EECSE'19

5th November ~ 7th November; 2019

NATIONAL CONFERENCE
ON

Electrical, Electronics and Computer Science Engineering

CONFERENCE PROCEEDING

AIET Bhubaneswar

Aryan Institute of Engineering and Technology Bhubaneswar

Organised by

Department of EE, ECE and CSE

Aryan Institute of Engineering and Technology

Bhubaneswar - 752050

Electrical, Electronics and Computer Science Engineering

5th Nov. – 7th Nov. 2019

Conference Proceeding

Organized by

Department of EE, EEE & CSE
Aryan Institute of Engineering and Technology
Bhubaneswar – 752050

List of Sponsors

Citicon Engineers Pvt. Ltd

Oritech Computers

Oltron Technology

GeoID Resources

ABOUT THE CONFERENCE

Science and Technology have continuously evolved through decades. EECSE 2019 was organized in Nov-2019 and was successful in capturing the development of materials and processing. Department of Mechanical Engineering, AIET, Bhubaneswar is organizing EECSE-2019 to showcase recent advances in materials processing and applications. In keeping up with the research interest of the materials community, EECSE-2019 will provide an update on scientific and technical aspects covering broad areas of interests in engineering materials, processing and applications.

ABOUT THE DEPARTMENT

The Department of Electrical Engineering, Electronics & Communication Engineering and, Computer Science Engineering has been in existence since 2009 with an initial intake capacity of 180 and is producing high quality technical manpower needed by State/Central Government, industry, R&D organizations, and academic institutions. The Department has full-fledged faculty members who are specialized in the fields of Network Device, Control Systems, MATLAB, Power Electronics, Electrical Machine Design etc . Modern Laboratories are established in the department for providing skill-oriented Hands–on training to all Engineering students while studying. Periodic industry trips and visits to various project sites are being arranged. Special guest lectures and seminars are held on a frequent basis with an aim to enhance student's knowledge in particular areas of interest and trying hard to transform them of even mild talent to professionals in their field. Already more than 400 no's of alumni have been produced so far, placed in different Government, private, Public & other sectors and some of them have pursued higher studies.

ABOUT THE INSTITUTE

Established in the year 2009, Aryan Institute of Engineering and Technology (AIET) is one of the premier engineering colleges in the self-financing category of Engineering education in eastern India. It is situated at temple city Bhubaneswar, Odisha and is a constituent member of Aryan Educational Trust. This reputed engineering college is accredited by NAAC, UGC and is affiliated to BPUT, Odisha. AIET aims to create disciplined and trained young citizens in the field of engineering and technology for holistic and national growth.

The college is committed towards enabling secure employment for its students at the end of their four-year engineering degree course. (The NAAC accreditation in the year 2018 vouches for the college's determination and dedication for a sustainable learning environment). The academic fraternity of AIET is a unique blend of faculty with industry and academic experience. This group of facilitators work with a purpose of importing quality education in the field of technical education to the aspiring students. Affordable fee structure along with approachable location in the smart city of Bhubaneswar, makes it a preferred destination for aspiring students and parents.

The Institute works with a mission to expand human knowledge beneficial to society through inclusive education, integrated with application and research. It strives to investigate on the challenging basic problems faced by Science and Technology in an Inter disciplinary atmosphere and urges to educate its students to reach their destination, making them come up qualitatively and creatively and to contribute fruitfully. This is not only its objective but also the ultimate path to move on with truth and brilliance towards success.

Organizing Committee Members

PATRON:

Dr. Madhumita Parida
Chairperson
Aryan Institute of Engineering and Technology

Director
Prof. Sasmita Parida

Convener
Prof. (Dr.) Amiya Kumar Sahoo

Co- Convener
Prof. Prakash Dehury

Organizing Secy.
Prof. Priaya Chandan Satpathy

Jt. Organizing Secy.
Prof. A. K. Panda

Treasurer
Prof. Abhishek Mohanty

Jt. Treasurer
Prof. Rudra Prasad Nanda

INTERNATIONAL ADVISORY COMMITTEE

Dr. Pradip Kr. Das
Professor
Department of Computer Science,
Rice University
Houston, USA

Dr. Shivashankar B. Nair
School of Electrical Engineering,
Singapore University
Singapore

Dr. Sreenath J G
Professor and Founding Chair
Department of Electrical and Electronics
Engineering, Yarmouk University
Irbid, Jordan

Dr. Mitjan Kalin
Seoul National University of Science and
Technology
Seoul, South Korea

Dr. Eric Jaegle
Chinese University of Hong Kong
Hong Kong

Dr. Shaik Rafi Ahamed
Professor
Department of Electrical Engineering
King Saud University, Saudi Arabia

NATIONAL ADVISORY COMMITTEE

Dr. Durga Prasad Mohapatra
Professor
Department of Computer Science Engineering
National Institute of Technology
Rourkela

Dr. Sanjay Kumar
Professor
Department of Computer Science Engineering
National Institute of Technology
Jamshedpur

Dr. Dipti Patra
Professor
Department of Electrical Engineering
National Institute of Technology
Rourkela

Dr. Ashok Kumar Akella
Professor
Department of Electrical Engineering
National Institute of Technology
Jamshedpur

Dr. Arun K Khosla
Professor
Department of Electronics and Communication Engineering
National Institute of Technology
Jalandhar

Dr. Ajay K Sharma
Professor
Department of Computer Science Engineering
National Institute of Technology
Jalandhar

Dr. S Baishya
Professor
Department of Electronics and Communication Engineering
National Institute of Technology, Silcher

Dr. Jyoti Prakash Mishra
Professor
Department of Electrical Engineering
National Institute of Technology, Silcher

Prof. K. K. Raina
Distinguished Professor
DIT University,
Dehradun

Dr. Vikas Kumar
Professor
Electrical and Electronics Engineering
University of Hydrabad
Hyderabad

LOCAL COMMITTEE MEMBERS

Prof. P. K. Rautray
Department of Computer Science Engineering

Prof. Sushree Sangita Jena
Department of Computer Science Engineering

Prof. R. B. Rao
Department of Civil Engineering

Prof. A. P. Das
Department of Civil Engineering

Assist. Prof. Prakash Dehury
Department of Computer Science Engineering

Prof. N. C. Mallik
Department of Mechanical Engineering

Prof. D. K. Sahoo
Department of Electrical Engineering

Prof. Subashish Mohanty
Department of Electrical Engineering

Prof. Ajit Kumar Panda
Department of Electrical Engineering

Prof. Sambit Parida
Department of Civil Engineering

Prof. Sagarika Patro
Department of Electrical and Electronics Engineering

Prof. Abhishek Mohanty
Department of Electrical and Electronics Engineering

Prof. Ipsita Pahi
Department of Electrical and Electronics Engineering

Prof. S. K. Panda
Department of Electronics and Communications Engineering

Prof. P. C. Satpathy
Department of Electronics and Communications Engineering

Prof. Biswajit Mishra
Department of Electronics and Communications Engineering

Prof. A. K. Jena
Department of Basic Science and Humanities

Prof. Deepak Sahoo
Department of Basic Science and Humanities

Conference Committee Management

1. Reception Management

- Rasmi Rekha Mahato
- Rajkumari Lopamudra
- Bidyabati Samal
- Urmila Sahoo
- Smita Digal
- Sunita Priyadarsini

2. Transit/Accommodation Management

- Krishna Naidu
- Biswanath Majhi
- Kishore Chandra Pradhan
- Duga Prasad Padhy
- Jyoti Prakash Khunti
- Deepen Kumar Jena
- Manoranjan Mahunta

3. Seminar Hall Management

- Prasannjeet Pattanaik
- Pravat Ranjan Mishra
- Priti Ranjan Jena
- Samrat Kharabela Senapati
- Bidyadhar Jena
- Chinmaya Mohapatra

4. Catering Management

- Pradyumna Badajena
- Pravat Kumar Sahoo
- Hara Prasad Mishra
- Asutosh Bal

5. Printing/Stationary Management

- Sumit Ghosh
- Akhilesh Singh
- Vikas Meher
- Vishal Gupta

6. Design Team

- Sridhar Jena
- Mahesh Nayak
- Nitesh Samal

7. Anchoring In Inauguration Ceremony

- Rudra Prasad Nanda
- Nilimashree Niharika

Conference Sub-Committee Management

- Dillip Kumar Pradhan
- Junaid Mohammad
- Chinmaya Mohapatra
- Naresh Sharma
- Pradeep Ghadei
- Dinesh Shah
- Narendra Mallick

CHAIRPERSON'S MESSAGE

I am delighted in acknowledging the International Conference **EECSE 2019** organized by the Mechanical Engineering Department of Aryan Institute of Engineering & Technology on **"Electrical, Electronics and Computer Science Engineering (EECSE-2019)".**

Aryan Institute of Engineering and Technology (AIET) was established in the year 2009 and it is one of the self-financing premier institutes in eastern Odisha. The Institute is accredited by NAAC, UGC, and is affiliated to BPUT, Odisha.

I ensure that this International Conference will motivate a large number of our B.Tech students and encourage them to actively participate in the program and gain some adequate knowledge. I congratulate the convener and members of the local, National and International organizing committees of this program.

I welcome on behalf of AIET to all the delegates and speakers for their participation in this International Conference. I am sure that this proceeding will be highly useful to researchers in their field.

I wish all the success to the conference.

Dr. Madhumita Parida

With regards,
Dr. Madhumita Parida
Chairperson
Aryan Institute of Engineering & Technology
Arya Vihar, Bhubaneswar, Odisha

DIRECTOR'S MESSAGE

I am glad to note that the Department of Mechanical Engineering is organizing an International Conference on "**Electrical, Electronics and Computer Science Engineering**" (EECSE-2019) from 5th November to 7th November 2019. I am sure that this conference deliberation will be highly stimulating embracing advancement in Electrical, Electronics and Computer Science Engineering.

I am sure that this conference will help in understanding the ever-changing corporate world and the corresponding reforms in India.

I congratulate the organizers of the Institute for their sincere effort to organize this conference.

I wish all the success to the conference.

Sasmita Parida

With regards,
Prof. Sasmita Parida
Director
Aryan Institute of Engineering & Technology
Arya Vihar, Bhubaneswar, Odisha

PRINCIPAL'S MESSAGE

I am immensely happy that the Mechanical Engineering department of our Institute is organizing an International Conference on **"Electrical, Electronics and Computer Science Engineering (EECSE-2019)"** (EECSE'19) on 5th November 2019 and is going to present a collection of various technical papers in the proceeding.

With the proper guidance of our management, the Aryan Institute of Engineering & Technology continues to march on the way to success with confidence.

I also congratulate Convener, staff members, students of our institute for their efforts in organizing this conference.

I wish the conference a grand success.

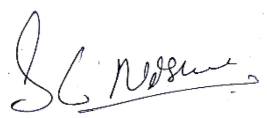

With regards,
Prof. (Dr.) Shart Chandra Mishra
Principal
Aryan Institute of Engineering & Technology
Arya Vihar, Bhubaneswar, Odisha

CONVENER'S MESSAGE

As the Convener of the of Conference EECSE'2019, I would like to cordially invite all academicians, researchers, and engineers in the broad disciplines of Electrical, Electronics & Computer Science Engineering to attend/present their papers at this conference. This conference is intended to boost the publication of research papers of Electrical, Electronics & Computer Science Engineering faculty members as well as be a platform for newcomers to present their technical papers. However, this conference is also open to all researchers throughout India to share their research findings.

The conference will be held from 5th November to 7th November 2019 at AIET, Bhubaneswar. Kindly mark your calendar, prepare your submissions, visit our website and keep in touch with me for updates. I hope you all will have a good deliberation during the conference and wish you all success in your research work. Looking forward to your participation in EECSE'2019.

With regards,
Prof. (Dr.) Amiya Kumar Sahoo

Dean of Academics, HOD of Computer Science Engineering
Aryan Institute of Engineering & Technology
Arya Vihar, Bhubaneswar, India

ORAL		Session 1		Session 2		Session 3	Poster(18:00 - 19:00)	
5-Nov	**Room 1**	Embedded Hardware	**Lunch**	Embedded Hardware	**Tea Break**	Sensor Applications and Deployments	**5-Nov**	Embedded Hardware
	Room 2	Network Reliability		Network Reliability		Embedded Hardware		Network Reliability
	Room 3	Sensor Applications and Deployments		Sensor Applications and Deployments		Human Centered Computing		Sensor Applications and Deployments
	Room 4	Human Centered Computing		Human Centered Computing		Machine Learning		Human Centered Computing
6-Nov	**Room 1**	Machine Learning		Machine Learning		Machine Learning		Machine Learning
	Room 2	Network Management		Network Management		Security Protocols		Security Protocols
	Room 3	Security Protocols		Security Protocols		World Wide Web	**6-Nov**	Network Management
	Room 4	Sensor Networks		Sensor Networks		Sensor Networks		Sensor Networks
7-Nov	**Room 1**	World Wide Web						World Wide Web
	Room 2	Mobile and Wireless Security						Mobile and Wireless Security
	Room 3	Supervised Learning by Classification						Supervised Learning by Classification

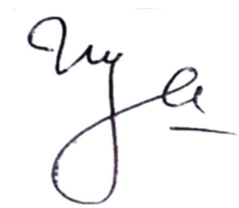

Contents

CONFERENCE PROCEEDING

ORAL PRESENTATION

For Hypertension Patients, Machine learning to promote health management through lifestyle changes

Debendra Kumar Sahoo, *Department of Electrical Engineering, Aryan Institute of Engineering & Technology, Bhubaneswar, dksahoo312@gmail.com*

Prithivraj Nayakmr, *Department of electrical Engineering , Raajdhani Engineering College, Bhubaneswar, p_nayakmr@gmail.com*

Purnya Prava Nayak, *Department of Computer Scinece Engineering , Capital Engineering College, Bhubaneswar, purnyaprava.nayak26@gmail.com*

Subhendu Sahoo, *Department of electrical Engineering and electronics Engineering, NM Institute of Engineering & Technology, Bhubaneswar, s.sahoo95@outlook.com*

A R T I C L E I N F O

Keywords:
Hypertension
Deep learning
Convolutional neural network
Health management
Perturbation-based simulation
Prediction

A B S T R A C T

The purpose of this paper is to investigate the use of machine learning models to develop a diagnostic system for hypertension patients so that people can modify their daily lifestyle to manage their condition. We propose this system by adopting the concepts of saliency maps for image data to non-image, lifestyle data with a data perturbation simulation technique. We trained the proposed system on a new lifestyle dataset that we extracted from a survey on Asian sub-population. The proposed system consists of a convolution neural network (CNN) as the diagnostic model, and is combined with simulation techniques to explain the concepts/insights learnt by the CNN. We compared classification performance of the CNN model with other baseline models fitted with other types of hypertension data including neural network, decision tree and other CNN model from literature. The CNN achieved a 68–70% accuracy on training and testing datasets. Comparing with other baseline models, our CNN model provided more consistent performance in terms of accuracy, sensitivity, specificity and area under receiver operating characteristic (ROC) curve. Using the simulations, we learnt that CNN captured not only direct correlation between the variables and the target, but also learnt group-based interactions. Our study reveals that age, gender, diabetes status, body mass index, smoking, occupation and education are some important lifestyle factors affecting hypertension. Avoiding smoking, maintaining a balanced diet to prevent unnecessary weight gaining, regular monitoring of blood sugar level for diabetic care, and stress relief exercise can reduce hypertension risk.

1. Introduction

Hypertension arises due to persistent level of high blood pressure, resulting from blood circulation within our body. Lacking symptoms, the “silent killer” hypertension is a major public health concern worldwide, and an important risk-factor for various non-communicable diseases such as stroke, cardiovascular and kidney disease. According to the World Health Organization (WHO) estimates, 1.13 billion people have hypertension worldwide, and over 80% of them are unable to control the condition [1]. Holding Year 2010 as baseline, WHO has taken a global initiative to reduce the prevalence of hypertension by 25% by 2025 [2]. [2–4] inform that low/middle-income families in South Asian countries are at highest risk, a condition worsened by the rare use of artificial intelligence (AI) in these regions. Thus, to stay updated with global trends to handle current healthcare challenges, it is imperative to develop objective, explainable decision-support systems for diagnosing and understanding hypertension.

While correct diagnosis is the first step towards achieving the goal set by WHO, the prevalence of hypertension will not decrease if patients are not also made aware of how they can manage their conditions within their life situations. Moreover, medical data, especially physiological data, has a higher chance of capturing the bodily variations that are *symptomatic* of hypertension. However, symptomatic variations do not necessarily always lead to effective treatment strategy or condition management. For example, medical physiological data can say that a patient has high blood pressure, but what should the patient do now? Is the patient genetically disposed? Should the patient simply rely on medication, or address the stimulation/stressors in his/her daily life that is causing the high blood pressure? Since genetic data is not easily available (and genetic conditions are not modifiable) and medication can be expensive especially for low/middle-income families/countries, the effective hypertension management strategy would probably involve addressing daily stressors or making changes in lifestyle, along with limited intake of medicine if necessary.

It is tempting to approach this problem with a simple diagnostic analysis using ML models. However, most analysis using ML models for diagnostic purposes stop at ML model predictive performance evaluation using metrics such as specificity, sensitivity, precision, f1-score, etc. While these evaluation metrics are standard in ML research community, they do not provide any insight into 'what' the ML model has actually learnt e.g. is the ML model diagnosing a patient with hypertension because of long history of stress, one instance of stressful experience or patient's gender? Does the model detect a correlation stress and gender? If the model detects a correlation (or not), should the correlation exist based on our current knowledge in medicine? Thus, the 'what' of ML models is directly related to the appropriate actionable strategy for managing a particular health (in this case, hypertension) condition, and this is likely to vary from patient to patient. After all, to make lifestyle changes, the affected person first needs to identify which lifestyle variable needs to be changed. And while some ML models, such as logistic regression or decision tree, have the ability to explain the 'what', they do not perform well on complex datasets that have non-linear patterns across class.

To the best of our knowledge, even though recent years have seen an explosion of research in this area (discussed in Section 2), currently there is no easy solution to this trade-off between the 'what' and performance of ML models, and many of these studies focus on using a second ML model (often a linear regression or decision tree model) as a post-hoc analysis to approximate the primary ML model under consideration. While this a valid approach, with the advantage that the primary ML model retains its performance capabilities, the feature interactions learnt by the primary ML model remains unexamined by the second model. In other words, feature interactions of the second model are used as approximation for the primary model, but there is no direct evaluation for this approximation except for the *fidelity* measure, which simply checks whether the primary and secondary models both provide the same label for a given instance. To complicate matters further for healthcare research, there is no easy way to automatically incorporate current medical knowledge into the evaluation of ML-based diagnostic models. Thus, in this paper, it is our aim to:

i. Leverage the predictive performance of a state-of-the-art ML model, most of which have the reputations of being "black-box" models for hypertension diagnosis.
ii. Leverage a post-hoc analysis methodology that does not rely on a second ML model, and instead tries to explain the feature interactions learned by the primary (and in this case also the "black-box") ML model.
iii. Investigate the feasibility of mapping the 'what' of the primary ML model to existing medical literature and knowledge.

Thus, we propose the following approach for this investigation:

i. To ensure that hypertension diagnosis can be followed up with an implementable action plan, we extract a life-style dataset (instead of a physiological dataset), which has not been analyzed for hypertension before, from India National Family Health Survey 2015–16, conducted by International Institute of Population Sciences, India and Bangladesh Demographic and Health Survey 2011 (BDHS 2011) conducted by National Institute of Population Research and Training, Bangladesh.
ii. Since image analysis technology from computer vision is one research area where models have been evaluated for the semantics of feature interactions learned by the primary state-of-the-art model (without the need for a second ML model), we modify, adapt and apply it to the lifestyle hypertension dataset. As such, we use convolution neural network (CNN) as our primary ML diagnostic model, and the concept of saliency maps to analyze the new hypertension lifestyle dataset. The adaptation involves a proposed simulation system that directly probes the trained CNN using synthetic instance data, and uses the changes in the CNN's response to make inference about the concepts learnt by the CNN
iii. To evaluate proper adaptation of the technique, we compare the accuracy of our system with the accuracy of hypertension prediction models found in literature. We also trained a decision tree on the same dataset to act as a benchmark.
iv. To investigate the feasibility of ML model obtaining medical knowledge from the dataset, we also compare the insights obtained from our system to insights from: a) statistical methods (including odds ratio from logistic regression), which are valued by the medical research community, b) a decision tree, one of the few intrinsically interpretable ML models, and c) published literature.

Thus, our contributions in this paper involve: i) creating a deep network for hypertension diagnosis using lifestyle dataset for low cost management of the condition, ii) providing a way to explain what the model has learnt without the aid of a second ML model, iii) adapting and interpreting the use of saliency map for non-image data, iv) evaluating what the ML model has learnt through comparison with domain knowledge, and v) addressing WHO's goal to reduce cases of hypertension in an Asian sub-population. While the research is still at rudimentary stage, we expect this research direction/approach to increase the awareness about healthcare needs and challenges that should be addressed by its analytics counterparts such as the ML research community.

In this investigation, we find that despite being a black-box model, the primary CNN model is able to find some feature associations that are collaborated by statistical methods and existing literature. Based only on our analysis of the CNN using the simulation technique (which does not consist of a second ML model), the CNN model saw gender, diabetes status, age, BMI, arm circumference, marital status, education, indoor pollution through smoking and possessing asset as important predictors of hypertension. In one interesting case of having geography as a predictor, the CNN model differed from the results of logistic regression, but was supported by existing literature. The CNN model also found some feature interactions for which we could not find evidence in literature, and thus are not presented in this paper (we list them in the Supplemental Material). However, to determine whether these interactions are just noise or hypertension patterns human beings have overlooked opens up new scientific queries and requires further investigation.

The rest of the paper is organized as follows: details of scientific studies relevant to our research is presented in Section 2. Section 3 describes the details relating to the methodology used with Sections 3.1-3.3 providing the background information about the ML models and statistical methods used in this paper. Details of the simulation technique can be found in Section 3.4, while information about the dataset is presented in Section 3.5. Section 4.1 presents the performance evaluation of the ML model (CNN), the comparisons, and our discussion about its performance. The results and discussion from the simulation to investigate what the CNN model learnt is provided in Section 4.2. We conclude with highlighting the limitations of our work and a brief discussion about future work.

2. Related works

For comprehensive understanding and comparison, we divide this section into four subsections.

2.1. Dataset, model, model explanation

In this subsection, we describe research work that used ML models for hypertension diagnosis. We compare each work in terms of the methodology approached e.g. the dataset type, the model type and the effort placed in understanding the model.

Lifestyle dataset, different model type, no model explanation: The work

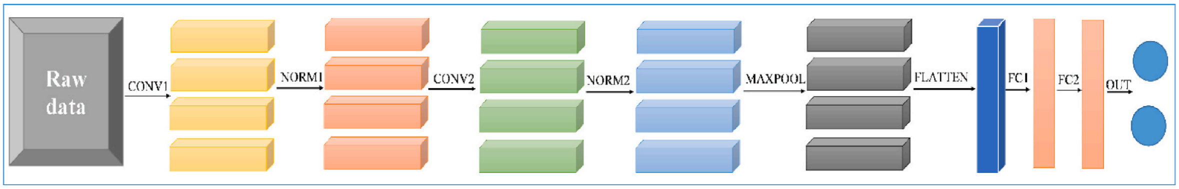

Fig. 1. Convolution Neural Network architecture to predict hypertension.

most similar to our research is [5] in that it also uses a lifestyle dataset and makes some ad-hoc effort to analyze the feature. However, their dataset was collected from an American population, and not South Asian population to address the WHO goal. Also, their ad-hoc effort (unlike our use of post-hoc simulation to explain CNN) to choose the important features for hypertension diagnosis using logistic regression is best described as a feature selection technique. Their approach involves using logistic regression to choose the important features, and then using this reduced feature set, they use an artificial neural network (ANN) with one fully connected hidden layer as the diagnostic model and uses the general ML metrics (accuracy, specificity, sensitivity, and area under the ROC curve) for model evaluation. The CNN model we used is based on two convolution layers along with layers for max-pooling and flattening (Fig. 1).

Different dataset type, same model type, no model explanation [6]: is closely related as they also used a CNN model to predict hypertension; however, they use a different CNN architecture that is more conducive to handling physiological and waveform data consisting of three pairs 1D convolution layers and pooling layers with ReLU as the activation function. The physiological dataset they use is taken from the public domain MIMIC II Waveform Database Matched Subset, and consists of a time series set of eight physiological parameters (HR, ABPSys, ABPDias, ABPMean, CVP, PULSE, RESP, and SpO2) collected every minute for 1 h. Unlike this work [6], neither uses lifestyle dataset nor provides explanation of what their CNN model is learning.

Different dataset type, different model type, no model explanation: [7,8] does not match our approach to any extent other than the fact that they too address hypertension diagnosis. Both uses one hidden layer artificial neural network (ANNs) with physiological data, focusing on features like blood pressure, high cholesterol, etc., and provide to model explanation. In this category, with regards to predicting hypertension, there are many other works in the literature that contributed greatly by making use of medical data (for example - electronic health records, echocardiogram, cardiorespiratory data, physiological waveforms and other clinical data), but do not directly relate to the work we are doing in terms of research approach [9]. used classification trees on college student data [10], applied Bayesian framework on respondents from Northeast Germany, and [11] studied prediction of echocardiographic pulmonary hypertension. Using different machine learning techniques [12], investigated hypertension risk by cardiorespiratory fitness data, whereas [13] used Canadian Primary Care Sentinel Surveillance Network data (clinical data) with a fully connected neural network (ANN).

Since [5,6] matches our approach to a certain extent, we use their models' performance (along with few others) as comparisons for our model in Section 4.1. Also, as can be seen from above, currently most hypertension studies aim to use state-of-the-art (deep and neural networks) diagnostic models, but provide no evaluation for what the model has learnt. Thus, in the next subsection, we provide the computational techniques that have been proposed to explain what is learnt by ML models.

2.2. *Model explanation strategies*

Multiple methods have been proposed over the last few years to solve the accuracy and interpretability trade-off problem of ML models. Among many others, these included the use of fuzzy logic to interpret neural networks [18], the use of linear models in the locality of an instance through data perturbation [19], the use of trained deep network results to train a decision tree, and the use of decision tree structures to train deep networks [20]. While these methods have their own merits [18], can only be used on neural networks, but not on other types of networks such convolutions networks, recurrent neural networks, etc. [20] achieved to create a decision tree very close to the accuracy of the deep network, but did not explore the deep network as a prediction model and instead treated it as the 'Oracle'. While using the deep network as an Oracle and using it to train the decision tree gives us some explanation, it still does not address the problem of whether the deep network originally learnt the right concepts from the data [19]. was the only one that attempts to explain the concepts learned by a complex decision model, but used a second linear classifier to explain only the locality of the boundary decision. In doing so [19], ignored the overall/global correlations that maybe present within the dataset, and it only explored the complex model indirectly through the lens of the simpler linear models. Also [19], focuses on text data only.

2.3. *Application of CNN in healthcare other than hypertension*

There is a plethora of research that uses CNN models in healthcare application. In this section we present a few of those articles to provide the breadth of the application area [42]. presents a case where a CNN model is used to create a general patient similarity network with electronic health records (EHR) patient [43]. uses a deep CNN model to identify indicative epileptic signatures in EEG (electroencephalogram) time series data. In an application of non-contact radar system to detect irregularities in respiration patterns [44], showed that 1D CNN model had a 15% higher accuracy than traditional ML models. ECG (electrocardiogram) time series data has the ability to capture abnormalities in the heart beat, including atrial fibrillation, and [45] achieves an accuracy as high as 89.60% in detecting atrial fibrillation using a LSTM-based (long short-term memory) CNN. In a very interesting human-machine system, [46] uses a CNN model to process low-quality images of head movements of disabled people to move the mouse on a computer screen.

Examples of other data driven systems solving medical problems but not involving hypertension include research on weight loss [14], obesity study [15], and evaluation of program cost effectiveness and classification of electronic health records [16,17].

2.4. *Our approach*

Unlike the methods (which are all great contributions in their own right) alienated above, the motivation for our methodological approach is to leverage the concept of saliency maps on non-image dataset. Generally, when used on a CNN trained on image data, a saliency map portrays the pixels of images that have the maximum contribution to the decision made by the model [21]. Saliency maps has the ability to inform about whether a CNN model classify based on presence or absence of target feature, or whether it is learning any latent feature related to the target feature. Thus, comparing the changes in the saliency maps due to changes in the input can guide researchers to investigate the concepts learnt by a CNN [21–23]. Thus, we propose to use a CNN as the diagnostic model, and propose a simulation technique that computes the changes in CNN output (e.g. saliency map for non-image data) for each change in the input values, such that it can handle both continuous and discrete feature variables. Note, the research approach we propose here is not restricted to the CNN architecture we use in this paper. For accuracy comparison we establish baseline models, and to validate the concepts learnt by the CNN we use statistical test, innately interpretable machine learning models, and published data.

3. Materials and methods

In this section, we briefly describe the CNN architecture used in this paper, the baseline models, statistical methods, proposed simulation technique, the details of the dataset and the pre-processing steps.

3.1. Convolutional neural network (CNN) as the diagnosis model

Due to their ability to find hidden relations in datasets, CNN models have been widely used as the prediction/diagnostic tool for various healthcare research. Its use of i) convolution layers, well known for selecting important features related to the target classification [24], ii) batch normalizer, for achieving fast convergence [25], and iii) dropout layers, to avoid possible overfitting [26], make it a highly efficient computational tool. Thus, for this paper, we use the CNN architecture presented in Fig. 1. Rectified linear units (ReLU) is used as the activation to address exploding/vanishing gradients [27]. Since our research consists of binary classification (hypertension versus normal) and class probability to aid personalized treatment, we use SoftMax activation function in output layer.

CNN is a multilayer deep neural network architecture which employs input layer, convolution layer, pooling layer, fully connected layers and output layer where the convolution layer is the core component of the structure. The local features are extracted from the input signal through convoluting by the convolution layer where the neurons belonging to same feature map share weights [6]. In this paper, as we have tabular form of data, we implemented one dimensional convolution layer. Features extracted from the convolution layer are normalized before transferring to the next layer. A pooling layer is added after two successive convolution layers followed by respective normalization. Next we add fully connected layers and output layer.

Convolution layer produce multiple feature maps which consist of multiple neurons where each neuron is connected through convolution kernel (weight matrix) to the upper feature surface. Different input features are extracted from the input by convolution operation here. The output of convolutional layer is computed by the dot product of input and weight factor of the kernel. In this study, we implemented two convolutional layers (Fig. 1). Rectified linear unit (ReLU), an activation function which prunes negative values to zero and keep positive values, is implemented to obtain feature map which is determined by the filters [6,43,46]. Considering the input denoted by $X^a_{i,j}$, the feature value $Y^{a+1}_{i,j,k}$ at the location (i,j) of kth feature map in (a+1) convolutional layer is calculated by,

$$Y^{a+1}_{i,j,k} = W^l_k \cdot Y^l_{i,j} + b^l_k$$

where W^l_k is the weight vector of the kth filter on lth layer and b^l_k is the corresponding bias component. In this paper, the first convolutional layer (CONV1) implements 48 filters; yielding a feature map of size (35, 48). Before transferring to the next convolution layer (CONV2), the feature values are normalized without changing dimension of the map. The second convolution layer implements ReLU activation function to produce 24 filters on the output of CONV1; yielding feature map of size (32, 24). The feature value obtained from the second convolution layer are again normalized before feeding to pooling layer [6,43,46].

Feature maps produced at convolution layers are often with high dimensions which need summarization to important signals. Pooling layers are often added next to convolution layers which efficiently reduce feature map dimension through achieving shift-invariance. The invariance includes any transformation, rotation, scaling, summarizing, and identifying existence of certain features. Other important contributions of pooling layer are retaining important features while reducing dimensions of the parameters and preventing overfitting. For feature map $Y^a_{i,j,k}$, the pooling layer output will take the expression as,

$$Q^{a+1}_{i,j,k} = pool\left(Y^{a+1}_{m,n,k}\right), \forall(m,n) \in \beta_{i,j}$$

where $\beta_{i,j}$ is local neighborhood around location (i,j). In this paper, we implement maximum pooling (max-pooling) layer which reduces feature dimension to (16,24) whereas average pooling is also very common in literature. After max-pooling, a flattening operation has been carried out to convert feature map into a one dimensional vector of size 384 using $\delta^L_{flatten} = flatten(\delta^L_{i,j})$ and the output vector is fed to a fully connected layer [6,43,46].

The main task of fully connected layer is to integrate the feature map of multiple convolution layer which are useful for classification. In this paper, we implement two fully connected dense layers having node size 12 and 8 respectively. ReLU activation function is used in both of the dense layers whereas the second dense layer is fully connected with the output layer having two nodes which is equal to the classification size. Softmax activation function is used to connect with output layer from the second dense layer [6,43,46].

3.2. Description of baseline models: decision tree and other neural network (NN) models from literature

Decision tree classification is one of the most popular classification techniques, which is both simple and explainable in terms of input features. The decision rules explicitly illustrate the feature contribution, which determine whether an instance will belong to positive or negative class. In this study, we implemented decision tree, DT (baseline), as a baseline model for both accuracy and concept comparison. To minimize misclassification probability, Gini impurity criterion was used. Besides, maximum tree depth of five and maximum leaf node of 20 were chosen based on optimum area under ROC value of train and test datasets.

The second baseline model, $NN_{\_lifestyle}$ (baseline), from Ref. [5] used multilayer perceptron neural network where the data were balanced using under-sampling technique. The model had one hidden layer fully connected with 11 input nodes for respective features such as age, sex, education, marital status, income, weight, height, exercise, diabetes status and others. Besides, they used *Tanh* activation function in hidden and output layers. We use this model for accuracy comparison only.

The final baseline model, $CNN_{\_other}$ (baseline), from Ref. [6] used CNN framework to predict hypertension using eight physiological variables. They compared performance of CNN with other machine learning models like K-nearest neighbors, random forest, naive Bayes, logistic etc. and identified CNN as the best performing model in terms of maximum accuracy. The CNN framework implemented three convolution layers separated with three pooling layers and a fully connected layer. They also identified *ReLU* activation function performing better than *sigmoid* and *Tanh* activation functions [6]. This model is used in this paper for accuracy comparison only.

3.3. Statistical method used for validating the concepts learned by CNN

In healthcare research, statistical analysis is considered more reliable because their results are easily interpreted. Thus, we used chi-squared test and odds ratio for benchmarking variable associations. These statistical tests handle the categorical and continuous variables in our dataset.

3.3.1. Chi-squared test

The chi-squared is a type of statistical hypothesis test, which is used to determine whether the frequency of occurrence of a variable is statistically significantly different between two (or more) target groups, in our case normal individuals versus individuals with hypertension. If the two groups are significantly different, i.e. the variable value is dependent on the target group; the associated p-value will be less than 0.05 with the error rate held at the most widely used value of 5%. Since chi-squared test uses frequency counts of variables, it is most commonly used with categorical variables.

3.3.2. Odds ratio (OR)

The odds ratio, OR, measures the magnitude of association between the target variable and the variable of interest, and a 95% confidence interval can be constructed (with an associated p-value) for the OR values to obtain an indirect evidence of significance. If OR = 1, then variable of interest does not affect the target variable (or the odds of outcome); if OR>1, the variable of interest is associated with higher odds of outcome; otherwise, the variable of interest is associated with lower odds of outcome. It can be calculated taking the exponent of the coefficients obtained from logistic regression. Besides, it can be used with both categorical and continuous variables.

3.4. Simulation algorithm to understand the concepts learnt by the trained CNN

To explore the concepts learnt by CNN, we design a data-perturbation simulation on a trained CNN, which learns a class distribution. Since data are expected to contain continuous and categorical variables, we conduct two simulations: i) the Categorical Simulation for assessing the categorical features, and ii) the Continuous Simulation for assessing the continuous features. We denote a general patient instance as $I(id, X_{id}, label)$, where *id* is a positive number for identifying individual patient, X is the set of all features for patient, and *label* is the associated class label. During both simulations, each iteration is denoted with $t \in \{1,2, \ldots, T\}$, and each newly-created instance is denoted as $I(id, F_t, x', label)$, where F is the set of changing variables, F_t is the feature/variable under consideration during t, $F_t \in F$, F is a subset of X_{id}, and x' are the variables that are kept constant.

For both (Continuous and Categorical) simulations, *each iteration* starts with one randomly chosen true instance, $I(id, X_{id}, label)$, from the real data with X_{id} containing the attribute information and *label* containing the class label. Both simulations divide X_{id} into two subsets, F and x'. For Categorical Simulation, F is equal to be the set of all categorical variables and x' is equal to the set of all continuous variables; for Continuous Simulation the opposite is true i.e. F is equal to be the set of all continuous variables and x' is equal to the set of all categorical variables. Holding x' fixed, both simulations go over each attribute, F_t, in F and create multiple new artificial instances $I(id, F_t = k, x', \sim)$, where k is any feasible value allowed in the real dataset for F_t. $\sim$ is used to denote that this new instance is not assigned to any class. If F_t is categorical and has m different nominal values then k takes on the $(m-1)$ different nominal values to create $(m-1)$ new artificial instances. There are $(m-1)$ new instances because at least one nominal value of the categorical variable is in form of the real data. If F_t is continuous, then value of k is derived from the estimated distribution of the variable; the distribution is sampled multiple times to create multiple new instances. The newly created instances from $I(id, X_{id}, label)$ are then passed through the trained CNN and changes in the CNN response (probability of class membership) are recorded. The algorithm for running the Categorical Simulation is given in Algorithm1 and a sample output of the Categorical Simulation can be found in Table 4. A sample output of Continuous Simulation can be found in Fig. 6. Both simulations are run using the same trained CNN.

Table 1

A list of 12 binary, 4 continuous (F1, F2, F6 and F15), and 6 are categorical lifestyle variables with multiple values.

SI.	Variable Description	SI.	Variable Description
1	Total number of household member [F1]	**12**	Household has cycle [F12] – *yes or no*
2	Age of the respondent [F2]	**13**	Has land [F13]– *yes or no*
3	Gender [F3] – *male or female*	**14**	Has livestock [F14]– *yes or no*
4	Area [F4] – *rural or urban*	**15**	Arm circumference [F15]
5	Self-reported diabetes status [F5] – *yes or no*	**16**	Cooking inside the room [F16]– *yes or no*
6	Body mass index (BMI) [F6]	**17**	Marital status – *currently married [$F17_{v1}$], divorced/ separated/ widowed [$F17_{v2}$], or never married [$F17_{v3}$]*
7	Household members smoke inside the house [F7] – *yes or no*	**18**	Education status – *higher than secondary [$F18_{v1}$], no education [$F18_{v2}$], primary [$F18_{v3}$], secondary [$F18_{v4}$]*
8	Country [F8]– *Bangladesh or India*	**19**	Occupation of respondent – *not working [$F19_{v1}$], agricultural work[$F19_{v2}$], non-agricultural work [$F19_{v3}$], domestic worker [$F19_{v4}$], or mid to high level job [$F19_{v5}$], others [$F19_{v6}$]*
9	Household has electricity [F9]– *yes or no*	**20**	Water source - *other improved drinking water sources [$F20_{v1}$], piped water on premises (improved source) [$F20_{v2}$], unimproved drinking water sources [$F20_{v3}$]*
10	Household has radio [F10]– *yes or no*	**21**	Floor material – *cement principal [$F21_{v1}$], dirt/sand/dung principal [$F21_{v2}$], or wood/plank principal [$F21_{v3}$]*
11	Household has refrigerator [F11]– *yes or no*	**22**	Roof material – *cement principal [$F22_{v1}$], dirt/sand/dirt/ plastic/others* [$F22_{v2}$], *or wood/plank/stone/tin principal*[$F22_{v3}$]

Algorithm1- *Algorithm: Categorical Simulation.*

Input: dataset, n_1, n_2, CNN

1) Randomly choose n_1 positive patient instances (i.e. hypertensive cases), and n_2 negative patient instances (i.e. non-hypertensive cases) from the dataset.
2)For each chosen instance, $I(id, X_{id}, label)$,
  a) Calculate base probability for the instance, e.g. CNN ($I(id, X_{id}, label)$)
  b) Set x' to the continuous variables in X_{id}.
  C) Let F be the list of all T categorical variables, where each variable takes on m different values.
  d) For $t \in \{1,2, \ldots, T\}$, do:
    i. Set F_t to the tth variable in F.
    ii. For $k \in \{1, \ldots, m\}$, do:
      - Create instance, $I(id, F_t = k, x', \sim)$
      - Find probability, p = CNN ($I(id, F_t = k, x', \sim)$);
      - Store p.

Output: Probability of each $I(id, F_t = k, x', \sim)$ of acquiring hypertension (over all values of t and k), which corresponds to labels for the created instance.

For the Continuous Simulation, each of the continuous variables is assumed to follow a normal distribution, and is standardized accordingly before training of the CNN model and executing the simulation. The algorithm for Continuous Simulation is similar to Algorithm 1, but has the following changes:

1) The respective categorical variables will remain same (Step 1) and held constant (Step 2b)
2) F contains all T continuous variables (Step 2c).

We run this simulation on 2000 subjects (1000 with hypertension, and 1000 healthy individuals) and 8 subjects (4 hypertensive and 4 normal) to infer the concepts learnt from categorical features and continuous features respectively (result is provided in Section 4.2, Table 4 and Fig. 6).

3.5. Dataset description

The dataset was gathered from two national representative, cross-

Table 2a
Six samples from the dataset with class label ("Hyp") variables 1 through 14. The abbreviations used in this table are explained as follows: "Mem" is the number of family members, "Gen" is gender of the subject, "Area" refers to whether person lives in rural or urban area, "Diab" indicates whether subject has diabetes or not, "Hhsm" refers to in-house smoking, "Coun" is the country the subject lives in, "Elec" indicates whether subject has electricity. "Rad", "Refr", and "Cyc" refers to whether the subject owns a radio, refrigerator, and/or cycle respectively. "Lstk" stands for livestock.

Hyp	Mem	Age	Gen	Area	Diab	BMI	Hhsm	Coun	Elec	Rad	Refr	Cyc	Land	Lstk
0	6	58	0	0	0	21.1	0	1	1	0	0	0	1	1
0	5	36	1	0	0	20.6	0	1	0	0	0	0	0	1
0	2	55	0	0	0	17.1	0	1	0	0	0	0	0	1
0	5	55	1	0	0	18.5	0	1	1	0	0	0	1	1
0	5	48	0	0	0	26.8	0	1	1	0	0	0	1	1
1	6	70	0	0	0	15.3	0	1	1	0	0	1	1	1

Table 2b
This is a continuation of Table 2.1, with the same samples for variables 15 through 22. "Crm" stands for cooking facilities within the room, "Mar"and "Edu" indicates marital and education status respectively. "Occ" stands for occupation and "Wa-Sou" for water source. "Floor" and "Roof" refers to the material used for their respective construction.

Arm	Crm	Mar	Edu	Occ	Wa_Sou	Floor	Roof
26	0	Currently married	No education	c1_not working	Other improved drinking water sources	dirt/sand/dung or other as principal floor	wood/plank/stone/tin principal roof
28	0	Currently married	Primary	c4_domesticworker	Other improved drinking water sources	dirt/sand/dung or other as principal floor	wood/plank/stone/tin principal roof
23	0	Currently married	No education	c1_not working	Other improved drinking water sources	dirt/sand/dung or other as principal floor	wood/plank/stone/tin principal roof
26	0	Currently married	Secondary	c5_midhi	Other improved drinking water sources	dirt/sand/dung or other as principal floor	wood/plank/stone/tin principal roof
25	0	Currently married	Secondary	c1_not working	Other improved drinking water sources	dirt/sand/dung or other as principal floor	wood/plank/stone/tin principal roof
22	0	Divorced/Separated/ Deserted/Widowed	No education	c1_not working	Other improved drinking water sources	dirt/sand/dung or other as principal floor	wood/plank/stone/tin principal roof

sectional health surveys – conducted by the *International Institute of Population Sciences, India* and *National Institute of Population Research and Training, Bangladesh*. The survey in Bangladesh was conducted on 2011 which was the sixth Bangladesh demographic and health survey based on a two-stage stratified cluster sampling method. About 18,000 residential households were selected in both rural and urban areas where a subset of eligible samples was selected for biomarker component such as blood pressure, blood glucose, height, and weight measurements. On the other hand, the survey conducted in India, the fourth National Family Health Survey (2015–16), was also employed two stage stratified cluster sampling technique. The respondents were chosen in such a way that the state territory and district representation as well as rural-urban level estimation was effectively performed. In total 699,686 eligible women of reproductive age and 112,122 men were interviewed whereas a selected number of respondents were provided biomarker components. In general, both of the survey collected background information of respondents, reproduction, family planning, maternal and child health, child nutrition, anthropometric and biomarker information of the respondents.

Patients with *systolic blood pressure* ≥ 140 *mmHg*, or *diastolic blood pressure* ≥ 90 *mmHg*, or who were taking hypertensive medication at time of the surveys were labeled as positive instances for hypertension [28–30]. [2,28,29,31] suggest relevant variables, whose details are given in Table 1. Out of all respondents in the surveys, 226, 953 were included in this study for having relevant feature information, resulting in 194,728 with normal blood pressure (negative class) and 32, 225 with hypertension (positive class). Out of all respondents in the surveys, 226,953 were included in this study for having relevant feature information, resulting in 194,728 with normal blood pressure (negative class) and 32,225 with hypertension (positive class). Tables 2a and 2b shows six samples with 22 variables from the dataset.

Preprocessing the dataset: Since the dataset is imbalanced (with 16% positive instances), we used a random oversampling method (using Scikit-learn library of Python) to ensure the proper training. Before training, the continuous features were transformed into respective standardized form, and all the categorical features were binarized. For example- F6 with range 70.21 (min: 4.87, max: 75.10), takes on the standardized values with range 17.12 (min: −4.11, max: 13.00), while F16 takes on the values of either 0 or 1.

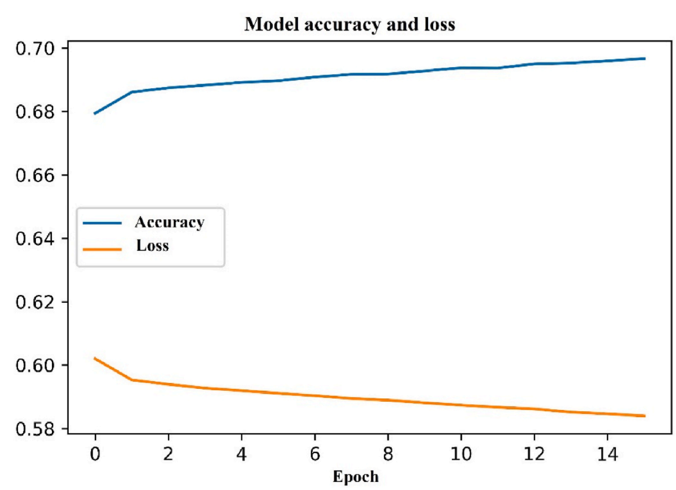

Fig. 2. The convergence curve of the CNN model.

4. Results and discussion

In this section, we present the performance of CNN as a diagnostic tool and compare it to accuracies obtained from baseline models and models from literature. Next, we will compare the concepts learnt by CNN with the correlations obtained from statistical tests, decision tree trained on the new lifestyle dataset, and evidence found in literature.

Table 3
Performance of deep-network model on training and testing data set. AUC = Area Under the ROC Curve.CNN_ lifestyle, DT (baseline), and DT_distill are models trained by us using the new lifestyle data. The other two models are from literature and trained on physiological data.

Model		Accuracy (%)	Sensitivity (%)	Specificity (%)	AUC (%)
CNN_lifestyle	*Train*	70.0	71.1	69.0	77.0
	Test	*68.4*	*69.0*	*68.4*	*74.4*
DT (baseline)	*Train*	*67.7*	*72.7*	*62.8*	*73.6*
	Test	*64.4*	*73.7*	*62.8*	*73.9*
DT_distill	*Train*	*88.3*	*84.1*	*92.6*	*94.4*
	Test	*70.0*	*64.0*	*71.0*	*71.1*
NN_lifestyle (baseline)		72	46.7	85.4	77.0
CNN_other (baseline)		90.0	Not reported	Not reported	Not reported

Table 4
Simulation of Categorical Features on the chosen data instances.

Feature	Feature value	Average probability change
Gender	Male	0.056
	Female	−0.055
Area	Rural	−0.001
	Urban	0.003
Diabetes status	No	−0.067
	Yes	0.065
Smoking inside the house	No	−0.012
	Yes	0.013
Country	Bangladesh	−0.012
	India	0.042
Electricity	No	−0.015
	Yes	0.004
Radio	No	0.002
	Yes	−0.010
Refrigerator	No	0.007
	Yes	−0.009
Cycle	No	0.042
	Yes	0.003
Land	No	−0.005
	Yes	0.004
Livestock	No	−0.005
	Yes	0.001
Cooking inside the room	No	0.017
	Yes	−0.011
Marital Status	Married	0.001
	Divorced	−0.003
	Never Married	−0.001
Education	No education	0.019
	Primary	0.009
	Secondary	−0.010
	Higher than secondary	−0.009
Occupation	Not working	0.017
	Agricultural	−0.017
	Non-agricultural	−0.015
	Domestic worker	−0.025
	Mid to high level	0.017
	Others	0.006
Water source	Piped water	0.007
	Other improved	−0.004
	Unimproved	0.001
Floor material	Cement	−0.009
	dirt/sand/dung	0.009
	wood/plank	0.011
Roof material	Cement	−0.015
	dirt/sand/dung	−0.004
	wood/plank	0.025

4.1. Diagnosis accuracy of CNN

The CNN was implemented in TensorFlow using Keras (Python 3.7) with binary cross-entropy as the loss function, and the Adam optimizer as the loss minimizer, which we define as *CNN_lifestyle* [24,32]. The dropout rate was set to 20%. 80% of the dataset were used for training and the rest for testing. We implemented decision tree (DT) as one of our baseline models for both accuracy and interpretability purposes. The literature models are used as baseline models for accuracy and performance only. The model accuracy and loss over the different epochs during the training phase is given in Fig. 2.

We implemented another recently proposed model, which is supposed to retain deep learning accuracy while being easier to interpret [20]. This model, also known as the distillation of CNN into soft decision tree (DT_distill) model. DT_distill is also included in our results for accuracy comparison. The binary soft decision tree incorporated learned filter F_i and bias b_i in each inner node i where as a whole it learned a hierarchy of filters with brunching decision based on the probability, $p_i(X) = \sigma(XF_i + b_i)$; here X is the input and σ is the sigmoid logistic function. Each sample was assigned to a particular *bigot* associated with a path probability and learned distribution of possible output classes [20]. Table 3 presents classification results over four evaluation measures for CNN.

The models NN_lifestyle [5] and CNN_other [6] were used as two of the benchmark models from literature for evaluating the performance of our CNN_lifestyle as a diagnosis model. While NN_lifestyle seem to have higher accuracy for predicting hypertension, it can be seen from Table 3 that NN_lifestyle has a very low sensitivity. Sensitivity less than 50% means that the model is not good at distinguishing true positives, and has a high number of false negatives. High sensitivity alone means that NN_lifestyle is good at recognizing the normal instances only; we got similar results with our model using the imbalanced dataset (not presented in Table 3). In comparison, our model is better at detecting both hypertension and normal instances. Since the specificity/sensitivity is not known for CNN_other, we cannot provide similar comparison, but we do expect physiological data to have a more direct correlation with hypertension than lifestyle choices. However, a CNN trained on physiological data cannot be used for actionable treatment plan in terms of lifestyle choices, and cannot recommend medication to patients. A thorough diagnosis model for hypertension requires both physiological and lifestyle data. However, collecting such dataset requires immense effort and coordination.

The CNN_lifestyle performs slightly better than decision tree model. Moreover, the distillation of CNN into a soft decision tree exhibits high training performance but the test sensitivity is not satisfactory (this might also be an indicator that this model requires more data for proper training than is currently available). Thus, we have not included the distilled model as a baseline model.

4.2. Understanding the diagnosis model

4.2.1. Interpretation results from statistical results

To compare the CNN performance on learning correlation between hypertension and features, we performed statistical analysis on our dataset. The chi-square test was used to check the association of each feature with hypertension. All features had a p-value less than 0.01, showing that they all contribute to hypertension classification.

We also performed a simple logistic regression to find the odds ratios [33] of being hypertensive and assess statistical significance. Broadly, we found that being male, living in urban area, being diabetic, living in Bangladesh, having electricity and related appliances, having no or low-level education, doing mid or high-level job, being older, having higher BMI and/or higher arm circumference significantly increased the odds of the getting hypertension. More specific results are presented in Supplementary Materials (Tables S1 and S2).

4.2.2. Interpretation results from decision tree

Fig. 3 shows decision tree diagram which depicts the classification flow of hypertension. First, the root node of training dataset was age (x_1) which created two subsets based on age of 30. For people of age less than 30 years, an internal node split the subset into two based on BMI (x_5) of

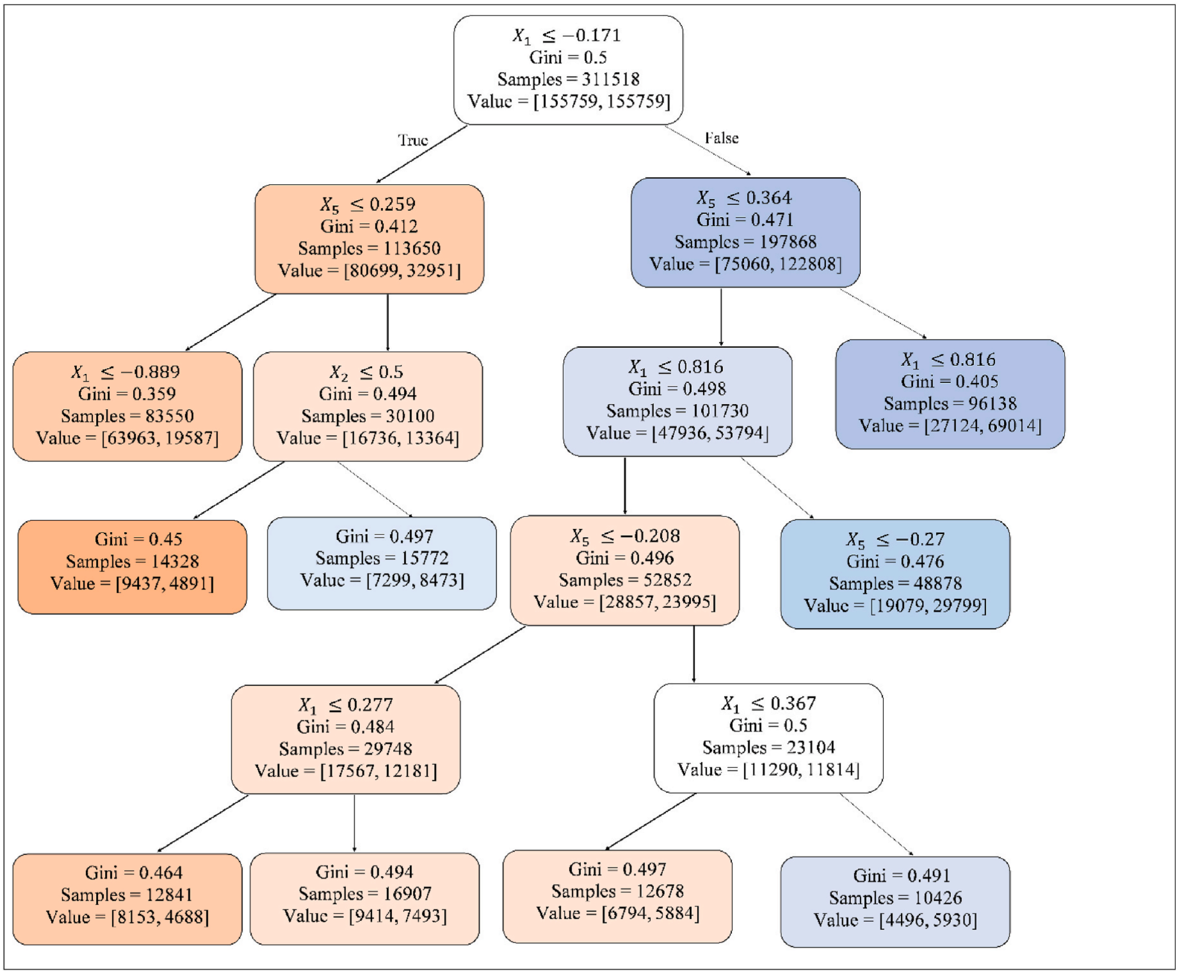

Fig. 3. Decision tree classification of hypertension.

22.8, but for people over 30, the BMI cut point was 23.3. An interesting pattern was that male (x_2) respondents under 30 years of age and having BMI 22.3 or more were identified as hypertensive but the respective female (x_2) respondents had normal blood pressure. The decision tree algorithm also included arm circumference (x_{14}) as splitting rule of internal node for age group of 22–30 years but seems redundant because of labeling normal case for both of the leaf nodes.

4.2.3. Interpretation results from simulations

Our input domain consists of two types of features – categorical and continuous. The main purpose of the categorical and continuous simulations of respective feature is to quantify the probability contribution of being hypertensive. For categorical simulation, we change one category at a time and compared the probability contribution. For continuous simulation, probabilities are being plotted against valid domain of respective continuous feature.

5. Results from categorical simulation

The Categorical Simulation was conducted by setting both n_1, and n_2 to 1000. This is equivalent to choosing one thousand hypertension (positive) instances and one thousand normal (negative) instances for the simulation which the CNN model classified accurately. For example, let two instances are represented by *I(1, F_t, x' = [Age = 35 years, Family Member = 4, BMI = 20.28, Arm Circumference =* 28 cm*], label = 0)* and *I (2, F_t, x' = [Age = 35 years, Family Member = 4, BMI = 20.28, Arm Circumference =* 28 cm*], label = 1),* where $t \in \{1,2, \ldots, T = 18\}$. For brevity, we refer to them as *I(1, X_1, label = 0)* and *I(2, X_2, label = 1).*

The base probability that CNN predicted before the simulation started for instances *I(1, X_1, label = 0)* and for *I(2, X_2, label = 1)* are 0.442 (normal) and 0.592 (hypertension), respectively. As the Categorical Simulation proceeds, according to the Algorithm1, the value of one categorical feature is changed during each iteration to create a new instance. For example, in the first iteration of the simulation, F_t is chosen to be "Gender" for the instances and change to 1 from 0 for *I(1, X_1, label = 0)* and to 0 from 1 for *I(2, X_2, label = 1)*. We calculate the probability of these synthetic samples. Table 4 shows the average effect of changing categorical variables on risk of hypertension for different individuals. There are some very prominent patterns in Table 4:

1) the CNN identifies gender and specific comorbidities to be important predictors of hypertension. In particular, being male increases the likelihood of hypertension (by 5.6% and vice versa), as does being diabetic (by 7% and vice versa). This concept matches with the results from chi-squared test and odds ratio from this study and findings from other literature [34]. Moreover, the CNN finds that smoking inside the house by any family member will contribute to the development of hypertension. This can also be a potential health hazard indication of both self-smoking as well as polluting household through smoking inside [35].
2) Our findings reveal that living in urban area increases the risk of hypertension [2]. Moreover, the risk of hypertension will increase by 4.2% because of living in India whereas the risk will decrease by only 1.2% in favor of Bangladesh. This result is directly opposite of the findings from logistic regression but supported by the recent literatures which indicate prevalence of hypertension is 30.7% in India

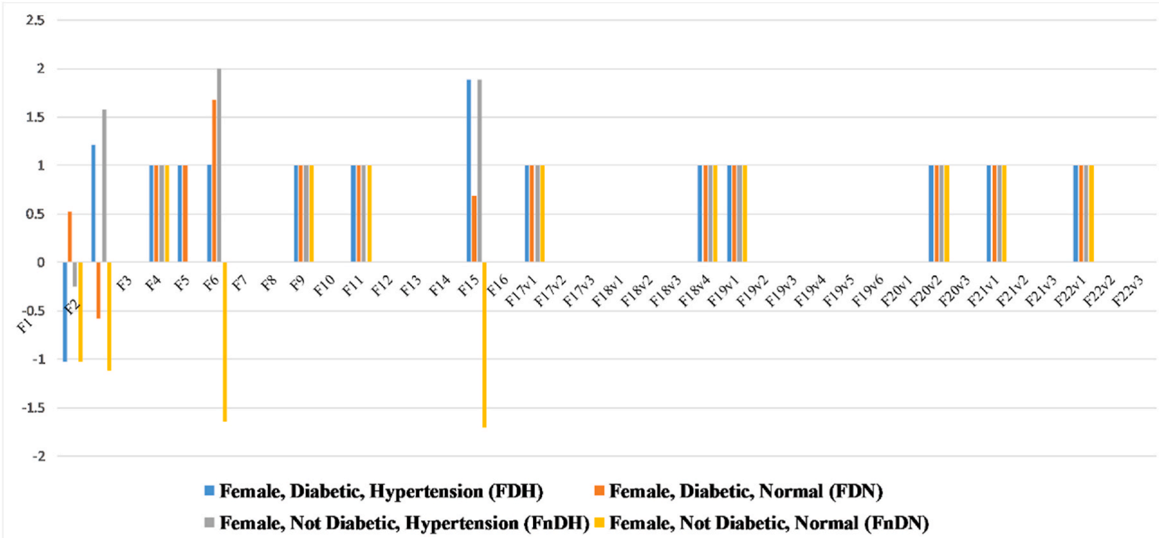

Fig. 4. The raw feature values of the female instances for Continuous Simulation.

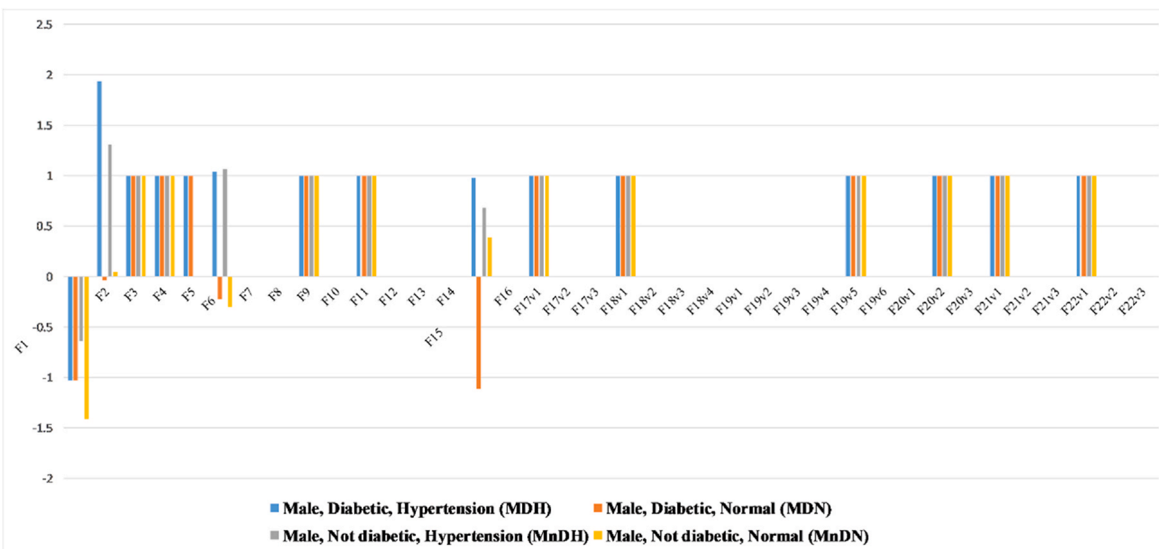

Fig. 5. The raw feature values of the male instances for Continuous Simulation.

and 21.0% in Bangladesh respectively [36,37]. In countries like India and Bangladesh, cemented floor, especially in conjunction with cemented roofs, usually represents an average (or higher) standard of living or stable income which indicates better access to hypertension control than others having low income [38].

3) Another interesting concept shows that hypertension is found inversely associated with level of education which supports the existing literature [39]. One possible reason might be that an educated person is more aware of non-communicable disease risk factors and appropriate health practices and behaviors.
4) Results show that the risk of hypertension is logically associated with the occupation of the respondent. Doing agricultural, non-agricultural and domestic works require physical activeness which reduces risk of hypertension whereas not working and doing mid to high level work indicate sedentary lifestyle which increases risk of hypertension [40,41].

6. Results from continuous simulation

For the Continuous Simulation, n_1, and n_2 were both set to 4. Since "Gender" and "Diabetes" were selected by both statistical method and the CNN model to have large influence as predictors for hypertension, the individuals were chosen as follows (Figs. 4–6):

1) I(3, F_t, x' = [Gender = Male, Diabetic = Yes], label = 1): Male, Diabetic, Hypertension (MDH); Base Probability = 0.84
2) I(4, F_t, x' = [Gender = Male, Diabetic = Yes], label = 0): Male, Diabetic, Normal (MDN); Base Probability = 0.38
3) I(5, F_t, x' = [Gender = Male, Diabetic = No], label = 1): Male, Not Diabetic, Hypertension (MnDH); Base Probability = 0.75
4) I(6, F_t, x' = [Gender = Male, Diabetic = No], label = 0): Male, Not Diabetic, Normal (MnDN); Base Probability = 0.42
5) I(7, F_t, x' = [Gender = Female, Diabetic = No], label = 1): Female, Not Diabetic, Hypertension (FnDH); Base Probability = 0.76
6) I(8, F_t, x' = [Gender = Female, Diabetic = No], label = 0): Female, Not Diabetic, Normal (FnDN); Base Probability = 0.15
7) I(9, F_t, x' = [Gender = Female, Diabetic = Yes], label = 1): Female, Diabetic, Hypertension (FDH); Base Probability = 0.77
8) I(10, F_t, x' = [Gender = Female, Diabetic = Yes], label = 0): Female, Diabetic, Normal (FDN); Base Probability = 0.36

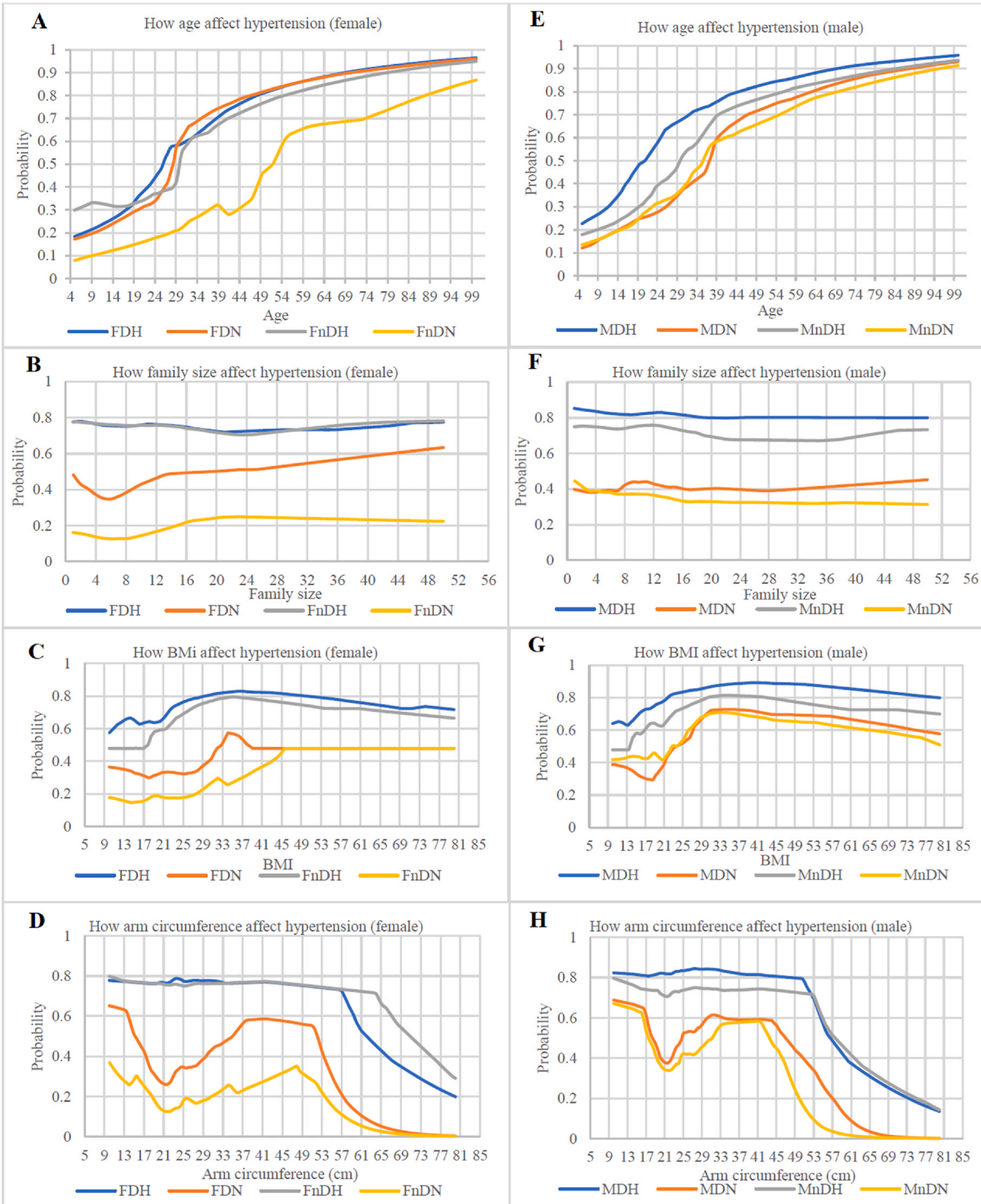

Fig. 6. Simulation of continuous features.

(F1: household member, F2: age, F3: gender, F4: area, F5:diabetes, F6:BMI, F7: smoking, F8: country, F9:electricity, F10: Radio, F11: refrigerator, F12: cycle, F13: land, F14: arm circumference, F16: cooking, F17: marital status – currently married (v1), divorced/ separated/ widowed (v2), never married (v3), F18: education – higher (v1), no (v2), primary (v3), secondary (v4), F19: occupation – not working (v1), agriculture (v2), non-agriculture (v3), domestic (v4), mod to high (v5), others (v6), F20: water source – other improved (v1), piped (v2), unimproved (v3), F21: Floor – cement (v1), dirt/sand (v2), wood/plank (v3), F22: roof – cement (v1), dirt/sand (v2), wood/plank (v3))

Continuous Simulation proceeds in a similar manner as the Categorical Simulation. The results are represented in Fig. 6.

In Figs. 4 and 5, we present visual representations of the raw features for a sample of eight individuals listed above to show that these individuals vary from one another only in terms of the continuous variables (F1- number of household members, F2- age, F6- BMI, and F15- arm circumference). Having constant categorical variables during the Continuous Simulation experiments allows us to control interaction between categorical and continuous variables, and thus, to ensure that the patterns and trends seen in Fig. 5 are solely due to the continuous variables and their interactions.

Fig. 6 shows that hypertension risk will generally increase with increasing age. The FnDN group, whose current age is 19 years, will become hypertensive after reaching 53, whereas FDN aged 25 years will become hypertensive at 29. The 49 years old FnDH, having BMI near 30, crossed hypertension probability threshold at 30. The behavioral pattern of age for male respondents are similar to that of female. Moreover, moderate family size, having 5–6 members, will provide minimum hypertension risk for FDN and FnDN. However, risk of hypertension increases gradually with BMI for FnDN, while there is a sharp increase for FDN after the BMI reaches 29. A dramatic increase of hypertension risk is found in MnDN (at BMI 21) and MDN (at BMI 18). In general, after certain level of BMI, the risk remains almost unchanged in both males and females. More interestingly, the pattern of arm circumference effect is similar for male and female. The risk of hypertension will attain minimum for the 4 non-hypertensive respondents at 21.5 of arm circumference, a common attainable measurement. Thus, based on these readings, a physician can suggest particular lifestyle changes to his/her patients.

The results obtained from categorical and continuous simulations identify gender, diabetes status, age, BMI, arm circumference, marital status, education, indoor pollution through smoking and possessing asset as influential factors.

The findings coincide with the results obtained from decision tree model, which depicts age, gender, BMI and arm circumference as leading factors associated with hypertension (Fig. 3).

7. Conclusion

This study aims at describing the learning of CNN to depict health care management of hypertension patients and a set of recommended lifestyle behaviors to prevent the disease. Even though CNNs are complex computational tools, carefully designed simulations can allow researchers good insights into the concepts they learn. In this study, we introduce two different types of simulations – categorical simulation (with total 2000 subjects; 1000 hypertensive and 1000 healthy individuals) and continuous simulation. Interestingly, CNN not only learned direct correlation of variables to hypertension, but also noticed group-based interactions. In addition, the simulations can be used to prepare and predict how lifestyle changes can affect their risk of developing hypertension. This has high potential in being developed into individual personalized healthcare systems and management recommendation.

Through our analysis, we find that hypertension in countries, such India and Bangladesh, is affected by a dynamic interaction between different lifestyle choices. Factors, such as gender, age, health (e.g. BMI) and comorbidities play a huge role in predicting the predisposition of individuals. A distinction between the possession of livelihood capitals and luxury good is also noted to have differing effects on individuals, along with possible work life conditions, cultural preferences and their social roles in the respected geographical areas. Thus, increasing exercise to maintain a healthy BMI, avoiding stress, maintaining good social standing, and self-care are highly recommended to achieve WHO's goal of reducing prevalence of hypertension. This correlates highly with literature, which finds rapid urbanization, increased sedentary lifestyle, and unhealthy diet as leading factors that increased the rate of hypertension [2–4].

The study has some limitations – the dataset is only subpopulation from India and Bangladesh, which does not include the other South Asian countries. Besides, it does not include some important hypertension related variables, such as family history, salt consumption, calories intake, physical exercise etc. With more data, the accuracy of CNN could be improved. As future work, we propose to include more variables such as dietary diversity, information on physical exercise, salt consumption, parental history of hypertension and more because of unavailability of the data. Although we have achieved fairly acceptable and better model performances comparing to decision tree, adding these variables could improve more in all of the four performance measures. Moreover, CNN has the ability to explain the concepts it has learnt using the proposed simulation technique. To the best of our knowledge, this is one of the first step towards creating a ML platform solely dedicated to addressing challenges in improving healthcare systems.

References

[1] World Health organization (WHO). Hypertension. Internet, https://www.who.int/news-room/fact-sheets/detail/hypertension. [Accessed 22 July 2019].
[2] Rahman M, Zaman MM, Islam JY, Chowdhury J, Ahsan HN, Rahman R, et al. Prevalence, treatment patterns, and risk factors of hypertension and pre-hypertension among Bangladeshi adults. J Hum Hypertens 2018;32:334–48. https://doi.org/10.1038/s41371-017-0018-x.
[3] Lloyd-Sherlock P, Beard J, Minicuci N, Ebrahim S, Chatterji S. Hypertension among older adults in low- and middle-income countries: prevalence, awareness and control. Int J Epidemiol 2014;43:116–28. https://doi.org/10.1093/ije/dyt215.
[4] Joshi P, Islam S, Pais P, Reddy S, Dorairaj P, Kazmi K, et al. Risk factors for early myocardial infarction in South Asians compared with individuals in other countries. J Am Med Assoc 2007;297:286. https://doi.org/10.1001/jama.297.3.286.
[5] Wang A, An N, Chen G, Li L, Alterovitz G. Predicting hypertension without measurement: a non-invasive, questionnaire-based approach. Expert Syst Appl 2015;42:7601–9. https://doi.org/10.1016/j.eswa.2015.06.012.
[6] Luo Y, Li Y, Lu Y, Lin S, Liu X. The prediction of hypertension based on convolution neural network. In: Ieee 4th int. Conf. Comput. Commun. IEEE; 2018. p. 2122–7. https://doi.org/10.1109/CompComm.2018.8780834. 2018.
[7] Sumathi B, Santhakumaran DA. Pre-diagnosis of hypertension using artificial neural network. Glob J Comput Sci Technol Glob J Comput Sci Technol 2011.
[8] Fang J, Zhang Z. Prediction of human blood pressure based on wavelet analysis and BP neural network. Comput Syst Appl 2017;26:157–61.
[9] Golino HF, Amaral LS de B, Duarte SFP, Gomes CMA, Soares T de J, Reis LA dos, et al. Predicting increased blood pressure using machine learning. J Obes 2014; 2014:1–12. https://doi.org/10.1155/2014/637635.
[10] Völzke H, Fung G, Ittermann T, Yu S, Baumeister SE, Dörr M, et al. A new, accurate predictive model for incident hypertension. J Hypertens 2013;31:2142–50. https://doi.org/10.1097/HJH.0b013e328364a16d.
[11] Seidler T, Hellenkamp K, Unsoeld B, Mushemi-Blake S, Shah A, Hasenfuss G, et al. A machine learning approach for the prediction of pulmonary hypertension. J Am Coll Cardiol 2019;73:1589. https://doi.org/10.1016/S0735-1097(19)32195-3.
[12] Sakr S, Elshawi R, Ahmed A, Qureshi WT, Brawner C, Keteyian S, et al. Using machine learning on cardiorespiratory fitness data for predicting hypertension: the Henry Ford exercise testing (FIT) project. PLoS One 2018;13:e0195344. https://doi.org/10.1371/journal.pone.0195344.
[13] LaFreniere D, Zulkernine F, Barber D, Martin K. Using machine learning to predict hypertension from a clinical dataset. In: IEEE symp. Ser. Comput. Intell. IEEE; 2016. p. 1–7. https://doi.org/10.1109/SSCI.2016.7849886. 2016.
[14] Goldstein SP, Zhang F, Thomas JG, Butryn ML, Herbert JD, Forman EM. Application of machine learning to predict dietary lapses during weight loss. J Diabetes Sci Technol 2018;12:1045–52. https://doi.org/10.1177/1932296818775757.
[15] Dugan TM, Mukhopadhyay S, Carroll A, Downs S. Machine learning techniques for prediction of early childhood obesity. Appl Clin Inf 2015:506–20. https://doi.org/10.4338/ACI-2015-03-RA-0036. 06.
[16] Haskew J, Rø G, Saito K, Turner K, Odhiambo G, Wamae A, et al. Implementation of a cloud-based electronic medical record for maternal and child health in rural

Kenya. Int J Med Inf 2015;84:349–54. https://doi.org/10.1016/j.ijmedinf.2015.01.005.

[17] Haskew J, Rø G, Turner K, Kimanga D, Sirengo M, Sharif S. Implementation of a cloud-based electronic medical record to reduce gaps in the HIV treatment continuum in rural Kenya. PLoS One 2015;10:e0135361. https://doi.org/10.1371/journal.pone.0135361.

[18] Benítez JM, Castro JL, Requena I. Are artificial neural networks black boxes? IEEE Trans Neural Network 1997;8:1156–64.

[19] Ribeiro MT, Singh S, Guestrin C. "Why should I trust you?" Explaining the predictions of any classifier. In: Proc. 22nd ACM SIGKDD int. Conf. Knowl. Discov. Data min. - KDD '16. New York, New York, USA: ACM Press; 2016. p. 1135–44. https://doi.org/10.1145/2939672.2939778.

[20] Frosst N, Hinton G. Distilling a neural network into a soft decision tree. 2017. ArXiv Prepr ArXiv171109784.

[21] Jermain N. Visualizing your convolutional neural network predictions with saliency paps. Open Data Sci 2019. https://opendatascience.com/visualizing-your-convolutional-neural-network-predictions-with-saliency-maps/. [Accessed 26 March 2021].

[22] Simonyan K, Vedaldi A, Zisserman A. Deep inside convolutional networks: visualising image classification models and saliency maps. 2014.

[23] John V, Yoneda K, Liu Z, Mita S. Saliency map generation by the convolutional neural network for real-time traffic light detection using template matching. IEEE Trans Comput Imaging 2015;1:159–73. https://doi.org/10.1109/TCI.2015.2480006.

[24] Chollet F. Keras: the python deep learning library. Astrophys Source Code Libr 2018.

[25] Ioffe S, Szegedy C. Batch normalization: accelerating deep network training by reducing internal covariate shift. 2015. ArXiv Prepr ArXiv150203167.

[26] Srivastava N, Hinton G, Krizhevsky A, Sutskever I, Salakhutdinov R. Dropout: a simple way to prevent neural networks from overfitting. J Mach Learn Res 2014; 15:1929–58.

[27] Brownlee J. Better deep learning: train faster, reduce overfitting, and make better predictions. 2018. Machine Learning Mastery.

[28] Chowdhury MAB, Uddin MJ, Haque MR, Ibrahimou B. Hypertension among adults in Bangladesh: evidence from a national cross-sectional survey. BMC Cardiovasc Disord 2016;16:22. https://doi.org/10.1186/s12872-016-0197-3.

[29] Bangladesh demographic and health survey 2011. Dhaka, Bangladesh and Calverton. Maryland, USA: NIPORT, Mitra and Associates, and ICF International; 2013.

[30] National family health survey (NFHS-4), 2015-16: India. Mumbai: IIPS; 2017.

[31] Bhansali A, Dhandania VK, Deepa M, Anjana RM, Joshi SR, Joshi PP, et al. Prevalence of and risk factors for hypertension in urban and rural India: the ICMR–INDIAB study. J Hum Hypertens 2015;29:204–9. https://doi.org/10.1038/jhh.2014.57.

[32] Kingma DP, Ba J. Adam: a method for stochastic optimization. ArXiv Prepr ArXiv14126980 2014.

[33] Agresti A. An introduction to categorical data analysis. John Wiley & Sons; 2018.

[34] Everett B, Zajacova A. Gender differences in hypertension and hypertension awareness among young adults. Biodemogr Soc Biol 2015;61:1–17. https://doi.org/10.1080/19485565.2014.929488.

[35] Park YS, Lee C-H, Kim Y-I, Ahn CM, Kim JO, Park J-H, et al. Association between secondhand smoke exposure and hypertension in never smokers: a cross-sectional survey using data from Korean National Health and Nutritional Examination Survey V, 2010–2012. BMJ Open 2018;8:e021217. https://doi.org/10.1136/bmjopen-2017-021217.

[36] Ramakrishnan S, Zachariah G, Gupta K, Shivkumar Rao J, Mohanan PP, Venugopal K, et al. Prevalence of hypertension among Indian adults: results from the great India blood pressure survey. Indian Heart J 2019;71:309–13. https://doi.org/10.1016/j.ihj.2019.09.012.

[37] Riaz BK, Islam MZ, Islam ANMS, Zaman MM, Hossain MA, Rahman MM, et al. Risk factors for non-communicable diseases in Bangladesh: findings of the population-based cross-sectional national survey 2018. BMJ Open 2020;10:e041334. https://doi.org/10.1136/bmjopen-2020-041334.

[38] Anstey DE, Christian J, Shimbo D. Income inequality and hypertension control. J Am Heart Assoc 2019;8. https://doi.org/10.1161/JAHA.119.013636.

[39] Wang Y, Chen J, Wang K, Edwards CL. Education as an important risk factor for the prevalence of hypertension and elevated blood pressure in Chinese men and women. J Hum Hypertens 2006;20:898–900. https://doi.org/10.1038/sj.jhh.1002086.

[40] Palatini P, Bratti P, Palomba D, Saladini F, Zanatta N, Maraglino G. Regular physical activity attenuates the blood pressure response to public speaking and delays the development of hypertension. J Hypertens 2010;1. https://doi.org/10.1097/HJH.0b013e328338a8e7.

[41] Twinamasiko B, Lukenge E, Nabawanga S, Nansalire W, Kobusingye L, Ruzaaza G, et al. Sedentary lifestyle and hypertension in a periurban area of Mbarara, South Western Uganda: a population based cross sectional survey. Int J Hypertens 2018; 2018:1–8. https://doi.org/10.1155/2018/8253948.

[42] Suo Q, et al. Deep patient similarity learning for personalized healthcare. In: IEEE transactions on nano bioscience, vol. 17; July 2018. p. 219–27. https://doi.org/10.1109/TNB.2018.2837622. 3.

[43] Abiyev R, Arslan M, Bush Idoko J, Sekeroglu B, Ilhan A. Identification of epileptic EEG signals using convolutional neural networks. Appl Sci 2020;10(12):4089. https://doi.org/10.3390/app10124089.

[44] Kim S, Han G. 1D CNN based human respiration pattern recognition using ultra wideband radar. In: 2019 international conference on artificial intelligence in information and communication (ICAIIC); 2019. p. 411–4. https://doi.org/10.1109/ICAIIC.2019.8669000.

[45] Ping Y, Chen C, Wu L, Wang Y, Shu M. Automatic detection of atrial fibrillation based on CNN-LSTM and shortcut connection. Healthcare 2020;8(2):139. https://doi.org/10.3390/healthcare8020139.

[46] Abiyev RH, Arslan M. Head mouse control system for people with disabilities. Expet Syst 2020;37:e12398. https://doi.org/10.1111/exsy.12398.

Deep learning computer vision for robotic disassembly and servicing applications

Prakash Chandra Sahu, *Department of Electrical Engineering, Aryan Institute of Engineering & Technology, Bhubaneswar, pksahoo88@gmail.com*

Manisha Pradhan, *Department of Computer Scinece Engineering , Raajdhani Engineering College, Bhubaneswar, manishapradhan456@gmail.com*

Sagarika Patro, *Department of Electrical and Electronics Engineering, Aryan Institute of Engineering & Technology, Bhubaneswar, sagarikapatro14@gmail.com*

Madhusmita Mohanty, *Department of Electronics and Communication Engineering , NM Institute of Engineering & Technology, Bhubaneswar, madhusmitamohanty@gmail.com*

ARTICLE INFO

Keywords:
Screw detection
YOLO
Robotic disassembly
Robotic servicing
Deep learning

ABSTRACT

Fastener detection is a necessary step for computer vision (CV) based robotic disassembly and servicing applications. Deep learning (DL) provides a robust approach for creating CV models capable of generalizing to diverse visual environments. Such DL CV systems rely on tuning input resolution and mini-batch size parameters to fit the needs of the detection application. This paper provides a method for determining the optimal compromise between input resolution and mini-batch size to determine the highest performance for cross-recessed screw (CRS) detection while utilizing maximum graphics processing unit resources. The Tiny-You Only Look Once v2 (Tiny-YOLO v2) DL object detection system was chosen to evaluate this method. Tiny-YOLO v2 was employed to solve the specialized task of detecting CRS which are highly common in electronic devices. The method used in this paper for CRS detection is meant to lay the ground-work for multi-class fastener detection, as the method is not dependent on the type or number of object classes. An original dataset of 900 images of 12.3 MPx resolution was manually collected and annotated for training. Three additional distinct datasets of 90 images each were manually collected and annotated for testing. It was found an input resolution of 1664 x 1664 pixels paired with a mini-batch size of 16 yielded the highest average precision (AP) among the seven models tested for all three testing datasets. This model scored an AP of 92.60% on the first testing dataset, 99.20% on the second testing dataset, and 98.39% on the third testing dataset.

1. Introduction

Electronic waste (e-waste) is a rapidly growing problem. In 2019 alone, 53.6 million metric tons (Mt) of e-waste was generated globally; however, only approximately 17.4% was formally recycled. It is estimated that the annual e-waste generation will increase to 74 Mt by 2030 , increasing at almost 2 Mt per year [1]. Over half of the e-waste gathered for recycling in developed countries is sent to developing countries for processing, where health and safety regulations are not enforced, and dangerous methods for recycling e-waste are used [2]. Methods to dispose of e-waste include destructive, semi-destructive, and non-destructive disassembly methods. Destructive disassembly methods involve destroying the product through shredding or metallurgical processes (hydro or pyro) to recover valuable resources. Non-destructive methods are more useful when the disassembly goal is to recycle or reuse parts of the product. However, non-destructive disassembly typically needs to be performed by trained workers, which can be expensive because of pay and safety [3]. Robotic disassembly offers an efficient non-destructive method for disassembling e-waste. This method can be used in situations where the goal is to reuse parts or disassemble parts that contain hazardous materials in a safe manner [4, 5]. Many products, such as laptops, cellphones, and electric vehicle batteries, have outer cases held together with fasteners which must be unfastened during non-destructive disassembly. To fully realize the potential of automated disassembly, it becomes necessary to implement a computer vision (CV) system capable of automatically recognizing and locating these screws on these outer cases [6].

Robotic servicing is another critical application of CV fastener detection. The amount of space debris reached 3 million kilograms in 2013 and continues to increase. This debris poses a serious threat to the safety of future space missions [7]. NASA suggests that retired satellites should either lower their orbits and reenter or raise their orbit to a graveyard region within 25 years of mission completion to mitigate space debris buildup, but this procedure has not been globally accepted because of the significant technical challenges and cost associated with it [8]. Robotic servicing can extend the life of current satellites without the need for sending more as replacements. Therefore, there is a need to develop on-orbit satellite servicing robots to increase the longevity of artificial satellites [9]. CV can be used to aid robotic servicing missions in the detection of important mechanical features such as fasteners and docking rings. The lighting and camera orientations are highly variable in this application and deep learning provides a possible solution for making generalized predictions in this variable environment. Robots are especially useful in satellite servicing missions, where sending humans can be much more costly [10].

Both automated disassembly and servicing robots require a CV system that detects (classifies and locates) fasteners and other objects so they can be engaged by the proper tool. This paper evaluates the detection of cross-recessed screws (CRS), a common fastener used in electronics.

The goal of many object detection systems is to detect large objects such as vehicles and people [11]. Having a high input resolution is not critical when detecting large objects because they typically occupy a large portion of the frame. In this case, it is usually desirable to use lower input layer resolutions as they can allow for faster detection speed at the expense of some average precision (AP) [12]. The challenge with detecting CRS and other small objects is they usually occupy a relatively small portion of the frame due to their size. Significant visual information about the screws' appearances is lost when processed by low resolution input layers.

The training and testing of deep learning (DL) object detection systems are usually highly dependent on available graphics processing unit (GPU) resources. The number of hidden layers in a neural network (NN), the input layer resolution, and the mini-batch size are all dependent on available GPU resources. Finding the optimal balance of these three parameters for a given GPU can be challenging, especially for detecting small objects. The Tiny-You Only Look Once v2 (Tiny-YOLO v2) DL object detection system was chosen for evaluation because YOLO v2 is highly documented in literature as a widely used state-of-the-art object detection system [12–17] and its Tiny configuration allowed for more GPU resources to be allocated for higher input resolutions. Tiny-YOLO v2 was set up using Darkflow [13], a Tensorflow translation of Darknet [18]. YOLO v2 has 32 hidden layers while Tiny-YOLO v2 has 16 hidden layers. Tiny-YOLO v2 is used so higher definition input layers at reasonable mini-batch sizes can be evaluated within the constraints of one NVidia Tesla V100 GPU with 32 Gigabytes (GB) of RAM. This paper provides a method for determining the optimal compromise between input resolution and mini-batch size to determine the highest performance for CRS detection while utilizing maximum GPU resources. The method used in this paper is defined in the numbered list below and was shown to work using the aforementioned GPU for the application of CRS detection using Tiny-YOLO v2.

1. Identify the highest input resolution the given GPU can support at the default mini-batch size.
    - NOTE: If the GPU is unable to support at least high definition (1280 x 720 pixels) at the default mini-batch size, a more capable GPU may be needed.
2. Select several evenly spaced mini-batch sizes above and below the default value and identify the maximum corresponding input resolution for each.
3. Obtain a training and testing dataset of images with a resolution equal to or greater than the highest input resolution value determined in the previous step.
4. Train one model at each input resolution/mini-batch size configuration using the discrete learning rate decay method discussed in this paper.
5. Evaluate the performance of each trained model on test datasets of images indicative of the desired operating regime.
6. Choose the highest performing model for use in the field.

1.1. Related work

1.1.1. Object recognition tasks

Recently, deep learning approaches have been applied to all CV application areas such as image classification [19,20], object recognition [21–23], semantic segmentation [24], depth estimation [25,26], and human detection [27,28]. The goal of object detection is to correctly classify the object as well as predict the object's location in an image [29]. Object detection research has primarily used deep convolutional neural network (DCNN), a feed-forward type of neural network which works by trying to match features across an image using convolution functions [30]. Wei et al. [31] compared the effectiveness of image processing and deep learning techniques on the detection of railway track fastener defects for missing or broken links. Four methods were compared: classical image processing, classification based on Dense-Scale Invariant Feature Transform (SIFT), classification based on the VGG16 DCNN, and classification based on Faster Region Based Convolutional Neural Network (R-CNN). The Dense-SIFT method scored the highest mean AP (mAP) of 99.26% but had the slowest image processing time of 2.21s per image. Faster R-CNN scored the second highest mAP of 97.90% with the fastest image processing time of 0.23s per image.

K. Zhang et al. [32] applied an attention mechanism, which made their model more sensitive to foreground pixels, to a custom CNN to improve the detection of foreign objects in coal processing. Their model correctly identified 97% of the foreign objects in their test set and resized images to 416 x 416 pixels with a batch size of 4 for training. The low resolution worked well for their application because the foreign objects of concern occupied a considerable portion of the frame. The small batch size seemed to work well because there is a high variation of possible foreign objects, so it is desirable to avoid over-normalizing the model to retain its sensitivity to such variation.

Y. Zhang et al. [33] examined how well a deep learning model could identify if a bolt was loose or tightened to monitor a structure's health (e.g., a bolt that loosens over time). For testing, bolts were loosened to various heights and the model was able to detect bolts that were loosened by just 0.5 cm. Overall, the model was able to achieve a mAP of 95.03%. Wang, Li, and Zhang [34] created a construction waste recycling robot capable of detecting loose nails and screws. Their vision system used the Faster R-CNN and their model achieved a mAP of 89.10% on their testing dataset of nails and screws. Li, Zhao, and Pan [35] used Fisher criteria in a four hidden-layer network to obtain the location and classification of defects in fabrics. Their model scored a detection rate (DR) of over 90% on their testing dataset, where DR is the ratio of correctly detected defective samples.

The YOLO framework in particular has led to the development of many promising applications [5,14,36–38]. Ding et al. [36] developed a novel Unmanned Aerial Vehicle (UAV) capable of semi-automated aerial drilling and screwing. Their design used the YOLO v3 CV system to detect targets and maintain alignment in real-time during drilling and screwing processes. A custom dataset of 600 images of targets at different angles and distances was used to train the YOLO v3 model and experiments successfully demonstrated high precision aerial drilling and screwing.

Zheng et al. [37] presented a dataset of 13,000 images of UAV flight scenarios and evaluated the performance of eight different DL CV systems on UAV detection. Their study evaluated RetinaNet, Single-Shot Detector, YOLO v3, Feature Pyramid Network, Faster R-CNN, RefineDet, Grid R-CNN, and Cascade R-CNN DL CV systems. Each system was trained using 70% of the dataset and the remaining 30% was used for testing. YOLO v3 achieved an AP of 72.3%, which is between the lowest performer, RefineDet, at 69.5%, and the highest performer, Grid R-CNN, at 82.4%. They reported that among all eight systems, Grid R-CNN had the slowest image processing time at 157 ms while YOLO v3 had the fastest image processing time at 32 ms.

Chen et al. [14] used a detection pipeline consisting of Super-Resolution CNN (SRCNN) and YOLO v3 to detect electrical components from UAV inspection images. They used SRCNN to enhance the resolution of blurry images before sending them to YOLO v3 for detection and were able to achieve a mAP of 93.60% with their detection pipeline.

Yildiz and Wörgötter [5] investigated several DL methods for screw detection in hard drives. The first method they evaluated used a Hough Transform to detect circles which acted as screw candidates. The screw candidates were sent to a classifier which predicted the class and location of those candidates. Their best model used a weighted decision of the predictions made by both the InceptionV3 and Xception classifier. This model scored an AP of 80.23% on their testing dataset. They compared these results to a model they trained using YOLO v3, which scored an AP of 66.47% on their testing dataset.

1.1.2. Transfer learning with neural networks

Transfer learning is the method of appending training to a pre-trained model to repurpose it for the needs of the desired application. A common issue that arises in many problems is limited training data because of the cost of obtaining and annotating new training data [39]. Various applications that have used the YOLO network such as object detection [40,41] and diagnosis of medical issues [42–44] have instituted transfer learning methods.

Li et al. [16] introduced a method based on transfer learning and sample enhancement with a small number of training samples that was able to classify 87.5% of objects. They first initialized training weights using unrelated sample data from the PASCAL Visual Object Classes (VOC) dataset with Tiny-YOLO v2 then used the Tiny-YOLO v2 network to further train the data.

Transfer learning can be used to improve detection results of models. Raza and Hong [41] designed a computer vision model using YOLO v3 to monitor for fish in a marine ecosystem. They used a transfer learning method that was pre-trained on 1.2 million samples of the ImageNet dataset. By incorporating the transfer learning method as well as some other improvement techniques, they were able to increase the mAP by 4.13%. Montalbo et al. [42] developed a model that could detect three types of brain tumors and used Tiny-YOLO v4 and pre-trained weights from the COCO dataset. They achieved a mAP of 93.14% which outperformed other studies that had tried to detect brain tumors using different deep learning networks.

1.1.3. Automatic screw detection for disassembly

In applications such as robotic disassembly, automated screw unfastening is an important task robots can execute. Robots already perform screw fastening for assembly operations [45,46], and there have been many studies detailing the designs of robotic systems [47,48] and end-effectors [49–51] for fastening applications. In these assembly applications, when screw locations are known in advance, fixtures and compliance devices can be used to achieve proper screw alignment. When screw locations are not known in advance, as is typically the case with disassembly operations [38,52], vision systems may be used to determine screw positions [45].

Gil et al. [53] used various computer vision techniques such as Douglas–Peucker's algorithm, adaptive thresholding, Canny edge detection, and region detection with template matching to identify features such as screws and other components (covers, wires, batteries, etc.) on electronic equipment to create a robotic system to perform disassembly tasks. Bdwidi et al. also designed a workstation to automatically disassemble electric vehicle motors. They used a Microsoft Kinect sensor capable of providing depth data, feature point detectors such as the Harris detector, and then multiple optimization steps to identify screws and remove false positives. A drawback of using these types of classifiers is that they can be heavily dependent on lighting and require controlled lighting environments. Vongbonyung et al. [54,55] designed a robotic system that could learn actions and revise them to make cuts to disassemble monitors. This system was also able to deal with uncertainties that can arise during automated disassembly. The system used computer vision to automatically determine the location of screws and was able to find over 80% of them however, the authors reported a high number of false positive (82.83%) and false negative (35.78%) detections. A false positive detection would lead to redundant cutting operations and would require human intervention for disassembly to proceed.

Wegener et al. [6] proposed a concept for a human-assisted robot workstation for the disassembly of electric vehicle batteries where fastener detection was a primary task for the robot. They investigated three methods of fastener detection: using a computer-aided design (CAD) database, physically demonstrating the location of the screws, and a CV algorithm. They determined that detailed CAD databases are usually not accessible by the recycler and physical demonstrations are too time-consuming, thus making these methods impractical. The final option of using a CV algorithm was investigated using a Haar-Cascade classifier trained on positive and negative images to create a model for detecting the desired object classes. Their model was only able to correctly detect 50% of the screws in their testing dataset.

DiFilippo and Jouaneh [4] developed an automated robotic disassembly system that combined CV and force sensing to remove screws from the back of laptops. The system comprised two webcams, a Microsoft Kinect sensor, and a 3-axis cartesian robot with an actuated sensor-equipped (SE) screwdriver. Once a laptop was placed on the workspace, the overhead webcam identified circles as screw candidates using a Hough Circle Transform. The robot would then move to the locations of these circles and, using a webcam attached to the robot's end-effector, perform classical computer vision techniques to center the screw. The SE screwdriver would then test if the circle was a screw by attempting to remove it. If a screw was detected, the robot removed the screw, and if no screw was detected, the robot would move to the following circle location. This process proved to be time-consuming. By using the Soar cognitive architecture [56], screw locations could be stored in semantic memory after the first pass, thus reducing screw removal time on subsequent passes. Even so, the fastest CV time per circle was 6.5s. This paper builds upon their previous work by proposing an optimized DL Tiny-YOLO v2 based CV system that can process high-resolution images at over 3 frames per second (FPS). The image processing speed of this method is not dependent on the number of screws/screw-like objects in each image.

2. Background on tiny-YOLO v2 object detection system

Tiny-YOLO v2 is a lightweight version of YOLO v2, which is derived from the original YOLO object detection system [12]. YOLO, YOLO v2, and Tiny-YOLO v2 are high performance DL object detection systems that can be applied to real-time applications. YOLO is unique from other object detection systems in that it simultaneously predicts bounding boxes and object classes with a single NN.

Tiny-YOLO v2 has 1 input layer, 9 convolutional layers and 6 maximum pooling layers. The unmodified Tiny-YOLO v2 input layer resizes images to 416 x 416 pixels, where the output is passed to convolutional layers for feature extraction. Max pooling is used to reduce the dimensionality of the convolutional layer outputs.

YOLO divides an image into an S x S grid, where each grid cell predicts B bounding boxes with corresponding confidence scores. The confidence, C, represents the probability that an object is encompassed in a bounding box and is represented as:

$$C = Pr(Object) * IOU_{pred}^{truth} \tag{1}$$

where intersection over union (IOU) is defined as the ratio of the area of overlap of the detection and ground truth bounding boxes divided by the area formed by their union. A graphical representation of IOU is shown in Fig. 1.

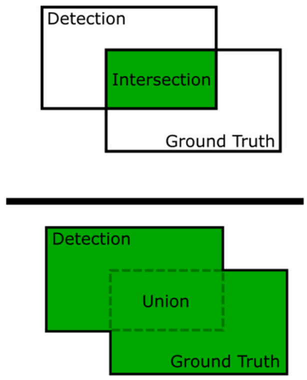

Fig. 1. Graphical representation of intersection over union metric.

Table 1
Tiny-YOLO v2 model configurations.

Model	Mini-batch size	Input resolution
A	8	2368 x 2368
B	12	1920 x 1920
C	16	1664 x 1664
D	20	1472 x 1472
E	24	1344 x 1344
F	28	1248 x 1248
G	32	1184 x 1184

3. Training method

Input resolution and mini-batch size are parameters that directly influence the performance of a deep NN. The input resolution is defined in the first layer of the Tiny-YOLO v2 network. In this layer, images of any size are accepted into the network and resized to the input resolution specified by the network's configuration. In this paper, high definition (pixel density equal to or greater than 1280 x 720) input resolutions are specified. The original aspect ratio is maintained during this process. A higher input resolution allows for the network to process higher resolution images.

At every step (gradient update), the model updates its weights based on the normalized training loss results from one mini-batch of images. The training loss reports the error between the model's predictions and the ground truth of the training dataset at the end of each step. A higher mini-batch size allows for more normalized learning whereas a smaller mini-batch size may evoke noise in the reported training loss.

Both input resolution and mini-batch size depend on the availability of GPU memory allocations. Therefore, it is desirable to determine the optimal compromise between these two parameters. A total of seven models were trained using different combinations of input resolutions and mini-batch sizes to determine the optimal training conditions. These combinations were chosen to represent a wide spread of reasonable combinations of mini-batch size and resolution from which a trend in reported AP should emerge. Table 1 shows the input resolution/mini-batch pairing for each model. The default mini-batch size for Tiny-YOLO v2 is 16 and mini-batch sizes above and below this default value were explored in evenly-spaced steps of four mini-batches from half of the default mini-batch value (8) to twice the default mini-batch value (32). Each model's mini-batch size was paired with a respective input resolution that fully utilizes the resources of the GPU. These input resolution values were identified by a trial-and-error process which finds the highest input resolution that does not give a memory error for a given batch size. The input resolution was chosen to be square to remain unbiased to one image orientation as input images may be landscape or portrait orientation. It should be noted the input resolution of Tiny-YOLO v2 can have rectangular dimensions.

All datasets were manually collected using a Google Pixel 12.3 MPx (3036 x 4048 pixels) camera to maintain uniform high resolution. Tiny-YOLO v2 automatically resizes these images down to specified input resolutions during training and testing. Thus, it is desirable to start with an image resolution that is the same or higher than the specified input resolution so that maximum visual information can be maintained.

Ground truth files containing the location and classification of screws were manually generated for each image. Tiny-YOLO v2 uses these ground truth files to train a model by associating the location and classification of screws with the respective images. The testing process also requires these ground truth images, as they are compared with detection results to determine AP.

The training dataset consists of 900 images of general electronics and hardware with embedded CRS. The objects in this dataset include laptops, computer towers, hard drives, oscilloscopes, power supplies, and other assorted hardware. Due to the diverse assortment of objects, this dataset contains many variations of CRS. These 900 images were taken in highly variable environments with various lighting conditions and distances to the object (ranging from approximately 4 to 8 inches from the surface of the objects). This dataset is intended to be highly variable as it is hypothesized this variability will improve the generalizing ability of the models. Fig. 2 shows a sample of the images included in this set.

Due to the relatively small training dataset of 900 images, a transfer learning approach similar to the one discussed in [16] is employed to avoid overfitting. Each model initializes training from the Tiny-YOLO v2 Visual Objects Classes (VOC) weights file from [18] which has been pre-trained on the VOC [11] dataset.

The generalizing ability of the model at a given training iteration is evaluated by a validation set. The validation set will be referred to as Test Set A, which contains 90 images of hardware with embedded CRS. The images in Test Set A are not present in the training dataset and are used to gauge the performance of the model throughout training. After training was completed, the final performance results from each model on Test Set A were recorded in Section 4.

The training method for each model is as follows. A discrete learning rate decay method was used to achieve the optimal AP on Test Set A. The learning rate is a parameter that dictates the amount of change applied to the model's weights after each training iteration in response to the reported error between the model prediction and the ground truth. Fig. 3 shows the learning rate progression method for each trained model. This method entails first training a model at a high learning rate of 5e-5 until a maximum attainable AP is reached on Test Set A for this learning rate. The model then continues training at a reduced learning rate of 2e-6 until a maximum attainable AP is reached on Test Set A for this reduced learning rate. To determine the maximum AP for both the high learning rate and the reduced learning rate, validation tests are performed where the loss convergence occurs that determine the AP where further training will cause the model to overfit the data. The final trained model is the result of this procedure.

Fig. 4(a) shows the overall view of training loss curves for all seven models. All loss curves closely follow the same trend, but models with higher input resolutions tend to initialize with a greater loss value. This higher loss is likely associated with there being more to learn from higher resolution images. Higher resolution images inherently contain more information, so it follows the initial training loss increases with input resolution. Models with higher resolution also generally take more steps to train; however, this trend is not followed exactly.

Fig. 4(b) shows a zoomed-in view of where the training loss for all seven models begins to converge. As mentioned earlier, models with lower batch sizes tend to evoke more noise in the reported training loss. This is represented clearly in Fig. 4(b) since Model A has the lowest batch size and shows the most noise, while Model G has the highest batch size and shows a smooth curve. All seven models consistently converge in the order of increasing initial loss values. While this appears negligible in the overall view, it is helpful to confirm this behavior in the zoomed-in view as it is expected that higher initial loss values should take longer to converge.

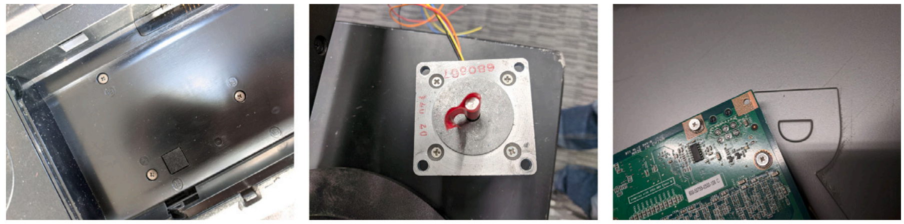

Fig. 2. Sample of images used for training each model.

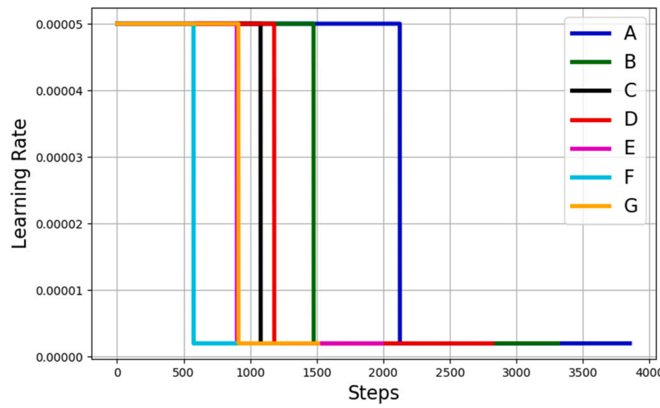

Fig. 3. Learning rate progression of each model throughout the training process.

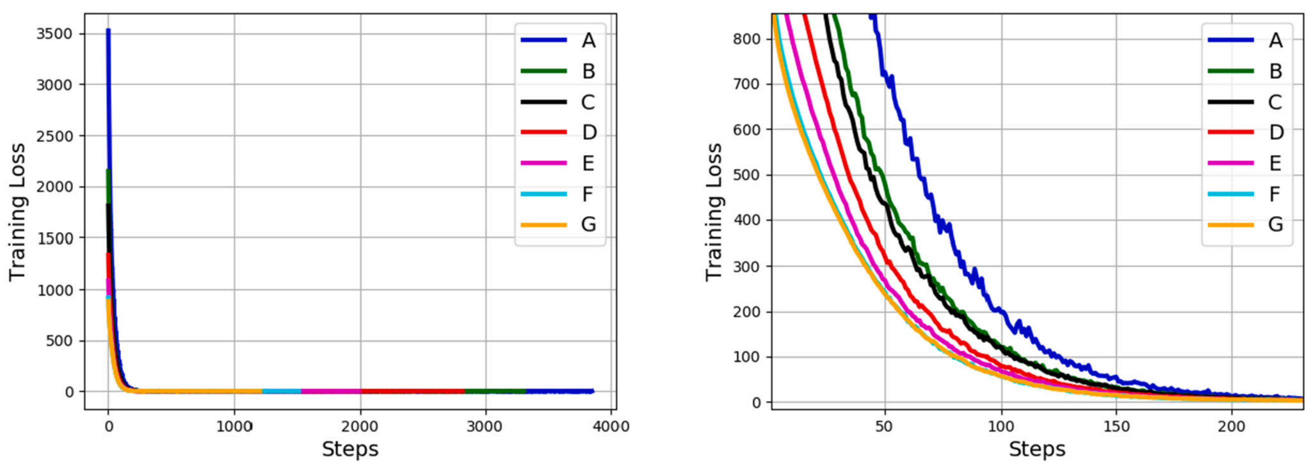

(a) (b)

Fig. 4. Training loss reported over steps. (a) Overall view of each model throughout the training process. (b) Zoomed-in view of initial convergence for each model.

4. Testing results and discussion

Each model was tested on three distinct datasets; Test Sets A, B, and C. The authors chose to make the visual environments (lighting, size of CRS relative to overall frame, distance, and camera angle) equally diverse between these test sets as to capture a broad representation of possible conditions that could be encountered by this vision system during nominal operation. As a result, the authors did not feel a need to do a systematic investigation of model performance as a function of the visual environment. Each testing dataset consists of 90 new images outside of the training dataset. Table 2 provides the total number of CRS, a description, and sample image for each test set.

Test Set A, which was also used for training validation, consists of images of general hardware with embedded CRS. This test set evaluates the ability of the models to make detections on new images of similar objects to those found in the training dataset.

It is useful to evaluate the models' performance when given specialized tasks they were not primarily trained to encounter. Test Sets B and C provide two different specialized tasks. Test Set B evaluates the ability of the models to perform CRS detection on laptops and Test Set C evaluates their ability to perform CRS detection on boxed electronics such as power supplies, power tools, and oscilloscopes.

The AP metric is used to evaluate the performance of each model. AP computes the area under a monotonically decreasing precision–recall curve for a single class as defined in [11]. For reference, Fig. 5 shows similar information to Table 3 but in a visual format for the precision–recall curve for Model C on Test Set A. Similar graphs can be constructed for all of the models (A–G) on all of the Test Sets (A,B,C). IOU is used to differentiate true positives (TP) from false positives (FP). A TP is defined as a prediction with the correct classification that has an IOU greater than 50%. A FP is defined as a detection with an IOU less than 50%. Python scripts developed by Cartucho, Ventura, and

Table 2
Test set descriptions.

Test Set	Total CRS	Description	Sample Image
A	164	General hardware	
B	131	Laptops	
C	200	Boxed Electronics	

Fig. 5. Model C precision–recall curve for CRS detection on Test Set A.

Veloso [17] were used to plot the AP and generate visual overlays of the detections over ground truth bounding boxes.

Table 3 shows the AP, TP, FP, network initialization time, total prediction time, and FPS for each model on Test Sets A, B, and C. The network initialization time is the amount of time Tiny-YOLO v2 takes to set up its network for testing. The total prediction time is the amount of time spent passing the entire dataset through the network while generating detection output files for each image in sequence. FPS is defined as the number of images passed through the network divided by the total prediction time. The reported network initialization time and total prediction time are averaged results taken from five trials for each model. These results are averaged to account for the GPU's slight variation in computing times. The AP, TP, and FP will always remain constant for a given trained model as neither the model's weights nor the input image pixels change during testing. Model C scored the highest AP on all three test sets.

Table 4 shows a sample of images representative of Model C's performance on all three test sets. Detections are shown as green or red boxes labeled "CRS", which stands for cross-recessed screw. Ground truth boxes associated with each detection are shown in blue. Green boxes represent TP and red boxes represent FP.

Test Set A contains a total of 164 screws. Model C correctly predicted 152 screws while only making one FP prediction. This shows Model C was more likely to miss a TP rather than assign a FP in Test Set A. As shown in Table 4, Model C performs exceedingly well when presented images with a blend of screws and screw-like objects. Grates, connectors, and holes are often screw-like in appearance and can be a source of difficulty for classical CV techniques. As shown, the approach used in this paper is robust in differentiating screws from screw-like objects. The top right picture in Table 4 shows the only FP Model C predicted in Test Set A, which is a circular indent in an electronics case. Model C scored 92.60% AP on Test Set A with an average speed of 2.535 FPS. This result reaffirms the value of using DL techniques for fastener detection as they can exhibit high performance and speed when optimized.

Table 3
Results on Test Sets A, B, and C.

Model	Test Set A					
	AP	TP	FP	Network Init. time (s)	Total Prediction time (s)	Frames Per second
A	85.54%	142	2	10.053	49.576	1.815
B	92.44%	154	4	10.052	42.014	2.142
C	92.60%	152	1	10.047	35.507	2.535
D	90.41%	151	4	10.022	32.989	2.728
E	91.74%	153	8	10.057	30.193	2.981
F	86.97%	146	4	10.039	28.915	3.113
G	83.66%	141	10	10.047	28.720	3.134
Model	**Test Set B**					
	AP	TP	FP	Network Init. time (s)	Total Prediction time (s)	Frames Per second
A	90.44%	120	4	10.084	49.869	1.805
B	98.88%	130	4	10.042	41.722	2.157
C	99.20%	130	2	10.045	35.541	2.532
D	95.01%	125	2	10.066	31.892	2.822
E	93.54%	123	4	10.058	30.599	2.941
F	92.01%	121	2	10.072	28.610	3.146
G	93.50%	123	4	10.016	28.470	3.161
Model	**Test Set C**					
	AP	TP	FP	Network Init. time (s)	Total Prediction time (s)	Frames Per second
A	84.82%	170	1	10.090	48.901	1.840
B	90.50%	181	0	10.090	40.497	2.222
C	98.39%	197	1	10.081	34.244	2.628
D	94.42%	189	2	10.048	30.033	2.997
E	91.21%	183	7	10.048	29.393	3.062
F	90.24%	183	4	10.065	28.016	3.212
G	90.10%	181	10	10.053	27.577	3.264

Test Set B contains a total of 131 screws. Model C correctly predicted 130 screws while making only 2 FP predictions. Both FP cases are shown in the center and mid-right pictures in Table 4, where the model mistook a power connector and another circular feature as a screw. Still, Model C is robust when presented with images containing holes that do not contain screws. Model C scored 99.20% AP on Test Set B with an average speed of 2.532 FPS.

Test Set C contains a total of 200 screws. Model C correctly predicted 197 screws while making only 1 FP prediction. The FP case is shown in the bottom right picture of Table 4, where the model did surround the CRS in a bounding box; however, the IOU was less than 50%, which resulted in a FP. Model C scored 98.39% AP on Test Set C with an average speed of 2.628 FPS. These results show that model C is highly robust when given the specialized task of CRS detection in boxed electronics.

Fig. 6 shows the FPS for all seven input resolutions on all three test sets. Average FPS decreases as input resolution increases for all test sets. This is expected since more computation is needed for evaluating higher resolution images. The FPS curves for Test Sets A, B, and C are nearly identical and follow the same trajectory. The minor variations between both curves can be attributed to the slight inconsistency of the GPU's processing speed. It should be noted the CV time spent using classical techniques is dependent on the number of screws and screw-like objects in an image [4,56]. Fig. 6 shows even when three different

Table 4
Model C detected output images from Test Sets A, B, and C.

Test Set	Detected Output Images		
A		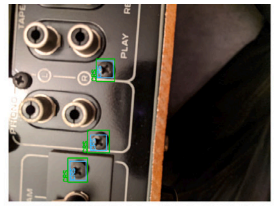	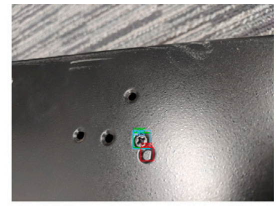
B	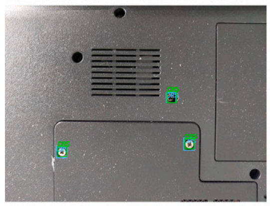	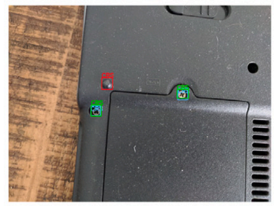	
C	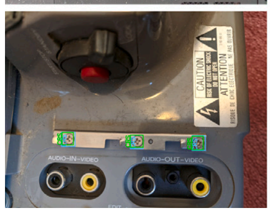		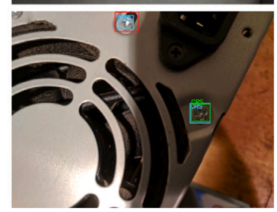

*Some images have been rotated 90° to better fit the table as the test sets contain both portrait & landscape images.

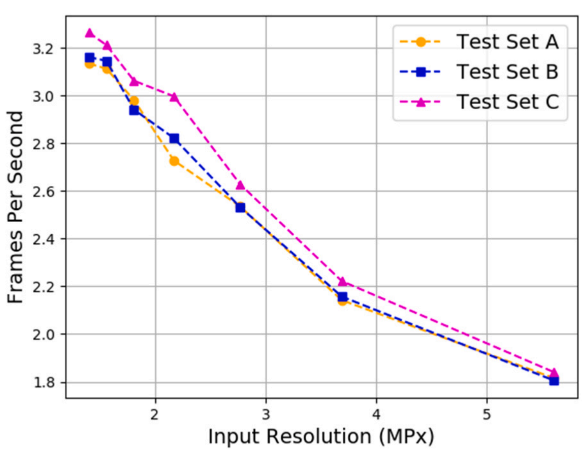

Fig. 6. Image processing speed reported as a function of input resolution for all test sets.

datasets with varying numbers of screws and screw-like objects are evaluated, the CV time is dependent almost exclusively on input resolution. This suggests an image with few screws would likely be evaluated in the same amount of time as an image with many screws.

Fig. 7a shows the AP vs. mini-batch size, Fig. 7b) shows the AP vs input resolution and Fig. 7c) shows a 3D plot of the AP scored on Test Sets A, B, and C as a function of input resolution and mini-batch size. Models scored highest on Test Set B likely because it has the smallest variety of objects. Models scored lowest on Test Set A likely because it contains the largest variety of objects. The general AP curve for all three test sets is similar, with all curves reaching optimal AP when a mini-batch size of 16 is paired with an input resolution of 2.77 MPx (1664 x 1664 pixels). This indicates the method used in this paper yields a configuration that shows consistently optimal performance across several variations of CRS detection tasks.

The results obtained in this paper show improvement over results that have been reported from previous work, either in the time to detect a screw or in the screw detection accuracy. A summary of this work compared with previous results can be found in Table 5 where the work described by this paper is referred to as Tiny-YOLO v2 (Model C). In terms of detection accuracy, Wegener et al. [6] used a Haar Cascade classifier but was only able to detect 50% of screws. Vongbunyong et al. [54,55] also used a Haar Classifier and reported being able to detect over 80% of screws [54], however they also indicated a high number of false-positive screw detections (82.32%) and false-negative screw detections (35.78%) [55]. Yildiz and Wörgötter [5] reported their custom deep learning model was able to achieve an AP of 80.23% on a testing dataset compared to the 66.47% YOLO v3 was able to do. DiFilippo and Jouaneh [56] tested multiple laptops using contour and blob detection, and the accuracy of detection was based on the color of the laptop and vision system settings. The system performed the best on lighter laptops and detected 86.7% of screws, and the fastest computer vision time was 6.5s per screw. For laptops that had darker cases, the percentage of screws that were correctly identified decreased. The work presented in this paper has a higher percentage, as the best-trained model (Model C) has an AP of 92.60% on Test Set A, 99.20% on Test Set B, and 98.39% on Test Set C. It was also faster than previous systems that reported the time it took to detect a screw [4,55], as one frame took approximately 0.4s to process.

5. Conclusions

In conclusion, fastener detection is a required step for CV based robotic disassembly and servicing applications. The use of DL for this task offers several advantages to classical CV techniques, including higher detection speed and performance. Fasteners typically occupy a small portion of an image, so it is important to use a high-resolution NN to capture maximum detail when detecting images. It is desirable to find the optimal compromise between input resolution and mini-batch size for a given NN as both parameters are dependent on available GPU resources.

This paper presents a method for determining the optimal compromise between input resolution and mini-batch size for CRS detection while utilizing maximum GPU resources. An optimal compromise for an NVidia Tesla V100 GPU with 32 GB of RAM was found with a mini-batch size of 16 and an input resolution of 1664 x 1664 pixels. At this

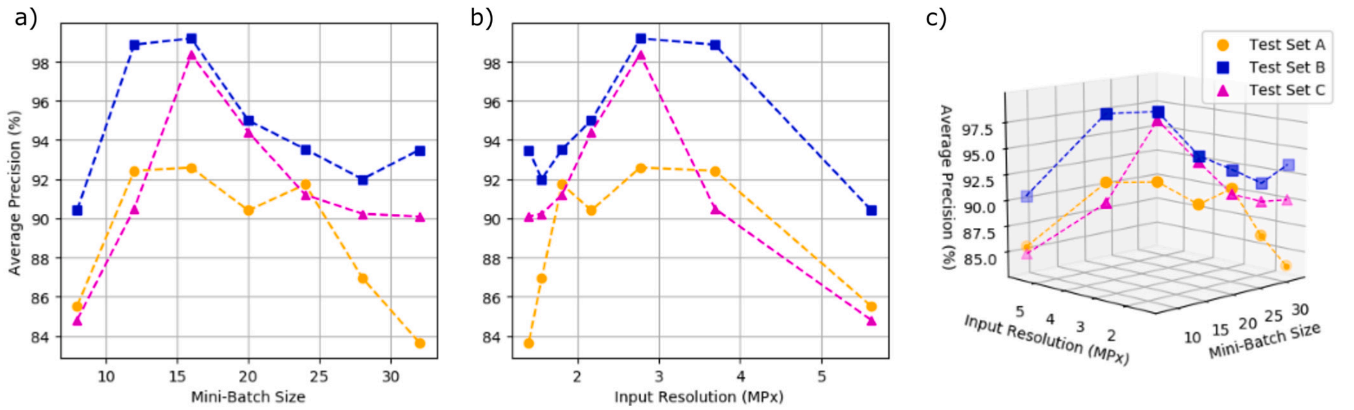

Fig. 7. (a) AP vs. mini-batch size for all test sets (b) AP vs. input resolution for all test sets (c) AP reported as a function of input resolution and mini-batch size for all test sets.

Table 5
Comparison of screw detection with previous results.

Authors	Accuracy (%)	Detection time (s)
Wegener et al. [6]	50	Not reported
Vongbunyong et al. [54,55]	>80 [54] 82.32 (False Positive) [55] 35.78 (False Negative) [55]	2.60
Yildiz and Wörgötter [5]	80.23 (custom DCNN) 66.47(YOLO v3)	Not reported
DiFilippo and Jouaneh [4]	86.7 (Light Laptop — Best Parameters)	6.7
Tiny-YOLO v2 (Model C)	92.6 (Test Set A) 99.20 (Test Set B) 98.39 (Test Set C)	0.4

configuration, Model C scored 92.60%, 99.20%, and 98.39% AP on Test Sets A, B, and C respectively. A limitation of the models in this paper is FPS must be sacrificed for such high input resolutions. While much faster than classical CV techniques, the fastest model in this paper ran at only around 3 FPS. These results from the best-performing model shows improvement over accuracy and detection time from previous models and approaches that have been presented in literature. Another limitation is the time spent upfront in manually creating a training dataset for the purpose of screw detection. Unless publicly available, the practitioner must generate their own training dataset for their specific application. For this reason, the authors have created a publicly available repository containing the manually generated datasets used in this paper. The repository may be accessed through the following link: https://github.com/Dan-Brogan/Cross-Recessed-Screw_Deep-Learning-Datasets.

Future work should include training a single Tiny-YOLO v2 network to detect multiple types of screws and even other useful features commonly found on electronics. Some considerations for multi-class detection include the requirement for additional training data on multiple object classes and the mAP metric should be used to evaluate performance in place of AP. It is hypothesized that the method used in this paper applies to any GPU; however, future work is needed to investigate this hypothesis. Future work should also investigate the integration of this CV system into a robotic test bed.

CRediT authorship contribution statement

Daniel P. Brogan: Methodology, Funding acquisition, Data curation, Formal analysis, Software, Visualization, Writing – original draft. **Nicholas M. DiFilippo:** Project administration, Supervision, Conceptualization, Writing – review & editing. **Musa K. Jouaneh:** Project administration, Supervision, Conceptualization, Writing – review & editing.

Declaration of competing interest

The authors declare that they have no known competing financial interests or personal relationships that could have appeared to influence the work reported in this paper.

Acknowledgments

The first author would like to acknowledge the NASA Rhode Island Space Grant (RISG) Consortium, USA for supporting his work on this project. The NASA RISG Consortium provided financial support independent of influencing the study design; collection, analysis, and interpretation of data; writing of the report; or in the decision to submit the article for publication. We also like to thank Harrison Decker and Indrani Mandal for providing access to the University of Rhode Island AI Laboratory GPU computing resources.

References

[1] Forti V, Baldé CP, Kuehr R, Bel G. The global e-waste monitor 2020. Tech. rep., Bonn/Geneva/Rotterdam: United Nations Univ., Int. Telecommun. Union & Int. Solid Waste Assoc. (ISWA); 2020.
[2] Sthiannopkao S, Wong MH. Handling e-waste in developed and developing countries: Initiatives, practices, and consequences. Sci Total Environ 2013;463:1147–53.
[3] Cui J, Forssberg E. Mechanical recycling of waste electric and electronic equipment: a review. J Hazard Mater 2003;99(3):243–63.
[4] DiFilippo NM, Jouaneh MK. A system combining force and vision sensing for automated screw removal on laptops. IEEE Trans Autom Sci Eng 2017;15(2):887–95.
[5] Yildiz E, Wörgötter F. Dcnn-based screw detection for automated disassembly processes. In: 15th Int. conf. signal-image technol. & internet-based syst. 2019, p. 187–92.
[6] Wegener K, Chen WH, Dietrich F, Dröder K, Kara S. Robot assisted disassembly for the recycling of electric vehicle batteries. Procedia CIRP 2015;29:716–21.
[7] Shan M, Guo J, Gill E. Review and comparison of active space debris capturing and removal methods. Prog Aerosp Sci 2016;80:18–32.
[8] Liou J-C. An active debris removal parametric study for LEO environment remediation. Adv Space Res 2011;47(11):1865–76.

[9] Hu H, Wang D, Gao H, Wei C, He Y. Vision-based position and pose determination of non-cooperative target for on-orbit servicing. Multimedia Tools Appl 2020;79(21):14405–18.

[10] On-orbit satellite servicing study project report. Tech. rep., Greenbelt, MD: National Aeronautics and Space Administration, Goddard Space Flight Center; 2010.

[11] Everingham M, Eslami SA, Van Gool L, Williams CK, Winn J, Zisserman A. The pascal visual object classes challenge: A retrospective. Int J Comput Vis 2015;111(1):98–136.

[12] Redmon J, Farhadi A. YOLO9000: better, faster, stronger. In: Proc. IEEE conf. comput. vis. pattern recognit. 2017, p. 7263–71.

[13] Thtrieu TH. Thtrieu/darkflow. 2019, [Online]. Available: https://github.com/thtrieu/darkflow. [Accessed 7 Nov. 2019].

[14] Chen H, He Z, Shi B, Zhong T. Research on recognition method of electrical components based on YOLO V3. IEEE Access 2019;7:157818–29.

[15] De Gregorio D, Tonioni A, Palli G, Di Stefano L. Semiautomatic labeling for deep learning in robotics. IEEE Trans Autom Sci Eng 2019;17(2):611–20.

[16] Li G, Song Z, Fu Q. A new method of image detection for small datasets under the framework of YOLO network. In: EEE 3rd Adv. Inf. Technol., Electron. Automat. Control Conf. 2018, p. 1031–5.

[17] Cartucho J, Ventura R, Veloso M. Robust object recognition through symbiotic deep learning in mobile robots. In: IEEE/RSJ int. conf. intell. robots and syst.. IEEE; 2018, p. 2336–41.

[18] Redmon J. Darknet: Open source neural networks in C. 2019, [Online]. Available: http://pjreddie.com/darknet. [Accessed 7 Nov. 2019].

[19] Krizhevsky A, Sutskever I, Hinton GE. Imagenet classification with deep convolutional neural networks. Adv Neural Inf Process Syst 2012;25:1097–105.

[20] Raj RJS, Shobana SJ, Pustokhina IV, Pustokhin DA, Gupta D, Shankar K. Optimal feature selection-based medical image classification using deep learning model in internet of medical things. IEEE Access 2020;8:58006–17.

[21] Zhao Z-Q, Zheng P, Xu S-t, Wu X. Object detection with deep learning: A review. IEEE Trans Neural Netw Learn Syst 2019;30(11):3212–32.

[22] Liu L, Ouyang W, Wang X, Fieguth P, Chen J, Liu X, et al. Deep learning for generic object detection: A survey. Int J Comput Vis 2020;128(2):261–318.

[23] Gupta A, Anpalagan A, Guan L, Khwaja AS. Deep learning for object detection and scene perception in self-driving cars: Survey, challenges, and open issues. Array 2021;100057.

[24] Lateef F, Ruichek Y. Survey on semantic segmentation using deep learning techniques. Neurocomputing 2019;338:321–48.

[25] Eitel A, Springenberg JT, Spinello L, Riedmiller M, Burgard W. Multimodal deep learning for robust RGB-D object recognition. In: IEEE/RSJ int. conf. intell. robots and syst. 2015, p. 681–7.

[26] Xu J, Zhou W, Chen Z, Ling S, Le Callet P. Binocular rivalry oriented predictive autoencoding network for blind stereoscopic image quality measurement. IEEE Trans Instrum Meas 2020;70:1–13.

[27] Kim Y, Moon T. Human detection and activity classification based on micro-Doppler signatures using deep convolutional neural networks. IEEE Geosci Remote Sens Lett 2015;13(1):8–12.

[28] Zhao Y, Cheng J, Zhou W, Zhang C, Pan X. Infrared pedestrian detection with converted temperature map. In: Asia-Pacific signal and information processing association annu. summit and conf. 2019, p. 2025–31.

[29] Guo Y, Liu Y, Oerlemans A, Lao S, Wu S, Lew MS. Deep learning for visual understanding: A review. Neurocomputing 2016;187:27–48.

[30] Pathak AR, Pandey M, Rautaray S. Application of deep learning for object detection. Procedia Comput Sci 2018;132:1706–17.

[31] Wei X, Yang Z, Liu Y, Wei D, Jia L, Li Y. Railway track fastener defect detection based on image processing and deep learning techniques: A comparative study. Eng Appl Artif Intell 2019;80:66–81.

[32] Zhang K, Wang W, Lv Z, Fan Y, Song Y. Computer vision detection of foreign objects in coal processing using attention CNN. Eng Appl Artif Intell 2021;102:104242.

[33] Zhang Y, Sun X, Loh KJ, Su W, Xue Z, Zhao X. Autonomous bolt loosening detection using deep learning. Struct Health Monit 2020;19(1):105–22.

[34] Wang Z, Li H, Zhang X. Construction waste recycling robot for nails and screws: Computer vision technology and neural network approach. Autom Constr 2019;97:220–8.

[35] Li Y, Zhao W, Pan J. Deformable patterned fabric defect detection with fisher criterion-based deep learning. IEEE Trans Autom Sci Eng 2016;14(2):1256–64.

[36] Ding C, Lu L, Wang C, Ding C. Design, sensing, and control of a novel UAV platform for aerial drilling and screwing. IEEE Robot Automat Lett 2021;6(2):3176–83.

[37] Zheng Y, Chen Z, Lv D, Li Z, Lan Z, Zhao S. Air-to-air visual detection of micro-UAVs: An experimental evaluation of deep learning. IEEE Robot Autom Lett 2021;6(2):1020–7.

[38] Chen WH, Wegener K, Dietrich F. A robot assistant for unscrewing in hybrid human-robot disassembly. In: IEEE int. conf. robotics and biomimetics. 2014, p. 536–41.

[39] Tan C, Sun F, Kong T, Zhang W, Yang C, Liu C. A survey on deep transfer learning, In: Int. conf. on artificial neural networks. 2018, p. 270–9.

[40] Wang C-C, Samani H. Object detection using transfer learning for underwater robot. In: Int. conf. advanced robotics and intelligent systems. 2020, p. 1–4.

[41] Raza K, Hong S. Fast and accurate fish detection design with improved YOLO-v3 model and transfer learning. Int J Adv Comput Sci Appl 2020;11:7–16.

[42] Montalbo FJP. A computer-aided diagnosis of brain tumors using a fine-tuned YOLO-based model with transfer learning. KSII Trans Internet & Inf Syst 2020;14(12).

[43] George J, Skaria S, Varun V, et al. Using YOLO based deep learning network for real time detection and localization of lung nodules from low dose CT scans. In: Medical imaging 2018: computer-aided diagnosis. vol. 10575, International Society for Optics and Photonics; 2018, p. 105751I.

[44] Al-Masni MA, Al-Antari MA, Park J-M, Gi G, Kim T-Y, Rivera P, et al. Simultaneous detection and classification of breast masses in digital mammograms via a deep learning YOLO-based CAD system. Comput Methods Programs Biomed 2018;157:85–94.

[45] Jia Z, Bhatia A, Aronson RM, Bourne D, Mason MT. A survey of automated threaded fastening. IEEE Trans Autom Sci Eng 2018;16(1):298–310.

[46] Lee NK, An Y, Tsung F. Studying effects of screw-fastening process on assembly accuracy. Int J Adv Manuf Technol 2005;25(5–6):493–9.

[47] Cherubini A, Passama R, Fraisse P, Crosnier A. A unified multimodal control framework for human–robot interaction. Robot Auton Syst 2015;70:106–15.

[48] Pitipong S, Pornjit P, Watcharin P. An automated four-DOF robot screw fastening using visual servo. In: IEEE/SICE int. symp. system integration. 2010, p. 379–83.

[49] Hu Z, Wan W, Koyama K, Harada K. A mechanical screwing tool for parallel grippers—Design, optimization, and manipulation policies. IEEE Trans Robot 2021.

[50] Bolmsjö G. Supporting tools for operator in robot collaborative mode. Procedia Manuf 2015;3:409–16.

[51] Matsuno T, Huang J, Fukuda T. Fault detection algorithm for external thread fastening by robotic manipulator using linear support vector machine classifier. In: IEEE int. conf. robotics and automation. 2013, p. 3443–50.

[52] Li R, Pham DT, Huang J, Tan Y, Qu M, Wang Y, et al. Unfastening of hexagonal headed screws by a collaborative robot. IEEE Trans Autom Sci Eng 2020;17(3):1455–68.

[53] Gil P, Pomares J, Diaz SvPC, Candelas F, Torres F. Flexible multi-sensorial system for automatic disassembly using cooperative robots. Int J Comput Integr Manuf 2007;20(8):757–72.

[54] Vongbunyong S, Kara S, Pagnucco M. Basic behaviour control of the vision-based cognitive robotic disassembly automation. Assem Autom 2013.

[55] Vongbunyong S, Kara S, Pagnucco M. Learning and revision in cognitive robotics disassembly automation. Robot Comput Integr Manuf 2015;34:79–94.

[56] DiFilippo NM, Jouaneh MK. Using the soar cognitive architecture to remove screws from different laptop models. IEEE Trans Autom Sci Eng 2018;16(2):767–80.

Industrial control system device classification using network traffic features and neural network embeddings

Abhishek Mohanty, *Department of Electrical and Electronics Engineering, Aryan Institute of Engineering & Technology, Bhubaneswar, abhishekmohanty226@gmail.com*

Pranay Rout, *Department of electrical Engineering , NM Institute of Engineering & Technology, Bhubaneswar, pranayrout93@gmail.com*

Romeo Jena, *Department of Electrical and Electronics Engineering, Capital Engineering College, Bhubaneswar, romeo_jena2@hotmail.com*

Madhusudan Das, Department of Electronics and Communication Engineering , Raajdhani Engineering College, Bhubaneswar, madhusudandas55@hotmail.com

ARTICLE INFO

Keywords:
Industrial Control Systems
SCADA
Device classification
Machine learning
Neural network embeddings
DNP2Vec

ABSTRACT

Characterization of modern cyber–physical Industrial Control System (ICS) devices is critical to the evaluation of their security posture and an understanding of the underlying industrial processes with which they interact. In this work, we address two related ICS device identification tasks: (1) separating ICS from non-ICS devices and (2) identifying specific ICS device types. We propose two distinct methods (one based on the existing IP2Vec method, and a novel traffic-features-based method) for achieving the first task. For transferability of the first task between two datasets, the traffic-features-based method performs significantly better (75% overall accuracy) compared to IP2Vec (22.5% overall accuracy). We further propose a novel method called DNP2Vec to address the second task. DNP2Vec is evaluated on two different datasets and achieves perfect multi-class classification accuracy (100%) for both datasets.

1. Introduction

Industrial Control Systems (ICS) are a general class of structures that carry out the automation of industrial processes. Some particularly complex and critical forms of ICS are those that support the processes of electricity generation, transmission and distribution, oil and natural gas extraction, transportation and delivery, and water distribution and treatment. Vast collections of physical devices, consisting of various sensing and actuation mechanisms, in combination with general-purpose computing devices, comprise cyber–physical systems that manifest within these types of modern critical infrastructure.

While these cyber–physical systems enable new paths towards improved efficiency, opportunities for misuse and abuse are increased due to the interconnections between mechanical devices that affect the real world and conventional communication networks. Consequently, intrusion and vulnerability analysis techniques which are relatively common in information technology networks, are being developed for ICS.

A broad goal of our ongoing work is to develop machine learning approaches that support the discovery and prediction of ICS network and host properties. In particular, we seek to discover the manufacturer, model number, and process-oriented behavior of cyber–physical ICS devices in a way that does not disturb the critical infrastructure process. While this process of passively "mapping" a network is not new, existing tools for mapping conventional computer networks are ill-suited to ICS networks due to a few factors: (1) active probing of ICS devices is often prohibited in production environments, (2) ICS networks make use of specialized application layer protocols that support a wide range of industrial processes, and the payloads of these protocols should be exploited in any ICS network mapping scheme, and (3) as new protocols are introduced, existing signature or rule-based tools must be updated to accommodate the protocol semantics; i.e. they must be explicitly programmed to recognize and interpret new protocols. Thus, an important underlying goal is the development of techniques that utilize passively collected ICS network traffic to enable characterization of ICS devices, which ultimately can be used to assess the security of a system.

Properties of ICS hosts can be used for a variety of critical infrastructure security-oriented applications. For example, critical infrastructure asset owners are often interested in verifying that the actual composition of their networks matches their current understanding. While ICS networks are often quite static by design, the addition, removal or modification of hosts – whether intentional due to upgrades or retirement of legacy systems, or unintentional due to a security breach – needs to be tracked. Often times, this exercise takes the form of periodic security assessments which utilize basic network flow information, including host IP addresses and source/destination ports, as the primary keys for host identification. Intuitively, the duration of analysis activities during these assessments is a function of the size of the network under study, the available analysis staff, and the capability of the tools employed. Properties of hosts automatically inferred by machine learning methods, such as whether a host is an ICS device, and if so what is the manufacturer and model number of the device, can both enhance asset identification fidelity and potentially decrease the analysis staffing requirements. This has the overall effect of improving the security assessment process for both small and large networks.

In this paper, we propose machine learning techniques for identifying ICS network flows as well as distinguishing specific types of ICS devices. Firstly, in the ICS vs. non-ICS classification task, we propose two methods, namely a method based on the IP2Vec [1] technique, and a traffic-features-based method. Moreover, we show that the traffic-features-based method is better in an "across-network" transfer-learning setting, and that both of these methods are insensitive to observation window length as long as it is "long enough" (at least 1 h). Secondly, for the ICS device type classification task, we propose a novel method called DNP2Vec, an embedding of DNP3 features that improves classification performance. DNP3 (Distributed Network Protocol, version 3) is a communications protocol used by devices in the kinds of controls systems employed, for example, by electric utilities.

This paper is structured as follows. In Section 2, we introduce the dataset and then formally introduce the problems we solve in this paper. Section 5 describes our two proposed methods used to solve the flow classification problem, along with the comparison of these two methods with the baseline. In Section 6, we evaluate the optimal data collection time required to achieve a desired classification accuracy. Finally in Section 7, we propose a new method for device classification and compare the classification performance with the baseline method.

1.1. Related work

Machine learning (ML) for ICS and Supervisory Control and Data Acquisition (SCADA) applications is an area of active research. Prior work in this area spans a variety of applications, including attack detection [2–5], failure/event prediction [3,6], adaptive control [7,8], and anomaly detection [4,5,9–11].

Work applying ML to SCADA network and device characterization appears to be sparse, likely inspired by early work on flow classification for IT systems [12]. In this work, the authors applied a Bayesian classifier to network flow statistics (packet inter-arrival time, packet length, mean and variance, flow size, and duration) to classify conventional Internet network flows as belonging to specific application classes (i.e. FTP, Telnet, DNS, HTTP, etc.). Feature selection was based on classifier performance, and reasonable classification accuracy was obtained across multiple network trace files. While this work established a workflow model for network flow classification, it was not applied to ICS network data, nor did the authors focus on identifying the characteristics of the network hosts themselves.

An assessment of the applicability of standard device fingerprinting techniques for ICS was undertaken several years later in [13]. This work analyzed traditional fingerprinting methods and assessed their applicability to ICS environments. The authors began by reviewing common device fingerprinting techniques and describing a new reference architecture for fingerprinting tools; manual creation and maintenance of fingerprints was cited as a major shortcoming of existing fingerprinting tools. Standard fingerprinting techniques were then tested and shown to be ineffective at identifying ICS devices, with the primary reasons being device heterogeneity, the use of proprietary protocols, low computational power, and the use of long-running TCP sessions. The authors recommended exploring the exploitation of temporal communication patterns and passive traffic capture techniques to classify ICS device component types and mentioned the use of ML to address the fingerprint creation and maintenance issue.

Following the fingerprinting assessment work, an effort was undertaken to characterize industrial control systems on the Internet [14]. In this work, active probes for 17 different ICS protocols were used to gather data from network hosts, which was then processed by a signature-based matching algorithm to identify ICS devices. A naïve Bayes classifier was also used to distinguish between real ICS devices and ICS honeypots. The classifier was trained on 281 devices and 16 honeypots, utilizing a feature set consisting of the number of open ports, the HTTP configuration, and two protocol-specific features (ModBus and S7 function codes). This mechanism was then applied to Internet hosts to determine location, ownership and functional characteristics of Internet-connected ICS devices, with reasonable accuracy. The authors recognized that the active probing method may be harmful to real ICS devices, and they implemented a heuristic that attempts to minimize the number of active probes send to a host. While this work makes progress towards distinguishing between ICS and non-ICS hosts, active probing methods are typically forbidden in live ICS networks and thus likely inapplicable to most industrial environments.

In the same year, [15] introduced two passive, ML-oriented fingerprinting methods for ICS devices in electric SCADA systems. The first, network-oriented, method exploits data response processing times of three common ICS protocols to identify ICS device types. The authors defined a "Cross-Layer Response Time" feature that captures the time delta between receiving a TCP ACK and an application layer response from a device. The second, physics-based, method exploits the physical operation times of devices. This method relies on physical operation timing differences between device vendors due to different methods of physical construction and is based on dynamic models of device hardware. These two methods were then evaluated in the context of supervised and unsupervised ML methods, and applied to real-world data, resulting in high device classification accuracy. This work makes significant progress towards the exploitation of network and physical features for ICS device classification. However, the Cross-Layer Response Time feature may not always be available for measurement due to transport-layer acknowledgments being incorporated into application layer response messages, a common method that TCP/IP stacks use to save bandwidth. Likewise, accurate and validated dynamic models of device hardware are needed to facilitate the physics-based fingerprinting approach, which is a manual and time-consuming effort; the authors recognize this and propose a hybrid black/white box ("grey box") modeling approach to address this issue.

Recently, much focus has been placed on characterization of IoT devices. For example, in [16,17], the authors explored fingerprinting for IoT and ICS devices. These works utilized active probing of Internet hosts, and feature sets based on network, transport and application layer characteristics. The study undertaken in [16] is similar in form to [14] but utilized a broader feature set and an Artificial Neural Network (ANN) model as opposed to a Bayesian classifier. Similarly, [17] utilized an ANN, but devised a feature set based on HTTP responses. Both efforts report reasonable accuracy in identifying device type and vendor. However, as mentioned earlier, methods that rely on active probing are often forbidden in industrial environments. Furthermore, feature sets based on HTTP responses may not be available for ICS devices due to disablement of HTTP services to reduce the device attack surface.

Recent work has also been undertaken that utilizes network traffic features. In [18], high accuracy classification of six different types of network video traffic was performed using two novel feature fusion methods, including computed network flow statistics. [19] proposed a method to extract signatures to identify different classes of network traffic, based on packet length statistics, and obtained 91% accuracy with a decision-tree classifier. Finally, [20] proposed a learning automata method to select network traffic features for a network intrusion detection system, and found that a SVM combined with their feature selection method obtained an intrusion detection rate of 93.8%. This work exemplifies the importance of network traffic features when characterizing network traffic across a variety of applications.

While our work is most closely related to both network host fingerprinting and network flow classification using traffic features, we propose a different approach that augments an existing, well-known machine learning method; this augmentation exploits both network flow statistics and ICS protocol application layer payload data in a hierarchical manner to produce high accuracy in determining whether a network host is an ICS device and, if so, the type of the device. This method allows ICS device characterization to be performed without explicitly programming for the protocol semantics as is typical for existing rule-based or signature/fingerprint-oriented methods. Furthermore, since we are concerned with automating this characterization process in a passive and unobtrusive manner, our method operates on passively collected network traffic only and does not require probing of network hosts.

1.2. Contribution of this paper

In this paper we propose a lower dimensional neural network embedding based framework, DNP2Vec. This framework utilizes the training fundamentals of Word2Vec [21], and improves upon the existing IP2Vec [1] method by incorporating features based on ICS protocol fields in the embedding process. The primary contribution of this paper is the successful use of ICS protocol features for device classification, through a lower dimensional embedding. We focused on the DNP3 ICS protocol in this work primarily due to data availability; however, this framework can be extended to other ICS protocols as well, and we discuss this briefly in Section 8.

Furthermore, we propose another method named the "traffic-feature" based method for ICS and non-ICS device classification, which uses network traffic features for classification. The traffic-feature based method utilizes network flow statistics for classification and is shown to be transferable between different ICS networks, unlike DNP2Vec which is shown to be ICS network specific and needs retraining when transferring to another ICS network.

The next section formally describes the machine learning tasks and the characteristics of the data sets used to evaluate the machine learning methods.

2. Dataset and problem description

A network flow is a sequence of packets from a specific source computer to a specific destination computer. Network flows from two separate and distinct systems were utilized for this work. The first system (Site A) is a production-level industrial electrical distribution system. The second system (Site B) is a non-production cyber–physical testbed. Network flow datasets were generated for each system by processing passively captured network traffic in PCAP form. Table 1 describes the endpoints of the distinct network flows present in both systems. Table 2 briefly describes the ICS devices present in these systems.

We begin by defining two data-collection related time parameters.

Nomenclature 1. ***Total Data Collection Time*** *(T) is the total duration of the PCAP data collection period.*

Nomenclature 2. ***Flow Observation Window*** *(ΔT) is the duration of each network flow.*

Both datasets consist of flow-based network data associated with the device types, such as their IP addresses, port numbers, protocol types, transferred bytes, etc. The datasets consist of a mixture of various data types, such as numeric (e.g., transferred bytes) and categorical (e.g., IP addresses) types. These datasets can be used to characterize different device types, which can then be used to identify and verify new devices that are introduced in the device network. If signatures can be developed for different devices in the ICS setting, it may be possible to translate passively collected network data into a network map of interconnected devices.

In this work, we propose a framework to identify different types of ICS devices present in a SCADA network. This comprises two distinct tasks, namely: separating ICS devices from non-ICS devices, and classifying the ICS devices. For the first task, we propose two distinct methods to distinguish ICS devices from non-ICS devices in a SCADA network. We pose this as a binary classification task, and propose two separate methods to obtain relevant features for classification. For the second task, we propose a novel framework which utilizes DNP3 fields and their embedding as features. The second task is posed as a multi-class classification task. Now we formally introduce the two tasks.

Table 1
Distinct flow types present in the dataset.

Site A	Site B
SEL-2240 → server	NI controller → unknown
server → SEL-2240	PDU → PDU
server → server	PDU → unknown
server → unknown	SEL-2414 → workstation
unknown → server	SEL-2740 → PDU
unknown → unknown	SEL-351A → unknown
workstation → SEL-735	unknown → workstation
workstation → SEL-751	workstation → SEL-351A
workstation → SEL-787	workstation → unknown
workstation → unknown	

Table 2
ICS device type and description.

Device Type	Description
SEL-2240	Modular Real-Time Automation Controller
SEL-735	Power Quality and Revenue Meter
SEL-751	Feeder Protection Relay
SEL-787	Transformer Protection Relay
SEL-2414	Transformer Monitor
SEL-2740	Software-Defined Network Switch
SEL-351A	Protection System
PDU	Power Distribution Unit

Task 1 (*ICS Flow Classification*)**.** *Given a network flow, determine whether it is an ICS flow (i.e., one or more endpoints is an ICS device) or a non-ICS flow (no ICS endpoints).*

For this task, we vary a number of important experimental parameters. Specifically, we investigate the effects of two generalization scenarios and two data collection parameters.

Generalization scenario: We evaluate Task 1 in both the within-network setting (train on Site A, test on Site A) and across-network setting (train on Site A, test on Site B).

Data collection parameters: For Task 1, classifier performance is affected by various data collection parameters. In this study, we quantify the effects of two specific data collection parameters on classifier performance: (1) total data collection time (T), (2) flow observation window (ΔT).

Task 2 (*ICS Device Classification*)**.** *Given all of the flows for an ICS device, determine the specific type of the ICS device.*

The complete framework is schematically shown in Fig. 1. Before describing the framework, we describe the experimental setup used for generating results related to all of the classifiers' training and testing.

2.1. Experimental setup

Throughout this paper, unless otherwise mentioned, we used standard k-fold cross validation ($k = 100$) to evaluate generalization performance of our classification methods.

3. Description of IP2Vec and DNP2Vec

IP2Vec and DNP2Vec are based on the Word2Vec algorithm for natural language processing [21]. Before describing the fundamentals of IP2Vec [1] and our DNP2Vec method, we introduce a few definitions.

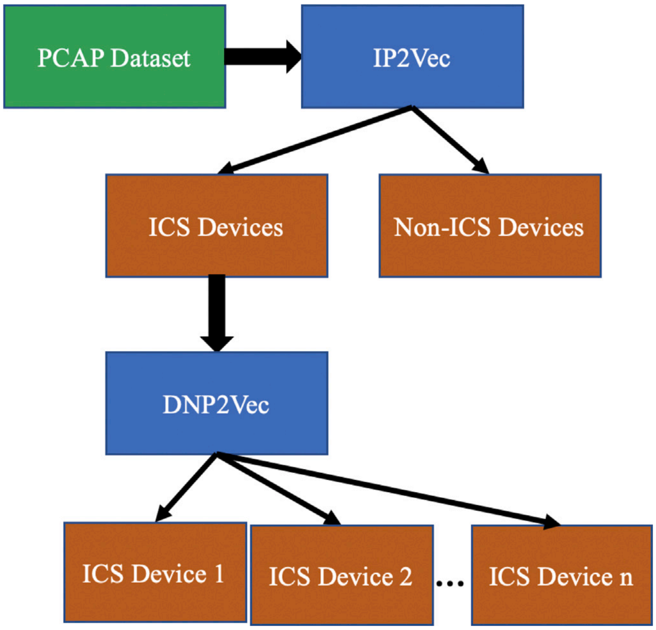

Fig. 1. Schematic of the overall proposed framework.

Definition 1 (*Definition of Corpus (w)*)**.** Similar to Word2Vec, an IP2Vec corpus consists of a collection of unique source IP addresses, destination ports and network protocols. A DNP2Vec corpus consists of unique source IP addresses.

Definition 2 (*Definition of Context (c)*)**.** Similar to Word2Vec, the context for each element in the corpus is defined as follows:

(1) For IP2Vec, the context for the source IP address corpus element is either destination IP address, destination port, or protocol,

(2) For IP2Vec, the context for the destination port corpus element is destination IP address,

(3) For IP2Vec, the context for the protocol corpus element is destination IP address,

(4) For DNP2Vec, the context for the source IP address corpus element is either destination IP address, destination MAC address, or DNP3 fields.

Definition 3 (*The Skip-gram Model*)**.** In this model we are given an element of corpus w and their contexts c. We consider the conditional probabilities $p(c|w)$, and given a corpus element, the goal is to set the parameters θ of $p(c|w;\theta)$ so as to maximize the corpus probability:

$$\arg\max \prod_{w \in \text{corpus element}} [\prod_{c \in C(w)} p(c|w;\theta)]$$

$C(w)$ indicates the context of the corpus element (as defined in Definition 2).

Now we parameterize the conditional probability of the skip-gram model defined in Definition 3 as

$$p(c|w;\theta) = \frac{\exp(v_c \dot{v}_w)}{\sum_{c' \in C} \exp(v_{c'} \dot{v}_w)}$$

where $v_c, v_w \in \mathbb{R}^d$ is the d-dimensional vector representation of the context, and the corpus element, respectively. The parameters θ are v_{ci} and w_{ci}, $i = 1, 2, \ldots, d$, which are solved to maximize the corpus probability defined in Definition 3.

4. Description of network traffic features

Network traffic was attributed to one of six different protocol groups: ARP, TCP/IP, DNP3, HTTP, TLS, and UDP. Before calculating

Table 3
Feature list per protocol per direction. In the 'Symbol' column 'a' is either sent or received, representing each direction of flow.

Description	Symbol
Number of packets	a_num_packets
Volume of bytes transferred	a_vol_bytes
Packet inter-arrival time- Average (Mean)	a_pinterarr_avg
Packet inter-arrival time- Minimum	a_pinterarr_min
Packet inter-arrival time- Maximum	a_pinterarr_max
Packet inter-arrival time- Standard Deviation	a_pinterarr_stdev
Packet size- Average (Mean)	a_psize_avg
Packet size- Minimum	a_psize_min
Packet size- Maximum	a_psize_max
Packet size- Standard Deviation	a_psize_stdev

the traffic features, the packets within each flow were subdivided according to these protocol types. Originally, LLDP was also included as one of the protocol groups, however, LLDP is a link-layer protocol and encapsulates Ethernet addresses only (no IP addresses). Thus, attributing this traffic to existing flows relied upon a pre-computed Ethernet to IP address mapping. Ten standard traffic features were selected for this classification task, shown in Table 3.

Traffic features are calculated for each captured network flow. These traffic features represent various statistics of the network flow, such as the total number of transferred packets, packet arrival time, packet size, etc. Network flows are captured for the collection time T, and traffic features are calculated during the flow observation window ΔT. Therefore, if the total data collection time T comprises N flow observation windows ΔT, where $N \in \mathbb{Z}^+$, then there will be 20 traffic features associated with each observation window (ten features in the send direction, and ten features in the receive direction).

The extracted traffic features are used as the feature set for classifying ICS and non-ICS devices. Therefore, the feature set will have a dimension of $\mathbb{R}^{N \times 20}$. We used a support vector machine (SVM) binary classifier for this task.

5. ICS vs. non-ICS device classification, solution of Task 1

Here we evaluate two approaches to separating ICS and non-ICS traffic, one based on IP2Vec as described in Section 3 and one based on network traffic features. We also compare to a baseline method based on PCAP flow features.

We collected the PCAP dataset for Site A with $T = 1$ h, $\Delta T = 10$ s, and for Site B with $T = 0.5$ h, $\Delta T = 10$ s. The difference in data collection time for Site A and Site B is due to each site having a different optimal collection time, as described in Section 6. Throughout this paper, if not explicitly mentioned, the data collection time is 1 h and 0.5 h, for Site A and Site B, respectively. The true labels for classifier training and evaluation were captured using the constant source port number associated with ICS flows. We used the experimental setup described in Section 2.1.

5.1. Baseline performance

Our baseline method is a binary SVM classifier trained using the following features: IP addresses associated with the source and destination devices, destination port number, protocol, and transferred bytes. The baseline classification performance was tested on both the Site A and Site B datasets and compared to the performance of our proposed methods.

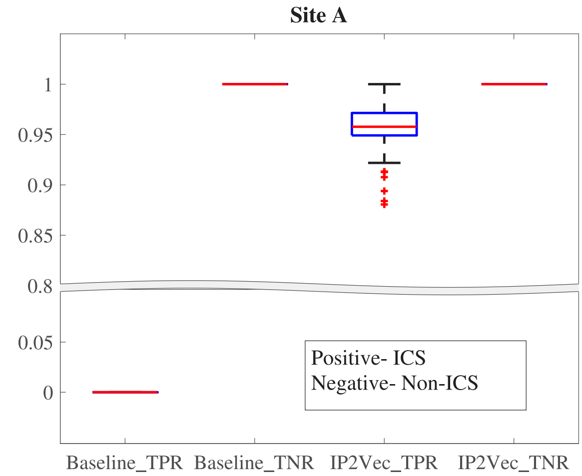

Fig. 2. Baseline and IP2Vec performance for ICS vs. non-ICS device classification, for Site A.

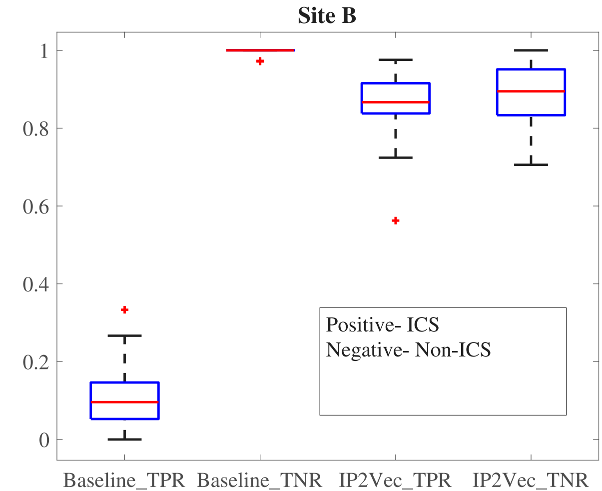

Fig. 3. Baseline and IP2Vec performance for ICS vs. non-ICS device classification, for Site B.

5.2. Classification using IP2Vec

In this section, we use IP2Vec, described in Section 3, for classifying ICS and non-ICS devices in the Site A and Site B datasets. For example, for each defined flow between a source and a destination device, using the IP2Vec training process discussed previously, our input will have a dimension of 500 (where the IP2Vec training batch size is 100) and a size of 60 is selected for the hidden dimension ($d = 60$ in accordance with the notation in Section 3). After successful training of the IP2Vec architecture, we use the embedding of the training sample from the hidden layer as features for training the SVM classifier.

Classification Performance Comparison: We compared the baseline performance (described in Section 5.1) with IP2Vec (described in Section 5.2) for the first classification task (Task 1) between ICS devices and non-ICS devices, applied to the Site A and Site B datasets. In Fig. 2, the boxplots are shown for the baseline and IP2Vec classification performance with the true positive (ICS devices) rate and the true negative (non-ICS devices) rate. The classification baseline fails to identify ICS devices (as shown by the boxplot in Fig. 2), unlike IP2Vec, which is able to classify ICS devices with a true positive rate of 0.95. Similarly, for the Site B dataset, we compared the baseline performance with IP2Vec as shown in Fig. 3. For the Site B dataset, the baseline method is able to classify ICS devices with a true positive rate of 0.1, unlike IP2Vec which gives a true positive rate of 0.88. We also evaluated the F1 score between IP2Vec and the baseline method for a class-independent comparison for Site A and Site B datasets as shown in Table 4. For Site A, baseline provides a F1 score of 0 compared to 0.974 for IP2Vec. Similarly, for Site B, baseline provides a F1 score of 0.18, when IP2Vec provides a F1 score of 0.91.

Visually, the classification performance using a two-dimensional t-SNE plot for the Site A test dataset is shown in Fig. 4. IP2Vec outperforms the baseline method significantly for classifying ICS devices and non-ICS devices. For the Site B dataset, similar performance is observed when comparing the IP2Vec and baseline methods.

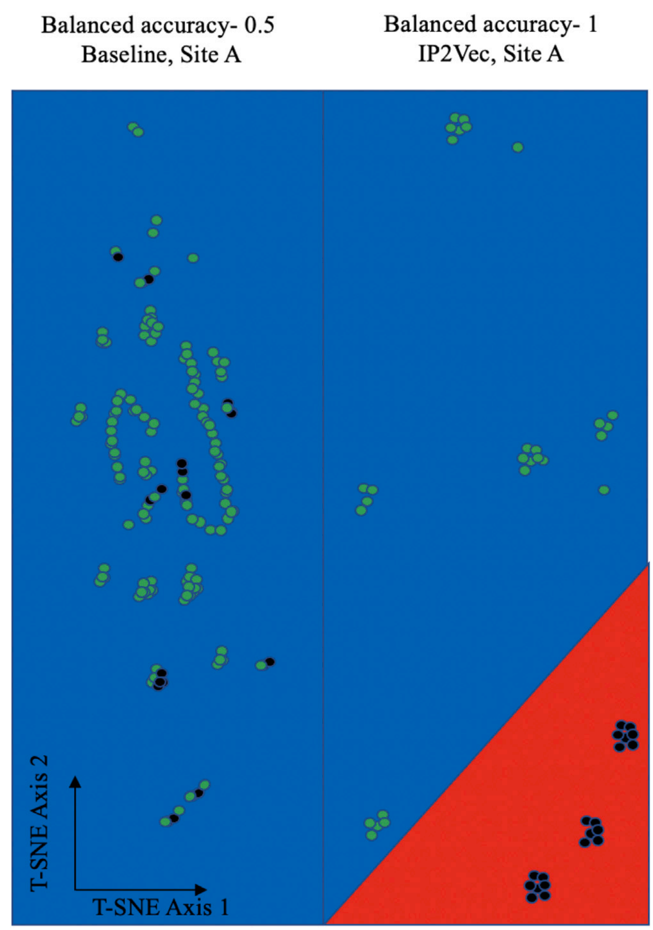

Fig. 4. t-SNE visualization-based comparison of baseline and IP2Vec methods for ICS and non-ICS device classification on a testing dataset from Site A, using a SVM with a linear kernel. For visual clarity, these plots are generated on 10% of the dataset. Green dots represent non-ICS devices and black dots represent ICS devices. IP2Vec with a linear SVM kernel and IP2Vec with a polynomial SVM kernel yield 100% and 84% classification improvement compared to baseline, respectively. Similar classification performance is observed for the Site B dataset, and the t-SNE plots are omitted for brevity.

5.3. Classification using traffic features

Before describing this method, the traffic features considered for classification will be introduced.

Classification Performance Comparison: The traffic features in Table 3 were calculated for the Site A and Site B datasets, with ΔT = 10 s for both. For both of the datasets, the experimental setup is considered as discussed in Section 2.1. For the Site A training data, the comparison between the baseline classifier (Section 5.1) and the traffic-features-based methods is shown in Fig. 5. As shown in Fig. 5, the baseline classifier completely misclassifies ICS devices, while the traffic-features-based method able to achieve a true positive rate 1 (complete

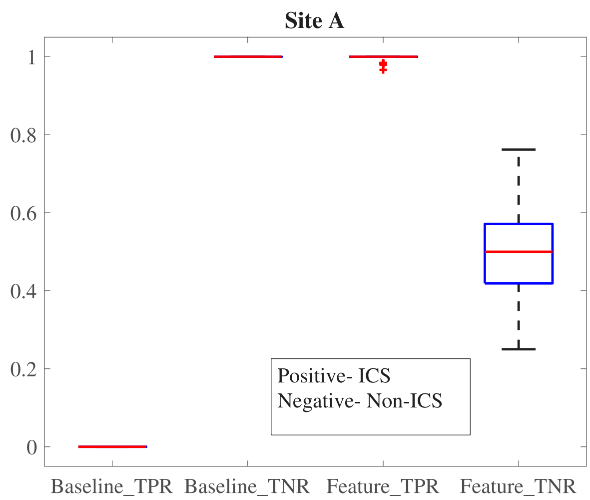

Fig. 5. Baseline performance and traffic-features-based performance for ICS vs. non-ICS device classification, for Site A.

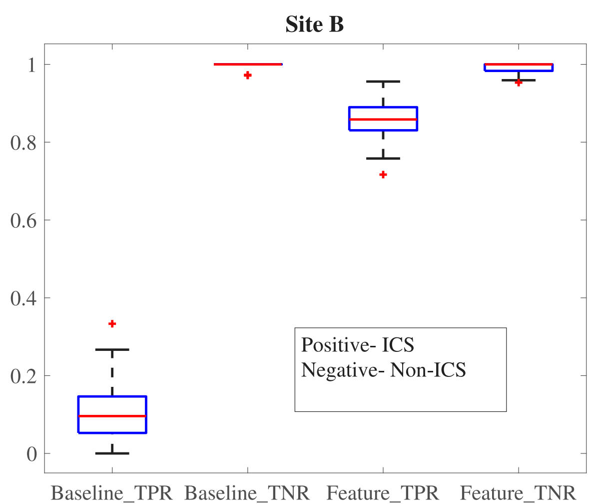

Fig. 6. Baseline performance and traffic-features-based performance for ICS vs. non-ICS device classification, for Site B.

classification) for ICS devices. However, the baseline method is able to completely classify non-ICS devices, unlike the traffic-features-based method, which only achieved a true negative rate of 0.5 for non-ICS devices. As shown in Table 4, the F1 scores of the baseline and traffic-features-based methods are 0 and 0.8, respectively.

Similarly, in Fig. 6 we plot an accuracy comparison between the baseline and traffic-features-based methods applied to the Site B training data. As shown in Fig. 6, the baseline method is able to achieve classification accuracy of 0.1 and 1 for ICS devices and non-ICS devices, respectively, with a total F1 score of 0.18. On the other hand, the traffic-features-based method achieves classification accuracy of 0.9 and 0.98 for ICS devices and non-ICS devices, respectively, with a total F1 score of 0.89. Finally, in Table 4 we tabulated four different performance metrics, TPR (true positive rate), TNR (true negative rate), F1 score and class-balanced accuracy, in the context of our proposed methods and the baseline method. Although both the proposed methods perform better in all metrics when comparing with the baseline method, IP2Vec performs better than the traffic-features-based method.

The traffic-feature based method performs better than the baseline method, for both the site datasets, due to the appropriately selected classification features (i.e. the packet size, packet inter-arrival time, etc.). Similarly, IP2Vec performs better than the traffic-feature based

Table 4
Performance comparisons of two proposed methods for ICS vs. non-ICS classification, compared to the baseline method. The results of the best performing method for both the datasets are boldfaced.

	TPR	TNR	F1 score	Balanced Accuracy
Site A (Baseline)	0	1	0	0.5
Site A (IP2Vec)	**0.95**	**1**	**0.974**	**0.975**
Site A (Traffic-feature)	1	0.5	0.8	0.755
Site B (Baseline)	0.1	1	0.18	0.55
Site B (IP2Vec)	**0.9**	**0.92**	**0.91**	**0.91**
Site B (Traffic-feature)	0.82	0.98	0.89	0.9

method due to the traffic-flow based embedding as demonstrated by IP2Vec in Section 3. Moreover, IP2Vec performs better than the traffic-feature based method for both sites, due to the associated lower dimensional embedding for the network flows as in the IP2Vec method, which provides better classification features than the traffic-feature based method.

Ranking of Features: In this section we will evaluate the importance of the features described in Table 3, in the context of ICS ad non-ICS traffic classification. For ranking the features, we used Recursive Feature Elimination (RFE, [22]) with a support vector classifier and a linear kernel as the estimator. The three most important features of the Site A and B datasets, as ranked by RFE, are the minimum value of received packet size (rcvd_psize_min), and the minimum and standard deviation of sent packet inter-arrival time (sent_pinterarr_min, sent_pinterarr_stdev). In Figs. 7 and 8, we have plotted the six highest priority features as a function of time, for both ICS and non-ICS flows, for Site A and Site B, respectively. These plots show the same conclusion regarding the feature ranks as found using RFE, for both the datasets. Figs. 7 and 8 also show the least important features in the context of Task 1, which is 'rcvd_vol_bytes' for both the datasets. These feature ranks will be useful in defining the transferability of classifying ICS and non-ICS devices, as mentioned in Section 5.4. In Section 5.4, we show that if two datasets share a similar feature ranking (as in the Site A and Site B datasets), then the classifier trained to distinguish ICS and non-ICS devices on one dataset will perform adequately on the other dataset. Also, the more similar the feature ranks are within the two datasets, the better the classifier will perform when transferring from one dataset to another.

5.4. Transferability

We trained a SVM classifier with a 10th order polynomial kernel, which uses the calculated network features for one dataset and tests on another dataset, to evaluate if the classifier is transferable and how well it performs ICS device vs. non-ICS device classification. For demonstrating transferability, we selected two scenarios. The first scenario uses network traffic features and flows from the Site A training dataset to train a SVM classifier, and tests the trained classifier on the Site A test dataset. The second scenario involves the same training step as the first scenario, but tests the trained classifier on the traffic flows from the Site B test dataset. In traffic flow calculations, T and ΔT play major roles, so for this transferability experiment, we kept ΔT constant at 10 s, while varying T from 0.1 to 2 h, with an interval of 10 min. The objective is to show if the transferability (defined here by the classifier's performance) changes while changing the total data collection time, defined by T. In Fig. 9 , the two subplots show the true positive and true negative

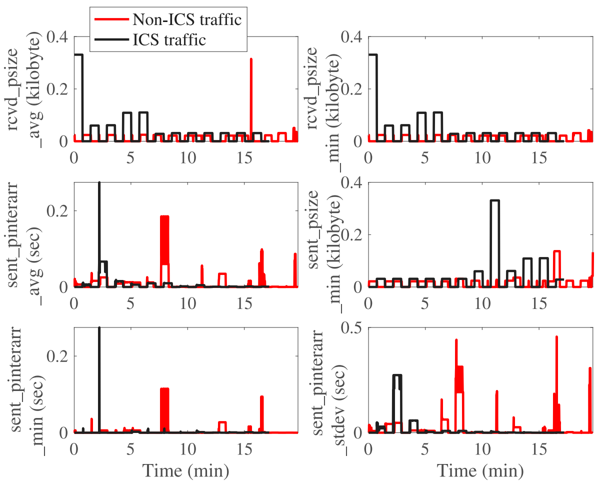

Fig. 7. Time series plots of ICS and non-ICS traffic related to the top six important features for Site B.

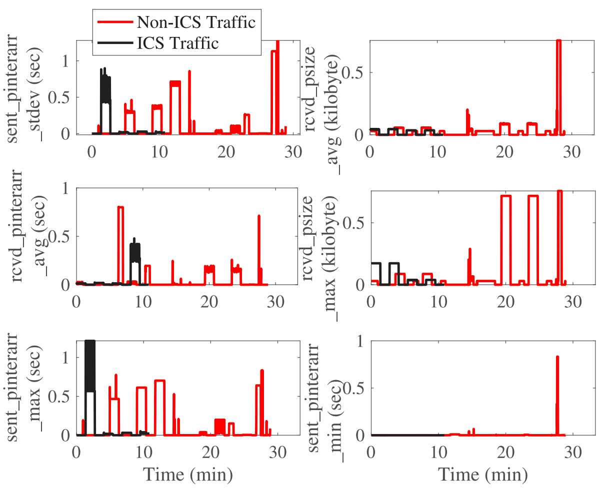

Fig. 8. Time series plots of ICS and non-ICS traffic related to the top six important features for Site A.

rates (here positive indicates ICS devices and negative indicates non-ICS devices), where the red and blue colors indicate the test dataset to be either Site B or Site A, respectively. Compared to the blue line (no-transfer), the red line (transfer) yields around a 0.25 reduction in true positive rate and a 0.07 reduction in true negative rate. Furthermore, for both transfer and no-transfer cases, both the rates saturate after a T value of 1 h, which further shows our previous claim of having 1 h of data with $\Delta T = 10$ s to be optimal.

Based on the findings from Figs. 7 and 8, we chose the three important features in common between Site A and Site B for classifying ICS and non-ICS flows. The feature ranking shows that Site A and Site B do not share the feature ranking for classifying ICS and non-ICS flows; this justifies the drop in classification accuracy between the transfer and no-transfer cases as shown in Fig. 9. As shown in Fig. 11, the two subplots show that by adding three extra features (based on the feature ranking) and retraining the transferred classifier, we can achieve the no-transfer accuracy for the Site B dataset (retraining here means transferring the trained classifier from Site A and replacing the respective features with those from Site B as mentioned in Fig. 11). In a similar transferability setting (training on Site A and testing on Site B), the feature-based-method performs significantly better than IP2Vec, as in Fig. 10. Although IP2Vec performs better than the feature-based-method within a dataset due to its inherent architecture of utilizing

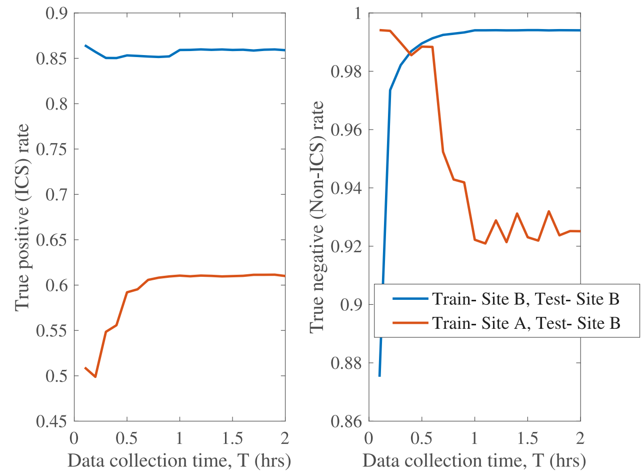

Fig. 9. Classification performance variation with varying T using the traffic-features-based method, when the classifier is trained on Site A and tested on Site A, and when the classifier is trained on Site A and tested on Site B.. (For interpretation of the references to color in this figure legend, the reader is referred to the web version of this article.)

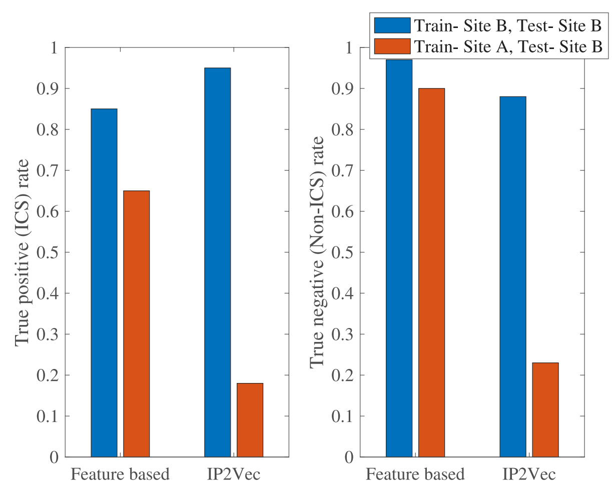

Fig. 10. Across-dataset performance comparison between IP2Vec and feature-based methods.

flow definition, IP2Vec is unable to extract generalizable features, unlike the feature-based-method, and therefore performs worse than the feature-based-method in an across-dataset setting.

6. Data collection parameters: Optimal T and ΔT

The amount of data needed to obtain a desired classification accuracy for differentiating ICS and non-ICS devices is crucial for understanding the applicability of this task in a near-real-time environment. The definition of "desired" is highly application-dependent. For example, a real-time intrusion detection system may require a low false negative rate to maximize the likelihood of detecting intruders, but be more tolerant of false positives. On the contrary, an off-line security assessment survey may tolerate both false negatives and false positives due to the non-time-critical nature of the assessment. An ideal method of differentiating ICS and non-ICS devices would produce perfect classification accuracy, but this may not always be achievable in practice. In this section, we evaluate the optimal data collection time required to achieve a classification accuracy between 80–95%.

We have iterated the amount of data available, by varying T between 0.1 to 2.5 h, with an interval of 5 min for the Site A dataset.

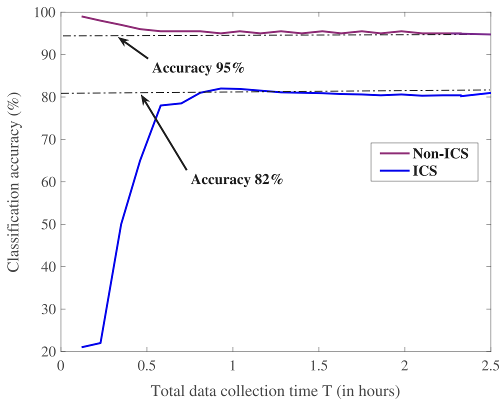

(a) Site A training dataset, selected T based on the convergence of classification, is 1 hour.

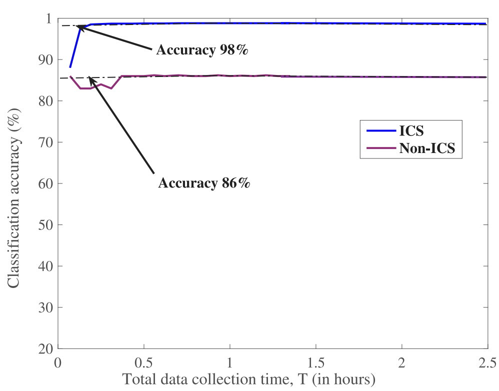

(b) Site B training dataset, selected T based on the convergence of classification, is 0.5 hour.

Fig. 11. Different cases of transfer with their respective accuracies: Case 1 indicates just the transfer from Site A to Site B. Case 2 indicates replacing rcvd_psize_min associated with Site A by the one from Site B, and retraining the classifier. Case 3 indicates replacing rcvd_psize_min and sent_pinterarr_avg associated with Site A by the ones from Site B, and retraining the classifier. Case 4 indicates replacing rcvd_psize_min, sent_pinterarr_avg and sent_psize_min associated with Site A by the ones from Site B, and retraining the classifier. Case 5 indicates retraining using all the features from Site B.

Similarly we have iterated the amount of data available, by varying T between 0.1 to 2.5 h, with an interval of 5 min. For each T, the classification accuracy for ICS devices and non-ICS devices was evaluated, as shown in Fig. 12(a) and Fig. 12(b). Moreover, we used standard k-fold cross validation ($k = 20$) for determining the classification accuracy, which eliminates variability over the accuracy number. As shown in Fig. 12(a), for the Site A dataset with a ΔT of 10 s, the minimum T is 1 h (after 1 h of data, both the classification accuracies converge). Similarly, in Fig. 12(b), for the Site B dataset with ΔT of 10 s, the optimal T is 0.5 h for achieving a converged classification accuracy. In both Fig. 12(a) and Fig. 12(b), the accuracy numbers are associated with the test classes, averaged over the 20 folds.

After fixing T at the optimal value of 0.5 h for the Site B dataset, ΔT was varied to show the effect of ΔT on the classification accuracy. The variation of classification accuracy with ΔT is shown in Fig. 13(b). Similarly, after fixing T at the optimal value of 1 h for the Site A dataset, ΔT was varied to capture its effect on the classification accuracy, as shown in Fig. 13(a). For both Fig. 13(a) and Fig. 13(b), there is a downward trend in classification accuracy with an increase in ΔT. This finding matches with intuition, as increasing ΔT (with a fixed value of T) results in a smaller number of individual flows in each dataset. However, we have selected a ΔT value of 10 s for both the datasets.

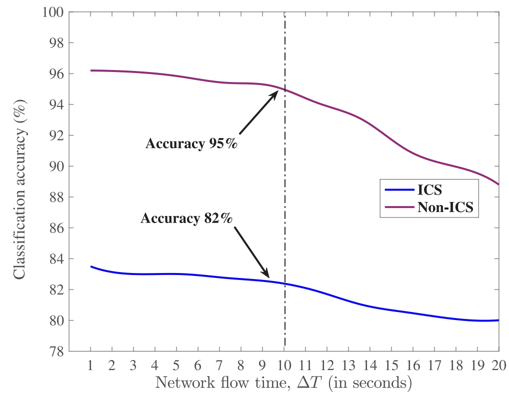

(a) Site A dataset, selected ΔT based on the convergence of classification is 10 seconds.

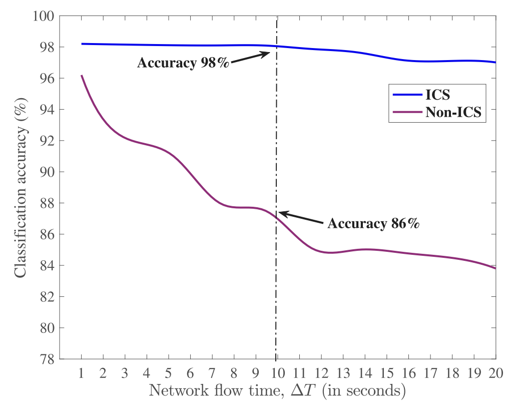

(b) Site B dataset, selected ΔT based on the convergence of classification is 10 seconds.

Fig. 12. Variation of classification accuracy with changing T, with $\Delta T = 10$ s.

Note that in both Figs. 12 and 13, the classification accuracy was evaluated using the traffic-features-based method described in Section 5.3. For IP2Vec, data from both Site A and Site B are collected based on the number of discrete flows and therefore the classification accuracy variation with respect to T and ΔT is not studied.

7. ICS device classification using DNP2Vec, solution of Task 2

In this section, we utilize DNP3 fields as features for classifying ICS devices. Before describing the details of the proposed framework, we rank the DNP3 features based on their importance in classifying ICS devices for both Site A and Site B datasets.

7.1. DNP3 field importance

There are 7 different types of ICS devices and 2 different types of ICS devices in the Site B dataset and Site A dataset, respectively. We used the labeled ICS devices to train a linear kernel-based SVM classifier, which utilizes 40 distinct DNP3 fields as features. Between these 40 different DNP3 features present in both the Site A and Site B datasets, we wanted to find the priority ranking of the fields in relation to the performance of ICS devices classification. First, we trained a linear kernel-based SVM classifier using 40 DNP3 features for classifying ICS devices for both datasets, and repeated the training activity while individually eliminating DNP3 features. This yields the effect of individual DNP3 features on device classification accuracy. dnp3.hdr.CRC and dnp3.al.obj fields have the highest priority, and rest of the 38 fields are at the same level of priority.

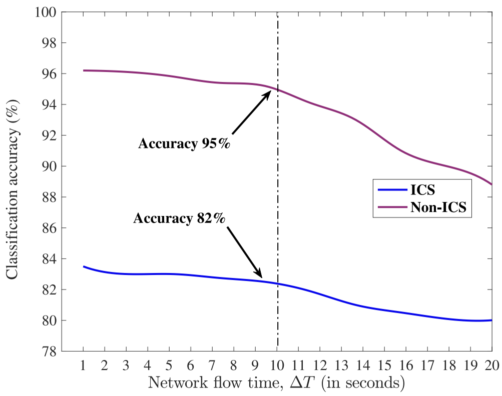

(a) Site A dataset, selected ΔT based on the convergence of classification is 10 seconds.

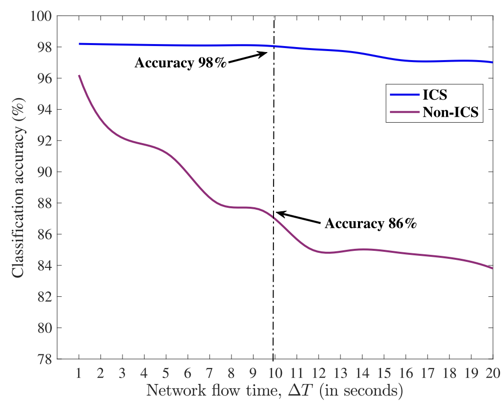

(b) Site B dataset, selected ΔT based on the convergence of classification is 10 seconds.

Fig. 13. Variation of classification accuracy with changing ΔT, with $T = 1$ h for Site A testing set and $T = 0.5$ h for Site B testing set.

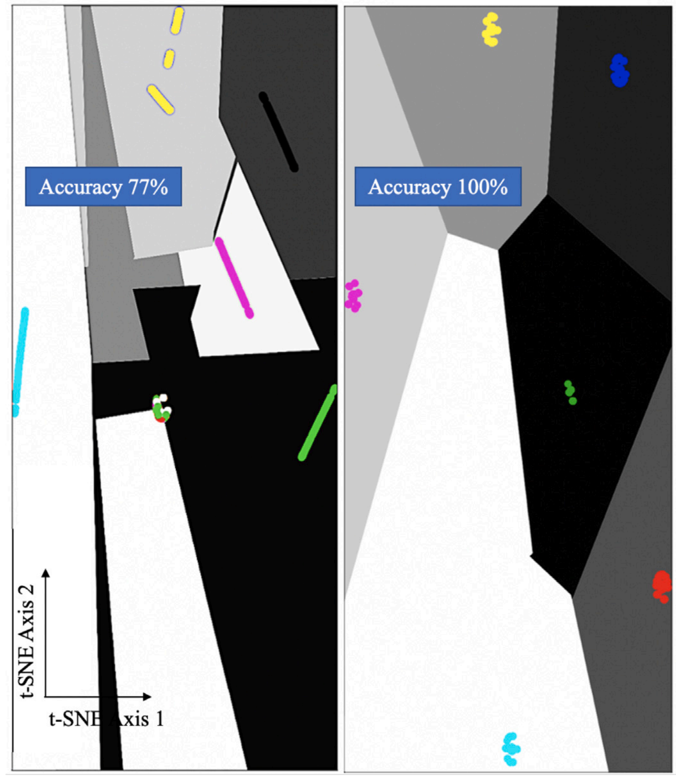

Fig. 14. t-SNE based classification performance comparison for ICS device classification using the baseline (left) and DNP2Vec methods (right), applied to the Site B test dataset. SVM with a linear-kernel gives an improvement of 23% when using the DNP3 feature embedding with DNP2Vec. SVM with a polynomial kernel via the DNP2Vec-based method gives an improvement of 8% compared to the baseline.

dnp3.hdr.CRC is the DNP3 data link header checksum. This unsigned integer is used for error detection in the data link header fields, and effectively encodes the message length, a multitude of information in the data link header control field, and the DNP3 source and destination addresses. Thus, this field appears to be relevant for device identification in that it captures some valuable characteristics of a message sender, as well as the state of the link between a sender and receiver.

dnp3.al.obj is the DNP3 application layer object type field. DNP3 uses the concept of objects to represent data from a device. Every object is identified by a group and variation that specifies the nature of the data encapsulated by the object. This unsigned integer specifies the object group and variation for data requested by a master or provided by an outstation response. It is conceivable that the identity of a device is in some way linked to the type of data that it requests or provides. Thus, this feature may be relevant for device identification.

7.2. Description of DNP2Vec

We modified the IP2Vec framework [1] for classifying the ICS devices present in the PCAP dataset. DNP2Vec is similar in architecture to IP2Vec, although dissimilar in generating the training samples for its training. We used the DNP3 feature ranking captured in Section 7.1 with the training sample to train DNP2Vec with a hidden dimension of 60. The input layer of training DNP2Vec uses the Source IP address as the only feature, while the output layer uses destination IP address, destination port, dnp3.al.obj, dnp3.hdr.CRC and dnp3.tr.fin, as shown in Fig. 1. This training sample generation method guarantees a unidirectional network flow similar to IP2Vec. Therefore, for a selected batch size of 100 when training DNP2Vec (this means 100 network flows), the input dimension will be 500 (as the Source IP will be repeated 5 times for generating the training sample associated with the five features in the output layer). Also, it is important to note that all of the network flows passing through the DNP2Vec framework are ICS device-type flows, which go through the sequence of operations (first IP2Vec and then DNP2Vec) mentioned in Fig. 1. Next, we demonstrate an experimental setup, similar to that mentioned in Section 2.1, for training the proposed DNP2Vec framework.

7.3. Performance of the proposed framework

The proposed framework is trained on the Site A and Site B datasets, using the experimental setup mentioned in Section 2.1. We trained a linear and a 10th order kernel-based SVM, as shown in Figs. 14 and 15. The baseline performance, using 40 DNP3 features for classifying ICS devices, is shown in Fig. 14 for the Site B testing dataset; the average class accuracy in this case is 77% for a linear-kernel, and 58% for a 10th order kernel. Our proposed DNP2Vec framework performs significantly better for classifying ICS devices: as shown in Fig. 14, using DNP2Vec gives perfect (100%) classification accuracy with a linear-kernel, and 77% classification accuracy with a 10th order kernel, when applied to the Site B testing dataset. Similarly, for the Site A testing dataset, the baseline method yields a classification accuracy of 70% for a linear-kernel, and 92% for a 10th order kernel, as shown in Fig. 15. The DNP2Vec method for the Site A testing dataset has perfect (100%) classification accuracy for both a linear and a 10th order kernel, as shown in Fig. 15.

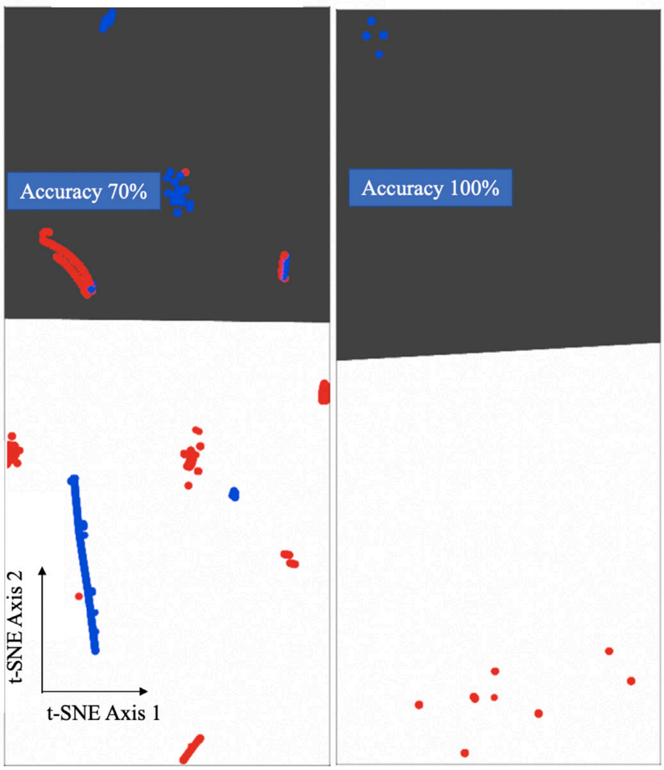

Fig. 15. t-SNE based classification performance comparison for ICS device classification using the baseline (left) and DNP2Vec methods (right), applied to Site A test dataset. SVM with linear-kernel gives an improvement of 30% when using the DNP3 feature embedding with DNP2Vec. SVM with polynomial kernel is also tried and the DNP2Vec-based method gives an improvement of 19% when compared to baseline.

8. Conclusion and future work

In this paper, we have proposed a framework for classifying ICS devices from PCAP datasets. The framework consists of two main tasks: first the classification of ICS vs. non-ICS devices and second, classifying the ICS device type. For the first task we proposed a method based on IP2Vec and network traffic features. We showed that although IP2Vec outperforms the traffic-features-based method in a "within-network" setting, the traffic-features-based method is better in an "across-network" transfer-learning setting. Furthermore, we have showed that both methods are insensitive to the observation window as long as it is "long enough" (at least 1 h for both the datasets we have tested our methods on). For the second task, we proposed the DNP2Vec method, which uses an embedding of DNP3 features for classifying ICS devices. We showed that our DNP2Vec method outperforms the baseline method for classifying ICS devices.

The architecture selection of IP2Vec and DNP2Vec is motivated by the desire to deploy our proposed methods to the field for the purpose of real-time network traffic monitoring. Deep learning methods, such as graph convolutional network, although applicable in the context of device classification, are much more computationally complex compared to our proposed architecture. Such methods might introduce additional processing delays.

General availability of ICS network data is a challenge due primarily to reasons of security; however, assuming that a data set has been obtained, the generalizability of classification methods can help to mitigate this to an extent. Additionally, in cases where network data to be classified is sparse, as illustrated in Fig. 12(a) and Fig. 12(b), we propose to use synthetic data generation frameworks such as generative adversarial networks or sequence-to-sequence models in future work.

Furthermore, while our device classification methods work well for traffic with unencrypted payloads, which is common for ICS networks where availability and integrity are more important than confidentiality, they are less effective when the payload is unavailable. However, when payload is available, our methods are easily extensible to the numerous other ICS protocols through the feature selection process described in Section 7. Through the feature selection and training processes, our models adapt to new protocols without the need to explicitly consider the semantics of specific protocol fields. This eliminates the need to write code that interprets ICS protocol field values and assign meaning to them; rather, what is needed is simply a decomposition of network packets into their constituent protocol fields, which is already performed by common open-source protocol analyzers.

Finally, while we focused on two specific learning tasks in this work, there are many other ICS device characterization tasks that might be amenable to our proposed methods, such as determination of firmware version or other configuration-oriented characteristics, and these should be investigated in future work.

References

[1] Ring M, Dallmann A, Landes D, Hotho A. Ip2vec: Learning similarities between IP addresses. In: 2017 IEEE international conference on data mining workshops (ICDMW). IEEE; 2017, p. 657–66.

[2] Beaver JM, Borges-Hink RC, Buckner MA. An evaluation of machine learning methods to detect malicious SCADA communications. In: 2013 12th international conference on machine learning and applications, vol. 2. IEEE; 2013, p. 54–9.

[3] Hink RCB, Beaver JM, Buckner MA, Morris T, Adhikari U, Pan S. Machine learning for power system disturbance and cyber-attack discrimination. In: 2014 7th International symposium on resilient control systems. IEEE; 2014, p. 1–8.

[4] Kravchik M, Shabtai A. Detecting cyber attacks in industrial control systems using convolutional neural networks. In: Proceedings of the 2018 Workshop on Cyber-Physical Systems Security and PrivaCy; 2018. p. 72–83.

[5] Maglaras LA, Jiang J. Intrusion detection in SCADA systems using machine learning techniques. In: 2014 Science and information conference. IEEE; 2014, p. 626–31.

[6] Rudin C, Waltz D, Anderson RN, Boulanger A, Salleb-Aouissi A, Chow M, Dutta H, Gross PN, Huang B, Ierome S, et al. Machine learning for the new york city power grid. IEEE Trans Pattern Anal Machine Intell 2011;34(2):328–45.

[7] Fukuda T, Shibata T. Theory and applications of neural networks for industrial control systems. IEEE Trans Indus Electron 1992;39(6):472–89.

[8] Anderson RN, Boulanger A, Powell WB, Scott W. Adaptive stochastic control for the smart grid. Proc IEEE 2011;99(6):1098–115.

[9] Bigham J, Gamez D, Lu N. Safeguarding SCADA systems with anomaly detection. In: International workshop on mathematical methods, models, and architectures for computer network security; Springer: 2003. p. 171–82.

[10] Düssel P, Gehl C, Laskov P, Bußer J-U, Störmann C, Kästner J. Cyber-critical infrastructure protection using real-time payload-based anomaly detection. In: International workshop on critical information infrastructures security; Springer: 2009. p. 85–97.

[11] Garitano I, Uribeetxeberria R, Zurutuza U. A review of SCADA anomaly detection systems. In: Soft computing models in industrial and environmental applications, 6th international conference SOCO 2011. Springer; 2011, p. 357–66.

[12] Zander S, Nguyen T, Armitage G. Automated traffic classification and application identification using machine learning. In: The IEEE conference on local computer networks 30th anniversary. IEEE; 2005, p. 250–7.

[13] Caselli M, Hadžiosmanović D, Zambon E, Kargl F. On the feasibility of device fingerprinting in industrial control systems. In: International workshop on critical information infrastructures security; Springer: 2013. p. 155–66.

[14] Feng X, Li Q, Wang H, Sun L. Characterizing industrial control system devices on the internet. In: 2016 IEEE 24th international conference on network protocols. IEEE; 2016, p. 1–10.

[15] Formby D, Srinivasan P, Leonard AM, Rogers JD, Beyah RA. Who's in control of your control system? device fingerprinting for cyber-physical systems. In: NDSS. 2016.

[16] Yang K, Li Q, Sun L. Towards automatic fingerprinting of IoT devices in the cyberspace. Comput Netw 2019;148:318–27.

[17] Lavrenovs A, Graf R, Heinaaro K. Towards classifying devices on the internet using artificial intelligence. In: 2020 12th International conference on cyber conflict. 1300, IEEE; 2020, p. 309–25.

[18] Yuan M, Dong Y. Network video traffic classification using feature fusion. In: 2020 IEEE 6th international conference on computer and communications; 2020. p. 1847–51. 10.1109/ICCC51575.2020.9345024.

[19] S. MC, H. S, Somu TE. Network traffic classification by packet length signature extraction. In: 2019 IEEE international WIE conference on electrical and computer engineering; 2019. p. 1–4. 10.1109/WIECON-ECE48653.2019.9019918.

[20] Su Y, Qi K, Di C, Ma Y, Li S. Learning automata based feature selection for network traffic intrusion detection. In: 2018 IEEE third international conference on data science in cyberspace; 2018. p. 622–27. 10.1109/DSC.2018.00099.

[21] Mikolov T, Sutskever I, Chen K, Corrado G, Dean J. Distributed representations of words and phrases and their compositionality. 2013, arXiv preprint arXiv:1310.4546.

[22] Guyon I, Weston J, Barnhill S, Vapnik V. Gene selection for cancer classification using support vector machines. Machine Learn 2002;46(1-3):389–422.

Machine learning in Agriculture Domain: A state-of-art survey

Pravat Kumar Subudhi, *Department of Electrical and Communication Engineering, Aryan Institute of Engineering & Technology, Bhubaneswar, pk.subudhi11@outlook.com*

Alekha Sahoo, *Department of Electrical Engineering , Raajdhani Engineering College, Bhubaneswar, alekha.sahoo241@gmail.com*

Manoj Mohanta, *Department of Electrical and Electronics Engineering, Capital Engineering College, Bhubaneswar, manoj.mohanta62@outlook.com*

Namrata Khamari, *Department of Computer Scinece Engineering , NM Institute of Engineering & Technology, Bhubaneswar, namrayakhamari@outlook.com*

A R T I C L E I N F O

Keywords:
Deep learning
Harvesting
Machine learning
Post-harvesting
Pre-harvesting
Precision agriculture

A B S T R A C T

Food is considered as a basic need of human being which can be satisfied through farming. Agriculture not only fulfills humans' basic needs, but also considered as source of employment worldwide. Agriculture is considered as a backbone of economy and source of employment in the developing countries like India. Agriculture contributes 15.4% in the GDP of India. Agriculture activities are broadly categorized into three major areas: pre-harvesting, harvesting and post harvesting. Advancement in area of machine learning has helped improving gains in agriculture. Machine learning is the current technology which is benefiting farmers to minimize the losses in the farming by providing rich recommendations and insights about the crops. This paper presents an extensive survey of latest machine learning application in agriculture to alleviate the problems in the three areas of pre-harvesting, harvesting and post-harvesting. Application of machine learning in agriculture allows more efficient and precise farming with less human manpower with high quality production.

1. Introduction

Agriculture is considered an important pillar of the world's economy and also satisfies one of the basic need of human being i.e. food. In most of the countries it is considered the major source of employment. Many countries like India still use the traditional way of farming, farmers are reluctant to use advanced technologies while farming because of either the lack of knowledge, heavy cost or because they are unaware about the advantages of these technologies. Lack of knowledge of soil types, yields, crops, weather, and improper use of pesticides, problems in irrigation, erroneous harvesting and lack of information about market trend led to the loss of farmers or adds to additional cost. Lack of knowledge in each stage of agriculture leads to new problems or increases the old problems and add the cost to farming. Growth in the population day by day also increases the pressure on the agriculture sector. Overall losses in the agriculture processes starting from crop selection to selling of products are very high. As per the famous saying "Information is the Power", keeping track of information about the crops, environment, and market, may help farmers to take better decisions and alleviate problems related to agriculture. Technologies like blockchain, IoT, machine learning, deep learning, cloud computing, edge computing can be used to get information and process it. Applications of computer vision, machine learning, IoT will help to raise the production, improves the quality, and ultimately increase the profitability of the farmers and associated domains. The Precision learning in the field of agriculture is very important to improve the overall yield of harvesting.

Blockchain technology, cloud computing, internet of things (IoT), machine learning (ML) and deep learning (DL) are the latest emerging trends in the computer field. It has been already used in different domains like healthcare, cybercrime, biochemistry, robotics, metrology, banking, medicine, food etc. to solve the complex problems by the researchers. Many applications of machine learning, IoT in different domains are presented [1–5]. Deep learning algorithms are making machine learning more powerful and accurate. By using automated machine learning (AutoML) one can cut the demand of ML experts, automate the ML pipeline with more accuracy.

While performing agriculture tasks the steps as below is generally followed by farmers.

Step 1: Selection of Crop
Step 2: Land Preparation
Step 3: Seed Sowing
Step 4: Irrigation & fertilizing
Step 5: Crop Maintenance [use of pesticides, crop pruning etc.]
Step 6: Harvesting
Step 7: Post-Harvesting activities

As per the above algorithm, the agriculture related tasks are categorized in the for major sub areas. Fig. 1 shows these four sub-domains of agriculture tasks.

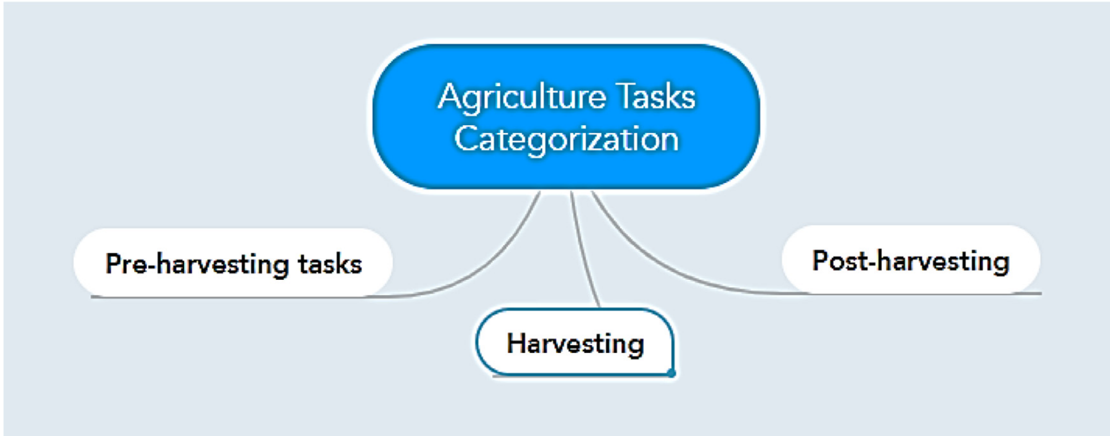

Fig. 1. General categorization of agriculture tasks.

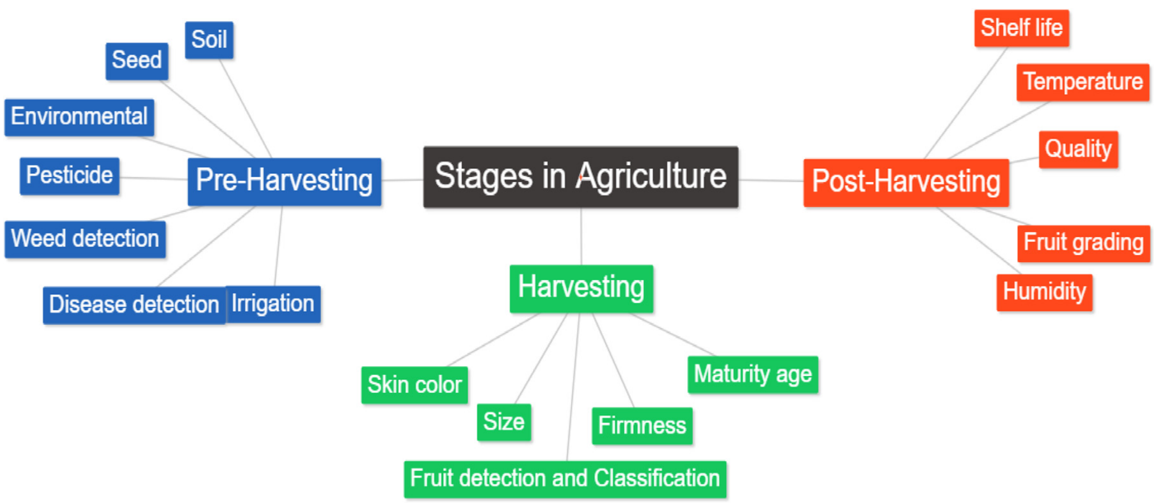

Fig. 2. Important parameters considered in each stage of farming.

Table 1
Important factors to be considered in each stage.

S. No.	Stage	Activities / Factors	References
1	Pre-harvesting	Soil, seeds quality, fertiliser/pesticide application, pruning, cultivar selection, genetic and environmental conditions, irrigation, crop load, weed detection, disease detection.	[6, 7, 9]
2	Harvesting	Fruit/crop size, skin color, firmness, taste, quality, maturity stage, market window, fruit detection and classification.	[7]
3	Post-harvesting	Factors affecting the fruit shelf-life such as temperature, humidity, gasses used in fruit containers, usage of chemicals in postharvest and fruit handling processes to retain the quality, fruit grading as per quality.	[7]

During pre-harvesting tasks farmers focuses on selection of crops, land preparation, seed sowing, irrigation, and crop maintenance which includes use pesticides, pruning etc. In yield estimation the farmers do the activities like yield mapping and counting the number of fruits so that they can predict the production and make the necessary arrangements required at the time of harvesting or post-harvesting. While harvesting farmers are focused on maturity of crops or fruits market need quality. Whereas in post-harvesting farmers are focused on post-harvest storage and processing systems. Fig. 2 shows the important factors that should be considered in each stage of farming. Table 1 summarizes few works in each stage of agriculture tasks.

The major branches of the agriculture are Agronomy, Horticulture, Forestry, Livestock, Fisheries, Agriculture Engineering and Economics. The scope of the paper is confined to use of machine learning in agriculture, specifically on fruits.

In the following sections, the review of the most recent techniques of machine vision systems used for classification and object detection in each stage of farming is presented. Section 2 explains the use of ML in the pre-harvesting stage. In Section 3, usage of ML in the stage of harvesting is explained and in Section 4 usage of ML in the post-harvesting stage is explained. Sections 5 and 6 focuses on discussion and challenges in use of the Artificial Intelligence (AI), ML, and DL.

2. Pre-harvesting

Pre-harvesting parameters play a key role in overall growth of crop/fruits. In pre-harvesting machine learning is used to capture the parameters of soil, seeds quality, fertilizer application, pruning, genetic and environmental conditions and irrigation. Focusing on each component it is important to minimize the overall losses in production. Here few important components in the pre-harvesting are considered and how neural networks and machine learning are used to capture the parameters of each component.

Table 2
Analysis of pre-harvesting parameter: Soil.

S. No.	Property	Important features	Classes defined in the work	Dataset used (Public / Own)	Total number of images used for training	Models / Method / Algorithms compared	Best model / method/ algorithm	Results	Reference
1	Soil	Village wise soil fertility indices of available Soil Reaction (pH), Organic Carbon (OC) and Boron (B), Phosphorus (P), and Potassium (K)	For P, K and OC three classes: Low, Medium, and High. For B six classes: Very Low, Low, Medium, Moderately High, High, and very High. For pH Four classes: Strongly Acidic (SA), Highly Acidic (HA), Moderately Acidic (MA), and Slightly Acidic (SLA).	public (reports available during the years 2014 to 2017)	NA	Extreme Learning Machine (ELM) with different activation functions like sine-squared, Gaussian radial basis, triangular basis, hyperbolic tangent, and hard limit	ELMs with Gaussian radial basis function	80% of accuracy	[10]
2		Soil Organic matter (SOM) and pH parameter	SOM and pH parameters	Own	523 soil samples	four Machine Learning models Cubist regression model (Cubist), extreme learning machines (ELM), least squares-support vector machines (LS-SVM), and partial least squares regression (PLSR)	ELM	R2 = 0.81	[11]
3		Moisture content (MC), organic carbon (OC), and nitrogen (TN)	Estimating moisture content (MC), organic carbon (OC), and nitrogen (TN)	Own	140 set	Cubist, partial least squares regression (PLSR), least squares support vector machines (LS-SVM), and principal component regression (PCR)	LS-SVM is best for MC and OC and TN is best by the Cubist	MC - RMSEP:0.457%, RPD:2.24 TN - RMSEP: 0.071 and RPD :1.96	[12]
4		soil moisture	Auto-regressive error function (AREF) combined with computational models	Own The soil moisture and density were determined by volumetric rings with 100 cm3 collected in eight positions along the plots, at depths from 25 mm to 75 mm	NA	One Neuro-Fuzzy model (ANFIS) and two artificial neural networks (a Multi-Layer Perceptron (MLP) and a Radial Basis Function (RBF)). Multiple linear regression (MLR) models with two and six independent variables	Neural Network with AREF	RMSE between 1.27% and 1.30%, R2 around 0.80, and APE between 3.77% and 3.75%	[13]
5		Soil Temperature	soil temperature (ST) at 6 different depths of 5, 10, 20, 30, 50 and 100 cm	Public (For Bandar Abbas, 10 years measured data sets for the period of 1996–2005 and for Kerman, 7 years measured data sets for the period of 1998–2004)	NA	ELM, SaE-ELM, genetic programming (GP) and artificial neural network (ANN)	SaE-ELM	MABE - 0.8660–1.5338 C R - 0.9084–0.9893	[14]

2.1. Soil

Liakos, et al. [8] and Sharma, et al. [9] presented a soil management survey with the application of ML techniques for prediction or identification of soil properties (estimation of soil temperature, soil drying, and moisture content). The categorization and estimation of the soil attributes help farmers in minimizing extra cost on fertilizers, cut the demand of soil analysis experts, increase profitability, and improve health of soil, whereas Suchithra and Pai [10] presented pH values and soil fertility indices classification and predication model. Yang, et al. [11] observed that important indicators of soil fertility are pH values and Soil Organic matter (SOM) and thus the authors have done prediction of SOM and pH parameters in paddy soil. Morellos, et al. [12] has predicted organic carbon (OC), nitrogen (TN), and moisture content (MC) parameters of the soil. The aim of study was to compare machine learning algorithms and linear multivariate algorithms on basis of their performance of prediction. As soil moisture is frequently associated with variability in yield, Johann, et al. [13] have estimated the moisture content of soil using with Auto-regressive error function (AREF) along with machine learning algorithms. Nahvi, et al. [14] developed a new model by employing Self-adaptive evolutionary (SaE) agent in extreme machine learning (ELM) architecture. This new model is used for the assessment of daily soil temperature (ST) at 6 different depths of 5, 10, 20, 30, 50 and 100 cm. The detail summary of work done by different authors on soli parameter is mentioned in Table 2.

2.2. Seeds

Seed germination is a vital factor for quality of seed, which is an important determining factor of yield and quality of production. Seed germination rate calculation is still done manually with the help of trained persons which is not only a tiresome process but also prone
to error. Thus, various machine leaning and image recognition techniques have been proposed by different authors to automate the process of seed sorting and calculation. Various computer vision, machine learning techniques, Convolution Neural Network (CNN) methods have been presented in D. Sivakumar, et al. [15], Huang, et al. [16], Zhu, et al. [17]. Image recognition technique for seed sorting with high accuracy is developed by Young, et al. [18]. Ke-ling, et al. [19] used a multilayer perceptron neural network model for improving the accuracy of the classification method to separate pepper seeds of high-quality from low-quality. Uzal, et al. [20] and Veeramani et al. [21] used the deep neural network (DNN) model using CNN for the assessment of the quantity of seeds per pod in soybean and for sorting of haploid seeds on basis of shape, phenotypic expression, and the embryo pose. Nkemelu, et al. [22], built a model using CNN for plant seedlings classification into 12 species. Medeiros, et al. [23] assessed the proficiency of computer vision as an alternative to routine vigor tests to expedite the process of accurate evolution of seed physiological potential. Amiryousefi, et al. [24] used image analysis technique, principal component analysis (PCA), to save time and cost of placing seeds in different clusters by reducing the features to be considered for clustering. Vlasov, et al. [25], Kurtulmuş, et al. [26] used machine learning (ML) techniques for efficient seed classification. The detail summary of work done by different authors is mentioned in Table 3.

2.3. Pesticides and disease detection

In-time disease detection is the most important task to save crops from major loss. Some farmers regularly analyze leaf or branches of tree while growing and identify the diseases or many times to avoid the diseases, they apply the pesticides on all the crops equally. Both the activities are based on human experience which is prone to errors and risky. Decision of which pesticide, when to apply and where to apply is totally dependent on type of disease, its stage and affected area. Application of unnecessary pesticide on all the crops may harm crops as well as farmer's health. Precision agriculture helps farmers for application of the right pesticide at right time at right place. Many works combined pesticides prediction with the detection of disease on plants. This section discusses bout disease detection using machine learning.

Alagumariappan, et al. [27], developed a real-time decision support system integrated with a camera sensor module for plant disease identification. In this work authors evaluated the performance of three machine learning algorithms namely, Extreme Learning Machine (ELM) and Support Vector Machine (SVM) with linear and polynomial kernels and observed that the performance of ELM is better when compared to other algorithms. Savary, et al. [28] studied how diseases cause the crop losses and their implications for global food production losses and food security. The objective of this work is to show that crop loss research is vital and should be consider as full branch of plant science.

Sujatha, et al. [29], compared the ML algorithms (SVM, RF, SGD) with DL algorithms (Inception-v3, VGG-16, VGG-19) in terms of citrus plant disease detection and observed that DL methods performed much better. Karadaˇg, et al. [30] studied detection of healthy and fusarium diseased peppers (capsicum annuum) from the reflections obtained from the pepper leaves with the help of spectroradiometer. Artificial Neural Networks (ANN), Naive Bayes (NB) and K-nearest Neighbor (KNN) machine learning algorithms were used for classification. Authors claimed that leaf reflections can be used in disease detection. Pandya [31], presented data about different types of pesticides, their applications and impact on environment. Arsenovic, et al. [32] discussed the shortcomings of available DL models used for plant disease detections. A novel model is built which consist of two-stage architecture Disease Net, for classification of plant disease, which achieved 93.67% training accuracy. Barbedo [33], explored the new approach by using DL to identify plant diseases from individual lesions and spots instead of considering entire leaf. This approach helps to detect multiple diseases on the same leaf with 12% higher accuracy. Saleem, et al. [34], presented a detail review of DL models used to envision different diseases of plant. Many research gaps have been enlisted in the plant disease detection and suggested that advanced DL algorithms should be used to increase the accuracy.

Liu, et al. [36], Kour, et al. [37] studied the apple leaf diseases and apple fruit diseases respectively. A CNN model was proposed to classify apple leaf diseases into Brown spot, Rust, Mosaic, and Alternaria leaf spot. A new dataset was created consisting of 13,689 images of diseased leaves which was used to train the novel architecture based on AlexNet in [34]. For apple disease detection and classification in Kashmir Valley, another model called Fuzzy Rule-Based Approach for Disease Detection (FRADD) was proposed in [35]. Though the accuracy of the model is good, it takes into account only one disease known as scab and limited numbers of fruit types. Xing, et al. [38] proposed a new model called Weakly DenseNet-16, to overcome the limitations of pre-trained models which are trained on ImageNet dataset. A dataset consisting of 17 species of citrus pests and seven types of citrus diseases (9051 images of citrus pests and 3510 images of citrus diseases) was created. Weakly DenseNet-16 performed well with the accuracy 93.33% as compared to MobileNet-v1 (85.04%), MobileNet-v2 (87.82%), ShuffleNet-v1 (83.44%), ShuffleNet-v2 (83.21%), NIN-16 (91.66%), SENet-16 (88.36%), and VGG-16 (92.93%). Doh, et al. [39] proposed a solution to detect the citrus fruit diseases using their physical attributes such as the texture, color, structure of holes on the fruit and morphology. The proposed solution composed of K-Means clustering technique, ANN and SVM algorithms. Results show that the use of SVM with ANN helps in increasing disease detection and classification rate. The detailed summary of the published works is presented in Table 4.

3. Harvesting

After taking care of parameters in pre-harvesting stage like soil, seeds, weeds etc., when the fruits/vegetables are ready then harvesting is the most important stage. The important parameters should be focused in this stage are fruit/crop size, skin color, firmness, taste, quality, maturity stage, market window, fruit detection and classification for harvesting. Careful and right harvesting of fruit is directly correlated with the profit. In the survey, we observed that auto-harvesting robots, machine learning, deep learning techniques are achieving better results and helping farmers in reducing the losses in harvesting stage. This section presents the application of ML, DL algorithms in the harvesting.

Hua, et al. [40] presented a detail survey on automated fruit harvesting systems for sweet pepper, tomato, apple and kiwifruit as an example to demonstrate the recent advances in intelligent automatic harvesting robots in horticulture. The use automatic robots in field helps to increase the production, saves the harvesting time which ultimately increase the profits of the farmers. Kushtrim, et al. [41] developed a CNN model based on single shot detector (YOLO) algorithm for on-tree fruit detection. A dataset consisting of real and synthetic images of apple and pear trees was created. For labeling the images, open-source labeling tool called as BBox-Label-Tool was used. More than 5000 images of pear and apple fruits were used while training the model. Amazon cloud platform was used to train the model. The model achieved more than 90% accuracy for on-tree fruit detection. Two deep neural network models were investigated in the proposed work, a small CNN model and a VGG-16

Table 3
Analysis of pre-harvesting parameter: Seed.

Sr. No.	Property	Important features	Classes defined in the work	Dataset used (Public / Own)	Total no of images used for training	Models / Method / Algorithms compared	Best model / method / algorithm	Results	Model evaluation technique	Reference
1	Seed	color, shape, and texture	maze seed	Own	4000	ensemble learning, K-nearest neighbor (KNN), logistic regression, support vector machine (SVM), and Speeded Up Robust Features (SURF) algorithm to classify the extracted features, GoogLeNet, VGG19	GoogleNet	95%	Confusion Table, Training loss. Testing loss. Training accuracy. Testing accuracy	[16]
2	Cotton Seed		Jinxin5, Jinxi7, Shennongmian1, Xinjiangzaomian13, Xinluzao-mian29, Xinluzhong52 and Xinluzhong42	own, dataset collected from Shihezi, Xinjiang Uyghur Autonomous Region, China	13,160	SVM, PLS-DA, and LR models based on deep features extracted by self-design CNN and ResNet models	self-design CNN	80%	classification accuracy	[17]
3	pepper seeds	15 features (ten color features: R, G, B, L*, a*, b*, hue, saturation, brightness, and Gray, three geometric features: width, length, and projected area, seed weight and density)	germinated seed (1) and un-germinated seed (0)	Own	400 seeds	multilayer perceptron (MLP); BLR binary logistic regression, single feature models	multilayer perceptron and binary logistic regression	90%	classification accuracy	[19]
4	soybean pods	38 tailored features, geometrical characteristics (area, perimeter, major and minor axis length), shape features (density, elongation, ompactness, rugosity and axis ratio), first 4 Hu moments, and finally a 25 bins histogram of the profile of the pod straighten mask added along the short axis	2-SPP, 3-SPP, and 4-SPP	Own	18,178	tailored features extraction (FE) followed by a Support Vector Machines (SVM), CNN	CNN	86.20%	accuracy	[20]
5	haploid maize seeds	texture, morphology, color and shape	True-Diploid, True-Haploid	Own	4021	DeepSort, Support Vector Machine (SVM), Random Forest (RF), and Logistic Regression (LR)	DeepSort	0.961	5-fold cross-validation	[21]

Table 4
Analysis of pre-harvesting parameter: Pesticides and disease detection.

Sr. No.	Property	Important features	Classes defined in the work	Dataset used (Public / Own)	Total no of images used for training	Models / Method / Algorithms compared	Best model / method / algorithm	Results	Model evaluation technique	Reference
1	Disease detection	color, shape, and texture	12 different species and 42 different classes (both healthy and diseased)	Own (PlantDisease)	79,265	AlexNet, VGG 19, Inception, DenseNet, ResNet, PlantDiseaseNet Object Detection: Two-Stage Methods - Faster R-CNN, Faster R-CNN with TDM, Faster R-CNN with FPN, One-Stage Methods - YOLOv3, SSD513, RetinaNet	PlantDiseaseNet	94%	TOP-1 Accuracy	[32]
2	Plant disease	individual lesions and spots	Healthy, Mildly diseased, Moderately diseased, Severely diseased	Own (Plant-Disease)	PDDB - 1575 XDB - 46,409	GoogLeNet CNN	GoogLeNet CNN	12% higher	Confusion matrices	[33]
3	Plant disease and pest detection	deep features	8 classes : 5 disease (Coryneum beijerinckii, Apricot monilia laxa, Peach monilia laxa, Cherry myzus cerasi, Xanthomonas arboricola); 3 pest (Walnut leaf mite ga, Peach sphaerolecanium prunastri, Erwinia amylovora)	Own	1965	extreme learning machine (ELM), support vector machine (SVM), and K-nearest neighbor (KNN), VGG16, VGG19, and AlexNet	ResNet50 model and SVM classifier	98%	accuracy, sensitivity, specificity, and F1-score, confusion matrix	[35]
4	Apple Leaf Diseases	edge, corner, color, shape and object,	4 classes: Brown spot, Rust, Mosaic, and Alternaria leaf spot	Own	13,689	AlexNet Precursor, VGG 19, Inception, DenseNet, ResNet, PlantDiseaseNet, SVM BP AlexNet GoogLeNet ResNet-20 VggNet-16 Our Work	AlexNet Precursor	97.62%	confusion matrix	[36]
5	Apple Fruit Disease	background and foreground pixels	4 classes: Poor, Average, Good, Excellent	Own (Two datasets)	NA	Fuzzy Rule-Based Approach for Disease Detection (FRADD)	FRADD	91.66	accuracy	[37]

fine-tuned model to classify the fruits by Hossain, et al. [42]. The first model was built with six layers while the second was fine-tuned visual geometry group-16 pre-trained DL model. Two datasets were used to evaluate the performance of the proposed models. Dataset-1 is publicly available and it consists of 2633 color images whereas dataset-2 consists of total 5946 images, distributed among 10 classes. It was claimed VGG-16 fine-tuned model achieved excellent accuracy on both datasets. Kirk, et al. [43] studied on improving network performance on unseen data through a structured approach and analysis of the network input. Instead of modifying network architecture and increasing depth of neural network, the fusion of features was chosen. Result shows that the model complexity for more accuracy and generalization capabilities can be avoided by using bio-inspired features. It is claimed that for the color centric data classes this approach shows more promising results with the robust DL model in real world. For this the work author created dataset consists of 6189 images over 2 months, August and September 2018, and manually annotated 150 of them. Altaheri, et al. [44] proposed a machine vision system to categorize date fruit images according their maturity stages which help in harvesting decision. A dataset of 8072 images were created consisting of five date types: Naboot Saif, Khalas, Barhi, Meneifi, and Sullaj with different pre-maturity and maturity stages. The images were captured in various angles, scales, illumination conditions, and there were few occluded images. Transfer learning from two famous CNN models AlexNet and VGGNet were used to build the three classification models to classify date fruit according to their maturity stage, type, and whether they are harvestable or not. Result shows that VGG-16 model outperformed with the accuracy of 99.01% in 20.6 msec. Bauer, et al. [45] developed a platform that chains up-to-date ML techniques, modern computer vision, and integrated software engineering practices to measure yield-related phenotypes from ultra-large aerial imagery named as AirSurf. Author claims that this platform help to increase the yield and crop marketability before the harvest. Zhang, et al. [46] developed a harvesting robot for autonomous harvesting which consists of low priced gripper and ML technique for detection of cutting-point. The purpose of the study was to develop an autonomous harvester system which can harvest any crop with peduncle rather than damaging to its flesh. Onishi, et al. [47] proposed a new system (robot arm) consisting of Single Shot MultiBox Detector (SSD) and stereo camera for autonomous detection and harvesting of fruits. The system was tested on apple tee called "Fuji". Robot arm detects the harvestable fruit position and harvest it by twisting the hand axis. An experimental result shows that system was able to detect 90% fruits and took only 16 s for harvesting. Liu, et al. [48] proposed a novel pipeline consisting of segmentation, 3D localization and frame to frame tracking for accurately counting the fruits from order of images. This model was evaluated on orange and apple fruits dataset. Table 5, presented the detail summary of harvesting techniques.

4. Post-harvesting

Post-harvesting is last and most crucial area in agriculture which require more attention. After successfully completing all stages starting from yield-estimation till harvesting, negligence in post-harvesting may spoil all the efforts and cause severe loss to farmers. The subtasks that

Table 5
Analysis of harvesting techniques.

Sr. No.	Property	Important features	Classes defined in the work	Dataset used (Public / Own)	Total no of images used for training	Models / Method / Algorithms compared	Best model / Method /Algorithm	Results	Model evaluation technique	Reference
1	Real-Time Fruit Detection within tree	fruit shapes, color and/or other attributes	apple and pear fruits	own	5000	Single-Shot Convolution Neural Network (YOLO)	YOLO	90%	confusion matrix.	[41]
2	fruit classification	NA	1st dataset: 15 classes, 2nd dataset: 10 classes	1st dataset: Public, 2nd Dataset: own	1st dataset: 2633, 2nd dataset:5946	2 deep learning Models : 1) light model of six CNN layers and 2)VGG-16 based architecture	VGG-16 based architecture	99.75%	Confusion matrix	[42]
3	Outdoor Fruit Detection	Bio-Inspired Features, fusion of features	3 classes: Ripe Strawberry, Unripe Strawberry, Both Classes	own (DeepFruit)	4219	Feature Pyramid Networks, Residual Neural Networks and RetinaNet	L*a*b*Fruits system	performance increase of 6.6 times	F1 score, the harmonic mean of precision and recall	[43]
4	Date Fruit Classification	local and spatial features and patterns	five date types in different pre-maturity and maturity stages: Naboot Saif, Khalas, Barhi, Menei, and Sullaj	own	8000	VGG-16, AlexNet	VGG-16	99.01%	Confusion matrix.	[44]
5	fruit harvesting robot	NA	apples Detected, Undetected	public	169	Single Shot MultiBox Detector (YOLO)	YOLO	0.9	precision, recall	[47]

can be consider in this stage are shelf-life of fruits and vegetables, post-harvest grading and export. Every country has their own standard rules and regulations for grading the fruits [49–51].

In [52], an information manual with directions for "Post-harvest management of mango for quality and safety assurance" was presented. This is very insightful for all the stakeholders of horticultural supply chain. Study showed that wrong post-harvest handling methods can affect the quality and quantity of fruits which increases the overall losses. 31% losses which are identified at retail level were caused by decay only. The other practices which add losses are poor harvesting, careless handling, and improper packaging and carriage conditions.

The wrong disease management during production causes the decay at high-level of pre-harvest infections. The decays in the form of anthracnose and stem end rot are very commonly observed. A training manual for "handling fresh fruits, vegetables and root crops" for Grenada was presented in [53], as a part of the "Agricultural Marketing Improvement" Project TCP/GRN/2901 which was implemented by Grenada Government and FAO. The goal of this project was to increase the profits for horticulture products and root crop growers through a well-organized agricultural marketing system. This document provides in detail study about all post-harvest stages with how to minimize the losses in every stage. Ucat, et al. [54] explored the use of image processing with deep leaning algorithm to classify Cavendish banana as per their grades. Python, OpenCV and Tensorflow were used to build the model to classify the bananas into different categories such as Class A big-hand or small-hand, Class B big-hand or small-hand and Cluster class (part of hand). Result shows that the model achieved more than 90% classification accuracy. Ireri, et al. [55] proposed a machine vision system for post-harvest tomato grading. The system works on RGB images given as an input to the system. Dataset was created by manually labeling the tomato images into four categories according to their defect, healthy and ripeness parameters. Four different models were built to classify image into one of the category according to the matching features, total 15 features were considered while taking the decision Result shows that RBF-SVM performed well as compared to others for category 1 i.e. healthy or defected with 0.9709 detection accuracy. Piedad, et al. [56] developed a system for banana (Musa acuminata AA Group 'Lakatan') classification using ML techniques based on tier-based. A non-invasive tier-based technique was used in this study. ANN, SVM and RF classifiers were used to classify bananas into extra class, class I, class II and rejected classes. Result shows that the random-forest algorithm outperformed as compared to others with the 94.2% accuracy. Lia, et al. [57] studied and compared two hyper-spectral imaging technologies namely long-wave near infrared (LW-NIR) and short-wave near infrared (SW-NIR) for early identification of Bruise of 'Pinggu' peaches. An improved watershed segmentation algorithm based on morphological gradient reconstruction and marker extraction was developed and tested on multispectral PC images in this study. Experimental result shows that a proposed algorithm accurately classified 96.5% of the bruised and 97.5% of sound peaches respectively. An automated real–time grading system with quality inspection for apple fruit was developed by Sofu, et al. [58]. The developed system comprises a roller, transporter and class conveyors joined with an enclosed cabin with camera, load cell and control panel units. System not only classifies the apples on the basis of color, size and weight parameters but also identifies defective apples. The proposed system took only 0.52 s to capture the apple image and process. Average 15 apples per seconds were sorted by the system. Author claims average sorting accuracy between 73 and 96% and the system can be used to sort different fruits like orange, potatoes and so on. A grading and sorting system based on machine vision for date fruit was developed by Ohali [59]. The system was able to categorize the date fruit into three classes (grade 1, 2 or 3) from the given RGB image as an input. A back-propagation algorithm was tested in the study which showed 80% accuracy. Fruits and vegetables quality depends on their parameters like shape, size, texture, color and defects. Different methods needs to apply in order to classify the fruits and vegetables according to their quality parameters like data collection, pre-processing of data, image segmentation, feature extraction, and finally classification. Bhargava, et al. [60] presented a detail survey to compare the various algorithms used in every stage of the fruits and vegetables quality inspection. Meshram, et al. [61] proposed a new framework called "MNet: Merged Net" to reduce the fruits misclassification problem. Author created his own dataset of top Indian fruits consists of 12,000 images with

Table 6
Analysis of post-harvesting works.

Sr. No.	Property	Classes defined in the work	Dataset used (Public / Own)	Total no of images used for training	Models / Method / Algorithms compared	Results	Model evaluation technique	Reference
1	POSTHARVEST GRADING CLASSIFI-CATION OF CAVENDISH BANANA	4 classes	own	1116	Python OpenCV and Tensorflow	0.9	accuracy	[54]
2	Defect discrimination and grading in tomatoes	4 classes: category 1, 2, 3, and 4. depends upon defect, healthy, and ripeness (red color intensity)	own	8000	linear-SVM, quadratic-SVM, cubic-SVM, and radial basis function (RBF-SVM), ANN, decision tree, and random forest	0.9709	Confusion matrix	[55]
3	Postharvest classification of banana (Musa acuminata)	extra class, class I, class II and reject class	own	1164	artificial neural network, support vector machines and random forest	0.942	Classification Accuracy, F-Score, Confusion matrix	[56]
4	Automatic apple sorting system	small, normal, large, light and dark, defective and non-defective	own	183	K-means, C4.5 decision tree	0.79	statistical test	[58]
5	Date fruit grading	3 classes: grades 1, 2 and 3	own	1860	back propagation neural network (BPNN)	0.8	Confusion matrix	[59]

six classes. Table 6, presented the detail summary of post-harvesting works.

5. Discussion

This paper has extensively reviewed the available literature on application of machine learning and deep learning in agriculture. Different state-of-the-art machine learning and deep learning models in different stages of agriculture, including pre-harvesting, harvesting and post-harvesting in different domains were reviewed. Deep learning technology is becoming mature day-by-day. This survey shows that use of CNN in agriculture is huge and it is also getting remarkable results. By exploiting depth, other structure and hardware support, the learning capacity and accuracy of the CNN is significantly improved. Still there are challenges like dataset creation, time required for training and testing, hardware support, deployment of big models on small devices like boards or android phones, user awareness etc.

A popular technique called “Transfer Learning” is often used to mitigate the problems of small dataset, time required for training and to improve the accuracy of the model. Internet of Things (IoT) systems combined with machine learning provides a beneficial solution to improve farming gains. Real time parameters of the farms are gathered using IoT, and the collected data is used by machine learning algorithms either to predict or for recommendations to farmers for improvements in farming. From the survey it is also observed that Single-Shot Convolution Neural YOLO (You only look once) is a state-of-the-art, real-time object detection system which must be used for detection and localization to increase the classification accuracy.

Automated machine learning (AutoML) is the latest approach which can be used to build highly efficient, more accurate, high quality ML models in a less time [62,63]. AutoML is used to automate the entire ML pipeline shown in the Fig. 3, starting from data cleaning to model selection and hyperparameters tuning. These are time-consuming and iterative tasks of machine learning model development. As compared to traditional ML model development which is time-consuming, resource-intensive, need domain expertize, AutoML can accelerate the complete process to get production-ready model in less time without requiring domain expertise. In depth surveys on automated machine learning (AutoML) is presented in [64–69].

6. Challenges and recommendations

From this survey one can comprehend the importance of machine learning in the agriculture domain. In each phase of agriculture starting from pre-harvesting to post-harvesting, researchers have applied machine learning algorithms to solve the complex problems. Today’s need is to develop precise and customized machine learning models which can perform fast, automatically analyze bigger, more complex data and help to optimize the agriculture processes like classification, recommendations or predications.

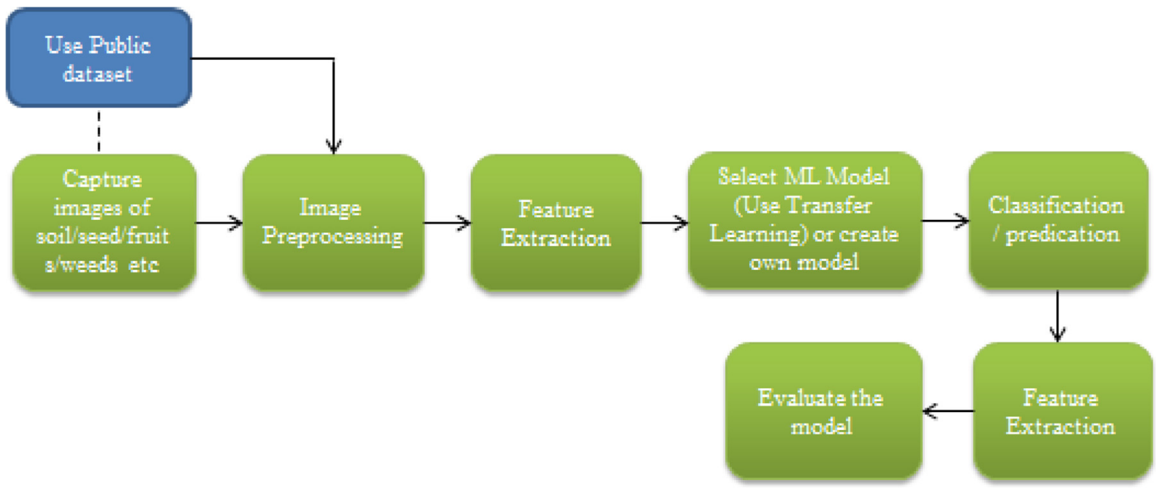

Fig. 3. Steps of Machine Learning used in literature.

The benefits of machine learning in agriculture domain are enormous. However, the benefits come with its challenges. Few such challenges while implementing machine learning algorithms in agriculture domain are listed as follows:

1) *Data:* Data is the most fundamental requirement to build the machine learning models. Many researchers faced the challenges regarding data like lack of data, unavailability of data in required format, poor quality of data, data may contain extraneous features etc. From this survey it is observed that, many researchers use data source sites like Kaggel, Meandly, IEEE Dataport etc. to get the data to build models. If the required data is not available then researchers need to build their own dataset [70–75].
2) *Pre-processing of the data:* As there are lot of problems associated with data, one has to apply the different pre-processing techniques to make the data suitable for training, testing, and validation testing the model. This might be time consuming process.
3) *Selection of machine learning algorithms:* Wide list of machine learning algorithm is available which make it difficult to find out more suitable algorithm to build the customize machine learning model. Many times, it is required to do random selection or after comparing results of multiple algorithms one can come to conclusion for best suitable algorithm. This trial-and error technique may delay the model deployment process.
4) *Training and testing of the machine learning model:* Building the accurate model needs huge data for training. Testing and validation are also important to check the accuracy of the model before its deployment. Building a model from scratch for best desired and possible outcomes needs long training and multiple time testing which are very time-consuming tasks. It needs high configuration hardware resources; domain knowledge programmers, testing tools etc. Overfitting and underfitting are the common challenges faced while building the models.
5) *Deployment of models:* This is the most challenging phase to bring the models in the production as there is absence of deployment skills, third party library dependencies, size of models, complex real-world scenarios, deployment platform hardware limitations, (like android phones, embedded boards) etc.

Some more challenges are important to make a note of:

1) Understanding the business need and identification of problem.
2) Understanding user and their interaction with technology
3) User friendly application design.
4) Performance of models in the real-word scenarios.
5) Power consumption by model and battery limitations to run the model on the devices.
6) For computer vision models camera configurations at user end.

The applications of machine learning and deep learning in the field of agriculture are huge with many challenges. After this in-depth survey following are a few recommendations to make the implementation process more fast, accurate, smooth and deployable.

1) Focus to build a machine learning model to solve specific problem like classification or recommendation.
2) For training the model try to create own dataset and make this available to other researchers through open platform like Kaggel, Meandly, IEEE Dataport etc.
3) For testing and validation of the models use publically available dataset.
4) To reduce the time required for training a model use the “Transfer Learning” techniques.
5) AutoML is the state-of-the-art approach which can be used to build more accurate, high quality ML models in a less time.
6) Deployment of the model in real-time application is recommended to help the intended users in their mundane work.

7. Conclusion

In this paper an in-depth survey of applications of machine learning algorithms in agriculture domain is presented. According to this review, agriculture activities are broadly categorized into three major areas as pre-harvesting, harvesting and post harvesting. Important parameters to be considered in each stage are shown in Fig. 2 and Table 1. Machine learning algorithms/techniques used in each stage are reviewed and presented in Tables 2, 3, 4, 5 and 6 respectively. Machine learning is the state-of-art technology which is used to solve complex problem in the agriculture and helping farmers to reduce their losses. In this survey it is seen that machine learning algorithms have obtained remarkable outcomes to solve agriculture related problems.

Our study indicated that there is need to follow the machine learning pipeline with standard experimental methods. Researches should create their own dataset and make this available to others through different platforms, so that others can use it for testing and validation of their own models. This comprehensive survey of various machine learning algorithms used in different stages of agriculture will be more helpful to other researches who are working in this field.

References

[1] Siqueira VS, Borges MM, Furtado RG, Dourado CN, MCosta R. Artificial Intelligence applied to support medical decisions for the automatic analysis of echocardiogram images: a Systematic Review. Artif Intell Med 2021;120(5):102165 doi.org/10.1016/j.artmed.2021.102165.

[2] Karie NM, Kebande VR, Venter HS. Diverging deep learning cognitive computing techniques into cyber forensics. Forensic Sci Int 2019;1:61–7 vol. 1, pp. 61-67doi.org/10.1016/j.fsisyn.2019.03.006.

[3] Doowon J. Artificial intelligence security threat, crime, and forensics: taxonomy and open issues. IEEE Access 2020;8 184560-184574. 10.1109/ACCESS.2020.3029280.

[4] Meshram VV, Patil K, Meshram VA, Shu FC. An Astute Assistive Device for Mobility and Object Recognition for Visually Impaired People. IEEE Trans Hum Mach Syst 2019;49(5):449–60 10.1109/THMS.2019.2931745.

[5] Patil K, Jawadwala Q, Shu FC. Design and construction of electronic aid for visually impaired people. IEEE Trans Hum Mach Syst 2018;48(2):172–82 10.1109/THMS.2018.2799588.

[6] Arah IK, Amaglo H, Kumah EK, Ofori H. Preharvest and postharvest factors affecting the quality and shelf life of harvested tomatoes: a mini review. Int J Agron 2015;2015 6,Article ID 478041http://dx.doi.org/10.1155/2015/478041.

[7] Prange RK. Pre-harvest, harvest and post-harvest strategies for organic production of fruits and vegetables. Acta Hortic 2012;933:43–50 DOI10.17660/ActaHortic.2012.933.3.

[8] Liakos KG, Busato P, Moshou D, Pearson S, Bochtis D. Machine learning in agriculture: a review. *Sensors* (Switzerland) 2018;18(8):1–29 10.3390/s18082674.

[9] Sharma A, Jain A, Gupta P, Chowdary V. Machine learning applications for precision agriculture: a comprehensive review. IEEE Access 2021;9:4843–73 10.1109/ACCESS.2020.3048415.

[10] Suchithra MS, Pai ML. Improving the prediction accuracy of soil nutrient classification by optimizing extreme learning machine parameters. Inf Process Agricul 2019;7(1):72–82.

[11] Yang M, Xu D, Chen S, Li H, Shi Z. Evaluation of machine learning approaches to predict soil organic matter and pH using vis-NIR spectra. *Sensors* (Switzerland) 2019;19(2):263–77 10.3390/s19020263.

[12] Morellos A, Pantazi X, Moshou D, Alexandridis T, Whetton R, Tziotzios G, Wiebensohn J, Bill R, Mouazen AM. Machine learning based prediction of soil total nitrogen, organic carbon and moisture content by using VIS-NIR spectroscopy. Biosyst Eng 2016;152:104–16 http://dx.doi.org/10.1016/j.biosystemseng. 2016.04.018.

[13] Johann AL, de Araújo AG, Delalibera HC, Hirakawa AR. Soil moisture modeling based on stochastic behavior of forceson a no-till chisel opener. Comput Electron Agricul 2016;121:420–8 http://dx.doi.org/10.1016/j.compag.2015 .12.020, 2016.

[14] Nahvi B, Habibi J, Mohammadi K, Shamshirband S, Saleh Al Razgan O. Using self-adaptive evolutionary algorithm to improve the performance of an extreme learning machine for estimating soil temperature. Comput Electron Agricul 2016;124:0168–1699 http://dx.doi.org/10.1016/j.compag.2016.03.025.

[15] Sivakumar D, SuriyaKrishnaan K, Akshaya P, Anuja GV, Devadharshini GT. Computerized growth analysis of seeds using deep learning method. Int J Recent Technol Eng 2019 Volume-7Issue-6S5.

[16] Huang S, Fan X, Sun L, Shen Y, Suo X. Research on classification method of maize seed defect based on machine vision. J Sens 2019;2019:9 Article ID 2716975https://doi.org/10.1155/2019/2716975.

[17] Zhu S, Zhou L, Gao P, Bao Y, He Y, Feng L. Near-infrared hyperspectral imaging combined with deep learning to identify cotton seed varieties. Molecules 2019;24:3268 10.3390/molecules24183268.

[18] Young J, Se JK, Dayeon K, Keondo L, Wan CK. Super-high-purity seed sorter using low-latency image-recognition based on deep learning. IEEE Robot Autom Lett 2018:2377–3766 https://doi.org/10.1186/s12859-018-2267-2.

[19] Ke-ling TU, Lin-juan LI, Li-ming YANG, Jian-hua WANG, Qun SUN. Selection for high quality pepper seeds by machine vision and classifiers. J Integr Agric 2018;17(9):1999–2006 10.1016/S2095-3119(18)62031-3.

[20] Uzal LC, et al. Seed-per-pod estimation for plant breeding using deep learning. Comput Electron Agricul 2018;150:196–204 https://doi.org/10.1016/j.compag.2018.04.024.

[21] Veeramani B, Raymond JW, Chanda P. DeepSort: deep convolutional networks for sorting haploid maize seeds. BMC Bioinformatics 2018;19(9):289 Suppl-https://doi.org/10.1186/s12859-018-2267-2.

[22] D. Nkemelu, D. Omeiza, and N. Lubalo,"Deep convolutional neural network for plant seedlings classification", 2018, arXiv:1811.08404v1 [cs.CV].

[23] Medeiros Dantas de, Pereira MDias, Fernanda Santos Neri Soares T, Gomes Noronha B, Teixeira Pinheiro D. Computer vision as a complementary method to vigour analysis in maize seeds. J Exp Agricul Int 2018;25(5):1–8 Article no.JEAI.43464.

[24] Amiryousefi MR, Mohebbi M, Tehranifar A. Pomegranate seed clustering by machine vision. Food Sci Nutr 2017;6(1):18–26 10.1002/fsn3.475.

[25] Vlasov AV, Fadeev AS. A machine learning approach for grain crop's seed classification in purifying separation. IOP Conf Ser 2017;803(2017):012177 10.1088/1742-6596/803/1/012177.

[26] Kurtulmuş F, Alibaş İ, Kavdir I. Classification of pepper seeds using machine vision based on neural network. Int J Agricul Biol Eng 2016;9(1):51–62 10.3965/j.ijabe.20160901.1790.

[27] Alagumariappan P, Dewan NJ, Muthukrishnan GN, Bojji Raju BK, Bilal RAA, Sankaran V. Intelligent plant disease identification system usingmachine learning. Eng Proc 2020;2:49 10.3390/ecsa-7-08160.

[28] Savary S, Ficke A, Aubertot J-N, Hollier C. Crop losses due to diseases and their implications for global food production losses and food security. Food Secur 2012 DOI 10.1007/s12571-012-0200-5.

[29] Sujatha R, Chatterjee JM, Jhanjhi NZ, Brohi SN. Performance of deep learning vs machine learning in plant leaf disease detection. Microprocess Microsyst 2021;80 https://doi.org/10.1016/j.micpro.2020.103615.

[30] Karada˘g K, Tenekeci ME, Tasaltın R, Bilgilic A. Detection of pepper fusarium disease using machine learningalgorithms based on spectral reflectance. Sustain Comput 2018:8 https://doi.org/10.1016/j.suscom.2019.01.001.

[31] Pandya IY. Pesticides and their applications in agriculture. Asian J Appl Sci Technol (AJAST) 2018;2(2):894–900 ISSN: 2456-883X.

[32] Arsenovic M, Karanovic M, Sladojevic S, Anderla A, Stefanovic D. Solving current limitations of deep learning based approaches for plant disease detection. Symmetry (Basel) 2019;11:939 10.3390/sym11070939.

[33] Barbedo JGA. Plant disease identification from individual lesions and spots using deep learning. Biosyst Eng 2019;180:96–107 https://doi.org/10.1016/j.biosystemseng.2019.02.002.

[34] Saleem MH, Potgieter J, Arif KM. Plant disease detection and classification by deep learning. Plants 2019;8:468 10.3390/plants8110468.

[35] Türkoğlu M, Hanbay D. Plant disease and pest detection using deep learning-based features. Turk J Electr Eng Comput Sci 2019;27:1636–51 10.3906/elk-1809-181.

[36] Liu B, Zhang Y, He D, Li Y. Identification of apple leaf diseases based on deep convolutional neural networks. Symmetry (Basel) 2018;10:11 10.3390/sym10010011.

[37] Kour V, Arora S. Fruit Disease Detection Using Rule-Based Classification. In: Proceedings of Smart Innovations in Communication and Computational Sciences, Advances in Intelligent Systems and Computing (ICSICCS-2018); 2019. p. 295–312. 10.1007/978-981-13-2414-7_28.

[38] Xing S, Lee M, Lee K. Citrus pests and diseases recognition model using weakly dense connected convolution network. Sensors 2019;19:3195 10.3390/s19143195.

[39] Doh B, Zhang D, Shen Y, Hussain F, Doh RF, Ayepah K. Automatic Citrus Fruit Disease Detection By Phenotyping Using Machine Learning. In: Proceedings of the 25th international conference on automation & computing. Lancaster UK: Lancaster University; 2019. 5-7 September.

[40] Hua Y, Zhang N, Yuan X, Quan L, Yang J, Nagasaka K, Zhou X. Recent advances in intelligent automated fruit harvesting robots. Open Agricul J 2019;13:101–6 10.2174/1874331501913010101.

[41] Kushtrim B, Demetrio P, Alexandra B, Brunella M, Grappa C. Single-shot convolution neural networks for real-time fruit detection within the tree. Front Plant Sci 2019;10:611 10.3389/fpls.2019.00611.

[42] Hossain MS, Al-Hammadi M, Muhammad G. Automatic fruit classification using deep learning for industrial applications. IEEE Trans Ind Inf 2019;15(2) 10.1109/TII.2018.2875149.

[43] Kirk R, Cielniak G, Mangan M. L*a*b*Fruits: a Rapid and Robust Outdoor Fruit Detection System Combining Bio-Inspired Features with One-Stage Deep Learning Networks. Sensors 2020;20:275 10.3390/s20010275.

[44] Altaheri H, Alsulaiman M, Muhammad G. Date fruit classification for robotic harvesting in a natural environment using deep learning. IEEE Access 2019;7:117115–33 10.1109/ACCESS.2019.2936536.

[45] Bauer A, Bostrom AG, Ball J, Applegate C, Cheng T, Laycock S, Rojas SM, Kirwan J, Zhou Ji. Combining computer vision and deep learning to enable ultra-scale aerial phenotyping and precision agriculture: a case study of lettuce production. Hortic Res 2019;6:70 https://doi.org/10.1038/s41438-019-0151-5.

[46] Zhang T, Huang Z, You W, Lin J, Tang X, Huang H. An autonomous fruit and vegetable harvester with a low-cost gripper using a 3D sensor. Sensors 2020;20:93 10.3390/s20010093.

[47] Onishi Y, Yoshida T, Kurita H, Fukao T, Arihara H, Iwai A. An automated fruit harvesting robot by using deep learning. Robomech J 2019;6:13 https://doi.org/10.1186/s40648-019-0141-2.

[48] X. Liu, S.W. Chen, S. Aditya, N. Sivakumar, S. Dcunha, C. Qu, C.J. Taylor, J. Das, and V. Kumar,"Robust Fruit Counting: Combining Deep Learning, Tracking, and Structure from Motion", arXiv:1804.00307v2 [cs.CV] 2 Aug 2018.

[49] United states department of Agriculture (USDA) Grade standards for Fruits, https://www.ams.usda.gov/grades-standards/fruits (Accessed: July 2021).

[50] EU, Fruit and Vegetables: Marketing Standards, 2011,https://ec.europa.eu/agriculture/fruit-and-vegetables/marketing-standards_en (Accessed: July 2021).

[51] Government Of India, AGMRK ("Agricultural Marketing Adviser"), 2004, https://upload.indiacode.nic.in/showfile?actid=AC_CEN_23_31_00011_193701_1535099362507&type=rule&filename=fruits_and_vegetables_grading_and_marking_rules,_2004.pdf (accessed:July 2021).

[52] Esguerra Elda B. Post-harvest management of mango for quality and safety assurance guidance for horticultural supply chain stakeholders. Rome: Food and Agriculture Organization of The United Nations; 2018.

[53] Gaetano Paltrinieri. Handling of fresh fruits, vegetables and root crops -a training manual- for grenadaAgricultural marketing improvement TCP/GRN/2901. Food and Agriculture Organization of the United Nations; 2021. http://www.fao.org/3/au186e/au186e.pdf. accessed:July.

[54] Ucat RC, Dela Cruz JC. Postharvest grading classification of cavendish banana using deep learning and tensorflow. In: 2019 International Symposium on Multimedia and Communication Technology (ISMAC); 2019. p. 1–6. 10.1109/ISMAC.2019.8836129.

[55] Ireri D, Belal E, Okinda C, Makange N, Ji C. A computer vision system for defect discrimination and grading in tomatoes using machine learning and image processing. Artif Intell Agricul 2019;2:28–37 https://doi.org/10.1016/j.aiia.2019.06.001.

[56] Jr Piedad E, Larada JI, Pojas GJ, Vithalie L, Ferrer V. Postharvest classification of banana (Musa acuminata) using tier-based machine learning. Postharvest Biol Technol 2018;145:93–100 https://doi.org/10.1016/j.postharvbio.2018.06.004.

[57] Lia J, Chena L, Huanga W. Detection of early bruises on peaches (Amygdalus persica L.) using hyperspectral imaging coupled with improved watershed segmentation Algorithm. Postharvest Biol Technol 2018;135:104–13 http://dx.doi.org/10.1016/j.postharvbio.2017.09.007.

[58] Sofu MM, Er O, Kayacan MC, Cetisli B. Design of an automatic apple sorting system using machine vision. Comput Electron Agric 2016;127:395–405 http://dx.doi.org/10.1016/j.compag.2016.06.030.

[59] Ohali YA. Computer vision based date fruit grading system: design and implementation. J King Saud Univ – Comput Inf Sci 2011;23:29–36 10.1016/j.jksuci.2010.03.003.

[60] Bhargava A, Bansal A. Fruits and vegetables quality evaluation using computer vision: a review. J King Saud Univ – Comput Inf Sci 2018;33:243–57 https://doi.org/10.1016/j.jksuci.2018.06.002.

[61] Meshram VA, Patil K, Ramteke SD. MNet: a framework to reduce fruit image misclassification. Ing Syst Inf 2021;26(2):159–70 https://doi.org/10.18280/isi.260203.

[62] Microsoft, "What is automated machine learning (AutoML)?" https://docs.microsoft.com/en-US/azure/machine-learning/concept-automated-ml, (Accessed: July 2021).

[63] Hibayesian, "awesome-automl-papers", 2017, https://github.com/hibayesian/awesome-automl-papers (Accessed: July 2021).

[64] X. He, K. Zhao, X. Chu, "AutoML: A Survey of the State-of-the-Art", 2021, arXiv:1908.00709v6 [cs.LG] 16 Apr 2021.

[65] Zoller M, Huber MF. Benchmark and survey of automated machine learning frameworks. J Artif Intell Res 2021;70:409–74. arXiv:1904.12054v5 [cs.LG] 26 Jan 2021.

[66] R. Elshawi, M. Maher, S. Sakr, "Automated machine learning: state-of-the-art and open challenges", 2019, arXiv:1906.02287v2 [cs.LG] 11 Jun 2019.

[67] Q. Yao, M. Wang, Y. Chen, W. Dai, Y. Li, W. Tu, Q. Yang, Y. Yu, "Taking the human out of learning applications: a survey on automated machine learning", 2019, arXiv:1810.13306v4 [cs.AI] 16 Dec 2019.

[68] L. Yang, and A. Shami, "On hyperparameter optimization of machine learning algorithms: theory and practice", 2020, arXiv:2007.15745v2 [cs.LG] 7 Aug 2020.

[69] H.J. Escalante, "Automated Machine Learning - a brief review at the end of the early years", 2020, arXiv:2008.08516v3 [cs.LG] 24 Aug 2020.

[70] Mihai Oltean. Fruits 360 dataset. Mendeley Data 2018;V1 10.17632/rp73yg93n8.1.

[71] prabira Kumar sethy. Indian Fruits-40. Mendeley Data 2020;V1 10.17632/bg3js4z2xt.1.

[72] Meshram VA, Thanomliang K, Ruangkan S, Chumchu P, Patil K. FruitsGB: top indian fruits with quality. IEEE Dataport 2020 https://dx.doi.org/10.21227/gzkn-f379.

[73] Meshram VA, Patil K. FruitNet: Indian Fruits Dataset with quality (Good, Bad & Mixed quality). Mendeley Data 2021;V1. doi:10.17632/b6fftwbr2v.1.

[74] Tripathi M, Maktedar D, Dhanajay D. Fruits and Vegetables. Mendeley Data 2020;V2 10.17632/73kpfrbcck.2.

[75] Math M, Kumar R, Dharwadkar V, Nagaraj Dr. Real-world tomato image dataset for deep learning and computer vision applications involving precision agriculture. Mendeley Data 2020;V1 10.17632/9zyvdgp83m.1.

An assessment of wind energy status, incentive mechanisms and market

Amiya Kumar sahoo, *Department of Computer Sciencel Engineering, Aryan Institute of Engineering & Technology, Bhubaneswar, aksahoo336@gmail.com*

Sachikanta Pati, *Department of Computer Scinece Engineering , NM Institute of Engineering & Technology, Bhubaneswar, sachikantapati98@outlook.com*

Ashis Acharya, *Department of Computer Scinece Engineering , Capital Engineering College, Bhubaneswar, ashisacharya12@gmail.com*

Rajesh Tripathy, *Department of Computer Scinece Engineering , Raajdhani Engineering College, Bhubaneswar, rajeshtripathy1@outlook.com*

Keywords:
Wind energy
Incentive mechanism
Market
Policy
Feasibility analysis
Turkey

A B S T R A C T

Turkey attaches great importance to energy diversification to reduce the energy dependence on fossil resources. In this regard, Turkey assigned energy targets by 2023 including 20 GW of installed wind capacity. Yet, despite the good efforts, the current wind installed capacity of 8 GW is far behind the assigned target. This study presents a comprehensive review of wind energy status in Turkey focusing on policies and incentives for improvement of wind energy progress in the country. To that end, the global wind energy market is evaluated and a set of recommendations is presented in the context of the importance of local employment and establishment of local wind energy industry. Then, a feasibility analysis is performed to discuss the current feed-in tariff scheme in Turkey. Lastly, Turkey's competitive position is evaluated over a SWOT analysis to give an overview of all positive and negative determinants, considering internal and external factors.

1. Introduction

Global energy consumption is increasing steadily with the rising population, energy-dependent habits of use, and technological developments. The world population of 6.84 billion in 2009 became 7.59 billion in 2018 with a growth rate of nearly 1.1% [1], and the global primary energy demand of 11,540.3 Mtoe in 2009 reached 13,864.9 Mtoe in 2018 with an average annual increase of 2.01% [2]. Meanwhile, the global electric energy consumption of 17,355 TWh in 2009 reached 22,964 TWh in 2018 with a growth rate of 3.23% [3]. The main reason for the higher growth rate of energy consumption than the global population and primary energy demand has become the rapid rise in the use of electrical devices due to technological advances. This situation prompted countries to look for new ways to meet their ever-increasing energy demands.

As the global energy demand increases, the countries seek new solutions to curtail their demand for fossil resources. The average ratio of electricity production from conventional resources was 66.5% between 2005 and 2015 [4]. The negative impacts on the environment along with the depletion of fossil sources and a large share of energy expenditures in the economy caused interest in renewables and their share gradually increased over the last decade [5]. Among the renewables, the average share of hydroelectric resources in the global electricity production was 16% between 2005 and 2015 [6]. The share of renewables except hydroelectric was increased from 1.96% in 2005 to 6.77% in 2015 and this increase is mostly provided by wind energy [7]. The electricity acquired from the wind energy had a share of 4.55% in the global electricity production in 2017 [8].

Turkey is one of the countries that comply with the global wind energy trend in recent years. The fact that Turkey is an energy importing country (mostly from Russia, Iran, and Iraq), and the electricity is mainly generated by fossil fuels, which has the largest share in energy expenses, made Turkey focus more on reducing its energy dependency by promoting renewable energy resources over the last decade. Wind energy takes the first place in the non-hydro renewable investments due to the country's high wind potential. Yet, despite the relatively good effort in the last decade, the wind energy potential has not been effectively utilized in Turkey.

1.1. Literature review

Currently, all wind power installations in Turkey are onshore, and review studies regarding Turkey have focused on onshore wind energy. Güler [9] presented the wind energy status of Turkey and examined the purchase guarantee for renewables introduced in 2005. Ilkilic [10] investigated the wind energy potential of dif-

Nomenclature

List of symbols

NCF_t	Net cash flow at time t (\$/year)
NCF_0	Initial investment cost (\$)
$O\&M_t$	annual operation & maintenance cost of the plant at time t (\$/year)
E	Annual wind electricity production (kWh)
P	Installed capacity of power plant (kW)
f	Expected inflation rate
i	Real interest rate
i'	Nominal discount rate
λ	selling price (\$/kWh)

List of abbreviations

CF	Capacity factor
DPBP	Discounted payback period
EIE	Electricity Affairs Survey Administration
MoENR	Ministry of Energy and Natural Resources
MoEU	Ministry of Environment and Urbanization
REPA	Wind energy potential atlas
SWOT	Strenghts, weaknesses, opportunities and threats
YEKA	Renewable Energy Resource Areas
YEKDEM	Renewable Energy Resources Support Mechanism

ferent regions in Turkey. Yaniktepe et al. [11] examined the installed wind power capacity in the context of countries and investigated the Renewable Energy Law (2011) which amended the purchase guarantee introduced in 2005. Camadan [12] separately assessed Turkey's priorities of wind energy policies in the short, medium, and long term. In short term priorities, support mechanisms, licensing and coordination, balance, and settlement market were evaluated, while in medium and long term, intermittency of wind energy, demand-side management, and ancillary services were examined. Dursun and Gokcol [13] examined the before and after of wind energy installations following the introduction of the existing Renewable Energy Law of Turkey. Kaplan [14] presented the legal regulations and expectations of the wind energy sector. None of the studies above explicitly examined the wind energy-related industry and local labor force in Turkey.

There is no offshore wind farm in Turkey and the studies in the literature regarding offshore focus on site selection, potential estimation, and feasibility analysis. Argin et al. [15] studied the offshore potential of 20 selected sites on the Black Sea coast of Turkey. Amasra was stated to have the highest potential. Satir et al. [16] conducted a feasibility study for the Aegean coasts of Turkey and made recommendations on the future development of offshore wind energy. Cali et al. [17] determined high-potential sites for offshore wind in Turkey using a multi-criteria site selection method and conducted a detailed techno-economic analysis of the regions. Bozcaada was determined as economically the most viable site. Argin et al. [18] investigated 55 different sites in coastal areas using a multi-criteria site selection method and determined the wind potential of the five most suitable points for offshore as 1,629 MW. Emeksiz and Demirci [19] proposed a novel method to identify suitable sites for offshore wind farms. 9021 MW of offshore capacity was estimated for the selected regions.

1.2. Content and contribution

In this review study, the current status of wind energy in the world and Turkey is evaluated and recommendations are made for Turkey to achieve its wind energy targets taking into account the incentives, wind energy market, wind energy jobs, and local wind turbine industry.

When the literature is examined, it is determined that a study focusing on the local wind turbine industry and the labor force is missing for Turkey. Thus, the study mainly aims to fill this missing part in the literature, comparing Turkey's policies with other countries.

The Turkish feed-in tariff scheme will end by the end of 2020. Its future for licensed generation is still unclear and is a great hesitation factor for the project investors. The second objective of the study is to make recommendations about the future of the Turkish feed-in tariff scheme. Also, a feasibility analysis is included not only to discuss the future of the feed-in tariff scheme of Turkey but also to enrich the comprehensive feature of the study.

Finally, a SWOT (strengths, weaknesses, opportunities, and threats) analysis is made to evaluate Turkey's competitive position considering internal and external factors and to give a clear overview of all positive and negative determinants.

2. Wind energy status in the world

2.1. Global installed capacity

After the oil crises in the 70 s and 80 s, the atmosphere of insecurity about energy resources [20] and the concept of "energy diversification" became one of the indispensable elements of energy policies [21]. As a result, wind energy gained importance especially in Europe and the USA [10]. During the 1980 s and 1990 s, modern wind farm constructions began and the cumulative wind installations in the world reached 6,100 MW in 1996 [22]. By the end of 2000, onshore wind energy capacity in the world was 16,863 MW and nearly 80% of this capacity belonged to Germany, the USA, Denmark, and Spain [23]. Global wind energy investments remarkably increased between 2000 and 2010. The global wind capacity grew 3.5 times in 2005 and 10 times in 2010 compared to 2000. During this period, new countries, such as China and India, joined the wind market. India and China increased their installed capacities by approximately 14 and 85 times, respectively over 10 years [24].

The total global installed wind capacity of 180,850 MW in 2010 (177,794 MW onshore) increased to 622,704 MW in 2019 (594,396 MW onshore) [23]. Fig. 1 shows the total onshore and offshore wind capacities in the world from 2010 to 2019. The cumu-

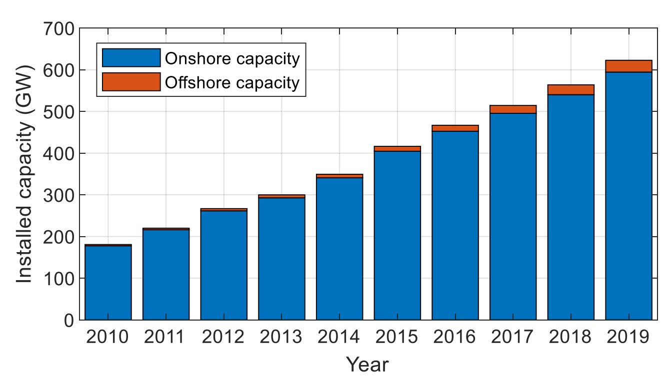

Fig. 1. The global installed onshore and offshore wind capacity [24].

lative installed capacities of the top 15 countries are listed in Table 1. The top 15 countries constitute 88.5% and 89.5% of global wind capacity for onshore and offshore, respectively. China is the leading country in onshore with installed wind capacity of 204,548 MW and the United Kingdom has the highest offshore wind capacity with 9,945 MW in the world [23].

2.2. Global electricity production

The share of renewables (especially wind) in total electricity production increased considerably in the last decade. The change in global electricity generation from wind energy between 2010 (342,092 GWh) and 2017 (1,134,451 GWh) is given in Fig. 2. It is seen that the wide majority of the generation belongs to onshore. According to the latest data for wind electricity production, the ratio of the electricity generation from the onshore wind energy to the total wind generation was 98% and 94.9% in 2010 and 2017 respectively [8]. The development of the offshore electricity generation is slower than the onshore mainly due to their high expenses, constructional difficulties, and unavailability of individual use [25,26].

The share of wind energy in the total electricity production for the top 15 countries is given in Fig. 3. It is seen that the countries invested in wind energy in the early 2000 s such as Denmark, Spain, and Germany have higher wind share today. At the beginning of the 2000 s, the global share of wind in the total electricity production was 0.2%, which reached to 4.55% in 2017. The top three countries in wind electricity generation were Denmark (12.72%), Spain (2.11%), and Germany (1.62%) in 2000. The other countries had lower shares of less than 1%.

The share of wind electricity production has increased for countries over the years due to technological advances and reduced costs. In 2017, the top three countries in wind electricity production were Denmark (40.67%), Portugal (20.76%), and Spain

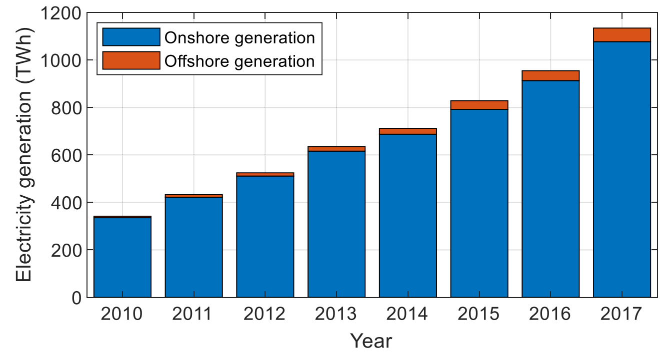

Fig. 2. Global electricity generation from the wind [24].

(17.86%). By 2017, six countries have wind share more than 10% and five countries have wind share between 5 and 10% in their total electricity production.

China's wind share (4.63%) is below 5% however above the world average. France, Canada, and India have a wind share below 5% and also below the world average among the top 15 countries.

2.3. Capacity factors by countries

Capacity factor (CF) is calculated as follows:

$$CF = \frac{E}{P \times 8760} \tag{1}$$

where E represents the annual wind electricity production (kWh) and P is the rated installed capacity (kW). Here, the average capacity factor values are calculated by the ratio of the annual energy production of the country to the installed power capacity output over a period of a whole year for the top 15 countries

Table 1
Onshore and offshore installed wind capacities of the top 15 countries and the world [23].

	[MW]	2010	2011	2012	2013	2014	2015	2016	2017	2018	2019
China	Onshore	29,534	46,145	61,306	76,314	96,379	130,489	147,037	161,587	180,077	204,548
	Offshore	100	210	291	417	440	559	1,480	2,788	4,588	5,930
USA	Onshore	39,135	45,676	59,075	59,973	64,232	72,573	81,257	87,568	94,388	103,555
	Offshore	–	–	–	–	–	–	29	29	29	29
Germany	Onshore	26,823	28,524	30,711	32,969	37,620	41,297	45,303	50,174	52,447	53,315
	Offshore	80	188	268	508	994	3,283	4,132	5,406	6,396	7,507
India	Onshore	13,184	16,179	17,300	18,420	22,465	25,088	28,700	32,849	35,288	37,505
	Offshore	–	–	–	–	–	–	–	–	–	–
Spain	Onshore	20,693	21,529	22,789	22,953	22,920	22,938	22,985	23,120	23,400	25,548
	Offshore	–	–	–	5	5	5	5	5	5	5
UK	Onshore	4,080	4,758	6,035	7,586	8,573	9,212	10,832	12,597	13,554	14,183
	Offshore	1,342	1,838	2,996	3,696	4,501	5,093	5,293	6,988	8,217	9,945
France	Onshore	5,912	6,723	7,562	8,250	9,110	10,258	11,567	13,497	14,898	16,258
	Offshore	–	–	–	–	–	–	–	–	–	–
Canada	Onshore	3,967	5,265	6,201	7,801	9,694	11,214	11,973	12,403	12,816	13,413
	Offshore	–	–	–	–	–	–	–	–	–	–
Brazil	Onshore	927	1,426	1,894	2,202	4,888	7,633	10,124	12,294	14,833	15,364
	Offshore	–	–	–	–	–	–	–	–	–	–
Italy	Onshore	5,794	6,918	8,102	8,542	8,683	9,137	9,384	9,737	10,230	10,758
	Offshore	–	–	–	–	–	–	–	–	–	–
Sweden	Onshore	1,854	2,601	3,443	3,982	4,875	5,606	6,232	6,408	7,097	8,685
	Offshore	163	163	163	212	213	213	203	203	203	203
Turkey	Onshore	1,320	1,729	2,261	2,759	3,630	4,503	5,751	6,516	7,005	7,591
	Offshore	–	–	–	–	–	–	–	–	–	–
Poland	Onshore	1,108	1,800	2,564	3,429	3,836	4,886	5,747	5,759	5,766	5,917
	Offshore	–	–	–	–	–	–	–	–	–	–
Denmark	Onshore	2,934	3,081	3,241	3,548	3,616	3,806	3,975	4,226	4,420	4,416
	Offshore	868	871	922	1,271	1,271	1,271	1,271	1,297	1,701	1,701
Portugal	Onshore	3,796	4,254	4,410	4,608	4,854	4,935	5,124	5,124	5,172	5,225
	Offshore	–	2	2	2	2	2	0	0	0	8
World	Onshore	177,794	216,244	261,575	292,749	340,808	404,559	452,485	495,565	540,191	594,396
	Offshore	3,056	3,776	5,334	7,171	8,492	11,718	14,342	18,837	23,629	28,308

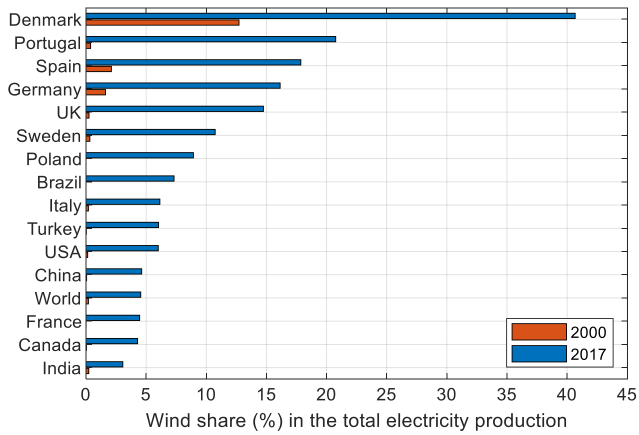

Fig. 3. Wind share (%) in the total electricity production for the top countries and the world.

between 2013 and 2017 (Fig. 4 and Fig. 5) for onshore and offshore wind energy, respectively [8,27]. From Fig. 4, it is seen that Brazil has the highest capacity factor for onshore followed by the USA and Turkey. The average capacity factor of Turkey is above its European neighbors for onshore wind energy. For the offshore, Denmark has the highest capacity factor, followed by the UK and Sweden.

3. Electricity production and targets of Turkey

Turkey is a developing country with a fast-growing population, industry, and economy. The population of Turkey which was 73.7 million in 2010 reached 83.2 million in 2019 with an average annual increase of %1.3 [28]. In the last decade, the Turkish economy had an average growth rate of 4.86% [29], and accordingly, the average increase rate of the gross electricity generation in Turkey became 4.5% [30]. The majority of electricity is supplied from conventional resources and Turkey imports almost all fossil resources except lignite from the other countries.

The electricity generation and installed capacities by sources for Turkey are given in Table 2 by the end of 2019 [30–32]. Coal has the highest share in electricity production (37.18%), followed by hydro (29.21%). The rest of the electricity demand is met by natural gas (18.64%), and non-hydro renewables (14.73%) as wind, solar, geothermal and biomass. The share of wind energy (7.07%) is ranked as the highest among the non-hydro renewables.

The on-going energy strategies of Turkey aim to reduce the dependency of the country on imported fossil fuels and to decrease

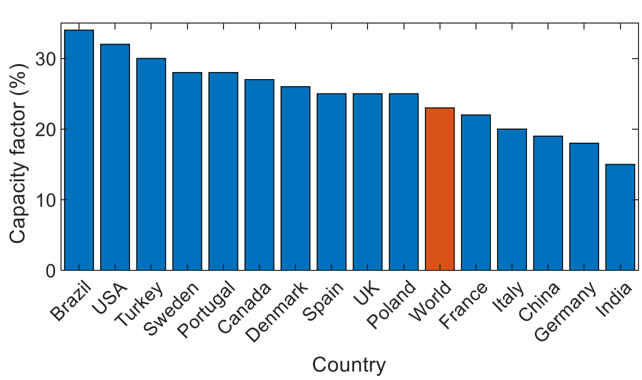

Fig. 4. Average capacity factor of the selected countries for onshore wind energy between 2013 and 2017.

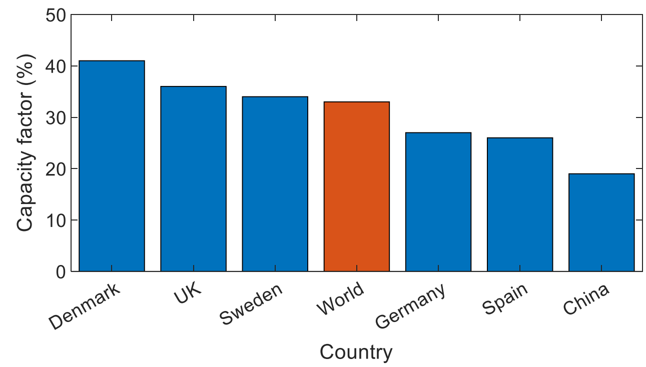

Fig. 5. Average capacity factor of the selected countries for offshore wind energy between 2013 and 2017.

the environmental impacts through measures to maximize the efficient use of renewable energy resources. For the 100th anniversary (2023) of the foundation of the Republic of Turkey, the Turkish government assigned a set of targets in many fields including energy. In 2009, the "Strategy Paper on Electricity Market Reform and Security of Supply" was issued to achieve an increased share of electricity generated from renewable resources by 30% with a specific target of 20 GW installed power capacity for wind energy, by 2023 [33].

The target of 30% renewable energy production by 2023 was not changed in Strategic Plan 2010–2014 published by the Ministry of Energy and Natural Resources (MoENR) and the Turkey Climate Change Strategy 2010–2020, published by the Ministry of Environment and Urbanization (MoEU) [34,35]. The development of renewable energy technologies was supported by the "Strategic Plan" of MoENR, and one of the long-term objectives of the "Climate Change Strategy" was determined as generating more electricity from wind energy.

Owing to its high installed hydropower capacity, as of 2018, Turkey is capable of meeting 30% of its electricity generation from the renewables. However, by the end of 2019, the total installed wind capacity is 7.59 GW and the average rate of new capacity installations of 627 MW per year in the last decade makes it impossible to reach the target of 20 GW in wind energy. Therefore, Turkey should introduce more effective policy measures to reach its 2023 targets in wind energy.

The other renewable targets of Turkey in terms of installed capacities of renewable sources are 1 GW for geothermal, 1 GW for biomass and 5 GW for solar photovoltaic (PV) [36]. The targets for geothermal and solar PV have already been achieved by the end of 2018 [30].

4. Wind energy status of Turkey

4.1. Wind energy potential of Turkey

Turkey is located between 36°-42° northern latitudes and 26°-45° eastern longitudes with a total surface area of 783,562 km^2. The Wind Energy Potential Atlas (REPA) is introduced in 2002 by the Electricity Affairs Survey Administration (EIE) to explore the wind energy potential in Turkey (Fig. 6) [37]. The REPA is a geographic information system (GIS) based map and has been compiled by using the collected data of EIE and General Directorate of State Meteorology Affairs (DMI) in 200 m × 200 m resolution [38].

According to the REPA, the wind speed at 50 m height is 6 – 7 m/s in the coasts and 5.5 – 6.5 m/s in northwestern and southeastern parts of Turkey. The western part of the country has the

Table 2
The distribution of electricity generation by sources in 2019 [30–32].

Source		Installed Capacity (MW)	Electricity Production (TWh)	Share in electricity production (%)
Non-renewables	Coal	20,283.7	113.12	37.18
	Natural gas	25,904.3	56.70	18.64
	Liquid fossils	311.6	0.73	0.24
Renewables	Hydro resources	28,503.0	88.89	29.21
	Wind	7,591.2	21.51	7.07
	Solar	5,995.2	10.07	3.31
	Geothermal	1,514.7	8.71	2.86
	Biomass	1,163.4	4.52	1.49
	Total	91,267.1	304.25	100.0

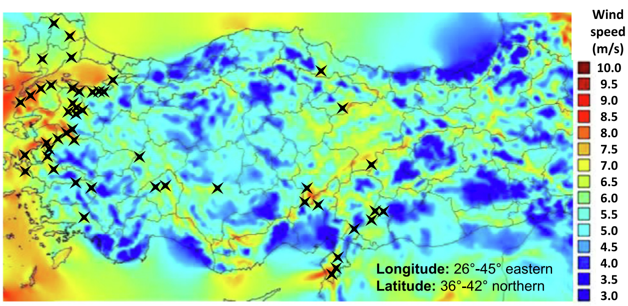

Fig. 6. The wind energy potential of Turkey at 50 m height and location of top 50 wind power plants above 50 MW (modified from [37]).

highest potential with a wind speed of 7 – 8.5 m/s in the coasts and 6.5 – 7 m/s in internal territories between western and northeastern parts [9]. According to EIE, onshore wind potential at 50 m height is 131,756 MW in Turkey [38].

The location of the top 50 wind plants above 50 MW installed capacity in Turkey are highlighted in Fig. 6. The distribution of the operational wind power plants by geographical regions of Turkey in 2019 is shown in Fig. 7 [31]. From Fig. 6, it can be seen that the high wind energy potential of the western parts of the country is already being exploited, whereas wind turbine installation rate stays low in the central and eastern parts of the country. In addition to high wind energy potential, the northern and western parts of Turkey have higher energy consumption. At the same time, the qualified labor force and industry are located in the same part of the country.

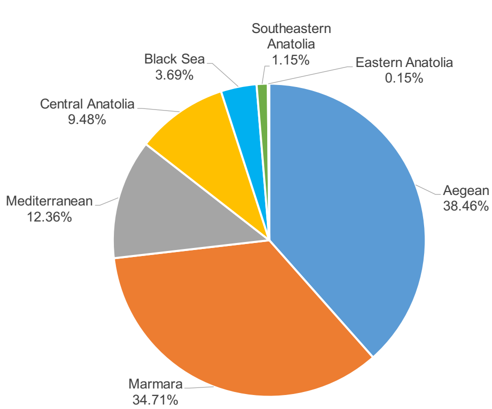

Fig. 7. The distribution of the operational wind power plants by regions of Turkey [31].

4.2. Wind energy installed capacity and generation in Turkey

The share of wind energy in the gross electricity production of Turkey has been rapidly growing. In 2010, the installed capacity of wind energy was 1,329 MW and the share of wind energy in the gross electricity production was 1.39%, whereas the total capacity reached 7,591 MW by the end of 2019, and the share of wind energy in the gross electricity production [39] became 7.07% (Fig. 8 and Fig. 9). In the last decade, the annual average capacity increase became 627 MW.

4.3. Feed-in tariff scheme for wind energy in Turkey-YEKDEM

Turkey put in place the country's first feed-in tariff scheme in 2005 under the Renewable Energy Resources Support Mechanism (YEKDEM) with the enactment of amendments to Law No. 5346 to promote renewable energy systems [40]. The rate was Turkish Lira-denominated which corresponded to 5.0 – 5.5 Euro cent/kWh [12]. This scheme, which was valid between 2005 and 2011 was not successful to promote renewable energy investments as expected. There were two main reasons for this. Firstly, the Turkish Lira-denominated feed-in tariff pushed the market participants into uncertainty due to exchange rate fluctuations. The profitability of renewable energy investments was not predictable in advance. Secondly, the feed-in tariff rates were not very attractive and most of the time the market players preferred to sell the electricity in the balancing market where the prices were slightly higher.

In 2011, the promotion law was amended. The replaced YEKDEM feed-in tariff is eligible for the first 10 years of operation [41]. To benefit from YEKDEM, the projects should be implemented before the end of 2020. In the new law, the feed-in tariff rate is US Dollar-denominated instead of Turkish Lira, also, the rate is

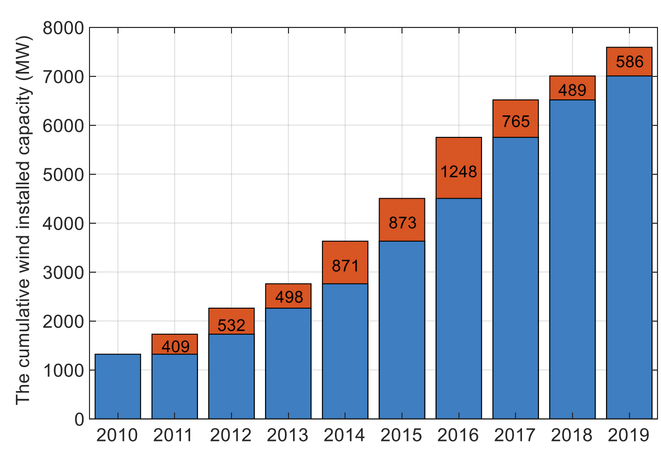

Fig. 8. The cumulative wind installed capacity in Turkey [31].

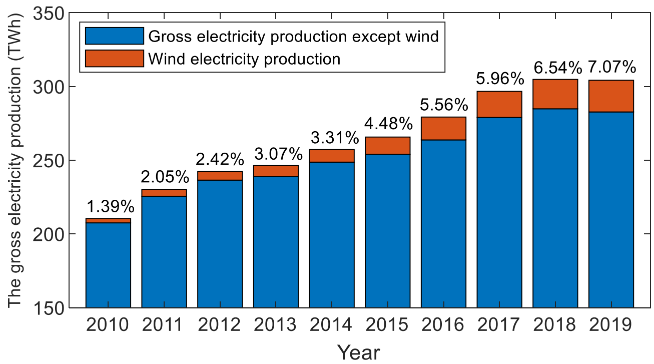

Fig. 9. The share of wind electricity in the gross electricity production of Turkey.

increased and differentiated for particular renewable technologies as:

- 7.3 $ cent/kWh for wind and hydropower
- 10.5 $ cent/kWh for geothermal
- 13.3 $ cent/kWh for biomass and solar PV

In addition to the base feed-in tariff amount, a local content bonus is introduced for locally produced mechanical and electromechanical equipment to promote the local manufacturing in Turkey. For wind energy, local content bonus varies between 0.6 and 3.7 $ cent/kWh as detailed in Table 3 [42]. The local content incentive is valid for the first 5 years of the operation.

The future of the feed-in tariff after 2020 is still unclear for the licensed production. Yet, it is clarified for the unlicensed production with the new Regulation of Unlicensed Electricity Production in Electricity Market and the Presidential Decree No. 1044 dated 10 May 2019 [43]. According to the new unlicensed law:

- The incentive rates have been Turkish Lira-denominated as it was before 2011.
- The new amount of rate is determined as the retail energy price (without distribution fee, and VAT) which is on average 45 kurus/kWh as of 2020, and corresponds to 7 $ cent/kWh depending on the currency rate.
- Unlike the previous law, the amount of rate varies according to the retail price of user groups (residential, commercial, industrial, agricultural, and lighting) [44].
- The differentiation of the incentives applying to the different renewable technologies has been ended, and the determined price applies to all technologies.
- The upper limit of 1 MW unlicensed capacity has been increased to 5 MW. Since wind technology is not a modular technology as PV, the increase in the upper limit causes a severe reduction in the unit cost of installations. It will be possible to use more cost-effective and higher capacity wind turbines.

Table 3
The list of local equipment bonus for wind energy power plants [42].

Local content	Bonus ($ cent/kWh)
Blades	0.8
Generator and power electronics	1.0
Tower	0.6
Other mechanical parts inside rotor and nacelle	1.3
Maximum local content bonus	3.7
Feed-in tariff (base)	7.3
Feed-in tariff (maximum)	11.0

- The new projects will be able to benefit from these incentives for 10 years once they are in operation.

The feed-in tariffs in YEKDEM may not always be the exact revenue of the projects. The project investors enter auctions for the allocation of connection capacity. As a result of the auctions, the owners pay a connection price to the state in terms of $ cent/kWh. The amount to be paid for the connection capacity is usually proportional to the capacity factor of a location.

In these auctions, some project investors may offer negative prices. This means these investors choose to sell the produced electricity in the free market and have a higher trust for the market prices than feed-in tariffs. In this case, the selling price becomes below the market-clearing price depending on the offered negative price [45]. Here, the market-clearing price can both become above and below the feed-in tariff rate. The risk belongs to project owners.

4.4. Wind energy auctions in Turkey - YEKA

In addition to YEKDEM feed-in tariff mechanism, Turkey has begun to apply a widely used auction mechanism to expand the capacity of renewable energy power plants since 2012 (2017 for wind energy power plants). Turkish auction model, Renewable Energy Resource Areas (YEKA) aims:

- Promotion of local manufacturing of high-technology wind and solar power equipment in Turkey
- Technology transfer
- Establishment of a competitive domestic market for low-cost renewable energy
- Efficient use of renewable energy resources with rapid investments
- Utilization of local labor force in wind energy

Turkey has established two YEKA auctions so far for onshore wind, with capacities of 1,000 MW and 4x250 MW, 2,000 MW in total. Also, an offshore wind auction with a capacity of 1,200 MW was planned to take place in October in 2018, however, postponed to a near unknown future [46]. With the realization of all the three YEKA auctions for wind energy, Turkey will add 3,200 MW wind capacity by the end of the projects.

4.4.1. The first YEKA auction

The first YEKA auction was held in 2017 both for onshore wind (1,000 MW) and solar PV (1,000 MW). Eight consortiums, all with foreign partners participated in the wind auction and Siemens-Turkerler-Kalyon consortium awarded the right to develop the announced 1,000 MW capacity for onshore wind. The auction started from the ceiling price of 7 $ cent/kWh and closed with 3.48 $ cent/kWh which was considered as a record-low price, below the 2017 global average of 6 $ cent/kWh [46,47]. The energy production license is given for 30 years with 15 years of guarantee of purchase for the first YEKA auction.

- The consortium is responsible for conducting R&D activities for 10 years in at least three of five areas, namely, Blade, Generator design, Material technologies, and manufacturing techniques, Software, and Innovative gearboxes.
- A budget of $ 5 million will be allocated for R&D activities every year.
- 50 technical personnel, 80 percent of whom are local engineers, will carry out R&D activities.
- A wind turbine factory with an investment cost of over $ 100 million will be established.

- The installation period of the factory will be 21 months from the date of signing the contract and the license period of the project will be 30 years.
- 300 – 450 wind turbines with a minimum capacity of 2.3 MW will be manufactured at the factory.
- The local content requirement in the turbines is determined to be 65% including tower and blades.

The winner consortium will invest more than $ 1 billion in wind plants. With this project, a minimum of 3 billion kWh of electricity will be generated each year with the commissioning of the power plants to be established, and the annual electricity demand of approximately 1.1 million households will be supplied from the wind energy. At the same time, an average annual reduction of 1.5 million tons of carbon emissions will be achieved [46,48].

Since the high wind energy potential of Turkey in the regions of Marmara and Aegean is already being exploited, the government plans to exploit the unused high wind energy potential especially in the region of Central Anatolia (Fig. 6). The domestic wind plants will be located in 5 provinces:

- Kayseri – Nigde (Central Anatolia)
- Sivas (Central Anatolia)
- Edirne – Kirklareli – Tekirdag (Marmara)
- Ankara – Cankiri – Kirikkale (Central Anatolia)
- Bilecik – Kutahya – Eskisehir (intersection of regions of Marmara, Central Anatolia, and Aegean)

4.4.2. The second YEKA auction

The second YEKA auction was made in 2019 for four areas for wind energy, each of 250 MW and 1,000 MW in total. The auction has started from 5.5 $ cent/kWh and closed with:

- 4.56 $ cent/kWh for the province of Aydin (Aegean)
- 4.00 $ cent/kWh for the province of Mugla (Aegean)
- 3.53 $ cent/kWh for the province of Balikesir (Marmara)
- 3.67 $ cent/kWh for the province of Canakkale (Marmara)

The lowest bids were given by Enerjisa Power Plants with Sabanci Holding and German E.ON in Aydin, Enercon in Mugla and Balikesir, and Enerjisa in Canakkale. As it was in the first YEKA auctions, the requirement of local content in the second YEKA auction is also determined as a minimum of 55% for wind turbines with at least 65% for turbine tower, 60% for blade and 51% for other parts. In the second YEKA, the produced turbines will have a minimum power of 3.0 MW [46,48]. In the second YEKA auction, the energy production license is given for 49 years with 15 years of guarantee of purchase.

4.4.3. Offshore YEKA

Turkey also aims to invest in the offshore wind through YEKA auctions. An offshore wind auction with a capacity of 1.2 GW was planned to take place in October in 2018, however, postponed to a near unknown future. Wind offshore auction ceiling prices were determined to be 8 $ cent/kWh and in the region of Marmara in locations of Saros, Gelibolu, and Kiyikoy. The local content requirement is set to be 60% with at least 80% of the employees are local [46].

5. Estimation of feasibility of wind energy projects in Turkey

In this part of the study, the discounted payback period (DPBP) of wind energy projects in Turkey is investigated. Wind power generation is calculated based on capacity factor, and the feasibility of the projects is evaluated through YEKDEM feed-in tariffs. Net cash flow NCF_t (\$/year) is calculated as follows [49]:

$$NCF_t = P \times CF \times 8760 \times \lambda - O\&M_t \tag{2}$$

where t is time, P is the installed capacity of energy plant (kW), CF is the capacity factor, λ is the selling price (\$/kWh) and $O\&M_t$ is annual operation & maintenance cost of the plant at time t (\$/year). The real interest rate i is calculated as [50]:

$$i = \frac{i' - f}{1 + f} \tag{3}$$

where, i' is the nominal discount rate and f is the expected inflation rate. The payback period is the time where the initial investment reaches the break-even point. DPBP is calculated as follows [51]:

$$DPBP \rightarrow \sum_{t=1}^{DPBP} \frac{NCF_t}{(1+i)^t} \equiv NCF_0 \tag{4}$$

where NCF_0 is the initial investment cost (\$), i is the real interest rate, and NCF_t is the net cash flow in year t (\$/year).

The feasibility of the projects for YEKDEM feed-in tariff is investigated through three cases:

- Base case (7.3 $ cent/kWh)
- Possible case - Tower and blade are locally manufactured and benefit from local content bonus (8.7 $ cent/kWh for the first 5 years and 7.3 $ cent/kWh for the second 5 years)
- The best case - All the components are locally manufactured and benefit from local content bonus (11 $ cent/kWh for the first 5 years and 7.3 $ cent/kWh for the second 5 years)

In the analysis, the wind turbine cost is taken as 945 USD/kW according to the average wind turbine cost data of Vestas and BloombergNEF [52]. The other costs such as grid connection, land rent, road construction, electrical installation, etc. constitute approximately 25% of total installation costs [53]. Therefore, the total installation cost is set as 1205 USD/kW. Operation and maintenance (O&M) cost is 2% of total investment [54]. The installed capacity is assumed as 5 MW which is also the upper limit for unlicensed installations. Thus, consistency is provided for unlicensed case analysis. The real interest rate is calculated as 0.03 by using the average of the nominal discount rate and the inflation rate of the last 10 years. The system lifetime is 25 years and the capacity factor is 0.3 as the average of Turkey.

The limitations of the study are as follows: Connection capacity cost is not included in the calculations considering the capacity factor is not high and there is no or low competition. Not to add another parameter to the sensitivity analysis and to keep the results more comprehensible, it is assumed that the land and construction costs will be the same throughout the country. Due to the currency rate fluctuations occurred in the last years in Turkey, the sell-back price in Section 5.2 can vary.

The net cash flows of the investment for three cases are shown in Fig. 10. According to the results of the feasibility analysis, the payback periods of large-scale wind energy projects in Turkey under the YEKDEM feed-in tariff are 4.96 years (best case), 6.94 years (possible case) and 8.21 years (base case). In Turkey there exist qualified manufacturers for tower and blade components as mentioned in Section 5 and project owners are very likely to benefit from the local content bonus provided for these two components. Therefore, the "possible case" can be considered as the most realistic case for Turkey.

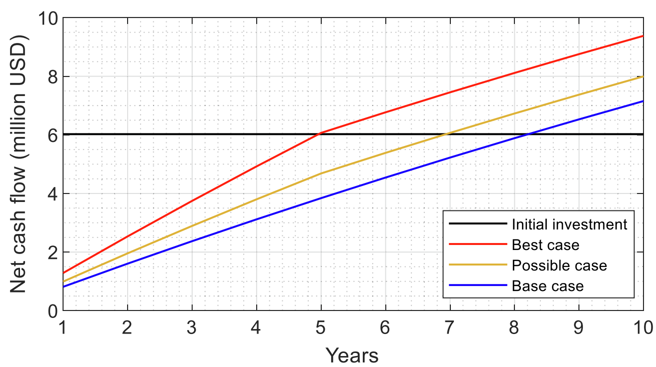

Fig. 10. Net cash flow for the feed-in tariff duration.

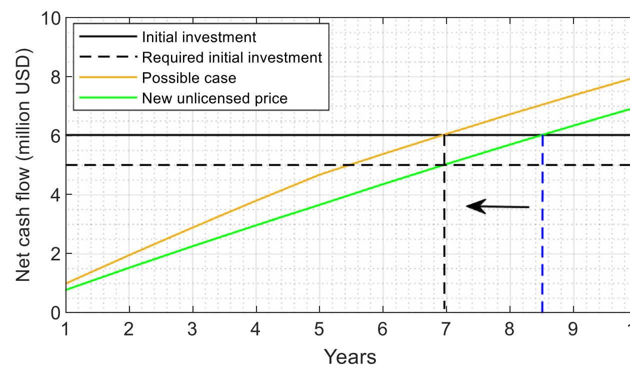

Fig. 12. Comparison of payback period under old YEKDEM (possible case) and new unlicensed production prices.

5.1. Sensitivity analysis

The capacity factor of a region directly affects the DPBP. Also, the initial investment cost of wind plants is still gradually decreasing and the real interest rate can change according to the economic situation of the country. Therefore, these three parameters are taken into consideration in the sensitivity analysis. The selling price used in the sensitivity analysis belongs to the "possible case".

The capacity factor in Turkey is investigated and found to be varying between 19.7% and 56.8% [55], thus, the capacity factor is set in the range of 20–50% in the analysis. The initial investment cost is assumed to decrease by at most 20% in the short-term. The results are evaluated under different real interest rates of 0.01, 0.03 (current average of last 10 years), and 0.05.

The results are presented in Fig. 11. The range of DPBP changes between 8.72 and 17.14 years for low capacity factor regions (20%) and 2.87 and 4.02 years for high capacity factor regions (50%). It can be seen that the regions which have low capacity factor are more vulnerable to the changes in real interest rate and initial investment cost, whereas, the high capacity factor regions have more stable DBPB.

5.2. Results for new unlicensed prices

The future of YEKDEM is unclear for licensed production. Yet, it has been clarified for unlicensed production [43]. Thus, here, the feasibility of unlicensed projects with new prices is analyzed. The new price is approximately 45 kurus/kWh as of 2020 which corresponds to 7 $ cent/kWh for the time being. This price is very close to the previous "base price" provided by YEKDEM.

The results are presented in Fig. 12. The payback period is found as 8.50 years for the "new unlicensed price" which is close to 8.21 years of the old "base price" (Fig. 10).

It is seen that in order to reach the previous payback period of the "possible case" of the YEKDEM scheme (6.94 years), the initial investment cost of the projects should decrease by 17% from 1.205 to 1.00 million USD or the state should maintain the local content bonus as in the previous YEKDEM. Presence of a local content bonus also overlaps with the country's willingness to establish a local wind energy industry. When there is a local content bonus, investors will want to invest in equipment that will be produced in Turkey.

6. Status of wind energy market

In the late 1970 s and early 1980 s, the wind turbines were on a small-scale around 20–30 kW. The first wind farm was established in 1980 in the USA with 30 kW-turbines [56]. At present, the turbine dimensions and power-scales are much higher than before and the turbines have reached a power rating of 9.5 MW [57]. The manufacturing processes today require high-technology, advanced production facilities, experience, and know-how. Notable countries working in this field are Germany, Denmark, Spain, the USA, and China. The turbine manufacturing companies of these countries comprise almost the entire global wind market. The leading manufacturers and their countries are given in Table 4 according to market shares based on sales in 2019 [58]. Although China

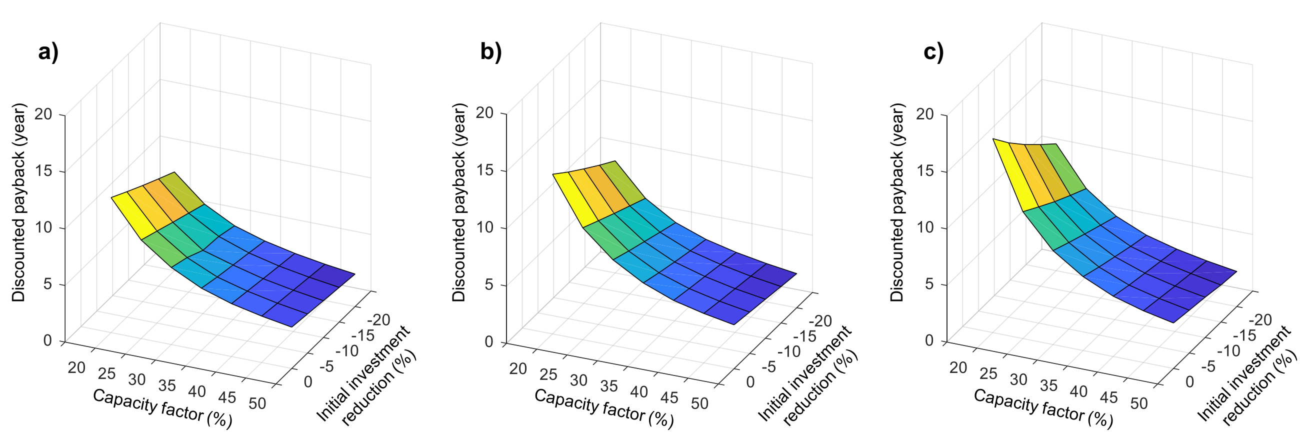

Fig. 11. The impact of capacity factor, initial investment cost, and real interest rate on DPBP of the wind farm investments in Turkey (a- Real interest rate: 1%, b- Real interest rate: 3% (current), c- Real interest rate: 5%).

Table 4
The shares of the leading wind turbine manufacturers in the market in 2019 [58].

Manufacturer	Country	Market share (%)
Vestas	Denmark	15.7
Siemens Gamesa	Spain	14.4
Goldwind	China	13.5
GE Renewable	USA	12.1
Envision	China	9.5
Mingyang	China	7.4
Windey	China	3.4
Nordex	Germany	3.2
Shanghai Electric	China	2.8
CSIC	China	2.4

has entered the wind turbine market later than the others, today it has become one of the leading countries in the market.

These companies are not only dominant in the global market but also their domestic markets. For instance, Siemens Gamesa has a 55% market share in Spain [59] and Suzlon (India) comprises 35% of the Indian market [60]. Nordex and Enercon (Germany) have a total market share of over 60% in Germany by 2018 [61]. China is the most remarkable country in this respect that the market share of Chinese manufacturers has reached almost 90% in their domestic markets [62].

They do not only manufacture wind turbines for their domestic and foreign markets but also contribute to employment in the countries they serve. The approximate number of employees of the wind turbine manufacturers [63–68] are given in Table 5. Vestas, Siemens Gamesa, and Enercon are the leading companies in terms of employment. It should be noted that the number of employees is not limited to these numbers. These complex devices feed many sub-sectors and further expand their businesses [69].

The wind energy sector creates remarkable employment. According to the International Renewable Energy Agency (IRENA) job report [70], the wind power sector provides 1.16 million jobs worldwide. Table 6 shows the number of jobs in the wind sector by the top 10 countries. The top 10 countries constitute 85.4% of the total employment. China alone comprises 44% of the total labor force, followed by Germany, the United States, India, and others. Turkey's labor force is 6,700 in the wind industry.

It should be noted that all the leading countries in terms of employment have their domestic wind turbine brands except one. Brazil distinguishes from others by holding a high labor force without having a notable wind turbine brand. Therefore, the unique aspect of Brazil and the policies in the country are examined in detail in the discussion part and compared to Turkey.

6.1. Status of the wind energy market in Turkey

In Turkey, almost all the active turbines used in wind power plants are imported products. The country does not have any notable domestic manufacturer in a megawatt-scale. Fig. 13 shows the distribution of the total installed wind capacity in Turkey by turbine manufacturers [31]. Nordex is the leading company (26.16%) in terms of installed wind capacity, followed by Vestas, Enercon,

Table 5
The approximate number of employees by the manufacturers.

Manufacturers	The approximate number of employees
Vestas	25,000
Siemens Gamesa	23,000
Enercon	18,000
Goldwind	8,000
Nordex	7,500
Suzlon	6,000

Table 6
The number of jobs in wind energy sector by countries [70].

Country	Number of jobs
China	510,000
Germany	140,800
United States	114,000
India	58,000
United Kingdom	44,140
Denmark	34,200
Brazil	34,000
Spain	20,500
France	18,500
Philippines	16,874

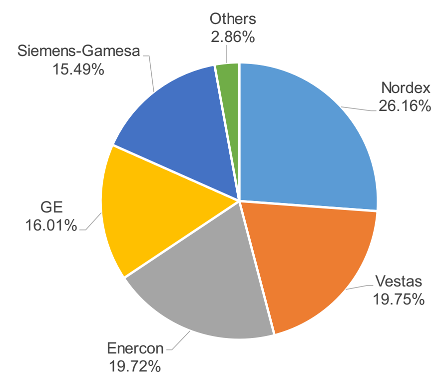

Fig. 13. The distribution of the installed wind capacities in Turkey by turbine manufacturers.

Siemens-Gamesa, and General Electric (GE) respectively. The other manufacturers are Suzlon, Sinovel, Goldwind and Senvion which have a 2.86% market share in Turkey.

There exist 25 wind power plants under construction which constitute 1309.79 MW in Turkey and majority of them are installed in Marmara (729.4 MW) and Aegean (410.49 MW) regions [31]. Among the new installations, Nordex and GE have large installation capacities with 732.79 MW and 350.20 MW respectively and the majority of these constructions are located in regions of Marmara and Aegean which have steady and high-speed wind potential, also contain the required industry and labor force.

As mentioned above, the wind energy sector in Turkey provides 6,700 jobs [70]. These jobs are mostly related to the construction processes of wind power plants, manufacturing of some of the wind turbine components such as blade, tower, and other sub-components. Also, blade manufacturers operating in Turkey are sub-companies established by global wind companies. For instance; Aero Wind and LM Wind are the sub-companies of Enercon and GE respectively. Turkey has advanced construction companies such as Alke, Çimtaş, Gesbey, and Temsan, and the country is capable of tower production in this regard.

7. Discussion

The discussion part is examined in four sub-sections for better understandability and concluded with a SWOT analysis to present a clear overview of all positive and negative factors.

7.1. Turkish Lira-denominated feed-in tariff

The future of YEKDEM is unclear for licensed production. Yet, it has been clarified for the unlicensed production. In the new law, the selling price is denominated in Turkish Lira for unlicensed production. Turkish Lira-denominated feed-in tariff had been in use between 2005 and 2011 before. Back then, the use of domestic currency became a matter of debate. Both financial corporations and sector stakeholders demanded US Dollar or Euro-denominated fixed-prices which are not subject to change due to exchange rate fluctuations. Especially banks demanded them to predict cash flows and offer debt ratio to investors. Such that, after 2011, with the amendment of the law, the amount has been denominated in US Dollar and the rate of new installations has increased significantly.

When the electricity selling price is Turkish Lira-denominated, it becomes a hesitation factor for the investors since the investments and loans are denominated in US Dollars or Euro. If the selling price is considered to be Turkish Lira-denominated, then, Turkey should wait until its domestic wind energy industry develops and becomes mature, that is:

- As the equipment to be used in projects will be locally produced and trade of these products will be Turkish Lira-denominated, the investment of a wind energy project will be Turkish Lira-denominated. Then, the incentives provided in Turkish Lira will be meaningful. Investors will have a lower risk factor and will not be affected by the exchange rate volatility.
- If Turkey decides to continue with Turkish-lira denominated feed-in tariffs, then Turkish banks should provide better loan options for these investments. Because the investors obtain loans from foreign banks denominated in US Dollar or Euro. In case the incentives (which means the cash flows of the project) are in another currency, and fragile to exchange rate volatility, these banks may want to avoid taking risks.
- In order to prevent the money loss that can be caused by currency fluctuations, Turkish Lira denominated feed-in tariff rates can be updated in short periods based on US Dollar/Euro or inflation rate.

7.2. Local wind energy industry and labor force in Turkey

The domestic wind energy industry highly contributes to the local labor force and technological know-how. Turkey which holds relatively cheap labor force and qualified staff can combine these features and get close to its target of 20 GW installed capacity in wind energy by reducing the risk factors mentioned in Section 7.1 for investors and establishing its local wind energy industry. The top countries holding the highest installed capacity in wind energy are the developed countries that started their wind energy investments earlier than others, except China and Brazil.

Although the installed wind power in China is very high and the Chinese market dominates a large part of the market share in the world (Table 4), China entered the wind market later than the others and turbine production is mainly directed to the domestic Chinese market [62]. To reduce carbon emissions and supply the energy demand, the Chinese government provided incentives and subsidiaries for wind energy such as tax reduction, feed-in-tariffs valid for 20 years, supports for local manufacturing of wind turbines such as availability of better funds from state-owned banks, funds given for research & development (R&D) projects, and grants given for wind turbine manufacturers for production of 1.5 MW or higher capacity wind turbine parts [71,72].

In Brazil, despite the country's high installed capacity, there are no domestic wind turbine manufacturers. Brazil has achieved its success in wind energy with its local content requirements set in wind auctions. Brazil's wind auctions strongly promote localization in wind turbine manufacturing. Although not obligatory, to benefit from the favorable credit options of the Brazilian Development Bank BNDES (a governmental funding agency responsible for most of the energy financing in Brazil), the companies should fulfill local content requirements. These requirements impose investors to manufacture or assemble at least three of the four main wind turbine components: towers, blades, nacelles, and hubs, in Brazil [73]. The local content requirements policy has become successful to promote low and medium technology manufacturing in Brazil. Wind turbine components that are difficult to transport such as parts of the nacelle, hubs, and blades are currently being produced in the country. Yet, expensive high technology and high-quality content, which requires a more qualified labor force, is still being imported [74].

In this respect, instead of creating a local wind turbine brand in the first stage, Turkey should consider establishing partnerships with large brands that maintain their production since the 80 s. Turkey has achieved such success in the automotive industry and become one of the top manufacturer countries [48]. Also, the Brazilian example shows the success of this method. Although Brazil does not have any domestic wind turbine brands, it has become one of the leading countries in wind energy and contains one of the highest labor force. This model was so successful that, especially after 2013, the country has increased its installed wind capacity significantly (Table 1).

One of the successes of Brazil's auction model is undoubtedly the country's highest capacity factor in the world. This is one of the main factors that attract firms to invest in Brazil. Likewise, Turkey is a country ranked with the third-highest capacity factor in the world, and with this feature, Turkey has a similar potential to attract investors, if necessary incentives and supports are supplied. If Turkey continues its YEKA auctions and insists on domestic labor and domestic industry stand out in these auctions, it is likely to be successful as can be seen from the example of Brazil.

The incentives and support mechanisms in wind energy provided by Brazil and China had a positive impact on the wind installations in their countries as well as on the labor force. As given in Table 6, these countries are among the top ten countries in the world concerning the number of wind-related jobs. China and Brazil have 510,000 and 34,000 wind-related jobs in their countries, respectively. This is also one of the factors that enhance the country's technological know-how and qualified manpower.

7.3. Wind energy auctions

Turkey has applied two YEKA auctions so far. Both auctions aimed to promote locally produced wind turbine equipment, conduct R&D in wind turbine technology, and use local labor force in wind energy projects. These two auctions were achieved with very low prices in the range of 3.48–4.56 cent/kWh while the global average of onshore wind auctions was 6 cent/kWh (2017) [46]. The low prices were caused by the high capacity factor of the project areas and the large capacity of the projects (1,000 MW of each).

The achieved low prices show that the YEKA auction model can be further expanded in Turkey. The authorities and decision-makers can develop YEKA-like auction models with lower capacity projects and in the regions with lower capacity factors while auction prices still stay below the global average. This might further expand the use of wind power, improve the wind industry, and increase local employment in Turkey.

Moreover, small-scale YEKAs can overcome another threat: a possible project failure. In big projects a failure may cause a valuable time loss in the process of Turkey's local wind industry establishment. Dividing the risk can be another option to be considered.

7.4. SWOT analysis

Lastly, a SWOT (strengths, weaknesses, opportunities, and threats) analysis is made to summarize the discussion part and evaluate Turkey's competitive position considering internal and external factors (Table 7). Turkey's industrial development and

Table 7
SWOT analysis of wind energy in Turkey.

(S)trenghts	(W)eaknesses	(O)pportunities	(T)hreats
• High capacity factor in the country. • Qualified and cheap labor force. • Governmental willingness to develop local wind energy industry. • Strong domestic demand of wind turbine equipment. • State policy of energy diversification and energy independency. • Increased know-how in Turkey over years	• Lower feed-in tariffs compared to developed countries. • The highest-potential wind sites are already occupied. • Some of the high-speed wind areas exist on bird migration routes. • Bureaucracy and institutional incoordination can be challenging from time to time. • Short duration of feed-in tariff (10 years).	• Untouched, high offshore wind potential. • Wind turbine raw materials are already being produced and in use in other sectors in Turkey. • Closeness to new markets. • Upper limit increase for unlicensed plants (1 MW to 5 MW). • Unexploited high-medium, medium wind speed sites. • Increase of infrastructural investments.	• Unclear future of feed-in tariffs after 2020. • Unwillingness of businesses to use Turkish Lira denominated feed-in tariff. • High exchange rate and interest rate volatility. • Country's vulnerability to economic crises. • High competition in the market due to lower production costs and higher technological development of India and China. • Removal of bonus price for use of domestic equipment in new unlicensed feed-in tariff.

low-cost, skilled workforce stand out as the country's "strengths". The industrial force, combined with the governmental willingness can help the country to achieve its goal of establishing a local wind energy industry. The bureaucracy and institutional incoordination in Turkey can be seen as a "weakness" in general but that can be eliminated with facilitating arrangements. Here, Turkey's main "opportunity" is the country's closeness to the new markets such as Mediterranean, Middle Eastern, North African and Central Asian. Turkey also already produces wind turbine raw materials and use them in various sectors, which can accelerate the country's achievement of its goal. Yet, the main "threat" is India and China, which have already established their industrial facilities with low production costs and high technological development. Taking a share from a market that is targeted by Indian and Chinese manufacturers will be one of the main challenges.

8. Conclusions

By the end of 2019, the total installed wind capacity reached 7.59 GW in Turkey which is far away from the country's target of 20 GW by 2023. The average rate of 627 MW capacity installations per year makes it impossible to reach the assigned target. Thus, to get close to "2023 targets" in wind energy, Turkey should increase the efficiency of the current policy measures. In this respect, the below recommendations are made and economic feasibility results are presented to give a broader view about the country's potential:

- Turkish Lira-denominated feed-in tariff is a hesitation factor for project owners due to the exchange rate and interest rate volatility. If Turkey wants to continue with the Turkish Lira-denominated feed-in tariff, then the Turkish banks should offer better credit options to attract investors.
- Turkish Lira-denominated feed-in tariff will be justified when Turkey establishes its local wind energy industry. Yet, until then, measures should be taken to prevent investors from a possible money loss. In this regard, Turkish Lira-denominated feed-in tariff rates can be updated in short periods.
- In the first stage, instead of creating a local wind turbine brand, Turkey should consider going into partnerships with well-established firms. Brazil's own success story in wind energy and Turkey's success in the automotive sector show that this model can work for Turkey and the country can develop a remarkable wind energy industry and employment with its qualified and relatively cheap labor force.
- The future of the YEKDEM feed-in tariff mechanism which ends by the end of 2020 should be clarified. The uncertainty causes hesitation for the investors.
- Turkey should maintain the local content requirements in its successful YEKA auctions and feed-in tariff scheme. Local content requirements can be provided for unlicensed projects as well. Especially taking into account that the definition of unlicensed projects is expanded from 1 to 5 MW, this may be required to boost the promotion of unlicensed projects.
- The duration of Turkey's feed-in tariff (10 years) is lower compared to many countries (15–20 years). A longer feed-in tariff (even with a lower feed-in tariff rate) can provide better predictability for both banks and project investors.
- While large capacity YEKA auctions were achieved with record low prices, the risk gets bigger as the capacity increases. A possible project failure may cause a valuable time loss in the process of Turkey's local wind industry development. Thus, mini-YEKAs with lower capacities should also be considered.
- Wind energy investments in Turkey are concentrated in certain regions (Fig. 6). This brings necessary infrastructure investments with an economic burden. Within a strategic plan, investments can be homogeneously shifted to other high-capacity regions that require less infrastructure investment.
- Although wind energy projects have not faced with strong opposition in Turkey so far, offshore projects can suffer from "Not in my backyard" (NIMBY) syndrome due to the touristic aspect of Turkish coasts. Suitable offshore locations having low public opposition can be mapped considering social effects.
- In the economic analysis, the DPBP of large-scale wind power plants are determined to be between 4.96 and 8.21 years depending on taking advantage of the local content bonus provided by YEKDEM feed-in tariff scheme. The DPBP of 4.96 years belongs to the best case where all the used equipment are locally produced. Yet, in the possible case DPBP is 6.94 years due to the limited availability of locally produced equipment in Turkey.
- It is seen that, the new unlicensed scheme to be used after 2020 provides a DPBP of 8.5 years which is close to the previous DPBP of 8.21 years under YEKDEM without any local content bonus. If the government decides to apply the same rates to the licensed projects after YEKDEM (as applied previously), then the local content bonus must be maintained in the new scheme to reach the old payback periods. This also overlaps with the country's willingness to establish a local wind energy industry. When there is a local content bonus, investors will want to invest in equipment that will be produced in Turkey.

References

[1] The World Bank, Population. World Bank 2019. https://data.worldbank.org/indicator/sp.pop.totl?end=2018&start=2009 (accessed January 25, 2020).
[2] British Petroleum (BP). BP Statistical Review of World Energy. 2019.
[3] Global Energy Statistical Yearbook 2019. Electricity domestic consumption. 2019.
[4] Electricity production from oil, gas and coal sources (% of total). World Bank 2019. https://data.worldbank.org/indicator/EG.ELC.FOSL.ZS?end=2015&start=2005 (accessed January 15, 2019).
[5] A. Aranizadeh, A. Zaboli, O. Asgari Gashteroodkhani, B. Vahidi, Wind turbine and ultra-capacitor harvested energy increasing in microgrid using wind speed forecasting, Eng Sci Technol an Int J 22 (5) (2019) 1161–1167, https://doi.org/10.1016/j.jestch.2019.08.006.
[6] Electricity production from hydroelectric sources (% of total). World Bank 2019. https://data.worldbank.org/indicator/eg.elc.hyro.zs?end=2015&start=2005 (accessed March 11, 2019).
[7] Electricity production from renewable sources, excluding hydroelectric (% of total). World Bank 2019. https://data.worldbank.org/indicator/EG.ELC.RNWX.ZS?end=2015&start=2005 (accessed February 1, 2019).
[8] I.R.E.N.A. Renewable Energy, Statistics (2019. 2019.).
[9] Ö. Güler, Wind energy status in electrical energy production of Turkey, Renew Sustain Energy Rev 13 (2) (2009) 473–478, https://doi.org/10.1016/j.rser.2007.03.015.
[10] C. İlkiliç, Wind energy and assessment of wind energy potential in Turkey, Renew Sustain Energy Rev 16 (2) (2012) 1165–1173, https://doi.org/10.1016/j.rser.2011.11.021.
[11] B. Yaniktepe, M.M. Savrun, T. Koroglu, Current status of wind energy and wind energy policy in Turkey, Energy Convers Manag 72 (2013) 103–110, https://doi.org/10.1016/j.enconman.2012.08.028.
[12] E. Camadan, An assessment on the current status and future of wind energy in Turkish electricity industry, Renew Sustain Energy Rev 15 (9) (2011) 4994–5002, https://doi.org/10.1016/j.rser.2011.07.055.
[13] B. Dursun, C. Gokcol, Impacts of the renewable energy law on the developments of wind energy in Turkey, Renew Sustain Energy Rev 40 (2014) 318–325, https://doi.org/10.1016/J.RSER.2014.07.185.
[14] Y.A. Kaplan, Overview of wind energy in the world and assessment of current wind energy policies in Turkey, Renew Sustain Energy Rev 43 (2015) 562–568, https://doi.org/10.1016/j.rser.2014.11.027.
[15] M. Argin, V. Yerci, Offshore wind power potential of the Black Sea region in Turkey, Int J Green Energy 14 (10) (2017) 811–818.
[16] M. Satir, F. Murphy, K. McDonnell, Feasibility study of an offshore wind farm in the Aegean Sea, Turkey. Renew Sustain Energy Rev 81 (2018) 2552–2562, https://doi.org/10.1016/J.RSER.2017.06.063.
[17] U. Cali, N. Erdogan, S. Kucuksari, M. Argin, Techno-economic analysis of high potential offshore wind farm locations in Turkey, Energy Strateg Rev 22 (2018) 325–336, https://doi.org/10.1016/J.ESR.2018.10.007.
[18] M. Argin, V. Yerci, N. Erdogan, S. Kucuksari, U. Cali, Exploring the offshore wind energy potential of Turkey based on multi-criteria site selection, Energy Strateg Rev 23 (2019) 33–46, https://doi.org/10.1016/J.ESR.2018.12.005.
[19] C. Emeksiz, B. Demirci, The determination of offshore wind energy potential of Turkey by using novelty hybrid site selection method, Sustain Energy Technol Assessments 36 (2019) 100562, https://doi.org/10.1016/j.seta.2019.100562.
[20] S. Alpanda, A. Peralta-Alva, Oil crisis, energy-saving technological change and the stock market crash of 1973–74, Rev Econ Dyn 13 (4) (2010) 824–842, https://doi.org/10.1016/j.red.2010.04.003.
[21] Z. Altuntasoglu, Renewable energy; Turkey and the European Union acquis. TMMOB V, Energy Symp., Ankara (2005) 249–261.
[22] IRENA, 30 Years of Policies for Wind Energy: Lessons from 12, Wind Energy Markets. (2013).
[23] I.R.E.N.A. Renewable Capacity, Statistics (2020. 2020.).
[24] IRENA. IRENA's renewable electricity capacity and generation statistics-Query tool. 2020.
[25] I.F.A. Vis, E. Ursavas, Assessment approaches to logistics for offshore wind energy installation, Sustain Energy Technol Assessments 14 (2016) 80–91, https://doi.org/10.1016/j.seta.2016.02.001.
[26] K. Angelakoglou, P.N. Botsaris, G. Gaidajis, Issues regarding wind turbines positioning: A benchmark study with the application of the life cycle assessment approach, Sustain Energy Technol Assessments 5 (2014) 7–18, https://doi.org/10.1016/j.seta.2013.10.006.
[27] Y.i. Li, X. Huang, K.F. Tee, Q. Li, X.-P. Wu, Comparative study of onshore and offshore wind characteristics and wind energy potentials: A case study for southeast coastal region of China, Sustain Energy Technol Assessments 39 (2020) 100711, https://doi.org/10.1016/j.seta.2020.100711.
[28] T.U.I.K. Address, Based Population Registration System Results. (2019).
[29] GDP growth (annual %). World Bank 2018. https://data.worldbank.org/indicator/NY.GDP.MKTP.KD.ZG?end=2018&locations=TR&start=2008 (accessed March 15, 2019).
[30] Turkish Electricity Transmission Corporation. Electricity generation and transmission statistics. 2019.
[31] Turkish Wind Energy Association. Turkish Wind Energy Statistic Report January 2020. 2020.
[32] Turkish Energy Exchange. Real-time generation (Transparency platform). 2020.
[33] State Planning Organization. Electricity Market and Security of Supply Strategy Paper. 2009.
[34] Ministry of Energy and Natural Resources (MoENR). Ministry of Energy and Natural Resources Strategic Report (2010-2014). 2010.
[35] Ministry of Environment and Urbanization. Turkey Climate Change Strategy 2010-2020. Ankara: 2012.
[36] , Ankara (2017).
[37] , Turkey Wind Energy Potential Atlas. (2012).
[38] Y. Malkoç, Wind energy resources of Turkey, (in Turkish) (2009).
[39] Turkish Electricity Transmission Corporation. Annual Development of Electricity Generation- Consumption and Losses in Turkey (1993-2017). 2018.
[40] Law on the Use of Renewable Energy Resources for the Purpose of Generating Electric Energy. Turkey: Official Gazette; 2005.
[41] Implementing Regulation on Certification and Support of Renewable Energy Resources. Turkey: 2011.
[42] Law on the Use of Renewable Energy Resources for the Purpose of Generating Electric Energy. Turkey: 2010.
[43] Presidency Of The Republic Of Turkey. Presidential Decree No: 30770. 2019.
[44] Energy Market Regulatory Board. Tariff Tables for Electricity Bills. 2019.
[45] Turkish Electricity Transmission Corporation. RES Yarışma Duyurusu 2017. https://www.teias.gov.tr/tr/duyuru/res-yarisma-duyurusu (accessed September 24, 2019).
[46] Sari AC, Saygin D, Lucas H. On the way to efficiently supplying more than half of Turkey's electricity from renewables: Opportunities to strengthen the YEKA auction model for enhancing the regulatory framework of Turkeýs power system transformation. 2019.
[47] IRENA. Renewable Power Generation Costs in 2017. 2018.
[48] TÜBA-Wind energy technologies report. Ankara: 2019.
[49] G. Xydis, A techno-economic and spatial analysis for the optimal planning of wind energy in Kythira island, Greece. Int J Prod Econ 146 (2) (2013) 440–452, https://doi.org/10.1016/j.ijpe.2013.02.013.
[50] R. Hosseinalizadeh, E.S. Rafiei, A.S. Alavijeh, S.F. Ghaderi, Economic analysis of small wind turbines in residential energy sector in Iran, Sustain Energy Technol Assessments 20 (2017) 58–71, https://doi.org/10.1016/j.seta.2017.02.018.
[51] O. Ozcan, F. Ersoz, Project and cost-based evaluation of solar energy performance in three different geographical regions of Turkey: Investment analysis application, Eng Sci Technol an Int J 22 (4) (2019) 1098–1106, https://doi.org/10.1016/j.jestch.2019.04.001.
[52] IRENA. Wind turbine costs 2010-2018. 2018.
[53] Søren K, Morthorst P-E, Awerbuch S. The Economics of Wind Energy. 2009.
[54] IRENA, Renewable Energy Technologies: Cost Analysis Series - Wind, Power. (2012).
[55] Seyit Ahmet Akdağ, Önder Güler, Evaluation of wind energy investment interest and electricity generation cost analysis for Turkey, Appl Energy 87 (8) (2010) 2574–2580, https://doi.org/10.1016/j.apenergy.2010.03.015.
[56] Breeze P. An Introduction to Wind Power. Wind Power Gener., 2016. doi:10.1016/b978-0-12-804038-6.00001-3.
[57] D. Borge-Diez, A. Comenar-Santos, A. Pérez-Hoyos, J.-J. Blanes-Peiró, E. Rosales-Asensio, Review of wind energy technology and associated market and economic conditions in Spain, Renew Sustain Energy Rev 101 (2018) 415–427, https://doi.org/10.1016/j.rser.2018.11.029.
[58] Henze V. Vestas still rules turbine market, but challengers are closing in. BloombergNEF 2020. https://about.bnef.com/blog/vestas-still-rules-turbine-market-but-challengers-are-closing-in/#_ftnref1 (accessed May 3, 2020).
[59] Siemens Gamesa to supply 92 of its newest wind turbine models at 10 wind farms in Spain. Siemens Gamesa Renew Energy 2018. https://www.siemensgamesa.com/en-int/newsroom/2018/07/180709-contratos-in-spain (accessed April 11, 2019).
[60] Suzlon maintains strong market position despite sector transition. Suzlon 2018. https://www.suzlon.com/press-release-detail/385/suzlon-maintains-strong-market-position-despite-sector-transition (accessed April 14, 2019).
[61] Market share 2019. https://www.enercon.de/en/company/market-share/ (accessed April 14, 2019).
[62] H. Dexin, D. Guangping, L. Bo, Chinese Wind Energy Association. (2018).
[63] Vestas annual report 2019. 2019.
[64] Shaping the renewable energy industry. Siemens Gamesa Renew Energy 2019. https://www.siemensgamesa.com/en-int/about-us (accessed May 2, 2019).
[65] Locations worldwide: Enercon Discover your opportunities. Enercon 2018. https://www.enercon.de/en/karriere-portal/corporate-divisions/#Sektion0 (accessed May 2, 2019).
[66] Goldwind-About us. Goldwind 2018. http://www.goldwindglobal.com/about/detail.html (accessed May 2, 2019).
[67] Suzlon provides renewable energy solutions worldwide. Suzlon 2020. https://www.suzlon.com/in-en/about-suzlon/corporate-profile (accessed February 2, 2020).
[68] Amazing perspectives for your career. Nordex 2020. https://www.nordex-online.com/en/career/ (accessed April 5, 2020).
[69] P. Ferreira, F. Lima, F. Ribeiro, F. Vieira, A mixed-method approach for the assessment of local community perception towards wind farms, Sustain

Energy Technol Assessments 33 (2019) 44–52, https://doi.org/10.1016/j.seta.2019.02.004.
[70] I.R.E.N.A. Renewable, Energy and Jobs: Annual Review (2019. 2019.).
[71] B.K. Sahu, Wind energy developments and policies in China: A short review, Renew Sustain Energy Rev 81 (2018) 1393–1405, https://doi.org/10.1016/J.RSER.2017.05.183.
[72] Y. Zhang, N. Tang, Y. Niu, X. Du, Wind energy rejection in China: Current status, reasons and perspectives, Renew Sustain Energy Rev 66 (2016) 322–344, https://doi.org/10.1016/J.RSER.2016.08.008.
[73] Market study: Wind energy in Brazil. 2014.
[74] Overcoming Barriers to International Investment in Clean Energy, OECD (2015), https://doi.org/10.1787/9789264227064-en.

Z-source converter integrated dc electric spring for power quality improvement in dc microgrid

Rakhi Jha, *Department of Computer Scinece Engineering , NM Institute of Engineering & Technology, Bhubaneswar, rakhijha91@yahoo.co.in*

Subrat Dash, *Department of Computer Scinece Engineering , Capital Engineering College, Bhubaneswar, subratdash43@gmail.com*

Ajit Kumar Panda, *Department of Electrical Engineering, Aryan Institute of Engineering & Technology, Bhubaneswar, akpanda555@hotmail.com*

Sulochana Nanda, *Department of Electronics and Communication Engineering , Capital Engineering College, Bhubaneswar, sulochananandal@hotmail.com*

Keywords:
DC electric spring
High gain
Z source converter
DC microgrid
Power quality

A B S T R A C T

Increasing penetration of renewable energy sources reveals the concept of dc microgrid which has the advantages of low cost and low losses because of the elimination of the AC/DC conversion processes. The most frequently encountered power quality problem in DC microgrid is voltage fluctuations due to the intermittent nature of renewable energy sources. Direct current (DC) electric spring (DCES), which is an emerging power quality device in DC microgrids, is employed in order to mitigate the effect of the related problem. In this paper, z source converter integrated DCES topology (zDCES) is proposed to provide a wide compensation voltage range with lower duty cycle range and a remarkable decrease in the battery nominal voltage in comparison with conventional systems. The proposed system composed of full-bridge converter, z source converter and battery pack. zDCES provides high voltage gain by using z source converter with passive components without any need for additional switches. The shoot-through control, which is used to achieve high gain in z source converter, is implemented using existing full-bridge switches. The performance of the proposed system is compared with the traditional DCES system. The performance of the zDCES is validated with a case study with different voltage fluctuation states.

1. Introduction

1.1. Overview

Nowadays, the interest in DC microgrids is growing in parallel with the rapidly increasing use of renewable energy sources (RES) powered systems such as photovoltaic (PV) systems and fuel cell (FC) systems. DC microgrids provide high reliability, high efficiency and ease of RES interconnection in comparison with ac microgrids. RESs that generate inherently DC output can be integrated into DC microgrids without any need for AC-DC converter interfaces as with dc loads such as LED systems, televisions and computers [1–3]. In addition, frequency and phase synchronization requirements are eliminated through DC microgrids. Because of such advantages, DC microgrids, which is one of the prominent emerging technologies, will play an important role in the improvement of the new generation grids [4].

The nonlinear behaviors of RESs due to natural events such as partial shading and temperature variations reveals the phenomenon of electrical power quality in DC microgrids. The most common power quality problems in dc microgrids are (i) DC bus faults, (ii) inrush current, (iii) communication failures, (iv) voltage fluctuations, (v) electromagnetic interference compatibility (EMC) issue, (vi) harmonics due to resonances and power electronics-based converters [5]. Since power quality is consumer-driven issue, sensitive loads such as computers and communications devices should be protected from power quality problems [6]. Voltage fluctuations are one of the most frequently encountered electric power quality problems in DC microgrids due to the nonlinear production behavior of RESs and abrupt load changes. To alleviate voltage fluctuations, RES-powered systems traditionally are equipped with large energy storage units and supply-side management is performed by providing power flow management [7–9]. Recently, electric spring (ES) technology, which is a demand-side management approach, is applied to mitigate the effects of voltage fluctuations on voltage-sensitive loads.

1.2. Literature survey

ES is an emerging power quality device that can provide electric active suspension functions to mitigate the effects of voltage instability from the integration of RESs with nonlinear characteristics in DC microgrids. Although numerous studies related with electric spring for AC microgrids have been performed in literature, there are a limited number of publications in this regard for DC microgrids.

Nomenclature

B	Boost factor
CL	Critical load
d	S_1-S_4 duty cycle
DCES	DC electric spring
d_{st}	Shoot-through duty cycle
ES	Electric spring
FC	Fuel cell
HFT	High frequency transformer
NCL	Non-critical load
NST	Non-shoot-through
P_{act}	Actual power consumption
PCC	Point of common coupling
P_{CL}	CL power consumption
P_{NCL}	NCL power consumption
P_{nom}	Nominal power consumption
P_{SL}	SL power consumption
PV	Photovoltaic
P_{zDCES}	zDCES power consumption
R_{CL}	CL resistance
RES	Renewable energy source
R_{NCL}	NCL resistance
SL	Smart load
ST	Shoot-through
T_S	Switching cycle
T_{ST}	Shoot-through time
V_{bus_act}	Actual busbar voltage
V_{bus_nom}	Nominal busbar voltage
V_{zDC}	Input voltage of zDCES
V_{zDCES}	Output voltage of zDCES
zDCES	z source integrated DC electric spring

The configuration of DCES is classified into two as series-type and shunt-type as shown in Fig. 1. The critical loads (CL) corresponds to voltage sensitive loads, and noncritical loads (NCL) corresponds to loads not affected by voltage variations. The series-type DCES is a voltage source connected in series with noncritical loads to form a smart load (SL) that is able to regulate the voltage of the busbar by controlling the charges stored in a capacitor. The shunt-type DCES is a current source connected in parallel with the point of common coupling (PCC) and is not associated with any noncritical loads [10]. A comparison study on the series-type and shunt-type DCESs is presented in [10]. Since the dynamic response of the series-type DCES depends on the serial impedance of the NCL, the series-type DCES has a slower dynamic response than shunt-type DCES.

However, the series-type DCES requires reduced battery capacity as it creates a smart load by connecting in series with NCLs. Thus, the related aspect of the series-type DCES makes it applicable in many DC microgrid implementations [1].

The shunt-type DCES topologies had derived from the buck, boost and buck-boost converter topologies because of the unipolar output voltage requirement [11]. The series-type DCES topologies are usually composed of the variations of the bridge topologies due to the requirement of the bipolar output voltage. In [1,2,10,12,13], full bridge converter based DCES concepts are proposed to regulate the busbar voltage at PCC. The related studies differ from each other in control aspects. The control methods coordinating the power flow of full-bridge converter based DCES are model predictive control [1], distributed control [13], decentralized control [12] and active damping control [14]. The performance of the full-bridge converter based DCES has been investigated in a bipolar DC distribution network in [15]. A complicated control system with double inputs and outputs are

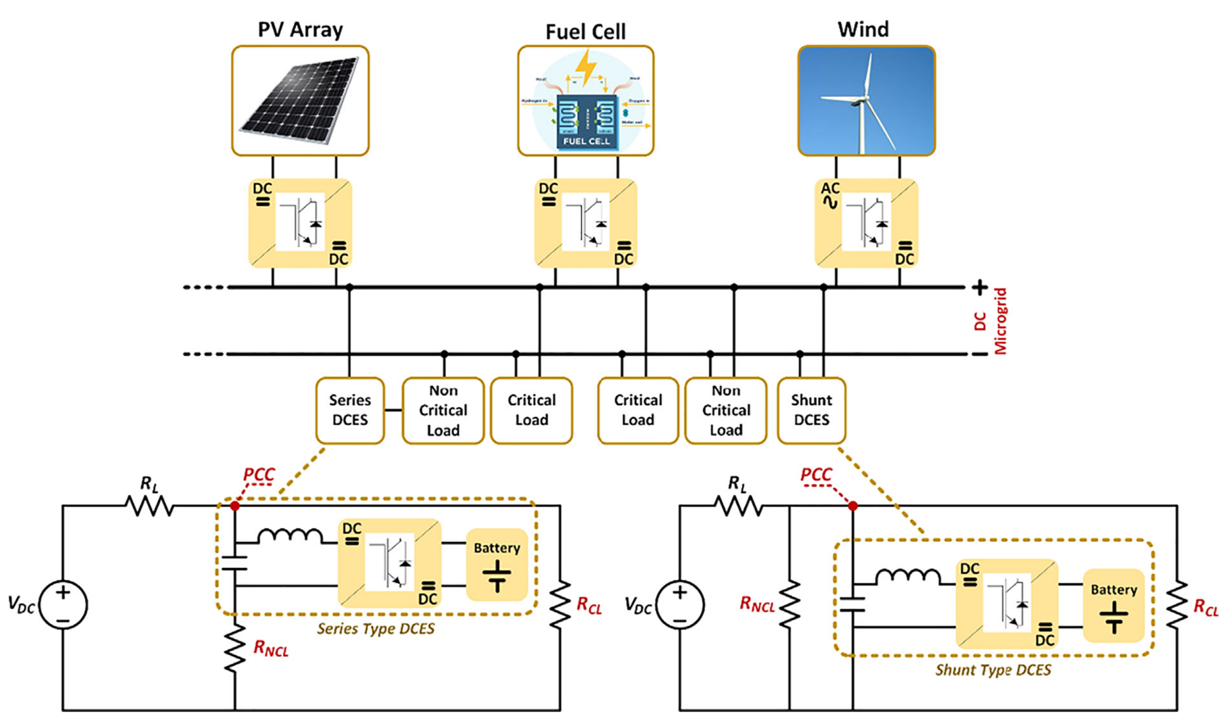

Fig. 1. Types of DC electric springs.

employed. In [3], a half-bridge topology based DCES is proposed for a dc microgrid with the drawback of specialized charge-balance control scheme requirement. The common drawback of the DCES topologies formed with bridge converters is the relatively high battery voltage requirement to provide bipolar high voltages at the output ports of the DCES. Some authors have addressed three-port and isolated DCES topologies to regulate the busbar voltage of DC microgrid [16,17]. The current topologies are equipped with high frequency transformers (HFTs) to provide both galvanic isolation and to regulate the voltage level. The bipolar high voltage requirement at the output of DCES is provided through the turns ratio of the HFTs while transformerless topologies endowed with batteries of higher voltage levels.

Recently, several studies have been conducted regarding the power electronic interfaces that are able to achieve high voltage gain with a reduced number of switches [18]. Some high-gain step-up converter topologies offered in the literature include mul-tiplier cells [19], switched-capacitors [20], cascaded boost [21], quadratic boost [22], and coupled inductor [23] converters. Although the related topologies provide high gain and high effi-ciency, they include additional switches in order to integrate into the DCESs which are the variations of the bridge topologies. Besides, the formed two-stage power electronic interface by integrating DCESs and high-gain converters requires independent control for each stage and increases the control complexity of the system. The impedance networks stand out with advantage of high-gain. In this regard, z source and quasi z source converters provide attrac-tive boost ability for aforementioned applications [24–26].

1.3. Key contributions

As it is understood from the literature review, the wide input voltage range of ES is essential to compensate the voltage fluctuations by producing various bipolar voltage levels at the output port of the ES. The wide voltage range is achieved by using the turns ratio of HFTs and battery packs composed of many series cells in traditional DCESs. In this study, a z-source converter integrated full bridge based DCES with reduced battery voltage is proposed to mitigate the effects of voltage instability occurred in DC microgrids. The proposed zDCES composed of a full-bridge converter, z source converter and reduced voltage battery. With the proposed system, the battery voltage requirement is remarkably decreased in comparison with conventional studies in the literature. Z source converter increases and adjusts the input voltage of the full-bridge converter. Shoot-through states of z source converter are controlled with the switches of full-bridge converter. Thus, the high voltage gain, which is achieved with passive components and no additional switches, has reduced the battery cost. Although the quasi z source converter has the superior aspects of z source converter as well as more advantages such as reduced voltage stress, the z source converter topology has been used because of the low ratings of the proposed system. The performance of the pro-posed system is verified with different case studies.

The rest of the paper is organized as follows: Section II introduces the proposed zDCES topology and describes its operation principle. Section III presents the design of the control for the proposed converter. The results of case studies are presented in Section IV. Section V puts forward conclusions with relevant discussion.

2. ZDCES design

In this paper, a z source converter integrated DCES topology is proposed to achieve a reduction in the nominal voltage rating of the battery. The proposed zDCES topology is illustrated in Fig. 2 consists of a full-bridge converter, a z source converter and a battery pack. While the full-bridge converter produces a bipolar voltage at the output port of the zDCES, the z source converter achieves the wide input voltage range for full-bridge converter. The zDCES is connected in series with NCL to form a smart load. Thus, the zDCES mitigates the voltage fluctuations at PCC by regulating the power flow of NCL that can tolerate large power and voltage variations and it prevents the CL from being affected by voltage fluctuation. The z source converter makes it possible to reach a wide range of bipolar voltage at the output ports of the zDCES with reduced battery voltage. The loads are fed from the PCC through the source and the power flow is performed considering the instantaneous voltage and power of PCC.

The proposed system operates at three different modes according to the power and voltage ratings of PCC as Mode 1, 2 and 3. Mode 1 corresponds to greater actual power consumption (P_{act}) than the nominal power consumption (P_{nom}) of loads. The fact that the actual busbar voltage is lower than its nominal voltage is compensated by the zDCES providing a positive polarity voltage. Mode 2 corresponds to lower actual power consumption than the nominal power consumption of loads. The fact that the actual busbar voltage (V_{bus_act}) is greater than its nominal voltage (V_{bus_nom}) is compensated by the zDCES providing a negative polarity voltage. Mode 3 corresponds to balanced actual power consumption and nominal power consumption of loads. In this state, the zDCES is deactivated with the output voltage of 0. The equivalent circuit of the proposed system illustrated in Fig. 3 represents all operation modes. Considering the equivalent circuit, the relations of voltages and current flow directions can be derived by the following formulation;

$$V_{zDCEC} = dV_{zDC} - (1-d)V_{zDC} - V_{L_{NC1}} - V_{L_{NC2}} \tag{1}$$

where V_{zDCES} and V_{zDC} are the output voltages of zDCES and z-source converter respectively, V_{LNC1} and V_{LNC2} are the inductor voltages. d represents the duty cycle of S_1 and S_4 switches while $(1\text{-}d)$ represents the duty cycle of S_2 and S_3 switches. At the steady state, the average voltages of inductors are zero for one switching cycle. Thus the voltage V_{zDCES} can be computed considering the duty cycle value.

The operation modes of zDCES are summarized in Eq. (2).

$$\begin{cases} V_{zDCES} > 0 \text{ when } V_{bus\_act} < V_{bus\_nom} \text{ and } P_{nom} > P_{act} \\ V_{zDCES} < 0 \text{ when } V_{bus\_act} > V_{bus\_nom} \text{ and } P_{nom} < P_{act} \\ V_{zDCES} = 0 \text{ when } V_{bus\_act} = V_{bus\_nom} \text{ and } P_{nom} = P_{act} \end{cases} \tag{2}$$

where P_{nom} and P_{act} are the nominal and actual power consumptions of loads respectively, V_{bus_nom} and V_{bus_act} are the nominal and actual busbar voltages respectively.

The power consumption of the smart load and CL are described as follows [1];

$$P_{act} = P_{NCL} + P_{zDCES} + P_{CL} \tag{3}$$

$$P_{act} = \underbrace{\underbrace{\frac{(V_{bus\_act} - V_{zDCES})^2}{R_{NCL}}}_{P_{NCL}} + \underbrace{\frac{(V_{bus\_act} - V_{zDCES})V_{zDCES}}{R_{NCL}}}_{P_{zDCES}}}_{smart\ \ load} + \underbrace{\frac{V_{bus\_act}^2}{R_{CL}}}_{P_{CL}} \tag{4}$$

where P_{NCL}, P_{zDCES} and P_{CL} represent the actual power consumption of NCL, zDCES and CL respectively. R_{NCL} is the NCL load, and R_{CL} is the CL load. From Eq (4), it is observed that the smart load power decreases linearly with positive V_{zDCES} while it increases linearly with negative V_{zDCES}. Eq(4) is valid for both voltage variations that occur in negative and positive directions in the DC busbar.

The voltage fluctuations occurred at PCC cause actual power variations in the loads. The power difference of the PCC can be expressed as;

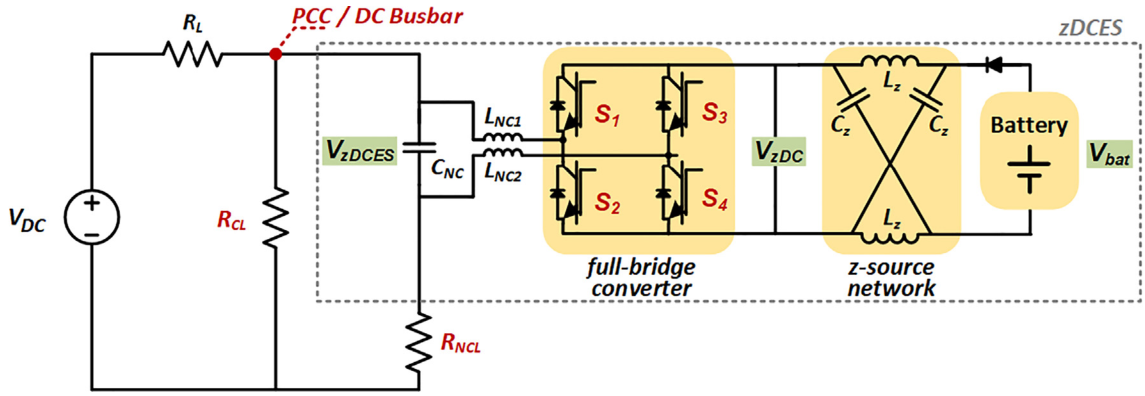

Fig. 2. Proposed zDCES topology.

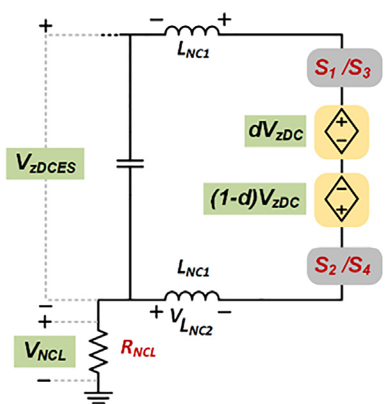

Fig. 3. Equivalent circuit of zDCES.

$$\Delta P = P_{nom} - P_{act} \tag{5}$$

The zDCES voltage is calculated according to;

$$P = \underbrace{\left(\frac{V^2_{bus\_nom}}{R_{NCL}} + \frac{V^2_{bus\_nom}}{R_{CL}} \right)}_{P_{nom}} - \underbrace{\left(\frac{(V_{bus\_act} - V_{zDCES\_act})^2}{R_{NCL}} + \frac{(V_{bus\_act} - V_{zDCES\_act})V_{zDCES\_act}}{R_{NCL}} + \frac{V^2_{bus\_act}}{R_{CL}} \right)}_{P_{act}} \tag{6}$$

$$V_{zDCES} = V_{bus\_act} - \frac{P_{SL}R_{NCL}}{V_{bus\_act}} \tag{7}$$

The voltage and power regulation of the SL are achieved via the full bridge converter the zDCES. The zDCES generate a suitable voltage (V_{zDCES}) and regulates the power flow to provide a stable voltage at PCC. With the control of the duty cycle in the full bridge converter, the zDCES voltage is defined as;

$$V_{zDCES} = V_{zDC}(2d - 1) \tag{8}$$

3. Control scheme of zDCES

The full-bridge converter is employed to manipulate the power flow of SL by providing bipolar voltage. A bipolar PWM method is adopted to provide a bipolar voltage at the output port of the zDCES. To be able to compensate for the voltage fluctuations by regulating the power flow of the PCC, the controller of the proposed system monitors the voltages and powers and detects the missing/excessive voltage. The compensation is performed by adjusting the duty cycles of switches in the full-bridge converter, which is interfacing battery and SL. The switching pairs of S_1-S_4 and S_2-S_3 are periodically triggered and have the complementary duty cycles as $(d)T_s$ and $(1\text{-}d)T_s$ respectively, where d is the duty cycle of S_1-S_4 and T_s is the switching cycle.

The zDCES is operated in different modes by considering Eq.2 via the controller. The difference (V_e) between the nominal voltage (V_{bus_nom}) and the measured actual voltage (V_{bus_act}) of the busbar is used to determine the instantaneous zDCES voltage. When the busbar voltage sags, zDCES voltage increases in the positive pole reducing the power consumption of the NCL. In addition, the busbar can also be fed by zDCES within the case of higher voltage sags. When the bus voltage exceeds its nominal voltage, zDCES voltage decreases in the negative pole, increasing the power consumption of the NCL. Thus, it ensures that the busbar voltage remains constant within the specified interval.

The controller of the zDCES is shown in Fig. 4. The duty cycles of h-bridge and shoot-through states are adjusted by the proportional-integral (PI) controllers which are operated simultaneously. The reference voltage of the busbar at PCC is subtracted from the measured busbar voltage to calculate the error. The error signal is applied to the PI controllers to generate the duty and shoot-through signals to be compared with a triangular carrier signal as illustrated in Fig. 5. Thus, bipolar PWM control is achieved. The change in duty cycles adjusts the voltage of the busbar and regulates the power flow at PCC.

~0.5 duty cycle is the critical value for the H-bridge since it represents the zero voltage output in mode 3. If the duty cycle is less than 0.5, the state represents mode 2 and the output voltage of the zDCES has a negative amplitude. If the duty cycle is more than 0.5, the state represents mode 1 and the output voltage of the zDCES has a positive amplitude.

The z source converter provides a high voltage in the input port of the full-bridge converter by regulating the battery voltage. Thus, a wide voltage range can be achieved with a smaller duty cycle ratio and lower battery voltage in comparison with the studies in the literature. It is achieved by an additional switching state called shoot-through which is an extra state corresponding to the shorting of one of the legs of a full-bridge converter [27,28]. The operation of the z source converter consists of two states as shoot-through (ST) and non-shoot-through (NST). During ST state, the upper and lower switches of one leg of the full-bridge converter are turned on simultaneously and the diode of the battery is reverse biased. Thus, the battery is isolated from the system and the SL is fed from the two capacitors. During NST state, the diode of the battery is forward biased and the SL is fed from the battery as well as the two inductors energy [29,30]. The DC voltage across

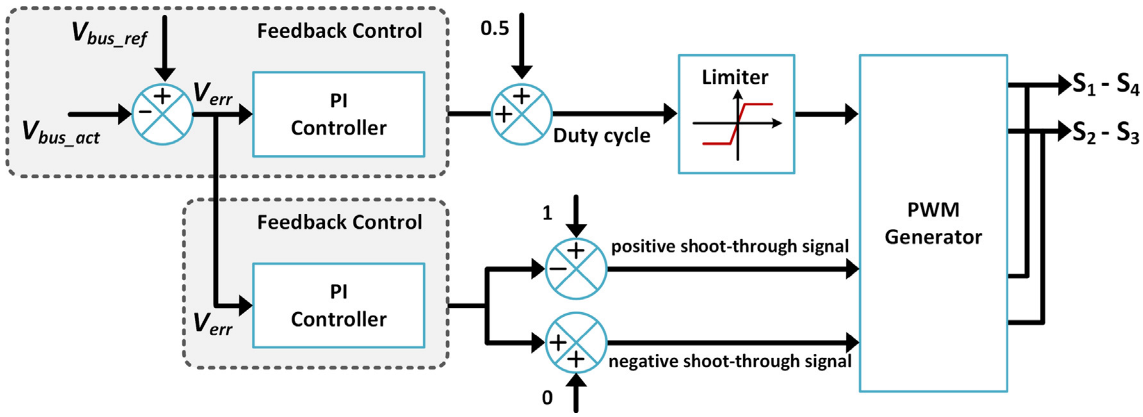

Fig. 4. Controller of the proposed zDCES.

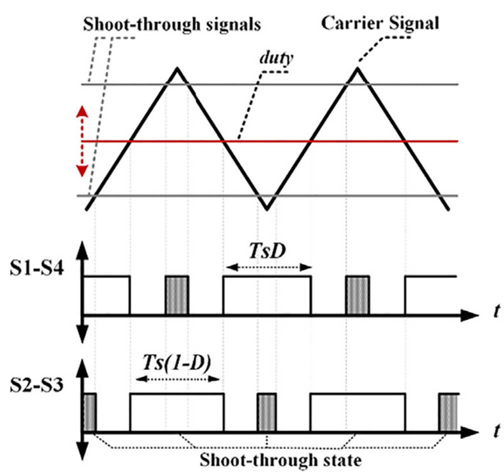

Fig. 5. Bipolar PWM control signals.

the input port of the full-bridge converter (V_{zDC}) is expressed as [27];

$$V_{zDC} = V_{bat}B \tag{9}$$

where B represents the boost factor and it is calculated according to the Eq.10 and Eq.11;

$$B = \frac{1}{1 - 2d_{st}} \tag{10}$$

$$d_{st} = T_{st}/T_S \tag{11}$$

where d_{st} represents the duty cycle of switches in shoot-through state and T_S and T_{st} represent the switching cycle and shoot-through time respectively.

The controller adjusts the d_{st} considering the difference between the reference and actual dc busbar voltages. In the state that the difference is high, the duty cycle of shoot-through state is also adjusted as a high value. Whereas the difference is low, the shoot-through duty cycle is also adjusted as a low value.

4. Performance analysis

This section presents the performance evaluation of the proposed system. In order to evaluate the performance of the designed zDCES topology and controller, a prototype is developed in MATLAB/Simulink environment for a dc microgrid. The presented system is tested under a case with different voltage fluctuation states and the performance results are compared with the conventional full-bridge converter based DCES topology. The switching elements of the power circuit are MOSFET because of the power rating and switching frequency of the system. The CL and NCL are designed as constant resistive loads with values of 14.05 O and 15.13 O respectively. The voltage at PCC is set to be 48 V and it fluctuates between 48.5 V and 51 V during the voltage fluctuation states. The parameters of the developed system are shown in Table 1.

The performance investigation of the proposed zDCES and the conventional full-bridge converter based DCES that is equipped with a 120 V battery pack is implemented using the same parameters. The only difference between the systems is the battery voltages. PI controllers generate a duty cycle considering dynamic variations of the voltage at PCC to trigger the switches of the electric springs. The generated duty cycles are presented in Fig. 6. The controllers respond dynamically during the instantaneous change in voltage. The results show that the proposed system provides the related compensation voltage with lower battery voltage and lower duty cycle range thanks to the high gain z source converter. The duty cycle values vary with using zDCES varies within the 40–60% whereas they vary within the 35–72% with using the conventional DCES topology.

The resulting PCC voltages that are obtained without using DCES, with using conventional DCES and the proposed zDCES during the voltage fluctuations are illustrated in Fig. 7. As can be seen from Fig. 7, the dc busbar voltage fluctuates without using DCES whereas it keeps constant within the specified values with using electric springs during the source voltage variations. In the same case, the proposed topology achieves to further increase the system performance by keeping the voltage fluctuation in a lower range in comparison with the conventional DCES.

Table 1
Parameters of the developed system.

System	Parameter	Value
DC Microgrid	Nominal Busbar Voltage	48 V
	Distribution Line Resistance (R_L)	0.37 O
	Critical Load Resistance (R_{CL})	14.05 O
	Non-critical Load Resistance (R_{NCL})	15.13 O
Full Bridge Converter	Switching Elements	MOSFET
	Filter Capacitor (C_{NC})	140 uF
	Filter Inductor (L_{NC1}, L_{NC2})	600 uH
	Switching Frequency	50 kHz
Z Source Converter	Capacitor (C_z)	1 mF
	Inductor (L_z)	12.8 mH
Battery	Nominal Voltage	65 V
	Capacity	10 Ah

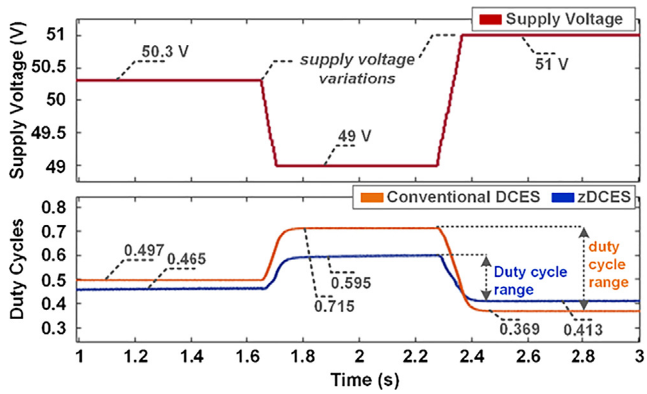

Fig. 6. Duty cycle variations during source voltage fluctuations.

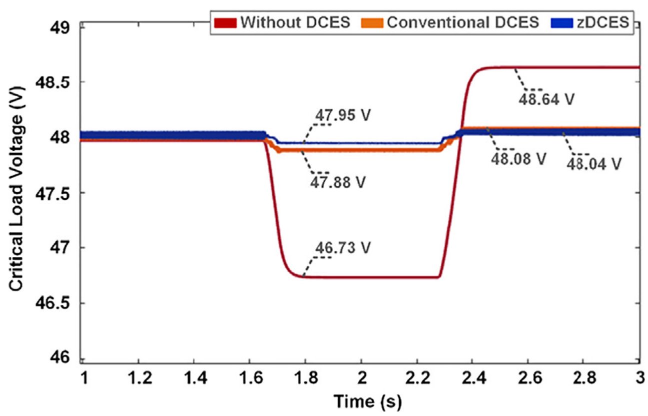

Fig. 7. PCC voltages during source voltage fluctuations.

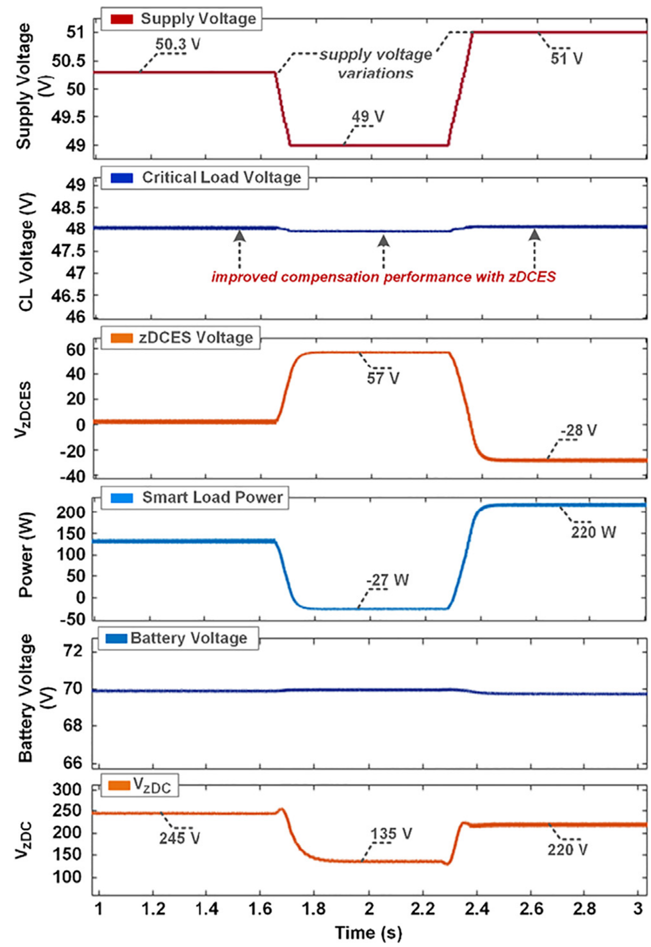

Fig. 8. Performance waveforms of the proposed zDCES.

The power consumption details of the SL are presented in Fig. 8. As illustrated in Fig. 8, the electric spring voltage is higher than zero when the busbar voltage sags. The SL power decreases linearly with the increasing electric spring voltage according to the depth of the voltage sag. The negative SL power corresponds to the injected power to the system by the zDCES. The electric spring voltage is lower than zero when the busbar voltage is higher than its nominal value. The SL power increases linearly with the decreasing electric spring voltage according to the depth of the voltage swell. As illustrated in Fig. 8, during the voltage fluctuations, the SL power is adjusted and the busbar voltage is kept under the desired voltage limits via zDCES. Besides, the z-source converter adaptively regulates the V_{zDC} voltage between 135 V and 245 V considering the related operation case with low battery voltage. So that the requirement for a high voltage battery is eliminated. The results prove that the proposed zDCES can quickly mitigate the effect of the dc microgrid fluctuations on the CL.

Table 2 outlines the advantages and disadvantages of the investigated systems in the DC microgrid. Among these systems, the proposed zDCES excels with the advantages of the reduced battery voltage, high gain, and lower duty cycle range. Besides, it has flexible operation voltage provided by the z-source converter thanks to the aspect of high gain.

5. Conclusion and discussion

In this paper, a z source converter integrated full-bridge converter based DCES topology and control method have been proposed. The main superior aspects of the proposed zDCES topology are reduced battery voltage and lower duty cycle range as well as providing a wider compensation voltage range. Also, a wide range bipolar voltage at the output ports of the zDCES is achieved by z source converter without additional switches rather than relatively high voltage battery packs or HFT conversion rate methods used in traditional DCES topologies.

Thus, a low cost solution has been developed to alleviate the voltage fluctuation problem. In order to verify the effectiveness

Table 2
Advantage/disadvantage benchmarking of the investigated systems.

Methods	Advantages	Disadvantages
zDCES	• Reduced battery voltage • Reduced series battery cells • Lower duty cycle range • High voltage gain • Adaptability voltage flexible applications • Four active switches • Bipolar voltage	• Additional passive components
H-Bridge Converter Based DCES	• Four active switches • Bipolar voltage	• High battery voltages • Restricted voltage applications • Limited compensation capability
Without DCES		• No compensation capability • Critical load damages

of the proposed zDCES system, a case study that includes different dynamic operational changes has been conducted. Besides, to show the superiority of the zDCES system is compared with conventional DCES. Performance results show that the proposed system can keep the busbar voltage constant with a lower duty cycle range while the other system requires a higher duty cycle range. Hence, a wide voltage range can be provided in the input port of the full-bridge converter by z source converter in contrast to other sys-tems. Besides, the zDCES can keep the voltage fluctuation in a lower range when compared with conventional DCES. As a result, zDCES shows better and more flexible mitigation performance for all operational conditions.

References

[1] Y. Yang, S. Tan, S.Y.R. Hui, Mitigating distribution power loss of DC microgrids with DC electric springs, IEEE Trans. Smart Grid 9 (2018) 5897–5906.
[2] M. Wang, S. Yan, S. Tan, S.Y. Hui, Hybrid-DC electric springs for DC voltage regulation and harmonic cancellation in DC microgrids, IEEE Trans. Power Electron. 33 (2018) 1167–1177.
[3] K. Mok, M. Wang, S. Tan, S.Y.R. Hui, DC electric springs—A technology for stabilizing DC power distribution systems, IEEE Trans. Power Electron. 32 (2017) 1088–1105.
[4] H. Zhao, M. Hong, W. Lin, K.A. Loparo, Voltage and frequency regulation of microgrid with battery energy storage systems, IEEE Trans. Smart Grid 10 (1) (2019) 414–424.
[5] D. Kumar, F. Zare, A. Ghosh, DC microgrid technology: system architectures, AC grid interfaces, grounding schemes, power quality, communication networks, applications, and standardizations aspects, IEEE Access 5 (2017) 12230–12256.
[6] M.M. Savrun, T. Köroğlu, A. Tan, M.U. Cuma, K.Ç. Bayindir, M. Tümay, Isolated H-bridge DC–DC converter integrated transformerless DVR for power quality improvement, IET Power Electron. 13 (5) (2020) 920–926.
[7] P. Sanjeev, N.P. Padhy, P. Agarwal, Peak energy management using renewable integrated DC microgrid, IEEE Trans. Smart Grid 9 (2018) 4906–4917.
[8] M. Farhadi, O. Mohammed, Adaptive energy management in redundant hybrid DC Microgrid for pulse load mitigation, IEEE Trans. Smart Grid 6 (1) (2015) 54–62.
[9] Z. Xin, W. Xuezhi, Y. Li, T. Hao, Energy management strategy of multiple supercapacitors in an autonomous DC microgrid using adaptive virtual impedance, in: 2016 IEEE 7th International Symposium on Power Electronics for Distributed Generation Systems (PEDG), 2016, pp. 1–8.
[10] M. Wang, K. Mok, S. Tan, S.Y. Hui, Multifunctional DC electric springs for improving voltage quality of DC grids, IEEE Trans. Smart Grid 9 (2018) 2248–2258.
[11] X. Chen, M. Shi, H. Sun, Y. Li, H. He, Distributed cooperative control and stability analysis of multiple DC electric springs in a DC microgrid, IEEE Trans. Ind. Electron. 65 (2018) 5611–5622.
[12] M. Wang, S. Yan, S. Tan, Z. Xu, S.Y. Hui, Decentralized control of DC electric springs for storage reduction in DC microgrids, IEEE Trans. Power Electron. 35 (2020) 4634–4646.
[13] X. Chen, Y. Hou, S.Y.R. Hui, Distributed control of multiple electric springs for voltage control in microgrid, IEEE Trans. Smart Grid 8 (2017) 1350–1359.
[14] A. Hosseinipour, H. Hojabri, Small-signal stability analysis and active damping control of DC microgrids integrated with distributed electric springs, IEEE Trans. Smart Grid 11 (5) (2020) 3737–3747.
[15] J. Liao, N. Zhou, Y. Huang, Q. Wang, Unbalanced voltage suppression in a bipolar DC distribution network based on DC electric springs, IEEE Trans. Smart Grid 11 (2020) 1667–1678.
[16] Q. Wang, D. Zha, F. Deng, M. Cheng, G. Buja, A topology of DC electric springs for DC household applications, IET Power Electron. 12 (2019) 1241–1248.
[17] D. Zha, Q. Wang, M. Cheng, F. Deng, and G. Buja, "Regulation Performance of Multiple DC Electric Springs Controlled by Distributed Cooperative System," Energies, vol. 12, 2019.
[18] M. İnci, M. Büyük, M.H. Demir, G. İlbey, A review and research on fuel cell electric vehicles: Topologies, power electronic converters, energy management methods, technical challenges, marketing and future aspects, Renew. Sustain. Energy Rev. 137 (2021) 110648, https://doi.org/10.1016/j.rser.2020.110648.
[19] W. Li, W. Li, X. Xiang, Y. Hu, X. He, High step-up interleaved converter with built-in transformer voltage multiplier cells for sustainable energy applications, IEEE Trans. Power Electron. 29 (6) (2014) 2829–2836.
[20] M. İnci, M. Büyük, M.M. Savrun, M.H. Demir, Design and analysis of fuel cell vehicle-to-grid (FCV2G) system with high voltage conversion interface for sustainable energy production, Sustain. Cities Soc. 67 (2021) 102753.
[21] B. Singh, V. Bist, A. Chandra, K. Al-Haddad, Power factor correction in bridgeless-luo converter-fed BLDC motor drive, IEEE Trans. Ind. Appl. 51 (2) (2015) 1179–1188.
[22] L.H.S.C. Barreto, E.A.A. Coelho, V.J. Farias, J.C. deOliveira, L.C. deFreitas, J.B. Vieira Jr., A quasi-resonant quadratic boost converter using a single resonant network, IEEE Trans. Ind. Electron. 52 (2) (2005) 552–557.
[23] S. M. P., M. Das and V. Agarwal, "Design and Development of a Novel High Voltage Gain, High-Efficiency Bidirectional DC–DC Converter for Storage Interface," IEEE Transactions on Industrial Electronics, vol. 66, no. 6, pp. 4490-4501, June 2019.
[24] Y. Liu, H. Abu-Rub, B. Ge, Z-source\/quasi-Z-source inverters: derived networks, modulations, controls, and emerging applications to photovoltaic conversion, IEEE Ind. Electron. Mag. 8 (4) (2014) 32–44.
[25] Y. Liu, H. Abu-Rub, B. Ge, Front-end isolated quasi-Z-source DC–DC converter modules in series for high-power photovoltaic systems—Part II: control, dynamic model, and downscaled verification, IEEE Trans. Ind. Electron. 64 (1) (2017) 359–368.
[26] M.M. Savrun, A. Atay, Multiport bidirectional DC–DC converter for PV powered electric vehicle equipped with battery and supercapacitor, IET Power Electron. 13 (17) (2020) 3931–3939.
[27] P. Fang Zheng, Z-source inverter, IEEE Trans. Ind. Appl. 39 (2) (2003) 504–510.
[28] A. Desmoort, O. Deblecker, Z.D. Grève, Active rectification for the optimal command of bidirectional resonant wireless power transfer robust to severe circuit parameters deviations, IEEE Trans. Ind. Appl. 56 (2020) 1640–1648.
[29] O. Ellabban, H. Abu-Rub, An overview for the Z-source converter in motor drive applications, Renew. Sustain. Energy Rev. 61 (2016) 537–555.
[30] A.M. Florez-Tapia, J. Vadillo, A. Martin-Villate, J.M. Echeverria, Transient analysis of a trans quasi-Z-source inverter working in discontinuous conduction mode, Electr. Power Syst. Res. 151 (2017) 106–114.

Electric power bidding model for practical utility system

Sudhansu Sekhar Khuntia, *Department of Electrical and Communication Engineering, Aryan Institute of Engineering & Technology, Bhubaneswar, sskhuntia88@gmail.com*

Prakash Kumar Behera, *Department of Electronics and Communication Engineering , Raajdhani Engineering College, Bhubaneswar, prakash_behera21@gmail.com*

Laxminarayan Mishra, *Department of Electrical and Electronics Engineering, Capital Engineering College, Bhubaneswar, laxminarayan.s@gmail.com*

Pranay Rout, *Department of electrical Engineering , NM Institute of Engineering & Technology, Bhubaneswar, pranayrout93@gmail.com*

Alekha Sahoo, *Department of electrical Engineering , Raajdhani Engineering College, Bhubaneswar, alekha.sahoo241@gmail.com*

KEYWORDS

Bidding strategy;
Day ahead electricity market;
Market clearing price;
Market clearing volume;
Block bid;
Intermediate value theorem

Abstract A competitive open market environment has been created due to the restructuring in the electricity market. In the new competitive market, mostly a centrally operated pool with a power exchange has been introduced to meet the offers from the competing suppliers with the bids of the customers. In such an open access environment, the formation of bidding strategy is one of the most challenging and important tasks for electricity participants to maximize their profit. To build bidding strategies for power suppliers and consumers in the restructured electricity market, a new mathematical framework is proposed in this paper. It is assumed that each participant sub-mits several blocks of real power quantities along with their bidding prices. The effectiveness of the proposed method is tested on Indian Utility-62 bus system and IEEE-118 bus system.

1. Introduction

The electricity industry around the world has been undergoing through a change from regulated to restructuring market structure and the government owned utilities have become privatized. In this environment, introduction of competitive energy market, unbundling electricity services and open access to the network have been created. In order to have the competitive market, market operator and policy makers need to study, analyze and monitor the behavior of market participants. In a competitive electricity market, both power suppliers and consumers are allowed to participate in the market. Due to limited number of power producers, long period of power plant construction, large size of capital investment, transmission constraints and transmission losses, the restructured power market behaves more like an imperfect competition. In such oligopolistic markets, an individual generator can exercise market power and manipulate the market price via its strategic bidding behavior and generating companies may achieve benefits by bidding at a price higher than their marginal production cost. This is called as a strategic bidding problem. In order to maximize the profit for suppliers and minimize the payments of customers, the building of bidding strategies is a major concern in the restructured power market because their profits depend on their bids.

In recent years, a number of strategic bidding models have been proposed by many researchers. There are three main methods to model the strategic bidding problems based on the estimation of market clearing price, probability of rival's bidding behavior and game theory approach [1]. The market clearing price (MCP) plays a significant role in the strategic bidding problem since it determines what blocks will be nominated by the market clearing mechanism. The MCP is determined by the following process. In the competitive electricity market, the sellers submit the offers to sell the energy and the buyers submit the bids to buy the energy. After accepting the offers and bids from the sellers and buyers, the market operator ranks the selling offers with buying bids. The stacked supply curve for seller and demand curve for buyer are formed by market operator. The point of intersection of the two curves sets the MCP. The determination of market clearing price is main operating function for a market operator in energy trading market.

Still now, a wide research work has been done on developing bidding strategies for generation side market participant only and little work on demand side participants. The problem of developing optimal bidding strategies for competitive generation companies was first introduced by David [2] and then surveyed by several researchers. Most of the researchers have used a linear bid function or quadratic bid function to build the bidding strategy for the electricity market participant. In [3,4], a linear bid function is assumed to build the bidding strategies for participant and the system is dispatched to maximize the social welfare. In [5], Market clearing price with and without wind power has been evaluated in double sided bidding for linear bid and block bid trading model. Using Graphical analysis, the MCP and schedules are determined under different market conditions in which quadratic bid function from both generating side and consumer side is considered [6]. In [7], a conceptual study is carried out on optimal bidding strategies of power suppliers in the operating Zhejiang provincial electricity market in which the step-wise bidding protocol is used. A normal probability distribution function is used to describe the bidding behaviors of rivals. The problem of building optimal bidding strategies for GENCOs is formulated as stochastic optimization problem which is solved by Monte-Carlo simulation method and the optimal bidding block price of GENCO is searched by Genetic Algorithm. Based on the stepwise bidding protocol in electricity markets, the impact of different numbers of bidding segments on the bidding strategies of generation companies is calculated in [8].

The published research work regarding solution methodology for bidding strategies can be grouped as optimization method, game theory based and evolutionary based model. In [9,10], strategic bidding problem has been formulated as an optimization problem in which producers try to maximize their profit based on the market clearing price. An analytical formulation was developed for building the optimal bidding strategy in England and Wales type electricity markets under an assumption that the MCP is independent of the bid of any supplier [11]. Some mathematical programming models [12] such as linear and nonlinear integer programming models were established to build optimal building problem for power producers in day ahead electricity auction markets. In [13], the bidding decision problem is formulated for GENCO with considering risk management and unit commitment. Using Graphical analysis, MCP and schedules are determined under different market conditions in double sided auction [14]. Li et al. [15] have presented a mathematical model to find out MCP in the electricity markets. In [16], a strategic bidding procedure based on stochastic programming is decomposed using the Benders technique. Zou [17] has designed bidding strategy model to maximize social welfare in the spot market. In [18], the supply function models of various bidding strategies with forward contracts are employed to simulate the bidding strategy of suppliers in the power pool. An improved PSO algorithm is proposed to solve the optimal bidding problem for GENCO's in a uniform price spot market [19]. Richter and Sheble have applied GA [20] and GP - Automata [21] to evolve appropriate bidding strategies in double auctions for electric utilities which trade electricity competitively.

Strategic bidding has been addressed by many researchers for a wide variety of market players. Researchers utilized many different modeling approaches and different solution methods. By analyzing the strategic bidding behavior of generating companies, a specific MLNB decision model for day-ahead electricity markets is created in [22]. Soleymani [23] has proposed a new method that was the combination of PSO and simulated annealing to predict the bidding strategy of generating companies in an electricity market where they have incomplete information about their opponents and market mechanism of payment is pay as bid. In [24], discrete cosine transforms based neural network approach is used to classify the electricity markets of Mainland Spain and New York. Agent based simulation is employed to study the power market operation under different pricing methods in [25]. The JAVA based power trading simulator is proposed to find out the market clearing price in single sided auction market in [26]. For the price-maker hydro-electric producers bidding problem, the most recent developments and a path for future efforts are illuminated in [27]. Jain et al. [28] have developed an optimal bidding strategy for a supplier considering double sided bidding, rivals bidding behavior, and unconstrained and constrained market scenario.

A number of strategic bidding models have been proposed by different researchers in recent years. In this paper, a mathematical model is developed for step bidding function for a day ahead market in the competitive environment. In most of the research work, a linear supply function model was presented to investigate strategic bidding behavior. However actual implementation of electricity markets requires the representation of supply offers and demand bids that aggregated into distinct steps. This paper presents mathematical model for stepwise bidding protocol for both supplier offer functions and customer bid functions of real power. Conventional method is used to solve this mathematical model for step bidding function. This proposed method is tested on Indian Utility-62 bus system and IEEE-118 bus system.

The Indian Energy Exchange actually uses piecewise-linear bids that are strict functions from price to quantity. Bidders in practice use these functions almost exclusively to closely approximate step functions with constant quantities for a range of prices. In this paper, bids to be assumed of a true step form throughout and do not use the linear interpolation of the exchange.

In the developing electricity markets, a suitable trading mechanism is required for all participants in order to achieve the profit. This paper employs conventional method to solve the bidding function of both suppliers and customers. The pricing mechanism in double side auction is uniform pricing method. The social welfare generated by the double auction will be improved greatly. The different case studies with block bids models are illustrated. It has been found that MCP may be higher when demand is increased. Case studies show that such a structure allows all power market participants to empower with more information about the market settlement. This method is more consistent than other simulation model.

This paper is organized as follows. Section 2 explains the mathematical formulation of the strategic bidding problem for double sided auction in a day ahead market. Section 3 describes the solution algorithm. Section 4 illustrates conceptual analysis for a practical utility system and results are presented. Conclusive remarks are given in Section 5.

2. Mathematical formulation

To realize the economic dispatch, maximize the profits of suppliers and minimize the customer payments, it is very important to create reasonable matching rule for the electricity auction market. In a day ahead electricity market, every electricity supplier and customer submits bids to the power market for every hour. Market operator sorts bids of customers and suppliers by their price offers in descending and ascending order respectively and the customer with the highest bid price is first matched with the lowest offer price of supplier. For that, the aggregated hourly supply and demand bid curves are constructed from the offers and bids submitted by participants. The point of intersection between aggregated demand and supply curve sets the market clearing price (MCP). Every supplier whose offering price is below or equal to the MCP will be allowed to sell the electricity at that hour. Similarly every customer whose bidding price is above or equal to the MCP will be accepted to buy the energy. All accepted participants will be paid at the same clearing price for the electricity, but not the price offered. Thus a system dispatch levels are fixed by a market operator by making maximize the profit of suppliers and minimize the customer payments. In this paper, it is assumed that each participant (supplier and customer) in day ahead electricity market submits its own bid as pairs of price and quantity with several blocks. Stepwise bidding is considered. Mathematical model is developed for bidding function of suppliers and customers. The solution methodology is also proposed for this mathematical model. The plant ramping, transmission and system security constraints and reserve have been ignored.

2.1. Mathematical model for suppliers

In a competitive electricity market, the participants can be allowed to bid their outputs and demands as blocks. The sales bid of suppliers are expressed in the following way.

Suppose that a system consists of 'm' independent power suppliers. Each supplier is required to submit a block bid function. Each supplier has $k_i (i = 1, 2, \ldots, m)$ blocks of power to sell which are arranged in ascending order of their cost of production as shown below.

$$S_i(q) = \begin{cases} p_{si1} & a_{i0} \leqslant q \leqslant a_{i1}, \\ p_{si2} & a_{i1} \leqslant q \leqslant a_{i2}, \\ p_{si3} & a_{i2} \leqslant q \leqslant a_{i3}, \\ \vdots & \vdots \quad \ddots \quad \vdots \\ p_{sik_i} & a_{ik_i-1} \leqslant q \leqslant a_{ik_i}, \quad i = 1, 2, \ldots m \end{cases} \tag{1}$$

where p_{si1} denotes offering price of first block for the ith supplier between the power quantity a_{i0} and a_{i1}.

The electricity supply curve is upward sloping curve which can be obtained by summing of all net sales bids of suppliers. The cumulative blocks of power for all suppliers can be written as

$$S(q) = \begin{cases} p_{s1} & a_0 \leqslant q \leqslant a_1, \\ p_{s2} & a_1 \leqslant q \leqslant a_2, \\ p_{s3} & a_2 \leqslant q \leqslant a_3, \\ \vdots & \vdots \quad \ddots \quad \vdots \\ p_{sk} & a_{k-1} \leqslant q \leqslant a_k \end{cases} \tag{2}$$

where p_{s1} denotes offering price of first block for the 'm' suppliers between the power quantity a_0 and a_1.

Using Heaviside's unit step function, these equations are expressed as a single equation and are given by the equation.

$$S(q) = p_{s1} + (p_{s2} - p_{s1})u_{a_1}(q) + (p_{s3} - p_{s2})u_{a_2}(q) + \cdots + (p_{sk} - p_{sk-1})u_{a_k-1}(q) \tag{3}$$

2.2. Mathematical model for customers

The demand bid of customers are expressed in the following way.

Let there are 'n' independent customers and each customer has l_j, $(j = 1, 2, \ldots n)$ blocks of power to purchase the energy which is given by the equations.

$$D_j(q) = \begin{cases} p_{di1} & b_{j0} \leqslant q \leqslant b_{j1}, \\ p_{di2} & b_{j1} \leqslant q \leqslant b_{j2}, \\ p_{di3} & b_{j2} \leqslant q \leqslant b_{j3}, \\ \vdots & \vdots \quad \ddots \quad \vdots \\ p_{djl_j} & b_{jl_{j-1}} \leqslant q \leqslant b_{jl_j}, \quad j = 1, 2, \ldots n \end{cases} \tag{4}$$

where p_{dj1} denotes offering price of first block for the jth customer between the power quantity b_{j0} and b_{j1}.

The electricity demand curve is downward sloping curve which can be obtained by summing up of all purchase bids of customers. The cumulative blocks of power for all customers can be written as

$$D(q) = \begin{cases} p_{d1} & b_0 \leqslant q \leqslant b_1, \\ p_{d2} & b_1 \leqslant q \leqslant b_2, \\ p_{d3} & b_2 \leqslant q \leqslant b_3, \\ \vdots & \vdots \quad \ddots \quad \vdots \\ p_{dl} & b_{l-1} \leqslant q \leqslant b_l \end{cases} \tag{5}$$

where p_{d1} indicates the bidding price of first block for 'n' customers between the power quantity b_0 and b_1.

Using Heaviside's unit step function, these equations are expressed as a single equation and are given by the equation.

$$D(q) = p_{d1} + (p_{d2} - p_{d1})u_{b_1}(q) + (p_{d3} - p_{d2})u_{b_2}(q) + \cdots + (p_{dl} - p_{dl-1})u_{b_l-1}(q) \tag{6}$$

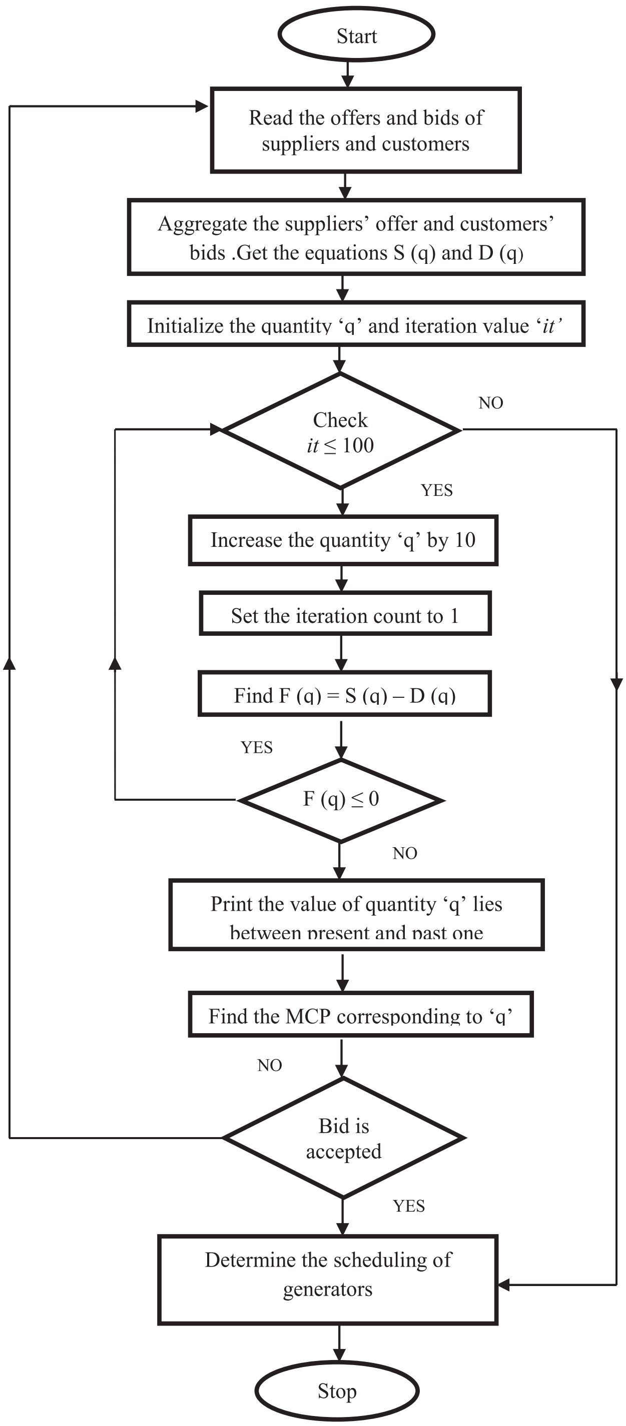

Figure 1 Step by step algorithm.

2.3. Solution methodology

Strategic bidding has been addressed in many research literature and different solution methods are proposed. From an organization point of view and according to bidding models for market participants' behavior taking into account, electricity market modeling can be classified into three main areas:

- Optimization models are involved with profit maximization problem for a single participant in electricity market.
- Equilibrium models represent the market behavior taking into consideration competition between all participants.
- Simulation models aim to model complexity of electricity market as collection of rule based agents interacting with one another dynamically.

Optimization models generally focus on one specific market participant in system by simplifying rest of the system as a set of exogenous variables. It is well established by mathematical foundation and difficult to model complex and dynamic system. This model is used to describe the players in electricity market with the objective of finding optimal solution [29,30]. Equilibrium models represent the overall market behavior taking into consideration and competition among all participants. The approach assumes that each player in the market tries to maximize its profit. Hence performance of market participant is affected by other participant behaviors. All players are assumed to be rational which does not generally hold in reality. This model is developed with aim of improving economic efficiency [31,32]. Simulation models are an alternative to equilibrium models when the problem under consideration is too complex to be addressed within a formal equilibrium frame work. Only few simple rules are followed by various agents participated in the network and interacting with one another intelligently and dynamically. It is based on agents that allow developing models to represent in more realistic way electricity markets. But actual performance of the system is limited by mathematical or logical relationship foundation [33,34].

In this research work, conventional method is used to find the solution of supply and demand equation. Intermediate value property is used to solve this mathematical model of step bidding function. The solution for this mathematical function is found by equating aggregated suppliers function and aggregated customers function. The MCP of the system is obtained by the intersection of the aggregated supply curve and the aggregated demand curve.

$$S(q) = D(q) \tag{7}$$

Eq. (7) is nothing but the solution of $F(q) = 0$ where $F(q) = S(q) - D(q)$.

The solution of $F(q) = 0$ can be found by using intermediate value property. The intermediate value theorem was first proved by Bernard Bolzano [35]. This theorem states that let 'a', 'b' real numbers with $a < b$ and let 'f' be a continuous function defined on the interval $[a, b]$ to R such that $f(a) < 0$ and $f(b) > 0$. Then there is some number 'c' between 'a' and 'b' such that $f(c) = 0$. According to this theorem, it is easy to see that, if we find two values q_r and q_{r-1} such that $F(q_r)F(q_{r-1}) < 0$ (i.e. one value is positive and another one is negative) then there exists a 'q' which lies between q_r and q_{r-1} such that $F(q) = 0$.

The iteration process is used to find value of q_r and q_{r-1} such that $F(q_r)F(q_{r-1}) < 0$. In this connection while finding the values of $F(q)$ for $q = 0, 10, 20, 30, \ldots$ at one stage we will have q_r and q_{r-1} such that $F(q_r)F(q_{r-1}) < 0$. We note the value of 'q' at which the sign of $F(q)$ changes. By intermediate value theorem we can find a 'q' in between q_r and q_{r-1} such that $F(q) = 0$. The corresponding price for this 'q' is known as market clearing price.

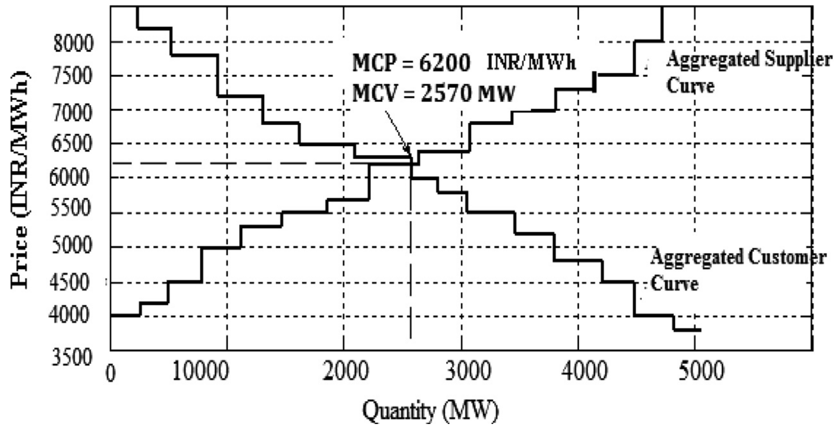

Figure 2 Matching of aggregated suppliers and customers curve.

Table 1 The effect of load variation.

Load demand	MCP (INR/MWh)	MCV (MW)
Base load	6200	2570
Increase in load	6400	3000
Decrease in load	6000	2210

In this paper, MCP for market participants in practical utility system is found by using step bidding function of suppliers and customers. MCP is set by the intersection of demand and supply at the market. In case of linear bidding, the exercise of market power creates an economic dead weight loss. It causes loss of benefit to society. In step bidding, the exercise of market power could not create an economic dead weight loss. This is the most efficient output because the exercise market power can be avoided. This paper also employs conventional method to solve this mathematical model. This proposed solution methodology gives unique solution. The optimal price and quantity occur at the intersection of supply curve and demand curve. This proposed method is an exact and efficient method.

3. Step by step algorithm

The step by step procedure to evaluate market settlement in double auction electricity market is illustrated in Fig. 1.

4. Results and discussion

<u>*Case 1*</u>

4.1. Indian Utility-62 bus system

A case study has been carried on Indian Utility 62 bus system with 19 generators and 29 customers interconnected by 89 transmission lines [36]. The different case studies are analyzed in this section.

4.1.1. Base load condition

In this case, under the base load condition the Market Clearing Price is determined. The bidding data are aggregated in ascending order of price from the 19 supplier's offers and descending order of price from 29 consumer's bids which is given in appendix. The supplier curve and customer curve are obtained and illustrated in Fig. 2. The point of intersection of two curves gives the market clearing price and corresponding quantity is called as market clearing volume. The market clearing price and transaction volume are given in Table 1.

4.1.2. The effect of load variation

In this case the load is varied with 20% increase and decrease from the base case. For these loads, the consolidated offer curve for suppliers and bid curve for customers are obtained and given in Fig. 3. By comparing the graphs with those of base load, it can be observed that the demand curve shifts upward or downward when the load is increased or decreased from the base load. The market clearing price and clearing volume for each case are listed in Table 1. From the table, it can be clearly seen that when the load is 20% more than the base case the estimated market clearing price is higher than the base case and 20% less than the base case the expected market clearing price is less than the base case. The market clearing price and market clearing volume for various load conditions are given in Table 1.

4.1.3. MCP and MCV for various system demands

The volume of system demand at various percentages is given in Fig. 4. In this case, the transaction of volume and market clearing price under different market conditions is obtained which is given in Fig. 5. The scheduling quantity of all 19 generators obtained by proposed method is shown in Fig. 6. After determining the market clearing price in base load condition, the offering price below and equal to MCP of suppliers is measured. For each offering price, the contributed generators and their clearing volume of each generator are given in Table 2.

<u>*Case 2*</u>

4.2. IEEE-118 bus system

This test case consists of 118-bus, 19 generators, 35 synchronous condensers, 177 lines, 9 transformers, and 91 loads. For this practical utility system, MCP is determined by assuming linear bid and as well as step bid function under base load conditions. Economic welfare between linear bid and step bid

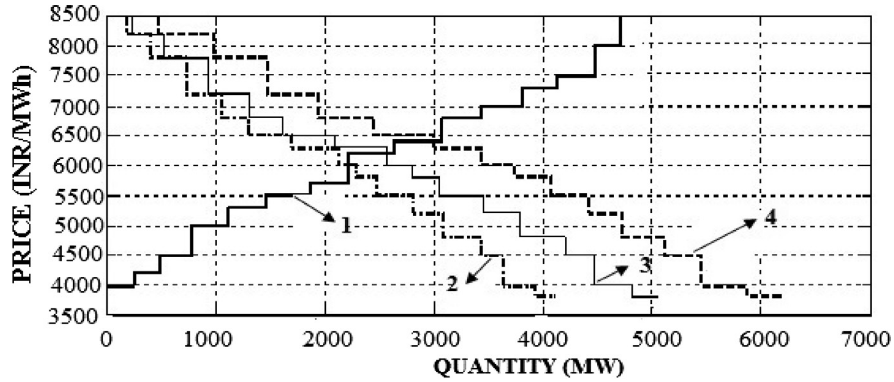

1--Aggregated suppply
2--Aggregated demand for decrease in load
3--Aggregated demand for base load
4--Aggregated demand for increase in load

Figure 3 Matching of aggregated suppliers and customers curve in different load conditions.

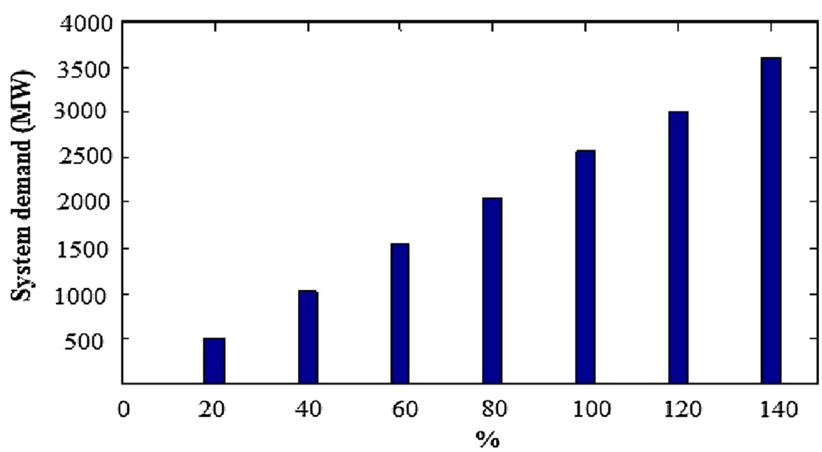

Figure 4 The volume of system demand.

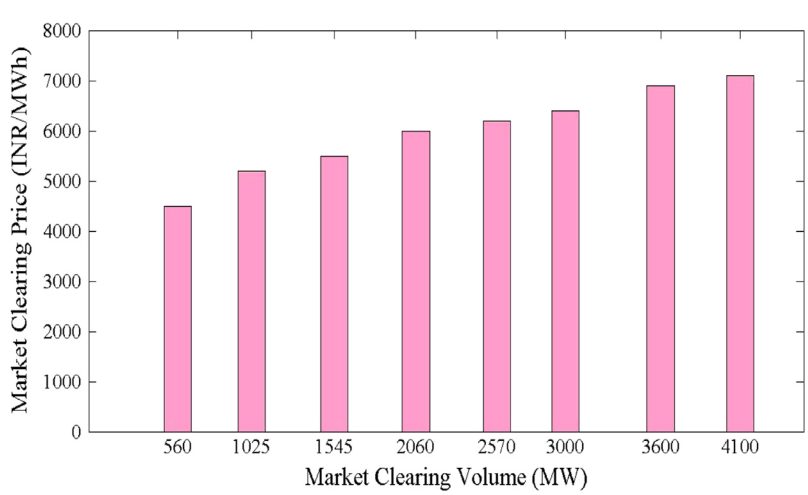

Figure 5 MCP and MCV for different system demands.

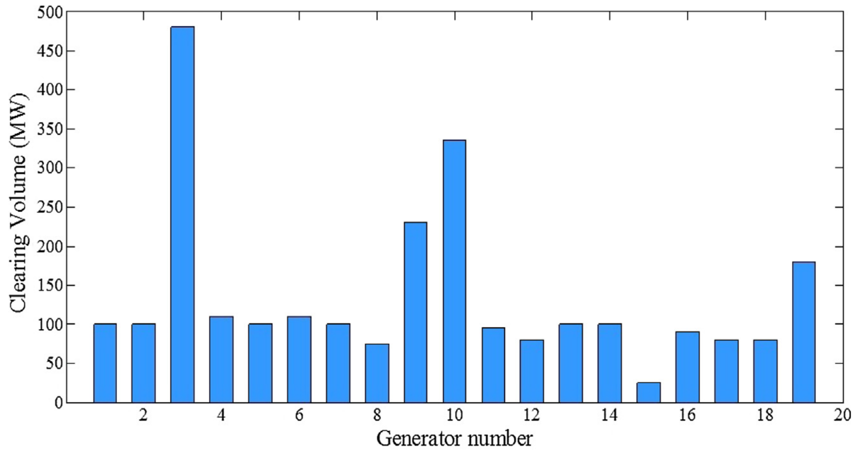

Figure 6 Clearing volume of each generator.

Table 2 Clearing volume of competitive generator.

Bid price (INR/MWh)	Contributed generators								Clearing volume of generators (MW)								Total volume (MW)
4000	G_1	G_3	G_9	G_{14}	G_{18}	–	–	–	50	50	75	50	25	–	–	–	250
4200	G_2	G_6	G_{10}	G_{16}	–	–	–	–	50	60	100	30	–	–	–	–	240
4500	G_1	G_3	G_{10}	G_{14}	G_{17}	G_{18}	–	–	50	50	75	50	35	30	–	–	290
5000	G_2	G_4	G_9	G_{10}	G_{16}	G_{19}	–	–	50	60	50	50	30	95	–	–	335
5300	G_3	G_6	G_7	G_{11}	G_{17}	G_{18}	G_{19}	–	50	50	50	95	45	25	30	–	345
5500	G_3	G_4	G_7	G_9	G_{10}	G_{12}	G_{15}	G_{19}	100	50	25	50	50	80	25	20	400
5700	G_3	G_5	G_8	G_{10}	G_{13}	–	–	–	80	60	75	35	100	–	–	–	350
6200	G_3	G_5	G_7	G_9	G_{10}	G_{16}	G_{19}	–	150	40	25	55	25	30	35	–	360

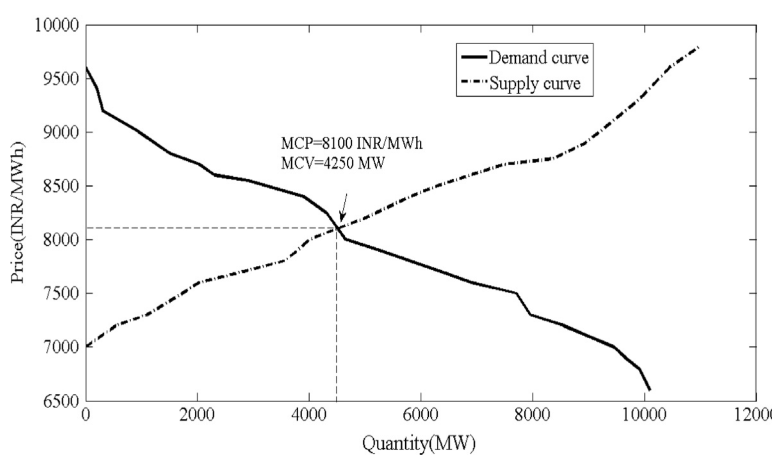

Figure 7 Linear bid curve.

is also analyzed. We assume that each generator specifies an offer function is equal to its marginal cost. For base load condition, suppliers offer function and customers bid function are aggregated and illustrated. Figs. 7 and 8 show matching of aggregated suppliers and customers curve for linear bid and step bid function. Under base load conditions, MCP is found as 8100 INR/MWh.

An individual supplier can exercise market power and manipulate the market price via strategic bidding behavior. Each market participant will maximize their profit at a point where marginal revenue (MR) equals to marginal cost (MC). Since demand curve is downward sloping, profit maximization level of output (MR) lies below the demand curve. Because of this market produces less than socially output amount. It

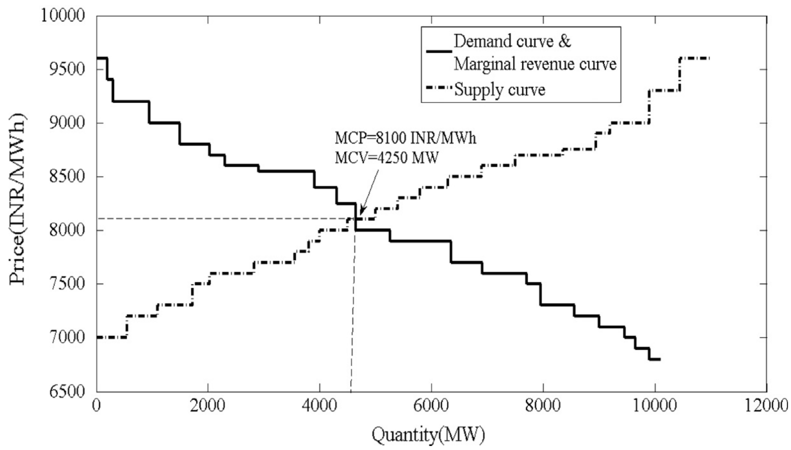

Figure 8 Step bid curve.

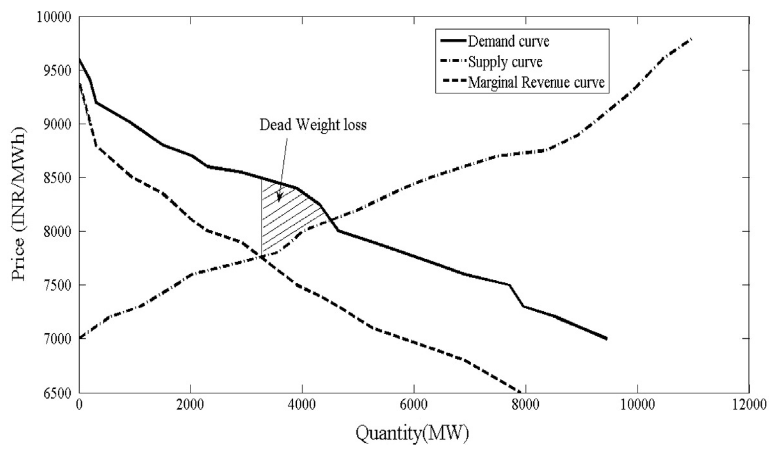

Figure 9 Dead weight loss.

Table 3 Bidding block and simulation result of optimization based method [7].

Ref. [7]							
GENCOs	Max. available capacity (MW)	Bidding block			MCP	Dispatched amount (MW)	Benefit
		I	II	III	$/MWh		$
GENCO X	600	200	200	200	49.99	400	8698
R_1	600	200	200	200			
R_2	600	200	200	200			
R_3	600	200	200	200			
R_4	600	200	200	200			
Rival bidding block		800	800	800			
Bidding price		10$	30$	50$			

causes dead weight loss. There is a loss in economic surplus within the market. Dead weight loss is the lined triangle shown in Fig. 9. In case of step bidding, the profit maximization output line (MR) is the same as the demand curve. Marginal revenue curve is the first order derivative of total revenue curve. Marginal revenue of step bidding function is the same as the total revenue function (i.e.) demand function. So marginal revenue curve lies on the demand curve, that is marginal revenue curve will be the same as the actual quantity demand curve illustrated in Fig. 8. Hence there is no dead weight loss on step bidding.

Case 3

In this case, we compare the results of dispatched power of GENCOs and their surplus amount. Both participants (suppli-

Table 4 Bidding block and simulation result of proposed method.

GENCOs	Max. available capacity (MW)	Bidding block I	Bidding block II	Bidding block III	Bidding block IV	Bidding block V	Bidding block VI	Bidding price I	Bidding price II	Bidding price III	Bidding price IV	Bidding price V	Bidding price VI	MCP $/MWh	Dispatched amount (MW)	Benefit $
G_1	600	100	100	100	100	100	100	10	20	35	52	58	65		300	8500
G_2	600	100	150	150	100	100	–	15	20	30	45	54	–		500	9000
G_3	600	200	200	200	–	–	–	20	35	55	–	–	–	50	400	9000
G_4	600	150	150	100	100	100	–	15	30	40	55	60	–		400	9250
G_5	600	100	150	150	200	–	–	10	30	50	60	-	-		400	9500

ers and customers) are considered in our proposed method. The registered capacities of all five GENCOs are same as those of Ref. [7] (i.e.) 600 MW each. Each participant can bid at more than one block with different prices for each period in power market. The solution of the system is obtained by intermediate value property. The MCP of the system obtained using proposed method is same for all GENCOs (i.e.) 50 $. Table 4 gives the simulation results obtained by proposed method against those given in optimization based method [7]. Table 3 shows the values of dispatched power and benefit of GENCO X. The dispatched output for all GENCOs and their benefit are given in Table 4. It is seen that the dispatched level for each participant in each period is based on the bidding prices and load forecast. Profits of generation companies depend on their bidding strategies. This trading mechanism maximizes the total value of the transactions between the participants by making each customer maximize its savings and each supplier maximize its gains.

5. Conclusion

In competitive electricity market, power suppliers and customers are required to bid stepwise bidding protocol function. For that a new mathematical model is proposed in this paper to build bidding strategies for power suppliers and customers in a day ahead electricity market. The solution methodology for the proposed mathematical model is also discussed. This methodology has been tested on Indian Utility-62 bus system and IEEE-118 bus system. The case studies are analyzed for different load conditions.

References

[1] A.K. David, F. Wen, Strategic bidding in competitive electricity markets: a literature survey, Proceedings of IEEE Power Engineering Society Summer Meeting, vol. 4, 2000, pp. 2168–2173.
[2] A.K. David, Competitive bidding in electricity supply, IEE Proc. Gener. Transm. Distrib. 140 (5) (1993) 421–426.
[3] A.K. David, F. Wen, Optimal bidding strategies and modeling of imperfect information among competitive generators, IEEE Trans. Power Syst. 16 (1) (2001) 15–21.
[4] J. Vijaya Kumar, D.M. Vinod Kumar, Optimal bidding strategy in an open electricity market using Genetic Algorithm, Int. J. Adv. Soft Comput. Appl. 3 (2011) 55–67.
[5] S.N. Singh, I. Erlich, Strategies for wind power trading in competitive electricity markets, IEEE Trans. Energy Convers. 23 (2008) 249–256.
[6] Tanay Joshi, Gagan Uberoi, Graphical scheme for determination of market clearing price using quadratic bid function, Int. J. Adv. Eng. Technol. 1 (2011) 144–150.
[7] Li Ma, Wen Fushuan, A.K. David, A preliminary study on strategic bidding in electricity markets with step-wise bidding protocol, IEEE/PES on Transmission and Distribution Conference and Exhibition, Asia Pacific, vol. 3, Dover, 2002, pp. 1960–1965.
[8] L. Wang, C.W. Yu, F.S. Wen, The impacts of different bidding segment numbers on bidding strategies of generation companies, Electr. Power Syst. Res. 78 (2008) 458–463.
[9] D. Zhang, Y. Wang, P.B. Luh, Optimization based bidding strategies in the deregulated market, IEEE Trans. Power Syst. 15 (2000) 981–986.
[10] J.D. Weber, T.J. Overbye, A two-level optimization problem for analysis of market bidding strategies, in: Proceedings of IEEE Power Engineering Society Summer Meeting, 1999, pp. 682–687.
[11] G. Gross, D.J. Finlay, Optimal bidding strategies in competitive electricity markets, in: Proceedings of 12th Power Systems Computation Conference (PSCC-96), Dresden, 1996, pp. 815–823.
[12] Roy H. Kwon, Daniel Frances, Optimization-based bidding in day-ahead electricity auction markets: a review of models for power producers, Handbook of Networks in Power Systems I, Springer, Berlin Heidelberg, 2012, pp. 41–59.
[13] Azmi Saleh, Takao Tsuji, Tsutomu Oyama, Optimal bidding strategies for generation companies in a day-ahead electricity market with risk management taken into account, Am. J. Eng. Appl. Sci. 2 (2009) 8–16.
[14] S. Prabhakar Karthikeyan, Sathish K. Kumar, Y. Janakinadh, V.V. Raviteja, I. Jacob Raglend, P. Kothari, Determining market clearing price using graphical analysis - impact of loss as a case study, in: International Conference and Utility Exhibition on Power and Energy Systems: Issues & Prospects for Asia (ICUE), 2011, pp. 1–8.
[15] Zuyi Li, Hossein Daneshi, Some observations on market clearing price and locational marginal price, IEEE Power Engineering Society General Meeting, vol. 2, 2005, pp. 2042–2049.
[16] Alvaro Baillo, Mariano Ventosa, M. Rivier, A. Ramos, Strategic bidding in a competitive electricity market: a decomposition approach, IEEE Power Tech Proc. 1 (2001) 8–13.
[17] Xiaoyan Zou, Double-sided auction mechanism design in electricity based on maximizing social welfare, Energy Policy 37 (2009) 4231–4239.
[18] Zhiqiang Yuan, Dong Liu, Chuanwen Jiang, Analysis of equilibrium about bidding strategy of suppliers with future contracts, Energy Convers. Manage. 48 (2007) 1016–1020.
[19] Karim Afshar, Saeedeh Ahmadi, Nooshin Bigdeli, Bidding strategy based on improved particle swarm optimization algorithm for a generation company, International Conference on Power and Energy Systems, vol. 13, 2012, pp. 157–162.

[20] C.W. Richter, G.B. Sheble, Genetic algorithm evolution of utility bidding strategies for the competitive market place, IEEE Trans. Power Syst. 15 (1998) 256–261.

[21] C.W. Richter, G.B. Sheble, D. Ash lock, Comprehensive bidding strategies with genetic programming/finite state automata, IEEE Trans. Power Syst. 14 (1999) 1207–1212.

[22] Guangquan Zhang, Guoli Zhang, Ya Gao, Jie Lu, Competitive strategic bidding optimization in electricity markets using bilevel programming and swarm technique, IEEE Trans. Power Syst. 58 (6) (2011).

[23] S. Soleymani, Bidding strategy of generation companies using PSO combined with SA method in the pay as bid markets, Electr. Power Energy Syst. 33 (2011) 1272–1278.

[24] S. Anbazhagan, N. Kumarappan, Day-ahead deregulated electricity market price classification using neural network input featured by DCT, Electr. Power Energy Syst. 37 (2012) 103–109.

[25] Hossein Haghighat, Hossein Seifi, Ashkan RahimiKian, Pay-as-bid versus marginal pricing: the role of suppliers strategic behaviour, Electr. Power Energy Syst. 42 (2012) 350–358.

[26] Sumit Saroha, Amit Rathee, Rohit Verma, JAVA based power trading simulator in electricity market, Int. J. Comput. Appl. 44 (2012) 8–13.

[27] Gregory Steeger, Luiz Augusto Barroso, Steffen Rebennack, Optimal bidding strategies for hydro-electric producers: a literature survey, IEEE Trans. Power Syst. 29 (4) (2014) 1758–1766.

[28] Arvind Kumar Jain, Suresh Chandra Srivastava, Sri Niwas Singh, Laxmi Srivastava, Bacteria foraging optimization based bidding strategy under transmission congestion, IEEE Syst. J. 9 (1) (2015) 141–151.

[29] G. Gross, D. Finlay, Optimal bidding strategies in competitive electricity markets, in: Proceedings of the 12th PSCC Conference, Germany, 1996.

[30] X. Guan, Y.C. Ho, F. Lai, An ordinal optimization based bidding strategy for electric power suppliers in the daily energy market, IEEE Trans. Power Syst. 16 (4) (2001) 788–797.

[31] S.D. Torre, A.J. Conejo, J. Contreras, Finding multi-period Nash equilibrium in pool-based electricity markets, IEEE Trans. Power Syst. 19 (1) (2004) 643–651.

[32] M. Lai, T. Tong, H. Yang, P. Bing, Dynamic bidding analysis in power market based on the supply function, Comput. Math. Appl. 58 (1) (2009) 25–38.

[33] P. Bajpai, S.K. Punna, S.N. Singh, Swarm intelligence-based strategic bidding in competitive electricity markets, IET Gener. Transm. Distrib. 2 (2) (2008) 175–184.

[34] A. Azadeh, S.F. Ghaderi, B. Pourvalikhan Nokhandan, M. Sheikhalishahi, A new genetic algorithm approach for optimizing bidding strategy viewpoint of profit maximization of a generation company, Expert Syst. Appl. 39 (2012) 1565–1574.

[35] S.B. Russ, A translation of Bolzano's paper on the intermediate value theorem, Hist. Math. 7 (2) (1980) 156–185.

[36] R. Gnanadass, Narayana Prasad Padhy, K. Manivannan, Assessment of available transfer capability for practical power systems with combined economic emission dispatch, Electr. Power Syst. Res. 69 (2004) 267–276.

On new computational and numerical solutions of the modified Zakharov–Kuznetsov equation arising in electrical engineering

Subhasish Mohanty, *Department of Electrical Engineering, Aryan Institute of Engineering & Technology, Bhubaneswar, subhasish.mohanty@hotmail.com*

Swadesh Ranjan Jena, *Department of Electrical and Electronics Engineering, Raajdhani Engineering College, Bhubaneswar, swadesh.jena@yahoo.co.in*

Malaya Tripathy, *Department of Electronics and Communication Engineering , Capital Engineering College, Bhubaneswar, malaya.tripathy43@gmail.com*

Smruti Ranjan Nayak, *Department of electrical Engineering , NM Institute of Engineering & Technology, Bhubaneswar, smrutinayak@live.com*

Sachikanta Pati, *Department of Computer Scinece Engineering , NM Institute of Engineering & Technology, Bhubaneswar, sachikantapati98@outlook.com*

KEYWORDS

Discrete electrical lattice;
Modified Zakharov–Kuznetsov equation;
Modified Khater method;
B–spline scheme;

AMS CLASSIFICATION

35E05;
35C08;
35Q51;
37L50;
37J25;
33F05

Abstract In this research, analytical and numerical solutions are studied of a two–dimensional discrete electrical lattice, which is mathematically represented by the modified Zakharov–Kuznetsov equation. Moreover, the stability property of the obtained analytical solutions is investigated based on the Hamiltonian system, and then it is used to evaluate the initial and boundary conditions that are used in the numerical investigation. Many kinds of analytical solutions are obtained, such as complex, exponential, hyperbolic, and trigonometric function solutions. The functioning of both schemes of both techniques is tested and investigated.

1. Introduction

Partial differential equations have considered as a fundamental in many applications. This kind of equations has used to formulate many of natural, engineering, mechanical, and physical phenomena. That happens because it contains beforehand unknown multi-variable functions and its derivatives. During the last decade, many phenomena have been formulated in partial differential equations. Studying and investigation the solitary wave of these models are considered as one of the basic interesting of many researchers. Solitary wave is that kind of waves which propagates without any chronological evolution in shape or size. These properties and abilities of the nonlinear partial differential equations are used to describe the natural phenomena. According to these properties, many mathematicians developed some methods and still trying to find new general methods to get exact and solitary traveling wave solutions of these models. For more details about these methods, you see [25–27,2,3,41,21,31,42,19,17,18,46,39,32,7,6,28,29,36–38,16,50].

In this paper, a discrete nonlinear transmission line equation [14,20,30,48,40] is investigated by the modified Khater (mK) method [45,5,34,23,24,1], the Hamiltonian system [9,8,33,11,43], and B–spline scheme [12,51,22,10,4]. This equation is also known by the modified Zakharov–Kuznetsov (mZK) equation that helps in understanding the mechanism of various phenomena [52,15,35,13,44]. For example; the electrical transmission lines which is considered as a good example of systems for the investigation of the nonlinear excitations behave inside nonlinear media as shown in Fig. 1.

The nonlinear electrical transmission line is constructed based on periodically loading with var–actors or, alternatively, by arranging inductors and var–actors in a one–dimensional lattice. The nonlinear network with some couple nonlinear LC with dispersive transmission line is consisted in this model. There are many identical dispersive lines which are coupled by means of capacitance C_s at each node, as represented in Fig. 1 where a conductor L and a nonlinear capacitor of capacitance $C(v_{n,m})$ are consist in each line in the shunt branch. The mathematical model which describes the discrete nonlinear transmission is given by mZK equation that is formulated by Duan when he applied the Kirchhoff law on the model, is given by

$$\frac{\partial^2 \mathcal{Q}_{n,m}}{\partial \mathcal{T}} = \frac{1}{\mathcal{L}}(\mathcal{V}_{n+1,m} - 2\mathcal{V}_{n,m} + \mathcal{V}_{n-1,m}) + \mathcal{C}_s \frac{\partial^2}{\partial \mathcal{T}^2}(\mathcal{V}_{n,m+1} - 2\mathcal{V}_{n,m} + \mathcal{V}_{n,m-1}), \tag{1}$$

where $\mathcal{V}_{n,m} = \mathcal{V}_{n,m}(\mathcal{T})$ is the voltage so that the nonlinear charge is derived in the following form

$$\mathcal{Q}_{n,m} = \mathcal{C}_0\left(\mathcal{V}_{n,m} + \frac{\beta_1}{2}\mathcal{V}_{n,m}^2 + \frac{\beta_2}{3}\mathcal{V}_{n,m}^3\right), \tag{2}$$

where β_1, β_2 are arbitrary constants. Substituting Eq. (2) into Eq. (1), yields

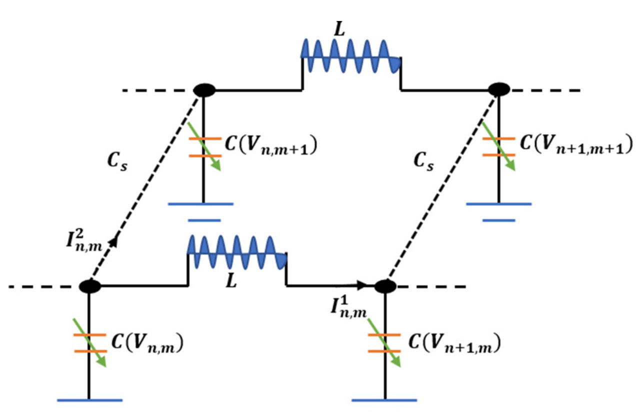

Fig. 1 Linear representation of the nonlinear electrical transmission line.

$$\mathcal{C}_0 \frac{\partial^2}{\partial \mathcal{T}}\left(\mathcal{V}_{n,m} + \frac{\beta_1}{2}\mathcal{V}_{n,m}^2 + \frac{\beta_2}{3}\mathcal{V}_{n,m}^3\right) = \frac{1}{\mathcal{L}}(\mathcal{V}_{n+1,m} - 2\mathcal{V}_{n,m} + \mathcal{V}_{n-1,m}) + \mathcal{C}_s \frac{\partial^2}{\partial \mathcal{T}^2}(\mathcal{V}_{n,m+1} - 2\mathcal{V}_{n,m} + \mathcal{V}_{n,m-1}). \tag{3}$$

Replacing $\mathcal{V}_{n,m}(T) = \mathcal{V}(n, m, \mathcal{T})$, leads to

$$\mathcal{C}_0 \frac{\partial^2}{\partial \mathcal{T}^2}\left(\mathcal{V} + \frac{\beta_1}{2}\mathcal{V}^2 + \frac{\beta_2}{3}\mathcal{V}^3\right) = \frac{1}{\mathcal{L}}\frac{\partial^2}{\partial n^2}\left(\mathcal{V} + \frac{1}{12}\frac{\partial^2 \mathcal{V}}{\partial n^2}\right) + \mathcal{C}_s \frac{\partial^4}{\partial \mathcal{T}^2 \partial m^2}\left(\mathcal{V} + \frac{1}{12}\frac{\partial^2 \mathcal{V}}{\partial m^2}\right). \tag{4}$$

Based on the reductive perturbation technique Eq. (4), is reduced to the following mZK equation

$$\mathcal{K}_t + l\mathcal{K}\mathcal{K}_x + m\mathcal{K}^2\mathcal{K}_x + d\mathcal{K}_{xxx} + q\mathcal{K}_{xyy} = 0, \tag{5}$$

where $\left[y = \sqrt{\chi}m,\ x = \sqrt{\chi}(n - v_s\mathcal{T}),\ t = \sqrt{\chi}\mathcal{T},\ \mathcal{V}(n, m, \mathcal{T}) = \chi\mathcal{K}(x, y, t),\ v_s^2 = \frac{1}{\mathcal{L}\mathcal{C}_0},\ l = -\beta_1 v_s,\ m = -\beta_2 v_s,\ d = \frac{1}{24\beta\beta_1 \mathcal{L} v_s},\ q = \frac{\beta_1}{288\mathcal{L}^2 v_s \mathcal{C}_0^2}\right]$ since x, y, t are independent transformation variables. Applying the following wave transformation $\mathcal{K} = \mathcal{K}(x, y, t) = \mathcal{K}(\hbar),\ \hbar = h_1 x + h_2 y + h_3 t$ and integrate the obtained ODE once with zero constant of integration, give

$$6h_3\mathcal{K} + 3lh_1\mathcal{K}^2 + 2mh_1\mathcal{K}^3 + 6h_1\left(dh_1^2 + qh_2^2\right)\mathcal{K}'' = 0. \tag{6}$$

Balancing the highest order derivative term and nonlinear terms, yields $n = 1$.

The remaining of this paper is organized as follows: In Section 2, the mK method is used to obtain computational solutions of the mZK equation then the stability property of these solutions is tested. Moreover, the stable solution is used to find the initial and boundary conditions that allow applying the B–spline schemes to the same model to investigate the accuracy of obtained solutions. In Section 3, the comparison between our obtained solutions and that obtained in different research papers is represented. In Section 4, the conclusion is given.

2. Application

Here we apply the mK method to the mZK equation to establish the explicit wave solutions of both of models then test the stability property of these solutions. Moreover, we use these solutions in the investigation of numerical solution of the same models.

2.1. Explicit solutions of the mZK equation

According to the homogeneous balance value and the suggested general solution in the modified Khater method, the general solutions of Eq. (6) is in the following formula:

$$\mathcal{K}(\hbar) = \sum_{i=1}^{N} a_i \mathcal{M}^{i\Psi(\hbar)} + \sum_{i=1}^{N} b_i \mathcal{M}^{-i\Psi(\hbar)} + a_0 = a_1\mathcal{M}^{\Psi(\hbar)} + a_0 + b_1\mathcal{M}^{-\Psi(\hbar)}, \tag{7}$$

where $a_0, a_1, b_1, \mathcal{M}$ are arbitrary constants. Additionally $\Psi(\hbar)$ is the solution function of the next auxiliary equation

$$f'(\hbar)=\frac{1}{ln(\mathcal{M})}\left(\chi+\vartheta\mathcal{M}^{-\Psi(\hbar)}+\rho\mathcal{M}^{\Psi(\hbar)}\right), \tag{8}$$

where ϑ, χ, ρ are arbitrary constants to be determine later. Replacing Eq. (7) along (8) into Eq. (6) and gathering all terms with the same power of $\left[\mathcal{M}^{i\Psi(\hbar)}, i=-3,-2,\ldots,2,3\right]$, lead to system of algebraic equations. Solving this system, yields

Family I

$$\left[a_0\to-\frac{l}{m}, a_1\to-\frac{l\rho}{m\chi}, b_1\to-\frac{l\vartheta}{m\chi}, h_2\to -\frac{\sqrt{-6dh_1^2m\chi^2-l^2}}{\sqrt{6}\sqrt{m}\sqrt{q}\chi}, h_3\to\frac{h_1l^2\chi^2-4h_1l^2\rho\vartheta}{6m\chi^2}\right.$$

where $\left(l\neq0,\ \rho\neq0,\ \vartheta\neq0,\ q>0, m>0, 6dh_1^2m\chi^2<l^2\right)]$

Thus, the explicit wave solutions of Eq. (5) are given by When $[\chi^2-4\rho\vartheta<0\,\&\,\rho\neq0]$

$$\mathcal{K}_1(x,y,t)=-\frac{l(\chi^2-4\rho\vartheta)\sec^2\left(\frac{\sqrt{4\rho\vartheta-\chi^2}\left(h_1\left(l^2t\left(\chi^2-4\rho\vartheta\right)+6m\chi^2x\right)-\frac{\sqrt{6}\sqrt{m}\chi y\sqrt{-6dh_1^2m\chi^2-l^2}}{\sqrt{q}}\right)}{12m\chi^2}\right)}{2m\chi\left(\chi-\sqrt{4\rho\vartheta-\chi^2}\tan\left(\frac{\sqrt{4\rho\vartheta-\chi^2}\left(h_1\left(l^2t(\chi^2-4\rho\vartheta)+6m\chi^2x\right)-\frac{\sqrt{6}\sqrt{m}\chi y\sqrt{-6dh_1^2m\chi^2-l^2}}{\sqrt{q}}\right)}{12m\chi^2}\right)\right)}, \tag{9}$$

$$\mathcal{K}_2(x,y,t)=-\frac{l(\chi^2-4\rho\vartheta)\csc^2\left(\frac{\sqrt{4\rho\vartheta-\chi^2}\left(h_1\left(l^2t\left(\chi^2-4\rho\vartheta\right)+6m\chi^2x\right)-\frac{\sqrt{6}\sqrt{m}\chi y\sqrt{-6dh_1^2m\chi^2-l^2}}{\sqrt{q}}\right)}{12m\chi^2}\right)}{2m\chi\left(\chi-\sqrt{4\rho\vartheta-\chi^2}\cot\left(\frac{\sqrt{4\rho\vartheta-\chi^2}\left(h_1\left(l^2t(\chi^2-4\rho\vartheta)+6m\chi^2x\right)-\frac{\sqrt{6}\sqrt{m}\chi y\sqrt{-6dh_1^2m\chi^2-l^2}}{\sqrt{q}}\right)}{12m\chi^2}\right)\right)}. \tag{10}$$

When $[\chi^2-4\rho\vartheta>0\,\&\,\rho\neq0]$

$$\mathcal{K}_3(x,y,t)=-\frac{l(\chi^2-4\rho\vartheta)\operatorname{sech}^2\left(\frac{\sqrt{\chi^2-4\rho\vartheta}\left(h_1\left(l^2t\left(\chi^2-4\rho\vartheta\right)+6m\chi^2x\right)-\frac{\sqrt{6}\sqrt{m}\chi y\sqrt{-6dh_1^2m\chi^2-l^2}}{\sqrt{q}}\right)}{12m\chi^2}\right)}{2m\chi\left(\sqrt{\chi^2-4\rho\vartheta}\tanh\left(\frac{\sqrt{\chi^2-4\rho\vartheta}\left(h_1\left(l^2t(\chi^2-4\rho\vartheta)+6m\chi^2x\right)-\frac{\sqrt{6}\sqrt{m}\chi y\sqrt{-6dh_1^2m\chi^2-l^2}}{\sqrt{q}}\right)}{12m\chi^2}\right)+\chi\right)}, \tag{11}$$

$$\mathcal{K}_4(x,y,t)=\frac{l(\chi^2-4\rho\vartheta)\operatorname{csch}^2\left(\frac{\sqrt{\chi^2-4\rho\vartheta}\left(h_1\left(l^2t\left(\chi^2-4\rho\vartheta\right)+6m\chi^2x\right)-\frac{\sqrt{6}\sqrt{m}\chi y\sqrt{-6dh_1^2m\chi^2-l^2}}{\sqrt{q}}\right)}{12m\chi^2}\right)}{2m\chi\left(\sqrt{\chi^2-4\rho\vartheta}\coth\left(\frac{\sqrt{\chi^2-4\rho\vartheta}\left(h_1\left(l^2t(\chi^2-4\rho\vartheta)+6m\chi^2x\right)-\frac{\sqrt{6}\sqrt{m}\chi y\sqrt{-6dh_1^2m\chi^2-l^2}}{\sqrt{q}}\right)}{12m\chi^2}\right)+\chi\right)}. \tag{12}$$

When $\left[\chi=\frac{\vartheta}{2}=\kappa\,\&\,\rho=0\right]$

$$\mathcal{K}_5(x,y,t)=\frac{l}{m}\left(-\frac{2}{\exp\left(h_1\left(\frac{\kappa l^2t}{6m}+\kappa x\right)-\frac{y\sqrt{-6dh_1^2\kappa^2m-l^2}}{\sqrt{6}\sqrt{m}\sqrt{q}}\right)-2}-1\right). \tag{13}$$

When $[\chi=\rho=\kappa\,\&\,\vartheta=0]$

$$\mathcal{K}_6(x,y,t)=\frac{l}{m\left(\exp\left(h_1\left(\frac{\kappa l^2t}{6m}+\kappa x\right)-\frac{y\sqrt{-6dh_1^2\kappa^2m-l^2}}{\sqrt{6}\sqrt{m}\sqrt{q}}\right)-1\right)}. \tag{14}$$

When $[\vartheta=0\,\&\,\chi\neq0\,\&\,\rho\neq0]$

$$\mathcal{K}_7(x,y,t)=-\frac{2l}{m\left(2-\rho\exp\left(h_1\left(\frac{l^2t\chi}{6m}+\chi x\right)-\frac{y\sqrt{-6dh_1^2m\chi^2-l^2}}{\sqrt{6}\sqrt{m}\sqrt{q}}\right)\right)}. \tag{15}$$

When $[\rho=0\,\&\,\chi\neq0\,\&\,\vartheta\neq0]$

$$\mathcal{K}_8(x,y,t)=\frac{l}{m}\left(\frac{\vartheta}{\vartheta-\chi\exp\left(h_1\left(\frac{l^2t\chi}{6m}+\chi x\right)-\frac{y\sqrt{-6dh_1^2m\chi^2-l^2}}{\sqrt{6}\sqrt{m}\sqrt{q}}\right)}-1\right). \tag{16}$$

Family II

$$\left[a_0\to-\frac{\frac{l\chi}{\sqrt{\chi^2-4\rho\vartheta}}+l}{2m}, a_1\to-\frac{l\rho}{m\sqrt{\chi^2-4\rho\vartheta}}, b_1\to0,\right.$$

$$h_2\to\frac{\sqrt{6dh_1^2m(\chi^2-4\rho\vartheta)+l^2}}{\sqrt{6}\sqrt{mq(4\rho\vartheta-\chi^2)}}, h_3\to\frac{h_1l^2}{6m}$$

where $\left(mq<0,\ \chi^2-4\rho\vartheta>0,\ 6dh_1^2m\left(\chi^2-4\rho\vartheta\right)+l^2>0,\right.$ $l\neq0,\ \rho\neq0,\ m\neq0,\ h_1\neq0)]$

Thus, the solitary wave solutions of Eq. (5) are given by When $[\chi^2-4\rho\vartheta>0\,\&\,\rho\neq0]$

$$\mathcal{K}_9(x,y,t)=\frac{l}{2m}\left(\tanh\left(\frac{1}{2}\sqrt{\chi^2-4\rho\vartheta}\left(\frac{y\sqrt{6dh_1^2m(\chi^2-4\rho\vartheta)+l^2}}{\sqrt{6}\sqrt{mq(4\rho\vartheta-\chi^2)}}+h_1\left(\frac{l^2t}{6m}+x\right)\right)\right)\right. \\ \left.+\frac{2\chi}{\sqrt{\chi^2-4\rho\vartheta}}+1\right), \tag{17}$$

$$\mathcal{K}_{10}(x,y,t)=\frac{l}{2m}\left(\coth\left(\frac{1}{2}\sqrt{\chi^2-4\rho\vartheta}\left(\frac{y\sqrt{6dh_1^2m(\chi^2-4\rho\vartheta)+l^2}}{\sqrt{6}\sqrt{mq(4\rho\vartheta-\chi^2)}}+h_1\left(\frac{l^2t}{6m}+x\right)\right)\right)\right. \\ \left.+\frac{2\chi}{\sqrt{\chi^2-4\rho\vartheta}}+1\right). \tag{18}$$

When $[\rho\vartheta<0\,\&\,\vartheta\neq0\,\&\,\rho\neq0\,\&\,\chi=0]$

$$\mathcal{K}_{11}(x,y,t)=\frac{l}{2m}\left(\tanh\left(\sqrt{\rho(-\vartheta)}\left(\frac{y\sqrt{l^2-24dh_1^2m\rho\vartheta}}{2\sqrt{6}\sqrt{mq\rho\vartheta}}+h_1\left(\frac{l^2t}{6m}+x\right)\right)\right)+1\right), \tag{19}$$

$$\mathcal{K}_{12}(x,y,t)=\frac{l}{2m}\left(\coth\left(\sqrt{\rho(-\vartheta)}\left(\frac{y\sqrt{l^2-24dh_1^2m\rho\vartheta}}{2\sqrt{6}\sqrt{mq\rho\vartheta}}+h_1\left(\frac{l^2t}{6m}+x\right)\right)\right)+1\right). \tag{20}$$

When $[\chi=0\&\vartheta=-\rho]$

$$\mathcal{K}_{13}(x,y,t)=\frac{1}{2m}\left(\frac{l\vartheta\coth\left(\frac{1}{6}\vartheta\left(\frac{\sqrt{\frac{3}{2}}y\sqrt{24dh_1^2m\vartheta^2+l^2}}{\sqrt{-mq\vartheta^2}}+h_1\left(\frac{l^2t}{m}+6x\right)\right)\right)}{\sqrt{\vartheta^2}}+l\right). \tag{21}$$

When $[\chi=\rho=\kappa\,\&\,\vartheta=0]$

$$\mathcal{K}_{14}(x,y,t)=\frac{l}{2\sqrt{\kappa^2}m}\left(\kappa\left(\coth\left(\frac{1}{12}\kappa\left(\frac{\sqrt{6}y\sqrt{6dh_1^2\kappa^2m+l^2}}{\sqrt{\kappa^2(-m)q}}+h_1\left(\frac{l^2t}{m}+6x\right)\right)\right)+2\right)+\sqrt{\kappa^2}\right). \tag{22}$$

2.2. Stability property

This section studies the stability property of the obtained solutions by using the properties of the Hamiltonian system. The momentum Υ in the Hamiltonian system is given by

$$\Upsilon = \frac{1}{2}\int_{-\varsigma}^{\varsigma} \mathcal{K}^2(\hbar)\, d\hbar, \tag{23}$$

where $\mathcal{K}(\hbar)$ is the solution of the model and the necessary condition for stability is formulated in the next form

$$\frac{\partial \mathcal{K}}{\partial h_3} > 0, \tag{24}$$

where h_3 is the wave velocity. Thus, the studying of the stability property of the mZK equation by using Eq. (19) when $[d = -1, h_1 = 2, l = 6, m = 3, \rho = 1, q = 4, \chi = 0, y = 0, \vartheta = -4]$:

$$\Upsilon = \frac{\log\left(e^{40-10h_3} + e^{10h_3}\right) - \log\left(e^{-10h_3} + e^{10(h_3+4)}\right)}{8h_3} + 100$$

and thus

$$\frac{\partial \Upsilon}{\partial \epsilon}|_{h_3=4} = 0.312500000 > 0.$$

Consequently, this solution is stable.

2.3. Numerical Simulations

This section studies the numerical solution of the mZK equation according to B–spline schemes and based on the obtained stable analytical solution (19). Applying the B–spline schemes to Eq. (6), allows obtaining the next values of absolute value of error.

Table 1 Absolute value of error by using B–spline schemes.

Value of $\hbar$	Cubic	Quintic	Septic
0	0	0	0
0.1	0.00122084	5.2426×10^{-6}	1.2709×10^{-7}
0.2	0.00201838	9.46474×10^{-6}	1.63978×10^{-7}
0.3	0.00222625	7.63285×10^{-6}	4.31598×10^{-8}
0.4	0.00196322	4.12028×10^{-6}	1.41841×10^{-8}
0.5	0.00147327	1.18457×10^{-6}	2.83815×10^{-8}
0.6	0.000965422	3.25168×10^{-7}	1.5585×10^{-8}
0.7	0.000552262	7.52359×10^{-7}	5.23207×10^{-9}
0.8	0.000264813	6.26445×10^{-7}	7.07674×10^{-10}
0.9	8.99409E−05	2.62173×10^{-7}	1.122×10^{-9}
1	0	2.22045×10^{-16}	2.22045×10^{-16}

3. Results and discussion

This section studies the novelty of our presented paper by making a comparison between our solutions and that obtained in previous research paper:

1. The analytical solutions:
   - In [49], E. Tala-Tebue, Z.I. Djoufacka, S.B. Yamgouéb, A. Kenfack–Jiotsac, T.C. Kofanéd applied the Jacobi elliptical function method to the mZK equation and by analysis our solutions and those solutions, we find Eq. (19) and Eq. (23) in [49] are equal when $\left[B = mA, \sqrt{-\rho\vartheta} = 1\right]$ and all our other solutions are different from that obtained in this paper.
   - In [47], A. Sardar, S. M. Husnine, S. T. R. Rizvi, M. Younis, and K. Ali used the $\left(\frac{G\prime}{G}\right)$–expansion method, Tanh method, and Sine–cosine method. Investigating their and our solution, we find Eq. (19) is equal to (18) when $\left[-2\rho\vartheta = \lambda^2 - 4\mu,\ A = \frac{-1}{3\lambda m} - \lambda, B = 24m^2 (r_1^2 M + r_2^2 N)\ (\lambda^2 - 4\mu)\right]$ and Eq. (19) is equal to Eq. (36) when $\left[B = \frac{6a_0}{12c_1 + r_1(1+3m)}, \rho\vartheta = -1\right]$.

2. Numerical solutions:
   - according to the shown Table 1 and Fig. 5, the septic B–spline scheme obtain the most accurate value of numerical solutions of the mZK equation.

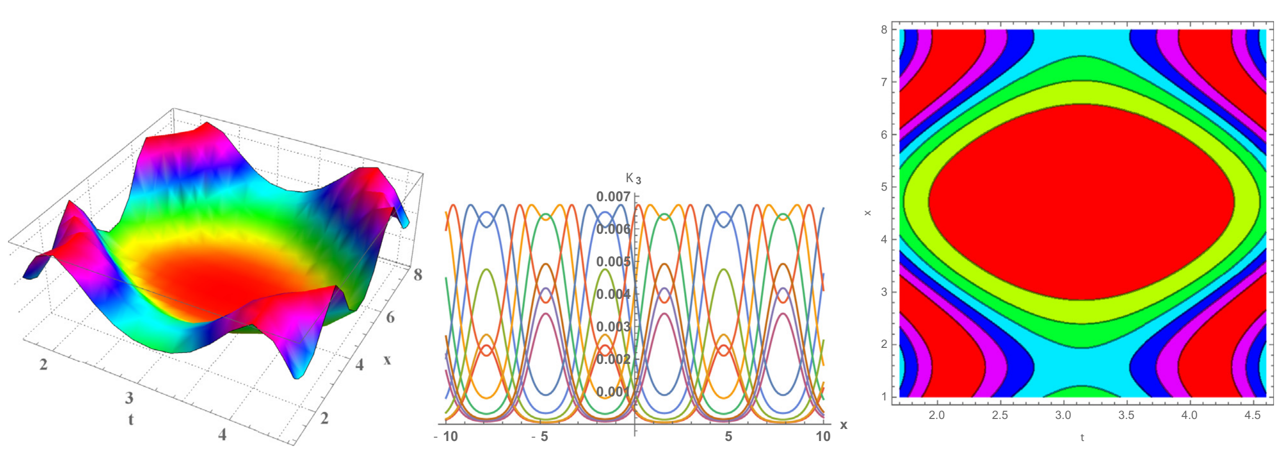

Fig. 2 Solitary wave of (11) in three, two-dimensional, and contour plots when $[h_1 = 2, l = -1, m = 3, \rho = 6, X = 5, y = 0, \vartheta = 1]$.

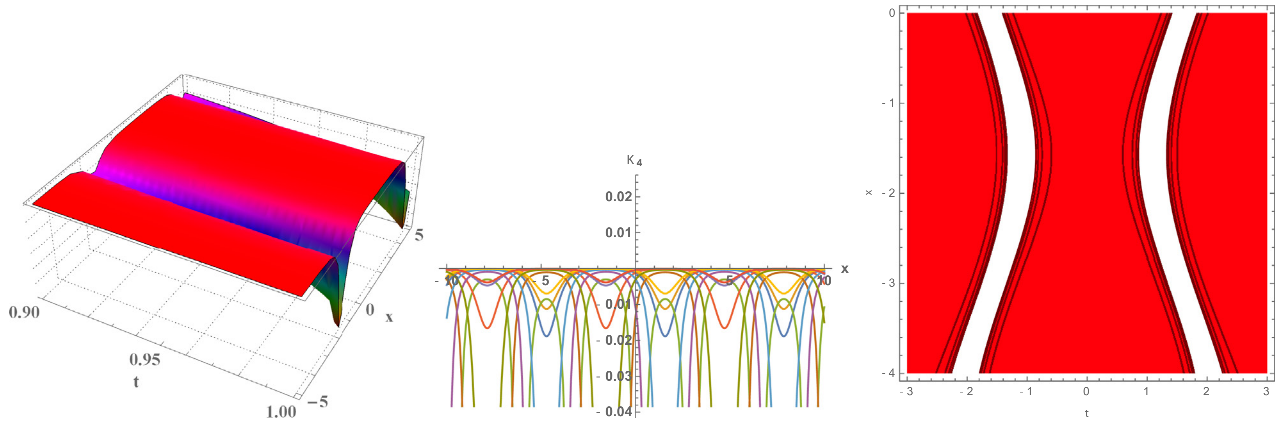

Fig. 3 Solitary wave of (12) in three, two-dimensional, and contour plots when $[h_1 = 2, l = -1, m = 3, \rho = 6, X = 5, y = 0, \vartheta = 1]$.

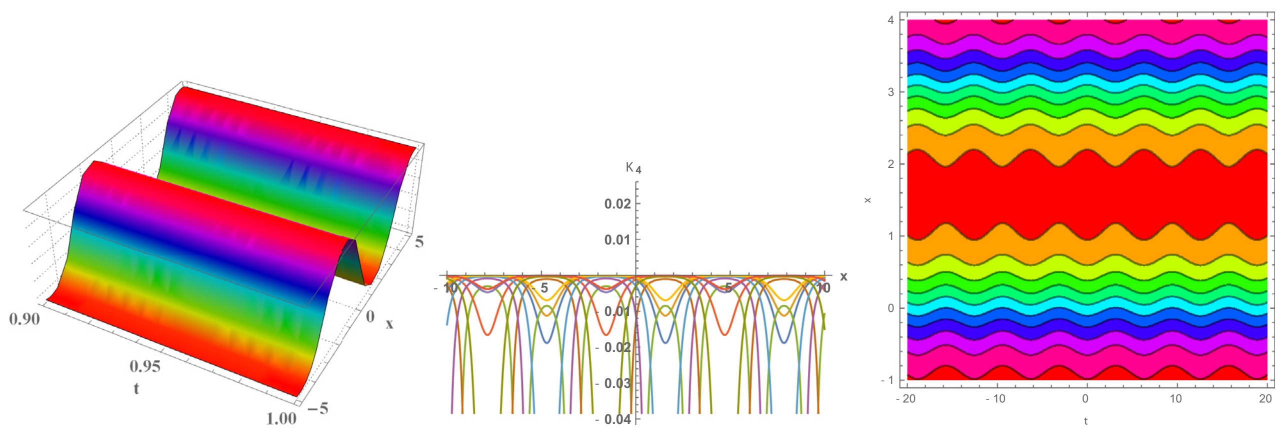

Fig. 4 Periodic solitary wave of (17) in three, two-dimensional, and contour plots when $[h_1 = 2, l = -1, m = 3, \rho = 6, X = 5, y = 0, \vartheta = 1]$.

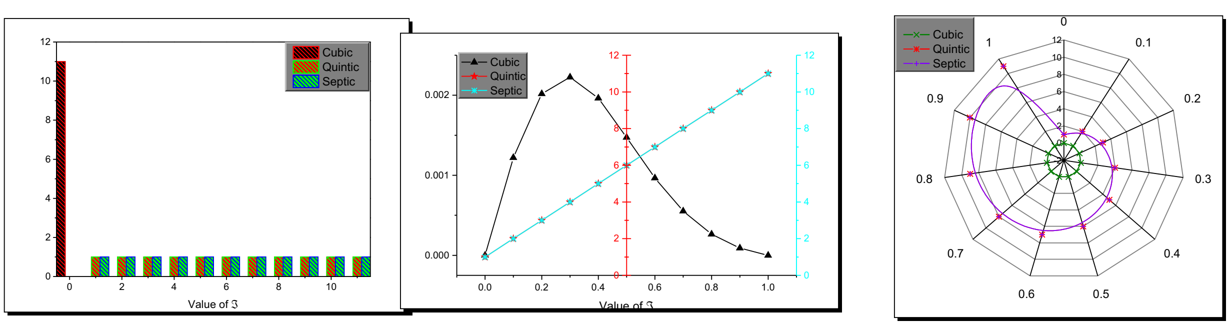

Fig. 5 Absolute value of error between exact and numerical solutions that obtained respectively by B–spline schemes (cubic & quintic & septic) to explain that the B–spline septic scheme is the most accurate method for this model (6).

4. Conclusion

This paper succeeded in the implementation of the mK method on the mZK equation to show more physical properties of the transportation of the energy in nonlinear electrical transmission lines. Moreover, the stability property of the obtained solutions was discussed and explained by using the momentum Υ in the Hamiltonian system. Some sketches were plotted to illustrate the more physical properties of these models (Figs. 2–4). The performance of the used method shows the effective and power of this method and its ability to apply other nonlinear evolutions equations.

Declarations of Competing Interest

None.

References

[1] Lump soliton wave solutions for the (2+ 1)-dimensional Konopelchenko-Dubrovsky equation and V equation, author = Khater, Mostafa M.A., Lu, Dianchen and Attia, Raghda AM, journal = Modern Physics Letters B, pages = 1950199, year = 2019, publisher = World Scientific.

[2] Mahmoud A.E. Abdelrahman, Mostafa M.A. Khater, Exact traveling wave solutions for Fitzhugh-Nagumo (FN) equation and modified Liouville Equation, Int. J. Comput. Appl. 113 (2015) 1–7.

[3] Mahmoud A.E. Abdelrahman, Mostafa M.A. Khater, Traveling wave solutions for the couple Boiti–Leon–Pempinelli system by using extended Jacobian elliptic function expansion method, J.: J. Adv. Phys. 11 (3) (2015).

[4] S.H. Alfalqi, J.F. Alzaidi, Dianchen Lu, Mostafa Khater, On exact and approximate solutions of (2+ 1)-dimensional Konopelchenko-Dubrovsky equation via modified simplest equation and cubic B-spline schemes, Therm. Sci. (2019) 349.

[5] Ahmad T. Ali, Mostafa M.A. Khater, Raghda A.M. Attia, Abdel-Haleem Abdel-Aty, Dianchen Lu. Abundant numerical and analytical solutions of the generalized formula of Hirota-Satsuma coupled KdV system. Chaos, Solitons Fract. 2019, p. 109473.

[6] Aliyu Isa Aliyu, Mustafa Inc, Abdullahi Yusuf, Dumitru Baleanu, A fractional model of vertical transmission and cure of vector-borne diseases pertaining to the Atangana-Baleanu fractional derivatives, Chaos, Solitons Fract. 116 (2018) 268–277.

[7] Ebru Cavlak Aslan, Mustafa Inc, Optical soliton solutions of the NLSE with quadratic–cubic–Hamiltonian perturbations and modulation instability analysis, Optik 196 (2019) 162661.

[8] Bjorn Augner, Well-posedness and stability of infinite-dimensional linear port-Hamiltonian systems with nonlinear boundary feedback, SIAM J. Control Optim. 57 (3) (2019) 1818–1844.

[9] Boris S. Bardin, Evgeniya A. Chekina, On the constructive algorithm for stability analysis of an equilibrium point of a periodic hamiltonian system with two degrees of freedom in the case of combinational resonance, Regul. Chaotic Dynam. 24 (2) (2019) 127–144.

[10] ALİ BAŞHAN, Seydi Battal Gazi Karakoc, Turabi Geyikli, Approximation of the KdVB equation by the quintic B-spline differential quadrature method, Kuwait J. Sci., 42(2) (2019).

[11] Alexander Batkhin. Some properties of doubly symmetric periodic solutions to Hamiltonian system, in: International Conference Polynomial Computer Algebra, 2019, pp. 15–20.

[12] QingZhen Bi, Jie Huang, Lu. YaoAn, LiMin Zhu, Han Ding, A general, fast and robust B-spline fitting scheme for micro-line tool path under chord error constraint, Sci. China Technol. Sci. 62 (2) (2019) 321–332.

[13] Amiya Das, Explicit weierstrass traveling wave solutions and bifurcation analysis for dissipative Zakharov-Kuznetsov modified equal width equation, Comput. Appl. Math. 37 (3) (2018) 3208–3225.

[14] Guy Roger Deffo, Serge Bruno Yamgoue, Francois Beceau Pelap, Modulational instability and peak solitary wave in a discrete nonlinear electrical transmission line described by the modified extended nonlinear Schrödinger equation, Eur. Phys. J. B 91 (10) (2018) 242.

[15] Zhongzhou Dong, Ling Wang, Solitary wave solutions and rational solutions for modified Zakharov-Kuznetsov equation with initial value problem, Scient. Res. Publish. 6 (2018) 949–959.

[16] Du. Xue-Dong, Chong-Chen Wang, Jian-Guo Liu, Xu-Dong Zhao, Jun Zhong, Yu-Xuan Li, Jin Li, Peng Wang, Extensive and selective adsorption of ZIF-67 towards organic dyes: performance and mechanism, J. Colloid Interface Sci. 506 (2017) 437–441.

[17] S.O. Edeki, I. Adinya, G.O. Akinlabi, O.P. Ogundile, Conformable decomposition for analytical solutions of a time-fractional one-factor markovian model for bond pricing, Appl. Math. 13 (4) (2019) 539–544.

[18] Feng Gao, Xiao-Jun Yang, Ju. Yang, Exact traveling-wave solutions for one-dimensional modified Korteweg–De Vries equation defined on cantor sets, Fractals 27 (01) (2019) 1940010.

[19] Laura R González-Ramírez, Mark A Kramer, The effect of inhibition on the existence of traveling wave solutions for a neural field model of human seizure termination, J. Comput. Neurosci. 44 (3) (2018) 393–409.

[20] Tiague Takongmo Guy, Jean Roger Bogning, Construction of Breather soliton solutions of a modeled equation in a discrete nonlinear electrical line and the survey of modulationnal instability, J. Phys. Commun. 2 (11) (2018) 115007.

[21] G.M. Ismail, H.R. Abdl-Rahim, A. Abdel-Aty, R. Kharabsheh, W. Alharbi, M. Abdel-Aty, An analytical solution for fractional oscillator in a resisting medium, Chaos, Solitons Fract. 130 (2020) 109395.

[22] C. Kadapa, W.G. Dettmer, D. Perić, A stabilised immersed framework on hierarchical b-spline grids for fluid-flexible structure interaction with solid–solid contact, Comput. Methods Appl. Mech. Eng. 335 (2018) 472–489.

[23] Mostafa Khater, Raghda A.M. Attia, Lu Dianchen, Explicit lump solitary wave of certain interesting (3+ 1)-dimensional waves in physics via some recent traveling wave methods, Entropy 21 (4) (2019) 397.

[24] Mostafa M.A. Khater, Dianchen Lu, Raghda A.M. Attia, Dispersive long wave of nonlinear fractional Wu-Zhang system via a modified auxiliary equation method, AIP Adv. 9 (2) (2019) 025003.

[25] Mostafa M.A. Khater, Aly R. Seadawy, Lu Dianchen, Dispersive solitary wave solutions of new coupled Konno-Oono, Higgs field and Maccari equations and their applications, J. King Saud Univ.-Sci. 30 (3) (2018) 417–423.

[26] Mostafa M.A. Khater, Aly R. Seadawy, Dianchen Lu, New optical soliton solutions for nonlinear complex fractional Schrödinger equation via new auxiliary equation method and novel (G′/G)-expansion method, Pramana, 90(5) (2018) 59.

[27] Mostafa MA Khater, Aly R Seadawy, Lu. Dianchen, Optical soliton and bright–dark solitary wave solutions of nonlinear complex Kundu-Eckhaus dynamical equation of the ultra–short femtosecond pulses in an optical fiber, Opt. Quant. Electron. 50 (3) (2018) 155.

[28] Zeliha Korpinar, Mustafa Inc, Numerical simulations for fractional variation of (1+ 1)-dimensional Biswas-Milovic equation, Optik 166 (2018) 77–85.

[29] Zeliha Korpinar, Mustafa Inc, Mustafa Bayram, Theory and application for the system of fractional burger equations with mittag leffler kernel, Appl. Math. Comput. 367 (124781) (2020).

[30] Md. Lukasz Krzczanowicz, Asif Iqbal, Ian Phillips, Mingming Tan, Pavel Skvortcov, Paul Harper, Wladek Forysiak, Low transmission penalty dual-stage broadband discrete raman amplifier, Opt. Exp. 26 (6) (2018) 7091–7097.

[31] D. Kumar, J. Singh, A. Prakash, R. Swroop, Numerical simulation for system of time–fractional linear and nonlinear differential equations, Progr. Fract. Differ. Appl. 5 (1) (2019) 65–77.

[32] Sachin Kumar, Qin Zhou, Wenjun Liu, Invariant traveling wave solutions of parity–time–symmetric mixed linear–nonlinear

optical lattices with three types of nonlinearity, Laser Phys. 29 (4) (2019) 045401.

[33] Chenhao Li, Yusheng Xue, Effects of cascading failure intervals on synchronous stability, Int. J. Electr. Power Energy Syst. 106 (2019) 502–510.

[34] Jing Li, Yuyang Qiu, Dianchen Lu, Raghda AM Attia, Mostafa Khater, Study on the solitary wave solutions of the ionic currents on microtubules equation by using the modified Khater method, Therm. Sci., (00) (2019) 370–370.

[35] Felipe Linares, Gustavo Ponce, On special regularity properties of solutions of the Zakharov-Kuznetsov equation, Commun. Pure Appl. Anal. 17 (4) (2018) 1561–1572.

[36] Jian-Guo Liu, Jian-Qiang Du, Zhi-Fang Zeng, Guo-Ping Ai, Exact periodic cross–kink wave solutions for the new (2+ 1)-dimensional KdV equation in fluid flows and plasma physics, Chaos: An Interdiscip. J. Nonlinear Sci. 26 (10) (2016) 103114.

[37] Jian-Guo Liu, Du. Jian-Qiang, Zhi-Fang Zeng, Bin Nie, New three-wave solutions for the (3+ 1)-dimensional Boiti–Leon–Manna–Pempinelli equation, Nonlinear Dyn. 88 (1) (2017) 655–661.

[38] Jian-Guo Liu, Yan He, Abundant lump and lump–kink solutions for the new (3+ 1)-dimensional generalized Kadomtsev-Petviashvili equation, Nonlinear Dyn. 92 (3) (2018) 1103–1108.

[39] Jian-Guo Liu, Yu Tian, Jian-Guo Hu, New non–traveling wave solutions for the (3+ 1)-dimensional Boiti–Leon–Manna–Pempinelli equation, Appl. Math. Lett. 79 (2018) 162–168.

[40] A.B. Togueu Motcheyo, C. Tchawoua, J.D. Tchinang Tchameu, Supratransmission induced by waves collisions in a discrete electrical lattice, Phys. Rev. E 88 (4) (2013) 040901.

[41] Saud Owyed, M.A. Abdou, Abdel-Haleem Abdel-Aty, S. Saha Ray, New optical soliton solutions of nolinear evolution equation describing nonlinear dispersion, Commun. Theor. Phys. 71 (9) (2019) 1063.

[42] Okkes Ozturk, Resat Yilmazer, On applications of the fractional calculus for some singular differential equations, Progr. Fract. Differ. Appl 4 (2018) 27–33.

[43] Orlando Ragnisco, Massimo Scalia, Stability for generalized volterra's model in the Hamiltonian formalism. Preprint on Researchgate, 2018, pages 22–11.

[44] Nauman Raza, Muhammad Abdullah, Asma Rashid Butt, Isma Ghulam Murtaza, Sultan Sial, New exact periodic elliptic wave solutions for extended quantum Zakharov-Kuznetsov equation, Opt. Quant. Electron., 50(4) (2018) 177.

[45] Hadi Rezazadeh, Alper Korkmaz, Mostafa M.A. Khater, Mostafa Eslami, Dianchen Lu, Raghda A.M. Attia, New exact traveling wave solutions of biological population model via the extended rational sinh-cosh method and the modified khater method, Modern Phys. Lett. B, 33(28) (2019) 1950338,.

[46] Hadi Rezazadeh, Jalil Manafian, Farid Samsami Khodadad, Fakhroddin Nazari, Traveling wave solutions for density-dependent conformable fractional diffusion–reaction equation by the first integral method and the improved Tanh-expansion method, Opt. Quant. Electron., 50(3) (2018) 121.

[47] Ali Sardar, S.M. Husnine, Syed Tahir Raza Rizvi, M. Younis, K. Ali, Multiple travelling wave solutions for electrical transmission line model, Nonlinear Dyn. 82 (3) (2015) 1317–1324.

[48] S. Shige, K. Miyasaka, W. Shi, Y. Soga, M. Sato, A.J. Sievers, Experimentally observed evolution between dynamic patterns and intrinsic localized modes in a driven nonlinear electrical cyclic lattice, EPL (Europhys. Lett.) 121 (3) (2018) 30003.

[49] E. Tala-Tebue, Z.I. Djoufack, S.B. Yamgoué, A. Kenfack-Jiotsa, T.C. Kofané, New soliton solutions for a discrete electrical lattice using the Jacobi elliptical function method, Chin. J. Phys. 56 (3) (2018) 1010–1020.

[50] Yu-Hang Yin, Wen-Xiu Ma, Jian-Guo Liu, Xing Lü, Diversity of exact solutions to a (3+ 1)-dimensional nonlinear evolution equation and its reduction, Comput. Math. Appl. 76 (6) (2018) 1275–1283.

[51] Baoxing Zhang, Hongchan Zheng, Lulu Pan, A generalized cubic exponential b-spline scheme with shape control, Math. Probl. Eng. 2019 (2019).

[52] Xuan Zhou, Wenrui Shan, Zhilei Niu, Pengcheng Xiao, Ying Wang, Lie symmetry analysis and some exact solutions for modified Zakharov-Kuznetsov equation, Mod. Phys. Lett. B 32 (31) (2018) 1850383.

Proposal of Block Bidding for Large-Scale Wind Power Energy

Shashi Bhusan Mohanty, *Department of electrical Engineering , Raajdhani Engineering College, Bhubaneswar, s.b.mohanty@gmail.com*

Rudra Prasad Nanda, *Department of Electrical and Communication Engineering, Aryan Institute of Engineering & Technology, Bhubaneswar, rudraprasad858@gmail.com*

Chinmaya Ranjan Pradhan, *Department of Electrical and Electronics Engineering, NM Institute of Engineering & Technology, Bhubaneswar, cr.pradhan23@gmail.com*

Malaya Tripathy, *Department of Electronics and Communication Engineering , Capital Engineering College, Bhubaneswar, malaya.tripathy43@gmail.com*

Abstract: It is necessary for power systems to provide flexible power to balance the fluctuation and intermittency of wind power. For the large-scale and central-integrated wind generation (such as that in China), the required flexible power may be very significant and expensive. In market environment, it is important to design a proper market mechanism and price signal which can promote conventional power and load demand to integrate wind power and gain corresponding profit. Firstly, the paper analyzes the current economy and dispatch policy for wind power in China. Then, a Block Bidding mode for wind power is presented. Unlike Timely Bidding mode that power is auctioned hourly by hourly, for Block Bidding the wind power energy is divided into different energy block. And these blocks are auctioned by conventional power resources and load demands. The Block Bidding mode has some advantages: 1) subdivides wind power by energy quality, and then the value of different parts can be revealed; 2) provides incentive for conventional power resource and load demand to integrate wind power; 3) is convenient for trading and dispatching wind power. Finally, a simple numerical case is given to illustrate the validity of Block Bidding mode.

1. INTRODUCTION

Renewable energy has received more and more attention with the increasing consumption of fossil fuel resources and the strength of public's environment consciousness. Wind power, as a kind of renewable clean energy that can be large-scale developed and utilized, has been developing rapidly worldwide in recent years. However, because of the fluctuation and intermittency of wind power, it is necessary to provide flexible power to balance its fluctuation and intermittency in power system operation. From the perspective of economy, when integrating wind power, other conventional resources (such as coal-thermal, gas, oil generation) should be paid because valuable contribution has been given by them to compensate the fluctuation of wind power. The more wind power is integrated, the more flexible capacity and compensatory cost are required.

The compensatory cost of wind power has been concerned by many studies. Based on the large amount of real data in UK market, the influence of wind power “balancing cost” in power systems is analyzed by Swinand and Godel (2012), results show that the balancing cost is increasing with the increasing capacity of wind power integration. Hannele et al. (2011) presents the opinion that high penetration of wind power would bring considerable integrating costs, including cost of operation balance and cost of grid strengthen. Andrianesis and Liberopoulos (2012) studies the “hidden cost” from the perspective of optimal dispatch, but it only gives a preliminary result with a simple numerical example without systematic analyses. Milligan et al. (2011) and Milligan and Kirby (2009) analyzes the problem of “integrating cost” of wind power systematically and discusses some problems in current research. Mills et al. (2009) focus on the “extra cost” of wind power integration in the sense of transmission cost. And Mount et al. (2011) analyzes the hidden cost in term of power market, but the electricity price is ignored. Makarov et al (2009) evaluates the impacts of wind power on the balance of power grid. Ummels (2006) presents the influence of integration of wind power on the Dutch power system. Holttinen (2005) concludes that the reserve demands would greatly increase with the increase of wind power penetration.

As a large-scale and rapid developed wind power country, China has constructed 75.3 GW wind power in 2012, which is shown in Fig.1. In the future ten years, the wind power of China will be continually increased in 3-5 times. Therefore, the required flexible power to balance wind power fluctuation may be significant. Especially for China power system that has few flexible powers (over 70% coal-fired powers), the required flexible power may be very expensive. Even currently, in some regions of China, the balance has become very difficult, which results expensive compensatory cost. For example, in Inner Mongolia, North China, North-east China, all of the coal-thermal generators should usually operate in their minimum output level.

As renewable energy, wind power should be sufficiently utilized. Many countries have made economy policies to encourage wind power development. For instance, in China 1) wind power should be fully dispatched in priority; 2) wind power is paid for high price that is the same as that for thermal power (Besides these policies, wind power can also get investment allowance and the profit of international carbon emissions). However, these policies do not give effectively incentive to conventional power, and then bring some problems (as shown in Table 1).

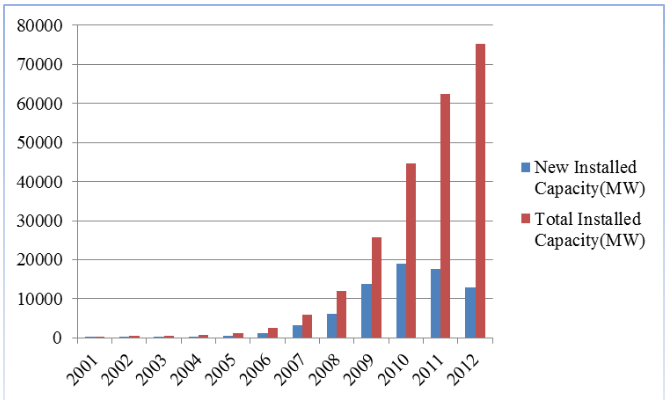

Fig.1. The installed capacity of wind power in China

Table 1. The problems of the wind power participants facing

Market Participants	Problems
Conventional power	should modify unit commitment and power schedule to balance the fluctuation and intermittency of wind power, but without any reward.
Wind power	without price and product option rights, either be accepted or to be abandoned.
Load demand	would prefer stable controllable hydro or thermal power with the same market price.

The key reason of above problems is that these policies do not deeply consider the following characters of wind power: 1) In power system dispatch, wind power is not an individual resource, it requires other resources' help to balance its fluctuation and intermittency; 2) The quality of wind power is different from that of other controllable generation resource. And in the sense of market, market price should be different according to the different products' quality.

In order to overcome above problems, a novel bidding mode of wind power, or Block Bidding mode, will be proposed in this paper. Firstly, the paper analyzes the quality of large-scale wind power. Then the block bidding mode is presented. Furthermore, a simple numerical example is provided to illustrate the validity of block bidding mode. Finally some discussions of block bidding are given.

2. THE COMPENSATORY COST AND VALUE OF WIND POWER IN A BLOCK VIEW

It is well-known that if wind power is dispatch in power system, its fluctuation and intermittency should be balanced by other generation resource to guarantee load balance and frequency stability of power systems. Therefore, extra cost (called compensatory cost in this paper) would arise to balance wind power fluctuation and intermittency. From the viewpoint of power systems or market, the total cost of integrating wind power includes not only its generation cost but also the compensatory cost:

$$IC_w = GC_w + CC_w \tag{1}$$

where, IC_w is the integration cost of wind power, GC_w is the generating cost of wind power, CC_w is the compensatory cost of wind power.

Generally, without fuel cost, the generating cost of wind power is very low. While, the compensatory cost may be high or low, which is determined by many factors, including the resource structure of system, penetration of wind power, flexible adjustment capacity of conventional power, etc. How to evaluate the compensatory cost is an interesting and challenging problem. Some calculation methods have been given to analyze this cost (Augustine et al 2012; Meibom et al. 2009). Here, the key idea is to find a proxy wind power generation and compare the differences.

(1) Although the compensatory cost can be calculated, this cost cannot be easily and correctly applied in timely power market that is the most popular market mechanism around the world and power is auctioned hourly by hourly because of the following reasons:

(2) The compensatory cost is relevant with unit commitment and ramp rate cost of other conventional generators. In other words, it is an optimization in a continuous time horizon with coupled and multiple time-interval constraints. And hourly by hourly bidding mode is unsuitable for the compensatory cost analysis.

In hourly by hourly bidding mode, the wind power of each hour is deemed as fluctuation power and requires to be balanced. This mode may underestimate wind power quality. In fact, some parts of wind energy quality are very good, especially for large-scale and centralized integrated wind power.

For example, Fig.2 gives an actual daily wind power output of Yumen area in northwest China. Large amount of wind generators form a complementary character in time and space intervals. The intermittency and fluctuation of total wind power output decrease. It can be found that at the bottom of output curves there is a continual and stable wind power output, and this output can be controllable dispatched without other generator's balance and compensatory cost.

Based on above analysis, we divide daily wind power into 3 horizontal blocks according to its continuity and stability, which is shown in Fig.2.

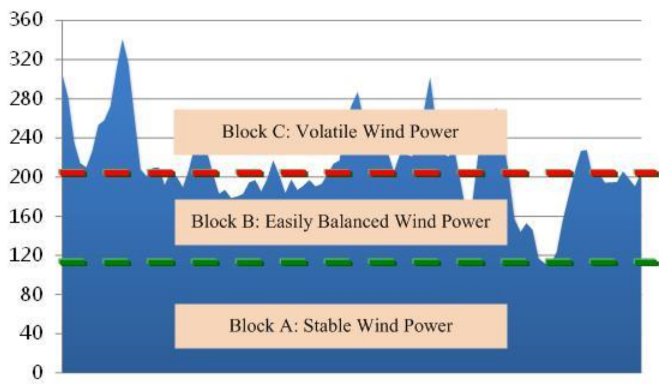

Fig.2. Typical daily wind power output of Yumen

The different block in Fig.2 has different wind power compensatory cost, as well as the quality or values:

- For Block A, the power quality is sustained and stable that does not need other conventional power to balance. Therefore, Block A is the energy that with the highest value and requires no compensatory cost. Here, it should be mentioned that the energy of Block A usually occupies about 50% of the total daily energy.
- For Block B, the power has a little fluctuation and is easy to be balanced. So the Block B is the energy with the higher value and requires a little compensatory cost.
- For Block C, the wind power fluctuates violently. So the Block C is the energy with the lowest value and requires large compensatory cost (even cannot be fully balanced in power system operation).

To a summary, when wind power is dispatched in power system, it needs other generation resources to balance its fluctuation and intermittency. In block view, not all wind power energy is fluctuation and intermittency, different block has different quality and value.

3. BLOCK BIDDING OF WIND POWER

Nowadays, timely bidding is the most popular market mechanism around the world. Timely Bidding divides the daily load into time intervals by hour or half hour. The power is auctioned by every time interval with a uniform market clearing price for each time interval. This bidding mode stimulates the development of power enterprises and improves the efficiency of power industry. However, Timely Bidding cannot distinguish quality and value for different component of wind power energy. And in current market, conventional power has not gained any distinct payment for balancing wind power (except conventional auxiliary reserve).

Unlike Timely Bidding that power is auctioned hourly by hourly, Block Bidding is a new mode that divides load demand into some load blocks according to continual hours, and the auction is carried out in the load blocks (Wang et al. 2002). Base on the idea of Block Bidding, a new Block Bidding mode for wind power is proposed in this paper.

In the proposed mode, wind power is divided into some horizontal blocks. And each block can submit different price and takes part in market auction. In economic theory, the wind power is authorized for option right of product subdivision with different price. At the same time, wind power should submit stable power output. Therefore, wind power should take compensatory cost into it bidding price.

For example, the specific steps and rules of bidding are described in Fig.3.

Firstly, the forecasting wind power curve is divided into some blocks, such as 3 blocks, indexed by l_1, l_2 and l_3 in Fig. 3.

Secondly, each block can bid separately. For each block, the bidding power output should be stable, such as a simple horizontal output curve in Fig.3. And the output of each block is denoted as pl_1, pl_2, pl_3 respectively.

$$pl_1 = P_1 \tag{2}$$

$$pl_2 = P_2 - P_1 \tag{3}$$

$$pl_3 = P_3 - P_2 \tag{4}$$

If the bid wins the auction, the stable power output should be provided. Therefore, wind farm should consider offer price high enough to pay for other conventional generator to balance the fluctuations of wind power.

In detail, the compensatory cost of each block is denoted as CC_{w_1}, CC_{w_2}, CC_{w_3}, respectively. And according to the fluctuation of each block, we can obtain:

$$CC_{w_1} = 0 \tag{5}$$

$$CC_{w_1} < CC_{w_2} < CC_{w_3} \tag{6}$$

Equation (5) means that for the block l_1, the wind power output is stable, and then it is unnecessary for other generator to balance fluctuation. So the compensatory cost is zero. Equation (6) means that with the increase of block index, the wind power energy decreases, and the required balance power increases more and more. So the compensatory cost increases.

Substitute (5) and (6) into (1):

$$IC_{w_1} < IC_{w_2} < IC_{w_3} \tag{7}$$

Where IC_{w_1}, IC_{w_2}, IC_{w_3} is the offer price for each block, respectively.

Equation (7) indicates that in Block Bidding mode, the wind power would submit an incremental price for the blocks. The more necessary compensatory cost is required; the more expensive energy is sold.

Finally, based on the wind power block bids, the whole market can be auctioned as usual. The system marginal price is set as clearing price, and the wined wind power block can gain excess profit.

In addition, to make incentive for balancing wind fluctuation, the excess profit is designed to be distributed among wind power and conventional power that provides balance. There may be many distribution methods, and a method based on cost-ratio is provided in this paper (shown in Fig. 4).

We may suppose the wind power's trading quantity of three blocks are Q_1, Q_2, Q_3, respectively and then the market clearing price is ρ.

For block l_1, as the wind power is steady and continuous, its compensatory cost is zero. The total excess profit belongs to wind power.

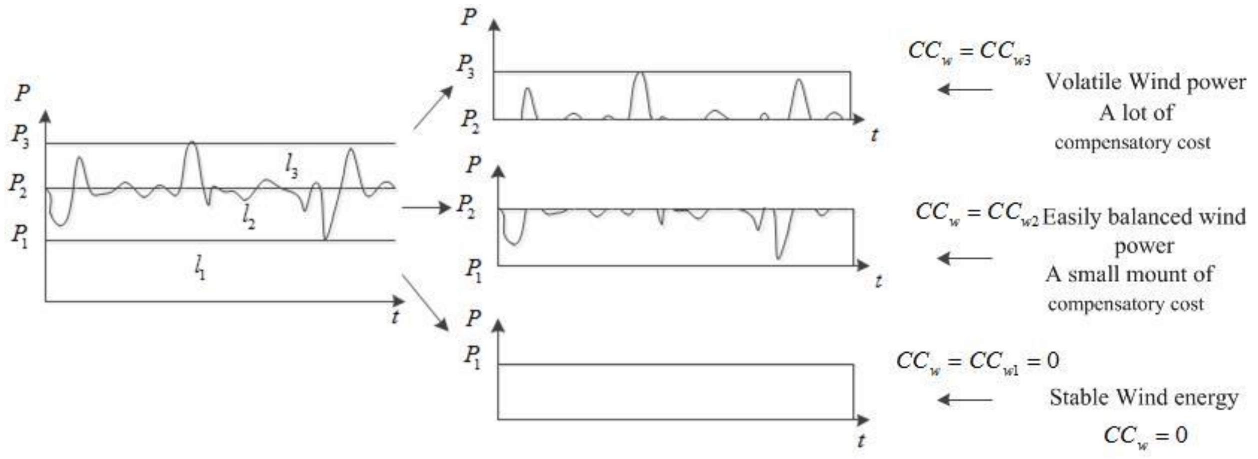

Fig. 3. Blocks bidding for wind power

For block l_2, the distribution ratio λ_2 between conventional power and wind power is:

$$\lambda_2 = \frac{(IC_{w2} - IC_{w1})Q_2}{IC_{w1}Q_2} = \frac{IC_{w2} - IC_{w1}}{IC_{w1}} \tag{8}$$

For block l_3, the distribution ratio λ_3 between conventional power and wind power is

$$\lambda_3 = \frac{(IC_{w3} - IC_{w1})Q_3}{IC_{w1}Q_3} = \frac{IC_{w3} - IC_{w1}}{IC_{w1}} \tag{9}$$

So the payment for wind power is:

$$P_w = \rho Q_1 + \rho Q_2 \frac{1}{1+\lambda_2} + \rho Q_3 \frac{1}{1+\lambda_3} \tag{10}$$

And the payment for conventional power which balances the fluctuation and intermittency of wind power is:

$$P_c = \rho Q_2 \frac{\lambda_2}{1+\lambda_2} + \rho Q_3 \frac{\lambda_3}{1+\lambda_3} \tag{11}$$

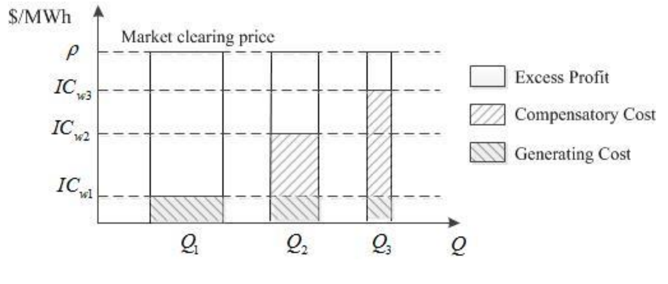

Fig. 4. The diagram of profit distribution for wind power block bidding mode

4. CASE STUDY

Here, a power system is chosen as an example to demonstrate the validity of the proposed block bidding mode. The system consists of the following components: one wind farm with 200MW capacity, two 50MW thermal power plants, and a load of 150MW. Firstly, the following assumptions are supposed:

(1) Wind power should be dispatched firstly as it is the clean energy. As shown in Fig. 5, when quoting, wind power is in the means of block mode and considers the compensatory cost. Here, the compensatory cost is determined according to the proportion of compensatory cost and generating cost.

(2) Conventional power (thermal power) is only used to complement the fluctuation of wind power, and does not directly participate in the bidding. Then, only three types of energy participate in the bidding: the high quality wind power, the wind power with a little compensatory cost and the wind power with massive compensatory cost.

(3) The daily output of wind power is divided into 24 time intervals and cleared by hourly and hourly. The power is auctioned by every time interval with a uniform market clearing price. The transaction price is determined by the marginal cost of the whole power systems.

(4) For the sake of simplification, the offer curve of wind power is supposed to be a straight line, as shown in Fig. 5.

As the generation cost of wind power is quite low, the major factor of integration cost is the compensatory cost. Then, the generation cost of different blocks can be supposed as the same. In period t, the marginal generating cost of wind power can be supposed as 10\$/MWh. From Fig. 5, it can be seen that the market clearing price is 70\$/MWh and the earning ratio of conventional power and wind power is

$$\lambda_2 = (\int_B^O pl_2 dp - \int_B^E pl_1 dp) / \int_B^E pl_1 dp = \frac{(70-10)\times 70/2}{10\times 70} = 3 .$$

So, in period t, the earning of wind power is

$$P_w = 70\times 80 + 70\times 70\times \frac{1}{3+1} = 6825$$

and the earning of conventional power which balances the fluctuation and intermittency of wind power is

$$P_c = 70\times 70\times \frac{3}{3+1} = 3675 .$$

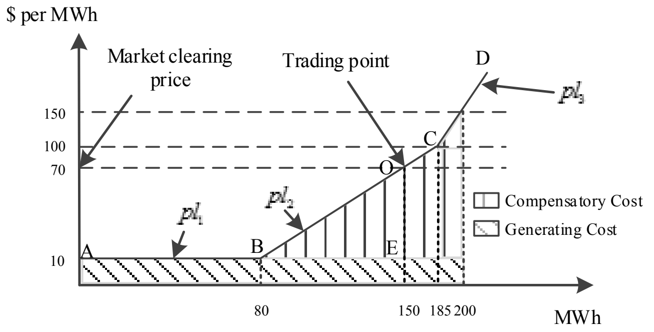

Fig. 5. The diagram of wind power clearing in period t

For the different load in the period t, the earnings of wind power and the conventional power are shown in Table 2. From the table, it can be seen that:

(1) When the volume of integrated wind power is less, the market clearing price is cheap because of the low generating cost of wind power. With the increase of the volume of integrated wind power, the second-block wind power is used and the quality of whole integrated wind power decreases. Then, the market clearing price increases. When the integrated volume of wind power reaches a certain level, the marginal value of wind power will be zero due to the massive compensatory cost.

(2) If the market clearing price is limited in 70$ per MWh, the volume of wind power integrated into grid is only 150MW which is located in the bottom of the output curve and has less compensatory cost due to their high quality and stability. The other valueless wind power can be abandoned.

Table 2. The earning distribution for different loads in period t

Load (MW)	Market clearing price ($ per MWh)	Earning of the first-block wind power ($)	Earning of the second-block wind power ($)	Earning ratio of conventional power and wind power (λ_2)	Total earning of wind power ($)	Total earning of conventional power ($)
60	10	600	0	0	600	0
80	10	800	0	0	800	0
100	27.1	2168	292.3	0.855	2460.2	250.2
120	44.	3544	652.7	1.715	4196.7	1119.3
140	61.4	4912	1031.9	2.57	5943.9	2652.1
150	70	5600	1225	3	6825	3675
160	78.6	6288	1419.4	3.43	7707.4	4868.6
170	87.1	6968	1614.6	3.855	8582.6	6224.4
180	95.7	7656	1810.8	4.285	9466.8	7759.2

5. DISCUSSION

In this paper, a novel bidding mode of wind power, or the Block Bidding mode, is proposed. This mode provides wind power the right to subdivide its energy product according to the different energy quality of its different blocks, and then the wind power suppliers can submit different bids for different energy block with the complement of conventional power suppliers.

It should be mentioned that many problems still need to be deeply investigated in the future, especially corresponding bidding mechanisms should be established. For example:

(1) The fluctuation and intermittency of wind power should be complemented by conventional power. Therefore, a sub-market should be established for wind power and conventional power to deal. In fact, some generation unions with both wind power and coal-thermal power have tried to coordinate the operation of wind and thermal power plants in China.

(2) How to evaluate the compensatory cost in market environment? By the mode of centralized optimization dispatching, or by the mode of negotiation? This is a question worthy of study.

(3) How to integrate Blocking Bidding and current Timely Bidding? This is also necessary to be investigated in detail.

(4) There are many methods to divide wind power into blocks. Which one is reasonable? If load-demand takes part in, the division of block and compensatory cost need to be analyzed again.

6. CONCLUSIONS

In order to accurately measure the cost of conventional power used to balance the fluctuation and intermittency of wind power, the concept of compensatory cost is proposed in the paper. By dividing the wind power into several blocks horizontally, the different compensatory cost of different blocks can be revealed clearly. Meanwhile, a block bidding mode for wind power energy is presented in the paper, which has the following advantages:

(1) In block bidding mode, wind power can be subdivided by energy quality. Then, different blocks can be set different prices according to their qualities.

(2) The scale of compensatory cost can be recognized clearly in the model of Block Bidding. Then, the benefit distribution of wind power plants and conventional power plants can be determined reasonably.

(3) Power grid can be guided to integrate the wind power

with high quality.

REFERENCES

Andrianesis, P. and G.. Liberopoulos (2012). The "Hidden Cost" of Renewable Energy Sources in Electricity Pool Markets. *European Energy Market (EEM), 2012 9th International Conference on the. IEEE*, p. 1-8.

Augustine, N., S. Suresh, P. Moghe and K. Sheikh (2012) Economic dispatch for a microgrid considering renewable energy cost functions. *Innovative Smart Grid Technologies (ISGT), 2012 IEEE PES,* p. 1-7.

Hannele, H., et al. (2011). Impacts of large amounts of wind power on design and operation of power systems, results of IEA collaboration. *Wind Energy*, 14(2):179–192.

Holttinen, H. (2005). Impact of hourly wind power variations on the system operation in the Nordic countries. *Wind Energy*, 8(2), p. 197-218.

Makarov, Y. V., et al. (2009). Operational impacts of wind generation on California power systems. *Power Systems, IEEE Transactions on*, 24(2), p. 1039-1050.

Meibom, P., et al. (2009). Operational costs induced by fluctuating wind power production in Germany and Scandinavia. *Renewable Power Generation, IET*, 3(1), p. 75-83.

Milligan, M., et al. (2011). Cost-causation and integration cost analysis for variable generation. *Contract,* 303, p. 275-3000.

Milligan, M. R. and B. Kirby (2009). *Calculating wind integration costs: separating wind energy value from integration cost impacts*. Golden: National Renewable Energy Laboratory.

Mills, A., et al. (2009). *The Cost of Transmission for Wind Energy: A Review of Transmission Planning Studies*. Ernest Orlando Lawrence Berkeley National Laboratory.

Mount, T., et al. (2010). The Hidden System Costs of Wind Generation in a Deregulated Electricity Market. *System Sciences (HICSS), 2010 43rd Hawaii International Conference on IEEE*, p. 1-10.

Swinand, G. P. and M. Godel (2012). Estimating the impact of wind generation on balancing costs in the GB electricity markets. *European Energy Market (EEM), 2012 9th International Conference on the. IEEE*, p. 1-8.

Ummels, B. C, .et al. (2006). Integration of wind power in the liberalized Dutch electricity market. *Wind Energy*, *9*(6), p. 579-590.

Wang, X., et al. (2002). Block bidding power markets. *Power System Technology*, 3, p. 1828-1832.

Optimal Sizing and Allocation of Fixed Reactive Power Compensation

Sanjeev Kumar Mishra, *Department of Electrical and Electronics Engineering, Aryan Institute of Engineering & Technology, Bhubaneswar, sk.mishra@outlook.com*

Prajnadipta Sahoo, *Department of Electrical and Electronics Engineering, NM Institute of Engineering & Technology, Bhubaneswar, prajnadipta567@gmail.com*

Anil Sahoo, *Department of electrical Engineering , Capital Engineering College, Bhubaneswar, anil_sahoo342@gmail.com*

Prakash Kumar Behera, *Department of Electronics and Communication Engineering , Raajdhani Engineering College, Bhubaneswar, prakash_behera21@gmail.com*

Abstract: This paper proposes an approach to optimize the sizing and allocation of a fixed capacitor in a radial distribution network to compensate reactive power. The optimization problem is formulated as a minimization of the line loss of the network with the load profile within 24 hours. Constraints refer to node voltage quality and power flow. The approach is tested on IEEE 33 nodes radial distribution network and the process of the optimization is analyzed from four aspects which are compensation nodes, power factor, active power load factor and compensation proportion to illustrate its feasibility and affectivity.

Keywords: Distribution network; Flow calculation; Reactive power compensation; Fixed capacitor; Static optimization problems.

1. INTRODUCTION

With the scale expansion of distribution power system, the line loss is getting more and more owing to the transmission of reactive power. The compensation of reactive power within the distribution network might reduce the line loss. However, the allocation and sizing of the compensation should be carefully chosen. The proper optimization can reduce line loss of network, and improve the voltage quality Wang, Yang, Wang, Wang, Huang and Zeng (2012). A reactive power optimization problem is a typical nonlinear programming problem with constraints.

At present, there are mainly two kinds of compensation strategies, namely, fixed compensation or adjustable compensation (centralized regulation or distributed regulation)YUAN and HAN (2003). The adjustable compensation, such as Static Var Compensator and Static Compensator, can output varying reactive power according to the supervisor's command or to the operational states of the distribution network to reach good operational performances (line loss and node voltages), which requires lots of information communication and computation. A fixed compensation, such as a fixed capacitor, outputs almost a constant reactive power no matter the system states are. The compensation performance might not be as good as the adjustable compensation. However, such a fixed capacity device requires no communication and computation, the operation is very simple and thus the fixed operational costs are very low. Distribution networks are usually characterized by radial topology. In radial distribution networks, the most widely-used device for reactive power compensation is a shunt capacitor Pires, Antunes and Martins (2012).

Reactive power compensation optimization problems often involve multiple and even conflicting objectives. There exists a global optimum in a single-objective optimization, while the multi-objective case has a set of solutions from different aspects instead of clear optimal solutions. Many objectives and approaches have been proposed in the scientific literature for reactive power compensation problems.

The optimal objectives are about power loss and/or economical savings in the following literature. In Antunes, Pires, Barrico, Gomes and Martins (2009), the problem of locating and sizing of capacitors for reactive power compensation in radial distribution network is modeled as a multi-objective programming problem, where two (conflicting) objective functions are involved: one is to minimize the line loss of the network and the other is to minimize the installation costs of new reactive power sources. In Pires et al. (2012) and Nojavan, Jalali and Zare (2014), the problem of optimal capacitor placement for the reactive power compensation is formulated to identify the network nodes to install capacitors and the dimension of each capacitor so as to minimize installation costs and power loss. The objective in Haque (1999) is to minimize the power losses and a two stage approach is applied. In the first stage, the objective is to find the nodes where the capacitor singly-installed having the significant effects on the feeder power loss. In the second stage, the capacitor sizes at the selected locations are optimized to overcome any over-compensation.

There are some various approaches applied to solve reactive power compensation optimization problem. For example, a teaching learning based optimization approach, consisting of a teaching phase and a learning phase is applied in Sultana and Roy (2014), while a direct search algorithm implicitly incorporating the power flow calculation is applied in Ramalinga Raju, Ramachandra Murthy and Ravindra (2012). In Kannan, Renuga, Kalyani and Muthukumaran (2011), differential evolution and multi agent particle swarm optimization (PSO) are applied to find the sizing and the allocation of the capacitors. A heuristic search based method and a bacterial foraging based method are applied in Hamouda and Sayah (2013) and Tabatabaei and Vahidi (2011) respectively. A fuzzy adaptive PSO approach is also proposed in Zhang and Liu (2008) to address the multi-objective problem for reactive power compensation. In Antunes et al. (2009), elitist genetic algorithm is applied to characterize the Pareto optimal frontier to obtain the minimized system loss and capacitor installation costs. In Varadarajan and Swarup (2008), the reactive power compensation optimiza-tion problem is formulated as a mixed integer power sys-tem optimization problem having non-convex, nonlinear objectives and nonlinear constraints and solved with a differential evolution based method.

In summary, the attention in the literature is focused on line power/energy loss and node voltages at a specific time and few efforts are involved in those indices within 24 hours for the radial distribution network, i.e., the power flow is only calculated according to specific load distribution of the network. Actually, the load distribution is varying with respect to the time. Generally, a typical load profile for a node is used to describe the load time-varying, from which the load variation can be seen. When the load profile is considered in the computation of the line loss of the network, reactive power compensation will bring better compensation effects for the actual situations.

This paper proposes an approach to optimize the reactive power compensation of a medium voltage radial distribution network to achieve minimization of the line loss within 24 hours. A typical daily load curve is applied to the network in order to obtain load power values at specific times. The approach is tested on IEEE 33 nodes radial distribution network, which implies the approach is feasible and effective.

In Section 1, the motivation of the study has been provided. The rest of this paper is organized as follows. In Section 2, the problem formulation of optimization of the reactive power compensation with the objective is given. Section 3 introduces optimization approach and solutions. Section 4 presents an example of the application to IEEE 33 nodes radial distribution network with the optimization results discussed. Finally, conclusions are drawn in Section 5.

2. PROBLEM FORMULATIONS

There are mainly two reasons for the installation of reactive power compensation devices: one is to regulate the voltages at load nodes to be in a specific range, and the other is to compensate the variable consumption to reduce the line loss. In this paper, the sizing and allocation of a fixed capacitor as a reactive power compensation device for a distribution network is studied. To make full advantages of the fixed capacitor, there are two problems should be answered. One is where the capacitor is installed and the other is that what the size of the capacitor is. The solu-tions to both problems will have impacts on the voltage regulation and line loss of the network. Here, an approach is proposed to optimize the sizing and allocation of the capacitor.

2.1 Line Loss Calculation

Reactive power compensation to a distribution network usually pursues two objectives Wang et al. (2012). One is to minimize the line power loss of the network to save the power energy loss and the other one is to reduce the installation cost of the compensation devices. As we know, a reactive power compensation device can be in operation for a long time (the lifespan of the device) once it is installed. Thus the installation cost of the device might be very small compared with the energy cost saving in the lifespan. Therefore, in this paper, only the line loss of the network is thought of as the objective.

The diagram of the IEEE 33 nodes radial distribution network with 33 nodes is shown in Fig. 1 Khodr, Olsina, Jesus and Yusta (2008).

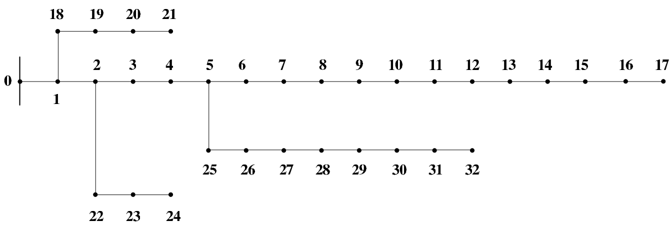

Fig. 1. Single-line diagram of the IEEE 33 nodes distribution network

According to Liao and Zheng (2011), for the given radial distribution network with N nodes, the line loss of the network within a day can be calculated as:

$$W = \int_{t_0}^{t_f} p_{i,j}(t)dt = 3\int_{t_0}^{t^f} \sum i_{i,j}^2(t)R_{i,j}dt \times 10^{-3} \quad (1)$$
$$i = 0, 1, 2, \cdots, N-1, j = 0, 1, 2, \cdots, N-1, i \neq j$$

where i and j represent the starting and ending nodes in branch (i, j) respectively, $p_{i,j}(t)$ is the active power of the (i, j) branch, $i_{i,j}(t)$ is the current of the (i, j) branch, $R_{i,j}$ is the resistance of the (i, j) branch and t is time, t_0 and t_f are the start time and stop time of the network respectively. To calculate W, the branch current $i_{i,j}(t)$ must be obtained firstly. Usually we use power flow calculation to obtain the branch currents.

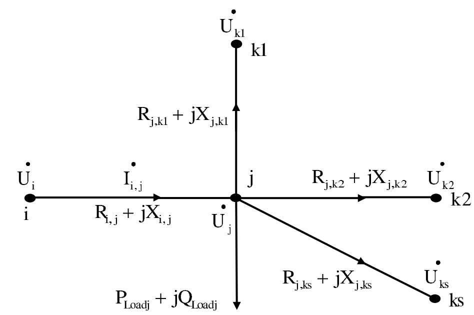

Fig. 2. A typical feeder line

For the distribution network, the voltage of the root node (U_0), the load power of the rest nodes ($P_{Loadi} + jQ_{Loadi}$) ($i = 1, 2, \cdots, N-1$), the topology structure of the distribution network and the impedance of the (i, j) branch ($Z_{i,j} = R_{i,j} + jX_{i,j}$) ($i = 0, 2, 3, \ldots, N-1, j = 0, 2, 3, \ldots, N-1, i \neq j$) are known. The voltage of each node (U_i) (i = 1, 2, 3, . . . , $N - 1$), the current through the (i, j) branch ($i_{i,j}(t)$) (i = 0, 2, 3, . . . , $N - 1$, j = 0, 2, 3, $\cdots$, $N - 1$, $i \neq j$) and the active power loss of the network are to be calculated Liu, Bi and Dong (2002).

For line loss calculation, branch currents are the focus of attention. An example is illustrated to obtain branch current. A typical branch of a feeder network is shown in Fig. 2.

According to Kirchhoff's current law, the following is true.

$$\dot{i_{i,j}}(t) = \frac{\dot{U_i} - \dot{U_j}}{R_{i,j} + jX_{i,j}} \tag{2}$$

$$\dot{i_{i,j}}(t) = \sum_{k \in d}^{d} \frac{\dot{U_j} - \dot{U_k}}{R_{j,k} + jX_{j,k}} + \frac{P_{Loadj} - jQ_{Loadj}}{\dot{U_j^*}} \tag{3}$$

Then one has

$$\frac{\dot{U_i} - \dot{U_j}}{R_{i,j} + jX_{i,j}} = \sum_{k \in d}^{d} \frac{\dot{U_j} - \dot{U_k}}{R_{j,k} + jX_{j,k}} + \frac{P_{Loadj} - jQ_{Loadj}}{\dot{U_j^*}} \tag{4}$$

where d is a set of the branches whose parent node is the node j.

The above equations are applicable to all branches. So for the N nodes radial distribution network, there are $N - 1$ equations and $N - 1$ node voltages to be calculated. And with the node voltages obtained, the branch currents can be calculated. The equations in the form of Equation (4) are nonlinear obviously, and there are no analytic solutions to the equations. Generally, numerical solutions can be obtained by iterative computation which will be introduced in Section 3.

With branch currents obtained, the line power loss of the network can be calculated. Generally, the theoretical calculation for line energy loss refers to the line energy loss in a day is done in an interval of one hour, which means

$$\begin{aligned} &i_{i,j}(t) = \text{constant} = I_{i,j} \\ &0 \leq k < t \leq k + 1 \leq 24 \end{aligned} \tag{5}$$

where k is positive integer.

So, $W(t)$ can be further expressed as

$$W(t) = \sum_{i=0}^{N-1} \sum_{j=1, j \neq i}^{N-1} 3I_{i,j}^2 R_{i,j} \times 10^{-3} \tag{6}$$

within the t-th hour.

For the network, the theoretical line loss within a day can be expressed as

$$W = \sum_{t=1}^{24} W(t) \tag{7}$$

When the reactive power compensation capacity Q_C is compensated to a node j in the distribution network, the power flow in the network can be changed with the branch current changed. Then, the equation (3) changes into (8)

$$\dot{i_{i,j}}(t) = \sum_{k \in d}^{d} \frac{\dot{U_j} - \dot{U_k}}{R_{j,k} + jX_{j,k}} + \frac{P_{Loadj} - j(Q_{Loadj} - Q_C)}{\dot{U_j^*}} \tag{8}$$

And the equation (4) changes into the equation (9)

$$\begin{aligned} \frac{\dot{U_i} - \dot{U_j}}{R_{i,j} + jX_{i,j}} = &\sum_{k \in d}^{d} \frac{\dot{U_j} - \dot{U_k}}{R_{j,k} + jX_{j,k}} + \\ &\frac{P_{Loadj} - j(Q_{Loadj} - Q_C)}{\dot{U_j^*}} \end{aligned} \tag{9}$$

The line loss of the network W changes with the branch current changed. Thus, appropriate compensation capacity of the reactive power Q_C may minimize the line loss W.

2.2 Operational Constraints

Two operational constraints for the distribution network must be taken into consideration. One is the node voltage constraint. For each node, the voltage must satisfy

$$(1 - 5\%)U_{rated} \leq U_i \leq (1 + 5\%)U_{rated} \tag{10}$$

where U_{rated} is the rated voltage.

The other is the security limitation on the branch current. For each branch, the branch current must satisfy

$$0 \leq I_{i,j} \leq I_{i,j}^s \tag{11}$$

where $I_{i,j}^s$ is the current carrying capacity of the (i, j) branch cable.

2.3 Optimization Problem

According to the power flow distribution, compensating reactive power to the node in the network will change the power flow distribution of the network. The optimization of the capacitor is to find the node and corresponding capacity of the capacitor in the network such that the line loss of the network within a day is minimized with the operational constraints satisfied. In this paper, the objective is f expressed as

$$\begin{aligned} &f = \min W \\ &\text{s. t.} \begin{cases} (1 - 5\%)U_{rated} \leq U_i \leq (1 + 5\%)U_{rated} \\ 0 \leq I_{i,j} \leq I_{i,j}^s \end{cases} \end{aligned} \tag{12}$$

3. APPROACH AND SOLUTIONS

The power flow equations are nonlinear. It is difficult to obtain analytic solutions to those equations. In engineering, such a problem is generally solved by numerical computation approach specifically. Here we use a numerical computation approach based on the forward and backward substitution method CONG and WANG (2008) which is usually used in engineering.

3.1 Forward and Backward Substitution Method

On the basis of analyzing the techniques for power flow calculations of distribution network, the topology structure of distribution network is defined by the tree structure which consisted of special circuit branch structure and node structure CHEN, CHEN, GU and LIU (2010). Branch currents are corrected by postorded-traversing the tree structure and node voltages are corrected by preorder-traversing the tree structure until constringency. With such a method, there is no need to number the distribution network and form admittance matrix. The power flow distribution of network can be obtained through this method.

Flow chart of the forward and backward substitution method is shown in Fig. 3. Specific calculation steps can refer to CHEN et al. (2010).

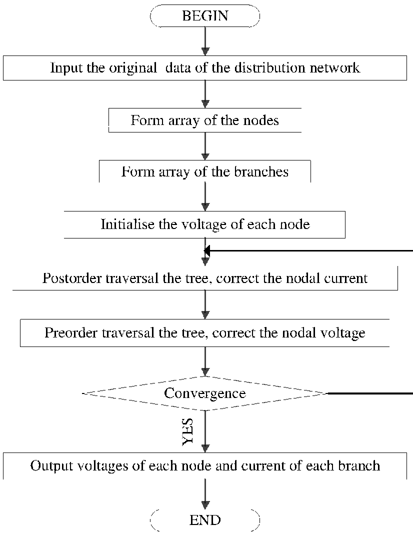

Fig. 3. Flow chart of the forward and backward substitution method

3.2 Steps of Approach

To solve the optimal problem, we use the approach with following steps:

(1) For a given sequence of Q_{C0} at a node, the line loss for each value of Q_{C0} could be found. Then we can find the optimum Q_{Ci} to the problem at this node.
(2) Choose another node to repeat step (1).
(3) After all nodes except the root node being checked, we can compare the optimums at those nodes to obtain the optimum Q_C for the problem in the global scope.

4. EXAMPLE AND RESULTS

4.1 Example

The proposed approach is tested on IEEE 33 nodes radial distribution network which is shown in Fig. 1. The parameters of the network can refer to Baran and Wu (1989). The convergence condition for the power flow calculation is that voltage difference values between the consecutive rounds for all nodes are less than 1.0×10^{-6}kV. The root node voltage is fixed as $U_0 = 12.66$kV.

In this example, active power of each node changes with the typical daily load curve, and the line loss of the network can be calculated one hour by one hour. For convenience, we assume that each node has the same shape for the typical daily active power load curve and power factor. A typical daily load curve in summer Zhang (2009) depicted in Fig. 4 is adopted, where P.U.=1 means the actual active power is the maximum.

4.2 Discussions and Analysis

When the results are shown in the following figures. In the figures, the proportion refers to the capacitor percentage that is Q_C/Q_ε.

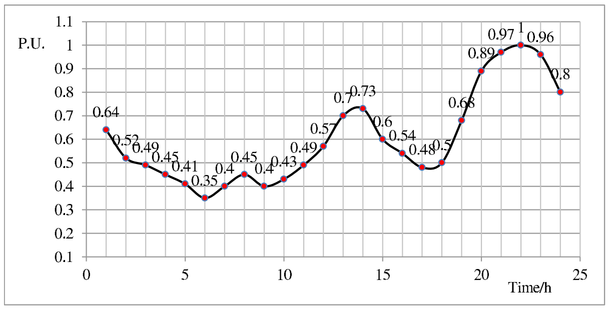

Fig. 4. A typical daily load curve in summer

The power factor is 0.85 and the maximum of compensation reactive power Q_ε in the network within a day is 2302.35021kVar. Fig. 5 shows the optimum for each node. From Fig. 5, we can see that the optimal proportions of reactive power compensation at different nodes are different and results in different line loss. With the topology structure of the radial distribution network and the optimization results investigated, some interesting information can be known. When the compensated node is near to the root node, the effect of compensation is not good. With the compensated node far away from the root node, the line loss decreases until reach the least at a node and the capacity of compensation decreases. Then, with the compensated node close to the ending node, the line loss increases while the capacity of compensation decreases. According to the parameters of the network, we can see that the resistance of the branch can influence the effective of the adjacent compensated nodes, but when the adjacent nodes are close and the resistance is small, their compensated effects are similar.

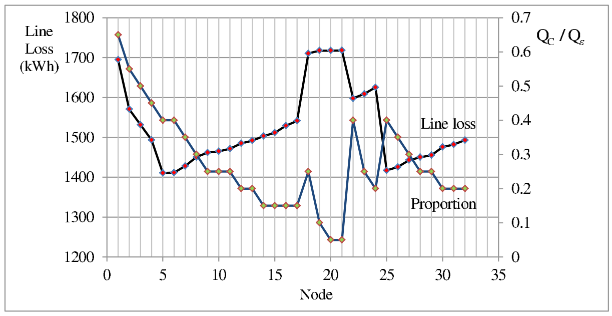

Fig. 5. Optimum at each node in the network

The results for some nodes with different proportions of compensation are shown in Fig. 6 and Fig. 7, from which it is seen that at a specific node, different compensation capacity generally results in different line loss, which is the motivation for the optimization of the compensation capacity. Meanwhile, we can see that even the same capacity of reactive power compensation for different compensated nodes, usually lead to different line loss of the network, which is the motivation for the optimization of the compensation allocation.

It is also seen that no matter what the compensation capacity is to the Node 1, the line loss changes little, while compensation capacity at any other nodes varies, the line loss has an obvious change. This probably because Node 1 is very close ($R_{0,1}$ is very small) to the root node (the source node). The compensation reduces branch current

$I_{0,1}$, which has little effect because of $R_{0,1}$ in Equation (6) is very small. Meanwhile, it can be seen that the curves of line loss with respect to the compensation capacity is convex. Therefore, compensation capacity could be optimized such that the line loss can be minimized.

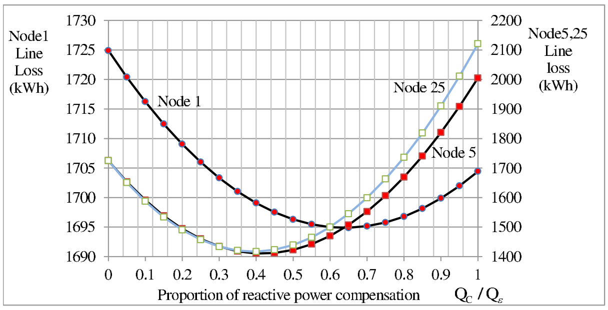

Fig. 6. Optimum result with power factor=0.85, Q_{ε}=2302.35022 kVar

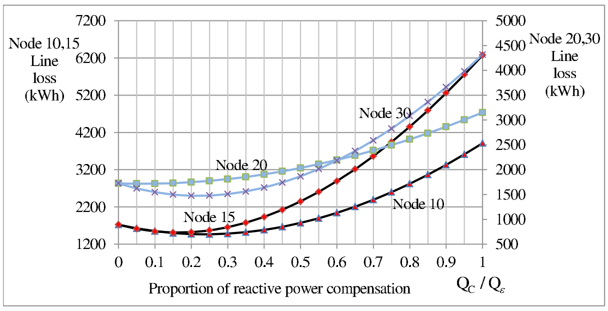

Fig. 7. Optimum result with power factor=0.85, Q_{ε}=2302.35022 kVar

We further investigate the optimization results in more scenarios, i.e., the scenarios with the active power and the power factor changed. In the rest of the paper, PLF represents active power load factor.

When P_{Loadj} is maintained and Q_{Loadj} is changed such that the power factor is 0.95, the optimization result is shown as Fig. 9, while $P_{i,j}$ is 0.4 times of the baseline (i.e., PLF=0.4).

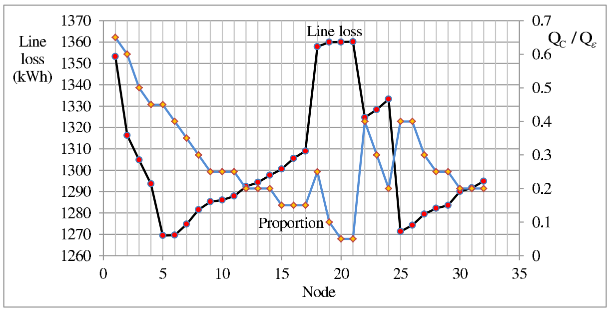

Fig. 8. Optimum result with power factor=0.95, PLF=1.0, Q_{ε}=1221.06145 kVar

Comparing Fig. 5 with Fig. 8 and Fig. 9, it is easy to find that the shapes of the two classes of optimization result curves are consistent, which implies that the relative effects of optimal compensation at different nodes are influenced by the topology structure of the distribution network.

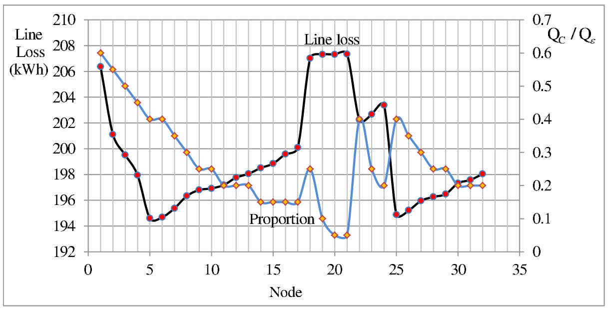

Fig. 9. Optimum result with power factor=0.95, PLF=0.4, Q_{ε}=488.42458 kVar

Comparing Fig. 5 with Fig. 8, it can be seen that the line loss of the network and compensation capacity decrease with the growth of power factor. This because the higher power factor is, the lower the reactive power Q_{ε} is and then the smaller the branch currents of the network. The higher power factor results in smaller line loss and compensation capacity. So improving power factor can reduce the line loss effectively.

Comparing Fig. 9 with Fig. 8, it can be seen that when the power factor is the same, the line loss of the network and compensation capacity increase with the increase of the PLF. This because the higher PLF is, the more reactive power compensation is required.

Fig. 10 shows the optimization results while the power load factor is different and the power factor is the same. With different PLF, Q_{ε} is different. In Fig. 10, Q_{ε} is as follows:

When PLF=0.4, Q_{ε}=1516.02323kVar.
When PLF=0.6, Q_{ε}=2274.03485kVar.
When PLF=0.8, Q_{ε}=3032.046470kVar.
When PLF=1.0, Q_{ε}=3790.05808kVar.
When PLF=1.2, Q_{ε}=4548.06970kVar.

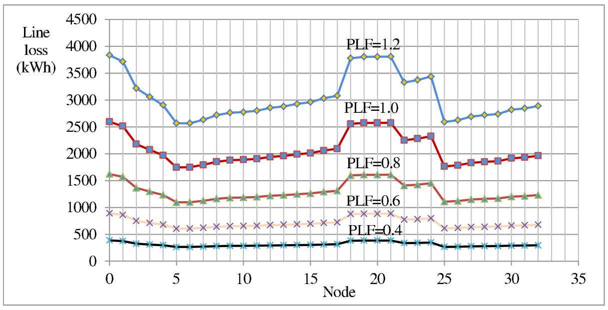

Fig. 10. Optimum results with power factor=0.7

Particularly, the line loss of Node 0 refers to the scenario that the compensation capacitor is installed at the bus node, implying the line loss is the result without compensation. It is obvious to see that the line loss grows with the increase of PLF in Fig. 10. But the optimum shapes of the curves in Fig. 10 are similar. Compare the curves in Fig. 10, it could be found that when PLF is low, the effects of the compensation at different nodes are not significant, this is because the optimum effect is not obvious compared with no compensation. When PLF is high, the differences of the compensation effects at different nodes are significant. So, with a high PLF, reactive power compensation can be optimized for sizing and allocating.

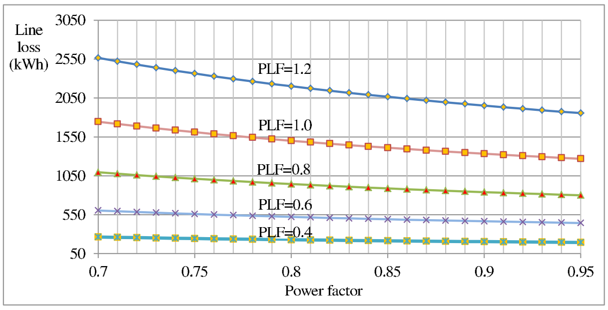

Fig. 11. Optimum results with compensating at Node 5

With different power factors, the optimum results are shown in Fig. 11. With the same PLF at Node 5, the optimum line loss of the distribution network varies with respect to the power factor. Obviously in Fig. 11, the line loss decreases with the increase of the power factor. From Fig. 11, we can see that when PLF is low, the optimized compensation effects are similar even with different power factors. However, when PLF is high, the differences of optimized compensation effects with different power factors are significant. Those are true for other nodes, too. Thus, the higher the PLF is, the more important the optimization of compensation.

5. CONCLUSIONS

This paper proposed an approach which is to find the optimal sizing and allocation of a fixed capacitor as the reactive power compensation device to minimize the line loss of a radial distribution network within a day. The approach is very simple and effective for practical engineering. The approach is tested on IEEE 33 nodes radial distribution network and the results are analyzed from some aspects which are compensation nodes, power factor, active power load factor and compensation proportion. The test illustrates the motivations and applicability of this study. The higher power load factor is and the lower the power factor is, the more important the optimization of reactive power compensation.

REFERENCES

Antunes, C. H., Pires, D. F., Barrico, C., Gomes, A. and Martins, A. G. (2009). A multi-objective evolutionary algorithm for reactive power compensation in distribution networks, *Applied Energy,* **86**(7): 977–984.

Baran, M. E. and Wu, F. F. (1989). Network reconfiguration in distribution systems for loss reduction and load balancing, *Power Delivery, IEEE Transactions on,* **4**(2): 1401–1407.

CHEN, W.-h., CHEN, Q.-z., GU, S.-p. and LIU, H.-t. (2010). A simple implement method of back/forward sweep distribution power flow, *Jiangsu Electrical Engineering,* **4**: 014.

CONG, P.-j. and WANG, Z. (2008). Power flow calculation for radial distribution network based on forward and backward substitution method, *Northeast Electric Power Technology,* **2**: 001.

Hamouda, A. and Sayah, S. (2013). Optimal capacitors sizing in distribution feeders using heuristic search based node stability-indices, *International Journal of Electrical Power & Energy Systems,* **46**: 56–64.

Haque, M. (1999). Capacitor placement in radial distribution systems for loss reduction, *IEE Proceedings-Generation, Transmission and Distribution,* **146**(5): 501–505.

Kannan, S., Renuga, P., Kalyani, S. and Muthukumaran, E. (2011). Optimal capacitor placement and sizing using fuzzy-de and fuzzy-mapso methods, *Applied Soft Computing,* **11**(8): 4997–5005.

Khodr, H., Olsina, F., Jesus, P. and Yusta, J. (2008). Maximum savings approach for location and sizing of capacitors in distribution systems, *Electric Power Systems Research,* **78**(7): 1192–1203.

Liao, X. and Zheng, D. (2011). *Line Loss Calculation Analysis and Management of Urban and Rural Power Grid*, China Electric Power Press, Beijing.

Liu, J., Bi, P. and Dong, H. (2002). *Simplified Analysis and Optimization of Complex Distribution Network*, China Electric Power Press, Beijing.

Nojavan, S., Jalali, M. and Zare, K. (2014). Optimal allocation of capacitors in radial/mesh distribution systems using mixed integer nonlinear programming approach, *Electric Power Systems Research,* **107**: 119–124.

Pires, D. F., Antunes, C. H. and Martins, A. G. (2012). NSGA-II with local search for a multi-objective reactive power compensation problem, *International Journal of Electrical Power & Energy Systems,* **43**(1): 313–324.

Ramalinga Raju, M., Ramachandra Murthy, K. and Ravindra, K. (2012). Direct search algorithm for capacitive compensation in radial distribution systems, *International Journal of Electrical Power & Energy Systems,* **42**(1): 24–30.

Sultana, S. and Roy, P. K. (2014). Optimal capacitor placement in radial distribution systems using teaching learning based optimization, *International Journal of Electrical Power & Energy Systems,* **54**: 387–398.

Tabatabaei, S. and Vahidi, B. (2011). Bacterial foraging solution based fuzzy logic decision for optimal capacitor allocation in radial distribution system, *Electric Power Systems Research,* **81**(4): 1045–1050.

Varadarajan, M. and Swarup, K. (2008). Network loss minimization with voltage security using differential evolution, *Electric Power Systems Research,* **78**(5): 815–823.

Wang, R.-t., Yang, Y.-l., Wang, B., Wang, X.-w., Huang, J.-w. and Zeng, S.-z. (2012). Application of optimization algorithm on simulating the fisher fishing in multi-objective optimal reactive power, *Energy Procedia,* **17**: 1482–1489.

YUAN, S. and HAN, S. (2003). *Reactive Power Optimization and Reactive Power Compensation Device*, China Electric Power Press, Beijing.

Zhang, W. and Liu, Y. (2008). Multi-objective reactive power and voltage control based on fuzzy optimization strategy and fuzzy adaptive particle swarm, *International Journal of Electrical Power & Energy Systems,* **30**(9): 525–532.

Zhang, Y. (2009). *Load forecasting based on the decomposition of the daily load curve*, Master's thesis, North China Electric Power University.

Bidding strategies for renewable energy generation with non stationary statistics

S. Sivasakthiselvan, *Department of Electronics and Communication Engineering , NM Institute of Engineering & Technology, Bhubaneswar, s.sivasakthiselavan@live.com*

Swarna Manjari Samal, *Department of Electrical Engineering, Aryan Institute of Engineering & Technology, Bhubaneswar, swarnamanjari88@gmail.com*

Balagoni Sampath Kumar, *Department of Electrical and Electronics Engineering, NM Institute of Engineering & Technology, Bhubaneswar, bs.kumar89@gmail.com*

Durga Prasanna Mohanty, *Department of electrical Engineering , Raajdhani Engineering College, Bhubaneswar, dp_mohanty@yahoo.co.in*

Abstract: The intrinsic variability in non-dispatchable power generation raises important challenges to the integration of renewable energy sources into the electricity grid. This paper studies the problem of optimizing energy bids for a photovoltaic (PV) power producer taking part into a competitive electricity market characterized by financial penalties for generation shortfall and surplus. To this purpose, an optimization procedure is devised to cope with the intermittent nature of PV generation and maximize the expected profit of the producer. Since the optimal offer turns out to be a suitable percentile of the PV power cumulative distribution function (*cdf*), we investigate two approaches to properly take into account the effects of seasonal variation and non stationary nature of PV power generation in the estimation of PV power statistics. The first one normalizes the generated power with the power obtainable under clear-sky conditions. The second approach estimates a time-varying PV power *cdf* using only power data in a moving window of suitable width. A numerical comparison of the different bidding strategies is performed on a real data set from an Italian PV plant.

1. INTRODUCTION

With the increasing penetration level of renewable energy sources (RES), grid system operators have to face more and more challenging technical issues. While RES bring in obvious advantages in terms of production costs and environmental impact, their intrinsic intermittent and non-dispatchable nature causes several difficulties for a correct grid operation. In order to mitigate such problems, several countries are promoting regulatory frameworks forcing the producers to actively participate in the technical and economical integration of renewables [Klessmann et al., 2008]. In an attempt to reduce the uncertainty affecting generation from RES, producers are required to provide day-ahead schedules of their generation. Energy is then remunerated according to the conformity of the actual generation profile to the schedule, by applying financial penalties to shortfall or surplus of energy generation. From a producer perspective, this calls for the development of suitable bidding strategies to offer the maximum amount of energy while avoiding imbalance costs.

Optimal bidding strategies for a wind power producer have been studied in [Bathurst et al., 2002, Matevosyan and Soder, 2006, Pinson et al., 2007, Morales et al., 2010, Dent et al., 2011], and recently in [Bitar et al., 2012]. In a market where penalties are applied whenever the delivered power deviates from the schedule, the optimal bid for a certain hour of the day turns out to be a suitable percentile of the cumulative distribution function (*cdf*) of the power generation at the same hour. Under the assumption of time-invariant statistics of power generation, the *cdf*s can be estimated from all past data of the power generated by the plant. In principle, one could apply the same bidding strategy to other RES. However, some RES like photovoltaic (PV) and hydro are characterized by remarkable seasonal variations of power generation and exhibit a significant non stationary behavior. Such a phenomenon may negatively affect the optimal bidding strategy, if not properly considered.

The main contribution of the paper is to present two approaches to account for the fluctuations of the generated power over the year and thus tune the optimal bidding strategies originally developed for a wind source to the case of a PV producer. The first solution consists in normalizing the generated power with respect to the power that could be obtained from the plant under clear-sky conditions. In the second approach, a moving window on the most recent power generation data is adopted to estimate a time-varying *cdf* of generated power. Both techniques are experimentally compared, in terms of average daily profit, to the straightforward application of the optimal bidding strategy for wind power producers.

The paper is organized as follows. Section 2 presents the mathematical formulation of the bidding problem for a generic non-dispatchable RES and recalls the optimal solution. Section 3 describes the proposed approaches to deal with the non stationarity of the PV power generation statistics. Section 4 reports experimental results obtained under different pricing scenarios using data from a real Italian PV plant. Finally, some conclusions are drawn in Section 5.

2. OPTIMAL BIDDING STRATEGY

In this section we consider a power producer from non-dispatchable RES (e.g. wind, solar), and formulate the problem of finding the optimal energy bids in an electricity market featuring financial penalties for energy imbalance. We also recall the optimal solution to this problem, which is derived in [Bitar et al., 2012] in terms of power statistics and imbalance penalties.

Let w_m be a random variable describing the energy generated by the power plant over the m-th hour of the day, $m = 1, \ldots, 24$, and let C_m denote the corresponding energy bid for the same interval. It is assumed that the power producer is remunerated with unitary price $p > 0$ for the actual generated energy. Moreover, the power producer is penalized whenever the generated energy differs from the bid. In particular, $\bar{q} \geq 0$ and $\bar{\lambda} \geq 0$ are the unitary penalties applied for energy shortfall ($w_m < C_m$) and surplus ($w_m > C_m$), respectively. It follows that the net hourly profit for the power producer amounts to

$$\begin{aligned} J(C_m, w_m) =& p w_m - \bar{q} \max\{C_m - w_m, 0\} \\ & - \bar{\lambda} \max\{w_m - C_m, 0\}. \end{aligned} \tag{1}$$

Since $J(C_m, w_m)$ in (1) is a stochastic quantity due to the uncertainty on the generated energy w_m, the optimal bidding problem consists in finding the bid C_m^* which maximizes the expected profit $\mathbf{E}[J(C_m, w_m)]$, i.e.

$$C_m^* = \arg\max_{C_m} \mathbf{E}[J(C_m, w_m)], \tag{2}$$

where $\mathbf{E}[\cdot]$ denotes expectation with respect to the statistics of w_m. We define $F_m(\cdot)$ the *cdf* of the random variable w_m, i.e. $F_m(\omega) \triangleq \Pr(w_m \leq \omega)$. Moreover, we let $F_m^{-1}(\nu) = \inf\{\omega : F_m(\omega) \geq \nu\}$, $\nu \in [0, 1]$, be the corresponding quantile function. It turns out (see [Bitar et al., 2012]) that the optimal solution to (2) is given by:

$$C_m^* = F_m^{-1}\left(\frac{\bar{\lambda}}{\bar{\lambda} + \bar{q}}\right). \tag{3}$$

Note that the optimal solution (3) depends only on the penalties $\bar{q}$ and $\bar{\lambda}$, and the *cdf* of w_m. If the penalties are stochastic variables independent of the generated energy w_m, the optimal bid (3) still holds by replacing $\bar{q}$ and $\bar{\lambda}$ with their mean values. Concerning $F_m(\cdot)$, in real applications it must be typically estimated from historical energy generation data. As will be discussed in the next section for the specific case of PV power producers, the way $F_m(\cdot)$ is estimated may have an important impact on the practical performance of the optimal bidding strategy (3).

In some cases, deviations from the bid are tolerated within a specified threshold. This applies, for instance, to the regulatory framework recently introduced in Italy. An extension of problem (1)-(2) to the framework with soft penalties is presented in [Giannitrapani et al., 2013b].

Remark 1. In some markets (e.g., the Italian one), it may happen that, depending on the network contingency, $\bar{q} < 0$ and/or $\bar{\lambda} < 0$. This means that deviations from the schedule are actually rewarded, rather than penalized, since they contribute to mitigate the overall network imbalance. In this case, the optimal solution to problem (2) boils down to offering either zero or the maximum producible power (see [Bitar et al., 2012] for details). In this paper, we will restrict our attention to a scenario in which $\bar{q} \geq 0$ and $\bar{\lambda} \geq 0$, so that the existence of a nontrivial solution (3) is guaranteed.

3. NON STATIONARY POWER GENERATION

As recalled in Section 2, the solution of the optimal bidding problem requires the knowledge of the generated power *cdf* at each hour of the day. In real applications, such a distribution is to be estimated on the basis of historical data of generated power. A distinctive feature of renewable sources is that the generated power statistics is strictly dependent on weather variables, e.g., wind velocity and direction for wind plants, or irradiance and air temperature for PV plants. It is well known that meteorological variables exhibit strongly non stationary behavior, which implies that special care must be taken in the estimation of power statistics from historical data.

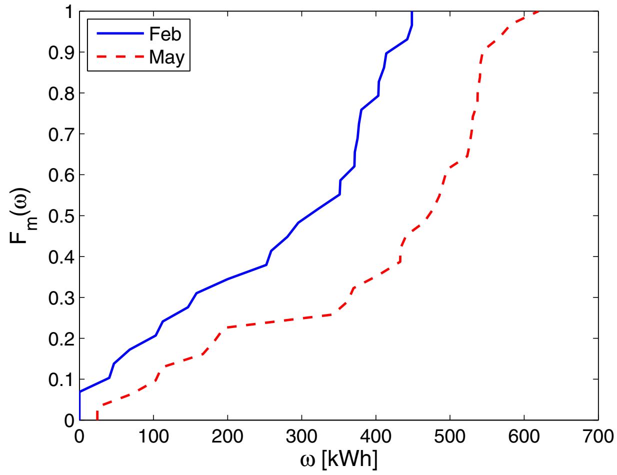

Fig. 1. Example of empirical *cdf* of the random variable w_{11} in two different months of year (solid: February, dashed: May).

With regard to PV generation, which is of concern in this paper, non stationarity is due to the time-varying patterns of solar irradiance in days of different periods of the year. To realize the importance of this issue, consider Fig. 1, which shows the estimated *cdf*s of the energy generated by a 825 kWp PV plant at a certain hour of the day, in two different months of the year, i.e., February and May. For example, it is clear even from a visual inspection of the two curves, that both the maximum and the average generated energy are different in the two cases. To deal with the time-varying nature of the statistics of PV power, we propose two alternative approaches, whose effectiveness will be successively tested on real data in Section 4.

The first approach consists in transforming the past power data according to a multiplicative deseasonalization model exploiting the concept of "clear-sky" power generation profile. This profile can be reliably computed for a PV plant at any fixed day of the year, by assuming that the plant is subject to the maximum solar irradiance achievable at the plant site, i.e., under cloudless sky. Clear-sky solar irradiance can be computed by means of well-known analytical models, e.g., [Wong and Chow, 2001].

The second approach consists in devising an adaptive mechanism for updating daily or weekly the estimates of power *cdf*s. The simple technique adopted consists in estimating the power *cdf* at a given hour based on most recent historical data, by selecting a moving window whose width in the past is optimized according to the best profit obtainable by the bidding strategy.

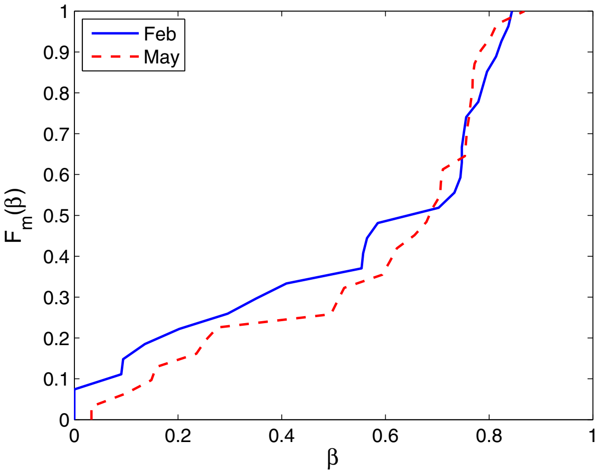

Fig. 2. Example of averaged *cdf*s of the normalized variable β_{11} (solid: February, dashed: May).

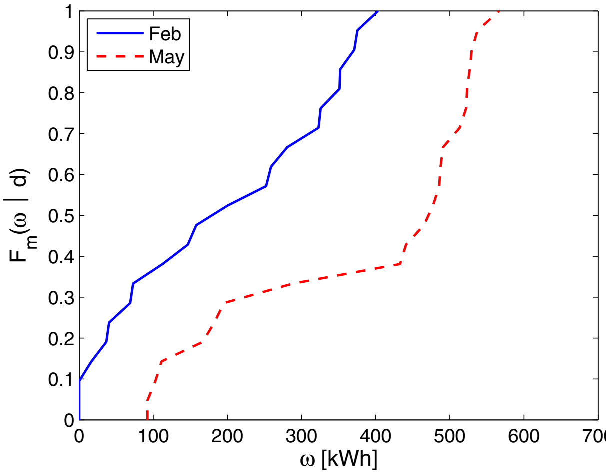

Fig. 3. Example of two moving window *cdf*s: $F_{11}^{(20)}(\omega \mid 46)$ and $F_{11}^{(20)}(\omega \mid 135)$ (solid: February, dashed: May).

3.1 Exploiting clear-sky generation profiles

In the first approach, we choose to normalize both the generated power and the bid at a given hour with respect to the maximum power obtainable from the plant at the same hour, i.e. under clear-sky conditions.

The solar irradiance at ground level takes maximum values in a cloudless day and is defined as clear-sky solar irradiance (I_{cs}). The generation profile of a PV plant hit by clear-sky solar radiation is called clear-sky generation profile (w_{cs}). It can be estimated by using clear-sky solar irradiance and the power curve of PV modules. An analytical form of the power curve of PV modules is provided by the PVUSA model (see [Dows and Gough, 1995]), which expresses the generated power w_m as a function of solar irradiance I_m and air temperature T_m according to the equation:

$$w_m = aI_m + bI_m^2 + cI_mT_m, \tag{4}$$

where a, b and c are the model parameters (typically $a > 0$, $b < 0$, $c < 0$). Although model (4) is linear-in-the-parameters, parameter estimation is complicated by the fact that measurements of solar radiation and air temperature may not be available at the plant site. A heuristic approach to estimate such parameters in the partial information case is presented in [Bianchini et al., 2013], which relies on historical data of generated power, air temperature forecasts and clear-sky solar irradiance. The clear-sky generation profile can be computed from (4) by replacing I_m with the clear-sky solar irradiance $I_{cs,m}$ and T_m with commonly available temperature forecasts.

Let us denote by $w_{cs,m}$ the clear-sky PV energy over the m-th hour of the day (to simplify notation, we omit the dependence of $w_{cs,m}$ on the day of the year), and let $w_m = \beta_m w_{cs,m}$, $\beta_m \in [0, 1]$. Moreover, the bid is parameterized as $C_m = \alpha_m w_{cs,m}$, $\alpha_m \in [0, 1]$. By substituting the expressions of w_m and C_m into (1), we obtain that $J(C_m, w_m) = w_{cs,m} J(\alpha_m, \beta_m)$, where

$$\begin{aligned} J(\alpha_m, \beta_m) =& p\beta_m - \bar{q}\max\{\alpha_m - \beta_m, 0\} \\ & - \bar{\lambda}\max\{\beta_m - \alpha_m, 0\}. \end{aligned} \tag{5}$$

The considered bidding problem can thus be reformulated as finding

$$\alpha_m^* = \arg\max_{\alpha_m} \mathbf{E}[J(\alpha_m, \beta_m)], \tag{6}$$

where $\mathbf{E}[\cdot]$ here denotes expectation with respect to the statistics of β_m. Let $F_{cs,m}(\beta)$ denote the *cdf* of the random variable β_m. Similarly to the previous case, the optimal solution to (6) is given by:

$$\alpha_m^* = F_{cs,m}^{-1}\left(\frac{\bar{\lambda}}{\bar{\lambda} + \bar{q}}\right). \tag{7}$$

The optimal bid is finally computed as

$$C_m^* = \alpha_m^* w_{cs,m}. \tag{8}$$

In this way, the seasonal variations of PV power generation are captured by the clear-sky PV energy profile $w_{cs,m}$. As a consequence, to a first approximation, the resulting normalized energy β_m can be regarded as a stationary process, thus mitigating the adverse effect of seasonality on the bidding strategy. Figure 2 shows the empirical *cdf*s of the normalized generated energy relative to the same hours of the day and months of the year as those of Fig. 1. Note the reduction of the discrepancies between the two curves, if compared with Fig. 1. The main advantage of the proposed bidding strategy is that the power *cdf* can be estimated on the basis of the entire historical data set of the generated power.

3.2 Moving Window

An alternative approach to tackle the non stationary behavior of PV power generation is to estimate the *cdf*s of the random variables w_m by using only the most recent portion of the data set.

Let $F_m^{(L)}(\omega \mid d)$ be the time-varying *cdf* describing the statistics of the random variable w_m estimated from the realizations of the random variables

$$w_{m,d-1}, w_{m,d-2}, \ldots, w_{m,d-L},$$

where $d = 1, \ldots, 365$ is the day the random variable w_m refers to, and L is the width of the window. In this case, the optimal bid for the m-th hour of day d is computed as:

$$C^*_m = F_m^{(L)^{-1}} \left(\frac{\bar{\lambda}}{\bar{\lambda} + \bar{q}} \,\middle|\, d \right). \tag{9}$$

This idea leads to an adaptive mechanism which aims at tracking the seasonal variations by selecting only most recent power data to estimate the *cdf*s. Differently from the approach in Section 2, in which for fixed hour of the day one has always the same *cdf*, independently of the day of the year, here the *cdf* changes every day. Figure 3 shows this adaptation process using a moving window of length $L = 20$ days.

Note that the length L of the moving window must be selected as a suitable trade-off between estimation accuracy and adaptation capability. If L is chosen too large, the effect of removing non stationarity by tracking the seasonal variations is not reached (the conditional *cdf* $F_m^{(L)}(\cdot \mid d)$ tends to resemble the unconditional one $F_m(\cdot)$, i.e. the *cdf* estimated using the whole dataset). On the other hand, if L is chosen too small, the conditional *cdf* turns out to be statistically inaccurate, since it is estimated using few data. In the experimental results of the next section, it will be shown how to tune the width of the moving window by evaluating the performance of the bidding strategy (9) for different values of L.

4. EXPERIMENTAL RESULTS

The performance of the bidding strategies described so far is evaluated in this section using experimental data from an Italian PV plant.

The basic bidding strategy introduced in Section 2 will be denoted by OB. The bidding strategies developed in Section 3, which use different techniques to mitigate the effects of seasonality of PV power generation, will be denoted by OB+N and OB+WI for the approaches exploiting normalization and moving window, respectively. Furthermore, the results obtained with the aforementioned bidding strategies are compared with those of two additional bidding strategies fully exploiting weather forecasts.

The first one, which uses weather forecasts along with the PV power curve (4) to compute the energy bids, will be denoted by WF+PC. This intuitive approach consists in offering the forecast energy derived by substituting the forecasts of solar irradiance and air temperature into the equation of the power curve (4).

The second one, which combines the normalization technique of Section 3.1 and the use of weather forecasts for the classification of the next day, will be denoted by WF+OB+N. In other words, this alternative approach consists in training a classifier which, given energy forecasts for the next day, in the simplest implementation labels the next day as “sunny” or “cloudy”, depending on the level of total daily generated energy. Then, the bid made for that day is the optimal contract computed as in (7)-(8), but using the conditional normalized PV power *cdf* of the corresponding class. The interested reader is referred to [Giannitrapani et al., 2013a] for further details.

The following data from a 825 kWp PV power plant are available:

- generated power w_m,

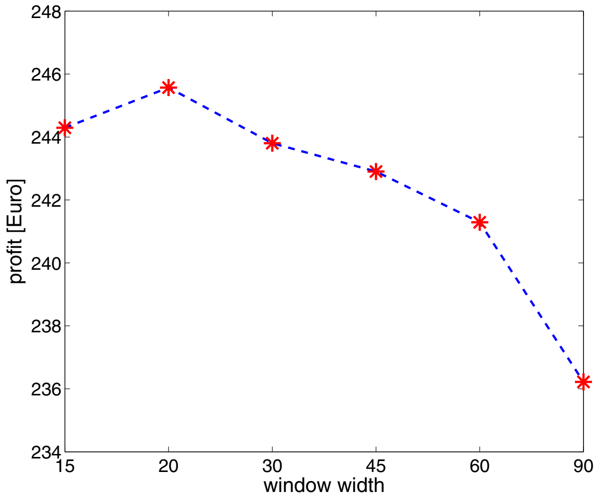

Fig. 4. Average daily profit for the bidding strategy OB+WI in the market scenario where $p = 0.1027$ €/kWh and $\bar{q} = \bar{\lambda} = 0.4p$.

- solar irradiance forecasts $\hat{I}_m$,
- air temperature forecasts $\hat{T}_m$.

The number of days spanned by the data set corresponds to one year of recordings in 2012. The data set is split into a training set (about two third of the data) and a validation set, containing the remaining data.

4.1 Selection of the window width

The performance of the bidding strategy OB+WI depends on the selection of the window width. Figure 4 shows how the results could change significantly for different values of the parameter L. Here, the average daily profits have been computed over the entire year.

The optimal value of the window width is chosen by simply selecting the one providing the highest average daily profit. According to the results shown in Fig. 4, in the next simulations we set $L = 20$ days.

4.2 Optimal bidding strategies

For the bidding strategies OB and OB+N, the training set is used to compute the empirical *cdf*s $F_m(\cdot)$ and $F_{cs,m}(\cdot)$. Then, the bids C_m are computed using (3) or (7)-(8), according to the strategy adopted. Concerning the strategy OB+WI, the bids are computed as in (9), where $F_m^{(L)}(\cdot \mid d)$ is estimated from the data gathered over the most recent L days. The proposed strategies have been evaluated using the data contained in the validation data set under four market scenarios. The values of the

Table 1. Simulation setup.

	$\bar{q} = \bar{\lambda}$
Scenario I	$0.25p$
Scenario II	$0.5p$
Scenario III	$0.75p$
Scenario IV	p

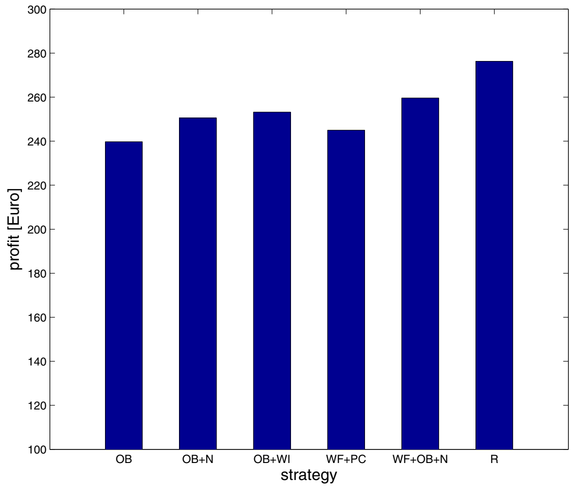

Fig. 5. Average daily profits in Scenario I.

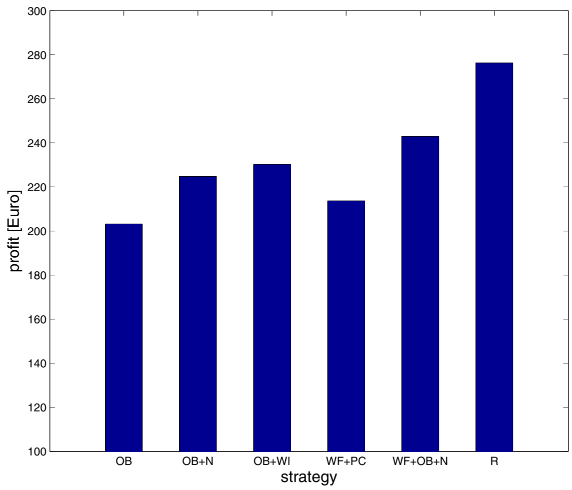

Fig. 6. Average daily profits in Scenario II.

surplus and shortfall penalties are summarized in Table 1 (it is always assumed $\bar{q} = \bar{\lambda}$), whereas the price p = 0.1027 €/kWh is taken to be the same in all scenarios.

The performance achieved by the proposed bidding strategies in the four test scenarios is reported in Figs. 5, 6, 7 and 8. The bars represent the average daily profit computed over 1000 simulations. In each simulation, different training and validation data sets have been obtained by selecting the days belonging to each set randomly but without overlapping. This method avoids that presented results could be biased by a specific choice of the two data sets (e.g. the first eight months as training set and the last four months as validation set).

4.3 Discussion

In all scenarios, OB performs significantly worse than the bidding strategies OB+N and OB+WI. In this respect, the approaches adopted to manage the non stationary behaviour of PV power generation seem to work by enhancing consistently the results of the base line strategy OB. In

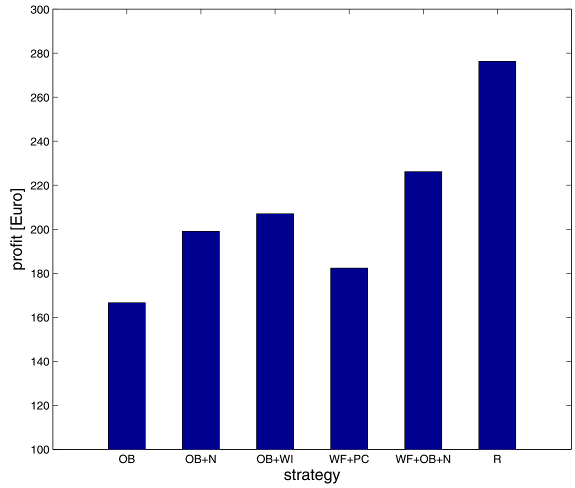

Fig. 7. Average daily profits in Scenario III.

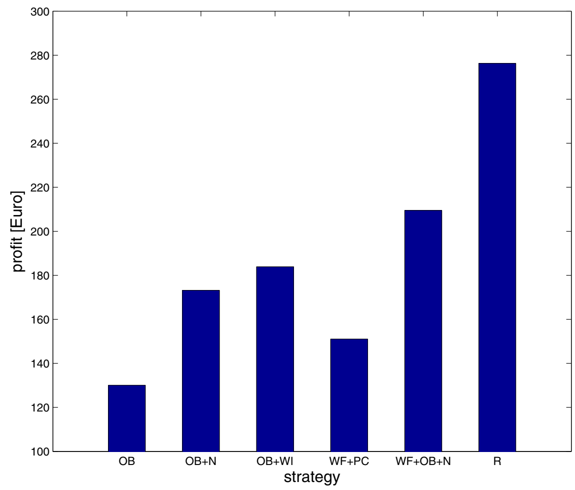

Fig. 8. Average daily profits in Scenario VI.

Scenario I the profit of the PV power producer increases up to 5.3%, in Scenario II up to 11.6%, in Scenario III up to 19.2% and in Scenario IV up to 28.7%. Note that the improvement increases with the entity of the penalty. Moreover, the strategy OB+WI performs slightly better than OB+N.

The strategy WF+PC is ranked poorly with respect to OB+N e OB+WI in all scenarios, despite using weather forecasts. Typically, such a naive approach may lead to unsatisfactory performance because it is strictly dependent on the accuracy of the weather forecasts and does not take into account the price p and the penalties $\bar{\lambda}$ and $\bar{q}$. On the other hand, the strategy WF+OB+N, which overcomes the above mentioned drawbacks through a different use of weather forecasts, turns out to be the most profitable one among all the strategies presented in the paper. We stress that both WF+PC and WF+OB+N exploit the same information, i.e. the weather forecasts provided by a commercial meteorological service. It is apparent that a classification-based approach to the use of weather forecasts turns out to be more robust to forecast errors, whereas the performance of a power curve-based approach degrades quickly as the forecast inaccuracy increases. This makes strategy WF+OB+N particularly favorable when having access to only moderately accurate weather forecasts.

The bar plots in Figs. 5, 6, 7 and 8 show the average results for each scenario. However, it is stressed that we observed profit(WF+OB+N) $\geq$ profit(OB+WI) $\geq$ profit(OB+N) $\geq$ profit(WF+PC) $\geq$ profit(OB) in 98% of the trials.

For comparison purposes, the ideal strategy R is also considered, where it is assumed that the exact generation profile of the next day is known in advance. This makes it possible to evaluate the performance of the proposed bidding strategies with respect to the maximum achievable. Although the profits go down when the penalties raise, for each scenario the bidding strategy OB+WI fills approximately 37% of the gap between OB and R, while WF+OB+N fills 54% of the same gap.

5. CONCLUSIONS

The optimal bidding strategy for a power producer from non-dispatchable renewable energy sources participating in a competitive market with financial penalties for generation imbalance, requires the knowledge of the cumulative distribution function of the power generation. However, when dealing with PV plants, the statistics of the power generation differ significantly over the year according to the seasonality of the solar irradiance. This work has focused on the development of suitable methodologies able to cope with the non stationary nature of PV power gener-ation. Two approaches have been proposed. The first one aims at removing the non stationarity by normalizing the energy generated hourly with the energy obtainable under clear-sky conditions. The second one consists in tracking the actual time-varying cumulative distribution function through the use of a moving window containing the most recent generation data.

Experimental results have shown that both solutions reach comparable performance and provide an effective means to adapt the bidding strategy to the case of a PV power producer. Indeed, a significant increase of the average daily profit has been observed, with respect to the bare application of a bidding strategy which simply neglects the power generation non stationarity. Remarkably, the proposed solutions perform even better than offering the predicted power generation profile computed by substituting the day-ahead forecasts of solar irradiance and air temperature into the equation of the PV plant power curve.

REFERENCES

G.N. Bathurst, J. Weatherill, and G. Strbac. Trading wind generation in short term energy markets. *IEEE Trans. Power Systems*, 17(3):782–789, 2002.

G. Bianchini, S. Paoletti, A. Vicino, F. Corti, and F. Nebiacolombo. Model estimation of photovoltaic power generation using partial information. In *Proc. of 4th IEEE PES Innovative Smart Grid Technologies Europe*, Copenhagen, DK, 2013.

E.Y. Bitar, R. Rajagopal, P.P. Khargonekar, K. Poolla, and P. Varaiya. Bringing wind energy to market. *IEEE Trans. Power Systems*, 27(3):1225–1235, 2012.

C.J. Dent, J.W. Bialek, and B.F. Hobbs. Opportunity cost bidding by wind generators in forward markets: Analytical results. *IEEE Trans. Power Systems*, 26(3): 1600–1608, 2011.

R.N. Dows and E.J. Gough. PVUSA procurement, acceptance, and rating practices for photovoltaic power plants. Technical report, Pacific Gas and Electric Company, San Ramon, CA, 1995.

A. Giannitrapani, S. Paoletti, A. Vicino, and D. Zarrilli. Exploiting weather forecasts for sizing photovoltaic energy bids. In *Proc. of 4th IEEE PES Innovative Smart Grid Technologies Europe*, Copenhagen, DK, 2013a.

A. Giannitrapani, S. Paoletti, A. Vicino, and D. Zarrilli. Wind power bidding in a soft penalty market. In *Proc. of 52nd IEEE Conf. on Decision and Control*, Florence, IT, 2013b. To appear.

C. Klessmann, C. Nabe, and K. Burges. Pros and cons of exposing renewables to electricity market risks - A comparison of the market integration approaches in Germany, Spain, and the UK. *Energy Policy*, 36(10): 3646–3661, 2008.

J. Matevosyan and L. Soder. Minimization of imbalance cost trading wind power on the short-term power market. *IEEE Trans. Power Systems*, 21(3):1396–1404, 2006.

J.M. Morales, A.J. Conejo, and J. Perez-Ruiz. Short-term trading for a wind power producer. *IEEE Trans. Power Systems*, 25(1):554–564, 2010.

P. Pinson, C. Chevallier, and G.N. Kariniotakis. Trading wind generation from short-term probabilistic forecasts of wind power. *IEEE Trans. Power Systems*, 22(3): 1148–1156, 2007.

L.T. Wong and W.K. Chow. Solar Radiation Model. *Applied Energy*, 69:191–224, 2001.

biDeepFM: A multi-objective deep factorization machine for reciprocal recommendation

Sanjay Kumar Padhi, *Department of Computer Sciencel Engineering, Aryan Institute of Engineering & Technology, Bhubaneswar, sk.padhi2@gmail.com*

Subrat Dash, *Department of Computer Scinece Engineering , Capital Engineering College, Bhubaneswar, subratdash43@gmail.com*

Niladri Bhusan Biswal, *Department of Computer Scinece Engineering , Raajdhani Engineering College, Bhubaneswar, niladribiswal26@gmail.com*

Rashmita Panigrahi, *Department of Computer Scinece Engineering , NM Institute of Engineering & Technology, Bhubaneswar, rashmitapanigrahi116@gmail.com*

A B S T R A C T

In this paper, we propose a multi-objective learning approach for online recruiting. Online recruiting and online dating are the most known reciprocal recommendation problems. However, the reciprocal recommendation has gained little attention in the literature due to the lack of public datasets consisting of reciprocal preferences of users in a network. We aim to resolve this shortage in our study. Since the satisfaction of both candidates and companies is indispensable for successful hiring as opposed to traditional recommenders, online recruiting should respect to expectations of all parties and meet their common interests as much as possible. For this purpose, we integrated our multi-objective learning approach into various state-of-the-art methods, whose success has been proven on similar prediction problems, and we achieved encouraging results. We named and proposed one of the prominent architectures that we've tested on the problem as a prototype of our multi-objective learning approach however our approach is applicable to any recommender system employing neural networks as its final decision-maker.

Keywords:
Recommender systems
Reciprocal recommendation
Online recruiting
Personalization
Explainable recommendation
Learning latent representation
Neural networks
Deep learning

1. Introduction

Online services, such as social media and e-commerce platforms, have gained impressive popularity, and thus, the number of users and the volume of content in such systems have rapidly increased. The existence of such systems with numerous users around the world has led to the emergence of massive data sources that makes it difficult for users to reach relevant information. Recommender systems have been developed to help users to overcome this information overload problem by increasing their chance to reach valuable information in a personalized fashion. In this sense, *Memorization* and *generalization* capabilities play essential roles in the success of recommender systems. Memorization is recalling the frequent co-occurrence of interactions and then utilizing the correlations known from the interaction history. Yet, by increasing the utility of correlations, exploring new feature combinations that have never or rarely seen in the historical data defines generalization and it may help more to model taste of user without being bounded by their small world. Accordingly, while memorization usually offers more local recommendations and so coherence, generalization is inclined to offer diverse recommendations. These two are essential properties of a prospering recommender system.

Job recommendation is a highly attractive application of recommender systems because of global changes that emphasize the importance and the necessity of fast and convenient recruiting. During the job-hunting process, directing candidates to the jobs they are ideal for and fulfill their expectations, not only shortens idle-waiting or seeking-time but also helps companies to be agile. Unlike traditional recommenders, a job recommendation should satisfy both parties involved, which makes it a reciprocal recommendation problem. Besides offering relevant jobs to people based on their interests and skills, a good job recommender should consider their chance of being hired for the job as well. In this problem, companies are the decision-makers, thus meeting their expectations is a prerequisite for the satisfaction of candidates. Accordingly, successful modeling of the recruiter's interest is much more critical for a job recommendation. For these reasons, a thriving recommender system for recruiting requires feedback from both the candidates and companies to model their preferences. The feedback of a candidate can be extracted from the candidate's applications. However, most companies are reluctant to give feedback about their interests in candidates. Thus, a reciprocal recommender system designed for recruiting websites should generate recommendations relying on a few available information from company preferences. In this paper, we propose a novel method to tackle this problem and to expel the sparsity of recruiters' interest by exploiting inferences under the domain knowledge.

In this study, we work on a reciprocal job recommendation problem. Reciprocal recommenders, as in online dating and online recruiting applications, pose new challenges that distinguish them from traditional recommenders. Ref. [1] summarizes these challenges as follows:

- Reciprocity: A successful recommendation depends on bilateral preferences, not solely on user preference who receives the recommendation.
- Capacity: In traditional recommenders, there is no limit on being preferred, e.g., a movie can be liked by thousands of users in a movie recommender system. However, in reciprocal recommenders, parties have limited availability towards other parties, e.g., an employee can simultaneously work at one or two jobs but certainly not at dozens of jobs.
- Limited-activity: In reciprocal recommenders, many users do passively use the system, for example, candidates in a job recommender system have to be selective because the interviewing process costs a waste of effort if the job is not really desirable by the candidate. To have a high recruitment rate in such a system and encourage people to use it, considering the limited activity of the users, is one of the key factors in reciprocal recommenders.
- Sparsity: Users in reciprocal communities would probably not come back to the system at least for a while if they are engaged to their preference. Therefore, reciprocal recommender systems suffer from insufficient activity considering large space shaped by a vast number of users and items.

Our proposed framework is designated for reciprocal recommendation, which cannot be easily come through by traditional recommenders. The framework uses multi-objective optimization that has been applied in many fields of science [2–4], including engineering, economics, and logistics, yet not applied in the reciprocal recommendation. The contribution of this work is summarized below:

1. We propose a generalized reciprocal recommendation framework, in which various challenges are tackled, e.g., reciprocity, capacity, limited-activity, and sparsity.
2. We perform an empirical evaluation on a real-world reciprocal data set to demonstrate the effectiveness and efficiency of our proposed framework.
3. Our proposed approach not only outperforms existing state-of-the-art approaches for prediction but also offers good explainability.

The outline of this work is as follows. Section 2 presents a brief summary of prior work relevant to the use of deep neural networks in recommender systems and reciprocal recommenders. In Section 3, we formalize the problem and introduces the details of the prototype of our proposed framework. In Section 4, we describe the experimental setup used in the experiments, including dataset preparation, negative sampling, and evaluation protocols. We then discuss the performance results in Section 5. Finally, Section 6 presents the outcomes of this study by a brief conclusion based on the empirical evaluation and also states the projected future works.

2. Related work

With the tremendous success of the deep learning in vision and language processing in recent years, by confirming the rapidly grown interest in machine learning in general, deep learning techniques have started to direct the tendency in recommender systems as well as other application domains. Unlike the conventional methods (e.g. matrix factorization), deep learning can effectively capture the non-linear and non-trivial feature interactions, and generalize interactions to avoid deterioration of the learning process due to the unseen feature combinations. For this reason, we also utilize deep learning techniques to solve reciprocal recommendation problem. In this section, we will briefly review key researches closely related to our work, including recommender systems with the deep learning aspect and reciprocal recommendation.

2.1. Deep neural networks in recommender systems

Feature engineering is the process of creating features from raw data by using domain knowledge in order to make machine learning algorithms work effectively, however, it is a time-consuming process and thus expensive. It has been accepted as an inevitable process of machine learning until recent years that deep learning achieved tremendous success against the carefully crafted feature detectors [5]. In recommender systems, various prospering methods avoiding extensive task-specific feature engineering have been proposed, mostly based on embeddings and neural networks. To learn high-order feature interactions, PNN [6] employs a pairwisely connected product layer on top of the embedding layer and sends the product vector to the succeeding fully-connected layer which is the first hidden layer of the architecture. Deep neural networks (DNN) have better generalization capability to unseen feature combinations through low-dimensional dense embeddings. However, they tend to over-generalize when data is sparse. To defeat this drawback, the Wide & Deep network [7] by Google is proposed as a concept. To model low- and high-order feature interactions simultaneously, they jointly trained wide and deep architectures on app recommendation. In addition to the generalization of DNN, Wide & Deep benefits from the memorization of linear models through a wide set of cross-product feature transformations. Memorization of feature interactions is effective and still interpretable in opposition to design pairwise feature interactions requiring manual labor and also resulting in increased complexity.

In later research, DeepFM [8] replaced the linear part of Wide & Deep with a neural network-based Factorization Machine (FM) while both FM and DNN parts are sharing the same feature embeddings. The sharing strategy of feature embedding lets the learning of feature representations to be influenced by both low- and high-order feature interactions via back-propagation. By doing so, the DeepFM model is able to make more precise recommendations on click-through-rate (CTR) prediction. FM is one of the most promising methods in the recommender systems area for years and feature engineering in conventional machine learning has been replaced by architecture engineering in deep learning. Therefore, there are many valuable attempts to use FM and DNN in varying setups. While NFM [9] applies DNN to learn high-order interaction on top of an FM network, FNN [10] takes advantage of FM to learn latent vectors, then utilizes them to initialize the embedding vectors feeding the first layer of DNN.

Attention mechanisms are first introduced by [11] for sequence modeling in the area of machine translation. These mechanisms allow the neural networks to attend to different parts of the input at each step so that the network can focus on both local and global features to have a broader understanding. After their proven success in vision and natural language processing, attentions are applied to recommender systems as well. In this regard, AFM [12] uses a simple multi-layer perceptron (MLP) to learn the strength of attention to the feature interactions. Unlike traditional

FM, which uniformly sums up the inner product of embedding vectors, it adjusts the importance of products and applies a weighted sum. AutoInt [13] uses a multi-head attention mechanism to model the different order feature interactions. Recently, attention mechanism is widely applied in various domains to increase personalization, including channel recommendation, resource recommendation for online learners [14–16]. We found these attempts very inspiring because the recommendation problem in definition already aims to find out the user's attention.

In the era of data, integrating complex data sources into recommender systems has been intended to supply more information to the learning process. However, extracting valuable information from these complex objects may be difficult. As discussed until here, previous works focused on mining from the recommended features, not on finding out the best features to contribute more to the mining process. A recent research, FGCNN [17], focused solely on feature learning by an automatic process. FGCNN uses Convolutional Neural Networks (CNN) to detect local patterns and generate new features from their combinations. These attempts point out the importance of automated feature learning by powerful computers.

2.2. Reciprocal recommendation

The earliest reference to reciprocal recommendation is done by Luiz Pizzato et al. [18] as a particular case of recommender systems. It is originally designed for online dating systems where people have the common goal of finding a partner. Finding friends, colleagues, communities to follow on social networks; matching mentors and mentees for information sharing; or any other matching applications in recommender systems are possible problems to solve with the reciprocal recommendation. In such systems, the preferences of both users participated are mutually considered and satisfied at the same time.

On a social networking website, Ref. [19] presents a method to combine both sender and recipient interest with a weighted harmonic mean. Ref. [20] proposes a content-based recommender for online dating (RECON) to predict the reciprocal compatibility of user pairs based on their profiles and actions. In their following work, RECON is extended to consider both positive and negative preferences [21], and collaborative filtering is applied with a stochastic matching algorithm [22].

Later approaches focus on graph-based solutions. Ref. [1] models the correlations of users as a bipartite graph by using both local utilities captured by bilateral preferences and global utilities extracted from the entire reciprocal network. Then, it proposes a generalized framework for a reciprocal recommendation in online dating and online recruiting. Ref. [23] takes the reciprocal links in the interaction graph into account and performs better in recommending both initial and reciprocal contacts for online dating. Ref. [24] formulates the user reply prediction as a link prediction problem of social networks. An edge (or link) in the constructed network may represent either an initial contact message or a reply to an initial contact message. Their reply prediction problem is to accurately predict whether a reciprocal link will occur given an initial contact link between two users and the current bipartite directed network. They compared several machine learning algorithms on this setup using content features from user-profiles and also graph-based features from interaction history. CoupleNet [25] redefines the problem as a stable relationship recommendation and seeks for the long-term and serious relationship instead of finding users that might reciprocate to each other. By considering users' attention, CoupleNet creates user representations based on users' social posts, i.e. tweets, and estimates their compatibility using cosine similarity.

Online recruiting where one group of users (candidates) aims to find a job and another group (companies) aims to find an employee for their needs is another example application of reciprocal recommendation. As opposite to online dating, online recruiting has received little attention in the literature. To find out the best matches in an online recruiting system, Ref. [26] builds two independent recommender systems: to recommend candidates to particular jobs of a recruiter, and to recommend jobs to a particular candidate. The natural behaviors of users in the system are used as training data. A recruiter manually labels the candidates as either a fit or a not-fit for their open positions; on the other hand, a candidate ranks the jobs to specify how well the position meets their preferences. Expectation–Maximization is used to build a prediction model for both recommender systems and achieved a promising performance on predictions of hiring. In a similarity-based reciprocal system [27], attributes, explicit and implicit preferences of users are used to strengthen recommendations via a better similarity calculation between entities. Differently, [28] adds bidirectional feedbacks to users' actions to calculate the similarity between the job seeker and the recruiter. The response of the user is considered as positive or negative feedback about the other user contacted. By using the bi-directional feedback exchanged between users, the method updates the similarity score between users and then creates a ranked list for each user based on similarities. Yet another similarity-based model, *MAJORE* [29], reported improved matching performance between jobs and resumes by using deep neural networks in cold start mode.

In respect to common approaches in the reciprocal recommendation, the proposed systems are either similarity-based or bonding a pair of independent recommended systems for reciprocity. In this work, we propose a novel approach based on deep learning methodology that efficiently assembles multiple aspects to have a compact and viable reciprocal model for online recruiting. As verified with experiments, jointly learning different aspects not only empowers overall recommendation quality but also enables learning from sparse data which is a common case when interactions of the reacting side are scarcely any or hard to acquire. Additionally, it is capable of giving explainable recommendations.

One issue that should be tackled in the reciprocal recommendation is to find a dataset to evaluate your model. For example, in online recruiting, [1] used Xiamen Talent Service Center data, and RecSys Challenge in 2017 made XING data available only for participants. The aim of RecSys Challenge is to identify users that may be interested in receiving a given job posting as a push recommendation and that are also appropriate candidates for the given job. However, these are not publicly available to other researchers due to the company's concerns. Therefore, as in other reciprocal recommendation studies, we could report our results on a single dataset given us under a nondisclosure agreement.

3. Bi-objective deep factorization machine

In the following sections, we first define the problem by introducing all parameters and representations used in this research, then present our proposed approach to the problem.

3.1. Problem statement

The problem that is handled in the research and our formulation to solve it by multi-objective learning is given below. The purpose of the reciprocal recommendation is to recommend relevant job postings to candidates, and relevant candidates to recruiters for their job postings by maximizing their satisfaction. The primary indicator of the satisfaction of both sides is to increase the hiring rate in the dataset. Thus, given the properties of a candidate and a job posting, a prospering model coherently gives a higher value for a true match between the pair. Each instance refers to an interaction between a candidate and a company through a respective job, either a single-acting or a reciprocal interaction.

Suppose the training dataset consists of N instances like $\mathcal{X}^{(i)} = (x^{(i)}; y_{candidate}, y_{company})$, where $i = [1, \dots, N], x^{(i)} \in \mathbb{R}^{n}_{x}, n_x$ is the input size, and $\{y_{candidate}, y_{company}\} \in \{0, 1\}$ is the associated labels indicating the interest of the candidate (a.k.a. job-seeker) and the company (a.k.a. recruiter), respectively. $y_{candidate}$ is 1 if the candidate clicks the job posting of the company, and 0 otherwise. Similarly, $y_{company}$ is 1 if the company views the phone number of the candidate, and 0 otherwise. Requesting the phone number of a candidate is assumed as a positive interaction of companies to candidates because it is the only way to contact a candidate for a possible interview. Besides, there is no mechanism on the recruiting website to collect information from companies about their preferences since companies are not reluctant to share such information. $\forall i, \mathcal{X}^{(i)}$ refers to an interaction between the candidate and the company through a job posting and $x^{(i)}$ is derived from the concatenation of features of candidate and job posting. $x^{(i)}$ may include categorical (e.g., gender, provinces, education) and numerical information (e.g., age). Each categorical field is represented as a vector of one-hot encoding, or multi-hot encodings if there are multiple choices, and each numerical field is represented with a normalized value or a vector of one-hot encoding after discretization. Then, assuming $x^{(i)}$ is an m-fields input where m refers to the total number of features in the interaction and all fields are l-dimensional vectors, each instance $\mathcal{X}^{(i)}$ is converted to $(x^{(i)}; y_{candidate}, y_{company})$ where $x^{(i)} = [x_1, x_2, \dots, x_j, \dots, x_m]$ is an n_x-dimensional vector $(\mathbb{R}^{n}_{x}; n_x = m \times l)$, x_j is the vector representation of the j-th field of $x^{(i)}$. Normally, $x^{(i)}$ is high-dimensional and extremely sparse. The task of reciprocal recruitment prediction is to build a prediction model $(\hat{y}_{candidate}, \hat{y}_{company}) = f(x^{(i)})$ to jointly estimate the probability of a candidate applying a specific job posting in a given context and the probability of a recruiter calling a specific candidate in the same context, respectively.

3.2. Model

We aim to predict both candidate and company interest while focusing on the company aspect because companies are the decision-makers of the recruitment process and also finding a perfect match passes through their decisions. For this aim, we propose a multi-objective learning framework shown in Fig. 1 for the reciprocal recommendation on online recruiting platforms. The model in the framework may be any neural-network-based model that gets a sparse list of features in an interaction input and creates a signal referring likelihood of this interaction to become true. By inheriting this approach, we create a prototype, bi-objective deep factorization machine (biDeepFM), a wide and deep network that takes advantage of memorization and generalization capabilities at the same time. As depicted in Fig. 2, biDeepFM optimizes two outputs; job recommendation for candidates ($y_{candidate}$) and candidate recommendation for companies ($y_{company}$). Both objectives are powered by the same input, embedding layer, and network. This shared network consists of an FM to learn low-order feature interactions and a DNN to learn high-order interactions. Its prediction layer can be written as follows:

$$\hat{y}_{candidate} = sigmoid(y_{FM} + y_{DNN}) \quad (1)$$

$$\hat{y}_{company} = sigmoid(y_{FM} + y_{DNN}) \quad (2)$$

where $\hat{y}_{\{candidate,company\}} \in \{0, 1\}$ is the predicted interest, y_{FM} is the output of FM component, and y_{DNN} is the output of DNN component.

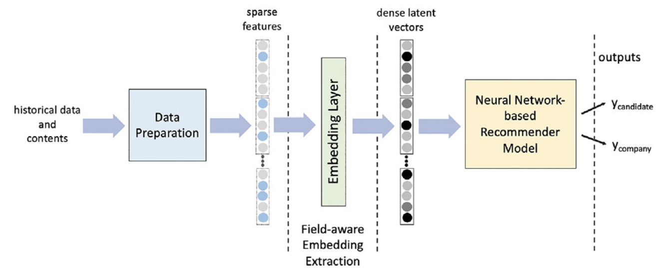

Fig. 1. The framework of the multi-objective learning approach for the reciprocal recommendation. The details of the data preparation step are given in the following sections.

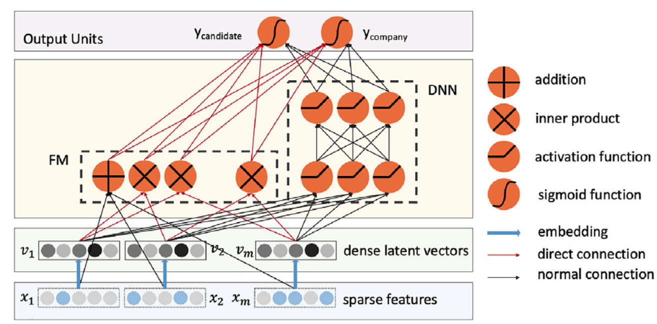

Fig. 2. The network architecture of the biDeepFM model. The candidate and company component share the same input raw feature vector and network layers, which enables biDeepFM to better learn feature interactions of candidates and jobs to model the company aspect. The gray and blue circles in the sparse features represent one and zero entries in the encodings (one- or multi-hot) of raw inputs, respectively. A normal connection in black refers to a connection with weight to be learned; a direct connection, red arrow, is a connection with weight 1 by default; embedding, blue thick arrow, means a latent vector to be learned.

The FM component is a factorization machine, which is first proposed by Rendle [30] to explicitly learn feature interactions for recommendation. The output of the FM component is calculated as follows:

$$y_{FM} = t \cdot f(X) = w_0 + \sum_{i=1}^{m} w_i x_i + \sum_{i=1}^{m} \sum_{j=i+1}^{m} \langle \mathbf{v}_i, \mathbf{v}_j \rangle x_i x_j \quad (3)$$

$$\langle \mathbf{v}_i, \mathbf{v}_j \rangle = \sum_{f=1}^{l} v_{i,f} \cdot v_{j,f} \quad (4)$$

where $w_0, \forall w_i$ and $\forall v_i$ are the model parameters that have to be learned. l equals to the embedding-size, m refers to the number of field and t is just a hyper-parameter to define the trade-off between the FM and DNN components, but we set t to 0.5 to let them affect the overall recommendation performance equally. While w_0 is the global bias, w_i describes the strength of feature i, so the first sum $(\sum_{i=1}^{m} w_i x_i)$ incorporates the direct impact of features into the model. x_i and v_i respectively refer to the sparse features and the dense latent vector representation (or embedding) of i-th feature, and $\langle \mathbf{v}_i, \mathbf{v}_j \rangle$ is the dot product of v_i and v_j that models the interaction between the i-th and j-th features. Hence, the second sum $(\sum_{i=1}^{m} \sum_{j=i+1}^{m} \langle \mathbf{v}_i, \mathbf{v}_j \rangle x_i x_j)$ involves the effect of pair-wise interactions in decision making. After jointly learning embeddings through both components, $\langle \mathbf{v}_i, \mathbf{v}_j \rangle$ is easily computed as in Eq. (4).

E.

The output of DNN component is calculated as follows:

$$\begin{aligned} y_{DNN} &= (1-t)\cdot f(X) = \phi_n \\ \phi_n &= \alpha_n\left(W_n^T\phi_{n-1}+b_n\right) \\ &\vdots \\ \phi_2 &= \alpha_2\left(W_2^T\phi_1+b_2\right) \\ \phi_1 &= \alpha_1\left(W_1^T X+b_1\right) \end{aligned} \tag{5}$$

where $\forall\alpha_i$ are the ReLU activation functions, except the final α_n which is a sigmoid, W_i and b_i denote the weight matrix and bias vector, respectively.

To learn the parameters in our model, we used the following multi-objective optimization formula which minimizes the cumulative empirical error of the output functions through a set of shared and task-specific parameters.

$$\min_{\boldsymbol{\theta}, \boldsymbol{\theta}^1, \ldots, \boldsymbol{\theta}^T} \sum_{t=1}^{T} w^t \hat{\mathcal{L}}^t(\boldsymbol{\theta}, \boldsymbol{\theta}^t) \tag{6}$$

where T is the number of tasks, w^t and $\hat{\mathcal{L}}^t$ respectively are the weight and the empirical loss of the task t; $\boldsymbol{\theta}$ and $\boldsymbol{\theta}^t$ refer to the shared and the task-specific set of parameters. Since the objectives share the same layers till the end of the network, the task-specific parameters only comprise the weights of the last layer of the network, which are connected to the sigmoid functions and define y_{FM} and y_{DNN} in both aspects. To measure the loss per task, we utilize cross-entropy (a.k.a. *LogLoss*) metric. The cross-entropy is an error measure when a network output can be interpretable as an independent hypothesis (e.g. interaction between candidate and company in our case) and the final activation refers to the probability that the hypothesis might be true. It measures the distance between the predicted probability and empirical distribution. Over and above, cross-entropy also deals with the vanishing gradient problem from which deep neural networks suffer. For binary classification problems where targets are either 0 or 1, it is calculated as follows:

$$LogLoss = -\frac{1}{N}\sum_{i=1}^{N}(y_i\log(\hat{y}_i) + (1-y_i)\log(1-\hat{y}_i)) \tag{7}$$

where y_i and $\hat{y}_i$ are ground truth of user interest (candidate or company) and estimated interest respectively, and N is the total number of training instances. During the training, the model parameters are updated via minimizing the weighted LogLoss using gradient descent.

It is worth pointing out that thismodel is capable of learning different order feature interactions by its parameters to be tuned during the training. For a feature i, a scalar w_i is used to learn its direct (first-order) impact. This linear part which is represented by an addition sign in Fig. 2 is a sub-function of the FM component. The latent vector representation of this feature, v_i is fed into both FM and DNN components, and by doing so, it is utilized to model second-order and high-order interactions of feature i with other features, respectively. Relying on the insights of the Wide & Deep [7], learning low- and high-order feature interactions simultaneously is expected to provide advancement over the attempts of learning either alone. Accordingly, learning aspect-dependent feature interactions simultaneously by multi-objective learning can additionally improve the reciprocal recommendation. The effectiveness of multi-objective approach is tested and evaluated in Section 5.1.

The number of parameters to be learned is completely the same as the single-objective network of the same architecture because the only change in multi-objective network is a sigmoid extension as output for each objective in Eqs. 1 and 2. Since the two objectives are simultaneously trained without increasing the complexity, multi-objective learning for reciprocal recommendation is more efficient than single-objective learning of the candidate and company aspects. The efficiency is investigated in Section 5.2.

The advantage of having an FM component to traditional approaches is the ability to work better, especially on sparse datasets. Previous methods before the emergence of factorization machines need to have both features i and j in a training instance at least once to learn the impact of their interaction. If they do not appear together even for once as is quite often in sparse datasets, their relation stays unknown and thus degrades the prediction performance. FM can train the relevant latent vectors whenever i or j appears in instances with no dependency over each other, then easily measure their relation by an inner product of their latent vectors v_i and v_j. Moreover, by means of explicit learning, it offers explainability as discussed in Section 5.3 and gives insights about user's decisions.

Reciprocity is the primary consideration in our approach since the proposed multi- objective learning jointly models the interests of both sides. Furthermore, by offering candidates to the jobs that they have a higher chance of being hired and directing candidates to the jobs that they will be interested in, our approach aims to decrease the number of false attempts on the recruitment process and to increase the hiring rate. Thus, this approach can help to candidates and recruiters by filling their capacity only with true matches without intervening in their limited-activity habit.

Two types of interaction are concurrently used in learning, and so the valuable information exists here intensify each other. Sparsity makes a challenge for many recommendation problems, but our model can help to alleviate sparsity by concurrent use. How we tackle the sparsity in our problem is explained in Section 4.1.

4. Experimental setup

4.1. Dataset statistics

The online recruiting dataset used in our study is obtained through a collaboration with Kariyer.Net, the largest online recruiting website in Turkey. Candidates use *Kariyer.Net* to find a suitable job, and recruiters use *Kariyer.Net* to find the right candidate for a job on behalf of their companies. We evaluate the effectiveness and efficiency of our proposed model on a dataset constructed of user profiles, job postings and user behaviours on this website in a limited time frame. Table 1 gives a brief summary of the dataset. Single links refer to the initial interaction of candidates (e.g. applying for a job); the positive interactions of recruiters (e.g. viewing candidate's phone number) are called reciprocal links.

As can be seen above, reciprocal links are extremely sparse in comparison to the number of candidates and jobs in the system. To model company interest and recommend favorable candidates to their recruiters is not feasible when only the known positive interactions of companies are used. Note that getting feedback directly from companies is not an option for the *Kariyer.Net* website since the recruiters leave the system once they get enough information to reach out to promising profiles, like the phone numbers of candidates. Therefore, positive interactions are extracted from the recruiters' behavior on the system by inference and domain knowledge, but yet an inadequate amount of feedback. Our multi-objective approach to the problem lets us model company interest even with a small amount of information by boosting the company feedback with the candidate feedback, which is comparatively generous.

Table 1
The summary of the dataset.

Dataset	Candidate#	Job#	Single-links#	Reciprocal-links#
Kariyer.Net	20,283	16,134	383,434	9,081

Table 2
Features in the dataset.

Feature (candidate)	Feature (job)	Feature type	Representation
id military service work status gender driving licence	id gender hidden posting position type language driving licence	categorical	one-hot encoding
education faculty university province	education military service industries provinces	categorical	multi-hot encoding
age	min experience max experience position level hiring capacity	numerical	$\{x \mid 0 \leqslant x \leqslant 1\}$

4.2. Dataset preparation

The dataset consists of numerical and categorical data types. To make its features meaningful and applicable for the recommendation task, we first applied some preprocessing steps, such as noise-cleaning, we then performed feature transformations Depending on the implementation details varying between the versions of the online recruiting website, there are many outliers and missing information in the data. We removed such outliers from the data and filled missing information with a common appropriate value per feature to indicate its loss. All features are transformed into proper representations in regard to their types. After preparation, each feature becomes a part of the input to the model, such as x_m given in the problem statement (Section 3.1) and shown in the illustration of the prototype (Fig. 2). Features that exist in the dataset are listed in Table 2 along with their types and representations as a reference for the rest of the paper. Apparently, a feature listed in the candidate's side is an attribute of candidates, while job features define desired attributes of candidates for a specific position. Feature names already give their semantics, however, some of them may be confusing and we would like to make them comprehensible. For instance, "military service" can be a single status entry for candidates, i.e. *completed*, *unfinished*, whereas companies may ask for multiple options, and "hiring capacity" refers to the number of employees to be hired for a specific job posting. For normalization of numerical values that are measured on different scales, outliers are removed by considering their statistics, then they are adjusted to the $[0, 1]$ scale.

Neural networks, as well as many other machine learning algorithms, require numeric input and output variables. To that end, the most primitive solution to use categorical features is to transform them into integer labels, a.k.a. integer encoding, where each category is represented by unique numbers. However, integer values have ordinal relationships between each other, whereas no such relation exists in categorical variables, so the learning process may result in poor performance. Therefore, we converted categorical features into one-hot or multi-hot representations that work better with learning algorithms. Depending on our implementation, the dense embedding layer gets a list of categories from one-hot and multi-hot sparse features as its input. In order to feed the dense embedding layers with inputs in equal length, we had to limit the number of represented categories per multi-hot feature based on the occurrence statistics given in Table 3.

4.3. Negative sampling

In some applications of recommender systems such as job recommendation and music recommendation, users do not reflect their negative preferences since the system is designed to allow positive interactions only. While there are some exceptional algorithms working fine with binary data, in many studies negative interactions have been artificially generated by inference to benefit from a wide range of algorithms in the literature [31]. As our original dataset as well contains positive instances only which means a true interest between a candidate-company pair, we sampled two negative instances per positive instance to ensure the generalization capability of the predictive model as is applied in [9]. For the interest of candidates, we randomly sampled two jobs that the candidate has not applied yet; for the interest of companies, we randomly sampled two candidates that have not been called yet for their jobs. The target value of 0 is assigned to each negative instance in sampling while positive instances already have the target value of 1. By this means, cases that $(y_{candidate}, y_{company}) = (0, 0)$ are added for the candidate interest; and cases that $(y_{candidate}, y_{company}) = (1, 0)$ for the company interest.

4.4. Evaluation protocols

We randomly divided the dataset into three parts of training (70%), validation (10%) and test (20%) as in many studies. The training set is used for training the models, the validation set is used for hyper-parameter tuning and the test set is used for performance reporting. To evaluate the performance of different models in terms of effectiveness, we adopted two popular metrics used in previous researches [13,8,6,17]: (1) LogLoss defined by Eq. (7) and (2) Area Under ROC (AUC).

Table 3
Occurrence statistics of features along with the number of represented categories ("length") for each multi-hot feature.

Object	Feature	Max	Mean	Std	Length
jobs	education	12	4.1100	2.2337	6
	provinces	82	2.5023	8.5675	10
	industries	6	1.4352	0.9516	2
	military service	4	1.4525	0.6708	2
candidates	education	2	1.0381	0.1913	2
	faculty	7	1.3930	0.6402	2
	university	6	1.3644	0.5945	2
	province	5	1.0390	0.2041	2

- **LogLoss** or binary cross-entropy is an indicator of the divergence of prediction probabilities from actual labels. This probability is a value ranging from 0 to 1, and a label is a binary value. The ambition here is to minimize LogLoss, which is an indicator for lower generalization error in real-world applications.
- **AUC** gives the probability that a binary classifier gives a randomly chosen positive test instance a higher score than a randomly chosen negative test instance. A higher AUC indicates better performance.

AUC and LogLoss are more convenient than precision and recall when the output of the model is a value indicating the likelihood of the given data record to belong to a certain class. For computing precision and recall, the probabilities are converted to class labels depending on a user-defined threshold and the choice of the threshold may drastically affect the results. However, AUC and LogLoss have the advantage to avoid such user-defined thresholds.

To evaluate the baseline models for their efficiency, we used the time spent during training and testing, and the speedup constant which is calculated by the following formula:

$$speedup = \frac{t_{single\_objective}}{t_{multi\_objective}} \quad (8)$$

5. Performance results

We compared 7 baseline models and their multi-objective versions in our experiments, which are implemented with TensorFlow,[1] and trained with Adam optimizer [32] which employs an adaptive learning rate for faster convergence. We set the embedding dimension of features to 8 in all experiments for a fair comparison. The details of the compared models are given below.

- PNN [6] consists of an embedding layer to learn a dense representation of the categorical data, a product layer to capture interactive patterns between the learned embeddings of categorical fields, and a series of fully connected layers to explore high-order feature interactions. It concatenates the products of embedding pairs to feed succeeding MLP layers. The product layer of PNN combines two types of products: the inner product (IPNN) and the outer product (OPNN).
- DeepFM [8] improves Wide&Deep [7] by replacing the linear part with an FM. Both deep and wide parts share the same embedding layer, so they contribute to each other on learning feature representations. DeepFM does not need a pre-trained FM to initialize the embedding vectors as in [10]. Embedding vectors are learned in an end-to-end fashion.
- DCN [33] combines a cross-network with a deep neural network to avoid task-specific feature engineering. The cross-network explicitly learns low and high dimensional feature interactions. The output of cross and deep networks are concatenated, then the concatenated vector is feed into a fully connected layer to get the prediction probability.
- AFM [12] is a special case of FM which pays attention to the impacts of feature interactions on predictions. Thus, while traditional FM uniformly sums the inner product of embedding vectors, AFM applies a weighted sum of feature interactions. The weights are learned by a simple neural network, then assigned to the relevant feature interactions.
- NFM [9] uses a bi-interaction pooling layer to utilize the linearity of FM in modeling second-order feature interactions, and also a neural network for its non-linearity in modeling higher-order feature interactions after bi-interaction pooling. Similar to Wide & Deep, it has a linear interaction part, and its output logit is added to the output logit of the neural network to get the prediction probability.
- AutoInt [13] uses interacting layers to model the different order feature interactions via a multi-head attention mechanism. For each interacting layer, high-order features are combined through the attention mechanism, and the multi-head mechanism maps the features into various subspaces. By stacking multiple interacting layers, different orders of feature interactions can be modeled.
- FGCNN [17] is one of the latest CTR prediction approaches which gives promising results and most likely to be the state-of-the-art model in the area. It consists of two components: Feature Generation and Deep Classifier. Feature Generation leverages the strength of CNN to detect local patterns and recombine them to generate new features. Deep Classifier adopts the structure of IPNN to learn interactions from the augmented feature space.
- biDeepFM is a prototype of our proposed multi-objective neural network model for reciprocal recommendation. The details of the model are given in Section 3.2. The same multi-objective learning approach can be easily applied to other neural network-based solutions as we already tested and reported in the following sections for all listed models above. Besides the effectiveness (see Section 5.1) and the efficiency (see Section 5.2) of biDeepFM, it takes advantage of its FM part for explainability (see Section 5.3), and also has the high-order feature learning capability by its DNN part.

All tests are carried out over Amazon Web Service (AWS) virtual machines. The used machine is a p2.xlarge instance with 4 core Intel Xeon (E5-2686v4) CPU, 61 GB memory and one NVIDIA K80 GPU. The model parameters are learned via backpropagation. To prevent overfitting and also long-running time for training, early stopping is applied with patience, which defines the number of epochs to wait before early stop if no progress on the validation loss. The patience is set to 3 in all our tests, and by means of callbacks, the most successful state is restored and used for testing.

Before starting to compare our multi-objective approach to the baselines, we would like to test how biDeepFM works as a whole architecture since it combines two components, FM and DNN, to benefit from both memorization and generalization. For this purpose, we first trained the FM and the DNN components alone as complete reciprocal recommender systems with our proposed multi-objective approach. We then compared their performance to the biDeepFM model, which is already multi-objective. They underperformed than biDeepFM (see Table 4) in a way to convince us to combine linear and deep models to improve recommendations as expected [7,8]. In job recommendation, understanding user's taste is much more complicated than the other domains like movie, application or partner recommendation because the underlying reason to apply/hire or not to apply/hire may depend on diverse parameters that we can even not think about and/or do not exist in input data. For instance, the candidate's decisions may depend on their partners, families, and even friends; companies may include their current financial status or even temporary political situations to their selection criterion. Therefore, this domain requires more generalization than memorization when compared to others. The experiment shows that DNN outperformed than FM and supports this claim.

Cold-start is one of the biggest considerations in recommender systems, and content helps to alleviate this problem for new coming items/users. Although we are not directly focusing on the cold-start problem in this research, we expect to overcome this in all models that we have compared with the help of content. Depending on how we define the problem (see Section 3.1 for details),

Table 4
Comparative results of architecture selection for our multi-objective approach. † and § are simplified architectures by removing a component from the prototype in Fig. 2. DNN for † and FM for §, respectively.

Architecture	Candidate		Company	
	Log Loss	AUC	Log Loss	AUC
FM†	0.4323	0.8633	0.0389	0.8394
DNN§	0.3172	0.9303	0.0316	0.9287
biDeepFM	0.3083	0.9351	0.0311	0.9348

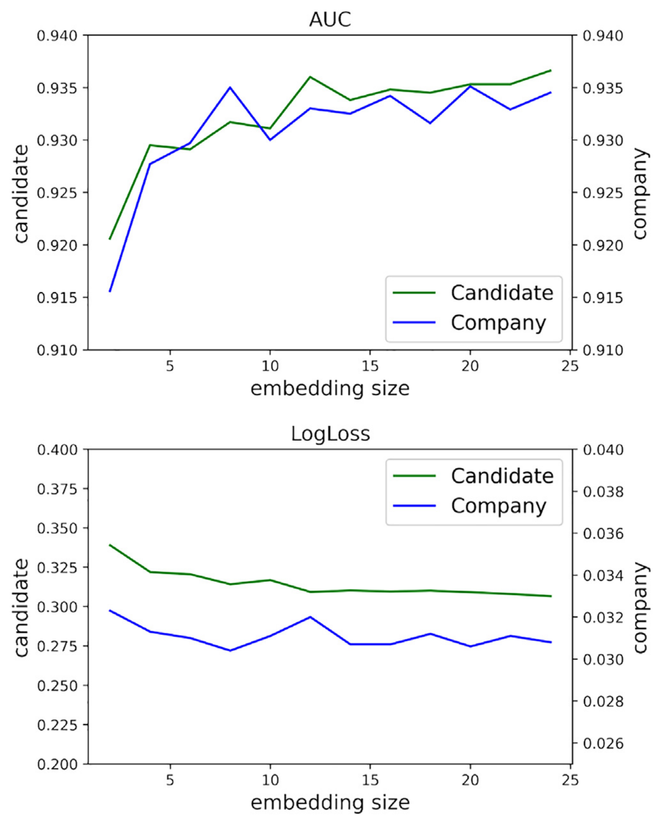

Fig. 3. AUC and LogLoss changes of biDeepFM by different embedding dimensions.

every instance in the dataset basically refers to an interaction represented by content features, and the models try to predict if there will be an interaction between a given user-item pair. Thereby, the models make use of historical and content data to have variety (globalization) and consistency (localization) in the recommendation. We conducted an experiment to see how much we can improve our model by adding content, so we trained biDeepFM with ids only and with all the features mentioned in Table 2. When the content is included into the system, AUC is increased by 5.23% (from 0.8886 to 0.9351) for the candidate aspect, $y_{candidate}$, and by 4.97% (from 0.8905 to 0.9348) for the company aspect, $y_{company}$; and LogLoss is decreased by 23.00% (from 0.4004 to 0.3083) for $y_{candidate}$ and by 18.80% (from 0.0383 to 0.0311) for $y_{company}$. The results meet the expectation and approve the previous works [34] in the literature.

We adapted the architecture used in [8] to create our prototype, however, we also tested the various embedding dimensions to better fit this architecture into our domain. Fig. 3 shows the change in performance by embedding dimension on reciprocal job recommendation problem. The results are inclined to increase with higher embedding dimension. While AUC is more sensitive to these changes, LogLos is more stable.

Table 5
Comparative results in terms of Log Loss and AUC metrics.

Method	Candidate		Company	
	Log Loss	AUC	Log Loss	AUC
PNN	0.3023	0.9397	0.0330	0.9098
DeepFM	0.3078	0.9353	0.0354	0.8788
DCN	0.3083	0.9350	0.0345	0.8928
AFM	0.5062	0.7976	0.0411	0.7785
NFM	0.3889	0.8968	0.0353	0.8827
AutoInt	0.3038	0.9381	0.0347	0.8975
FGCNN	0.3028	0.9395	0.0332	0.9121
biDeepFM	0.3083	0.9351	0.0311	0.9348

5.1. Effectiveness of multi-objective learning

Table 5 shows the predictive performance of all listed models above in terms of Log Loss and AUC. For each compared model to biDeepFM, two independent models are trained and tested: a candidate interest model and a company interest model. Then, their performance is compared to the biDeepFM model, which is simultaneously trained to model both candidate and company interests. All models except AFM and NFM perform similarly on candidate interest predictions, whereas biDeepFM has better performance on company interest. Note that in reciprocal recommendation final decision-maker is much more important because it defines the reciprocity in relation. Therefore, even if we could not improve the candidate model, we have an insight that our model is capable of recommending more convenient jobs to candidates. If we had the chance to interactively collect true labels after our recommendations, the performance evaluation of the candidate model would be more meaningful. Seemingly, multi-objective learning is competitive as much as single-objective on candidate interest but far better than it on company interest with an advantage of less effort. Despite the limited number of positive samples for company interest, it is very promising that our approach could improve the reciprocal recommendation performance.

In reciprocal recommendation, how to optimally balance the interest of both sides remains open and depends on the domain [35]. Even though the interest models are not independent in our approach, we conducted a set of experiments to learn the empirical importance of both objectives. Fig. 4 shows the performance changes of company and candidate interest models by adjusting the weight of the company model. The weight of the company model defines the trade-off between the two objectives. When the weight of the company model is set to w, the weight of the candidate model automatically turns into $(1 - w)$. Since each objective contributes to the learning of embeddings, a balanced combination of two objectives gave the best performing results. Moreover, listening to company interests only, i.e., in the case of $w = 1$, results in degrading the performance of the company interest model as well (see the slight decline in AUC in Fig. 4a). As the cumulative success is aimed to satisfy both parties, we adopted equal weight for the models in further experiments.

We also reported a group of experiments to evaluate the effect of multi-objective learning on company interest for all baselines in Table 6. Please note that biDeepFM is the multi-objective model of the DeepFM baseline, therefore the company model performance of our prototype given in Table 5 is identical to the multi-objective performance of DeepFM here. For each baseline, we created an output layer with two sigmoid functions, one for the candidate interest and one for the company interest; and then made the proper connections to the shared network which originally serves as a one-directional recommendation system. This group of experiments verifies that the multi-objective learning approach perfectly fits in the reciprocal recommendation problem. By multi-objective learning, each model is improved, ranging from 2.63% to

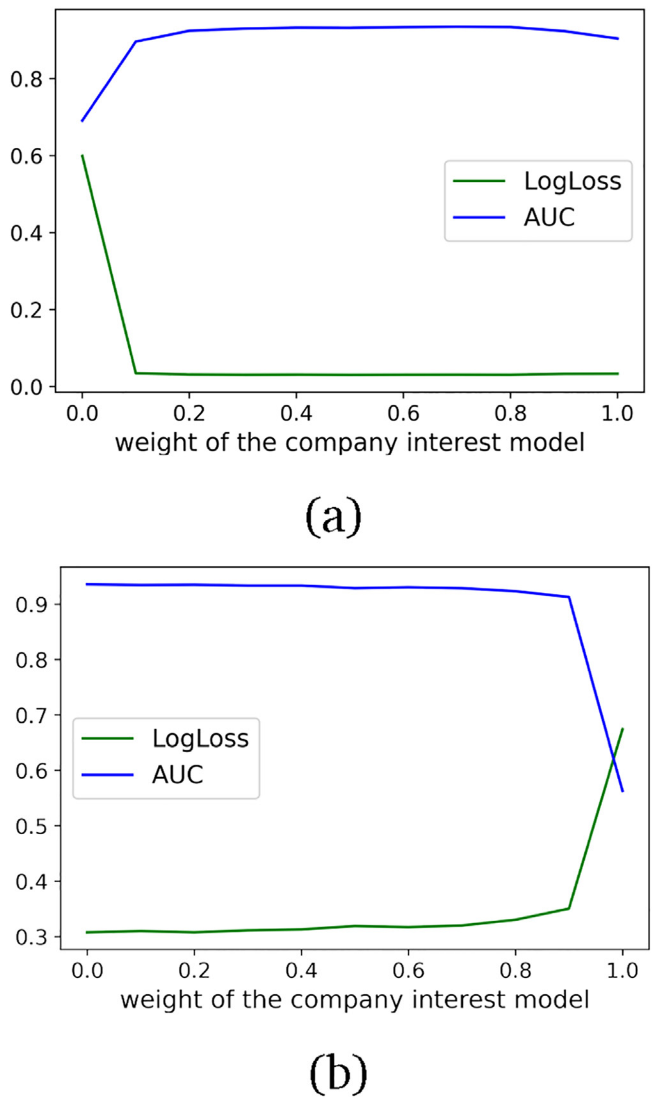

Fig. 4. (a) Performance of company interest model, and (b) Performance of candidate interest model. AUC and LogLoss changes by the weight of company interest model.

6.37% on AUC metric and up to 12.15% on Log Loss. Even though PNN and FGCNN respond slightly better to multi-objective learning in this setup, they both are computationally expensive models (see Section 5.2) and furthermore FGCNN does not offer explainability discussed further in Section 5.3. Due to their weaknesses against the recent incline moving forward to lightweight and transparent recommender systems and depending on the percentage improvements on Log Loss and AUC, the most effective results have been obtained by biDeepFM.

5.2. Efficiency of multi-objective learning

Table 7 shows the running time of all considered models during their train and test phases in HH:MM:SS format. Because single-objective learning requires two independent training operations to perform reciprocal recommendation, we keep track of train and test times for both models, then sum them up to find out the total elapsed time. The total elapsed time for the models is compared to the elapsed time of the relevant multi-objective model in one-shot. We also defined a speedup metric given in Eq. (8) to make a fair comparison of the model efficiencies. The speedup is shown along with the elapsed training and test time in Fig. 5. AFM not only had the weakest prediction performance on both candidate and company interest models in the comparison in Table 5 but also result in undesirable long running time. Despite their remarkable success, PNN and FGCNN did not show the same performance on time complexity. While FGCNN has the heavy burden of feature generation component consisting of many convolution layers, PNN has inefficient inner product operations, which slowing it down. DeepFM and DCN show similar performance while NFM and AutoInt need a bit more time. Actually, these methods require reasonable running time for both training and testing, even so, multi-objective learning results in almost two times faster running times for all baseline models. This makes the multi-objective learning approach once more meaningful for reciprocity in recommendation, especially for online platforms, which requires instant results.

5.3. Explainability of the proposed method

As we mentioned before, the FM component of our proposed method allows us to investigate the effect of feature interactions in depth. During the training, the latent vector representation of features (e.g. v_i) are jointly learned by FM and DNN components. After the learning process, we extracted the embedding weights of each feature, then pair-wisely multiplied them to calculate the interaction strength of the relevant features. Since our inputs (sparse features) consist of non-negative values only, the direction of the multiplication is used to determine the direction of their interaction. As expected, we observed that the strongest correlations are between the user and item features that share the same information, for instance, the gender of the candidate *(u_gender)* and the gender requested in job requirements *(i_gender)*. We omitted these interactions for simplicity and listed the top-10 strongest correlations in Table 8.

The strongest correlations are in this group of user features: {*u_gender*, *u_driving_licence*, *u_military_service*}. Based on the domain knowledge that we have in the recruiting process in Turkey, we can say that the combination of these features defines the non-desk jobs. Unfortunately, the job positions which require vehicle use are always thought suitable only for men in Turkey. So, this explains why these three user features are in high correlation in our dataset. The same behavior can be seen from the interactions of the user and item features in the same type (*gender*,

Table 6
Comparative results of single-objective and multi-objective company models in terms of Log Loss and AUC metrics. * symbol refers to our proposed biDeepFM model.

Method	Single-Objective		Multi-Objective	
(company)	Log Loss	AUC	Log Loss	AUC
PNN	0.0330	0.9098	**0.0310/-6.06%**	**0.9373/3.02%**
DeepFM	0.0354	0.8788	**0.0311*/-12.15%**	**0.9348*/6.37%**
DCN	0.0345	0.8928	**0.0309/-10.43%**	**0.9333/4.54%**
AFM	0.0417	0.7785	**0.0416/-0.24%**	**0.8006/2.84%**
NFM	0.0353	0.8827	**0.0348/-1.42%**	**0.9093/3.01%**
AutoInt	0.0347	0.8975	**0.0311/-10.37%**	**0.9333/3.99%**
FGCNN	0.0332	0.9121	**0.0300/-9.64%**	**0.9361/2.63%**

Table 7
Elapsed training and test time of models (HH:MM:SS).

		Single-Obj.			Multi-Obj.
Model	Phase	Cand.	Comp.	In-Total	One-shot
PNN	Train	00:25:39	00:21:16	00:46:55	**00:25:28**
	Test	00:00:23	00:00:19	00:00:42	**00:00:20**
DeepFM	Train	00:03:17	00:02:15	00:05:32	**00:03:52**
	Test	00:00:02	00:00:02	00:00:04	**00:00:02**
DCN	Train	00:02:54	00:02:28	00:05:26	**00:03:33**
	Test	00:00:02	00:00:02	00:00:04	**00:00:02**
AFM	Train	00:22:35	00:22:45	00:45:20	**00:24:00**
	Test	00:00:05	00:00:05	00:00:10	**00:00:03**
NFM	Train	00:04:40	00:03:37	00:08:17	**00:05:48**
	Test	00:00:05	00:00:05	00:00:06	**00:00:06**
AutoInt	Train	00:09:12	00:07:18	00:16:30	**00:08:20**
	Test	00:00:08	00:00:08	00:00:16	**00:00:08**
FGCNN	Train	00:57:04	01:02:37	01:59:41	**00:50:12**
	Test	00:00:41	00:00:52	00:01:33	**00:00:50**

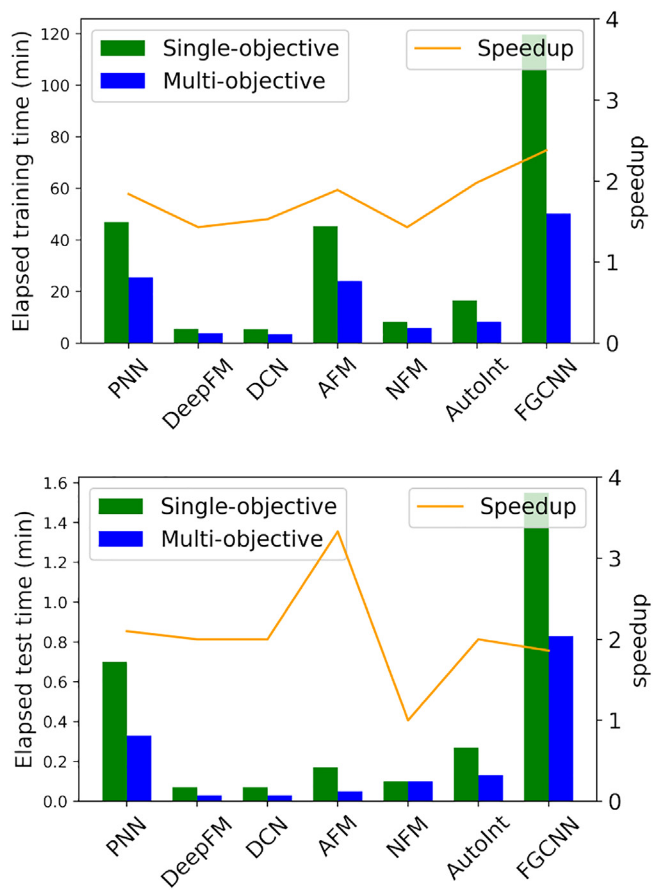

Fig. 5. Elapsed training and test time by method and learning type, and achieved speedup by the multi-objective approach. Speedup, the efficiency metric which is introduced in Eq. (8), is the ratio of time spent in single- and multi-objective approaches.

driving_licence, and *military_service*). The next outcome of this experiment is the correlation between the work status of the user and the position type of the job. We surmise that companies invite candidates according to their current work status for some certain type of positions, for instance, an unemployed candidate may be more favorable for a full-time position than a candidate currently working at a part-time job. Similarly, based on embedding weights, critical features or feature interactions can be extracted for certain jobs or candidates. Hereby, a recommender system may be tuned by using such information to direct candidates to convenient jobs that can hire them or the other way around. We suggest this to increase the recruitment rate in the system.

Table 8
The top-10 strongest correlations. Note that *u_* and *i_* prefixes refer to user and item, respectively. ↔ refers to bidirectional interaction.

Feature-*i*		Feature-*j*	Strength-of-correlation
u_gender	↔	i_driving_licence	7.96e−03
u_driving_licence	↔	i_military_service	7.24e−03
u_driving_licence	↔	i_gender	4.34e−03
i_driving_licence	↔	i_military_service	1.40e−03
i_driving_licence	↔	i_gender	1.36e−03
u_work_status	↔	i_position_type	1.35e−03
i_gender	↔	i_military_service	1.08e−03
u_military_service	↔	i_gender	9.88e−04
i_driving_licence	↔	i_gender	8.93e−04
u_driving_licence	↔	i_hidden	6.84e−04

6. Conclusion & future work

In this work, we proposed a multi-objective learning approach that perfectly fits into reciprocal recommendation problems. We tested our approach on an online recruiting problem. We observed valuable improvements over traditional single-objective models besides speeding up the process two times. Our prototype model biDeepFM achieved 12.15% improvement on Log Loss and 6.37% on AUC over its counterpart. We applied multi-objective learning on many state-of-the-art networks, which recently proposed for item prediction problems, such as CTR prediction. Our approach in almost all of the compared algorithms had tangible improvements. The reason for selecting DeepFM as a base method to create biDeepFM was that even though some of the other algorithms are highly competitive, they are either solely implicit learning or computationally expensive methods. Moreover, biDeepFM offers explainability by means of its FM part. Depending on the feature interactions, recommender systems can offer more insight to candidates about companies' preferences. This insight may direct job seekers' interest in the positions which are more probable to be hired or the other way around.

In future work, we will explore representations of user and item by using independent connections from their embedding layer to an additional representation layer, so that we can investigate the accordance of user-item pairs in detail. Besides, we are interested in explaining and visualizing the feature vectors learned by our models so that we can give insights to candidates to be favored amongst others and to find best-fit jobs for themselves. We will further apply this approach to other reciprocal tasks, such as online dating.

Declaration of Competing Interest

The authors declare that they have no known competing financial interests or personal relationships that could have appeared to influence the work reported in this paper.

.

References

[1] L. Li, T. Li, Meet: a generalized framework for reciprocal recommender systems, in: Proceedings of the 21st ACM International Conference on Information and Knowledge Management, ACM, 2012, pp. 35–44.
[2] O. Sener, V. Koltun, Multi-task learning as multi-objective optimization, in: Advances in Neural Information Processing Systems 31, 2018, pp. 527–538.
[3] K. Mason, J. Duggan, E. Howley, A multi-objective neural network trained with differential evolution for dynamic economic emission dispatch, International Journal of Electrical Power & Energy Systems 100 (2018) 201–221.
[4] S. Roth, A. Gepperth, C. Igel, Multi-objective neural network optimization for visual object detection, in: Multi-Objective Machine Learning, Springer, 2006, pp. 629–655.
[5] Y. Huang, W. Jin, Z. Yu, B. Li, Supervised feature selection through deep neural networks with pairwise connected structure, Knowledge-Based Systems 204 (2020) 106202.
[6] Y. Qu, H. Cai, K. Ren, W. Zhang, Y. Yu, Y. Wen, J. Wang, Productbased neural networks for user response prediction, in: 2016 IEEE 16th International Conference on Data Mining (ICDM), IEEE, 2016, pp. 1149–1154.
[7] H.T. Cheng, L. Koc, J. Harmsen, T. Shaked, T. Chandra, H. Aradhye, G. Anderson, G. Corrado, W. Chai, M. Ispir, et al., Wide & deep learning for recommender systems, in: Proceedings of the 1st Workshop on Deep Learning for Recommender Systems, ACM, 2016, pp. 7–10.
[8] H. Guo, R. Tang, Y. Ye, Z. Li, X. He, Deepfm: a factorizationmachine based neural network for ctr prediction, arXiv preprint arXiv:1703.04247..
[9] X. He, T.S. Chua, Neural factorization machines for sparse predictive analytics, in: Proceedings of the 40th International ACM SIGIR Conference on Research and Development in Information Retrieval, ACM, 2017, pp. 355–364.
[10] W. Zhang, T. Du, J. Wang, Deep learning over multi-field categorical data, in: European Conference on Information Retrieval, Springer, 2016, pp. 45–57.
[11] D. Bahdanau, K. Cho, Y. Bengio, Neural machine translation by jointly learning to align and translate, arXiv preprint arXiv:1409.0473..
[12] J. Xiao, H. Ye, X. He, H. Zhang, F. Wu, T.S. Chua, Attentional factorization machines: Learning the weight of feature interactions via attention networks, arXiv preprint arXiv:1708.04617..
[13] W. Song, C. Shi, Z. Xiao, Z. Duan, Y. Xu, M. Zhang, J. Tang, Autoint: Automatic feature interaction learning via self-attentive neural networks, arXiv preprint arXiv:1810.11921..
[14] G. Li, L. Qiu, C. Yu, H. Cao, Y. Liu, C. Yang, Iptv channel zapping recommendation with attention mechanism, IEEE Transactions on Multimedia..
[15] C.D. Wang, W.D. Xi, L. Huang, Y.Y. Zheng, Z.Y. Hu, J.H. Lai, A bp neural network based recommender framework with attention mechanism, IEEE Transactions on Knowledge and Data Engineering..
[16] J. Lin, G. Sun, J. Shen, D. Pritchard, T. Cui, D. Xu, L. Li, G. Beydoun, S. Chen, Deep-cross-attention recommendation model for knowledge sharing micro learning service, in: International Conference on Artificial Intelligence in Education, Springer, 2020, pp. 168–173.
[17] B. Liu, R. Tang, Y. Chen, J. Yu, H. Guo, Y. Zhang, Feature generation by convolutional neural network for click-through rate prediction, in: The World Wide Web Conference, ACM, 2019, pp. 1119–1129.
[18] L. Pizzato, T. Rej, T. Chung, K. Yacef, I. Koprinska, J. Kay, Reciprocal recommenders, ITWP 2010 (2010) 53.
[19] Y.S. Kim, A. Mahidadia, P. Compton, X. Cai, M. Bain, A. Krzywicki, W. Wobcke, People recommendation based on aggregated bidirectional intentions in social network site, in: Pacific Rim Knowledge Acquisition Workshop, Springer, 2010, pp. 247–260.
[20] L. Pizzato, T. Rej, T. Chung, I. Koprinska, J. Kay, Recon: a reciprocal recommender for online dating, in: Proceedings of the Fourth ACM Conference on Recommender Systems, ACM, 2010, pp. 207–214.
[21] L.A. Pizzato, T. Rej, K. Yacef, I. Koprinska, J. Kay, Finding someone you will like and who won't reject you, in: International Conference on User Modeling, Adaptation, and Personalization, Springer, 2011, pp. 269–280.
[22] L.A. Pizzato, C. Silvestrini, Stochastic matching and collaborative filtering to recommend people to people, in: Proceedings of the Fifth ACM Conference on Recommender Systems, ACM, 2011, pp. 341–344.
[23] K. Zhao, X. Wang, M. Yu, B. Gao, User recommendations in reciprocal and bipartite social networks–an online dating case study, IEEE Intelligent Systems 29 (2) (2013) 27–35.
[24] P. Xia, H. Jiang, X.Wang, C.X. Chen, B. Liu, Predicting user replying behavior on a large online dating site., in: ICWSM, Citeseer, 2014..
[25] Y. Tay, L.A. Tuan, S.C. Hui, Couplenet: Paying attention to couples with coupled attention for relationship recommendation, in: Twelfth International AAAI Conference on Web and Social Media, 2018..
[26] J. Malinowski, T. Keim, O. Wendt, T. Weitzel, Matching people and jobs: A bilateral recommendation approach, in: Proceedings of the 39th Annual Hawaii International Conference on System Sciences, 2006. HICSS'06, vol. 6, IEEE, 2006, pp. 137c–137c..
[27] H. Yu, C. Liu, F. Zhang, Reciprocal recommendation algorithm for the field of recruitment, Journal of Information & Computational Science 8 (16) (2011) 4061–4068.
[28] T. Mine, T. Kakuta, A. Ono, Reciprocal recommendation for job matching with bidirectional feedback, in: 2013 Second IIAI International Conference on Advanced Applied Informatics, IEEE, 2013, pp. 39–44.
[29] T. Schmitt, P. Caillou, M. Sebag, Matching jobs and resumes: a deep collaborative filtering task, 2016.
[30] S. Rendle, Factorization machines, in: 2010 IEEE International Conference on Data Mining, IEEE, 2010, pp. 995–1000.
[31] W.B. Feng, Z.S. Zhang, C.Z. Li, A.P. Song, Negative examples sampling based on factorization machines for occf, in: 2019 6th International Conference on Systems and Informatics (ICSAI), IEEE, 2019, pp. 1482–1485.
[32] D.P. Kingma, J. Ba, Adam: A method for stochastic optimization, arXiv preprint arXiv:1412.6980..
[33] R. Wang, B. Fu, G. Fu, M. Wang, Deep & cross network for ad click predictions, in: Proceedings of the ADKDD'17, ACM, 2017, p. 12..
[34] E. Yildirim, P. Azad, Ş.G. Öğüdücü, Neural hybrid recommender: Recommendation needs collaboration, in: M. Ceci, C. Loglisci, G. Manco, E. Masciari, Z. Ras (Eds.), New Frontiers in Mining Complex Patterns, Springer International Publishing, Cham, 2020, pp. 52–66.
[35] A. Kleinerman, A. Rosenfeld, F. Ricci, S. Kraus, Optimally balancing receiver and recommended users' importance in reciprocal recommender systems, in: Proceedings of the 12th ACM Conference on Recommender Systems, ACM, 2018, pp. 131–139.

Forecast electricity demand in commercial building with machine learning models to enable demand response programs

Prakash Dehury, *Department of Computer Sciencel Engineering, Aryan Institute of Engineering & Technology, Bhubaneswar, prakashdehury1@hotmail.com*

Arabinda Dash, *Department of Computer Scinece Engineering , Capital Engineering College, Bhubaneswar, arabindadash56@hotmail.com*

Abhishek Das, *Department of Electronics and Communication Engineering , Raajdhani Engineering College, Bhubaneswar, abhishekdas2256@gmail.com*

Rashmi Ranjan Behera, *Department of Electrical and Electronics Engineering, NM Institute of Engineering & Technology, Bhubaneswar, rr_behera@yahoo.co.in*

Keywords:
Deep neural network
Model assessment
Short-term load forecasting
Feature selection
Support Vector Machines
Artificial Neural Networks
Long Short-term Memory Networks
Demand response

A B S T R A C T

Electricity load forecasting is an important part of power system dispatching. Accurately forecasting electricity load have great impact on a number of departments in power systems. Compared to electricity load simulation (white-box model), electricity load forecasting (black-box model) does not require expertise in building construction. The development cycle of the electricity load forecasting model is much shorter than the design cycle of the electricity load simulation. Recent developments in machine learning have lead to the creation of models with strong fitting and accuracy to deal with nonlinear characteristics. Based on the real load dataset, this paper evaluates and compares the two mainstream short-term load forecasting techniques. Before the experiment, this paper first enumerates the common methods of short-term load forecasting and explains the principles of Long Short-term Memory Networks (LSTMs) and Support Vector Machines (SVM) used in this paper. Secondly, based on the characteristics of the electricity load dataset, data pre-processing and feature selection takes place. This paper describes the results of a controlled experiment to study the importance of feature selection. The LSTMs model and SVM model are applied to one-hour ahead load forecasting and one-day ahead peak and valley load forecasting. The predictive accuracy of these models are calculated based on the error between the actual and predicted loads, and the runtime of the model is recorded. The results show that the LSTMs model have a higher prediction accuracy when the load data is sufficient. However, the overall performance of the SVM model is better when the load data used to train the model is insufficient and the time cost is prioritized.

1. Introduction

There are many driving factors that make accurate electricity load forecasting models a pertinent issue, the most obvious and pressing of which is climate change. Carbon emissions are one of the most significant driving forces of climate change and with data being published [1] that shows carbon emissions rates are increasing, a solution is urgently needed. Emissions from electricity generation account for the 25% of the whole worldwide emissions [2]. Because of physical limitations in storing electricity, the production, transmission, and consumption of electricity must be carried out simultaneously with its demand [3], therefore the power supply and power consumption need to maintain a dynamic balance.

Considering buildings accounted for an estimated 41.1% of primary energy and 74% of the electricity, the necessity for accurate energy prediction models for buildings is obvious. According to [4], more than 25% of the 713 GW of the U.S electricity demand in 2010 could be dispatchable, meaning created and used on demand if buildings could use advanced building energy systems and employ advanced forecast techniques. This is massively appealing, not only because it will slow down climate change, which is projected to wreak irrevocable damage to the planet, but also partly because of the financial incentive tied to lowering carbon emissions for governments. The Effort Sharing Regulation [5] adopted by the European Union in 2018 sets out to lower carbon emissions across the EU by 30% before 2030. Under this regulation, if targets are not met for one member state, one available option is to buy carbon credits from member states who have exceeded their goals. Therefore, there is not only financial incentive for governments to reach their emission goals, so as to not have to pay for extra carbon credits, but also to surpass expectations and generate revenue through selling surplus carbon credits.

On a more demand node level, the introduction of accurate short term electricity forecasting will allow building operators to save money as they are no longer paying to offset wasted energy which could have been dispatched on-demand instead. Amidst the backdrop of climate change, coupled with the granular benefits of load prediction, it is easy to see why the pursuit of an accurate, scalable, and complete energy prediction solution is desirable. Accurate electricity load forecasting contributes to the supply demand stability of the power grid and it can provide a reference for the planning and operation of power systems [6], often through demand response programs. Demand Response (DR) is one of the Demand Side Management (DSM) measures that has been promoted as a mechanism to increase the percentage of renewable energies in the system [7]. It is defined as "changes in electricity use by demand-side resources from their normal consumption patterns in response to changes in the price of electricity or to incentive payments designed to induce lower electricity use at times of high wholesale market prices or when system reliability is jeopardised" [8]. A DR signals by a demand response aggregator or Trasmission System Operator (TSO), triggers the intentional reshape of the electricity demand profile. The variation can be measured as level of instantaneous demand or total electricity consumption deferred. DR assets can dynamically change the electricity demand curve, providing peak shaving, frequency control, load shifting and load forcing measures [9].

Therefore, predicting peak demand and short term forecasts could support energy management systems devices to actuate optimal strategies during demand response events [10]. Depending on the time period, electricity load forecasting can be divided into four types, which are very short-term, short-term, medium-term and long-term load forecasting [6,11].

- Very short-term load forecasting (VSTLF) focuses on electricity load within 1 h in the future. It is mainly used for real-time safety analysis of power systems and monitoring the operation of power equipment [12].
- Short-term load forecasting (STLF) refers to one-day ahead and one-week ahead load forecasting. In the four types of electricity load forecasting, STLF has important practical significance, which can help with electricity dispatching and management in power systems [13,14].
- Medium-term load forecasting (MTLF) focuses on predicting electricity load in the coming weeks or months. It is used for the operation and maintenance of power systems [15].
- Long-term power load forecasting (LTLF) is used for long-term planning of power systems. It is mainly used to predict the electrical load for the next year or even years. [16].

The work described in this paper focuses on STLF, which is an integral part of the smart grid in order to estimate the future electricity loads accurately and minimize errors between actual and predicted loads, which can help to improve the utilization of power generation equipment and the effectiveness of economic dispatch [14]. Predictive energy demand techniques for buildings can be broadly divided into white-box model and black-box model [17]. The former is physics-based model, which requires expertise in the field of building. The white-box model uses building energy simulation software with a set of detailed physical rules and building information to generate electrical load data [18]. The latter is used to find the correlation between electrical load and historical load data [3]. It is also known as a data-driven model, which does not require physical information about the building, but requires sufficient historical data [19]. Recent research is focused on exploring predictive techniques for electricity demand, targeting improving the accuracy of forecast results, whether using white-box model or black-box model. The white-box model is an essential tool for calculating and analyzing the building energy load and has been widely used [20]. The core of the white-box model is to transform the basic physical characteristics of the building into corresponding simulations [21]. If most of the detailed building information and energy transfer processes are considered in the BES model, the prediction accuracy of these models is high. However, some detailed data may not be available to the user during the simulation process, resulting in poor prediction performance [22]. The white-box model is computationally expensive and has a long development cycle. Many researchers have tried to simplify the white box model, however, the simplifications cannot solve the above problems and are prone to errors [21]. The black-box model predicts the electricity load by learning from historical load data and some external factors. It can avoid the inadequacy of the white-box model given that detailed building information is not required [22]. In addition, the high stability and accurate prediction of the black-box model is also the reason why the increasing number of research is taking place [19]. In the early stages of black-box model development, traditional forecasting methods for modeling electricity load through stochastic processes are widely used. They are the easy-to-use predictive methods that associate electricity load data with impact variables. Kalman filter [23], Time series analysis [24] and statistical regression [25] are typical representatives of such methods. These algorithms have the advantages of fewer parameters, lower computational complexity, and greater interpretability. They are able to achieve good forecast results when dealing with highly stable, periodic electricity load datasets. With the rise of machine learning, many network structures and training algorithms have emerged. These algorithms have powerful learning capabilities and the ability to handle complex nonlinear functions to adapt to the complex influencing factors [26]. Currently, among the most common technologies for electricity forecast there are Artificial Neural Networks (ANNs) [22] and Support Vector Machines (SVM) [27]. In [28], Support Vector Machines (SVM) are highlighted as the most accurate option for forecasting electricity load, with similar levels of complexity and accuracy of deep neural networks. Support Vector Machines (SVM) do suffer from some disadvantages not seen in ANNs such as low running speed. This is an issue, most notably in projects with large scope. Unfortunately this is a widespread issue with models which are accurate to a fair degree requiring a large computer memory and processing or computation time [29]. The upside of using Support Vector Machines (SVM)s is that they require few inputs, so this means the feature selection process is easier. They are also notable for having a relatively simple training process due to requiring a few inputs as mentioned earlier [21]. Statistical regression models are a prominent option for forecasting electricity load. These models are beneficial for evaluating the importance of potential inputs for models but struggle with short term predictions, with a relatively large amount of inaccuracy in this field.

A hybrid model is proposed [30] based on improved empirical mode decomposition (IEMD), autoregressive moving average (ARIMA) and wavelet neural network (WNN). The model is said to perform better in comparison to SVMs based upon case study data from America and Australia and can provide a robust, stable and accurate prediction result. A method is introduced [31] based on Gaussian Process Regression (GPR) which also incorporates physical insights about load data characteristics. It achieved an accuracy of up to 94.38% and 99.26% for long- and short-term forecasting, respectively, although interestingly as training data and forecast length increased, so did prediction error.

A new framework based on Long Short-Term Memory (LSTM) Network moving window-based technique is described by [32]. LSTMs are a form of Recurrent Neural Network, which excel at time-series forecasting due to "maintaining a memory cell to determine which unimportant features should be forgotten and which important features should be remembered during the learning process". This approach is said to outperform regression models, Support Vector Machines and Artificial Neural Networks. Recurrent Neural Networks can be used to predict electricity demand efficiently. There are numerous advantages such as handling non-linear complexities, minimum prediction errors and ease of generalization. Research into Long Short Term Memory (LSTM) shows promise, with many studies being conducted to show the efficacy of the model in handling time-series [32–34]. One such study cites the use of Convolutional Neural Network (CNN) layers in conjunction with LSTM layers as a method of improving accuracy [34].

The ability of Recurrent Neural Networks, and more specifically LSTMs alongside CNNs to make proven accurate predictions using time-series data makes them a model for consideration.

The aforementioned papers reproduce and improve the forecast models' accuracy using LSTM methods and compare with the performance of ANN and SVM on historical energy demand dataset. In the literature, the applicability of the methods on existing demand response programs is limited. The novelty of the current work is the use of the forecast models to predict both the electricity demand, daily peak load and valley load to dynamically optimize the local generator, the thermal storage and the demand for a new highly efficient commercial building equipped with advanced control systems, which is also a demand response unit. Additionally, the work explores the model's adaptability through multiple cases — on one-hour ahead load forecasting and one-day ahead peak and valley load forecasting that could be used to schedule demand response measures in response to grid signals. Such an objective has been validated comparing the performance of forecasting techniques and adapt the test cases for specific demand response programs such as day-ahead scheduling, and secondary reserve time resolution. The effects of outliers' processing and feature selection on prediction accuracy are also discussed. The paper is organized as follows: Section 2 provides the principles of these two common forecasting methods Artificial Neural Networks (ANNs) and Support Vector Machines (SVM) for STLF. An overview of the experiment is provided in Section 3. Section 4.1 describes the commercial building used for the experiment. Section 4 denotes the experimental setting, dataset details, and evaluation metrics. The experimental results are discussed in Sections 5 and 6 summarizes the work described in this paper.

2. Background work

2.1. Artificial Neural Networks

The design of ANNs is inspired by the structure of the human brain [21]. Typically, ANNs consists of the input layer, the hidden layer, and the output layer. Each layer contains multiple neurons and their corresponding activation functions. Multiple hidden layers can improve the ability to handle non linearities, making them more accurate for electricity load forecasting [22]. The Recurrent Neural Networks-based model has become an important technique for dealing with nonlinear and short-term dependence in sequence data in recent years [35]. However, during model training, the multiple uses of matrix multiplication lead to gradient disappearance or explosion.

Long Short-term Memory Networks (LSTMs) technique is a special type of RNNs. It retains the recursiveness of RNNs while having selective memory. The LSTMs avoids the problem of gradient disappearance and gradient explosion through the forgetting mode [36]. Like other neural network structures, the LSTMs consists of the input layer, the hidden layer, and the output layer. However, the internal structural unit of the LSTMs is a cell, also known as a memory unit. This memory unit contains the forget gate (blue circle), the input gate (orange circle) and the output gate (red circle), as shown in Fig. 1.

The LSTMs decides which information to discard through the forgot Gate. The function of the input gate is to determine the value of the updated memory state. The output gate is used to determine the output value of the current memory unit.

Bouktif et al. use the genetic algorithm to select the optimal time lag and the number of LSTMs layers to forecast short- and medium-term electrical loads [35]. The remaining parameters, such as the number of neurons in the hidden layers, activation functions, and optimizers, are determined experimentally. The main purpose of Bouktif et al.'s study is to compare the performance of LSTMs model and other machine learning models. This study initially evaluates the performance of various machine learning models, such as random forest, ridge and extra trees regressor. Secondly, the model with the best prediction result is selected as the benchmark model. Feature engineering and parameter tuning are used to improve the performance of the benchmark model further. Finally, Bouktif et al. compare the performance of this benchmark model with the LSTMs model. Experimental results show that the performance of the extra tree regression model is best in other machine learning models besides ANNs. Therefore, the extra tree regression model is used as the benchmark model for comparison with the LSTMs model. Through further comparative analysis, the prediction error of the LSTMs model is lower than that of the reference model. The authors conclude that the designed LSTMs model is more accurate and stable [35].

2.1.1. Support Vector Machines

SVM is a kernel-based machine learning algorithm with the ability to solve nonlinear classification and regression problems [22]. The process of SVM to solve nonlinear problems can be divided into two steps. SVM firstly determines the appropriate function for projecting nonlinear problems into high dimensional space. Secondly, the kernel function is used to make the complex nonlinear mapping a linear problem. It is worth mentioning that the SVM is outstanding in accuracy and can maintain good performance with only a small amount of training data [28].

Khan et al. use support vector machines and artificial neural networks as short-term electricity load forecasting models to compare their performance [27]. In the model design phase, the authors firstly select the Feed-Forward Neutral Network (FFNN) as the representative of ANNs. Secondly, Support Vector Regression (SVR) is used, which indicates SVM for solving regression problems. Then, three SVM models with different kernel functions are designed, which are Linear, Quadratic and Cubic SVM. It ensures that the best performing SVM model can be found because different kernel functions have an impact on their performance. Expressions of these three different kernel functions are as following:

$$\textit{Linear} \quad B\left(\mathrm{x_r}, \mathrm{x_q}\right) = \mathrm{x}_r' \mathrm{x_q} \tag{1}$$

$$\textit{Quadratic} \quad B\left(\mathrm{x_r}, \mathrm{x_q}\right) = \left(1 + \mathrm{x}_r' \mathrm{x_q}\right)^2 \tag{2}$$

$$\textit{Cubic} \quad B\left(\mathrm{x_r}, \mathrm{x_q}\right) = \left(1 + \mathrm{x}_r' \mathrm{x_q}\right)^3 \tag{3}$$

where $\mathrm{x_r}$, $\mathrm{x_q}$ stand for two input vectors. The transformation function, which are $\mathrm{x}_r'\mathrm{x_q}$, $\left(1 + \mathrm{x}_r'\mathrm{x_q}\right)^2$, and $\left(1 + \mathrm{x}_r'\mathrm{x_q}\right)^3$, map the input vector to a higher dimension space.

According to Khan et al. the experimental results show that the performance of SVM-based models is better than that of ANNs model. However, the authors only select the FFNN model as a benchmark to compare with the SVM model, which does not prove that the SVM model performs better than all neural networks-based models. In addition, the prediction of the Cubic SVM is the most accurate among the above three SVM-based models.

3. Methodology

This paper studies the existing electricity load forecasting models in order to improve the prediction accuracy, and applies the effective input features and prediction models for the actual electricity load of the commercial building described in Section 4.1. The workflow of the experimental methodology is shown in Fig. 2.

The pre-processing phase includes missing data processing, outlier processing, and normalization. Firstly, a suitable filling method is used to complement the missing data in order to ensure the integrity of the power load sequence. Secondly, the purpose of outlier processing is to identify and modify the random errors present in the electricity load by the characteristics of the actual load data. Finally, normalization is used to eliminate the effects of the order of magnitude of the data.

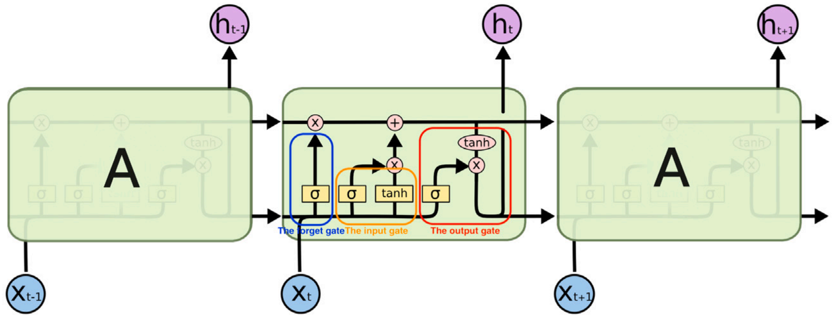

Fig. 1. LSTM internal structure [36]. (For interpretation of the references to color in this figure legend, the reader is referred to the web version of this article.)

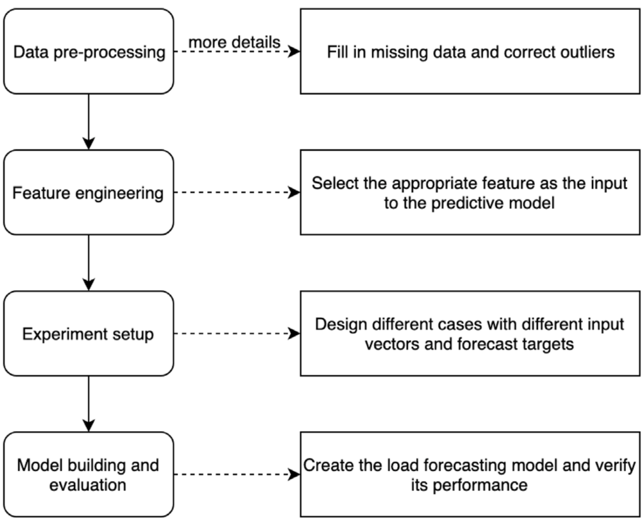

Fig. 2. Experimental methodology.

Many factors affect the performance of electricity load forecasting, and these factors can be divided into internal factors and external factors. Specifically, historical load data is an internal factor, and weather, date type, and economic are external factors. Correlation coefficients evaluate these factors in the feature selection phase because not all factors positively affect predictive accuracy. Following the correlation analysis, the appropriate influencing factors are selected as the input features of the load forecasting model. In terms of experiment setup, this paper uses the selected factors to create multiple cases to study the impact of different input features on the performance of the electrical load forecasting model.

As for model building and evaluation, this paper builds LSTM-based model and SVM-based model with appropriate model parameters and evaluates the predictions in the different cases.

3.0.1. Normalization

Machine learning models are sensitive to the scale of input data, therefore normalization is used to avoid the impact of data magnitude on them [35]. Therefore, the raw data is linearly transformed by min–max normalization, so that the data size is constrained between [0,1]. The min–max normalization formula is as follows:

$$x_n = \frac{x - x_{\min}}{x_{\max - x_{\min}}} \tag{4}$$

where x is the data to be processed, x_n stands for the normalized data, x_{max} and x_{min} are the maximum and minimum values in the load data, respectively.

After the data has been trained and predicted, a denormalisation operation is required. The formula is as follows:

$$\hat{x} = (x_{\max - x_{\min}})x_n + x_{\min} \tag{5}$$

where $\hat{x}$ x represents denormalized data.

In addition, in the normalization phase, the training set and test set use a uniform normalization standard. Therefore, the maximum and minimum electricity loads of the training set and the test set are the same.

3.1. Evaluation metrics

The difference between the predicted load and the actual load is called the prediction error. This section lists several commonly used methods for measuring the prediction error and their values can reflect the performance of the forecast model. These measurement standards are defined as follows:

$$MAE = \frac{1}{n}\sum_{i=1}^{n} |\hat{y}_i - y_i| \tag{6}$$

$$RMSE = \sqrt{\frac{1}{n}\sum_{i=1}^{n} (\hat{y}_i - y_i)^2} \tag{7}$$

$$MAPE = \frac{100\%}{n}\sum_{i=1}^{n} |\frac{\hat{y}_i - y_i}{y_i}| \tag{8}$$

Mean Absolute Error (MAE) [14,35] is one of the most commonly used average error metrics, calculated by the average of the sum of absolute errors. Root Mean Squared Error (RMSE) [14,27,35] is used to describe one of the most common metrics of uncertainty. It is worth mentioning that RMSE amplifies the value of larger error terms in the calculation process. Mean Absolute Percentage Error (MAPE) [14,27] represents the average absolute error percentage.

4. Experiment setup and dataset exploration

This section describes the case study and provide an analysis of the dataset used for training the models. Next section will describe the test case building.

4.1. Building description

The test bed building [20] is a building with a strong commercial profile, variability of HVAC systems, space usage and occupancy patterns and is located on the UCD campus in Dublin, Ireland. The building is used as a sports/entertainment center, consists of three floors with a total floor area of 11,000 m^2 and includes a 50 m *x* 25 m swimming pool, with related ancillary areas such as a wellness suite, fitness center, aerobics and dance studios, drama theater, multimedia and seminar rooms, offices, shops and cafe space. A front view of the building is depicted in Fig. 3.

The building electrical and space-conditioning requirements are provided by two identical CHP units (506 kW thermal and 400 kW electrical output each), two gas boilers (1146 kW each) and an air-cooled water chiller (865 kW). Additionally, heat is provided as well, when necessary, by the campus district heating installation (500 kW). The space conditioning delivery equipment consists of eight air handling

Fig. 3. SLLS building located at University College Dublin, Ireland.

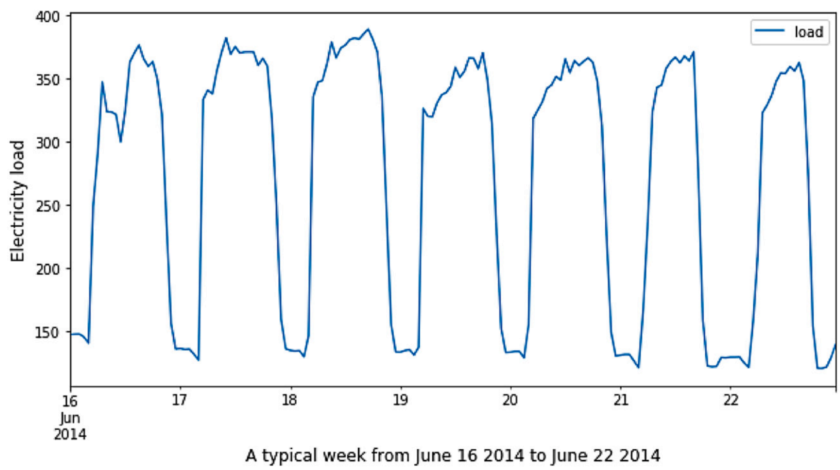

Fig. 4. The typical week of electricity load.

units, fan coil units, underfloor heating and baseboard heaters, while the ventilation throughout the building is mechanical.

The building energy rate is B2, which is a benchmark for excellent performance in a commercial building with such equipment and intended use [37]. An Energy Management System controls and monitors all the primary and ancillary HVAC equipment in the building. Operational EMS data has been recorded at 15 min intervals from September 2012 onwards. Total electricity and gas consumption are monitored and there are sub-meters on individual HVAC components (i.e., boilers, CHP units, and the chiller). Pressure, humidity, air temperature and CO_2 levels are measured at different points of the HVAC systems. Moreover, air temperature, relative humidity and CO_2 concentration are measured at zone level. The experimental data in this paper includes historical electrical load data and weather factor data from January 1, 2013, to December 31, 2018.

4.2. Data pre-processing

The data collection period of the electricity load is 15 min with 96 points per day, and a total of 220,336 data points in 6 years. The hourly outdoor temperature, wind speed and relative humidity are used as weather data, which is available on the Irish Meteorological Agency website [38]. A data pre-processing procedure has been applied to the time series to reduce abnormal prediction errors. The process has selected outliers and missing data. Both missing data and outliers can be caused by communication system failure or equipment maintenance. Some errors can also be caused by errors in the data collection hardware infrastructure.

4.2.1. Missing data processing

The dataset used in this paper contains 644 missing data, which account 0.3% of the entire dataset. As illustrated in Fig. 4, the electricity load curve can be divided into weekdays and non-working days based on the day type.

In particular, electricity loads at the same time point between different working days are similar, and that of non-working day also have the same characteristics. Special days such as national and local holidays have been analyzed to assess if they could have been clustered and used for data interpolation to fix missing data. However, demand profiles of special days are similar to non-working days. As per best practice, missing data are filled with the average of the electricity load at the same time point of the same day type.

4.2.2. Outliers processing

Outliers are those in which the data at some time point deviates from the range of most other data. A standard procedure described in [39] has been used to identify outliers in the dataset. The methodology uses the five statistical components, which are minimum, the first quartile (Q_1), the median, the third quartile (Q_3), and the maximum to describe the distribution of the data. Data should be allocated between

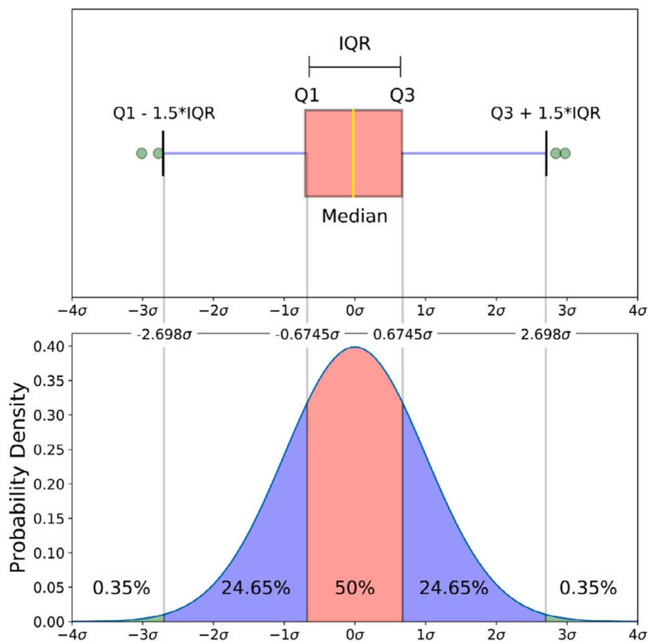

Fig. 5. The comparison the distribution of the box plot and the probability density function of the standard normal distribution [39].

$Q_1 - 1.5 * IQR$ and $Q_3 + 1.5 * IQR$, and data outside this range can be considered an outlier.

The outliers have been flagged, by comparing the distribution of the box plot and the probability density function of the standard normal distribution, as shown in Fig. 5. It can be seen that the outliers account for approximately 0.7% of the entire dataset. Through the box plot test, 2.9% of the data in the dataset have been flagged as outliers. The source of error can be correlated t sensor calibration for the electricity load data. These outliers are corrected using the same method as filling the missing data.

4.3. Feature selection

This paper evaluates the applicability of the factors as input features by correlation. According to Kapetanakis et al. the Pearson and the Spearman correlation coefficient can be used to measuring the linear correlation and monotonic relationship between these factors and the output [40]. While the Pearson correlation coefficient identifies a linear correlation between the variables, the Spearman correlation assesses if two variables are monotonically related. Both Pearson and Spearman correlation coefficients range between −1 and +1. The absolute value of the correlation coefficient is equal to 1, which represents a positive or negative correlation between the influencing factor and the output variable. There is no correlation between the influencing factor and the output variable when the correlation coefficient is equal to 0. The threshold for determining the influence factor suitable as an input feature is 0.5 [41]. As illustrated in [42], there are three main types of external factors that affect the commercial electricity load forecasting, which are weather, day type and economic factors. Among them, economic factors include population growth, power system regulations and economic development trends, which mainly impact on medium-term, long-term load forecasting [42]. Therefore, for VSTLF and STLF, these economic factors can be ignored. In terms of weather factors, some commonly used weather variables, including the outdoor temperature, wind speed and relative humidity, are evaluated for their applicability as input features. As for date types, this paper mainly considers the difference between workdays and non-workdays. The date type has a value of 0 and 1, which is marked as 1 from Monday to Friday and 0 on Saturday and Sunday. In addition, the correlation coefficient between the historical load and the output variable is calculated. Fig. 6 shows Pearson and Spearman correlation coefficients, respectively. In these figures, red indicates that the correlation coefficient exceeds the threshold, and the correlation coefficients that do not exceed the threshold are filled with green.

It can be seen that Pearson and Spearman correlation coefficients between the electrical load and external factors are very low, whether it is hourly load or daily peak and valley load. The absolute value of Pearson and Spearman correlation coefficient for most external factors is less than 0.2. However, the historical load is highly correlated with the output. Therefore, this paper only uses historical load data as input features for electricity load forecasting.

4.4. Daily peak and valley load analysis

For day-ahead scheduling the prediction of daily demand peaks and valleys could facilitate demand response programs behind the meters. In the current work, the number of peak or valley load occurrences per day for 2018 has been assessed. The result is shown in Fig. 7.

As illustrated in Fig. 7, although the peak and valley values of daily electricity load are not fixed at a certain moment, the distribution of their occurrence times is concentrated. At 1200 h and 1600 h daily, the peak load occurred the most, accounting for 33.9% of the total, while the daily valley load appeared at 1500 h and 2300 h, accounting for 36.2% of the total. In addition, daily peak and valley loads hardly appear at the same time, except between 1800 h and 1900 h. These two moments of the weekdays and the weekends have different meanings. In other words, the two moments are working hours during the weekdays and non-working hours at the weekends. Therefore, both peak loads and valley loads can occur at these two moments.

4.5. Experiment setup

For the purpose of the research described in this paper, various cases are created to compare the performance of the LSTM-based model and SVM-based model. These cases are divided into two parts, one for one-hour ahead load forecasting and the other for one-day ahead peak and valley load forecasting. The former is conducted using the historical hourly load data from 2013 to 2018, with a total of 52,584 data. The latter is based on the maximum and minimum daily load from 2013 to 2018, with 2191 data. All data is re-sampled from the original dataset.

According to Khan et al. this paper selects load sequences of different lengths as input features based on the auto-correlation function [27].

In terms of one-hour ahead load forecasting, Fig. 8 shows the auto-correlation between the load of 200 h in the hourly load dataset. It can be seen that the load of hour h-1 has the highest auto-correlation, and the hourly load sequence contains multiple periodicities. The load of h-24 and the load of h-24 multiple have peak auto-correlation.

As for one-day ahead peak and valley load forecasting, as shown in Fig. 9. It shows the auto-correlation between the 14-day loads. The auto-correlation coefficients between the daily peak load data sequences are periodic, while the auto-correlation between the daily valley load data sequences is not significant. Overall, the auto-correlation between the daily peak and valley load decreases as the time interval increases.

Based on the above conclusions, this paper creates 4 cases with different input features, case details are shown in Table 1.

- The input of Case 1 is a 8-dimensional vector that uses the load of hour h-1, h-24, h-48, h-72, h-96, h-120, h-144, h-168 to forecast the load of hour h.
- The input of Case 2 is a 168-dimensional vector that uses the load of hour h-1 to h-168, the hourly load of the previous week, to forecast the load of hour h.

	Historical load (t-1)	Outdoor temperature	Wind Speed	Relative humidity	Day type
Hourly load	0.930	0.172	0.112	-0.252	0.085
Daily peak load	0.946	-0.021	-0.003	0.155	0.072
Daily valley load	0.952	-0.145	0.041	0.190	0.040

The Pearson correlation coefficient

	Historical load (t-1)	Outdoor temperature	Wind Speed	Relative humidity	Day type
Hourly load	0.929	0.162	0.122	-0.241	0.088
Daily peak load	0.915	0.005	-0.017	0.132	0.084
Daily valley load	0.887	-0.175	0.056	0.224	0.064

The Spearman correlation coefficient

Fig. 6. Assessment of correlation for selected prediction features.

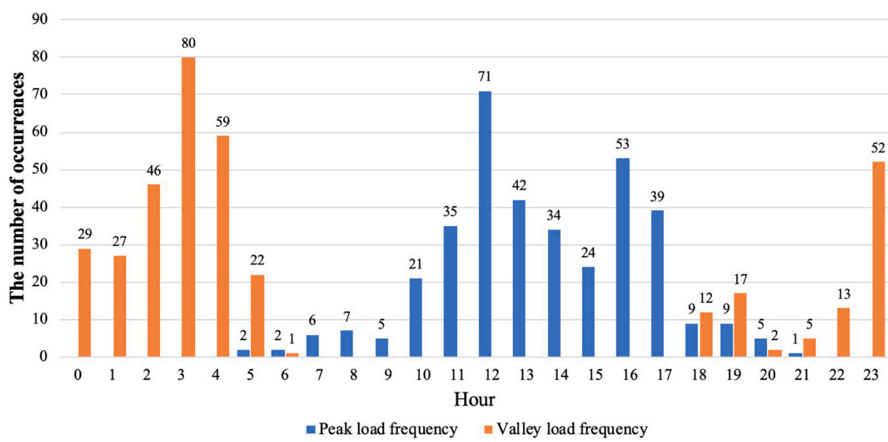

Fig. 7. The number of occurrences of peak or valley load per day for 2018.

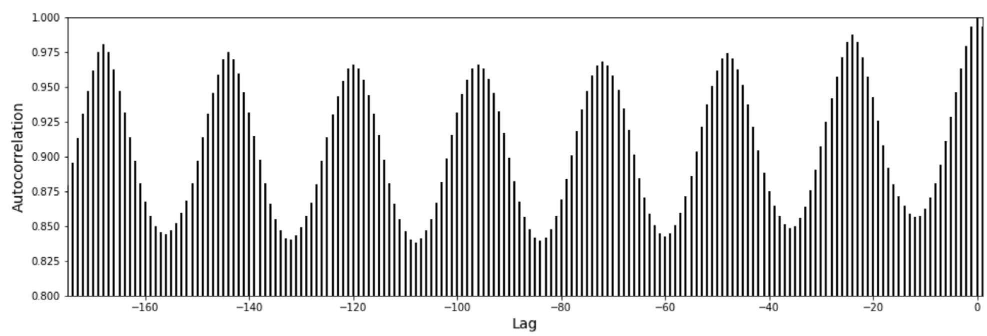

Fig. 8. The auto-correlation coefficient of hourly load data.

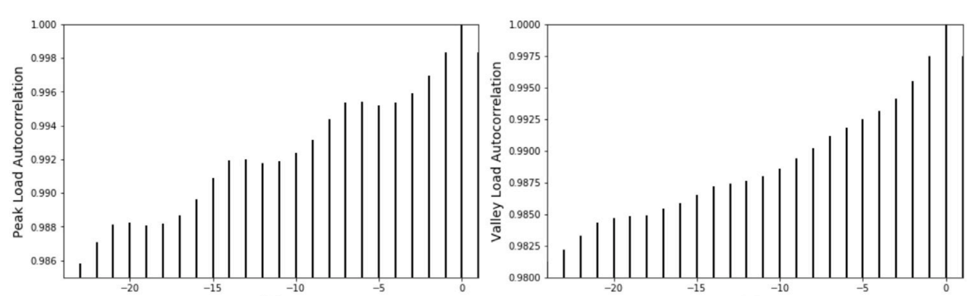

Fig. 9. The auto-correlation coefficient of daily peak and valley load data.

- The input of Case 3 is a 3-dimensional vector that uses the peak and valley load of day d-1, d-2, d-7 to forecast the peak and valley load of day d.
- The input of Case 4 is a 7-dimensional vector that uses the peak and valley load of day d-1 to d-7, the daily peak or valley load of the previous week, to forecast the peak and valley load of day d.

The input features of Cases 1 and 3 are selected based on the auto-correlation of hourly load data and that of daily peak and valley load data. The time point with a high auto-correlation coefficient and that with peak auto-correlation coefficient in the previous week are used as input features. In addition, it can be seen from Table 1 that the input features of Case 2 and Case 4 contain all of the input features of Case 1 and Case 3, respectively. In this paper, Case 2 and Case 4 are used as the control experiments to verify the accuracy and importance of feature selection.

Table 1
The details of each case.

	Forecast horizon	Input feature	Output (kW)
Case 1	1-h load	h-1,h-24,h-48,h-72,h-96,h-120,h-144,h-168	Load_(h)
Case 2	1-h load	h-1,h-2,h-3, …,h-167,h-168	Load_(h)
Case 3	Daily peak load Daily valley load	d-1, d-2, d-7	Peak load_(d) valley load_(d)
Case 4	Daily peak load Daily valley load	d-1,d-2,d-3,d-4,d-5,d-6,d-7	Peak load_(d) Valley load_(d)

4.6. Model setup

This paper creates standard LSTM-based model and SVM-based model based on background work. The SVM-based model used in the experiment is created with the scikit learning package, and the LSTM-based model is developed using Keras. The detailed parameters of these two models parameter settings are as follows:

- LSTM-based model: This model contains two LSTM layers and one fully connected layer. The first LSTM contains 100 units and the second LSTM layer contains 50 units. A dropout layer with 0.2 dropout rate is added between the first LSTM layer and the second LSTM layer to prevent overfitting. The activate function is rule. Mean square error is used as a loss function and Amda acts as an optimizer.
- SVM-based model: The linear function is used as the kernel of support vector regression model. The Tolerance for stopping criterion is set to 0.001. The penalty parameter C of the error term is 1.

4.7. Cross validation

Time series cross-validation [43] has been used to avoid over-fitting. Thus, the whole historical load dataset from 2013 to 2017 is used as a training set to ensure that there is a sufficient data training model. Then, the energy demand data for 2018 is treated as a verification set. Unlike the K-Fold cross-validation method, time series cross-validation method is trained using data prior to the test set sequence.

5. Results

The current section describes the results of the prediction models for each case study developed. The results presented in this section have been validated with data extracted by the building management system. Therefore, both the accuracy metrics and the validation refer to the physical building actual data. In particular one-hour ahead load (Section 5.1), and one-day ahead peak and valley load (Section 5.2).

5.1. Performance of one-hour ahead load forecasting models

This sub-section mainly evaluates the performance of LSTM-based model and SVM model for one-hour load forecasting. In terms of Case 1, the 2018 monthly RMSE is shown in Fig. 10.

The actual load and the predicted load for hourly load forecasting in June, 2018 are plotted in Fig. 11. The blue line is the actual power data, the green line represents the predicted electricity load by the LSTM-based model, and the red line stands for the predicted data by the SVM-based model. The absolute values of the predicted and actual load differences are displayed below the corresponding time step. Among them, the blue bar represents the LSTM-based model, and the orange bar stands for the SVM-based model.

It can be seen from Fig. 10 that the monthly RMSE trends of the two models are similar, and the RMSE changes are balanced. This shows that the performance of the two models is relatively stable and there is no over-fitting phenomenon. The monthly RMSE of the LSTM-based model is smaller compared to the monthly RMSE of the SVM-based model. It can also be seen from the predicted load curve and the actual load curve shown in Fig. 11 that the LSTM-based model performs better on the fitted hourly power load curve than the SVM-based model.

As for case 2, due to the influence of input feature selection, the 2018 monthly RMSE in Case 2 presents the opposite result of Case 1, as shown in Fig. 12. Fig. 13 shows the actual load and predicted load in Case 2 in June 2018.

It can be seen that the monthly RMSE of the SVM-based model is generally lower than that of the LSTM-based model. The predicted load of the SVM-based model fits better with the actual load.

In summary, considering both feature selection and hourly load forecasting, it can be concluded that the performance of the LSTM-based model is better than that of the SVM-based model. In addition, as shown in Table 2, the runtime of the LSTM-based model is much longer than that of the SVM-based model.

5.2. Performance of daily peak and valley load prediction models

This section assesses the performance of the LSTM-based model and the SVM-based model in one-day peak and valley load forecasting. As in the previous sub-section, RMSE is used to describe the performance of the model, and each month of 2018 is used as a test set. Figs. 14 and 15 plots the monthly RMSE of the model for peak load and valley load forecasting in Case 3 and in Case 4, respectively.

It can be seen that the trend of monthly RMSE in Case 3 and Case 4 is very similar whether it is one-day ahead peak forecasting or one-day ahead valley forecasting.

In order to more intuitively compare the performance of the two models, the actual load and predicted load for one-day ahead peak and valley load forecasting in June are plotted, as shown in Figs. 16 and 17. In these figures, the blue line is the actual power data, the red line represents the predicted electricity load by the LSTM-based model, and the yellow line stands for the predicted data by the SVM-based model. The absolute values of the difference between the predicted load and the actual load are displayed below the corresponding time step. Among them, the blue bar represents the LSTM-based model and the orange bar stands for the SVM-based model. It can be concluded from the above figures that the LSTM-based model and the SVM-based model have almost the same prediction accuracy in one-day ahead peak and valley load forecasting. In fact, the SVM-based model is able to perform better with small datasets compared to deep neural network.

The predictions have been tested using cross-validation and data analysis techniques to find outliers in the performance of the models. The validation analysis was also applied on special days such as national or local holidays, but it did not reveal any great variance from the average.

6. Discussion

The current work aims to forecast the electricity consumption of a large and high efficient commercial building using different machine learning techniques. The results of the four main case studies with the MAE, RMSE, MAPE, and runtime are summarized in Table 2. The current section discuss the performance of LSTM-based model and SVM-based model assessing the advantages and disadvantages of the models.

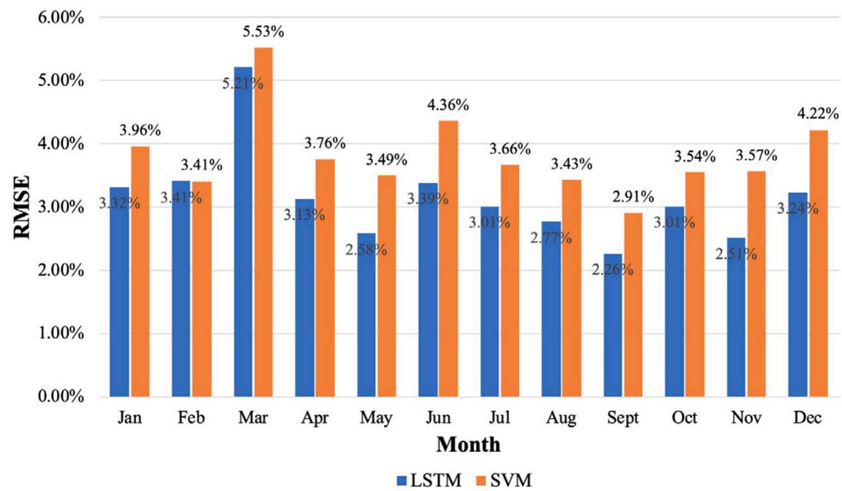

Fig. 10. The 2018 monthly RMSE for hourly load forecasting in Case 1.

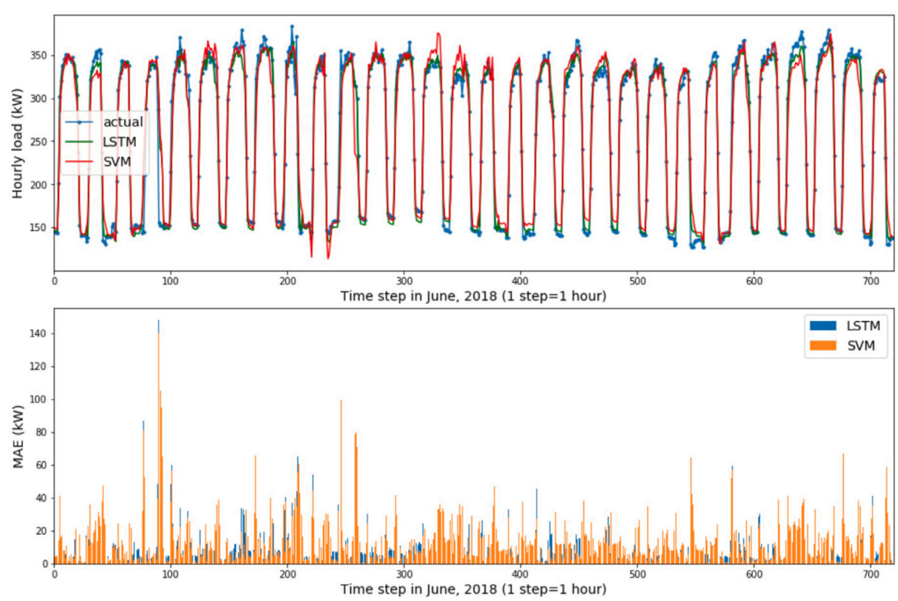

Fig. 11. The actual load and the predicted load in Case 1. (For interpretation of the references to color in this figure legend, the reader is referred to the web version of this article.)

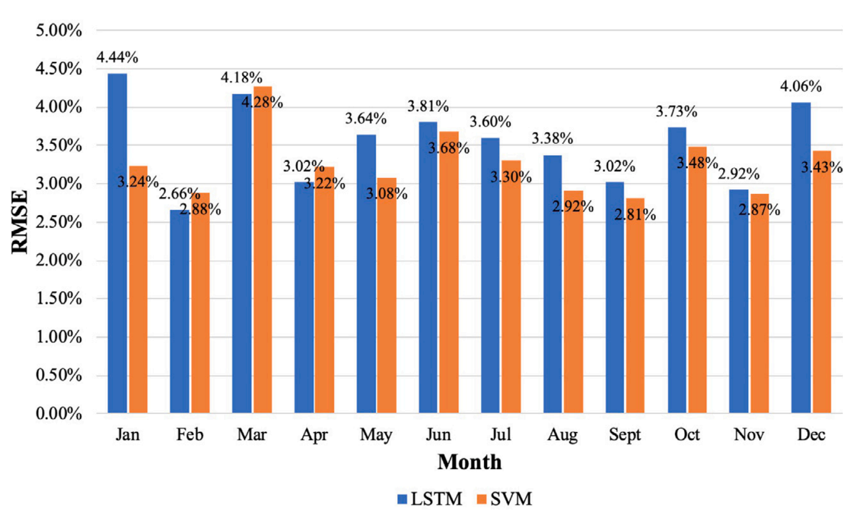

Fig. 12. The 2018 monthly RMSE for hourly load forecasting in Case 2.

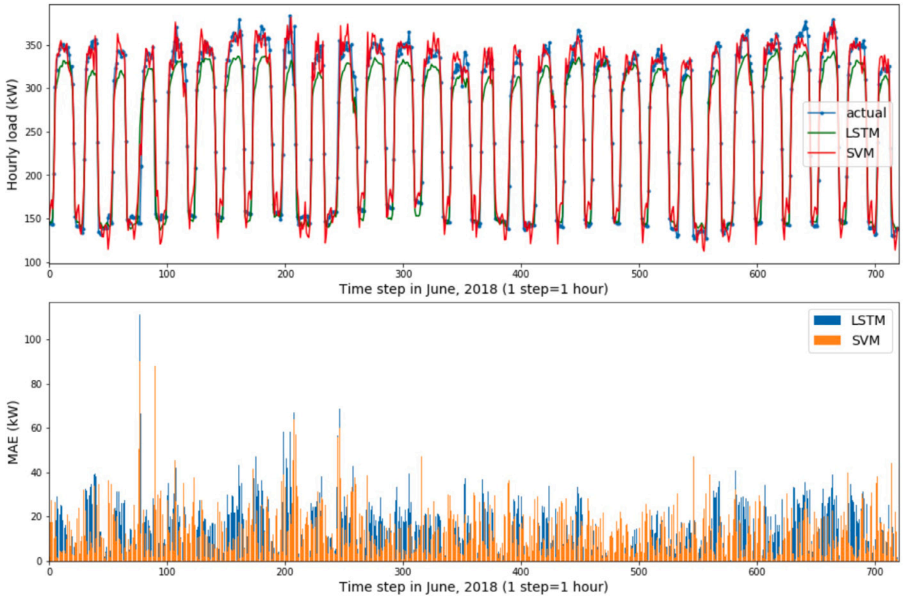

Fig. 13. The actual load and the predicted load in Case 2.

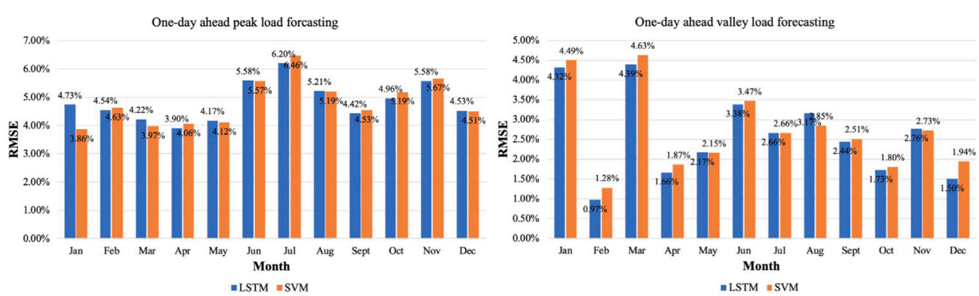

Fig. 14. The 2018 monthly RMSE for daily peak and valley load forecasting in Case 3.

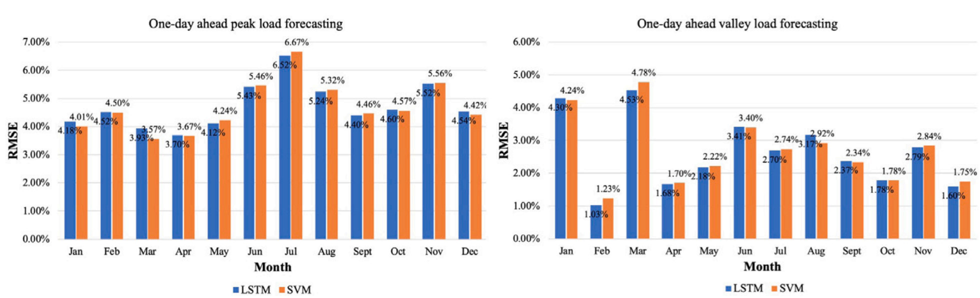

Fig. 15. The 2018 monthly RMSE for one-day ahead peak and valley load forecasting in Case 4.

Table 2
Comparison of models performances.

	Forecast	Model	MAE (kW)	RMSE (%)	MAPE (%)	Runtime
		LSTM	9.258	3.15	4.05	497.70
Case 1	1-h ahead load	SVM	11.940	3.82	5.30	4.21
		LSTM	12.642	3.54	5.54	706.96
Case 2	1-h ahead load	SVM	11.539	3.26	5.37	23.94
		LSTM	9.957	4.84	3.04	67.93
	1-day ahead peak load	SVM	9.873	4.81	3.01	0.05
		LSTM	3.603	2.60	2.57	66.96
Case 3	1-day ahead valley load	SVM	3.758	2.70	2.71	0.05
		LSTM	9.800	4.73	3.00	66.82
	1-day ahead peak load	SVM	9.709	4.70	2.96	0.06
		LSTM	3.683	2.63	2.63	69.60
Case 4	1-day ahead valley load	SVM	3.665	2.66	2.63	0.05

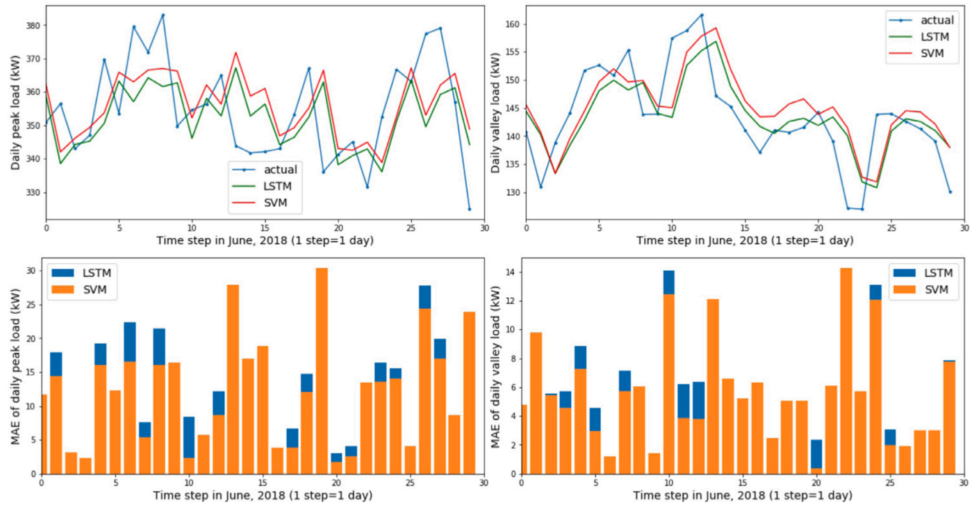

Fig. 16. The actual load and predicted load for daily peak and valley load forecasting in Case 3. (For interpretation of the references to color in this figure legend, the reader is referred to the web version of this article.)

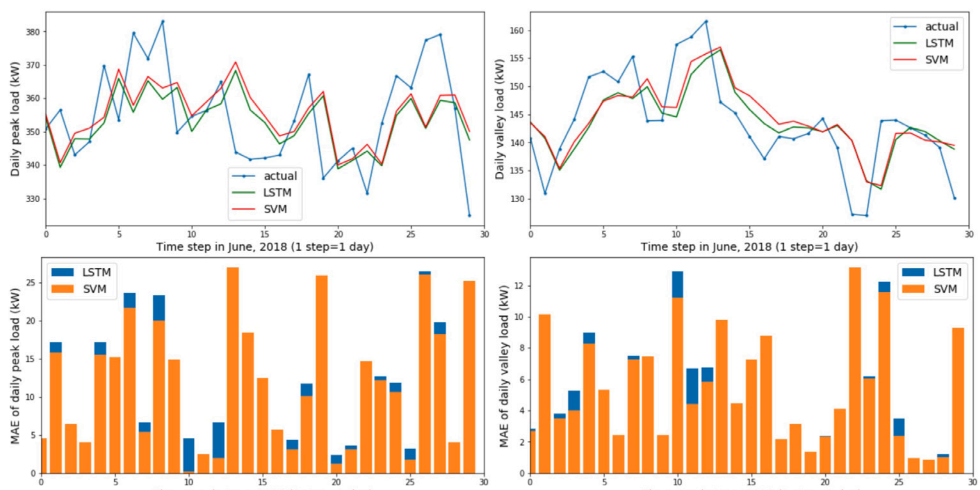

Fig. 17. The actual load and predicted load for daily peak and valley load forecasting in Case 4. (For interpretation of the references to color in this figure legend, the reader is referred to the web version of this article.)

In terms of one-hour ahead load forecasting, it can be seen that based on the LSTM-based model, the models produce more accurate results in Case 1 than Case 2 As mentioned in the experimental setup section, Case 1 contains only 8 features for the input of the predictive model, which is much smaller than the number of features included in Case 2. Therefore, it shows that feature selection based on auto-correlation plays a fundamental role in LSTM-based models. The input features with high auto-correlation are more important than the number of input features.

As for one-day ahead peak and valley load forecasting, the prediction accuracy of Case 3 using the LSTM-based model is not significantly different from that of Case 4. The reason for this result is that the auto-correlation of daily peak and valley load shows a downward trend as a whole. At this point, it is not effective to select the input features on the peak auto-correlation in each cycle.

For the SVM-based model, it can be seen from the experimental results that the more input features provided to the model, the higher the prediction accuracy of the model. In summary, the feature selection focusing on high auto-correlation features can improve the accuracy of the LSTM-based model. Therefore, another contribution of this paper is the method of feature selection. The input of the model can directly affect the predictive performance of the LSTM-based model. Thus, in the feature selection stage, the auto-correlation of historical load data is used to select the time point with high correlation as the input feature. This method is better than directly selecting the historical load of a certain cycle in the past as an input feature. Additionally, this paper evaluates and compares the performance of LSTM-based models and SVM-based models through four cases. Using time series cross-validation, each month of 2018 is used for validation of the model, and the monthly RMSE of the two models is recorded.

The comparison between a deep neural network prediction with a SVM model revealed that the trained LSTM model is more accurate than the SVM-based model in one-hour ahead load forecasting. In terms of one-day ahead peak and valley load forecasting, the performance of the SVM-based model is better. However, it is worth mentioning that the runtime of the SVM-based model is much shorter than the LSTM-based model, for both hourly load forecasting and daily peak and valley load forecasting. In fact, as illustrated in Table 2, the average runtime of the SVM-based model can be negligible, at 0.05 s, while the average runtime of the LSTM-based model is approximately 70 s.

In summary, the LSTM-based model is better at handling complex, unstable data based on sufficient training data. SVM-based model is suitable for load forecasting of small-scale datasets. In the case of sufficient data and the pursuit of high-precision load forecasting, the preferred choice is the LSTM-based model, while SVM-based model is a better choice when there is not enough training data or time cost is one of the main considerations.

Furthermore, when assessing technology for electricity demand forecast in buildings for day-ahead scheduling or short term prediction to implement demand response measures, training a deep neural network could result in a small if none advantage. In the case of commercial high efficient buildings, the prediction errors are relatively small and the accuracy is enough for an accurate overall assessment for a demand response aggregator to control the electricity generation or reduce the building electricity demand.

The forecast technique can be used to estimate valleys and peak consumption a day-ahead, allowing demand response aggregators to bid on the day ahead electricity market. Additionally, it could also support building managers to schedule a day ahead local CHP generators. The one hour ahead forecast will allow to have an accurate baseline to estimate the impact on DR measures on the buildings and for the optimal scheduling of local generators.

Although the model applied in this paper has good prediction results, it can be further improved to reduce the predicted and actual load difference. This paper only considers history load data for short-term load forecasting. The article uses the Pearson and Spearman correlation coefficients to rule out the effects of outdoor temperature and date types on load forecasting, however, other factors can be considered, such as the amount of renewable energy produced or occupancy profiles.

7. Conclusions

The provision of energy system services plays a critical role for the decarbonization of the power system and the integration of renewable energies at local and system levels. However, the growing penetration of renewable and controllable loads require accurate load forecasting techniques. In this paper, a commercial building has been used as a test-bed for a set of forecasting algorithms using machine learning techniques. Besides the hourly energy demand forecast, a day-ahead peak and valley prediction has been trained on the historical data. The current work developed state of the art forecast models to predict the electricity demand and compare it with the daily valley and peak to dynamically optimize the CHP generator, the thermal storage and electricity demand implementing demand response measures. The novelty of the work is the development of three different prediction models that can be combined for the evaluation of flexibility. In future work, hybrid models, for example, combining multiple forecast techniques, may be tested to improve prediction accuracy. Additionally, a more accurate model will be employed to identify anomalies such as power outages and unscheduled maintenance and the prediction models will be used to compute a metric to assess the flexibility of the building and to forecast the impact of the demand response measures on the potential flexibility.

Acronyms

ANNs Artificial Neural Networks

BES building energy simulation

CHP combined heat and power

DR Demand Response

DSM Demand Side Management

EMS energy management system

FFNN Feed-Forward Neutral Network

HVAC Heating, Ventilation and Air Conditioning

LSTMs Long Short-term Memory Networks

LTLF long-term power load forecasting

MAE Mean Absolute Error

MAPE Mean Absolute Percentage Error

MTLF medium-term load forecasting

RMSE Root Mean Squared Error

RNNs Recurrent Neural Networks

STLF short-term load forecasting

SVM Support Vector Machines

SVR Support Vector Regression

TSO Transmission System Operator

VSTLF very short-term load forecasting

References

[1] Le Quéré C, Andrew RM, Friedlingstein P, Sitch S, Hauck J, Pongratz J, Pickers PA, Korsbakken JI, Peters GP, Canadell JG, Arneth A, Arora VK, Barbero L, Bastos A, Bopp L, Chevallier F, Chini LP, Ciais P, Doney SC, Gkritzalis T, Goll DS, Harris I, Haverd V, Hoffman FM, Hoppema M, Houghton RA, Hurtt G, Ilyina T, Jain AK, Johannessen T, Jones CD, Kato E, Keeling RF, Goldewijk KK, Landschützer P, Lefèvre N, Lienert S, Liu Z, Lombardozzi D, Metzl N, Munro DR, Nabel JEMS, Nakaoka S, Neill C, Olsen A, Ono T, Patra P, Peregon A, Peters W, Peylin P, Pfeil B, Pierrot D, Poulter B, Rehder G, Resplandy L, Robertson E, Rocher M, Rödenbeck C, Schuster U, Schwinger J, Séférian R, Skjelvan I, Steinhoff T, Sutton A, Tans PP, Tian H, Tilbrook B, Tubiello FN, van der Laan-Luijkx IT, van der Werf GR, Viovy N, Walker AP, Wiltshire AJ, Wright R, Zaehle S, Zheng B. Global carbon budget 2018. Earth Syst Sci Data 2018;10(4):2141–94. http://dx.doi.org/10.5194/essd-10-2141-2018, URL https://essd.copernicus.org/articles/10/2141/2018/.
[2] International Energy Agency. Electricity information overview. 2020, URL https://www.iea.org/reports/electricity-information-overview.
[3] Alkhathami M. Introduction to electric load forecasting methods. J Adv Electr Comput Eng 2015;2(1):1–12.
[4] Li X, Wen J. Review of building energy modeling for control and operation. Renew. Sustain. Energy Rev. 2014;37:517–37. http://dx.doi.org/10.1016/j.rser.2014.05.056, URL https://www.sciencedirect.com/science/article/pii/S1364032114003815.
[5] Steininger K, Meyer L, Schleicher S, Riahi K, Williges K, Maczek F. Effort Sharing among EU Member States: Green Deal Emission Reduction Targets for 2030. Wegener Center Research Briefs 2-2020; 2020.
[6] Hong T, Fan S. Probabilistic electric load forecasting: A tutorial review. Int. J. Forecast. 2016;32(3):914–38. http://dx.doi.org/10.1016/j.ijforecast.2015.11.011.
[7] Albadi MH, El-Saadany EF. A summary of demand response in electricity markets. Electr. Power Syst. Res. 2008;78(11):1989–96.
[8] Gils HC. Assessment of the theoretical demand response potential in Europe. Energy 2014;67:1–18.
[9] Nolan S, O'Malley M. Challenges and barriers to demand response deployment and evaluation. Appl. Energy 2015;152:1–10. http://dx.doi.org/10.1016/j.apenergy.2015.04.083.

[10] Bampoulas A, Saffari M, Pallonetto F, Mangina E, Finn DP. A fundamental unified framework to quantify and characterise energy flexibility of residential buildings with multiple electrical and thermal energy systems. Applied Energy 2021;282:116096. http://dx.doi.org/10.1016/j.apenergy.2020.116096, https://www.sciencedirect.com/science/article/pii/S0306261920315191.

[11] Ahmad A, Javaid N, Mateen A, Awais M, Khan ZA. Short-term load forecasting in smart grids: An intelligent modular approach. Energies 2019;12(1):164. http://dx.doi.org/10.3390/en12010164.

[12] Ekonomou L, Christodoulou CA, Mladenov V. A short-term load forecasting method using artificial neural networks and wavelet analysis. Int J Power Energy Syst 2016;1:64–8.

[13] Yildiz B, Bilbao J, Sproul A. A review and analysis of regression and machine learning models on commercial building electricity load forecasting. Renew. Sustain. Energy Rev. 2017;73:1104–22. http://dx.doi.org/10.1016/j.rser.2017.02.023.

[14] Zhang J, Wei YM, Li D, Tan Z, Zhou J. Short term electricity load forecasting using a hybrid model. Energy 2018;158:774–81. http://dx.doi.org/10.1016/j.energy.2018.06.012.

[15] Kuo P-H, Huang C-J. A high precision artificial neural networks model for short-term energy load forecasting. Energies 2018;11(1):213. http://dx.doi.org/10.3390/en11010213.

[16] Raza MQ, Khosravi A. A review on artificial intelligence based load demand forecasting techniques for smart grid and buildings. Renew. Sustain. Energy Rev. 2015;50:1352–72. http://dx.doi.org/10.1016/j.rser.2015.04.065.

[17] Coakley D, Raftery P, Keane M. A review of methods to match building energy simulation models to measured data. Renew. Sustain. Energy Rev. 2014;37:123–41. http://dx.doi.org/10.1016/j.rser.2014.05.007.

[18] Prakash AK, Xu S, Rajagopal R, Noh HY. Robust building energy load forecasting using physically-based kernel models. Energies 2018;11(4):862. http://dx.doi.org/10.3390/en11040862.

[19] Li X, Wen J. Review of building energy modeling for control and operation. Renew. Sustain. Energy Rev. 2014;37:517–37. http://dx.doi.org/10.1016/j.rser.2014.05.056.

[20] Christantoni D, Flynn D, Finn DP. Modelling of a multi-purpose commercial building for demand response analysis. Energy Procedia 2015;78:2166–71. http://dx.doi.org/10.1016/j.egypro.2015.11.308, URL http://www.sciencedirect.com/science/article/pii/S1876610215020408.

[21] Wei Y, Zhang X, Shi Y, Xia L, Pan S, Wu J, Han M, Zhao X. A review of data-driven approaches for prediction and classification of building energy consumption. Renew. Sustain. Energy Rev. 2018;82:1027–47. http://dx.doi.org/10.1016/j.rser.2017.09.108.

[22] Amasyali K, El-Gohary NM. A review of data-driven building energy consumption prediction studies. Renew. Sustain. Energy Rev. 2018;81:1192–205. http://dx.doi.org/10.1016/j.rser.2017.04.095.

[23] Takeda H, Tamura Y, Sato S. Using the ensemble Kalman filter for electricity load forecasting and analysis. Energy 2016;104:184–98. http://dx.doi.org/10.1016/j.energy.2016.03.070.

[24] Nguyen AT, Reiter S, Rigo P. A review on simulation-based optimization methods applied to building performance analysis. Appl. Energy 2014;113:1043–58. http://dx.doi.org/10.1016/j.apenergy.2013.08.061.

[25] Feng Y, Ryan SM. Day-ahead hourly electricity load modeling by functional regression analysis. Appl. Energy 2016;170:455–65. http://dx.doi.org/10.1016/j.apenergy.2016.02.118.

[26] Kuster C, Rezgui Y, Mourshed M. Electrical load forecasting models: A critical systematic review. Sustainable Cities Soc. 2017;35:257–70. http://dx.doi.org/10.1016/j.scs.2017.08.009.

[27] Khan RA, Dewangan CL, Srivastava SC, Chakrabarti S. Short term load forecasting using SVM models. Power India Int Conf 2018;8:1–5. http://dx.doi.org/10.1109/POWERI.2018.8704366.

[28] Zhao H, Magoulès F. A review on the prediction of building energy consumption. Renew. Sustain. Energy Rev. 2012;16(6):3586–92. http://dx.doi.org/10.1016/j.rser.2012.02.049.

[29] Harish VSKV, Kumar A. A review on modeling and simulation of building energy systems. Renew. Sustain. Energy Rev. 2016;56:1272–92. http://dx.doi.org/10.1016/j.rser.2015.12.040.

[30] Alfares HK, Nazeeruddin M. Electric load forecasting: literature survey and classification of methods. Internat. J. Systems Sci. 2002;33(1):23–34.

[31] Prakash AK, Xu S, Rajagopal R, Noh HY. Robust building energy load forecasting using physically-based kernel models. Energies 2018;11(4). http://dx.doi.org/10.3390/en11040862, URL https://www.mdpi.com/1996-1073/11/4/862.

[32] Bedi J, Toshniwal D. Deep learning framework to forecast electricity demand. Appl. Energy 2019;238:1312–26. http://dx.doi.org/10.1016/j.apenergy.2019.01.113, URL https://www.sciencedirect.com/science/article/pii/S0306261919301217.

[33] Qing X, Niu Y. Hourly day-ahead solar irradiance prediction using weather forecasts by LSTM. Energy 2018;148:461–8. http://dx.doi.org/10.1016/j.energy.2018.01.177, URL https://www.sciencedirect.com/science/article/pii/S0360544218302056.

[34] Du Q, Gu W, Zhang L, Huang S-L. Attention-based LSTM-CNNs for time-series classification. In: Proceedings of the 16th ACM conference on embedded networked sensor systems. 2018. p. 410–411.

[35] Bouktif S, Fiaz A, Ouni A, Serhani MA. Optimal deep learning LSTM model for electric load forecasting using feature selection and genetic algorithm: Comparison with machine learning approaches. Energies 2018;11(7):1636. http://dx.doi.org/10.3390/en11071636.

[36] Colah. Understanding LSTM networks. 2015, URL https://colah.github.io/posts/2015-08-Understanding-LSTMs/.[accessed 26 August 2019].

[37] Non-domestic building energy ratings Q4 2017 - CSO - central statistics office. 2020, URL https://www.cso.ie/en/releasesandpublications/er/ndber/non-domesticbuildingenergyratingsq42017/.

[38] Met ÉireannDublin weather reports. 2019, URL https://www.met.ie/.[accessed 26 August 2020].

[39] Galarnyk M. Understanding boxplots. 2018, URL https://towardsdatascience.com/understanding-boxplots-5e2df7bcbd51.[accessed 26 August 2019].

[40] Kapetanakis D-S, Mangina E, Finn DP. Input variable selection for thermal load predictive models of commercial buildings. Energy Build. 2017;137:13–26. http://dx.doi.org/10.1016/j.enbuild.2016.12.016.

[41] Pallonetto F, Mangina E, Milano F, Finn DP. SimApi, a smartgrid co-simulation software platform for benchmarking building control algorithms. SoftwareX 2019;9:271–81. http://dx.doi.org/10.1016/j.softx.2019.03.003.

[42] Hong T. Short term electric load forecasting. North Carolina State University; 2010.

[43] Bergmeir C, Hyndman RJ, Koo B. A note on the validity of cross-validation for evaluating autoregressive time series prediction. Comput. Statist. Data Anal. 2018;120:70–83. http://dx.doi.org/10.1016/j.csda.2017.11.003.

Strategic bidding of distributed energy resources in coupled local and central markets

Aruna Rout, *Department of electrical Engineering , Capital Engineering College, Bhubaneswar, aruna.rout@hotmail.com*

Achyutananda Panda, *Department of Electrical and Electronics Engineering, NM Institute of Engineering & Technology, Bhubaneswar, achyutananda.panda55@gmail.com*

Ajit Kumar Panda, *Department of Electrical Engineering, Aryan Institute of Engineering & Technology, Bhubaneswar, akpanda555@hotmail.com*

Madhusudan Das, *Department of Electronics and Communication Engineering , Raajdhani Engineering College, Bhubaneswar, madhusudandas55@hotmail.com*

A B S T R A C T

This paper explores a revenue maximization problem for distributed energy resources in a local day-ahead and balancing market. The local market creates opportunities for competition among distributed energy resources, however it may also lead to exercising market power. In the day-ahead market, the strategic revenue maximization of the distributed energy resources is modelled through a bi-level optimization. The upper-level in the bi-level optimization is from the strategic distributed energy resource's perspective and the lower-level problem is from the local market operator's perspective. The balancing market (where there is perfect competition) is modelled by the shrinking rolling horizon approach. A wind farm with a storage system is considered as a case study of a strategic distributed energy resource to evaluate its profitability within the proposed revenue maximization problem. The revenue of the wind farm in the local market is compared with the one in a (business-as-usual) centralized market where it cannot exercise market power. Sensitivity analysis regarding the effect of changing the distribution system parameters e.g. the branch resistances and the loads, on the revenue of the wind farm and its bidding behaviour is performed. Moreover, the role of the storage system on the revenue of the wind farm is studied. Results show that an overloaded or weak distribution system will positively influence the strategic position of the wind farm. Finally, it is shown that depending on the existence of market power, a storage system can bring extra revenues for the wind farm, by hedging against its uncertain output.

Keywords:
Distributed energy resources
Distribution system constraints
Electrical storage systems
Local market
Market power
Wind energy

1. Introduction

The integration of distributed energy resources (DERs) such as electrical storage systems, small wind farms, PV systems, etc. are increasing in the distribution system. High penetration of DERs brings benefits and opportunities for power systems, among others, increasing the affordability and reliability and decreasing system costs [1]. However, in the current electricity markets, there are some challenges for the participation of the DERs in markets, among others, scalability issues and complexity of many DERs in one central market, a high bid size requirement for market participants, and a high market transaction fee [2]. To deal with these challenges, the concept of the local electricity market has emerged [3–7]. In these local electricity markets DERs participate directly within a market. What the bidding strategy of these DERs should be to maximize their profit within the specific case of a local market is still an open question.

Generally speaking, the bidding behaviour of market players in power systems can be classified into strategic bidding and non-strategic bidding. Non-strategic bidding means market players can only solve a self-scheduling problem to determine their most beneficial actions for given prices. In contrast, strategic bidding is behaviour by which a market player can affect market prices and as a result, increase its revenue [8]. There are several ways for a market player to perform market power in the electricity market. These ways, according to [9] are: using price bidding strategies to raise market prices independently of changes in underlying supply and demand conditions; exploiting market power resulting from local transmission network constraints; capacity withholding to increase market prices, in particular by manipulating the capacity payment mechanism under the existing trading arrangements; and manipulation of complex market rules to increase prices and earn excessive profits. Ref. [10] summarizes the market power behaviour of generating companies in three strategies: financial withdrawal (price increase), physical withdrawal (volume reduction), and physical withdrawal with free bilateral contracts. Ref. [11] classifies the exercise of market power in electricity markets in two broad strategies which a generator can use to artificially increase electricity market prices;

economic withholding and capacity withholding. In the capacity withholding, a strategic market participant can influence the market price by withdrawing its cheaper units [12]. In the economic withholding, a strategic market player can maximize its revenue mainly due to the system constraints [13]. DERs participating in local electricity markets can have market power despite their small size, as the market size is still smaller and location matters for economic withholding. Therefore, local electricity markets can create good opportunities for DERs to exercise market power [1]. Moreover, it is important to understand strategic bidding behaviour by the DERs in local markets, as the market power leads to unwanted consequences for social welfare and unfair income distribution [14]. However, there is yet limited amount of literature in which the strategic behaviour of DERs in the local electricity market is studied. Strategic bidding of market players in the centralized electricity market, however, has been studied thoroughly in the literature. Some of them are reviewed here.

The existing literature is classified in terms of a different strategic approach. In [15], the bidding behaviour of the storage system which acts strategically through economic withholding is studied. Ref. [16] is another example where the storage system is exercising market power, however, by withholding its capacity. In some literature, "capacity" refers to generation capacity expansion which can also be seen as a strategic behaviour by generating companies in imperfectly competitive power markets. For example, in [17], the strategic behaviour of companies facing generation capacity expansion decisions are studied through different game-theoretic models. Ref. [18] is another example in which different models of investments in generation capacity in an oligopolistic market are studied. However interesting, long-term investment decisions are out of scope of this paper, where we focus on day-ahead operational decisions. In the published literature in this area, mainly exercising market power by generators which are participating in the wholesale market is studied. However, the effect of transmission constraints on strategic bidding of market players mostly is discarded such as [19]. Ref. [20] also proposes a profit maximization problem for a wind turbine operating in a traditional wholesale market without considering system constraints. However, there is some literature such as [21] and [22] where transmission system constraints are considered through DC and AC power flow, respectively. Ref. [23] is another example that proposes a problem with mathematical programming with equilibrium constraints-based procedure for calculating oligopolistic price equilibria for an electric power market while taking into account transmission constraints. Ref. [24] studies the strategic behaviour of a wind turbine through a bi-level model for the jointly cleared wholesale energy and reserve markets where the transmission system is modelled through the DC power flow. This bi-level approach is also used in [25] which addresses the optimal bidding strategy problem of a commercial virtual power plant seeking to maximize its profit in the day-ahead market. Another example is [15] in which the bi-level optimization is used to maximize the profit of a storage system in the day-ahead and balancing markets without considering the transmission constraints. In [23], also the bi-level optimization is applied for profit maximization of dominant firms in an electric power network modelled through DC power flow. In recent years, there has been a growing interest in bi-level approaches to model many operational and planning problems in power systems. More information about the bi-level and its application in power systems can be found in [26].

In this paper, the bi-level approach is applied to the local electricity market to study the possibility of market power for a DER represented by a combination of wind farm and storage system. A local market model based on the coupled market concept introduced in [6] is selected. In this market, there is a local market for the participation of DERs which is operated by a distribution market operator. The distribution market operator can be considered as the distribution system equivalent of the market operator, which is responsible for managing the electricity market and scheduling power transfers to achieve the secure operation of the distribution system. This local market engages in an exchange of information and power with the central market, both in the day-ahead and real-time balancing time frames.

The reason for choosing this market model is as follows. Since the main research question of this paper is to address whether DERs are capable of exercising market power, a market model with certain characteristics should be chosen. When a local market is connected to a larger market, capacity withholding is a less feasible strategy for the DERs due to their small size and the risk of such a strategy backfiring by triggering imports of cheaper energy from the upstream transmission system. The distribution network constraints should, therefore, be taken into account in the market clearing process, so that a realistic picture can be obtained of any remaining possibilities for exercising market power, in particular economic withholding.

Next to that, a local balancing market needs to be included to fully model the behaviour of market participants, and uncover the possibility for exercising market power in this market as well. With a high level of DER penetration, the participation of DERs in the balancing market becomes non-negligible. However, the scalability issue for the TSO with regards to managing all the balancing resources which are available still exists. Therefore, DERs need to be aggregated in some way to allow participation in the central balancing market. In the proposed coupled market, the local balancing market acts as this aggregator. Note that the DMO participates in the central balancing market, and balancing remains a system-wide service. Lastly, the coupled market can belong to a future with a lot of (renewable-based) DERs in the distribution system, and there can be that balancing in distribution systems becomes part of the responsibility of the local market. It means that in the future, the local market can go towards being more independent of the upstream system. There is research on local balancing and its importance in the future, for example in [27]. Therefore, the coupled market design is chosen, because it enables both modelling of the distribution system constraints and the inclusion of a balancing market, both of which are essential ingredients for studying the possibilities of exercising market power by DERs.

To model the participation of the wind farm with the storage system in the balancing market a shrinking rolling horizon approach is used. In a shrinking rolling horizon approach, instead of having a horizon of fixed length, the endpoint of the horizon is fixed, leading to a shorter time window (horizon) for each solution performed at consecutive times t, after starting time t_0 [28]. This shrinking rolling horizon is applied in several pieces of literature, for example, in [29] which addresses the demand side management problem for smart grids where the users have energy generation and storage capabilities. In [30] also, a shrinking rolling horizon is used in unit commitment formulations to quantify the uncertainty in wind power generation.

With the behaviour of the wind farm with the storage system modelled, several questions about the exercising of market power in a local electricity market can be answered: Can the wind farm raise its revenue in the day-ahead market compared to a centralized market model? How do the distribution system parameters, e.g. resistance and loads, affect the use of the market power of the wind farm? How would the inclusion of the storage system affect the revenue of the wind farm? In short, the contributions of this paper are:

- Formulating a revenue maximization problem for a wind farm with a storage system in a local day-ahead market.

Table 1
Sets and indices.

$c(C)$	Index(set) of combined wind farm and energy storage systems.
$e(E)$	Index(set) of energy storage systems.
$g(G)$	Index(set) of generators.
$i(I)$	Index(set) of sending nodes.
$j(J)$	Index(set) of receiving nodes.
$l(L)$	Index(set) of line.
L_D	Set of distribution lines.
L_T	Set of transmission lines.
N_D	Set of distribution nodes.
N_T	Set of transmission nodes.
N_{D-T}	Set of interface nodes in distribution system.
N_{T-D}	Set of interface nodes in transmission system.
$s(S)$	Index(set) of scenarios.
$t(T)$	Index(set) of time steps.
$w(W)$	Index(set) of wind farms.

- Showing that a wind farm with a storage system can exercise its market power in a local market to generate a higher revenue than in a centralized (business-as-usual) market.
- Demonstrating the effect of the distribution system parameters on the ability to exercise market power by DERs in local markets.

The paper is organized as follows. In Section 2, the main nomenclature used in this paper is listed. In Section 3, the coupled market model is explained. In Section 4, the steps for the revenue maximization of the DERs in the day-ahead and balancing markets of the coupled market model are described. In Section 5, the corresponding mathematical formulation is presented. In Section 6, input data and case studies are explained. The result of simulations on the case studies is shown in Section 7. Finally, conclusions are summarized in Section 8.

2. Nomenclature

The main nomenclature used in this paper is listed in Tables 1–3. Other symbols and abbreviations are defined where they first appear.

3. Coupled market model

In this section, the proposed coupled market model in [6] is described. In this market model, there is a local day-ahead and balancing market where DERs that are connected to the distribution system level can participate. The local market for DERs is operated by the distribution market operator (DMO) which can be an independent entity or be a part of the distribution system operator (DSO) (if the local regulatory framework allows). In any case, there should be information exchange between DSO and DMO regarding the dispatching of DERs and the security of the system constraints. The DMO aggregates bids from DERs and participates in the central market on behalf of them. The central market is operated by the transmission market operator (TMO) which is equivalent to a power exchange in Europe (e.g. EPEX or Nordpool) or an independent system operator in the US. Note that for example, in Europe, the transmission system operator (TSO) is responsible for balancing and is a different entity than the power exchange which operates the day-ahead market. It could have been that in the coupled market, one TMO could be assigned for the day-ahead market operation and one other entity for the balancing market, separately. However, for the sake of simplicity, one TMO is introduced which clears both the balancing and day-ahead markets. Having one TMO in the market scheme does not affect results in comparison with the situation of two separate TMO organizations. In this market model, the TSO is responsible for managing the transmission system and guarantees the security and stability of its operation. The TSO and the TMO should, therefore, exchange information regarding the dispatching and the security of the transmission system. The DMO and bulk generators and consumers at the transmission system participate in this TMO-operated central market.

The DMO can be defined as the distribution level equivalent of the market operator, which is responsible for managing the electricity market and scheduling power transfers to achieve the optimal operation of the distribution system. The DMO serves as an intermediate entity between the TMO-operated central market and the DERs and is a separate entity from the DSO.

In Fig. 1, the time sequence of the coupled DMO–TMO market model is shown in the grey colour flowchart. In total there are six steps in Fig. 1: Step I is preliminary scheduling for the local day-ahead joint energy and reserve capacity market. This step happens in D-1, the day before the delivery time and at a time, before the clearing time of the day-ahead wholesale market. The day-ahead market at the local and national level is a joint energy and reserve market and is cleared every hour in a 24-hour time-horizon. The reasons for introducing a reserve capacity market and including this as part of a joint energy and reserve capacity market is as follows. Firstly, in the coupled market, the TSO relies on the DMO market for the balancing market. As the TSO does not have control over DERs and the distribution system, there is a chance that in the balancing market, there will be a lack of resources. To avoid this situation, the reserve market should be created to guarantee that there will be enough energy available for the balancing phase. Secondly, the European regulators are paying more attention to the reserve market and the simultaneous alignment of energy provision and reserve capacity as a more efficient market design [31]. Through this step, the DMO solves an optimization problem for determining the local day-ahead energy and reserve market prices and an initial limit for the power flow over the transmission-distribution interface transformer. Step II is the TMO day-ahead joint energy and reserve market and clears in D-1 with the time resolution of one hour and in a 24-hours time-horizon. The results for this step are the scheduled power of bulk generators which will be sent to the central balancing market (step V) and a final value of the power flow over the transmission-distribution interface transformer which will be sent back to the DMO. Right after clearing the day-ahead wholesale market, the local day-ahead joint energy and reserve market is cleared by the DMO in step III. The results of this market will be sent to the local balancing market in step IV.

The procedure in the balancing market is similar to that of the day-ahead market. The difference is the duration of the scheduling interval which is 15 min for the balancing market. Step IV which happens in D, the day of the delivery time, is preliminary scheduling for the local balancing market and happens near real-time. Through this step, the local balancing market price and an initial value for the power flow over the interface transformer are estimated. In step V (real-time), the TMO clears the central real-time balancing market according to the scheduled energy and reserve of market players. The TMO will send back the final value for the interface transformer power to the DMO. Finally, in step VI, the local balancing market is cleared by the DMO, based on the updated interface power flow from step V and the DER scheduled energy and reserve from step III. As mentioned in Section 1, the algorithm applied in the balancing market clearing is based on the shrinking rolling horizon which is explained further in Section 5.2.

Calculating the market clearing price in both day-ahead and balancing markets is based on marginal pricing. The reason for choosing this pricing mechanism is, firstly, because in Europe most countries apply marginal pricing as shown in [32]. Secondly,

Table 2
Parameters.

b_i	Nodal susceptance [p.u.].
B_l	Line shunt susceptance of transmission line l [p.u.].
E_e^{ini}	Initial energy value for the energy storage system [MWh].
E_e^{max}	Maximum ESS state-of-charge [MWh].
E_e^{min}	Minimum ESS state-of-charge [MWh].
G_i	Distribution nodal admittance [p.u.].
M	A large positive number.
$O_{e,t}^{Edis/Ech}$	Energy (upward/downward) offer price by the storage in the balancing market [€/MWh].
$O_{g,t}^{E}$	Energy offer price of generators in day-ahead market [€/MWh].
$O_{g,t}^{RUP}$	Upward reserve offer price of generators [€/MW].
$O_{g,t}^{RDN}$	Downward reserve offer price of generators [€/MW].
$O_{g,t}^{EUP/EDN}$	Energy (upward/downward) offer price of generators in balancing market [€/MWh].
$P_e^{ch,max}$	Maximum charging power of ESS [MW].
$P_e^{dis,max}$	Maximum discharging power of ESS [MW].
$P_{i,t}^{load}/Q_{i,t}^{load}$	Active/reactive power load demand [MW/MVAr].
$P_{w,t,s}^{Wact}$	Actual wind farm power production [MW].
P_w^{Wmax}	Installed wind farm power [MW].
$P_{g,t}^{gmax}/P_{g,t}^{gmin}$	Maximum/minimum active power of generator g [MVAr]
$Q_{g,t}^{gmax}/Q_{g,t}^{gmin}$	Maximum/minimum reactive power of generator g [MVAr]
r_l	Resistance of a distribution line.
$S_{g,t}$	Rated apparent power of generator g [MVA].
$S_{l,t}$	Rated apparent power of line l [MVA].
$SI_{t,s}$	Total system imbalance in scenario s and time t [MW].
TC_l	Transmission line capacity.
V_i^{max}/V_i^{min}	Maximum/minimum voltage of bus i $\in N_D$
x_l	Reactance of a distribution line.
α_{Imb}	Coefficient for total system imbalance in distribution system.
α_T	Coefficient for total reserve capacity requirement in transmission system.
η^{ch}/η^{dis}	Charging/discharging efficiency of the ESS [p.u.].
$\lambda_{t,s}^{TD}$	Wholesale day-ahead market price in scenario s and time t [€/MWh].
$\lambda_{t,s}^{+/-}$	Forecasted positive/negative imbalance prices [€/MWh].
π_s	Scenario probability.

for the most common alternative which is the pay-as bid mechanism, strategic behaviour of the other generators in the system cannot be ignored. By contrast, for marginal pricing, the assumption that each generator (which does not behave strategically) bids its marginal cost is tenable. Therefore, marginal pricing is used in this paper. The interested reader is referred to [33] for a more in-depth comparison on the effect of pricing mechanism on the exercise of market power.

4. Revenue maximization problem of DERs in the coupled market

In this section, the revenue maximization of the DERs in day-ahead and balancing markets in the coupled market model is described. The dark and light green bars in Fig. 1 – underneath the grey flowchart – are showing the steps taken by the DERs to bid into the day-ahead and balancing markets, respectively. These steps are explained as follows.

4.1. Day-ahead market

As it has been mentioned in Section 3, the day-ahead market is a joint energy and reserve capacity market in which the wind farm with a storage system (WF-ESS) actively bids. However, due to the uncertain nature of the wind, the wind farm alone can only actively bid into the day-ahead energy market and cannot participate in the reserve market.

As mentioned earlier, in the day-ahead market in the coupled market model, the WF-ESS can behave strategically. The reason is that in the coupled market, the DERs participate in the local market which has relatively small in size. Therefore, the chance for the DERs to act strategically will increase. Moreover, in the coupled market model, the distribution system constraint is taken into account in market-clearing. DERs knowing that they might be called due to the power flow limits are provoked to exercise market power. In the coupled market due to the system constraint in the market clearing, the market power can be performed through economic withholding. Capacity withholding is an unsafe strategy for market players. Because, in the coupled market, the local market is not independent and is in exchange for power with the wholesale market. Therefore, there is always a chance that cheaper energy from the higher-level becomes imported to the local market. In this situation, if DERs apply capacity withholding strategy, their chance of being dropped out of the market will rise. Note that, the other generators of the distribution system are price-takers.

The bidding process in the day-ahead market contains three steps, as shown by the dark green bar in Fig. 1. In step 1, the WF-ESS tries to generate its strategic bids in terms of price and quantities in the day-ahead market. This strategic bidding of the WF-ESS in the day-ahead market is modelled through a bi-level optimization shown in Fig. 2. The bi-level optimization contains two levels in which the upper-level problem is from the WF-ESS's perspective and the lower-level problem is from the DMO market clearing's perspective. Through this bi-level optimization, the

Table 3
Decision variables.

$E_{e,t}$	Energy stored (state-of-charge) in the ESS [MWh].
$f^p_{l,t}/f^q_{l,t}$	Active/reactive power over line l [MW/MVAr].
$I_{l,t}/I_{l,t,s}$	Square current over line l [A].
$\widehat{o}^E_{c,t}$	Energy offer price of WF-ESS [€/MWh].
$\widehat{o}^{Rech}_{e,t}$	Downward reserve offer price of ESS [€/MW].
$\widehat{o}^{Redis}_{e,t}$	Upward reserve offer price of ESS [€/MW].
$P^{ch/dis}_{e,t}$	Charging/discharging rate of ESS in day-ahead energy market [MW].
$\widehat{P}^{ch/BL}_{e,t}$	Energy quantity bid/offer ESS in balancing market (downward regulation) [MW].
$\widehat{P}^{dis/BL}_{e,t}$	Energy quantity bid/offer ESS in balancing market (upward regulation) [MW].
$P^{ch/BL}_{e,t}$	Charging rate of ESS in balancing market(downward regulation) [MW].
$P^{dis/BL}_{e,t}$	Discharging rate of ESS in balancing market (upward regulation) [MW].
$\widehat{P}^{DA}_{c,t}$	Energy quantity bid/offer by WF-ESS at time t, [MW].
$P^{DA}_{c,t}$	Scheduled energy from the WF-ESS in day-ahead energy market [MW].
$P^{DT/DN}_{i,t}/P^{DT/UP}_{i,t}$	Downward/upward regulation in the balancing market at N_{D-T} node at the distribution system [MW].
$P_{g,t}/Q_{g,t}$	Scheduled active/reactive power output from generator g [MW/MVAr].
$P^w_{w,t}$	Scheduled wind power in day-ahead market [MW].
$P^{TD}_{i,t}/Q^{TD}_{i,t}$	Real/reactive power injection in T-D interface node i [MW/MVAr].
$P^{DT}_{i,t}$	Real power injection in interface node i∈ N_{D-T} [MW].
$P^{DN/UP}_{g,t}$	Downward/upward regulation from generator g in balancing market [MW].
$P^{Totalrealtime}_{c,t,s}$	Actual power produced by the WF-ESS in scenario s and time t [MW].
$R^{DN/UP}_{g,t}$	Scheduled downward/upward reserve capacity of the generator g [MW].
$R^{ch/dis}_{e,t}$	Charging/discharging rate of ESS in reserve market (downward/upward reserve) [MW].
$\widehat{R}^{ch/dis}_{e,t}$	Upward/ downward reserve bid/offer by storage system e at time t, [MW].
$R^{DT/DN}_{i,t}$	Aggregated upward reserve at node i∈ N_{D-T} [MW].
$R^{DT/UP}_{i,t}$	Aggregated downward reserve at node i∈ N_{D-T} [MW].
$R^{DER}_{i,t}$	Aggregated reserve capacity from DERs at T-D node [MW].
$u_{e,t}$	Binary variable related to the charging state of storage.
$V_{i,t}$	Square bus voltage [p.u.] at node i∈ N_D
$y_{t,s}$	Binary variable defines the positive and negative imbalance of WF-ESS.
$z_{t,s}$	Binary variable related to the imbalance direction of WF-ESS.
$\Delta_{c,t,s}$	Imbalance of WF-ESS in scenario s and time t [MW].
$\Delta^+_{c,t,s}$	Positive imbalance of WF-ESS and time t [MW].
$\Delta^-_{c,t,s}$	Negative imbalance of WF-ESS and time t [MW].
$\Delta_{w,t,s}$	Imbalance of wind farm and time t [MW].
$\Delta^+_{w,t,s}$	Positive imbalance of wind farm and time t [MW].
$\Delta^-_{w,t,s}$	Negative imbalance of wind farm and time t [MW].
$\lambda^{DA}_{i,t}$	Local day-ahead energy market price [€/MWh].
$\lambda^{DN/UP}_t$	Downward/upward reserve market price [€/MW].
$\lambda^{BL}_{i,t}$	Balancing market price [€/MWh].
$\theta_{i,t}$	Transmission bus angle.

WF-ESS makes its offering decisions in the upper-level while anticipating the market behaviour of other market players which is modelled in the lower-level within the day-ahead market clearing by the DMO.

In step 2, the day-ahead market is cleared by the DMO. The reason for having this step – even though the day-ahead market clearing by the DMO is taking into account in the lower-level problem in step 1 – is that there is uncertainty in how much power flow over interface transformer between distribution and transmission system is. Therefore, the lower-level problem in step 1, cannot reflect the real market, and therefore, step 2 is needed. Step 2, the day-ahead market-clearing, contains all three steps (I–III) in the day-ahead market shown in the grey flowchart in Fig. 1 which are explained in Section 3. The output of step 2 is the cleared local market prices and the scheduled energy and reserve capacities for the DERs including the WF-ESS.

Finally, step 3 is the remuneration phase in which the WF-ESS calculates its day-ahead revenue based on the cleared market prices and its scheduled energy and reserve capacity obtained in step 2. The corresponding mathematical formulations are presented in Section 5.1.

4.2. Balancing market

Unlike the day-ahead market, in the balancing market, it is more difficult to exercise market power by the DERs. The reason is that first of all, the amount of MWh energy traded in the balancing market is significantly smaller than in the day-ahead market. Secondly, since in the balancing market, the exact location for the required imbalances is not known by the DERs, it can be risky to perform market power. As DERs would get their market power from possible congestion which arising from the imbalances or the reserve activation, the chance that they will not be called in the balancing market is significantly higher then

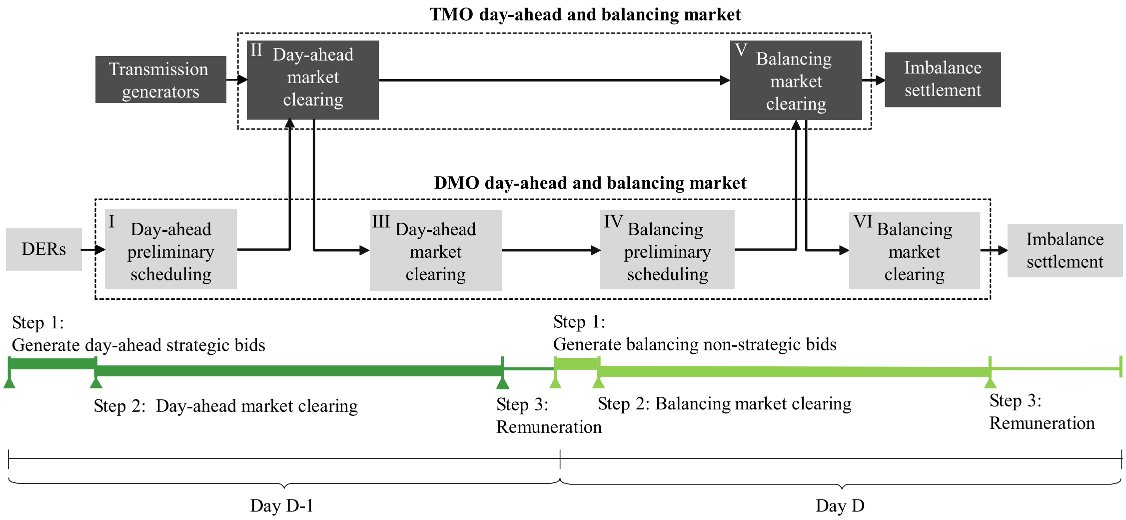

Fig. 1. Coupled market model and DER's bidding steps in day-ahead and balancing markets.

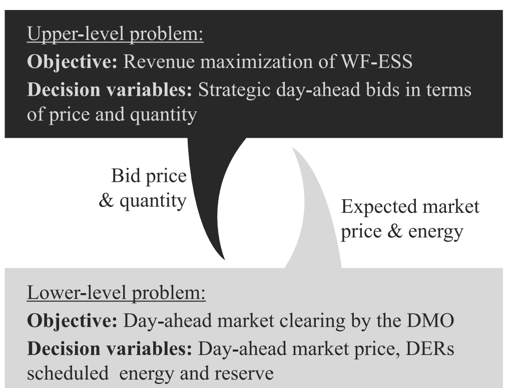

Fig. 2. Step 1: Generate day-ahead strategic bids through a bi-level optimization.

in the day-ahead market. Therefore, the revenue maximization problem for the WF-ESS in the balancing market is the same as the WF-ESS being non-strategic, i.e. a price-taker. Moreover, the balancing market clearing is modelled through a shrinking rolling horizon due to having a storage system, since the energy or the state of charge of the storage system at time t depends on its energy at the previous time $t-1$. The starting rolling time is reset to each time the day-ahead market is cleared. This period includes 96 intervals in 24 h. At the start of each interval, a new forecast becomes available. At each step inside the rolling horizon, the horizon is shrunk by one time-step and the balancing market is solved over the remaining horizon. Each of these shrinking horizon problems gives the bid for the current time. The last assumption is regarding the pricing mechanism in imbalance settlements. In this paper, the dual pricing is applied. The Ref. [34] explains the feature for the dual versus single pricing mechanism, in detail. The dual-pricing mechanism is more complicated than the single-pricing, therefore, to have a broader formulation, the dual-pricing mechanism has been chosen in this paper. However, the approach can easily be adapted for the single-pricing mechanism too.

The storage system of the WF-ESS can actively bid into the balancing market. However, the wind farm alone cannot participate in the balancing market, instead, it can only pay or being paid in the imbalance settlement depending on its imbalance direction with respect to the total system imbalance. The bidding in the balancing market also contains three steps shown in the light green bar in Fig. 1. Step 1 is generating non-strategic bids in terms of price and quantities. Therefore, the WF-ESS solves a self-scheduling problem to determine its most beneficial actions (bids) for given prices. Step 2, is the balancing market-clearing which contains all three steps (IV–VI) in the balancing market. The results of this step are local balancing market prices and quantities and imbalances. Finally, step 3 is the remuneration in the imbalance settlement phase based on the dual-pricing mechanism. if Wf-ESS's imbalance is in the opposite direction of the system imbalance, he has to pay the price equal to the day-ahead market price. But if its imbalance is in the same direction with the total system imbalance, he has to pay the price based on the marginal cost of the last balancing unit deployed, which is usually higher than the day-ahead market price. The corresponding mathematical formulations are presented in Section 5.2.

5. Mathematical formulations

In this section, the mathematical formulations for the revenue maximization of the WF-ESS are presented. The mathematical formulations are for the WF-ESS case, as this is a more complicated case study than the wind farm alone. However, the formulations can easily be adapted for the wind farm case by setting the storage system size equal to zero. Section 5.1 shows the mathematical formulation regarding the strategic optimization of the WF-ESS in the day-ahead market and Section 5.2 describes the mathematical formulation for the non-strategic optimization of the WF-ESS in the balancing market.

5.1. Mathematical formulations: Revenue maximization in the day-ahead market

As it has been explained, the revenue maximization problem of the WF-ESS in the day-ahead market consists of three steps. The mathematical formulation for steps 1–3 is described as follows.

- **Step 1. Generate day-ahead strategic bids**
  In step 1, through a bi-level optimization shown in Fig. 2, the WF-ESS tries to generate its strategic bidding in terms of price and quantities. The upper and lower levels of the bi-level optimization are formulated as follow:

  1. Upper-level problem:

The upper-level is from the WF-ESS's perspective which is maximizing the revenue of the WF-ESS and its objective function is shown in (1):

$$\text{Maximize} \sum_t [\sum_c \lambda^{DA}_{c\in i,t} \cdot P^{DA}_{c,t} + \sum_e \lambda^{UP}_t \cdot R^{dis}_{e,t} + \lambda^{DN}_t \cdot R^{ch}_{e,t}] \tag{1}$$

The objective function in (1) consists of several parts. The first part is the day-ahead energy bidding revenue of the WF-ESS. The expected day-ahead market price, $\lambda^{DA}_{c\in i,t}$, is the Lagrangian multiplier of the power balance equation in the lower-level problem. The second part is the revenue from selling upward and downward regulations by the storage in the reserve market. The expected reserve prices, λ^{UP}_t and λ^{DN}_t, are the Lagrangian multipliers belong to constraints (A.4) and (A.5) in the lower-level problem.
Following constraints need to be enforced:

$$\widehat{P}^{DA}_{c,t} = \sum_{w\in c} P^w_{w,t} + \sum_{e\in c}(P^{dis}_{e,t} - P^{ch}_{e,t}), \forall c, t \tag{2}$$

$$0 \le P^w_{w,t} \le P^{Wmax}_w, \forall w, t \tag{3}$$

$$-\sum_{e\in c} P^{ch,max}_e \le \widehat{P}^{DA}_{c,t} \le \sum_{e,w\in c}(P^{Wmax}_w + P^{dis,max}_e), \forall c, t \tag{4}$$

$$0 \le \widehat{R}^{ch}_{e,t} \le P^{ch,max}_e, \forall e, t \tag{5}$$

$$0 \le \widehat{R}^{dis}_{e,t} \le P^{dis,max}_e, \forall e, t \tag{6}$$

$$0 \le P^{ch}_{e,t} \le u_{e,t} \cdot P^{ch,max}_e, \forall e, t \tag{7}$$

$$0 \le P^{dis}_{e,t} \le (1 - u_{e,t}) \cdot P^{dis,max}_e, \forall e, t \tag{8}$$

$$0 \le P^{ch}_{e,t} + \widehat{R}^{ch}_{e,t} \le P^{ch,max}_e, \forall e, t \tag{9}$$

$$0 \le P^{dis}_{e,t} + \widehat{R}^{dis}_{e,t} \le P^{dis,max}_e, \forall e, t \tag{10}$$

$$\widehat{o}^{Redis}_{e,t}, \widehat{o}^{Rech}_{e,t}, \widehat{o}^{E}_{c,t} \ge 0, \forall c, e \in c, t \tag{11}$$

$$E^{min}_e \le E_{e,t} \le E^{max}_e, \forall e, t \tag{12}$$

$$E_{e,1} = E^{ini}_e, \forall e \tag{13}$$

$$E_{e,t} = E_{e,t-1} + (P^{ch}_{e,t} + \widehat{R}^{ch}_{e,t}) \cdot \eta^{ch} - \frac{(P^{dis}_{e,t} + \widehat{R}^{dis}_{e,t})}{\eta^{dis}}, \forall e, 1 < t \tag{14}$$

Constraint (2) defines the total energy bid by the WF-ESS in the day-ahead market which is a combination of the energy from the wind farm and the storage system. Constraint (3) limits the bidding by the wind farm in the day-ahead market to its installed capacity and (4) limits the total energy bids by the WF-ESS to the summation of the installed capacity of the wind farm and the storage system. Constraints (5) and (6) enforce limits for the downward and upward reserves by the storage system, $R^{ch}_{e,t}$ and $R^{cdis}_{e,t}$, respectively. Similarly, (7) and (8) limit the bidding by the storage system in the day-ahead energy market. Constraints (9) and (10) show that the total charging and discharging of the storage in the reserve and energy markets should be less than the charging and discharging capacity of the storage system, respectively. Constraint (11) shows the offer prices of the WF-ESS in the day-ahead energy and reserve markets should be more than zero. Finally, (12)–(14) enforce limits to the state of charge for the storage system.

2. Lower-level problem:
   The lower-level is from day-ahead market clearing by the DMO. This local day-ahead market is cleared by solving the optimization problem defined by constraints (15)–(A.16). The primal variable is set $\{P_{g,t}, Q_{g,t}, R^{UP}_{g,t}, R^{DN}_{g,t}, P^{DA}_{c,t}, R^{ch}_{e,t}, R^{dis}_{e,t}, V_{i,t}, I_{l,t}, f^p_{l,t}, f^q_{l,t}\}$. All dual variables are given in a parentheses in front of constraints.

$$\begin{aligned} \text{Minimize} & \sum_{t\in T}\sum_{g\in G_D}(O^E_{g,t} \cdot P_{g,t} + O^{RUP}_{g,t} \cdot R^{UP}_{g,t} + O^{RDN}_{g,t} \cdot R^{DN}_{g,t}) \\ & + \sum_{t\in T}[\sum_c \widehat{o}^E_{c,t} \cdot P^{DA}_{c,t} \\ & + \sum_{e\in c}(\widehat{o}^{Rech}_{e,t} \cdot R^{ch}_{e,t} + \widehat{o}^{Redis}_{e,t} \cdot R^{dis}_{e,t})] \\ & + \sum_t \sum_{i\in N_{D-T}} \sum_s \pi_s \cdot \lambda^{TD}_{t,s} \cdot P^{TD}_{t,i} \end{aligned} \tag{15}$$

   The objective function in (15) minimizes the total energy and reserve capacity costs from DERs (shown in the first line), and the energy and the reserve capacity cost form the WF-ESS (shown in the second line) in the joint day-ahead market. The objective function is subjected to the constraints which are mainly distribution system constraints. The distribution system is represented through a second-order cone programming (SOCP) relaxation, which is tight for radial distribution systems [35]. Through the SOCP relaxation, the distribution system constraints become convex which is a necessary condition for solving the bi-level optimization problems. The constraints are shown in Appendix A.
3. Solving the bi-level optimization problem:
   To solve the bi-level problem, first, the lower-level problem of DMO-market-clearing including Eqs. (15)–(A.16) are replaced by their Karush–Kuhn–Tucker (KKT) conditions. Note that these KKT conditions provide the optimality conditions since the lower-level problem is convex. Then, the KKT equations of the lower level problem will be added to the upper-level problem including Eqs. (1)–(14). The resulting single-level optimization model is a mathematical problem with equivalent constraints (MPEC). This problem, however, is non-linear. There are two sources of non-linearity that can be linearized as described below:

- The first source of non-linearity is the set of complementarity conditions that are within the KKT conditions. Each complementarity condition can be linearized using a "Big-M" approach [36].
- The second source of non-linearity comes from the bilinear terms in the objective function (1). Inspired from [37], we linearize those bilinear terms.

After solving the aforementioned non-linearity in the MPEC model, it turns into a mixed integer linear problem which its output is the strategic bidding prices ($\widehat{o}^{E}_{c,t}$, $\widehat{o}^{Redis}_{e,t}$, $\widehat{o}^{Rech}_{e,t}$) and quantities ($\widehat{P}^{DA}_{c,t}$, $\widehat{R}^{ch}_{e,t}$, $\widehat{R}^{dis}_{e,t}$) by which WF-ESS participates in the day-ahead market in step 2.

- **Step 2. Day-ahead market clearing**

In this step, the day-ahead market is cleared. As it is explained in Section 3, the day-ahead market in the coupled market model consists of three steps. The first step is the preliminary scheduling, the second step is the wholesale market clearing and the third step is the local day-ahead market clearing. A complete mathematical formulation for the day-ahead market in the coupled market model is explained in [6]. However, to clarify the inputs and outputs of this step, a short explanation together with a simplified formulation is presented below.

1. Step I: Day-ahead preliminary scheduling by the DMO:
The DMO first aggregates all the bids and offers from the DERs by solving a preliminary scheduling problem where the objective function is minimizing the total cost of energy and reserve capacity. The objective function is shown in (16).

$$\begin{aligned} Minimize \sum_{t\in T}\sum_{g\in G_D}&(O^{E}_{g,t}\cdot P_{g,t}+O^{RUP}_{g,t}\cdot R^{UP}_{g,t}+O^{RDN}_{g,t}\cdot R^{DN}_{g,t})\\ &+\sum_{t\in T}[\sum_{c}\widehat{o}^{E}_{c,t}\cdot P^{DA}_{c,t}\\ &+\sum_{e\in c}(\widehat{o}^{Rech}_{e,t}\cdot R^{ch}_{e,t}+\widehat{o}^{Redis}_{e,t}\cdot R^{dis}_{e,t})]\\ &+\sum_{t}\sum_{i\in N_{D-T}}\sum_{s}\pi_s\cdot\lambda^{TD}_{t,s}\cdot P^{TD}_{t,i} \end{aligned} \tag{16}$$

Eq. (16) minimizes the total cost of generation and reserve capacity of the DERs in the local market plus the expected cost of buying/selling energy and reserve from/to the TMO market. The cost of this energy is the day-ahead price in the wholesale market. This price has to be estimated by the DMO and is therefore based on a set of scenarios and their associated probabilities of occurrence. Note that $\widehat{o}^{E}_{c,t}$, $\widehat{o}^{Rech}_{e,t}$ and $\widehat{o}^{Redis}_{e,t}$ in (16) are no longer decision variables, but parameters which are the output of the bi-level optimization in step 1. Constraints of the objective function in (16) are similar to the ones in (A.1)–(A.16).
Through this preliminary scheduling, the local market price for energy and reserve will be determined. The energy price ($\lambda^{DA}_{i,t}$) is the Lagrange multiplier of the power balance equation at the interface node between the TSO and DSO, which can be determined by deriving the KKT conditions of the above convex optimization problem. Moreover, the Lagrangian multiplier of (A.4) and (A.5) symbolized with λ^{UP}_{t} and λ^{DN}_{t}, are the price for the upward and downward reserve capacity in the distribution system. The power injected at the interface node ($\widetilde{P^{TD}_{i,t}}$), total reserve capacity of DERs ($\widetilde{R^{UP/DN}_{g,t}}$), energy price ($\lambda^{DA}_{i,t}$) and reserve price ($\lambda^{UP/DN}_{t}$) are outputs of this step by which the DMO participates in the wholesale market.
2. Step II: Day-ahead market clearing by the TMO:
In this step, the wholesale day-ahead joint energy and reserve capacity market is cleared by the TMO. The DMO and transmission generators participate in this market. The objective of this market is maximizing social welfare. However, since in this paper the demand is considered to be inelastic, the social welfare is equivalent to minimizing the total generation cost.

$$\begin{aligned} Minimize \sum_{t\in T}\sum_{g\in G_T}&(O^{E}_{g,t}\cdot P_{g,t}+O^{RUP}_{g,t}\cdot R^{UP}_{g,t}+O^{RDN}_{g,t}\cdot R^{DN}_{g,t})\\ &+\sum_{t\in T}\sum_{i\in N_{T-D}}(\lambda^{DA}_{i,t}\cdot P^{DT}_{i,t}\\ &+\lambda^{UP}_{t}\cdot R^{DT/UP}_{i,t}-\lambda^{DN}_{t}\cdot R^{DT/DN}_{i,t}) \end{aligned} \tag{17}$$

The first line in (17) consists of the cost of energy and reserve capacity procured by the transmission generators. The second line accounts for the total costs of energy and reserve capacity procured by the DERs. The objective function is subjected to the transmission system constraints. In a transmission system, the error in the DC power flow is less than in the distribution system, therefore a DC power flow can be used to model the transmission system constraints. The constraints can be found in Appendix B. After clearing this market, the DMO is informed about the allocated power flow over the interface transformer ($\widetilde{P^{DT}_{i,t}}$) and the required reserve capacity from DERs ($\widetilde{R^{DT/UP}_{i,t}}$ and $\widetilde{R^{DT/DN}_{i,t}}$).
3. Step III: Day-ahead market clearing by the DMO:
In this step, the DMO clears the day-ahead joint energy and reserve capacity market based on the updated information from step II. This local day-ahead market is cleared with the objective function shown by (18):

$$\begin{aligned} Minimize \sum_{t\in T}\sum_{g\in G_D}&(O^{E}_{g,t}\cdot P_{g,t}+O^{RUP}_{g,t}\cdot R^{UP}_{g,t}+O^{RDN}_{g,t}\cdot R^{DN}_{g,t})\\ &+\sum_{t\in T}[\sum_{c}\widehat{o}^{E}_{c,t}\cdot P^{DA}_{c,t}\\ &+\sum_{e\in c}(\widehat{o}^{Rech}_{e,t}\cdot R^{ch}_{e,t}+\widehat{o}^{Redis}_{e,t}\cdot R^{dis}_{e,t})] \end{aligned} \tag{18}$$

The objective function in (18) is minimizing the total generation cost of DERs in the distribution system. The constraints in this step are mostly similar to the preliminary scheduling. The differences are in the power balance equation in (19) and the required upward and downward reserves in (20) and (21) which are written as follows:

$$\begin{aligned} &\sum_{l=(j,i)}(f^{p}_{l,t}-I_{l,t}\cdot r_l)+\sum_{g\in G_D}P_{g,t}+\sum_{c\in i}P^{DA}_{c,t}-\widetilde{P^{DT}_{i,t}}\\ &=P^{load}_{i,t}+\sum_{l=(i,j)}f^{p}_{l,t}+G_i\cdot V_{i,t},\forall i\in N_D,t \end{aligned} \tag{19}$$

$$\sum_{g\in G_D} R^{UP}_{g,t} + \sum_{e} R^{dis}_{e,t} \geq \widetilde{R^{DT/UP}_{i,t}}, \forall i \in N_{D-T}, t \tag{20}$$

$$\sum_{g\in G_D} R^{DN}_{g,t} + \sum_{e} R^{ch}_{e,t} \geq \widetilde{R^{DT/DN}_{i,t}}, \forall i \in N_{D-T}, t \tag{21}$$

In (19), $\widetilde{P^{DT}_{i,t}}$ is a parameter symbolizing the power flow injected at the interface node of the distribution system. In (20) and (21), $\widetilde{R^{DT/UP}_{i,t}}$ and $\widetilde{R^{DT/DN}_{i,t}}$ are parameters symbolizing the required upward and downward reserves in the distribution system, respectively, which are generated in step II. The rest of the constraints are similar with the ones in (A.1), (A.3), and (A.6)–(A.16) shown in Appendix A. The outputs of this step, regarding the upward and downward reserve capacity ($\widetilde{R^{UP/DN}_{g,t}}$ and $\widetilde{R^{dis/ch}_{e,t}}$) and the scheduled energy of dispatchable generators ($\widetilde{P_{g,t}}$ and $\widetilde{P^{DA}_{c,t}}$), are inputs for the balancing market which is explained further in Section 5.2.

- **Step 3. Remuneration**
  In this step, according to the cleared day-ahead market price ($\lambda^{DA}_{i,t}$ and $\lambda^{UP/DN}_{t}$) and quantities ($\widetilde{P^{DA}_{c,t}}$ and $\widetilde{R^{dis/ch}_{e,t}}$) obtained in step 2, the day-ahead revenue of the WF-ESS is calculated as shown in (22):

$$\sum_{t}[\sum_{c} \lambda^{DA}_{c\in i,t} \cdot \widetilde{P^{DA}_{c,t}} + \sum_{e} \lambda^{UP}_{t} \cdot \widetilde{R^{dis}_{e,t}} + \lambda^{DN}_{t} \cdot \widetilde{R^{ch}_{e,t}}] \tag{22}$$

5.2. Mathematical formulations: Revenue maximization in the balancing market

As explained earlier in Section 4.2, the bidding of the WF-ESS in the balancing market is non-strategic. The revenue calculations of the WF-ESS in the balancing market has three steps. Step 1 is to generate the bids through a self-optimization problem. Step 2 is the balancing market clearing process including three steps (4–6) of the coupled market model explained in Section 3. Lastly, step 3 is the remuneration phase in which the WF-ESS calculates its balancing revenue based on a dual-pricing mechanism.

These three steps need to be performed through a shrinking rolling horizon approach. The balancing market is cleared every 15 min in a time window of 24 h. At each time interval inside the rolling horizon, the horizon is shrunk by a one time step and the optimization is solved over the remaining horizon with the new forecasts of the current day. The forecast is for the uncertain parameters which are dependent on scenarios. Wind output ($P^{Wact}_{w,t,s}$), the imbalance prices ($\lambda^{+/-}_{t,s}$), and the total system imbalance ($SI_{t,s}$) are the uncertain scenario-based parameters in step 1. Indeed, there is no uncertainty in steps 2 and 3 which happen in real-time. Each of these shrinking horizon solutions gives the current variable outputs and at the current time. Mathematical formulations belong to steps 1–3 are described as follows.

- **Step 1: Generate balancing-non-strategic bids**
  In step 1, the WF-ESS solves a self-scheduling problem to determine its most beneficial actions in the balancing market in terms of its bidding volume for a given price and for the time-horizon of 24 h.

$$\begin{aligned}&\sum_{t}[\sum_{e\in c}\sum_{s}\pi_s \cdot ((\lambda^{+}_{t,s} \cdot P^{dis/BL}_{e,t,s} - \lambda^{-}_{t,s} \cdot P^{ch/BL}_{e,t,s})\\&+ \sum_{c}(\lambda^{DA}_{c\in i,t} \cdot (1 - z_{t,s}) \cdot \Delta_{c,t,s})\\&+ \sum_{c}(\lambda^{+}_{t,s} \cdot z_{t,s} \cdot y_{t,s} \cdot \Delta^{+}_{c,t,s} + \lambda^{-}_{t,s} \cdot z_{t,s} \cdot (1 - y_{t,s}) \cdot \Delta^{-}_{c,t,s}))]\end{aligned} \tag{23}$$

The objective function in (23) consists of three parts. The first term is the revenue obtained by the storage system due to actively bidding in the balancing market. The second and the third terms belong to the imbalance settlement in which the storage system pays or is being paid, depending on whether or not its imbalance is in the opposite direction with the total system imbalance. As the dual-pricing mechanism is applied, in the case in which the deviation is in the same direction with the total system imbalance, the WF-ESS has to pay with a price equal to the $\lambda^{DA}_{c\in i,t}$, otherwise, it is being paid by a price equal to $\lambda^{+}_{t,s}$ or $\lambda^{-}_{t,s}$ depending on having a short or long imbalance, respectively. As mentioned earlier, this step happens before the real-time, hence the wind power and imbalance prices and the total imbalance of the system are scenario-dependent. Constraints Eqs. (24)–(39) need to be enforced.

$$\Delta_{c,t,s} = P^{Totalrealtime}_{c,t,s} - \widetilde{P^{DA}_{c,t}}, \forall c, t, s \tag{24}$$

$$\Delta_{c,t,s} \cdot SI_{t,s} \leq z_{t,s} \cdot M, \forall c, t, s \tag{25}$$

$$\Delta_{c,t,s} \cdot SI_{t,s} \geq -(1 - z_{t,s}) \cdot M, \forall c, t, s \tag{26}$$

$$P^{Totalrealtime}_{c,t,s} = \sum_{w\in c} P^{Wact}_{w,t,s} + \sum_{e\in c}(\widehat{P}^{dis/BL}_{e,t,s} - \widehat{P}^{ch/BL}_{e,t,s}), \forall c, t, s \tag{27}$$

$$\Delta_{c,t,s} = \Delta^{+}_{c,t,s} - \Delta^{-}_{c,t,s}, \forall c, t, s \tag{28}$$

$$0 \leq \Delta^{+}_{c,t,s} \leq y_{t,s} \cdot (\sum_{w\in c} P^{Wact}_{w,t,s} + \sum_{e\in c} P^{dis,max}_{e}), \forall c, t, s \tag{29}$$

$$0 \leq \Delta^{-}_{c,t,s} \leq (1 - y_{t,s}) \cdot \widetilde{P^{DA}_{c,t}}, \forall c, t, s \tag{30}$$

$$\widehat{P}^{ch/BL}_{e,t,s} + \widetilde{P^{ch}_{e,t}} \leq P^{ch,max}_{e}, \forall e, t, s \tag{31}$$

$$\widehat{P}^{dis/BL}_{e,t,s} + \widetilde{P^{dis}_{e,t}} \leq P^{dia,max}_{e}, \forall e, t, s \tag{32}$$

$$0 \leq \widehat{P}^{ch/BL}_{e,t,s} \leq u_{e,t,s} \cdot P^{ch,max}_{e}, \forall e, t, s \tag{33}$$

$$0 \leq \widehat{P}^{dis/BL}_{e,t,s} \leq (1 - u_{e,t,s}) \cdot P^{dis,max}_{e}, \forall e, t, s \tag{34}$$

$$\widehat{P}^{ch/BL}_{e,t,s} \leq \widetilde{R^{ch}_{e,t}}, \forall e, t, s \tag{35}$$

$$\widehat{P}^{dis/BL}_{e,t,s} \le \widetilde{R^{dis}_{e,t}}, \forall e,t,s \tag{36}$$

$$E^{min}_e \le E_{e,t} \le E^{max}_e, \forall e,t,s \tag{37}$$

$$E_{e,1} = E^{ini}_e, \forall e \tag{38}$$

$$E_{e,t} = E_{e,t-1} + \sum_s \pi_s \cdot (P^{ch/BL}_{e,t,s} \cdot \eta^{ch} - \frac{P^{dis/BL}_{e,t,s}}{\eta^{dis}}), \forall e, t > 1 \tag{39}$$

Constraints (24) and (27) are related to the amount of the imbalances caused by the WF-ESS. Constraints (25) and (26) define the direction of the imbalance of the WF-ESS with respect to the total system imbalance. $SI_{t,s}$ indicates the total system imbalance and is scenario-based. Constraints (28)–(30) define the positive and negative imbalance by WF-ESS. Constraints (31) and (32) limit the upward and downward energy of the storage system in the balancing market. Constraints (33)–(36) limit the charging an discharging of the storage system with respect to the scheduled energy of the storage in the day-ahead market ($\widetilde{P^{dis}_{e,t}}$ and $\widetilde{P^{ch}_{e,t}}$). Finally, (37)–(39) depict the state of the charging of the storage systems. The output of this optimization is an estimated bidding energy of the WF-ESS by which it will participate in the balancing market.

- **Step 2: balancing market clearing**
This step includes steps IV–VI in the coupled market model shown in Fig. 1 and explained in Section 3. In [6], the formulation for each step is described in detail, but for clarity, each step is formulated briefly here as well. Note that, τ in the equations below is the time unit of the balancing market in the shrinking rolling horizon.

1. Step IV: Balancing preliminary scheduling:
In this step, the DMO estimates the local balancing market price by which it participates in the central real-time balancing market. The objective function is minimizing the expected cost of balancing services at the distribution system shown in (40).

$$\begin{aligned} Minimize\{ & \sum_{g \in G_D} (O^{EUP}_{g,\tau} \cdot P^{UP}_{g,\tau} - O^{EDN}_{g,\tau} \cdot P^{DN}_{g,\tau}) \\ & + \sum_e (O^{Edis}_{e,\tau} \cdot P^{dis/BL}_{e,\tau} - O^{Ech}_{e,\tau} \cdot P^{ch/BL}_{e,\tau}) \\ & + \sum_{i \in N_{D-T}} \sum_s \pi_s \cdot (\lambda^+_{\tau,s} \cdot P^{DT/UP}_{i,\tau} - \lambda^-_{\tau,s} \cdot P^{DT/DN}_{i,\tau})\} \end{aligned} \tag{40}$$

The first and the second term in (40) is the cost of the balancing services procured from the DERs and the third term belongs to the cost of balancing services procured by the transmission system. The following constraints need to be imposed:

$$\begin{aligned} (\lambda^{DBL}_{i,\tau}): \quad & \sum_{l=(j,i)} (f^p_{l,\tau} - I_{l,\tau}.r_l) + \sum_{g \in i} (\widetilde{P_{g,\tau}} + P^{UP}_{g,\tau} - P^{DN}_{g,\tau}) \\ & + (\widetilde{P^{DA}_{c,\tau}} + P^{dis/BL}_{e,\tau} - P^{ch/BL}_{e,\tau}) \\ & + \sum_{i \in N_{D-T}} (P^{DT/UP}_{i,\tau} - P^{DT/DN}_{i,\tau}) = \alpha_{Imb} \cdot SI_{\tau,s} \\ & + P^{load}_{i,\tau} + \sum_{l=(i,j)} f^p_{l,t} + G_i.V_{i,t}, \forall i \in N_D \end{aligned} \tag{41}$$

$$\widetilde{P_{g,\tau}} + P^{UP}_{g,\tau} \le P^{gmax}_g, \forall g \in G_D \tag{42}$$

$$\widetilde{P_{g,\tau}} - P^{DN}_{g,\tau} \ge P^{gmin}_g, \forall g \in G_D \tag{43}$$

$$-\widetilde{R^{UP/DN}_{g,\tau}} \le P^{UP/DN}_{g,\tau} \le \widetilde{R^{UP/DN}_{g,\tau}}, \forall g \in G_D \tag{44}$$

Constraint (41) is the power balance equation. α_{Imb} is the fraction of the total imbalance system which belongs to the distribution system. Constraints (42)–(44) limit the upward and downward balancing regulations. The rest of the constraints are related to the system constraint which is similar with the ones in (A.1), (A.3), and (A.6)–(A.16) shown in Appendix A. The output of this step is the local balancing market price ($\lambda^{DBL}_{i,\tau}$: the Lagrangian multiplier of (41)) and quantities ($P^{DT/UP}_{i,\tau}$ and $P^{DT/DN}_{i,\tau}$), by which the DMO participate in the TMO-balancing market in step V.

2. Step V: Balancing market clearing by the TMO:
In this step, the TMO clears the real-time central balancing market. Generators connected to the transmission system and the DMO with aggregated bids from the DERs participate in this market (see Fig. 1). This is the objective function:

$$\begin{aligned} Minimize & \sum_{g \in G_T} (O^{EUP}_{g,\tau} \cdot P^{UP}_{g,\tau} - O^{EDN}_{g,\tau} \cdot P^{DN}_{g,\tau}) \\ & + \sum_{i \in N_{T-D}} \lambda^{DBL}_{i,\tau} \cdot (P^{DT/UP}_{i,\tau} - P^{DT/DN}_{i,\tau}) \end{aligned} \tag{45}$$

The first term is related to the cost of balancing services from the transmission generators. In the second term, $\lambda^{DBL}_{i,\tau}$ is the price of balancing services form aggregated the DERs by the DMO. The system constraints of the transmission system are enforced as shown in (B.1)–(B.10) in Appendix B. The results of this step, which will be passed on to the DMO, is indicating the deployed energy from transmission to the distribution system.

3. Step VI: Balancing market clearing by the DMO:
In this step, the DMO clears the local balancing market. The objective function is minimizing the balancing service cost deployed by the DERs:

$$\begin{aligned} Minimize\{ & \sum_{g \in G_D} (O^{EUP}_{g,\tau} \cdot P^{UP}_{g,\tau} - O^{EDN}_{g,\tau} \cdot P^{DN}_{g,\tau}) \\ & + \sum_e (O^{Edis}_{e,\tau} \cdot P^{dis/BL}_{e,\tau} - O^{Ech}_{e,\tau} \cdot P^{ch/BL}_{e,\tau})\} \end{aligned} \tag{46}$$

The power balance equation is as follow:

$$\begin{aligned} (\lambda^{DBL}_{i,\tau}): \quad & \sum_{l=(j,i)} (f^p_{l,\tau} - I_{l,\tau}.r_l) + \sum_{g \in i} (\widetilde{P_{g,\tau}} + P^{UP}_{g,\tau} - P^{DN}_{g,\tau}) \\ & + (\widetilde{P^{DA}_{c,\tau}} + P^{dis/BL}_{e,\tau} - P^{ch/BL}_{e,\tau}) \\ & + \sum_{i \in N_{D-T}} (\widetilde{P^{DT/UP}_{i,\tau}} - \widetilde{P^{DT/DN}_{i,\tau}}) = P^{load}_{i,\tau} \\ & + \sum_{l=(i,j)} f^p_{l,\tau} + G_i.V_{i,\tau}, \forall i \in N_D \end{aligned} \tag{47}$$

In the power balance equation in (47), $\widetilde{\Delta P^{DT}_{i,\tau}}$ is the scheduled adjustment from transmission level to the distribution level which has been calculated in step V. The rest of the constraints are similar with the system constraints shown in Appendix A. The output of this step is the cleared balancing market price ($\lambda_{i,\tau}^{DBL}$) and quantities ($\widetilde{P_{e,\tau}^{dis/BL}}, \widetilde{P_{e,\tau}^{ch/BL}}$) by which the WF-ESS calculates its revenue in step 3.

- **Step 3: Remuneration**
This step, which happens at the imbalance settlement phase, calculates the revenue of the WF-ESS by the cleared balancing market price and quantities obtained in step VI of step 2. As explained in Section 3, in the imbalance settlement of the balancing market, the dual pricing mechanism is applied. Therefore, the revenue calculation is as follow:

$$\begin{aligned}&\sum_{e\in c}(\lambda_{\tau}^{DBL}\cdot\widetilde{P_{e,\tau}^{dis/BL}}-\lambda_{\tau}^{DBL}\cdot\widetilde{P_{e,\tau}^{ch/BL}})\\&-\sum_{c}(\lambda_{\tau}^{DA}\cdot a\cdot\widetilde{\Delta_{c,\tau,s_r}^{+}}+\lambda_{\tau}^{DA}\cdot b\cdot\widetilde{\Delta_{c,\tau,s_r}^{-}})\\&+\sum_{c}(\lambda_{\tau}^{DBL}\cdot c\cdot\widetilde{\Delta_{c,\tau,s_r}^{+}}+\lambda_{\tau}^{DBL}\cdot d\cdot\widetilde{\Delta_{c,\tau,s_r}^{-}})\end{aligned}\tag{48}$$

where a, b, c, d are binary parameters which at each moment only one of them is equal to one and the rest are zero. For example, $a = 1$ means that in the real-time the imbalance caused by the WF-ESS is positive ($Delta_{c,\tau,s_r}^{+}$) and is in-line with the direction of the total system imbalance. Therefore, the WF-ESS should pay for causing this imbalance in the system at the rate of the day-ahead market price. The definitions of $\widetilde{\Delta_{c,\tau,s_r}^{+}}$, $\widetilde{\Delta_{c,\tau,s_r}^{-}}$ are based on the (24)–(30). However, the difference is that in (48), $\widetilde{\Delta_{c,\tau,s_r}^{+}}$ and $\widetilde{\Delta_{c,\tau,s_r}^{-}}$ do not depend on the scenario, since this step is after scenario realizations. Note that s_r is one realized scenario. $\widetilde{P_{e,\tau}^{dis/BL}}$ and $\widetilde{P_{e,\tau}^{ch/BL}}$ are cleared charging and discharging of storage system in the balancing market obtained in step VI of step 2.

6. Input data and case studies

In this section, the input data and main case studies which have been used for the simulations are described.

6.1. Input data

The proposed coupled TMO–DMO market model is tested using a radial 30-bus medium voltage Dutch distribution system and the IEEE-24 bus transmission system [38] as shwon in Fig. 3. The data for the offer prices of distributed generators are from [39]. Tables 4 and 5 summarize the data for generators at transmission and distribution network level, respectively. The WF-ESS is located at bus number 19 (at the end of the feeder) of the distribution system with a wind farm with an installed capacity of 6 MW. The storage system has 5 MW charging and discharging capacity with an efficiency of 80%. The wind speed data are from the Royal Netherlands Meteorological Institute (KNMI) [40]. The day-ahead and imbalance market prices and total system imbalances are for the Netherlands and obtained from the ENTSO-e transparency platform [41]. The residential loads in the distribution system are generated with the method described in [42]. For the industrial loads, the data for the Netherlands from the NEDU profiles [43] has been used. To generate the scenarios an Artificial Neural Network modelling approach is applied in order to obtain a set of scenarios of wind power generation, day-ahead, and imbalance market prices. The time resolution of the day-ahead market is one hour with a time horizon of 24-hours

Table 4
Data for transmission generators.

Gens. bus no.	P_g^{gmax} MW	P_g^{gmin} MW	$O_{g,t}^{E}$ €/MWh	$O_{g,t}^{RUP/DN}$ €/MW
1	15.2	3,4	90.58	50
2	15.2	3,4	90.58	50
7	30	7.5	130.63	70
13	59.1	20,85	130.27	70
15	60	12	210	120
15	15.5	5,25	60.75	40
16	15.5	5,25	60.75	40
18	40	40	30.39	20
21	40	40	30.39	20
23	31	10,5	60.75	40
23	35	14	70.03	50

Table 5
Data for distribution generators.

Gens. bus no.	P_g^{gmax} MW	$O_{g,t}^{E}$ €/MWh	$O_{g,t}^{RUP/DN}$ €/MW
3	1.96	25	12
4	0.98	20	10
5	1.96	15	7.5
17	0.98	30	15
19	5	15	7.5
26	1.96	22	12
29	0.98	18	9
31	0.98	18	9

and the balancing market is 15 min. α_T is considered as 30% of the total installed generation at the transmission system and α_{Imb} is the ratio of the total installed DERs to the total load of the system. The mathematical models are formulated in the General Algebraic Modelling System (GAMS) and solved with the solvers CPLEX and MOSEK on a computer with CPU E5-2697 v3@2.6 GHz. The computational time for the participation of the WF-ESS in one time-step of the day-ahead market (i.e. 1 h) and the balancing market (i.e. 15 min) of the coupled market model is 34 s and 16 s, respectively.

6.2. Case studies

In this section, the case studies which are going to be analysed in the results section are introduced. The first one is regarding the market model and the second one is about different sorts of DERs.

6.2.1. Market model case studies

In this paper, in addition to the coupled market model which is explained earlier, a centralized market is also considered as the benchmark. This market model is more compatible with the current electricity market regulation. More detailed information about the centralized market and its mathematical formulation can be found in Appendix A.

As the WF-ESS is relatively small compared with the size of the market, the WF-ESS cannot behave strategically in the centralized market and therefore his behaviour does not affect the market price. Consequently, the WF-ESS is a price-taker in both day-ahead and balancing markets hence, it solves a self-scheduling problem to determine its most beneficial actions for given prices in day-ahead and/or balancing markets.

6.2.2. DER case studies

In the WF-ESS case, the storage system participates in the energy and reserve capacity market and actively bids into the balancing markets. The wind farm alone, however, is limited in how it can participate in the market. Due to the stochastic nature of wind power, the wind farm alone is considered unable to

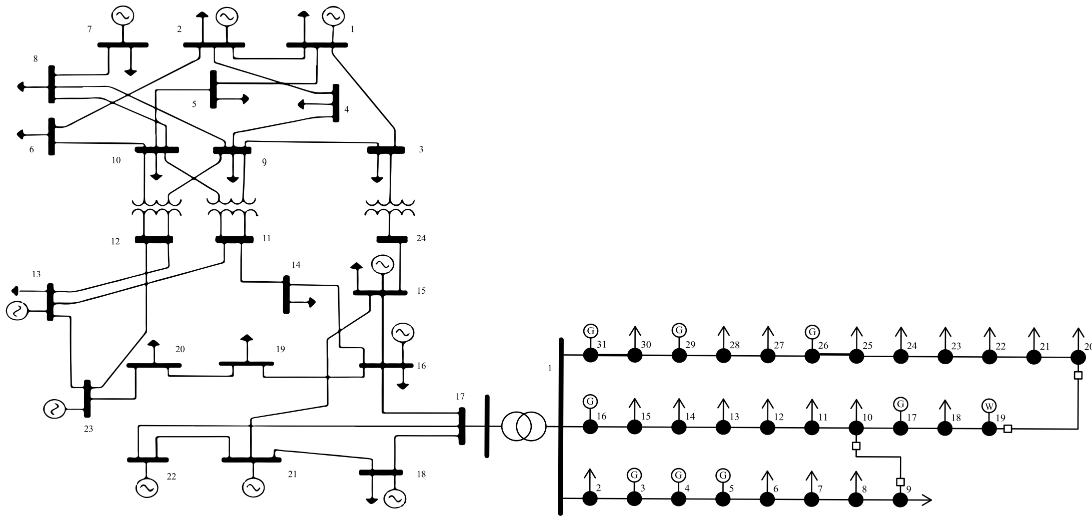

Fig. 3. Connected transmission and distribution system diagram for the case studies.

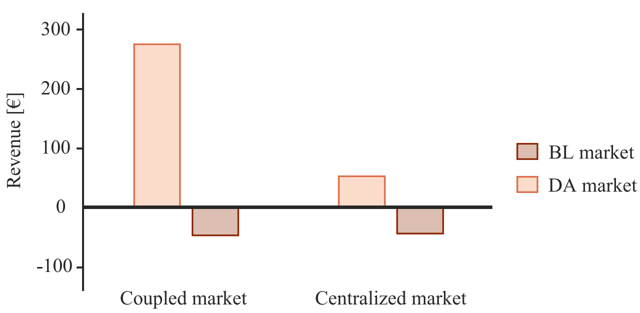

Fig. 4. The revenue of the wind farm in the coupled versus the centralized market.

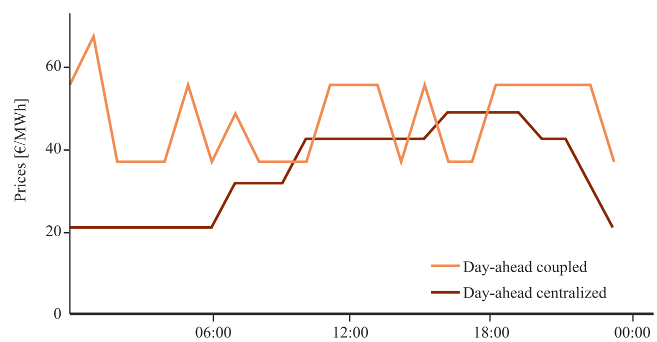

Fig. 5. The DA market price in the coupled versus centralized market.

participate in the reserve capacity market and/or actively bid into the balancing market, so it can only actively bid into the day-ahead energy market. However, in the balancing market, the wind farm may have to be paid or pay the market imbalance price (based on the assumed dual pricing scheme), depending on its real-time deviation with respect to the total system imbalance.

Because of higher complexity in the WF-ESS compared with the wind farm case, the mathematical formulations have been presented for the WF-ESS case. However, these formulations can be easily adapted for the wind farm alone, if one sets the capacity of the storage system equal to zero.

7. Results and discussion

In this section, the numerical results of the simulation are shown. In Section 7.1, the results of the wind farm's revenue in the coupled versus the centralized market are presented. In Section 7.2, the results of sensitivity analysis for changing the distribution system parameter, e.g. resistance and loads, and their effects on the day-ahead revenue and bidding wind energy by the wind farm are presented. In Section 7.3, the wind generation of the wind farm at different resistance rates in the coupled market is compared with the one in the centralized market model. Finally, in Section 7.4, the revenue of the wind farm is compared with the case in which the wind farm is equipped with a storage system. Therefore, the results of the performance of the WF-ESS in the coupled and centralized market is shown in this section.

7.1. Wind farm's revenues in the coupled versus centralized market

Fig. 4 shows the revenues of the wind farm in day-ahead and balancing markets for different market models. As this figure shows, in the coupled market model, the day-ahead revenue is significantly higher compared to the one in the centralized market model. The reason is indeed the strategic behaviour of the wind farm in the day-ahead coupled market which leads to higher market prices. For the comparison, Fig. 5 shows the day-ahead market prices in the coupled versus centralized market models and is showing a relatively higher value for day-ahead market prices in the coupled market.

As expected, the revenue in balancing markets is lower than the revenue in the day-ahead market for both market models. Moreover, for both market models, the balancing market revenue is negative which means that the wind farm has to pay the imbalance penalty cost to the system. Compared to the day-ahead market, there is not that much of a difference between the balancing revenue of coupled and centralized markets. The reason is that, as explained in Section 4.2, in the balancing market of the coupled market model, the wind farm cannot exercise market power. However, the difference is significantly higher in the day-ahead revenue of the wind farm when it participates strategically in the coupled market in comparison with its non-strategic day-ahead revenue in the centralized market.

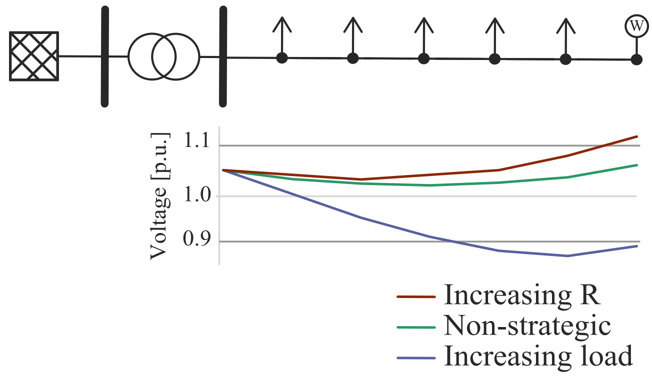

Fig. 6. The effect of increasing resistance and loads on the voltage through the feeder.

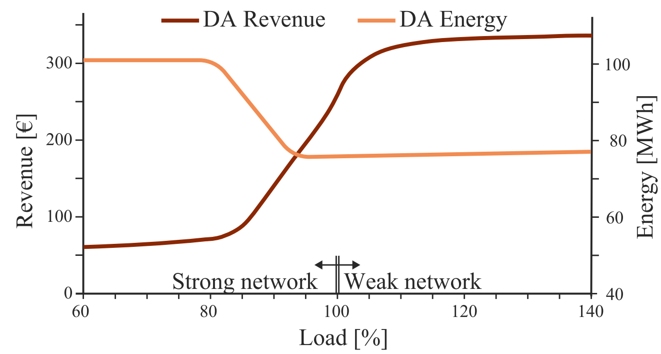

Fig. 7. The effect of increasing loads on the day-ahead energy and revenue of wind farm.

7.2. The effect of distribution system parameters on exercising market power by the strategic wind farm

To see the effect of distribution system parameters on the revenue of strategic market players, two parameters are being changed, loads, and the resistance of branches. In the distribution systems, cables are usually being used and their reactant compared with the resistance have smaller values. Therefore, changing the resistance of cables can be sufficient for studying the effect of branch parameters on the strategic biding of DERs. Performing this sensitivity analysis helps to understand whether or not changing loads and resistances, effects on the bidding volume and the revenue of the strategic wind farm. Before answering this question, one needs to study the effect of varying the resistance or loads on the security element of the distribution system, i.e. the voltage. To a better understanding of this effect, an example in Fig. 6 has been demonstrated. This figure shows a feeder where at its end, there is a generator, and in the middle, there are some loads. The generator's situation is almost comparable to the wind farm. In the diagram in Fig. 6, there are three curves showing voltage magnitude through the feeder in three different cases. The green curve in the middle is related to the normal situation where there is not increasing loads or resistance, hence the voltage along the feeder is always in the secure range. The red curve is related to the case where the resistance is increasing. As it is shown, the voltage along the feeder is increasing too, so that at the end of the feeder, there is an over-voltage. In contrast, by increasing the loads, the voltage along the feeder is decreasing in such a way that at the end of the feeder an under-voltage happens. This is shown by the blue curve in the diagram. Therefore, in both cases, i.e. either increasing the loads or increasing the resistance, the voltage at the end of the feeder-where the generator is located can be higher or lower than the security limits. Hence, the generator reacts differently to each of the two cases. In the case where the resistance is increasing, to counteract the over-voltage, the generator has to reduce its generation. This prevents the generator to exercise the market power because the generator knows that its power is not required by the system. In contrast, in the case where the loads are increasing, to counteract the under-voltages, the generator should inject more power to raise the voltage. Therefore, in this case, the generator by knowing this fact that its power is being required by the system operator might exercise market power. This market power is performed through an economic withholding which leads to a higher bidding price and a lower bidding quantity.

Now, back to the case study for the wind farm, the effect of increasing loads and resistance are being investigated. First starting with the loads. The effect of increasing the loads on the bidding behaviour of the wind farm is presented in Fig. 7. In the horizontal axis, a different percentage of the load is shown. When the load in the distribution system is decreasing with respect to the base-case, the system is indicated as strong and when the load is increasing, the system is indicated as weak. The red curve in the figure shows the day-ahead revenue of the wind farm in the coupled market model. As it is shown in Fig. 7, by increasing the loads, the day-ahead revenue has an overall increase. However, the revenue stays the same up to the point where the load is 80%. After this point, the revenue starts rising, since the wind farm realizes that it is required by the system operator thanks to its geographical location and the under-voltage which is happened there. Therefore, the wind farm raises the offer prices. On the other hand, at the point where the revenue is increasing, the energy bid by the wind farm is decreasing as it is shown by the orange curve in Fig. 7. In short, Fig. 7 depicts an exercising market power by the wind farm when the loads are increasing. The exercising of the market power by the wind farm is shown through a higher revenue for a lower amount of energy bid into the day-ahead market, which means a higher day-ahead price. As it has been mentioned earlier, this phenomenon is the basis of the economy withholding by which a strategic market player increases its revenue.

Fig. 8 shows an increase in the resistance and its effect on the bidding wind energy and the day-ahead prices. The horizontal axis is the difference percentage of the resistance of the cables. When the resistance of the cables is decreasing, the system is indicated as strong and when the resistance of the cables is increasing with respect to the base-case, the system is indicated as weak. As it is explained by Fig. 6, increasing the resistance will cause an over-voltage at the end of the feeder and therefore, the wind farm has to decrease its power. This is shown by the orange curve in Fig. 8 which has a downward trend. On the other hand, the day-ahead market prices — indicated by the red curve in Fig. 8, is also decreasing as the resistance is increasing. This, therefore, leads to a downward trend in the revenue of the winds farm as well. Therefore, it can be seen that by increasing the resistance, the wind farm cannot perform market power.

7.3. Renewable generation in the coupled versus centralized market

In this part, the difference between the bidding energy by the wind farm in the coupled versus centralized markets with different resistance rates is studied. In the centralized market, as it is explained in Appendix C, distribution system constraints are not taken into account during market clearing. This means that in the centralized market, the feasibility of the distribution system constraints when the DERs are getting dispatched is not considered, and therefore, there might be the chance that they

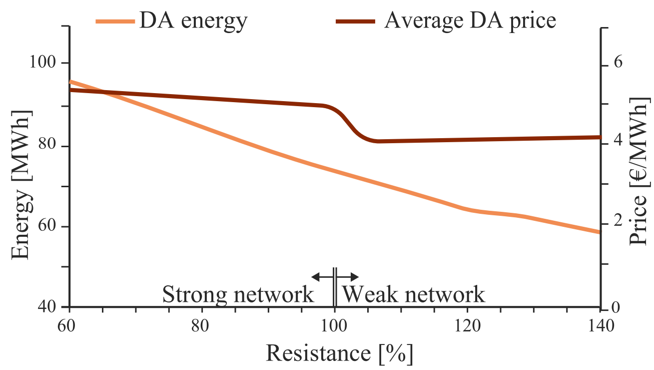

Fig. 8. The effect of increasing cable resistances on the day-ahead energy and revenue of the wind farm.

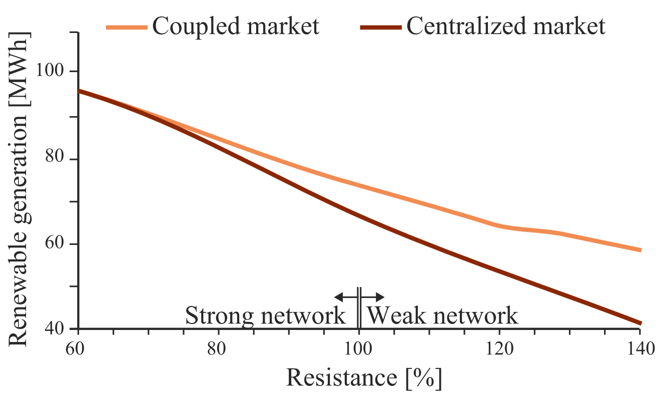

Fig. 9. Wind generation in the coupled and the centralized market.

cause system disturbances. To avoid this, a power flow for the distribution system with different resistance rates is performed, to determine the maximum energy allowed by the wind farm which does not cause disturbances in the distribution system. Then, the maximum energy allowed by the wind farm is getting compared with its bidding energy in the centralized market. If the bidding energy, in the centralized market and at a certain resistance rate, is lower than the maximum allowed energy, there will not be any wind curtailment, otherwise, there will be wind curtailments to reduce the bidding energy to the amount of the maximum allowed energy by the wind farm at that resistance rate.

Fig. 9 shows the bidding wind energy into the day-ahead market in the coupled versus the centralized market. The red curve shows the wind generated by the wind farm in the centralized market and the orange curve shows the one in the coupled market. As is expected, the wind generation in the centralized market has a downward trend by increasing the resistance, the same as that in the coupled market. However, at any resistance rate, the wind generation in the coupled market is higher than the wind generation in the centralized market. In other words, in the coupled market the distribution system is dynamically checked at each moment while in the centralized market, the distribution system is taken into account statically. Therefore, in a weak system where the resistance is higher and the distribution system is more often in danger of disturbance, the renewable-based DERs such as wind farms are more likely to be curtailed. In the coupled market, however, dynamically checking the distribution system let the wind farm to generate at a higher rate. This can be seen in Fig. 9 where for example at 140% resistance, the wind generation in the coupled market is almost 50% higher than the one in the centralized market.

7.4. *Effect of storage system on the wind farm's revenue*

In this section, the results for the difference between the wind farm alone and the WF-ESS, in terms of their revenues, are presented. These results want to show whether or not being equipped with a storage system is affordable for the wind farm. This comparison is performed for both market models.

Fig. 10 shows the revenues of the WF-ESS in day-ahead and balancing markets for different market models. To make the figure more readable, the results in Fig. 4 are added to Fig. 10 as well. As the figure shows, in the coupled market model, the day-ahead revenue either at the wind farm alone or the WF-ESS case is significantly higher compared to the ones in the centralized market model. The reason is indeed the strategic behaviour of the wind farm and the WF-ESS in the day-ahead coupled market which leads to higher market prices. As expected, Fig. 10 shows that the revenue in balancing markets, for both cases and at both market models are lower than the revenues in day-ahead markets. However, in the case where the wind farm is alone, at both market models, the balancing market revenue is negative which means that the wind farm has to pay the imbalance penalty cost to the system. In contrast, as the storage system can actively bid into the balancing market, the revenue in the balancing market for the WF-ESS either at coupled or centralized market models has positive values which means the WF-ESS can earn some revenue in the balancing market. There is slightly a higher balancing market revenue in the coupled compared to the

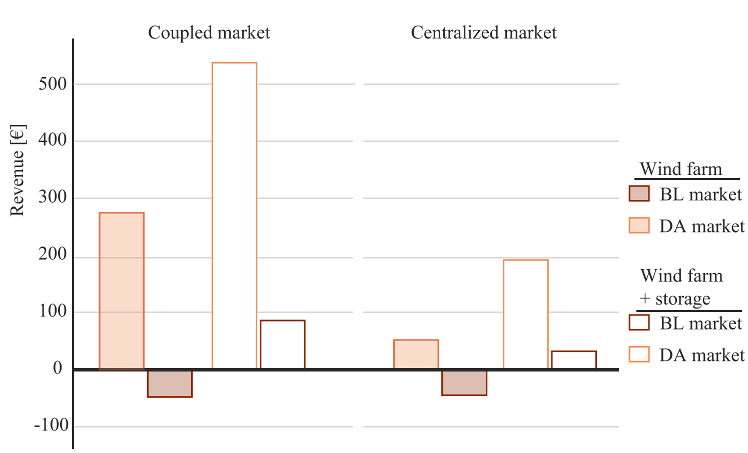

Fig. 10. Revenue of the wind farm and the WF-ESS in the coupled and the centralized market.

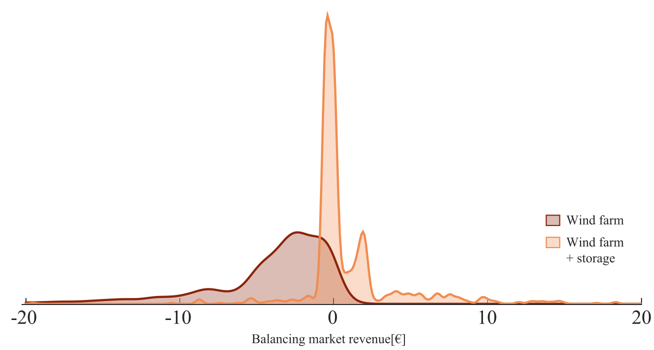

Fig. 11. The probability density function of the revenue in the balancing market for the wind farm and the WF-ESS.

centralized market but comparing this difference with the one in the day-ahead market, this difference is not very significant due to the non-strategic behaviour of market players in the balancing market.

To compare the balancing market revenues for different scenario realizations in two cases of wind farm versus WF-ESS, the probability density function (PDF) of balancing market revenues has been figured. Fig. 11 shows the PDFs for the wind farm versus WF-ESS case in the coupled market which are the results of 960 points consists of 10 scenarios realization for each of the 96-time intervals in the balancing market. The PDF belongs to the WF-ESS case has been shifted to the right in comparison with the one for the wind farm case and shows an increase in the balancing market revenue for the WF-ESS. This means that when the wind farm is provided with a storage system, for different scenario realization, there is a higher revenue compared with the case where the wind farm solely bid into the market and consequently has to pay a penalty cost due to its imbalances caused by the real-time wind power deviated from the bidding energy in the day-ahead market.

It should be mentioned here that to have a better comparison in terms of revenues between the wind farm case and the WF-ESS case, it is also important to take into account the cost of the storage system as well. If for the electrical storage system, a Li-ion battery is being considered, the Levelized cost of storage (LCOS) may be equal to 388 €/MWh. In this case the WF-ESS in the coupled market, with the deducted LCOS from its total revenue, results in a 227 €/MWh net revenue which is equal to the 227 €/MWh revenue of the case where the wind farm is alone. On the other hand, in the centralized market, deducting the LCOS from the total revenue requires a LCOS of 217 €/MWh to have an equal profit to a wind farm without a storage system. Therefore, depending on the market model and whether or not there is market power, a combined wind and storage unit can be an affordable or a non-affordable option in comparison with a case where the wind farm is alone and cannot act strategically.

8. Conclusions

This paper proposes a novel strategic bidding method for the revenue maximization of distributed energy resources (DERs) in a coupled market model. In a coupled market, as described in our earlier work [6], there is – in addition to a central market – a local market operated by the distribution market operator (DMO) to facilitate the participation of DERs. The size of the local market is relatively small, and this increases the chance of some DERs to act strategically. The coupled market consists of day-ahead and balancing markets on two geographical levels. The revenue maximization problem has been modelled through a bi-level shrinking rolling horizon optimization where its upper-level problem is from the strategic DER's perspective and the lower-level problem is from the market operator's (DMO's) perspective. In this paper, a wind farm is considered as the strategic DER, showing that under certain assumptions, also intermittent resources can exercise market power by economic withholding.

The first research question was to quantify the proposed strategic revenue maximization of the wind farm in the coupled market model. To answer this question, the results for the coupled market were compared with the ones for a state-of-art centralized market model where DERs cannot employ strategic behaviour. The results confirm the applicability of the proposed revenue maximization problem and they show that, in general, the wind farm earns higher revenues in the coupled market where it can exercise market power, as compared with the centralized market.

The second research question was whether or not changing the distribution system parameters can affect the revenue of the wind farm and its bidding strategy in the coupled market. Results show that a weak system, with longer feeders and thus higher branch resistances, leads to higher revenues for the wind farm, and lower amounts of energy cleared in the day-ahead market, while a stronger system has a reverse effect. In other words, a strategic market player in a weak system can increase its market power and therefore earn a higher income. In contrast, a strong system prevents exercising market power by market players. Note that these results have to do with the presence of the wind farm at the end of a feeder, therefore having a positive effect on the voltage profile. Moreover, it is seen that in a weak system, wind generation is significantly higher in the coupled market compared with the amounts cleared in the centralized market. This means that the coupled market can better unlock the potential of the renewable-based DERs which want to participate in the market.

The last research question was to see whether or not adding a storage system is affordable for the wind farm. Results show that in both coupled and centralized markets, the combined wind and storage system (WF-ESS) has a higher income compared with the case of the wind farm alone. However, taking into account the Levelized Cost of the Storage and deducting it from the revenue can lead to different net revenue for the wind farm with the storage system in coupled and centralized markets.

Finally, it is important to mention that exercising market power by market players leads to a higher end-user electricity price and consequently a higher social cost. Since in the coupled market design, this market power exists due to the presence of system constraints, the distribution system operator must also investigate the cost of upgrading the system to avoid the occurrence of market power.

CRediT authorship contribution statement

Mana Farrokhseresht: Conceptualization, Ideas, Methodology, Software, Formal analysis , Writing - original draft. **Han Slootweg:** Writing - review & editing, Supervision, Project administration. **Madeleine Gibescu:** Investigation, Writing - review & editing, Supervision, Project administration, Funding acquisition.

Declaration of competing interest

The authors declare that they have no known competing financial interests or personal relationships that could have appeared to influence the work reported in this paper.

Appendix A. Distribution system constraints

In this section, the constraints that need to be enforced for the distribution system are explained. Given a distribution node $i \in N_D$, j refers to its unique ancestor.

$$(\theta_{i,l,t}): \quad V_{i,t} = V_{j,t} + 2(r_l \cdot f^p_{l,t} + x_l \cdot f^q_{l,t}) + r_l^2 \cdot I_{l,t} + x_l^2 \cdot I_{l,t}, \quad \forall i \in N_D, l \in L_D, t \tag{A.1}$$

$$(\lambda^{DA}_{i,t}): \sum_{l=(j,i)} (f^p_{l,t} - I_{l,t} \cdot r_l) + \sum_{g \in G_D} P_{g,t} + \sum_{w \in i} P^{DA}_{c,t} + P^{TD}_{i,t} = P^{load}_{i,t} + \sum_{l=(i,j)} f^p_{l,t} + G_i \cdot V_{i,t}, \forall i \in N_D, t \tag{A.2}$$

$$(\mu_{i,t}): \quad \sum_{l=(j,i)} (f^q_{l,t} - I_{l,t} \cdot x_l) + \sum_{g \in i} Q_{g,t} + Q^{TD}_{i,t} = Q^{load}_{i,t} + \sum_{l=(i,j)} f^q_{l,t} - b_i \cdot V_{i,t}, \forall i \in N_D, t \tag{A.3}$$

$$(\lambda^{UP}_t): \sum_{g \in G_D} R^{UP}_{g,t} + \sum_{e \in i} R^{dis}_{e,t} \geq 0, \forall t \tag{A.4}$$

$$(\lambda^{DN}_t): \sum_{g \in G_D} R^{DN}_{g,t} + \sum_{e \in i} R^{ch}_{e,t} \geq 0, \forall t \tag{A.5}$$

$$(\varphi^+_{g,t}): \quad P_{g,t} + R^{UP}_{g,t} \leq P^{gmax}_g, \forall g \in G_D, t \tag{A.6}$$

$$(\varphi^-_{g,t}): \quad P_{g,t} - R^{DN}_{g,t} \geq P^{gmin}_g, \forall g \in GD, t \tag{A.7}$$

$$(\xi_{l,t}): \quad (f^p_{l,t})^2 + (f^q_{l,t})^2 \geq I_{l,t} \cdot V_{i,t}, \forall i \in N_D, l = (i,j) \in L_D, t \tag{A.8}$$

$$(\zeta_{l,t}): \quad (f^p_{l,t})^2 + (f^q_{l,t})^2 \leq S^2_{l,t}, \forall i \in N_D, l = (i,j) \in L_D, t \tag{A.9}$$

$$(\phi_{g,t}): \quad (P_{g,t})^2 + (Q_{g,t})^2 \leq S^2_{g,t}, \forall g \in G, t \tag{A.10}$$

$$(\sigma^+_{i,t}, \sigma^-_{i,t}): \quad V^{min}_i \leq V_{i,t} \leq V^{max}_i, \forall i \in N_D, t \tag{A.11}$$

$$(\delta^+_{g,t}, \delta^-_{g,t}): \quad Q^{gmin}_i \leq Q_{g,t} \leq Q^{gmax}_i, \forall g \in G, t \tag{A.12}$$

$$(\beta^+_{g,t}, \beta^-_{g,t}): \quad P^{gmin}_g \leq P_{g,t} \leq P^{gmax}_g, \forall g \in G, t \tag{A.13}$$

$$(\gamma^+_{c,t}, \gamma^-_{c,t}): \quad 0 \leq P^{DA}_{c,t} \leq \widehat{P}^{DA}_{c,t}, \forall c \in C, t \tag{A.14}$$

$$(\psi^+_{e,t}, \psi^-_{e,t}): \quad 0 \leq R^{dis}_{e,t} \leq \widehat{R}^{dis}_{e,t}, \forall e \in E, t \tag{A.15}$$

$$(\vartheta^+_{e,t}, \vartheta^-_{e,t}): \quad 0 \leq R^{ch}_{e,t} \leq \widehat{R}^{ch}_{e,t}, \forall e \in E, t \tag{A.16}$$

Constraint (A.1) accounts for the voltage difference which is induced by the power flow over a line. Constraints (A.2) and (A.3) are active and reactive power balance equations of the distribution system, respectively. In (A.4) and (A.5) the required upward and downward reserves procured from DERs are defined. This constraint guarantees that a certain amount of the total installed capacity from dispatchable generators is available for the balancing purpose. Constraints (A.6) and (A.7) are limits for the reserve capacity of generators. Constraints (A.8) shows the relation between voltage and current and active and reactive power flow over a line and is the conic equation of the distribution system. Constraint (A.9) imposes the congestion limit for the distribution lines. Constraint (A.10) is related to the generation capability curves and is linearized by the method explained in [44]. Constraints (A.11)–(A.16) impose limits on the involved decision variables.

Appendix B. Transmission system constraints

In this section, the constraints that need to be enforced for the transmission system are explained.

$$f^p_{l,t} = B_l(\theta_{i,t} - \theta_{j,t}), \forall (i,j) \in l, l \in L_T, t \tag{B.1}$$

$$-TC_l \leq f^p_{l,t} \leq TC_l, \forall l \in L_T, t \tag{B.2}$$

$$\sum_{g \in G_T} P_{g,t} + P^{DT}_{i,t} + \sum_{(j,i) \in l} f^p_{l,t} = P^{load}_{i,t} + \sum_{(i,j) \in l} f^p_{l,t}, \forall i \in N_T, l \in L_T, t \tag{B.3}$$

$$(R^{DT/UP}_{i,t} - R^{DT/DN}_{i,t}) + \sum_{g \in G_T} (R^{UP}_{g,t} - R^{DN}_{g,t}) \geq \alpha_T. \sum_{g \in G_T} P^{gmax}_g, \forall i \in N_{T-D}, t \tag{B.4}$$

$$P_{g,t} + R^{UP}_{g,t} \leq P^{gmax}_g, \forall g \in G_T, t \tag{B.5}$$

$$P_{g,t} - R^{DN}_{g,t} \geq P^{gmin}_g, \forall g \in G_T, t \tag{B.6}$$

$$P^{gmin}_g \leq P_{g,t} \leq P^{gmax}_g, \forall g \in G_T, t \tag{B.7}$$

$$0 \leq P^{DT}_{i,t} \leq \widetilde{P^{TD}_{i,t}}, \forall i \in N_{T-D}, t \tag{B.8}$$

$$0 \leq R^{DT/UP}_{i,t} \leq \sum_{g \in G_D} \widetilde{R^{UP}_{g,t}}, \forall i \in N_{T-D}, t \tag{B.9}$$

$$0 \leq R^{DT/DN}_{i,t} \leq \sum_{g \in G_D} \widetilde{R^{DN}_{g,t}}, \forall i \in N_{T-D}, t \tag{B.10}$$

Constraint (B.1) considers the power flow over a transmission line and (B.2) imposes a limit on this power flow to the transmission line capacity. In (B.3), the power balance equation is shown. Constraint (B.4) is the required reserve capacity in the transmission system level which is a ratio of the totalled generation directly connected to the transmission system. Constraints (B.5)–(B.6) correspond to limits for the reserve capacity procured from generators in the transmission system. Constraints (B.7) and (B.8) impose limits for the energy from transmission generators and the DMO, respectively. Eqs. (B.9) and (B.10) limit the reserve capacity from the DMO.

Appendix C. Centralized market model

A scheme consisting of centralized day-ahead and balancing markets is considered as the benchmark which has the most compatibility with the current electricity market regulation. The centralized market model is shown in the grey flowchart in Fig. C.12. As it is shown in the figure, there are no DMO-operated local markets, and distribution system constraints are not taken into account. DERs are considered to be connected at the interface node of the transmission system and the TMO operates both day-ahead and balancing markets for all DERs and generators in the transmission system. Same as the coupled market, the day-ahead market is the joint energy and reserve capacity market and there is a similar approach regarding the time resolution, time horizon, and market clearing. To avoid disturbing the distribution system, due to activating the DERs, after market clearing, a power-flow for the distribution system is performed by the distribution system operator, to determine the maximum energy allowed by the DERs which does not cause problems in the distribution system. The centralized market model merely consists of Step 2 and Step 5 (shown in Fig. 1) in the coupled market model. A more detailed explanation for the clearing process in the centralized market can be found in [6]. Below, the revenue maximization problem of the WF-ESS in the centralized market is explained.

C.1. Revenue maximization problem of DERs in the centralized market model

The steps and their sequences in the WF-ESS's bidding in centralized day-ahead and balancing markets are shown in the green bar in Fig. C.12. Relatively speaking, day-ahead and balancing markets in the centralized market model are much bigger than the WF-ESS, hence the WF-ESS cannot behave strategically and exercise market power in the day-ahead market nor the balancing market. The balancing market is also modelled through the rolling shrinking horizon in case of having a storage system, the same as the one in the coupled market model. The dual pricing mechanism is also applied in the imbalance settlement phase.

In both day-ahead and balancing markets, there are three steps. In step 1, generating the non-strategic bids, the WF-ESS solves a self-scheduling problem for given scenario-based market prices to determine its most beneficial actions in terms of bidding volume. Thereafter, in step 2, the unit participates in the day-ahead or balancing markets and the centralized market becomes clear. Finally, in step 3, according to the cleared price and quantities in step 2, the day-ahead or balancing revenue of the WF-ESS is calculated. The corresponding mathematical formulations of WF-ESS revenue in day-ahead and balancing markets are presented below.

C.2. Mathematical formulations: WF-ESS's revenue in the day-ahead market

In this section, the mathematical formulation for the revenue maximization of the WF-ESS in the day-ahead market is presented. As shown in Fig. C.12, there are three steps in day-ahead bidding which are as follows:

- **Step 1: Generate day-ahead non-strategic bids**
In this step, the WF-ESS solves the following optimization to determine its most optimum bidding volume in the day-ahead market.

$$\begin{aligned} Maximize \sum_t [\sum_c \sum_s \pi_s \cdot \lambda_{t,s}^{TD} \cdot P_{c,t}^{DA} \\ + \sum_e \sum_s \pi_s \cdot (\lambda_{t,s}^{UP} \cdot R_{e,t}^{dis} + \lambda_{t,s}^{DN} \cdot R_{e,t}^{ch})] \end{aligned} \tag{C.1}$$

The objective function in Eq. (C.1) consists of the revenue of WF-ESS in day-ahead energy market and the in the reserve market. The constraints for Eq. (C.1) are the same as the ones in Eqs. (2)–(14). The output of this step are the energy ($\widetilde{P_{c,t}^{DA}}$) and reserve ($\widetilde{R_{e,t}^{dis/ch}}$) bidding volume of WF-ESS in the day-ahead market.

- **Step 2: day-ahead market clearing**
The day-ahead joint market of the centralized model is quite similar to the day-ahead market clearing by the TMO in the coupled market model. The difference is that, for the objective function in the centralized model, $\lambda_{i,t}^{DA}$ and $\lambda_t^{UP/DN}$ in (17) are equal to zero. Moreover, $P_{g,t}$ and $R_{g,t}^{UP/DN}$ represent energy and reserve for all generators including DERs and generators at the transmission system. Therefore, the objective function and constraints are as follows:

$$\begin{aligned} Minimize \sum_{t\in T}[\sum_{g\in(G_T\cup G_D)} O_{g,t}^{E} \cdot P_{g,t} + O_{c,t}^{E} \cdot P_{c,t}^{DA} + O_{g,t}^{RUP} \cdot R_{g,t}^{UP} \\ + O_{g,t}^{RDN} \cdot R_{g,t}^{DN} \\ + O_{e,t}^{RUP} \cdot R_{e,t}^{dis} + O_{e,t}^{RDN} \cdot R_{e,t}^{ch}] \end{aligned} \tag{C.2}$$

The system constraints are quite similar with the constraints in the step of wholesale market clearing by the TMO in the coupled market model shown in Appendix B. The only difference is in the power balance equation in (B.3) where $P_{i,t}^{load}$ belongs to the loads of the transmission and distribution systems. The output of this step is cleared market prices ($\lambda_{i,t}^{DA}$, $\lambda_t^{UP/DN}$) and dispatching of energy and reserve of generators ($\widetilde{P_{g,t}}$, $\widetilde{P_{c,t}^{DA}}$, $\widetilde{R_{g,t}^{UP/DN}}$, $\widetilde{R_{e,t}^{dis/ch}}$).

- **Step 3: Remuneration**
In this step, the revenue of the WF-ESS is calculated based on the cleared day-ahead market price and quantities obtained in step 2:

$$Revenue = \sum_t[\sum_c \lambda_{c\in i,t}^{DA} \cdot \widetilde{P_{c,t}^{DA}} + \sum_e(\lambda_t^{UP} \cdot \widetilde{R_{e,t}^{dis}} + \lambda_t^{DN} \cdot \widetilde{R_{e,t}^{ch}})] \tag{C.3}$$

C.3. Mathematical formulations: WF-ESS's revenue in the balancing market

As the light green bar in Fig. C.12 shows, the revenue maximization of WF-ESS in the balancing market consists of three steps, the same as the one in the day-ahead market. These steps are explained below.

- **Step 1: Generate balancing non-strategic bids**
In this step, same as the one in the coupled market, the WF-ESS tries to calculate its energy bidding in the balancing market based on scenario-based positive and negative imbalance prices and the cleared day-ahead market prices:

$$\begin{aligned} \sum_t[\sum_{e\in c} \sum_s \pi_s \cdot (\lambda_{t,s}^{+} \cdot P_{e,t}^{dis} - \lambda_{t,s}^{-} \cdot P_{e,t}^{ch}) + \sum_c(\lambda_t^{DA} \cdot (1 - z_t) \cdot \Delta_{c,t} \\ + \sum_s \pi_s.(\lambda_{t,s}^{+} \cdot z_t \cdot y_t \cdot \Delta_{c,t}^{+} + \lambda_{t,s}^{-} \cdot z_t \cdot (1 - y_t) \cdot \Delta_{c,t}^{-}))] \end{aligned} \tag{C.4}$$

The formulation of the objective function in (C.4) is similar with the one in (23) hence its constraints are also the same as in (24)–(39). The output of this step is the bidding volume ($\widetilde{P_{e,t}^{dis/ch}}$) of the unit in the balancing market.

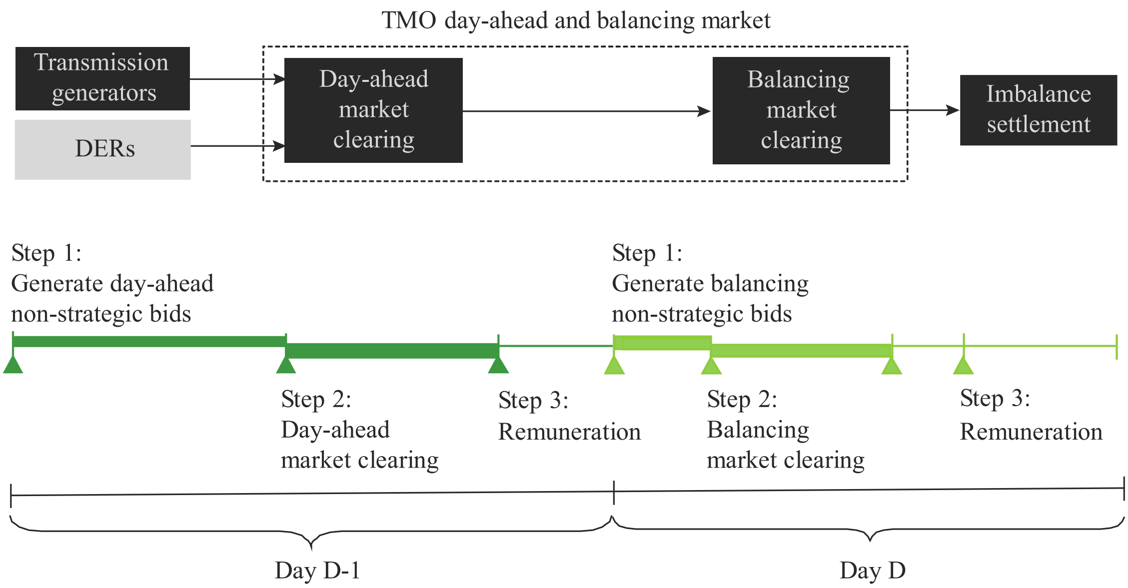

Fig. C.12. Centralized market model.

- **Step 2: balancing market clearing**

In this step, the balancing market is cleared. The shrinking rolling horizon approach is applied here as well to clear the balancing markets. The objective function is minimizing the total balancing service by the TMO as shown in (C.5):

$$\begin{aligned} Minimize \sum_{g\in G_T\cup G_D} (O^{EUP}_{g,\tau}.P^{UP}_{g,\tau} - O^{EDN}_{g,\tau}.P^{DN}_{g,\tau}) \\ + \sum_{e}(O^{Edis}_{e,\tau}\cdot P^{dis/BL}_{e,\tau} - O^{Ech}_{e,\tau}\cdot P^{ch/BL}_{e,\tau}) \end{aligned} \quad (C.5)$$

Following constraints need to be enforced:

$$\begin{aligned} (\lambda^{BL}_{i,\tau}): \quad & \sum_{g\in G_T\cup G_D} (\widetilde{P_{g,\tau}} + (P^{UP}_{g,\tau} - P^{DN}_{g,\tau})) \\ & + \sum_{c,e\in c}(\widetilde{P^{DA}_{c,\tau}} + P^{dis/BL}_{e,\tau} - P^{ch/BL}_{e,\tau}) \\ & + \sum_{(j,i)\in l} f^{p}_{l,\tau} = SI + P^{load}_{i,\tau} \\ & + \sum_{(i,j)\in l} f^{p}_{l,\tau}, \forall i \in N_T/N_{T-D}, l \in L_T, t \end{aligned} \quad (C.6)$$

$$P^{ch/BL}_{e,\tau} \leq \widetilde{P^{ch/BL}_{e,\tau}}, \forall e, \tau \quad (C.7)$$

$$P^{dis/BL}_{e,\tau} \leq \widetilde{P^{dis/BL}_{e,\tau}}, \forall e, \tau \quad (C.8)$$

The rest of the constraints are similar as the ones in Appendix B. The output of this step is the cleared balancing market price ($\lambda^{BL}_{i,\tau}$) and the cleared upward and downward energy ($\widetilde{P^{dis/BL}_{e,\tau}}$, $\widetilde{P^{ch/BL}_{e,\tau}}$) in the balancing market.

- **Step 3: Remuneration**

Finally, at the imbalance settlement phase, the WF-ESS calculates its revenue based on dual pricing mechanism and cleared balancing market prices ($\lambda^{BL}_{i,\tau}$) and the cleared upward and downward energy ($\widetilde{P^{dis/BL}_{e,\tau}}$, $\widetilde{P^{ch/BL}_{e,\tau}}$), obtained in step 2.

References

[1] Sweco, Ecofys, Tractbel Engineering, PWC, Study on the effective integration of demand energy recourses for providing flexibility to the electricity system, Final Report to The European Commission (April), 2015, p. 179.

[2] S. Minniti, N. Haque, P. Nguyen, G. Pemen, Local markets for flexibility trading: Key stages and enablers, Energies 11 (11) (2018) http://dx.doi.org/10.3390/en11113074.

[3] T. Sousa, T. Soares, P. Pinson, F. Moret, T. Baroche, E. Sorin, Peer-to-peer and community-based markets: A comprehensive review, Renew. Sustain. Energy Rev. 104 (January) (2019) 367–378, http://dx.doi.org/10.1016/j.rser.2019.01.036, arXiv:1810.09859.

[4] Decentralized Flexibility Market 2.0, A market based solution for organizing access to flexibility on the local distribution network, Tech. rep. Bundesverband Neue Energiewirtschaft e.V. (bne) / Association of Energy Market Innovators.

[5] C. Zhang, Y. Ding, N.C. Nordentoft, P. Pinson, J. Ostergaard, A Danish market solution for DSO congestion management through DER flexibility services, Power Syst. Clean Energy 2 (2014) 126–133.

[6] M. Farrokhseresht, N.G. Paterakis, H. Slootweg, M. Gibescu, Enabling market participation of distributed energy resources through a coupled market design, IET Renew. Power Gener. 14 (4) (2020) 539–550, http://dx.doi.org/10.1049/iet-rpg.2019.0598.

[7] P. Olivella-Rosell, E. Bullich-Massagué, M. Aragüés-peñalba, A. Sumper, S.Ø. Ottesen, J.A. Vidal-Clos, R. Villafáfila-Robles, Optimization problem for meeting distribution system operator requests in local fl exibility markets with distributed energy resources, Appl. Energy 210 (2017) (2018) 881–895, http://dx.doi.org/10.1016/j.apenergy.2017.08.136.

[8] C.A. Holt, Markets, Games, and Strategic Behavior: An Introduction to Experimental Economics, Princeton University Press, 2019.

[9] D. Electricity, M. Require, S.R. Rules, Market Power in Electricity Markets : Do Electricity Markets Require Special Regulatory Rules ? a Report Concerning the Competition Commission Electricity Generators Inquiry, 2000.

[10] E. Union, and an Evolution to Smart Grids, 2020, http://dx.doi.org/10.1016/B978-0-12-817770-9.00002-X.

[11] J.a. Dutton, Sources of market power in electricity markets, in: Introduction to Electricity Markets, PennState University. URL https://www.e-education.psu.edu/ebf483/node/2.

[12] J. Bergler, S. Heim, K. Hüschelrath, Strategic capacity withholding through failures in the German-Austrian electricity market, Energy Policy 102 (2016) (2017) 210–221, http://dx.doi.org/10.1016/j.enpol.2016.12.017.

[13] H. Zhou, B. Chen, Z.X. Han, F.Q. Zhang, Study on economic withholding in electricity market of Zhejiang Province, China, Commun. Nonlinear Sci. Numer. Simul. 14 (5) (2009) 2495–2501, http://dx.doi.org/10.1016/j.cnsns.2008.05.016.

[14] J.F. De Guevara, J. Maudos, Measuring welfare loss of markets power: An application to European banks, Appl. Econ. Lett. 11 (13) (2004) 833–836, http://dx.doi.org/10.1080/1350485042000263908.

[15] E. Nasrolahpour, J. Kazempour, H. Zareipour, W.D. Rosehart, A bilevel model for participation of a storage system in energy and reserve markets, IEEE Trans. Sustain. Energy 9 (2) (2018) 582–598, http://dx.doi.org/10.1109/TSTE.2017.2749434.

[16] Y. Ye, D. Papadaskalopoulos, R. Moreira, G. Strbac, Strategic capacity withholding by energy storage in electricity markets, in: 2017 IEEE Manchester PowerTech, IEEE, 2017, pp. 1–6, http://dx.doi.org/10.1109/PTC.2017.7981200.

[17] S. Wogrin, B.F. Hobbs, D. Ralph, E. Centeno, J. Barquín, Open versus closed loop capacity equilibria in electricity markets under perfect and oligopolistic competition, Math. Program. 140 (2) (2013) 295–322, http://dx.doi.org/10.1007/s10107-013-0696-2.

[18] H.K. Brøndbo, A. Storebø, T.K. Boomsma, C. Skar, S.E. Fleten, A Real Options Approach to Generation Capacity Expansion in Imperfectly Competitive Power Markets, vol. 11, Springer Berlin Heidelberg, 2020, http://dx.doi.org/10.1007/s12667-019-00325-3.

[19] N.-H.M. von der Fehr, D. Harbord, Spot market competition in the UK electricity industry, Econ. J. 103 (418) (1993) 531, http://dx.doi.org/10.2307/2234530.

[20] M. Vilim, A. Botterud, Wind power bidding in electricity markets with high wind penetration, Appl. Energy 118 (2014) 141–155, http://dx.doi.org/10.1016/j.apenergy.2013.11.055.

[21] S.S. Oren, Economic inefficiency of passive transmission rights in congested electricity systems with competitive generation, Energy J. 18 (1) (1997) 63–83, http://dx.doi.org/10.5547/ISSN0195-6574-EJ-Vol18-No1-3.

[22] R.W. Ferrero, V.C. Ramesh, Transaction analysis in deregulated power systems, Trans. Power Syst. 12 (3) (1997) 1340–1347.

[23] B.F. Hobbs, C.B. Metzler, J.S. Pang, Strategic gaming analysis for electric power systems: An MPEC approach, IEEE Trans. Power Syst. 15 (2) (2000) 638–645, http://dx.doi.org/10.1109/59.867153.

[24] E.G. Tsimopoulos, M.C. Georgiadis, Optimal strategic offerings for a conventional producer in jointly cleared energy and balancing markets under high penetration of wind power production, Appl. Energy 244 (March) (2019) 16–35, http://dx.doi.org/10.1016/j.apenergy.2019.03.161.

[25] E.G. Kardakos, C.K. Simoglou, A.G. Bakirtzis, Optimal offering strategy of a virtual power plant: A stochastic bi-level approach, IEEE Trans. Smart Grid 7 (2) (2016) 794–806, http://dx.doi.org/10.1109/TSG.2015.2419714.

[26] D. Pozo, E. Sauma, J. Contreras, Basic theoretical foundations and insights on bilevel models and their applications to power systems, Ann. Oper. Res. 254 (1–2) (2017) 303–334, http://dx.doi.org/10.1007/s10479-017-2453-z.

[27] J. Horta, D. Kofman, D. Menga, A. Silva, Novel market approach for locally balancing renewable energy production and flexible demand, in: 2017 IEEE International Conference on Smart Grid Communications, SmartGridComm 2017 2018-January, October, 2018, pp. 533–539, http://dx.doi.org/10.1109/SmartGridComm.2017.8340728, arXiv:1711.09565.

[28] H. Anis, Shrinking Horizon, Scenario-Based Optimal Liquidation with Lower Partial Moments Criteria By Shrinking Horizon, Scenario-Based Optimal Liquidation with Lower Partial Moments Criteria, 2018.

[29] R. Estrella, G. Belgioioso, S. Grammatico, A shrinking-horizon game-theoretic algorithm for distributed energy generation and storage in the smart grid with wind forecasting, IFAC-PapersOnLine 52 (3) (2019) 126–131, http://dx.doi.org/10.1016/j.ifacol.2019.06.022.

[30] E.M. Constantinescu, V.M. Zavala, M. Rocklin, S. Lee, M. Anitescu, A computational framework for uncertainty quantification and stochastic optimization in unit commitment with wind power generation, IEEE Trans. Power Syst. 26 (1) (2011) 431–441, http://dx.doi.org/10.1109/TPWRS.2010.2048133.

[31] A. van der Welle, Required adjustments of electricity market design for a more flexible energy system in the short term, Tech. rep. ECN, 2016.

[32] Frontier economics METIS technical note t4: Overview of European electricity markets, METIS Tech. Notes (February) (2016) 67, http://dx.doi.org/10.15614/ijpp.v9i01.n737.

[33] Y.U. Ren, F.D. Galiana, Pay-as-bid versus marginal pricing - Part II: Market behavior under strategic generator offers, IEEE Trans. Power Syst. 19 (4) (2004) 1777–1783, http://dx.doi.org/10.1109/TPWRS.2004.835650.

[34] J. Chaves-Ávila, R. Hakvoort, A. Ramos, The impact of European balancing rules on wind power economics and on short-term bidding strategies, Energy Policy 68 (2014) 383–393, http://dx.doi.org/10.1016/j.enpol.2014.01.010.

[35] M. Farivar, S.H. Low, Branch flow model: Relaxations and convexification-part i, IEEE Trans. Power Syst. 28 (3) (2013) 2554–2564, http://dx.doi.org/10.1109/TPWRS.2013.2255317.

[36] A.J. Fortuny-amat, B. Mccarl, J. Fortuny-amat, B. Mccarl, Linked references are available on JSTOR for this article : A representation and economic interpretation of a two-level programming problem, J. Oper. Res. Soc. 32 (9) (1981) 783–792.

[37] M.J. Rider, J. Contreras, J.M. López-Lezama, A. Padilha-Feltrin, Bilevel approach for optimal location and contract pricing of distributed generation in radial distribution systems using mixed-integer linear programming, IET Gener. Transm. Distrib. 7 (7) (2013) 724–734, http://dx.doi.org/10.1049/iet-gtd.2012.0369.

[38] C. Grigg, P. Wong, P. Albrecht, R. Allan, M. Bhavaraju, R. Billinton, Q. Chen, C. Fong, S. Haddad, S. Kuruganty, W. Li, R. Mukerji, D. Patton, N. Rau, D. Reppen, A. Schneider, M. Shahidehpour, C. Singh, The IEEE reliability test system-1996. A report prepared by the reliability test system task force of the application of probability methods subcommittee, IEEE Trans. Power Syst. 14 (3) (1999) 1010–1020, http://dx.doi.org/10.1109/59.780914.

[39] M. Xie, X. Ji, X. Hu, P. Cheng, Y. Du, M. Liu, Autonomous optimized economic dispatch of active distribution system with multi-microgrids, Energy 153 (2018) 479–489, http://dx.doi.org/10.1016/j.energy.2018.04.021.

[40] KNMI - Koninklijk Nederlands Meteorologisch Instituut, URL www.knmi.nl.

[41] E.N.T.S.O.-e, ENTSO-E Transparancy Platform, 2020, URL https://transparency.entsoe.eu/.

[42] M. Nijhuis, M. Gibescu, J. Cobben, Bottom-up Markov chain Monte Carlo approach for scenario based residential load modelling with publicly available data, Energy Build. 112 (2016) (2016) 121–129, http://dx.doi.org/10.1016/j.enbuild.2015.12.004.

[43] URL https://www.nedu.nl.

[44] M. Farrokhseresht, N.G. Paterakis, M. Gibescu, Oint day-ahead clearing of energy, active and reactive power reserves for systems with significant RES-related uncertainty, in: 2016 13th International Conference on the European Energy Market (EEM), IEEE, 2016, pp. 1–5, http://dx.doi.org/10.1109/EEM.2016.7521277.

Air-Gap Flow and Thermal Analysis of Rotating Machines using CFD

Debasish Mishra, *Department of Electrical Engineering, Aryan Institute of Engineering & Technology, Bhubaneswar, debasishmishra1@gmail.com*

Tapas Ranjan Baitharu, *Department of Computer Sciencel Engineering, Aryan Institute of Engineering & Technology, Bhubaneswar, tkbaitharu11@gmail.com*

Swaha Pattnaik, Department of Electronics and Communication Engineering , NM Institute of Engineering & Technology, Bhubaneswar, swaha.pattanayak@gmail.com

Nikunja Bihari Kar, Department of Computer Scinece Engineering , Raajdhani Engineering College, Bhubaneswar, nikunjabiharikar@gmail.com

Abstract

Thermal management of the rotating electrical machines is a very challenging area which needs appropriate solutions for each machine and operating condition. The heat is generated by the electromagnetic losses and the mechanical friction during the rotation. Computational Fluid Dynamics (CFD) is used in this study to predict and analyze the thermal performance of a rotating electrical machine where high speed rotation is coupled with small flow gaps. The investigation presented in this paper is based on a geometry used for model assessment and verification purposes. However, the approach outlined and the observations made are transferrable to other geometries. ANSYS Fluent has been used to perform CFD simulation where both the air velocity field and the temperature distribution are obtained. The results are qualitatively highly interesting to understand the thermal behavior within an electrical machine operations. The results show a periodic temperature distribution on the stator surface with similar periodic pattern for the heat transfer coefficient on the rotor surface. The simulated average heat transfer coefficient at the rotor surface is compared with the correlations from published literature with an overall good agreement.

1. Introduction

The air-gap between the rotor and the stator plays very important role in the design and performance of rotating machines. The air-gap thickness can be very different for different types of rotating machines based on their size and operating conditions. As an example, for smaller motor sizes, very small air-gap, often less than one millimetre, is maintained to reduce the electromagnetic losses and to increase the efficiency. On the other hand, in larger rotating machines, a very high magnetic field is formed which can drag the rotor towards the stator with very high force. Therefore, a larger gap is often maintained to avoid the contact between the rotor and the stator during machine operation.

Nomenclature

D_h	$=2g$, Hydraulic diameter (0.01m)	Ta	Taylor number
g	Gap size (0.005m)	Ta_{cr}	Critical Taylor number
h	Heat transfer coefficient (W/m^{2}K)	Nu	Nusselt number
h_{avg}	Average h (W/m^{2}K)	Nu_{avg}	Average Nusselt number
k	Thermal conductivity of air (W/m-K)	ν	Kinematic viscosity of air (m^2/s)
r_1	Outer radius of the rotor (0.075m)	Ω	Angular velocity of the rotor (157rad/s)
r_2	Inner radius of the stator (0.08m)	Ω_{cr}	Critical angular velocity (rad/s)
r_m	$=\frac{r_1+r_2}{2}$, Mean radius (0.0775m)		

The design process of the machine also requires the knowledge of the temperature distribution and the maximum internal temperature for a given operating condition. The performance and the life time of the machine depend on how well the temperature is maintained during the machine operation by following the guidelines and the design specifications. Moreover, the maximum output power is also limited by the temperature rise inside the electrical machines [1]. These considerations make the thermal management a very important and challenging issue for the rotating machines. Heat transfer modelling is therefore getting more and more attention within research community [2], [3], [4]. From a cooling perspective rotating machines can be broadly classified in two groups, ventilated and totally enclosed machines. For totally enclosed low voltage machines, the major heat transfer is governed by heat removal at the external surfaces (which can be achieved either by cooling ribs or a water jacket) and by the internal heat transfer which is mainly driven by the recirculating air inside the machine. The rib-cooled totally enclosed machine does in many cases have a shaft-mounted fan which forces air over the cooling ribs. For open machines, cooling is achieved by forcing ambient air through the machine. The convection inside the air-gap plays a very important role for both types of machines because the heat transfer behaviour from the rotor depends completely on the airflow pattern inside the air-gap.

Air-gap heat transfer has attracted a lot of attention from many researchers over the past few decades. It is addressed by several authors for different types of rotating machines with different operating conditions. Howey et al. [2] highlighted the importance of the air-gap for rotating electrical machines and discussed the convective heat transfer inside the air-gap in their review paper. The authors have also discussed different non dimensional parameters and presented the most commonly used convective heat transfer correlations for a wide range of operating conditions and air-gap size. Romanazzi and Howey [5] have analysed the rotor-stator air-gap heat transfer for a switched reluctance machine using Computational Fluid Dynamics (CFD) and have derived a new correlation to calculate the non-dimensional surface heat transfer coefficient. Anderson et al. [6] performed a CFD analysis to evaluate the forced air cooling and windage losses for high speed air-cooled electric motors and also proposed a new correlation to calculate the heat transfer coefficient. Deaconu et al. [7] analysed a non-uniform annulus gap between the rotor and stator for a permanent magnet synchronous motor using CFD where the authors confirmed highly nonlinear behaviour of the heat transfer.

The electrical machine is an energy conversion apparatus where electrical energy is converted into mechanical energy. A very important aspect for the rotating electrical machines is the heat produced during the energy conversion process. The heating of the electrical machines is an effect due to several types of loss mechanisms, for example, resistive losses or the so called joule losses, hysteresis losses, mechanical losses, windage losses etc. As an example, 15% of the total electrical energy is converted into heat in a usual totally enclosed 4kW induction motor [1]. This waste energy contributes to the temperature rise inside the machine as well as to the ambient which needs to be taken care of through ventilation. A detailed combined flow and heat transfer modelling will help to understand the complex flow and heat transfer behaviour inside the machine. This knowledge can then be translated into design choices which enables higher efficiency and longer lifetime of the product.

In this paper, we analyse the flow and heat transfer for a totally enclosed rotating machine. However, heat transfer from the end winding, which is e.g. investigated in [8] is not considered in this paper. The key focus in this article is to discuss the heat transfer within the air-gap between the rotor and the stator. The complex flow pattern due to the aerodynamic friction and its influence on the heat transfer are presented in this paper. The Taylor vortex flow [9] or the so called Taylor vortices are observed in the annulus shaped air-gap in our simulation which is in general a great modelling challenge. Taylor instability becomes a very interesting topic for number of engineering subjects due to its impact on the heat transfer and mechanical design. Number of studies have been performed to investigate this phenomena [10]–[13]. A strong influence of the Taylor instabilities on the heat transfer through the annulus air-gap is observed from our simulation results.

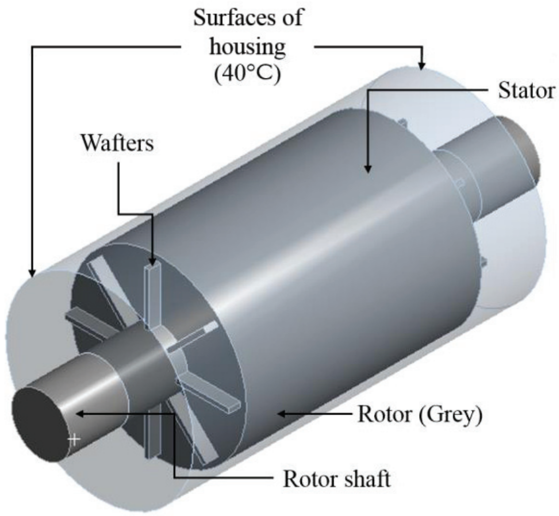

(a)

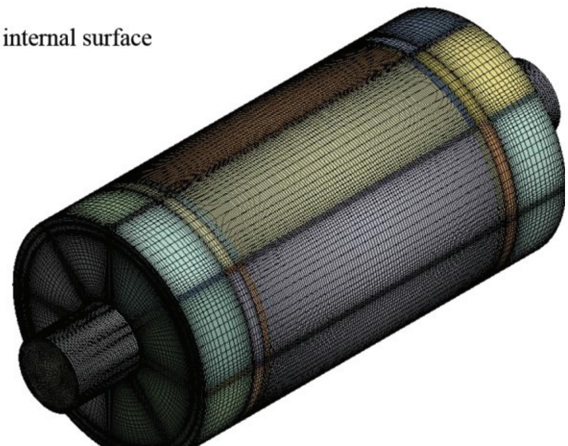

(b)

Fig. 1. Numerical domain (a) simplified motor geometry (b) mesh (2 million cells)

2. Rotating machine and operating conditions

The model geometry presented in this section is a design used for model assessment and verification purposes intended to resemble a low voltage motor. The intention of having a pure modelling-centred geometry is that different methods for fluid mechanics can be investigated and that there is a flexibility in re-defining the shape based on the varying demands from one verification case to the other. The computational domain consists of a rotor and the air surrounding the rotor enclosed by the internal surfaces of the stator and the surfaces of the housing of the machine (Fig. 1a). Fig. 2a presents a cross section of the numerical domain together with the dimensions. The rotor is modelled as a solid where the rotor is rotating at 1500 rpm. No slip boundary condition is used for the rotor surfaces with a constant temperature of 150°C. However, the surfaces of the shaft outside the air domain were kept at ambient temperature 40°C. On the other hand, the stator internal surface was modelled as a stationary wall where a virtual wall thickness of 50mm was considered. A convective heat transfer coefficient of 10 W/m^{2}K was imposed at the external surface of the virtual thick wall together with a free stream temperature of 40°C, which is the ambient temperature. The air properties are used at ambient temperature. The volume average air temperature (117°C) from the simulation is used as a reference temperature to calculate the heat transfer coefficient.

The mesh (Fig. 1b) contains about 2 million cells where very refined boundary layer is generated close to the solid walls. Realizable $k-\varepsilon$ two equations model is used to model the turbulence together with enhanced wall treatment for the boundary layer.

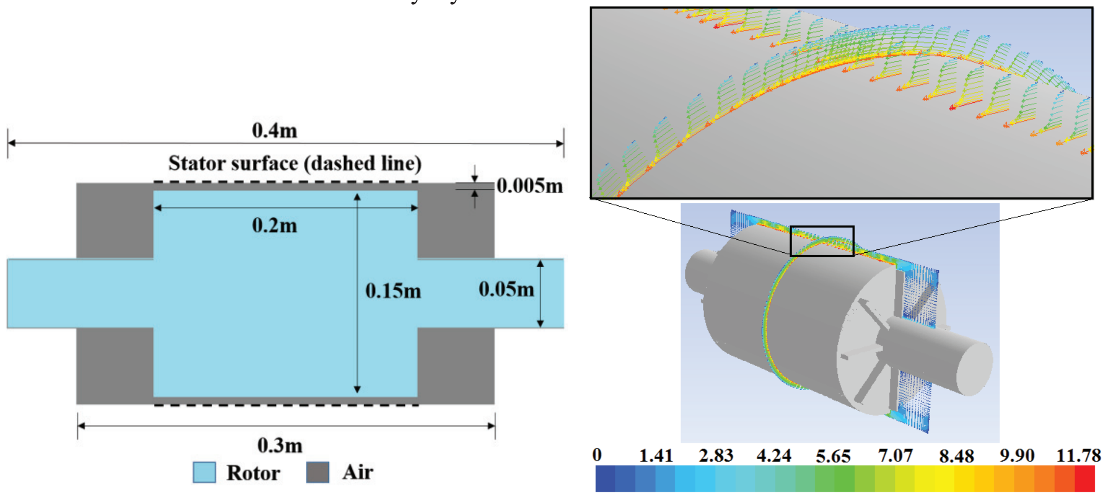

(a) (b)

Fig. 2. Domain together with velocity vectors (m/s) (a) Cross section of the domain together with dimensions (b) Boundary layer flow pattern in the air-gap surrounding the rotor

3. Results and discussions

The flow characteristics inside the cylindrical annulus air-gap can be determined by the non-dimensional Taylor number (Ta). Taylor number measures the importance of the inertial forces over the viscous forces for fluid rotation induced by the rotation of cylindrical surfaces. Taylor number is defined according to the following formula:

$$Ta = \Omega^2\, r_m\, (r_2 - r_1)^3/\nu^2 \tag{1}$$

The critical Taylor number can be defined as [14]:

$$Ta_{cr} = 1697F_g \tag{2}$$

Where F_g is defined as:

$$F_g = \frac{\pi^4}{1697}\left(1-\frac{r_2-r_1}{2r_m}\right)^{-2} S^{-1} \tag{3}$$

$$S = 0.0571\left[1-0.652\frac{r_2-r_1}{r_1}\right] + 0.00056\left[1-0.652\frac{r_2-r_1}{r_1}\right]^{-1} \tag{4}$$

Which gives the critical angular velocity:

$$\Omega_{cr}^2 = 1697\, F_g\, \nu^2/r_1(r_2-r_1)^3 \tag{5}$$

According to the theory, if the Taylor number is larger than the critical value, then Taylor vortices are most likely present in the flow inside the annulus. For our particular case the critical Taylor number is 1884 and the present Taylor number is 8.26×10^5, which clearly shows that Taylor vortices are present in our studied case (Fig. 3).

Since the flow is turbulent ($10^4 < Ta/F_g < 10^7$), the non-dimensional heat transfer coefficient, the Nusselt number (Nu) can be calculated using the following formulation [2]:

$$Nu = 0.409\left(Ta/F_g\right)^{0.241} \tag{6}$$

The convective heat transfer coefficient is then calculated from Nusselt number using the following formula:

$$h = \frac{Nu\, k}{D_h} \tag{7}$$

Now, for the studied geometry with the considered operating conditions, $Ta/F_g = 7.44 \times 10^5$. The average Nusselt number Nu_{avg} for the rotor surface and the average heat transfer coefficient h_{avg} are calculated using the correlation presented in (6) and (7) and compared with the simulation data in Table 1. The results presented in Table 1 show that the average heat transfer coefficient from the simulation agrees well with the correlations.

Table. 1. Comparison of the average surface Nusselt number and heat transfer coefficient for the rotor surface from the simulation with correlations (6) and (7)

	Correlation (6 & 7)	Simulation
Nu_{avg}	10.64	11.18
h_{avg}	28.82	30.3

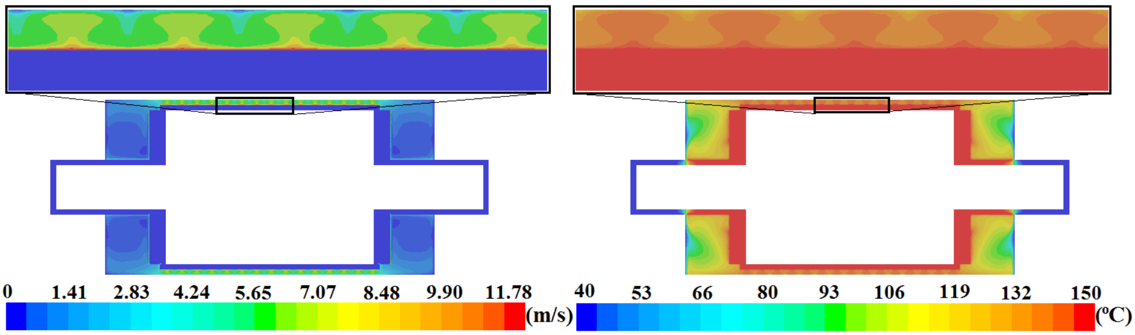

(a) (b)

Fig. 3. Taylor vortex flow and temperature distribution (a) Velocity contour (m/s) (b) Temperature contour (°C)

Fig. 2b shows the boundary layer flow pattern using the velocity vectors which represents the rotational and the viscous effect on the airflow inside the air-gap. Fig. 3a illustrates the Taylor vortex flow pattern inside the annulus air-gap which affects the temperature distribution following similar pattern (Fig. 3b).

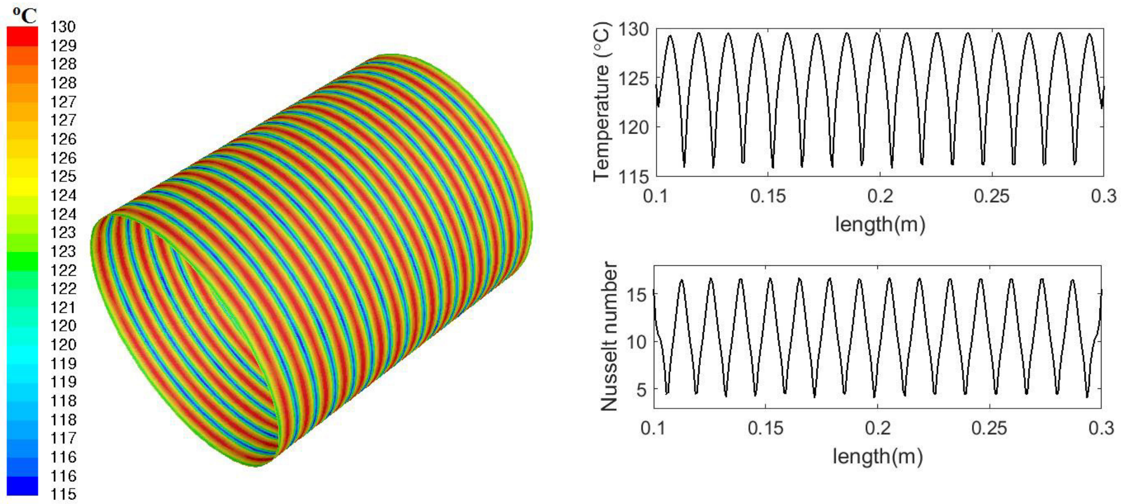

(a) (b)

Fig. 4. Taylor vortex flow effect on heat transfer performance (a) Temperature distribution on stator's internal surface (°C) (b) Temperature on a line along the length on the stator internal surface (top) and Nusselt number on a line along the length on the rotor surface

The effect of the Taylor instabilities can also be observed in fig.4. The temperature contour on the stator surface shows a periodic distribution with 15°C temperature variation which is a lot from the design perspective. A similar periodic pattern is observed also on the heat transfer coefficient for the rotor surface. The results obtained from the simulation can be very useful for the design and manufacturing of electrical rotating machines in general. However, the strong connection between the thermal and electromagnetic performance requires a combined analysis to find an optimum design. The thermal analysis can though on its own provide useful indications on design changes which are not related to the electromagnetic design. This is due to the induced temperature related effects e.g. a higher temperature will increase the resistance in the conductors, leading to that a higher voltage has to be applied in order to maintain a certain current. This means that the efficiency goes down when the temperature increases. At the same time, a higher temperature will lead to a loss reduction in the electrical steel, whether it is silicon steel (SiFe) [15] or nickel iron (NiFe) [16]. These effects, which are strongly coupled to temperature, and their consequences justify the present study where the electric machine is approached from the thermal physics side. A good understanding of the thermal behaviour will add additional paths to further improve the energy efficiency of motors and generators.

4. Conclusion

The model presented in this paper captures the complex Taylor vortex flow very well while providing detailed insight of the flow and heat transfer inside the air-gap. The model predicts the heat transfer coefficient with overall good accuracy. The simulation results pinpoint also the periodic heat transfer pattern from the rotor surface and this provides useful information for the prediction of the temperature distribution inside the rotating electrical machine.

The simulation results show about 15°C temperature variation on the stator surface. This kind of variation along the rotor cannot be resolved using less intricate modelling tools than those employed in this paper. It shows that a deep and detailed understanding of heat transfer phenomena and fluid dynamics enables additional degrees of freedom when it comes to design of rotating electrical machines.

References

[1] J. Pyrhönen, T. Jokinen, and V. Hrabovcová, *Design of rotating electrical machines*. John Wiley & Sons, Ltd, 2008.

[2] D. A. Howey, P. R. N. Childs, and A. S. Holmes, "Air-Gap Convection in Rotating Electrical Machines," *IEEE Trans. Ind. Electron.*, vol. 59, no. 3, pp. 1367–1375, Mar. 2012.

[3] M. Kuosa, P. Sallinen, and J. Larjola, "Numerical and experimental modelling of gas flow and heat transfer in the air gap of an electric machine," *J. Therm. Sci.*, vol. 13, no. 3, pp. 264–278, Aug. 2004.

[4] D. Staton and A. Cavagnino, "Convection heat transfer and flow calculations suitable for analytical modelling of electric machines," *IECON 2006-32nd Annu.*, 2006.

[5] P. Romanazzi and D. A. Howey, "Air-gap convection in a switched reluctance machine," in *2015 Tenth International Conference on Ecological Vehicles and Renewable Energies (EVER)*, 2015, pp. 1–7.

[6] K. R. Anderson, J. Lin, C. McNamara, and V. Magri, "CFD Study of Forced Air Cooling and Windage Losses in a High Speed Electric Motor," *J. Electron. Cool. Therm. Control*, vol. 05, no. 02, pp. 27–44, 2015.

[7] A. Deaconu and A. CHIRILĂ, "Air-Gap Heat Transfer of a Permanent Magnet Synchronous Motor," *Rev. Roum.*, 2015.

[8] S. La Rocca, C. N. Eastwick, P. Connor, S. J. Pickering, C. Gerada, and K. Rönnberg, "Challenges in modelling totally enclosed fan-cooled electrical machines," in *International Heat Transfer Symposium and Heat Powered Cycles Conference*, 2016.

[9] G. Taylor, "Stability of a viscous liquid contained between two rotating cylinders," *Philos. Trans. R. Soc.*, 1923.

[10] A. Ben Nachouane, A. Abdelli, G. Friedrich, and S. Vivier, "Numerical approach for thermal analysis of heat transfer into

a very narrow air gap of a totally enclosed permanent magnet integrated starter generator," in *2015 IEEE Energy Conversion Congress and Exposition (ECCE)*, 2015, pp. 1749–1756.

[11] N. Lancial, F. Torriano, F. Beaubert, S. Harmand, and G. Rolland, "Study of a Taylor-Couette-Poiseuille flow in an annular channel with a slotted rotor," in *2014 International Conference on Electrical Machines (ICEM)*, 2014, pp. 1422–1429.

[12] R. Maryami, M. Javadpoor, and S. Farahat, "Experimental investigation of head resistance reduction in bubbly Couette–Taylor flow," *Heat Mass Transf.*, pp. 1–16, Feb. 2016.

[13] S. Viazzo and S. Poncet, "Numerical simulation of the flow stability in a high aspect ratio Taylor–Couette system submitted to a radial temperature gradient," *Comput. Fluids*, vol. 101, pp. 15–26, 2014.

[14] K. Becker and J. Kaye, "The influence of a radial temperature gradient on the instability of fluid flow in an annulus with an inner rotating cylinder," *J. Heat Transfer*, 1962.

[15] N. Takahashi, M. Morishita, D. Miyagi, and M. Nakano, "Examination of Magnetic Properties of Magnetic Materials at High Temperature Using a Ring Specimen," *IEEE Trans. Magn.*, vol. 46, no. 2, pp. 548–551, Feb. 2010.

[16] A. Krings, S. A. Mousavi, O. Wallmark, and J. Soulard, "Temperature Influence of NiFe Steel Laminations on the Characteristics of Small Slotless Permanent Magnet Machines," *IEEE Trans. Magn.*, vol. 49, no. 7, pp. 4064–4067, Jul. 2013.

Recent advancement in smart grid technology

Sunil Kumar Mahapatro, Department of Electrical Engineering, Aryan Institute of Engineering & Technology, Bhubaneswar, skmahapatro78@outlook.com

Snigadha Sagarika, Department of electrical Engineering , NM Institute of Engineering & Technology, Bhubaneswar, snigadha216@gmail.com

Romeo Jena, Department of Electrical and Electronics Engineering, Capital Engineering College, Bhubaneswar, romeo_jena2@hotmail.com

Soumya Mishra, Department of Electronics and Communication Engineering , Raajdhani Engineering College, Bhubaneswar, soumyamishra96@gmail.com

A B S T R A C T

With the advancement in technology, there is an immense increase in the demand of electrical energy that has not only become challenge for its production but also its distribution. So this rising demand is growing the complexities of power grids by increasing requirement for greater reliability, efficiency, security and environmental and energy sustainability concerns. These feature in a power grid towards smartness which eventually known as a today's concept of "Smart Grid". This is a conceptual technique in which all smart features are implemented in order to increase the distribution system of electricity efficient, more reliable and sustainable. In this article an overview of "Smart Grids" with its features and its different aspects on power distribution industry has been presented. It is also explained that how these technologies change and have more potential to evolve and strength the distribution system.

Keywords:
Smart Grid
Transmission
Distribution
Automation
Energy management

1. Introduction

Urbanization, living standards and advancement in technology has increase the demand of energy requirement. This made electricity consumption rises to levels that may no longer be manageable if left unattended. This is an alarming situation not only for providing sustainable energy but also preservation of environment worldwide. Almost 75–80% of total energy consumption is consumed in cities which is responsible for 80% greenhouse gas emission [1,2]. Traditional and centrally-controlled system for the distribution of electrical energy is being used for a long day. This is commonly name as power grid. Since the use of electricity, globally electric grids have similar structure, dynamics and principles even with the advancement of technology. These traditional power grids are focused on only some of the basic functions like generation, distribution and control of electricity [3]. The electricity grid in present form is unreliable, has high transmission losses, poor power quality, prone to brownouts and blackouts, supplying inadequate electricity, discouraging to integration of distributed energy sources. There is a lack of monitoring and real time control in the traditional non-smart systems, which creates a challenging opportunity for smart grids to act as a real-time solution. Countering these issues requires a complete overhauling of power delivery structure. Electrical benefits are not only the encouraging force for the introduction of 'smart grid' concept, but environmental aspects too. Efficient usage of energy and dependency on renewable resources will also help to reduce the carbon foot print of human.

Smart Grid technology has a way for a solution for better generation of electric power and an efficient way for transmission and distribution of this power. Due to its versatility it can be more easily installed and required less space as compared to traditional grids. Concept of Smart Grid design is aimed for grid observability, create controllability of assets, enhance performance and security of power system and specially the economic aspects of operations, maintenance and planning [4]. That's why it is also consider that smart grid technology can be used to micro-grid level which eventually connect to all other micro-grids to form a large network of Smart Grid. These smart grids have a huge potential and could be a solution of reliability of power transmission and distribution in developing countries which lack infrastructure. In US only 20% of the all carbon dioxide is been emitted by transportation while generation of electricity has 40% of the carbon dioxide emitting share in it. This is due to the high demand rise of electricity. Smart Grids are been considering as a key role to address this problem by distributing electric power in an efficient way and ultimately reduce greenhouse gasses and pollutants like NOx and SOx [5]. It will also help the customer to forecast its demand and the best economical utilization of energy.

Smart Grid research has a long history with the start of its first concept implementation in 1997. This article will discuss an overview of the Smart Grid, its features and functions which includes reliability, security, energy management, self-healing. It will also discuss that how smart grid is changing the concept of grid technology and how much potential to revolutionized in modern electrical power grid. Some implemented technologies related to smart grids and pilot projects in different countries of the world are also part of this article.

2. Smart grid concept

There is no specific start of Smart Grid. This concept was start evolving with the start of distribution system of electrical networks. By the time different requirements were needed like control, monitor, prices and services of transmission and distribution of electrical power. Normally, Smart Grid implementation is associated with the installation of smart meter. In 1970s and 80s they were used to send the information of consumer back to the grid [6]. But the most important and fundamental need which is still under consideration even with latest advancement is reliability and efficiency of energy transmission and distribution via electric power grid. But in the latest advancement research is undergo that grids and network systems should not limit to transmission and distribution but also play a vital role in generating clean and sustainable energy in order to reduce greenhouse gases and carbon foot print.

2.1. Definition

For the distribution of electrical power to consumer one need a network of electrical conductor which is known as *grid*. If this network is intelligent with automated control and monitor system than it might be known as *Smart Grid.* Technically, smart grid is a concept for the conventional grids with some latest and automated features which make them more reliable and sustainable. Conventional grids were use just to transmit and distribute the electric power but this modern concept of smart grid could communicate, store or even decide according to the situation. Therefore, according to Strategic Deployment Document for Europe's Electricity Networks of future, a Smart Grid is an intelligent network of electricity that integrate the actions of all the stakeholders that are generators, consumers and one who does both in order to supply electricity with efficiency, sustainability, economically and securely [7]. So Smart Grid is not a single technology that is to be implemented. Its vastness and dependency increases by its stakeholders as shown in Fig. 1.

It provides its stakeholder an opportunity to maximize the efficiency, reliability, economic performance and security of their electrical network. An overview of its architecture is shown in Fig. 2.

2.2. Design

To understand the design and concept of smart grid one has to understand its difference with the traditional power grid. This comparison was done by Yu et al. in 2012 [8]. This comparison is shown in Table 1.

The design of the smart grid is flexible with its use and related objectives. A conceptual model of smart grid was presented by National Institute of Standards and Technology (NIST) which describe planning, development requirement, stakeholders that interconnected and equipments that are required [9]. NIST classifies these stakeholders in seven domains for modeling as shown in Table 2.

2.3. Characteristics of smart grid

For the modernization of the electric grid, Energy Independence and Security Act 2007 (EISA) developed a platform [10]. Features and functionalities of Smart Grid have a promise to full fill these requirements set by EISA.

2.3.1. Reliability

Success of the grid system depends upon the customer need which is measured as reliability. This mean as flaw less and error less system with continuous supply of electric power. Smart Grid has a potential to detect any fault and allow the self-healing of the system [11]. Conventional grids have issues regarding interaction of renewable resources, micro grid and demand response. With increase the size and complexity of these grids with demand it makes more difficult to analyze its reliability. But these issues are very well addressed by Smart Grids [12]. For this, Smart Grids have capability to monitor and store all the data and estimate its service reliability. It may also possible to monitor remotely for hybrid generation and management of the grid which enhance its reliability [13]. Technologies like Dynamic Stochastic Optimal Power Flow (DSOPF) helps in estimating and optimizing the flow of power in Smart Grid [4]. Therefore, Smart Grids can have better reliability with the advancement in communication system [14].

2.3.2. Security

Security is one of the challenging issues for the Smart Grid evolution. With the increase of automation, remote monitoring and controlling of the grid make the grid more vulnerable by cyber assault. According to Electric Power Research Institute, cyber security of the system is one of the biggest issue of the Smart Grid [15]. Suleiman et al propose a way to identify the weaknesses of the smart grids that usually attackers exploit by using Smart Grid Systems Treats Analysis and by integration of Systems Security Threat Model [16]. Similarly in 2014, Ashok et al proposed an approach to address cyber-physical security issue of Wide-Area Monitoring and protection and control from a coordinated cyber-attack perspective which will eventually enhance the security [17]. For assessing the Smart Grid security, one needs a review for its methodology. There are different agencies and organizations like IEEE Power & Energy Society (PES), IEC Smart Grid Standardization, National Institute of Standards and Technology (NIST) are involve and help in standardization and regulation for the smart grid [18]. Some of the promising ongoing research in different domains of security for smart grids include: Privacy-preserving smart metering with multiple data consumers, Ortho code privacy mechanism in Smart Grid using ring communication architecture and Security Threat Model [19–21]. As security is to be consider one of the biggest barrier for implementation of Smart Grid technology, so ongoing these researches have promise to resolve this barrier.

2.3.3. Demand side management system

Smart grid provides the demand side or user to interact with the grid by using two ways communication ability. It provides a chance for the consumer to use the electric power in an economical way. It will not only help for increasing efficiency at demand side but also at distribution end. It helps grid to reduce demand and stress during peak period by reducing or shifting power requirement to alternatives. This gives some financial incentive to consumer which encourage them to do so. Currently, a lot of investment is being made in this sector of the smart grids including demand side

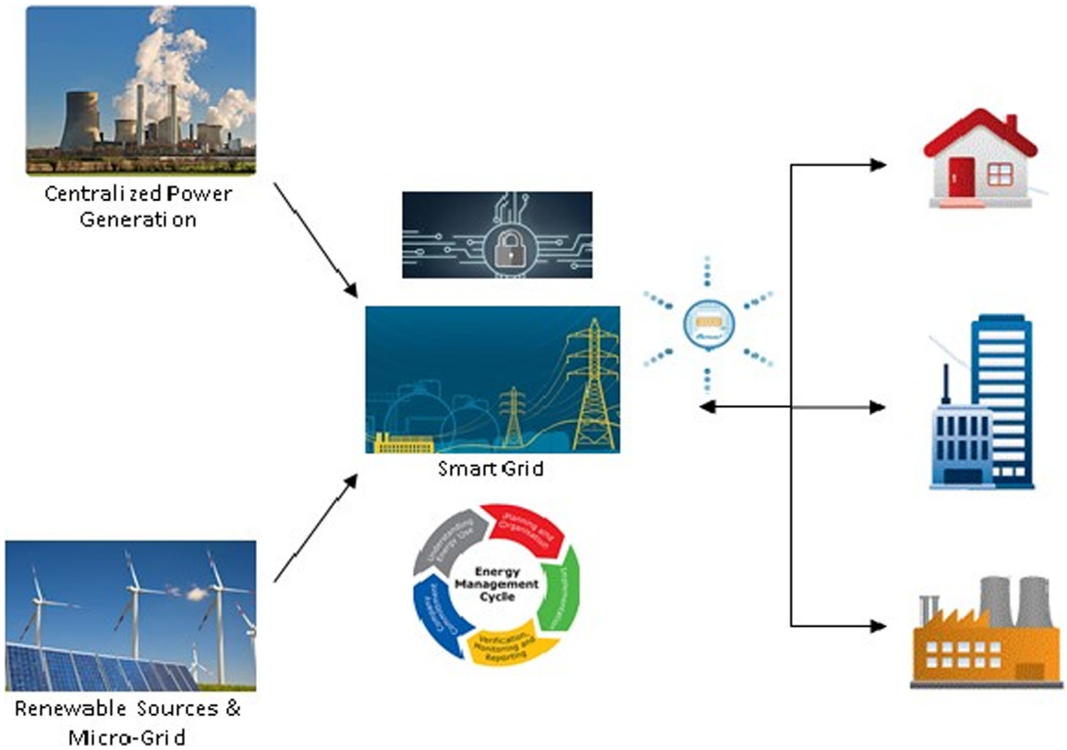

Fig. 1. Working concept of Smart Grid.

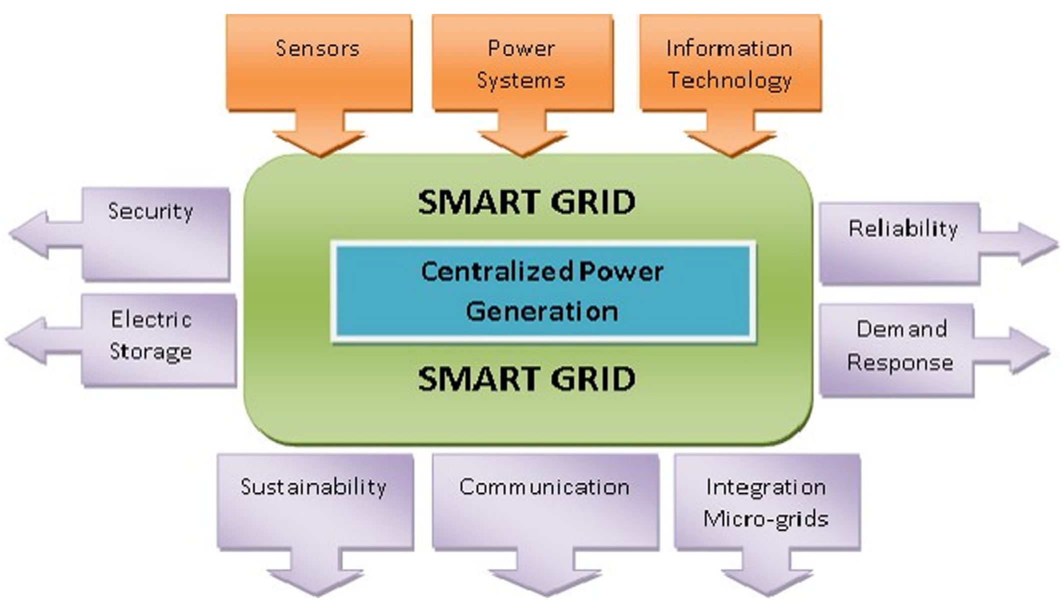

Fig. 2. Overview of Smart Grid architecture.

resources, load management systems and energy efficiency initiatives in order to address economical, reliability and economic perspectives [22]. Mostly demand side management systems focus only the communication between utility company and consumer. A new consumption scheduling technique is on the way to address the future grids in which each consumer can schedule their own consumption requirements. In this way it helps the distribution system to schedule itself accordingly to the requirement as peak loads for different consumers varies [23]. This also encourages the consumer to have financial incentives by scheduling their needs.

With the evolution of Smart Grid, this definition has also started revolution in the appliances and utilities to be "Smart" known as smart devices. These have ability to communicate with the grid which make house more autonomous and facilitate the user to use the electric power effectively and efficiently. These appliances shift demand of household electricity. Different networking protocols like 'ZigBee' provides a solution to have a wireless control of household appliances. These protocols have ability to communicate and coordinate with all the stakeholders involved in home energy management system hence providing the best optimal

Table 1
Difference between Smart and Conventional Grid.

Smart Grid	Conventional Grid
Two-way real-time communication	One-way communication
Distributed system of power generation	Centralized for power generation
Interconnected Network	Radial Network
A large number of sensors are involved	A small quantity of basic sensors are used
Digital Operation	Mechanical Operation
Automatic Control and Monitor	Manual Control and Monitor
Wide range of control	Limited control
Security and privacy concerns	No security or privacy concern

Table 2
Stakeholders of Smart Grid.

Stakeholder	Description
Customer	Electricity is consumed by consumer. It may be domestic, commercial or industrial
Operations	Operations related to power systems are performed. It comprises of regulatory authorities or management responsible for movement of electricity
Markets	Grid assets are used by stakeholders. Both operators and consumers are play role as market.
Generation	Electricity is generated. Generation companies in bulk quantity of electricity are involved as player.
Transmission	Electricity is transmitted. Companies or player responsible for transmission of generated electricity for distribution.
Distribution	Electricity is distributed to end consumer and monitored. They include distributor of electricity form and to customers.
Service Provider	Provide support services to all the stakeholders involved in generation, transmission and distribution of electric power.

solution to the user [24]. Therefore, smart grid is changing the trends of conventional household appliances to 'smart'.

2.3.4. Metering

Automation in distribution system is associated with the smart automatic meter. Metering provides a channel to enable two-way communication in Smart Grid concept between consumer and distributer. They not only help distributor for more accurate billing system but also help consumer to control their use of electrical energy. These meters are equipped with sensors for automation, power quality monitoring and power outage notifications. There are different drivers like price increase after electricity market deregulation, consumer dissatisfaction and monthly metering directives which encourages smart meters [25]. In traditional grid systems, SCADA was only used for communication purposes which provide a central control unit to monitor and control with second scan rate. But it's not much cost effective at different levels of electrical power distribution especially at utility end [26]. Advanced Metering Infrastructure (AMI) provides a real time solution that collects consumer data and provides a communication networks from grid to utility end. AMI provides opportunity to step forward for the modernization of the huge grids by combining consumer with the distribution system. It provides an opportunity for outage management, integration of electrical vehicles and smart devices, transformer and feeder monitoring and fault isolation [27]. Researchers have design a new system for the automation of distribution of power through a Substation Automation System (SAS). This system has ability to solve congestion through locally control actions with a minimum limitation of renewable energy resources [28].

2.3.5. Micro-grids and integration of renewable resources

Power generation from renewable resources likes, solar, wind, battery storage devices are bean of high consideration to full fill the increasing demand of electricity and reducing the greenhouse gasses. They even help to reduce the power stresses from grid during peak hours. Normally sites for these resources are far or in remote areas. Even sometimes it is not possible to have a complete functional grid to transmit or distribute electric power. Here micro-grids are used, which gather to form a big distribution network. So with this large number of micro-grids and sources will result in large amount of data to be handle. So researches like one by Penya et al. [29] have a solution for this problem by using an architecture that uses an intelligent system all over the grid to distribute the power effectively. This system will not be used as centralized but will handle individually by mean of individual intelligent nodes.

2.3.6. Self-Healing

For a robust Smart Grid, it should not limited diagnose the fault occur in the grid but could also be able to remove it for a constant supply of electricity. For a grid with a self-healing ability it uses real-time communication and digital components that are installed throughout the grid to monitor electrical characteristics of the grid. With this ability, grid is smart enough and capable to figure out the potential problem that may be caused naturally or by some human error. These intelligent systems react instantly to any such abnormalities and isolate the problem system before they snowball into a big problem and cause major blackout and automatically reroute the transmission of power for continuous services unless the error is removed. There are three main benefits of a smart grid with self-healing capability [30]: real-time monitoring and reaction, anticipation of problem, rapid isolation.

3. New technologies and research

A number of on-going research activities are being made for the advancement of the smart grid to make it more reliable and sustainable for the modern needs. These researches are focused on different technologies. It is difficult to cover all of these researches and advancement but this section includes some of the prominent and latest technologies and research activities associated with smart grid.

3.1. Energy management system

For a reliable grid, it's essential that all the components involve must be work together from generation to consumption. There are a lot of complex components involved in the grid. These components communicate and work together by mean of some computer software. So, planning and its implementation on grid are done by mean of interoperability. NIST initiated smart grid interoperability (SGIP) which was responsible to develop and maintain the standards for smart grids and all the components involve must communicate and operate efficiently. It was also liable to provide a platform for all the stakeholders of power grid including customer, markets, service provider, power system, generation, transmission and distribution network to work together to form a modern, reliable and efficient grid system [9]. For the understanding and implementation of energy management, both grids and consumer end must play their role. Technologies like advance metering infrastructure (AMI), communication network for grid and cyber security enables self-decision capabilities in grid which make energy management system more realistic for smart grid [31].

3.2. Internet of things (IoT)

Internets of things (IoT) take the internet to next step of evolution. It makes life easier, automate and handy by squeezing the whole world into one hand by computation and communication capabilities. With the advancement of smart grid and its components, a technology was needed to interact these components in an efficient, reliable and in more smart way. IoT has a promise to full fill all these characteristics taking smart grid into new era. But with this new technology, some serious security concern emerged which include impersonation, data tampering, overdoing, authorization, privacy issue and cyber-attack [32]. Researchers are doing study to deal with these issues. IoT base smart grid must have services like authentication, confidentiality, user's privacy and data integrity to avoid any security risk[32]. Connectivity that IoT provides to customer, enhance their experience and efficiency. It allows customer a flexible and easy interaction with the grid in order to reduce cost by diagnostics and neighborhood-wide meter reading capability [33]. In short, it makes smart grid smarter.

3.3. Smart grids with electric vehicles

As one of the biggest environmental issue is pollution due to vehicles. Use of electrical vehicles has the solution of this problem. There are several challenges for EVs to interact with the grid which include infrastructure, communication and control. Mostly it is seen that EVs are charged at home and even sometime charging take place at public or commercial Charging station [34]. Therefore, it is possible that it directly stresses the electric distribution network. But contrary it is possible that this EV charging can improve the quality of power and performance of grid if integration of EVs with the grid is well planned and follow the standards set for it [35].

As Smart Grids have advance technologies in the form of communication, smart meters and control. So it has a potential to offer electric vehicles not only as a load but can be used as a flexible energy source [36]. Smart meters play a vital role to address the challenges faced by the grid due to EV. As these meters have bidirectional communication ability and to monitor real time data so these smart meters can help in implementing a smart scheduling to optimize the available power in the grid [37]. An overview of this flow of communication and power was also describe by F. Mwasilu et al [38] in Fig. 3.

In vehicle to grid technology, one can predict the dynamics of power system. Charging is an essential part of vehicle to grid technology. A lot of research has been made in the area of this charging and discharging. A similar study was done in Portugal shows a good communication between charging of electric vehicle and solar energy [39]. In another study, Ota et al [40] proposed a way to consider charging request and battery condition for the next drive. There are very few cases of a weak grid that were reported while using V2G. Similarly renewable energy sources like solar and wind has a potential to overcome this weak grid scenario [38]. Understanding of dynamic behavior of the electric grid is essential to predict the reliability and effectiveness of the grid while operating with V2G.

3.4. Big data

Smart grid is full depended upon the data it receives. It is not just eyes of the grid but work as back bone for it. For a reliable and efficient working of a smart grid, a huge amount data is collected from power generation, transmission, transformation and power utilization [41]. All the decision made by the grid is depended upon it. It also plays a key role in the autonomous capabilities of the smart grid. There are numerous challenges for big data in smart grid technologies which include from storage to its visualization and security. Researchers have also focused on how to combine data into information and beneficial application. An overview of flow of data within components of the smart grid is shown in Fig. 4 [42].

A large amount of data gathered from different sensors, wireless transmission and communications is accumulated. All the data gather from generation to utilization is used by different algorithms to forecast and will also help full in recognizing the pattern of power utilization. This will ultimately useful for achieving a smart energy management system. Energy big data does not only include the data gather from meters but it has also a huge amount of data related to weather and environment. Characteristics of this data are incomplete without '4Vs' (volume, velocity, variety and value) and '3Es' (energy, exchange and empathy) [43]. Different algorithms and models were develop for the analysis of the big data but still there are some major issues related to big data like: IT infrastructure, Data Collection and governance, data processing and analysis, data integration and sharing and most importantly security and privacy which are to be address and are centrally focused by researchers [43].

4. Investment in smart grid

Different countries of the world have step forward in the era of smart grid and accept its reality. Many of them are working on smart grid pilot project or taking initiatives of this concept for testing and research in order to test feasibility before execution on full scale development and change. Government of different countries like Australia, United States, China, Britain, South Korea and Japan are already considering options like smart grid for reducing carbon emission and energy security. Some initiatives related to smart grid of different countries are following [44–46].

4.1. Australia

Australian government was interested in Smart Grid from 2009 when a call for proposal was given for smart grid, for which winner was announced in 2010. Government was interested to invest about $100 million initially. Government was more interested to raise awareness in customer about energy utilization and establishment of distributed demand as well as generation management system. Five different sites in New South Wales were selected for smart grid establishment and Energy Australia was selected for this purpose with collation of IBM, GE Energy and Grid Net. The idea was to build a WIMAX-based smart grid that has capabilities of automatic substation, able to accommodate electric vehicles and also supporting 50,000 smart meters' connections.

Another project was launch for testing network fault detection, isolation and restoration, power quality monitoring and automatic distribution of electric power via distribution management system. Australian government is also giving incentives for encouraging and investing in smart grid. Demand management, energy security and energy efficiency are the top priorities of Australian government.

4.2. Canada

Government of Canada made mandatory of installation of smart meters for business and households in Ontario by 2010 through legislation Energy Conservation Responsibility Act 2006. In the same year government also invested $32 million in a smart grid project for four years for research of problems associated of managing renewable energy. Federal government also took different initiatives like clean energy fund and eco-energy innovation initiative. Currently different pilot projects in province of Quebec and Ontario are going on. For the promotion and awareness campaign of Smart Grid, an association with the name Smart Grid Canada was formed which includes academia and all stakeholders involve. They were responsible to enable research and form different policies related to smart grid [44]. There are different

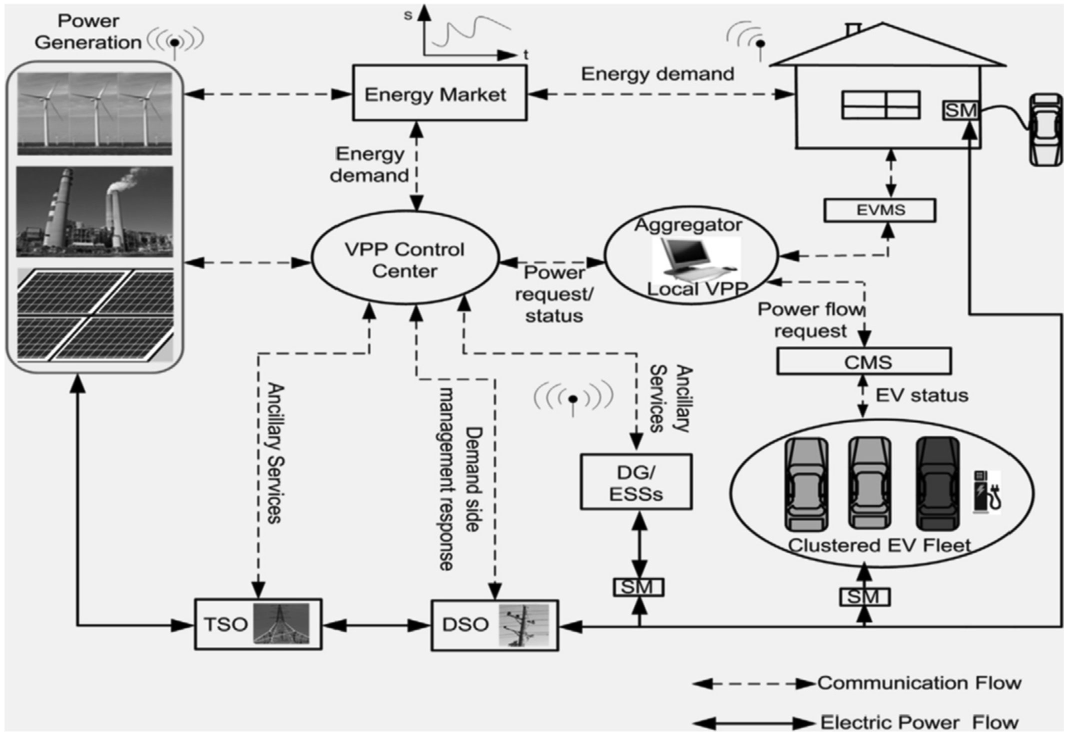

Fig. 3. Flow of communication and power in V2G.

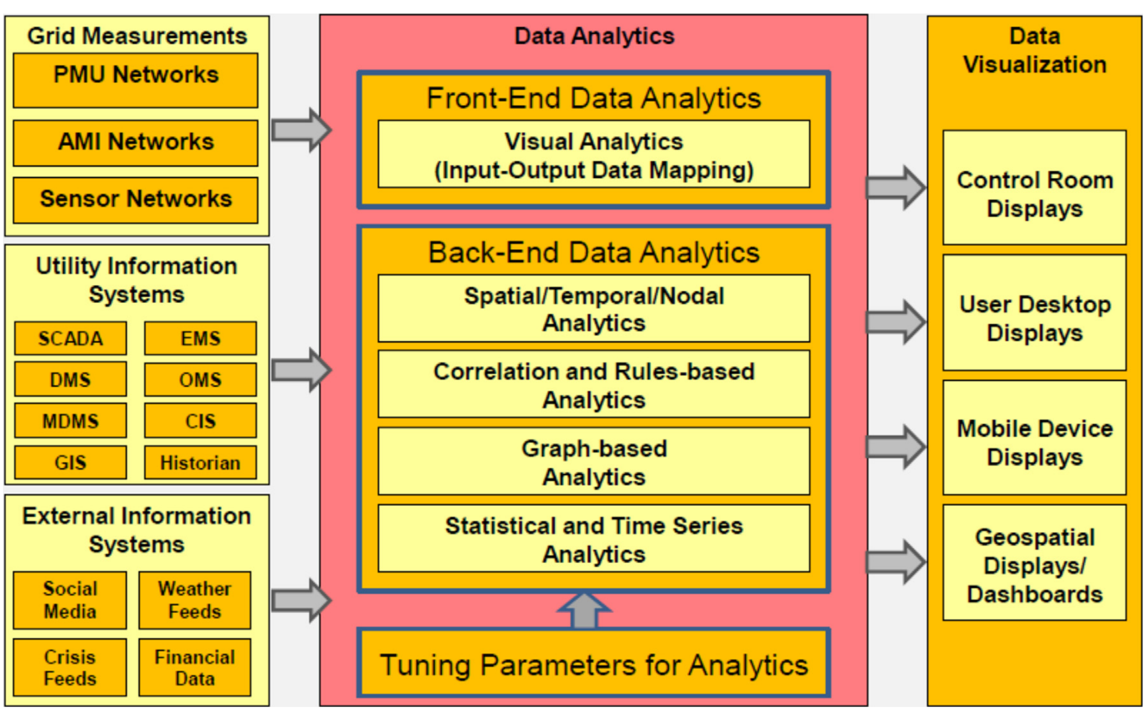

Fig. 4. Flow of data between components in Smart Grid.

entities like Natural Resource Canada, National Energy Board and National Smart Grid Technology and Standard task force which are being supported by government. National Smart Grid Technology and Standard task force was form for the development of all the aspects related to Smart Grid and also coordinate and involve provincial governments for the support and development of smart grid [47].

4.3. England

UK is one of the biggest producers of energy from photovoltaic. Low Carbon London institution integrated a number of technologies like photovoltaic, smart meters, electric vehicles and heat pump with the distribution system to reduce carbon emission. World's first cryogenic energy storage solution was implemented

Table 3
Ratio of GDP to Smart Grid cost for developing countries.

Nation	Population to be serviced	Initial Smart Grid Cost ($)	Nation's GDP	Ratio of GDP to Smart Grid cost
Afghanistan	8,686,000	3,136,862,040	19,331,000,000	6
Angola	11,022,000	3,980,485,080	102,627,000,000	25
Benin	4,782,000	1,726,971,480	8,291,000,000	4
Burkina Faso	5,406,000	1,952,322,840	10,678,000,000	5
Burundi	1,348,000	486,816,720	3,097,000,000	6
Cambodia	3,228,000	1,165,759,920	18,050,000,000	15
Central African Republic	1,962,000	708,556,680	1,584,000,000	2
Chad	3,154,000	1,139,035,560	10,889,000,000	9
Congo, Dem. Rep.	32,834,000	11,857,670,760	35,238,000,000	2
Congo, Rep.	3,021,000	1,091,003,940	8,553,000,000	7
Eritrea	1,000,000	361,140,000	2,600,000,000	7
Ethiopia	19,353,000	6,989,142,420	61,540,000,000	8
Gambia, The	1,187,000	428,673,180	939,000,000	2
Guinea	4,685,000	1,691,940,900	6,699,000,000	3
Haiti	6,282,000	2,268,681,480	8,765,000,000	3
Kenya	11,799,000	4,261,090,860	63,398,000,000	14
Lesotho	583,000	210,544,620	2,278,000,000	10
Liberia	2,238,000	808,231,320	2,053,000,000	2
Madagascar	8,508,000	3,072,579,120	9,739,000,000	3
Malawi	2,801,000	1,011,553,140	6,404,000,000	6
Mali	7,025,000	2,537,008,500	12,747,000,000	5
Mauritania	2,435,000	879,375,900	5,442,000,000	6
Mozambique	9,013,000	3,254,954,820	14,807,000,000	4
Namibia	1,147,000	414,227,580	11,492,000,000	27
Niger	3,728,000	1,346,329,920	7,714,000,000	5
Papua New Guinea	991,000	357,889,740	16,929,000,000	47
Rwanda	3,345,000	1,208,013,300	8,096,000,000	6
Sierra Leone	2,578,000	931,018,920	4,215,000,000	4
Solomon Islands	130,000	46,948,200	1,129,000,000	24
Somalia	4,266,000	1,540,623,240	5,925,000,000	3
South Sudan	2,320,000	837,844,800	9,015,000,000	10
Sudan	13,602,000	4,912,226,280	97,156,000,000	19
Swaziland	274,000	98,952,360	4,188,000,000	42
Tanzania	16,901,000	6,103,627,140	45,628,000,000	7
Timor-Leste	408,000	147,345,120	1,422,000,000	9
Togo	2,919,000	1,054,167,660	4,088,000,000	3
Tuvalu	6,000	2,166,840	33,000,000	15
Uganda	6,285,000	2,269,764,900	27,529,000,000	12
Vanuatu	69,000	24,918,660	742,000,000	29
Yemen, Rep.	9,286,000	3,353,546,040	37,734,000,000	11
Zambia	6,634,000	2,395,802,760	21,154,000,000	8
Zimbabwe	5,052,000	1,824,479,280	14,419,000,000	7

as a pilot project in Reading, UK. Similarly, in Ireland a successful trail of 9000 smart meters for homes and business was completed by Commission on Energy Regulation.

4.4. China

Chinese government is more focused on the policies related to conservation, encouraging diverse development, protecting environment and relying on domestic resources [48]. That is why development in Smart Grid is one of the priorities of Chinese policy which include increase renewable energy mix, improving energy efficiency and reducing carbon emission. Chinese agency National Development and Reform Commission (NDRC) is tasked for the research and development in smart grid technologies as its one of the priority in five year plan [49].

In 2011, China planned to build a Wide Area Monitoring System in a five-year plan and planned to implement phasor measurement units on all power generators above than 300 MW and substation above than 500 kV. China also announced a framework for smart grid in 2009 which was more transmission centric than other countries like US and Europe [50].

4.5. United States of America

US seem to be a promising region for the smart grid development since early 20th century. A federal policy was formed as Energy Independence and Security Act of 2007 which sets a funding of $100 million per year for five years from 2008 for developing and enhancing smart grid capabilities. According to this Act of 2007, National Institute of Standard and Technology will be responsible for looking after the development and modernization of grid and form a commission to access its benefits. It will also form standards to maintain the developments of smart grid. In 2009 a new act was formed as American Recovery and Reinvestment Act of 2009 which invested $11 billion for a smart grid pilot project. This was the result of the legislations and determination of US government that they demonstrated smart grid projects and related twenty-two utilities in five different states. A fully metering system with customer web portal and automatic notification features was developed by Houston's smart grid. Smart Texas also deploys a large number of smart meters for the automation of power distribution network.

4.6. Europe

In early 2005, European Union formed a European Technology Platform (ETP) for the development of smart grid technology. Its goal was to promote the vision 2020 of European electricity networks development. Portugal did a real time implementation of management and control system of smart grid in a pilot project [51]. Italy is playing a vital role in research and development of smart grid. Different pilot projects are on the way related to selec-

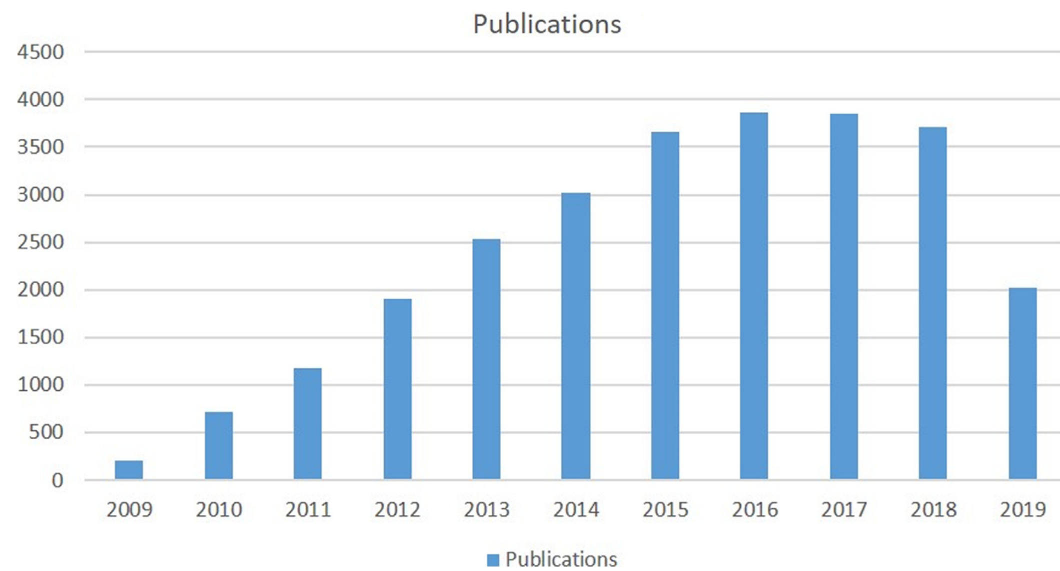

Fig. 5. Year wise publication of article on smart grid (data source science direct).

tion, assessment, regulation and instrumentation of smart distribution network [52,53]. University of Genoa is working on mathematical modeling of optimal operation for poly-generation microgrid which is stepping stone towards advance large scale metering [54,55]. A cost benefit analysis for smart grid was done by Czech Republic [56].

5. Economical potential of smart grid in developing world

Cost is one of the biggest constraints in the development and implementation of the smart grid especially in developing world. A lot of financial resources are associated with the transmission and distribution system, metering and other related technologies. A complete financial feasibility report is essential before implementation. This financial feasibility must include nation's capacity to pay development cost for smart grid infrastructure. This is normally calculated per consumer that is to be served. Young [57] in 2017 apply different test and calculate ratio of nation's GDP to cost of development for smart grids in developing countries. Most of the financial data for this calculation was used form World Bank's report of 2015. The summary of these results are given in Table 3 [57].

6. Future research in smart grid

A lot of research is undergoing for the development of smart grids. Still a lot of potential is available for future research for different aspects in different areas of smart grid. This include in area of forecasting, power flow optimization, communication, microgrid integration, demand and energy management system, conformance of standards for interoperability, scalability, economical factors, data encryption and most importantly automation of generation, transmission and distribution.

7. Conclusion

Advancement of the technologies and devices can change the utilization of energy in an economical and environmental friendly way. Evolution of Smart Grid concept has potential to meet all the future needs of utilization of energy in best possible manner by reducing carbon emission and integrate with more renewable energy mix. It can bring a considerable change in the conventional grid and consumer behavior towards utilization of energy by improving reliability, efficiency and quality of power delivery. Governmental policies are needed to facilitate smart grid implementation. This article pointed out the need of modernization of conventional grid and how researchers are implementing smart grid concept for electric power distribution networks. Still there is a lot of potential available for improving and implementation of this concept as it is just the start of the new era of modern grid. It is still difficult to predict that how far the research in smart grid is required to fully implement this concept but recent researches like smart meters, demand side management systems, self-healing and big data are source of encouragement in Smart grid technology.

8. Recent trends

Research and advancement on the smart grids have been seen tremendously increased in last decade. This is why smart grid technology has been shifted from virtual reality and concept to implementation phase. In last ten years 26,668 different research articles have been published on smart grids which shows a keen interest of researchers in this field. There was tremendous increase in the research in last five years (as shown in Fig. 5) in smart grid and soon this will be game changer in electrical power distribution with more flexibility and in efficient ways

References

[1] Mohanty SP, Choppali U, Kougianos E. Everything you wanted to know about smart cities: the internet of things is the backbone. IEEE Consum Electron Mag 2016;5:60–70.
[2] Nam T, Pardo TA. Smart city as urban innovation: Focusing on management, policy, and context. In: Proceedings of the 5th international conference on theory and practice of electronic governance. p. 185–94.
[3] Fang X, Misra S, Xue G, Yang D. Smart grid—the new and improved power grid: A survey. IEEE Commun Surv Tutorials 2012;14:944–80.
[4] Momoh JA. Smart grid design for efficient and flexible power networks operation and control. In: Power systems conference and exposition, 2009. PSCE'09. IEEE/PES; 2009. p. 1-8.
[5] U. S. D. o. E. b. L. S. Communication, The SMART GRID: An Introduction.
[6] (01-10-2018). The History of Making the Grid Smart. Available: https://ethw.org/The_History_of_Making_the_Grid_Smart.
[7] SmartGrids E. SmartGrids strategic deployment document for Europe's electricity networks of the future. Europ Technol Platform SmartGrids 2010.
[8] Yu Y, Luan W. Smart grid and its implementations. Proc CSEE 2009;29:1–8.

[9] Greer C, Wollman DA, Prochaska DE, Boynton PA, Mazer JA, Nguyen CT, et al. NIST framework and roadmap for smart grid interoperability standards, release 3.0; 2014.
[10] Congress U. Energy independence and security act. Public Law 2007;1–311.
[11] Xia S, Luo X, Chan KW. A framework for self-healing smart grid with incorporation of multi-agents. Energy Proc 2014;61:2123–6.
[12] Moslehi K, Kumar R. A reliability perspective of the smart grid. IEEE Trans Smart Grid 2010;1:57–64.
[13] Colmenar-Santos A, Pérez M-Á, Borge-Diez D, Pérez-Molina C. Reliability and management of isolated smart-grid with dual mode in remote places: Application in the scope of great energetic needs. Int J Electr Power Energy Syst 2015;73:805–18.
[14] Yan Y, Qian Y, Sharif H, Tipper D. A survey on smart grid communication infrastructures: Motivations, requirements and challenges. IEEE Commun Surv Tutorials 2013;15:5–20.
[15] Von Dollen D. Report to NIST on the smart grid interoperability standards roadmap. Electric Power Res Inst (EPRI) Nat Inst Stand Technol 2009.
[16] Suleiman H, Alqassem I, Diabat A, Arnautovic E, Svetinovic D. Integrated smart grid systems security threat model. Inform Syst 2015;53:147–60.
[17] Ashok A, Hahn A, Govindarasu M. Cyber-physical security of wide-area monitoring, protection and control in a smart grid environment. J Adv Res 2014;5:481–9.
[18] Wang Y, Ruan D, Gu D, Gao J, Liu D, Xu J, et al. Analysis of smart grid security standards. Computer science and automation engineering (CSAE) IEEE international conference on 2011;2011:697–701.
[19] Khan E, Adebisi B, Honary B. Location based security for smart grid applications. Energy Proc 2013;42:299–307.
[20] Rottondi C, Verticale G, Capone A. Privacy-preserving smart metering with multiple data consumers. Comput Netw 2013;57:1699–713.
[21] Li S, Choi K, Chae K. OCPM: Ortho code privacy mechanism in smart grid using ring communication architecture. Ad Hoc Netw 2014;22:93–108.
[22] US Department of Eenrgy. Demand side resource; 2008.
[23] Mohsenian-Rad A-H, Wong VW, Jatskevich J, Schober R, Leon-Garcia A. Autonomous demand-side management based on game-theoretic energy consumption scheduling for the future smart grid. IEEE Trans Smart Grid 2010;1:320–31.
[24] Mahmood A, Khan I, Razzaq S, Najam Z, Khan NA, Rehman M, et al. Home appliances coordination scheme for energy management (HACS4EM) using wireless sensor networks in smart grids. Proc Comput Sci 2014;32:469–76.
[25] Leysen R. An analysis of smart meter deployment in Sweden with applicability to the case of India; 2018.
[26] Hart DG. Using AMI to realize the smart grid. Power and energy society general meeting-conversion and delivery of electrical energy in the 21st Century IEEE 2008;2008:1–2.
[27] Hart DG. How advanced metering can contribute to distribution automation. IEEE Smart Grid 2012.
[28] Berizzi A, Bovo C, Ilea V, Merlo M, Miotti A, Zanellini F. Decentralized congestion mitigation in HV distribution grids with large penetration of renewable generation. Int J Electr Power Energy Syst 2015;71:51–9.
[29] Penya YK, Nieves JC, Espinoza A, Borges CE, Pena A, Ortega M. Distributed semantic architecture for smart grids. Energies 2012;5:4824–43.
[30] Amin M. Smart grid. Public Utilities Fortnightly; 2015.
[31] Vikram K, Sahoo SK. Energy management system in smart grids. In: Smart Grid Systems. Apple Academic Press; 2018. p. 241–72.
[32] Bekara C. Security issues and challenges for the IoT-based smart grid. Procedia Comput Sci 2014;34:532–7.
[33] D. U. S. C. B. Patel. IoT Enabled Smart Grid; 2016.
[34] Su W. Smart grid operations integrated with plug-in electric vehicles and renewable energy resources. North Carolina State University; 2013.
[35] Lopes JAP, Soares FJ, Almeida PMR. Integration of electric vehicles in the electric power system. Proc IEEE 2011;99:168–83.
[36] Su W, Eichi H, Zeng W, Chow M-Y. A survey on the electrification of transportation in a smart grid environment. IEEE Trans Ind Inf 2012;8:1–10.
[37] Guo Q, Wang Y, Sun H, Li Z, Xin S, Zhang B. Factor analysis of the aggregated electric vehicle load based on data mining. Energies 2012;5:2053–70.
[38] Mwasilu F, Justo JJ, Kim E-K, Do TD, Jung J-W. Electric vehicles and smart grid interaction: A review on vehicle to grid and renewable energy sources integration. Renew Sustain Energy Rev 2014;34:501–16.
[39] Nunes P, Farias T, Brito MC. Enabling solar electricity with electric vehicles smart charging. Energy 2015;87:10–20.
[40] Ota Y, Taniguchi H, Nakajima T, Liyanage KM, Baba J, Yokoyama A. Autonomous distributed V2G (vehicle-to-grid) satisfying scheduled charging. IEEE Trans Smart Grid 2012;3:559–64.
[41] Song Y, Zhou G, Zhu Y. Present status and challenges of big data processing in smart grid. Power System Technol 2013;37:927–35.
[42] Qiu R, Antonik P. Big data and smart grid. Smart Grid Using Big Data Anal Random Matrix Theory Approach 2014:485–91.
[43] Zhou K, Fu C, Yang S. Big data driven smart energy management: From big data to big insights. Renew Sustain Energy Rev 2016;56:215–25.
[44] Lee S. The global smart grid federation report. Canada: The Global Smart Grid Federation; 2012.
[45] Pazheri F, Khan H, Ahamed I. Smart grid implementation across the globe: A survey. In: Innovative Smart Grid Technologies-India (ISGT India), 2011 IEEE PES; 2011. p. 1-5.
[46] Tuballa ML, Abundo ML. A review of the development of Smart Grid technologies. Renew Sustain Energy Rev 2016;59:710–25.
[47] Popescu S, Roberts C, Bento G. Canada - smart grid developments. International Trade Administration; 2010.
[48] Xu Z, Xue Y, Wong KP. Recent advancements on smart grids in China. Electr Power Compon Syst 2014;42:251–61.
[49] Smart Grid in China - a R&D Perspective; 2013.
[50] Du X-W, Ye Q. Notice of retraction review of smart grid and its development prospect in Sichuan. In: Power and Energy Engineering Conference (APPEEC), 2010 Asia-Pacific; 2010. p. 1-4.
[51] Gouveia C, Rua D, Soares FJ, Moreira C, Matos P, Lopes JP. Development and implementation of Portuguese smart distribution system. Electr Power Syst Res 2015;120:150–62.
[52] Delfanti M, Fasciolo E, Olivieri V, Pozzi M. A2A project: A practical implementation of smart grids in the urban area of Milan. Electr Power Syst Res 2015;120:2–19.
[53] Delfanti M, Falabretti D, Fiori M, Merlo M. Smart Grid on field application in the Italian framework: The AS SE. M. project. Electr Power Syst Res 2015;120:56–69.
[54] Bracco S, Delfino F, Pampararo F, Robba M, Rossi M. A mathematical model for the optimal operation of the University of Genoa Smart Polygeneration Microgrid: Evaluation of technical, economic and environmental performance indicators. Energy 2014;64:912–22.
[55] López G, Moreno J, Amarís H, Salazar F. Paving the road toward smart grids through large-scale advanced metering infrastructures. Electr Power Syst Res 2015;120:194–205.
[56] Adamec M, Pavlatka P, Stary O. Costs and benefits of smart grids and accumulation in Czech distribution system. Energy Proc 2011;12:67–75.
[57] Young JR. Smart grid technology in the developing world; 2017.

Methods of finding losses and cooling methods to increase efficiency of electric machines

Ajanta Priyadarshinee, *Department of Electrical Engineering, Aryan Institute of Engineering & Technology, Bhubaneswar, ajantapriyadarshinee10@gmail.com*

Subhendu Sahoo, *Department of Electrical and Electronics Engineering, NM Institute of Engineering & Technology, Bhubaneswar, s.sahoo95@outlook.com*

Pravas Behera, *Department of Electrical Engineering , Raajdhani Engineering College, Bhubaneswar, p_behera91@outlook.com*

Smruti Samantray, *Department of Electronics and Communication Engineering , Capital Engineering College, Bhubaneswar, smrutisamantray23@hotmail.com*

Keywords:

Electric motor
Losses
Cooling
Efficiency

A B S T R A C T

Performance of electric motors and losses in terms of heat and temperature are reviewed in this paper. Airgap eccentricity, electromagnetic performance, effect of temperature and losses are shown as factors affecting the efficiency. Several methods of computer aided analyses are listed. Temperature distribution in an induction motor is shown through the results of a simulation. Different cooling methods are reviewed. Future directions for research include cryogenic cooling, heat pipes and usage of phase change materials.

1. Introduction

Electric motors have been utilized since 1834, and they have played a vital role in our day to day lives. Today, they continue to replace diesel and gas engines, as well as hydraulic cylinders, while evolving into new designs optimized for EVs (electric vehicles) and other technologies. "Electric motors are being used more widely in ships, airplanes, trains, and cars. We're also seeing a lot more electric motors in electric vehicles. "The ongoing transition from gas to electric is primarily driven by the need for more efficient devices that run with cleaner energy sources. Yet, electric motors also tend to be more responsive, and are more adaptable to new applications, especially in Electric truck. There is an increasing need to improve the fuel economy and reduce Green House Gas (GHG) emissions of heavy duty trucks due to high fuel prices, regulatory pressures, and climate change. Three approaches can be used to improve the fuel economy and/or reduce GHG emissioans of heavy-duty trucks: non-electrification efficiency-improving technologies on conventional powertrains and vehicles [1–3], hybrid powertrain technologies [3,4], and the substitution of natural gas, electricity or hydrogen for diesel fuel [5,6]. So far different types of motors have been used in electric truck. The main difference between electric propulsion on ships vs. cars is related to torque requirements, says Kirtley [7,8]. The variable speeds used in a car require that "the gearbox adapt the engine to the road, You can generate an electric motor that can propel an automobile without a gear shift. In the past, Kirtley has consulted with Tesla Motors on its electric cars, and both agree that "the induction motor" is the best for electric automobiles.

2. Performance of electric motors

The types of high-speed machines include induction machines, permanent-magnet machines and switched reluctance machines. Electric motors have a very high efficiency and high-power density, hence they find a perfect application in vehicle traction. They are fit for the downsizing concept also because they can produce maximum torque at low rotational speed. In all the types of electric machines, the squirrel-cage induction motor is the most opted one. A motor failure can result in the loss of large revenues, hence a thorough thermal analysis is done [9–11].

Electric motors and drive systems account for 64% of industrial electricity consumption. Energy which is not converted into useful work results in heating of the various motor components, and accounts for the motor losses. Heat generated during operation causes a negative effect on motor efficiency. The torque/rotational speed of the electric motor is being affected by temperature and internal losses viz. winding conduction losses, stator core losses, rotor core losses, and permanent magnet eddy current losses as well. To ensure a satisfactory life span for the motor, temperature rise must be limited to safe values. Obviously, the quantity of heat generated must be effectively removed to prevent damage to the machine using appropriate cooling methods [12–14].

Fig. 1 shows the contributors for developing high torque. Maximum torque can be obtained by the electric motor using power electronics, and high voltage battery, but increases the weight as well. In addition, although they have high efficiency, they produce a significant amount of heat that has to be removed. Much lower temperature can be accepted and higher values can request **power de-rating** in order to preserve their functionality. High voltage battery is even more critic, since it can work correctly only in a specific temperature window and outside this, it has a **rapid thermal degradation**. Maximum torque at different speeds possible for a specified winding and rotor temperature. Peak torque envelope for thermal transient condition can be calculated for a set amount of time that gives a certain maximum winding temperature [15].

2.1. Factors affecting the efficiency of electric motors

The calculation of losses in induction motors is particularly important, as it directly influences the temperature distribution, and also the overall motor efficiency. Predicting the temperature distribution is made difficult because of the uncertainties associated with assigning losses and thermal coefficients. These losses play an important role in determining the efficiency and temperature rise, and hence, the rating of a machine. The importance of **stray load losses** in induction machines was illustrated, indicating that a small improvement of the efficiency would mean about five times reduction in the losses of the input power. Hence, a small improvement of the average effective efficiency of the industrial motor would save energy [16,17]. Fig. 2 shows the factors affecting the motor efficiency.

2.1.1. Airgap eccentricity

One of the types of faults that can occur in Induction motors is **air gap eccentricity**. Static eccentricity is displacement of the rotation axis of the rotor with regard to the geometric center of the stator, hence the field distribution in the air–gap is unsymmetrical. The reasons for eccentricity include intrinsic shaft tolerance, ball-bearings defects or problems related with the fixing of these motor parts. This would cause the eccentricity to create additional motor vibrations and unbalanced magnetic pull (UMP). The static eccentricity leads to a non-uniform temperature distribution and the small eddy-current losses which occur in the magnets, contributes to the rise of the highest temperature spot in the motor, potentially shortening the lifespan of the **stator insulation system**. In Dynamic eccentricity the rotation axis of the rotor do not coincidence with its geometric center [11,18–22].

2.1.2. Electromagnetic performance

Mass, volume and material properties of electric motor have to be temperature-dependent so that temperatures inside the machine can work with a good **electromagnetic performance**. This analysis makes it easier for designers to maximize the winding current density to achieve the highest possible torque/power ratings within thermal limits set by the winding insulation or **demagnetization** limits [23,24]. The electrical machines in the automotive industry use permanent magnets in their rotors as they possess very good efficiency and high power density. On the other hand, sensitivity of the magnets in high temperatures is the major drawback. The losses caused by the eddy-currents induced in the rotor magnets are relatively small compared to the other losses generated in the electric machine. But due to the relatively poor

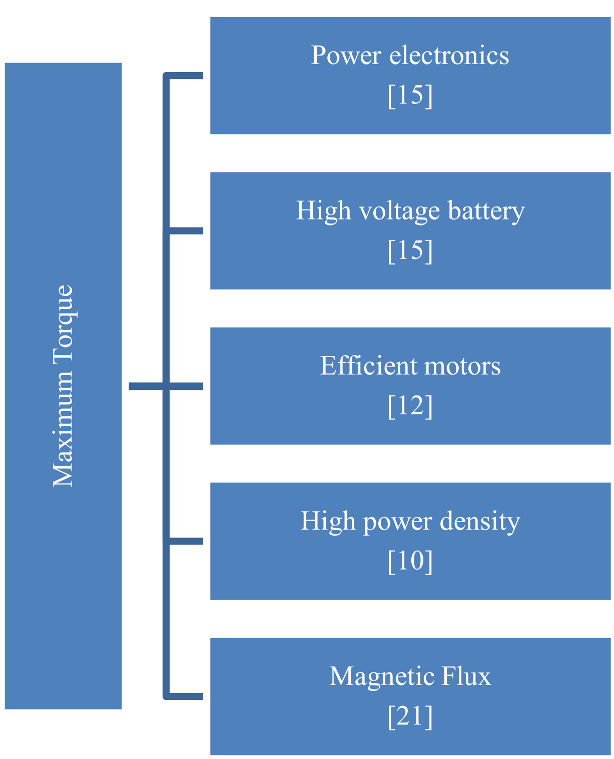

Fig. 1. Contributors for high torque.

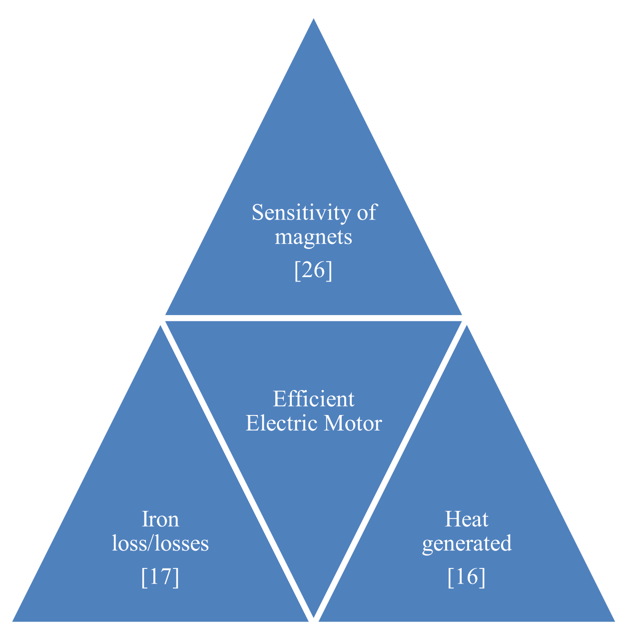

Fig. 2. Factors affecting the motor efficiency.

heat dissipation of the rotor, these losses can cause significant heating of the magnets. Increased temperature in the magnets may result in partial irreversible **demagnetization** of them as shown in Fig. 3. Abnormal high temperature will also affect the **core resistivity, thus affecting the eddy current loss** [25].

2.1.3. Temperature rise and losses

Operating point of the permanent magnet is subjective to the exposed temperature. Hence, the distribution of the **magnetic field** inside the motor, the **magnetic flux density** in the **air gap** and the core will change. Changes in magnetic field will affect **iron losses** and **permanent magnet eddy current losses**. Rise in temperature may alter the thermal conductivity, the resistance of the copper core, the permanent magnet remanence and intrinsic coercivity.

In general the highest temperature appears in the winding copper core, and the lowest temperature appears in the housing as shown in Fig. 4. Because the winding copper core is the main heat source and the small heat dissipation factor of the insulation layer leads to poor heat dissipation, the peak value of the temperature is located at the center of the stator winding. The eddy current losses are regarded as heat sources. With the increase of the load, the temperatures of the housing, stator core, winding copper core increases non-linearly. As the main heat source, the copper core is located in the middle of the stator and surrounded by insulations. The temperature will sharply rise because of the eddy current loss in the permanent magnet and poor thermal conduction ability of the rotor [26].

Increase of the power density would allow the motor temperature rise in the range of allowable limit value. Reducing the temperature rise can happen by improving the cooling capacity of motor and by reducing the losses. With the high speed and large carrier frequency, the **eddy current loss** of the permanent magnet is large [27]. Heat generated by a running induction motor and the temperature raise, eventually leading to thermal stresses. If the thermal stress is more than the limiting stress of the structure of the cage, it may lead to **broken bar fault** and the **cage fracture in the joint of the bars and the rings**. This is a very serious acci-dent as it would lead to asymmetric rotor operation. Temperature rise is a key performance parameter of concern in the industrial arena. The temperature rise can limit the rated power and reduce the motor efficiency, and it also imposes special demands on the material of the motor. Hence, thermal mapping is crucial for satisfying the requirements of functionality and safety [28].

The influence of the end of the stator and rotor on axial temperature distribution also contributes to thermal loss. The temperature of stator and rotor increase rapidly in the beginning and the rotor temperature is higher than the stator temperature all the time. The maximum temperature point is around the axial center of the rotor bar. The axial temperature difference of the rotor core

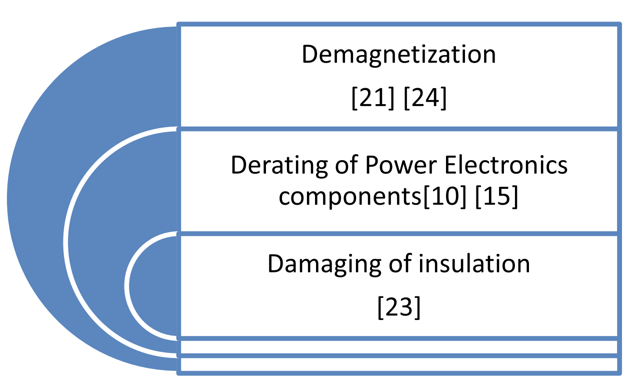

Fig. 3. Damages caused by temperature rise.

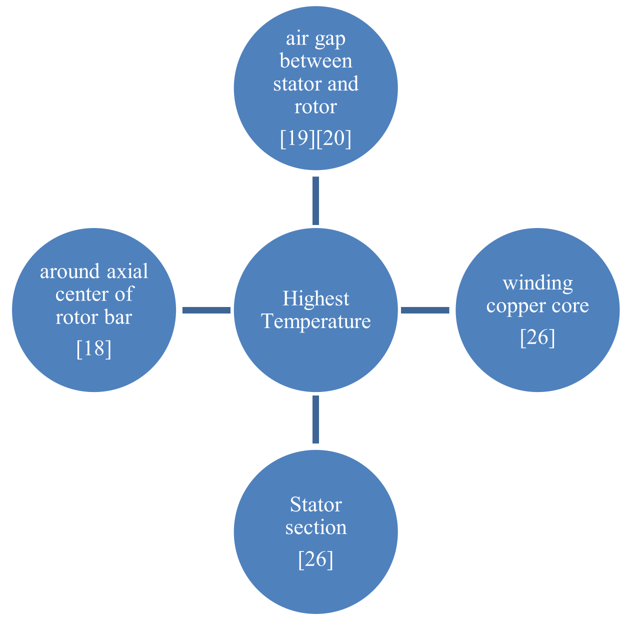

Fig. 4. Hottest spots in the motor.

is larger than that of the stator core while the radial temperature difference of the stator core is larger than that of the rotor core [18].

2.1.4. Power losses

Fixed losses are losses in the active iron, and additional no load losses in other metal parts, Losses due to friction and windage loss in the machine. Load losses are copper losses in primary windings, losses in secondary windings and additional load losses. Stator losses,

a. Stator Copper losses: losses are produced when the current passing through the stator windings, and generates the heat and consequently, the temperature of the motor rises. These losses are dependent on the square of stator current.
b. Rotor bars losses: losses are produced when the current passing through the rotor bars, they are dependent on the square of rotor current.
c. Iron losses or core losses: losses are generated in the conducting core laminations, due to hysteresis, eddy-current. These play an important role in design of the machine and in determination of its thermal rating.
d. Mechanical losses contain air friction losses and bearing friction losses. Air friction losses result following the air circulation around the rotor during its operation. The air friction losses are divided in to two parts: the losses corresponding to the rotor seen as a rotating cylinder and the losses corresponding to the end surfaces of the rotor. Bearing friction losses are the results of the relative motion in bearings.

Copper losses are due to Joule losses, iron losses are due to eddy current and hysteresis effect. Compared to the conventional engine losses, they are quite low because the power is generally lower and the efficiency is much higher. Electric motors have very high efficiency, however their power losses produce a significant amount of heat. All the power losses become heat and increase the temperature of the component. The maximum temperature have an important effect on the **de-rating** of the power electronic components. In order to avoid premature de-rating, it is important to leave the temperature as low as possible [10]. **Core loss** seen in Fig. 5 is much greater than other losses and is the main source of heat due to the high operating frequency. Therefore, it is of crucial importance to calculate the core loss accurately, taking operating temperature into account. The **core eddy current loss and hysteresis loss** are due to temperature-induced changes in core material resistivity [9]. In order to design a high-efficiency motor, the iron loss generated in the motor should be reduced. The **stator loss, armature winding loss, rotor loss, and axial structure loss** are assigned as the heat sources in the electrical machine. The large rotor's **eddy current loss** will cause the temperature of permanent magnet to increase considerably [29–32].

2.1.5. Methods of reducing losses

A speed vector control system of induction motor (IM) with minimization of the copper and iron losses has been introduced. This method reduces heat losses from the rotor windings and stator and core losses from eddy currents [52]. Results of a sensitivity analysis of the heat sources and the properties of the structural changes within a 3D-model are presented. Iron losses and ohmic losses in copper are examined on the basis of electromagnetic design. The criteria for future design of electric motors are shown [53]. High temperature superconductor (HTS) machines have been designed to use an iron core to reduce the HTS tape length. Further study is required to find the arrangement of HTS tape in iron core to reduce losses [54]. A stator magnetic core from segments of amorphous steel is developed. Ducts inside the stator are used as cooling ducts. These arrangements promote the dissipation of heat from the stator and minimize temperature [55]. Three different types of tape-wound laminations were analysed viz. heat treated (HT), glued and heat treated (GHT) and conventional non-treated (NT). HT and GHT type laminations have lower iron losses than NT and conventional stacked laminations [56]. Lumped parameter thermal network (LPTN) was used to find the thermal performance. Optimization of the reduction in iron loss and copper loss, eddy current loss in permanent magnet was carried out considering harmonics to improve thermal performance [57]. Experiments were carried out using lamination sheets fabricated through different manufacturing processes: insulation, laser cutting, electrical discharge machining (EDM) and thermal treatment. The best manufacturing processes were found to be the bonding varnish insulation and EDM cutting. Second stress-relieving thermal treatment on CoFe alloy reduced iron loss by 28% [58]. Hybrid excited axial field flux-switching machine (HEAFFSM) with permanent magnets (PMs) and excitation windings in its stator is a novel hybrid excited flux-switching PM machine. Experimental results show that the minimum-copper-loss (MCL) strategy minimises the copper loss of the HEAFFSM drive system [59]. Another study focused on the core losses in the stator region of high-speed permanent magnet synchronous motors, magnetic field characteristics in the load region, and variations in iron losses caused by changes in these areas. It was demonstrated that the running status of high speed motors is closely related to the stator iron losses [60].

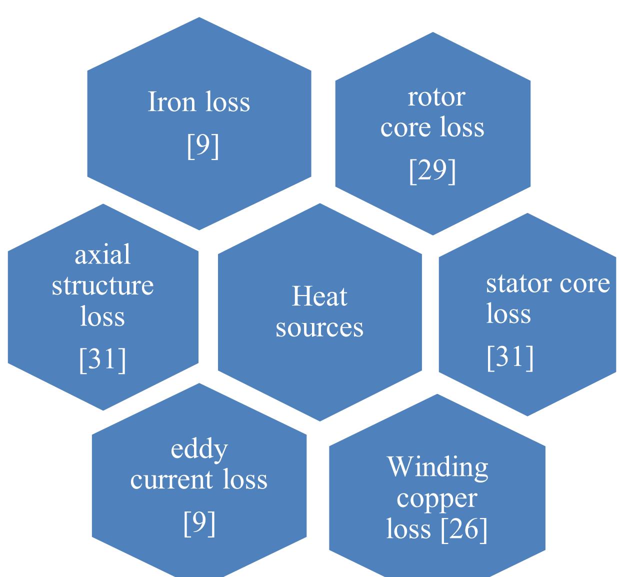

Fig. 5. Different type of losses acting as heat sources.

2.2. Temperature distribution in an induction motor

The temperature distribution in the induction motor is not uniform and there is a risk of local overheating. The **winding** is a main heat source and its insulation is thermally sensitive, so reducing the winding temperature rise is the key to the improvement of the reliability of the motor. Large end winding is required for high electrical loading and for the high torque density. The nature of the low speed, high torque application means that the losses in the machine are dominated by those from the winding [33,34]. Fig. 6 shows the temperature distributions inside an induction motor.

The maximum torque of a motor is directly proportional to the flux produced by the magnets. By keeping the working temperature of the magnets low, higher power density can be achieved [21]. Using cast copper instead of cast aluminum as rotor bars and end rings can reduce the temperature of rotor effectively [18]. The influence of temperature on the relative permeability of iron core material can be obtained. Thermoelectric materials allow converting a temperature gradient into electricity [35]. The material properties of the motor impose the temperature limit. The maximum limit of temperature is linked to silicon properties [10]. The thermal model explains the temperature distribution inside the induction motor, to give a precaution about problems which will occur during the operating conditions, like the **induction motor insulation**.

2.3. Computer aided analysis to find losses

Fig. 7 shows the computer aided analysis and modelling techniques used by different researchers during the past 10 years.

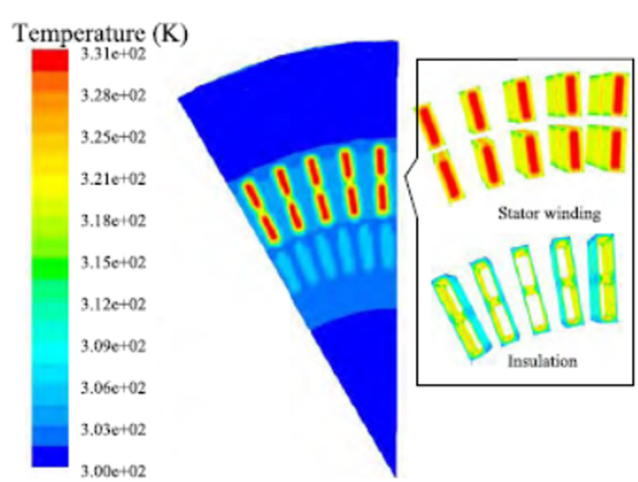

Fig. 6. Temperature distributions inside the induction motor [36].

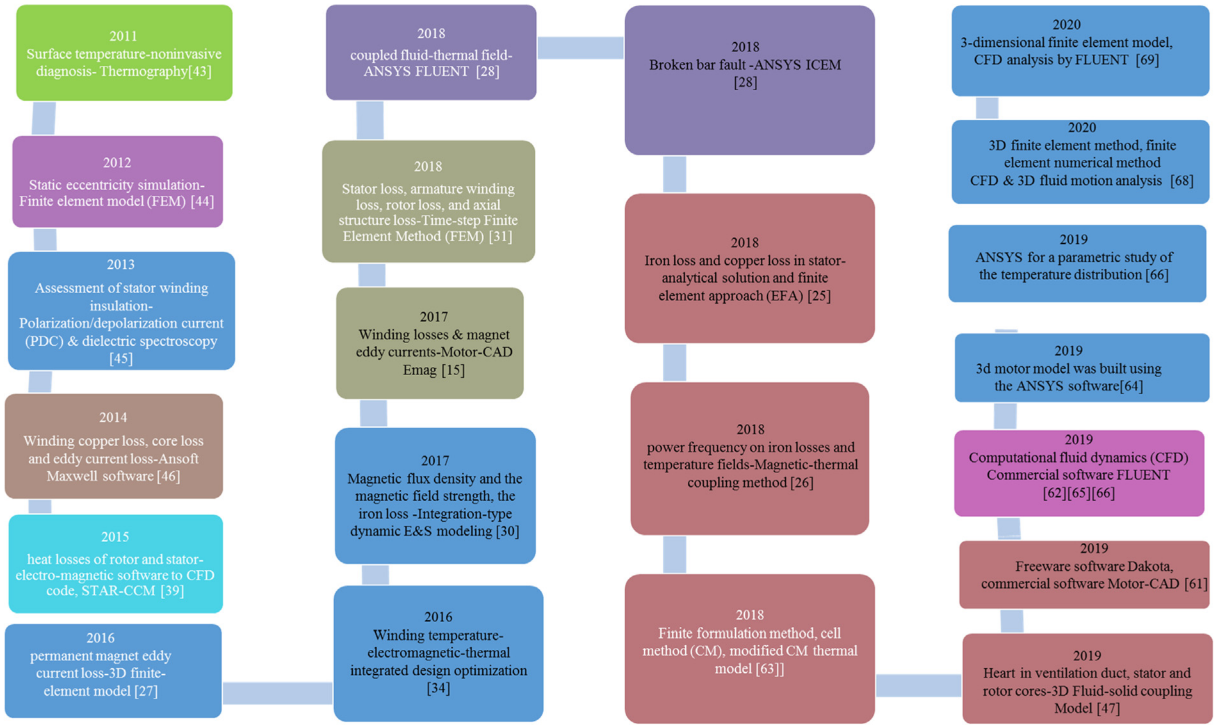

Fig. 7. Computer aided analysis to find losses.

The following techniques were used: Thermography, Simulation using FEM, PDC & dielectric spectroscopy, Ansoft Maxwell software, dynamic E&S modelling, design optimization, CFD, Motor CAD Emag, ANSYS FLUENT, ANSYS-ICEM, FEA method, SOLIDWORKS, commercial software Motor-CAD, cell method (CM), modified CM thermal model, 3D motor model using the ANSYS software, 3D fluid motion analysis and software Dakota. Taguchi methods are utilized to optimize the models.

3. Cooling methods

Motor cooling depends on conduction of lamination stacks, slot windings and end windings. It also depends upon the performance of the cooling jacket [37]. In thermal model, directions of the heat flows in the induction motor are important.

1. heat flow from the rotor bars through the air gap towards the stator winding and then to the stator iron then finally to the ambient through the round frame by convection.
2. heat flow from the stator end-winding and the rotor bars sides towards the end-cap air by convection and then to the ambient through the side frame by convection.

3.1. Cooling techniques for improving efficiency

Efficient cooling systems are essential to minimize the operating temperatures of the motor hot spots, and in particular of the copper windings. Thus, an accurate thermal modelling of the motor and of the coupled cooling system is important to optimize the thermal management of the engine. Water jacket cooling system removes more than 99.5% of the heat generated while the remaining portion is removed by natural convection [61]. By convection, heat is transferred from solid to either gas or liquid through the surface layer and can be either natural or forced convection [38]. The optimal flow rate for cooling is determined through an unsteady state analysis to predict according to the insulation grade [39]. A liquid-cooling system is often adopted where a cooling fluid (usually a 50% mix of water and glycol) is pumped into the components to be cooled and in a liquid–air heat exchanger, forced air cooled by means of cooling fans [40]. Oil spraying technique is used to cool the magnets in a safe operating temperature, increase their performance and also reducing their manufacturing cost. The oil-spraying cooling system, was designed to spray oil on the inside of the rotor of the electrical machine. Due to the high rotational speed the oil forms a thin film that absorbs the heat generated by the magnets [21].Water-ethylene glycol (WEG) circulated through three cooling channels within the cooling jacket [41]. The main technologies used in cooling electric motors include forced air cooling, direct water cooling, alternative cooling fluids, immersion cooling, heat pipes, phase change materials, vapour compression refrigeration, thermo electric cooling and Stirling cycle cooling. The novel cooling systems such as Malone refrigeration, pulse tube refrigeration, thermo ionic cooling, thermo acoustic refrigeration, magnetic refrigeration and ejector expansion refrigeration are still being studied or at research status [42]. Thermal diagnostics of motor windings, stator windings and temperature distribution inside the electric motors are presented [43–45]. Analysis of temperature rise, thermal losses and thermal performance are carried out in detail [46–48]. Forced convection on enhanced surfaces, different oil cooling systems and cooling of traction motors by combination of methods are reviewed [49–51]. Heat pipes are effectively used in thermal management of electric motors which simplify the system structure and save more space compared with the other methods [62]. Rotor is cooled using spiral stator water jacket that uses forced convection with water ethylene glycol mixture (50–50%) and oil spray cooling system. A new ventilation Cooling structure of the radial–axial mixed ventilation system is designed to safeguard the structure of the motor [63]. Temperature-rise rate of oil-cooled motor under rated working conditions viz. same electromagnetic structure, is slower than that of water-jacketed cooled motor and can work for longer periods. The oil-cooled method is one of the best methods to cool sta-

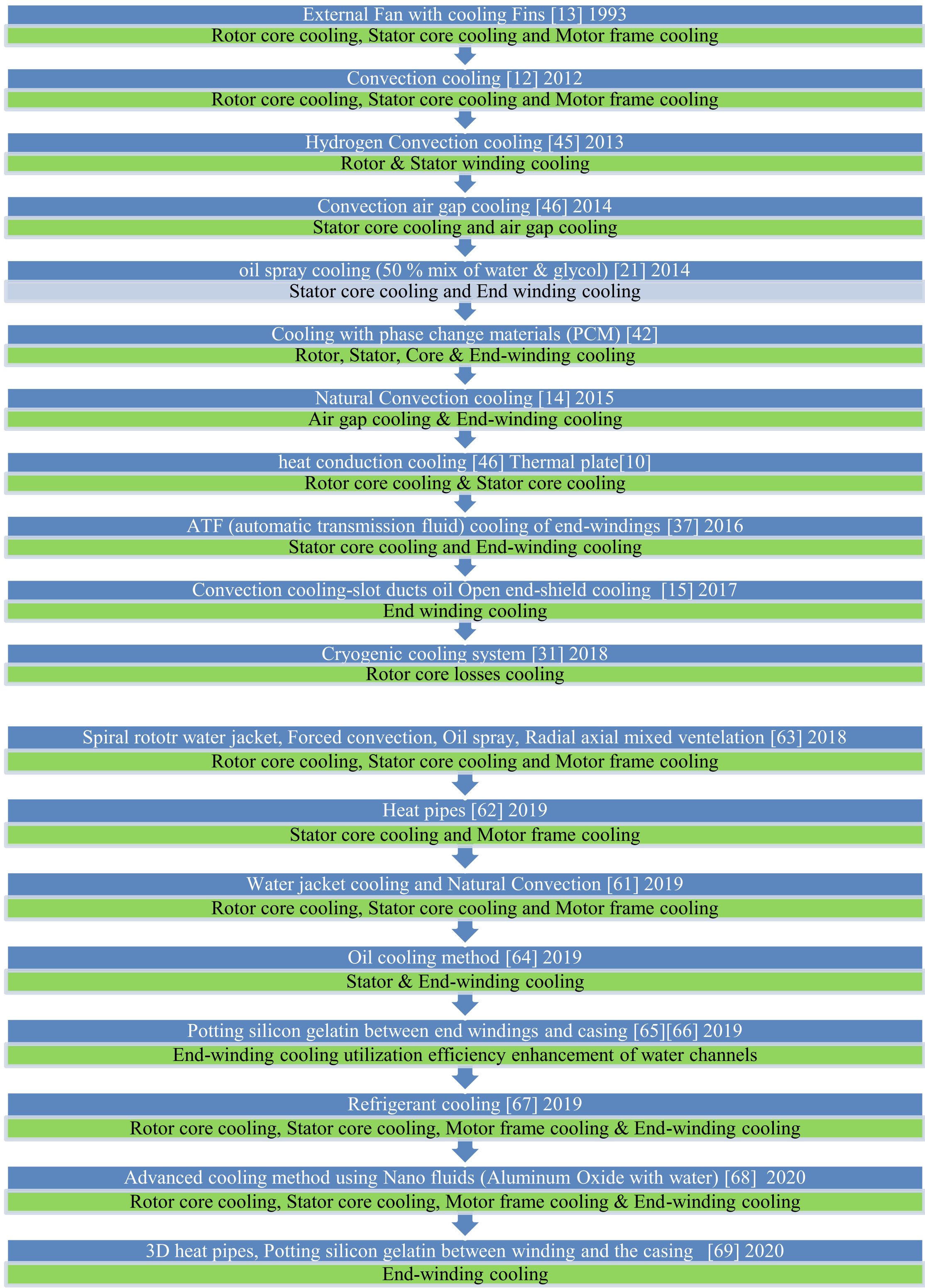

Fig. 8. Applied cooling methods.

tor and a direct oil-cooling method is proposed in the cooling the end winding with oil immersion [64]. Potting silicon gelatin is encapsulated in the gaps between the end windings and the casing to dissipate the heat generated in the end windings quickly and to enhance the utilization efficiency of the whole water channels [65,66]. In the recent research, the exprimental results predict higher cooling performance of electric motor with a refrigerant. Obtained rated torque with a refrigerant cooled motor is around 60% higher than that of water cooled motor [67]. Recently nanofluids are used as advance coolants in order to increase the heat transfer capability of the cooling system and to keep the temperature of the electric motor at operational level. A 4% of nanoparticle of

Aluminum-oxide with base fluid (pure water) increases the heat transfer capability of the cooling system up to 40% [68]. A very recent research is on introducing 3-dimensional heat pipes into the gap between the winding and the casing. Potting silicon gelatin is used to fix the heat pipes which also increase the contact area and the heat pipes with the combination of potting silicon gelatin can effectively improve the heat dissipation efficiency of the water-cooling. This technique is one of the best solution to solve the problem of high winding temperature [69]. A review on increasing efficiency of electric motors using cooling methods, lightweight materials and novel manufacturing processes is avail-able [70]. Fig. 8 shows the applied cooling methods.

4. Research gap and future directions for research

In this review it is observed that thermal mapping tempature at various parts of the motor is not very clear. All the researchers pointed out ther there is rise in temperature but quantitative analysis is missing. High Temperature Superconductor (HTS) technology has to be investigated to improve efficiency of motors. Further study is required to find the arrangement of HTS tape in iron core to reduce losses. Vector control system of electric motors can be explored to reduce losses. Secondly, various cooling methods are studied but comparison of results and quantitative analysis are not explicitly mentioned. Further research can be done in Cryogenic cooling method, Hydrogen cooling method and cooling using phase change materials (PCM)/Heat pipe. Experimental studies are to be done on the novel cooling systems such as Malone refrigeration, pulse tube refrigeration, thermo ionic cooling, thermo acoustic refrigeration, magnetic refrigeration and ejector expansion refrigeration. Even combinations of various cooling methods for the parts of the motor may be applied since the parts of the motor are not equally stressed thermally. Hence, by adopting appropriate cooling methods, the temperature in the motor can be controlled which will enhance torque and efficiency of the electric machines. Optimized thermal management is required to be studied to visualize the electromagnetic effects brought by geometric changes dictated by thermal considerations. The selection of Grade F insulation material has to be studied further to meet the requirements of the motor for short-term temperature rise. Also, Impacts of adding three different amount of nanoparticles in the base fluid has to be studied to predict the thermal performance of the cooling system. An optimized efficient electric motor is the need of the hour for high torque transport applications leading to the mitigation of the effects of climate change.

Declaration of Competing Interest

The authors declare that they have no known competing financial interests or personal relationships that could have appeared to influence the work reported in this paper.

References

[1] Miller P. Reducing heavy-duty long haul combination truck fuel consumption and CO_2 emissions. Boston: Northeast States Center for a Clean Air Future; 2009.
[2] Bachman LJ, Bynum CL. Effects of single wide tires and trailer aerodynamics on fuel economy and NOx Emissions of class 8 line-haul tractor-trailers. 2005 SAE commercial vehicle engineering conference, Rosemont, 2005.
[3] Zhao H, Burke A, Miller M. Analysis of class 8 truck technologies for their fuel savings and economics. Transp Res Part D: Transp Environ 2013;23:55–63.
[4] Karbowski D, Delorme A, Rousseau A. Modeling the hybridization of a class 8 line-haul truck. In: SAE 2010 commercial vehicle engineering congress, Chicago. Technical Paper 2010-01-1931. doi: https://doi.org/10.4271/2010-01-1931.
[5] Davis BA, Figliozzi MA. A methodology to evaluate the competitiveness of electric delivery trucks. Transp Res Part E 2013;49(2013):8–23.
[6] NREL report. Advanced technology vehicle evaluation: advanced vehicle testing activity – Norcal prototype LNG truck fleet; 2004. http://www.nrel.gov/docs/fy04osti/35427.pdf.
[7] Kirtley Jr. James L. Traction motor design considerations. http://web.mit.edu/kirtley/www/doe_kirtley_may_2011.pdf.
[8] Kirtley Jr JL, Schiferl RF, Peters DT, Brush Jr EF. The case for induction motors with die-cast copper rotors for high efficiency traction motors. Society of automotive engineers world congress, April 22, 2009, Detroit, 2009.
[9] Hong Do-K Wan, Choi Jae-Hak, Kim Dong-Jun, Chun Yon-Do, Woo Byung-Chul, Koo Dae-Hyun. Development of high speed induction motor for spindle systems. IEEE Trans Magn 2013;49(7):4088–91.
[10] Morini Lorenzo, Cavina Nicolò. Thermal management model for a plug-in hybrid electric vehicle-thesis. France: Anno Accademico, University; 2016.
[11] Faiz J, Ebrahimi BM, Akin B, Am Toliyat H. Finite-element transient analysis of induction motors under mixed eccentricity fault. IEEE Trans Magn 2008;44 (1):66–74.
[12] Croitorescu Valerian, Anthonis Jan, Vasiliu Nicolae. Thermal modeling of an electric motor used on road vehicle powertrain. University POLITEHNICA of Bucharest, LMS International, Engineering Services; 2012.
[13] Bousbaine Amar. An investigation into the thermal modelling of induction motors. Thesis submitted to the University of Sheffield for the degree of Doctor of Philosophy; 1993.
[14] Zhou Kan. Computationally-efficient finite-element-based thermal and electromagnetic models of electric machines A dissertation submitted in partial fulfillment of the requirements for the degree of Doctor of Philosophy. University of Michigan; 2015.
[15] Goss James. Multi-physics electric motor simulation workflow; Motor design software by Motor design engineers. In: CADFEM Ireland 13th October 2017, www.motor-design.com. Motor Design Limited; 2017.
[16] Jimoh AA, Findlay RD, Poloujadoff M. Stray losses in induction machines: Part I, Definition, origin and measurement. IEEE Trans Power Apparat Syst 1985;PAS-104(6):1500–5.
[17] Benamrouche N, Haddad S, Bousbaine A, Low FW. Measurement of iron and stray load losses in induction motors using the temperature-time method. Measurement 1997;20(2):91–6. ISSN 0263-2241.
[18] Tai Y, Liu Z. Analysis on three-dimensional transient temperature field of induction motor. Electric power industry; Proceedings of the CSEE, 2010. ISSN: 0258-8013.
[19] Barbour A, Thomson WT. Finite element study of rotor slot designs with respect to current monitoring for detecting static air-gap eccentricity in squirrel-cage induction motors. Industry Applications Conference, 1997. Thirty-Second IAS Annual Meeting, IAS '97., Conference Record of the 1997 IEEE, vol. 1. p. 112–9.
[20] Bannae Sharifian MB, Faiz Jawad, Ebrahimi Bashir Mahdi. Analysis of induction motor static eccentricity using time stepping finite element. International conference on electrical machines, ICEM 2006, Conf. Publ. No. 289, 2006.
[21] Frob Johan, Lykartsis Odyssefs. Advanced cooling of electric machine in a hybrid vehicle application. Master of Science Thesis, Division of Electric Power Engineering, Department of Energy and Environment, Chalmers University of Technology, Goteborg, Sweden 2014, Report No. 1; 2014.
[22] Nandi S, Ilamparithi TC, Lee Sang Bin, Hyun Doosoo. Detection of eccentricity faults in induction machines based on nameplate parameters. IEEE Trans Ind Electron 2011;58(5):1673–83.
[23] Jiang W, Jahns TM. Coupled electromagnetic-thermal analysis of electric machines including transient operation based on finite element techniques. In: IEEE energy conversion congress and exposition, Denver, CO, 2013. p. 4356–63.
[24] Prabhu, Chandrasekar V, Karthikeyan P, Lenin NC, Arumugam R. Vibration and thermal analysis of switched reluctance hub motor. Eur J Sci Res 2012;68 (1):12–20.
[25] Yanan Yu, Liang Deliang, Liang Zhe, Ze Qiji. Calculation for stator loss of high-speed permanent magnet synchronous machine in torque-speed envelope and restraint approach for circulating current in windings. CES Trans Electr Mach Syst 2018;2(2).
[26] Si Jikai, Zhao Suzhen, HaichaoFeng Yihua Hu, Cao Wenping. Analysis of temperature field for a surface-mounted and interior permanent magnet synchronous motor adopting magnetic-thermal coupling method. CES Trans Electr Mach Syst 2018;2(1).
[27] Li Bing, Li Ming. Calculation and analysis of permanent magnet eddy current, loss fault with magnet segmentation. Math Problems Eng 2016;2016.
[28] Xie Ying, Guo Jinpeng, Chen Peng, Li Zhiwei. Coupled fluid-thermal analysis for induction motors with broken bars operating under the rated load. Energies 2018;11(8):2024.
[29] Huang Yunkai, Hu Qiansheng, Zhu Jianguo. Magneto-thermal analysis of a high-speed claw pole motor considering rotational core loss. Trans China Electro Tech Soc 2010;25(5).
[30] Sato Takeru, Enokizono Masato. Evaluation of stator core loss of high speed motor by using thermography camera. Department of Electrical and Electronic Engineering, Oita University, Oita 870-1192, Japan. Vector Magnetic Characteristic Technical Laboratory, USA, Oita 879-0442; 2017.
[31] Li Dong, Wen Yinghong, Li Weili, Feng Bo, Cao Junci. Three-dimensional temperature field calculation and analysis of an axial-radial flux-type permanent magnet synchronous motor. Energies 2018;11. paper no. 1208.
[32] Kou BQ, Cao HC, Li WL. Analysis of Losses in high speed slot less PM synchronous motor integrated the added leakage inductance. Energies, Proc of

2015 Intl conference on power electronics and energy engineering (PEEE 2015-1)., 2015.
[33] Godbehere J, Wrobel R, Drury D, Mellor PH. Experimentally calibrated thermal stator modeling of AC machines for short-duty transient operation. IEEE Trans Ind Appl 2017;53(4):3457–66.
[34] Li Quanwu, Dou Manfeng, Tan Bo, Zhang Haitao, Zhao Dongdong. Electromagnetic-thermal integrated design optimization for hypersonic vehicle short-time duty PM brushless DC motor. Int J Aerosp Eng 2016;2016. Article ID 9725416.
[35] Chahine Khaled, Ramadan Mohamad, Merhi Zaher, Jaber Hadi, Khaled Mahmoud. Parametric analysis of temperature gradient across thermoelectric power generators. J Electr Syst 2016;12(3):623–32.
[36] Xia Y, Han Y, Xu Y, Ai M. Analyzing temperature rise and fluid flow of high-power-density and high-voltage induction motor in the starting process. IEEE Access 2019;7:35588–95.
[37] Bennion Kevin. Thermal management enables more efficient and cost-effective motors. National Renewable Energy Laboratory, 2016 Annual Merit Review; 2016.
[38] Huai Ying, Melnik Roderick VN. Computational analysis of temperature rise phenomena in electric induction motors. Appl Therm Eng 2003;23(7):779–95.
[39] Lee Jun Ho, Lee Gee Soo, Yu Byung Hun, Kim Hyun Chul, Kim Kyu Sik, Lee Bong Hyun. Design and thermal analysis of wheel hub motors of electric vehicles using analytical and CFD methods. International electric vehicle symposium and exhibition (EVS28), KINTEX, Korea, May 3–6, 2015, 2015.
[40] Mapelli Ferdinando Luigi, Tarsitano Davide. Modelling of full electric and hybrid electric vehicles, new generation of electric vehicles. INTECH open science/open minds, New Generation of Electric Vehicles https://doi.org/10.5772/45641. Milan (Italy): Mechanical Department, Politecnico di Milano; 2012.
[41] Bennion Kevin. Electric motor thermal management R&D. Annual report. National Renewable Energy Laboratory, U.S. Department of Energy; 2016. www.nrel.gov/publications.
[42] Rajapakshe Prathibha Chinthana. Heat storage application in electric motor cooling system smoke ventilation motors. Master's Thesis in Sustainable Energy Engineering. Sweden: KTH Industrial Engineering and Management, Univesity of Gavle; 2004.
[43] Barański Marcin, Polak Artur, Komel Bobrme. Thermal diagnostic in electrical machines. Electr Rev; 2011. ISSN 0033-2097, R. 87 NR 10.
[44] Baptista Bruno, Mendes André, Cruz Sérgio, Cardoso António. Temperature distribution inside a three-phase induction motor running with eccentric air gap. Electr Rev 2012. ISSN 0033-2097.
[45] Stone GC. Power, condition monitoring and diagnostics of motor and stator windings – A review. IEEE Trans Dielectr Electr Insul 2013;20:No. 6.
[46] Chen Qiping, Yang Xuelan. Calculation analysis of thermal loss and temperature field of in-wheel motor in micro-electric vehicle. J Mech Sci Technol 2014;28(8):3189–95.
[47] Xia Yunyan, Han Yongsen, Xu Yongming, Ai Mengmeng. Analyzing temperature rise and fluid flow of high-power-density and high-voltage induction motor in the starting process. IEEE Access 2019.
[48] Badran Omar, Sarhan Hussein, Alomour B. Thermal performance analysis of induction motor. Int J Heat Technol 2012;30:75–88.
[49] Almaghrabi Mohammed. Forced convection cooling of electric motors using enhanced surfaces. Electronic Theses and Dissertations, Masters Thesis (Open Access), 5272, University of Central Florida; 2016.
[50] Davin Tanguy, Pelle Julien, Harmand Souad, Yu Robert. Experimental study of oil cooling systems for electric motors. Appl Therm Eng 2015;75:1–13.
[51] Gai Yaohui, Kimiabeigi Mohammad, Chong Yew Chuan, Widmer James D, Deng Xu, Popescu Mircea, Goss James, Staton Dave, Steven Andrew. Cooling of automotive traction motors: schemes, examples and computation methods– A review. IEEE Trans Ind Electron 2018.
[52] Tolochko Olga, Kaluhin Dany Lo, Burmelov Oleksii. speed vector control of induction motor with copper and iron losses minimization. In: EEE 2nd Ukraine conference on Electrical and Computer Engineering, Lviv, Ukraine; 2019. p. 408–13.
[53] Beck Christopher, Keller Daniel, Echtle Harald, Haug Sebastian, Kruger Christian, Bargende Michael. Sensitivity study on heat source distribution and heat transport of electrical machines. E & I Electrotechnik und Informationstechnik 2019;136:195–201.
[54] Ogawa Jun, Fukui Satoshi, Oka Tetsuo, Sato Takao, Fushimi Atsumu, Shoda Takuya. Influence of the arrangement of HTS tapes inserted in an iron core on AC loss characteristics. IEEE Trans Appl Conduct 2014;24(3):6600204.
[55] Ismagilov Flur R, Vyacheslav E, Vavilov Ruslan D. Karimov. Improving the efficiency of electrical high-rpm generators with permanent magnets and tooth winding. Progr Electromagn Res M 2018;63:93–105.
[56] Syed Qurban Ali Shah, Solovieva Veronika, Hahn Ingo. Magnetization characteristics and loss measurements of the axial flux permanent magnet motor's stator. In: IEEE international conference on electric machines and drives (IEMDC); 2019. p. 1061–6.
[57] Seo Myung-Ki, Ko Young-Yoon, Lee Tae-Yong, Kim Yong-Jae, Jung Sang-Yong. Loss reduction optimization for heat capacity improvement in interior permanent magnet synchronous machine. IEEE Trans Magn 2018;54 (11):8207705.
[58] Boubaker Nadhem, Matt Daniel, Enrici Philippe, Nierlich Florent, Durand Guillaume. CoFe and SiFe lamination sheets and stemmed from different manufacturing processes. IEEE Trans Magn 2019;55(1):8100309.
[59] Zhao Jilong, Lin Mingyao, Da Xu. Minimum-copper-loss control of hybrid excited axial field flux-switching machine. IET Electr Power Appl 2016;10 (2):82–90.
[60] Tao Dajun, Zhou Kai Liang, Lv Fei, Dou Qingpeng, Jianxiao Wu, Sun Yutian, Zou Jibin. Magnetic field characteristics and stator core losses of high-speed permanent magnet synchronous motors. Energies 2020;13:535. doi: https://doi.org/10.3390/en13030535.
[61] Cavazzuti Marco, Gaspari Gloria, Pasquale Stefano, Stalio Enrico. Thermal management of a Formula E electric motor: Analysis and optimization. Appl Therm Eng 2019;2019:157. doi: https://doi.org/10.1016/j.applthermaleng.2019.113733.
[62] Fang Guoyun, Yuan Wei, Yan Zhiguo, Sun Yalong. Yong Tang (2019) Thermal management integrated with three-dimensional heat pipes for air-cooled permanent magnet synchronous motor. Appl Therm Eng 2019;152:594–604. doi: https://doi.org/10.1016/j.applthermaleng.2019.02.120.
[63] Zhu Gaojia, Zhu Yinghao, WenmingTong Xueyan Han, Zhu Jianguo. Double-circulatory thermal analyses of a water-cooled permanent magnet motor based on a modified model. IEEE Trans Magn 2018;2018:54. doi: https://doi.org/10.1109/TMAG.2017.2759805.
[64] Guo Fulai, Zhang Chengning. Oil-cooling method of the permanent magnet synchronous motor for electric vehicle. Energies 2019;14:1–11. doi: https://doi.org/10.3390/en12152984.
[65] Sun Yalong, Zhang Shiwei, Yuan Wei, Tang Yong, Li Jingrong, Tang Kairul. Applicability study of the potting material based thermal management strategy for permanent magnet synchronous motors. Appl Therm Eng 2019;149:1370–8. doi: https://doi.org/10.1016/j.applthermaleng.2018.12.141.
[66] Patrick McCluskey F, Yonatan Saadon, Zhaoxi Yao, Alexander Camacho. Cooling for electric aircraft motors. In: Intersoc. Conf. Therm. Thermomechanical Phenom. Electron. Syst. ITHERM, vol. 2019–May, 2019, p. 1134–8. https://doi.org/10.1109/ITHERM.2019.8757435.
[67] Hidemasa Fujita H, Itoh Atshushi, Urano Tohru. Newly developed motor cooling method using refrigerant. World Electr Veh J 2019;2019:10. doi: https://doi.org/10.3390/wevj10020038.
[68] Deriszadeh Ali, de Monte Filippo. On heat transfer performance of cooling systems using nanofluid for electric motor applications. Entropy 2020;22:99. doi: https://doi.org/10.3390/e22010099.
[69] Sun Yalong, Zhang Shiwei, Chen Gong, Tang Yong, Liang Fuye. Experimental and numerical investigation on a novel heat pipe based cooling strategy for permanent magnet synchronous motors. Appl Therm Eng 2020;2020:170. doi: https://doi.org/10.1016/j.applthermaleng.2020.114970.
[70] Solomon Darius Gnanaraj, Greco Adriana, Masselli Claudia, Gundabattini Edison, Rassiah Raja Singh, Kuppan Ravi. A review on methods to reduce weight and to increase efficiency of electric motors using lightweight materials, novel manufacturing processes, magnetic materials and cooling methods. Annals de Chimie – Science des Materlaux 2020;44(1):1–14.

A novel scheduling technique for improving cell-edge performance in 4G/5G systems

Priya Chandan Satpathy, *Department of Electrical and Communication Engineering, Aryan Institute of Engineering & Technology, Bhubaneswar, priyachandan.satpathy57@outlook.com*

Chinmaya Ranjan Pradhan, *Department of Electrical Engineering , NM Institute of Engineering & Technology, Bhubaneswar, cr_pradhan@outlook.com*

Smruti Samantray, *Department of Electronics and Communication Engineering , Capital Engineering College, Bhubaneswar, smrutisamantray23@hotmail.com*

Swadesh Ranjan Jena, *Department of Electrical and Electronics Engineering, Raajdhani Engineering College, Bhubaneswar, swadesh.jena@yahoo.co.in*

Keywords:

Wireless networks
Cellular system
5G
LTE schedulers
Cell-edge

A B S T R A C T

In cellular networks, users near the edge of the cell are usually suffering from low signal-to-noise-plus-interference-ratio (SINR) levels as a result from being far away from the base-station (BS). Many factors could lead to huge attenuation of the received signal in the cell-edge area such as path-loss and multipath fading. Increasing the BS transmit power is not always feasible as this could lead to an increased inter-cell-interference (ICI). Hence, the cell-edge problem arises. In this paper, a new scheduling technique has been developed to increase the probability of assigning the available resource blocks (RBs) to the cell-edge users so that their achieved throughput would increase. A performance comparison with state-of-the-art schedulers indicates that our proposed scheduling mechanism leads to a significant improvement in the average throughput for cell-edge users, with negligible performance degradation for cell-center users.

1. Introduction

Since the development of mobile wireless communication systems in the late 1970s, huge efforts have been devoted to improve both the capacity of the system, and the quality-of-service (QoS) experienced by the users. To achieve these goals, many approaches have been taken such as well-planned networks, massive antenna configurations and Inter Cell Interference Coordination (ICIC) methods. In conventional cellular networks, the full area of coverage is composed of multiple cells, where each cell is assigned a predetermined amount of radio resources and power allocation levels. Accordingly, the overall limited network resources will be distributed among the cells based on the capacity of each cell, and the corresponding service data rates needed to assure a fair performance among all users' requirements. Users located at the edge of the cell, i.e., far away from the base station (BS), typically experience a low signal-to-interference-plus-noise-ratio (SINR), which leads to considerably low achievable data rates. This is known as the cell-edge problem. Increasing the BS transmit power in an attempt to improve the cell-edge users' experience is typically limited by the resulting amount of inter-cell-interference (ICI) towards adjacent cells.

Most specifications of wireless communication systems have been using a frequency reuse of unity due to the shortage of available frequency resources (see, e.g., [1]). Frequency reuse may lead to ICI, especially at the cell boundaries, further negatively impacting the throughput of cell-edge users. 5G systems are expected to be based on an ultra-high densification of base stations to improve the overall system capacity [2]. This densification, however, together with frequency reuse and high traffic loads, will further negatively affect the throughput of cell-edge users. This motivates us to study methods for improving the cell-edge user throughput for 4G and 5G systems.

LTE [3] and LTE-Advanced (LTE-A) [4,5] are the leading systems for 4G as stated by the 3rd Generation Partnership Project (3GPP) [6]. Both LTE and LTE-A use orthogonal frequency division multiple access (OFDMA) in the downlink. OFDMA divides the available transmission bandwidth into multiple sub-carriers, which can carry independent data flows. A physical resource block (RB) is defined as 12 subcarriers in the frequency domain (180 kHz) and seven OFDM symbols in the time domain, which is equivalent to one time slot (0.5 ms). RBs are periodically allocated by the sched-uler to the active users in a cell every transmission time interval (TTI) that is equal to 1 ms.

This paper focuses on improving cell-edge user throughput via intelligently scheduling RBs among the users of the cell. The rest of the paper is organized as follows: state-of-the-art techniques for RB scheduling are reviewed in Section 2. In Section 3, The proposed scheduling technique is explained. In Section 4, Simulation parameters and setup are demonstrated. Simulation experiments and performance results are discussed in Section 5. Finally, Section 6 concludes the paper.

2. Related work

The related literature can be classified into three categories: (1) the main scheduling techniques (in LTE and LTE-A), (2) scheduling schemes tailored towards improving cell-edge user throughput and (3) work on cell-edge throughput improvement via other methods (not scheduling). In what follows we review the main related literature from each category.

The main scheduling techniques for LTE and LTE-A can be summarized as follows (more details can be found in [7,8]).

- Largest Weighted Delay First (LWDF) scheduler ensures that each packet has to be received within a certain deadline to avoid packet drops. The scheduler collects information about the creation time of a specific packet, as well as its deadline. The user with the most stringent requirements in terms of acceptable loss rate and deadline expiration will be preferred for allocation. This scheduler does not take the channel quality variation into consideration.
- Blind Equal Throughput (BET) attempts to achieve throughput fairness among all users. In particular, the scheduler allocates resources to flows that have been served with lowest average throughput in the past. Again, this scheduler is unaware of the channel quality variation.
- Maximum Throughput (MT) scheduler assigns RB to the user that achieves the maximum throughput. This is usually performed by selecting the user with the largest channel quality indicator (CQI) for each RB assignment. The major disadvantage is that the scheduler does not consider fairness among users.
- Proportional Fair (PF) scheduler strikes a balance between fairness and throughput, by taking both CQI and resource allocation history. In particular, the user with largest ratio of CQI and average past throughput is selected for each RB assignment.

Heuristics optimization algorithms, such as [9–11], are rarely used in LTE resource scheduling [12,13] because of the time complexity needed in such algorithms. RB scheduling and allocation in LTE is a real-time operation which has to be performed each TTI (i.e., 1 ms), which is not the case in heuristics optimization algorithms that assume plenty of computation power and time to find the solution as in offline applications. Works done in [12,13] use very low number of RBs (i.e., maximum one quarter the number of the used RBs in our paper) to bypass the delay caused from used heuristics. Due to its fast response, and consideration of both fairness and throughput, PF becomes the most supported scheduling technique for LTE system [14]. None of the above-mentioned schedulers, however, pays explicit attention to cell-edge users.

Scheduling techniques that are particularly devoted to cell-edge user throughput enhancement do exist. See, e.g., [15–17]. The authors of [15] consider allocating RBs to the users based on weighted signal-to-noise (SNR) ratios for both cell-centric and cell-edge users, then allocating transmit powers, as two separate steps. Their approach relies on combinatorial optimization and graph-theoretic techniques, which add to the complexity of the system. In contrast, this paper introduces a low-complexity, probabilistic approach for the dynamic allocation of RBs among cell-centric and cell-edge users. A detailed description for the proposed approach is illustrated in the next section. Throughout our experiments, our proposal has proven to achieve larger improvements as compared to [15], as will be illustrated in the results section.

In [16], a dynamic PF scheduler has been proposed to increase the performance of the cell-edge scheduler. The authors of [16] modified in the PF scheduler itself to adapt to the individual user conditions (e.g., location in the cell or QoS requirement). The proposed modification aims to give a chance to the cell-edge users to utilize some of the RBs seeking improvement of their ability to get the service. This is done by varying the exponent of the dominator of the scheduling equation used in conventional PF (i.e., βparameter) to be not fixed to unity as conventional PF use. The dominator is representing the past achieved average throughput by the user prior to the processed RB. The algorithm is adapting βsuch that the users near cell center will be discredited since their βtends to be larger than 1, while the users in the cell edge will be compensated since their βtends to be smaller than 1. The dynamic PF algorithm uses a time counter to record the duration in which a user stays in the cell-edge area. Hence, if a user stays in the cell-edge for a relatively long time, the user will be then prohibited from being favored by additional RBs. We will demonstrate in the results section that our algorithm will outperform this dynamic PF's performance.

Studies on improving cell-edge user throughput using other methods (than scheduling) do exist. For example, Coordinated Multi-Point transmission and reception (CoMP) was introduced in LTE-A [4,5] and refers to a family of functionalities involving multiple BSs coordinating transmissions to a cell-edge user, including joint processing and coordinated scheduling. The studies in [17–20] focus on improving cell-edge throughput via CoMP. However, CoMP comes at the cost of coordination and communication across multiple cells. Therefore, this paper focuses on cell-edge user improvement via low-complexity uncoordinated techniques that can be readily implemented within the cell. Furthermore, cell-edge user throughput can also be improved via power control. Typically, power control is applied as a separate step after RB scheduling (see, [15]). Therefore, our introduced scheduling mechanism can further benefit from intelligent power allocation performed separately. This paper, however, focuses on scheduling.

Improving cell-edge performance could be implicitly achieved using techniques enhancing the overall cell throughput. In addition to the COMP and power control techniques, the smart scheduler introduced by NOKIA in [17] is capable to improve cell-edge data rate as well as other users using the following techniques:

- Frequency Selective Scheduling (FSS): FSS uses Channel Aware Scheduling (CAS) and Interference Aware Scheduling (IAS) to select non-faded RBs to each user. Information about fading channels can be obtained from CQI reports.
- Modifying the parameters of handover between adjacent cells based on the information exchange of the X2 interface. This technique is known as "Intra-frequency load balancing" and used when the load in two adjacent cells is not balanced.
- Interference shaping to avoid ICI.
- QoS differentiation by allocating more re-sources for users in weak channel conditions.

Our proposed scheduler can further benefit from any of the above techniques used in NOKIA scheduler to add to the overall scheduling. This paper, however, focuses on scheduling. In light of the above, the contribution of this paper can be summarized as follows.

- A new scheduling algorithm is proposed to enhance the throughput achieved by cell-edge users. The proposed algorithm is an extension to the pro-portional fair scheduler. In particular, it is based on probabilistically replacing a cell-centric user by a cell-edge user at some RBs, where the allocation probability changes dynamically across RBs according to the concept of sampling without replacement to give a chance to the cell-edge users for scheduling and utilizing some RBs. However, this probability should decay gracefully to avoid poor system utilization if significant RBs are assigned to poor signal strengths cell-edge users.
- Our proposed scheduler has a low complexity, and is suitable to be invoked every TTI.

Our proposed scheduler aims to improve the cell-edge throughput, while maintaining the required throughput for cell-centric users to continue achieving an acceptable level of performance.

3. Edge User Friendly Scheduler (EUFS)

A new packet scheduling technique is developed to enhance the performance of cell-edge users, or more generally, users experiencing bad channel conditions. The proposed algorithm is an extension to the proportional fair scheduler. In particular, it is based on probabilistically replacing a cell-centric user by a cell-edge user at some RBs, where the allocation probability changes dynamically across RBs to give a chance to the cell-edge users for scheduling and utilizing some RBs. However, this probability should decay gracefully to avoid poor system utilization if significant RBs are assigned to cell-edge users experiencing poor signal strengths. Network operators could offer this feature to the all cell-edge users, or to a selected subset of cell-edge users according to some criteria (such as in return for additional fees). Accordingly, at each TTI, the core network controller classifies a user as featured user (FU), i.e., a user that can potentially benefit from the proposed scheduler, by checking two conditions. These conditions can be summarized as follows.

- FU classification criteria:
  1. *The user has been classified as a cell-edge user: (Obligatory)* Classifying users between cell-centric and cell-edge is very critical. A user is considered as cell-edge if its instantaneous throughput is below some threshold. This threshold value is chosen to be the 5th percentile point of the overall cell throughput, as stated in [21]. CQI reports are used to measure the instantaneous throughput of a user. Those users only will be eligible for requesting improved service.
  2. *The user is agreeing on paying additional fees for the improved service: (Optional)* Operators could decide to associate the level of system performance provided to users with pricing, as done in [22,23] based on the recording of RBs utilization. Nowadays, most of the operators are using fixed price charging models that set constant rental fees for users per time or per consumed bit rate. This works well for systems that include scheduling techniques implementing blind fairness to users/connections without any prioritization towards users suffering from degraded channel conditions (e.g., cell-edge users). Hence, operators could use different pricing schemes to cope with the proposed scheduling technique, as to strike a balance between featured users (who gain more privileges in terms of throughput and extra RBs) and non-featured users (who sacrifice some resources).

The proposed technique uses two-level scheduling. In the first level, PF scheduling is applied to identify a PF user to potentially utilize the RB. Then, a second scheduling level will probabilistically decide whether to allocate that RB to the chosen PF user, or to one of the FUs. In contrast to conventional PF scheduling [24] that selects the candidate user to utilize RB based on the ratio between the current instantaneous and the accumulated average throughput by the user, our algorithm involves putting the selected PF user into a second round of competition for the RB with all FUs (cell-edge users who probably experience weak signal strength). The selection between PF and FU is probabilistic, where the selection probabilities vary dynamically as to strike a balance between improving cell-edge user throughput and minimizing the reduction in overall system throughput. To describe the details of our proposed algorithms, we first make the following definitions.

- The set of FUs in the cell is denoted as {FU1, FU2, ..., FUN}, where N is the number of FUs in the cell.
- The set of available RBs in the cell per TTI is denoted as {RB1, RB2, ..., RBM}, where M is the number of RBs in the cell.
- The minimum required probability of selecting the PF candidate for RB1 is denoted as P(PF). This is a design parameter that should be identified by the network operator. The effect of the choice of P(PF) on the overall system performance will be explored later.
- The initial number of chances for the PF user at RB1 is denoted as PF_C.
- The initial number of chances for FUi at RB1 is denoted as FU_Ci.
- Hence, the total number of chances at RB1 could be denoted as:

$$UE\_C = PF\_C + \sum_{n=1}^{N} FU\_C_i$$

We assume that each FU has the same number K of initial chances of being selected for the first RB (i.e., RB1). In other words, initially,

$$FU\_C_i = K, \quad for\ i = 1, 2, \ldots, N. \tag{1}$$

Guidelines for choosing the scaling factor K as to achieve the best performance is discussed in Section 5.

Therefore, and since the probability of selecting a user is calculated by dividing the number of chances for that user by the total number of chances, it is straightforward to see that the initial probability of selecting the PF candidate for the first RB (i.e., RB1) is given by PF_C/(PF_C + NK).

Since the minimum required initial probability of selecting a PF user (for RB1) is P(PF), the following condition on the number of chances needs to be satisfied:

$$\frac{(PF\_C)}{(PF\_C + NK)} >= P(PF) \tag{2}$$

The latter implies that PF_C, the initial number of chances for the PF user at RB1, will be set according to:

$$PF\_C >= \frac{(P(PF) \times N \times K)}{(1 - P(PF))} \tag{3}$$

For the first RB, a user is selected among the PF and FU candidates depending on their respective selection chances initialized using (1) and (3), respectively. For every other RB, the selection chances are updated according to the statistical concept of sampling without replacement (SWR). In particular, the user chosen in one RB will be either assigned lower chance/ probability, or even totally removed from competing with others for the next RB, and so on. Consequently, users not selected in a RB will have higher chances in the next RBs. If all chances (PF $C$and all FU C_i)reach zero, the chance values PF $C$and all FU $C_i$will be reset according to (1) and (3), respectively. The process continues until all RBs are utilized by users.

The overall scheduling algorithm (for each cell, at the beginning of each TTI) can be summarized as follows.

Algorithm EUFS

1. Among all UEs in the cell, identify the featured set {FU1, FU2, ..., FUN} based on the FU classification criteria.
2. Set the initial chances $PF_C$and $FU_C_i(for 1 <= i <= N)$according to (1) and (3), respectively.
3. For each RB1, RB2, ..., RBM, do:
a. Invoke the PF scheduler to select a PF user.
b. Create the set U of users containing PF_Ccopies of the PF user, and FU_C_icopies of $FU_i(for 1 <= i <= N)$.
c. Select one user from U according to a uniform distribution, to utilize the RB.
d. Update the selection chances as follows:
- If the selected user is a PF user, then $PF\_C := PF\_C - 1$;
- If the selected user is $FU_i(for any 1 <= i <= N)$, then $FU\_C_i := FU\_C_i - 1$.

e. If all chances $(for PF and all FUs)$reach zero, reset $PF_C$and $FU_C_i(for 1 <= i <= N)$according to (1) and (3), respectively.

This algorithm ensures allowing the users who previously suffered from lower instantaneous throughputs (namely cell-edge users) to utilize additional RBs to improve their throughputs and avoid throttling them. The stolen RBs from PF users are substituted gradually from other users in the same cell who already have better throughput in a dynamic manner that would not affect their assigned bandwidth seriously as well. This purpose has been maintained and proven as will be shown in the results and analysis section.

4. Experimental setup

The proposed algorithm has been deployed into the Vienna LTE system-level simulator [25,24], which runs on top of MATLAB. The simulation parameters used in our experiments are shown in Table 1. The used system bandwidth and carrier frequency is supported in LTE Release-8 [26]. The remaining parameters have been selected to be compatible with the system bandwidth used and to be applicable in the realistic world as well. Without loss of generality, we assume that all cell-edge users are considered as FUs. If some of the cell-edge users refuse the condition of the additional pricing to be granted the improved performance, this would imply that the number of featured users will be decreased. Hence, the average throughput for the other users in both categories (cell-centric and cell-edge) will be even better than the results provided in next section.

For performance evaluation, three state-of-the-art algorithms are used as benchmarks to be compared against our proposal. The first algorithm is the conventional PF algorithm which is adopted by the standard LTE system [14]. The other two algorithms are the weighted SNR algorithm [15] and the dynamic PF algorithm

Table 1
Simulation parameters.

Parameter	Value
System Bandwidth	20 MHz
Carrier Frequency	2.14 GHz
Channel Model	Fast Fading
Total No. of RBs per TTI	100
Antenna per RRH	3
eNodeB Transmit Power	40 W
No. of eNodeBs	7
Total No. of active UEs	210 to 1260
User Mobility	No Mobility
No. of Cells	21
No. of TTIs	100

[16] which have been discussed in the "related work" section. Throughout our experiments, the proposed algorithm (i.e., "EUFS") is deeply investigated and compared to the best recently proposed algorithms. It is easily seen that algorithm EUFS is based on dynamically changing the chances (probabilities) of selecting PF and FU candidates, respectively, across the different consecutive RBs. The first experiment investigates the optimal value of the scaling factor K that achieves the best performance using EUFS algorithm. The purpose of the second experiment is to assess the proposed algorithm EUFS against the state-of-the-art techniques from [15,16]. The throughput achieved by cell-edge and cell-centric users is used as the comparison metric. The third experiment also assesses the performance the proposed algorithm EUFS against the state-of-the-art techniques from [15,16]. The performance metric used, however, is the signal-to-noise-ratio (SNR). In the fourth experiment, we use Jain's fairness index [27] to assess the fairness of the system across all scheduling algorithms. The concept of Jain's fairness index is close to the variance measure in statistical analysis, as it measures the deviation of the achieved throughput by each user from the fair throughput. Jain's fairness index is maximum (i.e., unity) when all users achieve the same throughput. The closer the users' throughputs are to each other, the larger Jain's fairness index could be attained by the system. In the fifth (last) experiment, the execution time is compared across all scheduling algorithms to investigate the speed of each, and make sure that the proposed algorithm could fit in LTE online RB scheduling and allocation.

5. Results and analysis

5.1. Assessing the initial scaling factor

The first study is performed on the choice of the best value for the initial number of chances (K) as used the EUFS algorithm. Our empirical approach is based on experimenting with a wide range of values for K, then choose the best performing value for the remaining experiments of the paper. The selection of K will depend on the performance of the cell-edge users; the effect of EUFS algorithm on cell-centric users, however, is discussed in details in the following experiments. Fig. 1 shows the average throughput of cell-edge users using EUFS relative to their average throughputs obtained from a static probability approach, (on the y-axis) using different values for K (on the x-axis). According to (1), K represents the initial chances assigned to each cell-edge user per cell (i.e., FU_C_i). However, to keep the initial probability for PF user P(PF) fixed while changing K, scaling K directly indicates a corresponding scaling for the PF user (i.e., PF_C) accordingly. At the first RB0, P(PF) is the only effective factor in assigning RB0 to either Cell-edge or cell-centric user. However, the choice of K would take effect while stepping up in the following RBs as the chances adaptation after each

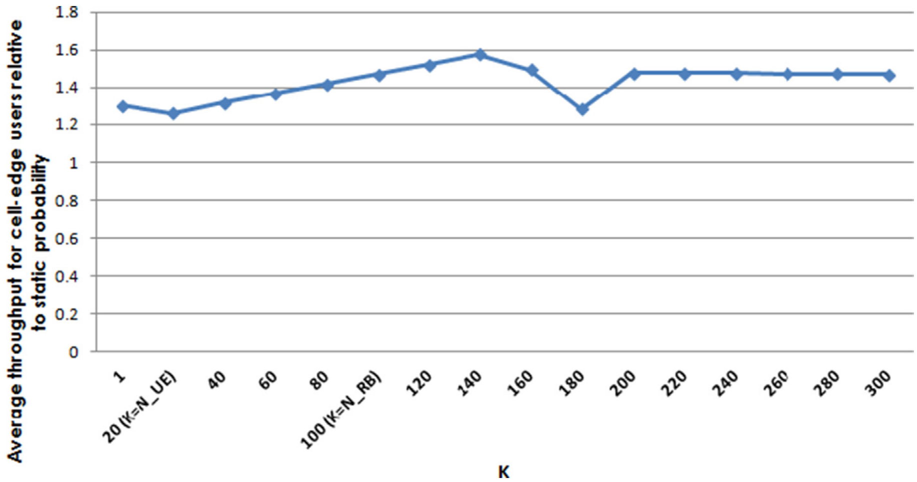

Fig. 1. Average throughput for cell-edge users using EUFS relative to the average throughput for cell-edge users using fixed probabilities, across different K.

RB would be dissimilar. Small K values (i.e., $K \ll number\ of\ RBs$) indicate an abrupt change to the total number of chances across the different RBs. Although this will guarantee the alternation between cell-edge and cell-centric users from one RB to the next (the change in chances changes the probability sharply), the algorithm quickly runs out of chances and mandates a reset for the chances as described in EUFS part (e) since the total number of chances (i.e. UE_C) is directly proportional to K. Hence, for the total number of RBs, static probability is effectively performed due to the very frequent reset to the total number of chances. Still with K = 1, as shown in Fig. 1, the dynamic probability assignment through EUFS achieves around 20% performance improvement over static probabilities. For small K values, the system memory is shallow, which implies a behavior closer to fixed probabilities. While increasing the value of K, deeper memory is preserved and more adaptive RB assignment to the users is performed. Accordingly, a better performance is achieved. On the other hand, the extreme case of increasing the K value as compared to the number of RBs (i.e., $K \gg number\ of\ RBs$) indicates too much initial chances for any user (edge-user or cell-centric user). This again reduces the effectiveness of the dynamic probability algorithm (EUFS), since for each RB only one chance is deducted from the total chances. With a very high number of total chances, the effect of the dynamic probability changes across RBs is minor and the algorithm again is getting closer to the static probability assignment. Fig. 1 indicates that the maximum throughput is achieved at K = 140. Accordingly, we decide to only consider this value of K for EUFS algorithm in the following experiments in order not to deviate from the main objectives of these experiments. That is, to compare the proposed algorithm with the state-of-the-art algorithms while keeping the scaling factor fixed.

5.2. Assessing the throughput

According to 3GPP [6], the user throughput is defined as the ratio of the number of information bits that the user successfully receives divided by the total simulation time. If user k has p downlink packet transmissions during the simulation period "T(sim)", and if there are q(k,i) packets in the ith transmission, and if b(k,i, j) denotes the number of correctly received bits in the jth packet; then the average user throughput for user k is:

$$R(K) = (\sum_{i=1}^{p(k)}\sum_{j=1}^{q(k)} b(k,i,j))/T(sim)$$

Now, the average throughput of all considered cell-edge users (featured users) has been observed for different initial probabilities of the PF candidate user. To this end, we keep the total number of users at 420, and the maximum number of FUs at 21. Fig. 2 shows the average throughput relative to a pure PF scheduler (on the y-axis) for different scheduling techniques (on the x-axis) as well as different initial P(PF) for our proposed EUFS. Probabilities for PF candidates less than 70% yield a sharp degradation in cell-centric user throughput since PF users are unlikely to be chosen, which could not be preferable. Hence, we run the algorithm using initial PF probabilities larger than 70% only. The average throughput for the EUFS algorithm decreases in a sub-linear rate by increasing the probability of PF candidate. This is because the number of assigned RBs to cell-edge users decreases as the probability of PF candidates is increased. The highest throughput increase using our algorithm compared to the pure PF algorithm occurs at the lowest probabilities assigned to PF candidates. As seen in Fig. 2, we got an increase of 2x of cell-edge user performance when the initial probability of PF candidates is 70%. The increase is about 1.5x when increasing the PF probability between 80% and 90%.

Next, we examine the average throughput across all cell-centric users while decreasing the PF candidates' probability. As shown in Fig. 2, the average throughput for cell-centric users relative to a pure PF scheduler (on the y-axis) is decreasing in a sub-linear manner while the probability assigned to the PF candidate (on the x-axis) decreases. By decreasing the probability of PF candidates, more RBs are given to cell-edge users and less are given to cell-centric users as compared to a pure PF scheduler. The proposed EUFS algorithm guarantees that the amount of RBs drawn from conventional PF candidates, as supposed to be carried out in pure PF scheduler, to be given to cell-edge users do not degrade the overall performance of the latter that much because the taken RBs is drawn in a distributive manner to avoid concentrating the losses in one or few users which could cause degradation to their accomplished throughputs. It is also shown in Fig. 2 that the largest decrease to all cell-centric users throughput occurs at the lowest probability for PF candidates. Regarding the EUFS algorithm, the maximum decrease in cell-centric user throughput was approximately 25%, and this occurred when the initial probability of PF can-didates was set to 82%. This decrease is shrinking to about 10% when increasing the probability of PF can-didates beyond 70%.

By investigating the performance of both cell-edge and cell-centric users simultaneously while changing the probability of PF candidates, the best tradeoff is to assign probabilities to PF candi-

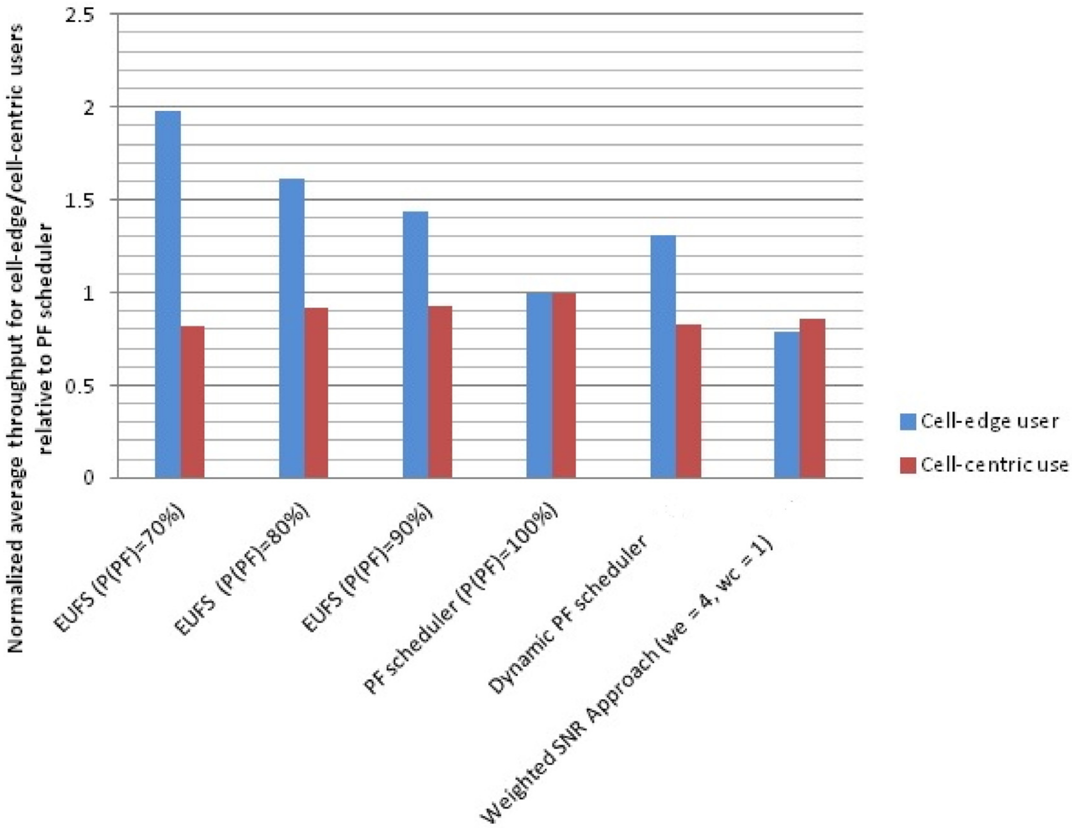

Fig. 2. Performance comparison for cell-edge/cell-centric users using different scheduling algorithms and fixed number of users.

dates from 80% to 90%. This increases the average throughput for cell-edge users to about 150%, while reducing the average throughput for cell-centric users by only about 10%. Operators could decide to further improve the cell-edge performance on the cost of additional degradation for the cell-centric user performance. To achieve that, operators could use higher probabilities for PF candidates as demonstrated in the experiments.

Fig. 2 indicates also that our proposed algorithm clearly outperforms the weighted SNR algorithm from [15] in all cases of used PF probabilities. Our algorithm protects the users from being affected sharply by re-adjusting the probabilities when moving from any RB to the next as discussed in Section 3. However, in the weighted SNR algorithm, using fixed weights across the whole TTI does not maintain the adaptability needed, causing aggressive distribution for the RBs among the users. The same behavior is repeated when observing the average throughput of all cell-centric users as shown in Fig. 2.

Furthermore, Fig. 2 indicates that our proposed EUFS algorithm outperforms the dynamic PF algorithm from [16] in all cases of used PF probabilities. Updating scheduling priorities for users to be based on user's averaged SINR - as performed in dynamic PF - seems to be less efficient than using user instantaneous throughput - as used in our proposed algorithm.

Finally, the average throughput of all considered cell-edge users (featured users) has been observed for different number of users per cell. To this end, we keep the initial probabilities of the PF candidate user at 80%. Fig. 3 shows the average throughput for cell-edge users relative to a pure PF scheduler across the different scheduling techniques (on the y-axis) versus the total number of users per cell as well as the number of cell-edge users per cell (on the x-axis). Our proposed EUFS algorithm outperforms other scheduling algorithms in all values of number of UEs/cell. When comparing EUFS to PF algorithm, we could notice that at lower number of UEs/cell, the amount of increase in the average throughput is higher due to the abundance of RBs/users ratio unlike at higher number of UEs/cell. For instance, at 10 UEs/cell, the average throughput for cell-edge users using EUFS algorithm is about 150% compared to PF algorithm. While at 60 UEs/cell, the average throughput for cell-edge users using EUFS algorithm is about only 125% compared to PF algorithm. As explained before, EUFS algorithm guarantees that more RBs are given to cell-edge users compared to the pure PF scheduler, which add to their achieved throughput.

Fig. 3 indicates also that our proposed algorithm is better than the weighted SNR algorithm [15], since EUFS algorithm implies dynamic probabilities by re-adjusting the probabilities when moving from any RB to the next as discussed in Section 3. However, in the weighted SNR algorithm, fixed weights are used across the whole TTI which does not maintain the adaptability needed, causing aggressive distribution for the RBs among the users. Furthermore, Fig. 3 indicates that our proposed EUFS algorithm outperforms the dynamic PF algorithm from [16] as updating scheduling priorities for users to be based on user's averaged SNR - as performed in dynamic PF - seems to be less efficient than using user instantaneous throughput - as used in our proposed algorithm.

5.3. Assessing the SNR

In the third experiment, we examine the average SNR for cell-edge and cell-centric users while varying the total number of users per cell and keeping the number of total RBs fixed at 100 RBs/cell. The goal is to test the scalability of our proposal compared to other algorithms. Figs. 4 and 5 depict the average SNR relative to a pure PF scheduler operating at 60 users/cell (on the y-axis) versus the used number of users per cell (on the x-axis) for cell-edge users and cell-centric users, respectively. The average SNR for cell-edge

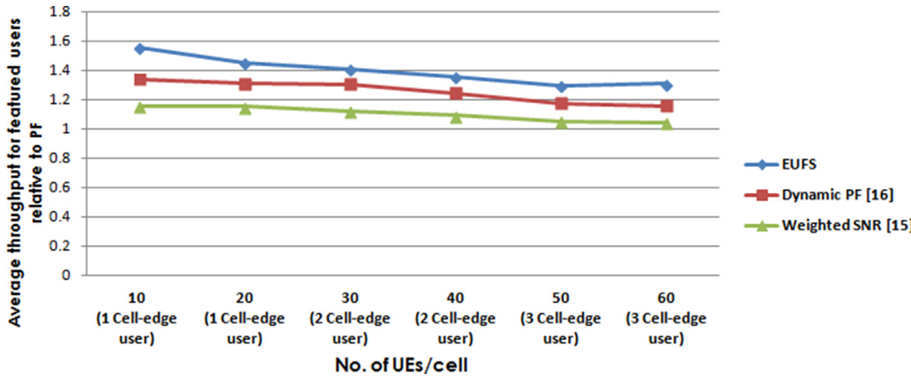

Fig. 3. Performance comparison for cell-edge users using different scheduling algorithms and variable number of users.

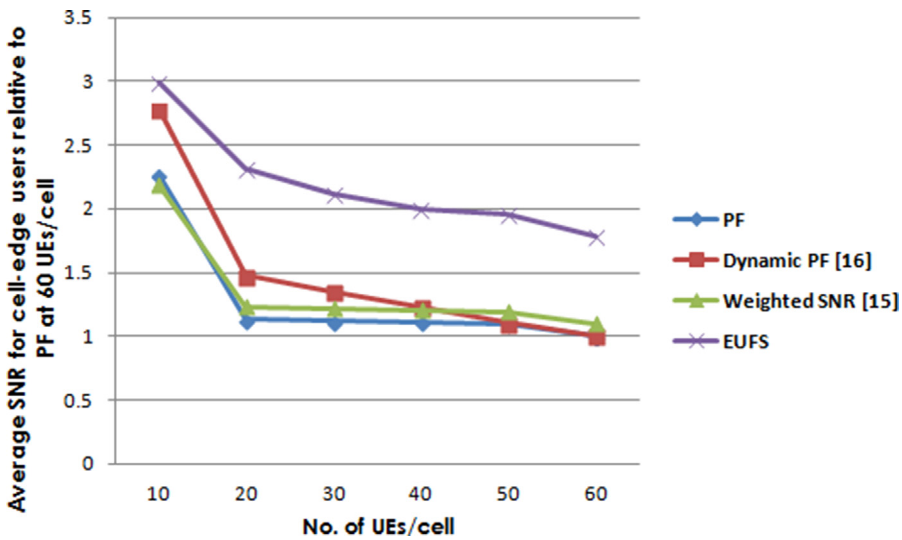

Fig. 4. Comparing SNR for cell-edge users using different scheduling algorithms.

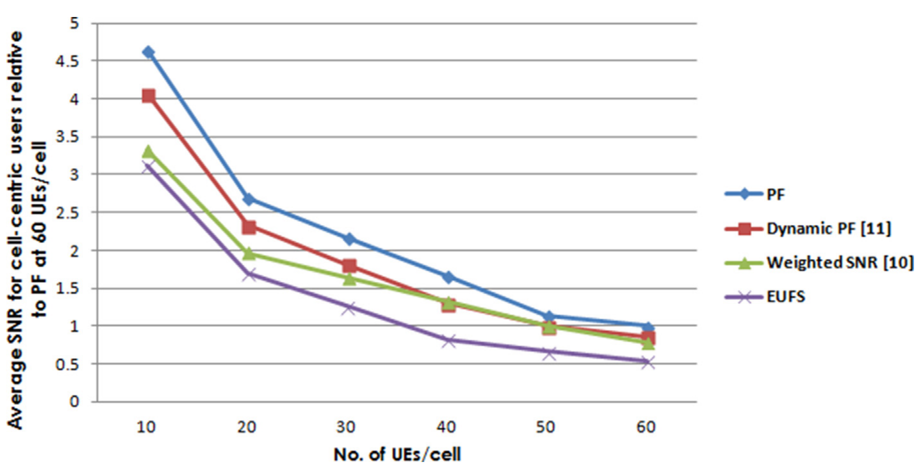

Fig. 5. Comparing SNR for cell-centric users using different scheduling algorithms.

users in EUFS algorithm is the highest compared to other algorithms as shown in Fig. 4. In other words, EUFS algorithm is the most beneficial to cell-edge users. This comes at the expense of the SNR for cell-centric users which is the lowest using EUFS algorithm, as shown in Fig. 5. However, for the EUFS algorithm, cell-edge users gain 80% increase in the SNR relative to PF at 60 UEs/-cell, compared to only 45% reduction in the SNR for cell-centric users relative to PF at 60 UEs/cell.

At lower numbers of users (e.g., 10 users/cell), the increase in the average SNR for cell-edge users using the EUFS algorithm is noticeable, as the average number of RBs/users is high (≈ 10 RBs/user/cell). On the contrary, the percentage of increase in the average SNR for cell-edge users using the EUFS algorithm shrinks at higher number of users per cell as the average number of RBs/users becomes low. By increasing the number of users per cell, the boost of SNR for cell-edge users increases from 55% to 80%. While the loss

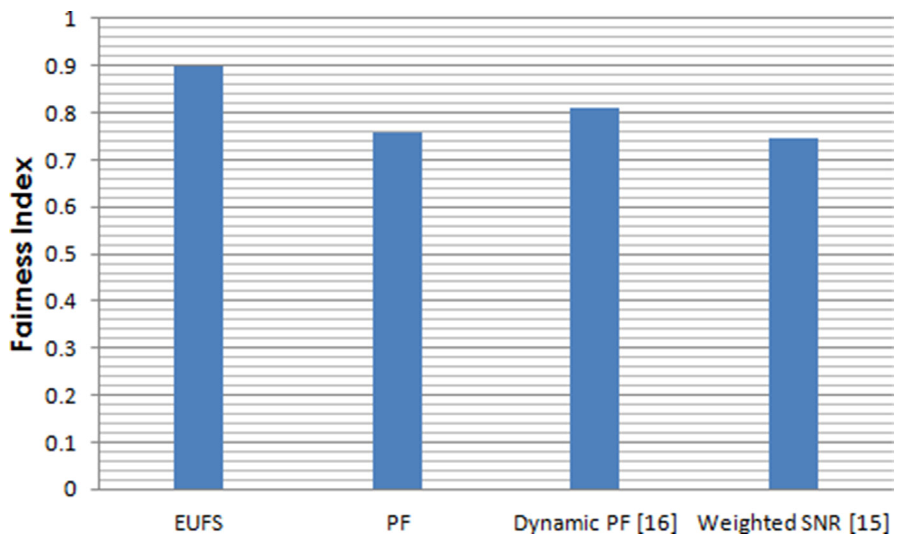

Fig. 6. Fairness Index Comparison.

in SNR for cell-centric users ranges from 45% to 35% compared to PF. Several techniques are available in the literature to enhance the achieved SNR more such as COMP [17–20] and heterogeneous networks [2], which are beyond the scope of this paper.

Fig. 4 indicates also that our proposed algorithm is better than the Dynamic PF algorithm [15] for cell-edge users as the latter implies a threshold for the maximum time in which the cell-edge users would be favored within. Hence, using the dynamic PF scheduler, cell-edge users staying relatively long in the cell-edge area are assigned lower RBs than when using the EUFS algorithm. The EUFS algorithm serves cell-edge users as long as they experience poor signal strengths and with no limitation in time, as explained in Section 3. At the lowest number of UEs/cell used (i.e., 10 UEs/cell), the average RBs per user is 10 RBs/user/cell. Hence, the dynamic PF scheduler will compensate the cell-edge users, which have been punished due to their long stay in the cell-edge area, more efficiently by exploiting the relatively high average RBs per user compared to other cases. As a result, the SNR achieved by the dynamic PF scheduler at 10 UEs/cell is significantly higher and approaching the SNR results of the EUFS algorithm compared to other cases of number of UEs/cell.

5.4. Assessing the fairness

In the fourth experiment, we use Jain's fairness index [27] to measure the fairness of the system across all algorithms. Jain's fairness index is maximum (i.e., unity) when all users achieve the same throughput. The closer all user throughputs are to each other, the larger Jain's fairness index. Fig. 6 indicates that the EUFS algorithm outperforms the other algorithms in terms of the fairness index achieved (i.e., 0.897). According to the definition of Jain's fairness index provided in Section 4, and the nature of operation for the EUFS algorithm, we could notice that while increasing the throughput of cell-edge users and decreasing the throughput of cell-centric users simultaneously, the two throughputs seem to be approaching their mean (i.e., the fair throughput). Therefore, this makes EUFS algorithm maintain a longer term of fairness than other methods.

5.5. Assessing the execution time

In the fifth experiment, we investigate the execution time needed for each algorithm to make sure that the EUFS algorithm fits our real-time application. Since the EUFS includes implementing the PF algorithm as a preliminary step as discussed in Section 3, it consumes more time than PF algorithm. However, this increase do not exceed 7.5% from total PF execution time.

6. Conclusion

The proposed algorithm has proven to achieve better performance for cell-edge users compared to PF scheduler used in LTE. In addition, it has shown that the side effects on cell-centric users' performance resulting from decreasing the RBs that they were supposed to take in PF technique are limited. A performance comparison with the leading scheduling methodology in LTE has been quantitatively evaluated for featured and non-featured users. Performed experiments have been shown that the best trade-off is to assign probabilities to PF candidates from 80% to 90% so as to multiply the average throughput for beneficial users approximately about 150%. Consequently, this will reduce the average throughput for non-beneficial users to only about 10%. Our algorithm could further take advantage of COMP and joint scheduling techniques to increase the overall system performance among all users.

References

[1] W.N.. D.B.. J.L.. I. Kang. Advanced interference management for 5g cellular networks. IEEE Commun Mag 2014;52(5):52–60. doi:10.1109/MCOM.2014.6815893.
[2] J.G.A.. S.B.. W.C.. S.V.H.. A.L.. A.C.K.S.. J.C. Zhang, What will 5g be?, IEEE J Sel Areas Commun 2014;32(6):1065–82. doi:10.1109/JSAC.2014.2328098.
[3] Evolved universal terrestrial radio access (e-utra); user equipment (ue) radio transmission and reception, version 10.4.0; 2011. https://www.3gpp.org/ [accessed: 2019-8-22].

[4] Evolved universal terrestrial radio access (e-utra) and evolved universal terrestrial radio access network (e-utran); overall description; stage 2; 2012. https://www.3gpp.org/ [accessed: 2019-8-22].
[5] Evolved universal terrestrial radio access (e-utra): Physical layer procedures. v11.11.0; 2013. https://www.3gpp.org/ [accessed: 2019-8-22].
[6] Third generation partnership project. https://www.3gpp.org/ [accessed: 2019-10-22].
[7] G.P.. L.A.G.. G.B.. F.C.. P. Camarda, Simulating lte cellular systems: an open source framework. IEEE Trans Veh Technol 2011;60(2):52–60. doi:10.1109/TVT.2010.2091660.
[8] P.K.. S.K.. C. Dabas. Comparative analysis of downlink scheduling algorithms for a cell affected by interference in lte network. Ann Data Sci 2016;3(2):135–53. doi: https://doi.org/10.1007/s40745-016-0076-x [Springer-Verlag Berlin Heidelberg].
[9] Kumar M. Fractional order fir differentiator design using particle swarm optimization algorithm. Int J Numer Model Electron Netw Dev Fields 2019;32(2):e2514. doi: https://doi.org/10.1002/jnm.2514.
[10] S.S.. A.A.. M.K.. T.K. Rawat, Adaptive infinite impulse response system identification using teacher learner based optimization algorithm. Appl Intell 2019;49:1785–802. doi: 10.1007/s10489-018-1354-4.
[11] Aggarwal A, Rawat T, Kumar M, Upadhyay D. Design of optimal band-stop fir filter using l1-norm based rcga. Ain Shams Eng J 2018;9(2):277–89. doi: https://doi.org/10.1016/j.asej.2015.11.022.
[12] L.S. P.W. F. Liu. Particle swarm optimization based resource block allocation algorithm for downlink lte systems. In: 18th Asia-Pacific Conference on Communications (APCC), Jeju Island; 2012. p. 970–4.
[13] F.H.T.V.. B.H.P.G.. F.G.C.R.. L.L.L.. M.V.G. Ferreira. Dynamic resource allocation in lte systems using an algorithm based on particle swarm optimization and bmwm network traffic modeling. In: Proceedings of IEEE 6th Latin American Symposium on Circuits & Systems (LASCAS). Montevideo, Uruguay: IEEE; 2015. p. 1–13.
[14] E.D.. S.P.. J.S.. P. Beming. 3G Evolution: HSPA and LTE for Mobile Broadband. Academic Press; 2008.
[15] Y.Y.. D.E.. X.H.. M.M. Downlink resource allocation for next generation wireless networks with inter-cell interference. IEEE Trans Wireless Commun 2013;12:1793–83. doi: 10.1109/TWC.2013.030413.120760.
[16] X.N.. V.G.. Z.W.. Q. Yongquan. A dynamic pf scheduler to improve the cell edge performance. In: Proceedings of IEEE 68th Vehicular Technology Conference (VTC 2008-Fall). Moscow, Russia: IEEE; 2008. p. 1–5.
[17] Nokia lte smart scheduler white paper. https://onestore.nokia.com/asset/200170?download [accessed: 2019-8-22].
[18] S.K.. S.D.. H.M. Gupta, Co-operative downlink scheduling for cell edge and handoff users. In: Proceedings of IEEE Wireless Communications and Networking Conference (WCNC): Mobile and Wireless Networks. Paris, France: IEEE; 2012. p. 1–6.
[19] G.V.. A.T.. J.J.. M. Juntti. Iterative scheduling for cell-edge in multi-cell mu-mimo. In: Proceedings of IEEE Global Conference on Signal and Information Processing (GlobalSIP). Texas, USA: IEEE; 2013. p. 1–6.
[20] M.A.. M. Mehrjoo. Improving the performance of cell edge users with fractional coordinated fair scheduling. Inst Eng Technol (IET) Commun 2014;8(13):2315–21. doi:10.1109/MCOM.2014.6815893.
[21] S.M.. J. Rodriguez. Green Communication for 4G Wireless Systems. River Publishers; 2013.
[22] A.-M.B.. N.N.. H.H. Downlink scheduling with economic considerations for future wireless networks. IEEE Trans Veh Technol 2009;58(2):835–824. doi:10.1109/TVT.2008.927039.
[23] Y.-C.W.. T.-Y. Tsai. A pricing-aware resource scheduling framework for lte networks. IEEE/ACM Trans Netw 2017;25(3):1–14. doi: 10.1109/TNET.2016.2629501.
[24] G.P.. L.A.G.. G.B.. R.F.. P. Camarda. Two-level downlink scheduling for real-time multimedia services in lte networks. IEEE Trans Multimedia 2011;13(5):1052–65. doi:10.1109/TMM.2011.2152381.
[25] Vienna lte-a simulators, https://www.nt.tuwien.ac.at/research/mobile-communications/vienna-lte-a-simulators [accessed: 2019-8-22].
[26] 3gpp lte release-8. http://www.3gpp.org/specifications/releases/72-release-8 [accessed: 2019-8-22].
[27] A quantitative measure of fairness and discrimination for resource allocation in shared computer systems; 1984.

Model of the DFIG considering coordinated control strategy of grid and rotor-side converters

Achyutananda Panda, *Department of Electrical and Electronics Engineering, NM Institute of Engineering & Technology, Bhubaneswar, achyutananda.panda55@gmail.com*

Sunita Baral, *Department of Electrical Engineering , Capital Engineering College, Bhubaneswar, sunita.baral95@gmail.com*

Srinivas, *Department of Electrical and Electronics Engineering, Aryan Institute of Engineering & Technology, Bhubaneswar, srinivas225@gmail.com*

Asheerbad Pradhan, *Department of Electronics and Communication Engineering , Raajdhani Engineering College, Bhubaneswar, asheerbadpradhan46@gmail.com*

Keywords:
Wind power
DFIG
Coordinated control
Equivalent calculation model
Short-circuit calculation
Slip speed

A B S T R A C T

The short-circuit current calculation is of vital importance for the power system. With a high proportion of new energy sources, the setting of relay protection and the selection of electrical equipment have been severely degraded. An accurate short-circuit current calculation model of new energy source is necessary for the short-circuit calculation of power grid with new energy sources. However, due to the DFIG's control system is a "black box", and an accurate fault characteristics and short-circuit current calculation models of DFIG is difficult to obtained. Currently, for the fault current of the DFIG, lots of research works is carried out under symmetrical fault or the crowbar protection is activated condition. However, under crowbar protection is not activated and unsymmetrical fault condition, there are no unified short-circuit calculation models of DFIG. In this paper, the transient process of DFIG under those condition is analyzed, and mathematical expressions are derived. Moreover, the comprehensive and unified short-circuit calculation models of DFIG have established under different low voltage ride through control conditions. The influence of GSC and slip rate of DFIGs can be considered. The test results show that the LVRT control strategies, the GSC and slip have an important influence on the DFIG's short-circuit calculation model. The quantitative research results are of important significance for relay protection setting calculation, grid operation and control, and the selection of electrical equipment of power grid with DFIGs.

1. Introduction

In power systems, an short-circuit current calculation is of vital importance for the power system, it is very important for the setting calculation of relay protection, the selection of electrical equipment and operation control of the power grid. In the traditional power system, the short-circuit current of a synchronous generator is generally more than 3 times the rated value. In order to retain a certain margin, the protection setting value or equipment selection value is generally taken as 1.1∼1.3 times the actual value. However, for a new energy source, the short-circuit current of a new energy source(the crowbar is not activated) is generally less than or equal to 1.3 times of the rated current. At present, as large-scale new energy sources are connected to the power grid, the power system has become a high-proportion new energy power system, it means that the traditional setting methods of relay protection and traditional selection methods of equipment are not applicable. In China, the mis-operation of relay protection system occurs many times in real power grid due to the inaccurate short-circuit model of DFIG. Therefore, the accurate short-circuit calculation model of new energy is necessary for the short-circuit calculation of power grid with new energy sources.

For double-fed induction generator (DFIG), the DFIG into the grid has increased steadily in recent years, the grid codes require wind power generators to not be tripped from the grid but stay connected during fault conditions (Jauch et al., 2005). Thus, wind turbines must have the capability of low voltage ride through (LVRT) (National Grid Plc, 2008; Transmission code, 2007; Technical Rule, 2011). The operation characteristics of a DFIG under the LVRT condition have a large influence on the fault characteristics of current (Howard et al., 2012a). The conventional voltage behind the reactance model typically used for short-circuit calculations is inappropriate for DFIGs. However, because of the trade secrets of the DFIG equipment manufacturer, the DFIG's control system is a "black box", and it is difficult to obtain accurate fault characteristics and short-circuit current calculation models of DFIG. The results of equipment selection and relay protection setting will be seriously affected. Especially, with the increased capacity of DFIG in power grid, this problem is becoming more and more serious in a high-proportion new energy source of power grid, even a 100% new energy source of power grid.

For the fault current characteristics of the DFIG, under symmetrical fault condition or the crowbar protection is activated condition, lots of research works have been carried out (Morren, 2007; Howard et al., 2012b; SnehapravaSwain and KumarRay, 2017; Sulla et al., 2011; Kong et al., 2014; Ouyang and Xiong, 2014). In Morren (2007), Howard et al. (2012b), SnehapravaSwain and KumarRay (2017) and Sulla et al. (2011), the fault characteristics and fault equivalent model of DFIG have been studied under crowbar protection is activated condition. In Kong et al. (2014), Ouyang and Xiong (2014) and Chang et al. (2018a), the fault current characteristics of the DFIG have been studied under crowbar protection is not activated and symmetrical fault condition. In Howard et al. (2015), the short-circuit modeling of DFIGs has been proposed under crowbar protection is not activated and symmetrical fault condition. In Chang et al. (2018b), The short-circuit current characteristics of DFIG before the crowbar protection is activated and the crowbar protection is activated are analyzed. For enhanced operation, the control strategy for suppressing negative sequence current is adopted in unbalanced DFIG conditions (Erlich et al., 2013). Nevertheless, the proposed control targets are only applied to the RSC, and the coordinated control scheme of GSCs and RSCs are not discussed in Chang et al. (2018b) and Erlich et al. (2013). However, under crowbar protection is not activated and unsymmetrical fault condition, the research results are based on simulation analysis and there are no analytical expressions of the fault current of DFIG. Moreover, the influence of different control strategies, GSC and slip rate of DFIGs are not considered, and they have a great influence on the fault current of DFIG under asymmetrical fault and crowbar protection is not activated condition. Hence, further research works on the unified short-circuit current calculation model of DFIG should be conducted.

In this paper, the coordinated control strategies for the RSC and the GSC under unbalanced fault conditions are discussed in Section 2. Then, the corresponding calculation models of the stator and fault currents of the GSC are presented in Section 3. On this basis, the comprehensive and unified short-circuit calculation models of DFIG have established under different low voltage ride through control conditions. Finally, the analytical results have been validated by simulation system with PSCAD/EMTDC and a real test system in Section 4.

2. Coordinated control strategy of DFIG

DFIG is a wound rotor induction generator that is excited by the back-to-back converters, as shown in Fig. 1. The converters are often referred to as RSC and GSC. As shown in Fig. 1, the fault current of DFIG includes the stator current and the fault current of the GSC.

Under fault condition, to provide sufficient reactive current that meets the requirements of the grid code (Technical Rule, 2011), the reactive current reference signal during grid fault and denoted by I_T should be

$$I_T = \begin{cases} 0 & \lambda > 0.9 \\ 1.5 \cdot (0.9 - \lambda) & 0.2 \le \lambda \le 0.9 \end{cases} \tag{1}$$

where all parameters are given in per unit system, and λ represents the magnitude of the positive-sequence grid voltage after a fault occurs.

Moreover, under unsymmetrical fault conditions, the incoming power from the wind and the power flowing into the grid are imbalanced instantaneously, resulting in negative-sequence currents in the stator circuits. The negative-sequence stator currents will result in unbalanced heating on the three-phase stator winding. Hence, the service life of the stator winding will be seriously influenced. Moreover, under unsymmetrical fault conditions, a second harmonic component exists in the electromagnetic torque and output active power of the stator winding, which will result in unreasonable mechanical stress on the turbine system and the fluctuation of the active power in the DFIG. Hence, various control strategies are available, or the DFIG is under balanced and unbalanced grid voltage conditions (Chang et al., 2018b; Erlich et al., 2013). On this basis, the comprehensive coordinated control targets of the GSC and the RSC under unsymmetrical fault conditions can be obtained. **Target A**: Balanced stator current and balanced output current of the DFIG. **Target B**: Eliminate the ripple in the output active power of the stator winding and the active power of the DFIG. **Target C**: Eliminate the ripple in the electromagnetic torque and the reactive power of the DFIG.

The DFIG model is commonly known as the "Park model" in Leonhard (1995), and the GSC model in the positive $(dq)^+$ and negative $(dq)^-$ synchronous rotating reference frames is discussed in Raghavendran et al. (2020).

3. Short-circuit calculation model of DFIG considering coordinated control of RSC and GSC

To analyze the fault current characteristics of the DFIG under the coordinated control for the RSC and GSC conditions, the corresponding short-circuit calculation models of the stator current and the GSC are established according to the different coordinated control targets.

3.1. Short-circuit calculation model of stator current

3.1.1. Calculation model of stator current under the condition of balanced stator current

Under fault conditions, according to the requirements of reactive power support for a DFIG, the q-axis components of the stator current can be expressed as follows:

$$i_{sq}^+ = -1.5 \cdot (0.9 - u_{sd}^+) \tag{2}$$

Under asymmetric fault conditions, the negative-sequence current must be eliminated to ensure balanced heating on the three-phase stator winding. Then, $i_{sd-}^- = i_{sq-}^- = 0$.

Moreover, the stator resistance is extremely small that it can be ignored. In addition, under stable operating condition, $p\psi_{sd+}^+ = p\psi_{sq+}^+ = p\psi_{sd-}^- = p\psi_{sq-}^- = 0$. Consequently, the stator flux linkages of the DFIG in the $(dq)^+$ and $(dq)^-$ reference frames can be obtained as follows:

$$\begin{cases} \psi_{sd+}^+ = 0 \\ \psi_{sq+}^+ = -u_{sd+}^+/\omega_1 \\ \psi_{sd-}^- = 0 \\ \psi_{sq-}^- = u_{sd-}^-/\omega_1. \end{cases} \tag{3}$$

Then, the active and reactive powers provided by the stator of the DFIG can be expressed as follows:

$$\begin{cases} P_{s0} = L_m/L_s \cdot (u_{sd+}^+ i_{rd+}^+ + u_{sd-}^- i_{rd-}^-) \\ Q_{s0} = u_{sd+}^+ i_{sq+}^+ + u_{sd-}^- i_{sq-}^-. \end{cases} \tag{4}$$

where, the $i_{rd+}^+, i_{rq+}^+, i_{rd-}^-$ and i_{rq-}^- are the rotor current in the $(dq)+$ and $(dq)-$ reference frames, respectively.

By substituting (2), (3), (4), and $i_{sd-}^- = i_{sq-}^- = 0$ into the electromagnetic equation, the reference signals of the rotor current in the $(dq)^+$ and $(dq)^-$ reference frames can be obtained as follows:

$$\begin{cases} i_{rd+}^{+*} = (P_{s0}L_s) / \left(u_{sd+}^+ L_m\right) \\ i_{rq+}^{+*} = -u_{sd+}^+ / (\omega_1 L_m) - 1.5 \times \left(0.9 - u_{sd+}^+\right) \cdot L_s/L_m \\ i_{rd-}^{-*} = \psi_{sd-}^-/L_m = 0 \\ i_{rq-}^{-*} = \psi_{sq-}^-/L_m = u_{sd-}^-/(\omega_1 L_m). \end{cases} \tag{5}$$

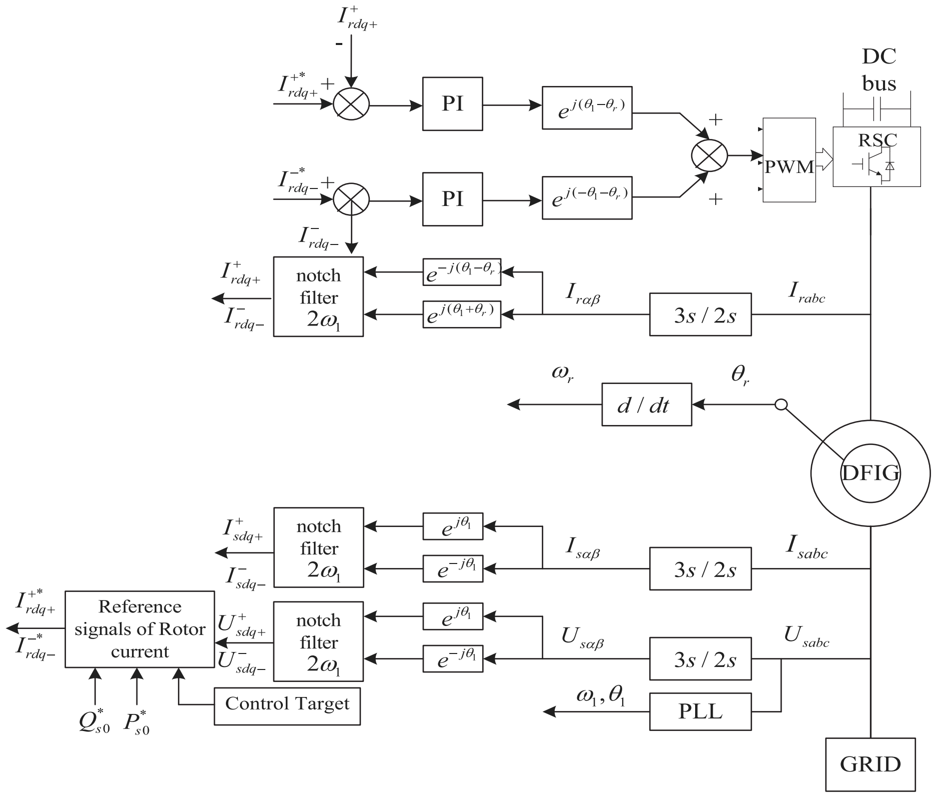

Fig. 1. Control diagram of DFIG under unbalanced grid voltage conditions.

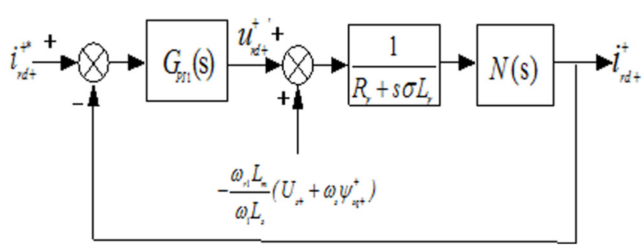

Fig. 2. Simplified block diagram of *d*-axis component in inner rotor current control loop.

In addition, the maximum output current of the RSC is I_{rset}. Therefore, the reference signals of the rotor current will be modified if the real rotor current is higher than the maximum output current. Under this condition, the *q*-axis components of the rotor current in the $(dq)^+$ reference frames can be obtained as follows:

$$i^{+*}_{rd+} = \sqrt{I^2_{rset} - i^{-*2}_{rd-} - i^{+*2}_{rq+} - i^{-*2}_{rq-}} \quad (6)$$

Taking the control diagram of the *d*-axis as an example, the simplified block diagram of the rotor current control loop of the RSC is shown in Fig. 2, where $G_{PI1}(s)$ is the transfer function of the PI controller.

Fig. 2 shows that the open-loop transfer function of the control system without time delay can be presented as

$$G_{PI}(s)G_r(s)N(s) = (k_{irp+} + \frac{k_{iri+}}{s})(\frac{1}{R_r + s\sigma L_r})(\frac{s^2+\omega_n^2}{s^2+2\varepsilon\omega_n s+\omega_n^2}) \quad (7)$$

As shown in Fig. 2, the *d*-axis component of the rotor current in the $(dq)^+$ reference frame is

$$i^+_{rd+}(s) = G^+_{ird1+}(s)i^{+*}_{rd+}(s) - G^+_{ird2+}(s)p\psi^+_{sd+}(s) \quad (8)$$

where:

$$G^+_{ird1+}(s) = \frac{G_{PI1}(s)N(s)}{R_r + s\sigma L_r + G_{PI1}(s)N(s)} \quad (9)$$

and:

$$G^+_{ird2+}(s) = \frac{N(s)}{R_r + s\sigma L_r + G_{PI1}(s)N(s)} \quad (10)$$

In (9), the range of the imaginary part for the dominant pole is between 610 and 640. Thus, the response component of the dominant poles of the system will be limited by the notch filters. Hence, $G^+_{ird1+}(s) \approx 1$.

Correspondingly, the bode diagram of $G^+_{ird2+}(s)$ is shown in Fig. 3. It can be seen form Fig. 3, the maximum gain of the closed-loop transfer function to the disturbance component at $\omega = \omega_1$ is nearly −55 dB. Hence, i^+_{rd+2} is approximately equal to 0.

Hence, during the fault transient period, the rotor currents in the $(dq)^+$ reference frame are

$$\begin{cases} i^+_{rd+} \approx i^{+*}_{rd+} \\ i^+_{rq+} \approx i^{+*}_{rq+}. \end{cases} \quad (11)$$

Consequently, for Target A, the stator currents in the $(dq)^+$ reference frame can be derived as

$$\begin{cases} i^+_{sd+} = -\frac{L_m}{L_s}\min\left[(P_{s0}L_s)/(u^+_{sd+}L_m), \sqrt{I^2_{rset} - i^{+*2}_{rq+} - i^{-*2}_{rq-}}\right] \\ i^+_{sq+} = 1.5 \times (0.9 - u^+_{sd+}) \\ i^-_{sd-} = 0 \\ i^-_{sq-} = 0. \end{cases} \quad (12)$$

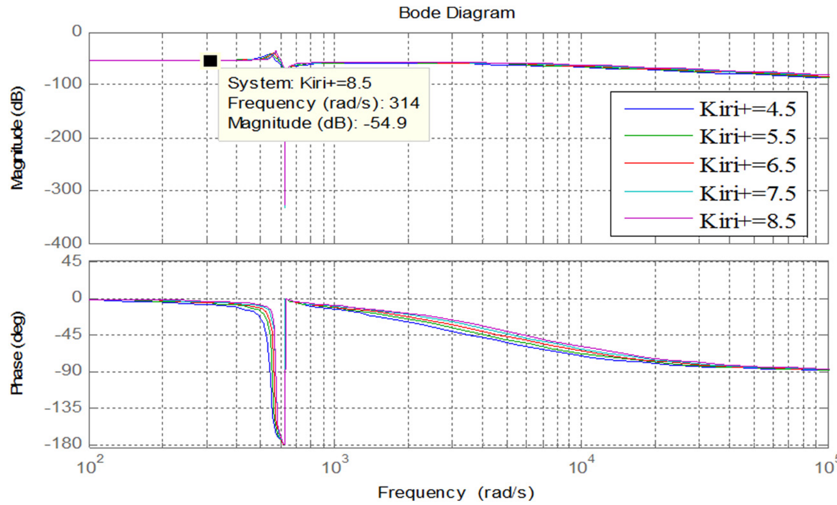

Fig. 3. Bode diagram of the harmonic component in $p\Delta\varphi_{sd}$.

3.1.2. Calculation model of stator current under condition to eliminate the $2\omega_1$ ripple in the output active power

Under unsymmetrical fault conditions, a second harmonic component exists in the stator active power.

$$\begin{cases} P_{s0} = L_m/L_s \cdot (u^+_{sd+}i^+_{rd+} + u^-_{sd-}i^-_{rd-}) \\ P_{s\sin 2} = -\dfrac{2u^+_{sd+}u^-_{sd-}}{\omega_1 L_s} + L_m/L_s \cdot (-u^-_{sd-}i^+_{rq+} + u^+_{sd+}i^-_{rq-}) \\ P_{s\cos 2} = L_m/L_s \cdot (u^-_{sd-}i^+_{rd+} + u^+_{sd+}i^-_{rd-}) \end{cases} \tag{13}$$

The $2\omega_1$ ripple in the output active power of the stator winding can be eliminated as follows:

$$P_{s\sin 2} = P_{s\cos 2} = 0. \tag{14}$$

Accordingly, the reference signals of the rotor current can be obtained as follows:

$$\begin{cases} i^{+*}_{rd+} = \left(L_s u^+_{sd+}P_{s0}\right) / \left[L_m(u^{+2}_{sd+} - u^{-2}_{sd-})\right] \\ i^{-*}_{rd-} = -u^-_{sd-}/u^+_{sd+} \cdot i^{+*}_{rd+} \\ i^{-*}_{rq-} = 2u^-_{sd-}/\left(\omega_1 L_m\right) + u^-_{sd-}/u^+_{sd+} \cdot i^{+*}_{rq+}. \end{cases} \tag{15}$$

To meet the reactive requirements of the grid code, the output reactive power of the stator winding can be obtained as

$$Q_{s0} = u^+_{sd+}i^+_{sq+} + u^-_{sd-}i^-_{sq-} = 1.5 \times \left(0.9 - u^+_{sd+}\right) u^+_{sd+}. \tag{16}$$

Accordingly, the q-axis components of the stator current can be expressed as follows:

$$i^+_{sq+} = \left[1.5 \times \left(0.9 - u^+_{sd+}\right) u^{+2}_{sd+}\right] / \left(u^{+2}_{sd+} - u^{-2}_{sd-}\right). \tag{17}$$

Consequently, the q-axis components of the rotor current can be obtained as

$$i^{+*}_{rq+} = -\frac{u^+_{sd+}}{\omega_1 L_m} - \frac{1.5L_s\left(0.9 - u^+_{sd+}\right) u^{+2}_{sd+}}{L_m\left(u^{+2}_{sd+} - u^{-2}_{sd-}\right)}. \tag{18}$$

If $\left(i^{+*}_{rd+}\right)^2 + \left(-u^-_{sd-}/u^+_{sd+} \cdot i^{+*}_{rd+}\right)^2 + i^{+*2}_{rq+} + i^{-*2}_{rq-} \geq I^2_{\mathrm{rset}}$, then the d-axis components of the rotor current can be obtained as follows:

$$i^{+*\prime}_{rd+} = \frac{u^+_{sd+}}{\sqrt{u^{+2}_{sd+} + u^{-2}_{sd-}}}\sqrt{I^2_{\mathrm{rset}} - i^{+*2}_{rq+} - i^{-*2}_{rq-}}. \tag{19}$$

Consequently, if Target B is applied in the DFIG, then the dc component of the stator currents can be derived as

$$\begin{cases} i^+_{sd+} = -\dfrac{L_m}{L_s}\min\left(\dfrac{u^+_{sd+}P_{s0}}{u^{+2}_{sd+} - u^{-2}_{sd-}}, \dfrac{u^+_{sd+}}{\sqrt{u^{+2}_{sd+} + u^{-2}_{sd-}}}\sqrt{I^2_{\mathrm{rset}} - i^{+*2}_{rq+} - i^{-*2}_{rq-}}\right) \\ i^+_{sq+} = \left[1.5 \times \left(0.9 - u^+_{sd+}\right) u^{+2}_{sd+}\right] / \left(u^{+2}_{sd+} - u^{-2}_{sd-}\right) \\ i^-_{sd-} = -\dfrac{u^-_{sd-}}{u^+_{sd+}}i^+_{sd+} i^-_{sq-} = \dfrac{u^-_{sd-}}{u^+_{sd+}}i^+_{sq+}. \end{cases} \tag{20}$$

3.1.3. Calculation model of stator current under condition to eliminate the $2\omega_1$ ripple in the electromagnetic torque

Under unsymmetrical fault conditions, the second harmonic and fundamental frequency components of the electromagnetic torque can be expressed as follows:

$$\begin{cases} P_{e0} = \dfrac{L_m\omega_r}{L_s\omega_1}(u^+_{sd+}i^+_{rd+} - u^-_{sd-}i^-_{rd-}) \\ P_{e\sin 2} = \dfrac{L_m\omega_r}{L_s\omega_1}(u^-_{sd-}i^+_{rq+} + u^+_{sd+}i^-_{rq-}) \\ P_{e\cos 2} = \dfrac{L_m\omega_r}{L_s\omega_1}(-u^-_{sd-}i^+_{rd+} + u^+_{sd+}i^-_{rd-}) \end{cases}. \tag{21}$$

The $2\omega_1$ ripple in the output active power of the stator winding can be eliminated as follows:

$$P_{e\sin 2} = P_{e\cos 2} = 0. \tag{22}$$

Accordingly, the reference signals of the rotor current can be obtained as

$$\begin{cases} i^{+*}_{rd+} = \left(L_s u^+_{sd+}P_{s0}\right) / \left[L_m(u^{+2}_{sd+} + u^{-2}_{sd-})\right] \\ i^{-*}_{rd-} = u^-_{sd-}/u^+_{sd+} \cdot i^{+*}_{rd+} \\ i^{-*}_{rq-} = -u^-_{sd-}/u^+_{sd+} \cdot i^{+*}_{rq+}. \end{cases} \tag{23}$$

To meet the reactive requirements of the grid code, the q-axis components of the stator current can be expressed as follows:

$$i^+_{sq+} = \left[1.5 \times \left(0.9 - u^+_{sd+}\right) u^{+2}_{sd+}\right] / \left(u^{+2}_{sd+} + u^{-2}_{sd-}\right). \tag{24}$$

Consequently, the q-axis components of the rotor current in the $(dq)^+$ reference frames can be obtained as follows:

$$i^{+*}_{rq+} = -\frac{u^+_{sd+}}{\omega_1 L_m} - \frac{1.5L_s\left(0.9 - u^+_{sd+}\right) u^{+2}_{sd+}}{L_m\left(u^{+2}_{sd+} + u^{-2}_{sd-}\right)}. \tag{25}$$

If $\left(i_{rd+}^{+*}\right)^2 + \left(-u_{sd-}^{-}/u_{sd+}^{+} \cdot i_{rd+}^{+*}\right)^2 + i_{rq+}^{+*2} + i_{rq-}^{-*2} \geq I_{rset}^2$, then the d-axis components of the rotor current in the $(dq)^+$ reference frames can be obtained as follows:

$$i_{rd+}^{+*\prime} = \frac{u_{sd+}^{+}}{\sqrt{u_{sd+}^{+2} + u_{sd-}^{-2}}}\sqrt{I_{rset}^2 - i_{rq+}^{+*2} - i_{rq-}^{-*2}}. \tag{26}$$

Then, if Target C is applied in the DFIG, the dc component of the stator currents can be derived as

$$\begin{cases} i_{sd+}^{+} = -\dfrac{L_m}{L_s}\min\left(\dfrac{u_{sd+}^{+}P_{s0}}{u_{sd+}^{+2} + u_{sd-}^{-2}},\right. \\ \left.\dfrac{u_{sd+}^{+}}{\sqrt{u_{sd+}^{+2} + u_{sd-}^{-2}}}\sqrt{I_{rset}^2 - i_{rq+}^{+*2} - i_{rq-}^{-*2}}\right) \\ i_{sq+}^{+} = \dfrac{1.5 \times \left(0.9 - u_{sd+}^{+}\right)u_{sd+}^{+2}}{u_{sd+}^{+2} + u_{sd-}^{-2}} \\ i_{sd-}^{-} = \dfrac{u_{sd-}^{-}}{u_{sd+}^{+}}i_{sd+}^{+} i_{sq-}^{-} = -\dfrac{u_{sd-}^{-}}{u_{sd+}^{+}}i_{sq+}^{+}. \end{cases} \tag{27}$$

3.2. Short-circuit calculation model of the output current of GSC

3.2.1. Calculation model of the GSC under condition of the balanced stator current

Under unsymmetrical fault conditions, the negative-sequence components of the GSC must be eliminated. Then, $i_{gd-}^{-*} = i_{gq-}^{-*} = 0$. The output active power form the GSC to the power grid is $P_{g0} = -u_{gd+}^{+}i_{gd+}^{+} - u_{gd-}^{-}i_{gd-}^{-}$. Hence, the reference signals of the d-axis components on the GSC can be obtained as follows:

$$i_{gd+}^{+*} = -P_{g0}/u_{gd+}^{+}. \tag{28}$$

Under the stable operating condition, the DC bus voltage is constant. Then, $pu_{dc} = 0$. Hence, the output active power of the RSC is equal to that of the GSC according to (6).

$$P_{g0} = P_{r0} = P_{e0} - P_{s0} \tag{29}$$

Then,

$$P_{g0} = -\frac{\omega_{slip+}L_m}{L_s}u_{sd+}^{+}i_{rd+}^{+} + \frac{\omega_{slip-}L_m}{L_s}u_{sd-}^{-}i_{rd-}^{-}. \tag{30}$$

The voltage equations of the rotor winding can be obtained as follows:

$$\begin{cases} u_{rd+}^{+} = -\omega_{slip+}(L_m i_{sq+}^{+} + L_s i_{rq+}^{+}) \\ u_{rd-}^{-} = -\omega_{slip-}(L_m i_{sq-}^{-} + L_s i_{rq-}^{-}) \end{cases}. \tag{31}$$

Accordingly, if Target A is applied in the GSC, the DC component of the GSC can be derived as

$$i_{gd+}^{+} = -P_{g0}/u_{gd+}^{+}, i_{gq+}^{+} = 0, i_{gd-}^{-} = 0, i_{gq\_}^{-} = 0\ . \tag{32}$$

Given that the capacity of the RSC is equal to that of the GSC, the corresponding current-limiting scheme of the GSC cannot be considered.

3.2.2. Calculation model of the GSC under condition to eliminate the $2\omega_1$ ripple in the output active power

Under unsymmetrical fault conditions, the second harmonic and fundamental frequency components of the output active power can be expressed as

$$\begin{cases} P_{g0} = -u_{gd+}^{+}i_{gd+}^{+} - u_{gd-}^{-}i_{gd-}^{-} \\ Q_{g0} = u_{gd+}^{+}i_{gq+}^{+} + u_{gd-}^{-}i_{gd-}^{-} \\ P_{g\sin 2} = u_{gd-}^{-}i_{gq+}^{+} - u_{gd+}^{+}i_{gq-}^{-} \\ P_{g\cos 2} = -u_{gd-}^{-}i_{gd+}^{+} - u_{gd+}^{+}i_{gd-}^{-} \end{cases} \tag{33}$$

The $2\omega_1$ ripple in the output active power of the GSC can be eliminated as follows:

$$P_{g\sin 2} = P_{g\cos 2} = 0 \tag{34}$$

Hence, under unsymmetrical fault conditions, the dc component of the GSC can be derived as

$$\begin{cases} i_{gd+}^{+} = -\left(u_{gd+}^{+}P_{g0}\right)/\left(u_{gd+}^{+2} - u_{gd-}^{-2}\right)i_{gq+}^{+} = 0 \\ i_{gd-}^{-} = \left(u_{gd-}^{-}P_{g0}\right)/\left(u_{gd+}^{+2} - u_{gd-}^{-2}\right)i_{gq-}^{-} = 0 \end{cases} \tag{35}$$

3.2.3. Calculation model of the GSC under condition to eliminate the $2\omega_1$ ripple in the reactive power of the DFIG

Under unsymmetrical fault conditions, the second harmonic component of the reactive power of the DFIG can be expressed as

$$\begin{cases} Q_{s\sin 2} = L_m/L_s \cdot -u_{sd-}^{-}i_{rd+}^{+} + u_{sd+}^{+}i_{rd-}^{-} \\ Q_{s\cos 2} = -L_m/L_s \cdot u_{sd-}^{-}i_{rq+}^{+} + u_{sd+}^{+}i_{rq-}^{-} \end{cases} \tag{36}$$

If Target C is applied in the DFIG, then (26) shows that the $2\omega_1$ ripple has been eliminated not only in the electromagnetic torque of the DFIG but also in the output reactive power of the stator winding. Then, the second harmonic and fundamental frequency components of the reactive power in the GSC can be expressed as

$$\begin{cases} Q_{g0} = u_{gd+}^{+}i_{gq+}^{+} + u_{gd-}^{-}i_{gd-}^{-} \\ Q_{g\sin 2} = u_{gd-}^{-}i_{gd+}^{+} - u_{gd+}^{+}i_{gd-}^{-} \\ Q_{g\cos 2} = u_{gd-}^{-}i_{gq+}^{+} + u_{gd+}^{+}i_{gq-}^{-} \end{cases} \tag{37}$$

Assume that the second harmonic components of the reactive power in the GSC are equal to zero, $Q_{g\sin 2} = Q_{g\cos 2} = 0$. Hence, the dc component of the GSC in the $(dq)^+$ and $(dq)^-$ reference frames can be derived as

$$\begin{cases} i_{gd+}^{+} = -\left(u_{gd+}^{+}P_{g0}\right)/\left(u_{gd+}^{+2} + u_{gd-}^{-2}\right),\ i_{gq+}^{+} = 0 \\ i_{gd-}^{-} = -\left(u_{gd-}^{-}P_{g0}\right)/\left(u_{gd+}^{+2} + u_{gd-}^{-2}\right),\ i_{gq-}^{-} = 0 \end{cases} \tag{38}$$

3.3. Short-circuit calculation model of DFIG

The positive-sequence component of the output current of the DFIG can be represented as a controlled positive-sequence current source, $\dot{I}_{DFIG(1)} = f_{DFIG(1)}\left(\dot{V}_{DFIG(1)}, \dot{V}_{DFIG(2)}\right)$. The amplitude and angle of the controlled positive-sequence current source can be expressed as

$$\begin{cases} I_{DFIG(1)} = \sqrt{\left(-i_{sd+}^{+} - i_{gd+}^{+}\right)^2 + \left(-i_{sq+}^{+}\right)^2} \\ \delta_{i(1)} = \arctan\left[-i_{sq+}^{+}/\left(-i_{sd+}^{+} - i_{gd+}^{+}\right)\right] + \delta_{v(1)} \end{cases} \tag{39}$$

where $\delta_{v(1)}$ is the phase angle of the positive-sequence terminal voltage vector.

Likewise, the negative-sequence component of the output current of the DFIG can be represented as a controlled negative-sequence current source, $\dot{I}_{DFIG(2)} = f_{DFIG(2)}\left(\dot{V}_{DFIG(1)}, \dot{V}_{DFIG(2)}\right)$. The amplitude and angle of the controlled negative-sequence current source can be expressed as

$$\begin{cases} I_{DFIG(2)} = \sqrt{\left(-i_{sd-}^{-} - i_{gd-}^{-}\right)^2 + \left(-i_{sq-}^{-}\right)^2} \\ \delta_{i(2)} = \arctan\left[-i_{sq-}^{-}/\left(-i_{sd-}^{-} - i_{gd-}^{-}\right)\right] + \delta_{v(2)} \end{cases} \tag{40}$$

where $\delta_{v(2)}$ is the phase angle of the negative-sequence terminal voltage vector.

On this basis, the steady-state equivalent circuits of the DFIG in positive- and negative-sequence networks are shown in Fig. 4.

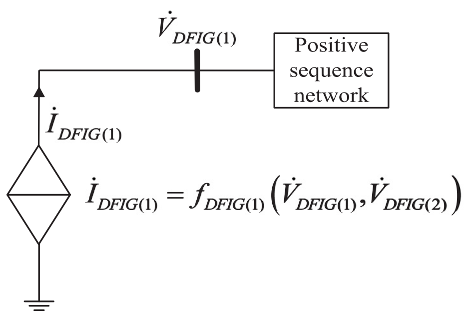

(a) Positive sequence grid network with DFIG

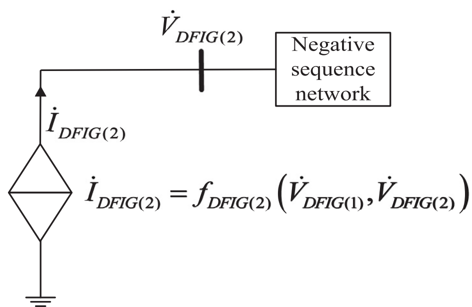

(b) Negative sequence grid network with DFIG

Fig. 4. Equivalent fault circuit of DFIG.

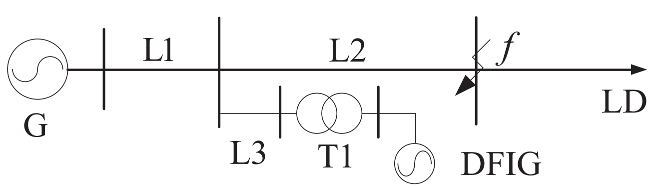

Fig. 5. Test system with DFIG.

4. Simulation study

To validate the short-circuit calculation model of the DFIG, a simulation model of the test system with a DFIG was constructed with PSCAD/EMTDC, as shown in Fig. 5. From the figure, the transmission lines are of the same type, and the line parameters are $r_{(1)} = r_{(2)} = 0.17$ Ω/km, $x_{(1)} = x_{(2)} = 0.394$ Ω/km, $r_{(0)} = 0.19$ Ω/km, and $x_{(0)} = 0.43$ Ω/km. The total lengths of L1, L2, and L3 are 2, 3, and 0.2 km, respectively. The rated capacity of T1 is 2/2 MVA, the turn ratio is 0.69 kV/36.7 5 kV, the winding type is/D, and the leakage reactance is 0.0622 p.u. The equivalent impedance of LD is 120+ j 39.11 Ω. The parameters of the 1.5-MW-rated DFIG are as follows: $U_{sn} = 690$ V, $f_n = 50$ Hz, $L_s = L_r = 2.3192$ p.u., $L_m = 2.1767$ p.u, $R_s = 0.00756$ p.u., $R_r = 0.00533$ p.u., $\omega_c = 7\omega_1$, $p = 2$, and $n_{\max} = 1800$ r/min.

4.1. Three-phase fault

When a three-phase fault occurs at *f*, the calculated and measured values of the fault currents of the DFIG with GSC and the calculated values of the fault currents of the DFIG without GSC for different control targets are compared, as shown in Table 1.

Table 1 shows that the measured values of the output fault current of the DFIG with GSC are approximately equal to the calculated values. It can been seen from Table 1 that, with and without considering GSC, the maximum amplitude error of positive sequence current of DFIG's short-circuit current calculation model is 25.1%, and the angle error is 4.2°. Hence, the influence of the GSC on the fault current of the DFIG cannot be ignored. Moreover, under different LVRT strategies conditions, the differences between the simulation and theoretical analysis results of the DFIG's fault current are small. Therefore, under symmetrical fault conditions, the fault current of DFIG is not necessary to consider the influence of different LVRT control strategies.

Table 1
Fault current on condition that 3-phase fault occurs at f, DFIG is fully loaded before the fault occurs.

	Target A	Target B	Target C
	$I_{DFIG}(1)$	$I_{DFIG}(1)$	$I_{DFIG}(1)$
Measured values (with GSC)	$1.08\angle -5.7°$	$1.08\angle - 5.5°$	$1.07\angle - 5.2°$
Calculated values (with GSC)	$1.05\angle - 4.6°$	$1.05\angle -4.6°$	$1.05\angle -4.6°$
Calculated values (without GSC)	$1.24\angle -1.5°$	$1.24\angle -1.5°$	$1.24\angle -1.5°$

4.2. Unbalanced fault

For asymmetrical fault conditions, the transient characteristics are verified. Among them, a Phase-C ground fault that occurs at f is used for the simulation example. Fig. 6 illustrates the amplitude of the positive- and negative-sequence fundamental frequency components of the stator currents (AMP_{Isa1pp} and AMP_{Isa1nn}), the phase angle of the positive-sequence fundamental frequency component (PH_{Isa1pp}), and the dampened DC component ($AMP_{Isa\ dc}$). The figure shows that the amplitude and phase angle of the positive-sequence fundamental frequency components in the stator currents are related to the corresponding control target of the DFIG and the amplitude of the positive-sequence stator voltage component. Similarly, the negative-sequence current has the same characteristics.

A Phase-B-to-Phase-C fault that occurs at f is used for the simulation example to analyze the steady-state characteristic of the short-circuit current. The output fault currents of the DFIG are studied at various fault conditions, including different fault types and fault points. Under this fault condition, the calculated and measured values of the fault currents of the DFIG with GSC and the calculated values of the fault currents of the DFIG without GSC for different control targets are compared, as shown in Table 2.

Table 2 indicates that the measured values of the output fault currents of the DFIG with GSC under asymmetrical fault conditions are approximately equal to the calculated values. It means that the proposed short-circuit calculation model of the DFIG is valid.

Moreover, it can been seen from Table 2 that, with and without considering different LVRT control strategies, the maximum amplitude error of positive sequence current of DFIG's short-circuit current calculation model is 40.2%, and the angle error is 6.7°. Especially, the negative sequence short-circuit current of DFIG is zero if Target A is applied in the DFIG, and the maximum amplitude of the negative sequence short-circuit current in the DFIG is 0.31 if Target B or Target C is applied in the DFIG. It means that the influence of LVRT control strategies on the DFIG's fault current cannot be ignored.

In addition, under the same LVRT control strategy condition, the maximum amplitude error of positive sequence current of DFIG's short-circuit current calculation model is 35.8%, and the angle error is 4.7°, and the maximum amplitude error of negative sequence current of DFIG's short-circuit current calculation model is 56.5%, and the angle error is 5.5°. It also means that the influence of the GSC on the fault currents of the DFIG cannot be ignored.

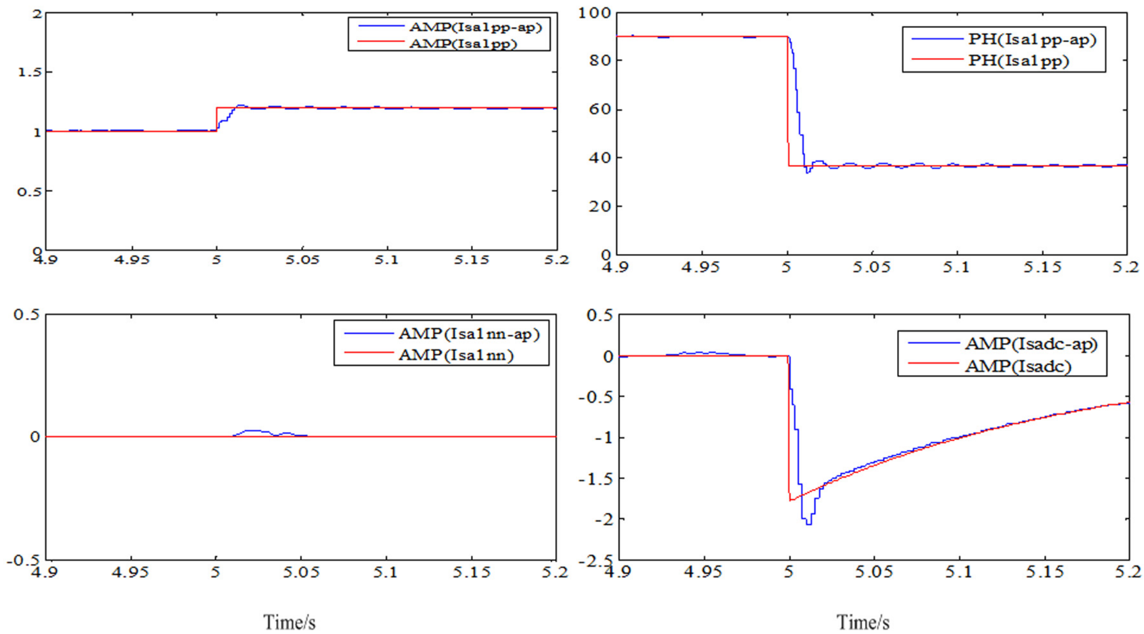

Fig. 6. The A phase current under condition of a Phase-C ground fault.

Table 2
Fault current on condition that BC-phase fault occurs at f, DFIG is fully loaded before the fault occurs.

	Target A		Target B		Target C	
	$I_{DFIG}(1)$	$I_{DFIG}(2)$	$I_{DFIG}(1)$	$I_{DFIG}(2)$	$I_{DFIG}(1)$	$I_{DFIG}(2)$
Measured values (with GSC)	1.08∠12.1°	0.00∠–	1.15∠14.5°	0.27∠149.3°	0.92∠9.1°	0.23∠−0.2°
Calculated values (with GSC)	1.04∠13.6°	0.00∠–	1.12∠15.4°	0.28∠151.8°	0.90∠10.3°	0.22∠−9.3°
Calculated values (without GSC)	1.29∠15.8°	0.00∠–	1.25∠17.5°	0.31∠157.15°	1.25∠13.8°	0.31∠−5.7°

Table 3
Fault current when 3-phase fault occurs at f, DFIG under different rotor speeds.

ω_r/pu.	I_S/kA		I_{GSC}/kA		I_{DFIG}/kA	
	Measured values	Calculated values	Measured values	Calculated values	Measured values	Calculated values
0.7	−1.25∠7.4°	−1.24∠7.6°	0.46∠31.8°	0.45∠31.0°	0.84∠-5.1°	0.84∠−4.8°
0.9	−1.24∠7.1°	−1.24∠7.6°	0.16∠31.2°	0.15∠31.0°	1.11∠4.5°	1.10∠4.4°
1.1	−1.24∠7.3°	−1.24∠7.6°	−0.14∠30.8°	−0.15∠31.0°	1.36∠10.4°	1.38∠10.1°
1.3	−1.24∠7.7°	−1.24∠7.6°	−0.45∠31.5°	−0.45∠31.0°	1.66∠14.5°	1.67∠14.8°

4.3. Slip speed

As shown in (25) and (26), the output currents of the GSC are influenced by the slip speed. Moreover, the rotor speed should be within a range of 70%–130% of the synchronous speed (i.e., 1 p.u.) (Xie et al., 2013). Taking control Target B as example, the influence of the slip speed on the fault currents of the DFIG under symmetric and asymmetric fault conditions are shown in Tables 3 and 4, respectively. In Table 4, MV and CV represent the measured and calculated values, respectively. With and without considering a slip, it can be seen from Tables 3 and 4 that the maximum amplitude error of positive sequence current of DFIG's short-circuit current calculation model is 110%, and the angle error is 6.6°, and the maximum amplitude error of negative sequence current of DFIG's short-circuit current calculation model is 117%, and the angle error is 6.2°. Therefore, it can be seen form the test results that the slip have an important influence on the DFIG's short-circuit calculation model. It also means that the influence of the slip on the fault currents of the DFIG cannot be ignored.

Moreover, Tables 3 and 4 show that the output current of the GSC is influenced by the slip. Then, the output current of the DFIG is influenced. When Wr < W_1 in Table 3, the output current of the DFIG is smaller than that of the stator current. When Wr > W_1, the output current of the DFIG is greater than that of the stator current. Therefore, the influence of the slip on the output current of the GSC also cannot be ignored.

In addition, it can be seen from Tables 3 and 4 that the error of the output current between the simulated and theoretical values is less than 4%. Therefore, the proposed short-circuit current calculation models of DFIG is valid. Based on this, the comparisons between traditional research and proposed method are shown in Table 5.

Compared with traditional methods, it can be seen from Table 5 that the transient process of DFIG under asymmetric faults and crowbar protection is not activated condition is analyzed, and mathematical expressions are derived. Moreover, the comprehensive and unified short-circuit calculation models of DFIG have established under different low voltage ride through control conditions. The influence of GSC and slip rate of DFIGs is also considered. This paper is of important significance for relay protection setting calculation, grid operation and control, and the selection of electrical equipment of power grid with DFIGs.

Table 4
Fault current when BC-phase fault occurs at f, DFIG under different rotor speeds.

ω_r/pu.	I_S/kA				I_{GSC}/kA				I_{DFIG}/kA			
	Pos.-Seq. comp.		Neg.-Seq.comp.		Pos.-Seq. comp.		Neg.-Seq.comp.		Pos.-Seq. comp.		Neg.-Seq.comp.	
	MV	CV	MV	CV	MV	CV	MV	CV	MV	CV	MV	CV
0.7	1.24∠ −155.9°	1.25∠ −155.7°	0.31∠ 157.9°	0.31∠ 158.1°	0.54∠ 30.2°	0.55∠ 31.0°	0.13∠ −29.1°	0.14∠ −28.6°	0.71∠ 19.5°	0.70∠ 19.1°	0.17∠ −17.0°	0.17∠ −16.7°
0.9	1.25∠ −155.8°	1.25∠ −155.7°	0.30∠ 157.6°	0.31∠ 158.1°	0.31∠ 31.5°	0.30∠ 31.0°	0.07∠ −28.5°	0.07∠ −28.6°	0.96∠ 22.1°	0.96∠ 22.3°	0.22∠ −19.5°	0.23∠ −19.9°
1.1	1.25∠ −154.9°	1.25∠ −155.7°	0.31∠ 158.3°	0.31∠ 158.1°	0.04∠ −147.9°	0.04∠ −149.0°	0.01∠ 150.7°	0.01∠ 151.4°	1.30∠ 24.7°	1.29∠ 24.5°	0.33∠ −21.3°	0.32∠ −21.7°
1.3	1.24∠ −155.1°	1.25∠ −155.7°	0.31∠ 158.0°	0.31∠ 158.1°	0.22∠ −148.6°	0.22∠ −149.0°	0.04∠ 152.1°	0.05∠ 151.4°	1.46∠ 26.1°	1.47∠ 25.3°	0.37∠ −23.0°	0.37∠ −22.9°

Table 5
Comparison between traditional research and proposed method.

	Traditional research		Proposed method	
	Transient process	Short-circuit current calculation model	Transient process	Short-circuit current calculation model
Symmetrical fault	Considered	Considered	Be applicable	Be applicable
Asymmetrical fault	Not consider	Not consider	Considered	Considered
Cowbar	Considered	Considered	Not consider	Not consider
GSC	Not consider	Not consider	Considered	Considered
Different LVRT strategies	Not consider	Not consider	Considered	Considered
Slip	Not consider	Not consider	Considered	Considered

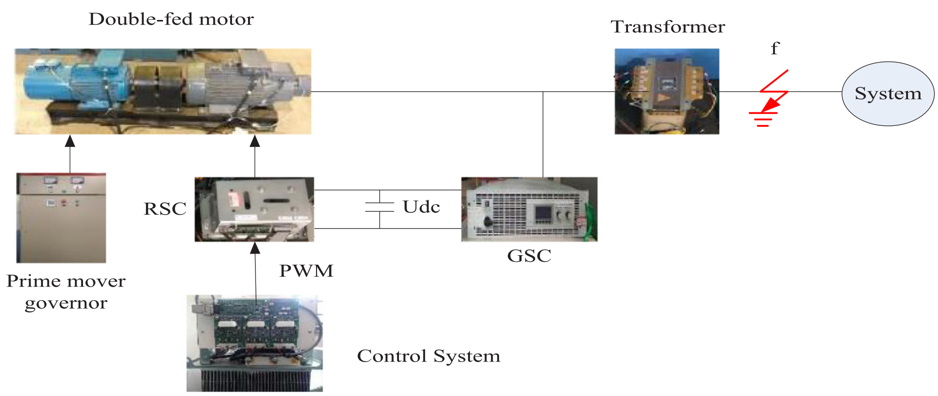

Fig. 7. The experimental testbed of power grid with a DFIG.

4.4. Hardware experimental testbed

Moreover, in order to validate the analytical results presented in this paper, a hardware experimental testbed of power grid with a DFIG has been established. The experimental testbed at the laboratory is shown in Fig. 1. Based on the experimental testbed, the influence of different low voltage ride-through strategies, different slip rates, and GSC for the fault current of the DFIG have been tested. The experimental testbed is shown in Fig. 7.

In Fig. 7, the parameters of the 10-kVA rated DFIG are: $U_{sn} = 180$ V, $f_n = 50$ Hz, $R_s = 0.078$ p.u., $R_r = 0.011$ p.u.,Ls = Lr = 2.378 p.u., $U_{DC} = 650$ V, Kp = 0.6, Ki = 8, $f_{PWM} = 10$ kHZ. For the following test examples, the output active power of the DFIG is 0.1 p.u. and the grid voltage is 1.0 p.u. before the fault occurs. Taking Phase-A fault at node f as example, the test results and the theoretical values are compared. Under this fault condition, the phase-A voltage dip down to 78%. Fig. 8 shows the test results of three-phase voltage for DFIG, the blue curve is phase-A voltage.

In Fig. 9, under phase-A grounding fault condition, the test results, theoretical values, the software results, and the software results without considered the slip and GSC (in Kong et al. (2014)) of DFIG's phase-A current and phase-B current are compared The red curve represents the test result, the blue curve represents the theoretical value, the sky blue curve represents the software value, and the green curve represents the software value, which is not considered the GSC and the slip is different from other test conditions.

As shown in Figs. 9 and 10, the differences between the test results, theoretical analysis results and the software results are very small. Notice that there are abrupt changes at the moment that the fault occurs, which are impossible in practice. The reason for this phenomenon is that some lagging elements are neglected for simplification during the theoretical analysis. Therefore, as Figs. 9 and 10 show, the influence of the aforementioned simplification is very small and it is within the allowable range. It means that the effectiveness of the proposed fault current models of DFIG are validate.

Moreover, no matter at the moment of the fault or under the fault steady condition, it also can been seen from Figs. 9 and 10 that there are a big difference between the other values and the software value, which is not considered the slip and GSC in Kong et al. (2014). It means that the slip and the GSC of a DFIG cannot be ignored, and the slip and the GSC have an important influence on the short-circuit current of DFIG.

5. Conclusions

An accurate short-circuit current calculation model of DFIG is of vital importance for the setting calculation of relay protection,

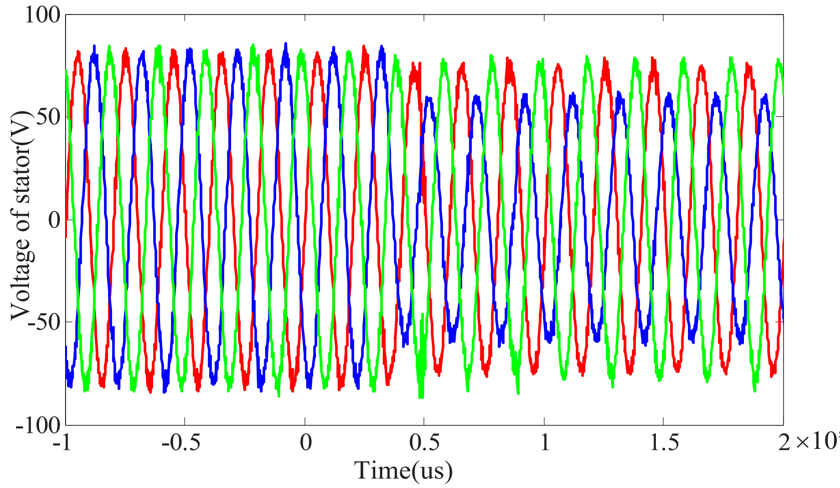

Fig. 8. Three-phase voltage of DFIG under Phase-A grounding fault condition. . (For interpretation of the references to color in this figure legend, the reader is referred to the web version of this article.)

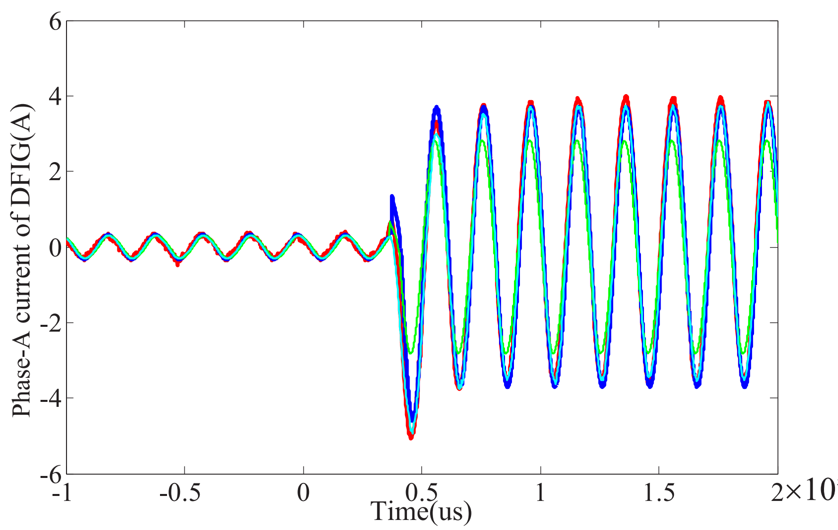

Fig. 9. Phase-A current of DFIG under Phase-A grounding fault condition. . (For interpretation of the references to color in this figure legend, the reader is referred to the web version of this article.)

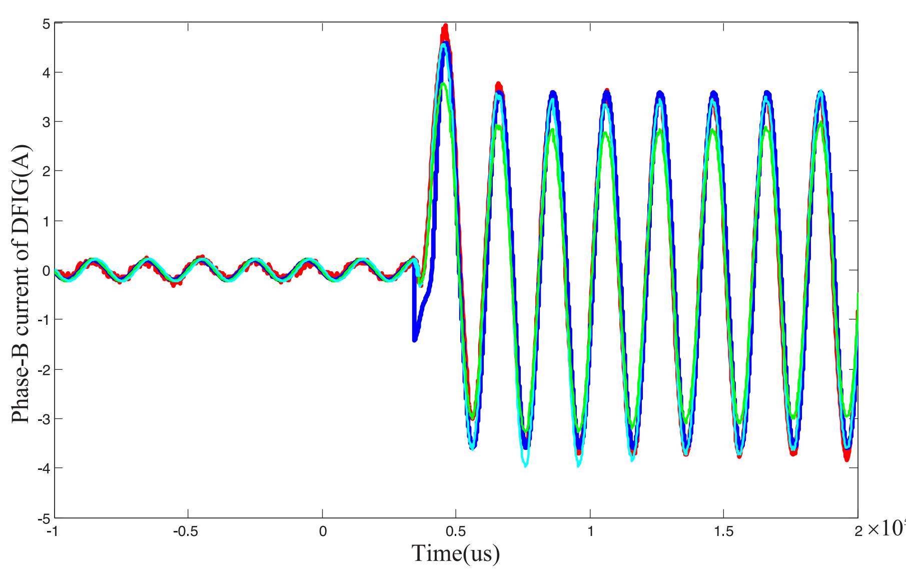

Fig. 10. Phase-B current of DFIG under Phase-A grounding fault condition.

grid operation and control, and the selection of electrical equipment. Due to the DFIG's control system is a "black box", the fault current characteristics of the DFIG have been studied under crowbar protection is activated or symmetrical fault condition, and it is difficult to obtain accurate fault characteristics and short-circuit current calculation models of DFIG under crowbar protection is not activated and unsymmetrical fault condition. In order to meet the requirements of short-circuit calculation of power grid with DFIGs, the transient process of DFIG under asymmetric faults and crowbar protection is not activated condition is analyzed, and mathematical expressions are derived. Moreover, the unified short-circuit calculation models of DFIG have established under different low voltage ride through control conditions. The influence of GSC and slip rate of DFIGs also have considered. The effectiveness of the proposed short-circuit calculation models have been validated by the hardware experimental testbed and EMTDC/PSCAD software. The analytical results shown that the LVRT control strategies, the GSC and slip have an important influence on the DFIG's short-circuit calculation model. Them must be considered in the short-circuit calculation models of DFIG. This paper is helpful for the relay protection setting calculation, grid operation and control, and the selection of electrical equipment

References

Chang, Y., Hu, J., Tang, W., Song, G., 2018a. Fault current analysis of type-3 WTs considering sequential switching of internal control and protection circuits in multi time scales during LVRT. IEEE Trans. Power Syst. 33 (6), 6894–6903.

Chang, Y., Hu, J., Tang, W., Song, G., 2018b. Fault current analysis of type-3 WTs considering sequential switching of internal control and protection circuits in multi time scales during LVRT. IEEE Trans. Power Syst. 33 (6), 6894–6903.

Erlich, I., Neumann, T., Shewarega, F., Schegner, P., Meyer, J., 2013. Wind turbine negative sequence current control and its effect on power system protection. In: 2013 IEEE Power & Energy Society General Meeting, Vancouver, BC, pp. 1–5.

Howard, D.F., Habetler, T.G., Harley, R.G., 2012a. Improved sequence network model of wind turbine generators for short-circuit studies. IEEE Trans. Energy Convers. 27 (2), 968–977.

Howard, D.F., Habetler, T.G., Harley, R.G., 2012b. Improved sequence network model of wind turbine generators for short-circuit studies. IEEE Trans. Energy Convers. 27 (2), 968–977.

Howard, Dustin F., Liang, Jiaqi, Harley, Ronald G., 2015. Short-circuit modeling of dfigs with uninterrupted control. IEEE J. Emerg. Sel. Top. Power Electron. 22 (1), 47–57.

Jauch, C., Matevosyan, J., Ackermann, T., Bolik, S., 2005. International comparison of requirements for connection of wind turbines to power systems. Wind Energy 8 (1), 295–306.

Kong, Xiangping, Zhang, Zhe, Yin, Xianggen, 2014. Study of fault current characteristics of the DFIG considering dynamic response of the RSC. IEEE Trans. Energy Convers. 29 (5), 278–287.

Leonhard, W., 1995. Control of Electrical Drives. Springer-Verlag, Berlin, Germany.

Morren, J., 2007. Short-circuit current of wind turbines with doubly-fed induction generator. IEEE Trans. Energy Convers. 22 (1), 174–180.

National Grid Plc, 2008. The grid code. (3). [Online]. Available: www.Nationalgrid.com/uk/Electricity/Codes/gridcode.

Ouyang, J., Xiong, Xiaofu, 2014. Dynamic behavior of the excitation circuit of a doubly-fed induction generator under a symmetrical voltage drop. Renew. Energy 71 (25), 629–638.

Raghavendran, C.R., Preeth Roselyn, J., Devaraj, D., 2020. Development and performance analysis of intelligent fault ride through control scheme in the dynamic behaviour of grid connected DFIG based wind systems. Energy Rep. 6, 2560–2576.

SnehapravaSwain, ., KumarRay, Pravat, 2017. Short circuit fault analysis in a grid connected DFIG based wind energy system with active crowbar protection circuit for ride through capability and power quality improvement. Int. J. Electr. Power Energy Syst. 84, 64–75.

Sulla, F., Svensson, J., Samuelsson, O., 2011. Symmetrical and unsymmetrical short-circuit current of squirrel-cage and doubly-fed induction generators. Electr. Power Syst. Res. 81 (5), 1610–1618.

Technical Rule, 2011. Technical Rule for Connecting Wind Farm To Power System. GB/T 19963-2011.

Transmission code, 2007. Network and System Rules of the German Transmission System Operators. Verband der Netzbetreiber VDN e.v. Beim BDEW, [Online]. Available www.bdew.de.

Xie, D., Xu, Z., Yang, L., et al., 2013. A comprehensive LVRT control strategy for DFIG wind turbines with enhanced reactive power support. IEEE Trans. Power Syst. 28 (5), 3302–3310.

Further reading

Xu, L., Andersen, B.R., Cartwright, P., 2005. VSC Transmission system operating under unbalanced network conditions – Analysis and control design. IEEE Trans. Power Deliv. 20 (4), 427–434.

Yazdani, A., Iravani, R., 2006. A unified dynamic model and control for the voltage sourced converter under unbalanced grid conditions. IEEE Trans. Power Deliv. 21 (6), 1620–1629.

An approach to estimate the frequency support from large-scale PV plants in a renewable integrated grid

Dillip Kumar Nayak, *Department of Electrical Engineering, Aryan Institute of Engineering & Technology, Bhubaneswar, dknayak225@yahoo.co.in*

Sanjay Kumar Nayak, *Department of Electrical Engineering , Raajdhani Engineering College, Bhubaneswar, sk.nayak24@gmail.com*

Rashmi Ranjan Behera, *Department of Electrical and Electronics Engineering, NM Institute of Engineering & Technology, Bhubaneswar, rr_behera@yahoo.co.in*

Sudipt Mandal, *Department of Electrical Engineering , Capital Engineering College, Bhubaneswar, sudiptmandal@hotmail.com*

Keywords:
Deloaded PV system
Frequency stability
Renewable energy integration
ROCOF
MLRA
BESS

A B S T R A C T

Photovoltaic systems, one of the major renewable energy systems (RESs), are getting integrated into conventional power grids in large-scale, substituting synchronous generators. However, PV systems lack inertia inherently and cannot provide any reserve power. Consequently, large-scale PV integrated grid faces severe frequency instability problems following a synchronous generator tripping event. Although various kinds of external storage systems are utilized to improve frequency response, they pose substantial economic challenges for grid operators. Deloaded PV systems, on the other hand, can assist in enhancing frequency stability without any external supporting mechanisms. In order to maintain frequency stability with minimal expenditure, an accurate estimation of the deloading percentage of PV systems is required. To this end, this paper proposes a novel methodology of estimating appropriate deloading percentages for PV systems in terms of frequency response parameters, using multiple linear regression analysis (MLRA). Simulations are conducted for different PV penetration levels on modified IEEE 39 bus test system. Additionally, a thorough performance comparison of deloaded PV integrated grid with both battery energy storage system (BESS) and synchronous condenser (SC) installed PV integrated grid is conducted. The findings support the feasibility of our method, allowing for accurate estimation and justifying the deployment of grid-connected deloaded PV systems. Deloaded PV systems also outperform other supporting mechanisms in terms of performance. Moreover, they provide insights on how the required deloading percentage decreases with increasing PV penetration. This paper can be used as a guide for grid designers to ensure that PV systems are properly deloaded to maintain frequency stability in large-scale PV integrated grids.

1. Introduction

Renewable energy systems are being integrated into conventional power grids in an increasing manner to implement clean energy targets by reducing global warming and greenhouse gas emission associated with fossil-fuel based generation (Basit et al., 2020; Qazi et al., 2019; Nassar et al., 2019). According to a recent finding (IRENA, 2020), total renewable power generation capacity around the world has become more than twofold in last ten years. Following this trend, solar photovoltaic (PV) based systems have the second-largest generation growth among the various renewable technologies. Specifically, PV power generation capacity increase by 22% over the last few years (IEA, 2021). These PV generators include both small-scale (i.e., in distribution level) and large-scale (i.e., in transmission level) plants.

Penetration of large-scale PV systems into power grids replaces the conventional synchronous generators from the generation mix. These PV plants are connected to the grid via power electronics interface that introduces several challenges regarding stable operation of the network (Rajakumar and Anbukumar, 2018). These encompass frequency stability (Ayamolowo et al., 2020), voltage stability (Petinrin and Shaabanb, 2016), small-signal stability (Eftekharnejad et al., 2013) and power quality issues (Bajaj and Singh, 2019). Among them, frequency stability is one of the most crucial concerns that needs more focus for conducting further research (Al-Shetwi and Sujod, 2018). Unlike synchronous generators, PV generators usually do not provide inertia (i.e., rotational energy) and headroom (i.e., frequency responsive reserve) to aid the frequency response following a contingency such as the tripping of a large generator. As a result, frequency stability of a power grid may severely decline due to prolific penetration of PV generators (Seneviratne and Ozansoy, 2016). Rajan et al. investigated a microgrid with high PV penetration and found adverse effect on frequency response after being subjected to a disturbance (Rajan et al., 2021). In Bueno et al. (2016), the authors used a typical transmission system with realistic loading situations and high PV integration levels to simulate and analyse transient and small-signal stability. The voltage and frequency conditions were thoroughly examined. However, no remedy to the increasing frequency instability caused by high PV penetration has been presented in this work. Nevertheless, it gives a proper insight how increased PV penetration can hamper frequency stability.

To address the above issue, different mechanisms are usually adopted to preserve satisfactory frequency response in PV integrated grids. For instance, Battery Energy Storage System (BESS) is a well-known device for improving frequency stability with instant active power injection after a large load-generation imbalance (Zhang et al., 2018; Chen et al., 2020; Shaqsi et al., 2020; Jawad et al., 2020). In addition, deployment of synchronous condenser (SC) (Arayamparambil Vinaya Mohanan et al., 2020), supercapacitors (Rocabert et al., 2019), superconducting magnetic energy storage (Said et al., 2020) etc. are reported in the literature. In Hernández et al. (2018), the authors have presented a detailed V2G (Vehicle to Grid) model with a hybrid energy storage system (HESS). These V2G models provide ancillary service like primary frequency control to the grid and act as a generator in case of emergency. Moreover, in Hernández et al. (2017), the authors propose a model of a utility-scale photovoltaic unit (USPVU) with an integrated HESS that is suited for transmission system stability assessments. The fundamental purpose of this approach was to provide primary frequency control and dynamic grid support at the same time. Although the system's performance has improved as a result of the enhanced USPVU model integration, it still has some shortcomings. The HESS system incorporates a BESS and a supercapacitor, which can put a serious financial strain on grid operators.

Note that for the above approaches, external devices need to be installed in the grid. Consequently, it increases the overall operational and maintenance costs. Therefore, an alternative mechanism has been developed that excludes the use of any external devices. In this approach, a certain percentage of PV generation is kept as reserve, i.e., not injected to the grid during normal operating condition. This reserve is utilized following a contingency to minimize the mismatch between load and generation. Eventually, a PV plant itself can participate in frequency regulation by this strategy. Such an operational mode is known as deloading of PV plants (Zarina et al., 2012).

A number of research works have been conducted on deloaded PV system to improve frequency response (Zarina et al., 2012, 2014; Xin et al., 2013; Yan et al., 2019; Rahmann and Castillo, 2014; Tavakkoli et al., 2018; Verma et al., 2021; Zarina and Mishra, 2016). For instance, Zarina et al. proposes an approach to mitigate the frequency transients considering load changes in a microgrid (Zarina et al., 2012). The same authors present a controller for deloading of PV systems considering frequency deviations in the grid and available reserve in PV plants (Zarina et al., 2014). However, in both studies, a micro grid was selected to conduct simulations. In addition, large-scale PV integration cases were not thoroughly investigated. Furthermore, Xin et al. recommends two different modes for deloaded operation of PV systems (Xin et al., 2013). These are frequency droop control mode and emergency control mode to support frequency response of the grid. Yan et al. utilizes an adaptive deloading technique with three controller loops, viz. droop controller, active power-voltage matching controller and vector controller (Yan et al., 2019). These loops enable the possibility of adjusting the output power of PV for frequency regulation of the grid. Rahamann and Castilo investigate the effects of deloaded PV plants on an isolated power system of northern Chile (Rahmann and Castillo, 2014). They found that this approach is a worthwhile choice for retaining frequency stability during significant penetration of large-scale PV power plants in a network. In addition, Tavakkoli et al. observes that deloaded PV systems decrease the overshoot and undershoot of frequency excursion as well as improves settling time (Tavakkoli et al., 2018). Besides, the cost-effectiveness of the deloaded PV systems compared to BESS is investigated in the literature (Verma et al., 2021; Zarina and Mishra, 2016).

Note that deloading of PV restricts a certain percentage of PV generation to be dispatched during normal operating condition. Therefore, plant owners may face financial consequences due to this power wastage. If an excessive reserve is kept, it will result in economic loss. In contrast, inadequate deloading may fail to meet the frequency response adequacy after a contingency. Therefore, it is extremely important to determine the appropriate percentage of deloading that serves dual purposes such as attainment of satisfactory frequency response and averting unnecessary reserve. It is evident from the literature review that a significant amount of work is done on the deloading of PV plants. However, the existing works do not explicitly suggest any systematic approach to find the appropriate deloading percentage of large-scale PV plants. Considering all the discussed literature, the crucial research gaps can be identified as follows:

- Several ways for deloading PV systems are provided in current studies (as stated above). However, no efficient method for determining the proper deloading requirement for grid-connected PV systems is presented in any of the studies. In addition, when estimating the required deloading of PV systems, no existing work takes the frequency response characteristics into consideration.
- PV systems and other types of storage system integrated grids have been thoroughly researched in the literature. There are a few studies available that consider the concept of deloaded PV. However, the majority of the existing research focused on small to medium-scale PV integration in mini or micro grids. As a result, further study is needed to examine the influence of large-scale deloaded PV integration into large power grids on system's frequency stability.
- The cost effectiveness of deloaded PV in comparison to BESS is comprehensively shown in the past studies. However, there is no comparison of performance between these mechanisms in the literature.
- Furthermore, synchronous condensers are getting popular as a tool for assisting large-scale renewable integrated grids. Existing research, however, does not provide a thorough comparison of SC and deloaded PV systems in terms of frequency response.

Taking into account all of the aforementioned gaps, the goal of this research is to provide a systematic technique based on frequency response characteristics for determining the needed deloading percentage of PV systems in a power grid. The proposed method is utilized to accurately estimate required deloading of PV systems efficiently. In addition, the effect of large-scale PV integration is explored while performance is compared to that of other supporting mechanisms. The following is a summary of the paper's key contribution.

- A systematic approach is proposed to find the most appropriate deloading percentage for maintaining frequency stability following a large contingency. Two key indices of frequency stability, viz. frequency nadir and Rate of Change of Frequency (ROCOF) are taken into account in the proposed method.
- Detailed investigations are carried out to find the required deloading percentage under various PV penetration levels in a renewable integrated grid.

- The proposed approach is validated by comparing the frequency response performances against two existing techniques such as deployment of BESS and synchronous condensers.

The rest of the paper is organized as follows. Section 2 describes the basic working mechanism of PV systems incorporated with the deloading mechanism. In Section 3, our proposed methodology is presented step by step with a relevant flowchart. Section 4 presents the details of the test system and simulation scenarios. It also describes the simulated models, for various cases, with measurements of goodness-of-fit for every constructed model. Additionally, performance analysis and validation of constructed models compared with both BESS and SC are conducted in Section 5. Section 6 introduces some important discussions on the applicability of the proposed method. Finally, a brief conclusion of our findings and insights are discussed in Section 7.

2. System modelling

In this section, the working mechanism of grid-connected photovoltaic systems is described along with deloaded PV system modelling. In this paper, DIgSILENT PowerFactory is used to model all the grid elements and conducting dynamic simulations (DIgSILENT, 2013).

2.1. Photovoltaic system working mechanism

PV system comprises photovoltaic modules that emulate the working mechanism of a p–n junction. When it is exposed to light, carriers are generated that create a current proportional to the incident radiation. To increases current and voltage ratings, PV modules are connected in series and parallel respectively (Kumar and Singh, 2018). The output current of a PV array, I_{PV} is expressed by

$$I_{PV} = n_p I_{SC} - n_p I_s \left(e^{\frac{qU_{DC}}{kTAn_s}} - 1 \right) \tag{1}$$

where n_p and n_s represent the number of cells in parallel and series respectively. Further, I_s and I_{SC} are the reverse saturation current and short circuit current of a cell (in A) respectively, k is the Boltzmann's constant (1.3806503×10^{23} J/K), A is the ideality factor, T is the temperature (in K), and U_{DC} is the dc output voltage (in V). I_{SC} is dependent on temperature and irradiance, G (in Wm^{-2}) and represented by Eq. (2).

$$I_{SC} = \frac{G \times I_{SC(STC)}}{G_{STC}} [1 + T_{C1}(T - T_{STC})] \tag{2}$$

where T_{C1} is the temperature coefficient, and $I_{SC(STC)}$, G_{STC}, T_{STC} are corresponding short circuit current, irradiance, and temperature respectively in standard test conditions i.e., the temperature of 25 °C and irradiation of 1000 Wm^{-2} (Sidrach-de-Cardona and López, 1999).

Conventionally, a PV system works using the Maximum Power Point Tracking Algorithm (MPPT). According to this algorithm, the PV system gives highest possible power, P_{MPP} at voltage U_{MPP} for a specific temperature and irradiance. The voltage is a function of U_{MPP0}, a value defined by PV module manufacturer, irradiance (G), and temperature (T) and temperature correction factor (T_{C2}) as shown in Eq. (3).

$$U_{MPP} = U_{MPP0} \times \frac{\ln(G)}{\ln(G_{STC})} \times [1 + T_{C2}(T - T_{STC})] \tag{3}$$

2.2. Deloaded PV system modelling

A PV system utilizing the MPPT algorithm always operates in a way to extract the maximum available active power. Therefore, no power reserve is kept when MPPT is followed. To allow a PV system to preserve a certain amount of reserve, it is operated at a higher voltage, U_{deload} instead of U_{MPP} as shown in Fig. 1. As a result, the PV system supplies lower power output, P_{red} compared to P_{MPP}. Eventually, it ensures a reserve P_{deload} according to Eq. (4).

$$P_{deload} = P_{MPP} - P_{red} \tag{4}$$

Such kind of PV system providing reduced active power in normal operating condition is called a deloaded PV system (Zarina et al., 2012). To utilize this additional power in the event of frequency disturbance, a signal proportional to frequency deviation (Δf) is added to the DC output voltage. It produces a new operating voltage, U_{DCref}, which is calculated by

$$U_{DCref} = U_{MPP} + U_{deload} - K_g \times \Delta f \tag{5}$$

where, K_g is the proportional gain constant. This approach is called frequency droop control method (Shutang, 2020).

In case of frequency decline following a contingency, U_{DCref} decreases. As a result, power output from the PV system increases. In other words, a deloaded PV system is able to inject additional active power support following a contingency. It eventually emulates the governor response akin behaviour of a synchronous generator. It can increase power output instantly and can reach up to P_{MPP}, thus, providing additional active power support, P_{deload} to the connected grid when a frequency reduction event occurs. The schematic diagram of the frequency droop control mechanism is illustrated in Fig. 2.

3. Proposed methodology

This section presents a methodology to estimate the required deloading percentage of installed PV systems in a power grid for maintaining frequency stability. The methodology uses two performance parameters associated with frequency response analysis, frequency nadir and ROCOF. Here, the deloading percentages of installed PV systems are varied for a major synchronous generator tripping event. A working relation between required additional PV support and the mentioned metrics is constructed from the results. The constructed prediction models are also evaluated in terms of R^2, adjusted R^2, and RMSE (Root mean square error). This whole process is shown as a flowchart in Fig. 3 and steps associated with the proposed methodology are presented below:

Step 1. Imposing initial deloading on PV systems: First, PV systems are assigned an initial deloading percentage, DL_{io} and a final deloading percentage, DL_f in terms of total PV penetration. Additionally, the percentage of total PV integration in the grid, $\%P_{total}^{PV}$ is calculated using Eq. (6).

$$\%P_{total}^{PV} = \frac{P_{total}^{PV}}{P_{total}} \times 100\% \tag{6}$$

where, P_{total}^{PV} denotes total installed PV system's output capacity (in MW) and P_{total} represents total active power generation of the grid (in MW).

As deloading percentage is varied in every distinct simulation, a fixed incremental deloading percentage, DL_{in} is considered. The number of total steps in between initial and final deloading is determined following Eq. (7).

$$n = \frac{DL_f - DL_{io}}{DL_{in}} + 1 \tag{7}$$

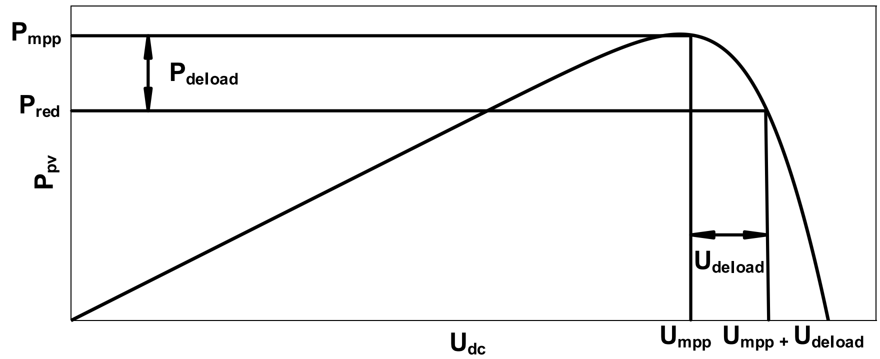

Fig. 1. Deloaded operation of a PV system.

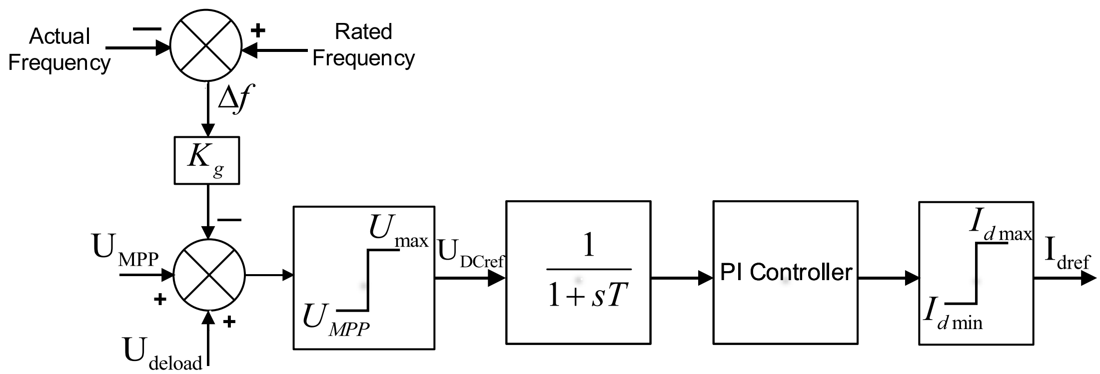

Fig. 2. Frequency droop control for active power support from a deloaded PV system.

Step 2. Execution of time-domain simulation: After fixing the deloading amount on PV systems, the next step requires time-domain simulation for a major synchronous generator outage event. The tripping event will impose abrupt changes in system frequency, thus causing severe frequency instability. For conducting frequency response analysis, an accurate measurement of the grid frequency is a requisite. As multiple synchronous generators run simultaneously in the grid, there is a possibility of small signal oscillations. This necessitates an equivalent system frequency calculation. This equivalent system frequency, f_{equ} is determined using the following equation for a generator tripping event (Athay et al., 1979).

$$f_{equ} = \frac{\sum_{i=1}^{i=m} H_i \times S_i \times f_i}{\sum_{i=1}^{i=m} H_i \times S_i} \quad (8)$$

where, H_i, S_i, f_i represent the inertia constant (in s), rated apparent power (in MVA), and frequency (in Hz) of the ith synchronous generator, respectively. Here, m represents the total number of available synchronous generators after the tripping event.

Step 3. Calculation of frequency nadir and ROCOF: In assessing frequency stability of a power system, multiple performance metrics are mentioned in the literature. Among them, we consider two metrics, frequency nadir and ROCOF, to create a dataset for conducting our deloading percentage estimation method. Frequency nadir (f_{nadir}), indicates the lowest point in the frequency response curve of a system following generation disturbance event. It is calculated by taking the minimum value of f_{equ} from Eq. (8) after power disturbance occurs. ROCOF is another frequency response evaluation parameter indicating the initial degree of frequency decrease following a disturbance event (in Hz/s). This parameter is calculated by Eq. (9) (Athay et al., 1979).

$$ROCOF = \frac{df}{dt} = \frac{1}{2} \times \frac{P_{dis} \times f_o}{IR} \quad (9)$$

where, P_{dis} represents the tripped synchronous generator size (in MW), f_o stands for the nominal frequency of the system, and IR denotes total system inertia (in MWs).

Step 4. Formation of dataset: After computation of frequency nadir and ROCOF, a dataset is formulated where the frequency parameters are stored. The corresponding deloaded PV support (in MW), calculated from the assigned deloading percentage is also included in the dataset. Then deloading percentage is again calculated using the following equation for the next simulation,

$$DL_i = DL_{io} + (i-1) \times DL_{in} \quad for\ i = 2, 3, 4, \ldots, n. \quad (10)$$

Steps 2 and 3 are repeated, and corresponding data for every simulation is stored in the dataset until i equates the number of total steps, n. After that, the workflow proceeds to the next step.

Step 5. Construction of MLRA model: MLRA is a well-known technique in predicting a dependent variable from two or more independent variables by fitting a linear equation to observed data. Assuming linear relation among the variables, an MLRA model is constructed in this stage. The independent variable here is the deloaded PV support (P_{deload}). Furthermore, both the frequency nadir (f_{nadir}) and the $ROCOF$ function as dependent variables. Eq. (11) represents the MLRA model whose regression coefficients β_0, β_1, β_2 are to be determined using the method of least square.

$$P_{deload} = \beta_0 + \beta_1 \times f_{nadir} + \beta_2 \times ROCOF \quad (11)$$

According to this method, minimization of the sum of squared error between observed and modelled response gives the best estimation of unknown coefficients. Eq. (11) can be written in a more generalized format by,

$$y = \beta_0 + \beta_1 x_1 + \beta_2 x_2 \quad (12)$$

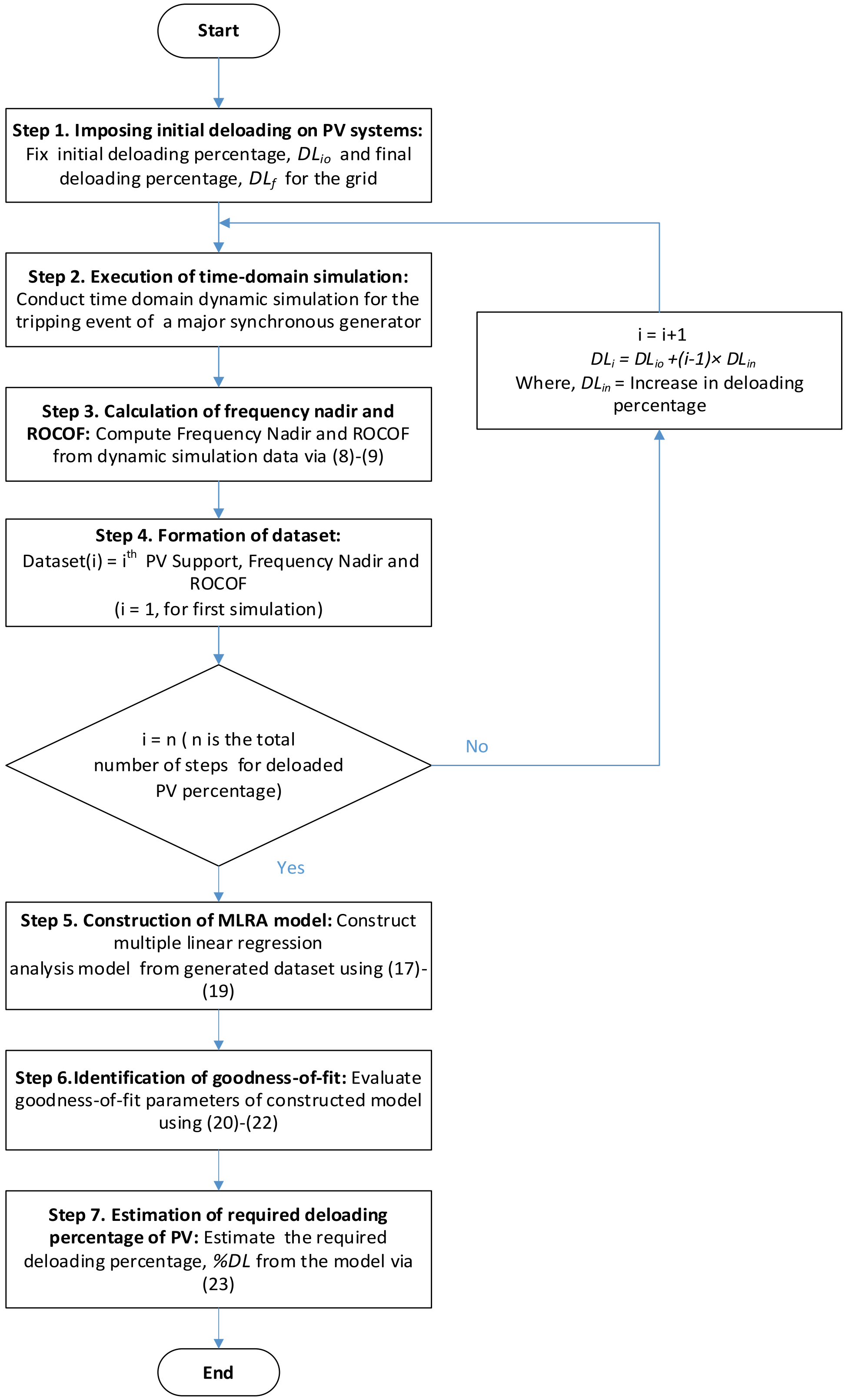

Fig. 3. Flowchart of the proposed methodology to estimate the deloading percentage of PV systems.

From the dataset formed in step 4, with total n samples, the best fitting model's sum of squared error can be described by,

$$E = \sum_{i=1}^{n} [y_i - (\beta_0 + \beta_1 x_1 + \beta_2 x_2)]^2 \tag{13}$$

It is necessary to achieve the best possible values for the regression coefficients β_0, β_1, and β_2. To obtain this, first derivative of Eq. (13) with respect to each coefficient must be zero. Therefore, the conditions stated in Eqs. (14)–(16) must be satisfied.

$$\frac{\partial E}{\partial \beta_0} = 2\sum_{i=1}^{n} [y_i - (\beta_0 + \beta_1 x_1 + \beta_2 x_2)] = 0 \tag{14}$$

$$\frac{\partial E}{\partial \beta_1} = 2\sum_{i=1}^{n} [y_i - (\beta_0 + \beta_1 x_1 + \beta_2 x_2)] = 0 \tag{15}$$

$$\frac{\partial E}{\partial \beta_2} = 2\sum_{i=1}^{n} [y_i - (\beta_0 + \beta_1 x_1 + \beta_2 x_2)] = 0 \tag{16}$$

Simplifying above equations,

$$\sum_{i=1}^{n} y_i = \beta_0 \sum_{i=1}^{n} 1 + \beta_1 \sum_{i=1}^{n} x_{1i} + \beta_2 \sum_{i=1}^{n} x_{2i} \tag{17}$$

$$\sum_{i=1}^{n} x_{1i} y_i = \beta_0 \sum_{i=1}^{n} x_{1i} + \beta_1 \sum_{i=1}^{n} x_{1i}^2 + \beta_2 \sum_{i=1}^{n} x_{1i} x_{2i} \tag{18}$$

$$\sum_{i=1}^{n} x_{2i} y_i = \beta_0 \sum_{i=1}^{n} x_{2i} + \beta_1 \sum_{i=1}^{n} x_{1i} x_{2i} + \beta_2 \sum_{i=1}^{n} x_{2i}^2 \tag{19}$$

The regression coefficients β_0, β_1, and β_2 can be determined by solving Eqs. (17)–(19) where y, x_1 and x_2, i.e., inputs are chosen from the available dataset.

Step 6. Identification of goodness-of-fit: In order to determine the success of the predicted model formed in step 5, three parameters are evaluated, R^2, Adjusted R^2, and RMSE. R^2 represents the square of the correlation between the response values and the predicted response values. The value is generally between 0 and 1. Here, a value closer to 1 indicates a more significant proportion of variance is accounted for by the model; i.e., how successful the fit is to explain the variation of the data.

$$R^2 = 1 - \frac{\sum_{i=1}^{n} w_i (y_i - u_i)^2}{\sum_{i=1}^{n} w_i (y_i - y_{av})^2} = 1 - \frac{SSE}{SST} \tag{20}$$

where, u_i is the predicted value from the fit, y_{av} is the mean of the observed data and y_i is the observed data value. w_i is the weighting factor, usually $w_i = 1$. SST is the total sum of squares, and SSE is the sum of squares due to error.

Adjusted R^2 is a modified version of R^2 based on the residual degrees of freedom (v). It is defined as the difference between the number of response values (N) and the number of fitted coefficients (M) estimated from the response values. A value closer to 1 indicates high fit quality of the predicted model, similar to R^2, and is formulated following Eq. (21).

$$Adjusted\_R^2 = 1 - \frac{SSE \times (N-1)}{SST \times \mathrm{v}} \tag{21}$$

RMSE, the standard deviation of the residual, indicates the absolute fit of the model to the data. Lower values of RMSE, i.e., close to 0, is a good measure of the accuracy of the response provided by the predicted model. This parameter is calculated using Eq. (22).

$$RMSE = \sqrt{\sum_{i=1}^{N} \frac{(y_i - u_i)^2}{N}} \tag{22}$$

Step 7. Estimation of required deloading percentage of PV: In the last step of this method, required deloaded PV support is calculated from the regression model formed in step 5. Following grid code, required values are assigned to the input variables of the estimation model. Finally, the required deloading percentage of PV is determined in terms of total PV penetration in the grid following Eq. (23).

$$\%DL = \frac{P_{deload}}{P_{total}^{pv}} \times 100\% \tag{23}$$

Before finalizing PV systems in a particular power grid, this process is executed. It supplies accurate prediction of the required deloading percentage to preserve the system's frequency stability in the event of synchronous generator tripping.

4. Simulation results and analysis

The purpose of this section is to assess the proposed method for estimating the appropriate deloading percentage of PV systems in a grid. Total simulations are categorized into five different situations based on PV penetration level in the grid for comprehensive analysis. Starting with the description of the test system, every simulation scenario is thoroughly discussed. Additionally, the simulation results are presented with relevant figures in each case with concise description. The proposed approach of incorporating frequency response metrics to estimate required deloading of grid-connected PV systems is justified after a thorough analysis of each scenario.

4.1. Test system

In this research work, the IEEE 39-bus New England test system is used for conducting time-domain dynamic simulation (Cabrera-Tobar et al., 2016). This test system comprises ten synchronous generators initially supplying power to 19 load buses. The total active power demand in this system is 6097.1 MW. It has a nominal system frequency of 60 Hz and base MVA of 100 MVA. Here, Generator 1(G01) is the aggregate of several synchronous generators connecting rest of USA/CANADA. The conventional synchronous generators are modelled with suitable automatic voltage regulator (AVR) control and governor controls with built-in models. The whole system is modelled to emulate real power grids when faced with a disturbance in the grid. A modified version of this test system is utilized in our research, replacing several synchronous generators with PV systems. These PV systems are installed at bus 37, 35, 36, 32 and bus 38 consecutively to emulate different levels of PV penetration in the grid. The scheduled generation of the replaced synchronous generators are assigned to the installed PV systems. Considering the time duration of the required dynamic simulations in this research work, PV intermittency is ignored. Consequently, PV systems are modelled to provide fixed amount of active power as assigned. Moreover, deloading mechanism as described in Section 2 is also incorporated in the PV systems to provide support when required. For every modification in this system, total demand and scheduled generation is kept constant while varying PV integration level. A single line diagram of the modified 50% PV integrated grid is shown in Fig. 4.

4.2. Simulation scenarios

In order to implement our proposed methodology, total simulations are divided into five separate cases based on PV integration level into the grid. The cases represent 20% to 60% PV penetration levels, with an increment of 10% PV in a successive manner. The details of the cases are presented in Table 1 in

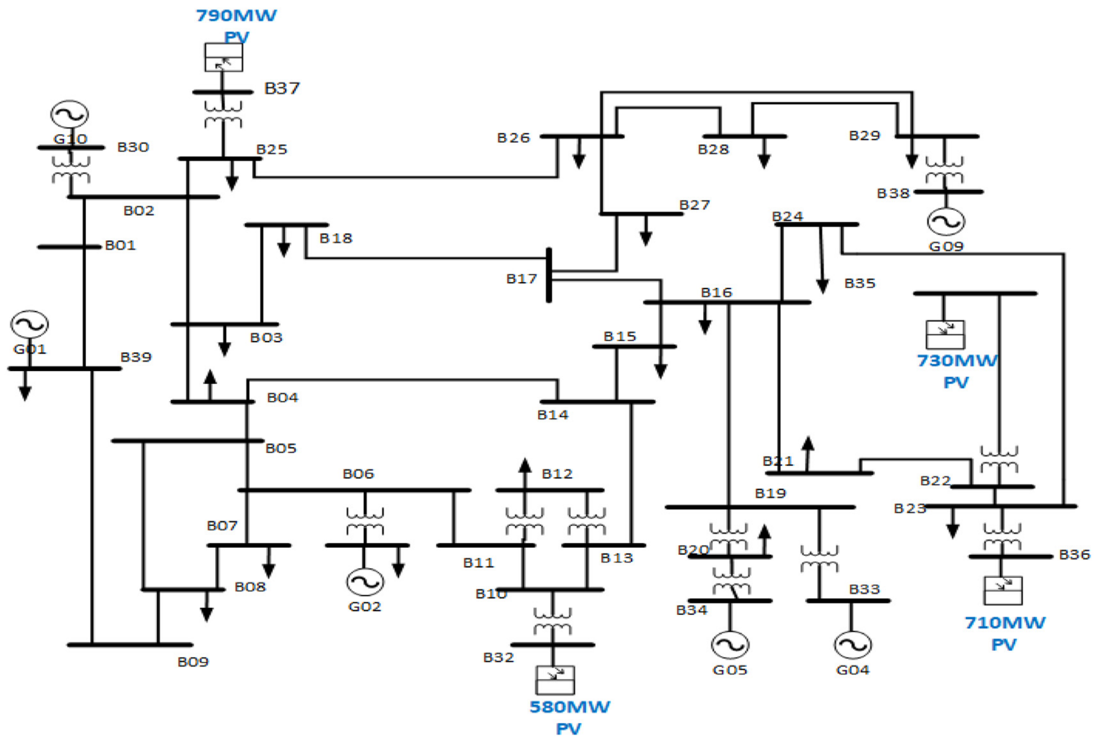

Fig. 4. Single line diagram of modified IEEE 39 bus test system.

Table 1
Simulation scenarios.

Simulation case	Synchronous generation (MW)	PV generation (MW)	PV penetration (%)
Case 1	4246	1120	20
Case 2	3686	1680	30
Case 3	3136	2230	40
Case 4	2556	2810	50
Case 5	2056	3310	60

brief. Solar irradiance and temperature values of PV systems are kept constant to conduct time-domain simulations in this paper. For each case, both initial deloading percentage, DL_{io} and final deloading percentage of PV systems, DL_f are assigned; the values being 0.25% and 10% respectively. Typically, the deloading percentage remains within 20% of the maximum possible generation (Cabrera-Tobar et al., 2016). In this paper, the final deloading percentage is allocated considering economic constraints for the grid planners. However, grid planners can choose any suitable percentage level for calculation. In the simulations, DL_{in}, incremental deloading percentage, is chosen to be 0.25%, and from Eq. (7), total step size n is determined to be 40.

Following that, tripping of Generator 5 (508 MW), is chosen to simulate an outage event in a time domain dynamic simulation. This synchronous generator is selected to observe the effects in frequency response of the grid after its outage. Additionally, frequency response parameters, f_{nadir} and $ROCOF$ for each simulation is calculated using Eqs. (8)–(9). According to the methodology described in Section 3, all simulations are carried out in DIgSILENT PowerFactory environment (DIgSILENT, 2013). Simultaneously, dataset is formulated consisting of PV support and corresponding frequency parameters.

4.3. Result analysis

The objective of this subsection is to evaluate the suggested approach using the simulation results from each described case. For every scenario, MLRA model is formulated using simulation data, and the goodness-of-fit is checked. In addition, a clear and concise analysis of the outcomes from each case is provided to substantiate our proposed method.

4.3.1. Case 1 (20% PV)

In this case, a time-domain simulation of Generator 5's outage event is considered for analysis. All of the needed simulations are carried out by varying deloading percentage using Eq. (10). A dataset is created by obtaining frequency nadir and ROCOF values for each simulation. The dataset is used to formulate MLRA model with 95% confidence bounds. It correlates required PV support with frequency nadir and ROCOF. The coefficients of the model are determined using Eqs. (17)–(19) from the dataset. The corresponding fitted curve using MATLAB is shown in Fig. 5. The frequency nadir and ROCOF values show a linear relationship with the deloaded PV support, as seen in the figure. This regression line backs up the claim that these frequency response metrics are effective indicators to estimate deloaded PV support.

Moreover, to verify the goodness-of-fit of the model, parameters R^2, Adjusted R^2, and RMSE are calculated using Eqs. (20)–(22). The corresponding values of these parameters are 1, 1, and 0.09542 respectively. As all of these parameters are in the acceptable range for successful estimation, the MLRA model's coefficients can be accepted for calculation. These parameters again justify the working relation between the frequency response metrics and PV support. The resultant MLRA model of PV support vs frequency nadir, ROCOF is expressed by,

$$P_{deload} = -1.074 \times 10^4 + 184.7 \times f_{nadir} + 491.6 \times ROCOF \qquad (24)$$

Conventionally, the accepted frequency range for a 60 Hz system is 59–61 Hz, and ROCOF range is within ±1 Hz/s (Hartmann et al., 2019). From the dataset for the 20% PV case, all ROCOF values remain within that range. However, frequency nadir deteriorates towards unacceptable values when additional

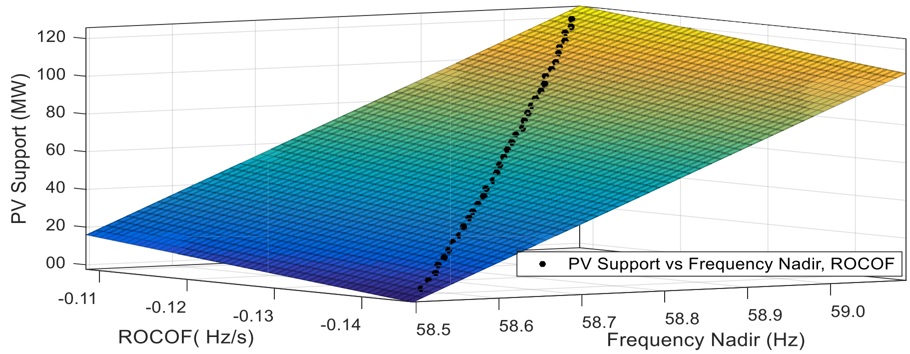

Fig. 5. Multiple linear regression model of PV support vs frequency nadir, ROCOF (20% case).

PV support is insufficient, making it the prime concern in improving frequency stability. To this end, f_{nadir} is set at 59 Hz and ROCOF at −0.1 Hz/s in the model. It will result in the minimum required deloading percentage of the PV systems to preserve frequency stability. From Eq. (24), required deloaded PV support, P_{deload} is found to be 111.76 MW. Finally, the required deloading percentage of PV, $\%DL$ is determined to be 9.976% in terms of total PV penetration in the grid from Eq. (23).

In this 20% PV penetration case, all the steps outlined in Section 3 are performed to formulate the MLRA model and calculate the required deloading percentage of installed PV systems. The figure, as well as the derived goodness-of-fit parameters, support the proposed method in this case.

4.3.2. Case 2 (30% PV)

To make a 30% PV penetration level in the grid, PV capacity is increased to 1680 MW in this case. A dataset is formed like the previous case for the tripping event of Generator 5. With 95% confidence bounds, a new MLRA model is formed, and parameters are calculated like case 1. The fitted curve is presented in Fig. 6. The figure clearly shows that, as in the preceding case, there is a linkage between the frequency response parameters and PV support. As a result, the claim in the proposed approach is strengthened even further. The corresponding equation of the constructed model is shown by

$$P_{deload} = -8917 + 154.9 \times f_{nadir} + 997.4 \times ROCOF \tag{25}$$

Corresponding R^2, Adjusted R^2, and RMSE values are 0.9998, 0.9998, and 0.7545, which verifies the model's compatibility. Using the same values for frequency nadir and ROCOF, calculated P_{deload} is 122.36 MW which in terms corresponds to $\%DL$ of 7.283%.

The constructed figure and goodness-of-fit characteristics for the 30% PV penetration case demonstrate the high accuracy of the models used in this study again. Although the required deloaded PV support is higher than in the preceding scenario, the necessary deloading percentage in terms of total PV penetration in the grid has decreased significantly here.

4.3.3. Case 3 (40% PV)

In this case, PV penetration is again increased, replacing synchronous generators, making the grid more susceptible to frequency instability. Following the same procedure as previous cases, the MLRA model is formulated shown in Fig. 7. Although there are more deviations in the data points for this case, the figure shows a linear relationship like previous cases. The constructed MLRA model is expressed by,

$$P_{deload} = -1.055 \times 10^4 + 182 \times f_{nadir} + 422.5 \times ROCOF \tag{26}$$

Additionally, goodness of fit parameters, i.e., R^2, Adjusted R^2, and RMSE are calculated to be 0.999, 0.999, and 2.057, respectively. RMSE value has increased compared to the preceding ones in account of more variability introduced in the grid for large-scale PV penetration. In spite of that, these parameters are well within acceptable ranges. The resultant MLRA model of PV support vs frequency nadir, ROCOF is expressed by

Keeping the same parameters, corresponding P_{deload}, according to Eq. (26) is 145.75 MW which is equivalent to $\%DL$ of 6.536%. Showing the same trend as previous cases, the total required deloaded PV support increases, whereas the deloading percentage decreases. The accuracy of the constructed model following the methodology is still satisfactory which is evident from the figure and calculated parameter values.

4.3.4. Case 4 (50% PV)

For this simulation case, PV penetration level is increased to 50%. Here, an MLRA model is created utilizing the synchronous generator tripping event dataset, as illustrated in Fig. 8. This figure indicates that the PV support variable is linearly related to the frequency nadir and ROCOF values. The observed pattern corresponds to prior simulated cases. The formulated MLRA model is given by Eq. (27). The goodness-of-fit parameters are also measured in this scenario and found to be 0.9986, 0.9986, and 2.265 for R^2, Adjusted R^2, and RMSE, consecutively. It is observed that the RMSE shows a slightly increased value than the previous case. However, all the parameters are still within the acceptable range to estimate the required deloaded PV support with high accuracy. According to Eq. (27), P_{deload} is found to be 178.037 MW. Frequency nadir remains the dominant factor as ROCOF always remains within the acceptable range as seen from Fig. 8. Finally, $\%DL$ is found to be 6.335% for 50% PV integration case according to Eq. (23).

$$P_{deload} = -1.106 \times 10^4 + 190.6 \times f_{nadir} + 73.63 \times ROCOF \tag{27}$$

The results obtained in this case imply the same trend as earlier cases, further justifying the constructed model using proposed methodology. The required demand from deloaded PV increases as PV integration in the grid increases. On the other hand, deloading percentage shows a decreasing pattern from low to high PV integrated cases.

4.3.5. Case 5 (60% PV)

This case has the highest overall PV penetration in the grid when compared to previous cases (60%). The outage event of generator 5 is simulated using deloaded PV support, as in previous instances. A MLRA model is developed using the dataset obtained from all simulations, as illustrated in Fig. 9. The correlation between PV support and the other two variables, ROCOF and frequency nadir, is depicted in the figure. Due to the high PV penetration in the grid, there is increased frequency instability,

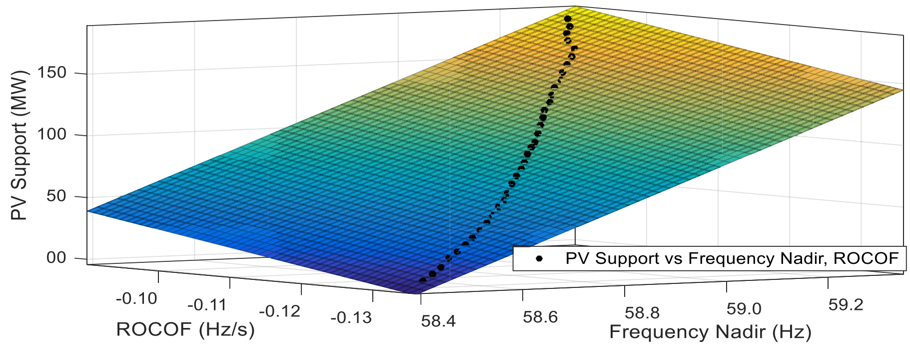

Fig. 6. Multiple linear regression model of PV support vs frequency nadir, ROCOF (30% case).

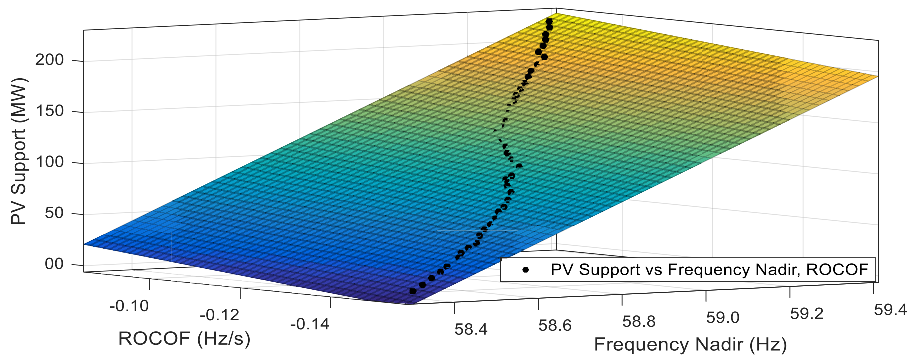

Fig. 7. Multiple linear regression model of PV support vs frequency nadir, ROCOF (40% case).

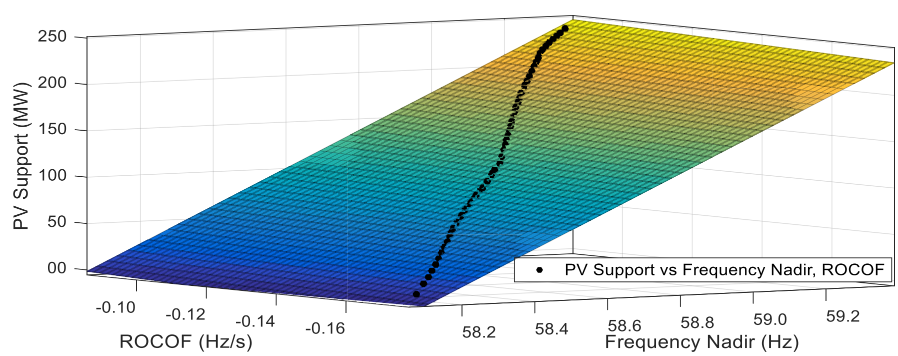

Fig. 8. Multiple linear regression model of PV support vs frequency nadir, ROCOF (50% case).

resulting in increased data fluctuation. Despite this, the linear relationship is still valid, as seen in the figure. Eq. (28) expresses the formulated MLRA model equation.

$$P_{deload} = -1.065 \times 10^4 + 183.6 \times f_{nadir} - 60.83 \times ROCOF \quad (28)$$

In this case, the goodness-of-fit parameters are also assessed and determined to be 0.9981, 0.9981, and 2.399 for R^2, Adjusted R^2, and RMSE, respectively. Because of the increased fluctuation in the grid with high level PV penetration, R^2 and RMSE have increased by a small amount. However, even in this scenario of substantial PV integration, all of the parameters are within permissible limits. This finding also supports the claim that this approach can accommodate very high levels of PV grid integration. Additionally, P_{deload} is determined to be 188.483 MW using Eq. (28). According to the obtained equation, frequency nadir is still the most significant factor. Moreover, *%DL* is calculated to be 5.694% for 60% PV integration case according to Eq. (23).

All the MLRA models constructed in this section show acceptable goodness-of-fit parameters, predicting satisfactory accuracy of the models. Evidently, the parameter values justify the relation generated between required PV support and frequency nadir, ROCOF for preserving frequency stability of the grid. The proposed method's justification is supported by all of the outcomes and associated figures. In addition, the data have shown an intriguing trend. The required deloading percentage of PV installations is lowering as PV adoption in the grid increases. In addition, a summary of all the models in all simulated cases is given in Table 2.

5. Validation of methodology & performance analysis

In this section, constructed model and corresponding deloading percentage of PV system for each case from Section 4 is validated. Deloaded PV enabled grid's ability to maintain frequency stability following a synchronous generator tripping event is evaluated. Furthermore, a performance comparison with two different additional support mechanisms included grids is performed. The two additional support mechanisms are briefly described below.

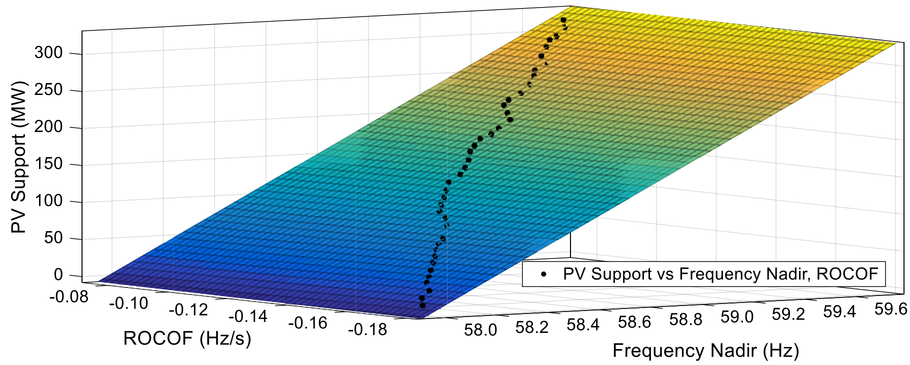

Fig. 9. Multiple linear regression model of PV support vs frequency nadir, ROCOF (60% case).

Table 2
Summary of simulation outcomes.

Case study	MLRA model equation	Goodness-of-fit			PV support (MW)	Deloading percentage %DL
		R^2	Adjusted R^2	RMSE		
20% PV	$P_{deload} = -1.074 \times 10^4 + 184.7(f_{nadir}) + 491.6(ROCOF)$	1	1	0.09542	111.74	9.976%
30% PV	$P_{deload} = -8917 + 154.9(f_{nadir}) + 997.4(ROCOF)$	0.9998	0.9998	0.7545	122.36	7.283%
40% PV	$P_{deload} = -1.055 \times 10^4 + 182(f_{nadir}) + 422.5(ROCOF)$	0.999	0.999	2.057	145.75	6.536%
50% PV	$P_{deload} = -1.106 \times 10^4 + 190.6(f_{nadir}) + 73.63(ROCOF)$	0.9986	0.9986	2.265	178.037	6.335%
60% PV	$P_{deload} = -1.065 \times 10^4 + 183.6(f_{nadir}) - 60.83(ROCOF)$	0.9981	0.9981	2.399	188.483	5.694%

BESS: Battery Energy Storage System (BESS) can store and supply active power with a quick response time. Thus, BESS can provide additional support to stop and recover the frequency excursion, which is particularly beneficial for renewable-rich grids (Zhang et al., 2018). A typical BESS comprises two main parts. The first part stores energy via electrochemical process. The second part contains rectifier–inverter set to transform AC to DC and vice versa (DIgSILENT, 2010). Total three controllers, i.e., frequency controller, real and reactive power (PQ) controller, and charge controller are used to generate additional output power to enhance frequency response (Jawad et al., 2020). A comprehensive overview of the utilized BESS model in this paper is demonstrated in DIgSILENT (2010).

Synchronous Condenser: With the increasing penetration of renewable energy into conventional grids, synchronous condensers can serve as a supporting device to enhance frequency response by providing supplementary inertia (Arayamparambil Vinaya Mohanan et al., 2020). High inertia synchronous condensers can be deployed to enhance frequency response. Alternatively, retired synchronous generators can be retrofitted as synchronous condensers to improve the frequency response of the renewable dominated grids (Masood et al., 2016). The later mentioned approach is applied in this work.

5.1. Simulation scenarios

For simulation purposes, the same test system as described in Section 4.1, i.e., IEEE 39 bus system, is chosen. The same cases of PV penetration levels as in Table 2 are considered for validation. The tripping event of Generator 5 (508 MW) is again selected for performing the time-domain simulation. Furthermore, a detailed comparison of deloaded PV integrated grid scenario with both BESS and SC integrated scenarios is carried out. Note that, the capacity of BESS and SC are kept the same as required deloaded PV support to perform thorough comparison. Under frequency load shedding (UFLS) scheme is also deployed to emulate standard power grids, which gets activated when system frequency goes below 59 Hz. 15% of the total load shed is considered to preserve system frequency stability in this paper. In brief, every case comprises three scenarios, i.e., deloaded PV, BESS, and SC integrated grid scenario, consecutively. Additionally, each scenarios' frequency response curve is compared in terms of frequency nadir, ROCOF, and the activation of UFLS scheme after generator tripping event.

5.2. Performance analysis

5.2.1. 20% PV integrated grid

From Section 5.1, the estimated deloaded PV support calculated from Eq. (24) is 111.74 MW to maintain frequency above 59 Hz with a nominal ROCOF. At first, a synchronous generator tripping event is simulated, keeping additional PV support per calculation, with a UFLS scheme installed. Also, BESS and SC having the same capacity of 111.74 MW and 111.74 MVAR are installed in the grid in two distinct scenarios. The same simulations are performed for each scenario. As observed from Fig. 10(a), frequency nadir points of deloaded PV, BESS, and SC integrated grid scenarios are 59.0635 Hz, 58.9966 Hz, 58.9865 Hz, respectively. It indicates that the UFLS scheme gets activated for both BESS and SC integration scenario. In contrast, the proposed deloaded PV system successfully preserves frequency within 59 Hz without activating the UFLS scheme. Moreover, corresponding ROCOF magnitudes calculated from Eq. (9) are 0.1102 Hz/s, 0.1232 Hz/s, 0.1606 Hz/s consecutively. Although ROCOF values in all scenarios are within acceptable range, deloaded PV scenario gives the lowest ROCOF after disturbance. Thus, our recommended model shows viable results.

After performing the same simulations without any UFLS schemes, the difference among frequency nadir points of the three scenarios becomes more evident. The corresponding values are 59.0635 Hz, 58.9238 Hz, and 58.2497 Hz, respectively for the three scenarios. Although BESS support comes close to deloaded PV support, SC support is far below considering frequency nadir points. Corresponding frequency response curves are shown in Fig. 10(b).

5.2.2. 30% PV integrated grid

Following the same procedure as the previous case, simulations are performed for the three scenarios of deloaded PV, BESS, and SC integrated grid. Additional support size is 122.36 MW

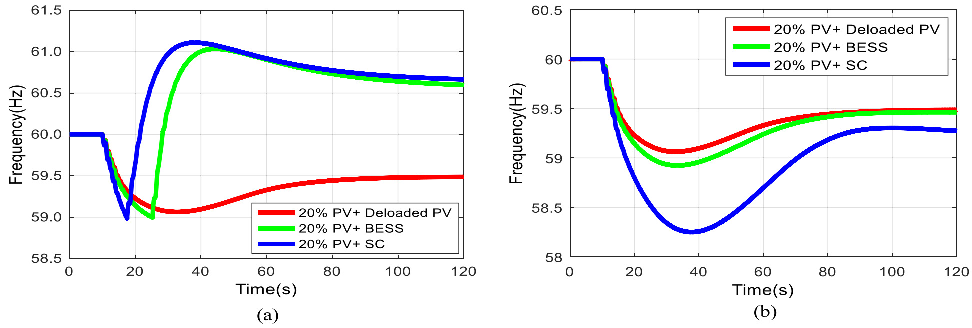

Fig. 10. Frequency response curves due to synchronous generator tripping (20% PV integrated grid) (a) with UFLS scheme, (b) without UFLS scheme.

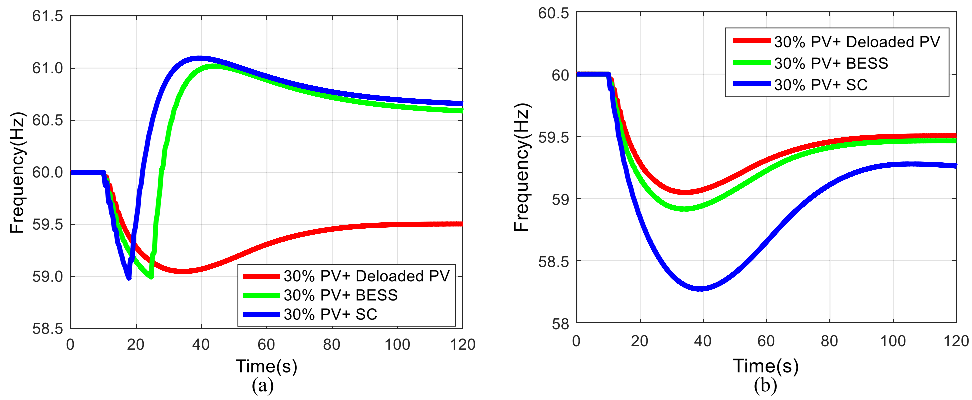

Fig. 11. Frequency response curves due to synchronous generator tripping (30% PV integrated grid) (a) with UFLS scheme, (b) without UFLS scheme.

according to Eq. (25) for the first two scenarios and 122.36 MVAR for the last one. The observed curves for simulations with UFLS schemes from Fig. 11(a) are similar to previous case. As estimated, Deloaded PV support preserves frequency within 59 Hz with frequency nadir of 59.0488 Hz where both BESS and SC fail to maintain frequency within the acceptable range.

In addition, calculated ROCOF magnitudes for each scenario are 0.0865 Hz/s, 0.1150 Hz/s, and 0.1457 Hz/s. Deloaded PV support again produces the best result among these supporting mechanisms in maintaining frequency stability. For the simulations without UFLS, Fig. 11(b) shows that frequency nadir points are 59.0488 Hz, 58.9152 Hz, and 58.2726 Hz, respectively. The results imply that using SC of the estimated amount is not enough to improve frequency nadir. However, BESS produces comparatively good results than SC. Still, using deloaded PV is the best possible support mechanism among them, considering the same support size.

5.2.3. 40% PV integrated grid

In this case, the estimated required deloaded PV support is 145.75 MW from Table 2. Assigning the same support size to BESS and SC, simulations are conducted. From Fig. 12(a), it is observed that estimated deloaded PV support was sufficient in retaining frequency above 59 Hz with a frequency nadir of 59.0407 Hz. But, two later scenarios fail to do so, as a result, UFLS scheme is activated, and load shedding takes place. Corresponding frequency nadir points are 58.9961 Hz and 58.9805 Hz.

Furthermore, the associated ROCOF magnitudes for these scenarios are 0.1072 Hz/s, 0.1243 Hz/s, 0.1555 Hz/s. For the simulations without UFLS scheme, frequency nadir points are observed to be 59.0407 Hz, 58.9223 Hz, and 58.2364 Hz for these three scenarios from Fig. 12(b). The findings are similar to the prior instance, in which deloaded PV outperforms BESS with the same support size.

5.2.4. 50% PV integrated grid

For the 50% PV integrated case, the requisite deloaded PV support following a synchronous generator tripping event is 178.037 MW. The frequency response curves for the simulations are presented in Fig. 13(a). The corresponding frequency nadir points are 59.0196 Hz, 58.9951 Hz, and 58.9809 Hz, respectively. Moreover, corresponding ROCOF magnitudes are 0.1094 Hz/s, 0.1227 Hz/s, and 0.1613 Hz/s, respectively. The results again validate the effectiveness of our proposed methodology as no UFLS scheme gets activated while utilizing deloaded PV support. Performing simulation without UFLS generates frequency nadir of 59.0196 Hz, 58.8674 Hz, and 58.0166 Hz successively, shown in Fig. 13(b). The values dictate a distinct difference in the performance of deloaded PV scenario with BESS and SC integrated scenario, confirming the feasibility of using deloaded PV support in the grid.

5.2.5. 60% PV integrated grid

With the highest level of PV integration in the grid, the required deloaded PV support was determined to be 188.483 MW. The BESS and SC sizes are set to 188.483 MW and 188.483 MVAR, respectively, following the same pattern as in earlier cases. Fig. 14(a) shows the frequency response curves with UFLS schemes enabled. Even in this case, with a frequency nadir of 59.0062 Hz, deloaded PV support was able to preserve frequency nadir above 59 Hz. Both BESS and SC, like the preceding examples, fail to keep frequency above 59 Hz, with frequency nadir points of 58.9936 Hz and 58.9820 Hz, respectively. The calculated ROCOF values for PV, BESS and SC scenarios are 0.1084 Hz/s, 0.1254 Hz/s, and 0.1648 Hz/s, respectively. As a consequence, as compared to other circumstances, adopting deloaded PV produces a more convenient outcome in terms of ROCOF value.

Fig. 14(b) depicts the frequency response curves for the three scenarios in simulations without the UFLS scheme. The corresponding frequency nadir points are 59.0062 Hz, 58.9255 Hz, and

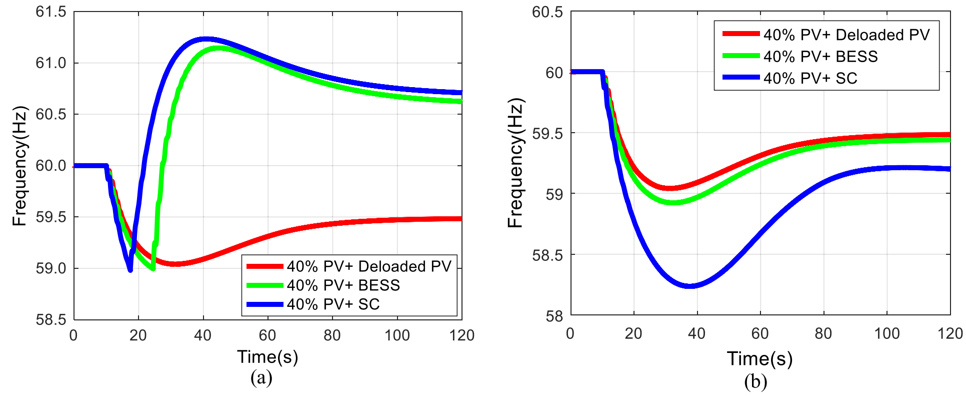

Fig. 12. Frequency response curves due to synchronous generator tripping (40% PV integrated grid) (a) with UFLS scheme, (b) without UFLS scheme.

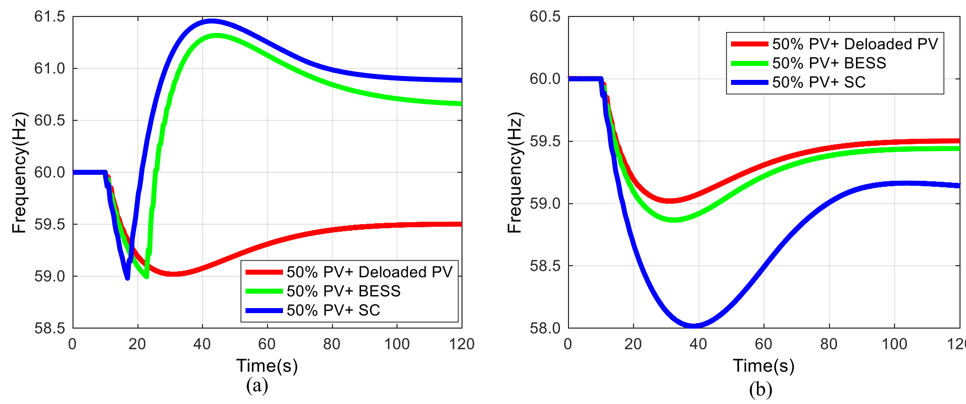

Fig. 13. Frequency response curves due to synchronous generator tripping (50% PV integrated grid) (a) with UFLS scheme, (b) without UFLS scheme.

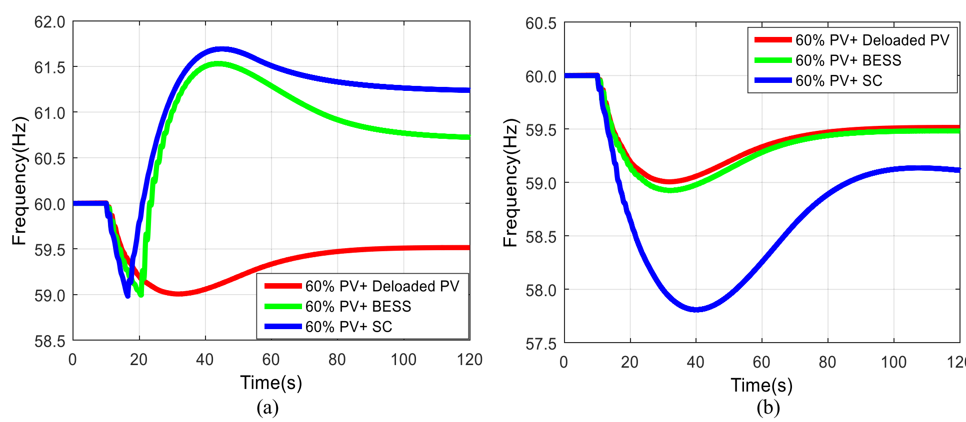

Fig. 14. Frequency response curves due to synchronous generator tripping (60% PV integrated grid) (a) with UFLS scheme, (b) without UFLS scheme.

57.8095 Hz, respectively. The significant variation in frequency nadir is apparent in the figure, with deloaded PV having the greatest frequency nadir. Although BESS comes close to deloaded PV in terms of frequency nadir, SC is significantly lower than the other two scenarios. So, even in the event of a 60% PV integration, deloaded PV support still provides the highest frequency stability.

The above five cases combinedly show the validity of the proposed methodology. As in every case, the estimated additional deloading percentage can keep frequency nadir and ROCOF within the allowable range. Moreover, after assigning the same size to deloaded PV, BESS, and SC, the deloaded PV showed better results in every case. It prevented the system from going through load shedding after generation tripping event. Total findings from these cases are summarized in Table 3 for convenience.

6. Discussions

6.1. Scalability of the proposed approach

The proposed method of calculating adequate deloaded PV support for grid frequency stability is based on two frequency response metrics: frequency nadir and ROCOF. Before grid integration, simulations will be needed to determine the relationship between deloaded PV support and frequency response characteristics for a major synchronous generator outage. The required deloaded PV percentage can then be calculated using the approach provided. Note that these frequency response characteristics can be obtained in the same way for any type of power system, with no changes to the method's steps. Consequently, this technique

Table 3
Summary of performance analysis.

Case study	Simulation scenarios	Performance analysis		
		Frequency nadir (Hz)		$\lvert ROCOF \rvert$ (Hz/s)
		With UFLS	Without UFLS	
20% PV integrated Grid	Deloaded PV	59.0635	59.0635	0.1102
	BESS	58.9966	58.9238	0.1232
	SC	58.9865	58.2497	0.1606
30% PV integrated Grid	Deloaded PV	59.0488	59.0488	0.0865
	BESS	58.9955	58.9152	0.1150
	SC	58.9857	58.2726	0.1457
40% PV integrated Grid	Deloaded PV	59.0407	59.0407	0.1072
	BESS	58.9961	58.9223	0.1243
	SC	58.9805	58.2364	0.1555
50% PV integrated Grid	Deloaded PV	59.0196	59.0196	0.1094
	BESS	58.9951	58.8674	0.1227
	SC	58.9809	58.0166	0.1613
60% PV integrated Grid	Deloaded PV	59.0062	59.0062	0.1084
	BESS	58.9936	58.9255	0.1254
	SC	58.9820	57.8095	0.1648

can be scaled up to larger power systems in addition to functioning for small grid systems. Moreover, if the grid planners want to add more synchronous generators or PV systems to an existing grid, they can repeat the same approach to figure out the appropriate parameters. As a result, this method can be used in any new or existing grid system, large or small.

6.2. Controlling parameters and tuning

The primary governing parameters for the accuracy of the proposed method can be separated into two categories. The first category involves deciding the step size for increasing the deloading percentage in subsequent PV system simulations. Setting up the initial and final deloading percentages of the PV systems is also an important aspect of the first category. The second category includes dictating the grid system's desired frequency response characteristics, such as frequency nadir and ROCOF. These two categories are critical for implementing the suggested approach effectively.

For the first segment, if the step size is chosen to be excessively large for successive increment of deloading percentage, the resultant values from the simulations can create excessive variety in data. This can drastically reduce the accuracy of the MLRA model built for a certain amount of PV integration in the grid. Furthermore, selecting a very small size increases the computing burden, making the operation more tedious. After several trial-and-error simulations, a reasonable amount of increment (0.25%) was found to strike a compromise between these two possibilities. This procedure was tested at various levels of PV penetration, which helped to justify the chosen percentage. Note that, that the quantity may vary based on the size of the test system. The next crucial tuning element was deciding on the final percentage. Running simulations up to 10% of total PV deloading resulted in the satisfactory frequency response outcome starting at 0.25 percent penetration for the 20% PV integration case. This result indicated that for the necessary simulations, adopting a higher deloading percentage was unnecessary. Furthermore, as the level of PV integration increases in the grid, the required deloading percentage from PV systems decreases. So, the chosen values were also applicable for higher PV integration cases. This is how deloading percentage parameters were tuned for this research work, which resulted in precise results in every PV integration situation.

Following the successful formulation of the MLRA model, the frequency response parameters, which are the second controlling parameters, are set. The frequency nadir and ROCOF values were determined based on typically used values in the literature. However, recognizing the dominating element is critical for accurate parameter adjustment. ROCOF values were considerably lower in the case of the used test system. As a result, varying permissible ROCOF values had little impact on the requisite deloaded PV. In this context, the frequency nadir eventually became the main controlling parameter. Because the UFLS system was designed to function below 59 Hz, 59 Hz was chosen as the lowest permissible frequency nadir point. Fixing both of these parameters yielded the intended result in all PV integration scenarios, proving the validity of the proposed method.

6.3. Limitations and practical applicability

Although the proposed approach is scalable even for large-scale PV integrated grids, it does have some limitations. The following are the details:

- Due to the short period of the simulations, PV output was kept constant for the simulated situations. PV output, on the other hand, is strongly dependent on temperature and irradiation levels in practice. As a result, their fluctuation over time is not taken into account in this study.
- Load demand in the electricity system may fluctuate over time. As a result, the required generation from synchronous generators and PV systems may vary. This study does not take into account the load side fluctuation.

These factors will be taken into account in future studies in order to produce more accurate estimation.

In order to put this strategy into practice, the model formulation and determining the appropriate deloading percentage must be done during the grid planning stage. As a result, there will be no variation in the procedure for implementing grids in practice. Even under extreme conditions, the proposed approach will suffice if calculations are made for the maximum load demand and lowest PV generation condition. Furthermore, if any changes are made to the grid, repeating the same process will generate the appropriate deloading percentage for PV systems. Therefore, the proposed method can be extended in practical applications.

7. Conclusions

This paper proposes a novel methodology of estimating the appropriate deloading percentage of PV systems in order to preserve frequency stability. To create a correlation with requisite deloading of PV systems, two frequency response performance metrics, frequency nadir and ROCOF, are utilized. MLRA models are formed using this methodology for different case scenarios in predicting required deloaded PV support, with acceptable goodness-of-fit parameters. According to the results, an intriguing trend is revealed; as PV integration increases in the grid, the required deloading percentage of PV systems to preserve frequency response reduces. Moreover, our estimation is validated by performance comparison with other supporting mechanisms, i.e., BESS and SC. Simulations are conducted for each supporting mechanism allocating the same support size as derived from MLRA models. Corresponding results indicate the success of the proposed methodology. Deloaded PV shows more effective outcomes than other mechanisms in terms of frequency nadir and ROCOF and protect the system from undergoing load shedding. Thus, the utilization of deloaded PV systems for preserving frequency stability in grids with significant PV penetration is justified. This paper also gives an insight into the appropriate deloading percentage of PV systems for different levels of PV penetration in the grid. Moreover, the proposed methodology will be helpful for grid planners to effectively estimate the required deloading percentage of PV systems for large PV integration. In future works, estimation of required deloaded PV systems will be carried out, taking into account more constraints and comparing the costs of each supporting mechanism.

References

Al-Shetwi, A., Sujod, M., 2018. Grid-connected photovoltaic power plants: A review of the recent integration requirements in modern grid codes. Int. J. Energy Res. 42 (5), 1849–1865. http://dx.doi.org/10.1002/er.3983.

Arayamparambil Vinaya Mohanan, V., Mareels, I., Evans, R., Kolluri, R., 2020. Stabilising influence of a synchronous condenser in low inertia networks. IET Gener. Transm. Distrib. 14 (17), 3582–3593. http://dx.doi.org/10.1049/iet-gtd.2020.0178.

Athay, T., Podmore, R., Virmani, S., 1979. A practical method for the direct analysis of transient stability. IEEE Trans. Power Appar. Syst. PAS-98 (2), 573–584. http://dx.doi.org/10.1109/tpas.1979.319407.

Ayamolowo, O., Manditereza, P., Kusakana, K., 2020. Exploring the gaps in renewable energy integration to grid. Energy Rep. 6, 992–999. http://dx.doi.org/10.1016/j.egyr.2020.11.086.

Bajaj, M., Singh, A., 2019. Grid integrated renewable DG systems: A review of power quality challenges and state-of-the-art mitigation techniques. Int. J. Energy Res. 44 (1), 26–69. http://dx.doi.org/10.1002/er.4847.

Basit, M., Dilshad, S., Badar, R., Sami ur Rehman, S., 2020. Limitations, challenges, and solution approaches in grid-connected renewable energy systems. Int. J. Energy Res. 44 (6), 4132–4162.

Bueno, P., Hernández, J., Ruiz-Rodriguez, F., 2016. Stability assessment for transmission systems with large utility-scale photovoltaic units. IET Renew. Power Gener. 10 (5), 584–597. http://dx.doi.org/10.1049/iet-rpg.2015.0331.

Cabrera-Tobar, A., Bullich-Massagué, E., Aragüés-Peñalba, M., Gomis-Bellmunt, O., 2016. Review of advanced grid requirements for the integration of large scale photovoltaic power plants in the transmission system. Renew. Sustain. Energy Rev. 62, 971–987. http://dx.doi.org/10.1016/j.rser.2016.05.044.

Chen, J., Jiang, X., Li, J., et al., 2020. Multi-stage dynamic optimal allocation for battery energy storage system in distribution networks with photovoltaic system. Int. Trans. Electr. Energy Syst. 30 (12).

DIgSILENT, 2010. DIgSILENT PowerFactory application example battery energy storing systems BESS.

DIgSILENT, 2013. DigSILENT GmbH, DIgSILENT PowerFactory V15.1- User Manual. DIgSILENT.

Eftekharnejad, S., Vittal, V., Heydt, G., Keel, B., Loehr, J., 2013. Small signal stability assessment of power systems with increased penetration of photovoltaic generation: A case study. IEEE Trans. Sustain. Energy 4 (4), 960–967. http://dx.doi.org/10.1109/tste.2013.2259602.

Hartmann, B., Vokony, I., Táczi, I., 2019. Effects of decreasing synchronous inertia on power system dynamics—Overview of recent experiences and marketisation of services. Int. Trans. Electr. Energy Syst. 29 (12), http://dx.doi.org/10.1002/2050-7038.12128.

Hernández, J., Bueno, P., Sanchez-Sutil, F., 2017. Enhanced utility-scale photovoltaic units with frequency support functions and dynamic grid support for transmission systems. IET Renew. Power Gener. 11 (3), 361–372. http://dx.doi.org/10.1049/iet-rpg.2016.0714.

Hernández, J., Sanchez-Sutil, F., Vidal, P., Rus-Casas, C., 2018. Primary frequency control and dynamic grid support for vehicle-to-grid in transmission systems. Int. J. Electr. Power Energy Syst. 100, 152–166. http://dx.doi.org/10.1016/j.ijepes.2018.02.019.

IEA, 2021. Solar PV – Tracking Power 2020 – Analysis - IEA. IEA, https://www.iea.org/reports/tracking-power-2020/solar-pv. Published 2021. (Accessed 10 May 2021).

IRENA, 2020. Renewable energy statistics. Irena.org https://irena.org/publications/2020/Jul/Renewable-energy-statistics-2020. Published 2021. (Accessed 10 May 2021).

Jawad, A., Naim, S., Saha, C., Masood, N., 2020. Frequency stability enhancement of a large-scale PV integrated grid. In: 2020 11Th International Conference on Electrical and Computer Engineering, ICECE. IEEE, Dhaka, Bangladesh, http://dx.doi.org/10.1109/ICECE51571.2020.9393073. (Accessed 4 May 2021).

Kumar, R.Vinod, Singh, S., 2018. Solar photovoltaic modeling and simulation: As a renewable energy solution. Energy Rep. 4, 701–712. http://dx.doi.org/10.1016/j.egyr.2018.09.008.

Masood, N., Yan, R., Saha, T., Bartlett, S., 2016. Post-retirement utilisation of synchronous generators to enhance security performances in a wind dominated power system. IET Gener. Transm. Distrib. 10 (13), 3314–3321. http://dx.doi.org/10.1049/iet-gtd.2016.0267.

Nassar, I., Hossam, K., Abdella, M., 2019. Economic and environmental benefits of increasing the renewable energy sources in the power system. Energy Rep. 5, 1082–1088. http://dx.doi.org/10.1016/j.egyr.2019.08.006.

Petinrin, J., Shaabanb, M., 2016. Impact of renewable generation on voltage control in distribution systems. Renew. Sustain. Energy Rev. 65, 770–783. http://dx.doi.org/10.1016/j.rser.2016.06.073.

Qazi, A., Hussain, F., Rahim, N., Hardaker, G., Alghazzawi, D., Shaban, K., Haruna, K., 2019. Towards sustainable energy: A systematic review of renewable energy sources, technologies, and public opinions. IEEE Access 7, 63837–63851.

Rahmann, C., Castillo, A., 2014. Fast frequency response capability of photovoltaic power plants: The necessity of new grid requirements and definitions. Energies 7 (10), 6306–6322. http://dx.doi.org/10.3390/en7106306.

Rajakumar, V., Anbukumar, K., 2018. Enhancement of power quality using double-band hysteresis controller for the grid integrated renewable energy system. Int. Trans. Electr. Energy Syst. 28 (11), e2623. http://dx.doi.org/10.1002/etep.2623.

Rajan, R., Fernandez, F., Yang, Y., 2021. Primary frequency control techniques for large-scale PV-integrated power systems: A review. Renew. Sustain. Energy Rev. 144, 110998. http://dx.doi.org/10.1016/j.rser.2021.110998.

Rocabert, J., Capo-Misut, R., Munoz-Aguilar, R., Candela, J., Rodriguez, P., 2019. Control of energy storage system integrating electrochemical batteries and supercapacitors for grid-connected applications. IEEE Trans. Ind. Appl. 55 (2), 1853–1862. http://dx.doi.org/10.1109/tia.2018.2873534.

Said, S., Aly, M., Balint, H., 2020. An efficient reactive power dispatch method for hybrid photovoltaic and superconducting magnetic energy storage inverters in utility grids. IEEE Access 8, 183708-183721. http://dx.doi.org/10.1109/access.2020.3029326.

Seneviratne, C., Ozansoy, C., 2016. Frequency response due to a large generator loss with the increasing penetration of wind/PV generation – a literature review. Renew. Sustain. Energy Rev. 57, 659–668. http://dx.doi.org/10.1016/j.rser.2015.12.051.

Shaqsi, A.AL., Sopian, K., Al-Hinai, A., 2020. Review of energy storage services, applications, limitations, and benefits. Energy Rep. 6, 288–306. http://dx.doi.org/10.1016/j.egyr.2020.07.028.

Shutang, Y., 2020. Photovoltaic (PV) virtual inertia and fast frequency regulation in high pv power grids. ArXiv abs/2010.11340.

Sidrach-de-Cardona, M., López, Ll Mora, 1999. Performance analysis of a grid-connected photovoltaic system. Energy (ISSN: 0360-5442) 24 (2), 93–102. http://dx.doi.org/10.1016/S0360-5442(98)00084-X.

Tavakkoli, M., Adabi, J., Zabihi, S., Godina, R., Pouresmaeil, E., 2018. Reserve allocation of photovoltaic systems to improve frequency stability in hybrid power systems. Energies 11 (10), 2583. http://dx.doi.org/10.3390/en11102583.

Verma, P., Kaur, T., Kaur, R., 2021. Cost assessment of deloaded photovoltaic systems. IOP Conf. Ser. Mater. Sci. Eng. 1033, 012001. http://dx.doi.org/10.1088/1757-899x/1033/1/012001.

Xin, H., Liu, Y., Wang, Z., Gan, D., Yang, T., 2013. A new frequency regulation strategy for photovoltaic systems without energy storage. IEEE Trans. Sustain. Energy 4 (4), 985–993. http://dx.doi.org/10.1109/tste.2013.2261567.

Yan, G., Liang, S., Jia, Q., Cai, Y., 2019. Novel adapted de-loading control strategy for PV generation participating in grid frequency regulation. J. Eng. 2019 (16), 3383–3387. http://dx.doi.org/10.1049/joe.2018.8481.

Zarina, P., Mishra, S., 2016. Cost benefit of using deloaded PV instead of battery. In: 2016 IEEE International Conference on Power Electronics, Drives and Energy Systems, PEDES. IEEE, pp. 1–4. http://dx.doi.org/10.1109/PEDES.2016.7914468. (Accessed 12 May 2021).

Zarina, P., Mishra, S., Sekhar, P., 2012. Deriving inertial response from a non-inertial PV system for frequency regulation. In: 2012 IEEE International Conference on Power Electronics, Drives and Energy Systems, PEDES. IEEE, Bengaluru, India, pp. 1–5.

Zarina, P., Mishra, S., Sekhar, P., 2014. Exploring frequency control capability of a PV system in a hybrid PV-rotating machine-without storage system. Int. J. Electr. Power Energy Syst. 60, 258–267. http://dx.doi.org/10.1016/j.ijepes.2014.02.033.

Zhang, C., Wei, Y., Cao, P., Lin, M., 2018. Energy storage system: Current studies on batteries and power condition system. Renew. Sustain. Energy Rev. 82, 3091–3106. http://dx.doi.org/10.1016/j.rser.2017.10.030.

Using a new hybrid methodology for optimal allocation of FACTS devices

Laxmi, *Department of Computer Science Engineering, Aryan Institute of Engineering & Technology, Bhubaneswar, laxmi3349@gmail.com*

Biraja Nayak, *Department of Computer Scinece Engineering , Capital Engineering College, Bhubaneswar, birajanayak21@gmail.com*

Asheerbad Pradhan, *Department of Electronics and Communication Engineering , Raajdhani Engineering College, Bhubaneswar, asheerbadpradhan46@gmail.com*

Balagoni Sampath Kumar, *Department of Electrical and Electronics Engineering, NM Institute of Engineering & Technology, Bhubaneswar, bs.kumar89@gmail.com*

Keywords:
FACTS devices
Hybrid AGPSO-GWO
Multi-objective optimization
Power loss minimization

A B S T R A C T

The proposed research article introduces a new hybrid heuristic algorithm based on Autonomous Groups Particle Swarm and Grey Wolf optimizers (AGPSO-GWO) via multi-objective function for the allocation of the Flexible Alternating Current Transmission Systems (FACTS) controllers in power grids to minimize the active power system losses, voltage deviation, and the system operational costs. In this research work, the Static Var Compensator (SVC), Thyristor-Controlled Series Compensator (TCSC), and Unified power flow controller (UPFC) are used as FACTS controllers. A comparative analysis is conducted with other proposed heuristic optimization algorithms such as Particle Swarm Optimization (PSO), Autonomous Group Particle Swarm Optimization (AGPSO) Grey Wolf optimizer (GWO), and improved grey wolf optimization (IGWO) algorithms to confirm and validate the superiority of the proposed technique. Moreover, the proposed AGPSO-GWO has been compared with the previous existing Simulated Annealing (SA) in the literature to prove its superiority and ensure its validity. The proposed scheme has been validated and applied on 30-bus and 118-bus IEEE electric power systems. The numerical results had been carried out using MATLAB and MATPOWER packages. The simulation results show that the proposed algorithm offers the best performance among all algorithms to achieve the optimum global minimum solutions with the highest convergence rate.

1. Introduction

The rise in global demand for electricity due to socio-economic developments and the constraints on expanding power generation plants' construction and transmission lines has resulted in a significant gap between power generation and demand. Consequently, it resulted in improper performance of the power systems, such as excessive power losses, congested lines, voltage instabilities, reliability, and stability problems. Furthermore, several critical demands are very sensitive to power quality degradations. The heavy industrials, radiations and nuclear installations, hospitals, etc., can be considered as a part of such critical loads. Also, the reliable on-site power supply of nuclear installations' aspects with insuring the power quality plays a valuable role in ensuring the safety of nuclear reactors operation and protect the public and environment against radiation hazards. Therefore, the optimal use of the grids is vital to enable the high performance of the electrical power systems (Gaur and Mathew, 2018; Singh and Agrawal, 2018; Muhammad et al., 2020). Effective implementation of reactive power compensation in transmission systems can address these problems. Recently, the area of reactive power compensation has become increasingly important. If properly planned, it can significantly improve the performance of the power system, i.e., improving the voltage profile, reducing power system losses, increasing the permissible power transfer capability, and enhancing the stability and reliability of the system (Hema Sekhar et al., 2020; Guo et al., 2020; Muhammad et al., 2021).

One of the most popular reactive power compensation devices is the flexible alternating current transmission system (FACTS), which refers to power electronics-based devices that enable better control of the alternating current system and enhance the performance of the power system. FACTS controllers ensure that the efficient use of existing power generation and transmission systems with significantly less investment as compared to the additional costs by building new transmission and generation units (Lee et al., 2019).

Abbreviations

AGPSO-GWO	Autonomous Groups Particle Swarm and Grey Wolf optimizers
FACTS	Flexible Alternating Current Transmission Systems
SVC	Static Var Compensator
TCSC	Thyristor-Controlled Series Compensator
UPFC	Unified power flow controller
PSO	Particle Swarm Optimization
AGPSO	Autonomous Group Particle Swarm Optimization
GWO	Grey Wolf optimizer
SA	Simulated Annealing
IGWO	Improved Grey Wolf Optimization
STATCOM	Static Synchronous Compensator
VSC	Voltage Source Converters
MFO	Moth Flame Optimization
BBO	Biogeography Based Optimization
WIPSO	Weight Improved PSO
OC	Operating Cost
VD	Voltage Deviation
PL	Active power losses
DLH	Dimension Learning-based Hunting strategy
RE	Relative error
MAE	Mean absolute error
RMSE	Root mean square error
SD	Standard deviation

Symbols

x_{TL}^{new}	Transmission line reactance after TCSC installation
x_{TL}	Transmission line reactance without TCSC installation
x_{TCSC}	Reactance of the TCSC
V	Magnitude of the bus voltage
B_{SVC}	Susceptance of the SVC
G_k	Conductance of the kth line
NL	Total number of transmission lines
δ_{ij}	Angle difference between the voltages of the buses i and j.
Nl	Total number of load buses
C_{PL}	Annual energy losses of the power system
C_{FACTS}	installation cost of FACTS
C_{SVC}	installation cost of the SVC
C_{TCSC}	installation cost of the TCSC
C_{UPFC}	installation cost of the UPFC
S	Operating range of the FACTS devices
$PL_{\_FACTS}, PL_{\_base}$	Real power losses with and without connecting the FACTS controller to the power system
$VD_{\_FACTS}, VD_{\_base}$	Voltage deviation with and without installation of FACTS controllers
$OC_{\_FACTS}, OC_{\_base}$	System operating cost with and without installation of FACTS controllers
P_{Gi}, P_{Di}	Active power generated and demanded at bus i
Q_{Gi}, Q_{Di}	Reactive power generated and demanded at bus i
N	Total number of buses, S_{ij} represents the apparent power flow inline i-j
$S_{ij\_\max}$	Is the thermal limit of line i-j,
G_{ij}, B_{ij}	Transfer conductance and susceptance between bus i and bus j, respectively
$Q_{svc}^{\max}, Q_{svc}^{\min}$	SVC reactive power's maximum and minimum limits
$X_{TCSC}^{\max}, X_{TCSC}^{\min}$	Maximum and minimum TCSC reactance limits
t	Current iteration
v_i^{t+1}	Velocity vector of a particle i in iteration $t+1$
$gbest, pbest_i$	Best global position and best particle position, respectively
T	Maximum iteration number
c_1, c_2	Are acceleration coefficients
r_1, r_2	Random numbers
ω	Inertia weight constant
x_i^{t+1}	Position vector of particle i in iteration $t+1$
$\omega_{\min}, \omega_{\max}$	Minimum and maximum values of the inertia weight
X_α, D_α	Position and coefficient vectors of the alpha wolf.
X_β, D_β	Position and coefficient vectors of the beta wolf.
X_δ, D_δ	Position and coefficient vectors of the delta wolf
$X_i(t)$	Position vector of ith grey wolf in the current iteration
X_{i_GWO}	Position vector of ith grey wolf
A, C	Coefficient vectors
cg_1, cg_2, cg_3	Variables
D_i	Euclidean distance
pop	population matrix
$X_{i-DLH,d}$	Position vector of ith grey wolf based on the DLH strategy
X_{i-GWO}	Position vector of ith grey wolf in the next iteration based on the GWO algorithm
$X_{n,d}(t)$	d[th] dimension of a random neighbor in the current iteration
$X_{r,d}(t)$	d[th] dimension of a random neighbor selected from the whole group of wolves
$rand$	random number.

The power that is transmitted through the transmission line is a function of three parameters, which are the impedance of the line, voltages at both ends, and the angle phase difference between buses at both ends. FACTS controllers can significantly affect these parameters, which contribute to controlling the power flow, maintaining the voltage within the permissible limits, reducing the power losses, and increasing the power transfer capability of the existing transmission lines (Mitiku Teferra and Ngoo, 2021; Singh et al., 2020).

On the basis of technological features, FACTS devices can be classified into two generations. The first generation uses thyristor-switched reactors and condensers such as the Static Var Compensator (SVC) and Thyristor-Controlled Series Compensator (TCSC). The second-generation utilizes Voltage Source Converters (VSC) as the Unified Power Flow Controller (UPFC) and the Static Synchronous Compensator (STATCOM) (Chow and Sanchez-Gasca, 2019). The optimal location and size of the FACTS devices should be considered to achieve the desired improvement in the performance of the power system (Mokhtari et al., 2021). Optimal allocating of the SVC controller can provide voltage regulation, dampening power oscillations in the grid after a contingency, improving the voltage profile, and minimizing system power losses. The TCSC can rapidly and continuously change the transmission line impedance, reducing power losses, minimizing subsynchronous resonance, and eliminating harmonic current. The STATCOM can correct power factor, control reactive power, and dampen low-frequency power oscillations. The UPFC devices have the ability to control the active and reactive power of the system, controlling the transmission angle and two-way power flows control. (Shehata et al., 2021a; Daealhaq et al., 2021; Ananth et al., 2021).

Throughout the literature, several methods have been applied to obtain the appropriate size and location of the FACTS controllers, which can be categorized into four groups: analytical methods, conventional optimization-based methods, metaheuristic optimization methods and, hybrid methods. The optimal allocation of FACTS is a nonlinear, multi-modal, mixed-integer, and highly constrained problem. Metaheuristic optimization techniques are remarkably efficient in dealing with these problems, so they are commonly applied to identify the optimum allocation of FACTS controllers (Singh and Kumar, 2020). Researchers have recently used various metaheuristic methods to determine the optimal allocation of the FACTS devices.

In Shehata et al. (2020), the optimum placement and capacity of the FACTS devices were determined using the Multi-Objective Multi-Verse Optimizer technique to jointly minimize three objective functions simultaneously, namely, voltage deviation, active power loss, and the installation cost of the FACTS devices. The SVC and TCSC were installed in the power system in two forms: single and combined. The proposed approach was implemented on the IEEE 57 bus test system. Based on the obtained results, the reduction of active power losses and voltage deviation is the highest when a combination of TCSC and SVC controllers is installed. A hybrid approach, namely, JAYA blended-moth flame, is considered in Dash et al. (2020b) to alleviate the transmission losses by installing SVC and TCSC in the IEEE 14 and 30 bus systems. Compared algorithms such as Particle Swarm Optimization (PSO) and Moth Flame Optimization (MFO) algorithms have been outperformed by the proposed algorithm. The researcher did not demonstrate the computational CPU time (speed) for the proposed approach to evaluate the optimal solution time performance. In addition, the proposed algorithms have not been tested on the large-scale power system. In order to achieve the maximum benefit of the FACTS device installation in the power system, Ref. (Kavitha and Neela, 2018) applied the Biogeography Based Optimization (BBO), PSO, and Weight Improved PSO (WIPSO) algorithms to obtain the optimum allocation of the FACTS controller to enhance a multi-objective function comprised of load bus voltage deviations, line loading, and FACTS devices' cost. The study has been executed using standard IEEE 14, 30, and 57 bus systems under different load conditions. The SVC, TCSC, and UPFC were considered as FACTS devices. The results obtained have shown that the BBO technique provided the best performance among the other methods used. The authors did not consider the statistical calculation to illustrate the performance of each proposed technique, clarifying the global minimum solutions. The issue of allocating FACTS devices to maximize the loading of the network at the lowest installation cost of FACTS without violating the voltage thermal constraints using a hybrid approach has been investigated in Dash et al. (2020a). This study implemented a metaheuristic–metaheuristic hybrid approach consisting of Ant Lion-Moth Flame-Slap Swarm optimization algorithms. The suggested approach has been performed using the standard IEEE 6 and 30 bus systems. But, the proposed method has not been implemented on a large-scale network. According to (Kanaan and Mehanna, 2020), the Simulated Annealing (SA) algorithm has been suggested to find the appropriate capacity and sitting of the SVC, TCSC, and UPFC to improve power system performance by reducing the system losses and voltage deviations. The objectives were analyzed separately and also combined into a single weighted goal function. The IEEE 30 bus system was used to verify the proposed method's performance. The proposed method has not been tested on a large network. Furthermore, this approach has not been validated by comparison with other optimization methods. From Kanaan et al. (2020), the PSO and SA have been utilized to find the optimal location and size of SVC to reduce the system overloading, losses, and voltage deviation. The proposed approaches are applied to the modified IEEE 30 bus system. The proposed methods have not been implemented on a large-scale network. In Shehata et al. (2021b), the Autonomous Group Particle Swarm Optimization (AGPSO) approach has been used to obtain an optimum size and placement of the SVC to reduce the real power losses in the transmission lines. The attitude of the proposed technique was validated on IEEE 14 and 30 bus standard systems. Even though the proposed technique outstripped the comparative algorithms, the multi-objective fitness function has not been considered in the study. The Grey Wolf optimizer (GWO) algorithm was used in Gautam et al. (2019) to determine the optimal size of the TCSC, while the optimal setting was determined using the A.C. power transfer distribution factor as a sensitivity factor. From Gautam et al. (2019), the prepared objective function had the capability to reduce the power loss and improve the available transfer capability of the system without violating the constraints of the power system. The proposed method has not been implemented and validated on a large scale network.

None of the studies have clarified the reasons for selecting the weight values for the weighted sum optimization problems. The presented study utilizes a strategy for selecting appropriate weight values. The GWO technique, widely used in the literature, suffers from the imbalance between exploitation and exploration phases, premature convergence, early loss of diversity, and entrapment in local optimums (Lu et al., 2018; Tu et al., 2019).

For addressing these drawbacks, this article presents a novel robust and well-established hybrid optimization approach that combines the AGPSO algorithm with the GWO algorithm, namely the AGPSO-GWO hybrid technique. This technique has not been implemented or applied before in electric power systems. The novel hybrid AGPSO-GWO technique uses the privilege of the diversity of the particle behavior provided by the AGPSO technique to improve the GWO algorithm's performance. The proposed algorithm enhances the performance of GWO using the autonomous group's methodology of the AGPSO method. The search agents of the proposed algorithm have diverse social and personal behaviors to avoid local optima trapping and improve convergence speed. Furthermore, a time-varying strategy based on nonlinear time-varying coefficients has been implemented to balance the exploitation and exploration phases and avoid losing diversity.

The research contributions can be deduced as the following:

This study proposes a novel hybrid AGPSO-GWO technique to improve the performance of the traditional GWO algorithm.

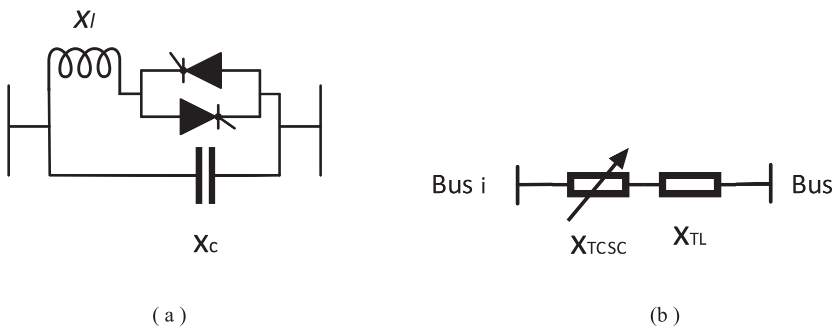

Fig. 1. (a) The TCSC Schematic diagram, (b) Model of TCSC in the transmission line.

The suggested algorithm is implemented to improve the power system performance by allocating FACTS devices optimally. The appropriate allocation of the FACTS devices such as SVC, TCSC, and UPFC is determined to minimize the power system's real power losses, bus voltage deviation, and system operating costs. Below are the article's key points.

- Simulations are performed and compared with various optimization algorithms, such as PSO, AGPSO, GWO, and IGWO, to verify the effectiveness of the AGPSO-GWO.
- To validate the performance of the AGPSO-GWO algorithm, the findings are compared with an existing study that used the SA technique.
- The AGPSO-GWO is applied to IEEE 30 and 118-bus systems with and without optimal allocations of the UPFC, TCSC, and SVC devices to reduce voltage deviation, active power losses, and operating cost.

Following the introduction, the modeling of the FACTS devices is presented in Section 2. The problem formulation is illustrated in Section 3. The description of the techniques is provided in Section 4. The existing results are analyzed in Section 5. The statistical evaluation of the proposed techniques is proposed in Section 6. Finally, the conclusion is given in Section 7.

2. FACTS modeling

FACTS are power electronic-based devices used in power systems to improve power grid controllability and power transfer capability by altering various electrical parameters in transmission systems (Balamurugan and Muthukumar, 2019). In this paper, all generations of the FACTS devices are considered; the SVC and TCSC represent the first generation, and the UPFC represents the second generation. These controllers are the most widely used FACTS systems in power grids (Jmii et al., 2017; Bakir et al., 2018). The FACTS controllers are allocated to minimize the active power losses, system operating cost, and bus voltage deviation. The following section discusses the modeling of the considered FACTS devices.

2.1. TCSC modeling

The TCSC is one of the series-connected FACTS controllers to the transmission lines, which can change the transmission line series impedance by adding an inductive or capacitive reactance (Dash et al., 2020b). The TCSC consists of a series-connected, thyristor-controlled reactor shunted by a condenser, as shown in Fig. 1. In this work, the TCSC is modeled as a controlled variable reactance that is connected in series to the transmission lines.

The modified reactance of the transmission line is given in Eq. (1) after the installation of the TCSC.

$$x_{TL}^{new} = x_{TL} + x_{TCSC} \tag{1}$$

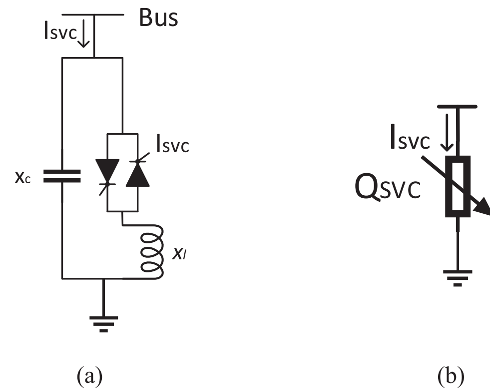

Fig. 2. (a) The SVC Schematic diagram, (b) Static model of the SVC.

where, x_{TL}^{new} represents the transmission line reactance after TCSC installation, x_{TL} is the transmission line reactance without installation of the TCSC, x_{TCSC} is the reactance of the TCSC. In order to avoid overcompensation when installing TCSC, the operating range of the TCSC is set as follows:

$$-0.8x_{TL} \leq x_{TCSC} \leq 0.2x_{TL} \tag{2}$$

2.2. SVC modeling

The SVC is a shunt-connected FACTS controller whose output can be regulated to interchange reactive power with the grid to improve the voltage profile, reduce active power loss, and enhance system load-ability and security (Agrawal et al., 2020; Singh et al., 2019). The SVC consists of a parallel combination of a condenser and a thyristor-controlled reactor, as shown in Fig. 2. The SVC controller is represented as a reactive power injection device in this paper. This power can be defined as follows:

$$Q_{svc} = -V^2 \times B_{svc} \tag{3}$$

where, V indicates the magnitude of the bus voltage and B_{svc} is the susceptance of the SVC.

The operating range of the SVC is given in Eq. (4)

$$-100MVAR \leq Q_{svc} \leq 100MVAR \tag{4}$$

2.3. UPFC modeling

The UPFC controller is a multifunctional FACTS device. It can influence phase angle, voltage, impedance, active and reactive power flow in the power system. The UPFC is modeled as a combination of TCSC and SVC connected in the line and bus with their operating ranges (Kanaan and Mehanna, 2020; Balamurugan and Muthukumar, 2019; Balamurugan et al., 2015) as given by Eqs. (2) and (4).

3. Problem formulation

Three fitness functions are minimized in this paper while considering the power system constraints. These fitness functions are optimized in two forms: mono-objective function and multi-objective function, as shown in the subsections below:

3.1. Mono-objective function

The active power losses, bus voltage deviation, and system operating cost are individually optimized in the mono-objective function form. The mathematical expression of these objectives can be expressed as:

3.1.1. Active power losses minimization (PL)

The reduction of active power losses in the power system can be represented as follows (Mamdouh et al., 2019; ben oualid Medani et al., 2018):

$$\min p_L = \min \sum_{k=1}^{NL} G_k[V_i^2 + V_j^2 - 2V_iV_j cos(\delta_{ij})] \tag{5}$$

where, G_k represents the conductance of the kth line, NL indicates the total number of transmission lines, V_i and V_j are the magnitudes of voltages at buses i and j, δ_{ij} refers to the angle difference between the voltages of the buses i and j.

3.1.2. Minimization of the bus voltage deviation (VD)

The reduction of the bus voltage deviation enhances the voltage of buses to remain within the allowable limits, which can be expressed as:

$$\min VD = \min \sum_{i=1}^{Nl} (V_i - 1.0)^2 \tag{6}$$

where, V_i denotes the magnitude of the voltage of the ith bus, Nl refers to the total number of load buses.

3.1.3. Minimization of the operating cost (OC)

In this paper, the operating cost (OC) includes two parts: cost related to energy losses and a cost due to the investment cost of FACTS controllers. Therefore, the objective function requires decreasing the cost of energy losses by alleviating active power losses with FACTS devices and reducing FACTS investment costs. The fitness function can be expressed as (Balamurugan and Muthukumar, 2019; Balamurugan et al., 2015; Nadeem et al., 2020; Saravanan et al., 2007):

$$\min(C_{PL} + C_{FACTS}) \tag{7}$$

where,

$$C_{PL} = (real power losse) \times 0.09 \times 365 \times 24 \tag{8}$$

$$C_{FACTS} = C_{SVC} + C_{TCSC} + C_{UPFC} \tag{9}$$

$$C_{SVC} = 0.0003S^2 + 0.3051S + 127.38 \tag{10}$$

$$C_{TCSC} = 0.0015S^2 - 0.7130S + 153.75 \tag{11}$$

$$C_{UPFC} = 0.0003S^2 - 0.2691S + 188.22 \tag{12}$$

where, C_{PL}, C_{FACTS} are the annual energy losses and installation cost of FACTS controller in $ respectively, 0.09 represents the cost associated with the power losses measured in $/KWhr, 365 indicates the days per year, 24 is the number of hours per day, $C_{SVC}, C_{TCSC}, C_{UPFC}$ are the installation cost of the SVC, TCSC, and UPFC devices in $/KVAR, respectively, S is the operating range of the FACTS devices in MVAR.

3.2. Multi-objective function

In the mono-objective function form, the considered objective functions are optimized simultaneously by combining them into a single objective function F, as given in Eq. (13).

$$F = w_1 \cdot J_1 + w_2 \cdot J_2 + w_3 \cdot J_3 \tag{13}$$

where, w_1, w_2, w_3 are weight coefficients to measure the contribution of each term in the fitness function.

$$J_1 = \frac{PL\_FACTS}{PL\_base}, J_2 = \frac{VD\_FACTS}{VD\_base}, J_3 = \frac{OC\_FACTS}{OC\_base} \tag{14}$$

where, $PL_{\_FACTS}$ and $PL_{\_base}$ are the real power losses with and without connecting the FACTS controller to the power system, $VD_{\_FACTS}$ and $VD_{\_base}$ are the voltage deviation with and without installation of FACTS controllers, $OC_{\_FACTS}$ and $OC_{\_base}$ are the system operating cost with and without installation of FACTS controllers.

3.3. Constraints

The following constraints are applied to the considered optimization problems:

$$P_{G_i} - P_{D_i} - \sum_{j=1}^{N} V_iV_j[G_{ij}cos(\delta_{ij}) + B_{ij}sin(\delta_{ij})] = 0 \tag{15}$$

$$Q_{G_i} - Q_{D_i} - \sum_{j=1}^{N} V_iV_j[G_{ij}sin(\delta_{ij}) - B_{ij}cos(\delta_{ij})] = 0 \tag{16}$$

$$V_{j\_\min} \le V_j \le V_{j\_\max} \tag{17}$$

$$S_{ij} \le S_{ij\_\max} \tag{18}$$

$$Q_{svc}^{\min} \le Q_{svc} \le Q_{svc}^{\max} \tag{19}$$

$$X_{TCSC}^{\max} \le X_{TCSC} \le X_{TCSC}^{\min} \tag{20}$$

Where P_{G_i} and P_{D_i} indicate the active power generated and demanded at bus i, Q_{G_i} and Q_{D_i} represent the reactive power generated and demanded at bus i, N refer to the total number of buses, S_{ij} represents the apparent power flow inline i-j, $S_{ij\_\max}$ is the thermal limit of line i-j, G_{ij} and B_{ij} indicate the transfer conductance and susceptance between bus i and bus j, respectively, $Q_{svc}^{\max}$ and $Q_{svc}^{\min}$ are the SVC reactive power's maximum and minimum limits, $X_{TCSC}^{\max}$ and $X_{TCSC}^{\min}$ are the maximum and minimum TCSC reactance limits.

4. Brief description of the optimization techniques

In addition to the classic PSO algorithm, the proposed method is compared with the AGPSO, GWO, and IGWO algorithms, which are briefly described in the following subsections.

4.1. Particle Swarm Optimization Technique (PSO)

The PSO is a metaheuristic optimization algorithm originally introduced by Kennedy and Eberhart, which simulates the behavior of birds flying in a swarm to obtain the best solution for the optimization problems. Each particle's motion is represented by two vectors, the position vector and the velocity vector (Wang et al., 2018). The particle's updated position is influenced by the best location the particle has previously acquired and the best position the whole swarm has achieved so far. Eqs. (21)–(23) generate the updated position and velocity of the particle during the optimization process (Faisal et al., 2020).

$$v_i^{t+1} = \omega v_i^t + c_1 r_1(pbest_i - x_i^t) + c_2 r_2(gbest - x_i^t), \tag{21}$$

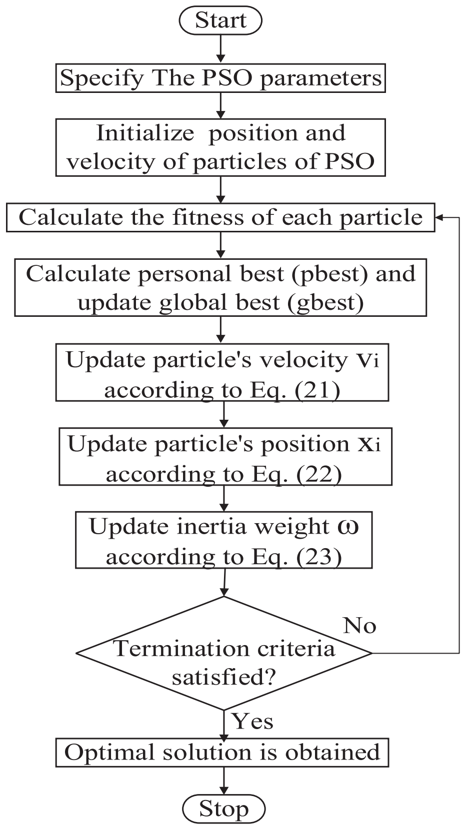

Fig. 3. PSO process.

$$x_i^{t+1} = x_i^t + (v_i^{t+1})T, \tag{22}$$

$$\omega_t = \omega_{\max} - \left(\frac{\omega_{\max} - \omega_{\min}}{T}\right)t, \tag{23}$$

where, v_i^{t+1} is the velocity vector of a particle i in iteration $t+1$, t is the current iteration, *gbest* and *pbest*$_i$ are the best global position and best particle position, respectively, T is the maximum iteration number, c_1 and c_2 are acceleration coefficients, r_1 and r_2 are random numbers, ω is the inertia weight constant, x_i^{t+1} is the position vector of particle i in iteration $t+1$, $\omega_{\min}$ and $\omega_{\max}$ are the minimum and maximum values of the inertia weight. The PSO process is depicted in Fig. 3

4.2. Autonomous Group Particle Swarm Optimization Technique (AGPSO)

There are some flaws in the PSO algorithm's performance, such as the rapid convergence without adequate exploration of the entire search space, trapped in the local optima, and the slow convergence rate (Rezaee Jordehi et al., 2015; Mirjalili et al., 2014a; Li et al., 2020). The AGPSO method has been introduced to address these deficiencies, wherein the swarm is divided into four independent groups inspired by the termite colony. In contrast to the traditional PSO algorithm, the acceleration coefficients (c_1, c_2) in the AGPSO algorithm have variable values using different models, as shown in Table 1. As a result, the algorithm's exploration phase has been strengthened to explore the whole search area. The optimization process's exploration and exploitation phases had been balanced to avoid premature convergence and quickly find the optimal global solution (Mirjalili et al., 2014a). The flowchart of the AGPSO algorithm is as shown in Fig. 4.

4.3. Gray Wolf Optimization Technique (GWO)

The GWO is a metaheuristic optimization algorithm implemented by Mirjalili et al. which emulates the leadership hierarchy and the hunting strategy of the grey wolves to solve the optimization problems. The flock of the grey wolves combines four levels of the leadership hierarchy: alpha (α), beta (β), delta (δ), and omega (ψ). Alpha is the leader and decision-maker of the flock that dominates all the wolves and lies at the top of the grey wolves' hierarchy. Delta and beta are the second and third levels in the hierarchy; they obey and help the alpha to make decisions and dominate all the rest of the wolves. Finally, omega is the last level of the hierarchy dominated by the wolves mentioned above. The hunting process is guided by alpha-called leaders followed by beta and delta. In the GWO method, the best fitness solution is analogous to alpha. The second-best solution is analogous to beta, the third-best solution analogous to delta, and the rest of the candidates' solutions are analogous to omega (Mirjalili et al., 2014b; Gutierrez et al., 2019).

For the mathematical modeling of the hunting mechanism, it is assumed that alpha, beta, and delta have a good knowledge of the possible position of prey and that the omega wolves update their location based on the three mentioned wolves. In this context, the following equations have been applied:

$$\vec{D}_\alpha = \left|\vec{C}_1.\vec{X}_\alpha - \vec{X}_i(t)\right|, \vec{D}_\beta = \left|\vec{C}_2.\vec{X}_\beta - \vec{X}_i(t)\right|, \vec{D}_\delta = \left|\vec{C}_3.\vec{X}_\delta - \vec{X}_i(t)\right| \tag{24}$$

$$\vec{X}_1 = \left|\vec{X}_\alpha - \vec{A}_1.\vec{D}_\alpha\right|, \vec{X}_2 = \left|\vec{X}_\beta - \vec{A}_2.\vec{D}_\beta\right|, \vec{X}_3 = \left|\vec{X}_\delta - \vec{A}_3.\vec{D}_\delta\right| \tag{25}$$

$$X_{i-GWO}(t+1) = \frac{\vec{X}_1 + \vec{X}_2 + \vec{X3}}{3} \tag{26}$$

where, X_α, and $D_\alpha$are the position and coefficient vectors of the alpha wolf, X_β and $D_\beta$are the position and coefficient vectors of the beta wolf, X_δ, and $D_\delta$are the position and coefficient vectors of the delta wolf, $X_i(t)$ indicates the position vector of the ith grey wolf, $X_{i-GWO}(t+1)$ represents the position vector of the ith grey wolf in the next iteration, A and C indicate the coefficient vectors. The vectors A and $C$are defined as follows:

$$\begin{aligned} \vec{A} &= 2\vec{a} \cdot \vec{r_1} - \vec{a} \\ \vec{C} &= 2 \cdot \vec{r_2} \end{aligned} \tag{27}$$

where, r_1 and $r_2$are vectors have random values in range [0,1] and a is a variable that has been reduced from 2 to 0 during iterations according to Eq. (28).

$$a = 2\left(1 - \frac{t}{T}\right) \tag{28}$$

The flowchart of the GWO algorithm is as shown in Fig. 5.

4.4. Improved Grey Wolf Optimization Algorithm (IGWO)

Despite the simplicity of the implementation, efficiency, and rapid convergence of the GWO algorithm, the disadvantage of this approach is that the wolves' updated location is based on the positions of the three wolves: alpha, beta, and delta. This causes the population to lose diversity too early, an imbalance between exploitation and exploration, and the wolves trapped in local optima may be far from the global minimum (Lu et al., 2018; Tu et al., 2019). In order to tackle these deficiencies, the IGWO approach was introduced in Nadimi-Shahraki et al. (2021). In addition to the candidate's updated wolf's position based on Eq. (26), the IGWO proposed another candidate's updated position based on a new search strategy called Dimension Learning-based Hunting (DLH) strategy, inspired by the natural behavior of

Table 1
Update strategies of c_1 and c_2.

Groups of particles	Update model of c_1	Update model of c_2
Group 1	$1.95 - 2t^{t/3}/T^{1/3}$	$2t^{t/3}/T^{t/3} + 0.05$
Group 2	$-2t^3/T^3 + 2.5$	$2t^3/T^3 + 0.5$
Group 3	$1.95 - 2t^{1/3}/T^{1/3}$	$2t^3/T^3 + 0.5$
Group 4	$-2t^3/T^3 + 2.5$	$2t^{1/3}/T^{1/3} + 0.05$

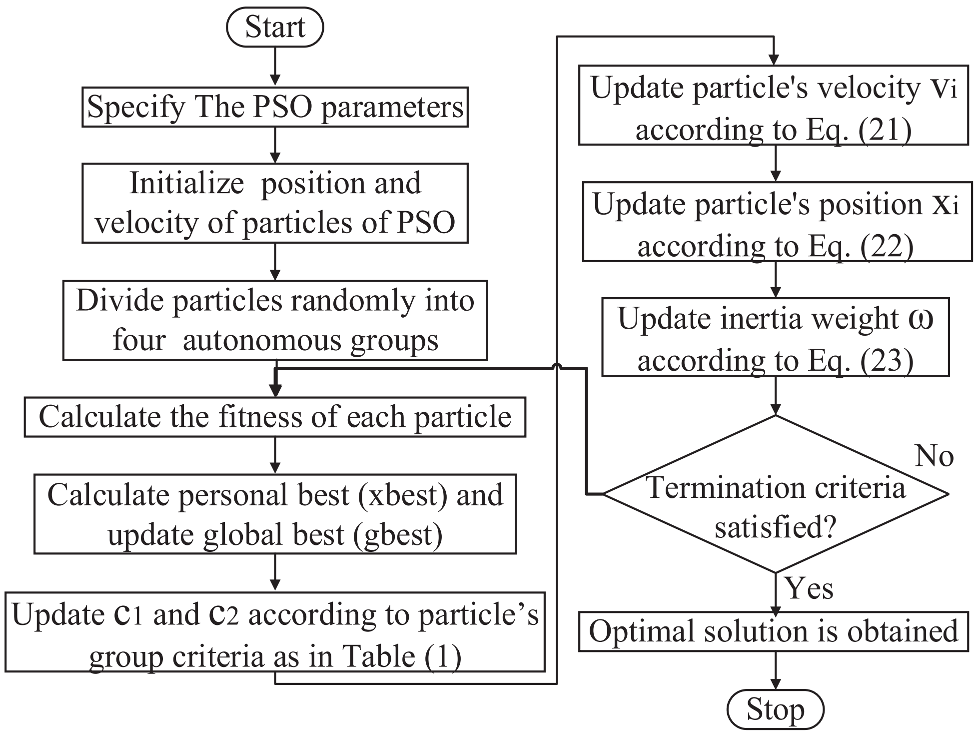

Fig. 4. Flowchart of the AGPSO algorithm.

individual hunting of grey wolves. The DLH search strategy improves the balance between local and global search and reduces the lack of population diversity (Nadimi-Shahraki et al., 2021).

Two updated positions of the wolves have been suggested in the IGWO technique: one by group hunting as in the classical GWO method according to Eq. (26) and the other by individual hunting using the DLH strategy. Following the identification of the updated position of wolves using Eq. (26), the IGWO method proposed an additional selection and updating stage, as shown below (Nadimi-Shahraki et al., 2021).

The radius R is computed using the following equation:

$$R_i(t) = \|X_i(t) - X_{i-GWO}(t+1)\| \tag{29}$$

Then, the neighbors of $X_i(t)$ denoted by $N_i(t)$ are constructed using Eq. (30) :

$$N_i(t) = \left\{X_j(t) D_i(X_i(t), X_j(t)) \le R_i(t), X_j(t) \in pop\right\} \tag{30}$$

where, D_i is the Euclidean distance between $X_i(t)$ and $X_j(t)$, pop is the population matrix.

After that, another updated position is proposed according to DLH strategy as follows:

$$X_{i-DLH,d}(t+1) = X_{i-d}(t) + rand \times (X_{n,d}(t) - X_{r,d}(t)) \tag{31}$$

where, $X_{n,d}(t)$ is the dth dimension of a random neighbor selected from $N_i(t)$, $X_{r,d}(t)$ the dth dimension of a random neighbor selected from the whole group of wolves, $rand$ is a random number.

The location of the individual is updated by comparing the two proposed new positions, which are calculated based on Eqs. (26) and (31), as expressed in Eq. (32).

$$X_i(t+1) = \begin{cases} X_{i-GWO}(t+1), & iff(X_{i-GWO}) \prec f(X_{i-DLH}) \\ X_{i-DLH}(t+1) & otherwise \end{cases} \tag{32}$$

The flowchart of the IGWO algorithm is as depicted in Fig. 6.

4.5. Hybrid AGPSO-GWO algorithm

A novel hybrid optimization technique has been developed in the present work known as the Autonomous Group Particle Swarm Grey Wolf Optimization (AGPSO-GWO) algorithm to address the drawback of the classical GWO algorithm. In order to eliminate the possibility of trapping in a local optimum and increase the efficiency of the classic GWO algorithm, the proposed AGPSO-GWO algorithm used the enhanced exploitation and exploration capabilities of the particles in the AGPSO algorithm. In the AGPSO technique, the swarm is divided into four groups. Each group has its coefficients to search the whole search space, avoid the premature convergence, and trap in local optimums. This search strategy is applied to the classical GWO algorithm's wolf population to obtain the global optimum solution of the optimization problem at a high conversion rate without trapping into local optimum.

In the AGPSO-GWO algorithm, the best three agents' position is updated using the inertia weight constant as given in

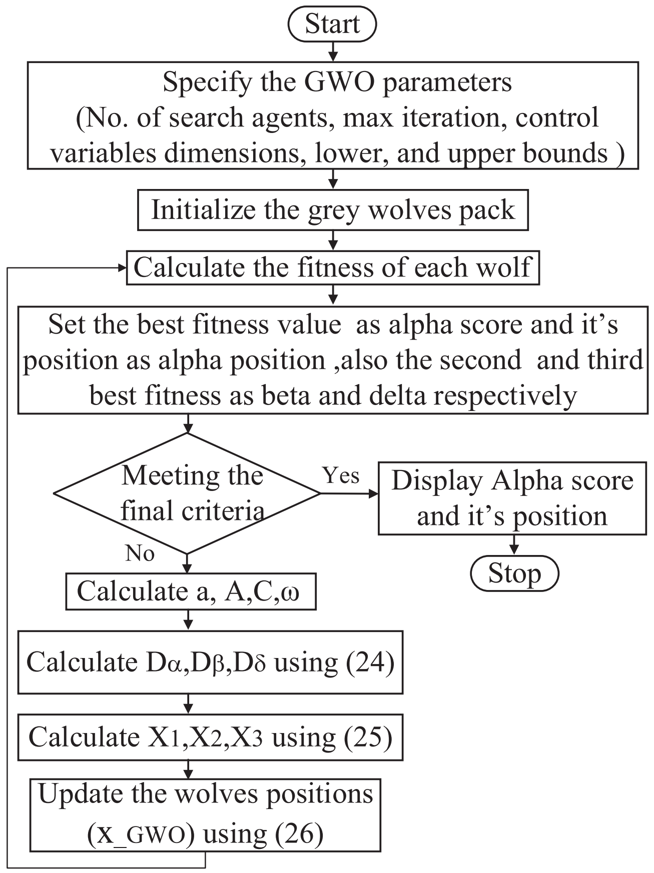

Fig. 5. Flowchart of the GWO algorithm.

Eqs. (33), (34).

$$\begin{aligned}\vec{D_\alpha} &= \left|\vec{C_1}.\vec{X_\alpha} - \omega \cdot \vec{X}(t)\right| \\ \vec{D_\beta} &= \left|\vec{C_2}.\vec{X_\beta} - \omega \cdot \vec{X}(t)\right| \\ \vec{D_\delta} &= \left|\vec{C_3}.\vec{X_\delta} - \omega \cdot \vec{X}(t)\right|\end{aligned} \tag{33}$$

$$\vec{X_1} = \left|\vec{X_\alpha} - \vec{A}_1.\vec{D_\alpha}\right|, \vec{X_2} = \left|\vec{X_\beta} - \vec{A_2}.\vec{D_\beta}\right|, \vec{X_3} = \left|\vec{X_\delta} - \vec{A_3}.\vec{D_\delta}\right| \tag{34}$$

As shown in Eq. (33), the wolf's exploitation and exploration are controlled in the search space by inertia weight constant. Update the position of the first three categories of the population according to Eq. (34). Then, the whole population is divided into four groups, each of which has a mathematical model for updating the values of the acceleration parameters cg_1, cg_2, and cg_3 as given in Table 2. Finally, the updated position $X_i(t+1)$ of the grey wolves is controlled through the velocity as shown below:

$$\begin{aligned}V_i(t+1) = \omega \cdot (V_i(t) + cg_1 r_1 (X_1 - X_i(t)) \\ + cg_2 r_2 (X_2 - X_i(t)) + cg_3 r_3 (X_3 - X_i(t)))\end{aligned} \tag{35}$$

$$X_i(t+1) = X_i(t) + V_i(t+1) \tag{36}$$

where r_1, r_2, r_3 are random values [0, 1], cg_1, cg_2, and cg_3 are variables determined using Table 2.

As shown in Table 2, The wolves are divided into four autonomous groups in the proposed algorithm, with different behaviors of the wolves in the groups. The core concept of autonomous groups is inspired by the diversity of individuals in the animal herd. The wolves' movement is controlled by acceleration parameters. These parameters' updating models are shown in Table 2. The mathematical models of these parameters are nonlinear time-varying models with varying slopes, interception points, and curvatures. The variety of models adds value to the algorithm by allowing the wolves to explore the search space both locally and globally thoroughly. The parameters can be tuned to achieve a balance between the exploitation and exploration phases, as well as convergence on the global optimal solution. During the early stages of optimization, search agents are incentivized to disperse across the entire search space. As a result, rather than grouping around local minima, search agents explore the entire search space. The wolves use the information collected in the later stages to converge on the optimal global solution.

Fig. 7 depicts the AGPSO-GWO algorithm flowchart. Firstly, all individuals are randomly initialized in the search space. For each iteration, the best solution is stored as alpha, the second as beta, and the third as delta. Then, the position of alpha, beta, and delta is updated according to Eq. (34). After that, the wolves are randomly divided into four predefined autonomous groups, and the coefficients cg_1, cg_2, and cg_3 are altered by the mathematical model for each group. After that, the wolves' velocities and positions are updated using Eqs. (35) and (36). The optimal solution is defined if the maximum number of iterations is reached. If not, proceed to the next iteration.

5. Simulation results and discussion

In order to recognize the effectiveness and applicability of the AGPSO-GWO technique, the IEEE 30 and 118 bus systems have been tested to find the optimum sitting and capacity of the FACTS controller. The results of the proposed AGPSO-GWO approach are compared with PSO, AGPSO, GWO, and IGWO algorithms to verify the performance of the proposed AGPSO-GWO approach over other reported methods for the optimum allocation of the FACTS problem. Besides, the proposed techniques had been compared to SA (Kanaan and Mehanna, 2020) from the literature to assure their validity. The parameters settings of the comparative techniques are listed in Table 3. The load flow analysis is obtained with the MATPOWER toolbox using the newton Raphson method in the MATLAB packages. The proposed scheme is installed in an Intel® Core™ i-8550U CPU @ 1.80 GHz 1.99 GHz with a setup memory of 8.00 GB & a 64-bit operating system.

In terms of the objective function formulation, the optimization problem is carried out with two cases: (1) mono-objective optimization and (2) multi-objective optimization. The optimization problems are implemented on the two tested systems as the following.

5.1. IEEE 30 bus system

The tested IEEE 30 bus system consists of six generators, 41 transmission lines. The system total active and reactive load demands are 265.16 MW, 150.64 MVAR, respectively (Kanaan and Mehanna, 2020).

5.1.1. Mono-objective optimization

Each objective function described in Eqs. (5)–(12) is performed individually on the IEEE30-bus system with three different FACTS device installation scenarios: SVC only, TCSC only, and UPFC only.

5.1.1.1. Installation of the SVC only. Table 4 provides the optimal SVC controller settings obtained from the proposed algorithms to diminish the bus voltage deviation and active power losses of the IEEE 30-bus system. As shown in Table 4, in the case of minimizing the total active power losses as an individual objective function, the integration of SVC in the power system based on the different tested techniques reduced the total actual power losses

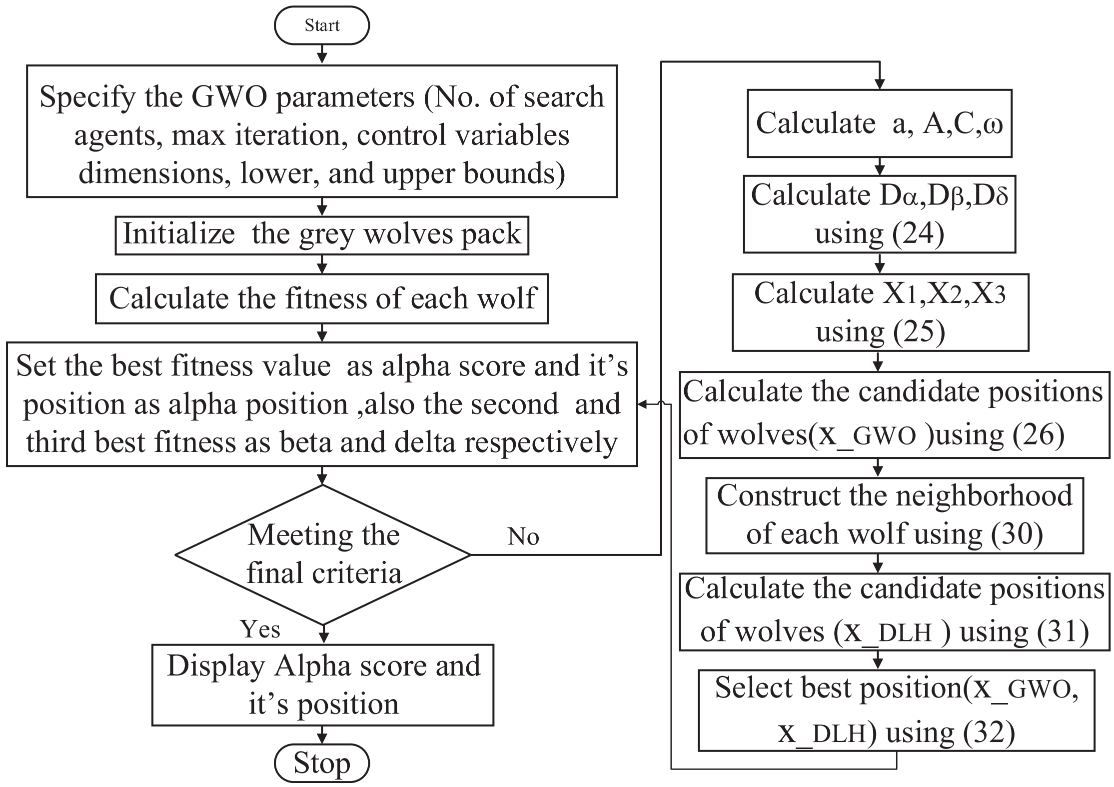

Fig. 6. Flowchart of the IGWO algorithm.

Table 2
Update scheme of cg_1, $cg_2$and cg_3.

Groups	Update model of cg_1	Update model of cg_2	Update model of cg_3
Group 1	$1.95 - 2t^{1/3}/T^{1/3}$	$2t^{1/3}/T^{1/3} + 0.05$	$-2t^{1/3}/T^{1/3} + 2.5$
Group 2	$-2t^3/T^3 + 2.5$	$2t^3/T^3 + 0.5$	$t/T + 1.25$
Group 3	$1.95 - 2t^{1/3}/T^{1/3}$	$2t^3/T^3 + 0.5$	$-2t^3/T^3 + 2.5$
Group 4	$-2t^3/T^3 + 2.5$	$2t^{1/3}/T^{1/3} + 0.05$	$t/T + 1.25$

Table 3
Parameters settings of the comparative techniques.

Algorithm	Setting
PSO	$c_1 = c_2 = 2$, $\omega = 0.4$ - 0.9, r_1, r_2 = [0,1]
AGPSO	c_1, c_2 as in Table 1, $\omega = 0.4$ - 0.9, r_1, r_2 = [0,1]
GWO	a decreased from 2 to 0, r_1, r_2 = [0,1]
IGWO	a decreased from 2 to 0, r_1, r_2 = [0,1]
AGPSO-GWO	cg_1, cg_2, cg_3 as in Table 2, $\omega = 0.4$ - 0.9, r_1, r_2 = [0,1], a decreased from 2 to 0

from 7.44 to 6.7258 MW. The proposed AGPSO-GWO technique provides the smallest SVC size to obtain the global minimum value of total active power losses compared to the other methods. In contrast, the SA technique provides the maximum size of the SVC among the tested algorithms.

In addition, in the case of minimizing the bus voltage deviation of the system as an individual objective function, the SVC installation in the power system based on the proposed algorithms, excepting the SA algorithm, reducing the voltage deviation from 0.0324 p.u to 0.01271 p.u. In contrast, the SA algorithm has achieved the highest VD value equal to 0.0141 p.u compared to other algorithms.

Table 5 shows the individual objective function of minimizing the operational Cost (OC) based on SVC installation in the power system. The OC of the power system is $5.8671*10^6$ $ without the installation of SVC devices. The results show that the integration of SVC based on the proposed AGPSO-GWO, PSO, IGWO, and AGPSO algorithms at bus 8 with size −21.1183 MVAR reduces the OC to $5.6462*10^6$ $. Although the GWO has the lowest power losses and VD, it has the highest OC compared to other techniques.

The comparative convergence curves of the proposed techniques are shown in Figs. 8–10 based on three individual objective functions (i.e., PL, VD, and OC) with the installation of the SVC device. It is noted that the AGPSO-GWO algorithm provides a better and faster solution than any other optimization technique. It is also observed that the AGPSO-GWO algorithm finds the global optimum in a small number of iterations compared to the other algorithms. The GWO algorithm was trapped in a local optimum and did not achieve the optimum global solution, as shown in Figs. 8 and 10.

5.1.1.2. Installation of the TSCS only. Table 6 presents the optimal settings of the TCSC controller obtained based on various proposed algorithms to minimize the active power losses and voltage division of the IEEE30 bus system. From Table 6, in the case of minimizing total active power losses as the individual objective function, the installation of the TCSC in the power

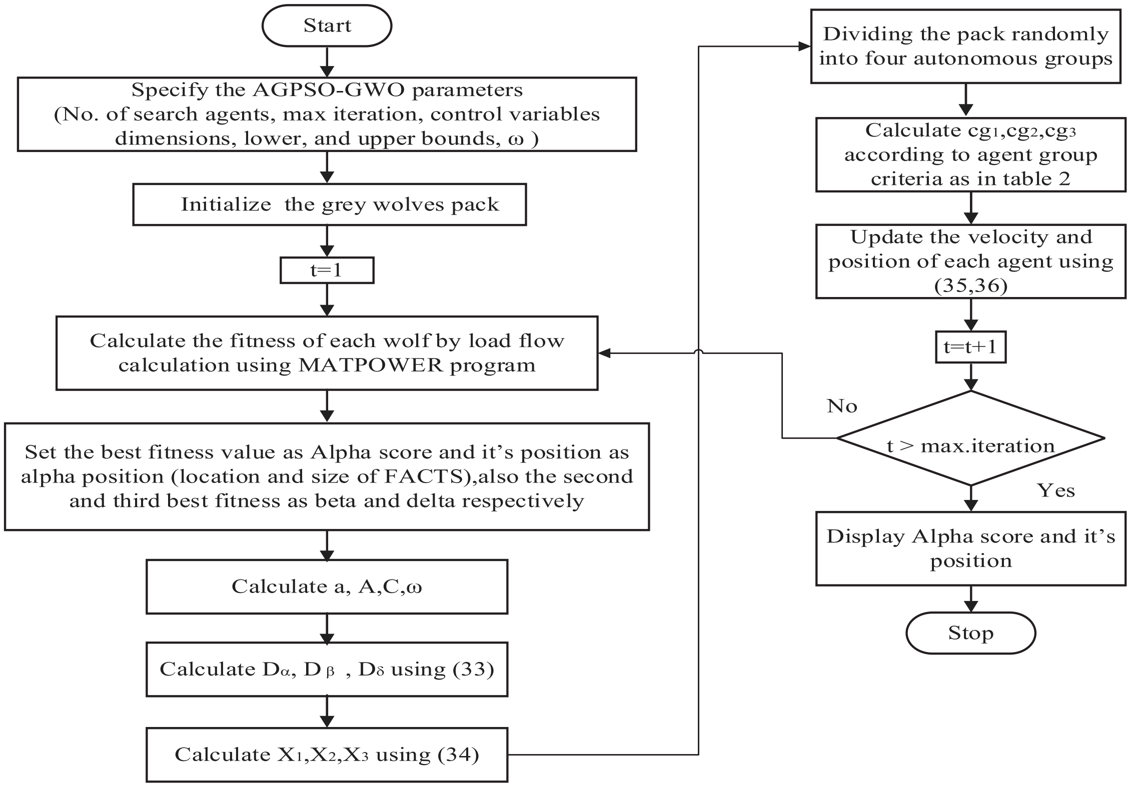

Fig. 7. Flowchart of the AGPSO-GWO algorithm.

Table 4
The optimal solution of all algorithms to reduce the active power losses and bus voltage deviation by installing SVC only.

	Items	PL is the only objective function				VD is the only objective function			
	Without FACTS	7.44 MW				0.0324 p.u.			
	Algorithms	LOC. (bus)	Size (MVAR)	PL (M.W.)	VD (p.u.)	LOC (bus)	Size (MVAR)	PL (M.W.)	VD (p.u.)
SVC	SA Kanaan and Mehanna (2020)	8	−57.1700	6.7258	0.0170	8	79.6900	6.8232	0.0141
	AGPSO	8	−57.1655	6.7258	0.0170	6	−100	6.9358	0.01271
	IGWO	8	−57.1655	6.7258	0.0170	6	−100	6.9358	0.01271
	AGPSO-GWO	**8**	**−57.1635**	**6.7258**	**0.0170**	**6**	−100	**6.9358**	**0.01271**
	GWO	8	−57.1655	6.7265	0.0170	6	−100	6.9358	0.01271
	PSO	8	−57.1655	6.7258	0.0170	6	−100	6.9358	0.01271

* Bold technique is referred to the best values as compared to the others.

Table 5
The optimal solution of all algorithms for minimization of OC at installation of SVC only.

Operational Cost (OC) is the only objective function						
	Without FACTS	$5.867088*10^6$ $				
	Algorithms	LOC (bus)	Size (MVAR)	OC ($)	PL (MW)	VD (pu)
SVC	SA Kanaan and Mehanna (2020)	–	–	–	–	–
	AGPSO	8	−21.1183	$5.6462*10^6$	6.9999	0.0252
	IGWO	8	−21.1183	$5.6462*10^6$	6.9999	0.0252
	AGPSO-GWO	**8**	**−21.1183**	**$5.6462*10^6$**	**6.9999**	**0.0252**
	GWO	8	−26.7726	$5.6617*10^6$	6.9188	0.0236
	PSO	8	−21.1183	$5.6462*10^6$	6.9999	0.0252

system based on the SA algorithm reduced total actual power losses from 7.44 to 7.1960 MW. The installation of the TCSC in the power system based on the AGPSO-GWO, GWO, IGWO, and AGPSO algorithms reduces the voltage deviation from 0.0324 to 0.0252 p.u. The optimal proposed location of the TCSC is at line 36, which is connected between buses 27 and 28 with the optimal size −0.8 of the reactance of the connected line. Whereas the SA algorithm suggested connecting the TCSC to the same line with a different size equal to −0.7920 of the reactance of the connected line, resulting in a higher voltage deviation value (0.0254 p.u.) with higher power losses (7.2607 MW). On the other hand, the PSO algorithm proposed the location of the TCSC at line No. 16, connected between busses 12 and 13, with the size −0.8 of the reactance of the connected line, leading to the highest voltage deviation value (0.0273 p.u.) as compared to other proposed methodologies.

The optimal solution of all algorithms to minimize the OC based on the integration of TCSC in the power system is shown

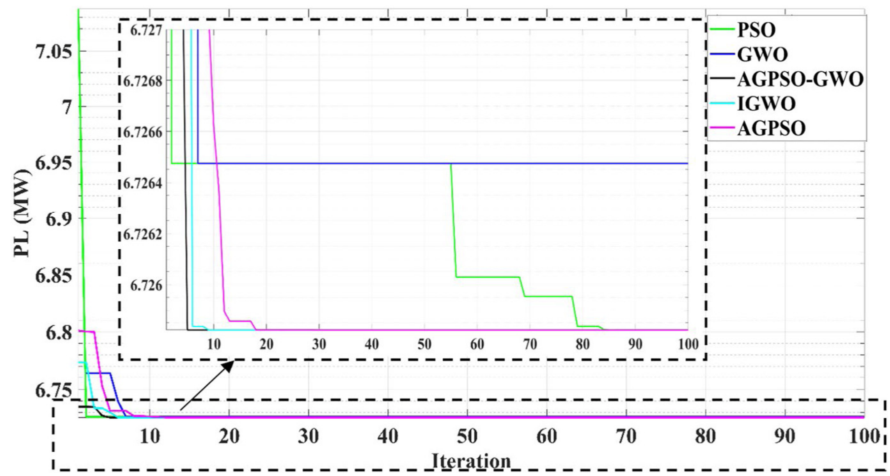

Fig. 8. Convergence curves of all algorithms for the installation SVC in the system for minimization of active power losses.

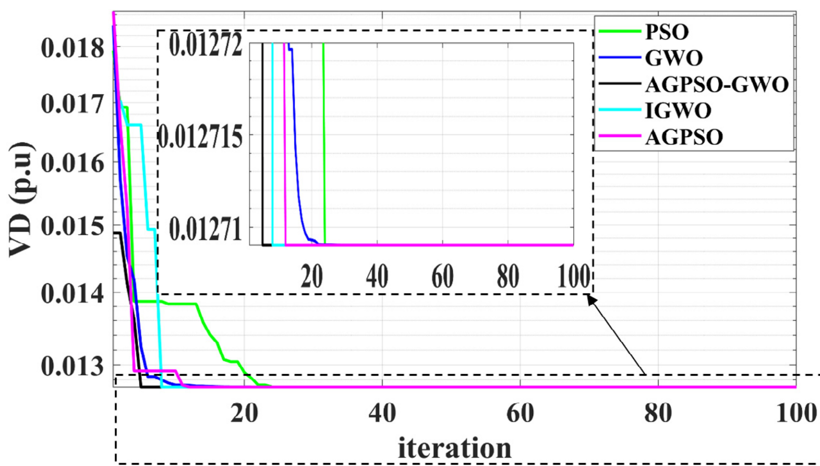

Fig. 9. Convergence curves of all algorithms for the installation of SVC in the system for minimization of voltage deviation.

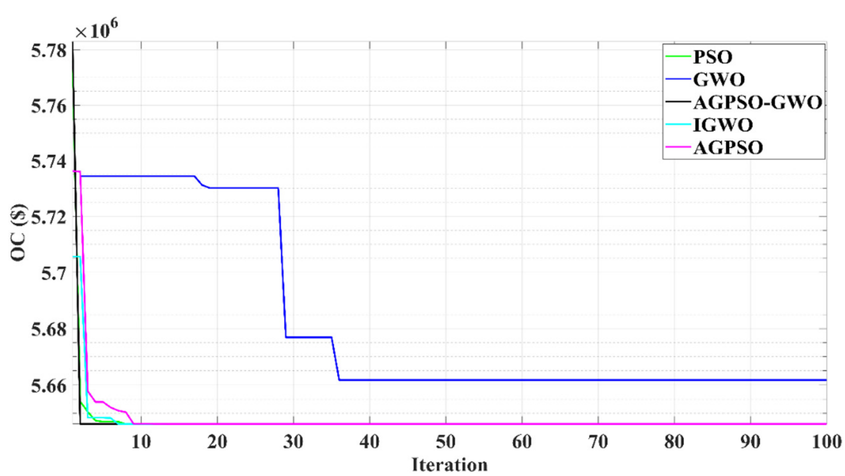

Fig. 10. Convergence curves of all algorithms for the installation of SVC in the system for minimization of the OC.

in Table 7. In this case, the proposed AGPSO-GWO, PSO, IGWO, and AGPSO techniques minimize the OC to 5.7975*10^6 $. In contrast with other algorithms, the optimal sitting and capacity of the TCSC based on the AGPSO-GWO approach resulted in a simultaneous reduction of the VD and OC to the minimum values.

In conclusion, although the SA algorithm has the best results with the power losses objective function, it has the highest values with VD and OC objective functions.

As shown in Figs. 11–13, the AGPSO-GWO algorithm exhibits the best performance during the optimization process. The AGPSO-GWO algorithm finds the global optima in fewer numbers of iterations than other algorithms. The PSO algorithm

Table 6
The optimal solution of all algorithms for active power losses and voltage deviation at installation of TCSC.

Items		PL is the only objective function				VD is the only objective function			
	Without FACTS	7.44 MW				0.0324 p.u			
	Algorithms	LOC. (line)	Size (%)	PL (MW)	VD (pu)	LOC. (line)	Size (%)	PL (MW)	VD (pu)
TCSC	SA Kanaan and Mehanna (2020)	16	**−0.7999**	**7.1960**	0.0274	36	−0.7920	7.2607	0.0254
	AGPSO	16	−0.8	7.1986	0.0274	36	−0.8	7.2586	0.0252
	IGWO	16	−0.8	7.1986	0.0274	36	−0.8	7.2586	0.0252
	AGPSO-GWO	16	−0.8	7.1986	0.0274	**36**	**−0.8**	**7.2586**	**0.0252**
	GWO	16	−0.8	7.1986	0.0274	36	−0.8	7.2586	0.0252
	PSO	16	−0.8	7.1986	0.0274	16	−0.8	7.1986	0.0273

Table 7
The optimal solution of all algorithms for minimization of OC at installation of TCSC only.

Operational Cost (OC) is the only objective function						
	Without FACTS	$5.867088*10^6$ $				
	Algorithms	LOC (line)	Size (%)	OC ($)	PL (MW)	VD (pu)
TCSC	SA	–	–	–	–	–
	AGPSO	11	−0.7253	$5.7975*10^6$	7.3152	0.0326
	IGWO	11	−0.7253	$5.7975*10^6$	7.3152	0.0326
	AGPSO-GWO	**11**	**−0.7262**	$\mathbf{5.7975*10^6}$	**7.3150**	**0.0326**
	GWO	11	−0.8	$5.7995*10^6$	7.3018	0.0326
	PSO	11	−0.7253	$5.7975*10^6$	7.3152	0.0326

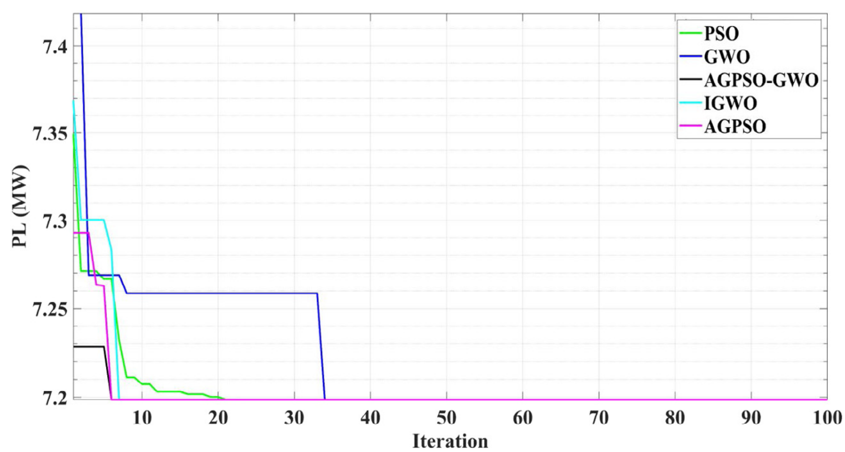

Fig. 11. Convergence curves of all algorithms for the TCSC only in the system for minimization of real power losses.

was trapped in a local optimum and did not achieve the optimum global minimum voltage deviation value as illustrated in Fig. 12. In addition, the GWO algorithm was trapped in a local optimum and did not achieve the optimum global minimum of OC value as illustrated in Fig. 13.

5.1.1.3. Installation of the UPFC only. Table 8 displays the optimal settings of the UPFC device for minimizing the active power losses and voltage division of the IEEE 30 bus system based on different proposed techniques. From Table 8, in the case of minimizing total active power losses as the only objective function, the installation of the UPFC based on the SA algorithms reduced the total real power losses from 7.44 to 6.5440 MW with high capacities values as compared to the AGPSO-GWO technique. The proposed locations of the UPFC are at bus 9 and line 11 with sizes −89.284 MVAR and −0.7474 of the reactance of the connected line. The non-optimized location of FACTS controllers results in poor objective values, as shown in Table 8. Whereas the non-optimum UPFC location and size result in higher objective values than the optimized location. According to the GWO, PSO, and AGPSO algorithms, the PL value is 6.5991, 6.7258, and 6.5565 MW, respectively. In comparison, the optimal location using the AGPSO-GWO, IGWO, and SA yields 6.5467, 6.5467, and 6.5440 MW, respectively.

Also, Table 8 demonstrates that in the case of minimizing the voltage deviation of the system as the individual objective function, the installation of the UPFC based on the AGPSO-GWO, IGWO, and AGPSO algorithms reduces the voltage deviation from 0.0324 to 0.0123 p.u as the best results as compared to SA, GWO, and PSO algorithms. The optimal proposed location of the UPFC is at bus 6 and line 12, which is connected between buses 6 and 10 with sizes −99.6857 MVAR and −0.8 of the reactance of the connected line. Whereas, the SA algorithm suggested connecting the UPFC at bus 8 and line 10 which is connected between buses 6 and 8 with size −99.8000 MVAR and −0.6231 of the reactance of the connected line, resulting in a higher voltage deviation (0.0124 p.u.). On the other hand, the PSO algorithm proposed the optimal location of the UPFC at bus 6 and line 41, which is connected between buses 6 and 28, with sizes −99.6857 MVAR and 0.2 of the reactance of the connected line, resulting in the highest voltage deviation value (0.0127 p.u.).

The optimal solution of all algorithms to minimize the OC based on the location of UPFC is shown in Table 9. The installation of the UPFC based on the AGPSO-GWO, IGWO, and AGPSO algorithms minimizes the OC to $5.6675*10^6$ $. On the other hand, the optimum location and size of the UPFC based on the PSO and GWO technique resulted in the highest OC values that equal to $5.7394*10^6$ and $5.7414*10^6$ $, respectively.

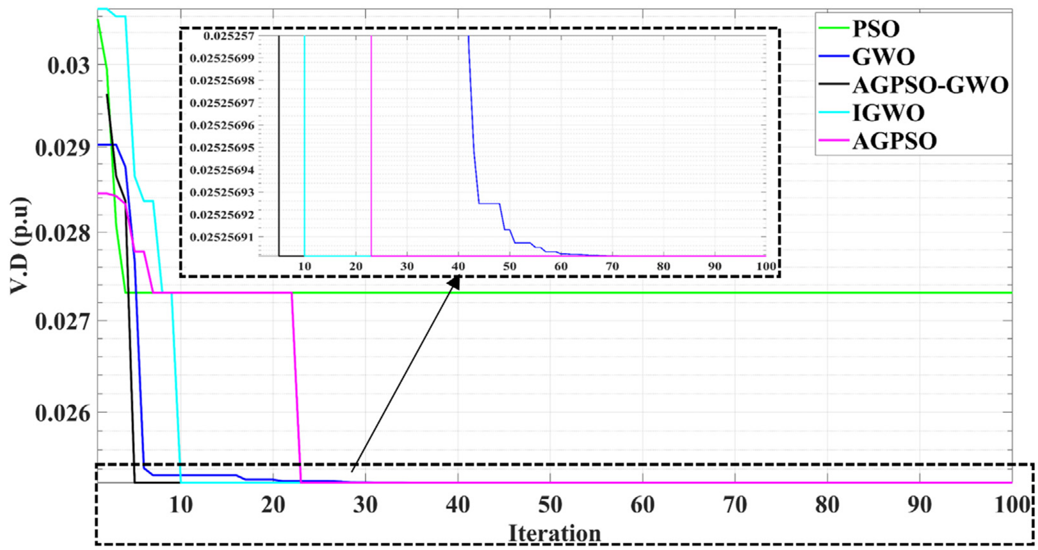

Fig. 12. Convergence curves of all algorithms for the TCSC only in the system for minimization of voltage deviation.

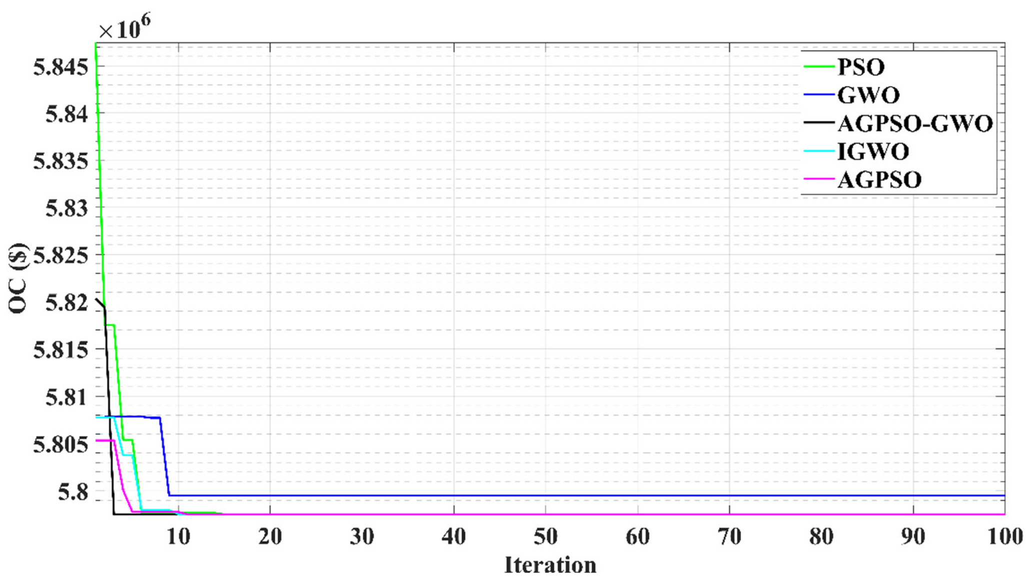

Fig. 13. Convergence curves of all algorithms for the installation of TCSC in the system for minimization of the OC.

Table 8
The optimal solution of all algorithms for active power losses and voltage deviation at installation of UPFC.

Items		PL is the only objective function					VD is the only objective function				
Without FACTS		7.44 MW					0.0324 p.u.				
	Algorithms	LOC.		Size	PL (MW)	VD (pu)	LOC		Size	V.D (pu)	PL (MW)
UPFC	SA Kanaan and Mehanna (2020)	bus line	9 11	−89.284 −0.7474	6.5440	0.0144	bus line	8 10	−99.8000 −0.6231	0.0124	7.1053
	AGPSO	bus line	10 12	−71.7483 −0.8	6.5565	0.0175	bus line	6 12	−99.6857 −0.8	0.0123	6.6788
	IGWO	bus line	9 11	−88.3250 −0.7247	6.5467	0.0146	bus line	6 12	−99.6857 −0.8	0.0123	6.6787
	AGPSO-GWO	**bus** **line**	**9** **11**	**−88.3249** **−0.7247**	**6.5467**	**0.0146**	**bus** **line**	**6** **12**	**−99.6857** **−0.8**	**0.0123**	**6.6787**
	GWO	bus line	10 12	−88.3250 −0.8	6.5991	0.0155	bus line	6 6	−100 0.2	0.0126	6.9150
	PSO	bus line	8 40	−57.1574 0.0168	6.7258	0.0170	bus line	6 41	−99.6857 0.2	0.0127	6.9313

As illustrated from Figs. 14–16, the AGPSO-GWO technique exhibits the best performance during the optimization process. The AGPSO-GWO algorithm finds the global optima in fewer numbers of iterations as compared to other algorithms. From

Table 9
The optimal solution of all algorithms for minimization of OC at installation of UPFC only.

Operational Cost (OC) is the only objective function							
	Without FACTS	5.8671*10^6 $					
	Algorithms	LOC		Size	OC ($)	PL (MW)	VD (pu)
UPFC	SA Kanaan and Mehanna (2020)	bus line	– –	– –	-	-	-
	AGPSO	bus line	6 11	−18.2164 −0.8	5.6675*10^6	7.0378	0.0271
	IGWO	bus line	6 11	−18.2164 −0.8	5.6675*10^6	7.0378	0.0271
	AGPSO-GWO	**bus line**	**6 11**	**−18.2146 −0.8**	**5.6675*10^6**	**7.0378**	**0.0271**
	GWO	bus line	8 40	−27.3498 0.1455	5.7414*10^6	6.9122	0.0253
	PSO	bus line	10 25	−16.0963 −0.263651	5.7394*10^6	7.1762	0.0282

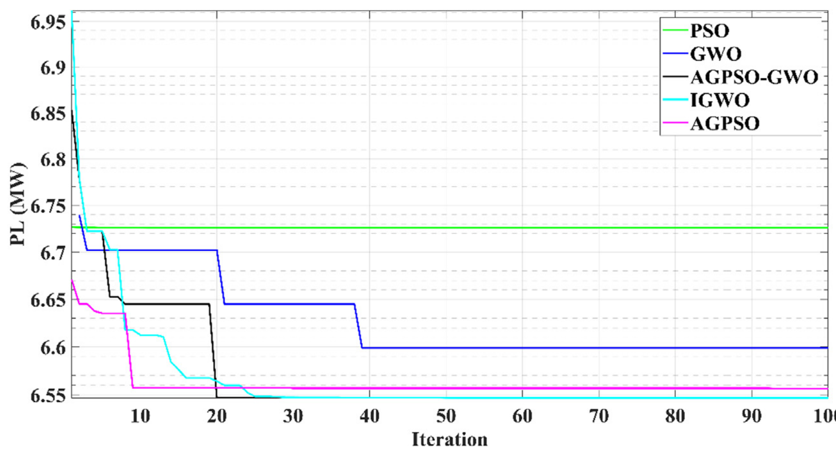

Fig. 14. Convergence curves of all algorithms for the UPFC only in the system for minimization of real power losses.

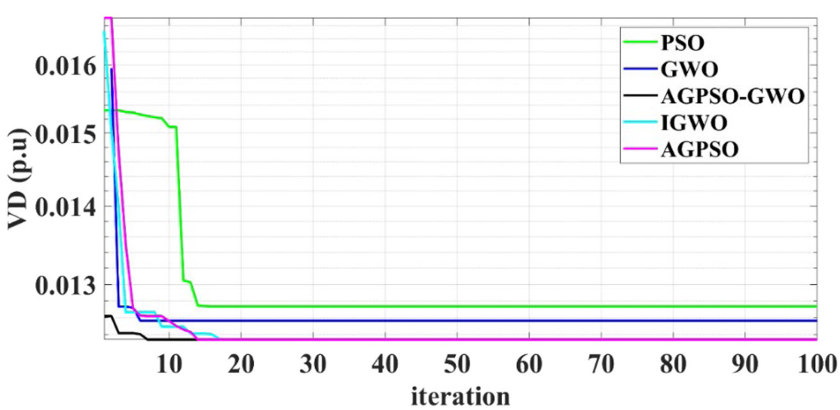

Fig. 15. Convergence curves of all algorithms for the UPFC only in the system for minimization of voltage deviation.

Fig. 14, it is noted that the AGPSO algorithm was almost trapped in a local optima. The PSO and GWO algorithms were trapped in a local optimum and did not achieve the optimum global minimum values of the PL, VD, and OC as shown in Figs. 14, 15, and 16, respectively.

5.1.2. Multi-objective optimization

In this article, the multi-objective function via the proposed techniques are performed to minify the active power losses, voltage deviation, and system operating cost simultaneously in three cases of FACTS device installation: SVC only, TCSC only, and UPFC.

The multi-objective function plays an important role in the performance of the optimization technique process for ensuring the global minimum. This issue can be achieved only based on the optimal evaluating of the weighting factors of the proposed fitness function. Therefore, the AGPSO-GWO algorithm has been carried out via multi-objective function (F) using Eq. (13) to evaluate the most suitable weighting factors' values via selecting the optimum capacity and sitting of the SVC as a case study. In this regard, for the 30-bus IEEE system, Table 10 illustrates the variation of the targeted quantities values (PL, VD, and OC) with changes in the weighting factors' values. The most applicable weighting factors are 0.1, 0.1, and 0.8; these values simultaneously ensure the balance between PL, VD, and OC values with the lowest capacity of the SVC device installation, unlike all cases in Table 10.

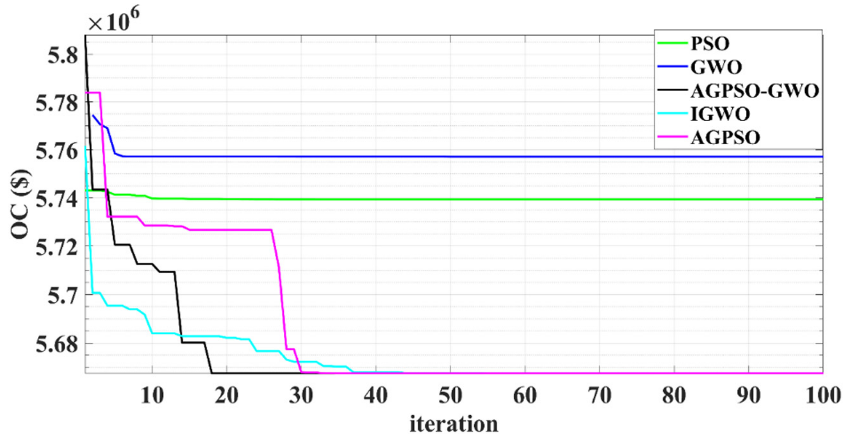

Fig. 16. Convergence curves of all algorithms for the installation of UPFC in the system for minimization of the OC.

Table 10
The optimal solution of all algorithms at different values of weight factors by the installation of SVC for multi-objective optimization problem.

Weighting factors	F	Bus	SVC_ size (MVAR)	OC ($)	PL (MW)	VD (pu)
(1,1,1)	2.4965	8	−54.9657	6.1931*10^6	6.7268	0.0174
(0.8,0.1,0.1)	0.8825	8	−56.1313	6.2310*10^6	6.7260	0.0172
(0.1,0.8,0.1)	0.5745	8	−73.0000	6.9175*10^6	6.7744	0.0148
(0.1, 0.1, 0.8)	**0.9377**	**8**	**−28.5686**	**5.6732*10^6**	**6.8961**	**0.0232**
(0.7,0.2,0.1)	0.8433	8	−63.3989	6.4953*10^6	6.7335	0.0161
(0.2,0.7,0.1)	0.6198	8	−73.0000	6.9175*10^6	6.7744	0.0148
(0.2,0.1,0.7)	0.9334	8	−30.5925	5.6897*10^6	6.8724	0.0226
(0.6,0.3,0.1)	0.8009	8	−69.6569	6.7611*10^6	6.7562	0.0152
(0.3,0.6,0.1)	0.6652	8	−73.0000	6.9175*10^6	6.7744	0.0148
(0.1,0.3,0.6)	0.9284	8	−33.0394	5.7150*10^6	6.8461	0.0220
(0.6,0.2,0.2)	0.8610	8	−55.4875	6.2099*10^6	6.7264	0.0173
(0.2,0.2,0.6)	0.9027	8	−37.8722	5.7817*10^6	6.8021	0.0208
(0.2,0.6,0.2)	0.6920	8	−73.0000	6.9175*10^6	6.7744	0.0148
(0.5,0.1,0.4)	0.9155	8	−38.8247	5.7974*10^6	6.7947	0.0206
(0.5,0.4,0.1)	0.7559	8	−73.0000	6.9175*10^6	6.7744	0.0148
(0.5,0.2,0.3)	0.8748	8	−48.6472	6.0094*10^6	6.7404	0.0186
(0.5,0.3,0.2)	0.8224	8	−61.3813	6.4171*10^6	6.7293	0.0164
(0.1,0.5,0.4)	0.7800	8	−59.1743	6.3358*10^6	6.7266	0.0167
(0.4,0.1,0.5)	0.9226	8	−34.4230	5.7318*10^6	6.8325	0.0217
(0.3,0.5,0.2)	0.7374	8	−71.7734	6.8590*10^6	6.7673	0.0150
(0.2,0.3,0.5)	0.8649	8	−47.8983	5.9901*10^6	6.7431	0.0187

5.1.2.1. Installation of the SVC only. In this section, all tested programs determined the optimum allocation of the SVC in the IEEE 30-bus system to minimize active power losses, bus voltage deviation, and system operating cost at the same time using the Eq. (13) as multi-objective function (F). As illustrated from Table 11, the optimal installation of the SVC with size −28.5666 MVAR at bus 8, based on AGPSO-GWO, AGPSO, and IGWO techniques is resulting in a reduction of active power losses, bus voltage deviation, and system operating cost to be 6.8961 MW, 0. 0231 p.u, and 5.6731*10^6 $, respectively. Without optimal SVC installation, these values were 7.44MW, 0.0324 p.u, 5.8671*10^6 $, respectively. Table 11 also revealed that the GWO algorithm failed to achieve the optimal solution, as it chose a non-optimal SVC allocation, resulting in higher PL and VD values than other programs. Whereas the PL and VD values of GWO are 6.9433 MW and 0. 0241 p.u, respectively. From Fig. 17, the AGPSO-GWO algorithm shows the best performance during the optimization process. The AGPSO-GWO algorithm finds a global optimum solution faster than other algorithms. The GWO algorithm has been trapped in a local optimum and has not achieved the optimum global minimum value of F.

5.1.2.2. Installation of the TCSC only. As seen from Table 12, the optimal sittings of the TCSC based on AGPSO-GWO, AGPSO, and IGWO algorithms is resulting in a reduction of active power losses, bus voltage deviation, and system operating costs to 7.2542 MW, 0. 0286 p.u, and 5.8234*10^6 $, respectively. The optimal placement of the TCSC is the connection to line 16 with a size −0.6521 MVAR. Whereas, the GWO algorithm provided the largest size of the TCSC resulted in a minimum PL value that required the highest OC value compared to the other algorithms. Table 12 also shows that the size of the TCSC based on the PSO algorithm results in minimum PL and OC values compared to the other techniques. As depicted in Fig. 18, the AGPSO-GWO algorithm shows the best performance during the optimization process, among other algorithms. Fig. 18 also illustrates that the GWO algorithm has been trapped in a local optimum and has not achieved the optimum global minimum value of F.

5.1.2.3. Installation of the UPFC only. In this section, the UPFC is installed in the IEEE 30-bus system to minimize the considered multi-objective function. Table 13 illustrates the minimum value of the PL that is 6.9120 MW. This issue can be achieved by installing the UPFC in the system based on the IGWO and AGPSO-GWO algorithms. AGPSO-GWO technique achieved the optimal global solutions compared to other algorithms by installing UPFC at bus 6 and line 11 with a size of −29.6436 MVAR and −0.8 of the connected line's reactance. According to the optimal UPFC setting based on the AGPSO-GWO algorithm, the system's bus

Table 11
The optimal solution of all algorithms for minimization of the multi-objective optimization problem at installation of SVC only.

PL, VD, and OC values at weighting factors 0.1, 0.1, 0.8 (best Fitness)							
Without FACTS		7.44 MW, 0.0324 pu, 5.8671*10^6 $					
	Algorithms	LOC bus	Size MVAR	Pl value MW	VD pu	OC $	F
SVC	AGPSO	8	−28.5666	6.8961	0.0231	5.6731*10^6	0.9377
	IGWO	8	−28.5666	6.8961	0.0231	5.6731*10^6	0.9377
	AGPSO-GWO	8	−28.5666	**6.8961**	**0.0231**	**5.6731*10^6**	**0.9377**
	GWO	8	−24.9490	6.9433	0.0241	5.6533*10^6	0.9387
	PSO	8	−28.7136	6.8943	0.0231	5.6742*10^6	0.9377

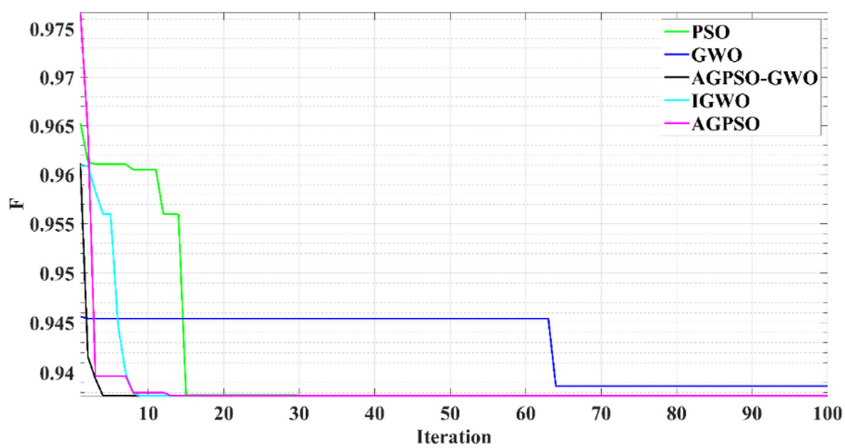

Fig. 17. Convergence curves for minimization of the multi-objective optimization problem at installation of SVC only.

Table 12
The optimal solution of all algorithms for minimization of the multi-objective optimization problem at the installation of TCSC only.

PL, VD, and OC values at weighting factors 0.1, 0.1, 0.8 (best Fitness)							
	Without FACTS	7.44 MW, 0.0324 pu, 5.867088*10^6 $					
	Algorithms	LOC line	Size	PL MW	VD pu	OC $	F
TCSC	AGPSO	16	−0.6521	7.2542	0.0286	5.8234*10^6	0.9798
	IGWO	16	−0.6521	7.2542	0.0286	5.8234*10^6	0.9798
	AGPSO-GWO	**16**	**−0.6521**	**7.2542**	**0.0286**	**5.8234*10^6**	**0.9798**
	GWO	16	−0.8000	7.1986	0.0273	5.8802*10^6	0.9828
	PSO	16	−0.6360	7.2599	0.0287	5.8202*10^6	0.9798

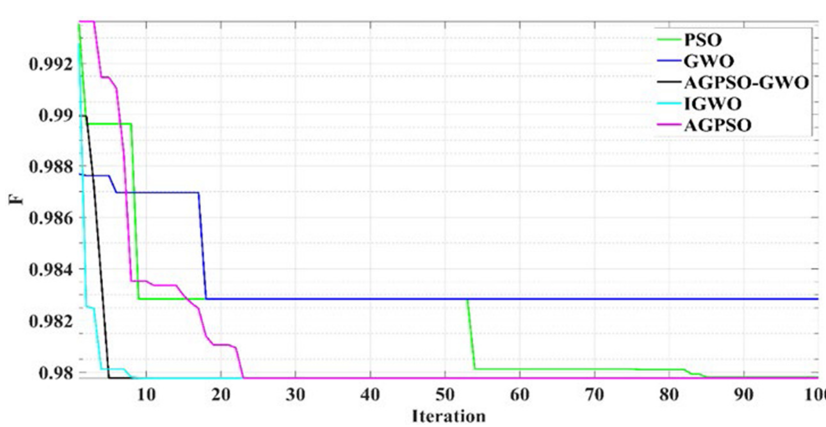

Fig. 18. Convergence curves for the multi-objective optimization problem minimization at the TCSC installation only.

voltage deviation and operating costs were reduced to 0.0241 pu and 5.7054*10^6 $, respectively.

As shown in Fig. 19, the AGPSO-GWO algorithm finds the global optimum solution faster than the other algorithms. The GWO and PSO algorithms were trapped at the optimum local value of F, resulting in the GWO achieving the highest OC value and the PSO algorithm achieving the highest PL value.

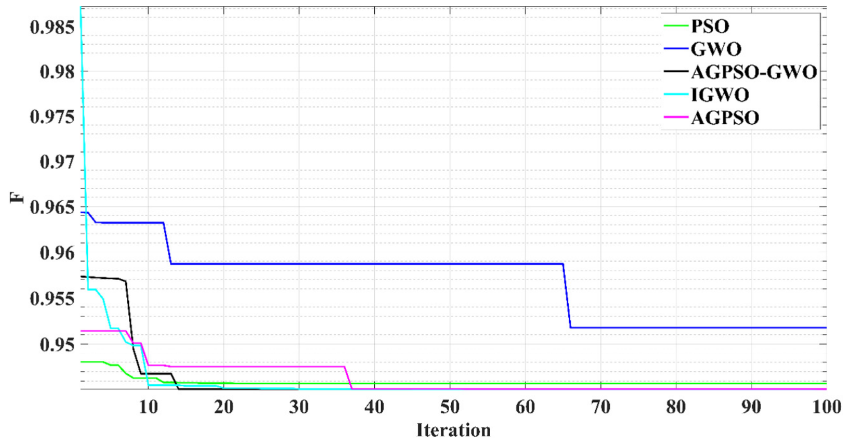

Fig. 19. Convergence curves for minimization of the multi-objective optimization problem at installation of UPFC only.

Table 13
The optimal solution of all algorithms for minimization of the multi-objective optimization problem at installation of UPFC only.

PL, VD, and OC values at weighting factors 0.1, 0.1, 0.8 (best Fitness)								
	Without FACTS	7.44&0.0324&5.8671*10^6						
	Algorithms	LOC		Size	OC ($)	PL (MW)	VD (pu)	F
UPFC	SA	Bus Line	– –	– –	-	-	-	-
	AGPSO	Bus Line	6 11	−29.5166 −0.8	5.7046*10^6	6.9133	0.0241	0.9451
	IGWO	Bus Line	6 11	−29.6441 −0.8	5.7054*10^6	6.9120	0.0241	0.9451
	AGPSO-GWO	Bus Line	**6** **11**	**−29.6436** **−0.8**	**5.7054*10^6**	**6.9120**	**0.0241**	**0.9451**
	GWO	Bus Line	8 40	−28.1192 −0.8	5.7720*10^6	6.9330	0.0232	0.9518
	PSO	Bus Line	8 40	−23.9598 0.4023	5.6985*10^6	6.9599	0.0244	0.9457

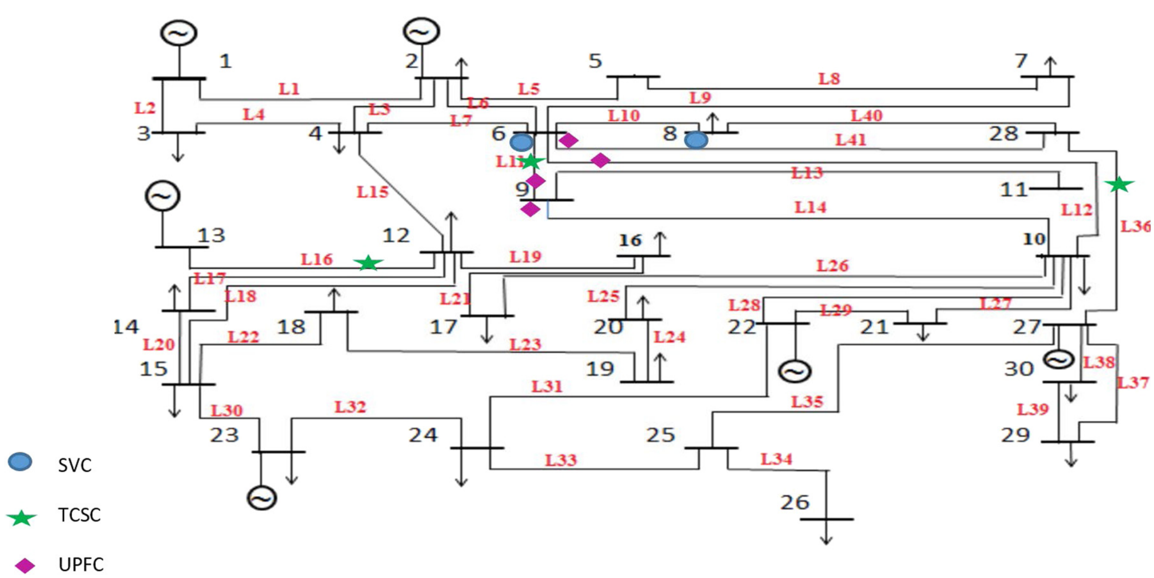

Fig. 20. The placement of FACTS devices on the IEEE-30 bus system.

Fig. 20 shows a single-line diagram of the IEEE 30 bus system, as well as a visual demonstration of the optimal placement of various FACTS controllers on the system based on the AGPSO-GWO technique, as seen in Tables 11–13.

5.2. IEEE 118

The standard IEEE 118-bus test system consists of 54 generating units interconnected with 186 transmission lines. Their 11 branches are equipped with tap changing transformers, and the three branches having shunt capacitors. Bus 1 is selected as a slack bus. The total active power demand is 4242 MW, and

Table 14
The optimal solution of all algorithms for different values of weight factors for the multi-objective optimization problem.

Weighting factors	F	Bus	SVC_ size (MVAR)	OC ($)	PL (MW)	VD (pu)
(1,1,1)	2.9464	52	−45.3705	$1.0554*10^8$	133.1035	0.0811
(0.8,0.1,0.1)	0.9953	52	−33.3965	$1.0511*10^8$	132.9149	0.0820
(0.1,0.8,0.1)	0.9466	52	−63.4427	$1.0647*10^8$	133.5398	0.0806
(0.1, 0.1, 0.8)	**0.9973**	**52**	**−13.3092**	**$1.0474*10^8$**	**132.7948**	**0.0843**
(0.7,0.2,0.1)	0.9894	52	−43.7966	$1.0548*10^8$	133.0740	0.0812
(0.2,0.7,0.1)	0.9540	52	−61.9732	$1.0638*10^8$	133.4979	0.0806
(0.2,0.1,0.7)	0.9966	52	−23.5326	$1.0488*10^8$	132.8239	0.0830
(0.6,0.3,0.1)	0.9828	52	−50.1218	$1.0575*10^8$	133.2011	0.0809
(0.3,0.6,0.1)	0.9614	52	−60.2165	$1.0628*10^8$	133.4492	0.0806
(0.1,0.3,0.6)	0.9965	52	−23.9170	$1.0488*10^8$	132.8263	0.0829
(0.6,0.2,0.2)	0.9899	52	−41.5569	$1.0539*10^8$	133.0344	0.0813
(0.2,0.2,0.6)	0.9916	52	−37.9717	$1.0526*10^8$	132.9771	0.0816
(0.2,0.6,0.2)	0.9624	52	−58.4684	$1.0618*10^8$	133.4023	0.0806
(0.5,0.1,0.4)	0.9961	52	−27.9666	$1.0497*10^8$	132.8574	0.0825
(0.5,0.4,0.1)	0.9758	52	−54.5703	$1.0597*10^8$	133.3037	0.0807
(0.5,0.2,0.3)	0.9904	52	−39.7436	$1.0532*10^8$	133.0045	0.0815
(0.5,0.3,0.2)	0.9835	52	−48.0636	$1.0566*10^8$	133.1573	0.0810
(0.1,0.5,0.4)	0.9718	52	−60.3827	$1.0629*10^8$	133.4537	0.0806
(0.4,0.1,0.5)	0.9963	52	−26.8111	$1.0494*10^8$	132.8475	0.0826
(0.3,0.5,0.2)	0.9696	52	−55.6604	$1.0603*10^8$	133.3304	0.0807
(0.2,0.3,0.5)	0.9852	52	−42.6402	$1.0543*10^8$	133.0532	0.0813

Table 15
Solution of all algorithms at the installation of the SVC in the IEEE 118-bus system for the multi-objective minimization problem.

PL, VD, and Oc values at weighting factors 0.1,0.1,0.8 (best Fitness)							
SVC	Without FACTS	132.8629 MW, 0.0866 pu, $1.0475*10^8$ $					
	Algorithms	LOC bus	Size MVAR	PL value M.W.	VD pu	OC $	F
	AGPSO	52	−13.3756	132.7948	0.0843	$1.0475*10^8$	0.9973
	IGWO	52	−13.3754	132.7948	0.0843	$1.0475*10^8$	0.9973
	AGPSO-GWO	**52**	**−13.3092**	**132.7948**	**0.0843**	**$1.0474*10^8$**	**0.9973**
	GWO	52	−12.7451	132.7952	0.0844	$1.0474*10^8$	0.9974
	PSO	51	−14.1667	132.7948	0.0847	$1.0475*10^8$	0.9978

Table 16
Solution of all algorithms at the installation of the TCSC in the IEEE 118-bus system to minimize the multi-objective optimization problem.

PL, VD, and OC values at weighting factors 0.1, 0.1, and 0.8 (best Fitness)							
TCSC	Without FACTS	132.8629 MW& 0.0866 pu & $1.0475*10^8$ $					
	Algorithms	LOC (line)	Size (%)	PL (MW)	VD (pu)	OC ($)	F
	AGPSO	96	−0.5473	130.4431	0.0858	$1.0337*10^8$	0.9868
	IGWO	96	−0.5473	130.4431	0.0858	$1.0337*10^8$	0.9868
	AGPSO-GWO	**96**	**-0.5483**	**130.4395**	**0.0858**	**$1.0337*10^8$**	**0.9868**
	GWO	105	0.2000	132.5572	0.0866	$1.0452*10^8$	0.9981
	PSO	38	−0.6877	131.1699	0.0859	$1.0350*10^8$	0.9883

reactive power demand is 1438 MVAR. The system data of 118-bus IEEE power system can be deduced in ben oualid Medani et al. (2018). Initially, the system's total real power loss and voltage deviation without FACTS installation is 132.8629 MW and 0.0866 p.u., respectively, with an operating cost of $1.0475*10^8$ $. The optimum placement and sizing of the SVC, TCSC, and UPFC in the IEEE 118 bus system have been calculated to minimize the multi-function described in Eq. (13). Therefore, the AGPSO-GWO algorithm has been carried out via a multi-objective function (F) process to evaluate the most suitable weighting factors' values (w_1, w_2, w_3) via selecting the optimum capacity and sitting of the SVC as a case study, as illustrated in Table 14. The results obtained from Table 14 reveal that the changes in the values of the weight factors lead to changes in the values of the target quantity (PL, DV, and OC). The most applicable weighting factors are 0.1, 0.1, and 0.8, whereas these values ensure the simultaneous balance between PL, VD, and OC values with the lowest values of the SVC capacity, OC, and PL, unlike all cases in Table 14., unlike all cases in Table 14.

5.2.1. Installation of the SVC only

The optimal location and capacity of the SVC in the IEE118-bus system based on the proposed algorithms to minimize the multi-objective function are shown in Table 15. The proposed AGPSO-GWO technique provided the optimum size of the SVC, which yielded the minimum OC value compared to other algorithms. The PL, DV, and OC values are reduced to 132.7948 MW, 0.0843 p.u, and $1.0474*10^8$ $, respectively. As can be seen in Table 15, the GWO method obtained the highest power losses value, while the PSO algorithm obtained the highest bus voltage deviation value. The convergence curves of all proposed algorithms via SVC device installation in the IEEE 118 system are demonstrated in Fig. 21. From this figure, the AGPSO-GWO algorithm finds the global optimum solution faster than the other algorithms. On the other hand, the GWO and PSO algorithms were trapped at the local optimum value of F and did not achieve the optimal solutions.

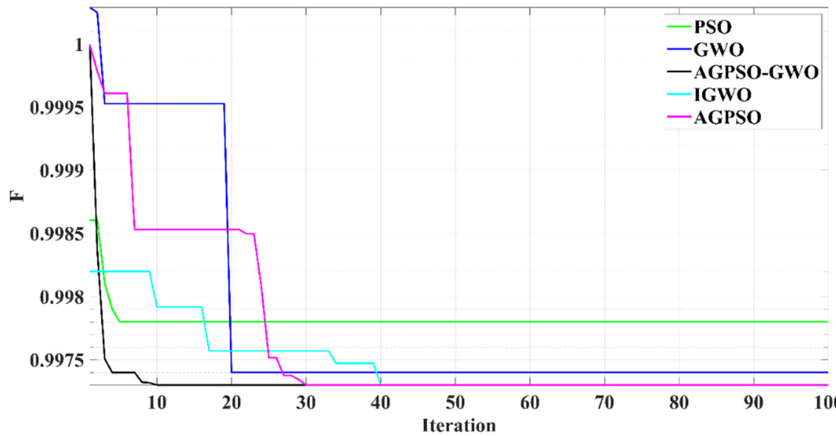

Fig. 21. Convergence curves of all algorithms when the SVC is connected in the IEEE 118-bus system to minimize the multi-objective optimization problem.

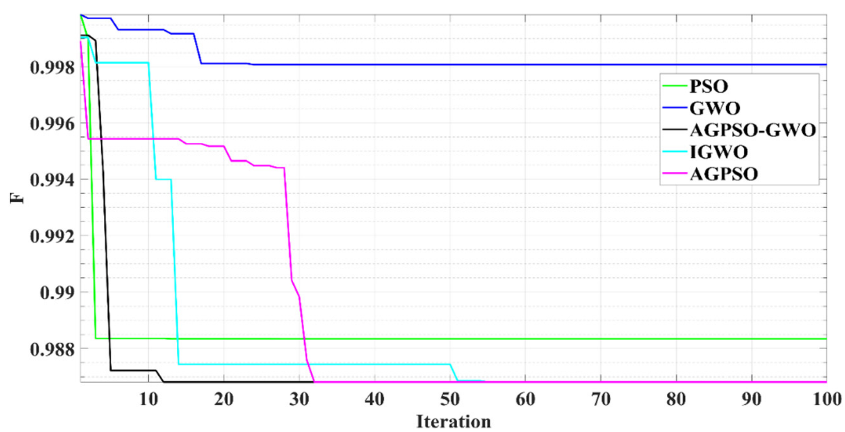

Fig. 22. Convergence curves of all algorithms when the TCSC is installed in the IEEE 118 system to minimize the multi-objective optimization problem.

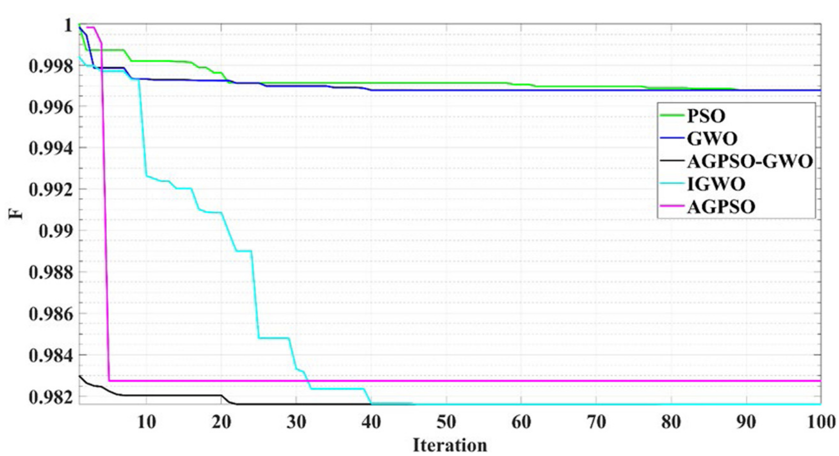

Fig. 23. Convergence curves of all algorithms when the UPFC is installed in the IEEE 118 system to minimize the multi-objective optimization problem.

5.2.2. Installation of the TCSC only

As shown in Table 16, the proposed AGPSO-GWO approach outperformed other compared programs by providing optimum TCSC settings that ensured the minimizing of the PL, DV, and OC values and obtained the global minimum value of F. From Table 16, the proposed AGPSO-GWO technique achieved the lowest PL value compared to other comparison algorithms.

As shown in Fig. 22, the AGPSO-GWO algorithm achieves the best performance during the optimization procedure. The AGPSO-GWO algorithm finds the global optimal value of the fitness function in the fewest iterations. It is noticed that the PSO and GWO algorithms failed to obtain the minimum global value of the fitness function.

Table 17
Solution of all algorithms at the installation of the TCSC in the IEEE 118-bus system to minimize the multi-objective optimization problem.

PL, VD, and OC values at weighting factors 0.1, 0.1, and 0.8 (best Fitness)								
	Without FACTS	132.8629 MW, 0.0866 pu, and $1.0475^{*}10^{8}$ $						
	Algorithms	LOC		Size	PL (MW)	VD (pu)	OC ($)	F
UPFC	AGPSO	bus line	38 96	−20.4460 −0.8	129.8099	0.0851	$1.0301^{*}10^{8}$	0.9827
	IGWO	bus line	38 96	−3.0025 −0.7296	129.9801	0.0854	$1.0280^{*}10^{8}$	0.9816
	AGPSO-GWO	**bus** **line**	**38** **96**	−3 **−0.7299**	**129.9798**	**0.0854**	$\mathbf{1.0280^{*}10^{8}}$	**0.9816**
	GWO	bus line	21 27	−17.3277 0.2	132.7883	0.0836	$1.0478^{*}10^{8}$	0.9968
	PSO	bus line	21 27	−17.4416 0.2	132.7886	0.0836	$1.0478^{*}10^{8}$	0.9968

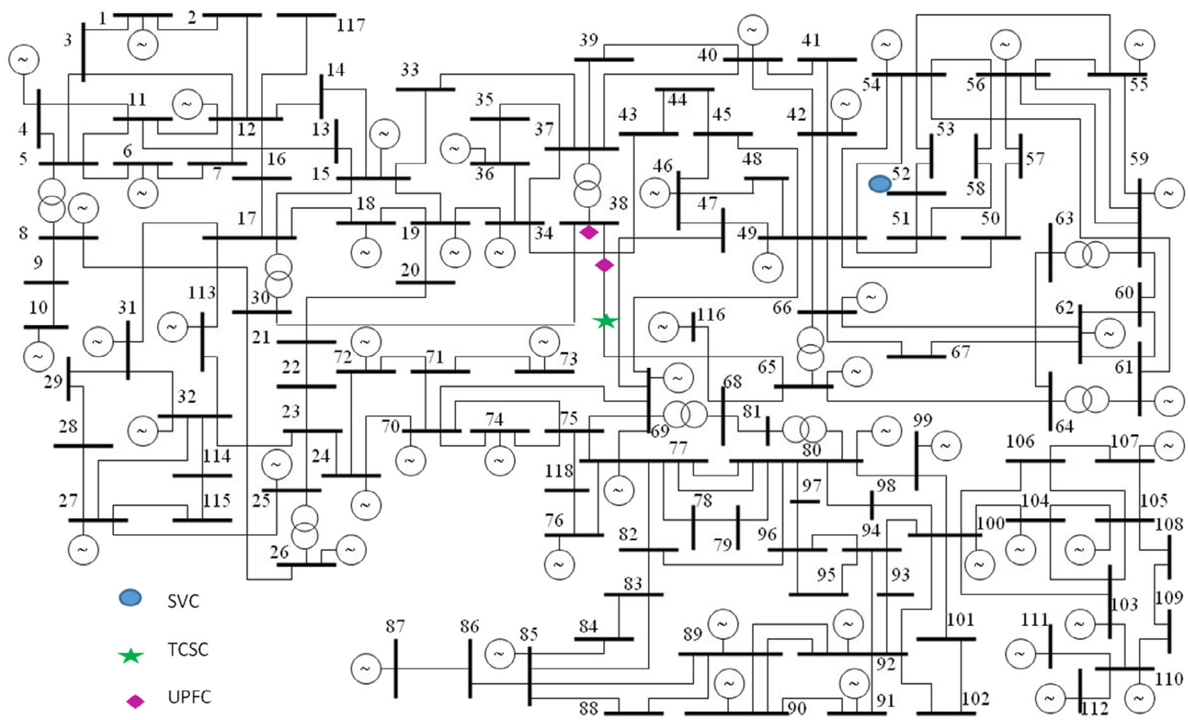

Fig. 24. The placement of FACTS devices on the IEEE-118 bus system.

5.2.3. Installation of the UPFC only

Table 17 summarizes the simulation results and lists the optimal size and location of UPFC based on the proposed algorithms. For each technique, Table 17 also reports the corresponding PL, VD, and OC values for the tested IEEE 118 bus system without FACTS installation.

The optimal settings of the UPFC based on the AGPSO-GWO algorithm have been achieved the smallest size of UPFC (MVAR) with balanced and optimum values of PL, VD, and OC compared to the other algorithms. Although the AGPSO has the lowest power losses and VD values, it has the largest UPFC size and OC value compared to the other proposed techniques.

As shown in Fig. 23, the AGPSO-GWO approach has a significant convergence profile relative to all other algorithms. It quickly achieves the optimal solution, followed by an IGWO algorithm, while the other algorithms have not attained the global minimum value of the fitness function.

Fig. 24 shows a single-line diagram of the IEEE 118-bus system, as well as a visual demonstration of the optimal placement of various FACTS controllers on the system based on the AGPSO-GWO technique, as seen in Tables 15–17.

Table 18
Criteria of evaluations of the proposed techniques Tolba et al. (2020).

Criteria	Equation
Relative error (RE)	$\frac{\sum_{i=1}^{nr}(F_i - F_{\min})}{F_{\min}}.100\%$
Mean absolute error (MAE)	$\frac{\sum_{i=1}^{nr}(F_i - F_{\min})}{nr}$
Root mean square error (RMSE)	$\sqrt{\frac{\sum_{i=1}^{nr}(F_i - F_{\min})^2}{nr}}$
Standard deviation (S.D.)	$\sqrt{\frac{\sum_{i=1}^{nr}(F_i - \overline{F}_{\min})^2}{nr}}$

6. Statistical evaluation of the results

In order to demonstrate the robustness of the AGPSO-GWO method, a statistical performance assessment based on Ref. (Tolba et al., 2020) is carried out for all methods at 30 runs and 50 search agents. The mathematical expressions of the assessment criteria are shown in Table 18. The numerical values of the evaluation criteria for all algorithms when installing SVC, TCSC, and UPFC in the IEEE 30 bus system to optimize the multi-objective function are set out in Table 19. As illustrated in Table 19, the proposed

Table 19
Numerical values for evaluation criteria.

Installation of the SVC					
Criteria	Technique				
	PSO	GWO	AGPSO	IGWO	AGPSO-GWO
RE	$6.1905*10^{-2}$	$6.02*10^{-4}$	$3.1346*10^{-7}$	$4.0808*10^{-10}$	$\mathbf{1.1067*10^{-12}}$
MAE	$6.0198*10^{-4}$	$4.5171*10^{-4}$	$3.0482*10^{-9}$	$3.9683*10^{-12}$	$\mathbf{1.0762*10^{-14}}$
RMSE	$3.2937*10^{-3}$	$2.4715*10^{-3}$	$1.6696*10^{-8}$	$9.6048*10^{-12}$	$\mathbf{4.9343*10^{-14}}$
SD	$3.2936*10^{-3}$	$2.4714*10^{-3}$	$1.6475*10^{-8}$	$8.8962*10^{-12}$	$\mathbf{4.8978*10^{-14}}$
Installation of the TCSC					
Criteria	Technique				
	PSO	GWO	AGPSO	IGWO	AGPSO-GWO
RE	$3.5401*10^{-2}$	$1.2001*10^{-3}$	$1.6626*10^{-12}$	$6.4929*10^{-13}$	$\mathbf{1.9754*10^{-13}}$
MAE	$3.4685*10^{-4}$	$1.1795*10^{-4}$	$1.6577*10^{-12}$	$6.3616*10^{-15}$	$\mathbf{1.9355*10^{-15}}$
RMSE	$1.8998*10^{-3}$	$1.7650*10^{-4}$	$1.6864*10^{-12}$	$1.1394*10^{-14}$	$\mathbf{2.9250*10^{-15}}$
SD	$1.8997*10^{-3}$	$1.3355*10^{-4}$	$3.1503*10^{-13}$	$9.6150*10^{-15}$	$\mathbf{2.2310*10^{-15}}$
Installation of the UPFC					
Criteria	Technique				
	PSO	GWO	AGPSO	IGWO	AGPSO-GWO
RE	$8.7419*10^{-2}$	$9.0761*10^{-2}$	$6.3382*10^{-2}$	$5.9018*10^{-2}$	$\mathbf{7.2659*10^{-3}}$
MAE	$8.2622*10^{-4}$	$9.0364*10^{-4}$	$5.9905*10^{-4}$	$5.5780*10^{-4}$	$\mathbf{6.8672*10^{-5}}$
RMSE	$2.8540*10^{-3}$	$1.2736*10^{-2}$	$2.1702*10^{-3}$	$1.9965*10^{-3}$	$\mathbf{1.9492*10^{-4}}$
SD	$2.8381*10^{-3}$	$4.5285*10^{-3}$	$2.7957*10^{-3}$	$1.9498*10^{-3}$	$\mathbf{1.8554*10^{-4}}$

AGPSO-GWO algorithm is superior with accurate performance to deduce the optimum allocation of FACTS devices in the IEEE 30-bus power in comparison with the other proposed techniques.

7. Conclusion

Meta-heuristic algorithms have been extensively used to allocate different types of FACTS devices such as Static Var Compensator (SVC), Thyristor-Controlled Series Compensator (TCSC), and Unified power flow controller (UPFC). One of the most popular techniques is the GWO algorithm, characterized by an easy implementation, a few variables that have to be adapted, and fast conversion to the final solution. Despite these advantages, it suffers from a loss of diversity that results in trapping in local optima. This paper proposed a new hybrid algorithm, namely the AGPSO-GWO algorithm, to address the standard GWO algorithm's issues. The suggested technique used the enhanced strategy of the AGPSO technique to improve the accuracy and efficiency of the classic GWO algorithm. The AGPSO-GWO algorithm has been applied on the IEEE 30 and 118 bus power systems (as a medium and large scale) to determine the optimum location and size of the SVC, TCSC, and UPFC individually. The FACTS are allocated to minimize active power loss, voltage deviation, and power system operating cost. These objectives have been optimized in single and multi-objective forms. Simulation results proved the effectiveness of the new approach (AGPSO-GWO technique) in optimizing the single and multi-objective functions. Besides, the locations of FACTS devices and ratings have been determined simultaneously. The findings show that optimal FACTS devices allocation diminishing power loss and voltage deviation as well as the system operating cost. In addition, the non-optimized location leads to poor objective values for single and multi-objective optimization. The PSO, GWO, SA, AGPSO, and IGWO algorithms have been used to confirm the validity of the proposed method. Numerical results and conversion curves illustrated that the AGPSO-GWO technique had outperformed the other comparable algorithms. The simulation evidently reveals that the AGPSO-GWO approach has a significantly higher convergence profile than all other algorithms. The proposed algorithm finds the optimum global value quickly while avoiding local optimum trapping. Statistical analyses such as RE, MAE, RMES, SD have been performed on the proposed algorithm and compared to other existing algorithms used in the literature. The results validate the suggested algorithm's superiority over other algorithms. The authors intend to apply the proposed algorithm to a real-network in future work. Moreover, the current paper is considered as the first stage of the proposed research idea to integrate the SVC, TCSC, and the UPFC as a combination of TCSC and SVC. The second stage is considering the active power balance in DC bus of the UPFC besides studying its effect on the proposed system.

References

Agrwal, R., Bharadwaj, S.K., Muley, K.C., 2020. Optimal location of static VAR compensator using evolutionary optimization techniques. Int. J. Emerg. Technol. 11 (1).

Ananth, D.V.N., Sureshkumar, L.V., Boddepalli, M., 2021. Modelling and design of static compensator and UPFC based FACTS devices for power system oscillations damping and voltage compensation. In: Lecture Notes in Electrical Engineering, vol. 702, http://dx.doi.org/10.1007/978-981-15-8439-8_29.

Bakir, H., Öztürk, A., Tosun, S., 2018. Investigation of power flow effect of serial and parallel FACTS devices. Balk. J. Electr. Comput. Eng. 6–11. http://dx.doi.org/10.17694/bajece.410204.

Balamurugan, K., Muralisachithanandam, R., Dharmalingam, V., 2015. Performance comparison of evolutionary programming and differential evolution approaches for social welfare maximization by placement of multi type FACTS devices in pool electricity market. Int. J. Electr. Power Energy Syst. 67, http://dx.doi.org/10.1016/j.ijepes.2014.12.007.

Balamurugan, K., Muthukumar, K., 2019. Differential evolution algorithm for contingency analysis-based optimal location of FACTS controllers in deregulated electricity market. Soft Comput. 23 (1), http://dx.doi.org/10.1007/s00500-018-3141-x.

ben oualid Medani, K., Sayah, S., Bekrar, A., 2018. Whale optimization algorithm based optimal reactive power dispatch: A case study of the Algerian power system. Electr. Power Syst. Res. 163, http://dx.doi.org/10.1016/j.epsr.2017.09.001.

Chow, J.H., Sanchez-Gasca, J.J., 2019. Power System Modeling, Computation, and Control.

Daealhaq, H.M., kfajey, Y.F., Tukkee, A.S., 2021. Power loss reduction and voltage profile improvement using optimal placement of FACTS devices. IOP Conf. Ser. Mater. Sci. Eng. 1067 (1), http://dx.doi.org/10.1088/1757-899x/1067/1/012128.

Dash, S., Subhashini, K.R., Satapathy, J., 2020a. Efficient utilization of power system network through optimal location of FACTS devices using a proposed hybrid meta-heuristic ant lion-moth flame-salp swarm optimization algorithm. Int. Trans. Electr. Energy Syst. 30 (7), http://dx.doi.org/10.1002/2050-7038.12402.

Dash, S.P., Subhashini, K.R., Satapathy, J.K., 2020b. Optimal location and parametric settings of FACTS devices based on JAYA blended moth flame optimization for transmission loss minimization in power systems. Microsyst. Technol. 26 (5), 1543–1552. http://dx.doi.org/10.1007/s00542-019-04692-w.

Faisal, M., Hannan, M.A., Ker, P.J., Rahman, M.S.A., Begum, R.A., Mahlia, T.M.I., 2020. Particle swarm optimised fuzzy controller for charging–discharging and scheduling of battery energy storage system in MG applications. Energy Rep. 6, 215–228. http://dx.doi.org/10.1016/J.EGYR.2020.12.007.

Gaur, D., Mathew, L., 2018. Optimal placement of FACTS devices using optimization techniques: A review. IOP Conf. Ser. Mater. Sci. Eng. 331 (1), 012023. http://dx.doi.org/10.1088/1757-899X/331/1/012023.

Gautam, A., Sharma, P.R., Kumar, Y., 2019. Sensitivity based ATC maximization by optimal placement of TCSC applying grey wolf optimization. In: 2019 3rd International Conference on Recent Developments in Control, Automation and Power Engineering. RDCAPE 2019, http://dx.doi.org/10.1109/RDCAPE47089.2019.8979016.

Guo, C., Zhong, L., Zhao, J., Gao, G., 2020. Single-phase reactive power compensation control for STATCOMs via unknown system dynamics estimation. Math. Probl. Eng. 2020, http://dx.doi.org/10.1155/2020/8394513.

Gutierrez, E.H., Conde, A., Shih, M.Y., Fernández, E., 2019. Execution time enhancement of DOCR coordination algorithms for on-line application. Electr. Power Syst. Res. 170, 1–12. http://dx.doi.org/10.1016/J.EPSR.2019.01.004.

Hema Sekhar, A., Haritha, A., Vandana, A., Chaitanya Teja, P., 2020. Novel hybrid optimization techniques for analyzing the performance of transmission lines using SVC device. Int. J. Electr. Eng. Technol. 11 (1).

Jmii, H., Meddeb, A., Chebbi, S., 2017. An approach for improving voltage stability by combination of SVC and TCSC. In: 2016 7th International Conference on Sciences of Electronics, Technologies of Information and Telecommunications. SETIT 2016, http://dx.doi.org/10.1109/SETIT.2016.7939855.

Kanaan, H.M., EL-Gazaar, M., Mehanna, M.A., 2020. Optimal location and sizing of SVC considering system losses, voltage division and system overload. J. Al-Azhar Univ. Eng. Sect. 15 (57), http://dx.doi.org/10.21608/auej.2020.120371.

Kanaan, H.A.M., Mehanna, M.A.A., 2020. Application of simulates annealing algorithm for optimal location and sizing of FACTS devices considering system losses and voltage division corresponding author : engamdy08@gmail.com. Int. J. Adv. Sci. Technol. 29 (6), 5279–5289.

Kavitha, K., Neela, R., 2018. Optimal allocation of multi-type FACTS devices and its effect in enhancing system security using BBO, WIPSO & PSO. J. Electr. Syst. Inf. Technol. 5 (3), 777–793. http://dx.doi.org/10.1016/j.jesit.2017.01.008.

Lee, H.J., Lee, D.S., Yoon, Y.D., 2019. Unified power flow controller based on autotransformer structure. Electron 8 (12), http://dx.doi.org/10.3390/electronics8121542.

Li, W., Meng, X., Huang, Y., Fu, Z.H., 2020. Multipopulation cooperative particle swarm optimization with a mixed mutation strategy. Inf. Sci. (Ny). 529, http://dx.doi.org/10.1016/j.ins.2020.02.034.

Lu, C., Gao, L., Yi, J., 2018. Grey wolf optimizer with cellular topological structure. Expert Syst. Appl. 107, http://dx.doi.org/10.1016/j.eswa.2018.04.012.

Mamdouh, K.A., Shehata, A.A., Korovkin, N.V., 2019. Multi-objective voltage control and reactive power optimization based on multi-objective particle swarm algorithm. IOP Conf. Ser. Mater. Sci. Eng. 643, 012089. http://dx.doi.org/10.1088/1757-899X/643/1/012089.

Mirjalili, S., Lewis, A., Sadiq, A.S., 2014a. Autonomous particles groups for particle swarm optimization. Arab. J. Sci. Eng. 39 (6), 4683–4697. http://dx.doi.org/10.1007/s13369-014-1156-x.

Mirjalili, S., Mirjalili, S.M., Lewis, A., 2014b. Grey wolf optimizer. Adv. Eng. Softw. 69, 46–61. http://dx.doi.org/10.1016/j.advengsoft.2013.12.007.

Mitiku Teferra, D., Ngoo, L., 2021. Improving the voltage quality and power transfer capability of transmission system using FACTS controller. Int. J. Energy Power Eng. 10 (1), http://dx.doi.org/10.11648/j.ijepe.20211001.12.

Mokhtari, M.S., Gitizadeh, M., Lehtonen, M., 2021. Optimal coordination of thyristor controlled series compensation and transmission expansion planning: Distributionally robust optimization approach. Electr. Power Syst. Res. 196, http://dx.doi.org/10.1016/j.epsr.2021.107189.

Muhammad, Y., Akhtar, R., Khan, R., Ullah, F., Raja, M.A.Z., Machado, J.A.T., 2021. Design of fractional evolutionary processing for reactive power planning with FACTS devices. Sci. Rep. 11 (1), http://dx.doi.org/10.1038/s41598-020-79838-2.

Muhammad, Y., Khan, R., Raja, M.A.Z., Ullah, F., Chaudhary, N.I., He, Y., 2020. Solution of optimal reactive power dispatch with FACTS devices: A survey. Energy Rep. 6, http://dx.doi.org/10.1016/j.egyr.2020.07.030.

Nadeem, M., et al., 2020. Optimal placement, sizing and coordination of FACTS devices in transmission network using whale optimization algorithm. Energies 13 (3), http://dx.doi.org/10.3390/en13030753.

Nadimi-Shahraki, M.H., Taghian, S., Mirjalili, S., 2021. An improved grey wolf optimizer for solving engineering problems. Expert Syst. Appl. 166 (2020), 113917. http://dx.doi.org/10.1016/j.eswa.2020.113917.

Rezaee Jordehi, A., Jasni, J., Abd Wahab, N., Kadir, M.Z., Javadi, M.S., 2015. Enhanced leader PSO (ELPSO): A new algorithm for allocating distributed TCSC's in power systems. Int. J. Electr. Power Energy Syst. 64, http://dx.doi.org/10.1016/j.ijepes.2014.07.058.

Saravanan, M., Slochanal, S.M.R., Venkatesh, P., Abraham, J.P.S., 2007. Application of particle swarm optimization technique for optimal location of FACTS devices considering cost of installation and system loadability. Electr. Power Syst. Res. 77, 3–4. http://dx.doi.org/10.1016/J.EPSR.2006.03.006.

Shehata, A.A., Korovkin, N.V., Tolba, M.A., Tulsky, V.N., 2021a. Efficient utilization of the power grid using FACTS devices based on a new metaheuristic optimizer. In: Proceedings of the 3rd 2021 International Youth Conference on Radio Electronics, Electrical and Power Engineering. REEPE 2021, http://dx.doi.org/10.1109/REEPE51337.2021.9387974.

Shehata, A.A., Refaat, A., Ahmed, M.K., Korovkin, N.V., 2021b. Optimal placement and sizing of FACTS devices based on autonomous groups particle swarm optimization technique. Arch. Electr. Eng. 70 (1), 161–172. http://dx.doi.org/10.24425/aee.2021.136059.

Shehata, A.A., Refaat, A., Korovkin, N.V., 2020. Optimal allocation of FACTS devices based on multi-objective multi-verse optimizer algorithm for multi-objective power system optimization problems. In: 2020 International Multi-Conference on Industrial Engineering and Modern Technologies, FarEastCon 2020. http://dx.doi.org/10.1109/FarEastCon50210.2020.9271359.

Singh, B., Agrawal, G., 2018. Enhancement of voltage profile by incorporation of SVC in power system networks by using optimal load flow method in MATLAB/Simulink environments. Energy Rep. 4, 418–434. http://dx.doi.org/10.1016/J.EGYR.2018.07.004.

Singh, B., Kumar, R., 2020. A comprehensive survey on enhancement of system performances by using different types of FACTS controllers in power systems with static and realistic load models. Energy Rep. 6, 55–79. http://dx.doi.org/10.1016/J.EGYR.2019.08.045.

Singh, B., Mukherjee, V., Tiwari, P., 2019. Ga-based optimization for optimally placed and properly coordinated control of distributed generations and static var compensator in distribution networks. Energy Rep. 5, 926–959. http://dx.doi.org/10.1016/J.EGYR.2019.07.007.

Singh, P., Tiwari, R., Singh, A.K., Sangwan, V., 2020. Optimal allocation and comparative investigation of unified power flow controller using ASMO. In: 2020 International Conference on Power Electronics and IoT Applications in Renewable Energy and Its Control. PARC 2020, http://dx.doi.org/10.1109/PARC49193.2020.236663.

Tolba, M.A., Rezk, H., Al-Dhaifallah, M., Eisa, A.A., 2020. Heuristic optimization techniques for connecting renewable distributed generators on distribution grids. Neural Comput. Appl. 32 (17), http://dx.doi.org/10.1007/s00521-020-04812-y.

Tu, Q., Chen, X., Liu, X., 2019. Hierarchy strengthened grey wolf optimizer for numerical optimization and feature selection. IEEE Access 7, http://dx.doi.org/10.1109/ACCESS.2019.2921793.

Wang, D., Tan, D., Liu, L., 2018. Particle swarm optimization algorithm: an overview. Soft Comput. 22 (2), 387–408. http://dx.doi.org/10.1007/s00500-016-2474-6.

In electric vehicle technologies, the state-of-the-art of power electronics converters configurations

Subhrajit Sahoo, *Department of Electrical Engineering , Capital Engineering College, Bhubaneswar, subhrajitsahoo23@yahoo.co.in*

Umakanta Dash, *Department of Computer Scinece Engineering , Raajdhani Engineering College, Bhubaneswar, umakanta.das221@gmail.com*

Laxmi, *Department of Computer Science Engineering, Aryan Institute of Engineering & Technology, Bhubaneswar, laxmi3349@gmail.com*

Prajnadipta Sahoo, *Department of Electrical and Electronics Engineering, NM Institute of Engineering & Technology, Bhubaneswar, prajnadipta567@gmail.com*

Keywords:
Renewable energy
DC-DC bidirectional converter
Electric vehicle
Battery electric vehicle
Fuel cell vehicle
Hybrid electric vehicle
Plug-in electric vehicle

A B S T R A C T

Today, the Internal Combustion Engine (ICE) is gradually being replaced by electric motors, which results in higher efficiency and low emission of greenhouse gases. The electric vehicle either works wholly or partially on electrical energy generated from batteries and ultra-capacitors. The battery or ultra-capacitor is either charged from the AC supply connected to a grid line in a plug-in electric vehicle or from ICE in a hybrid electric vehicle. Alternatively, the battery charges from the traction motor by regenerative braking. In the reverse direction, the energy from the battery or ultra-capacitor is injected into the AC grid line in the plug-in electric vehicle. Power electronic converters play a vital role in the conversion process from grid line to traction motor and in the reverse direction. In this paper, the role of power electronics converters in an electric vehicle is elaborated. The bidirectional DC-DC converter plays a vital role in the power conversion process of electric vehicles. The existing bidirectional DC-DC converter topologies are discussed with a comprehensive review, comparison, and application. Additionally, the advancement in power electronics converters to improve the efficiency and reliability of the vehicular system is elaborated.

1. Introduction

Fossil fuel is depleting gradually due to excessive use to propel in the conventional vehicular system (Bhaskar, Padmanaban & Holm-Nielsen, 2019b; Ida, Murakami & Tanaka, 2014; Querini, Dagostino, Morel & Rousseaux, 2012; Shareef, Islam & Mohamed, 2016; Williamson, Rathore & Musavi, 2015; Yong, Ramachandaramurthy & Tan, 2015a). Moreover, the demand for fossil fuel is also gradually increasing due to advancements in the vehicular system (Afonso, Marques & Fuinhas, 2017; Gielen et al., 2019; Guo, Liu, Sun & Jin, 2018; Jenniches, 2018). The efficiency of conventional ICE is nearly 20%. The remaining energy is wasted as heat and Greenhouse Gases (GHG) as a by-product after combustion (Adams, Klobodu & Apio, 2018; Awasthia et al., 2017). Some key features of EVs are ease of operation; fewer moving parts that reflect increasing efficiency, pollutant-free, capable of frequently starting and stopping operation, and high starting torque (Adams et al., 2018). Apart from this, the electric vehicle is becoming an emerging concept in renewable generating facilities and advanced grid systems (Awasthia et al., 2017). In a Plug-in Electric Vehicle (PEV), the battery injects power into the gridline to overcome the overload problem and to provide ancillary services (Gough, Rowley & Walsh, 2014; Mukherjee & Gupta, 2015; Schaltz, Khaligh & Rasmussen, 2009; Subramaniam et al., 2019). All these features of electric vehicles are encouraging researchers to take this technology to the next level.

In recent advancements in automobile system, advanced Power Electronics Converters (PECs) and motor drives play an essential role in vehicular technology (Baha & Thomas, 2013; Bhaskar et al., 2019a; Bhaskar, Sanjeevikumar, Holm-Nielsen, Pedersen & Leonowicz, 2019c; Emadi, Rajashekara, Williamson & Lukic, 2005; Krishna, Daya, Sanjeevikumar & Mihet-Popa, 2017; Un-Noor, Padmanaban, Mihet-Popa, Mollah & Hossain, 2017). In EVs, PECs and electric motor drives control the flow of electrical energy within the vehicle or from the external charging station or grid to the vehicle and vice versa (Awasthia et al., 2017; Subramaniam et al., 2019). This makes EVs pollutant-free, more efficient, higher performance and increases the durability of the vehicle (Bhaskar et al., 2018; Daramy-Williams, Anable & Grant-Muller, 2019; Daya et al., 2016; Lane et al., 2018; Li, Khajepour & Song, 2019; Tahami, Kazemi & Farhanghi, 2003; Wu & Gao, 2006; Zhao, He, Yao & Huang, 2019; Zhou, Yang, Cai & Ying, 2018). In a conventional ICE

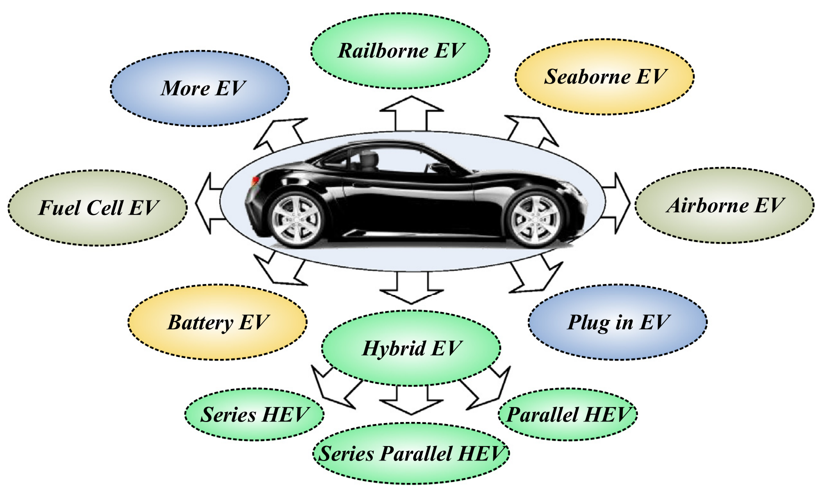

Fig. 1. General classification of electric vehicle.

vehicle, 6 V to 12 V is needed to start up and to run other electric equipment (Miller & Webster, 1997). The hydraulic system such as brake and mechanically driven system such as steering is being replaced by an electrically driven system, which makes it more efficient and safer (Adams et al., 2018). The luxurious load such as power windows, high power headlamp, and auto start-up is introduced in advanced automobile systems that demand higher power with different voltage ratings to work. Hence, power electronics converters are responsible for the advancement in EVs (Chan, 2002).

This paper will elaborate on the state-of-the-art of the PECs in the battery, hybrid, fuel cell, and plug-in electric vehicle systems and compare the associated advantages and disadvantages of the existing PECs for theze vehicular systems. In this paper, section-II elaborates the classifications of an electric vehicles, their structures, modes of operation, and the role of PECs in each vehicular system. Section-III deals with the role of PECs in existing electrical vehicular technology and discusses the non-isolated bidirectional DC-DC converter. Section-IV includes the challenges in power electronics vehicular systems.

2. Types of electrical vehicle and role of power electronics converter

EVs use electrical energy to drive the vehicle and for the electrical appliances in the vehicle to function. According to the International Electro-Technical Commission's Technical Committee (IETCTC), if the vehicle uses two or more energy sources, storage device, and converter to drive the vehicle, then it's called a Hybrid Electric Vehicle (HEV) as long as at least one source is providing electrical energy (Awasthia et al., 2017). EVs are classified into different types according to the combination of sources (Bayindir, Gozukucuk & Teke, 2011). The battery alone works as a source in the Battery Electric Vehicle (BEV), fuel cell and battery in Fuel Cell Electric Vehicle (FCEV), battery and ICE in HEV, and battery and grid or external charging station in PEV as shown in Fig. 1. The details of the EV types are discussed in the following section.

2.1. Battery electric vehicle

2.1.1. Architecture of battery electric vehicle

In a BEV, the battery provides power to drive the train of the vehicle (Cassani & Williamson, 2009; Ehsani, Gao & Gay, 2005; Grunditz & Thiringer, 2016). The rechargeable battery storage unit acts as a fuel tank in BEV. Therefore, the range of a BEV depends on the capacity of the battery unit. Typically, once it is fully charged, the BEV covers 100 km to 250 km distance (Awasthia et al., 2017). In BEV, ICE is replaced by an electric motor to propel which makes it a pollution-free vehicle. The typical structure of BEV is shown in Fig. 2(a). The 14 V to 300 V rechargeable batteries is used in BEV according to the type of vehicle. Light-duty, mid-duty, and heavy-duty vehicles need 14 V, 120 V and 150 V DC batteries, respectively (Hegazy, Barrero & Van Mierlo, 2013; Musavi, Craciun & Gautam, 2014; Rodatz, Garcia & Guzzella, 2003). Two operating modes are observed in BEV. The power from the battery is transferred to the vehicle through a DC-DC converter and an inverter in the battery operating mode. In regenerative braking mode, the power generated by traction motor transfers to the battery via rectifier and DC-DC converter.

2.1.2. Role of PECs in battery electric vehicle

In BEV, the unidirectional step-up DC-DC converter is adopted to boost the voltage as per the demand of the propelling system and electrical load (Adams et al., 2018; Awasthia et al., 2017). The low voltage/power rated equipment, such as mobile charger receives supply from the battery. The DC voltage of the battery is transferred to a high voltage DC bus through the step-up converter. The high voltage DC bus supply power to higher voltage rated equipment such as projector lamps. The function of the DC-AC inverter is to convert DC into a variable (voltage and frequency) three-phase AC to drive the AC motor. To drive the vehicle, and other electronic types of equipment, the DC power supply from the battery is used as fuel. The voltage controller controls the DC-DC converter to maintain the charging level of the battery at its maximum and minimum limits (Miller & Webster, 1997) as shown in Fig. 2(b).

2.2. Fuel cell electric vehicle

2.2.1. Architecture of fuel cell electric vehicle

The hybrid FCEV is a type of electric vehicle in which both the fuel cell and the battery provide electrical power to drive the train of the vehicle (Lai & Nelson, 2007; Marchesoni & Vacca, 2007; Thomas, 2009). In FCEV, oxygen from the air is combined with the stored hydrogen to generate power for driving the electric motor. From a fuel tank, hydrocarbon gas is transferred to the fuel reformer to achieve purity of hydrogen gas and is stored in the fuel cell stack (Tazelaar, Veenhuizen & Jagerman, 2013). As per the requirement of power, hydrogen for fuel cell stacks is combined with oxygen from the air to generate electricity, and excess electricity can be saved in batteries or ultra-capacitors.

There are different types of fuel cells available in the market, such as polymer electronic membrane (PEM), direct methanol fuel cells, phosphoric acid fuel cells, regenerative fuel cells, reformed methanol fuel cells, solid oxide fuel cells, and molten carbonate fuel cells (Das, Tan & Yatim, 2017). Both hybrid and fuel cell vehicles are pollutant-free, and the by-product is water. The schematic block diagram of hybrid and fuel cell vehicle is shown in Fig. 3(a). The operating mode of FCEV is divided

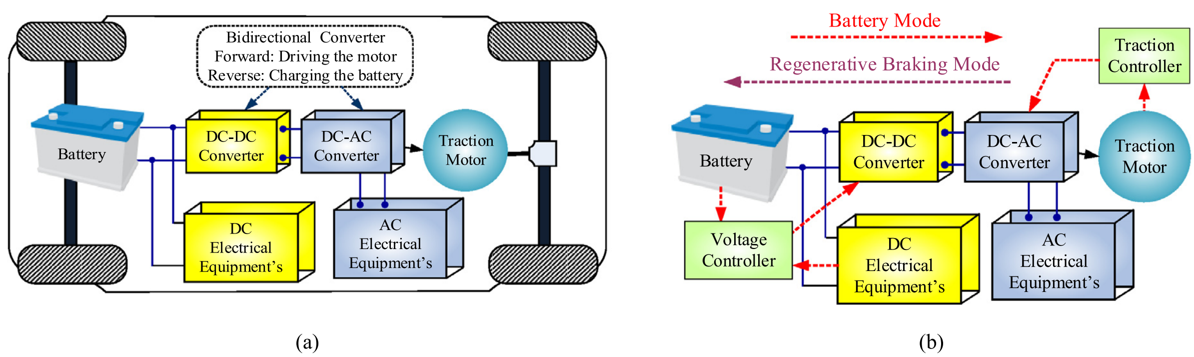

Fig. 2. Battery Electric Vehicle (a) Typical structure of BEV, (b) Control scheme operating modes of BEV.

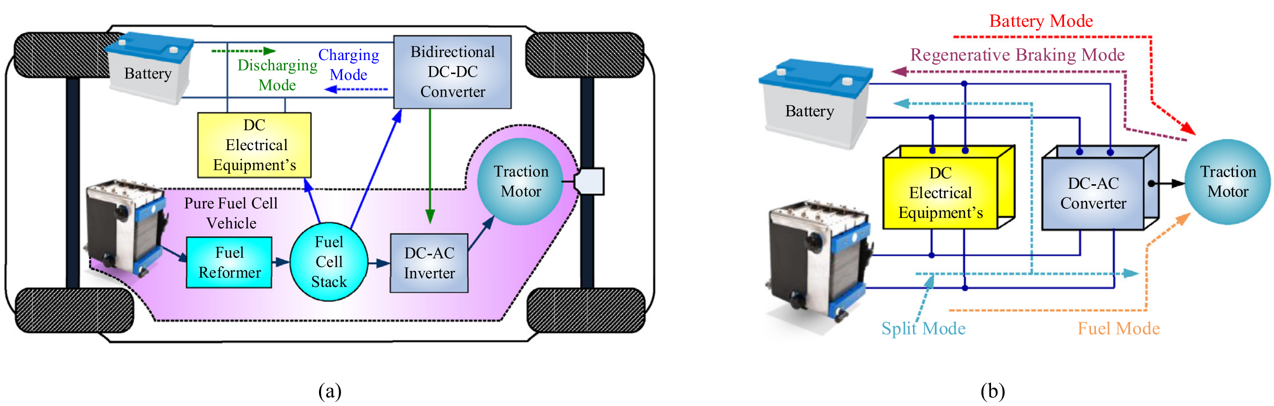

Fig. 3. Fuel Cell Electric Vehicle (a) Typical structure of FCEV, (b) Operating modes of FCEV.

into five modes, as shown in Fig. 3(b). In fuel mode, the fuel cell acts as a source of energy to propel the train individually. In battery mode, the battery works as a source of energy to drive the train. If both the battery and fuel supply are together, then it is called a "combined mode" (Miller & Webster, 1997). In split mode, the fuel cell supplies power to drive the vehicle, and excess energy is utilized to charge the battery. In a regenerative mode, the traction motor acts as a source to charge the battery (Jafri & Gupta, 2016; Schaltz, 2010).

2.2.2. Role of PECs in fuel cell electric vehicle

In FCEV, the electric energy is generated from the battery and fuel cell. The main goal of FCEVs is to convert electrical energy from fuel cells to usable power for various loads of the vehicle by using an efficient method to improve the efficiency and performance of the vehicle (Adams et al., 2018; Awasthia et al., 2017).

Low voltage DC equipments, such as mobile charger, auto starters receives power directly from a battery or fuel cell. For motor drive and high voltage applications, the low voltage is stepped-up to 300 V using a step-up DC-DC converter. The traction controller is adapted to maintain the required speed of the vehicle by varying the amplitude and frequency of the inverter output. The voltage controller is adapted to maintain the maximum and minimum charging levels of the battery and to increase its life, as shown in Fig. 4. In FCEV electrical system, a bidirectional DC-DC power converter plays a key role to controlling the energy flow from the fuel cell to a traction motor during motor mode and from the motor to the battery during regenerative braking mode in hybrid FCEV. The bidirectional DC-DC power converter controls the energy flow with the help of traction and voltage controllers.

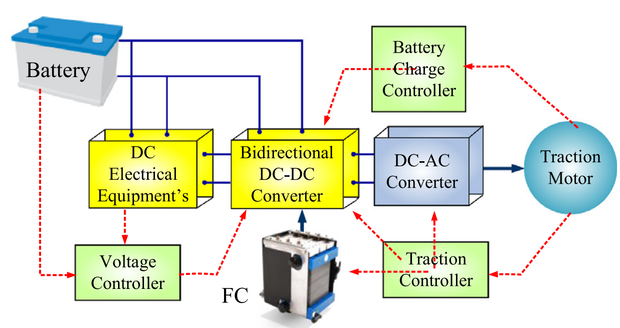

Fig. 4. Control scheme of FCEV.

2.3. Hybrid electric vehicles (HEVS)

The hybrid electric vehicle is a combination of an ICG vehicle and a BEV (Gao, Ehsani & Miller, 2005). The ICE provides the necessary propelling power to drive the train of vehicles. By regenerative mechanism, the lost energy during the braking mechanism is stored in the battery to increase the efficiency and economy of the vehicle. Customarily, there are two types of hybrid electric vehicles, namely Series Hybrid Electric Vehicle (SHEV) and Parallel Hybrid Electric Vehicle (PHEV) (Chiu & Lin, 2006; Gruosso, 2014; Zhang & Williamson, 2008). To improve power, performance and fuel economy, a third series-parallel hybrid vehicle (SPHEV) was introduced by combining the features of SHEV and PHEV (Gurkaynak, Khaligh & Emadi, 2009).

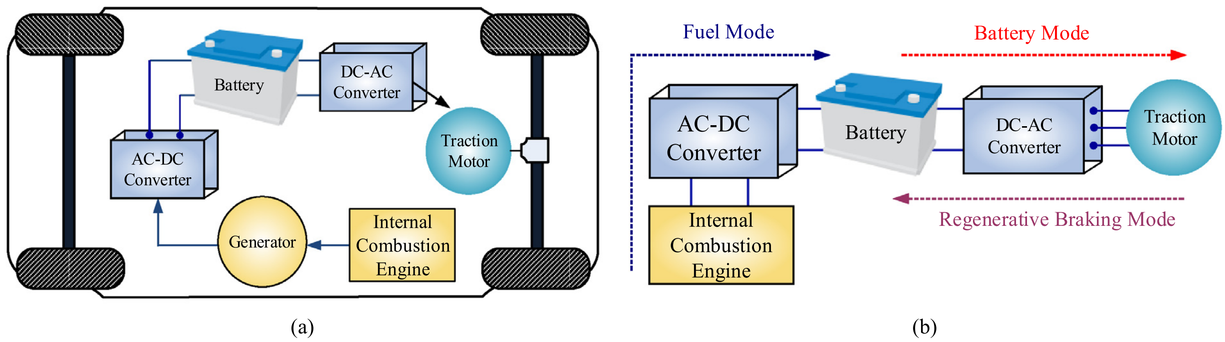

Fig. 5. SHEV (a) Typical structure of SHEV (b) Different operating mode of SHEV.

2.3.1. Series hybrid electric vehicle

In SHEV, both ICE and the battery is modeled in such a way that they can generate the necessary power to propel the train and peripheral electric/electronic equipment (Parag Jose & Meikandasivam, 2016; Roche, Shabbir & S., 2017). In SHEV, the mechanical energy from ICE is converted to electrical form by using a generator. The generated AC power is converted into the DC form to charge the battery by using an AC-DC rectifier (Akbarian, Pillay & Lopes, 2015). In SHEV, the ICE is not directly connected to the traction motor to drive the train. In between ICE and the traction motor, the battery is the intermediate unit. To drive the train, SHEV requires three propulsion devices. ICE will generate mechanical energy, and the generator will convert mechanical energy into electrical energy, whereas the traction motor will convert the electrical energy to mechanical energy for propelling the vehicle (Nayanatara, Shanmugapriya & Gurusivakumar, 2014; Razavian, Azad & McPhee, 2012). Therefore, the efficiency of SHEV is lower. The typical structure of SHEV is shown in Fig. 5(a).

In SHEV, the battery is the primary source of power to drive the train. The ICE runs at the optimal speed to drive the generator and charge the battery. When the State of Charge (SOC) of the battery is minimized, the ICE starts to charge the battery. As the SOC reaches its maximum level of around 65%–70%, the ICE stops charging the battery. The battery is the source of power to drive the train, which reduces the fuel consumption and emissions of the vehicle. The SHEV is a viable solution when the frequent starting and stopping of the vehicle is required, such as in city rides (Miller & Webster, 1997). Three operating modes are observed in SHEV. First, in the fuel mode, ICE is utilized to charge the battery according to the SOC of the battery. In the battery mode, the propelling power is gained from the battery. The traction motor also acts as a source during braking operations to charge the battery, which is called regenerative braking mode, as shown in Fig. 5(b).

2.3.2. Parallel hybrid electric vehicle

The PHEV is another type of HEV in which both the ICE and the battery act as a source to drive the train of the vehicle (Desai & Williamson, 2009; Li, Yu & Ding, 2010). Both the ICE and the battery can drive the train individually, as shown in Fig. 6(a). Both the ICE and the electrical motor are coupled to the driving shaft via two clutches. The ICE is directly connected to the mechanical shaft of the drive train to propel the vehicle (Adams et al., 2018). As there are no intermediate conversion stages between ICE and the drive train, the efficiency of PHEV is greater when compared to SHEV. For long distance range, a PHEV is a viable solution due to no intermediate conversion state as in SHEV. Hence, the vehicle is fuel efficient (Olson & Sexton, 2000).

In a PHEV, there are three different ways to utilize the ICE and battery, as shown in Fig. 6(b). In motor mode, the battery is utilized to power the train, which is a viable solution for lower speeds. In fuel mode, the ICE runs at an optimal speed to drive the train at high speed. During braking or deceleration operations, the traction motor acts as a generator to charge the battery in regenerative braking mode (Miller & Webster, 1997).

In PHEV, the lowest DC voltage is boosted by a bidirectional DC-DC converter to feed the high voltage DC bus. The function of the three-phase inverter is to convert the constant DC voltage into variable AC voltage and frequency to maintain the torque and speed of the traction motor.

2.3.3. Series-Parallel hybrid electric vehicle

The Series-Parallel Hybrid Electric Vehicle (SPHEV) configuration incorporates the features of SHEV and PHEV (Gruosso, 2014; Gurkaynak et al., 2009; Zhang & Williamson, 2008). In SPHEV, the generator is introduced in between ICE and the battery to charge the battery as compared to PHEV and ICE is directly connected to the mechanical shaft to drive the vehicle as compared to SHEV as shown in Fig. 7(a). From the architecture, it is clear that SPHEV is more complicated and expensive as compared to the other two HEV (Khaligh & Dusmez, 2012).

There are five different ways to utilize the ICE and battery to propel the vehicle and other electrical equipment function, as shown in Fig. 7(b). In fuel mode, the ICE works to drive the vehicle. However, the propelling power is received from the battery in the battery mode. During split mode, the ICE transfers power to the traction motor, and the excess power is utilized to charge the battery. Both the ICE and the battery provides power to the traction motor in combine mode. During braking and deceleration operations, the traction motor acts as a generator and supplies power to the battery in regenerative braking mode. The most adopted strategy for effective utilization of battery and ICE in SPHEV is that the battery is utilized to start operation and propel at low speed after the ICE works alone to drive at high speed, which increases the vehicle's fuel efficiency. When acceleration is needed, the battery mode is in an active state to give extra power along with the ICE (Kim & Kum, 2016).

2.3.4. Role of PECs in hybrid electric vehicle

As discussed earlier, the HEVs work on electric energy generated from the battery, mechanical energy from the ICE, and from both battery and ICE (Adams et al., 2018; Awasthia et al., 2017). The PECs maintain and control the flow of energy from the battery or ICE to the traction motor and the traction motor to the battery with the help of a voltage and traction controller. The low voltage from the battery is supplied to the low voltage rated DC equipment such as mobile chargers and auto start-up. The AC-DC rectifier adopted converts the variable AC to a constant DC voltage during regenerative braking mode. In battery mode, high DC voltage is converted into variable AC quantities to maintain the required torque and speed. The control schemes of SHEV, PHEV and SPHEV are shown in Fig. 8(a)–(c), respectively.

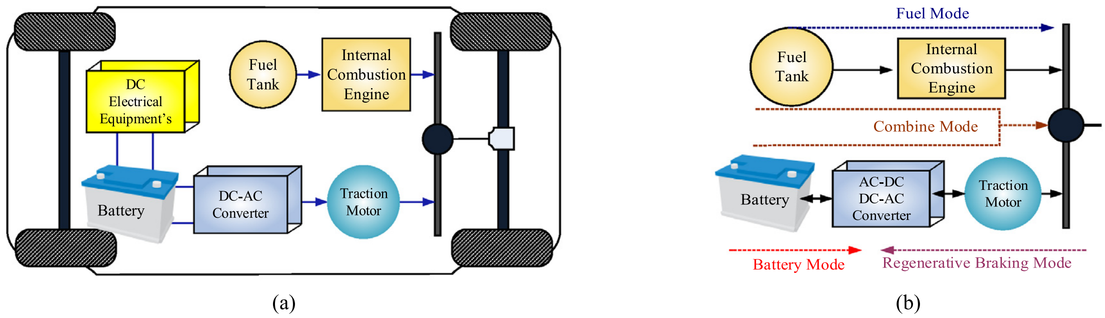

Fig. 6. PHEV (a) Typical structure of PHEV (b) Different operating mode of PHEV.

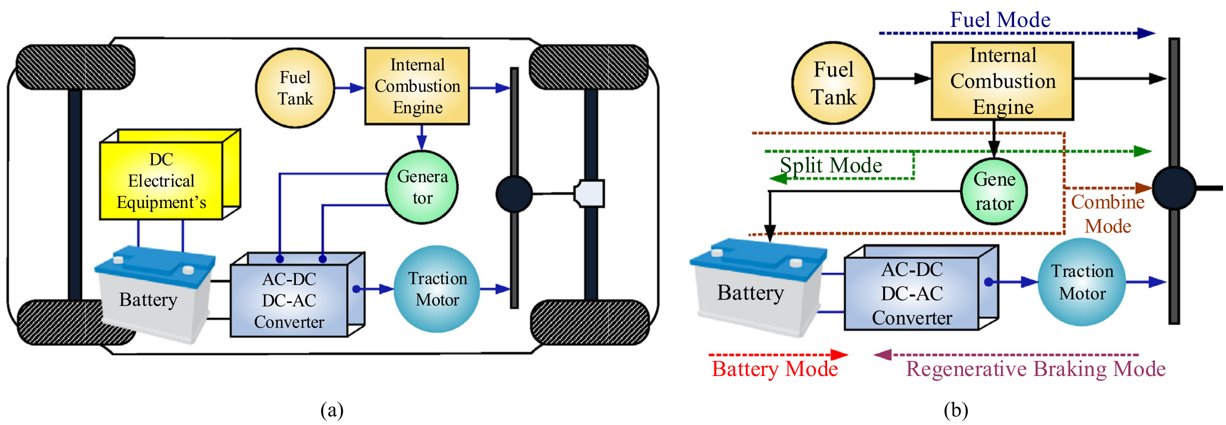

Fig. 7. SPHEV (a) Typical structure of SPHEV (b) Different working mode of SPHEV.

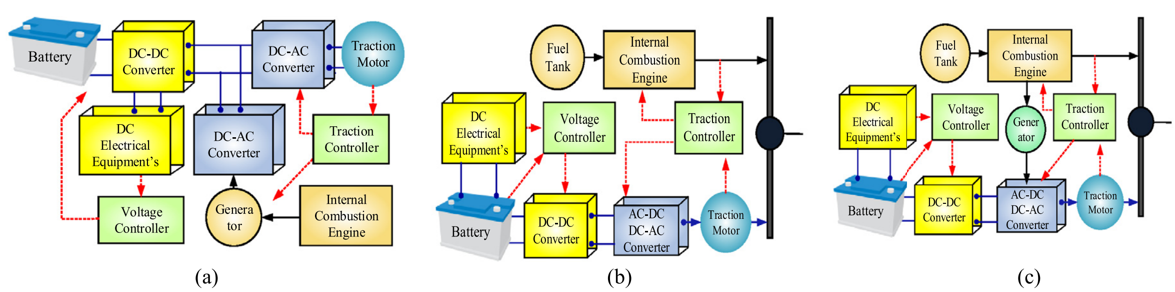

Fig. 8. Control schemes of (a) SHEV, (b) PHEV and (c) SPHEV.

2.4. Plug-In electric vehicles

2.4.1. Architecture of plug-in electric vehicle

The PEV is a type of HEV in which the battery is charged from an external source. The ICE is not sufficient to convert the fuel energy to mechanical energy to drive the shaft. Most of the energy is lost as heat during conversion (Li & Williamson, 2007; Li, Sharkh & Walsh, 2011; Mwasilu, Justo & Kim, 2014). Moreover, the ICE emits greenhouse gases as a by-product. To overcome the drawback of ICE, ICE is replaced by the battery. PEV has less maintenance cost due to fewer moving parts. The typical structure of PEV is shown in Fig. 9(a) and it is similar to SHEV. PEVs have an external charge unit for charging the battery, whereas SHEVs have it on board (Li, Lopes & Williamson, 2009; Williamson, 2007). The PEV works on the electrical supply, where the battery is charged at the battery charging station. The charging station may be at home or grid. Conceptually, PEV works in two modes, grid to the vehicle (G2V), in which the battery charges from the grid, and the other is the vehicle to grid (V2G), where the battery injects power into the grid, as shown in Fig. 9(b).

In the V2G concept (Subramaniam et al., 2019), battery energy can be injected into the grid to solve the overloading problem of the grid. In G2V mode, the power from the grid is utilized to drive the vehicle and charge the battery, mostly during no-load conditions on the grid line through various PECs. In regenerative braking mode, the traction motor acts as a generator to charge the battery. In V2G mode, the charged battery from either regenerative braking or from the grid is utilized to inject power into the grid power line to overcome the problem of peak load overvoltage and ancillary services, or used as an uninterrupted power supply during blackouts (Awasthia et al., 2017).

2.4.2. Role of PECs in plug-in electric vehicle

In a PEV, the power from the grid is transferred to the traction motor to propel the vehicle and charge the battery. Alternatively, the energy from the battery is injected into the grid. In both cases, to transfer the energy from one end to the other end, voltage conversion should be done in between the two ends. The rectifier unit is utilized to convert the three-phase or single-phase power to constant DC power to charge the battery through a step-down DC-DC converter (Adams et al., 2018;

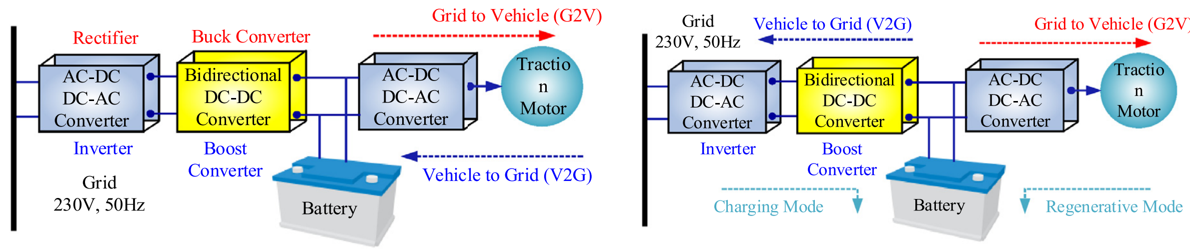

(a) (b)

Fig. 9. PEV (a) Typical structure of PEV, (b) Different operating mode of PEV.

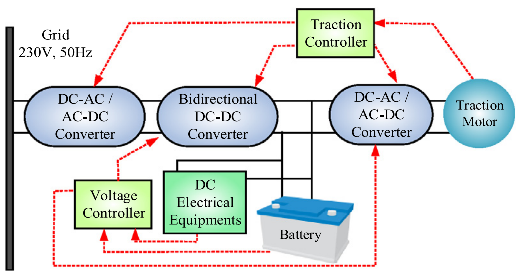

Fig. 10. Control scheme of PEV.

Table 1
Operating Modes of Evs.

Types of Vehicle	Mode of energy flow				
	Fuel	Battery	Split	Combine	Regenerative
BEV		√			√
FCEV	√	√	√	√	√
SHEV		√			√
PHEV	√	√		√	√
SPHEV	√	√	√	√	√
PEV		√			√

Awasthia et al., 2017). For maintain the speed and torque of the traction motor, traction control is adopted. The voltage controller controls the power flow from the battery in/out directions. In PEV, the bidirectional DC-DC converter plays a vital role in controlling the bidirectional flow of energy. It operates in step-up mode during V2G mode and acts as a step-down converter in G2V mode. The operating mode of the bidirectional DC-DC converter is controlled by the voltage controller, as shown in Fig. 10 (Elnozahy & Salama, 2014; Yong, Ramachandaramurthy & Tan, 2015b).

2.5. Summary of electric vehicles

As discussed above, five different operating modes in EVs that describe the flow of power from the battery, fuel cell, or ICE to the vehicle and from the vehicle to the battery or grid are articulated in Table 1. As per the operating modes of EVs, the different types of PECs utilized for specific operations are articulated in Table 2. The bidirectional DC-DC converter is adopted in EVs to allow regenerative braking to charge the battery.

3. Power electronics converters in electric, hybrid and fuel cell vehicle

3.1. Existing power electronics converter in EVs

In EVs, the power from battery/ultra-capacitor, fuel cell or ICE is utilized to drive the vehicle and functions of onboard electrical/electronic load (Amjadi & Williamson, 2010; Cabezuelo, Andreu & Kortabarria, 2017; Chan & Chau, 1997; Elnozahy & Salama, 2014; Emadi, Lee & Rajashekara, 2008; Helsper & Ruger, 2014; Hofmann, Schäfer & Ackva, 2014; Naghizadeh & Williamson, 2013; Onar, Kobayashi & Khaligh, 2013; Rajashekara, 2003). In fuel mode, the voltage from the fuel cell is not sufficient to drive the vehicle. Therefore, it is boosted by the unidirectional boost converter (Jafri & Gupta, 2016). Various electrical/electronic loads are present on the vehicle, which increase the luxurious features and comfort of the vehicle, as shown in Fig. 11.

Some electrical loads require high AC voltage, such as air conditioner and power windows, which receive power from a DC-AC converter. Mirror adjustment and drive seat adjustment work on a DC motor feed from a battery or fuel cell through a DC-DC converter. All these electrical loads operate at different voltage ratings (Adams et al., 2018). The projector lamp requires 42 V for projecting the light, and the interior lamp requires 12 V for its operation. Electronic loads such as sensors, communication systems and tacho-metre require low voltage for their operation. The need of different rated voltage supplies increases as the electrical/electronic load increases on the vehicle, which is not possible from a single battery supply as discussed in previous sections. The number of DC-DC converters increases with increasing different rated loads, which results in a lower efficiency of a single battery structure vehicular system. According to Adams et al. (2018), two types of architecture are adopted in the hybrid automobile system. One is a vehicular system that works on ICE or a fuel cell with a single battery (36 V). Another is the ICE, or fuel cell, which works with a double battery (14 V and 42 V).

The typical structure of the dual battery system is shown in Fig. 12. In the dual battery system (Cabezuelo et al., 2017), dual voltage is generated from a generator in HEV or from the grid in a PEV. The 36 V battery is utilized for mid voltage applications and the 12 V battery for low voltage applications. However, 36 V from the battery is boosted to 42 V for the drive and high voltage applications. The typical electrical system of EVs is shown in Fig. 13. The voltage generated from the generator optimizes to charge the battery with the help of the rectifier and unidirectional DC-DC converter in SHEV and SPHEV, to drive the vehicle in PHEV and FCEV (Elnozahy & Salama, 2014; Yong et al., 2015b). The voltage from the fuel cell and the battery is boosted by the unidirectional and bidirectional DC-DC converters, respectively. The boosted voltage supplies to high voltage DC applications and is converted into the variable frequency and voltage with the help of a three-phase inverter. Advanced EVs can utilize the wasted energy during deceleration and braking to charge the battery. In regenerative braking mode, the three-phase converter works as a three-phase rectifier. The rectified output is converted to the battery voltage with the help of a bidirectional DC-DC converter (Amjadi & Williamson, 2010; Choubey & Lopes, 2017; Chung, Chow & Hui, 2000; Di Napoli, Crescimbini & Solero, 2002; Dobbs & Chapman, March, 2003; Dusmez, Hasanzadeh & Khaligh, 2014; Emadi, 2005; Emadi, Lee & Rajashekara, 2008; Ha, Lee & Hwang, 2012; Khaligh, 2008; Khaligh & Li, 2010; Khan, Ahmed & Husain, 2015; Kuo, Lo & Chiu, 2014; Lulhe & Date, 2015; Ni, Patterson &

Table 2
Utilization of PEC in EVs.

Types of Vehicle		Power Electronics Converters			
		DC-DC converter		Rectifier	Inverter
		Uni-directional	Bi-directional		
BEV			√	√	√
FCEV		√		√	√
HEV	SHEV		√	√	√
	PHEV		√	√	√
	SPHEV		√	√	√
PEV	G2V		√	√	√
	V2G		√	√	√

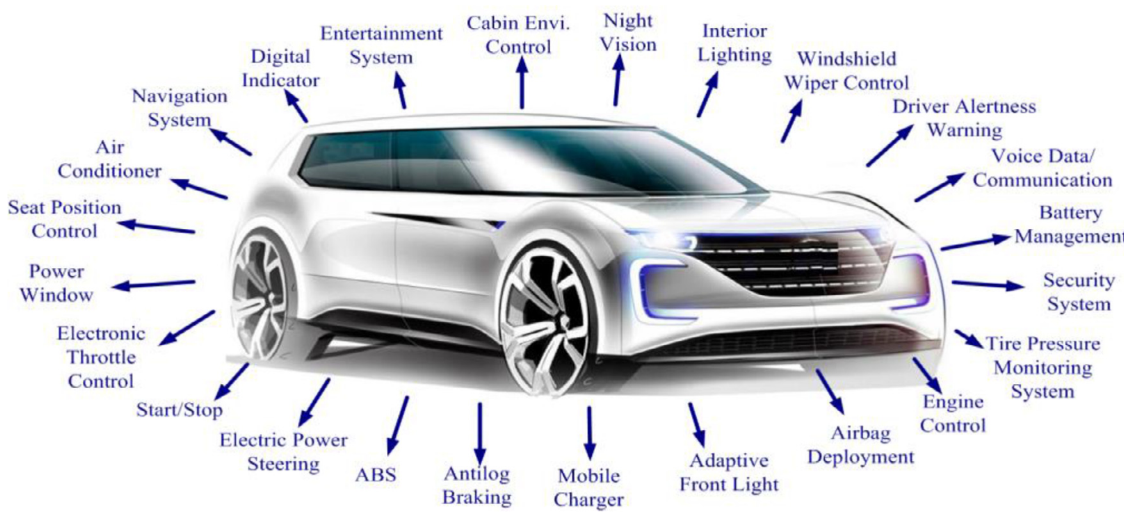

Fig. 11. Electrical appliances of EVs.

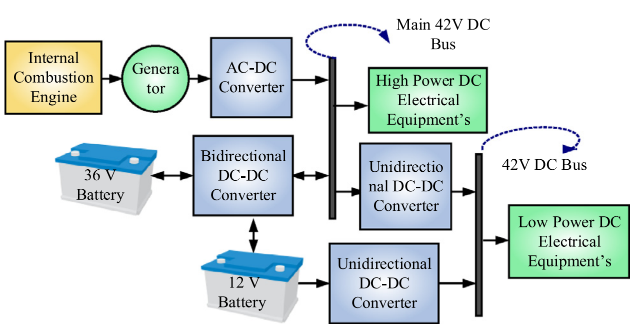

Fig. 12. Dual battery scheme for EVs.

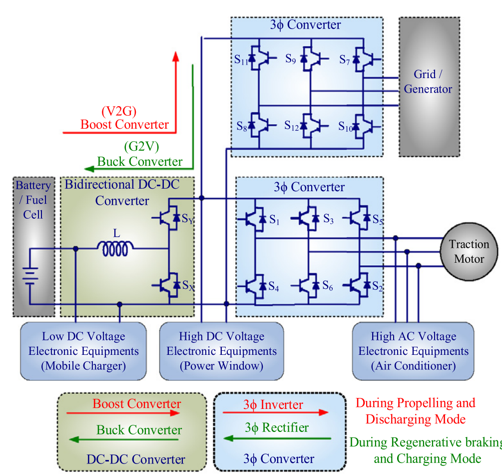

Fig. 13. General electrical structure of EVs.

Hudgins, 2012; Onwuchekwa & Kwasinski, 2011; Waffler & Kolar, 2009; Wu, Lu, Shi & Xing, 2012; Yang, Guan, Zhang, Jiang & Huang, 2018).

In a recent vehicular system, a three-phase converter acts as an inverter during fuel, battery, split and combine mode whereas rectifier in regenerative mode. The selection of converter mode is sophisticated and controlled by the traction controller unit. The traction controller generates the controlled pulses for the three-phase converter according to the received signal from the traction motor and vehicle drivers. The controlled pulse decides the operation of the three-phase converter as an inverter or rectifier. The voltage control unit controls the SOC of the battery at the maximum and minimum level. The voltage controller continuously receives the SOC level signal from the battery and compare it with the reference voltage signal, consistent with this controlled pulse generate for DC-DC converter to maintain the SOC of the battery to increase its lifespan and avoid power wastage.

3.2. Classification of power electronics converters

The general classification of PECs is shown in Fig. 14. As discussed in the previous section, each converter has its own functional/role. In this section, we will discuss the existing non-isolated bidirectional DC-DC converters for EVs. The bidirectional DC-DC converter is a basic conversion unit in EVs. It acts as a boost converter from low voltage to high voltage side direction and a buck converter from high voltage to low voltage side direction.

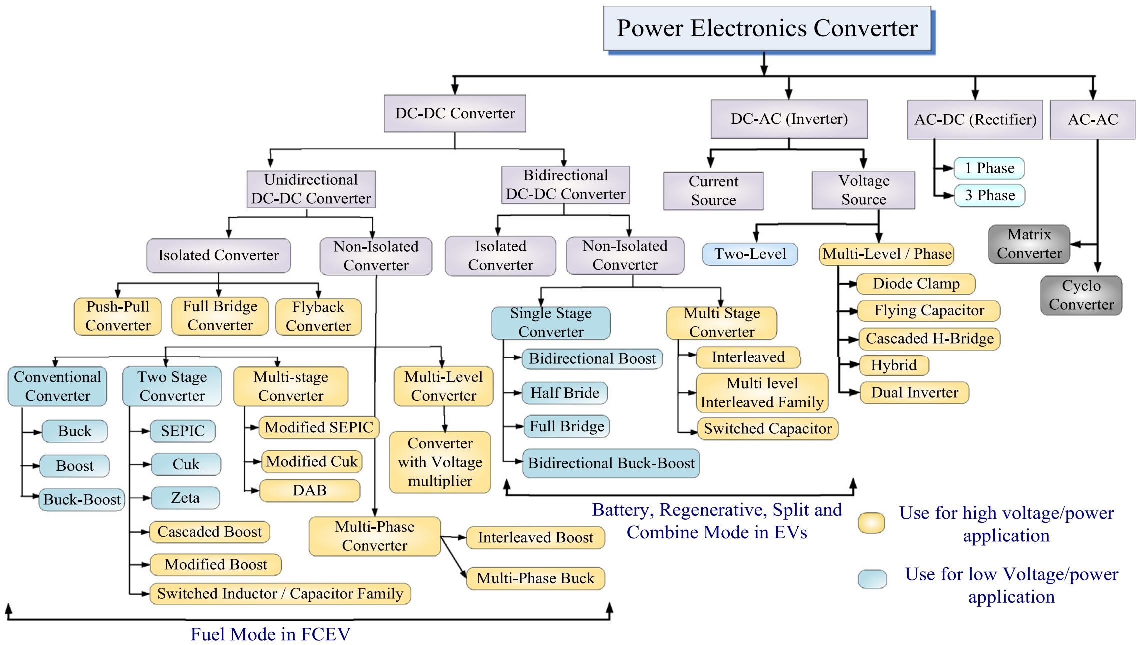

Fig. 14. Classification of Power Electronics Converters.

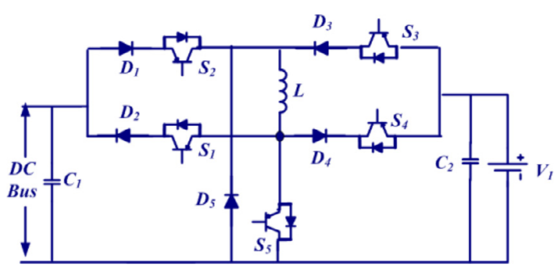

Fig. 15. Universal Bidirectional DC-DC Converter (Onar et al., 2013).

Table 3
Operating Modes of Bidirectional DC-DC Converter.

Direction	Mode	S_1	S_2	S_3	S_4	S_5
V_{DC} to V_1	Boost	ON	OFF	OFF	ON	PWM
V_{DC} to V_1	Buck	PWM	OFF	OFF	ON	OFF
V_1 to V_{DC}	Boost	OFF	ON	ON	OFF	PWM
V_1 to V_{DC}	Buck	OFF	ON	PWM	OFF	OFF

The universal bidirectional DC-DC converter in Onar et al. (2013) is shown in Fig. 15. The converter operates in both buck and boost mode with non-inverting output. The different operating modes are articulated in Table 3. Apart from the universal bidirectional converter, single input, multi-input, multistage, and multiphase non-isolated converters are adopted for bi-directional power flow. Fig. 16(a)–(c) and Fig. 17(a),(b) shows the single input non-isolated bidirectional DC-DC converter. Amjadi and Williamson (2010) Represent the buck-boost bidirectional converter for EV applications, as shown in Fig. 16(a). It works in both modes depending upon the switching pattern. It consists of two active and two passive components with lower electrical and thermal stress. It has the disadvantage of higher ripple current, which damages the battery, and discontinuous output current during boost mode mode, which the size of output capacitors. Fig. 16(b) represents the improved buck-boost converter (Emadi, 2005) where the anti-parallel diode reduces the stress across the power MOSFET and eventually increases the efficiency of conversion. The cascaded bidirectional buck-boost converter (Choubey & Lopes, 2017; Lulhe & Date, 2015; Waffler & Kolar, 2009; Wu et al., 2012) is shown in Fig. 16(c). It can maintain the SOC of the battery and recuperate the braking energy from the electrical motor.

However, it has double the number of active components as compared to the conventional bidirectional buck-boost converter. The bidirectional CUK and SEPIC with Luo converter are shown in Fig. 17(a) and (b), respectively (Amjadi & Williamson, 2010). The converter can operate in both buck and boost mode. The input and output current ripple are reduced in the CUK converter. In SEPIC with a Luo converter, the SEPIC converter works as a boost converter, and the Luo converter works as a buck converter. The disadvantage of SEPIC with the Luo converter is the discontinuous output current.

The numbers of active and passive components in single input non-isolated bidirectional DC-DC converters are articulated in Table 4, where L represents the inductor, C for the capacitor, S for the active switch, and D represents the diode. In addition to the single input topologies, multiple-input topologies are also adopted for bi-directional power flow in EVs. Fig. 18 shows the existing non-isolated bidirectional DC-DC converter with multiple inputs. The input may be the battery, fuel cell, or ultra-capacitor. The response from a fuel cell or ICE to the DC bus is slower as compared to battery (Khan et al., 2015). The battery and ultra-capacitor are utilized to provide the power for DC bus, as shown in Fig. 18(a). By utilization of two sources in one application permits the relatively low voltage from each source and controls the current from multiple inputs. Fig. 18(b) represents the multi-input hybrid conversion topology (Khaligh, 2008; Khan et al., 2015).

The presented topology is capable of diversifying the energy amongst the different energy sources with different voltage-current characteristics. The advantage of the multiple-input bidirectional converters is the least number of components and a positive output voltage without the transformer. The circuit works as a buck, boost, or buck-boost independently. Fig. 18(c) represents a multi-input cascaded boost converter for FCEV. According to Marchesoni and Vacca (2007), the multi-input hybrid boost converter has the advantage of three controlled power devices as compared to conventional boost converter.

The limitation of representing topology is that the voltage sum of two energy sources should be less than a DC link bus. The efficiency is higher if the power of both sources is in the same direction. In Di Napoli et al. (2002); Dusmez et al. (2014); Onwuchekwa and Kwasin-

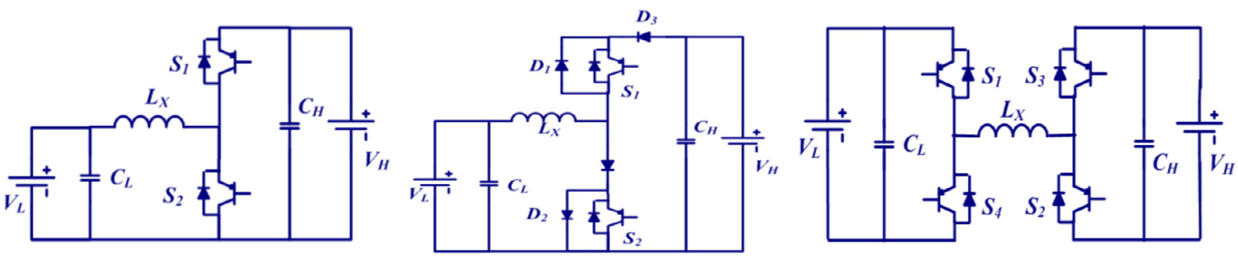

(a) (b) (c)

Fig. 16. Single input non-isolated bidirectional DC-DC Converters (a) buck-boost converter (Amjadi & Williamson, 2010), (b) improved buck-boost Converter (Emadi, 2005), (c) full bridge converter (Waffler & Kolar, 2009).

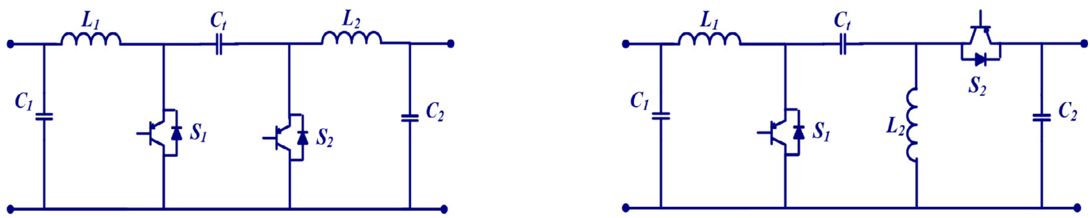

(a) (b)

Fig. 17. Single input non-isolated bidirectional DC-DC Converters (a) bidirectional CUK converter (Amjadi & Williamson, 2010) and (b) bidirectional SEPIC with Luo converter (Z. Amjadi & Williamson, 2010).

Table 4
The number of components in Single Input converters.

Converter	Passive Components		Active Components	
	L	C	S	D
Conventional Buck-boost Amjadi and Williamson (2010)	1	2	2	0
Improved Buck-boost Emadi (2005)	1	2	2	4
Cascaded Buck-boost Waffler and Kolar (2009)	1	2	4	0
CUK (Amjadi and Williamson (2010)	2	3	2	0
SEPIC with Luo Amjadi and Williamson (2010)	2	3	2	0

Table 5
Number of components in Multiple Input converters.

Converter	Passive Components		Active Components	
	L	C	S	D
Multi input Buck-boost Khan et al. (2015)	2	0	4	0
Multi input boost Khaligh (2008)	2	1	3	0
Multi input converter Marchesoni and Vacca (2007)	1	0	3	0
MI-PEC Di Napoli et al. (2002)	2	3	4	0

ski (2011) MI-PEC represents for the EV application shown in Fig. 18(d) in which VH represents DC power from different energy sources to the DC bus and operates in step-down mode to transfer power from the DC bus to the bus voltage. The MI-PEC works in step-up mode to transfer charge to the battery or ultra-capacitor. In Table 5, the number of components of multi-input non-isolated bidirectional DC-DC converters is articulated. As the number of active and passive components increases, it affects the efficiency of conversion. In Table 5, L represents the inductor, C represents the capacitor, S represents the active switch, and D represents the diode. Fig. 19 shows the multiphase non-isolated bidirectional DC-DC converters for EVs applications. Fig. 19(a) represents the three-phase interleaved boost converter (Khaligh & Li, 2010; Yang et al., 2018). The multiphase converter overcomes the drawbacks of the conventional bidirectional DC-DC converter by reducing the input-output current ripples. Several phases increase the ripple content in the current decreases, but eventually, it decreases the efficiency by increasing the number of active and passive components per phase. Fig. 19(b) shows the different structures of the interleaved boost converter (Ni et al., 2012). Several phases increase, the size of the input and output filter decreases. The represented topology has a greater number of active and passive components as compared to the topology shown in Fig. 19(a).

Fig. 20 shows the Switched Capacitor (SC) structure topologies for EVs. In Amjadi and Williamson (2010); Chung et al. (2000); Ni et al. (2012), SC topology was explained, and the structure is shown in Fig. 20(a). The SC structure offers the features of step-up, step-down, and both for bidirectional flow of power. The topology works in two modes, A and B. The efficiency of the represented topology is 85% in mode-A and 80% in mode-B. Fig. 20(b) and (c) show zero current switchings switched capacitor quasi-resonant converter with single-level and two-level configurations, respectively (Lee & Chiu, 2005). The configuration improves the problem of current stress during the bidirectional flow using SC structure and one inductor. With the help of L and C, the converter achieves zero switching currents and reduces the losses. The semiconductor device MOSFET is turned ON and OFF in a zero current

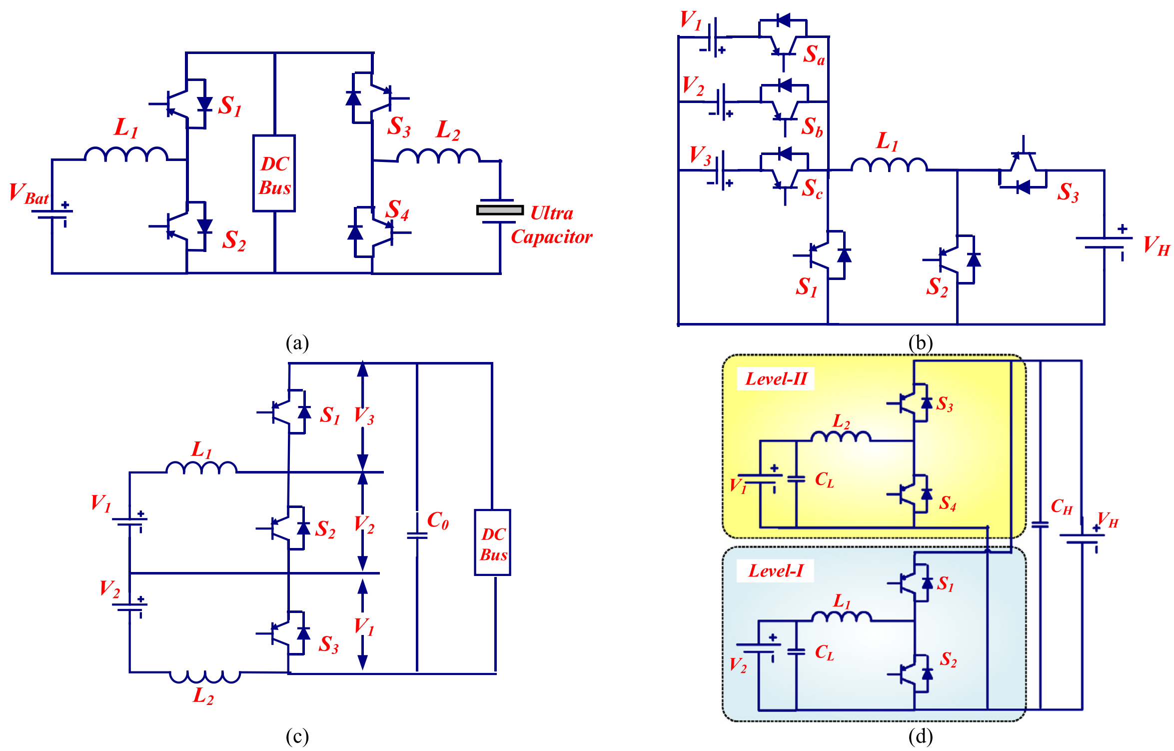

Fig. 18. Multiple input non-isolated bidirectional DC-DC converters (a) Multi input buck-boost converter (Khan et al., 2015), (b) Multi input converter (Khaligh, 2008), (c) multi input cascaded boost converter (Marchesoni & Vacca, 2007) and (d) MI-PEC (Di Napoli et al., 2002) .

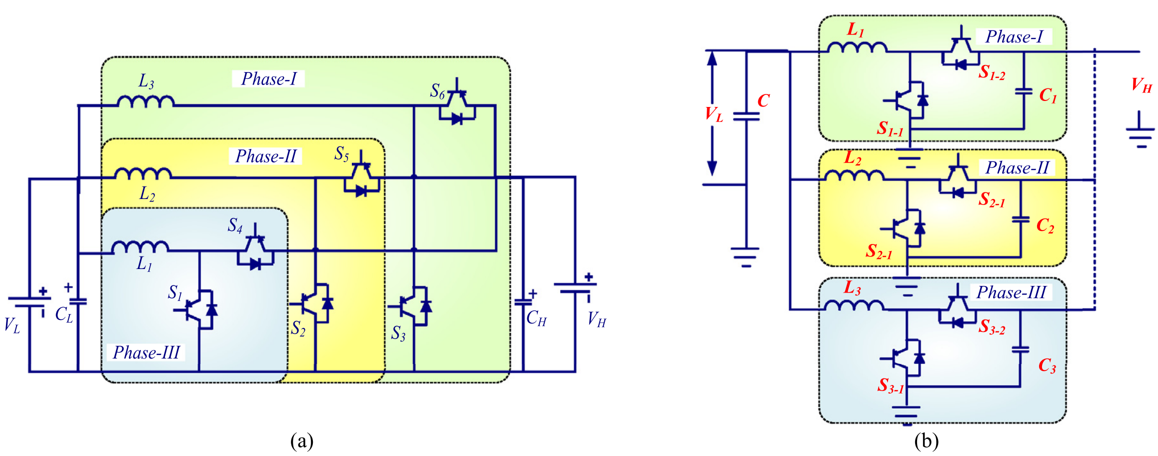

Fig. 19. Multiphase non-isolated bidirectional DC-DC converters (a) Multiphase interleaved boost converter (Yang et al., 2018), (b) 16 Phase IBC (Ni et al., 2012).

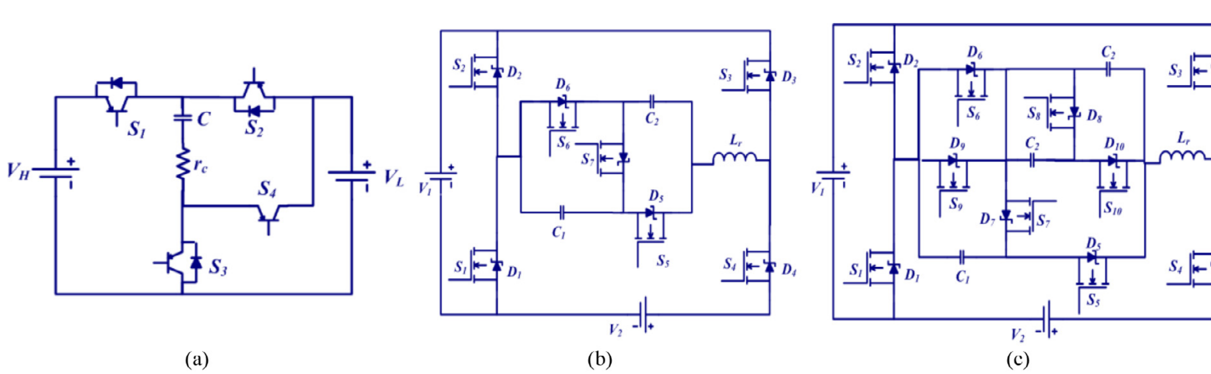

Fig. 20. Switched Capacitor Topologies (a) Switched bidirectional converter (Amjadi & Williamson, 2010) (b) zero current switching switched capacitor quasi resonant converter with single level (Lee & Chiu, 2005) (c) zero current switching switched capacitor quasi resonant converter with two level (Lee & Chiu, 2005).

state, which reduces the EMI problem. The converter gives 93% efficiency. The number of switched-capacitor stages increases to achieve a higher voltage conversion ratio.

4. Challenges in power electronics vehicular system

4.1. Improve efficiency

Firstly, in EVs, mechanical and hydraulic shaft are replaced by an electric motor for propelling operation. In HEV, selecting the perfect combination of ICE and fuel cell or battery in the proper way helps to
improve the efficiency. In the battery or fuel mode, PECs play a significant role to improve efficiency by selecting a proper power converter. The selection of PECs, switching strategies of converters, system integration and packing of individual units are essential to achieve the goal of power electronics in the vehicular system. The converters are selected according to the load demand and input supply. The efficiency of PEC depends on the number of components, control strategies, and EMI effects.

4.2. Increase the durability of EVs

The durability of EVs depends on the life of the electrical unit present in EVs. The durability of the battery increases by continuously maintaining the charging and discharging level with the help of the voltage controller. The life span of PEC depends on semiconductor devices. The converter should need to be withstood for high vibration and thermal condition at extreme condition. The challenges lie in selecting the proper converter with high efficiency, rigidness, low cost, and small size.

4.3. Increase the performance of EVs

Fast and high-power industrial motion control is a demanding trend in the modern automobile system. The PE technique is combined with Digital Signal Processing (DSP) to achieve the high performance of EVs.

4.4. Increase the luxurious feature

Today's advanced EVs are more focused on making high comfort EVs. Some high comfort applications are shown in Fig. 20. Each application requires a different voltage rating to work. The multistage or multi-output DC-DC converter provide different ratings power supply for DC appliances. The AC load receives power from the three-phase inverter.

4.5. Increase the safety in EVs

Apart from power conversion and propelling control, monitoring the condition of the traction motor to detect any failure like stator, rotor, and bearing faults are essential. In advance EVs, ABS and airbags require high power actuators. The PEC with DSP technique can increase the safety features in EVs in the future.

4.6. Decrease the overall cost of EVs

The number of power conversion unit and component uses, decide the cost of the vehicular electrical system in EVs. As the luxurious load increases on the vehicle, it is responsible for demanding a higher number of PEC. The challenge is to reduce the cost of the vehicle by selecting a smaller number of power conversion units for a more significant number of luxurious loads.

5. Conclusion

A state-of-the-art review of the current status and opportunities of PECs in electric, hybrid, and fuel cell vehicles is presented. This paper summarized the impact of PECs on cost, efficiency, and performance of EVs. From the review of EVs, the SPHEV has the perfect combination of two energy sources for propelling and other functions. With the advancement in the vehicular electrical system, the demand for different ratings of supply increases, which is not fulfilled by one battery or two battery structure. The bidirectional DC-DC converter plays a vital role in the power conversion process of EVs. The existing non-isolated bidirectional DC-DC converter topologies are discussed with a comprehensive review and comparison along with the advantages and disadvantages of PEC in the present vehicular system in detail. Finally, the paper explains the various challenges for PECs to improve efficiency, durability, performance, and cost reduction.

References

Adams, S., Klobodu, E. K. M., & Apio, A. (2018). Renewable and non-renewable energy, regime type and economic growth. *Renewable Energy, 125*, 755–767 Sep..

Afonso, T. L., Marques, A. C., & Fuinhas, J. A. (2017). Strategies to make renewable energy sources compatible with economic growth. *Energy Strategy Reviews, 18*, 121–126 Dec..

Akbarian, H., Pillay, P., & Lopes, L. (2015). Design of a power electronic emulator for series hybrid electric vehicle powertrains. In *Proceedings of the IEEE vehicle power and propulsion conference (VPPC)* (pp. 1–5).

Amjadi, Z., & Williamson, S. S. (2010a). Power-electronics-based solutions for plug-in hybrid electric vehicle energy storage and management systems. *IEEE Transactions on Industrial Electronics, 57*(2), 608–616 Feb..

Amjadi, Z., & Williamson, S. S. (2010b). A novel control technique for a switched-capacitor-converter-based hybrid electric vehicle energy storage system. *IEEE Transactions on Industrial Electronics, 57*(3), 926–934 Marc. 10.1109/TIE.2009.2032196.

Awasthia, A., Karthikeyan, V., Sanjeevikumar, P., Rajasekar, S., Blaabjerg, F., & Singh, A. K. (2017). Optimal planning of electric vehicle charging station at the distribution system using hybrid optimization algorithm. *Energy Journal, Elsevier Journal Publications, 133*, 70–78 August.

Baha, M. A. A., & Thomas, H. B. (2013). Review of hybrid, plug-in hybrid, and electric vehicle market modeling Studies. *Renewable and Sustainable Energy Reviews, 21*, 190–203 MaPages.

Bayindi, K. C., Gozukucuk, M. A., & Teke, A. (2011). A comprehensive overview of hybrid electric vehicle: Powertrain configurations, powertrain control techniques and electronic control units. *Energy Conversion and Management, 52*(2), 1305–1313 Issue-FebruarPages.

Bhaskar, M. S., Ben-Brahim, L., Iqbal, A., Padmanaban, S., Meraj, M., & Rahman, S. (2019a). Hardware implementation of a new single input double output L-l converter for high voltage auxiliary loads in fuel-cell vehicles. In *IEEE applied power electronics conference and exposition (APEC)* (pp. 1595–1600). Mar..

Bhaskar, M. S., Padmanaban, S., & Holm-Nielsen, J. B. (2019b). Double stage double output dc–dc converters for high voltage loads in fuel cell vehicles,". *Energies, 12*(19) Art. no. 19, Jan.

Bhaskar, M. S., Padmanaban, S., Iqbal, A., Meraj, M., Howeldar, A., & Kamuruzzaman, J. (2018). L-L Converter for fuel cell vehicular power train applications: hardware implementation of primary member of X-Y converter family. In *Proceedings of the IEEE international conference on power electronics, drives and energy systems (PEDES)* (pp. 1–6). Dec..

Bhaskar, M. S., Sanjeevikumar, P., Holm-Nielsen, J. B., Pedersen, J. K., & Leonowicz, Z. (2019c). 2L-2L converter: Switched inductor based high voltage step-up converter for fuel cell vehicular applications. In *Proceedings of the IEEE international conference on environment and electrical engineering and IEEE Industrial and Commercial Power Systems Europe* (pp. 1–6). 11-14 Jun..

Cabezuelo, D., Andreu, J., Kortabarria, I., et al. (2017). Powertrain systems of electric, hybrid and fuel-cell vehicles: State of the technology. In *Proceedings of the IEEE 26th international symposium on industrial electronics (ISIE)* (pp. 1445–1450).

Cassani, P. A., & Williamson, S. S. (2009). Feasibility analysis of a novel cell equalizer topology for plug-in hybrid electric vehicle energy-storage systems. *IEEE Transactions on Vehicular Technology, 58*(8), 3938–3946 Oct..

Chan, C. C. (2002). The state of the art of electric and hybrid vehicles. In *Proceedings of the IEEE: 90* (pp. 247–275). Feb.

Chan, C. C., & Chau, K. T. (1997). An overview of power electronics in electric vehicles. *IEEE Transactions on Industrial Electronics, 44*(1), 3–13.

Chiu, H. J., & Lin, L. W. (2006). A bidirectional DC-DC converter for fuel cell electric vehicle driving system. *IEEE Transaction on Power Electronics, 21*(4), 950–958 july.

Choubey, A., & Lopes, L. A. C. (2017). A tri-state 4-switch bi-directional converter for interfacing supercapacitors to DC micro-grids. In *Proceedings of the IEEE 8th international symposium on power electronics for distributed generation systems (PEDG)* (pp. 1–6).

Chung, H. S. H., Chow, W. C., Hui, S. Y. R., et al. (2000). Development of a switched-capacitor DC-DC converter with bidirectional power flow. *IEEE Transactions on Circuits and Systems I: Fundamental Theory and Applications, 47*(9), 1383–1389 Se.

Daramy-Williams, E., Anable, J., & Grant-Muller, S. (2019). A systematic review of the evidence on plug-in electric vehicle user experience. *Transportation Research Part D: Transport and Environment, 71*, 22–36 Jun..

Das, H. S., Tan, C. W., & Yatim, A. H. M. (2017). Fuel cell hybrid electric vehicles: A review on power conditioning units and topologies. *Renewable and Sustainable Energy Reviews, 76*, 268–291.

Daya, F. J. L., Sanjeevikumar, P., Blaabjerg, F., Wheeler, P. W., Ojo, J., & Ertas, A. H. (2016). Analysis of wavelet controller for robustness in electronic differential of electric vehicles: An investigation and numerical developments". *Electric Power Components and Systems, 44*(7), 763–773.

Desai, C., & Williamson, S. S. (2009). Optimal design of a parallel hybrid electric vehicle using multi-objective genetic algorithms. In *Proceedings of the IEEE vehicle power and propulsion conference* (pp. 871–876).

Di Napoli, A., Crescimbini, F., Solero, L., et al. (2002). Multiple-input DC-DC power converter for power-flow management in hybrid vehicles. In *Proceedings of the conference record of the IEEE industry applications conference. 37th IAS Annual Meeting (Cat. No.02CH37344): 3* (pp. 1578–1585).

Dobbs, B. G., & Chapman, P. L. (2003, March). A multiple-input DC-DC converter topology. *IEEE Power Electronics Letters, 1*(1), 6–9.

Dusmez, S., Hasanzadeh, A., & Khaligh, A. (2014). Loss analysis of non-isolated bidirectional DC/DC converters for hybrid energy storage system in EVs. In *Proceedings of the IEEE 23rd international symposium on industrial electronics (ISIE)* (pp. 543–549).

Ehsani, M., Gao, Y., Gay, S. E., et al. (2005). *Modern electric, hybrid electric, and fuel cell Vehicles- Fundamentals, theory, and design*. CRC Press LLC.

Elnozahy, M. S., & Salama, . M. (2014). 'A comprehensive study of the impacts of PHEVs on residential distribution networks. *IEEE Transactions on Sustainable Energy, 5*, 332–342.

Emadi, A.: (2005). 'Handbook of automotive power electronics and motor drives'. (1st ed.). New York: Taylor & Francis.

Emadi, A., Lee, Y. J., & Rajashekara, K. (2008). Power electronics and motor drives in electric, hybrid electric, and plug-in hybrid electric vehicles. *IEEE Transactions on Industrial Electronics, 55*(6), 2237–2245.

Emadi, A., Lee, Y. J., & Rajashekara, K. (2008). Power electronics and motor drives in electric, hybrid electric, and plug-in hybrid electric vehicles. *IEEE Transactions on Industrial Electronics, 55*(6), 2237–2245 Jun..

Emadi, A., Rajashekara, K., Williamson, S. S., & Lukic, S. M. (2005). Topological overview of hybrid electric and fuel cell vehicular power system architectures and configurations. *IEEE Transactions on Vehicular Technology, 54*(3), 763–770 May.

Ga, Y., Ehsani, M., & Miller, J. M. (2005). Hybrid electric vehicle: Overview and state of the art. In *Proceedings of the IEEE international symposium on industrial electronics* (pp. 307–316). ISIE 2005.

Gielen, D., Boshell, F., Saygin, D., Bazilian, M. D., Wagner, N., & Gorini, R. (2019). The role of renewable energy in the global energy transformation. *Energy Strategy Reviews, 24*, 38–50 Apr..

Gough, B., Rowley, P., & Walsh, C. (2014). What impact will the journey patterns of electric vehicles have on their capability to provide ancillary services? In *Proceedings of the 5th IET hybrid and electric vehicles conference (HEVC 2014)* (pp. 1–5).

Grunditz, E. A., & Thiringer, T. (2016). Performance analysis of current bevs based on a comprehensive review of specifications. *IEEE Transactions on Transportation Electrification, 2*(3), 270–289 Sept..

Gruosso, G. (2014). Optimization and management of energy power flow in hybrid electrical vehicles. In *Proceedings of the 5th IET hybrid and electric vehicles conference (HEVC 2014)* (pp. 1–5).

Guo, S., Liu, Q., Sun, J., & Jin, H. (2018). A review on the utilization of hybrid renewable energy. *Renewable and Sustainable Energy Reviews, 91*, 1121–1147 Aug..

Gurkaynak, Y., Khaligh, A., & Emadi, A. (2009). State of the art power management algorithms for hybrid electric vehicles. In *Proceedings of the IEEE vehicle power and propulsion conference*.

Ha, S. P., Lee, J. H., Hwang, J. P., et al. (2012). Two phase interleaved bidirectional DC-DC converter for electric vehicle using variable DC-link voltage. In *Proceedings of the IEEE vehicle power and propulsion conference* (pp. 748–752). pp..

Hegazy, O., Barrero, R., Van Mierlo, J., et al. (2013). An advanced power electronics interface for electric vehicles applications. *IEEE Transactions on Power Electronics, 28*(12), 5508–5521 Dec.

Helsper, M., & Ruger, N. (2014). Requirements of hybrid and electric buses – A huge challenge for power electronics. In *Proceedings of the 16th European conference on power electronics and applications*.

Hofmann, M., Schäfer, M., & Ackva, A. (2014). Bi-directional charging system for electric vehicles: A V2G concept for charging and discharging electric vehicles. In *Proceedings of the 4th international electric drives production conference (EDPC)* (pp. 1–5).

Ida, T., Murakami, K., & Tanaka, M. (2014). A stated preference analysis of smart meters, photovoltaic generation, and electric vehicles in Japan: Implications for penetration and GHG reduction. *Energy Research & Social Science, 2*, 75–89 Jun..

Jafri, N. H., & Gupta, S. (2016). An overview of fuel cells application in transportation. In *Proceedings of the IEEE transportation electrification conference and expo*.

Jenniches, S. (2018). Assessing the regional economic impacts of renewable energy sources – A literature review. *Renewable and Sustainable Energy Reviews, 93*, 35–51 Oct..

Khaligh, A. (2008). A multiple-input dc-dc positive buck-boost converter topology. In *Proceedings of the Twenty-third annual IEEE applied power electronics conference and exposition* (pp. 1522–1526). 10.1109/APEC.2008.4522926.

Khaligh, A., & Dusmez, S. (2012). Comprehensive topological analysis of conductive and inductive charging solutions for plug-in electric vehicles. *IEEE Transactions on Vehicular Technology, 61*(8), 3475–3489 Oct..

Khaligh, A., & Li, Z. (2010). Battery, ultracapacitor, fuel cell, and hybrid energy storage systems for electric, hybrid electric, fuel cell, and plug-in hybrid electric vehicles: State of the Art. *IEEE Transactions on Vehicular Technology, 59*(6), 2806–2814 July.

Khan, M. A., Ahmed, A., Husain, I., et al. (2015). Performance analysis of bidirectional DC–DC converters for electric vehicles. *IEEE Transactions on Industry Applications, 51*(4), 3442–3452 July-Aug.

Kim, H., & Kum, D. (2016). Comprehensive design methodology of input- and output-split hybrid electric vehicles: In search of optimal configuration. *IEEE/ASME Transactions on Mechatronics, 21*(6), 2912–2923 Dec..

Krishna, M., Daya, F., Sanjeevikumar, P., & Mihet-Popa, L. (2017). Real-time analysis of a modified state observer for sensorless induction motor drive used in electric vehicle applications. *Energies, MDPI, Open Access Journal, 10*(8), 1–23 pagesJuly.

Ku, S. W., Lo, Y. K., Chiu, H. J., et al. (2014). 'A high-performance bidirectional DC-DC converter for DC micro-grid system application. In *Proceedings of the international power electronics conference (IPEC-Hiroshima 2014 - ECCE ASIA)* (pp. 3185–3189).

Lai, J. S., & Nelson, D. J. (2007). Energy management power converters in hybrid electric and fuel cell vehicles. In *Proceedings of the IEEE: 95* (pp. 766–777). Apr..

Lane, B. W., Dumortier, J., Carley, S., Siddiki, S., Clark-Sutton, K., & Graham, J. D. (2018). All plug-in electric vehicles are not the same: Predictors of preference for a plug-in hybrid versus a battery-electric vehicle. *Transportation Research Part D: Transport and Environment, 65*, 1–13 Dec..

Lee, Y. S., & Chiu, Y. Y. (2005). Zero-current-switching switched-capacitor bidirectional DC-DC converter. In *Proceedings of the IEE electric power applications: 152* (pp. 1525–1530). 4 Nov..

Li, J., Yu, X., & Ding, H. (2010). Ping Sun: Design and control of the propulsion for a series hybrid electric vehicle. In *Proceedings of the 8th world congress on intelligent control and automation*.

Li, S. G., Sharkh, S. M., Walsh, F. C., et al. (2011). Energy and battery management of a plug-in series hybrid electric vehicle using fuzzy logic. *IEEE Transactions on Vehicular Technology, 60*(8), 3571–3585 Oct.

Li, X., Lopes, L. A. C., & Williamson, S. S. (2009). On the suitability of plug-in hybrid electric vehicle (PHEV) charging infrastructures based on wind and solar energy. In *Proceedings of the IEEE power & energy society general meeting*.

Li, X., & Williamson, S. S. (2007). Comparative investigation of series and parallel hybrid electric vehicle (HEV) efficiencies based on comprehensive parametric analysis. In *Proceedings of the IEEE vehicle power and propulsion conference*.

Li, Z., Khajepour, A., & Song, J. (2019). A comprehensive review of the key technologies for pure electric vehicles. *Energy, 182*, 824–839 Sep..

Lulhe, A. M., & Date, T. N. (2015). 'A technology review paper for drives used in electrical vehicle (EV) & hybrid electrical vehicles (HEV). In *roceedings of the international conference on control, instrumentation, communication and computational technologies (ICCICCT)* (pp. 632–636).

Marchesoni, M., & Vacca, C. (2007). New DC-DC converter for energy storage system interfacing in fuel cell hybrid electric vehicles. *IEEE Transactions on Power Electronics, 22*(1), 301–308 Jan..

Miller, J. F., Webster, C. E., Tummillo, A. F., et al. (1997). Testing and evaluation of batteries for a fuel cell powered hybrid bus. In *Proceedings of the energy conversion engineering conference: 2* (pp. 894–898). 27 July–1 Augus.

Mukherjee, J. C., & Gupta, A. (2015). A review of charge scheduling of electric vehicles in smart grid. *IEEE Systems Journal, 9*(4), 1541–1553 Dec..

Musavi, F., Craciun, M., Gautam, D. S., et al. (2014). Control strategies for wide output voltage range LLC resonant DC–DC converters in battery chargers. *IEEE Transactions on Vehicular Technology, 63*(3), 1117–1125 Marc.

Mwasil, F., Justo, J. J., Kim, E. K., et al. (2014). Electric vehicles and smart grid interaction: A review on vehicle to grid and renewable energy sources integration. *Renewable and Sustainable Energy Reviews Volume, 34*, 501–516 Jun.

Naghizadeh, N., & Williamson, S. S. (2013). A comprehensive review of power electronic converter topologies to integrate photovoltaics (PV), AC grid, and electric vehicles. In *Proceedings of the IEEE Transportation Electrification Conference and Expo (ITEC)* (pp. 1–6).

Nayanatara, C., Shanmugapriya, P., Gurusivakumar, G., et al. (2014). 'Design & development of series hybrid electric vehicle. In *Proceedings of the international conference on computation of power, energy, information and communication (ICCPEIC)* (pp. 114–117).

Ni, L., Patterson, D. J., & Hudgins, J. L. (2012). High power current sensorless bidirectional 16-phase interleaved DC-DC converter for hybrid vehicle application. *IEEE Transactions on Power Electronics, 27*(3), 1141–1151 March.

Olson, J. B., & Sexton, E. D. (2000). 'Operation of lead–acid batteries for HEV applications. In *Proceedings of the 15th battery conference on applications and advances* (pp. 205–210). 11–14 Januar.

Onar, O. C., Kobayashi, J., & Khaligh, A. (2013). A fully directional universal power electronic interface for EV, HEV, and PHEV applications. *IEEE Transactions on Power Electronics, 28*(12), 5489–5498 Dec..

Onwuchekwa, C. N., & Kwasinski, A. (2011). Analysis of boundary control for a multiple-input DC-DC converter topology. In *Proceedings of the 26th annual IEEE applied power electronics conference and exposition (APEC)* (pp. 1232–1237).

Parag Jose, C., & Meikandasivam, S. (2016). A review on the trends and developments in hybrid electric vehicles. In *Lecture notes in mechanical engineering* (pp. 211–229). Singapore: Springer.

Querini, F., Dagostino, S., Morel, S., & Rousseaux, P. (2012). Greenhouse gas emissions of electric vehicles associated with wind and photovoltaic electricity. *Energy Procedia, 20*, 391–401.

Rajashekara, K. (2003). 42V architecture of automobiles. In *Proceedings of the electrical manufacturing & coil winding expo* Sep..

Razavian, R., Azad, N. L., & McPhee, J. (2012). On real-time optimal control of a series hybrid electric vehicle with an ultra-capacitor. In *Proceedings of the american control conference (ACC)* (pp. 547–552).

Roche, M., Shabbir, W., & S, A. (2017). Evangelou: 'Voltage control for enhanced power electronic efficiency in series hybrid electric vehicles. *IEEE Transactions on Vehicular Technology, 66*(5), 3645–3658 May.

Rodatz, P., Garcia, O., Guzzella, L., et al. (2003). Performance and operational characteristics of a hybrid vehicle powered by fuel cells and supercapacitors. In *Proceedings of the SAE world congress and exhibition: 112* (pp. 692–703). 3 Marc.

Schaltz, E. (2010). *Design of a fuel cell hybrid electric vehicle drive system*. Aalborg, Denmark: The Department of Energy Technology, Aalborg University Ph.D. dissertation.

Schaltz, E., Khaligh, A., & Rasmussen, P. O. (2009). Influence of battery/ultracapacitor energy-storage sizing on battery lifetime in a fuel cell hybrid electric vehicle. *IEEE Transactions on Vehicular Technology, 58*(8), 3882–3891 Oct..

Shareef, H., Islam, M. M., & Mohamed, A. (2016). A review of the stage-of-the-art charging technologies, placement methodologies, and impacts of electric vehicles. *Renewable and Sustainable Energy Reviews, 64*, 403–420 Oct..

Subramaniam, U., Ganesan, S., Bhaskar, M. S., Padmanaban, S., Blaabjerg, F., & Almakhles, D. J. (2019). Investigations of AC microgrid energy management systems using distributed energy resources and plug-in electric vehicles. *Energies, 12*(14) Art. no. 14, Jan.

Tahami, F., Kazemi, R., & Farhanghi, S. (2003). A novel driver assist stability system for all-wheel-drive electric vehicles. *IEEE Transactions on Vehicular Technology, 52*(3), 683–692 May.

Tazelaar, E., Veenhuizen, B., Jagerman, J., et al. (2013). Energy management strategies for fuel cell hybrid vehicles; an overview. *2013 World Electric Vehicle Symposium and Exhibition (EV S27)*.

Thomas, C. E. (2009). 'Fuel cell and battery electric vehicles compared. *International Journal of Hydrogen Energy, 34*, 6005–6020.

Un-Noor, F., Padmanaban, S., Mihet-Popa, L., Mollah, M. N., & Hossain, E. (2017). A comprehensive study of key electric vehicle (EV) components, technologies, challenges, impacts, and future direction of development. *Energie, 10*, 1217.

Waffler, S., & Kolar, J. W. (2009). A novel low-loss modulation strategy for high-power bidirectional buck-boost converters. *IEEE Transactions on Power Electronics, 24*(6), 1589–1599 June.

Williamson, S. S. (2007). Electric drive train efficiency analysis based on varied energy storage system usage for plug-in hybrid electric vehicle applications. In *Proceedings of the IEEE power electronics specialists conference*.

Williamson, S. S., Rathore, A. K., & Musavi, F. (2015, May). Industrial electronics for electric transportation: Current state-of-the-art and future challenges. *IEEE Transactions on Industrial Electronics, 62*(5), 3021–3032.

Wu, H., Lu, J., Shi, W., & Xing, Y. (2012). Nonisolated bidirectional DC–DC converters with negative-coupled inductor. *IEEE Transactions on Power Electronics, 27*(5), 2231–2235 May.

Wu, Y., & Gao, H. (2006). Optimization of fuel cell and super capacitor for fuel cell electric vehicles. *IEEE Transactions on Vehicular Technology, 55*(6), 1748–1755 Nov..

Yang, Y., Guan, T., Zhang, S., Jiang, W., & Huang, W. (2018). More symmetric four-phase inverse coupled inductor for low current ripples & high-efficiency interleaved bidirectional buck/boost converter. *IEEE Transactions on Power Electronics, 33*(3), 1952–1966 March.

Yong, J. Y., Ramachandaramurthy, V. K., Tan, K. M., et al. (2015a). A review on the state-of-the-art technologies of electric vehicle, its impacts and prospects. *Renewable and Sustainable Energy Reviews, 49*, 365–385 Sep.

Yong, J. Y., Ramachandaramurthy, V. K., Tan, K. M., et al. (2015b). Bi-directional electric vehicle fast charging station with novel reactive power compensation for voltage regulation. *International Journal of Electrical Power & Energy Systems, 64*, 300–310.

Zhan, P., & Williamson, S. S. (2008). Recent status and future prospects of integrated starter-generator based hybrid electric vehicles. In *Proceedings of the IEEE vehicle power and propulsion conference* (pp. 1–8).

Zhao, Y., He, X., Yao, Y., & Huang, J. (2019). Plug-in electric vehicle charging management via a distributed neurodynamic algorithm. *Applied Soft Computing, 80*, 557–566 Jul..

Zhou, W., Yang, L., Cai, Y., & Ying, T. (2018). Dynamic programming for new energy vehicles based on their work modes part I: Electric vehicles and hybrid electric vehicles. *Journal of Power Sources, 406*, 151–166 Dec..

Harmonic compensators and Optimal design of controllers for three-level cascaded control in stationary reference frame for grid-supporting inverters-based AC microgrid

Pranay Rout, *Department of Electrical Engineering , NM Institute of Engineering & Technology, Bhubaneswar, pranayrout93@gmail.com*

Laxminarayan Mishra, *Department of Electrical and Electronics Engineering, Capital Engineering College, Bhubaneswar, laxminarayan.s@gmail.com*

Debasish Mishra, *Department of Electrical Engineering, Aryan Institute of Engineering & Technology, Bhubaneswar, debasishmishra1@gmail.com*

Swadesh Ranjan Jena, *Department of Electrical and Electronics Engineering, Raajdhani Engineering College, Bhubaneswar, swadesh.jena@yahoo.co.in*

Keywords:
Hierarchical control
Harmonic compensators
Microgrids
Optimization techniques
Power quality
Proportional-resonant controller

A B S T R A C T

In this paper, new optimal procedures are introduced to design the finest controllers and harmonic compensators (HCs) of three-level cascaded control for three-phase grid-supporting inverters based-AC microgrid. The three control levels, comprising primary, secondary and synchronization control levels, are developed in stationary $\alpha\beta$-frame and based on the proportional–integral (PI) controllers and the proportional-resonant controllers along with additional HCs. The new optimal design guidelines of microgrid's controllers and HCs are aimed to fulfill the study requirements. The optimization objectives and constraints are employed to minimize both the total harmonic distortion (THD) and individual harmonics of microgrid's voltage to enhance the quality of microgrid's output power. The THD of microgrid's voltage can be reduced to 0.19% under the nonlinear loads. Moreover, the microgrid's voltage and frequency can be perfectly regulated with zero deviations. Furthermore, these new optimal procedures accelerate the speed of synchronization process between the external power grid and the microgrid to be accomplished in time less than 20 ms. Additionally, an accurate power-sharing among paralleled operated inverters can be achieved to avoid overstressing on any one. Also, seamless transitions can be guaranteed between grid-tied and isolated operation mode. The optimal controllers and HCs are designed by a new optimization algorithm called H-HHOPSO, which is created by hybridizing between Harris hawks optimization and particle swarm optimization algorithms. The effectiveness and robustness of the H-HHOPSO-based controllers and HCs are compared with other meta-heuristic optimization algorithms-based controllers and HCs. A microgrid, including two grid-supporting inverters based optimal controllers and optimal HCs, are modeled and carried out using MATLAB/SIMULINK to test the performance under linear and nonlinear loads, and also during the interruption of any one of two inverters. The performance is investigated according to IEC/IEEE harmonic standards, and compared with the conventional control strategy developed in synchronous *dq*-frame and based on only PI controllers.

1. Introduction

Recently, the shortage of fossil fuel resources and the increase of greenhouse gas emissions have motivated researchers to use renewable energy resources (RERs) to alleviate the energy crisis and overcome environmental and economic issues (Andishgar et al., 2017; Meng et al., 2019). The distributed energy resources (DERs), including RERs and energy storage elements (ESEs), can be grouped as a locally controllable microgrid in the main power grid to supply the electrical power with minimum losses to the local loads (Farrokhabadi et al., 2020). These DERs can be interfaced with the main power grid and local loads through either a conventional synchronous generator or power electronic converter. The grid-supporting voltage source inverters (VSIs) in AC microgrids are the most significant part which is able not only to harmonious operate in parallel with each other but also has high flexibility to connect or disconnect from the external power grid (Guo and Mu, 2016).

A high penetration level of converters-interfaced RERs into microgrids causes several challenges to the stability and operation of power systems due to the intermittent nature and uncertainties of RERs. Therefore, appropriate microgrid architectures and control approaches for VSIs based-DERs are essential to enhance the quality of output power and guarantee the efficiency, reliability, safety and stability of power systems (Zhou and Ngai-Man Ho, 2016). Many hierarchical control architectures have been addressed in Guerrero et al. (2011, 2013) and Bidram and Davoudi

Nomenclature

DERs	Renewable energy resources
DG	Distribution generation
ESEs	Energy storage elements
FF	Fitness function
HCs	Harmonic compensators
ITAE	Integral time absolute error
LF	Levy flight
PCL	Primary control level
PI	Proportional–integral
PR	Proportional-resonant
RERs	Renewable energy resources
SCL	Secondary control level
TCL	Tertiary control level
THD	Total harmonic distortion
VSIs	Voltage source inverters
C_1, C_2, C_3, C_4, C_5, C_6, C_8, C_9, q, r	Random coefficients which are often in the range [0–1] and updated in each iteration
C_7	Random vector with dimension 1 × d
d	Dimension of variables
E_0	Initial value of escaping energy of the rabbit
E_{pry}	Escaping energy of the prey
e_P, e_Q	Errors in active and reactive powers of droop control
e_{secf}, e_{secE}	Errors in frequency and voltage amplitude of SCL
$e_{syn\theta}$, e_{synE}	Errors in phase angle and voltage amplitude of synchronization control level
$e_{V\alpha}$, $e_{V\beta}$, $e_{I\alpha}$, $e_{I\beta}$	Errors of voltage and current in α- and β-axis
$G(s)$, $Z_{o\alpha\beta}$	Closed-loop transfer function of voltage and output impedance of inverter in $\alpha\beta$-frame
$I_{o\alpha\beta}$	Output currents in $\alpha\beta$-frame
J	Random jump strength of the prey during the escaping behavior
K	Total hawks number
K_{hI}, ω_{chI}, K_{hV}, ω_{chV}	Resonant gain and cut-off frequency around resonant-frequency hω_o of current and voltage HCs for harmonic order h
K_{pDP}, K_{iDP}	Proportional and integral droop coefficients for active power control
K_{pDQ}	Proportional droop coefficient for reactive power control
K_{pI}, K_{rI}, ω_{cI}, K_{pV}, K_{rV}, ω_{cV}	Proportional gain, resonant gain and cut-off frequency around fundamental-frequency ω_o of PR current and voltage controllers
K_{psf}, K_{isf}, K_{psE}, K_{isf}	Proportional and integral gains of frequency and voltage amplitude secondary PI controllers
$K_{p\theta}^{syn}$, $K_{i\theta}^{syn}$, K_{pE}^{syn}, K_{iE}^{syn}	Proportional and integral gains of frequency and voltage amplitude PI synchronization controllers
LB, UB	Lower and upper bounds of optimization problem variables
L_f, R_f	Inductance and capacitance of LC-filter
M	Maximum number of iterations
P, Q, P^*, Q^*	Active and reactive powers, and their references
R_{vir}, L_{vir}	Resistance and inductance of the virtual impedance
T_{sa}	Sampling time
V^*, $\varnothing^*$, V_r, $\varnothing_r$	Reference and nominal values of the voltage amplitude and its phase angle
$v(t)$	Current velocity of particle in PSO
$v\ (t+1)$	Updated velocity of particle in PSO
$V_{cf\alpha}$, $V_{cf\beta}$, $i_{Lf\alpha}$, $i_{Lf\beta}$	Voltage across filter capacitor and current through filter inductor in α- and β-axis
$V_{cf\alpha\beta}$, $V^*_{c\alpha\beta}\ (s)$	Voltages across the filter capacitor in $\alpha\beta$-frame and their references
V_{oi}, V_{bus}	Amplitude of the VSI output voltage and the amplitude of network bus voltage
$v_{MG\alpha}$, $v_{MG\beta}$, $v_{EG\alpha}$, $v_{EG\beta}$	Microgrid and external grid voltages in α- and β-axis
$V_{vir\alpha}$, $V_{vir\beta}$	Voltage correction signal of virtual impedance loop in α-and β-axis
$X(t)$	Current positions of hawks
$X(t+1)$	Updated positions of hawks in the next iteration t
$X_{av}(t)$	Average location of the current hawks population
X_{dl}	Reactance of distribution line
$X_i(t)$	The hawk i position in iteration t
$X_{pry}(t)$	Position of the prey
$X_{rnd}\ (t)$	Hawk position which is selected randomly from the current population
$Z_{vir\alpha\beta}$	Virtual impedance in $\alpha\beta$-frame
$\propto_1$, $\propto_2$	Priority weights for terms in the proposed multi-objective function
$\beta\ (t)$	PSO time-varying inertia weight
β_{max}, β_{min}	Maximum and minimum inertia weights of PSO algorithm
γ	Constant adjust to 1.5
$\delta\omega_{sec}^{comp}$, δE_{sec}^{comp}	Compensation signals of SCL
$\Delta\theta_{syn}$, ΔE_{syn}	Compensation signals of synchronization control level
$\varnothing$	Angle between V_{bus} and V_{oi}, which is called the load angle
ω_{cL}	Cut-off frequency of the low pass filter
ω_o	Fundamental angular frequency of the microgrid
ω^*_{MG}, ω^{meas}_{MG}, E^*_{MG}, E^{meas}_{MG}	Reference and measured values of angular frequency and voltage amplitude

(2012) to make the grid-supporting VSIs-based microgrid capable of working in both isolated and grid-connected modes of operation. This hierarchical control has three control levels comprising of primary control level (PCL), secondary control level (SCL) and tertiary control level (TCL). The PCL is applied locally at each distribution generation (DG) unit to achieve its responsibilities represented in the regulation and stabilization of the frequency and voltage, a realization of accurate power-sharing

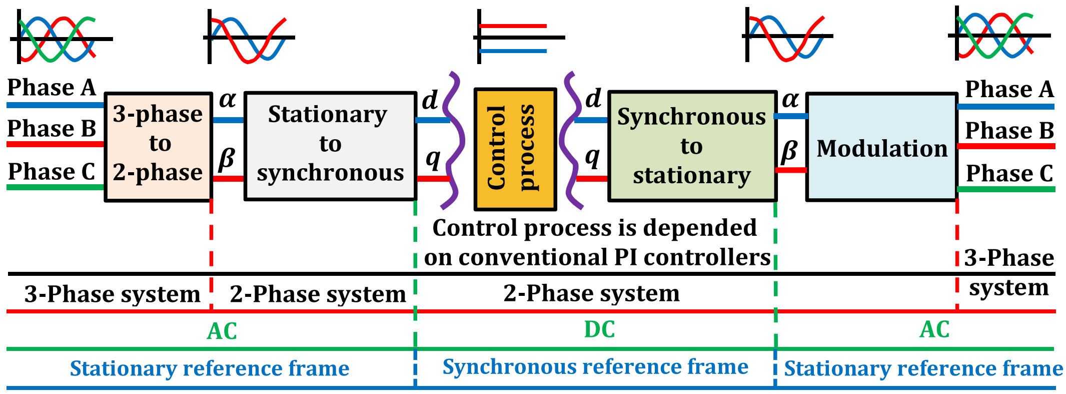

(a) Conventional control strategy developed in synchronous dq reference frame

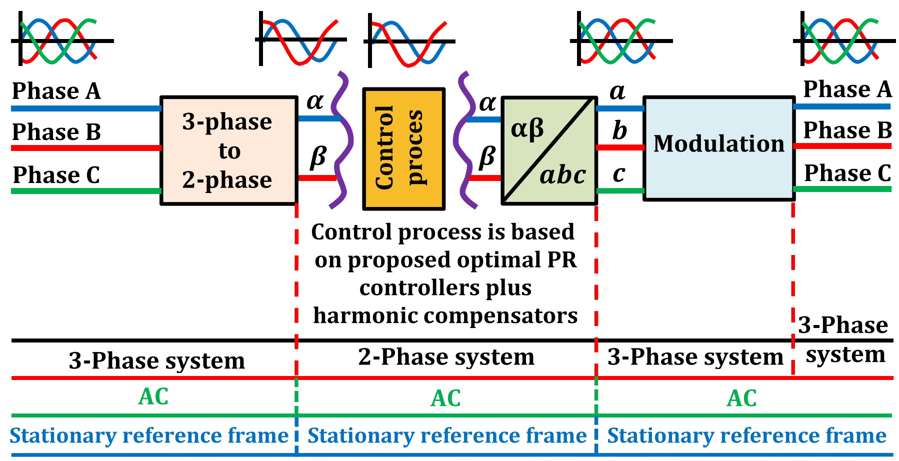

(b) Control approach developed in stationary $\alpha\beta$ frame and based on the proposed optimal PR controllers and HCs

Fig. 1. Two control methodologies developed in different reference frames.

among paralleled DG units via droop control strategy, and enhancement of output power quality. Another level of control is needed for remedying the drawback of the droop control technique which makes the voltage and frequency to deviate from their nominal values. Therefore, the centralized SCL is responsible for nullifying these deviations created by droop loops in PCL for restoring the frequency and voltage to their nominal values. Moreover, the synchronization process between the external main grid and the microgrid is achieved through the SCL. The TCL is the upper centralized layer of control required to optimize the microgrid's operational cost, and also to manage the power flow in grid-connected mode from the microgrid to the external power grid, and vice versa (Shrivastava et al., 2018).

Due to the unbalanced and nonlinear loads involved in the microgrids, the power quality issues are produced in the form of voltage/frequency deviations and fluctuations, current and voltage distortions, power variations, flickers, and voltage swell/sag. The microgrid entity is capable of dealing with these power quality issues using proper control techniques to meet acceptable standards. In the literature, the existing methodologies for power quality enhancement vary significantly including multiple current-loop active damping schemes-based hierarchical control architecture (Han et al., 2017), voltage harmonic compensation using active power filter and coordinated control of DERs VSIs (Hashempour et al., 2016), resonance damping and control of DERs converters (Li, 2009), voltage harmonic reduction for inverters using harmonic droop controller (Zhong, 2013), hybrid voltage/current control technique for grid-interfaced DERs converters (He and Li, 2013), and compensation and sharing of nonlinear and unbalanced loads (Yazdavar et al., 2019; Golsorkhi et al., 2017; Sreekumar and Khadkikar, 2016; He et al., 2015). In Han et al. (2017), the total harmonic distortion (THD) of inverter's output voltage under nonlinear load reduced from 5.45% in the case of without harmonic loops compensation to 1.2% in the case of adding the proposed harmonic loops compensation. The authors of Vasquez et al. (2013) suggested a PCL based on proportional-resonant (PR) controller along with additional harmonic compensators (HCs) in stationary $\alpha\beta$-frame to suppress the inverter's output voltage harmonics generated by nonlinear loads. In this reference, the THD of the inverter's output voltage under nonlinear load decreased from 5.61% in the case of deactivating HCs loops to 0.63% in the case of activating HCs loops. T.K. Vu, S.J. Seong presented a comparative study of proportional–integral (PI) and PR controller for single-phase grid-interfaced inverter system (Vu and Seong, 2010). The simulation results concluded that the current THD reduced from 10.32% for PI controller to 6.73% for PR controller. Other previous research works have focused on the voltage and frequency regulation in AC and DC microgrids for uncertain stochastic nonlinear system with application to energy Internet. A non-fragile robust H_∞ control methodology was employed in Hua et al. (2018) for isolated DC microgrids to regulate intelligently the deviation of DC bus voltage within an Internet energy scenario. In Hua et al. (2020), a mixed H_2/H_∞ control approach with Markov chains was introduced and used for AC microgrids to share the energy and regulate the frequency in Internet energy.

In the literature, most of the control approaches for AC microgrids are developed in either stationary $\alpha\beta$ reference frame or synchronous dq reference frame. Fig. 1a shows the conventional control strategy developed in dq reference frame. It can be observed that the three-phase voltages and currents are converted from three-phase time-variant quantities (i.e., x_a, x_b and x_c) to two-phase time-variant quantities (i.e., x_α and x_β) using Clarke transformation matrix. Then, the two-phase time variant quantities are converted to two-phase time-invariant quantities (i.e., x_d and x_q) using Park transformation matrix. The control laws are carried out under synchronous dq reference frame using the conventional PI controllers. The obtained references of dq voltages must be converted back to $\alpha\beta$ voltages for space vector pulse width modulation or abc voltages for sinusoidal pulse width modulation. This can be achieved using the inverse matrices of Clarke and Park. The transformation matrices between the reference frames can be found in Shuvo et al. (2020). Fig. 1b presents the control approach based on the proposed optimal PR controllers with their HCs. It can be noticed that the control laws are carried out under stationary $\alpha\beta$ reference frame without needing $\alpha\beta - \text{to} - dq$ transformations and vice versa. In contrast to the conventional control strategy developed in synchronous dq frame and based on PI controllers, the control approach developed in $\alpha\beta$ frame and based on PR controllers has a superior performance in tracking a sinusoidal waveform reference without steady-state error and also has a high capability in disturbance rejection (Gui et al., 2018). Moreover, the PR controllers can be integrated along with their HCs to suppress the selective negative and positive harmonics. Due to the control techniques based on PR controllers and their HCs are developed in stationary $\alpha\beta$-frame instead of synchronous dq-frame as in PI controllers-based control approaches, no feed-forward parts and no decoupling terms are required (Vasquez et al., 2013). Consequently, the op-timal control approach in this work is developed in stationary $\alpha\beta$-frame and based on PR controllers along with their additional HCs. The major challenge to using these PR controllers with addi-tional HCs is how to design their many parameters to achieve the control objectives and enhance the power quality. The existing design procedures of PR controllers and their HCs in Han et al.(2017), Vasquez et al. (2013), Gui et al. (2018) and Zammit et al.(2017) are based on the trial-error method, root-locus plots, bode plots and MATLAB's SISO Design Tool. These conventional design methods are inaccurate and ineffective procedures and consume more time. Subsequently, the vision of this article is to introduce artificial intelligence (AI) algorithms-based new optimal design procedures of PR controllers and HCs for control schemes ap-plied to grid-supporting VSIs-based microgrids. In contrast to the previous studies in the same research area mentioned in this paper, our proposed optimal PR controllers and HCs have a superior performance and better results. Unlike the adaptive PI controller which is suggested in Elnady and AlShabi (2019) for microgrid under balanced loads where the microgrids's voltage THD was 1.6%, our proposed optimal PR controllers and HCs under nonlinear loads can reduce the THD to 0.19%. Moreover, a comparison between various types of controllers, including conventional PI, PI plus HCs, and PI-P plus HCs, has been done for isolated microgrids under nonlinear load in Ortega Gonzalez et al. (2014). The microgrid's voltage THD values are found to be 8.8% for conventional PI, 5.2% for PI plus HCs, and 2.2% for PI-P plus HCs. This implies that the suggested optimal PR controllers and HCs in this study are more effective and efficient than those mentioned in the previous research works.

Previous research works focused on employing AI algorithms in the microgrids to select the optimal parameters of PI controllers. In Ebrahim et al. (2021), a novel hybrid algorithm, namely H-HHOPSO, is implemented by hybridization between Harries hawks optimization (HHO) and particle swarm optimization (PSO) algorithms. This reference applied H-HHOPSO algorithm on the new microgrid architecture to optimize the PI controllers' parameters of four control levels. The authors of Jumani et al. (2018) employed the grasshopper optimization algorithm to find the best PI controllers' gains for one control level-based islanded microgrid. M. A. Ebrahim, et al. used a self-adaptive salp swarm optimization algorithm in an isolated microgrid for choosing its PI controllers' coefficients (Ebrahim et al., 2020). In contrast to the PI controllers, the design of PR controllers and their HCs is insufficiently studied in the literatures. In yan Jiang et al. (2020), an optimal PR controller without any HCs is designed by using PSO algorithm for AC microgrid. In Gao et al. (2020), only the resonant term of PR controller was designed and used as active damping approach for grid-connected inverters. To the best of the authors' knowledge, no previous research works employ the AI algorithms in AC microgrids to design optimally the coefficients of PR controllers with their HCs.

The main contributions of the research work introduced in this article can be summarized as follows

- New design guidelines, based on the new H-HHOPSO algorithm cooperated with new proposed multi-objective functions, are presented for tackling one of the most popular microgrid technical issues represented in the optimal parameter-tuning of its controllers and HCs. In this paper, the optimal control approach has three levels of control developed in stationary $\alpha\beta$-frame, including PCL, SCL and synchronization control level, based on PR controllers along with additional HCs and PI controllers. New formulations are developed for optimization problem of three-level control-based microgrid. The optimization problem of three-level control-based microgrid is formulated. The optimal design procedures are carried out throughout two stages. The first stage is employed for the PCL to optimize its voltage/current PR controllers with additional HCs to regulate perfectly both the voltage and frequency and also to suppress the fifth, seventh, eleventh and thirteenth harmonics in microgrid's output voltage under linear and nonlinear loads. The second stage is used to get the best droop controller's coefficients, and also to optimize the voltage and frequency PI controllers for SCL and synchronization control level. The proposed multi-objective function in the second stage is aimed to eliminate the differences in voltage amplitude, frequency and phase angle between the microgrid and the external power grid, and also to achieve accurate power-sharing among paralleled operated grid-supporting inverters.
- A solid comparative study is done among the conventional PI controllers in synchronous dq-frame, other controllers introduced in the literatures, the proposed H-HHOPSO-based PR controllers and HCs in stationary $\alpha\beta$-frame and other meta-heuristic optimization algorithms-based PR controllers with additional HCs in stationary $\alpha\beta$-frame. This comparative study is to prove and confirm the robustness of the proposed optimal controllers and HCs.

The organizational structure of the rest of the paper is as follows: mathematical modeling of the H-HHOPSO optimization algorithm is expressed in Section 2. Section 3 introduces the PCL methodology for grid-supporting VSIs, while the SCL and synchronization control level are described in Section 4. Section 5 presents the proposed optimal design procedures of microgrid's controllers and HCs. The simulation results with a comparative study between various types of microgrid's controllers and HCs are introduced and discussed in Section 6. Finally, the work done in this article can be concluded in Section 7.

2. H-HHOPSO optimization algorithm

The H-HHOPSO is created by hybridizing between HHO and PSO algorithms. The strength of PSO in exploration is synthesized

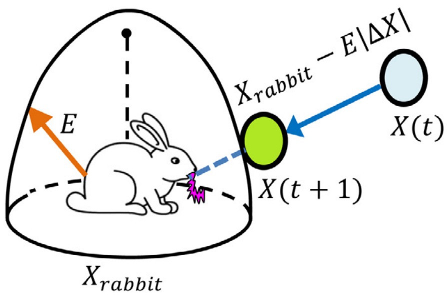

(a) Hard besiege

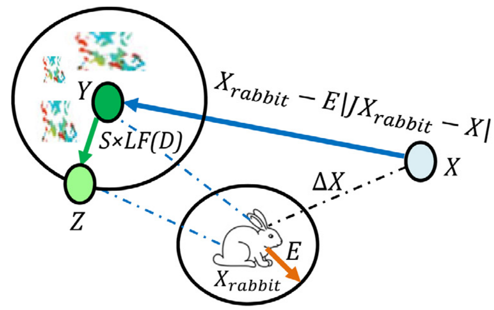

(b) Soft besiege

Fig. 2. Two main strategies of Harries hawks.

with the strength of HHO in exploitation to get a more efficient and effective algorithm. The PSO algorithm was introduced in Kennedy and Eberhart (1995) and inspired by nature from the social behavior of birds and fishes swarms in seeking food. Recently, a new algorithm called HHO has been suggested in Heidari et al. (2019) and nature-inspired by the cooperative behavior and attacking mechanism of Harris hawks to grasp the prey (rabbit). The Harries hawks change their positions for catching the prey according to two main strategies, namely hard and soft besiege strategy. The hard besiege strategy is shown in Fig. 2a. In this strategy, the hawks will change their positions from $X(t)$ to $X(t+1)$ and catch the rabbit. The soft besiege strategy is depicted in Fig. 2b. In this strategy, the hawks are having a lesser chance to grasp the rabbit and therefore they will change their locations to the next possible positions Y or Z and will try to grasp the rabbit from location Y or location Z using the strategy of Levy Flight (LF).

The H-HHOPSO is a novel hybrid algorithm presented in Ebrahim et al. (2021). This algorithm combines the advantages of both HHO and PSO algorithms, hence gives a balance for both the exploitation and exploration performance to achieve the best solutions. The effectiveness of H-HHOPSO algorithm has been confirmed in Ebrahim et al. (2021) through using it to solve twenty-three well-known benchmark problems with different dimensions and ranges. The mathematical model of H-HHOPSO algorithm can be represented as follows: Firstly, the Harris hawks are in the phase of exploration and the prey's escaping energy $|E_{pry}|$ is greater than or equal one, in which the hawks roost randomly on some positions and use two mechanisms to detect a rabbit. The two mechanisms are modeled as the following (Ebrahim et al., 2021)

$$\begin{cases} X(t+1) = \beta(t) * (X_{md}(t) \\ \quad -C_1 |X_{md}(t) - 2C_2 X(t)|) & q \geq 0.5 \\ X(t+1) = \beta(t) * \left(X_{pry}(t) - X_{av}(t)\right) \\ \quad -C_3 (LB + C_4 (UB - LB)) & q < 0.5 \end{cases} \tag{1}$$

$$v(t+1) = \beta(t) * \left(v(t) + C_5 * \left(X(t+1) - X_{pry}(t)\right)\right) \tag{2}$$

$$X(t+1) = X(t+1) + v(t+1) \tag{3}$$

where,

$$E_{pry} = 2E_0 (1 - t/M) \tag{4}$$

$$\beta(t) = \beta_{max} - ((\beta_{max} - \beta_{min}) * t/\mathrm{M}) \tag{5}$$

$$X_{av}(t) = 1/K \sum_{i=1}^{K} X_i(t) \tag{6}$$

Here, $X(t+1)$ are the new locations of hawks after one iteration t; $X(t)$ are the current locations of Harris' hawks; $X_{pry}(t)$ is the prey location; X_{rnd} is the hawk location, which is selected randomly from the current population; $\beta(t)$ is the time-varying inertia weight of PSO; β_{min} and β_{max} are the minimum and maximum PSO inertia weights, which equal 0.2 and 0.9, respectively; UB and LB are the upper bound and lower bound of variables; C_1, C_2, C_3, C_4, C_5 and q are coefficients varied randomly from 0 to 1 and updated in each iteration t; M is the maximum iteration number; $X_{av}(t)$ is the average location of the current hawks population; K is the total hawks number; $X_i(t)$ is the hawk i position in iteration t; $v(t+1)$ is the updated velocity of PSO particle; E_0 is the initial prey's escaping energy and M is the maximum number of iterations.

Secondly, the Harris hawks are transferred from the exploration to exploitation phase and the prey's escaping energy $|E_{pry}|$ is less than one. In this situation, the hawks attack the prey using four strategies based on the value of the prey's escaping energy and a random variable of r. The updated positions of hawks in the exploitation phase are represented as the following (Ebrahim et al., 2021)

$$X(t+1) = \begin{cases} X_1 & if \ |E_{pry}| < 0.5 \ and \ r \geq 0.5 \\ X_2 & if \ |E_{pry}| \geq 0.5 \ and \ r \geq 0.5 \\ X_3 & if \ |E_{pry}| \geq 0.5, r < 0.5 \ and \ F(X_3) < F(X(t)) \\ X_4 & if \ |E_{pry}| \geq 0.5, r < 0.5 \ and \ F(X_4) < F(X(t)) \\ X_5 & if \ |E_{pry}| < 0.5, r < 0.5 \ and \ F(X_5) < F(X(t)) \\ X_6 & if \ |E_{pry}| < 0.5, r < 0.5 \ and \ F(X_6) < F(X(t)) \end{cases} \tag{7}$$

$$v(t+1) = \alpha(t) * \left(v(t) + C_5 * \left(X(t+1) - X_{pry}(t)\right)\right) \tag{8}$$

$$X(t+1) = X(t+1) + v(t+1) \tag{9}$$

where

$$X_1 = \beta(t) * \left(X_{pry}(t) - E_{pry} \left|X_{pry}(t) - X(t)\right|\right) \tag{10}$$

$$X_2 = \beta(t) * \left(X_{pry}(t) - X(t)\right) - E_{pry} \left|JX_{pry}(t) - X(t)\right| \tag{11}$$

$$X_3 = \beta(t) * \left(X_{pry}(t) - E_{pry} \left|JX_{pry}(t) - X(t)\right|\right) \tag{12}$$

$$X_4 = \beta(t) * \left(\frac{X_3}{\beta(t)} + C_7 * LF(d)\right) \tag{13}$$

$$X_5 = \beta(t) * \left(X_{pry}(t) - E_{pry} \left|X_{pry}(t) - X_{av}(t)\right|\right) \tag{14}$$

$$X_6 = \beta(t) * \left(\frac{X_5}{\beta(k)} + C_7 * LF(d)\right) \tag{15}$$

$$J = 2(1 - C_6) \tag{16}$$

$$LF(x) = 0.01 * C_8 * \mu / |C_9|^{1/\gamma} \tag{17}$$

$$\mu = \left(\frac{\Gamma(1+\gamma) * sin(\pi\gamma/2)}{\Gamma((1+\gamma)/2) * \gamma * 2^{(\gamma-1)/2}}\right)^{1/\gamma} \tag{18}$$

Here, C_6, C_8, r, and C_9 are random coefficients in the range [0–1]; $LF(x)$ is the levy-flight function; d is the dimension of the variables; C_7 is a random vector by length $1 \times$ d; γ is a constant

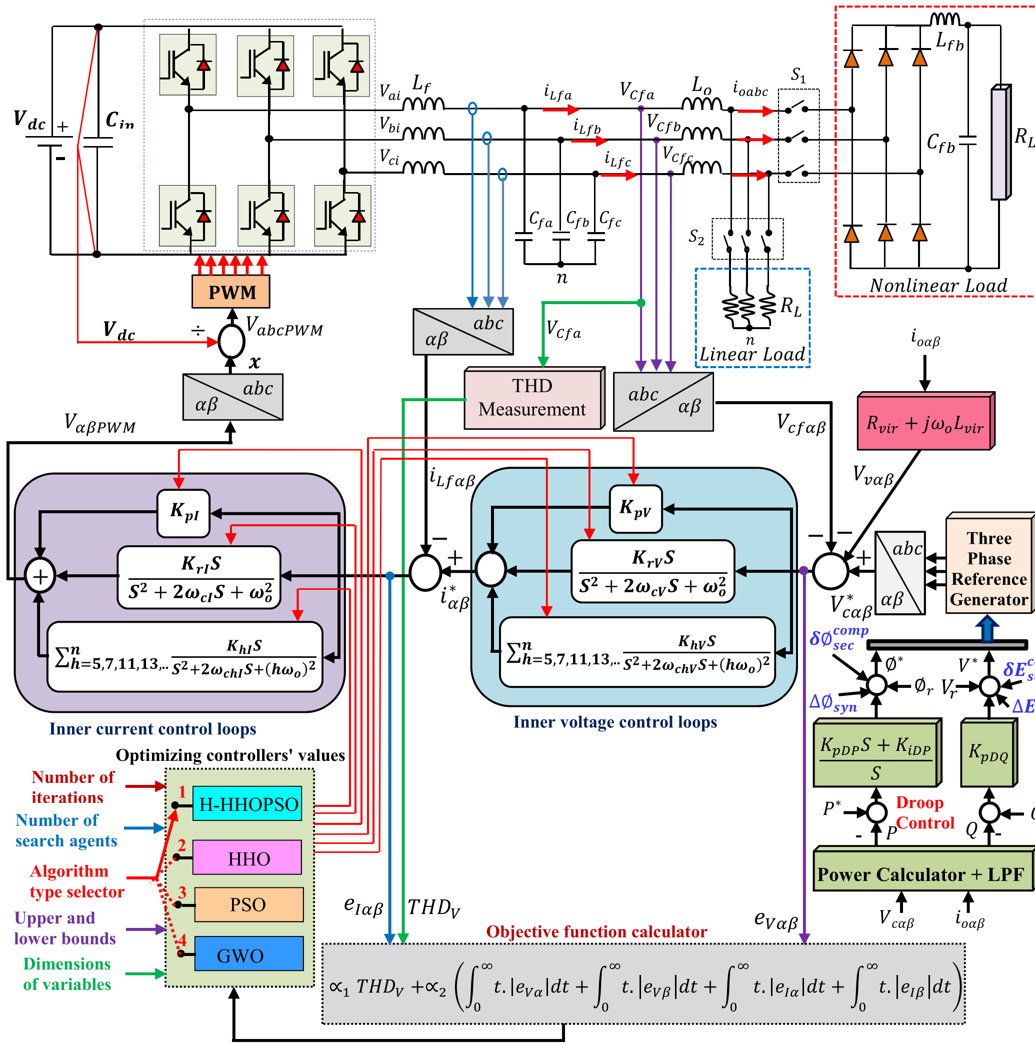

Fig. 3. Proposed primary control strategy for grid-supporting VSIs developed in stationary $\alpha\beta$-frame and based on optimal current/voltage PR controllers and their HCs.

of 1.5; and J is the strength of the prey's random jump which mimics the prey's escaping behavior.

3. Primary control of grid-supporting VSIs

Fig. 3 describes the power stage of a grid-supporting VSI and its proposed primary control methodology developed in stationary $\alpha\beta$-frame and based on optimal droop controllers as well as optimal current/voltage PR controllers along with their additional HCs. The power stage comprises a three-phase pulse width modulation inverter and an LC-filter with an additional output inductor. The PCL approach for grid-supporting inverter, presented in Fig. 3, consists of eight feedback loops of control (1) four inner current and voltage control loops for regulating properly the $\alpha\beta$-axis currents and voltages $i_{Lf\alpha}$, $i_{Lf\beta}$, $V_{cf\alpha}$ and $V_{cf\beta}$, respectively (2) two outer active/reactive power loops (i.e., droop control loops) for realizing accurate active/reactive power-sharing among the paralleled grid-supporting VSIs (3) two intermediate virtual impedance loops for controlling the output impedance of grid-supporting inverter.

3.1. Inner voltage and current control loops

As illustrated in Fig. 3, the voltage controllers track the reference signals produced by active/reactive power controllers and generate the references for the current controllers. The current controllers' output is transformed from stationary $\alpha\beta$-frame to stationary abc-frame and then divided by a dc-link voltage to obtain the three-phase voltage references for the PWM. The inner voltage and current control loops are based on the PR controllers along with HCs to overcome the difficulties of using PI controllers to follow AC signals. The PR controllers have a superior performance in following the current and voltage signals in stationary $\alpha\beta$-frame without any steady-state error. The PR controller includes a proportional term plus a resonant term tuned at the fundamental frequency. The HCs can be included with the PR controller for selective harmonics compensation. In this paper, there are four HCs for both current and voltage PR controllers to suppress the 5th, 7th, 11th and 13th microgrid's voltage harmonics generated by nonlinear loads. Each harmonic compensator includes only a resonant term which is tuned at the frequency of the selective harmonic order.

The dynamics of the closed-loop system, shown in Fig. 4, can be analyzed as follows

$$V_{cf\alpha\beta}(s) = G(s)V^{*}_{c\alpha\beta}(s) - I_{o\alpha\beta}(s)Z_{o\alpha\beta}(s) - G(s)Z_{vir\alpha\beta}(s) \qquad (19)$$

where

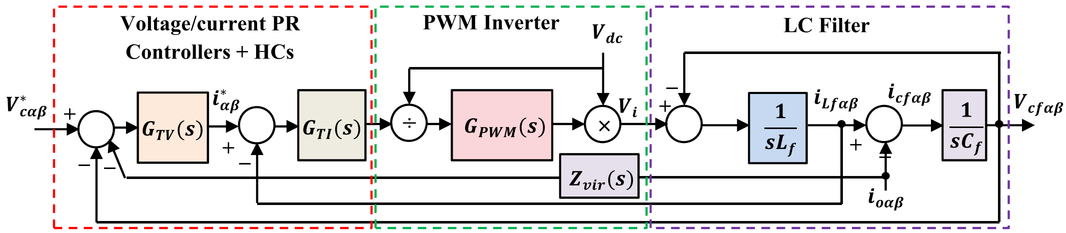

Fig. 4. Block diagram of the closed loops for grid-supporting VSIs based on PR controllers with HCs.

The closed-loop transfer function of the microgrid's output voltage can be derived as

$$G(s) = \frac{G_{TV}(s)G_{TI}G_{PWM}(s)}{L_fC_fS^2 + \left(C_fS + G_{TV}(s)\right)G_{TI}G_{PWM}(s) + 1} \tag{20}$$

The transfer function of the output impedance is expressed as

$$Z_{o\alpha\beta}(s) = \frac{L_fS + G_{TI}(s)G_{PWM}(s)}{L_fC_fS^2 + \left(C_fS + G_{TV}(s)\right)G_{TI}(s)G_{PWM}(s) + 1} \tag{21}$$

Here, $V_{cf\alpha\beta}$ and $V^*_{c\alpha\beta}$ (s) are the voltages across the filter capacitor in $\alpha\beta$-frame and their references, respectively; $I_{o\alpha\beta}$ are the output currents in $\alpha\beta$-frame; $G(s)$ and $Z_{o\alpha\beta}$ are the closed-loop transfer function of voltage and output impedance of inverter in $\alpha\beta$-frame, respectively; L_f and C_f are the inductance and capacitance of LC-filter, respectively; and $Z_{vir\alpha\beta}$ is the virtual impedance in $\alpha\beta$-frame. The transfer functions of the current PR controller and its HCs are represented by Han et al. (2017)

$$G_{TI}\ (s) = G^I_{PR}\ (s) + G^I_{HCs}\ (s) \tag{22}$$

$$G^I_{PR}\ (s) = K_{pI} + \frac{K_{rI}S}{S^2 + 2\omega_{cI}S + \omega_o^2} \tag{23}$$

$$G^I_{HCs}(s) = \sum_{h=5,7,11,13}^{n} \frac{K_{hI}S}{S^2 + 2\omega_{chI}S + (h\omega_o)^2} \tag{24}$$

The transfer functions of the voltage PR controller and its HCs can be expressed as (Han et al., 2017)

$$G_{TV}\ (s) = G^V_{PR}\ (s) + G^V_{HCs}\ (s) \tag{25}$$

$$G^V_{PR}\ (s) = K_{pV} + \frac{K_{rV}S}{S^2 + 2\omega_{cV}S + \omega_o^2} \tag{26}$$

$$G^V_{HCs}(s) = \sum_{h=5,7,11,13}^{n} \frac{K_{hV}S}{S^2 + 2\omega_{chV}S + (h\omega_o)^2} \tag{27}$$

The transfer function of the PWM delay is as follows

$$G_{PWM}\ (s) = \frac{1}{1 + 1.5T_{sa}s} \tag{28}$$

Here, K_{pI}, K_{rI}, ω_{cI}, K_{pV}, and ω_{cV} are the proportional gain, resonant gain and cutoff frequency around the fundamental-frequency ω_o of PR current and voltage controller, respectively; K_{hI}, ω_{chI}, K_{hV} and ω_{chV} are the resonant gain and cutoff frequency around resonant-frequency $h\omega_o$ of current and voltage harmonic compensator for harmonic order h; ω_o is the fundamental frequency of microgrid; and T_{sa} is the sampling time.

By using the model of the voltage closed-loop represented by (19)–(21), the bode plot diagrams of the voltage closed-loop in case of current/voltage PI controllers and also in case of current/voltage PR controllers with 5th, 7th, 11th and 13th harmonics tracking are depicted in Fig. 5. It can be observed that unlike PI controllers, the PR controllers with HCs provide a unity gain for voltage closed-loop response at the fundamental frequency and frequencies of 5th, 7th, 11th and 13th harmonics.

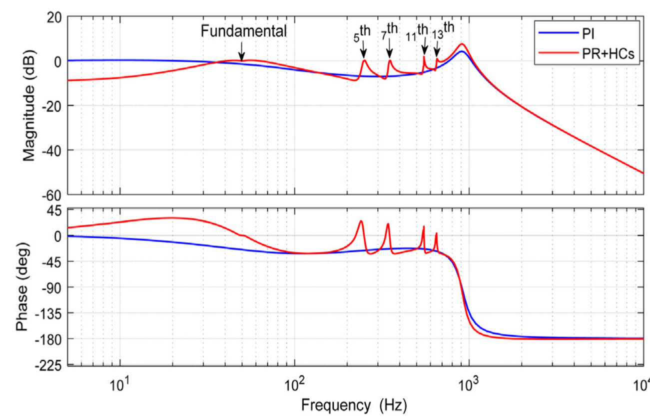

Fig. 5. Bode plot diagrams of the voltage closed-loop in case of current/voltage PI controllers and also in case of current/voltage PR controllers with 5th, 7th, 11th and 13th harmonics tracking.

Consequently, the system based on PR controllers and HCs has a superior performance in tracking capability without any steady-state error at both the fundamental frequency and frequencies of target harmonics.

3.2. Outer droop control loops

The droop control loops are responsible for realizing a proper active/reactive power-sharing among the paralleled grid-supporting VSIs-based DG units by using only low bandwidth communications. It is assumed that the grid-supporting VSIs-based DG units are integrated into the electrical power network via predominantly inductive distribution lines. Therefore, the active and reactive powers between the DG unit and the power network can be determined approximately as follows

$$P = \frac{V_{oi}V_{bus}}{X_{dl}}\varnothing \tag{29}$$

$$Q = \frac{V_{oi}}{X_{dl}}\left(V_{bus} - V_{oi}\right) \tag{30}$$

Here, V_{oi} and V_{bus} are the amplitude of the VSI output voltage and the amplitude of network bus voltage, respectively; X_{dl} is the reactance of distribution line; and $\varnothing$ is the angle between V_{bus} and V_{oi} , which is called the load angle. Considering the network voltage has zero phase angle, the phase angle of inverter voltage will be equal to $\varnothing$. Consequently, the droop control strategy can be employed to control and adjust the amplitude and phase angle of the voltage reference signal according to the reactive and active power, respectively, guaranteeing reactive and active flow control. According to this, the droop control characteristics can be defined as follows:

$$\varnothing^* = \varnothing_r - \frac{K_{pDP}S + K_{iDP}}{S}(P - P^*) \tag{31}$$

$$\overset{*}{V} = V_r - K_{pDQ}(Q - Q^*) \tag{32}$$

Here, V^* and $\varnothing^*$ are the references of the voltage amplitude and its phase angle, respectively; V_r and $\varnothing_r$ are the nominal values of the voltage amplitude and phase angle, respectively; K_{pDP} and K_{iDP} are the proportional and integral droop coefficients for active power control, respectively; K_{pDQ} is the proportional droop coefficient for reactive power control; and P, Q, P^* and Q^* are the active and reactive powers, and their references, respectively. The P^* and Q^* must be adjusted to zero in the islanded operation. The active and reactive powers can be calculated in stationary $\alpha\beta$-frame as follow (Vasquez et al., 2013)

$$\begin{cases} P = \dfrac{\omega_{cL}}{S + \omega_{cL}} \left(V_{c\alpha} i_{o\alpha} + V_{c\beta} i_{o\beta}\right) \\ Q = \dfrac{\omega_{cL}}{S + \omega_{cL}} \left(V_{c\beta} i_{o\alpha} + V_{c\alpha} i_{o\beta}\right) \end{cases} \tag{33}$$

Here, $V_{c\alpha}$, $V_{c\beta}$, $i_{o\alpha}$ and $i_{o\beta}$ are the voltage across filter capacitor and the inverter output current in α- and β-axis, respectively; and ω_{cL} is the cutoff frequency of the low pass filter, which is used to eliminate the ripples in active and reactive powers.

3.3. Intermediate virtual impedance loops

The virtual impedance loops are employed to make the inverter output impedance more inductive for decreasing the cross-coupling between active and reactive power, improving the VSIs stability, reducing the circulating currents and damping the active/reactive power oscillations. The stability of the droop control approach is enhanced by adding the virtual impedance without causing power losses and additional cost. The loops of virtual impedance can be represented in $\alpha\beta$-frame as follow (Vasquez et al., 2013)

$$\begin{cases} V_{vir\alpha} = R_{vir} i_{o\alpha} - \omega_o L_{vir} i_{o\beta} \\ V_{vir\beta} = R_{vir} i_{o\beta} - \omega_o L_{vir} i_{o\alpha} \end{cases} \tag{34}$$

Here, R_{vir} and L_{vir} are the resistance and inductance of the virtual impedance, respectively; and $V_{vir\alpha}$ and $V_{vir\beta}$ are the voltage correction signal of the virtual impedance loop in α-and β-axis, respectively.

4. Secondary and synchronization controls of grid-supporting VSIs

The droop control characteristics lead the microgrid's frequency and voltage amplitude to deviate from their nominal values. Consequently, the SCL is necessary to eliminate these voltage/frequency deviations for restoring their reference values. The frequency deviation should be corrected by the SCL to be within the permissible limits recommended by the grid exigencies in Technical Paper (2008). The block diagram of the SCL is demonstrated in Fig. 6. To generate the restoration signals of secondary control to nullify the voltage/frequency deviations created by droop loops, the amplitude and angular frequency of the microgrid voltage, ω_{MG}^{meas} and E_{MG}^{meas}, are sensed and compared with their references ω_{MG}^* and E_{MG}^*. Afterward, the different errors are remedied throughout PI controllers to produce the correction signals of SCL to be sent to the control loops of the droop approach for each grid-supporting VSI. The SCL compensation signals $\delta\omega_{\sec}^{comp}$ and $\delta E_{\sec}^{comp}$ can be expressed as (Vasquez et al., 2013)

$$\delta\omega_{\sec}^{comp} = K_{psf}(\omega_{MG}^* - \omega_{MG}^{meas}) + K_{isf} \int \left(\omega_{MG}^* - \omega_{MG}^{meas}\right) dt + \Delta\theta_{syn} \tag{35}$$

$$\delta E_{\sec}^{comp} = K_{psE}(E_{MG}^* - E_{MG}^{meas}) + K_{isE} \int \left(E_{MG}^* - E_{MG}^{meas}\right) dt + \Delta E_{syn} \tag{36}$$

Here, K_{psf}, K_{isf}, K_{psE} and K_{isE} are the proportional and integral gains of frequency and voltage amplitude secondary PI controllers, respectively; ω_{MG}^*, ω_{MG}^{meas}, E_{MG}^* and E_{MG}^{meas} are the reference and measured values of angular frequency and voltage amplitude, respectively; and $\Delta\theta_{syn}$ and ΔE_{syn} are the compensation signals of synchronization control level which are zero when the external power grid is not present.

In order to prepare the microgrid to be connected to the external power grid, the microgrid's frequency, and voltage amplitude and phase should be synchronized with those of the external main grid to ensure a seamless transition. Before reconnecting back the microgrid to the external power grid, the error differences in frequency, and voltage amplitude and phase between them must be met by the recommendations of DG units' synchronization by IEEE Standard 1547–2003. The block diagram of the synchronization control level is displayed in Fig. 6. The synchronization signals, $\Delta\theta_{syn}$ and ΔE_{syn}, should be fed to the control loops of droop approach to compensate the error differences in frequency, and voltage amplitude and phase can be expressed as (Sun et al., 2017)

$$\Delta\theta_{syn} = \left(K_{p\theta}^{syn} + K_{i\theta}^{syn}/S\right)\left(-v_{EG\alpha} v_{MG\beta} + v_{EG\beta} v_{MG\alpha}\right) \tag{37}$$

$$\Delta E_{syn} = \left(K_{pE}^{syn} + K_{iE}^{syn}/S\right)\left(\sqrt{v_{EG\alpha}^2 + v_{EG\beta}^2} - \sqrt{v_{MG\alpha}^2 + v_{MG\beta}^2}\right) \tag{38}$$

Here, $K_{p\theta}^{syn}$, $K_{i\theta}^{syn}$, K_{pE}^{syn} and K_{iE}^{syn} are the proportional and integral gains of frequency and voltage amplitude PI synchronization compensators, respectively; and $v_{MG\alpha}$, $v_{MG\beta}$, $v_{EG\alpha}$ and $v_{EG\beta}$ are the microgrid and external grid voltages in α- and β-axis, respectively.

5. Optimal design procedures of microgrid's controllers and HCs

The proposed optimal design procedures of microgrid controllers and HCs are employed to achieve the study objectives mentioned above. These procedures are based on a new H-HHOPSO algorithm that cooperated with proposed multi-objective functions. In this paper, the design procedures are carried out through two stages. In the first stage, the parameters of current/voltage PR controllers with their additional HCs for the PCL are optimally designed. However, the second stage is used to design the controllers' coefficients of droop control, SCL and synchronization control level.

5.1. First stage optimization procedure

The first stage is employed to tackle the design problem of twenty-two parameters of current/voltage PR controllers with their HCs for the PCL. The proposed multi-objective error function, mentioned in (39), was selected to reduce the THD in the microgrid voltage, and also to minimize the arithmetic summation of the following: the integral time absolute error (ITAE) of α-axis voltage, ITAE of β-axis voltage, α-axis current and ITAE of β-axis current. The optimization problem for optimal designing the parameters of current/voltage PR controllers with their HCs, which is proposed by the authors, can be formulated as Consider $\overrightarrow{x}$ which is given in Box I

$$\text{Minimize } FF = \propto_1 THD_V + \propto_2 \left(\int_0^\infty t.\left|e_{V\alpha}\right| dt + \int_0^\infty t.\left|e_{V\beta}\right| dt + \int_0^\infty t.\left|e_{I\alpha}\right| dt + \int_0^\infty t.\left|e_{I\beta}\right| dt\right)$$

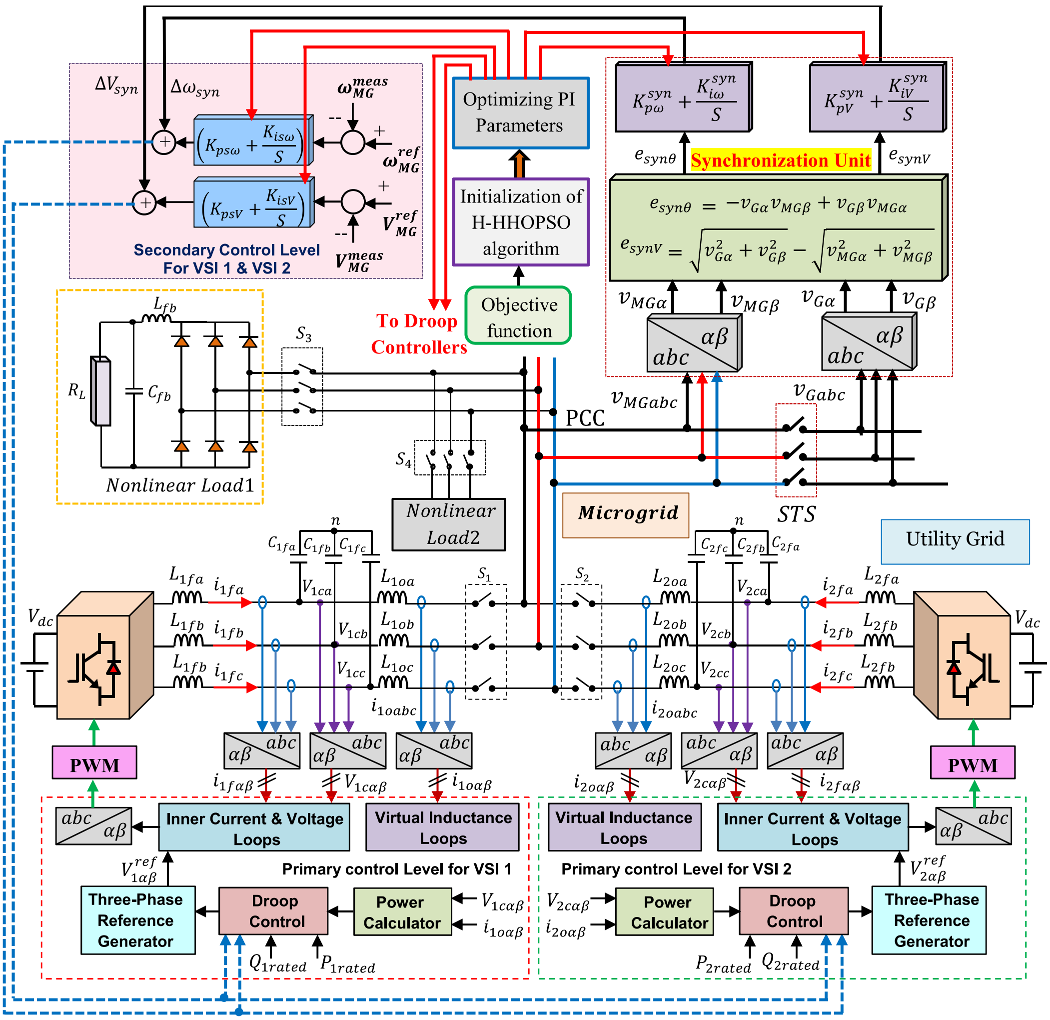

Fig. 6. Block diagram of the whole microgrid system including two grid-supporting VSIs based on the proposed control approach developed in $\alpha\beta$-frame and depended on the optimal controllers and HCs.

$$\text{Consider } \vec{x} = \begin{bmatrix} \vec{X}_V \\ \vec{X}_I \end{bmatrix} = \begin{bmatrix} K_{pV} & K_{rV} & K_{5V} & K_{7V} & K_{11V} & K_{13V} & \omega_{cV} & \omega_{c5V} & \omega_{c7V} & \omega_{c11V} & \omega_{c13V} \\ K_{pI} & K_{rI} & K_{5I} & K_{7I} & K_{11I} & K_{13I} & \omega_{cI} & \omega_{c5I} & \omega_{c7I} & \omega_{c11I} & \omega_{c13I} \end{bmatrix}$$

Box I.

$$\text{Variable range} \begin{cases} 0.05 \le K_{pV} \le 5 \\ 100 \le K_{rV} \le 1000 \\ 2 \le K_{hV} \le 100 \\ 2 \le K_{pI} \le 20 \\ 20 \le K_{rI} \le 200 \\ 1 \le K_{hI} \le 100 \\ 1 \le 2\omega_{cV} \le 10 \\ 5 \le 2\omega_{chV} \le 250 \\ 1 \le 2\omega_{cI} \le 5 \\ 20 \le 2\omega_{chI} \le 250 \end{cases} \tag{39}$$

Here, $e_{V\alpha}$, $e_{V\beta}$, $e_{I\alpha}$ and $e_{I\beta}$ are the errors of the voltage and current in α- and β-axis, respectively; THD_V is the THD in the microgrid voltage, and $\propto_1$ and $\propto_2$ are the priority weights for terms in the above multi-objective function. Fig. 7 depicts a flowchart of the first stage of the proposed design guidelines for obtaining the optimal parameters of current/voltage PR controllers with HCs. Initially, the fitness function (FF) is calculated during the run of the simulation model. The FF will be fed as input to the H-HHOPSO algorithm with other inputs, including search agents' number, upper/lower limits of variables, maximum iterations number and search agent's dimension. The H-HHOPSO algorithm will generate an initial random vector of controllers' parameters for each search agent, which represents a possible solution in search space. Then, the initial vector will be updated throughout the strategy of H-HHOPSO algorithm. Finally, the obtained results of H-HHOPSO algorithm are evaluated and compared with those of other meta-heuristic optimization algorithms, including grey wolf optimizer (GWO) (Mirjalili et al., 2014), particle swarm optimization (PSO) and HHO, to get the finest parameters. In this optimization problem, each

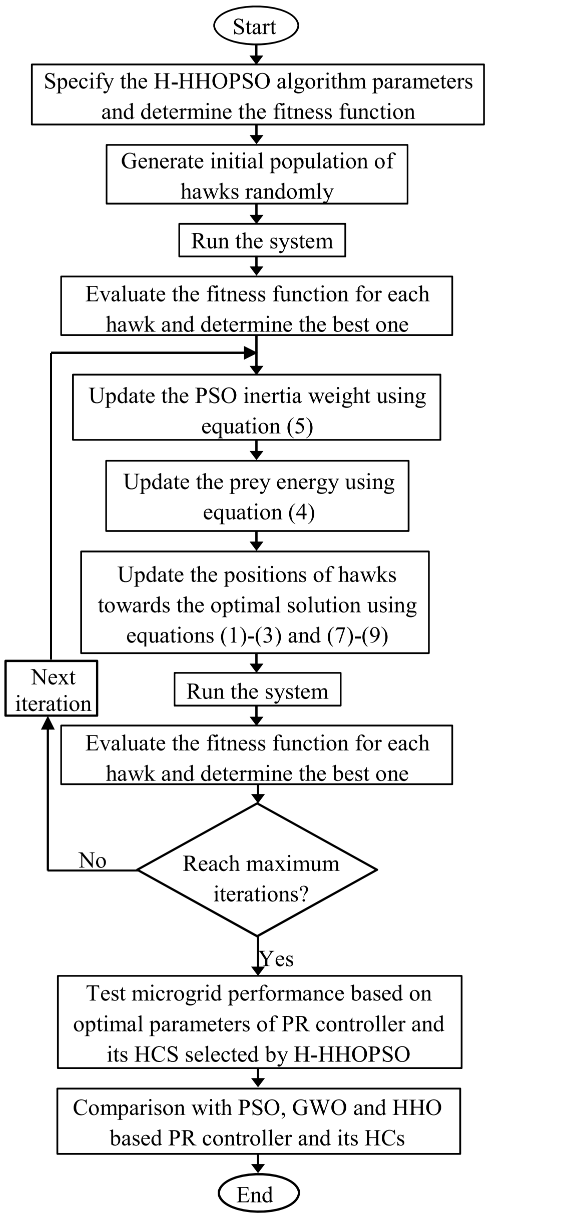

Fig. 7. A flowchart of the first stage of the proposed design guidelines for obtaining the optimal parameters of current/voltage PR controllers with HCs.

Harris hawk represents a search agent exploited to search and find the best parameters of current/voltage PR controllers and their HCs. In this paper, the initial parameters of algorithms are selected as following: maximum iteration number = 30, search agents number = 20, search dimension in first stage = 22, search dimension in second stage = 11 and number of runs for each algorithm = 10. Fig. 8 shows the convergence curves of the PSO, GWO, HHO and H-HHOPSO algorithms for minimizing the multi-objective function illustrated in (39). The optimization objective was to minimize the multi-objective function, and therefore its lowest value has been considered as the best value. It can be observed from Fig. 8 that the minimum obtained values of multi-objective are 3.922133, 2.978833, 2.36785 and 1.231183 in the cases of PSO, GWO, HHO and H-HHOPSO algorithm, respectively. Consequently, the H-HHOPSO algorithm gives a better optimum solution than the other algorithms.

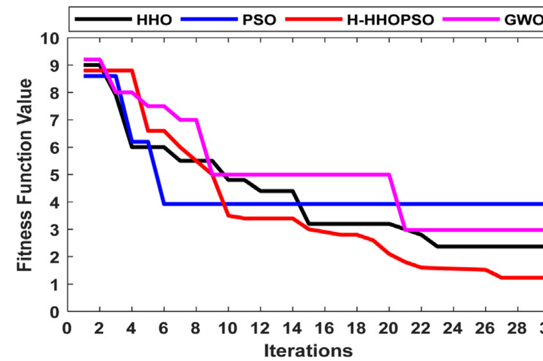

Fig. 8. Convergence curves of the PSO, GWO, HHO and H-HHOPSO algorithms for minimizing the multi-objective function illustrated in (39).

5.2. Second stage optimization procedure

After the first stage is performed, the second stage is conducted in this subsection. The second stage is used to optimally tune eleven controllers' parameters for both the SCL and synchronization control levels. The suggested objective function, mentioned in (40), was designated to minimize the arithmetic summation of the following: ITAE in both real and reactive powers of droop control, ITAE in both frequency and voltage amplitude of SCL, and ITAE in both phase angle and voltage amplitude of synchronization control level. In this stage, the formulation of the optimization problem can be proposed as follows

Consider

$$\begin{bmatrix} K_{pDP} & K_{iDP} & K_{pDQ} & K_{psf} & K_{isf} & K_{psE} & K_{isE} & K_{p\theta}^{syn} & K_{i\theta}^{syn} & K_{pE}^{syn} & K_{iE}^{syn} \end{bmatrix}$$

$$\text{Minimize } FF = \int_0^\infty t.\left|e_P\right|dt + \int_0^\infty t.\left|e_Q\right|dt + \int_0^\infty t.\left|e_{secf}\right|dt + \int_0^\infty t.\left|e_{secE}\right|dt + \int_0^\infty t.\left|e_{syn\theta}\right|dt + \int_0^\infty t.\left|e_{synE}\right|dt$$

$$\text{Variable range} \begin{cases} 1e-6 \le K_{pDP} \le 1e-4 \\ 0.0001 \le K_{iDP} \le 0.001 \\ 0.0005 \le K_{pDQ} \le 0.01 \\ 0.001 \le K_{psf} \le 0.1 \\ 0.01 \le K_{isf} \le 15 \\ 0.01 \le K_{psE} \le 1 \\ 0.1 \le K_{isE} \le 100 \\ 0.001 \le K_{p\theta}^{syn} \le 0.1 \\ 0.0001 \le K_{i\theta}^{syn} \le 0.01 \\ 0.01 \le K_{pE}^{syn} \le 0.2 \\ 0.0001 \le K_{iE}^{syn} \le 0.03 \end{cases} \tag{40}$$

Here, e_P and e_Q are the errors in active and reactive powers of droop control, respectively; e_{secf} and e_{secE} are the errors in frequency and voltage amplitude of SCL, respectively; and $e_{syn\theta}$ and e_{synE} are the errors in phase angle and voltage amplitude of synchronization control level, respectively.

6. Simulation results and discussions

The feasibility of two-stage optimal design procedures is examined throughout the two scenarios. The first scenario evaluates the efficiency of the first design stage for the inner current and voltage feedback loops which depend on PR controllers with their HCs. After the first stage is investigated, the whole microgrid system is tested and evaluated in the second scenario. This whole

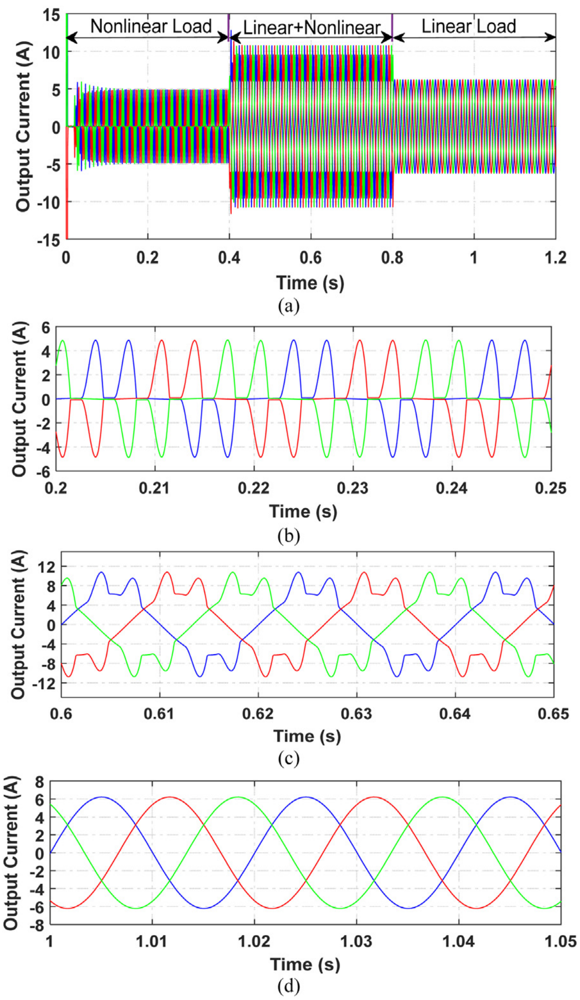

Fig. 9. Three-phase output currents during linear, nonlinear and composite loads in the case of the proposed voltage and current PR controllers plus their HCs (a) Three-phase output currents; (b) zoomed-in view for nonlinear load currents; (c) zoomed-in view for linear plus nonlinear load currents; (d) Zoomed-in view for linear load currents.

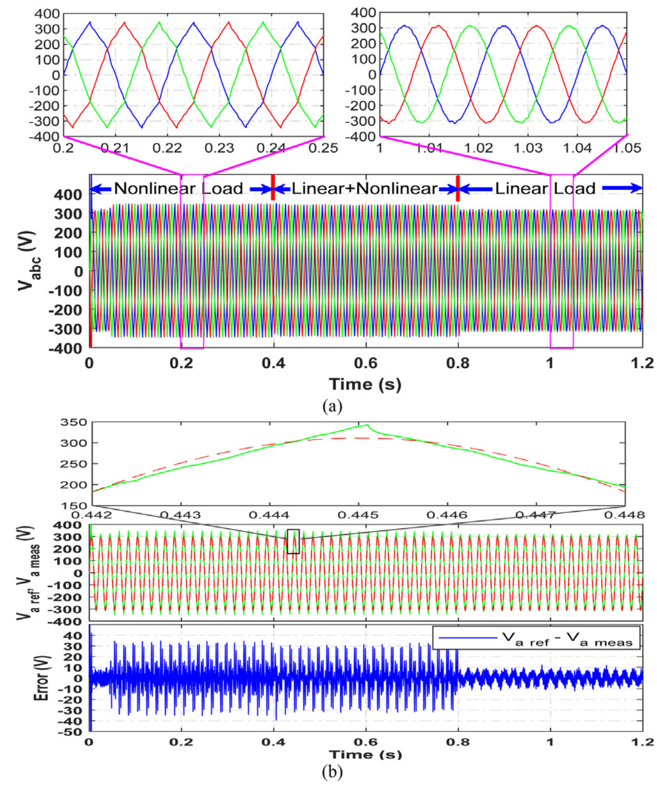

Fig. 10. Output voltages during linear, nonlinear and composite loads in the case of the proposed voltage and current PI conventional controllers (a) three-phase output voltages; (b) phase-a actual voltage and its reference with the error between them.

system has three control levels based on the controllers and HCs designed by the proposed optimal procedures conducted through two stages.

6.1. Scenario I

In this scenario, it is necessary to evaluate the first stage effectiveness of design procedures for voltage/current PR controllers with their HCs. Consequently, a microgrid comprising of one DG unit, based on only the primary control approach, shown in Fig. 3, is modeled and simulated through a MATLAB environment. In this case, the control system consists of only inner feedback control loops of voltage and current, in which the three-phase voltage references are generated internally not from droop control loops. The optimal voltage/current PR controllers with their HCs, based on H-HHOPSO algorithm, are examined under the linear load of 50 Ω, nonlinear load comprising diode bridge rectifier connected to 300 Ω resistive load and both the two loads (i.e. linear + nonlinear). The performance is evaluated and compared with the conventional PI controllers, PR controllers without HCs, and PSO, HHO and GWO-based PR controllers with HCs. Fig. 9 depicts the three-phase output currents during linear, nonlinear and linear + nonlinear (composite) loads in the case of the proposed voltage/current PR controllers plus their HCs. Figs. 10–12 illustrate the three-phase output voltages as well as phase-a actual voltage and its reference with the error between them during linear, nonlinear and composite loads in cases of conventional PI controllers, PR controllers without HCs and proposed optimal PR controllers with their HCs, respectively. It can be observed that the proposed optimal PR controller with their HCs has a superior performance in tracking the sinusoidal reference voltage with only slight oscillations. However, the PR controllers without HCs suffer from significant fluctuations in sinusoidal output voltage, which are increased in the case of conventional PI controllers. Figs. 13–15 demonstrate the harmonics spectrum of the output voltage during linear, nonlinear and composite loads in the cases of conventional PI controllers, PR controllers without HCs and proposed optimal PR controllers with their HCs, respectively. It can be observed that the THD in the output voltage during nonlinear load decreased from 5.23% in the case of conventional PI controllers to 4.18% in the case of PR controllers without HCs to 0.16% in the case of optimal PR controllers with their HCs. Table 1 gives the individual harmonics amplitudes and THD of output microgrid voltage during linear, nonlinear and composite loads in the cases of current/voltage PI controllers, PR controllers without HCs and optimal PR controllers plus their HCs. It can be observed that unlike the PI controllers and PR controllers without HCs, the optimal PR controllers with their HCs have the minimum values of both individual harmonics amplitudes and THD in the output voltage during linear, nonlinear and composite loads. Fig. 16 shows a comparative graph of individual harmonic magnitudes between

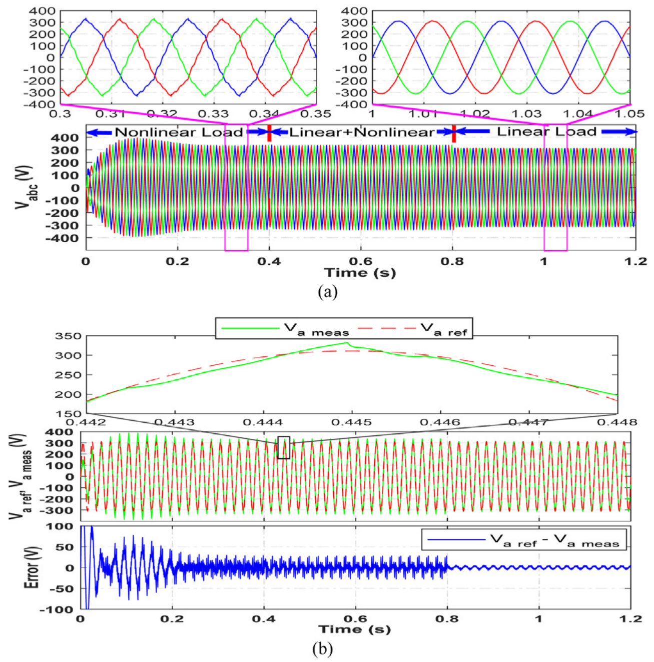

Fig. 11. Output voltages during linear, nonlinear and composite loads in the case of the proposed voltage and current PR controllers without HCs (a) three-phase output voltages; (b) phase-a actual voltage and its reference with the error between them.

the proposed optimal PR controller plus its HCs, PR controllers without HCs, and conventional PI controller under different types of load. Fig. 17 demonstrates the six switching pulses for grid-supporting inverter in the case of H-HHOPSO algorithm. Table 2 represents the optimal parameters obtained by the proposed design guidelines for PR voltage/current PR controllers with their HCs. The only limitation of the work presented in this paper is that the parameters obtained from the proposed guidelines may only need to fine-tune in practical and realistic operating condition. It can be observed from Table 2 that the computational times for H-HHOPSO, HHO, GWO and PSO algorithms are 159.213 min, 167.845 min, 182.357 min and 162.638 min, respectively. The proposed H-HHOPSO algorithm has a lower computational time than the other studied algorithms. The studied algorithms were run through a computer with installed memory (RAM) of 8.0 GB and processor of Intel(R) Core(TM) i7-4510U CPU@ 2.0 GHz. The computational times for the studied algorithms in this paper can be extremely reduced by using high performance computing facility. Fig. 18 clarifies the harmonics spectrum of the output voltage during nonlinear load in the cases of PSO, GWO and HHO-based voltage/current PR controllers with their HCs. It can be observed that the THD in the output voltage during nonlinear load decreased from 3.28% to 2.81% to 1.75% in cases of PSO, GWO and HHO-based voltage/current PR controllers with their HCs, respectively. Table 3 presents the individual harmonics amplitudes and THD of output microgrid voltage during linear, nonlinear and composite loads in the cases of H-HHOPSO, HHO, GWO and PSO-based voltage/current PR controllers with their HCs. At any operating conditions, the proposed optimal PR controllers with their HCs meet the exigencies recommended by IEEE/IEC harmonics standards and also have the best performance in minimizing both individual harmonic amplitudes and THD of the microgrid's output voltage.

6.2. Scenario II

In this scenario, the whole microgrid system, based on three control levels that cooperated with the optimal controllers and

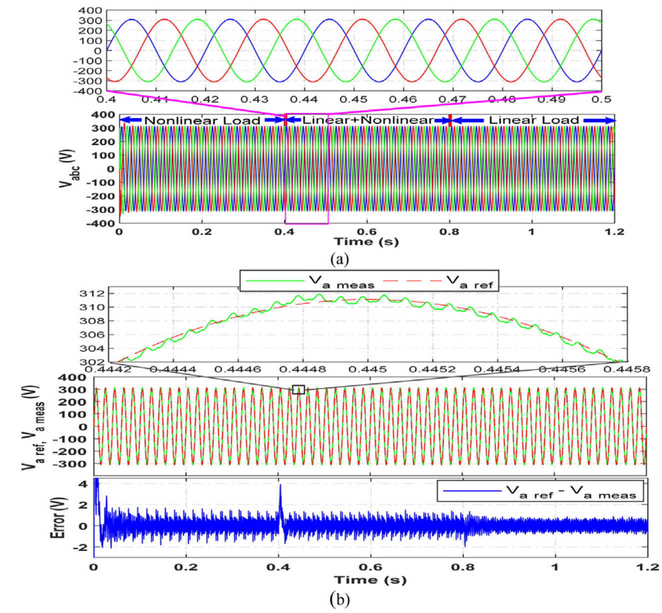

Fig. 12. Output voltages during linear, nonlinear and composite loads in the case of the proposed voltage and current PR controllers plus their HCs (a) three-phase output voltages; (b) phase-a actual voltage and its reference with the error between them.

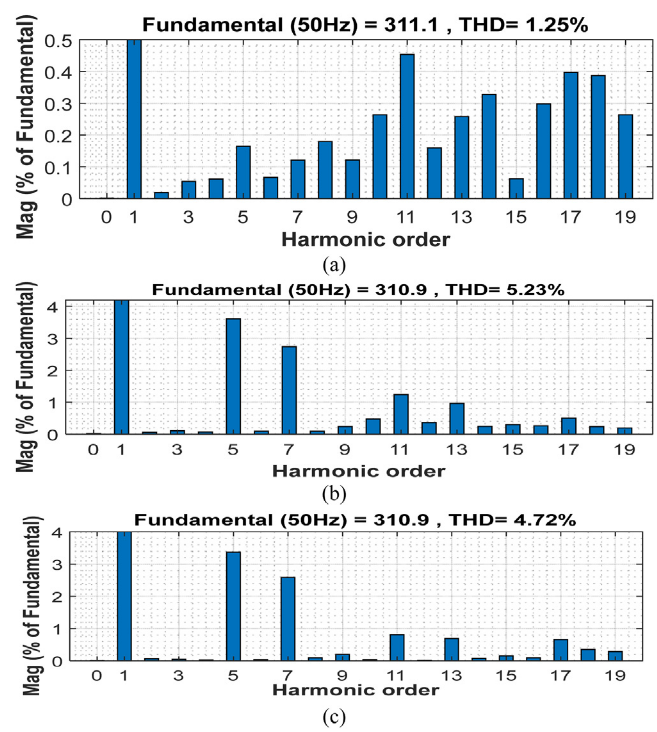

Fig. 13. Harmonics spectrum of the output voltage during linear, nonlinear and composite loads in the case of the voltage and current PI conventional controllers (a) linear load; (b) nonlinear load; (c) composite load.

HCs designed by the proposed guidelines, is examined. In order to test the effectiveness of the proposed control methodology based on the optimal controllers and HCs, a microgrid consisting of two identical grid-supporting VSIs was modeled in stationary $\alpha\beta$-frame and simulated in MATLAB environment. The microgrid under test, including the three control levels, is shown in Fig. 6 with the power circuit parameters and the optimal coefficients of the controllers and HCs listed in Tables 2 and 4.

Table 1
The individual harmonics amplitudes and THD of output microgrid voltage during linear, nonlinear and composite loads in the cases of current/voltage PI controllers, PR controllers without HCs and optimal PR controllers plus their HCs.

Fundamental/ Harmonic order/ THD	Controller type								
	PI controller			PR controller without HCs			Proposed PR controller Plus HCs		
	Nonlinear	Linear	Linear + Nonlinear	Nonlinear	Linear	Linear + Nonlinear	Nonlinear	Linear	Linear + Nonlinear
Fundamental	310.9 V (peak) (100%)	311.1 V (peak) (100%)	310.9 V (peak) (100%)	311 V (peak) (100%)	311 V (peak) (100%)	311.2 V (peak) (100%)	311.1 V (peak) (100%)	311 V (peak) (100%)	311 V (peak) (100%)
3rd	0.1044%	0.05365%	0.04772%	0.08611%	0.03597%	0.03493%	0.001025%	0.001471%	0.002291%
5th	3.609%	0.1647%	3.369%	2.273%	0.04128%	2.215%	0.03411%	0.00438%	0.02893%
7th	2.739%	0.1205%	2.588%	2.224%	0.01596%	2.29%	0.03667%	0.000956%	0.03492%
9th	0.2413%	0.121%	0.1989%	0.08025%	0.02327%	0.04919%	0.00199%	0.002389%	0.005536%
11th	1.239%	0.4539%	0.809%	1.049%	0.05646%	1.005%	0.06105%	0.006113%	0.05723%
13th	0.9645%	0.2584%	0.6902%	0.8718%	0.06237%	0.698%	0.03738%	0.000959%	0.03775%
15th	0.3004%	0.06279%	0.1516%	0.1841%	0.04342%	0.0365%	0.0001332%	0.000428%	0.001305%
17th	0.5013%	0.3973%	0.6586%	1.912%	0.1461%	1.072%	0.02925%	0.002429%	0.02984%
19th	0.1941%	0.2639%	0.2853%	1.122%	0.13%	0.3699%	0.02938%	0.001787%	0.02923%
THD	5.23%	1.25%	4.72%	4.18%	0.63%	3.64%	0.16%	0.12%	0.16%

Table 2
The optimal parameters were obtained by the proposed design guidelines for PR voltage and current PR controllers with their HCs.

Parameters of PR controllers and their HCs	H-HHOPSO	HHO	PSO	GWO
K_{pV}	1.833792	3.370431	0.10303	1.328514
K_{rV}	796.9437	764.6223	672.7865	346.5463
K_{5V}	80.62862	18.38088	80.47264	57.14535
K_{7V}	94.61034	27.30676	40.03947	77.5617
K_{11V}	17.7901	27.01649	27.01085	23.63293
K_{13V}	91.04992	4.28428	29.09901	50.16397
$2\omega_{cV}$	5.02142	1.870677	8.856286	4.112025
$2\omega_{c5V}$	5.274829	85.3602	99.27128	55.75242
$2\omega_{c7V}$	104.6628	129.9165	141.9648	49.75813
$2\omega_{c11V}$	160.7646	10.75371	95.93607	51.4355
$2\omega_{c13V}$	117.5536	239.1812	31.68606	216.4337
K_{pI}	17.84921	7.767538	14.30152	4.344418
K_{rI}	148.7882	27.79968	58.97532	195.2092
K_{5I}	45.67919	35.45971	58.42796	30.38284
K_{7I}	1.065081	51.02254	25.49977	68.90601
K_{11I}	5.719752	53.75801	93.65477	37.71907
K_{13I}	22.12468	40.88535	56.89113	39.22372
$2\omega_{cI}$	4.280542	3.985016	1.109482	1.221704
$2\omega_{c5I}$	59.82435	99.92674	38.97316	86.59314
$2\omega_{c7I}$	91.6601	81.81544	83.95773	125.5591
$2\omega_{c11I}$	28.68581	161.1439	184.5246	93.71798
$2\omega_{c13I}$	192.0994	196.4462	233.61	192.9981
FF value at nonlinear load	1.231183	2.36785	3.922133	2.978833
THD_v at nonlinear load	0.16%	1.75%	3.28%	2.81%
THD_v at computed parameters+10%	0.18%	1.87%	3.58%	2.97%
THD_v at computed parameters−10%	0.21%	1.95%	3.74%	3.26%
Computational cost (Min)	159.213	167.845	182.357	162.638

The system parameters, listed in Table 4, were taken as the following: the parameters of power circuit were taken from the literature (Vasquez et al., 2013). However, the control parameters were selected by the optimal design procedures discussed in this paper. The performance of the proposed model is tested under ±10% variations around the computed parameters listed in Table 2. When the values of the controllers' parameters are varied in the range of ±10%, the THD in microgrid's voltage is slightly affected. The tested microgrid is loaded by two nonlinear loads, each represented by a three-phase diode bridge rectifier connected to a resistive load of 8 ohm through an LC filter. The performance of the microgrid is examined under the nonlinear load change, and also during the suddenly disconnecting of one grid-supporting inverter. Moreover, the compensation of deviations in phase angle, frequency and voltage amplitude, by using SCL and synchronization control level, is verified and confirmed in this section. Fig. 19 describes the microgrid voltage during nonlinear loads in case of using the optimal current/voltage PR controllers with HCs. When the HCs are deactivated, the voltage THD is 5.82% decreased to 0.19% by activating voltage/current PR controllers with HCs. Table 5 presents a comparative study between our proposed optimal PR controllers with their HCs and the previously introduced controllers in the literatures. It can be observed that the proposed optimal procedures in this paper have better results than the previously published researches in this scope. Fig. 20 depicts the waveforms of output currents for the two paralleled grid-supporting inverters sharing the two nonlinear loads via the droop control methodology.

It is worth mentioning that Figs. 21 and 22 demonstrate the transient response of the microgrid's frequency and voltage, respectively, with and without secondary control under the nonlinear load change at t = 0.5 s and during the suddenly disconnecting of one inverter at t = 1 s. At any operating conditions, it can be observed that the deviations in microgrid's voltage amplitude

Table 3
The individual harmonics amplitudes and THD of output microgrid voltage during linear, nonlinear and composite loads in the cases of H-HHOPSO, HHO, GWO and PSO-based voltage and current PR controllers with their HCs.

Fundamental/ Harmonic order/ THD	Controller type											
	H-HHOPSO based PR+HCs			HHO based PR+HCs			GWO based PR+HCs			PSO based PR+HCs		
	Nonlinear	Linear	Linear + Nonlinear	Nonlinear	Linear	Linear + Nonlinear	Nonlinear	Linear	Linear + Nonlinear	Nonlinear	Linear	Linear + Nonlinear
Fundamental	311.1V (peak) (100%)	311V (peak) (100%)	311V (peak) (100%)	311.3 V (peak) (100%)	311.1 V (peak) (100%)	311 V (peak) (100%)	311.1 V (peak) (100%)	311.1 V (peak) (100%)	310.9 V (peak) (100%)	311 V (peak) (100%)	311 V (peak) (100%)	310.9 V (peak) (100%)
3rd	0.00103%	0.001471%	0.00229%	0.04547%	0.014%	0.0179%	0.0661%	0.0416%	0.01%	0.0353%	0.0443%	0.0244%
5th	0.0341%	0.00438%	0.02893%	0.1896%	0.025%	0.1173%	0.2629%	0.0777%	0.2118%	0.4879%	0.1385%	0.4627%
7th	0.03667%	0.000956%	0.03492%	0.1442%	0.0426%	0.1535%	0.1537%	0.1297%	0.1354%	0.5232%	0.1583%	0.645%
9th	0.00199%	0.002389%	0.00554%	0.05449%	0.001%	0.0622%	0.0852%	0.0186%	0.052%	0.0516%	0.1788%	0.1308%
11th	0.06105%	0.006113%	0.05723%	0.08558%	0.0477%	0.0493%	0.1999%	0.0447%	0.1207%	0.4692%	0.0908%	0.4014%
13th	0.03738%	0.000959%	0.03775%	0.03992%	0.0262%	0.0456%	0.1556%	0.0828%	0.1162%	0.1958%	0.0542%	0.116%
15th	0.00013%	0.000428%	0.0013%	0.02133%	0.0149%	0.0371%	0.0805%	0.0679%	0.0558%	0.2747%	0.121%	0.2299%
17th	0.02925%	0.00243%	0.02984%	0.01926%	0.0295%	0.0366%	0.116%	0.0589%	0.0852%	0.4589%	0.1849%	0.5%
19th	0.02938%	0.00178%	0.02923%	0.04736%	0.0458%	0.0643%	0.0894%	0.0602%	0.0523%	0.4767%	0.1275%	0.1767%
THD	0.16%	0.12%	0.16%	1.75%	1.18%	1.59%	2.81%	1.42%	2.3%	3.28%	1.74%	2.76%

Table 4
The parameters of the microgrid under study and its optimal controllers' coefficients.

Parameter	Symbol	Value
Power stage		
Nominal microgrid voltage	V	311.13 V
Nominal microgrid frequency	f	50 Hz
DC-bus voltage	V_{dc}	750 V
Capacitance of filter	C_f	25 µF
Inductance of filter	L_f	1.8 mH
Inductance of output	L_o	1.8 mH
Linear resistive load	R_L	50 Ω
Nonlinear linear load	L_{fb}, C_{fb}, R_L	84 µH, 235 µF, 8/300 Ω
Switching frequency	f_{sw}	15 kHz
Droop Control		
Proportional droop coefficient of frequency	K_{pDP}	6.57e−5 rad/W s
Integral droop coefficient of frequency	K_{iDP}	0.0008396 rad/W
Proportional droop coefficient of voltage amplitude	K_{pDQ}	0.001288 V/VAR
Resistance of virtual impedance	R_{vir}	0.8 Ω
Inductance of virtual impedance	L_{vir}	3.6 mH
Secondary control level		
Proportional and integral terms of frequency secondary controller	K_{psf}	0.065
	K_{isf}	6.84
Proportional and integral terms of voltage secondary controller	K_{psE}	0.573
	K_{isE}	80.42
Synchronization control level		
Proportional and integral terms of frequency synchronization controller	$K_{p\theta}^{syn}$	0.036
	$K_{i\theta}^{syn}$	0.00038
Proportional and integral terms of frequency synchronization controller	K_{pE}^{syn}	0.016
	K_{iE}^{syn}	0.00086

and frequency, generated by the control loops of droop approach and virtual impedance, are successfully nullified utilizing the SCL strategy. The microgrid's voltage amplitude and frequency are recovered smoothly with a faster response than those clarified in Technical Paper (2008) required by the grid. Furthermore, Fig. 23 displays the achievement of the synchronization procedure between the external main grid and the microgrid. It can be observed that the instantaneous voltage waveforms of the external power grid and the microgrid are synchronized, and the difference (error) between them is decreased rapidly. This result highlights the high performance of the synchronization control level for realizing the seamless transitions during connecting/disconnecting to/from the external main power grid. The synchronization process is accomplished considering the synchronization requirements of DG units presented in IEEE standard (2014) demanded by IEEE Std. 1547–2014.

Finally, the active/reactive power-sharing between the two grid-supporting VSIs is illustrated in Fig. 24. From the initiation to t = 0.5 s, the two grid-supporting inverters are connected to the isolated microgrid and supplied the two local nonlinear loads. The power and current demanded by these loads are shared equally between two inverters. After t = 0.5 s, one load is suddenly disconnected; therefore the output active/reactive power and current for each inverter are decreased with equally sharing to only compensate the active/reactive power and current required by one load. From t = 1 s to the end of simulation

Table 5
A comparative study between the proposed optimal PR controllers with their HCs and the previously introduced controllers in the literatures.

Controller type	Conventional PI (Ortega Gonzalez et al., 2014)	Adaptive PI (Elnady and AlShabi, 2019)	PI Plus HCs (Ortega Gonzalez et al., 2014)	PI-P plus HCs (Ortega Gonzalez et al., 2014)	Single input interval type-2 fuzzy integral (Gheisarnejad et al., 2020)	Virtual impedance and voltage compensation scheme (Baghaee et al., 2018)	Harmonic droop compensation (Moussa et al., 2019)	PR plus HCs (Vasquez et al., 2013)	Proposed optimal PR plus HCs
THD_v (%)	8.8	1.6	5.2	2.2	1.66	4.5	1.88	0.63	0.19

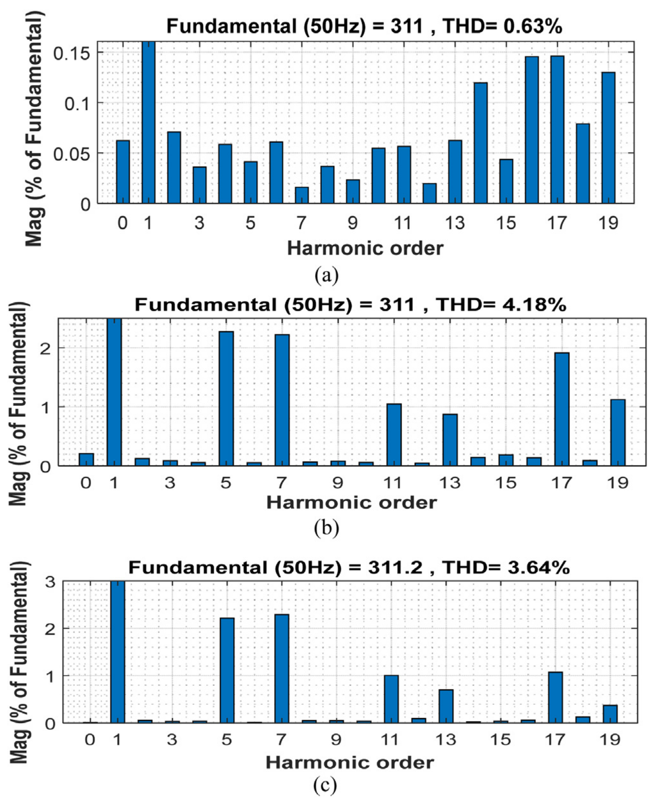

Fig. 14. Harmonics spectrum of the output voltage during linear, nonlinear and composite loads in the case of the voltage and current PR controllers without HCs (a) linear load; (b) nonlinear load; (c) composite load.

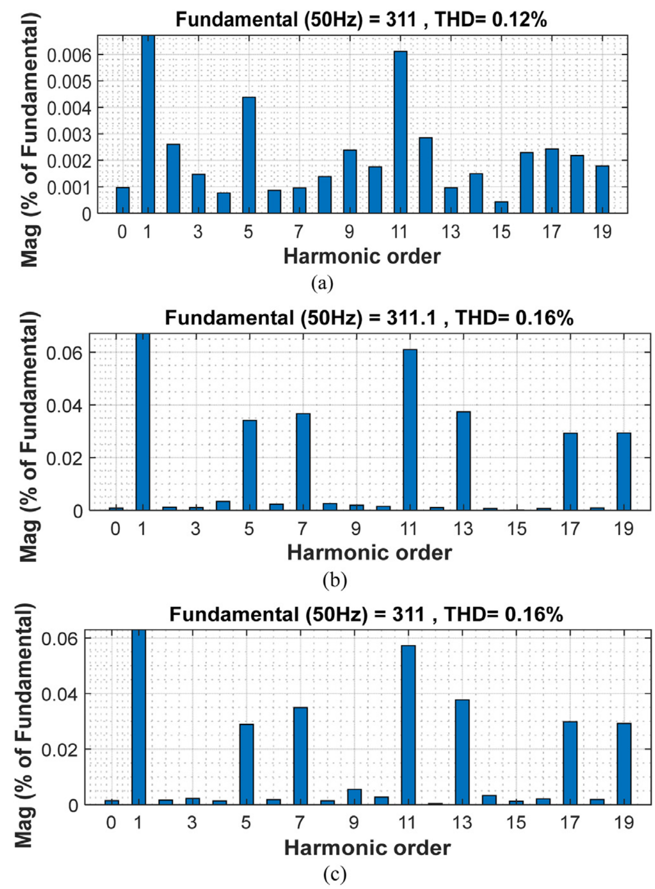

Fig. 15. Harmonics spectrum of the output voltage during linear, nonlinear and composite loads in the case of the proposed voltage and current PR controllers plus their HCs (a) linear load; (b) nonlinear load; (c) composite load.

time, the first grid-supporting VSI is suddenly tripped, the output active/reactive power and current of it becomes zero while those of the second inverter are doubled to compensate the interrupted amounts of the first inverter. The continuity of power supply to the connected load is maintained throughout only one grid-supporting VSI which is alone able to keep the system stability and regulate the microgrid's frequency and voltage. This result indicates that the microgrid system has high reliability and flexibility.

7. Conclusion

This paper has introduced new optimal design guidelines of both the PR controllers along with additional HCs and the PI controllers for three-layer cascaded control implemented on grid-supporting VSIs-based AC microgrid. The three-layer cascaded control approach is carried out in stationary $\alpha\beta$-frame, and comprised of the PCL, SCL and synchronization control level. The design procedures were conducted throughout two stages. The first stage was applied to the PCL to optimally adjust the parameters of its PR controllers along with additional HCs. In this stage, the optimization constraints/objectives aimed to improve the quality of the microgrid's output power represented in minimizing the voltage's harmonics and THD and eliminating the tracking errors for the voltage, current and frequency of the PCL. However, the second stage was employed for the SCL and the synchronization control level to appropriately design their PI controllers' coefficients. The goals of optimization in this stage were to remove the differences in voltage amplitude, frequency and phase angle between the microgrid and the external power grid, and also to reduce the overshoot/undershoot, settling time and steady-state error for the voltage and frequency of the SCL. The two stages are based on a new hybrid optimization algorithm between the HHO and PSO algorithms, namely H-HHOPSO. The suggested microgrid system, based on optimal controllers and HCs, has been modeled and simulated in a MATLAB environment to confirm the effectiveness of the proposed control approach. For the PCL, the performance of proposed H-HHOPSO-based voltage/current PR controllers with additional HCs was evaluated

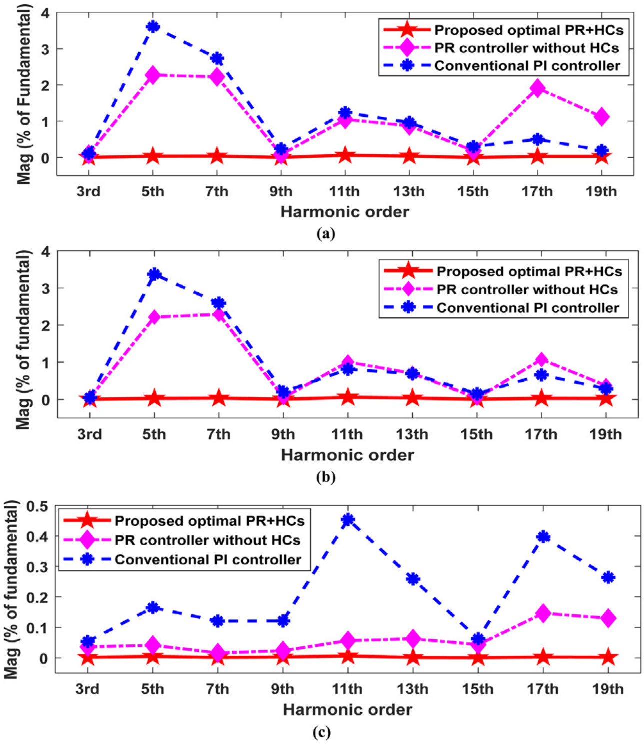

Fig. 16. Comparative graph of individual harmonic magnitudes between the proposed optimal PR controller plus its HCs, PR controllers without HCs, and conventional PI controller under different types of load (a) Nonlinear load (b) Linear plus nonlinear load (c) Linear load.

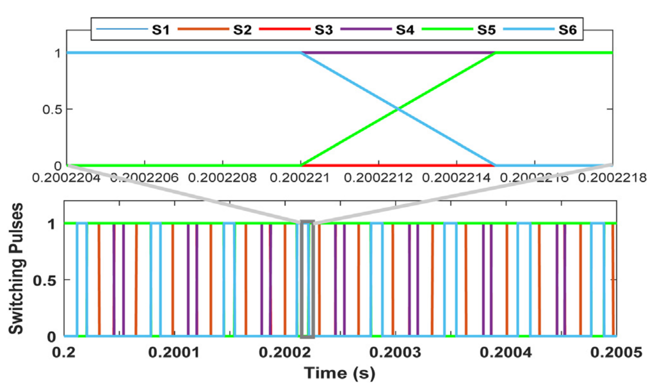

Fig. 17. Six switching pulses for grid-supporting inverter in the case of H-HHOPSO algorithm.

according to IET/IEEE harmonic standards and compared with the conventional PI controllers, and also compared with PSO, GWO and HHO-based PR controllers along with additional HCs. It was noticed that the THD of the microgrid's output voltage under nonlinear load decreased from 5.23% to 4.18% to 3.28% to 2.81% to 1.75% to 0.16% in the cases of conventional PI voltage/current controllers, PR controllers without additional HCs, PSO-based PR controllers with HCs, GWO-based PR controllers with HCs, HHO-based PR controllers with HCs and H-HHOPSO-based PR controllers with HCs, respectively. It can be concluded that the proposed optimal controllers and HCs have a superior performance in minimizing both individual harmonic amplitudes and THD of the microgrid's output voltage. Moreover, they have a high tracking behavior for the references of voltage, current and

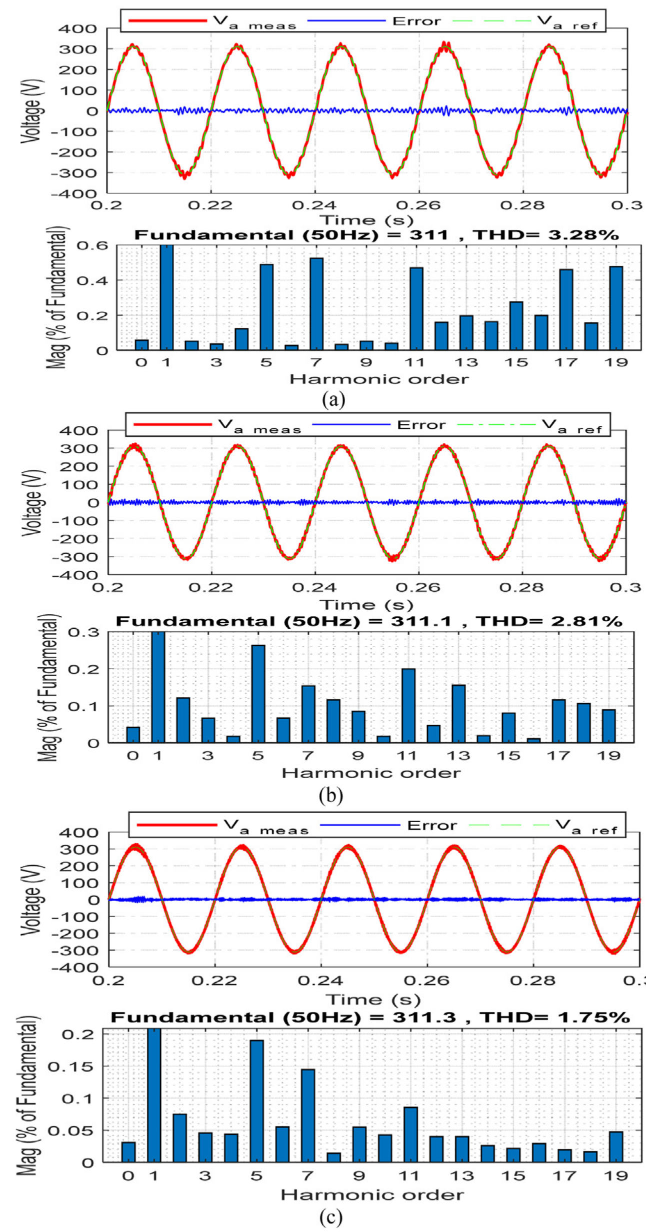

Fig. 18. Harmonics spectrum of the output voltage during nonlinear load in the cases of PSO, GWO and HHO-based voltage and current PR controllers with their HCs (a) PSO (b) GWO (c) HHO.

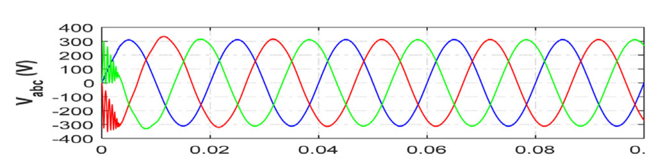

Fig. 19. The microgrid voltage during nonlinear loads in case of using the optimal current/voltage PR controllers with HCs.

frequency with the minimum values of oscillations. Additionally, the synchronization process between the external main grid and the microgrid is achieved fast and accurately with acceptable insignificant differences in voltage, frequency and phase angle. Furthermore, the active/reactive power-sharing is appropriately

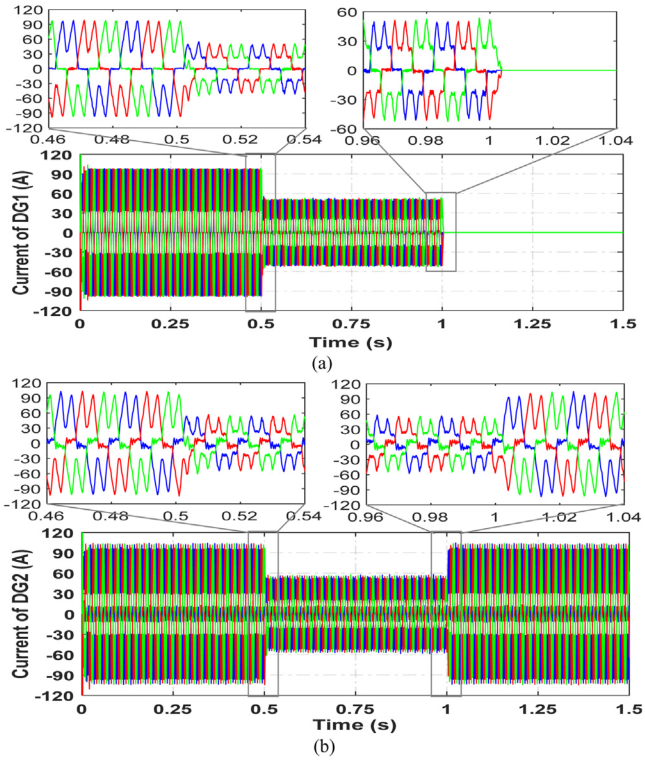

Fig. 20. The waveforms of output currents for the two paralleled grid-supporting inverters sharing the two nonlinear loads via the droop control methodology (a) DG1; (b) DG2.

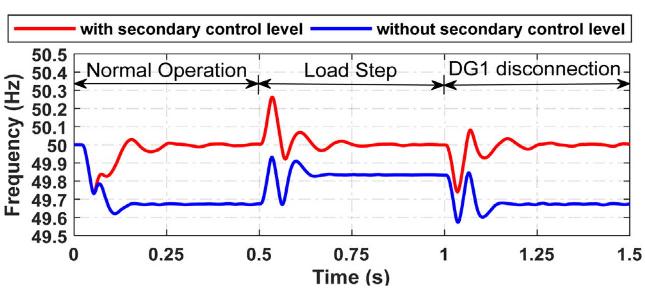

Fig. 21. The microgrid's frequency with and without secondary control.

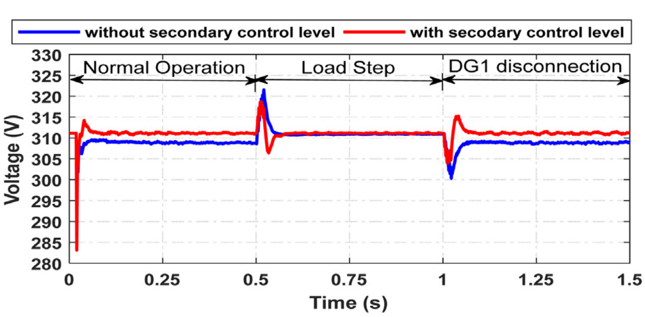

Fig. 22. The microgrid's voltage amplitude with and without secondary control.

realized among the parallel grid-supporting VSIs. It can be concluded that the proposed optimal controllers and HCs have a superior performance in minimizing both individual harmonic amplitudes and THD of the microgrid's output voltage.

Our future work will be extended in this research area to test the effectiveness of the proposed optimal controllers and HCs

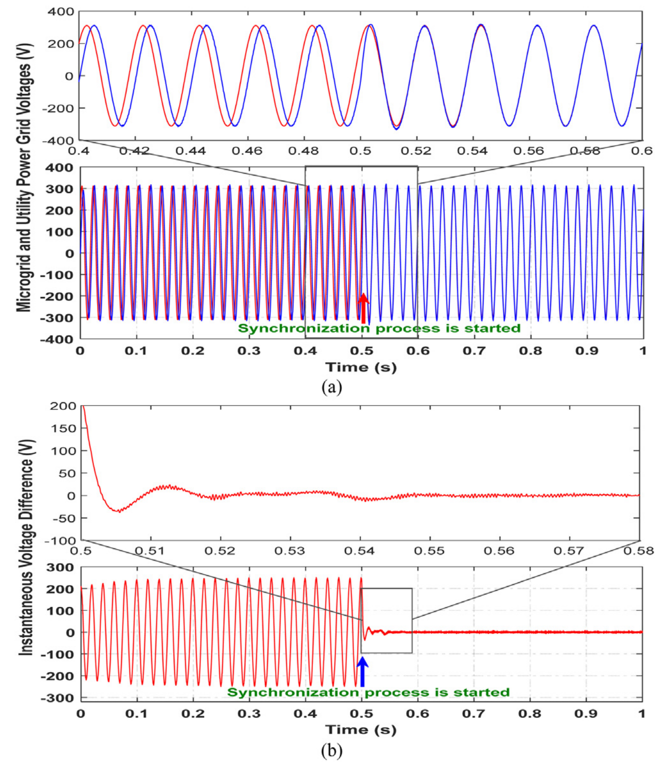

Fig. 23. The achievement of the synchronization procedure between the external main grid and the microgrid (a) External main grid and microgrid voltage during synchronization process (b) difference error of synchronization.

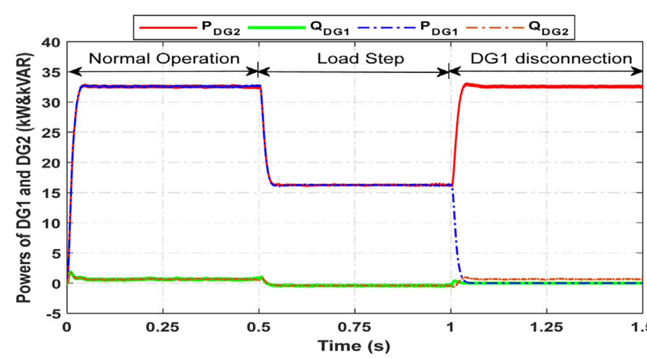

Fig. 24. The active/reactive power-sharing between the two grid-supporting VSIs.

under the unbalanced loads and voltage flickers. Moreover, our future work will employ these proposed optimal controllers with their HCs in AC microgrid architecture including multiple micro-sources such as PV panels, wind turbines, batteries and fuel cells. Furthermore, in the future work, the challenge represented in the complexity of experimental validation for the proposed system will be overcome using low cost hardware-in-the-loop testbed.

References

Andishgar, M.H., Gholipour, E., Hooshmand, R.A., 2017. An overview of control approaches of inverter-based microgrids in islanding mode of operation. Renew. Sustain. Energy Rev. 80, 1043–1060.

Baghaee, H.R., Mirsalim, M., Gharehpetan, G.B., Talebi, H.A., 2018. Nonlinear load sharing and voltage compensation of microgrids based on harmonic power-flow calculations using radial basis function neural networks. IEEE Syst. J. 12 (3), 2749–2759.

Bidram, A., Davoudi, A., 2012. Hierarchical structure of microgrids control system. IEEE Trans. Smart Grid 3 (4), 1963–1976.

Ebrahim, M.A., Ayoub, B.A.A., Nashed, M.N.F., Osman, F.A.M., 2021. A novel hybrid-HHOPSO algorithm based optimal compensators of four-layer cascaded control for a new structurally modified AC microgrid. IEEE Access 9, 4008–4037.

Ebrahim, M.A., Fattah, R.M.A., Saied, E.M.M., Maksoud, S.M.A., Khashab, H.E., 2020. Real-time implementation of self-adaptive salp swarm optimization-based microgrid droop control. IEEE Access 8, 185738–185751.

Elnady, A., AlShabi, M., 2019. Operation of parallel inverters in microgrid using new adaptive PI controllers based on least mean fourth technique. Math. Probl. Eng..

Farrokhabadi, M., Cañizares, C.A., Simpson-Porco, J.W., Nasr, E., Fan, L., 2020. Microgrid stability definitions, analysis, and examples. IEEE Trans. Power Syst. 35 (1), 13–29.

Gao, T., Lin, Y., Chen, D., Xiao, L., 2020. A novel active damping control based on grid-side current feedback for LCL-filter active power filter. Energy Rep. 6 (Supplement 9), 1318–1324.

Gheisarnejad, M., Mohammadi-Moghadam, H., Boudjadar, J., Khooban, M.H., 2020. Active power sharing and frequency recovery control in an islanded microgrid with nonlinear load and nondispatchable DG. IEEE Syst. J. 14 (1), 1058–1068.

Golsorkhi, M.S., Savaghebi, M., Lu, D.D., Guerrero, J.M., Vasquez, J.C., 2017. A GPS-based control framework for accurate current sharing and power quality improvement in microgrids. IEEE Trans. Power Electron. 32 (7), 5675–5687.

Guerrero, M., Chandorkar, M., Lee, T., Loh, P.C., 2013. Advanced control architectures for intelligent microgrids—Part I: Decentralized and hierarchical control. IEEE Trans. Ind. Electron. 60 (4), 1254–1262.

Guerrero, J.M., Vasquez, J.C., Matas, J., de Vicuna, L.G., Castilla, M., 2011. Hierarchical control of droop-controlled AC and DC microgrids—A general approach toward standardization. IEEE Trans. Ind. Electron. 58 (1), 158–172.

Gui, Y., Wei, B., Li, M., Guerrero, J.M., Vasquez, J.C., 2018. Passivity-based coordinated control for islanded AC microgrid. Appl. Energy 229, 551–561.

Guo, W., Mu, L., 2016. Control principles of micro-source inverters used in microgrid. Prot. Control Mod. Power Syst. 1 (1), 1–7.

Han, Y., Shen, P., Zhao, X., Guerrero, J.M., 2017. Control strategies for islanded microgrid using enhanced hierarchical control structure with multiple current-loop damping schemes. IEEE Trans. Smart Grid 8 (3), 1139–1153.

Hashempour, M.M., Savaghebi, M., Vasquez, J.C., Guerrero, J.M., 2016. A control architecture to coordinate distributed generators and active power filters coexisting in a microgrid. IEEE Trans. Smart Grid 7 (5), 2325–2336.

He, J., Li, Y.W., 2013. Hybrid voltage and current control approach for DG-grid interfacing converters with LCL filters. IEEE Trans. Ind. Electron. 60 (5), 1797–1809.

He, J., Li, Y.W., Blaabjerg, F., 2015. An enhanced islanding microgrid reactive power, imbalance power, and harmonic power sharing scheme. IEEE Trans. Power Electron. 30 (6), 3389–3401.

Heidari, A.A., Mirjalili, S., Faris, H., Aljarah, I., Mafarja, M., Chen, H., 2019. Harris hawks optimization: Algorithm and applications. Future Gener. Comput. Syst. 97, 849–872.

Hua, H., Cao, J., Yang, G., Ren, G., 2018. Voltage control for uncertain stochastic nonlinear system with application to energy internet: Non-fragile robust h∞ approach. J. Math. Anal. Appl. 463 (1), 93–110.

Hua, H., Qin, Y., He, Z., Li, L., Cao, J., 2020. Energy sharing and frequency regulation in energy internet via mixed H2/H∞ control with Markovian jump. CSEE J. Power Energy Syst..

2014. Ieee standard for interconnecting distributed resources with electric power systems - amendment 1. In: IEEE Std 1547a-2014 (Amendment To IEEE Std 1547-2003). pp. 1–16.

Jumani, T.A., Mustafa, M.W., Rasid, M.M., Mirjat, N.H., Leghari, Z.H., Saeed, M.S., 2018. Optimal voltage and frequency control of an islanded microgrid using grasshopper optimization algorithm algorithm. Energies 11 (11), 3191.

Kennedy, J., Eberhart, R.C., 1995. Particle swarm optimization. In: Proceedings of ICNN'95- International Conference on Neural Networks IV. IEEE Service Center, USA, Piscataway, NJ, pp. 1942–1948.

Li, Y.W., 2009. Control and resonance damping of voltage-source and current-source converters with LC filters. IEEE Trans. Ind. Electron. 56 (5), 1511–1521.

Meng, X., Liu, J., Liu, Z., 2019. A generalized droop control for grid-supporting inverter based on comparison between traditional droop control and virtual synchronous generator control. IEEE Trans. Power Electron. 34 (6), 5416–5438.

Mirjalili, S., Mirjalili, S.M., Lewis, A., 2014. Grey wolf optimizer. Adv. Eng. Softw. 69, 46–61.

Moussa, H., Martin, J.-P., Pierfederici, S., Meibody-Tabar, F., Moubayed, N., 2019. Voltage harmonic distortion compensation with nonlinear load power sharing in low-voltage islanded microgrid. Math. Comput. Simulation 158, 32–48.

Ortega Gonzalez, R., Sosa Saavedra, J.C., Carranza Castillo, O., Garcia Ortega, V., 2014. Comparison controllers for inverter operating in island mode in microgrids with linear and nonlinear loads. IEEE Lat. Amer. Trans. 12 (8), 1441–1448.

Shrivastava, S., Subudhi, B., Das, S., 2018. Distributed voltage and frequency synchronisation control scheme for islanded inverter-based microgrid. IET Smart Grid 1 (2), 48–56.

Shuvo, S., Hossain, E., Khan, Z.R., 2020. Fixed point implementation of grid tied inverter in digital signal processing controller. IEEE Access 8, 89215–89227.

Sreekumar, P., Khadkikar, V., 2016. A new virtual harmonic impedance scheme for harmonic power sharing in an islanded microgrid. IEEE Trans. Power Deliv. 31 (3), 936–945.

Sun, Y., Zhong, C., Hou, X., Yang, J., Han, H., Guerrero, J.M., 2017. Distributed cooperative synchronization strategy for multi-bus microgrids. Int. J. Electr. Power Energy Syst. 86, 18–28.

2008. Technical paper – definition of a set of requirements to generating units. UCTE.

Vasquez, J.C., Guerrero, J.M., Savaghebi, M., Eloy-Garcia, J., Teodorescu, R., 2013. Modeling, analysis, and design of stationary-reference-frame droop-controlled parallel three-phase voltage source inverters. IEEE Trans. Ind. Electron. 60 (4), 1271–1280.

Vu, T.K., Seong, S.j., 2010. Comparison of PI and PR controller based current control schemes for single-phase grid-connected PV inverter. Korea Acad. Ind. Soc. 11 (8), 2968–2974.

yan Jiang, X., He, C., Jermsittiparsert, K., 2020. Online optimal stationary reference frame controller for inverter interfaced distributed generation in a microgrid system. Energy Rep. 6, 134–145.

Yazdavar, A.H., Azzouz, M.A., El-Saadany, E.F., 2019. A novel decentralized control scheme for enhanced nonlinear load sharing and power quality in islanded microgrids. IEEE Trans. Smart Grid 10 (1), 29–39.

Zammit, D., Staines, C.S., Apap, M., Licari, J., 2017. Design of PR current control with selective harmonic compensators using matlab. J. Electr. Syst. Inf. Technol. 4 (3), 347–358.

Zhong, Q., 2013. Harmonic droop controller to reduce the voltage harmonics of inverters. IEEE Trans. Ind. Electron. 60 (3), 936–945.

Zhou, Y., Ngai-Man Ho, C., 2016. A review on microgrid architectures and control methods. In: 2016 IEEE 8th International Power Electronics and Motion Control Conference (IPEMC-ECCE Asia). pp. 3149–3156.

Load frequency control strategy using large-scale multi-agent deep reinforcement learning

Priya Chandan Satpathy, *Department of Electrical and Communication Engineering, Aryan Institute of Engineering & Technology, Bhubaneswar, priyachandan.satpathy57@outlook.com*

Supriya Nayak, *Department of Electronics and Communication Engineering , NM Institute of Engineering & Technology, Bhubaneswar, supriyanayak443@gmail.com*

Manoj Mohanta, *Department of Electrical and Electronics Engineering, Capital Engineering College, Bhubaneswar, manoj.mohanta62@outlook.com*

Alekha Sahoo, *Department of Electrical Engineering , Raajdhani Engineering College, Bhubaneswar, alekha.sahoo241@gmail.com*

Keywords:
Performance-based frequency regulation market mechanism
Deep reinforcement learning
Grid-area coordinated load frequency control strategy
Multi-agent deep deterministic policy gradient algorithm
Interconnected power grid
Load frequency control

A B S T R A C T

In order to enable full participation of high-performance units controlled by different dispatching centers in the performance-based frequency regulation market, a data-driven grid-area coordinated load frequency control (GAC-LFC) strategy using unified performance-based frequency regulation market mechanism is proposed. The strategy takes into account the coordination of LFC controllers in different areas of the interconnected power grid, and accommodates a large number of high-performance units controlled by dispatching centers in secondary frequency regulation. In addition, an effective exploration-based multi-agent deep deterministic policy gradient (EE-MADDPG) algorithm is proposed as the framework algorithm. In this algorithm, the LFC controller controlled by the grid-dispatching center and the LFC controller controlled by the area-dispatching center in each area are treated as different agents. Through centralized training with decentralized execution, the coordination of LFC controllers controlled by different levels of dispatching centers in different areas can be realized. Moreover, the algorithm introduces effective exploration strategies, agents operating on various principles, and artificial intelligence functions based on imitation learning and curriculum learning, which altogether constitute a more robust strategy. Through the simulation of the four-area LFC model of the China Southern Grid (CSG), it is demonstrated that the proposed method can simultaneously call more high-performance units, improve multi-area LFC control performance, and reduce the frequency regulation mileage payment in each area.

1. Introduction

Automatic Generation Control (AGC) is an important means of realizing active frequency control in the power system. The grid-dispatching center and the area-dispatching center monitor the area control error (ACE) in real time, and they control ACE by regulating the output of the grid-units and area-units, respectively (Xi et al., 2018). An interconnected power grid composed of multiple regional power grids uses Control Performance Standard (CPS) and frequency regulation mileage criteria to assess the performance of the LFC in each area (Xi et al., 2021).

Most of the independent system operators (ISOs) designed for high power supply area coverage and for covering many areas adopt the grid-area dispatch LFC operation mode termed "unified dispatch and hierarchical management", for example, the State Grid Corporation of China (SGCC), PJM, China Southern Power Grid (CSG), etc. (Zhang et al., 2020). In the LFC structure of these ISOs, the power grid (Ghasempour and Lou, 2017) usually includes a grid-dispatching center and several area-dispatching centers (Li et al., 2022b). Each area-dispatching center corresponds to an LFC area, and each different dispatching center is autonomous. AGC units are divided into grid-units and area-units; and LFC control is divided into grid-control areas and area-control areas (Yu et al., 2011a).

However, this LFC mode is affected by the following problems:

(1) There are coordination problems between the LFC in different areas, and the LFC among grid-control areas and area-control areas. The variation in response speeds among the area-units to frequency changes leads to overregulation or under-regulation, thereby causing the system frequency to fluctuate.

(2) The grid-unit controlled by the grid-dispatching center plays a limited role in frequency regulation. The grid-unit does not actively participate in frequency regulation. It will participate in the secondary frequency regulation only when the frequency deviation is large, which increases the difficulty of regulating the frequency and tie power in each area.

Nomenclature

A_i	Control penalties of $agent^i{}_A$
a_i^j	The action of the i agent in j step
a_i	Actions of agent
a_j^i	Generation factor of jth unit in ith Area
$a_A{}^{Area}$	Action of $\text{agent}_A{}^{\text{Area}}$
$a_B{}^{Area}$	Action of $\text{agent}_B{}^{\text{Area}}$
$a_C{}^{Area}$	Action of $\text{agent}_C{}^{\text{Area}}$
$a_D{}^{Area}$	Action of $\text{agent}_D{}^{\text{Area}}$
$a^j_{system-5-T}$	Action of 5-follows
$a^j_{system-7-T}$	Action of 7-follows
$a_A{}^{grid}$	Action of $\text{agent}_A{}^{\text{grid}}$
$a_B{}^{grid}$	Action of $\text{agent}_B{}^{\text{grid}}$
$a_C{}^{grid}$	Action of $\text{agent}_C{}^{\text{grid}}$
$a_D{}^{grid}$	Action of $\text{agent}_D{}^{\text{Grid}}$
B_i	Natural frequency coefficient of ith area
B	Coefficient
C_{CF1}	CF1 indicator
C_{CPS1}	CPS1 indicator
D_i^j	Total regulation mileage payment of jth unit in ith Area
D	Coefficient
$D_{\text{total}}^{i-\text{ grid}}$	Regulation mileage payment of ith grid-unit
$D_{\text{total}}^{i-\text{ area}}$	Regulation mileage payment of ith area-unit
e_i^{ACE}	ACE of ith Area
$e_{\text{ACE}_{\text{AVEmin}}}$	Average value in one minute of ACE
e_i^D	The sample created by the Demonstrator
e_i^e	The sample created by the explorer
$F\ (t)$	Objective function of controller in the Demonstrator
f_c	Objective function of GAC-LFC
G_i	Control reward term of $agent^i{}_G$
g	Deterministic policy gradient
H_i	Coefficient of ith area
$J(\theta)$	The objective function of the agent
$L(\theta^Q)$	Loss function
$L_A{}^{grid}$	Loss of $\text{agent}_A{}^{\text{grid}}$
$L_B{}^{grid}$	Loss of $\text{agent}_B{}^{\text{grid}}$
$L_C{}^{grid}$	Loss of $\text{agent}_C{}^{\text{grid}}$
$L_D{}^{grid}$	Loss of $\text{agent}_D{}^{\text{Grid}}$
$L_A{}^{Area}$	Loss of $\text{agent}_A{}^{\text{Area}}$
$L_B{}^{Area}$	Loss of $\text{agent}_B{}^{\text{Area}}$
$L_C{}^{Area}$	Loss of $\text{agent}_C{}^{\text{Area}}$
$L_D{}^{Area}$	Loss of $\text{agent}_D{}^{\text{Area}}$
N	Number of control intervals of regulation services
$N_{Gaussian}$	Gaussian noise
N_{OU}	OU noise
n	Number of AGC units
o_i^j	Observation of the ith agent
P_j^i	Output of jth unit in ith Area
P_{jG}^{max-i}	Maximum adjustable power of jth unit in ith Area
P_{ci}	Generation command
P_i^{max}	Maximum adjustable capacity
$\bar{Q}^*(s', a')$	Target Q function
R_i	Rewards of agent
$r(k)$	Reward function of kth control interval
S_i^{pre}	Regulation accuracy of the ith unit
s_i	States of agent
T_{ti}	Time constant of ith area
T_{gi}	Unit time constant of ith area
$V_i(s)$	Value function
$\lvert V_i \rvert$	ith node voltage
$\lvert V_j \rvert$	jth node voltage
X_{ij}	Reactance of transmission line ij
y_t^1	Target value of critic 1
y_t^2	Target value of critic 2

Greek symbols

γ	Discount factor
ΔA_m	The amplitude of the sine function of Area A
ΔB_m	The amplitude of the sine function of Area C
ΔC_m	The amplitude of the sine function of Area B
ΔD_m	The amplitude of the sine function of Area D
$\Delta f_{\text{AVE1 min}}$	Average value in one minute of Frequency deviation
Δf_i	Frequency deviation of ith Area
Δf_i	Frequency deviation of ith Area
$\Delta P^i_{order-\Sigma}$	Total generation power commends of ith area
ΔP_j^{min-i}	Minimum adjustable capacity of jth unit in ith Area
$\Delta P_j^{\text{out}-i}(k)$	Regulation power output of jth unit in ith Area
$\Delta P^i_{order-j}$	Generation power commends of jth unit in ith Area
ΔP_i^{in}	Input of generation power commend of ith unit
ΔP_i^{min}	Minimum AGC regulation capacity of the ith frequency regulation unit
ΔP_i^{out}	Regulation output of the ith unit
ΔP_i^{rate}	Maximum regulation rate of ith unit
ΔP_i^{out}	Output of ith unit
ΔP_i^{max}	Maximum regulation capacity of the ith frequency regulation unit
ΔP_i^{rate}	Ramp rate of the ith unit
ΔP_j^{max-i}	Maximum adjustable capacity of jth unit in ith Area

(3) In the conventional regulation mode, the grid-units and area-units are separately regulated and divided into different control areas, which leads to wastage of frequency regulation resources. Therefore, the conventional regulation mode is not suitable for the performance-based frequency regulation market. In this mode, the grid-unit will be repeatedly regulated. In addition, as a high-quality frequency regulation unit, the grid-unit exists in a different control area from other area-units that belong

$\Delta P_j^{\text{rate}-i}$	Ramp rate of *jth* unit in *ith* Area
ΔP_i^{out}	Regulation power output of units in *ith* Area
$\Delta P_{\text{error}\,i}^2(t)$	Power error of *ith* Area
$\Delta P_{\text{order}}^{i-\text{ Area}}$	Power generation command of *i*th Area-unit
$\Delta P_{\text{order}}^{i-\text{ grid}}$	Power generation command of *i*th grid-unit
$\Delta P_{Gi}^{\text{area}}$	Output of *i*th area-unit
$\Delta P_{Gi}^{\text{grid}}$	Output of *i*th grid-unit
$\nabla J(\phi)$	Policy gradient
$\nabla_{\phi^\pi} J_A^{grid}$	Policy gradient of $\text{agent}_A{}^{\text{grid}}$
$\nabla_{\phi^\pi} J_B^{grid}$	Policy gradient of $\text{agent}_B{}^{\text{grid}}$
$\nabla_{\phi^\pi} J_C^{grid}$	Policy gradient of $\text{agent}_C{}^{\text{grid}}$
$\nabla_{\phi^\pi} J_D^{grid}$	Policy gradient of $\text{agent}_D^{\text{Grid}}$
$\nabla_{\phi^\pi} J_A^{Area}$	Policy gradient of $\text{agent}_A{}^{\text{Area}}$
$\nabla_{\phi^\pi} J_B^{Area}$	Policy gradient of $\text{agent}_B{}^{\text{Area}}$
$\nabla_{\phi^\pi} J_C^{Area}$	Policy gradient of $\text{agent}_C{}^{\text{Area}}$
$\nabla_{\phi^\pi} J_D^{Area}$	Policy gradient of $\text{agent}_D{}^{\text{Area}}$
$\nabla_{\theta_i^\pi} J_i$	Gradient of actor in agent_i
ε	Noise
ε_1	The root-mean-square control target
θ_A^{rand}	The phase of the sine function disturbance of Area A
θ_C^{rand}	The phase of the sine function disturbance of Area C
θ_B^{rand}	The phase of the sine function disturbance of Area B
θ_D^{rand}	The phase of the sine function disturbance of Area D
θ^Q	Critics network parameters
μ_1	Weight coefficient
μ_2	Weight coefficient
μ_3	Weight coefficient
π	Policy of agent
π^*	Optimal policy
π_i (s)	Policy function of agent_i
$\pi'\left(s_{i+1}\vert\theta^{\mu'}\right)$	Target policy function
π^*	Optimal policy
$\pi_\phi{}^l(s)$	Policy of *lth* ε-explorer
$\pi_\phi{}^j(s)$	Policy of *jth* OU-explorer
$\pi_\phi{}^m(s)$	Policy of *mth* Gaussian-explorer
χ	Target entropy coefficient
ω_3	Weighting coefficient

to the same area geographically, and cannot participate in the performance-based frequency regulation market (Li et al., 2021a,b,c).

To date, it has not been possible to realize the coordinated operation of grid-LFC and area-LFC coordinated for each ISO (Zhang et al., 2021). At present, scholars have focused mainly on the following techniques for realizing coordination between LFC controllers in different area-dispatching centers covering different areas:

(1) *Fuzzy control*: Yousef et al. (2014) proposed an adaptive fuzzy logic control and applied it to a three-area LFC model, which improved the adaptability of LFC controllers in different areas and improved the frequency regulation performance accordingly. However, because the fuzzy control rules adopted by this algorithm are too simple, the control accuracy of the algorithm is low, which leads to the problem of frequency overregulation. Ghafouri et al. (2018) proposed a hierarchical coordinated control algorithm based on an adaptive fuzzy algorithm to achieve load frequency control, and designed an adaptive fuzzy algorithm to optimize the weight vector of the coordinated control performance, while considering the coordination of multi-area LFC controllers and the coordination of grid-LFC controllers. However, because this type of algorithm still divides grid-units and area-units into different control areas, its system frequency regulation ability is restricted.

(2) *Sliding mo*de control. Kumar et al. (2017) proposed a sliding mode control algorithm and applied it to a multi-area LFC model, and designed a sliding mode control strategy based on nonlinear switching sliding mode surfaces to advantageously achieve optimal control of multi-system load frequencies. Klimontowicz et al. (2016) designed a sliding mode controller as the load frequency controller of the interconnected power grid, and used genetic algorithms (Shirazi and Menhaj, 2006) to optimize the gain parameters and polynomial coefficient vectors in the sliding mode controller to achieve the optimal control of multi-area LFC. However, due to the chattering problem associated with sliding mode control algorithm, this type of algorithm cannot be applied for LFC control in an interconnected power grid.

(3) *Robust control*

An adaptive robust control was proposed in Wang et al. (1994), which can improve the secondary frequency regulation performance of the interconnected power grid. Overall, the above robust control methods all have good adaptive capabilities and can improve the frequency regulation capability of a multi-area LFC. However, because robust controllers generally do not work in the optimal state, the steady-state accuracy of this type of controller is poor.

Li et al. (2014) used the active disturbance rejection controller to control the interconnected power system containing photovoltaics, and used the adaptive ability of the active disturbance rejection controller to adapt to the influence of LFC in other areas. However, the authors did not consider the non-linear characteristics of the multi-area interconnected power system, with which the method is incompatible.

Most of the above algorithms consider the coordination of multi-area LFC controllers in the interconnected grid, but few consider the coordination of grid-LFC and area-LFC. Nowadays, the coordination of grid-LFC and area-LFC is realized mainly via a layered optimization method, in which the grid-units and the area-units are divided into different control areas. Zhang et al. (2015) proposed a predictive control algorithm with a multi-area hierarchical distributed model, in order to improve the coordination performance of multi-area controllers. However, because MPC requires accurate modeling of the system, it cannot easily be adapted for complex power systems. Variani and Tomsovic (2013) proposed an LFC method based on the method of differential flatness, in which a hierarchical distributed LFC strategy involving global optimization objectives was constructed, and the global optimization of multi-area LFC in the grid-area coordination control framework was considered. However, this requires each controller to obtain the state variables of the whole system when making online decisions, which in a grid-LFC framework is a difficult objective.

In general, researchers have not yet managed to solve the problem of poor coordination between the grid-LFC and area-LFC and the inter-area LFC controller, which leads to low frequency regulation performance of the system and significant wastage of frequency regulation resources.

With the development of AI technology, a large number of learning-based multi-agent algorithms have been proposed, including the "wolf climbing" reinforcement learning algorithm (Xi et al., 2015), multi-agent deep double Q learning action discovery (DDQN-AD) algorithm (Xi et al., 2020), and multi-agent deep deterministic policy gradient (MADDPG) algorithm (Yan and Xu, 2020). Since they combine the perception ability of deep learning with the adaptability of reinforcement learning, these learning-based algorithms can consider the coordination of multiple agents using data-driven strategies, and each can be regarded as an ideal coordinated control algorithm. However, due to their low robustness, their LFC performance is poor.

Therefore, based on learning-based multi-agent algorithms, a data-driven grid-area coordinated LFC strategy for a unified performance-based frequency regulation market is proposed. The strategy solves the coordination of poor LFC controllers in different areas in the interconnected power grid as it calls more high-performance units controlled by different levels of dispatching centers to participate in the unified performance-based frequency regulation market and realize their coordination. In addition, an effective exploration-based multi-agent deep deterministic policy gradient (EE-MADDPG) algorithm is proposed as the framework algorithm. In this algorithm, the LFC controller controlled by the grid-dispatching center and the LFC controller controlled by the area-dispatching center in each area are regarded as different agents. Through centralized training with decentralized execution, the coordination of LFC controllers controlled by different levels of dispatching centers in different areas can be realized. Moreover, the algorithm introduces effective exploration strategies, agents operating on a variety of principles, and AI functions based on imitation learning and curriculum learning, which altogether improve the training efficiency and exploration capabilities of the algorithm, thus realizing a more robust strategy. Through a simulation of a four-area LFC model based on CSG, it is demonstrated that the proposed method can simultaneously call more high-performance units, improve multi-area LFC control performance, reduce the frequency regulation mileage payment in each area, and realize optimal grid-area coordinated load frequency control.

The innovations proposed in this study are presented below:

(1) An area-unified performance-based frequency regulation market mode considering grid-LFC and area-LFC coordination is developed. Based on such a this, the grid-unit and area-unit are regulated in the identical control area and then managed by different agents. Compared with traditional frequency regulation mode (Li et al., 2021a,b,c; Xi et al., 2018, 2021; Zhang et al., 2020; Yu et al., 2011a; Li and Yu, 2021a; Li et al., 2021; Li and Yu, 2021b), this mode calls more high-quality frequency regulation units to participate in the regulation of the system, thus reducing wastage of frequency regulation resources.

(2) The robustness and adaptability exhibited by traditional area-grid control coordination strategies (Yousef et al., 2014; Ghafouri et al., 2018; Klimontowicz et al., 2016; Zhang et al., 2015; Xi et al., 2020) are low and ineffective. To improve the performance exhibited by area-grid control coordination strategies, a data-driven grid-area coordinated LFC strategy is proposed based on a unified performance-based frequency regulation market mechanism. The LFC controller controlled by the grid-dispatching center and the LFC controller controlled by the area-dispatching center in the respective area are treated as different agents. Through centralized training with decentralized execution, it is possible to coordinate the LFC controllers controlled by different levels of dispatch centers in different areas.

(3) The robustness and low learning efficiency of traditional deep reinforcement learning algorithms (Xi et al., 2020; Yan and Xu, 2020; Horgan et al., 2018; Fujimoto et al., 2019; Lowe et al., 2017). To improve the robustness and training efficiency of deep reinforcement learning algorithms, the EE-MADDPG algorithm is proposed as the framework algorithm. Such an algorithm can introduce effective exploration strategies, agents operating on various principles, as well as AI functions by complying with imitation learning and curriculum learning, thereby constituting a more robust strategy on the whole.

(4) Traditional area-grid control coordination strategies (Yousef et al., 2014; Ghafouri et al., 2018; Klimontowicz et al., 2016; Zhang et al., 2015; Xi et al., 2020) can only achieve single-objective optimal control, whereas they fail to achieve comprehensive optimal of performance and regulation mileage payment. The proposed method is capable of simultaneously calling more high-performance units to participate in the performance-based frequency regulation market, effectively improving the performance and CPS1 index of multi-area LFC, reducing the frequency regulation mileage payment, and achieving the optimal grid-area coordinated load frequency control of the multi-area LFC.

The structure of the paper is as follows: the LFC model is introduced in Section 2, and the proposed method introduced in Section 3; the case studies are introduced in Section 4, and the conclusions are proposed in Section 5.

2. LFC model for the performance-based frequency regulation market

2.1. Interconnected grid

2.1.1. LFC model

By analyzing the transfer function of the tie line, a dynamic model of the tie line can be established. In the process of frequency regulation, the regulation output is the difference between $\Delta P_{T,i}$ and the load increment $\Delta P_{D,i}$. It is balanced by three factors related to power.

The power increment brought by the kinetic energy of the units- $\frac{d}{dt}W_i$,

Load power change due to the frequency regulation effect of the load- $\Delta P'_{D,i}$,

Line power of the tie line- $\Delta P_{tie,i}$

Therefore, its energy balance equation is shown as follows (Li et al., 2021a,b,c):

$$\Delta P_{T,i} - \Delta P_{D,i} = \frac{d}{dt}W_i + \Delta P'_{D,i} + \Delta P_{te,i} \tag{1}$$

The power increment $\Delta P_{tie,i}$ on the tie line is the sum of the power changes of the area i and all other areas.

$$\Delta P_{\text{tie},i} = \sum_{j=1,i\neq j}^{n} \Delta P_{\text{tie, ij}} \tag{2}$$

The transmission power in the transmission line is (Li et al., 2021a,b,c):

$$P_{ij} = -P_{ji} = \frac{|U_i|\,|U_j|}{X}\sin\left(\theta_i - \theta_j\right) \tag{3}$$

$$\Delta\dot{f}_i = \frac{1}{2H_i}\left(\Delta P_{mi} + \Delta P_{RESi} - \Delta P_{Li} - \Delta P_{tie,i}\right) - \frac{D}{2H_i}\Delta f_i \tag{4}$$

$$\Delta\dot{P}_{mi} = \frac{1}{T_{ti}}\Delta P_{gi} - \frac{1}{T_{ti}}\Delta P_{mi} \tag{5}$$

$$\Delta\dot{P}_{gi} = \frac{1}{T_{gi}}\Delta P_{ci} - \frac{1}{R_i T_{gi}}\Delta f_i - \frac{1}{T_{gi}}\Delta P_{gi} \tag{6}$$

2.1.2. Conventional load frequency regulation mode

Interconnected large power grids generally use ACE to control frequency and power exchange. In the frequency control mode of the China Southern Power Grid, flat frequency control (FFC) is adopted in the grid-dispatch control area (Li et al., 2021a,b,c):

$$ACE = K\Delta f \tag{7}$$

The method proposed in this paper does not set the grid-dispatching control area specifically, but divides all the grid-units into control areas. Nevertheless, the area-LFC controller and the grid-LFC controller are still regarded as agents. The four areas represent four provinces, whereby each province has two LFC controllers. The four-region LFC model employs TBC according to the following equation (Li et al., 2022a):

$$ACE = \Delta P_{\mathrm{tie}} + B\Delta f \tag{8}$$

2.2. Frequency regulation mileage

In the unified performance-based frequency regulation market, frequency regulation mileage is a new quantitative indicator that reflects the actual output of each unit. According to the CSG rules, both grid-unit and area-unit need to count frequency regulation mileage, the calculation formula of frequency regulation mileage of the ith unit in each control interval is (Zhang et al., 2021):

$$M_i(k) = \left|\Delta P_i^{\mathrm{out}}(k+1) - \Delta P_i^{\mathrm{out}}(k)\right| \tag{9}$$

Frequency regulation mileage payment can be calculated by the equation as follows (Zhang et al., 2021):

$$D_i = \sum_{k=1}^{N} \lambda \cdot S_i^{\mathrm{p}} \cdot M_i(k) \tag{10}$$

S_i^{p} is composed of the following three different values.

(1) Regulation rate: it refers to the rate at which the LFC frequency regulation unit responds to the power generation command. Its calculation equation is (Zhang et al., 2021):

$$S_i^{\mathrm{rate}} = \frac{\Delta P_i^{\mathrm{rate}}}{\Delta P_{\mathrm{a}}^{\mathrm{rate}}} \tag{11}$$

(2) Response time: it refers to the time delay for the LFC frequency regulation unit to respond to the power generation command, which is (Zhang et al., 2021):

$$S_i^{\mathrm{delay}} = 1 - \frac{T_i^{\mathrm{d}}}{5\ \mathrm{min}} \tag{12}$$

(3) Regulation accuracy value: The regulation accuracy is evaluated according to the deviation between the allocated LFC generation power command input and the actual unit output, as shown below,

$$S_i^{\mathrm{pre}} = 1 - \frac{1}{N}\sum_{k=1}^{N}\left|\frac{\Delta P_i^{\mathrm{in}}(k) - \Delta P_i^{\mathrm{out}}(k+1)}{\Delta P_{i,\mathrm{a}}}\right| \tag{13}$$

$\Delta P_{i,\mathrm{a}}$ is the allowable regulation error of the ith frequency regulation unit in each cycle, which is 1.5% of the rated output of the ith frequency regulation unit.

Therefore, the comprehensive frequency regulation performance value is equal to the sum of the product of the three value and the weight. The result is (Zhang et al., 2021):

$$S_i^p = \omega_1 S_i^{rate} + \omega_2 S_i^{delay} + \omega_3 S_i^{pre} \tag{14}$$

$$\omega_1 + \omega_2 + \omega_3 = 1, \omega_1 \geq 0, \omega_2 \geq 0, \omega_3 \geq 0 \tag{15}$$

wherein, ω_1, ω_2 and ω_3 respectively represent the weight coefficients of different regulation value, which is respectively 0.50, 0.25 and 0.25 in the frequency regulation market of CSG.

2.3. CPS assessment index

The most common frequency regulation performance standard currently adopted by operators is the CPS proposed by the North American Electric Reliability Council. The CPS standard includes CPS 1 and CPS 2 standards. Within the assessment period (10 min), frequency control should meet (Zhang et al., 2021):

$$\frac{A_{\mathrm{AVE-min}}\Delta F_{\mathrm{AVE-min}}}{10\ \mathrm{B}} \leq \varepsilon_1^2 \tag{16}$$

CPS 1 standard: it mainly records the relationship between ACE variation and frequency deviation, and tends to evaluate the effect of LFC on frequency control (Zhang et al., 2021):

$$C_{\mathrm{CPS1}} = (2 - C_{\mathrm{F}}) \times 100\% \tag{17}$$

Wherein, $C_{\mathrm{F}} = \frac{\sum(A_{\mathrm{AVE-min}}\Delta F_{\mathrm{AVE-min}})}{10Bn\varepsilon_1^2}$ n is the number of minutes in the assessment period.

CPS2 standard (Zhang et al., 2021):

$$\begin{aligned} C_{\mathrm{CPS2}} &= \left|\sum A_{\mathrm{AVE-min}}/10\right| \leq L_{10} \\ L_{10} &= 1.65\varepsilon_{10}\sqrt{100BB_{\mathrm{net}}} \end{aligned} \tag{18}$$

2.4. GAC-LFC

2.4.1. Control framework

As shown in Fig. 1, under the GAC-LFC framework, eight agents are set up. These eight agents represent four area-LFC controllers and four grid-LFC controllers. The control interval of each agent is set at 4 s. Each area contains a grid-LFC agent and an area-LFC agent. The grid-LFC agent in each area is responsible for outputting the total power generation command of the grid-unit in the area, and then dispatching the power generation command to each grid-unit based on the PROP algorithm. The area-LFC agent in each area is responsible for outputting the total power generation command of area-units in the area, and then dispatching the power generation command to each area-unit based on the PROP algorithm. During pre-learning, each grid-LFC agent and area LFC agent need to formulate a reasonable global reward function and adopt centralized training. In centralized training, each agent can observe the global state, and then train the global optimal strategy. The Energy Management System (EMS) system of each area monitors, calculates and stores the "ACE/Δf/CPS data and total unit output" of each area of the interconnected power grid in real time, and inputs these states into the grid-LFC agent and area-LFC agent in the area. In the interconnected grid, the grid-LFC agent and the area LFC agent can make a global optimal decision after observing the state of their own area, without having to know the state of all areas.

2.4.2. Dispatch of unit

Since the frequency regulation units includes a large number of distributed power sources and flexible loads, the units are divided into the following categories: coal power units, gas power units, hydroelectric power units, virtual power plant (VPP). There are a large number of distributed power sources in the VPP. The distributed power sources are integrated into several VPPs by category. The EE-MADDPG algorithm calculates and outputs the total power generation commands of the VPP, and then the virtual power plant control center distributes the commands to each distributed power generation unit using PROP method. The VPP control center distributes the generation power commands to each distributed generation unit using the PROP dispatch method, as shown in the following equation (Zhang et al., 2021):

$$\Delta P_i^{\mathrm{in}}(k) = \frac{P_i^{\max}}{\sum_j^n P_j^{\max}} * \Delta P_{total}^{\mathrm{in}}(k) \tag{19}$$

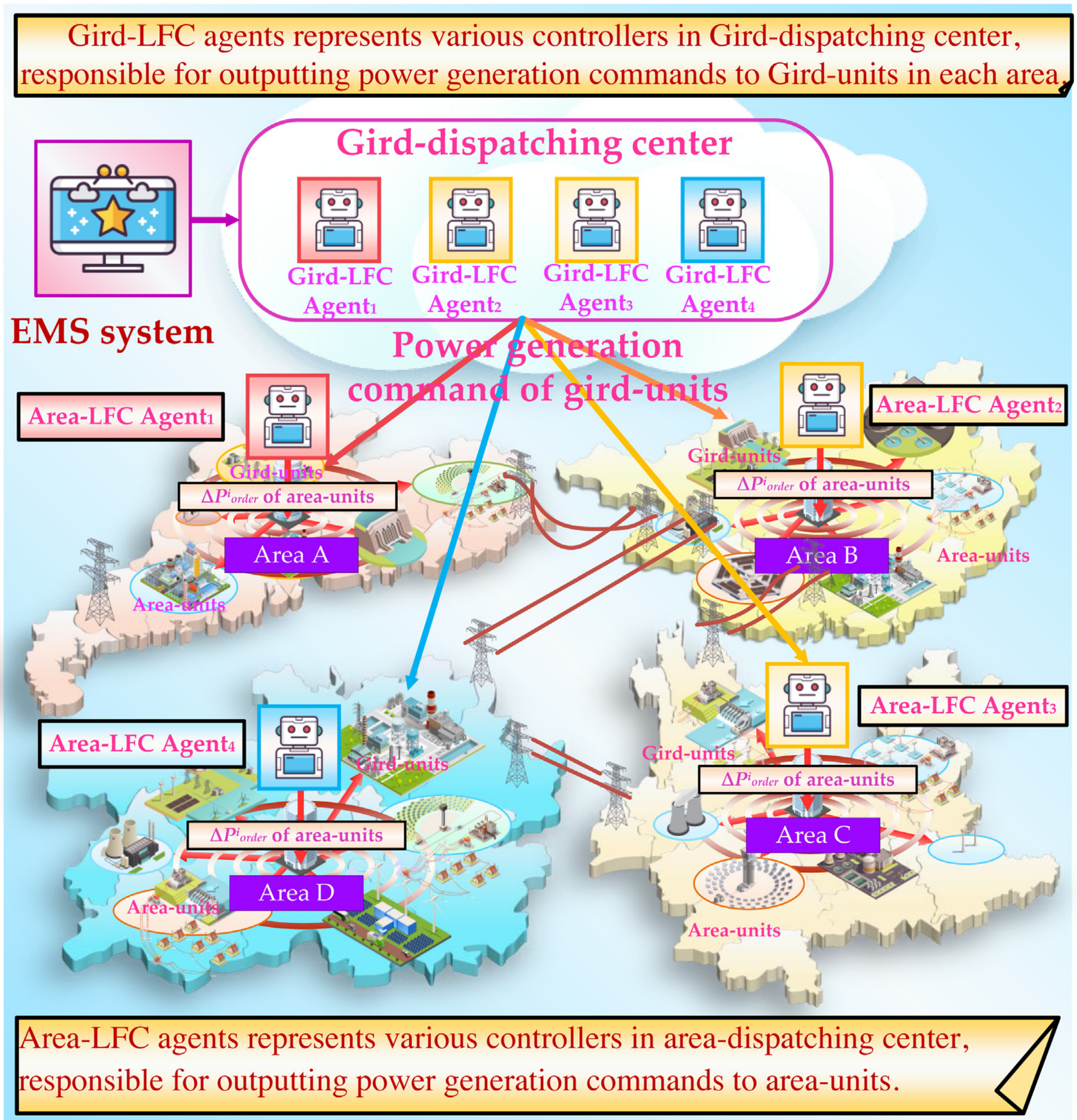

Fig. 1. GAC-LFC of Four-area system.

2.5. Objective function

GAC-LFC aims to achieve the optimal dynamic performance of LFC in multiple areas (thus realizing comprehensive economic benefits), which means achieving the minimum ACE in multiple areas while reducing the total frequency regulation mileage payment. Thus, to achieve the optimization of both dynamic performance and economic benefits in the respective area, this method addresses the following three parameters, i.e., total control area deviation, the total regulation mileage payment of area-unit, as well as the total regulation mileage payment of grid-unit, as expressed below:

$$\min f_C = \mu_1 \sum_{i=1}^{4} \left(\sum_{k=1}^{N} \left| e^i_{ACE}(k) \right| + \left(\mu_2 \sum_{j=1}^{n} D_i^j + \sum_{x=1}^{m} D_i^x \right) \right) \tag{20}$$

$$\begin{cases} e^i_{ACE}(k) = \Delta P^i_{tie}(k) + B\Delta f^i(k) \\ D_i^j = \sum_{k=1}^{N} \lambda \cdot S_j^{p} \cdot M_j(k) \\ D_i^x = \sum_{k=1}^{N} \lambda \cdot S_x^{p} \cdot M_x(k) \end{cases} \tag{21}$$

where e_i^{ACE} denotes the ACE of ith Area; $\Delta P^i_{tie}(k)$ represents the Tie line power of ith Area; Δf^i expresses the frequency of ith Area; D_i^j is the total regulation mileage payment of area-unit; D_i^x denotes the total regulation mileage payment of grid-unit; μ_1 and μ_2 is the weight coefficients; B is the frequency coefficient.

2.6. Constraint conditions

Constraints for the thermal power generating unit, gas generating units, oil-fired generating units, and hydropower generating units comprise power balance constraint, frequency regulation direction constraint, LFC regulation capacity upper and lower limit constraints, as well as power generation climbing rate constraint:

$$\begin{cases} \sum_{i=1}^{n} \Delta P_i^{in}(k) = \Delta P_{order-\Sigma}(k) \\ \Delta P_{order-}(k) * \Delta P_i^{in}(k) \geq 0 \\ \Delta P_i^{min} \leq \Delta P_i^{in}(k) \leq \Delta P_i^{max} \\ \left| \Delta P_i^{out}(k+1) - \Delta P_i^{out}(k) \right| \leq \Delta P_i^{rate} \end{cases} \tag{22}$$

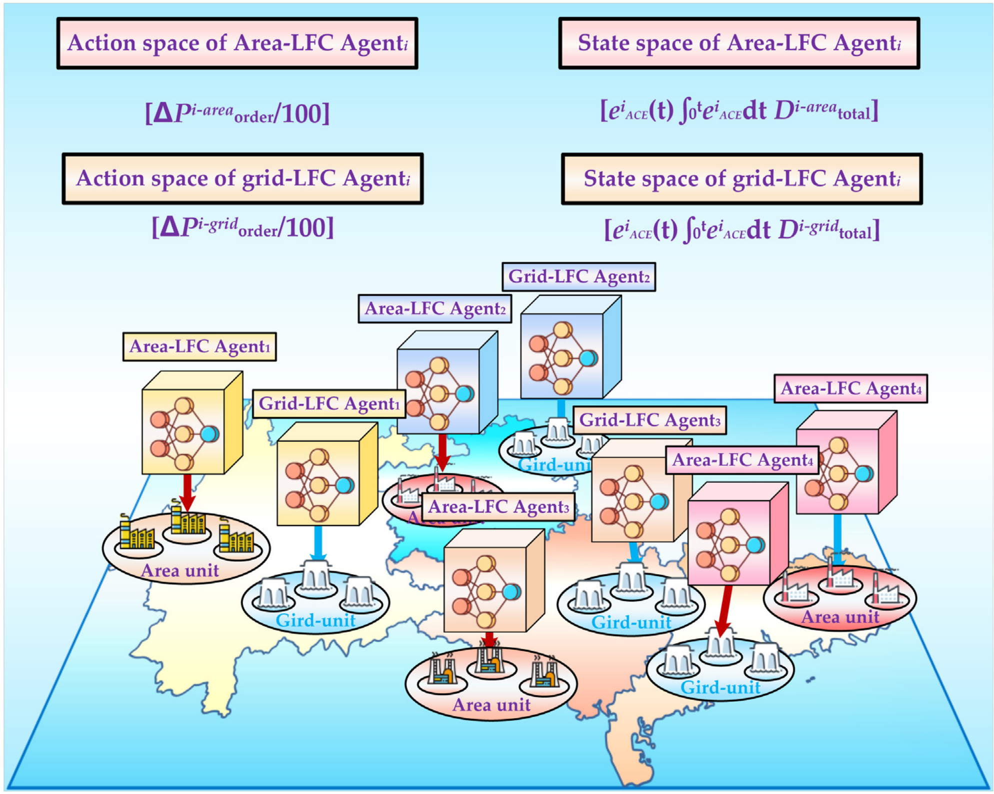

Fig. 2. Application of the proposed algorithm.

3. Proposed method

3.1. Application of the proposed algorithm

The proposed algorithm employs the strategy of centralized training with decentralized execution, with the aims of obtaining an optimal LFC coordination strategy, and realizing the coordination between the multi-area grid-LFC agent and the area LFC agent in the interconnected grid. Since the final area-regulated output is affected by both the grid-LFC agent and the area LFC agent in the area, it is necessary to first consider the coordination of the grid-LFC agent and the area-LFC agent in the same area. The specific framework is shown in Fig. 2.

During pre-learning, each grid-LFC agent and area-LFC agent can observe the state and actions of other agents and thus make the training environment stable. By separately formulating different reward functions and observing the actions of other agents, it can be determined whether their own strategies $\pi_G{}^i(s)$ and $\pi_A{}^i(s)$ are the global optimum.

The global optimal multi-area LFC can be achieved by continuously regulating their own strategies in pre-learning, so that the coordinated control strategy of LFC can fully consider the coordination of secondary frequency regulation between multiple areas, so as to improve the frequency regulation performance of each area and reduce wastage of frequency regulation resources in each area. Finally, agent$^i{}_G$ and agent$^i{}_A$ in each area obtain the global optimal strategy functions $\pi_G{}^i(s)$ and $\pi_A{}^i(s)$ respectively.

During online application, agent$^i{}_G$ and agent$^i{}_A$ in area i input the state of the area into their own policy functions $\pi_G{}^i(s)$ and $\pi_A{}^i(s)$, and output the total power generation commands of the grid-unit and area-unit in the area. Just as each agent considers the strategies of other agents in the area and other areas during pre-learning, so during online application agent$^i{}_G$ and agent$^i{}_A$ can make a global optimal action according to the state of their own area, which gives the proposed method an advantage over existing optimal control algorithms.

3.2. Modeling of Markov decision process

The environment of reinforcement learning can be described by the Markov decision process, which is a memory-less stochastic process that can describe the fully observable environment. It can be described as a set of tuples 〈 S, A_1,..., A_n, R_1,..., R_n, P 〉. For the problem proposed in this paper, the LFC decision can be modeled as a Markov decision process. The specific modeling method is as follows:

3.2.1. MDP modeling of agent$^i{}_G$

(1) Action space

Considering that the role of agent$^i{}_G$ is to output the total power generation command of all the grid-units in the ith area, a total of one action is set in order to be able to use smaller exploration noise during the exploration process, as shown in the following equation:

$$\left[P^{i-grid}_{\text{order}}/100\right] \tag{23}$$

(2) State space

The State space of agent$^i{}_G$ includes a total of three states as follows: the ACE in the ith area, the integral of time to the ACE in the ith area, and the total frequency regulation mileage payment of the grid-units in the ith area, as shown:

$$[e^i_{ACE}(t) \int_0^t e^i_{ACE} dt\, D^{i-grid}_{total}] \tag{24}$$

(3) Selection of reward functions

According to Eq. (20), in order to reduce the ACE in this area and the total frequency regulation mileage payment, the reward function item in this paper includes the e_{ACE} of current control interval, and the total frequency regulation mileage payment of all grid-units. In addition, in order to make the agent explore in the direction of reducing the frequency deviation, a penalty term G is set in the function. When the frequency deviation is too large, a large positive number will be subtracted to punish the agent. The value of comprehensive frequency regulation performance index of frequency regulation mileage used in this paper uses the historical average value obtained through long-term simulation to ensure that the form of the reward function is consistent. The comprehensive reward function is as follows:

$$r(t) = -\left[\mu_1 \left|e_{ACE}(t)\right|^2 + \mu_2 \sum_{j=1}^{n} D_j^i(t)\right] + G \tag{25}$$

$$D_j(t) = \lambda^* S_j^{p*} \left|\Delta P_{Gi}^{grid}(t) - \Delta P_{Gi}^{grid}(t-1)\right| \tag{26}$$

$$G = \begin{cases} 0 & |\Delta f(t)| < 0.03 \text{ Hz} \\ -1 & |\Delta f(t)| \geq 0.03 \text{ Hz} \end{cases} \tag{27}$$

3.2.2. MDP modeling of agent$^i{}_A$

(1) Action space

Similar to agent$^i{}_G$, considering that the role of agent$^i{}_A$ is to output the total power generation command of all the grid-units in the *i*th area, which is shown in the following equation:

$$\left[P_{\text{order}}^{i-\text{area}}/100\right] \tag{28}$$

(2) State space

The State space of agent$^i{}_A$ includes a total of three states as follows: the ACE in the *i*th area, the integral of time to the ACE in the *i*th area, and the total frequency regulation mileage payment of the area-units in the *i*th area, as shown follows:

$$[e_{ACE}^i(t) \int_0^t e_{ACE}^i dt \; D_{total}^{i-\text{area}}] \tag{29}$$

(3) Selection of reward functions

As shown in Eq. (20), in order to reduce the ACE in this area and the total frequency regulation mileage payment, ACE is used as the penalty item, which is different from agent$^i{}_A$. This is because agent$^i{}_G$ has greater effect on ACE and reduces tie-line power mainly based on fine-tuning, while agent$^i{}_A$ mainly relies on high-performance units to reduce frequency deviation. Therefore, the comprehensive reward function is as follows:

$$r(t) = -\left[\mu_1 \left|e_{ACE}(t)\right|^2 + \mu_2 \sum_{j=1}^{n} D_j^i(t)\right] + A \tag{30}$$

$$D_j(t) = \lambda^* S_j^{p*} \left|\Delta P_{Gi}^{area}(t) - \Delta P_{Gi}^{area}(t-1)\right| \tag{31}$$

$$A = \begin{cases} 0 & |e_{ACE}(t)| < 0.5 \text{ MW} \\ -1 & |e_{ACE}(t)| \geq 0.5 \text{ MW} \end{cases} \tag{32}$$

3.3. MADDPG

MADDPG (Lowe et al., 2017) is an actor–critic algorithm. It uses centralized training with decentralized execution to solve the environmental instability problem of conventional multi-agent deep reinforcement learning algorithms.

In MADDPG, each agent has an independent critic network and actor network. In the training of agent, in addition to the state collected by the agent, additional global information is provided to the agent based on the idea of centralized training with decentralized execution; However, in online applications, agents can only make decisions based on their own observations. Specifically, in pre-learning, the input of the critic network includes not only its own observations and actions, but also the states and actions of other agents (Global information); In contrast, the actor network only input its own state. Through the central training method, all agents' observations and actions can be observed by each agent. Therefore, even if the strategy of other agents changes, the environment is still static for the critic network. In addition, because the critic network is less disturbed by the non-static environment, the critic network can evaluate the performance of the strategy network more accurately, so that the agent is able to search for the optimal strategy in the entire state action space. At the moment, the loss function of the critic network of the agent is:

$$L\left(\theta_g^Q\right) = E_{(o,a,r_g,\theta') \sim D}\left[\left(y_g\left(r_g, o'\right) - Q\left(o, a; \theta_g^Q\right)\right)^2\right] \tag{33}$$

Wherein,

$$y_g\left(r_g, o'\right) = r_g + \gamma Q\left(o', a_1', \ldots, a_g', \ldots, a_N'; \theta_g^{Q,-}\right)\Big|_{a_g' = \pi\left(o_g' : \theta_g^{\pi-}\right)} \tag{34}$$

Through decentralized execution, the agent requires no additional priori knowledge when making decisions. Therefore, the agent g's policy gradient expression is:

$$\nabla_{\theta_g^\pi} J\left(\theta_g^\pi\right) = E_{(o,a)\sim \mathrm{D}}\left[\nabla_{\theta_g^\pi} \pi\left(o_g; \theta_g^\pi\right) \nabla_{a_g} Q\left(o, a; \theta_g^Q\right)\right] \tag{35}$$

3.4. EE-MADDPG framework

The MADDPG algorithm exhibits low robustness. The main reasons for this problem are presented below:

(1) Critics have overestimated the Q value. (2) The MADDPG algorithm has low values for samples at the initial training stage, and the problem of sparse rewards occurs. (3) The algorithm stochastically selected samples from the experience pool for training, so the training efficiency is relatively low.

(4) Offline training. The simple exploration strategy adopted by the MADDPG algorithm is not guided to explore in various action spaces. (5) The guidance technology of the MADDPG algorithm is insufficiently effective, so the algorithm can easily fall to a local optimum.

EE-MADDPG refers to a multi-agent deep reinforcement learning algorithm based on MA-DDPG, aiming at improving the robustness and exploration ability exhibited by the MADDPG algorithm. The EE-MADDPG algorithm exploits a distributed multi-agent deep reinforcement learning training framework by complying with on the MADDPG algorithm. There are a variety of agents with different principles in the framework participating in large-scale exploration. Different agents play different roles in exploring the environment to improve the robustness of the algorithm. As shown in Fig. 3, the following techniques are used in the EE-MADDPG algorithm: (1) Comprehensive anti-Q overestimation strategy is used to solve the problem 1. (2) The experience replay mechanism based on Aronson effect is employed to address the problem 2; (3) Multi-agent distributed exploration and Action space guidance strategy is used to solve the problem 3,4 of the MADDPG algorithm; (4) Curriculum learning strategies is used to solve the problem 5;

(1) The method proposed in this study refers to a coordinated control strategy that can consider multiple objectives. The original intention of this strategy is to be able to coordinate different types of units extensively. In such an algorithm, the LFC controller regulated by the grid-dispatching center and the LFC controller controlled by the area-dispatching center in the respective area are treated as different agents. Through centralized training with decentralized execution, LFC controllers controlled by different levels of dispatching centers in different areas can be coordinated.

(2) The algorithm proposed in this study has higher robustness and adaptability. It uses some techniques to improve the training efficiency and robustness of the algorithm. This improves the generalization, scalability and applicability of the algorithm. If it is overall trained, most control problems can be addressed by using this algorithm, i.e., a scalable deep reinforcement learning algorithm.

3.4.1. Overview of training framework with roles-based framework

(1) Overview of agents

The structure of the algorithm includes the parallel systems, explorers, teachers, followers, leaders, and public experience pools.

As shown in Fig. 4, Parallel systems: each parallel system includes a complete four-area LFC model environment and 8 agents. Each area i includes an $\text{agent}^i{}_G$ and an $\text{agent}^i{}_A$. Each $\text{agent}^i{}_G$ and $\text{agent}^i{}_A$ may be any combination of 8 explorers, 8 teachers, and 8 followers. The specific combination is shown in Eq. (35). The environment in each parallel system is stochastic.

$$\begin{cases} \text{agent}_G^1 = \text{agent}_G^2 = \text{agent}_G^3 = \text{agent}_G^4 \\ \quad = \text{agent}_A^1 = \text{agent}_A^2 = \text{agent}_A^3 = \text{agent}_A^4 \\ \quad = \exp \mathit{lorer}(\varepsilon \text{ greedy}) & \text{Parallel system 1} \\ \text{agent}_G^1 = \text{agent}_G^2 = \text{agent}_G^3 = \text{agent}_G^4 \\ \quad = \text{agent}_A^1 = \text{agent}_A^2 = \text{agent}_A^3 = \text{agent}_A^4 \\ \quad = \exp \mathit{lorer}(\mathit{OU\ noise}) & \text{Parallel system 2} \\ \text{agent}_G^1 = \text{agent}_G^2 = \text{agent}_G^3 = \text{agent}_G^4 \\ \quad = \text{agent}_A^1 = \text{agent}_A^2 = \text{agent}_A^3 = \text{agent}_A^4 \\ \quad = \exp \mathit{lorer}(\mathit{Gaussian\ noise}) & \text{Parallel system 3} \\ \text{agent}_G^1 = \text{agent}_G^2 = \text{agent}_G^3 = \text{agent}_G^4 \\ \quad = \text{agent}_A^1 = \text{agent}_A^2 = \text{agent}_A^3 = \text{agent}_A^4 \\ \quad = \text{Teacher}(\mathit{Fuzzy\ PID\ and\ PSO}) & \text{Parallel system 4} \\ \text{agent}_G^1 = \text{agent}_G^2 = \text{agent}_G^3 = \text{agent}_G^4 \\ \quad = \text{agent}_A^1 = \text{agent}_A^2 = \text{agent}_A^3 = \text{agent}_A^4 \\ \quad = \text{Follow}(\mathit{OU\ noise}) & \text{Parallel system 5} \\ \text{agent}_G^1 = \text{agent}_G^2 = \text{agent}_G^3 = \text{agent}_G^4 \\ \quad = \text{agent}_A^1 = \text{agent}_A^2 = \text{agent}_A^3 = \text{agent}_A^4 \\ \quad = \text{Teacher}(\mathit{Fuzzy\text{-}FOPID\ and\ GA}) & \text{Parallel system 6} \\ \text{agent}_G^1 = \text{agent}_G^2 = \text{agent}_G^3 = \text{agent}_G^4 \\ \quad = \text{agent}_A^1 = \text{agent}_A^2 = \text{agent}_A^3 = \text{agent}_A^4 \\ \quad = \text{Follow}(\mathit{Gaussian\ noise}) & \text{Parallel system 7} \end{cases} \tag{36}$$

Leaders: Leaders are the agents that are deployed in the GAC-LFC coordination strategy in online applications. All other agents act as sample providers in the pre-learning which provide samples to each leader for learning. The main responsibility of each leader is to collect samples from the public experience pool in each step and update its own neural network parameters, and then regularly transmit these network parameters to the relevant explorer for updating.

Explorers: The main responsibility of explorers is to use multiple strategies to explore the environment of their respective parallel systems, and provide the obtained exploration samples to the relevant leader. There is only one actor network in each explorer, and different explorers use different exploration principles to conduct distributed exploration of environments.

Teachers: On the basis of imitation learning, there is a controller in each teacher. The controllers in different parallel systems all use different algorithms and are able to obtain outstanding performance. The main responsibility of each teacher is to effectively interact with the environment to obtain demonstration samples, and then provide them to the leaders for learning. These demonstration samples are high-value samples that can effectively guide the training of each leader.

Followers: The responsibility of the followers is to explore around each teacher's motion locus and obtain more high-value tracking samples. Drawing on the concept of imitation learning, each follower observes the relevant teacher's movements and explores the small area around its motion locus to obtain high-value samples. Since in parallel systems 4 and 6 the teachers are used to explore the demonstration samples, the environment of parallel systems 4 and 6 is copied to parallel systems 5 and 7 in each step in order to track each teacher's motion locus and explore the small area around it. The followers add noises of different sizes based on each teacher's motion to explore the periphery of its motion locus, thus increasing the possibility of obtaining higher-value samples.

Public experience pools: There are two independent public experience pools in each leader. Public Experience Pool 1 stores samples from the explorers and followers, and Public Experience Pool 2 stores samples from the teachers.

(2) Algorithm flow overview

This algorithm uses a large-scale centralized training model. Leader is responsible for centralized training, and explorer, Teacher, Follows are responsible for real-time execution and exploration of environment. The training process is as follows:

(i) Initialize the parameters of leaders, explorers, follows, and teacher in each area.

(ii) Set up explorer or Teacher in areas A, B, C, and D of each parallel system according to the episode.

(iii) For each parallel system, a stochastic-phase sine wave is added to the area A, area B, area C, and area D. Each episode lasts 1800 s. The amplitude of the sine function increase with the increase of episode, as shown in the Eq. (37).

$$\begin{cases} \text{Disturbance}_A = \sin(0.0001t + \theta_A^{rand}) \quad 0\text{ s} \le t \le 3600\text{ s} \\ \text{Disturbance}_B = \begin{cases} 0 \quad 0\text{ s} \le t \le 900\text{ s} \\ \sin(0.0001t + \theta_B^{rand}) \quad 900\text{ s} \le t \le 3600\text{ s} \end{cases} \\ \text{Disturbance}_C = \begin{cases} 0 \quad 0\text{ s} \le t \le 1800\text{ s} \\ \sin(0.0001t + \theta_C^{rand}) \quad 1800\text{ s} \le t \le 3600\text{ s} \end{cases} \\ \text{Disturbance}_D = \begin{cases} 0 \quad 0\text{ s} \le t \le 2700\text{ s} \\ \sin(0.0001t + \theta_D^{rand}) \quad 2700\text{ s} \le t \le 3600\text{ s} \end{cases} \end{cases} \tag{37}$$

(iv) The explorer, Teacher, and follows in each parallel system i respectively obtain the actions that need to be executed according to the current state and input them into the environment.

(v) Explorers or Teachers in each parallel system i respectively

interact with the environment to obtain samples of different agents in each area (For example, the sample of $\text{agent}^i{}_G$ in area A is $e_A^i = (s_{t-A}^i, a_{t-A}^i, r_{t-A}^i, s_{(t+1)-A}^i, a_{t-B}^i, a_{t-C}^i, a_{t-D}^i)$), and store these samples into their corresponding public experience pools of A-leader, B-leader, C-leader, and D-leader.

(vi) After all agents interact with the environment, each leader stochastically selects experience from its own public experience pool to train its own actor neural network, and regularly transmits network parameters to the corresponding explorer. In training, the Critics input not only its own state, but also the actions taken by all other agents in the same parallel system. Critics updates the network parameters by minimizing the loss. The strategy loss is

$$\begin{cases} L_A^{area} = \frac{1}{K}\sum_{j=1}^{K}\left(y_j - Q_1\left(s_j, \ldots, a_B^{area}, a_C^{area}, a_D^{area}, a_A^{grid}, a_B^{grid}, a_C^{grid}, a_D^{grid}, \theta^{Q_1}\right)\right)^2, \\ L_A^{grid} = \frac{1}{K}\sum_{j=1}^{K}\left(y_j - Q_1\left(s_j, a_A^{area}, a_B^{area}, a_C^{area}, a_D^{area}, a_B^{grid}, a_C^{grid}, a_D^{grid}, \theta^{Q_1^{'}}\right)\right)^2, \\ L_B^{area} = \frac{1}{K}\sum_{j=1}^{K}\left(y_j - Q_2\left(s_j, \ldots, a_A^{area}, a_C^{area}, a_D^{area}, a_A^{grid}, a_B^{grid}, a_C^{grid}, a_D^{grid}, \theta^{Q_2}\right)\right)^2, \\ L_B^{grid} = \frac{1}{K}\sum_{j=1}^{K}\left(y_j - Q_2\left(s_j, a_A^{area}, a_B^{area}, a_C^{area}, a_D^{area}, a_A^{grid}, a_C^{grid}, a_D^{grid}, \theta^{Q_2^{'}}\right)\right)^2, \\ L_C^{area} = \frac{1}{K}\sum_{j=1}^{K}\left(y_j - Q_3\left(s_j, \ldots, a_A^{area}, a_B^{area}, a_D^{area}, a_A^{grid}, a_B^{grid}, a_C^{grid}, a_D^{grid}, \theta^{Q_3}\right)\right)^2, \\ L_C^{grid} = \frac{1}{K}\sum_{j=1}^{K}\left(y_j - Q_3\left(s_j, a_A^{area}, a_B^{area}, a_C^{area}, a_D^{area}, a_A^{grid}, a_B^{grid}, a_D^{grid}, \theta^{Q_3^{'}}\right)\right)^2, \\ L_D^{area} = \frac{1}{K}\sum_{j=1}^{K}\left(y_j - Q_4\left(s_j, \ldots, a_A^{area}, a_B^{area}, a_C^{area}, a_A^{grid}, a_B^{grid}, a_C^{grid}, a_D^{grid}, \theta^{Q_4}\right)\right)^2, \\ L_D^{grid} = \frac{1}{K}\sum_{j=1}^{K}\left(y_j - Q_4\left(s_j, a_A^{area}, a_B^{area}, a_C^{area}, a_D^{area}, a_A^{grid}, a_B^{grid}, a_C^{grid}, \theta^{Q_4^{'}}\right)\right)^2, \end{cases} \tag{38}$$

Then the gradient descent method is used to calculate and update the parameters of the current actor in each leader. The gradient calculation equation is

$$\begin{cases} \nabla_{\theta_1{}^{\pi}} J_A^{area} = \frac{1}{K}\sum_{j=1}^{K}\nabla_{\theta_1{}^{\pi}}\pi\left(o, \theta_1{}^{\pi}\right)\nabla_a \\ \quad \times Q_1\left(s_j, \ldots, a_B^{area}, a_C^{area}, a_D^{area}, a_A^{grid}, a_B^{grid}, a_C^{grid}, a_D^{grid}, \theta^{Q_1}\right) \\ \nabla_{\theta_2{}^{\pi}} J_B^{area} = \frac{1}{K}\sum_{j=1}^{K}\nabla_{\theta_2{}^{\pi}}\pi\left(o, \theta_2{}^{\pi}\right)\nabla_a \\ \quad \times Q_2\left(s_j, \ldots, a_A^{area}, a_C^{area}, a_D^{area}, a_A^{grid}, a_B^{grid}, a_C^{grid}, a_D^{grid}, \theta^{Q_2}\right) \\ \nabla_{\theta_3{}^{\pi}} J_C^{area} = \frac{1}{K}\sum_{j=1}^{K}\nabla_{\theta_3{}^{\pi}}\pi\left(o, \theta_3{}^{\pi}\right)\nabla_a \\ \quad \times Q_3\left(s_j, \ldots, a_A^{area}, a_B^{area}, a_D^{area}, a_A^{grid}, a_B^{grid}, a_C^{grid}, a_D^{grid}, \theta^{Q_3}\right) \\ \nabla_{\theta_4{}^{\pi}} J_D^{area} = \frac{1}{K}\sum_{j=1}^{K}\nabla_{\theta_4{}^{\pi}}\pi\left(o, \theta_4{}^{\pi}\right)\nabla_a \\ \quad \times Q_4\left(s_j, \ldots, a_A^{area}, a_B^{area}, a_C^{area}, a_A^{grid}, a_B^{grid}, a_C^{grid}, a_D^{grid}, \theta^{Q_4}\right) \end{cases} \tag{39}$$

$$\begin{cases} \nabla_{\theta_1{}^{\pi'}} J_A^{grid} = \frac{1}{K}\sum_{j=1}^{K}\nabla_{\theta_1{}^{\pi'}}\pi\left(o, \theta_1{}^{\pi'}\right)\nabla_a \\ \quad \times Q_1\left(s_j, a_A^{area}, a_B^{area}, a_C^{area}, a_D^{area}, a_B^{grid}, a_C^{grid}, a_D^{grid}, \theta^{Q_1^{'}}\right) \\ \nabla_{\theta_2{}^{\pi'}} J_B^{grid} = \frac{1}{K}\sum_{j=1}^{K}\nabla_{\theta_2{}^{\pi'}}\pi\left(o, \theta_2{}^{\pi'}\right)\nabla_a \\ \quad \times Q_2\left(s_j, a_A^{area}, a_B^{area}, a_C^{area}, a_D^{area}, a_A^{grid}, a_C^{grid}, a_D^{grid}, \theta^{Q_2^{'}}\right) \\ \nabla_{\theta_3{}^{\pi'}} J_C^{grid} = \frac{1}{K}\sum_{j=1}^{K}\nabla_{\theta_3{}^{\pi'}}\pi\left(o, \theta_3{}^{\pi'}\right)\nabla_a \\ \quad \times Q_3\left(s_j, a_A^{area}, a_B^{area}, a_C^{area}, a_D^{area}, a_A^{grid}, a_B^{grid}, a_D^{grid}, \theta^{Q_3^{'}}\right) \\ \nabla_{\theta_4{}^{\pi'}} J_D^{grid} = \frac{1}{K}\sum_{j=1}^{K}\nabla_{\theta_4{}^{\pi'}}\pi\left(o, \theta_4{}^{\pi'}\right)\nabla_a \\ \quad \times Q_4\left(s_j, a_A^{area}, a_B^{area}, a_C^{area}, a_D^{area}, a_A^{grid}, a_B^{grid}, a_C^{grid}, \theta^{Q_4^{'}}\right) \end{cases} \tag{40}$$

Since the interaction of agents can affect the control effect of the LFC in each area, during intensive training, each agent can fine-tune its own actions according to the actions of other agents observed, so as to coordinate with agents in other areas to achieve a mutually balanced state and obtain a balanced optimal solution.

3.4.2. Parallel system

In this method, a total of 7 parallel systems are set up, and each parallel system has different environments, that is, different stochastic load disturbances, as shown in Eq. (41). In addition, the amplitude of the sine function in Eq. (41) increases as the number of episodes increases, as shown in Eq. (41). Such simple techniques enable the environment in each parallel system to continuously transit from a simple ACE environment with a small error to a complex ACE environment with a large error, even to some stochastic environment with complex scenes. In accordance with the concept of curriculum learning, the agent progresses from simple to difficult stages in training, thus its training efficiency increases over time.

$$\begin{cases} |\Delta A_m|, |\Delta B_m|, |\Delta C_m|, |\Delta D_m| \subseteq [0, 150) & 0 \le episodes < 1000 \\ |\Delta A_m|, |\Delta B_m|, |\Delta C_m|, |\Delta D_m| \subseteq [150, 300) & 1000 \le episodes < 2000 \\ |\Delta A_m|, |\Delta B_m|, |\Delta C_m|, |\Delta D_m| \subseteq [300, 450) & 2000 \le episodes < 3000 \\ |\Delta A_m|, |\Delta B_m|, |\Delta C_m|, |\Delta D_m| \subseteq [450, 600) & 3000 \le episodes < 4000 \\ |\Delta A_m|, |\Delta B_m|, |\Delta C_m|, |\Delta D_m| \subseteq [600, 750) & 4000 \le episodes < 5000 \\ |\Delta A_m|, |\Delta B_m|, |\Delta C_m|, |\Delta D_m| \subseteq [750, 900) & 5000 \le episodes < 6000 \\ |\Delta A_m|, |\Delta B_m|, |\Delta C_m|, |\Delta D_m| \subseteq [900, 1050) & 6000 \le episodes < 7000 \\ |\Delta A_m|, |\Delta B_m|, |\Delta C_m|, |\Delta D_m| \subseteq [1050, 2600) & 7000 \le episodes < 8000 \end{cases} \tag{41}$$

In addition, for agents in parallel systems in different episodes, it is necessary to limit the action space of the agents in it in order to improve the exploration ability of the algorithm. The specific action space of the agent is as follows:

$$\begin{cases} a(\text{agent}_G^i), a(\text{agent}_A^i) \subseteq [0, 600) & 0 \le episodes < 1000 \\ a(\text{agent}_G^i), a(\text{agent}_A^i) \subseteq [150, 1200) & 1000 \le episodes < 2000 \\ a(\text{agent}_G^i), a(\text{agent}_A^i) \subseteq [300, 1800) & 2000 \le episodes < 3000 \\ a(\text{agent}_G^i), a(\text{agent}_A^i) \subseteq [450, 2400) & 3000 \le episodes < 4000 \\ a(\text{agent}_G^i), a(\text{agent}_A^i) \subseteq [600, 3000) & 4000 \le episodes < 5000 \\ a(\text{agent}_G^i), a(\text{agent}_A^i) \subseteq [750, 3600) & 5000 \le episodes < 6000 \\ a(\text{agent}_G^i), a(\text{agent}_A^i) \subseteq [900, 4200) & 6000 \le episodes < 7000 \\ a(\text{agent}_G^i), a(\text{agent}_A^i) \subseteq [1050, 8400) & 7000 \le episodes < 10000 \end{cases} \tag{42}$$

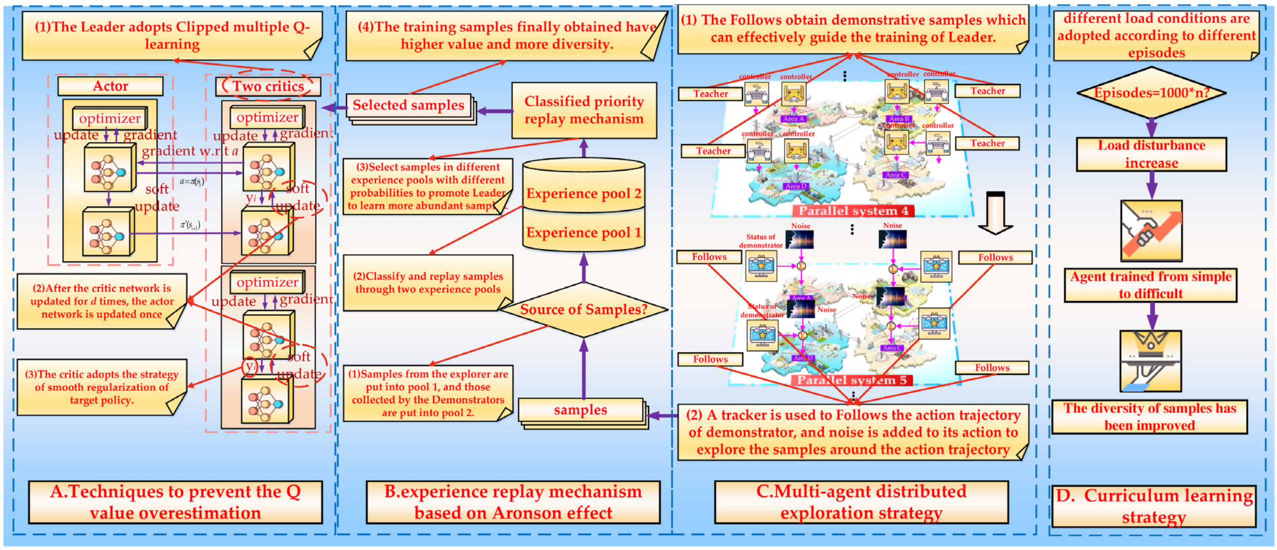

Fig. 3. Techniques used in the EE-MADDPG algorithm.

Therefore, as more and more episodes are completed, the action space changes and adapts to different stochastic disturbance ranges, thereby ensuring that each action is an effective action that can change the environment and obtain the best results.

3.4.3. *Explorer*

In this paper, the explorer structure includes one actor network and different network models. Explorers of different parallel systems use different exploration principles. There are three different exploration principles as follows: greedy strategy, Gaussian noise, and OU noise.

The exploration strategy of the explorer in a parallel system is set as greedy strategy, named: ε-explorer, and its exploration actions are as follows:

$$a_{\varepsilon}^{l}=\begin{cases}\pi_{\phi}^{l}(s) & \text{With } \varepsilon \text{ probability}\\ a_{\text{rand}}^{l} & \text{With } 1-\varepsilon \text{ probability}\end{cases} \tag{43}$$

The exploration strategy of the explorer in a parallel system is set as OU noise, named OU-explorer. Different OU-explorer uses stochastic OU noise with different variances to explore, and its exploration actions are as follows:

$$a_{OU}^{j}=\pi_{\phi}^{j}(s)+N_{OU}^{j} \tag{44}$$

The exploration strategy of the explorer in a parallel system is set as Gaussian noise, named Gaussian-explorer. Different Gaussian-explorer uses stochastic Gaussian noise with different variances, and its exploration actions are as follows:

$$a_{\text{Gaussian}}^{m}=\pi_{\phi}^{m}(s)+N_{\text{Gaussian}}^{m} \tag{45}$$

3.4.4. *Teacher and imitation learning strategy*

A conventional algorithm cannot obtain more high-value samples at the beginning of training, and so it falls into the local optimal solution. Drawing on the concept of imitation learning, the proposed method creates expert samples to improve the proportion of high-quality samples in the algorithm. In each area of a parallel system, there are two types of teachers: Teacher$_{\mathrm{G}}$, which represents the grid-LFC controller with different control principles; and, Teacher$_{\mathrm{A}}$, which represents the area-LFC controller. During pre-learning, these two types of teachers can interact with the parallel system environment to obtain more high-value samples and add them to the public experience pool.

The different controllers adopted by each teacher include fuzzy PID and fuzzy FOPID. The coefficients of each controller are set manually, and the following IAE indicators are mainly considered in the coefficient optimization:

$$F(t)=\int_{0}^{\infty} t(e(t))^{2}\mathrm{d}t \tag{46}$$

3.4.5. *Follower and imitation learning effect*

There is a "top-down rule" in the imitation law, the founder of the imitation learning method: the inferior imitates the superior; likewise, lower-level characters imitate upper-level characters. In human psychology, imitation is a prerequisite for fulfillment. Importing this concept into AI, in order to obtain more high-value samples in the initial stage of training, followers add noise to the actions given by the teacher in order to effectively study its surrounding area. They imitate the motion locus of the teacher, producing high-value samples.

In Parallel System 5, there are 8 followers in each area corresponding to the 8 teachers in Parallel System 4. In Parallel System 5, there are 8 followers in each area corresponding to teachers in Parallel System 6. The structure of each followers includes a replicator and a noise generator. Parallel systems 5 and 7 include a complete LFC model. During the training, the state of Parallel System 4 and the actions and states of teachers are completely copied to Parallel System 5, and Gaussian noise is added on the basis of the original actions of teachers, as shown in the Eq. (47). The state of Parallel System 6 and the actions and states of teachers are completely copied to Parallel System 7, and an OU noise is added on the basis of the original actions of teachers, as shown in the Eq. (48). Following this operation, high-value tracking samples can be obtained and stored in Public Experience Pool 1 of the corresponding leader. According to the parallel system, they are named 5-follows, and 7-follows.

The OU noise detection strategy is used in the parallel space 5-follows. Followers use square-differentiated stochastic Gaussian noise. The specific solutions discussed are as follows:

$$a_{system-5-T}^{j}=u_{\text{Fuzzy}-PID}^{j}(s)+N_{\text{Gaussian}}^{j} \tag{47}$$

Different parallel spaces 7-follows uses stochastic OU noise with different variances:

$$a_{system-7-T}^{j}=u_{\text{Fuzzy-FOPID}}^{j}(s)+N_{OU}^{j} \tag{48}$$

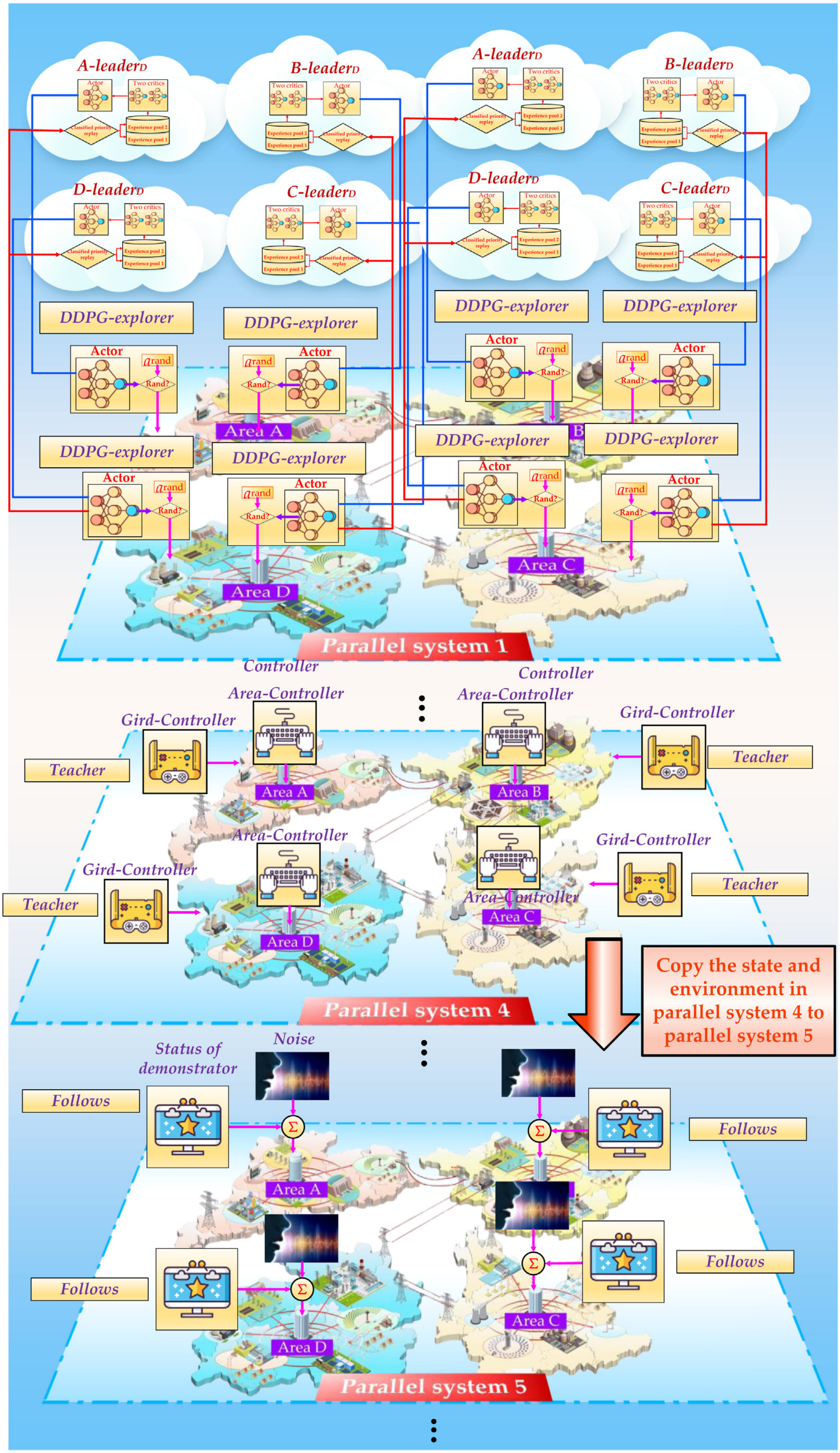

Fig. 4. Framework of the EE-MADDPG algorithm.

3.4.6. Leader

Each leader consists of 2 critic networks, 2 target critic networks, an actor network, a target actor network, and 2 public experience pools. Each parallel space has a total of 8 leaders. Explorers, teachers and followers put samples into the public experience pool for leader to regularly collect and learn, and then update its own parameters. Further the parameters in the corresponding target actor are transmitted to the actor of explorer in each parallel system. It uses the following three techniques to solve the Q value overestimation problem.

(i) Clipped multiple Q-learning is used to calculate the target value

$$y_t^1 = r(s_t, a_t) + \gamma \min_{i=1,2} Q_{\theta_i'}\left(s_{t+1}, \pi_{\phi_1}(s_{t+1})\right) \tag{49}$$

(ii) Policy delay update strategy. The critic adopts a delayed update strategy. After updating the critic network d times, the actor network is updated once.

(iii) The critic uses the smooth regularization policy. Citric estimates the Q value by bootstrapping the estimated value of the similar state action pair:

$$y_t = r(s_t, a_t) + \mathrm{E}_\varepsilon\left[Q_{\theta'}\left(s_{t+1}, \pi_{\phi'}(s_{t+1}) + \varepsilon\right)\right] \tag{50}$$

Smooth regularization is achieved by adding a stochastic noise to the target strategy and averaging on the mini-batch:

$$y_t = r(s_t, a_t) + \gamma \min_{i=1,2} Q_{\theta_t}\left(s_{t+1}, \pi_{\phi'}(s_{t+1}) + \varepsilon\right) \tag{51}$$

3.4.7. Experience replay mechanism based on Aronson effect

The Aronson effect refers to the psychological phenomenon of a person's attitude gradually becoming more negative as rewards decrease, and gradually becoming positive as rewards increase. The Aronson effect also refers to the psychological phenomenon of people gravitating towards other people or things that increase their own sense of self-worth. In reference to this construct, more samples with high rewards should be gradually added for the leader to learn in order to enable the leader to learn more effectively. Therefore, the algorithm uses two independent experience pools to store samples. The samples collected by explorers and followers are put into Public Experience Pool 1, and the samples collected by Teachers are put into Public Experience Pool 2.

During training, the experience samples in the buffer experience pool 1 are selected with a probability ξ, and the samples in the experience pool 2 are selected with a probability 1-ξ. Since it is impossible for other agents to obtain high-value samples at the beginning of training (at the moment, the quality of samples collected by Teachers are the highest), the probability ξ is very small in order to obtain more high-value samples at the beginning of the training. As the episodes increase, the value of the samples collected by the explorer in the later stage exceeds the model samples of Teachers, so this probability gradually increases as the episodes increase, as shown in Eq. (52).

$$\xi = \begin{cases} 0.8 & \text{Episodes} \le 1000 \\ 0.9 & 1000 < \text{Episodes} \le 2000 \\ 1 & \text{Episodes} > 2000 \end{cases} \tag{52}$$

3.4.8. Training flow

As shown in Fig. 5, the flow of the proposed algorithm is as follows

3.4.9. Parameter selection principle

(1) Learning rate α ($0 < \alpha < 1$). Weigh the stability of the proposed algorithm qualitatively, a larger α can increase the learning speed, and a smaller α can enhance the system stability. To exhibit a faster learning while ensuring stability, α is selected as 0.001.

(2) Discount factor γ($0< \gamma < 1$). The discount factor reflects the attenuation value of the future reward of the function. A value close to 1 should be selected. Simulation verification, choosing γ as 0.97, will get better control effect.

(3) Greedy factor of ε-*explorer* ($0< \varepsilon < 1$). The greedy strategy is exploited to select the action by complying with the probability of ε, and the random strategy is adopted to select the action in accordance with the probability of (1-ε), The explorer employs a low-probability random strategy to break the local optimum, so choose a value close to 1. As revealed from the simulation, selecting ε as 0.90 will achieve better control effects.

(4) Noise variance of Gaussian-DDPG-explorer, OU-DDPG-explorer. As impacted by the use of multiple Gaussian-DDPG-explorer, OU-DDPG-explorer, a noise sequence is proposed to improve the exploration ability. Noise variance of jth OU-DDPG-explorer is 0.07+0.009*j, and the noise variance of mth Gaussian-DDPG-explorer is 0.07+0.09*m.

The mentioned represents the four main parameters applied, and all the optimal parameters are given. The above parameters are determined by conducting a theoretical analysis combined with the trial-and-error methods, other than relying solely on trial and error methods.

4. Case studies

In order to demonstrate the superior qualities of the proposed algorithm, a series of simulations were carried out, each consisting of two stages: pre-learning, and online application. In each experiment, or case study, the EE-MADDPG algorithm-based GAC-LFC has been compared against the following similar algorithms: Apex-MADDPG algorithm-based GAC-LFC (Horgan et al., 2018), MATD3-based GAC-LFC (Fujimoto et al., 2019), and MADDPG-based GAC-LFC (Lowe et al., 2017). In addition, the following conventional algorithms are included: PSO optimized fuzzy PID controller (PSO-Fuzzy-PID) (Bahrami et al., 2014), GA optimized fuzzy PID controller (GA-Fuzzy-PID) (Tan, 2009), Takagi Sugeno fuzzy PID controller (Zhang et al., 2021), and PI controller optimized by PSO (PSO-PID) (Tan, 2010), PID optimized by GA (GA-PID) (Ray et al., 2009), Fuzzy-FOPID (Zeng et al., 2017), FOPID algorithm (Pan and Das, 2015), are used as comparison.

Both the simulation model and programs presented above are developed with a server comprising 48 CPUs. The single CPU is a 2.10 GHz Intel Xeon Platinum processor and the RAM of the server is 192 GB. The simulation software package applied in this study is MATALB/Simulink version 9.8.0 (R2020a).

The four-area LFC model consists of areas A, B, C, and D, which are, respectively, Guangdong Province, Guangxi Province, Guizhou Province, and Yunnan Province.

4.1. Pre-learning

In the pre-learning stage, a continuous sinusoidal load disturbance with a period of 1800 s, an amplitude of 900 MW, a duration of 1800 s, and a phase 0.5*π is applied to Area A. The training diagram is shown in Fig. 6.

In Fig. 6, the curve represents the average value of rewards of episodes in the respective algorithm. As indicated from Fig. 6, the learning speed of the MA-TD3 and MADDPG algorithms is slow, and significant oscillations occur in the learning process. Although the final average reward values of the Ape-x-MADDPG algorithm and the EE-MADDPG algorithm are slightly inconsistent, the EE-MADDPG algorithm converges to the optimal solution earlier and the process is more stable. Furthermore, since the training method of large-scale deep reinforcement learning

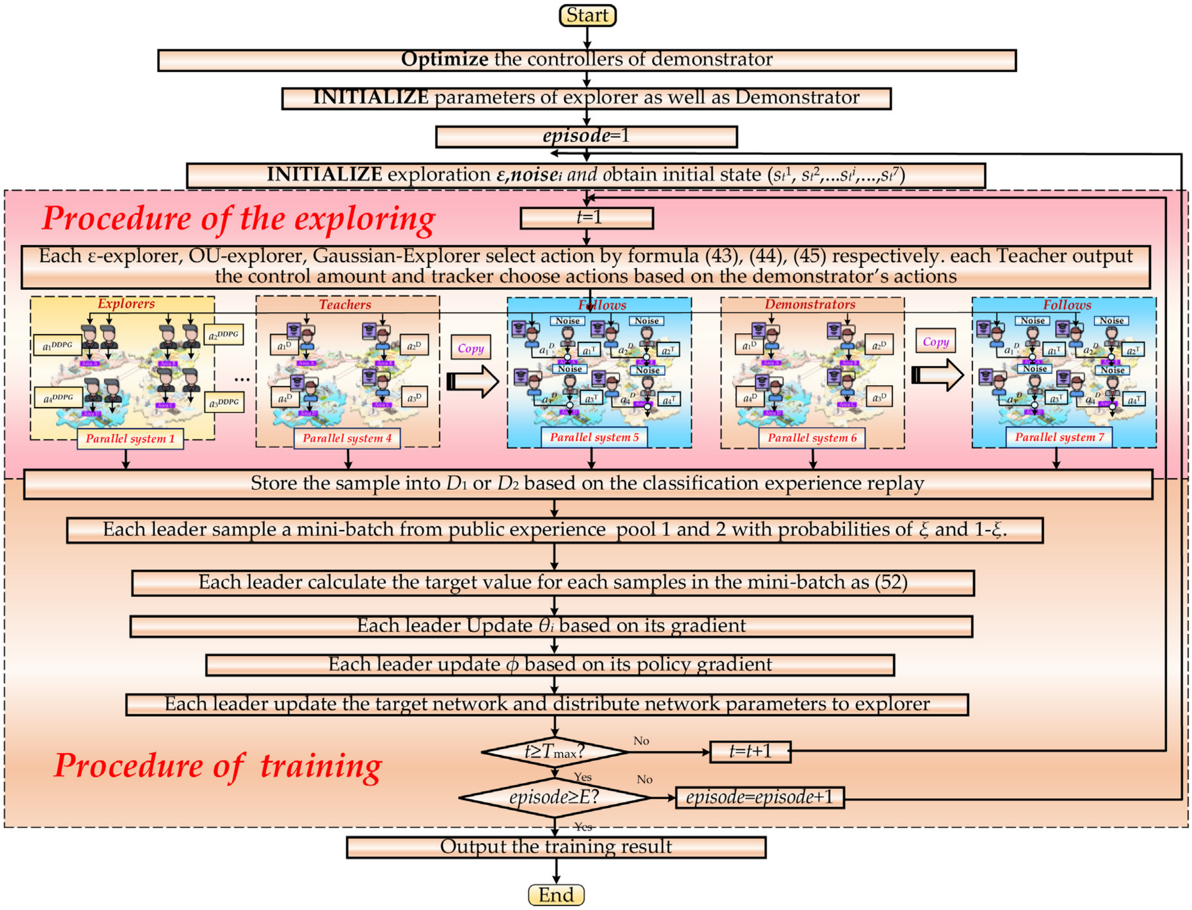

Fig. 5. EE-MADDPG flow.

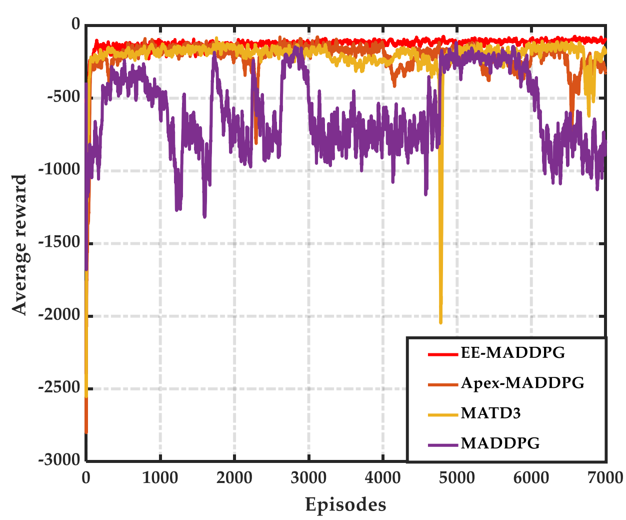

Fig. 6. Convergence curve of MA-DRLs.

is employed in the EE-MADDPG algorithm, under the identical conditions, the learning time of the EE-MADDPG algorithm is significantly shorted than that of the MA-TD3 and MADDPG algorithms. Moreover, the average reward value of the EE-MADDPG and Ape-x-MADDPG algorithm after convergence exceeds that of the MA-TD3 and MADDPG algorithms, thereby demonstrating that the distributed training methods are capable of improving the quality of the solutions obtained by training.

In this study, the computational cost is determined by adopting the computation time of the respective algorithm for training. As indicated from the data listed in Table 1, the computation time required for the EE-MADDPG algorithm and the Apex-MADDPG algorithm by employing the distributed deep reinforcement learning training framework reaches 18 213.6 s and 27 321.9 s, respectively. In comparison, the computation time required for MATD3 and MADDPG by applying the traditional

Table 1
Computation time of each algorithm for training.

Algorithm	Time (s)
EE-MADDPG	18 213.6
Apex-MADDPG	27 321.9
MATD3	92 232.1
MADDPG	99 321.2

deep reinforcement learning training framework reaches 92 232.1 s and 99 321.2 s, respectively. The computation time of the deep reinforcement learning algorithm by applying the distributed reinforcement learning framework is significantly less as compared to the algorithm by applying the traditional deep reinforcement learning training framework. The computation time of the EE-MADDPG algorithm is about 0.13 times that of the MATD3 algorithms. The distributed deep reinforcement learning training framework helps lower the computational cost significantly since the distributed deep reinforcement learning training framework is dependent of multiple agents in multiple parallel systems for distributed exploration, which can expedite the exploration and increase the efficiency of agent training. It is noteworthy that the EE-MADDPG algorithm introduces comprehensive anti-Q overestimation strategy, the experience replay mechanism based on Aronson effect, action space guidance strategy as well as curriculum learning strategies, thereby effectively up-regulating the probability of exploring and training to high-value samples in training, expediting the agent training process, and lowering computational costs. Accordingly, the EE-MADDPG algorithm achieves a shorter computation time. It is therefore concluded that the computational cost of the EE-MADDPG algorithm is significantly lower than that of other algorithms, thereby demonstrating that the EE-MADDPG algorithm can significantly reduce the computational cost in training and satisfy the time requirements of actual applications.

4.2. Online application

4.2.1. Case 1: Stochastic step disturbance

Stochastic step load disturbances with amplitude between +5000 MW and −5000 MW are used, and the EE-MADDPG algorithm is compared with the other algorithms. Fig. 7(a)–(f) and Table 2 provide the online optimization results of the algorithms.

The results in Table 2 show that, compared to the other three MA-DRL algorithms and other algorithms, the CPS1 of the EE-MADDPG algorithm in all four areas (A, B, C, and D) is the largest. In addition, the $|\Delta f|_{\text{avg}}$ and $|E_{ACE}|_{\text{avg}}$ results in each area for the EE-MADDPG algorithm are the smallest among all algorithms. Moreover, the frequency regulation mileage payment of the EE-MADDPG algorithm in the four areas is much lower compared with the other algorithms. Therefore, in contrast with the other algorithms, EE-MADDPG can achieve the optimal multi-area control performance and economic benefits within the context of grid-area coordinated control. Compared with other algorithms, the CPS1 value of the EE-MADDPG algorithm in Area A is 1.73%–8.14% higher, its $|\Delta f|_{\text{avg}}$ result is 41.66%–88.13% lower, its $|E_{ACE}|_{\text{avg}}$ results is 23.11%–73.92% lower, and its regulation mileage payment is 2.59%–123.5%.

These patterns indicate that the EE-MADDPG algorithm, which uses a MA-DDRL training framework and uses a variety of techniques to improve the agent's exploration ability and robustness, is more capable of delivering a higher-performance LFC coordinated control strategy. Under different step disturbances, the EE-MADDPG algorithm can coordinate grid-LFC agents and area-LFC agents, so that each agent can output a sufficiently coordinated total power generation command to the corresponding unit. As shown in Fig. 7(b) and (c), such a coordination strategy can ensure that there is no overregulation and fluctuation in the output of each unit in Area A (Fig. 7(b) and (c)), so that there is no overregulation of total regulated output in Area A (Fig. 7(a)). Moreover, as shown in Fig. 7(d), since the grid-LFC agent and the area-LFC agent in different areas under the control of the EE-MADDPG algorithm can effectively coordinate, the amount of overregulation of the tie line power is also small. Therefore, such stable regulation can reduce wastage of frequency regulation resource of units in Area A, and avoid repeated regulation of units, thereby reducing the frequency regulation mileage payment. In addition, the EE-MADDPG algorithm can call more fast units to participate in the secondary frequency regulation, including hydropower units (G9, G10) in the area-units and hydropower units that have fast capabilities in the grid-units (GG1-GG5). Thus, EE-MADDPG has a faster response speed, and it can restore the frequency and ACE to stable values more smoothly and quickly (Fig. 7(e) and (f)). By contrast, the other MA-DRL algorithms lack the complex techniques needed for enhanced exploration ability, and they apply sub-optimal coordinated control strategies, and in some cases even have difficulties with converging. Therefore, such algorithms are unable to use the optimal

Table 2
Statistical results of Case 1.

Area	Algorithm	$\lvert\Delta f\rvert_{\text{avg}}$/Hz	$\lvert ACE\rvert_{\text{avg}}$/MW	C_{CPS1}/%	Payment/$
Area A	**EE-MADDPG**	**0.00893**	**40.873**	**172.61**	**4434**
	Ape-MADDPG	0.01316	50.319	169.62	8620
	MATD3	0.01265	50.321	167.58	7431
	MADDPG	0.01526	59.217	165.14	9890
	PSO-Fuzzy-PID	0.01377	52.238	166.59	7583
	GA-Fuzzy-PID	0.01680	62.093	161.42	8472
	TS-Fuzzy-PID	0.01396	52.582	166.66	7852
	PSO-PID	0.01656	62.095	165.36	11 440
	GA-PID	0.01424	71.086	158.56	4549
	Fuzzy-FOPID	0.01424	53.258	167.63	8474
	FOPID	0.01427	53.663	167.66	8632
Area B	**EE-MADDPG**	**0.00766**	**2.378**	**198.21**	**431**
	Ape-MADDPG	0.01037	2.448	197.05	580
	MATD3	0.01026	2.655	197.35	544
	MADDPG	0.01214	2.555	196.85	667
	PSO-Fuzzy-PID	0.01143	3.176	197.51	534
	GA-Fuzzy-PID	0.01374	2.766	196.50	680
	TS-Fuzzy-PID	0.01156	2.864	197.65	554
	PSO-PID	0.01284	2.855	197.54	846
	GA-PID	0.01369	4.627	202.80	1601
	Fuzzy-FOPID	0.01154	2.579	196.45	542
	FOPID	0.01151	2.519	196.73	595
Area C	**EE-MADDPG**	**0.00757**	**2.452**	**197.52**	**349**
	Ape-MADDPG	0.00916	2.977	196.69	438
	MATD3	0.00931	2.930	196.88	414
	MADDPG	0.01075	3.459	196.08	473
	PSO-Fuzzy-PID	0.01057	3.511	195.15	332
	GA-Fuzzy-PID	0.01242	3.288	196.67	526
	TS-Fuzzy-PID	0.01065	3.497	195.34	348
	PSO-PID	0.01113	3.447	196.85	620
	GA-PID	0.01183	4.327	197.58	679
	Fuzzy-FOPID	0.01031	3.204	196.46	451
	FOPID	0.01026	3.220	196.42	457
Area D	**EE-MADDPG**	**0.00758**	**3.036**	**196.95**	**515**
	Ape-MADDPG	0.00901	3.188	196.94	626
	MATD3	0.00926	3.129	197.12	590
	MADDPG	0.01053	3.626	196.56	647
	PSO-Fuzzy-PID	0.01021	3.271	196.77	547
	GA-Fuzzy-PID	0.01183	3.938	195.67	708
	TS-Fuzzy-PID	0.01029	3.143	196.95	569
	PSO-PID	0.01108	4.048	195.88	654
	GA-PID	0.01108	3.657	196.83	725
	Fuzzy-FOPID	0.01187	3.246	196.80	646
	FOPID	0.01006	3.306	196.92	691

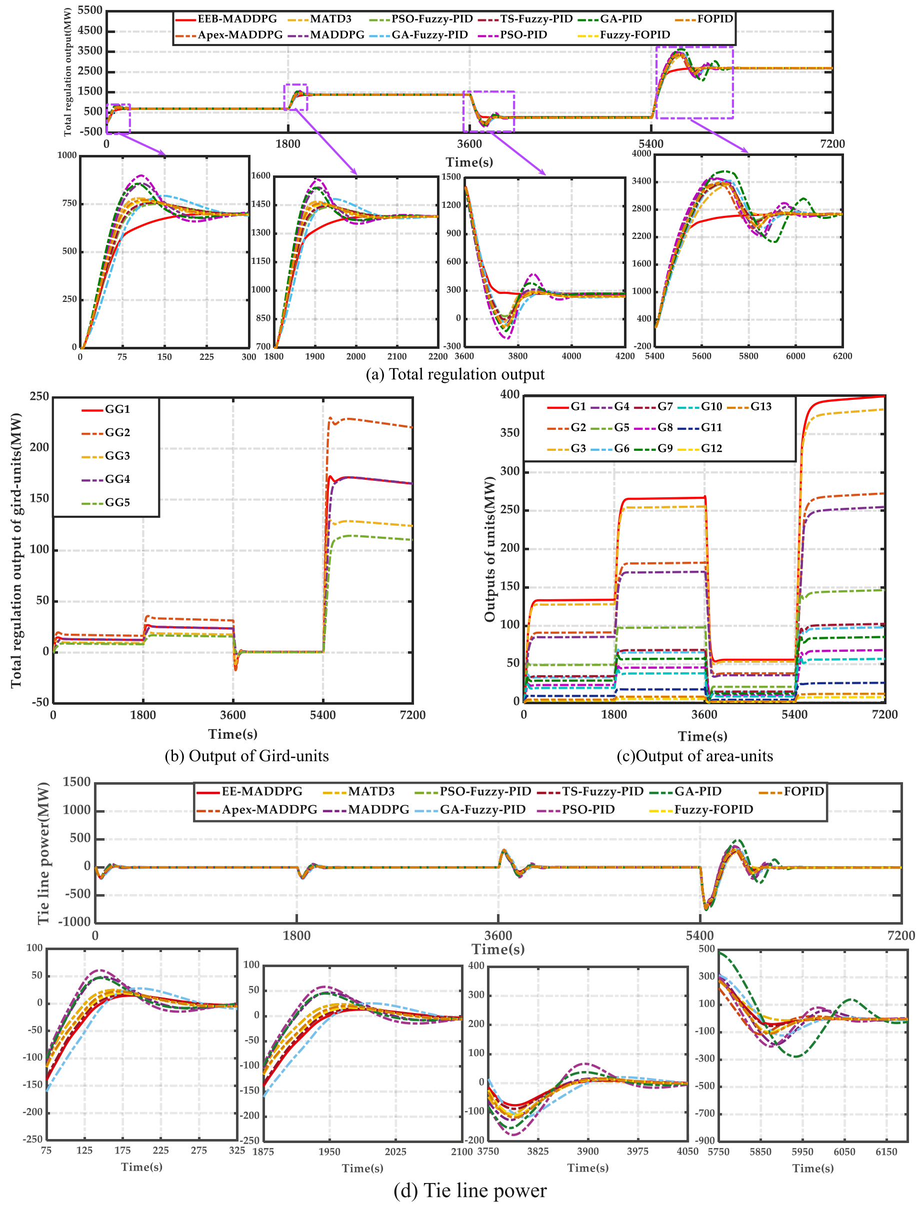

Fig. 7. Results of Case 1.

control allocation strategy to improve their own performance, and they are affected by larger regulation power overregulation, which in turn causes continuous fluctuation of Δf and ACE, and affects LFC performance and frequency regulation mileage payment.

The other conventional control algorithms include fuzzy-based algorithms and optimization-based algorithms. Among them, the Fuzzy-based algorithms has the ability to self-regulate parameters, so it can adjust the parameters of the controller according to the real-time state of the system to adaptively deal with the highly stochastic environment. As shown in Fig. 7(a) and (d), fuzzy-based algorithms obviously have better performance compared with the optimization-based algorithms, with faster response speed of units and smoother recovery speed, and so the fuzzy algorithms have better frequency regulation performance (Fig. 7(e) and Fig. (f)). However, although the fuzzy-based algorithms can adaptively regulate the controller parameters to reduce such fluctuations, this type of regulation cannot play a practical role because the rules are too simple, and there occur mutual coupling and huge influence between the many controllers.

However, neither of these two algorithms considers the coordination between the LFC controllers in different levels and in the multiple areas, which results in the overregulation of the total regulated output of the units in Area A (Fig. 7(a)). In addition, because the controllers between multiple areas cannot be coordinated, the power of the tie line becomes very large, and the amount of overregulation increases greatly (Fig. 7(d)).

This results in a serious waste of frequency regulation resources, which produces a decrease in control performance and an increase in the frequency mileage (Fig. 7(e), (f), (g)), which increases the fluctuation of frequency deviation and fluctuation of ACE.

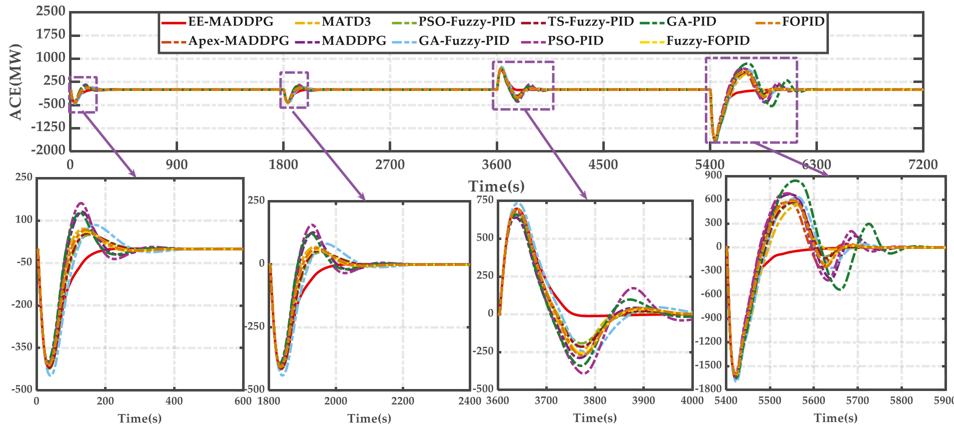

(e)ACE

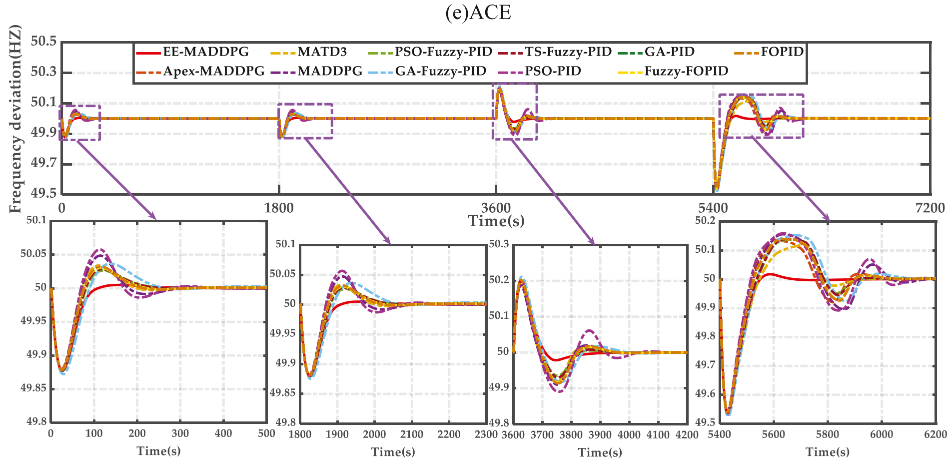

(f)Δf

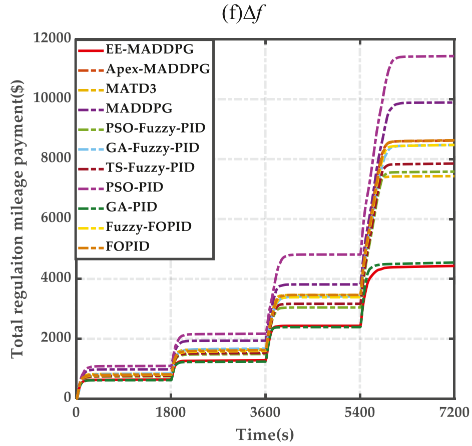

(g) Frequency regulation mileage payment

Fig. 7. (*continued*).

In summary, compared to other algorithms, the EE-MADDPG algorithm has the best multi-area control performance and the smallest frequency regulation mileage payment under stochastic step load disturbances.

4.3. Case 2: A four-area interconnected grid system with distributed power source disturbances

In this model, the actual wind power disturbance, photovoltaic disturbance and stochastic disturbance are introduced to the four-area model.

As shown in Table 3, in Area A, compared with the other algorithms, the $|\Delta f|_{avg}$ result for the proposed algorithm is 3.01%–56.02% lower, its $|E_{ACE}|_{avg}$ result is 1.31%–45.81% lower, its regulation mileage payment is 0.03%–58.69% lower, and its CPS1 is 0.24%–0.87% higher. Similarly, in areas B, C and D the EE-MADDPG algorithm also has the smallest $|\Delta f|_{avg}$ and $|E_{ACE}|_{avg}$ and the largest CPS1.

However, the EE-MADDPG algorithm does not obtain the lowest frequency regulation mileage payment result. This is because when there occur disturbances in areas A and B, the amplitude of the disturbances is so large that areas B and C lend too much power support, which increases the frequency regulation mileage payment in the two areas. However, Fig. 8(k) shows that the total frequency regulation mileage payment of the EE-MADDPG algorithm is the smallest out of all algorithms, indicating that the EE-MADDPG algorithm, which can consider the coordination between the area-LFC agent and the grid-LFC agent, and

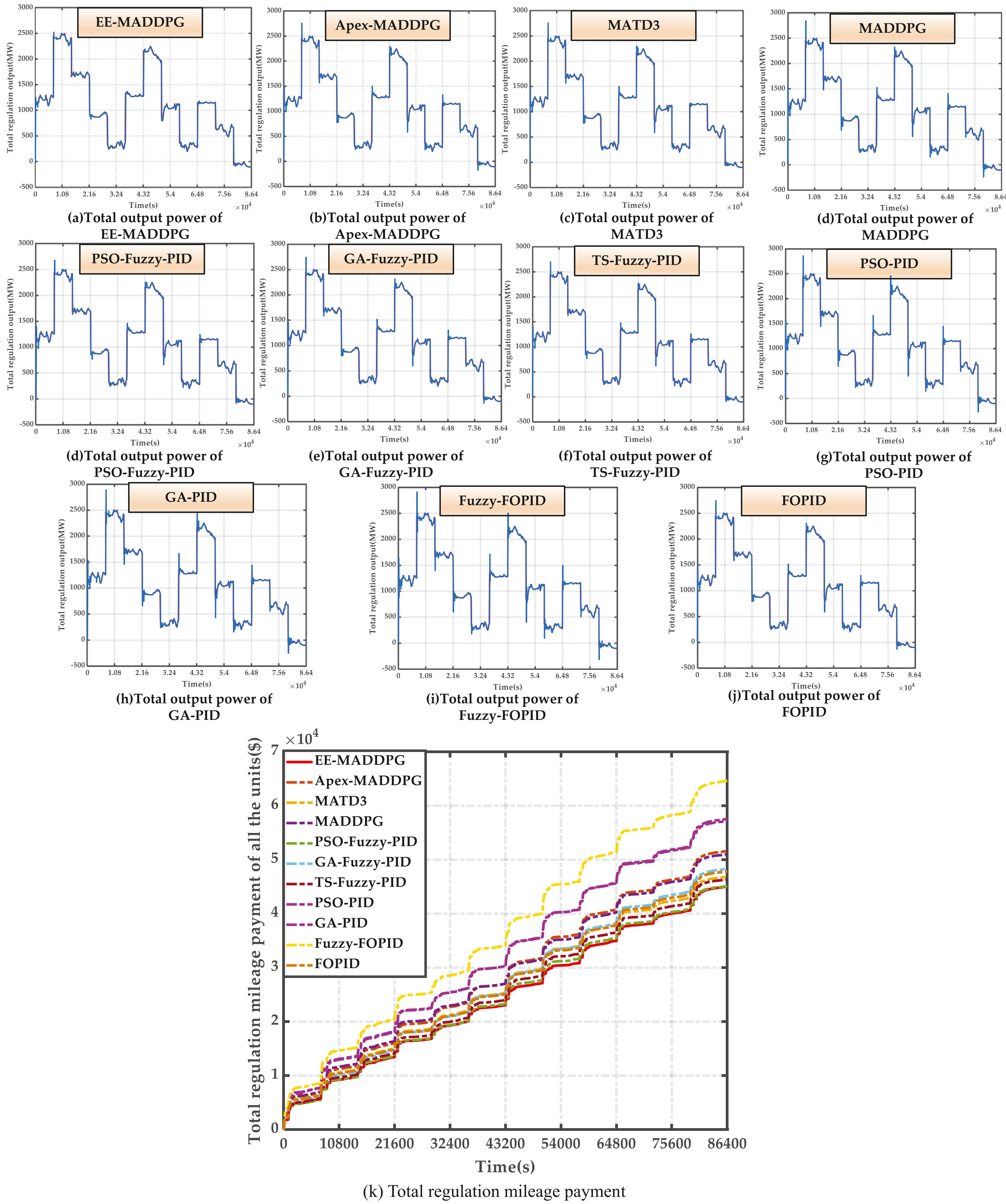

Fig. 8. Results of Case 2.

which has greater exploration ability and robustness, not only can improve the ACE regulation ability of LFC, but also reduce the frequency regulation mileage payment. In addition, it is able to effectively reduce wastage of frequency regulation resources under any stochastic disturbance due to its greater robustness.

Moreover, Fig. 8(a)–(j) shows that, since the EE-MADDPG algorithm can consider the coordination between area-LFC agents and grid-LFC agents, when there occurs a disturbance in the area, the area-LFC agents and the grid-LFC agents. The LFC agents respond quickly. While avoiding the reduction in control performance and economic performance caused by the combination of the area-LFC and the grid-LFC in the area, the algorithm also considers the area-LFC agent and grid-LFC in multiple areas. In addition, the LFC system in other areas can also give more emergency support power to the area, thus improving the frequency regulation ability in the disturbed area. In addition, Fig. 8(a) shows that

Table 3
Statistical results of Case 2.

Area	Algorithm	$\lvert \Delta f \rvert_{avg}$/Hz	$\lvert ACE \rvert_{avg}$/MW	C_{CPS1}/%	Payment/$
Area A	**EE-MADDPG**	**0.00332**	**9.91**	**198.70**	**23 034**
	Ape-MADDPG	0.00452	10.04	198.16	25 445
	MATD3	0.00341	12.95	198.22	24 007
	MADDPG	0.00382	11.37	197.85	27 975
	PSO-Fuzzy-PID	0.00487	10.73	197.92	23 042
	GA-Fuzzy-PID	0.00422	10.73	197.43	24 738
	TS-Fuzzy-PID	0.00466	10.61	197.92	23 650
	PSO-PID	0.00392	11.49	197.76	32 425
	GA-PID	0.00391	11.78	197.69	30 777
	Fuzzy-FOPID	0.00518	14.45	196.98	36 553
	FOPID	0.00342	10.23	198.12	24 380
Area B	**EE-MADDPG**	**0.00423**	**5.02**	**193.69**	11 674
	Ape-MADDPG	0.00362	5.50	193.27	12 655
	MATD3	0.00357	5.49	193.28	11 633
	MADDPG	0.00386	5.35	193.38	12 321
	PSO-Fuzzy-PID	0.00494	10.44	189.63	**11 135**
	GA-Fuzzy-PID	0.00422	10.44	193.23	12 213
	TS-Fuzzy-PID	0.00475	9.54	190.27	11 345
	PSO-PID	0.00388	5.18	193.50	13 293
	GA-PID	0.00390	6.24	193.96	14 484
	Fuzzy-FOPID	0.00511	6.03	193.12	16 159
	FOPID	0.00367	5.54	193.24	11 651
Area C	**EE-MADDPG**	**0.00344**	**2.99**	**197.74**	**4938**
	Ape-MADDPG	0.00345	3.13	197.38	7281
	MATD3	0.00363	3.12	197.39	5003
	MADDPG	0.00361	3.31	197.37	4918
	PSO-Fuzzy-PID	0.00467	5.81	197.45	5243
	GA-Fuzzy-PID	0.00403	5.81	197.38	5428
	TS-Fuzzy-PID	0.00446	5.59	197.53	5613
	PSO-PID	0.00378	3.29	196.74	5414
	GA-PID	0.00359	3.29	197.29	6076
	Fuzzy-FOPID	0.00463	4.40	196.78	6076
	FOPID	0.00350	3.23	197.33	4977
Area D	**EE-MADDPG**	**0.00354**	**3.17**	**198.46**	**5377**
	Ape-MADDPG	0.00356	3.26	198.06	6212
	MATD3	0.00355	3.25	198.07	6170
	MADDPG	0.00367	3.30	198.17	5795
	PSO-Fuzzy-PID	0.00485	3.36	198.30	5652
	GA-Fuzzy-PID	0.00404	3.36	198.06	5911
	TS-Fuzzy-PID	0.00463	3.27	198.30	5714
	PSO-PID	0.00463	3.52	198.12	6404
	GA-PID	0.00371	3.42	197.96	5828
	Fuzzy-FOPID	0.00374	5.24	197.93	5828
	FOPID	0.00461	3.37	197.90	6823

because the EE-MADDPG algorithm uses a variety of techniques to improve the generalization of the algorithm, thereby improving the robustness of the overall strategy, the algorithm attains better performance in each stochastic disturbance. Among the other algorithms, other MA-DRL algorithms have sub-optimal robustness, so they show completely different performances in each stochastic disturbance, which increases wastage of resources caused by repeated LFC regulation, thus reducing LFC performance and increasing regulation mileage payment. The Fuzzy-based algorithms have relatively better frequency regulation performance and less regulation mileage payment due to their adaptive regulation ability. However, because this type of algorithm cannot consider the coordination of grid-LFC and area-LFC controllers in multiple areas, it does not achieve optimal performance. The instantaneous CPS1 result obtained by the EE-MADDPG algorithm in Area A is smoother and more stable, and the maximum CPS1 deviation is smaller. As evidenced in Fig. 8(k), the overregulation problem of ACE is solved because the EE-MADDPG algorithm considers the problem of multi-area LFC coordination. More high-quality frequency regulation resources are used to improve frequency regulation capabilities and reduce wastage of frequency regulation resources, and so frequency regulation mileage is reduced. Therefore, under each disturbance, the algorithm's final total frequency regulation mileage payment is the smallest, and the multi-area economic benefits are optimal.

5. Conclusion

Based on the above analysis, the following conclusions are drawn:

(1) In order to enable full participation of high-performance units controlled by different dispatching centers in the performance-based frequency regulation market, a data-driven grid-area coordinated load frequency control strategy using unified performance-based frequency regulation market mechanism is proposed. Thus, the strategy solves the problem of poor coordination among LFC controllers in different areas of the interconnected power grid.

(2) In addition, an effective exploration based multi-agent depth deterministic policy gradient (EE-MADDPG) algorithm is proposed as the framework algorithm. In this algorithm, the LFC controller controlled by the grid-dispatching center and the LFC controller controlled by the area-dispatching center in each area are treated as agents. Through centralized training and decentralized execution, the coordination of LFC controllers controlled by different levels of dispatching centers in different areas can be realized. Moreover, the algorithm introduces (i) Comprehensive anti-Q overestimation strategy (ii) The experience replay mechanism based on Aronson effect; (iii) Multi-agent distributed exploration and Action space guidance strategy (iv) Curriculum learning strategies, which altogether improve the training efficiency and exploration ability of the algorithm and amount to a more robust strategy.

(3) In the simulation of the four-area LFC model of CSG, in which the EE-MADDPG algorithm is compared with MA-DRLs and other conventional algorithms, it is found that, compared with other algorithms, the CPS1 result is 0.24%–0.87% higher, its $\lvert \Delta f \rvert_{avg}$ result is 3.01%–56.02% lower, its $\lvert E_{ACE} \rvert_{avg}$ result is 1.31%–45.81% lower, and its regulation mileage payment is 0.03%–58.69% lower. Therefore, this method can significantly reduce the system frequency deviation of each area, and effectively reduces the frequency regulation mileage payment, so as to finally realize coordinated control of grid-area LFC.

The main reasons why the algorithm cannot be employed practically are presented below. The EE-MADDPG algorithm cannot be trained on the actual power grid since the actual grid fails to withstand unexpected results (e.g., the serious collapse of the grid frequency attributed to training). If it is required to be achieved, a digital twin system with the identical response performance as the actual power grid should be built.

(4) Future work: Our subsequent work aims to build a digital twin system and verify the method in the actual power grid system. Moreover, more techniques will be exploited to improve algorithm performance.

Declaration of competing interest

The authors declare that they have no known competing financial interests or personal relationships that could have appeared to influence the work reported in this paper.

References

Bahrami, S., Hooshmand, R.-A., Parastegari, M., 2014. Short term electric load forecasting by wavelet transform and grey model improved by PSO (particle swarm optimization) algorithm. Energy 72, 434–442. http://dx.doi.org/10.1016/j.energy.2014.05.065.

Fujimoto, S., Hoof, H., Meger, D., 2019. Addressing function approximation error in actor-critic methods. In: Proceedings of the 35th International Conference on Machine Learning. PMLR, Stockholm, Sweden, pp. 1587–1596.

Ghafouri, A., Milimonfared, J., Gharehpetian, G.B., 2018. Fuzzy-adaptive frequency control of power system including microgrids, wind farms, and conventional power plants. IEEE Syst. J. 12 (3), 2772–2781. http://dx.doi.org/10.1109/JSYST.2017.2715819.

Ghasempour, A., Lou, J., 2017. Advanced Metering Infrastructure in Smart Grid: Requirements, Challenges, Architectures, Technologies, and Optimizations. Smart Grids: Emerging Technologies, Challenges and Future Directions. Nova Science Publishers, New York.

Horgan, D., Quan, J., Budden, D., Barth-Maron, G., Hessel, M., Van Hasselt, H., Silver, D., 2018. Distributed prioritized experience replay. In: 6th International Conference on Learning Representations. Vancouver, BC, Canada.

Klimontowicz, M., Al-Hinai, A., Peng, J.C.H., 2016. Optimal LFC SMC for three-area power system with high penetration of PV. J. Electr. Syst. 12 (1), 68–84, https://www.ingentaconnect.com/content/doaj/11125209/2016/00000012/00000001/art00005#Refs.

Kumar, L.V.S., Kumar, G.V.N., Madichetty, S., 2017. Pattern search algorithm based automatic online parameter estimation for AGC with effects of wind power. Int. J. Electr. Power 84, 135–142. http://dx.doi.org/10.1016/j.ijepes.2016.05.009.

Li, Y., Dong, L., You, Y., Gao, Y., Liao, X., 2014. Load frequency control based on ADRC for inter connected power system. In: Proceedings of the 33rd Chinese Control Conference. IEEE, pp. 8158–8163. http://dx.doi.org/10.1109/ChiCC.2014.6896366.

Li, J., Li, Y., Yu, T., 2021a. An optimal coordinated proton exchange membrane fuel cell heat management method based on large-scale multi-agent deep reinforcement learning. Energy Rep. 7, 6054–6068. http://dx.doi.org/10.1016/j.egyr.2021.09.015.

Li, J., Yu, T., 2021a. A novel data-driven controller for solid oxide fuel cell via deep reinforcement learning. J. Clean. Prod. 321, 128929. http://dx.doi.org/10.1016/j.jclepro.2021.128929.

Li, J., Yu, T., 2021b. A new adaptive controller based on distributed deep reinforcement learning for PEMFC air supply system. Energy Reports 7, 1267–1279. http://dx.doi.org/10.1016/j.egyr.2021.02.043.

Li, J., Yu, T., Yang, B., 2021. A data-driven output voltage control of solid oxide fuel cell using multi-agent deep reinforcement learning. Appl. Energy 304, 117541. http://dx.doi.org/10.1016/j.apenergy.2021.117541.

Li, J., Yu, T., Zhang, X., 2021b. Emergency fault affected wide-area automatic generation control via large-scale deep reinforcement learning. Eng. Appl. Artif. Intell. 106, 104500. http://dx.doi.org/10.1016/j.engappai.2021.104500.

Li, J., Yu, T., Zhang, X., 2022a. Coordinated load frequency control of multi-area integrated energy system using multi-agent deep reinforcement learning. Appl. Energy 306, 117900. http://dx.doi.org/10.1016/j.apenergy.2021.117900.

Li, J., Yu, T., Zhang, X., Li, F., Lin, D., Zhu, H., 2021c. Efficient experience replay based deep deterministic policy gradient for AGC dispatch in integrated energy system. Appl. Energy 285, 116386. http://dx.doi.org/10.1016/j.apenergy.2020.116386.

Li, J., Yu, T., et al., 2022b. Coordinated automatic generation control of interconnected power system with imitation guided exploration multi-agent deep reinforcement learning. Int. J. Electr. Power Energy Syst. 136, 107471. http://dx.doi.org/10.1016/j.ijepes.2021.107471.

Lowe, R., Wu, Y., Tamar, A., Harb, J., Abbeel, P., Mordatch, I., 2017. Multi-agent actor-critic for mixed cooperative-competitive environments. In: Proceedings of the 31st Conference on Neural Information Processing Systems (NIPS 2017). pp. 1–12, https://proceedings.neurips.cc/paper/2017/file/68a9750337a418a86fe06c1991a1d64c-Paper.pdf.

Pan, I., Das, S., 2015. Fractional-order load-frequency control of interconnected power systems using chaotic multi-objective optimization. Appl. Soft Comput. 29, 328–344. http://dx.doi.org/10.1016/j.asoc.2014.12.032.

Ray, G., Prasad, A.N., Prasad, G.D., 2009. A new approach to the design of robust load-frequency controller for large scale power systems. Electr. Power. Syst. Res. 51 (1), 13–22. http://dx.doi.org/10.1016/S0378-7796(98)00125-4.

Shirazi, SAG., Menhaj, MB., 2006. A new genetic based algorithm for channel assignment problems. In: Computational Intelligence, Theory and Applications. Springer, Berlin, Heidelberg, pp. 85–91.

Tan, W., 2009. Tuning of PID load frequency controller for power systems. Energ. Convers. Manage 50 (6), 1465–1472. http://dx.doi.org/10.1016/j.enconman.2009.02.024.

Tan, W., 2010. Unified tuning of PID load frequency controller for power systems via IMC. IEEE Trans. Power Syst. 25 (1), 341–350. http://dx.doi.org/10.1109/TPWRS.2009.2036463.

Variani, M.H., Tomsovic, K., 2013. Distributed automatic generation control using flatness-based approach for high penetration of wind generation. IEEE Trans. Power Syst. 28 (3), 3002–3009. http://dx.doi.org/10.1109/TPWRS.2013.2257882.

Wang, Y., Zhou, R., Wen, C., 1994. New robust adaptive load frequency control with system parametric uncertainties. IET Gener. Transm. Distrib. 141 (3), 184–190. http://dx.doi.org/10.1049/ip-gtd:19949757.

Xi, L., Chen, J., Huang, Y., Xu, Y., Liu, L., Zhou, Y., Li, Y., 2018. Smart generation control based on multi-agent reinforcement learning with the idea of the time tunnel. Energy 153, 977–987. http://dx.doi.org/10.1016/j.energy.2018.04.042.

Xi, L., Wu, J., Xu, Y., Sun, H., 2021. Automatic generation control based on multiple neural networks with actor-critic strategy. IEEE Trans. Neural Netw. Learn. 32 (6), 2483–2493. http://dx.doi.org/10.1109/TNNLS.2020.3006080.

Xi, L., Yu, L., Xu, Y., Wang, S., Chen, X., 2020. A novel multi-agent DDQN-AD method-based distributed strategy for automatic generation control of integrated energy systems. IEEE Trans. Sustain. Energy 11 (4), 2417–2426. http://dx.doi.org/10.1109/TSTE.2019.2958361.

Xi, L., Yu, T., Yang, B., Zhang, X., 2015. A novel multi-agent decentralized win or learn fast policy hill-climbing with eligibility trace algorithm for smart generation control of interconnected complex power grids. Energ. Convers. Manage. 103, 82–93. http://dx.doi.org/10.1016/j.enconman.2015.06.030.

Yan, Z., Xu, Y., 2020. A multi-agent deep reinforcement learning method for cooperative load frequency control of a multi-area power system. IEEE Trans. Power Syst. 35 (6), 4599–4608. http://dx.doi.org/10.1109/TPWRS.2020.2999890.

Yousef, H.A., Al-Kharusi, K., Albadi, M.H., Hosseinzadeh, N., 2014. Load frequency control of a multi-area power system: An adaptive fuzzy logic approach. IEEE Trans. Power Syst. 29 (4), 1822–1830. http://dx.doi.org/10.1109/TPWRS.2013.2297432.

Yu, T., Wang, Y.M., Ye, W.J., Zhou, B., Chan, K.W., 2011a. Stochastic optimal generation command dispatch based on improved hierarchical reinforcement learning approach. IET Gener. Transm. Distrib. 5 (8), 789–797. http://dx.doi.org/10.1049/iet-gtd.2010.0600.

Zeng, G.-Q., Xie, X.-Q., Zhang, Z.-J., Yan, Z.-B., Sun, J.-L., Wu, L., Wang, H., Dai, Y.-X., 2017. Distributed fractional-order PID control of multi-area interconnected power systems by population based cxtremal optimization. In: Proceedings of the IECON 2017-43rd Annual Conference of the IEEE Industrial Electronics Society. IEEE, pp. 227–232. http://dx.doi.org/10.1109/IECON.2017.8216042.

Zhang, Y., Liu, X., Yan, Y., 2015. Model predictive control for load frequency control with wind turbines. J. Control Sci. Eng. 2015, 282740. http://dx.doi.org/10.1155/2015/282740.

Zhang, X., Tan, T., Yang, B., Wang, J., Li, S., He, T., Yang, L., Yu, T., Sun, L., 2020. Greedy search based data-driven algorithm of centralized thermoelectric generation system under non-uniform temperature distribution. Appl. Energy 260, 114232. http://dx.doi.org/10.1016/j.apenergy.2019.114232.

Zhang, X., Tan, T., Zhou, B., Yu, T., Yang, B., Huang, X., 2021. Adaptive distributed auction-based algorithm for optimal mileage based AGC dispatch with high participation of renewable energy. Int. J. Electr. Power 124, 106371. http://dx.doi.org/10.1016/j.ijepes.2020.106371.

In electric vehicle technologies, the state-of-the-art of power electronics converters configurations

Smruti Samantray, Department of Electronics and Communication Engineering , Capital Engineering College, Bhubaneswar, smrutisamantray23@hotmail.com

Rudra Prasad Nanda, *Department of Electrical and Communication Engineering, Aryan Institute of Engineering & Technology, Bhubaneswar, rudraprasad858@gmail.com*

Smruti Ranjan Panda, *Department of Electrical and Electronics Engineering, Raajdhani Engineering College, Bhubaneswar, sr_panda@outlook.com*

Romeo Jena, *Department of Electrical and Electronics Engineering, Capital Engineering College, Bhubaneswar, romeo_jena2@hotmail.com*

Keywords:
Renewable energy
DC-DC bidirectional converter
Electric vehicle
Battery electric vehicle
Fuel cell vehicle
Hybrid electric vehicle
Plug-in electric vehicle

A B S T R A C T

Today, the Internal Combustion Engine (ICE) is gradually being replaced by electric motors, which results in higher efficiency and low emission of greenhouse gases. The electric vehicle either works wholly or partially on electrical energy generated from batteries and ultra-capacitors. The battery or ultra-capacitor is either charged from the AC supply connected to a grid line in a plug-in electric vehicle or from ICE in a hybrid electric vehicle. Alternatively, the battery charges from the traction motor by regenerative braking. In the reverse direction, the energy from the battery or ultra-capacitor is injected into the AC grid line in the plug-in electric vehicle. Power electronic converters play a vital role in the conversion process from grid line to traction motor and in the reverse direction. In this paper, the role of power electronics converters in an electric vehicle is elaborated. The bidirectional DC-DC converter plays a vital role in the power conversion process of electric vehicles. The existing bidirectional DC-DC converter topologies are discussed with a comprehensive review, comparison, and application. Additionally, the advancement in power electronics converters to improve the efficiency and reliability of the vehicular system is elaborated.

1. Introduction

Fossil fuel is depleting gradually due to excessive use to propel in the conventional vehicular system (Bhaskar, Padmanaban & Holm-Nielsen, 2019b; Ida, Murakami & Tanaka, 2014; Querini, Dagostino, Morel & Rousseaux, 2012; Shareef, Islam & Mohamed, 2016; Williamson, Rathore & Musavi, 2015; Yong, Ramachandaramurthy & Tan, 2015a). Moreover, the demand for fossil fuel is also gradually increasing due to advancements in the vehicular system (Afonso, Marques & Fuinhas, 2017; Gielen et al., 2019; Guo, Liu, Sun & Jin, 2018; Jenniches, 2018). The efficiency of conventional ICE is nearly 20%. The remaining energy is wasted as heat and Greenhouse Gases (GHG) as a by-product after combustion (Adams, Klobodu & Apio, 2018; Awasthia et al., 2017). Some key features of EVs are ease of operation; fewer moving parts that reflect increasing efficiency, pollutant-free, capable of frequently starting and stopping operation, and high starting torque (Adams et al., 2018). Apart from this, the electric vehicle is becoming an emerging concept in renewable generating facilities and advanced grid systems (Awasthia et al., 2017). In a Plug-in Electric Vehicle (PEV), the battery injects power into the gridline to overcome the overload problem and to provide ancillary services (Gough, Rowley & Walsh, 2014; Mukherjee & Gupta, 2015; Schaltz, Khaligh & Rasmussen, 2009; Subramaniam et al., 2019). All these features of electric vehicles are encouraging researchers to take this technology to the next level.

In recent advancements in automobile system, advanced Power Electronics Converters (PECs) and motor drives play an essential role in vehicular technology (Baha & Thomas, 2013; Bhaskar et al., 2019a; Bhaskar, Sanjeevikumar, Holm-Nielsen, Pedersen & Leonowicz, 2019c; Emadi, Rajashekara, Williamson & Lukic, 2005; Krishna, Daya, Sanjeevikumar & Mihet-Popa, 2017; Un-Noor, Padmanaban, Mihet-Popa, Mollah & Hossain, 2017). In EVs, PECs and electric motor drives control the flow of electrical energy within the vehicle or from the external charging station or grid to the vehicle and vice versa (Awasthia et al., 2017; Subramaniam et al., 2019). This makes EVs pollutant-free, more efficient, higher performance and increases the durability of the vehicle (Bhaskar et al., 2018; Daramy-Williams, Anable & Grant-Muller, 2019; Daya et al., 2016; Lane et al., 2018; Li, Khajepour & Song, 2019; Tahami, Kazemi & Farhanghi, 2003; Wu & Gao, 2006; Zhao, He, Yao & Huang, 2019; Zhou, Yang, Cai & Ying, 2018). In a conventional ICE

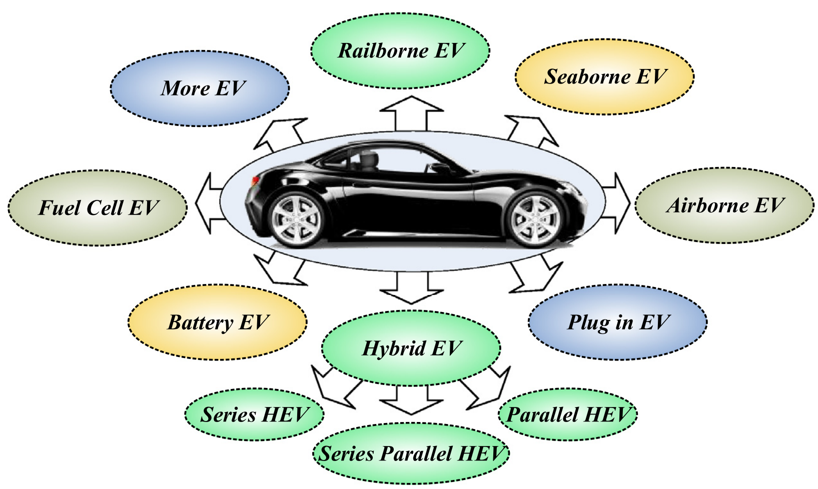

Fig. 1. General classification of electric vehicle.

vehicle, 6 V to 12 V is needed to start up and to run other electric equipment (Miller & Webster, 1997). The hydraulic system such as brake and mechanically driven system such as steering is being replaced by an electrically driven system, which makes it more efficient and safer (Adams et al., 2018). The luxurious load such as power windows, high power headlamp, and auto start-up is introduced in advanced automobile systems that demand higher power with different voltage ratings to work. Hence, power electronics converters are responsible for the advancement in EVs (Chan, 2002).

This paper will elaborate on the state-of-the-art of the PECs in the battery, hybrid, fuel cell, and plug-in electric vehicle systems and compare the associated advantages and disadvantages of the existing PECs for theze vehicular systems. In this paper, section-II elaborates the classifications of an electric vehicles, their structures, modes of operation, and the role of PECs in each vehicular system. Section-III deals with the role of PECs in existing electrical vehicular technology and discusses the non-isolated bidirectional DC-DC converter. Section-IV includes the challenges in power electronics vehicular systems.

2. Types of electrical vehicle and role of power electronics converter

EVs use electrical energy to drive the vehicle and for the electrical appliances in the vehicle to function. According to the International Electro-Technical Commission's Technical Committee (IETCTC), if the vehicle uses two or more energy sources, storage device, and converter to drive the vehicle, then it's called a Hybrid Electric Vehicle (HEV) as long as at least one source is providing electrical energy (Awasthia et al., 2017). EVs are classified into different types according to the combination of sources (Bayindir, Gozukucuk & Teke, 2011). The battery alone works as a source in the Battery Electric Vehicle (BEV), fuel cell and battery in Fuel Cell Electric Vehicle (FCEV), battery and ICE in HEV, and battery and grid or external charging station in PEV as shown in Fig. 1. The details of the EV types are discussed in the following section.

2.1. Battery electric vehicle

2.1.1. Architecture of battery electric vehicle

In a BEV, the battery provides power to drive the train of the vehicle (Cassani & Williamson, 2009; Ehsani, Gao & Gay, 2005; Grunditz & Thiringer, 2016). The rechargeable battery storage unit acts as a fuel tank in BEV. Therefore, the range of a BEV depends on the capacity of the battery unit. Typically, once it is fully charged, the BEV covers 100 km to 250 km distance (Awasthia et al., 2017). In BEV, ICE is replaced by an electric motor to propel which makes it a pollution-free vehicle. The typical structure of BEV is shown in Fig. 2(a). The 14 V to 300 V rechargeable batteries is used in BEV according to the type of vehicle. Light-duty, mid-duty, and heavy-duty vehicles need 14 V, 120 V and 150 V DC batteries, respectively (Hegazy, Barrero & Van Mierlo, 2013; Musavi, Craciun & Gautam, 2014; Rodatz, Garcia & Guzzella, 2003). Two operating modes are observed in BEV. The power from the battery is transferred to the vehicle through a DC-DC converter and an inverter in the battery operating mode. In regenerative braking mode, the power generated by traction motor transfers to the battery via rectifier and DC-DC converter.

2.1.2. Role of PECs in battery electric vehicle

In BEV, the unidirectional step-up DC-DC converter is adopted to boost the voltage as per the demand of the propelling system and electrical load (Adams et al., 2018; Awasthia et al., 2017). The low voltage/power rated equipment, such as mobile charger receives supply from the battery. The DC voltage of the battery is transferred to a high voltage DC bus through the step-up converter. The high voltage DC bus supply power to higher voltage rated equipment such as projector lamps. The function of the DC-AC inverter is to convert DC into a variable (voltage and frequency) three-phase AC to drive the AC motor. To drive the vehicle, and other electronic types of equipment, the DC power supply from the battery is used as fuel. The voltage controller controls the DC-DC converter to maintain the charging level of the battery at its maximum and minimum limits (Miller & Webster, 1997) as shown in Fig. 2(b).

2.2. Fuel cell electric vehicle

2.2.1. Architecture of fuel cell electric vehicle

The hybrid FCEV is a type of electric vehicle in which both the fuel cell and the battery provide electrical power to drive the train of the vehicle (Lai & Nelson, 2007; Marchesoni & Vacca, 2007; Thomas, 2009). In FCEV, oxygen from the air is combined with the stored hydrogen to generate power for driving the electric motor. From a fuel tank, hydrocarbon gas is transferred to the fuel reformer to achieve purity of hydrogen gas and is stored in the fuel cell stack (Tazelaar, Veenhuizen & Jagerman, 2013). As per the requirement of power, hydrogen for fuel cell stacks is combined with oxygen from the air to generate electricity, and excess electricity can be saved in batteries or ultra-capacitors.

There are different types of fuel cells available in the market, such as polymer electronic membrane (PEM), direct methanol fuel cells, phosphoric acid fuel cells, regenerative fuel cells, reformed methanol fuel cells, solid oxide fuel cells, and molten carbonate fuel cells (Das, Tan & Yatim, 2017). Both hybrid and fuel cell vehicles are pollutant-free, and the by-product is water. The schematic block diagram of hybrid and fuel cell vehicle is shown in Fig. 3(a). The operating mode of FCEV is divided

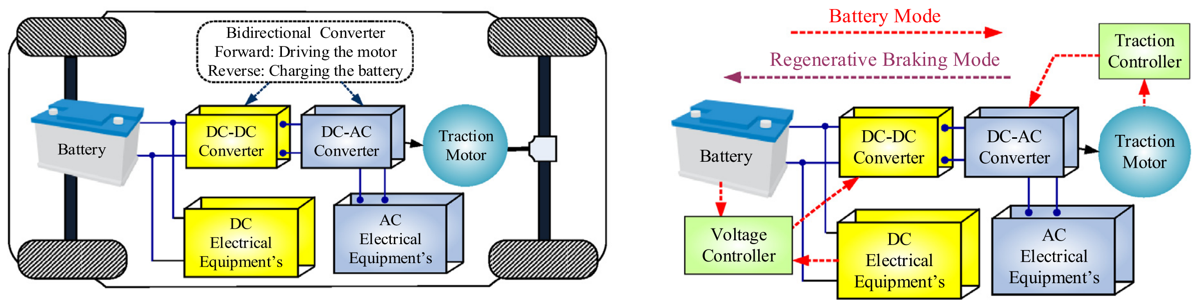

(a) (b)

Fig. 2. Battery Electric Vehicle (a) Typical structure of BEV, (b) Control scheme operating modes of BEV.

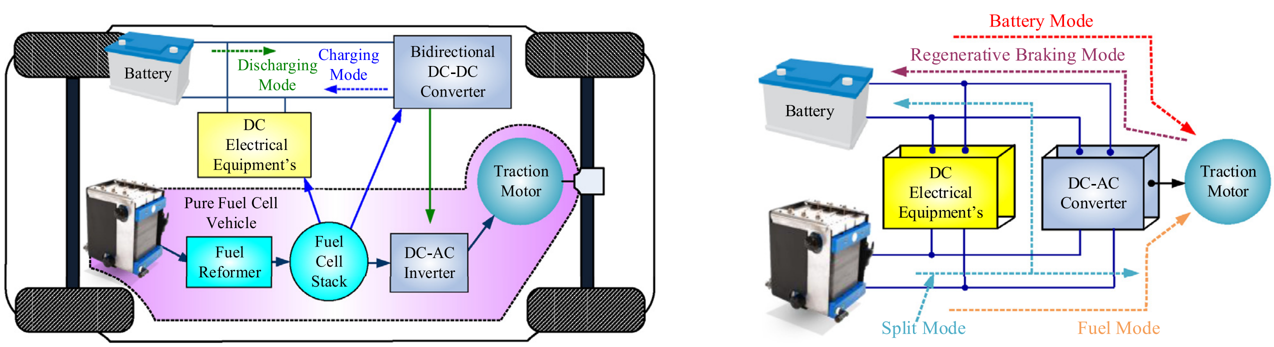

(a) (b)

Fig. 3. Fuel Cell Electric Vehicle (a) Typical structure of FCEV, (b) Operating modes of FCEV.

into five modes, as shown in Fig. 3(b). In fuel mode, the fuel cell acts as a source of energy to propel the train individually. In battery mode, the battery works as a source of energy to drive the train. If both the battery and fuel supply are together, then it is called a "combined mode" (Miller & Webster, 1997). In split mode, the fuel cell supplies power to drive the vehicle, and excess energy is utilized to charge the battery. In a regenerative mode, the traction motor acts as a source to charge the battery (Jafri & Gupta, 2016; Schaltz, 2010).

2.2.2. *Role of PECs in fuel cell electric vehicle*

In FCEV, the electric energy is generated from the battery and fuel cell. The main goal of FCEVs is to convert electrical energy from fuel cells to usable power for various loads of the vehicle by using an efficient method to improve the efficiency and performance of the vehicle (Adams et al., 2018; Awasthia et al., 2017).

Low voltage DC equipments, such as mobile charger, auto starters receives power directly from a battery or fuel cell. For motor drive and high voltage applications, the low voltage is stepped-up to 300 V using a step-up DC-DC converter. The traction controller is adapted to maintain the required speed of the vehicle by varying the amplitude and frequency of the inverter output. The voltage controller is adapted to maintain the maximum and minimum charging levels of the battery and to increase its life, as shown in Fig. 4. In FCEV electrical system, a bidirectional DC-DC power converter plays a key role to controlling the energy flow from the fuel cell to a traction motor during motor mode and from the motor to the battery during regenerative braking mode in hybrid FCEV. The bidirectional DC-DC power converter controls the energy flow with the help of traction and voltage controllers.

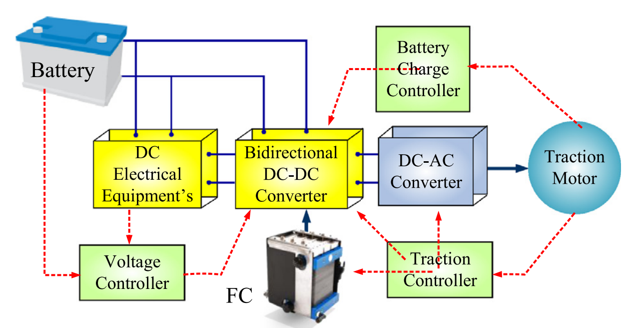

Fig. 4. Control scheme of FCEV.

2.3. *Hybrid electric vehicles (HEVS)*

The hybrid electric vehicle is a combination of an ICG vehicle and a BEV (Gao, Ehsani & Miller, 2005). The ICE provides the necessary propelling power to drive the train of vehicles. By regenerative mechanism, the lost energy during the braking mechanism is stored in the battery to increase the efficiency and economy of the vehicle. Customarily, there are two types of hybrid electric vehicles, namely Series Hybrid Electric Vehicle (SHEV) and Parallel Hybrid Electric Vehicle (PHEV) (Chiu & Lin, 2006; Gruosso, 2014; Zhang & Williamson, 2008). To improve power, performance and fuel economy, a third series-parallel hybrid vehicle (SPHEV) was introduced by combining the features of SHEV and PHEV (Gurkaynak, Khaligh & Emadi, 2009).

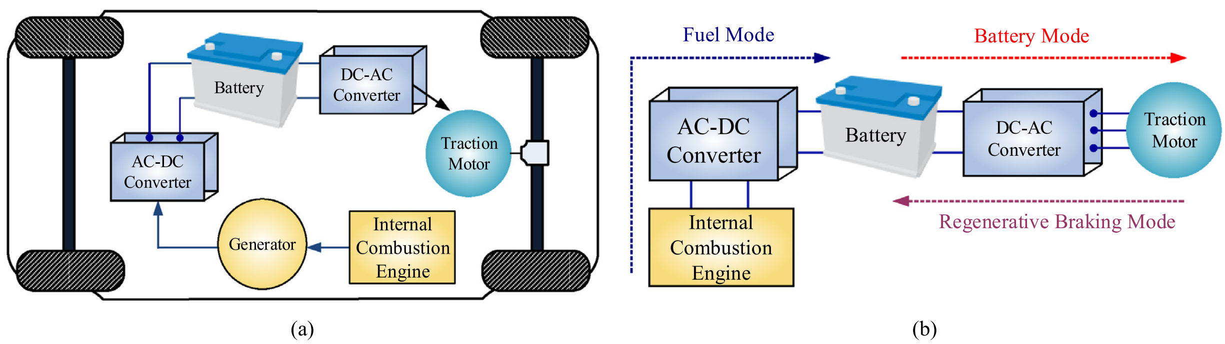

Fig. 5. SHEV (a) Typical structure of SHEV (b) Different operating mode of SHEV.

2.3.1. *Series hybrid electric vehicle*

In SHEV, both ICE and the battery is modeled in such a way that they can generate the necessary power to propel the train and peripheral electric/electronic equipment (Parag Jose & Meikandasivam, 2016; Roche, Shabbir & S., 2017). In SHEV, the mechanical energy from ICE is converted to electrical form by using a generator. The generated AC power is converted into the DC form to charge the battery by using an AC-DC rectifier (Akbarian, Pillay & Lopes, 2015). In SHEV, the ICE is not directly connected to the traction motor to drive the train. In between ICE and the traction motor, the battery is the intermediate unit. To drive the train, SHEV requires three propulsion devices. ICE will generate mechanical energy, and the generator will convert mechanical energy into electrical energy, whereas the traction motor will convert the electrical energy to mechanical energy for propelling the vehicle (Nayanatara, Shanmugapriya & Gurusivakumar, 2014; Razavian, Azad & McPhee, 2012). Therefore, the efficiency of SHEV is lower. The typical structure of SHEV is shown in Fig. 5(a).

In SHEV, the battery is the primary source of power to drive the train. The ICE runs at the optimal speed to drive the generator and charge the battery. When the State of Charge (SOC) of the battery is minimized, the ICE starts to charge the battery. As the SOC reaches its maximum level of around 65%–70%, the ICE stops charging the battery. The battery is the source of power to drive the train, which reduces the fuel consumption and emissions of the vehicle. The SHEV is a viable solution when the frequent starting and stopping of the vehicle is required, such as in city rides (Miller & Webster, 1997). Three operating modes are observed in SHEV. First, in the fuel mode, ICE is utilized to charge the battery according to the SOC of the battery. In the battery mode, the propelling power is gained from the battery. The traction motor also acts as a source during braking operations to charge the battery, which is called regenerative braking mode, as shown in Fig. 5(b).

2.3.2. *Parallel hybrid electric vehicle*

The PHEV is another type of HEV in which both the ICE and the battery act as a source to drive the train of the vehicle (Desai & Williamson, 2009; Li, Yu & Ding, 2010). Both the ICE and the battery can drive the train individually, as shown in Fig. 6(a). Both the ICE and the electrical motor are coupled to the driving shaft via two clutches. The ICE is directly connected to the mechanical shaft of the drive train to propel the vehicle (Adams et al., 2018). As there are no intermediate conversion stages between ICE and the drive train, the efficiency of PHEV is greater when compared to SHEV. For long distance range, a PHEV is a viable solution due to no intermediate conversion state as in SHEV. Hence, the vehicle is fuel efficient (Olson & Sexton, 2000).

In a PHEV, there are three different ways to utilize the ICE and battery, as shown in Fig. 6(b). In motor mode, the battery is utilized to power the train, which is a viable solution for lower speeds. In fuel mode, the ICE runs at an optimal speed to drive the train at high speed. During braking or deceleration operations, the traction motor acts as a generator to charge the battery in regenerative braking mode (Miller & Webster, 1997).

In PHEV, the lowest DC voltage is boosted by a bidirectional DC-DC converter to feed the high voltage DC bus. The function of the three-phase inverter is to convert the constant DC voltage into variable AC voltage and frequency to maintain the torque and speed of the traction motor.

2.3.3. *Series-Parallel hybrid electric vehicle*

The Series-Parallel Hybrid Electric Vehicle (SPHEV) configuration incorporates the features of SHEV and PHEV (Gruosso, 2014; Gurkaynak et al., 2009; Zhang & Williamson, 2008). In SPHEV, the generator is introduced in between ICE and the battery to charge the battery as compared to PHEV and ICE is directly connected to the mechanical shaft to drive the vehicle as compared to SHEV as shown in Fig. 7(a). From the architecture, it is clear that SPHEV is more complicated and expensive as compared to the other two HEV (Khaligh & Dusmez, 2012).

There are five different ways to utilize the ICE and battery to propel the vehicle and other electrical equipment function, as shown in Fig. 7(b). In fuel mode, the ICE works to drive the vehicle. However, the propelling power is received from the battery in the battery mode. During split mode, the ICE transfers power to the traction motor, and the excess power is utilized to charge the battery. Both the ICE and the battery provides power to the traction motor in combine mode. During braking and deceleration operations, the traction motor acts as a generator and supplies power to the battery in regenerative braking mode. The most adopted strategy for effective utilization of battery and ICE in SPHEV is that the battery is utilized to start operation and propel at low speed after the ICE works alone to drive at high speed, which increases the vehicle's fuel efficiency. When acceleration is needed, the battery mode is in an active state to give extra power along with the ICE (Kim & Kum, 2016).

2.3.4. *Role of PECs in hybrid electric vehicle*

As discussed earlier, the HEVs work on electric energy generated from the battery, mechanical energy from the ICE, and from both battery and ICE (Adams et al., 2018; Awasthia et al., 2017). The PECs maintain and control the flow of energy from the battery or ICE to the traction motor and the traction motor to the battery with the help of a voltage and traction controller. The low voltage from the battery is supplied to the low voltage rated DC equipment such as mobile chargers and auto start-up. The AC-DC rectifier adopted converts the variable AC to a constant DC voltage during regenerative braking mode. In battery mode, high DC voltage is converted into variable AC quantities to maintain the required torque and speed. The control schemes of SHEV, PHEV and SPHEV are shown in Fig. 8(a)–(c), respectively.

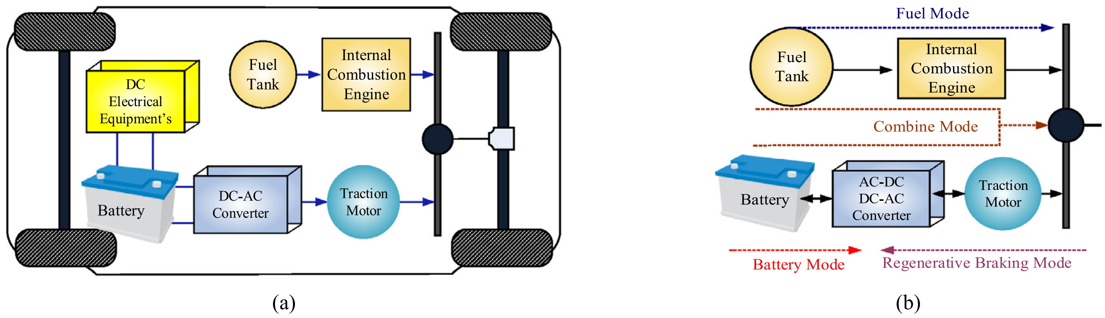

Fig. 6. PHEV (a) Typical structure of PHEV (b) Different operating mode of PHEV.

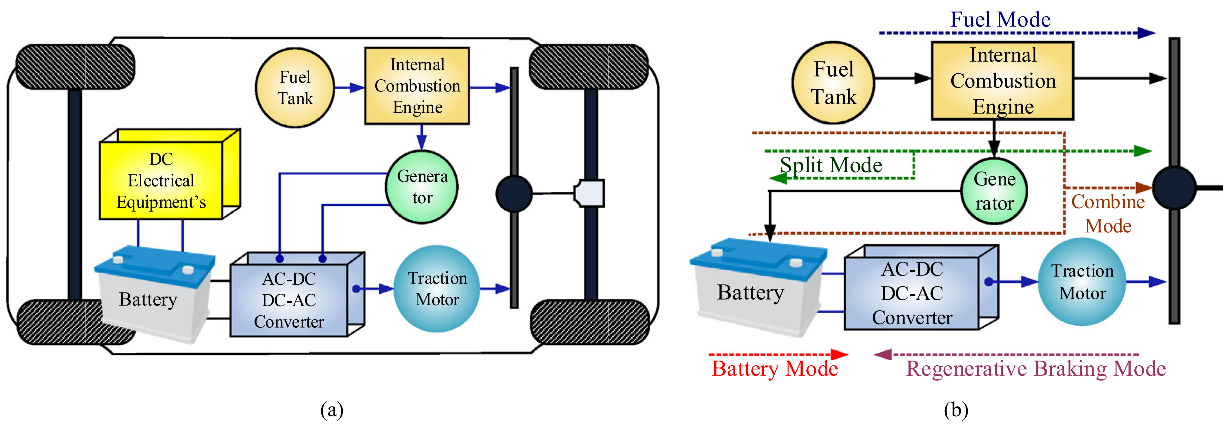

Fig. 7. SPHEV (a) Typical structure of SPHEV (b) Different working mode of SPHEV.

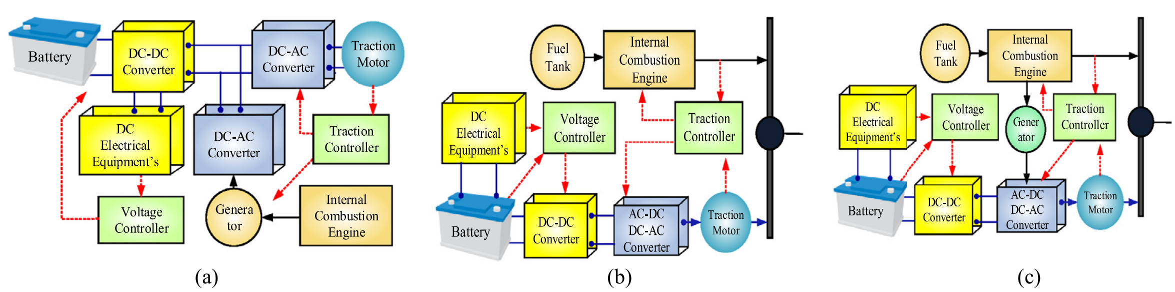

Fig. 8. Control schemes of (a) SHEV, (b) PHEV and (c) SPHEV.

2.4. *Plug-In electric vehicles*

2.4.1. *Architecture of plug-in electric vehicle*

The PEV is a type of HEV in which the battery is charged from an external source. The ICE is not sufficient to convert the fuel energy to mechanical energy to drive the shaft. Most of the energy is lost as heat during conversion (Li & Williamson, 2007; Li, Sharkh & Walsh, 2011; Mwasilu, Justo & Kim, 2014). Moreover, the ICE emits greenhouse gases as a by-product. To overcome the drawback of ICE, ICE is replaced by the battery. PEV has less maintenance cost due to fewer moving parts. The typical structure of PEV is shown in Fig. 9(a) and it is similar to SHEV. PEVs have an external charge unit for charging the battery, whereas SHEVs have it on board (Li, Lopes & Williamson, 2009; Williamson, 2007). The PEV works on the electrical supply, where the battery is charged at the battery charging station. The charging station may be at home or grid. Conceptually, PEV works in two modes, grid to the vehicle (G2V), in which the battery charges from the grid, and the other is the vehicle to grid (V2G), where the battery injects power into the grid, as shown in Fig. 9(b).

In the V2G concept (Subramaniam et al., 2019), battery energy can be injected into the grid to solve the overloading problem of the grid. In G2V mode, the power from the grid is utilized to drive the vehicle and charge the battery, mostly during no-load conditions on the grid line through various PECs. In regenerative braking mode, the traction motor acts as a generator to charge the battery. In V2G mode, the charged battery from either regenerative braking or from the grid is utilized to inject power into the grid power line to overcome the problem of peak load overvoltage and ancillary services, or used as an uninterrupted power supply during blackouts (Awasthia et al., 2017).

2.4.2. *Role of PECs in plug-in electric vehicle*

In a PEV, the power from the grid is transferred to the traction motor to propel the vehicle and charge the battery. Alternatively, the energy from the battery is injected into the grid. In both cases, to transfer the energy from one end to the other end, voltage conversion should be done in between the two ends. The rectifier unit is utilized to convert the three-phase or single-phase power to constant DC power to charge the battery through a step-down DC-DC converter (Adams et al., 2018;

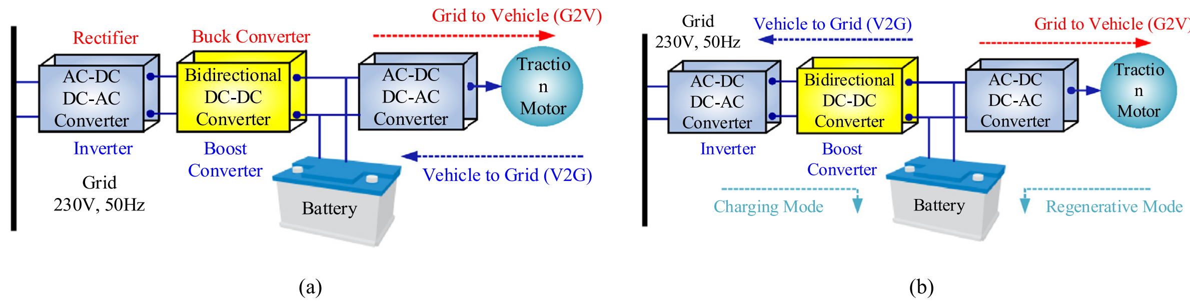

Fig. 9. PEV (a) Typical structure of PEV, (b) Different operating mode of PEV.

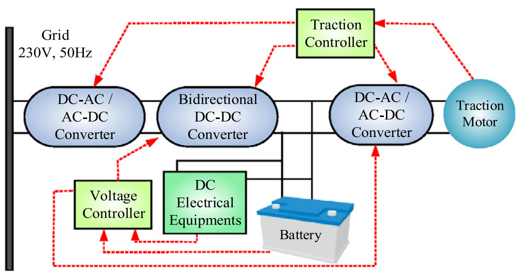

Fig. 10. Control scheme of PEV.

Table 1
Operating Modes of Evs.

Types of Vehicle	Mode of energy flow				
	Fuel	Battery	Split	Combine	Regenerative
BEV		√			√
FCEV	√	√	√	√	√
SHEV		√			√
PHEV	√	√		√	√
SPHEV	√	√	√	√	√
PEV		√			√

Awasthia et al., 2017). For maintain the speed and torque of the traction motor, traction control is adopted. The voltage controller controls the power flow from the battery in/out directions. In PEV, the bidirectional DC-DC converter plays a vital role in controlling the bidirectional flow of energy. It operates in step-up mode during V2G mode and acts as a step-down converter in G2V mode. The operating mode of the bidirectional DC-DC converter is controlled by the voltage controller, as shown in Fig. 10 (Elnozahy & Salama, 2014; Yong, Ramachandaramurthy & Tan, 2015b).

2.5. *Summary of electric vehicles*

As discussed above, five different operating modes in EVs that describe the flow of power from the battery, fuel cell, or ICE to the vehicle and from the vehicle to the battery or grid are articulated in Table 1. As per the operating modes of EVs, the different types of PECs utilized for specific operations are articulated in Table 2. The bidirectional DC-DC converter is adopted in EVs to allow regenerative braking to charge the battery.

3. Power electronics converters in electric, hybrid and fuel cell vehicle

3.1. *Existing power electronics converter in EVs*

In EVs, the power from battery/ultra-capacitor, fuel cell or ICE is utilized to drive the vehicle and functions of onboard electrical/electronic load (Amjadi & Williamson, 2010; Cabezuelo, Andreu & Kortabarria, 2017; Chan & Chau, 1997; Elnozahy & Salama, 2014; Emadi, Lee & Rajashekara, 2008; Helsper & Ruger, 2014; Hofmann, Schäfer & Ackva, 2014; Naghizadeh & Williamson, 2013; Onar, Kobayashi & Khaligh, 2013; Rajashekara, 2003). In fuel mode, the voltage from the fuel cell is not sufficient to drive the vehicle. Therefore, it is boosted by the unidirectional boost converter (Jafri & Gupta, 2016). Various electrical/electronic loads are present on the vehicle, which increase the luxurious features and comfort of the vehicle, as shown in Fig. 11.

Some electrical loads require high AC voltage, such as air conditioner and power windows, which receive power from a DC-AC converter. Mirror adjustment and drive seat adjustment work on a DC motor feed from a battery or fuel cell through a DC-DC converter. All these electrical loads operate at different voltage ratings (Adams et al., 2018). The projector lamp requires 42 V for projecting the light, and the interior lamp requires 12 V for its operation. Electronic loads such as sensors, communication systems and tacho-metre require low voltage for their operation. The need of different rated voltage supplies increases as the electrical/electronic load increases on the vehicle, which is not possible from a single battery supply as discussed in previous sections. The number of DC-DC converters increases with increasing different rated loads, which results in a lower efficiency of a single battery structure vehicular system. According to Adams et al. (2018), two types of architecture are adopted in the hybrid automobile system. One is a vehicular system that works on ICE or a fuel cell with a single battery (36 V). Another is the ICE, or fuel cell, which works with a double battery (14 V and 42 V).

The typical structure of the dual battery system is shown in Fig. 12. In the dual battery system (Cabezuelo et al., 2017), dual voltage is generated from a generator in HEV or from the grid in a PEV. The 36 V battery is utilized for mid voltage applications and the 12 V battery for low voltage applications. However, 36 V from the battery is boosted to 42 V for the drive and high voltage applications. The typical electrical system of EVs is shown in Fig. 13. The voltage generated from the generator optimizes to charge the battery with the help of the rectifier and unidirectional DC-DC converter in SHEV and SPHEV, to drive the vehicle in PHEV and FCEV (Elnozahy & Salama, 2014; Yong et al., 2015b). The voltage from the fuel cell and the battery is boosted by the unidirectional and bidirectional DC-DC converters, respectively. The boosted voltage supplies to high voltage DC applications and is converted into the variable frequency and voltage with the help of a three-phase inverter. Advanced EVs can utilize the wasted energy during deceleration and braking to charge the battery. In regenerative braking mode, the three-phase converter works as a three-phase rectifier. The rectified output is converted to the battery voltage with the help of a bidirectional DC-DC converter (Amjadi & Williamson, 2010; Choubey & Lopes, 2017; Chung, Chow & Hui, 2000; Di Napoli, Crescimbini & Solero, 2002; Dobbs & Chapman, March, 2003; Dusmez, Hasanzadeh & Khaligh, 2014; Emadi, 2005; Emadi, Lee & Rajashekara, 2008; Ha, Lee & Hwang, 2012; Khaligh, 2008; Khaligh & Li, 2010; Khan, Ahmed & Husain, 2015; Kuo, Lo & Chiu, 2014; Lulhe & Date, 2015; Ni, Patterson &

Table 2
Utilization of PEC in EVs.

Types of Vehicle		Power Electronics Converters			
		DC-DC converter		Rectifier	Inverter
		Uni-directional	Bi-directional		
BEV			√	√	√
FCEV		√		√	√
HEV	SHEV		√	√	√
	PHEV		√	√	√
	SPHEV		√	√	√
PEV	G2V		√	√	√
	V2G		√	√	√

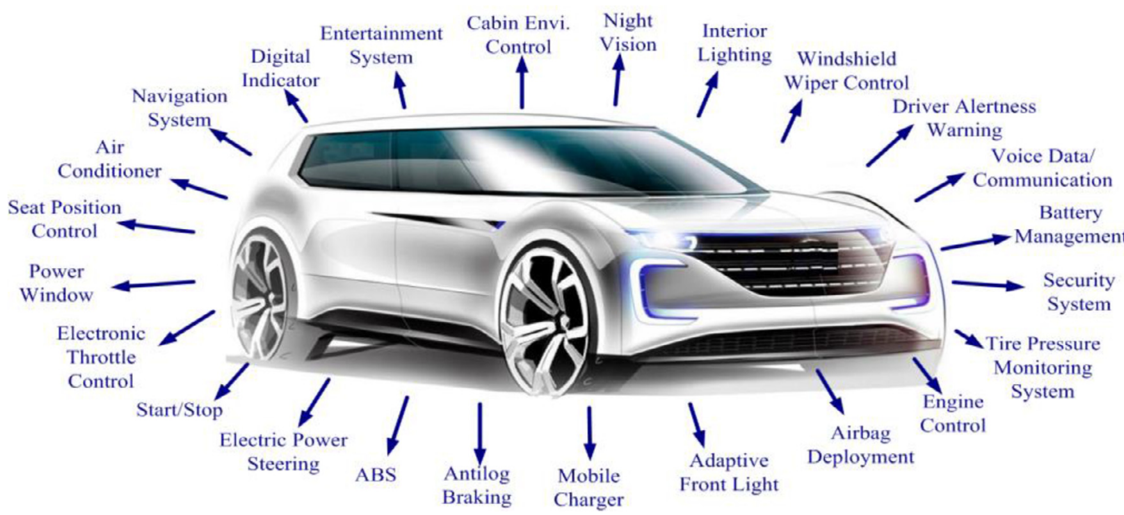

Fig. 11. Electrical appliances of EVs.

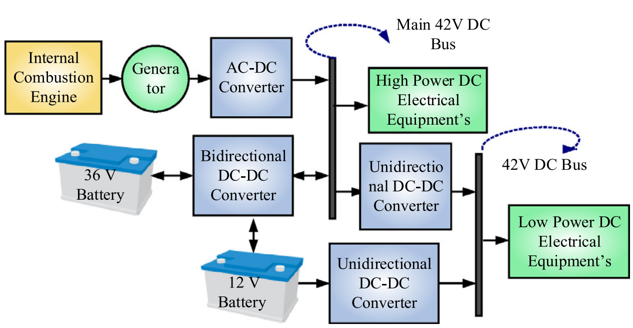

Fig. 12. Dual battery scheme for EVs.

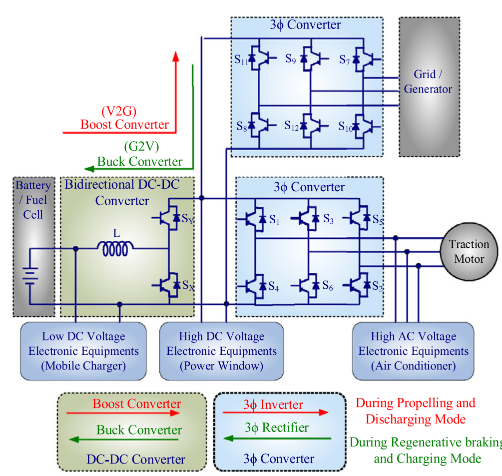

Fig. 13. General electrical structure of EVs.

Hudgins, 2012; Onwuchekwa & Kwasinski, 2011; Waffler & Kolar, 2009; Wu, Lu, Shi & Xing, 2012; Yang, Guan, Zhang, Jiang & Huang, 2018).

In a recent vehicular system, a three-phase converter acts as an inverter during fuel, battery, split and combine mode whereas rectifier in regenerative mode. The selection of converter mode is sophisticated and controlled by the traction controller unit. The traction controller generates the controlled pulses for the three-phase converter according to the received signal from the traction motor and vehicle drivers. The controlled pulse decides the operation of the three-phase converter as an inverter or rectifier. The voltage control unit controls the SOC of the battery at the maximum and minimum level. The voltage controller continuously receives the SOC level signal from the battery and compare it with the reference voltage signal, consistent with this controlled pulse generate for DC-DC converter to maintain the SOC of the battery to increase its lifespan and avoid power wastage.

3.2. *Classification of power electronics converters*

The general classification of PECs is shown in Fig. 14. As discussed in the previous section, each converter has its own functional/role. In this section, we will discuss the existing non-isolated bidirectional DC-DC converters for EVs. The bidirectional DC-DC converter is a basic conversion unit in EVs. It acts as a boost converter from low voltage to high voltage side direction and a buck converter from high voltage to low voltage side direction.

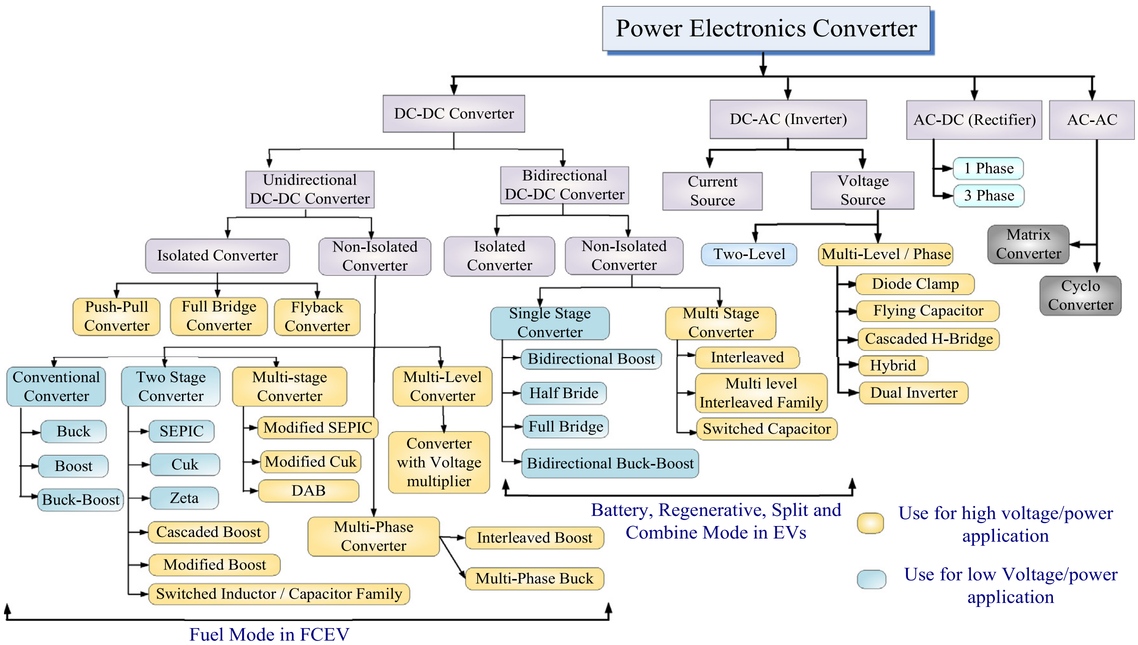

Fig. 14. Classification of Power Electronics Converters.

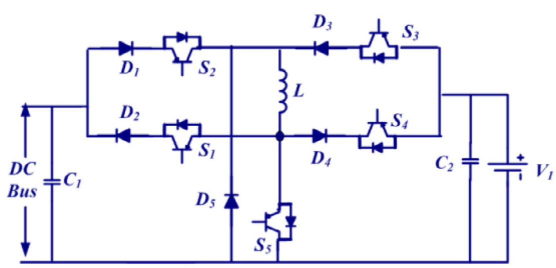

Fig. 15. Universal Bidirectional DC-DC Converter (Onar et al., 2013).

Table 3
Operating Modes of Bidirectional DC-DC Converter.

Direction	Mode	S_1	S_2	S_3	S_4	S_5
V_{DC} to V_1	Boost	ON	OFF	OFF	ON	PWM
V_{DC} to V_1	Buck	PWM	OFF	OFF	ON	OFF
V_1 to V_{DC}	Boost	OFF	ON	ON	OFF	PWM
V_1 to V_{DC}	Buck	OFF	ON	PWM	OFF	OFF

The universal bidirectional DC-DC converter in Onar et al. (2013) is shown in Fig. 15. The converter operates in both buck and boost mode with non-inverting output. The different operating modes are articulated in Table 3. Apart from the universal bidirectional converter, single input, multi-input, multistage, and multiphase non-isolated converters are adopted for bi-directional power flow. Fig. 16(a)–(c) and Fig. 17(a),(b) shows the single input non-isolated bidirectional DC-DC converter. Amjadi and Williamson (2010) Represent the buck-boost bidirectional converter for EV applications, as shown in Fig. 16(a). It works in both modes depending upon the switching pattern. It consists of two active and two passive components with lower electrical and thermal stress. It has the disadvantage of higher ripple current, which damages the battery, and discontinuous output current during boost mode mode, which the size of output capacitors. Fig. 16(b) represents the improved buck-boost converter (Emadi, 2005) where the anti-parallel diode reduces the stress across the power MOSFET and eventually increases the efficiency of conversion. The cascaded bidirectional buck-boost converter (Choubey & Lopes, 2017; Lulhe & Date, 2015; Waffler & Kolar, 2009; Wu et al., 2012) is shown in Fig. 16(c). It can maintain the SOC of the battery and recuperate the braking energy from the electrical motor.

However, it has double the number of active components as compared to the conventional bidirectional buck-boost converter. The bidirectional CUK and SEPIC with Luo converter are shown in Fig. 17(a) and (b), respectively (Amjadi & Williamson, 2010). The converter can operate in both buck and boost mode. The input and output current ripple are reduced in the CUK converter. In SEPIC with a Luo converter, the SEPIC converter works as a boost converter, and the Luo converter works as a buck converter. The disadvantage of SEPIC with the Luo converter is the discontinuous output current.

The numbers of active and passive components in single input non-isolated bidirectional DC-DC converters are articulated in Table 4, where L represents the inductor, C for the capacitor, S for the active switch, and D represents the diode. In addition to the single input topologies, multiple-input topologies are also adopted for bi-directional power flow in EVs. Fig. 18 shows the existing non-isolated bidirectional DC-DC converter with multiple inputs. The input may be the battery, fuel cell, or ultra-capacitor. The response from a fuel cell or ICE to the DC bus is slower as compared to battery (Khan et al., 2015). The battery and ultra-capacitor are utilized to provide the power for DC bus, as shown in Fig. 18(a). By utilization of two sources in one application permits the relatively low voltage from each source and controls the current from multiple inputs. Fig. 18(b) represents the multi-input hybrid conversion topology (Khaligh, 2008; Khan et al., 2015).

The presented topology is capable of diversifying the energy amongst the different energy sources with different voltage-current characteristics. The advantage of the multiple-input bidirectional converters is the least number of components and a positive output voltage without the transformer. The circuit works as a buck, boost, or buck-boost independently. Fig. 18(c) represents a multi-input cascaded boost converter for FCEV. According to Marchesoni and Vacca (2007), the multi-input hybrid boost converter has the advantage of three controlled power devices as compared to conventional boost converter.

The limitation of representing topology is that the voltage sum of two energy sources should be less than a DC link bus. The efficiency is higher if the power of both sources is in the same direction. In Di Napoli et al. (2002); Dusmez et al. (2014); Onwuchekwa and Kwasin-

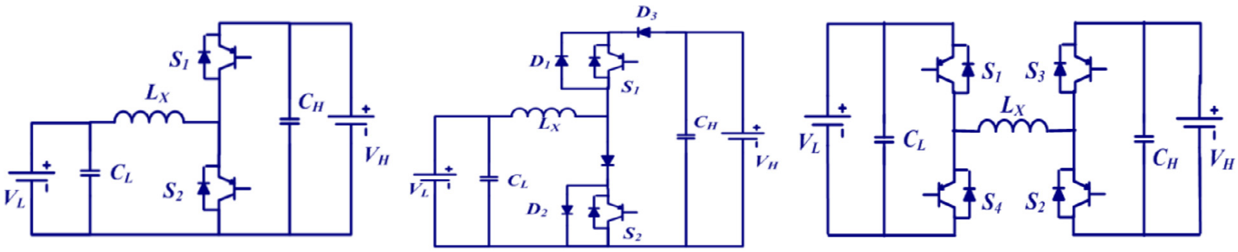

(a) (b) (c)

Fig. 16. Single input non-isolated bidirectional DC-DC Converters (a) buck-boost converter (Amjadi & Williamson, 2010), (b) improved buck-boost Converter (Emadi, 2005), (c) full bridge converter (Waffler & Kolar, 2009).

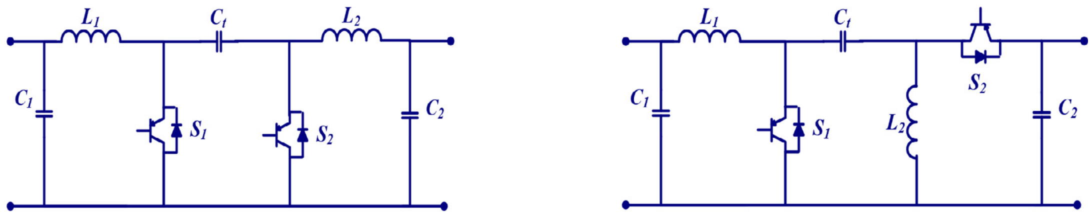

(a) (b)

Fig. 17. Single input non-isolated bidirectional DC-DC Converters (a) bidirectional CUK converter (Amjadi & Williamson, 2010) and (b) bidirectional SEPIC with Luo converter (Z. Amjadi & Williamson, 2010).

Table 4
The number of components in Single Input converters.

Converter	Passive Components		Active Components	
	L	C	S	D
Conventional Buck-boost Amjadi and Williamson (2010)	1	2	2	0
Improved Buck-boost Emadi (2005)	1	2	2	4
Cascaded Buck-boost Waffler and Kolar (2009)	1	2	4	0
CUK (Amjadi and Williamson (2010)	2	3	2	0
SEPIC with Luo Amjadi and Williamson (2010)	2	3	2	0

Table 5
Number of components in Multiple Input converters.

Converter	Passive Components		Active Components	
	L	C	S	D
Multi input Buck-boost Khan et al. (2015)	2	0	4	0
Multi input boost Khaligh (2008)	2	1	3	0
Multi input converter Marchesoni and Vacca (2007)	1	0	3	0
MI-PEC Di Napoli et al. (2002)	2	3	4	0

ski (2011) MI-PEC represents for the EV application shown in Fig. 18(d) in which VH represents DC power from different energy sources to the DC bus and operates in step-down mode to transfer power from the DC bus to the bus voltage. The MI-PEC works in step-up mode to transfer charge to the battery or ultra-capacitor. In Table 5, the number of components of multi-input non-isolated bidirectional DC-DC converters is articulated. As the number of active and passive components increases, it affects the efficiency of conversion. In Table 5, L represents the inductor, C represents the capacitor, S represents the active switch, and D represents the diode. Fig. 19 shows the multiphase non-isolated bidirectional DC-DC converters for EVs applications. Fig. 19(a) represents the three-phase interleaved boost converter (Khaligh & Li, 2010; Yang et al., 2018). The multiphase converter overcomes the drawbacks of the conventional bidirectional DC-DC converter by reducing the input-output current ripples. Several phases increase the ripple content in the current decreases, but eventually, it decreases the efficiency by increasing the number of active and passive components per phase. Fig. 19(b) shows the different structures of the interleaved boost converter (Ni et al., 2012). Several phases increase, the size of the input and output filter decreases. The represented topology has a greater number of active and passive components as compared to the topology shown in Fig. 19(a).

Fig. 20 shows the Switched Capacitor (SC) structure topologies for EVs. In Amjadi and Williamson (2010); Chung et al. (2000); Ni et al. (2012), SC topology was explained, and the structure is shown in Fig. 20(a). The SC structure offers the features of step-up, step-down, and both for bidirectional flow of power. The topology works in two modes, A and B. The efficiency of the represented topology is 85% in mode-A and 80% in mode-B. Fig. 20(b) and (c) show zero current switchings switched capacitor quasi-resonant converter with single-level and two-level configurations, respectively (Lee & Chiu, 2005). The configuration improves the problem of current stress during the bidirectional flow using SC structure and one inductor. With the help of L and C, the converter achieves zero switching currents and reduces the losses. The semiconductor device MOSFET is turned ON and OFF in a zero current

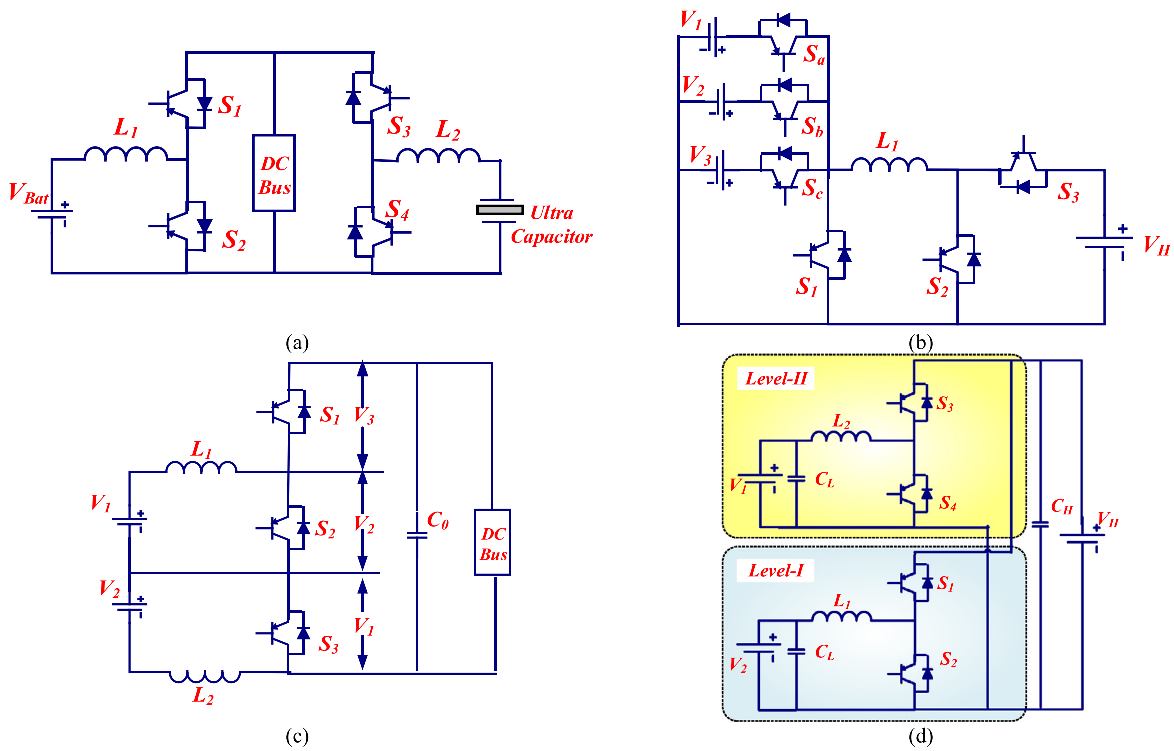

Fig. 18. Multiple input non-isolated bidirectional DC-DC converters (a) Multi input buck-boost converter (Khan et al., 2015), (b) Multi input converter (Khaligh, 2008), (c) multi input cascaded boost converter (Marchesoni & Vacca, 2007) and (d) MI-PEC (Di Napoli et al., 2002) .

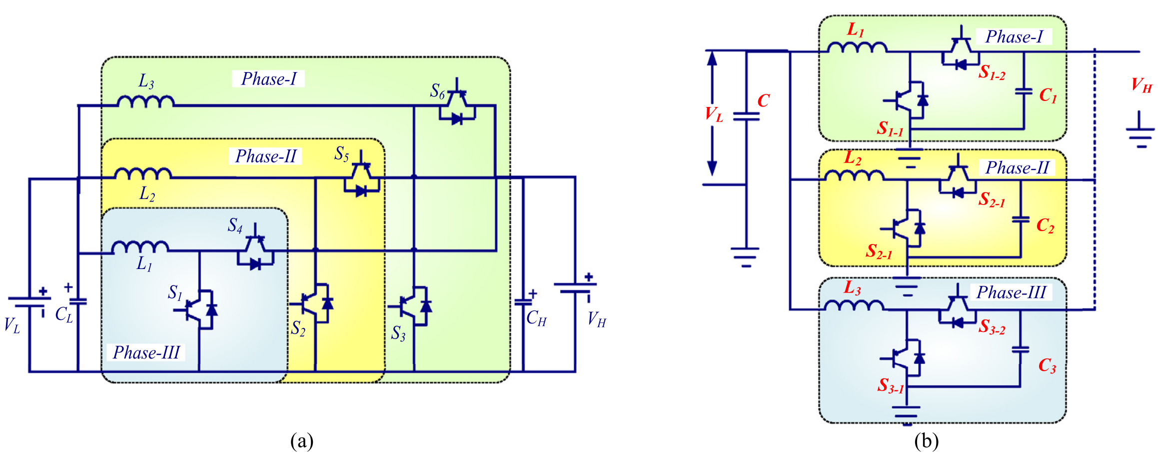

Fig. 19. Multiphase non-isolated bidirectional DC-DC converters (a) Multiphase interleaved boost converter (Yang et al., 2018), (b) 16 Phase IBC (Ni et al., 2012).

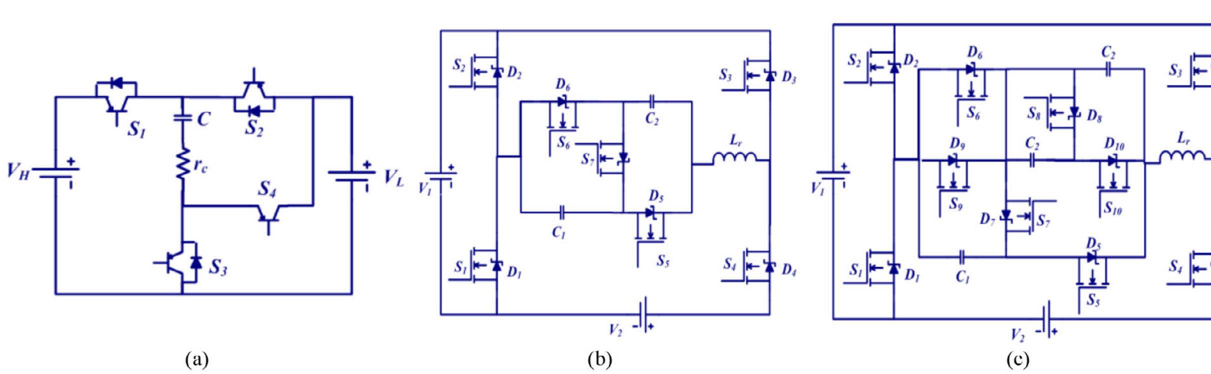

Fig. 20. Switched Capacitor Topologies (a) Switched bidirectional converter (Amjadi & Williamson, 2010) (b) zero current switching switched capacitor quasi resonant converter with single level (Lee & Chiu, 2005) (c) zero current switching switched capacitor quasi resonant converter with two level (Lee & Chiu, 2005).

state, which reduces the EMI problem. The converter gives 93% efficiency. The number of switched-capacitor stages increases to achieve a higher voltage conversion ratio.

4. Challenges in power electronics vehicular system

4.1. Improve efficiency

Firstly, in EVs, mechanical and hydraulic shaft are replaced by an electric motor for propelling operation. In HEV, selecting the perfect combination of ICE and fuel cell or battery in the proper way helps to
improve the efficiency. In the battery or fuel mode, PECs play a significant role to improve efficiency by selecting a proper power converter. The selection of PECs, switching strategies of converters, system integration and packing of individual units are essential to achieve the goal of power electronics in the vehicular system. The converters are selected according to the load demand and input supply. The efficiency of PEC depends on the number of components, control strategies, and EMI effects.

4.2. Increase the durability of EVs

The durability of EVs depends on the life of the electrical unit present in EVs. The durability of the battery increases by continuously maintaining the charging and discharging level with the help of the voltage controller. The life span of PEC depends on semiconductor devices. The converter should need to be withstood for high vibration and thermal condition at extreme condition. The challenges lie in selecting the proper converter with high efficiency, rigidness, low cost, and small size.

4.3. Increase the performance of EVs

Fast and high-power industrial motion control is a demanding trend in the modern automobile system. The PE technique is combined with Digital Signal Processing (DSP) to achieve the high performance of EVs.

4.4. Increase the luxurious feature

Today's advanced EVs are more focused on making high comfort EVs. Some high comfort applications are shown in Fig. 20. Each application requires a different voltage rating to work. The multistage or multi-output DC-DC converter provide different ratings power supply for DC appliances. The AC load receives power from the three-phase inverter.

4.5. Increase the safety in EVs

Apart from power conversion and propelling control, monitoring the condition of the traction motor to detect any failure like stator, rotor, and bearing faults are essential. In advance EVs, ABS and airbags require high power actuators. The PEC with DSP technique can increase the safety features in EVs in the future.

4.6. Decrease the overall cost of EVs

The number of power conversion unit and component uses, decide the cost of the vehicular electrical system in EVs. As the luxurious load increases on the vehicle, it is responsible for demanding a higher number of PEC. The challenge is to reduce the cost of the vehicle by selecting a smaller number of power conversion units for a more significant number of luxurious loads.

5. Conclusion

A state-of-the-art review of the current status and opportunities of PECs in electric, hybrid, and fuel cell vehicles is presented. This paper summarized the impact of PECs on cost, efficiency, and performance of EVs. From the review of EVs, the SPHEV has the perfect combination of two energy sources for propelling and other functions. With the advancement in the vehicular electrical system, the demand for different ratings of supply increases, which is not fulfilled by one battery or two battery structure. The bidirectional DC-DC converter plays a vital role in the power conversion process of EVs. The existing non-isolated bidirectional DC-DC converter topologies are discussed with a comprehensive review and comparison along with the advantages and disadvantages of PEC in the present vehicular system in detail. Finally, the paper explains the various challenges for PECs to improve efficiency, durability, performance, and cost reduction.

References

Adams, S., Klobodu, E. K. M., & Apio, A. (2018). Renewable and non-renewable energy, regime type and economic growth. *Renewable Energy, 125*, 755–767 Sep..

Afonso, T. L., Marques, A. C., & Fuinhas, J. A. (2017). Strategies to make renewable energy sources compatible with economic growth. *Energy Strategy Reviews, 18*, 121–126 Dec..

Akbarian, H., Pillay, P., & Lopes, L. (2015). Design of a power electronic emulator for series hybrid electric vehicle powertrains. In *Proceedings of the IEEE vehicle power and propulsion conference (VPPC)* (pp. 1–5).

Amjadi, Z., & Williamson, S. S. (2010a). Power-electronics-based solutions for plug-in hybrid electric vehicle energy storage and management systems. *IEEE Transactions on Industrial Electronics, 57*(2), 608–616 Feb..

Amjadi, Z., & Williamson, S. S. (2010b). A novel control technique for a switched-capacitor-converter-based hybrid electric vehicle energy storage system. *IEEE Transactions on Industrial Electronics, 57*(3), 926–934 Marc. 10.1109/TIE.2009.2032196.

Awasthia, A., Karthikeyan, V., Sanjeevikumar, P., Rajasekar, S., Blaabjerg, F., & Singh, A. K. (2017). Optimal planning of electric vehicle charging station at the distribution system using hybrid optimization algorithm. *Energy Journal, Elsevier Journal Publications, 133*, 70–78 August.

Baha, M. A. A., & Thomas, H. B. (2013). Review of hybrid, plug-in hybrid, and electric vehicle market modeling Studies. *Renewable and Sustainable Energy Reviews, 21*, 190–203 MaPages.

Bayindi, K. C., Gozukucuk, M. A., & Teke, A. (2011). A comprehensive overview of hybrid electric vehicle: Powertrain configurations, powertrain control techniques and electronic control units. *Energy Conversion and Management, 52*(2), 1305–1313 Issue-FebruarPages.

Bhaskar, M. S., Ben-Brahim, L., Iqbal, A., Padmanaban, S., Meraj, M., & Rahman, S. (2019a). Hardware implementation of a new single input double output L-l converter for high voltage auxiliary loads in fuel-cell vehicles. In *IEEE applied power electronics conference and exposition (APEC)* (pp. 1595–1600). Mar..

Bhaskar, M. S., Padmanaban, S., & Holm-Nielsen, J. B. (2019b). Double stage double output dc–dc converters for high voltage loads in fuel cell vehicles,". *Energies, 12*(19) Art. no. 19, Jan.

Bhaskar, M. S., Padmanaban, S., Iqbal, A., Meraj, M., Howeldar, A., & Kamuruzzaman, J. (2018). L-L Converter for fuel cell vehicular power train applications: hardware implementation of primary member of X-Y converter family. In *Proceedings of the IEEE international conference on power electronics, drives and energy systems (PEDES)* (pp. 1–6). Dec..

Bhaskar, M. S., Sanjeevikumar, P., Holm-Nielsen, J. B., Pedersen, J. K., & Leonowicz, Z. (2019c). 2L-2L converter: Switched inductor based high voltage step-up converter for fuel cell vehicular applications. In *Proceedings of the IEEE international conference on environment and electrical engineering and IEEE Industrial and Commercial Power Systems Europe* (pp. 1–6). 11-14 Jun..

Cabezuelo, D., Andreu, J., Kortabarria, I., et al. (2017). Powertrain systems of electric, hybrid and fuel-cell vehicles: State of the technology. In *Proceedings of the IEEE 26th international symposium on industrial electronics (ISIE)* (pp. 1445–1450).

Cassani, P. A., & Williamson, S. S. (2009). Feasibility analysis of a novel cell equalizer topology for plug-in hybrid electric vehicle energy-storage systems. *IEEE Transactions on Vehicular Technology, 58*(8), 3938–3946 Oct..

Chan, C. C. (2002). The state of the art of electric and hybrid vehicles. In *Proceedings of the IEEE: 90* (pp. 247–275). Feb.

Chan, C. C., & Chau, K. T. (1997). An overview of power electronics in electric vehicles. *IEEE Transactions on Industrial Electronics, 44*(1), 3–13.

Chiu, H. J., & Lin, L. W. (2006). A bidirectional DC-DC converter for fuel cell electric vehicle driving system. *IEEE Transaction on Power Electronics, 21*(4), 950–958 july.

Choubey, A., & Lopes, L. A. C. (2017). A tri-state 4-switch bi-directional converter for interfacing supercapacitors to DC micro-grids. In *Proceedings of the IEEE 8th international symposium on power electronics for distributed generation systems (PEDG)* (pp. 1–6).

Chung, H. S. H., Chow, W. C., Hui, S. Y. R., et al. (2000). Development of a switched-capacitor DC-DC converter with bidirectional power flow. *IEEE Transactions on Circuits and Systems I: Fundamental Theory and Applications, 47*(9), 1383–1389 Se.

Daramy-Williams, E., Anable, J., & Grant-Muller, S. (2019). A systematic review of the evidence on plug-in electric vehicle user experience. *Transportation Research Part D: Transport and Environment, 71*, 22–36 Jun..

Das, H. S., Tan, C. W., & Yatim, A. H. M. (2017). Fuel cell hybrid electric vehicles: A review on power conditioning units and topologies. *Renewable and Sustainable Energy Reviews, 76*, 268–291.

Daya, F. J. L., Sanjeevikumar, P., Blaabjerg, F., Wheeler, P. W., Ojo, J., & Ertas, A. H. (2016). Analysis of wavelet controller for robustness in electronic differential of electric vehicles: An investigation and numerical developments". *Electric Power Components and Systems, 44*(7), 763–773.

Desai, C., & Williamson, S. S. (2009). Optimal design of a parallel hybrid electric vehicle using multi-objective genetic algorithms. In *Proceedings of the IEEE vehicle power and propulsion conference* (pp. 871–876).

Di Napoli, A., Crescimbini, F., Solero, L., et al. (2002). Multiple-input DC-DC power converter for power-flow management in hybrid vehicles. In *Proceedings of the conference record of the IEEE industry applications conference. 37th IAS Annual Meeting (Cat. No.02CH37344): 3* (pp. 1578–1585).

Dobbs, B. G., & Chapman, P. L. (2003, March). A multiple-input DC-DC converter topology. *IEEE Power Electronics Letters, 1*(1), 6–9.

Dusmez, S., Hasanzadeh, A., & Khaligh, A. (2014). Loss analysis of non-isolated bidirectional DC/DC converters for hybrid energy storage system in EVs. In *Proceedings of the IEEE 23rd international symposium on industrial electronics (ISIE)* (pp. 543–549).

Ehsani, M., Gao, Y., Gay, S. E., et al. (2005). *Modern electric, hybrid electric, and fuel cell Vehicles- Fundamentals, theory, and design*. CRC Press LLC.

Elnozahy, M. S., & Salama, . M. (2014). 'A comprehensive study of the impacts of PHEVs on residential distribution networks. *IEEE Transactions on Sustainable Energy, 5*, 332–342.

Emadi, A.: (2005). 'Handbook of automotive power electronics and motor drives'. (1st ed.). New York: Taylor & Francis.

Emadi, A., Lee, Y. J., & Rajashekara, K. (2008). Power electronics and motor drives in electric, hybrid electric, and plug-in hybrid electric vehicles. *IEEE Transactions on Industrial Electronics, 55*(6), 2237–2245.

Emadi, A., Lee, Y. J., & Rajashekara, K. (2008). Power electronics and motor drives in electric, hybrid electric, and plug-in hybrid electric vehicles. *IEEE Transactions on Industrial Electronics, 55*(6), 2237–2245 Jun..

Emadi, A., Rajashekara, K., Williamson, S. S., & Lukic, S. M. (2005). Topological overview of hybrid electric and fuel cell vehicular power system architectures and configurations. *IEEE Transactions on Vehicular Technology, 54*(3), 763–770 May.

Ga, Y., Ehsani, M., & Miller, J. M. (2005). Hybrid electric vehicle: Overview and state of the art. In *Proceedings of the IEEE international symposium on industrial electronics* (pp. 307–316). ISIE 2005.

Gielen, D., Boshell, F., Saygin, D., Bazilian, M. D., Wagner, N., & Gorini, R. (2019). The role of renewable energy in the global energy transformation. *Energy Strategy Reviews, 24*, 38–50 Apr..

Gough, B., Rowley, P., & Walsh, C. (2014). What impact will the journey patterns of electric vehicles have on their capability to provide ancillary services? In *Proceedings of the 5th IET hybrid and electric vehicles conference (HEVC 2014)* (pp. 1–5).

Grunditz, E. A., & Thiringer, T. (2016). Performance analysis of current bevs based on a comprehensive review of specifications. *IEEE Transactions on Transportation Electrification, 2*(3), 270–289 Sept..

Gruosso, G. (2014). Optimization and management of energy power flow in hybrid electrical vehicles. In *Proceedings of the 5th IET hybrid and electric vehicles conference (HEVC 2014)* (pp. 1–5).

Guo, S., Liu, Q., Sun, J., & Jin, H. (2018). A review on the utilization of hybrid renewable energy. *Renewable and Sustainable Energy Reviews, 91*, 1121–1147 Aug..

Gurkaynak, Y., Khaligh, A., & Emadi, A. (2009). State of the art power management algorithms for hybrid electric vehicles. In *Proceedings of the IEEE vehicle power and propulsion conference*.

Ha, S. P., Lee, J. H., Hwang, J. P., et al. (2012). Two phase interleaved bidirectional DC-DC converter for electric vehicle using variable DC-link voltage. In *Proceedings of the IEEE vehicle power and propulsion conference* (pp. 748–752). pp..

Hegazy, O., Barrero, R., Van Mierlo, J., et al. (2013). An advanced power electronics interface for electric vehicles applications. *IEEE Transactions on Power Electronics, 28*(12), 5508–5521 Dec.

Helsper, M., & Ruger, N. (2014). Requirements of hybrid and electric buses – A huge challenge for power electronics. In *Proceedings of the 16th European conference on power electronics and applications*.

Hofmann, M., Schäfer, M., & Ackva, A. (2014). Bi-directional charging system for electric vehicles: A V2G concept for charging and discharging electric vehicles. In *Proceedings of the 4th international electric drives production conference (EDPC)* (pp. 1–5).

Ida, T., Murakami, K., & Tanaka, M. (2014). A stated preference analysis of smart meters, photovoltaic generation, and electric vehicles in Japan: Implications for penetration and GHG reduction. *Energy Research & Social Science, 2*, 75–89 Jun..

Jafri, N. H., & Gupta, S. (2016). An overview of fuel cells application in transportation. In *Proceedings of the IEEE transportation electrification conference and expo*.

Jenniches, S. (2018). Assessing the regional economic impacts of renewable energy sources – A literature review. *Renewable and Sustainable Energy Reviews, 93*, 35–51 Oct..

Khaligh, A. (2008). A multiple-input dc-dc positive buck-boost converter topology. In *Proceedings of the Twenty-third annual IEEE applied power electronics conference and exposition* (pp. 1522–1526). 10.1109/APEC.2008.4522926.

Khaligh, A., & Dusmez, S. (2012). Comprehensive topological analysis of conductive and inductive charging solutions for plug-in electric vehicles. *IEEE Transactions on Vehicular Technology, 61*(8), 3475–3489 Oct..

Khaligh, A., & Li, Z. (2010). Battery, ultracapacitor, fuel cell, and hybrid energy storage systems for electric, hybrid electric, fuel cell, and plug-in hybrid electric vehicles: State of the Art. *IEEE Transactions on Vehicular Technology, 59*(6), 2806–2814 July.

Khan, M. A., Ahmed, A., Husain, I., et al. (2015). Performance analysis of bidirectional DC–DC converters for electric vehicles. *IEEE Transactions on Industry Applications, 51*(4), 3442–3452 July-Aug.

Kim, H., & Kum, D. (2016). Comprehensive design methodology of input- and output-split hybrid electric vehicles: In search of optimal configuration. *IEEE/ASME Transactions on Mechatronics, 21*(6), 2912–2923 Dec..

Krishna, M., Daya, F., Sanjeevikumar, P., & Mihet-Popa, L. (2017). Real-time analysis of a modified state observer for sensorless induction motor drive used in electric vehicle applications. *Energies, MDPI, Open Access Journal, 10*(8), 1–23 pagesJuly.

Ku, S. W., Lo, Y. K., Chiu, H. J., et al. (2014). 'A high-performance bidirectional DC-DC converter for DC micro-grid system application. In *Proceedings of the international power electronics conference (IPEC-Hiroshima 2014 - ECCE ASIA)* (pp. 3185–3189).

Lai, J. S., & Nelson, D. J. (2007). Energy management power converters in hybrid electric and fuel cell vehicles. In *Proceedings of the IEEE: 95* (pp. 766–777). Apr..

Lane, B. W., Dumortier, J., Carley, S., Siddiki, S., Clark-Sutton, K., & Graham, J. D. (2018). All plug-in electric vehicles are not the same: Predictors of preference for a plug-in hybrid versus a battery-electric vehicle. *Transportation Research Part D: Transport and Environment, 65*, 1–13 Dec..

Lee, Y. S., & Chiu, Y. Y. (2005). Zero-current-switching switched-capacitor bidirectional DC-DC converter. In *Proceedings of the IEE electric power applications: 152* (pp. 1525–1530). 4 Nov..

Li, J., Yu, X., & Ding, H. (2010). Ping Sun: Design and control of the propulsion for a series hybrid electric vehicle. In *Proceedings of the 8th world congress on intelligent control and automation*.

Li, S. G., Sharkh, S. M., Walsh, F. C., et al. (2011). Energy and battery management of a plug-in series hybrid electric vehicle using fuzzy logic. *IEEE Transactions on Vehicular Technology, 60*(8), 3571–3585 Oct.

Li, X., Lopes, L. A. C., & Williamson, S. S. (2009). On the suitability of plug-in hybrid electric vehicle (PHEV) charging infrastructures based on wind and solar energy. In *Proceedings of the IEEE power & energy society general meeting*.

Li, X., & Williamson, S. S. (2007). Comparative investigation of series and parallel hybrid electric vehicle (HEV) efficiencies based on comprehensive parametric analysis. In *Proceedings of the IEEE vehicle power and propulsion conference*.

Li, Z., Khajepour, A., & Song, J. (2019). A comprehensive review of the key technologies for pure electric vehicles. *Energy, 182*, 824–839 Sep..

Lulhe, A. M., & Date, T. N. (2015). 'A technology review paper for drives used in electrical vehicle (EV) & hybrid electrical vehicles (HEV). In *roceedings of the international conference on control, instrumentation, communication and computational technologies (ICCICCT)* (pp. 632–636).

Marchesoni, M., & Vacca, C. (2007). New DC-DC converter for energy storage system interfacing in fuel cell hybrid electric vehicles. *IEEE Transactions on Power Electronics, 22*(1), 301–308 Jan..

Miller, J. F., Webster, C. E., Tummillo, A. F., et al. (1997). Testing and evaluation of batteries for a fuel cell powered hybrid bus. In *Proceedings of the energy conversion engineering conference: 2* (pp. 894–898). 27 July–1 Augus.

Mukherjee, J. C., & Gupta, A. (2015). A review of charge scheduling of electric vehicles in smart grid. *IEEE Systems Journal, 9*(4), 1541–1553 Dec..

Musavi, F., Craciun, M., Gautam, D. S., et al. (2014). Control strategies for wide output voltage range LLC resonant DC–DC converters in battery chargers. *IEEE Transactions on Vehicular Technology, 63*(3), 1117–1125 Marc.

Mwasil, F., Justo, J. J., Kim, E. K., et al. (2014). Electric vehicles and smart grid interaction: A review on vehicle to grid and renewable energy sources integration. *Renewable and Sustainable Energy Reviews Volume, 34*, 501–516 Jun.

Naghizadeh, N., & Williamson, S. S. (2013). A comprehensive review of power electronic converter topologies to integrate photovoltaics (PV), AC grid, and electric vehicles. In *Proceedings of the IEEE Transportation Electrification Conference and Expo (ITEC)* (pp. 1–6).

Nayanatara, C., Shanmugapriya, P., Gurusivakumar, G., et al. (2014). 'Design & development of series hybrid electric vehicle. In *Proceedings of the international conference on computation of power, energy, information and communication (ICCPEIC)* (pp. 114–117).

Ni, L., Patterson, D. J., & Hudgins, J. L. (2012). High power current sensorless bidirectional 16-phase interleaved DC-DC converter for hybrid vehicle application. *IEEE Transactions on Power Electronics, 27*(3), 1141–1151 March.

Olson, J. B., & Sexton, E. D. (2000). 'Operation of lead–acid batteries for HEV applications. In *Proceedings of the 15th battery conference on applications and advances* (pp. 205–210). 11–14 Januar.

Onar, O. C., Kobayashi, J., & Khaligh, A. (2013). A fully directional universal power electronic interface for EV, HEV, and PHEV applications. *IEEE Transactions on Power Electronics, 28*(12), 5489–5498 Dec..

Onwuchekwa, C. N., & Kwasinski, A. (2011). Analysis of boundary control for a multiple-input DC-DC converter topology. In *Proceedings of the 26th annual IEEE applied power electronics conference and exposition (APEC)* (pp. 1232–1237).

Parag Jose, C., & Meikandasivam, S. (2016). A review on the trends and developments in hybrid electric vehicles. In *Lecture notes in mechanical engineering* (pp. 211–229). Singapore: Springer.

Querini, F., Dagostino, S., Morel, S., & Rousseaux, P. (2012). Greenhouse gas emissions of electric vehicles associated with wind and photovoltaic electricity. *Energy Procedia, 20*, 391–401.

Rajashekara, K. (2003). 42V architecture of automobiles. In *Proceedings of the electrical manufacturing & coil winding expo* Sep..

Razavian, R., Azad, N. L., & McPhee, J. (2012). On real-time optimal control of a series hybrid electric vehicle with an ultra-capacitor. In *Proceedings of the american control conference (ACC)* (pp. 547–552).

Roche, M., Shabbir, W., & S, A. (2017). Evangelou: 'Voltage control for enhanced power electronic efficiency in series hybrid electric vehicles. *IEEE Transactions on Vehicular Technology, 66*(5), 3645–3658 May.

Rodatz, P., Garcia, O., Guzzella, L., et al. (2003). Performance and operational characteristics of a hybrid vehicle powered by fuel cells and supercapacitors. In *Proceedings of the SAE world congress and exhibition: 112* (pp. 692–703). 3 Marc.

Schaltz, E. (2010). *Design of a fuel cell hybrid electric vehicle drive system*. Aalborg, Denmark: The Department of Energy Technology, Aalborg University Ph.D. dissertation.

Schaltz, E., Khaligh, A., & Rasmussen, P. O. (2009). Influence of battery/ultracapacitor energy-storage sizing on battery lifetime in a fuel cell hybrid electric vehicle. *IEEE Transactions on Vehicular Technology, 58*(8), 3882–3891 Oct..

Shareef, H., Islam, M. M., & Mohamed, A. (2016). A review of the stage-of-the-art charging technologies, placement methodologies, and impacts of electric vehicles. *Renewable and Sustainable Energy Reviews, 64*, 403–420 Oct..

Subramaniam, U., Ganesan, S., Bhaskar, M. S., Padmanaban, S., Blaabjerg, F., & Almakhles, D. J. (2019). Investigations of AC microgrid energy management systems using distributed energy resources and plug-in electric vehicles. *Energies, 12*(14) Art. no. 14, Jan.

Tahami, F., Kazemi, R., & Farhanghi, S. (2003). A novel driver assist stability system for all-wheel-drive electric vehicles. *IEEE Transactions on Vehicular Technology, 52*(3), 683–692 May.

Tazelaar, E., Veenhuizen, B., Jagerman, J., et al. (2013). Energy management strategies for fuel cell hybrid vehicles; an overview. *2013 World Electric Vehicle Symposium and Exhibition (EV S27)*.

Thomas, C. E. (2009). 'Fuel cell and battery electric vehicles compared. *International Journal of Hydrogen Energy, 34*, 6005–6020.

Un-Noor, F., Padmanaban, S., Mihet-Popa, L., Mollah, M. N., & Hossain, E. (2017). A comprehensive study of key electric vehicle (EV) components, technologies, challenges, impacts, and future direction of development. *Energie, 10*, 1217.

Waffler, S., & Kolar, J. W. (2009). A novel low-loss modulation strategy for high-power bidirectional buck-boost converters. *IEEE Transactions on Power Electronics, 24*(6), 1589–1599 June.

Williamson, S. S. (2007). Electric drive train efficiency analysis based on varied energy storage system usage for plug-in hybrid electric vehicle applications. In *Proceedings of the IEEE power electronics specialists conference*.

Williamson, S. S., Rathore, A. K., & Musavi, F. (2015, May). Industrial electronics for electric transportation: Current state-of-the-art and future challenges. *IEEE Transactions on Industrial Electronics, 62*(5), 3021–3032.

Wu, H., Lu, J., Shi, W., & Xing, Y. (2012). Nonisolated bidirectional DC–DC converters with negative-coupled inductor. *IEEE Transactions on Power Electronics, 27*(5), 2231–2235 May.

Wu, Y., & Gao, H. (2006). Optimization of fuel cell and super capacitor for fuel cell electric vehicles. *IEEE Transactions on Vehicular Technology, 55*(6), 1748–1755 Nov..

Yang, Y., Guan, T., Zhang, S., Jiang, W., & Huang, W. (2018). More symmetric four-phase inverse coupled inductor for low current ripples & high-efficiency interleaved bidirectional buck/boost converter. *IEEE Transactions on Power Electronics, 33*(3), 1952–1966 March.

Yong, J. Y., Ramachandaramurthy, V. K., Tan, K. M., et al. (2015a). A review on the state-of-the-art technologies of electric vehicle, its impacts and prospects. *Renewable and Sustainable Energy Reviews, 49*, 365–385 Sep.

Yong, J. Y., Ramachandaramurthy, V. K., Tan, K. M., et al. (2015b). Bi-directional electric vehicle fast charging station with novel reactive power compensation for voltage regulation. *International Journal of Electrical Power & Energy Systems, 64*, 300–310.

Zhan, P., & Williamson, S. S. (2008). Recent status and future prospects of integrated starter-generator based hybrid electric vehicles. In *Proceedings of the IEEE vehicle power and propulsion conference* (pp. 1–8).

Zhao, Y., He, X., Yao, Y., & Huang, J. (2019). Plug-in electric vehicle charging management via a distributed neurodynamic algorithm. *Applied Soft Computing, 80*, 557–566 Jul..

Zhou, W., Yang, L., Cai, Y., & Ying, T. (2018). Dynamic programming for new energy vehicles based on their work modes part I: Electric vehicles and hybrid electric vehicles. *Journal of Power Sources, 406*, 151–166 Dec..

For electricity and freshwater production Thermodynamic-economic optimization of a solar-powered combined energy system with desalination

Sunil Kumar Mahapatro, *Department of Electrical Engineering, Aryan Institute of Engineering & Technology, Bhubaneswar, skmahapatro78@outlook.com*

Ajaya Kumar swain, *Department of Electrical and Electronics Engineering, Aryan Institute of Engineering & Technology, Bhubaneswar, ajayaswain9@gmail.com*

Sambhunath Biswas, *Department of Electronics and Communication Engineering , Raajdhani Engineering College, Bhubaneswar, s.biswas09@outlook.com*

Subhendu Sahoo, Department of Electrical and Electronics Engineering, NM Institute of Engineering & Technology, Bhubaneswar, s.sahoo95@outlook.com

Manoj Mohanta, *Department of Electrical and Electronics Engineering, Capital Engineering College, Bhubaneswar, manoj.mohanta62@outlook.com*

Keywords:
Solar energy
Cogeneration
Multi-objective optimization
Thermoeconomics
Genetic algorithm
Isfahan

A B S T R A C T

This study starts by modeling and analyzing a smart combined energy system that includes a concentrated solar power plant, steam Rankine, Brayton, organic Rankine cycles, reverse osmosis unit, and a thermoelectric generator. The system is then subjected to bi-criteria optimization, using non-dominated sorting genetic algorithm II (NSGA-II) and minimizing annual costs and maximizing exergy efficiency. The system is located in Isfahan (central Iran) and intended to produce electricity and freshwater. The thermodynamic results indicated the most critical parameters affecting system performance: direct normal irradiance, number of heliostats, turbine efficiency and inlet temperature, compressor pressure ratio, and steam Rankine cycle pump inlet temperature. A Pareto frontier was charted, producing a set of optimal points, where a decrease in costs was achieved if the exergy efficiency was slightly compromised, leading to the identification of an optimal location within the Pareto frontier.

1. Introduction

Although most energy transition programs have deaccelerated worldwide due to the impacts of the COVID-19 pandemic, highly integrated energy systems can and must be part of energy efficiency solutions. The aim is to enhance economic competitiveness, provide more affordable energy services, and reduce environmental impacts. The principle of combined energy systems is to optimize the planning, design, and implementation of energy supply technologies, including the incorporation of renewable energy sources. Combined energy schemes can generate many configurations and present ample design flexibility that accommodates specific regional conditions [1,2].

Water scarcity in arid areas (for example, the Middle East) has led to the progressive implementation of desalination schemes, with significant potential for energy savings by employing energy integration strategies [3,4]. Gunawan et al. [5] mentioned that the development of innovative, efficient, and sustainable engineering systems should recognize the water-energy nexus as crucial.

Regarding the analysis of these highly integrated energy systems producing freshwater and other energy services, Yilmaz [6] evaluated the thermodynamic performance of a novel solar-based polygeneration[1] system designed to produce hydrogen, cooling, heating, and freshwater. The energy and exergy efficiencies were 78.93% and 47.56%, respectively, with hydrogen and freshwater productions of 0.04663 kg/s and 0.8862 kg/s, respectively. A case was made to adopt renewable energy-supported multigeneration systems, which will become more attractive for green and sustainable energy applications. Ghorbani et al. [7] developed an innovative combined energy system, based on phase change materials (PCM) and an organic Rankine cycle (ORC), to produce power and freshwater. The system was able to produce 3628 kg/h water alongside 459.9 MW electrical power. Alirahmi and Assareh [8] went a step further and carried out energy, exergy, and exergoeconomics (3E) assessments plus optimization for a geothermal-

Nomenclature

A_{hel}	aperture of heliostat, m^2
A_r	area of heliostats
c	cost per unit exergy, \$/GJ
cp	specific heat, J/kg.K
$\dot{C}$	cost rate, \$/hr
CSP	concentrated solar power
DNI	direct normal irradiance
$\dot{E}x$	exergy rate, kW
F_1	collector efficiency factor
F_R	heat transfer factor
G_b	solar radiation intensity, W/m^2
h_x	specific enthalpy at point x, kJ/kg
HEX	heat exchanger
k	thermal conductivity, kW/m
k_ω	water permeability through membrane
M	mass, kg
$\dot{m}$	mass flow rate, m^3/h, kg/s
n_{cp}	number of collectors in parallel
n_{cs}	number of collectors in series
N_{hel}	number of heliostats
ORC	organic Rankine cycle
$\dot{Q}$	heat rate, kW
r_p	compressor pressure ratio
S	amount of heat collected
s	specific entropy, kJ/kg.K
SRC	steam Rankine cycle
SES	smart energy system
T	temperature, °C
T_r	receiver local temperature
TEG	thermoelectric generator
U_L	overall heat loss coefficient, kW/K
v_a	wind speed
$\dot{W}$	power, kW
w	width of collector, m
X	salinity, g/kg
$\dot{Z}$	levelized cost of components, \$/hr

Greek letters

α	absorbance of the receiver
γ	correction factor
ε	Surface emissivity of the receiver
η	efficiency, %
ρ	density, kg/m^3
τ_C	transmissivity of the cover glazing

Subscripts

0	reference state
av	average
b	brine
Con	condenser
D	destruction
Evp	evaporator
en	energy
f	feed
Gen	generator
hel	heliostat
HEX	heat exchanger
HP	high pressure
i, in	input condition
o, out	output condition
p	pump
pp	pinch point
ph	physical
s	isentropic
Tur	turbine

assisted polygeneration system, which produced hydrogen, electricity, freshwater, heat, and cooling. The NSGA-II optimization minimized cost rate and maximized exergy efficiency, with the optimal solution presenting exergy efficiency of 31.66% and a cost rate of 21.9 GJ/$. Salehi et al. [9] developed a 3E environmental analysis of a biomass-based cogeneration system assisted by molten carbonate fuel cell (MCFC). The highest achievable exergy efficiency was 50.18%, with CO_2 emissions at 0.289 $t.MW.h^{-1}$.

Assareh et al. [10] evaluated an extensive thermo-economic evaluation and optimization of an integrated system empowered by a solar-wind-ocean energy converter for electricity generation. The results indicate that the system can potentially supply 38 Iranian households with electricity all year-round. Ghorbani et al. [11] worked on a system where parabolic solar collectors were used as a thermal source alongside re-gasification operations to heat an ORC condenser. The system produced freshwater (3628 kgmol/h) and electricity (459.9 MW). Anvari et al. [12] carried out thermodynamic and environmental assessments for a renewable-based system based on syngas and concentrated solar power (CSP). The system consisted of a Brayton cycle and Steam Rankine Cycle (SRC) to generate 13.4 MW of electricity. The addition of a solar unit to the syngas-primed system increased electricity production by 25% and reduced carbon emissions by around 31%. Ozturk et al. [13] conducted the thermodynamic modeling of a cogeneration system comprised of steam and gas turbines, supplied by a CSP plant. The gas and steam turbines could produce 3.87 MW and 1.76 MW of electricity, respectively, with energy and exergy efficiencies of 69.2% and 37.3%, individually. Pourrahmani and Moghimi [14] carried out the exergoeconomic analysis and optimization of a CSP energy system for electricity, hydrogen, and cooling production. PCM was employed to alleviate the intermittency of solar energy, and a gas turbine exported electricity to the grid. The highest output of the gas turbine was 2.499 MW, with hydrogen production of 8.65 kg/h, and cooling production of 1.722 MW.

Behzadi et al. [15] assessed a solar-assisted energy system that produced electricity, cooling, and hydrogen. Utilizations of a compressor and thermoelectric generator (TEG) were compared, and it was demonstrated that TEG could enhance efficiency and lead to lower costs. Mohammadi et al. [16] designed a gas turbine combined cycle to produce electricity, freshwater, and cooling. Using a reverse osmosis unit was more economical than using multi-effect distillation (MED) and reverse osmosis (RO) desalination. The costs for electricity, freshwater, and cooling were 0.0648 \$/kWh, 0.7219 \$/m^3, and 0.0402 \$/h, respectively. Assareh et al. [17] used TEG within a geothermal-solar energy system that produced freshwater and electricity. Using TEG instead of a condenser reduced costs and increased exergy efficiency, 10.41 \$/GJ and 20.52%, respectively.

Although most desalination studies have been developed in the Middle East, some locations in Brazil have been suffering from a shortage of freshwater from rivers, and brackish water from artesian wells is commonly used. In the municipality of São Mateus

(Southeast Brazil), a Rankine-based steam power plant was proposed with a set of mechanical vapor compression desalination modules [18]. Coconut husk briquettes were used to produce electricity and freshwater, and the energy system could meet more than 70% of the water demand of the municipality. Fossil diesel was compared with soybean diesel by Lourenço and Carvalho [3], who proposed a novel off-grid desalination plant where part of the seawater is used to cool the radiator of the internal combustion engine and the condenser of the Rankine cycle, substituting the use of cooling towers.

Relating to previous smart energy research, combined energy systems are essential players in Smart Energy Systems (SES), which take an integrated, holistic focus on the supply of energy services [19], easing the transition into future renewable and sustainable energy solutions. This transition means moving away from freely dispatchable energy services and introducing renewable resources (along with their intermittency and variability) [20]. To ensure a smooth introduction of renewables and avoid black-outs, research efforts must focus on the redesign of energy systems, which requires knowledge on the dynamics of SES [21].

Next-generation smart regions or cities can take advantage of the proximity of multiple energy vectors (e.g., electricity, heat, cooling) [22], which are clear opportunities for energy systems integration. SES can also go a step further, benefitting from optimal design and management as well as including decentralization [23]. Using the SES approach, Bačeković and Østergaard mention [24] that it is possible to envision a 100% renewable energy system. However, the main point is that energy integration and renewable energy resources can increase energy security and create a low carbon system with lower financial costs than the current systems. Simultaneous utilization of various energy vectors in an optimal manner has led to the *Smart Energy Hub* concept [25]. The management of a smart system that included a desalination plant powered by renewables with energy storage was studied by [26], who employed NSGA-II optimization to consider embodied energy and hydraulic loss of power supply. Nevertheless, the authors recommend that the financial aspect (levelized cost of energy) be incorporated in future studies. A smart urban energy system was modeled by [27], which included interactions between electricity, cooling, and water desalination within a linear optimization problem. The authors tested six scenarios for 2030 and verified that the best economic performance was associated with 48% lower socio-economic costs and 68% lower carbon emissions compared to a business-*as*-usual case.

Recognizing that solar power coupled desalination can be crucial in helping solve the water-energy nexus and aiming at the stable supply of electricity throughout the year, an interesting configuration integrates a CSP plant with Brayton as the topping cycle and two Rankine cycles as the bottoming cycles. However, there are limited studies on the thermodynamic modeling of these combined systems. The overarching aim of this study is to model and analyze a combined energy system constituted by a CSP plant, steam Rankine, Brayton, and organic Rankine cycles, reverse osmosis unit, and a thermoelectric generator. The system is then subject to bi-criteria optimization, using a genetic algorithm (NSGA-II) that considers the minimization of annual costs and maximization of exergy efficiency. The further novelty of the present study embarks on employing the system in Isfahan, which faces severe water shortages and environmental concerns and at the same time has high potential in solar irradiation, which is a signpost for using this system. Also, solar irradiation is considered on an hourly basis, considering the actual conditions for Isfahan. In addition, since the compressor power is highly affected by ambient temperature, this impact is explored independently.

2. Material and methods

2.1. Energy system

The schematic of the proposed system is shown in Fig. 1. The heliostats reflect solar radiation to a central receiver, which can reach high temperatures (60°C-800°C). Air is the working fluid in the receiver, which operates as a heat absorbent that can enter the gas turbine and drive it for power generation purposes. The thermal energy (flow #3) is transferred to the Brayton cycle. The working fluid absorbs the thermal energy and carries it to the heat exchangers (flows #4 and #5) to heat the working fluid, mostly water, in sub-cycles. The heat converts the working fluid in the sub-cycles (green cycle, 7-8-9-10, and pink cycle, 13-14-15-16) into a superheated fluid at pre-designed pressure and temperature to run the turbines and produce power.

A heat recovery unit can be coupled to the gas turbine, providing an SRC with steam for more electricity production. Herein, high-pressure water in the central receiver is converted into superheated steam that flows to the turbine for electricity generation. The residual heat can be stored for further use. Additionally, in the next cycle, the steam enters the multi-stage water desalination condenser to be cooled. The fluid, after being pumped, flows to a heat exchanger to be reheated and is then utilized within the ORC. In this section, the temperature can be as low as 150°C. The steam is pumped into the turbine.

2.2. Thermodynamic analysis

For the thermodynamic analysis of the energy system, mass and energy balances are developed for each control volume. The following simplifying assumptions are applied:

- Steady-state conditions;
- Turbines and pumps are isentropic;
- Pressure drops within pipelines are negligible;
- The condenser output is saturated liquid, and the evaporator output is saturated steam;
- Variations on potential and kinetic energies are negligible;
- No heat losses were considered from the components to the ambient environment;
- The dead state temperature and pressure are 25 °C and 101.3 kPa, respectively;
- The pressure drop after passing through the steam generator and condenser is 5%.

The working fluids are isobutene in the ORC and water in the SRC. The initial parameters are shown in Table 1.

Application of the first law of thermodynamics (Eq. (1)) to each control volume yields Table 2 [28].

$$\dot{Q} - \dot{W} = \sum_{e} \dot{m}_e \left(h_e + \frac{v_e^2}{2} + gZ_e \right) - \sum_{i} \dot{m}_i \left(h_i + \frac{v_i^2}{2} + gZ_i \right) \quad (1)$$

The net power in the system can be calculated as shown by Equation (2).

$$\dot{W}_{net} = \dot{W}_{Brayton} + \dot{W}_{net,steam} + \dot{W}_{net,ORC} + \dot{W}_{TEG} \quad (2)$$

2.3. Heliostats analysis

Although the utilization of solar energy has been addressed in the literature [29–32], the importance of further studies in this area

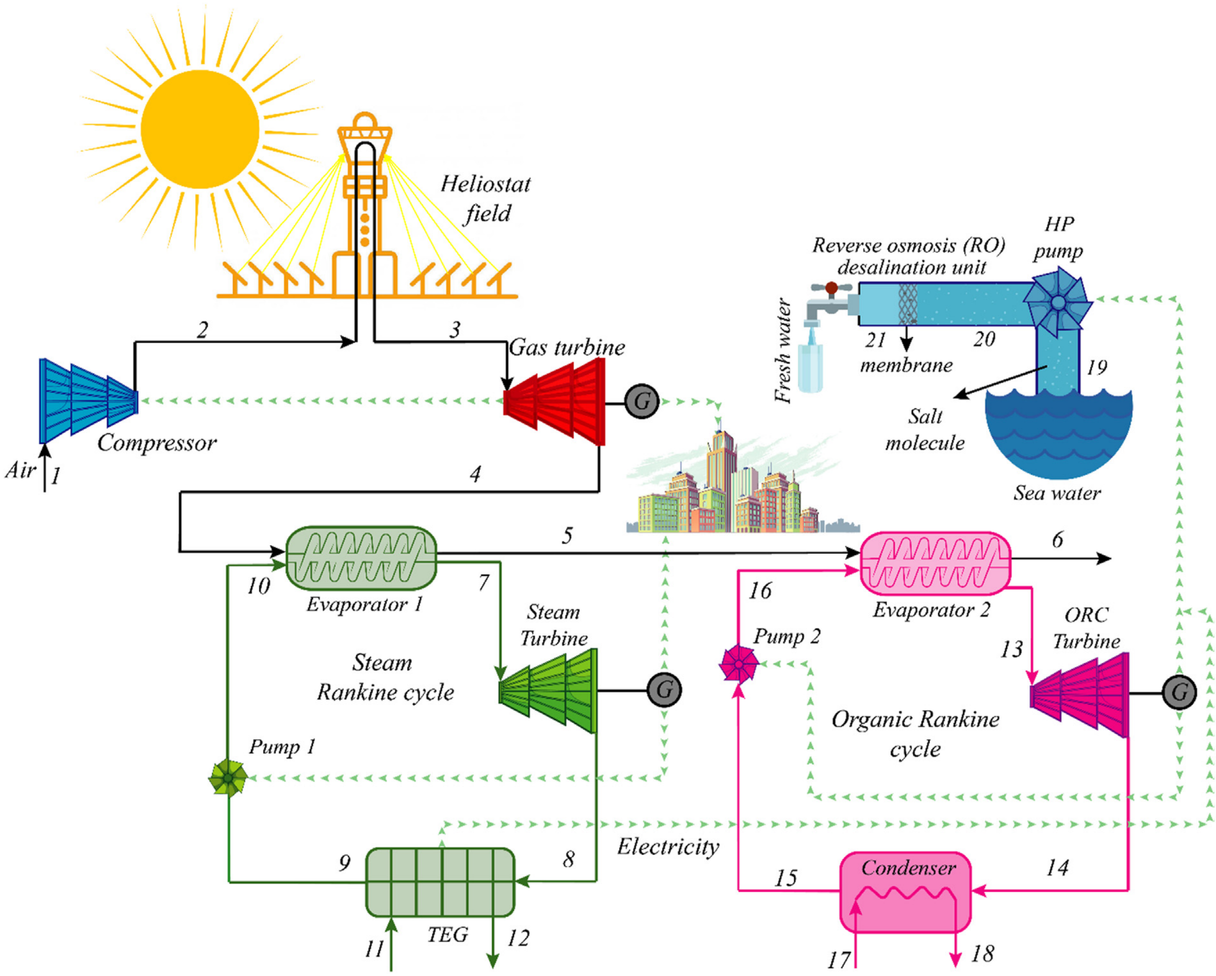

Fig. 1. Schematic of the proposed energy system.

Table 1
Modeling input parameters.

Parameter	Definition	Amount
N_{hel}	Number of heliostats	350
T_0	Ambient temperature	25 [°C]
P_0	Ambient pressure	101.3 [kPa]
T_{0K}	Temperature conversion formula	T_0 [K] = T_0[°C] + 273.15
r_P	Compressor pressure ratio	10
P_7	Turbine inlet pressure	4000 [kPa]
η_h	Heliostat efficiency	0.71
A_{hel}	Area of heliostats	11 × 11 [m^2]
DNI	Direct normal irradiance	750 [W/ m^2]
A_r	The area of heliostats	60 [m^2]
T_r	The receiver local temperature	1000 [°C]
ε	Surface emissivity of the receiver	0.88
v_a	Wind speed	5 [m/s]
P_9	SRC inlet pressure	90 [kPa]
η_{pump}	Pump efficiency	0.8
η_{turbin}	Gas turbine efficiency	0.85
pp_{evva}	Evaporator pinch point	10 [°C]
PP_{cond}	Condenser pinch point	10 [°C]
T_{15}	Pump 2 inlet temperature	40 [°C]
T_{13}	SRC turbine inlet temperature	80 [°C]

must be highlighted. The total amount of solar energy in heliostats is given by Equations (3) and (4) [33].

$$\dot{Q}_{Sun} = A_h \times N \times DNI \tag{3}$$

$$\dot{Q}_h = \eta_h \times \dot{Q}_{Sun} \tag{4}$$

A_h, η_h, and N refer to the area of one heliostat, efficiency, and the number of mirrors, respectively. Heat losses can be quantified by Equation (5).

$$\dot{Q}_{loss} = h_a A_h (T_r - T_0) + \sigma \varepsilon A_h \left(T_r^4 - T_0^4\right) \tag{5}$$

$$h_a = 10.45 - v_a + 10\sqrt{v_a} \quad \left(\mathrm{W} \big/ \mathrm{m^2 K}\right) \tag{6}$$

v_a represents wind speed. Finally, the heat transfer coefficient between air and receiver is expressed by Equation (7).

$$\dot{Q}_r = \dot{Q}_h - \dot{Q}_{loss} = \dot{m}(h_{out} - h_{in}) \tag{7}$$

2.4. Thermoelectric generator (TEG) analysis

A TEG uses residual heat to produce electricity, and its power can be calculated by Equation (8) [34].

Table 2
Energy and exergy balance equations for each control volume.

Component	Energy balance	Exergy balance
Compressor	$\dot{W}_{comp} = \dot{m}_1 \times (h_2 - h_1)$	$\dot{E}x^D_{Comp} = \dot{E}x_1 + \dot{W}_{comp} - \dot{E}x_2$
Brayton cycle	$\dot{W}_{Brayton} = \dot{W}_{turbine,\ steam} - \dot{W}_{comp}$	
Pump 1	$\dot{W}_{pump1} = \dot{m}_9 \times (h_{10} - h_9)$	$\dot{E}x^D_{Pump1} = \dot{E}x_9 + \dot{W}_{Pump1} - \dot{E}x_{10}$
Steam turbine	$\dot{W}_{turbine,\ steam} = \dot{m}_7 \times (h_7 - h_8)$	$\dot{E}x^D_{turbine,steam} = \dot{E}x_7 - \dot{W}_{turbine,\ steam} - \dot{E}x_8$
SRC	$\dot{W}_{net\_steam} = \dot{W}_{turbine,\ steam} - \dot{W}_{pump1}$	
Gas turbine	$\dot{W}_{turbine,\ gas} = \dot{m}_3 \times (h_3 - h_4)$	$\dot{E}x^D_{turbine,gas} = \dot{E}x_3 - \dot{W}_{turbine,\ gas} - \dot{E}x_4$
Pump 2 (ORC)	$\dot{W}_{pump2} = \dot{m}_{15} \times (h_{16} - h_{15})$	$\dot{E}x^D_{Pump2} = \dot{E}x_{15} + \dot{W}_{Pump2} - \dot{E}x_{16}$
ORC turbine	$\dot{W}_{turbine,\ ORC} = \dot{m}_{13} \times (h_{13} - h_{14})$	$\dot{E}x^D_{turbine,ORC} = \dot{E}x_{13} - \dot{W}_{turbine,\ ORC} - \dot{E}x_{14}$
ORC	$\dot{W}_{net\_ORC} = \dot{W}_{turbine,\ ORC} - \dot{W}_{pump2}$	
Evaporator 1	$Q_{Eva\ 1} = \dot{m}_{10} \times (h_7 - h_{10})$	$\dot{E}x^D_{Eva\ 1} = \dot{E}x_4 + \dot{E}x_{10} - \dot{E}x_5 - \dot{E}x_7$
Evaporator 2	$Q_{Eva\ 2} = \dot{m}_{16} \times (h_{13} - h_{16})$	$\dot{E}x^D_{Eva\ 2} = \dot{E}x_5 + \dot{E}x_{16} - \dot{E}x_6 - \dot{E}x_{13}$

$$\dot{m}_8 h_8 + \dot{m}_{11} h_{11} = \dot{m}_9 h_9 + \dot{m}_{12} h_{12} + \dot{W}_{TEG} \tag{8}$$

The efficiency of TEG and its figure of merit (Z-factor) are given by Equations (9) and (10).

$$\eta_{TEG} = \eta_{carnot} \times \left(\times \left(\sqrt{(1+ZT_M)} - 1\right) \Big/ \left(\sqrt{(1+ZT_M)} + \left(T_L \big/ T_H\right)\right)\right) \tag{9}$$

$$ZT_M = 0.8 \tag{10}$$

The capability of a substance to produce electricity holds a relationship with the figure of merit, which is a dimensionless number. For TEG efficiency, Equations (11)–(15) are applied [34].

$$\eta_{TEG} = \dot{W}_{TEG} \Big/ \dot{Q}_{Elegant} \tag{11}$$

$$\eta_{carnot} = 1 - (T_L / T_H) \tag{12}$$

$$\dot{Q}_{Elegant} = \dot{m}_{TEG} \times (h_H - h_C) \tag{13}$$

$$T_L = 0.5 \times (T_{11} + T_{12}) \tag{14}$$

$$T_H = 0.5 \times (T_8 + T_9) \tag{15}$$

2.5. Exergy analysis

Exergy analysis determines the location and degree of thermodynamic inefficiencies in a system, and is the maximum useful work extracted from a system as it reversibly comes into equilibrium with its environment [16,35]. The exergy of a flow is calculated by Equation (16).

$$\mathrm{ex} = \mathrm{h} - \mathrm{h}_0 + \mathrm{T}_0(\mathrm{s} - \mathrm{s}_0) \tag{16}$$

Exergy efficiency is calculated from [36], as shown in Equation (17).

$$\eta_{exe\_tot} = (\dot{W}_{net} + \dot{E}x_{21}) \,/\, \dot{E}x_{Sun} \tag{17}$$

$$T_{sun} = 5800[K] \tag{18}$$

$$\dot{E}x_{sun} = \dot{Q}_{sun} \times (1 - (T_{0K} / T_{sun})) \tag{19}$$

The exergy balance equations for system components are charted in Table 2.

2.6. Economic analysis

The capital recovery factor (CRF) is given by Equation (20) [37].

Table 3
Economic cost equations for the components [34,39].

Component	Equation
Compressor	$Z_{comp} = (75 \times \dot{m}_1)/(0.9 - \eta_{comp}) \times ((P_2 / P_1) \times \ln(P_2 / P_1))$
Gas turbine	$Z_{tubine,\ gas} = ((479.3 \times \dot{m}_1)/(0.92 - \eta_{turbin,gas})) \times \ln(P_3 / P_4) \times (1 + \exp(0.036 \times T_3 - 54.4))$
Heliostat	$Z_{solar,\ Heliostat,\ hel} = 150 \times A_{hel} \times N_{hel}$ $Z_{solar,\ Heliostat,\ rec} = A_r \times (79 \times T_r - 42000)$
SRC turbine	$Z_{Turbine,\ steam} = 2210 \times \dot{W}_{turbine,\ steam}{}^{0.75}$
Evaporator	$Z_{Evap} = 276 \times (A_{Evap1}{}^{0.88})$ $A_{Evap1} = Q_{Evap1} / (u_{Evap} / \Delta T_{lnEvap1})$ $\Delta T_{lnEvap1} = ((T_4 - T_7) - (T_5 - T_{10}))/\ln((T_4 - T_7) - (T_5 - T_{10}))$
Pump	$Z_{Pump} = 3540 \times \dot{W}_{Pump1}{}^{0.71}$
TEG	$Z_{TEG} = 1500 \times \dot{W}_{TEGT}$
RO unit	$Z_{RO} = 0.98 \times m^3_{Freshwater}$
Condenser	$Z_{cond} = 1173 \times m_{14}$
ORC turbine	$Z_{ORC\_turbin} = 4750 \times \dot{W}_{ORC\_turbin}{}^{0.7}$

Table 4
Validation of the RO unit with Nafey and Sharaf [40].

Variable	This research	Nafey and Sharaf [40]	Deviation (%)
$\dot{W}_{Pump,\ RO}$ (kW)	1121	1131	0.97
M_f (m^3/h)	486	485.9	0
SR (−)	0.994	0.9944	0
X_b (ppm)	64,181	64,180	0
X_d (ppm)	253	250	0.8
ΔP (kPa)	6840	6850	0.1

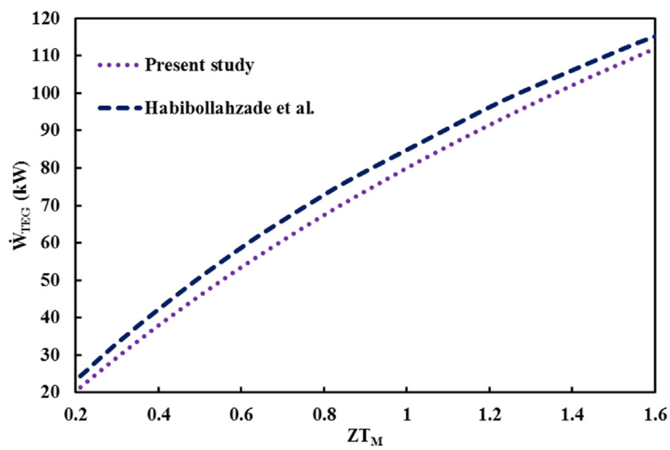

Fig. 2. Validation of TEG model with Habibollahzade et al. [41].

$$CFR = \frac{ix(1+i)^n}{(1+i)^n - 1} \tag{20}$$

i and n are the interest rate and lifetime of the system, equal to 0.1 and 20 years, respectively.

By assuming the lifetimes of each component, $\dot{Z}$ indicates the cost rate associated with sub-cycles, as shown in Equation (21) [38].

$$\dot{Z} = \frac{Z_{total} CRF \varnothing}{T_{cost}} \tag{21}$$

T_{cost} refers to the annual operation hours. Because the system location is Isfahan, it receives solar irradiation for 8.5 h a day, on average, throughout one operational year, yielding T_{cost} = 3102 h. Also, $\varnothing$ is the coefficient of maintenance, equal to 1.06 [39]. Table 3 shows the economic cost equations for the system components.

3. Results and discussion

3.1. Validation

The study of Nafey and Sharaf [40] is used as a benchmark to validate the RO unit modeling, as shown in Table 4. The study of Habibollahzade et al. [41] is utilized to validate TEG modeling, as depicted in Fig. 2.

Table 4 demonstrates a good agreement of the results obtained herein with the study of Nafey and Sharaf [40]. At the same time, Fig. 2 confirms the validation of the TEG model following Habibollahzade et al. [41].

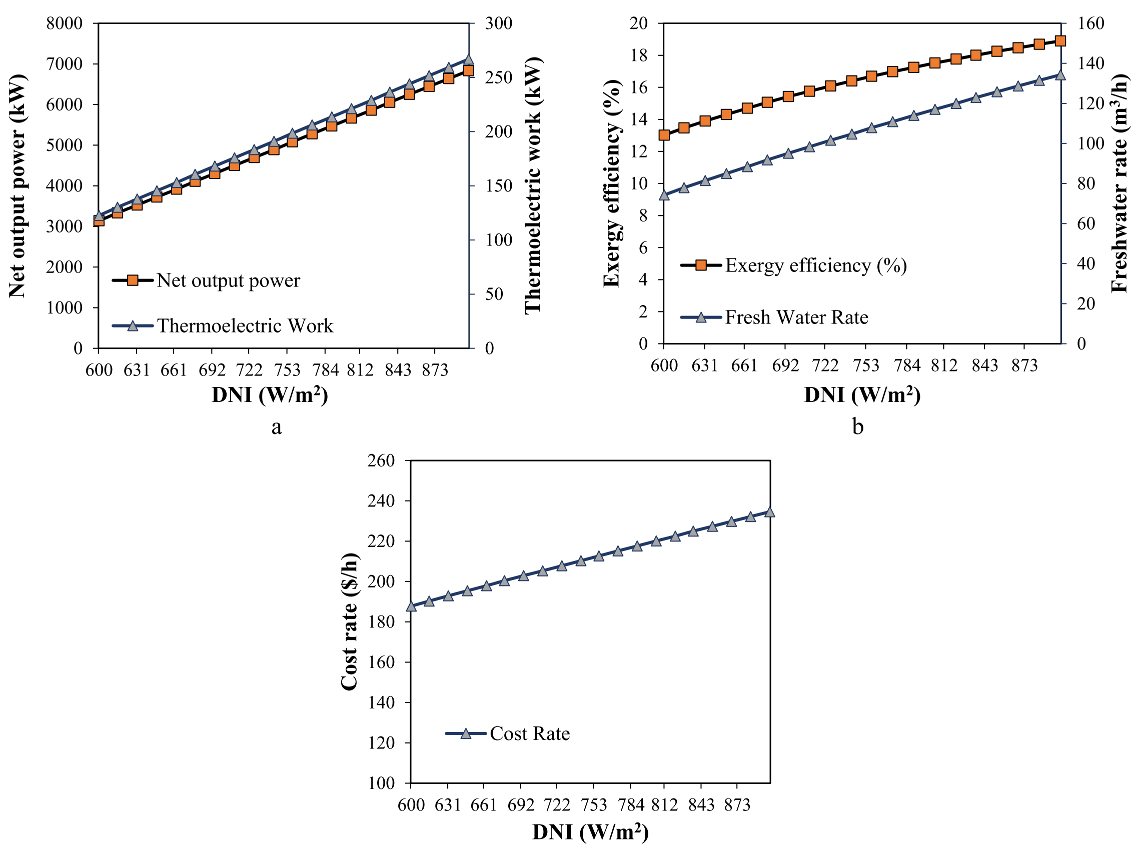

Fig. 3. The impact of DNI on (a) net output power and thermoelectric work, (b) exergy efficiency and freshwater production rate, and (c) cost rate.

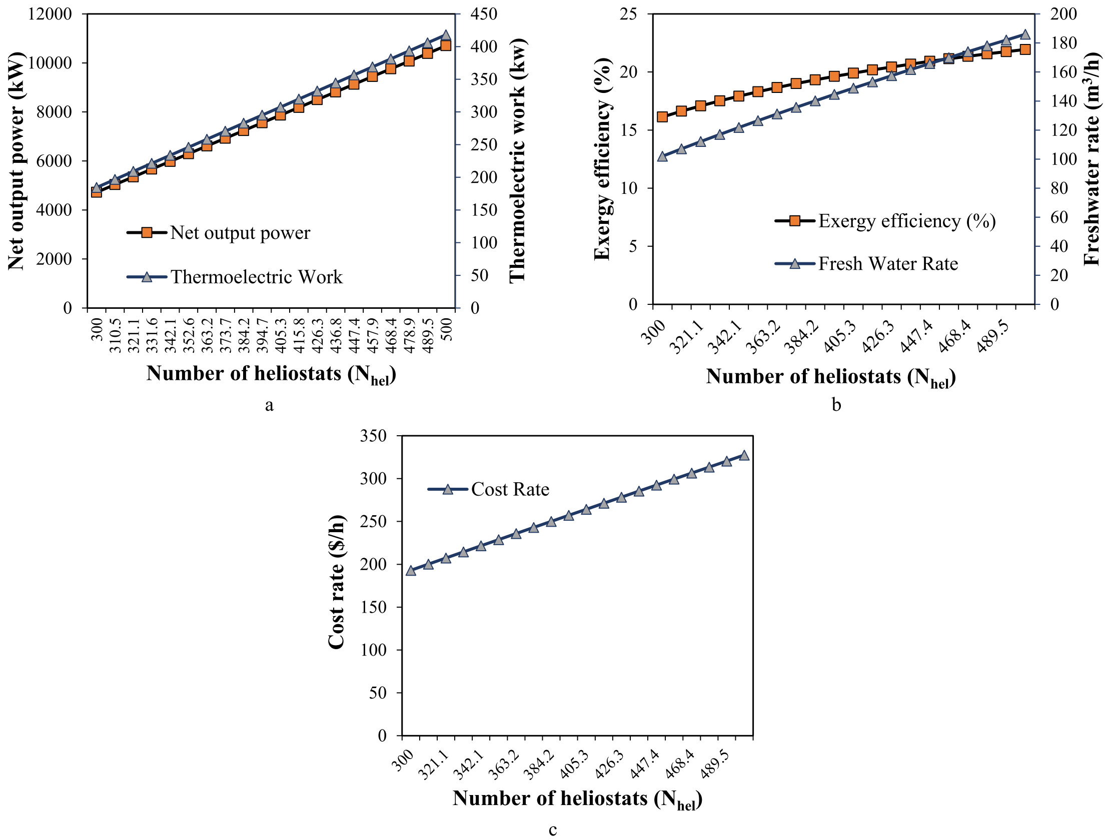

Fig. 4. The impact of the number of heliostats (N_{hel}) on (a) net output power and thermoelectric work, (b) exergy efficiency and freshwater production rate, and (c) cost rate.

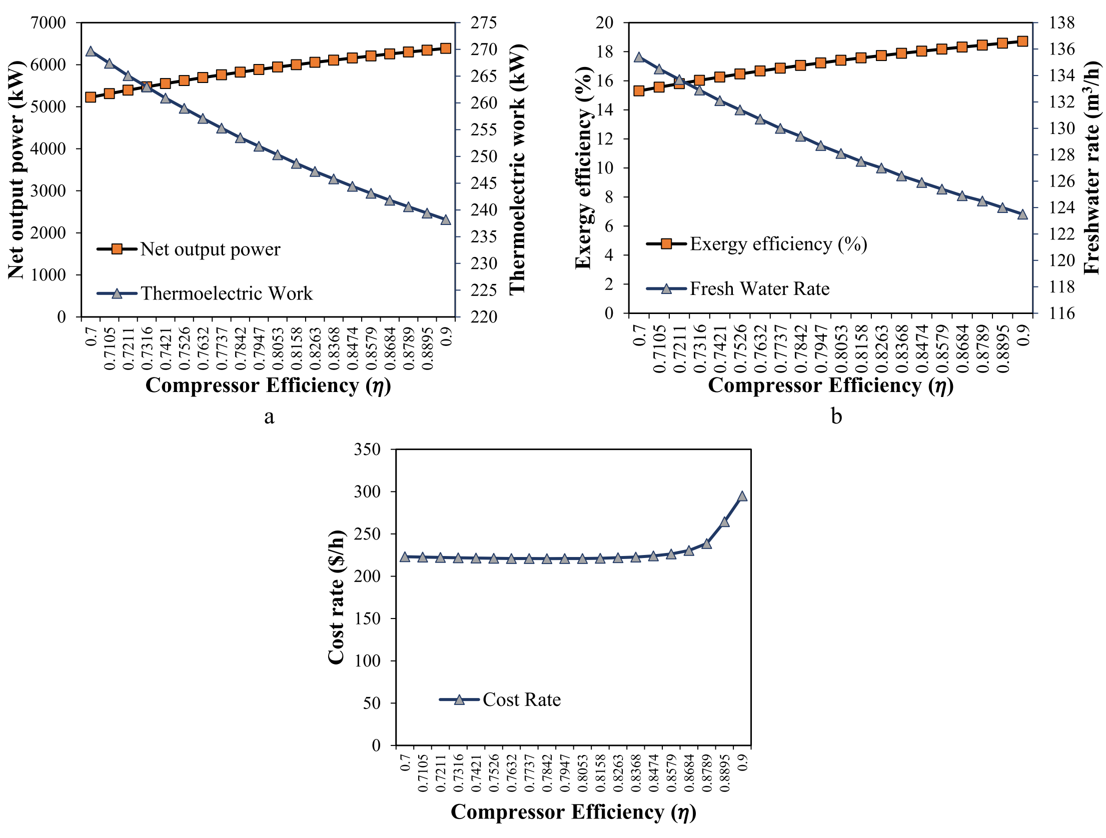

Fig. 5. The impact of compressor efficiency (η) on (a) net output power and thermoelectric work, (b) exergy efficiency and freshwater production rate, and (c) cost rate.

3.2. Parametric study

The main challenge in designing renewable-based multi-generation systems lies in finding the optimal point for efficiency, costs and defining suitable design parameters. This section analyzes the effects of evaporator pinch point, compressor efficiency, turbine efficiency, SRC turbine inlet pressure, ORC turbine inlet pressure, SRC turbine inlet temperature, SRC pump inlet temperature, compressor pressure ratio, number of heliostats, and direct normal irradiance (DNI).

Firstly, the impact of DNI is assessed. DNI is varied from 600 W/m^2 to 900 W/$m^{2,}$ and Fig. 3 depicts the effects on net output power, thermoelectric work, exergy efficiency, freshwater rate, output work, and cost rate. Fig. 3a illustrates that the net output power and thermoelectric work increase by increasing DNI from 600 W/m2 to 900 W/m2. Fig. 3b demonstrates that 300 W/m^2 enhancements DNI lead to increases in exergy efficiency, from 13.02% to 18.9%. The freshwater production rate increases as well, which is pertinent to exergy efficiency and net output power. According to Fig. 3c, the same enhancement in DNI increases systems cost rate from 187.5$/h to 234.6 $/h, resulting from a direct relationship between cost rate and net output power. As output power increases, larger equipment is required, so the costs increase.

Fig. 4 shows the influence of the number of heliostats from 300 to 500. As indicated in Fig. 4a, output power and thermoelectric work increase along with the number of heliostats. By adding 200 heliostats, the net output power goes up by almost 5500 kW, and thermoelectric work increases from 184.4 kW to 418.1 kW. Fig. 4b proves the positive correlation between changes in the number of heliostats, exergy efficiency, and freshwater production rate. Increasing the number of heliostats from 300 to 500 increases the exergy efficiency and freshwater production rate up to 21.94% and 186 m^3/h, respectively. Fig. 4c shows that with the same increase in the number of solar heliostats, the system cost rate increases from 193 $/h to 327.5 $/h. The reason for such an increase is the direct relationship between cost rate and output power. In other words, for achieving higher amounts of output work, more expensive equipment should be utilized.

Fig. 5 represents the impact of the increase in compressor efficiency. Two significant parameters in determining the performance of compressors are pressure ratio and compressor efficiency. Fig. 5a shows that by increasing compressor efficiency from 0.7 to 0.8, the net output power rises from 5225 kW to 6388 kW; however, the thermoelectric work reduces to 238.2 kW. In the course of compressing the gas, the temperature of compressors increases, requiring a cooling system. As the compressor efficiency augments, the gas cycle flow rate decreases, thus reducing the mass flow rate of the steam cycle, which inherently reduces the thermoelectric work. Fig. 5b shows that the increase in compressor efficiency increases exergy efficiency by around 6.5%. Whereas in contrast, the freshwater production rate decreases. As illustrated in Fig. 5c, a 20% rise in compressor efficiency increases system costs from 248.2223.1 $/h to 295 $/h, due to the need for more expensive equipment for higher amounts of output power. The increase

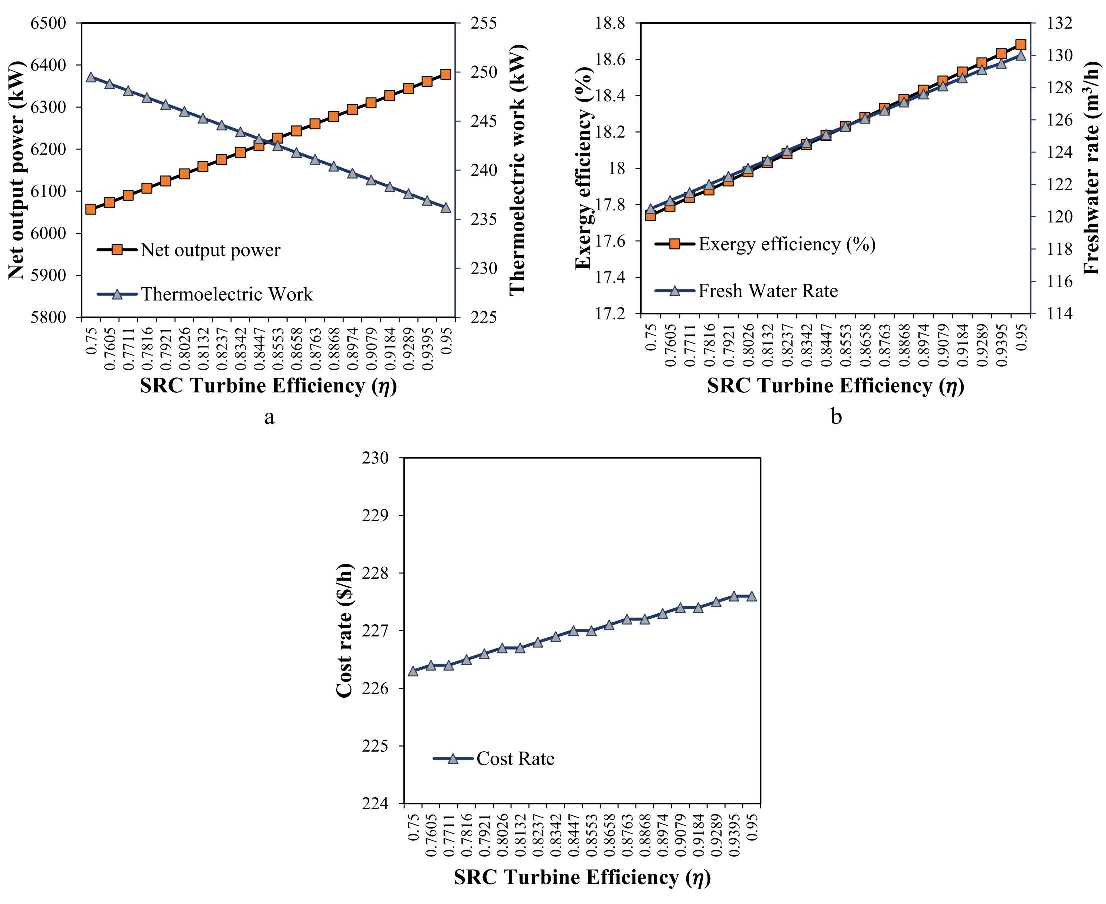

Fig. 6. The effect of increasing SRC turbine efficiency (η) on (a) net output power and thermoelectric work, (b) exergy efficiency and freshwater rate, and (c) cost rate.

occurs in the range of 0.868–0.9, and the cost rate remains approximately constant up to a 0.868 compressor efficiency. Furthermore, the hidden costs, including maintenance costs, are another reason which causes the costs to step up.

Fig. 6 shows the effect of increasing the SRC turbine efficiency from 0.75 to 0.95. Fig. 6a shows that higher turbine efficiency leads to higher net output power, incrementing from 6057 kW to 6378 kW. Nevertheless, the thermoelectric work sees a downward trend from 249.5 kW to 236.2 kW; this occurs because the effi-ciency exceeds its standard and allowable range, thereby lessening the system efficiency. Fig. 6b demonstrates that with increasing turbine efficiency, the system exergy efficiency changes from 17.74%to 18.68%, and the freshwater production rate increases from 120.5 m^3/h to 130m^3/h. As depicted in Fig. 6c, when turbine effi-ciency increases, the cost rate increases from 226.3 $/h to 227.6 $/h. Because cost and output work have a direct relationship, higher output power requires larger, more expensive equipment.

Fig. 7 shows the effect of increasing the SRC turbine inlet pressure from 3000 kPa to 5000 kPa. Fig. 7a shows that, as the SRC turbine inlet pressure rises, the net output power increases from 6217 kW to 6259 kW, whereas the thermoelectric work decreases from 242.8 kW to 228.6 kW. Because the turbine standard operating conditions exceed its standard and allowable range for boundary conditions, there is an unfavorable impact on system efficiency. There is also thermoelectric depreciation resulting from operating in inappropriate situations such as high temperature, uncontrolled pressure, enthalpy, increased entropy, and working in undersigned operational conditions. Fig. 7b shows that as the inlet pressure of the SRC turbine increases, the exergy efficiency of the system increases from 18.21% to 18.33%, and the freshwater production rate changes from 125.3 m^3/h to 132.2 m^3/h. As shown in Fig. 7c, as the SRC turbine inlet pressure is higher, the cost rate rises from 227 to 227.4 $/h, which can be said that the cost rate isn't affected by the SRC turbine inlet pressure changes.

The effect of increasing the evaporator pinch point temperature from 5°C to 15°C is depicted in Fig. 8. Fig. 8a displays a decrease in the net output power and the thermoelectric work. This happens due to undesirably high evaporator temperature and out-of-standard operating conditions. Fig. 8b demonstrates a decline in exergy efficiency, from 18.28% to 18.14%. The freshwater production rate also decreases from 126 m^3/h to 124.6 m^3/h. Fig. 8c shows that cost rate drops from 228.1 $/h to 226 $/h.

Fig. 9 shows that when increasing compressor pressure ratio from 10 to 20, the net output work follows an increasing decreasing trend, and at a pressure ratio of 14.76, the highest net output power (6310 kW) is obtained. Considering Fig. 9a, the increase in compressor pressure ratio decreases the thermoelectric work, from 242.8 kW to 188.5 kW. Fig. 9b shows that, with the increase in compressor pressure ratio, exergy efficiency increases from 18.21% to 18.48%, and after the 14.74 ratio, it decreases to 18.22%. Also, freshwater production follows a downward-upward increase from 125.3 m^3/h to 127.2 m^3/h. Fig. 9c shows an increase in cost rate, from 227 $/h to 277.8 $/h, due to the direct relationship between cost and output power.

Fig. 10 assesses the effect of increasing the ORC turbine inlet temperature from 70°C to 100°C. Fig. 10a and b shows that as the ORC turbine inlet temperature rises, the system's net output power and exergy efficiency increase from 6177 kW to 6259 kW and from

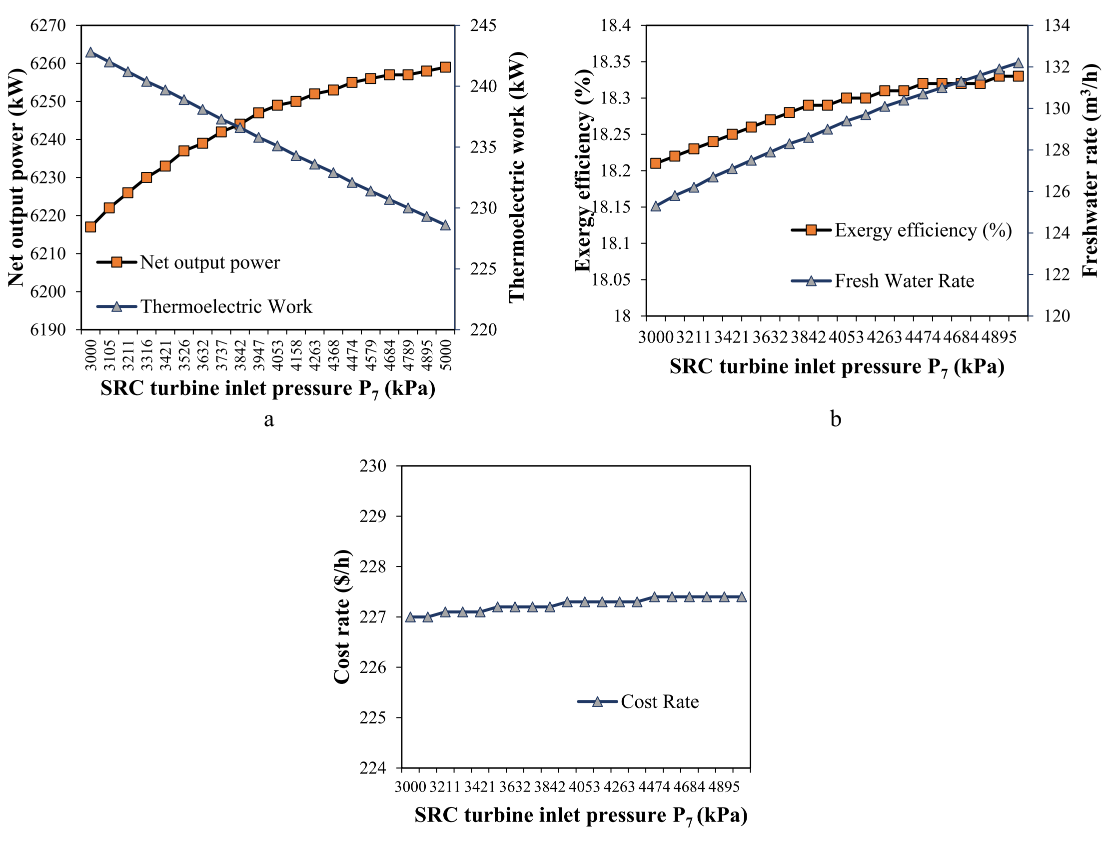

Fig. 7. The effect of increasing the SRC turbine inlet pressure (P_7) on (a) net output power and thermoelectric work, (b) exergy efficiency and freshwater rate, and (c) cost rate.

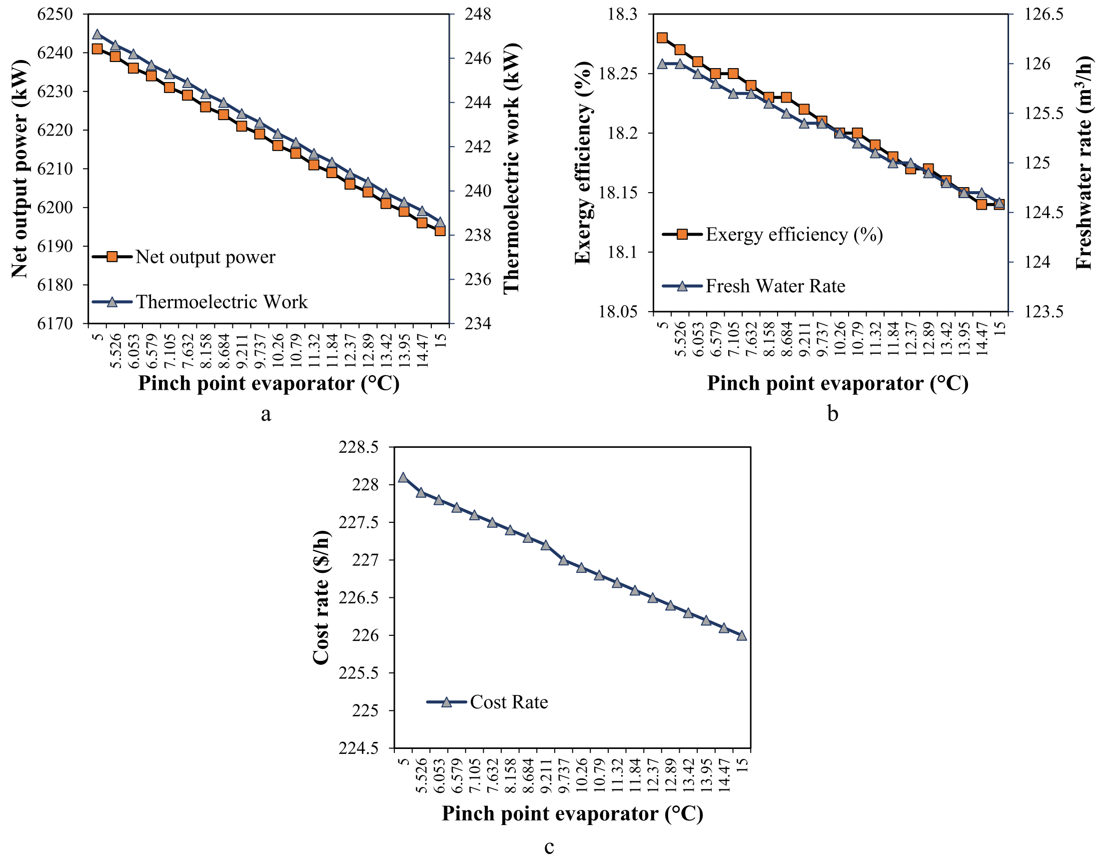

Fig. 8. The effect of increasing evaporator pinch point temperature on (a) net output power and thermoelectric work, (b) exergy efficiency and freshwater rate, and (c) cost rate.

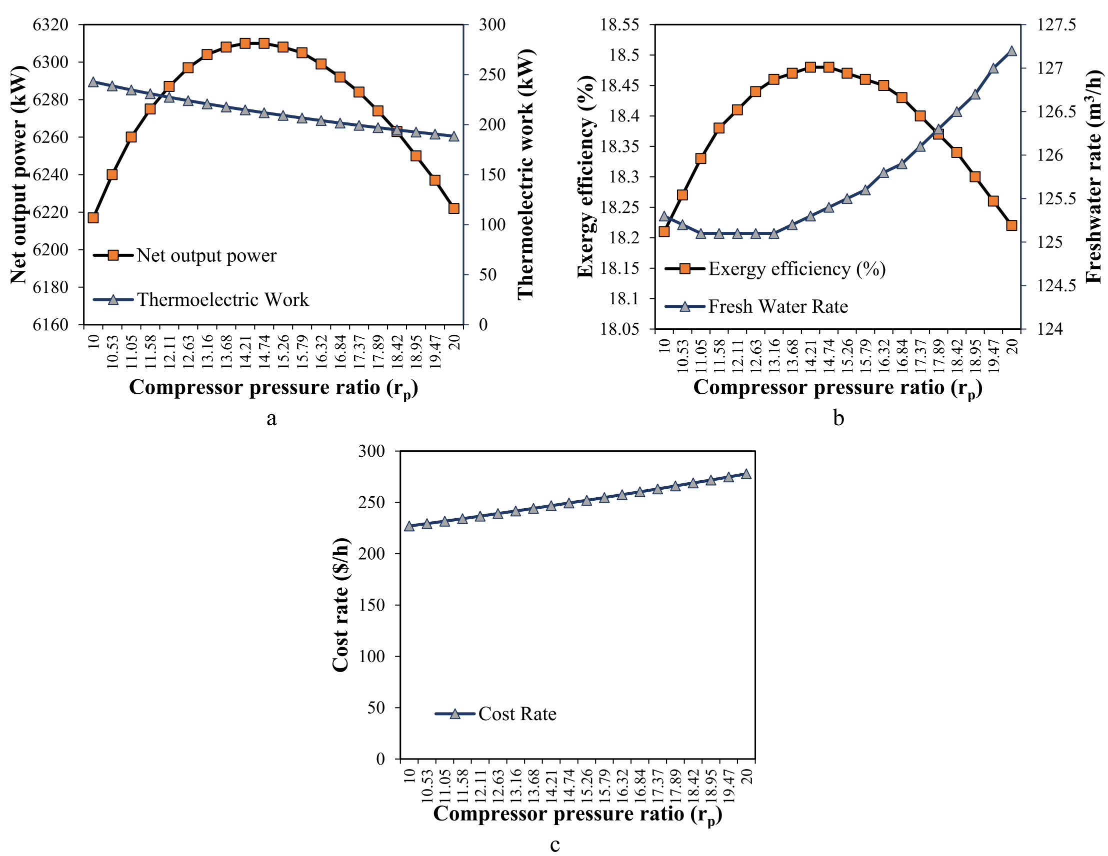

Fig. 9. The effect of increasing the compressor pressure ratio (r_p) on (a) net output power and thermoelectric work, (b) exergy efficiency and freshwater rate, and (c) cost rate. 1

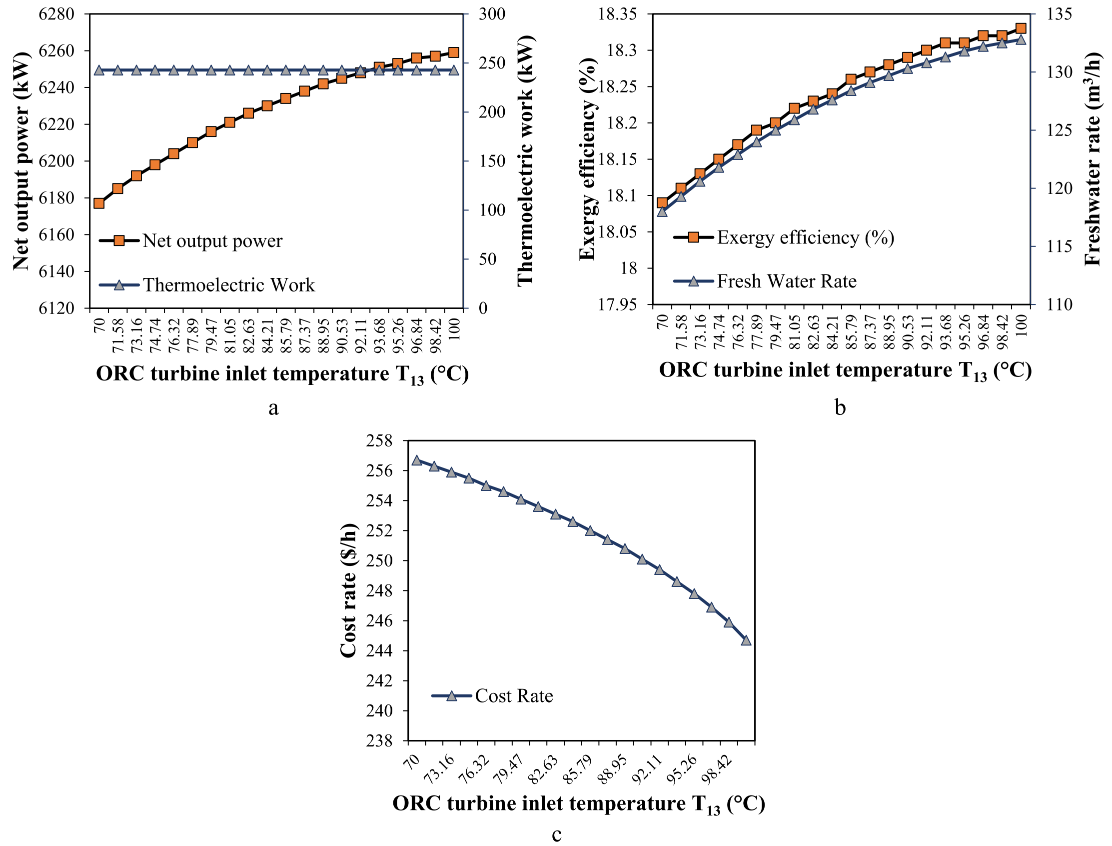

Fig. 10. The effect of increasing the ORC turbine inlet temperature (T_{13}) on (a) net output power and thermoelectric work, (b) exergy efficiency and freshwater rate, and (c) cost rate.

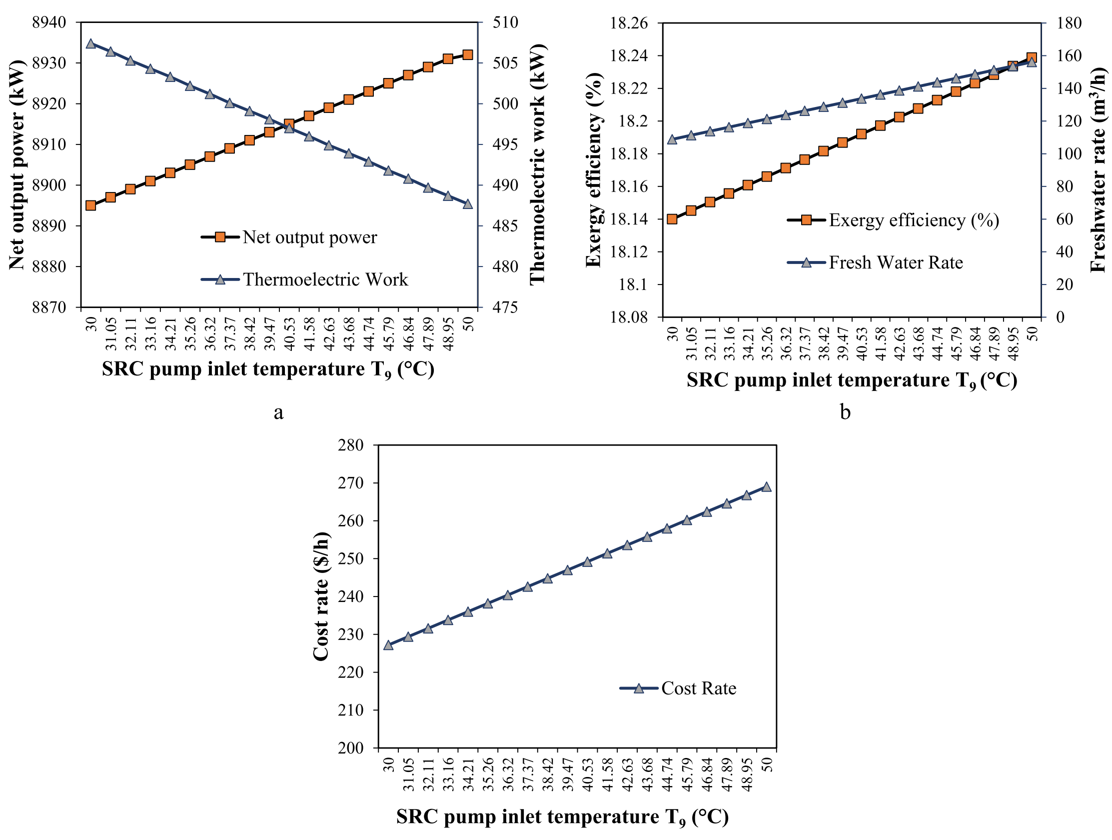

Fig. 11. The effect of increasing the SRC pump inlet temperature (T_9) on (a) net output power and thermoelectric work, (b) exergy efficiency and freshwater rate, and (c) cost rate.

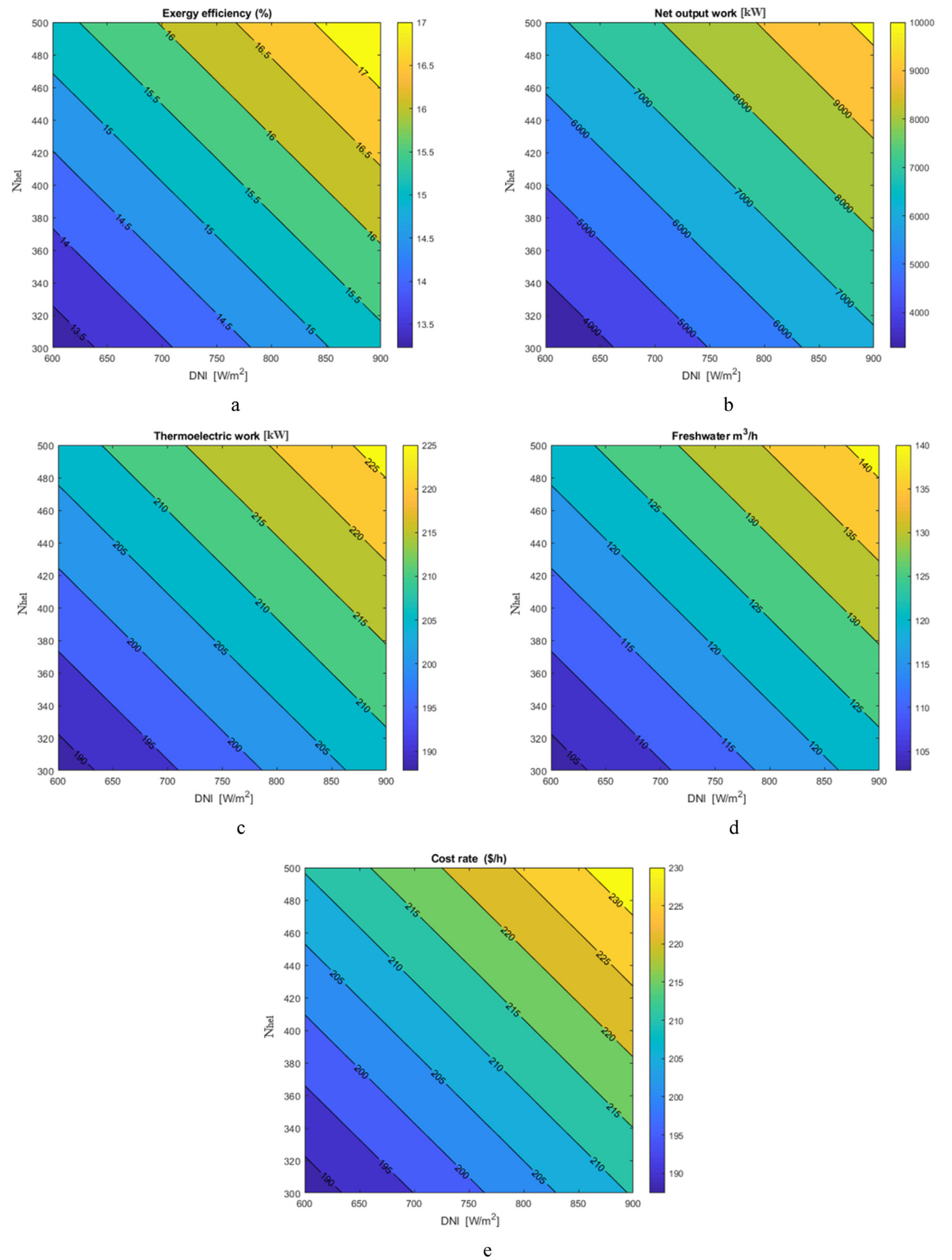

Fig. 12. The effect of increasing the number of heliostats (N_{hel}) and solar radiation (DNI) on (a) exergy efficiency, (b) net output power, (c) thermoelectric work, (d) freshwater production rate, and (e) cost rate.

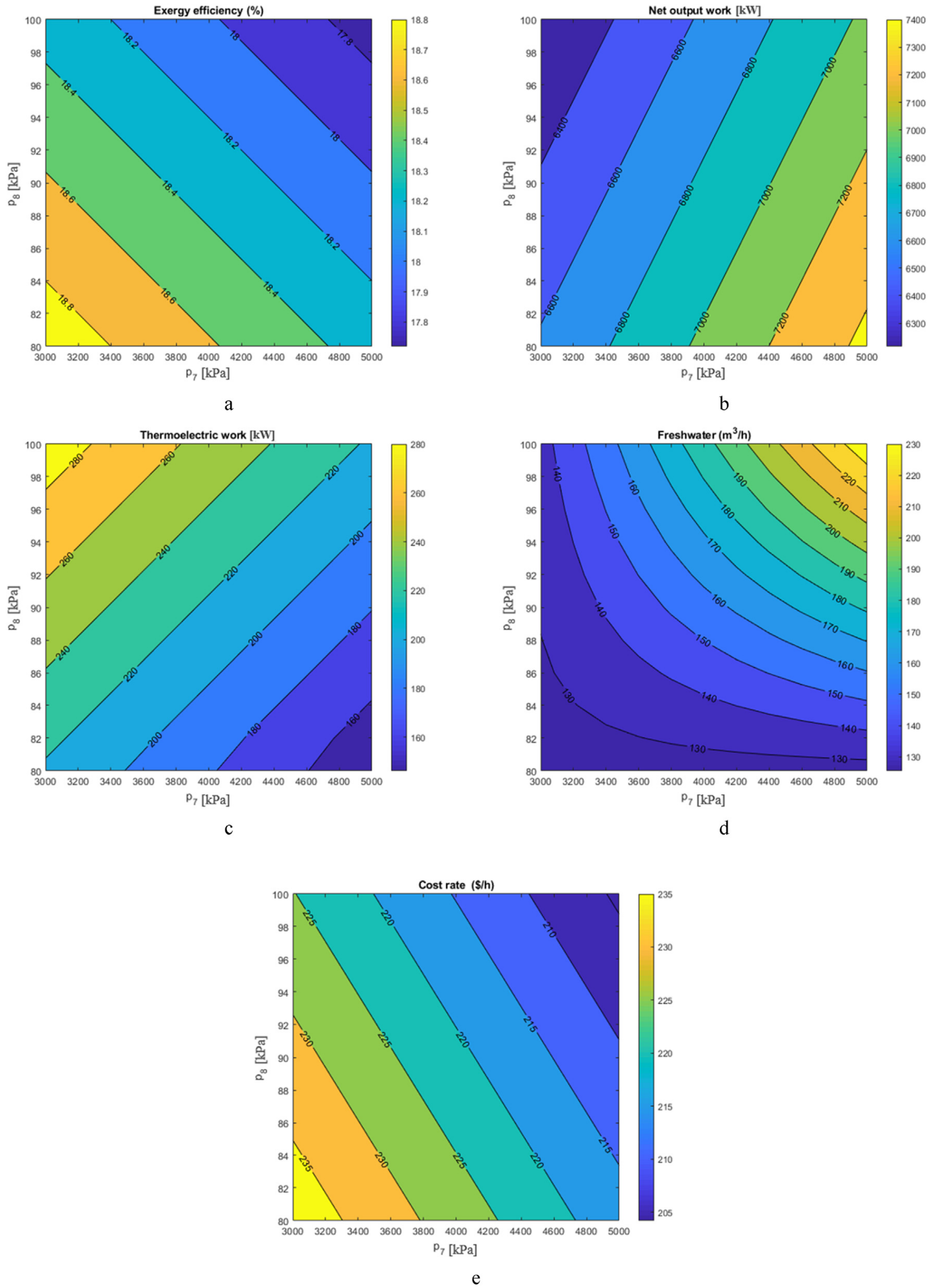

Fig. 13. The effect of increasing inlet (P_7) and outlet (P8) pressure of SRC turbine on (a) exergy efficiency, (b) net output power, (c) thermoelectric work, (d) freshwater production rate, and (e) cost rate.

18.09% to 18.33%, respectively. Exergy efficiency and output power are directly related. Fig. 10a illustrates that the thermoelectric work was unaffected by the ORC turbine inlet temperature. Fig. 10b shows that freshwater production increases from 118 m^3/h to 132.8 m^3/h. Fig. 10c shows a decrease in system cost rate from 227.6$/h to 225.7 $/h.

Fig. 11 analyzes the effect of increasing the SRC pump inlet temperature from 30°C to 50°C. Fig. 11a displays an increase in net output power, from 8895 kW to 8932 kW. Exergy efficiency also increases, as shown in Fig. 11b, from 18.14% to 18.23%. Exergy efficiency and net output power are directly related. As the fluid temperature entering the SRC pump rises, the enthalpy of the fluid also rises, thus increasing the output power. Fig. 11a shows that the thermoelectric work decreases from 507.4 kW to 487.7 kW. Fig. 11b shows that the system's freshwater production rate also increases with the increase in SRC pump inlet temperature. Fig. 11c shows an increase in the system cost rate from 227.2 $/h to 269 $/h, as cost and output power are directly related.

The parameters with the most substantial effect on system performance were DNI, number of heliostats (N_{hel}), turbine efficiency, turbine inlet pressure, compressor pressure ratio (r_p), and SRC pump inlet temperature (T_9).

Fig. 12 illustrates the effect of increasing the number of heliostats and the amount of solar radiation on system parameters. Fig. 12a shows the beneficial impact on exergy efficiency. Fig. 12b shows an increase in the net output power of the system, and Fig. 12c and d demonstrate that the increase in solar radiation and the number of heliostats increases thermoelectric work and freshwater production. Fig. 12e illustrates an expected increase in cost rate. It should be added that most costs are related to the heating system.

Fig. 13 shows the effect of increasing SRC turbine inlet and outlet pressures. Fig. 13a presents an obvious decrease in exergy efficiency. Fig. 13b shows that net output power increments with the rise in inlet pressure and decrease in outlet pressure. Fig. 13c demonstrates that the thermoelectric work rises with the decrease in inlet pressure and increase in outlet pressure. Fig. 13d reveals that increasing the inlet and the outlet pressure of the SRC turbine increases freshwater production rate. Fig. 13e depicts a decrease in cost rate with the rise in inlet and outlet pressure because net output work and exergy efficiency have already decreased.

3.3. *Case study: Isfahan*

Isfahan is a city in Central Iran (435 km from Tehran), located at 32.6539° N, 51.6660° E. The climate of Isfahan is temperate and dry, with moderate rain and snow precipitations (due to climate change, arid conditions have become ultra-arid) [42]. Summers are hot and dry, with maximum temperatures around 39°C. The minimum temperature in winter can reach −18°C. Isfahan is facing severe water shortages and environmental concerns. On this line, the seawater is transferred from the Persian Gulf to Isfahan for desalination purposes. Fig. 14 shows the location of Isfahan within Iran and its Solarimetric potential.

Fig. 15a and b depict air temperature solar radiation throughout the year on an hourly basis [43].

Fig. 16 summarizes the yearly net electrical energy, thermoelectric electrical energy, and freshwater production for the case study in Isfahan concerning DNI. As seen, July is the month with the highest electrical energy (110763 kWh, Fig. 16a), highest thermoelectric electrical energy (4085.8 kWh, Fig. 16b), and highest freshwater production (2759 m^3, Fig. 16c).

Table 5 summarizes the annual outputs of the system in Isfahan with regard to DNI.

Ambient temperature affects the output energy of solar-based systems. Fig. 17 summarizes the yearly net electrical energy, thermoelectric electrical energy, and freshwater production for Isfahan's case study regarding ambient temperature.

Fig. 17a indicates that the highest amount of net electrical energy (35774 kWh) occurs in July. As displayed in Fig. 17b, the highest amount of thermoelectric electrical energy is related to January, equal to 7722 kWh. As shown in Fig. 17c, the highest amount of freshwater production is in July and is 3900 m^3. These results agree with Abdulrahim and Chung [44], where power and water cogeneration plant located in a hot arid climate was analyzed

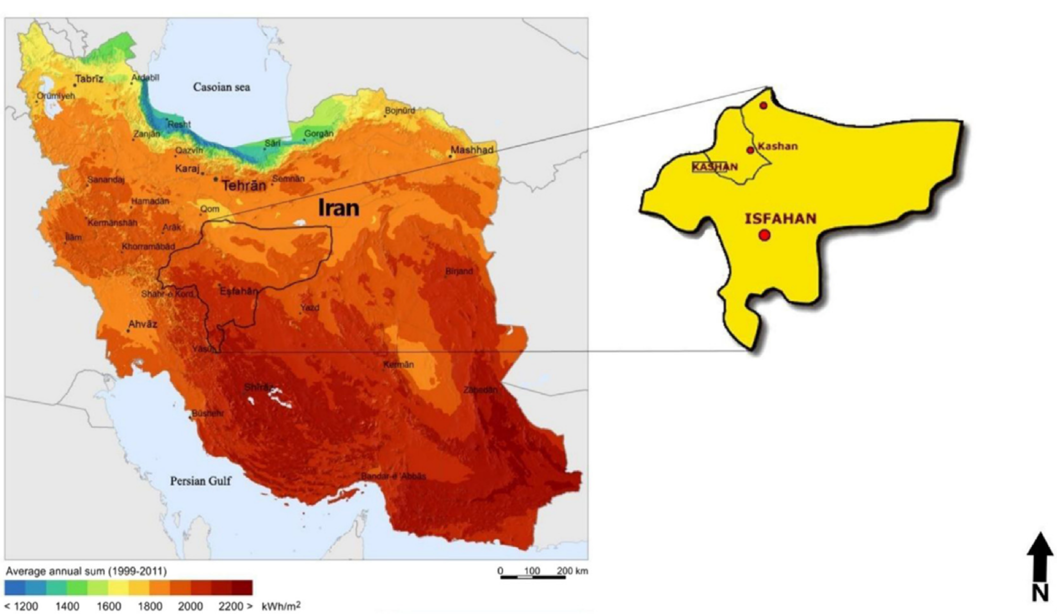

Fig. 14. Location of Isfahan and average amount solar energy [42].

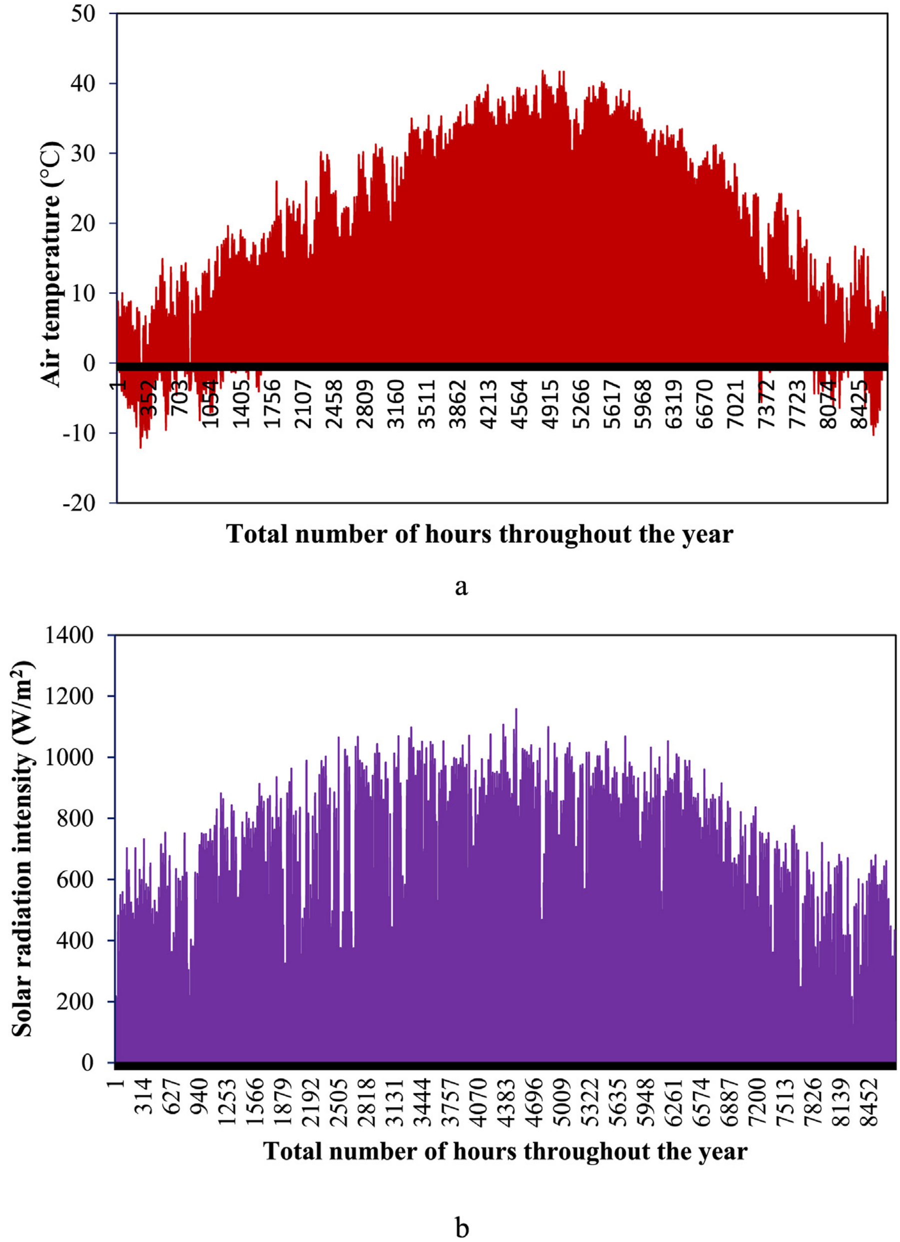

Fig. 15. (a) Air temperature and (b) solar irradiation throughout the year on an hourly basis at Isfahan.

in Kuwait. Table 6 summarizes the annual outputs of the system in Isfahan concerning ambient temperature.

3.4. Optimization

3.4.1. Artificial neural network (ANN)

Artificial neural networks (ANNs) are computational models based on biological theory and contain a large number of computing elements (linear or nonlinear) called neurons [38]. An ANN is a programmable method for learning from data. An initial set of neurons are linked together so they can send data to each other. After that, a problem is identified that the network must solve. The network attempts this process repeatedly, verifying the successful links and eliminating those that fail. With sufficient training samples and computing power, the ANN can answer any question. In an ANN, three layers exist: input layer, hidden layer, and output layer. The ability of ANNs to simulate and model nonlinear processes makes them useful in various fields, such as optimizing energy systems [45–47]. 700 samples from input-output points are taken from the results of the proposed thermodynamic analysis to train the network. Multi-objective optimization is carried out on the trained network using the multi-objective NSGA-II algorithm. The mean squared error (MSE) is calculated to determine how accurate the network is in determining output results. A significant advantage of the proposed method is the reduction of time since the thermodynamic calculations have only to be performed in the first step and not again during the optimization process. An analysis that integrates both thermodynamics for the proposed system and neural network, as well as neural network and the NSGA-II. There are

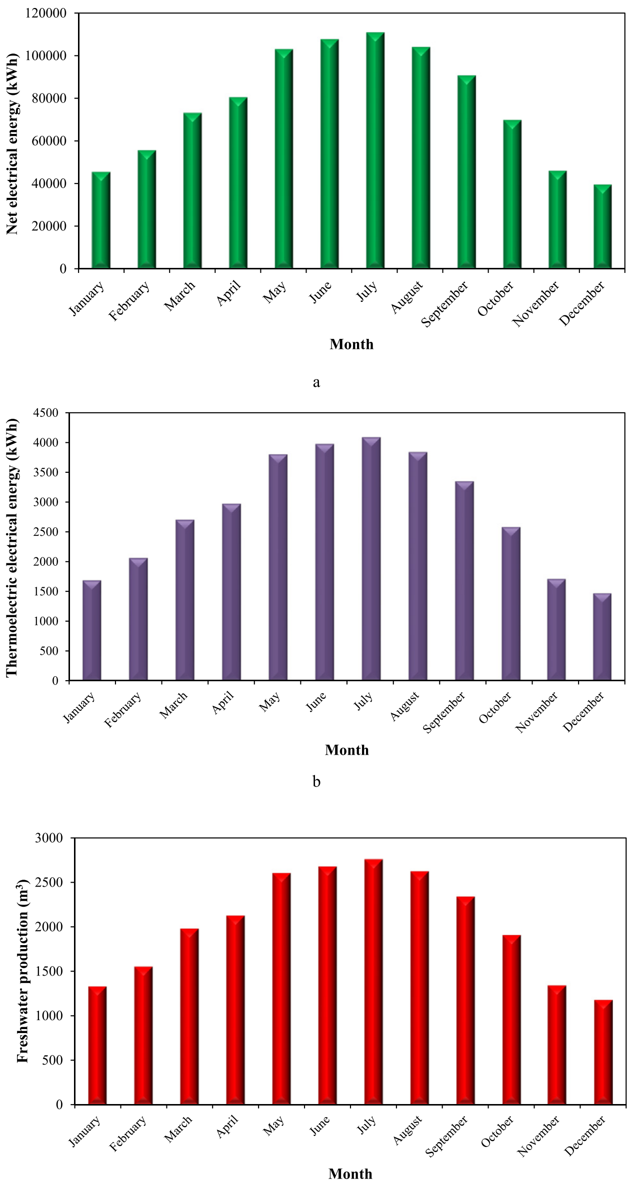

Fig. 16. (a) net electrical energy, (b) the thermoelectric electrical energy, and (c) freshwater production changes concerning DNI in Isfahan.

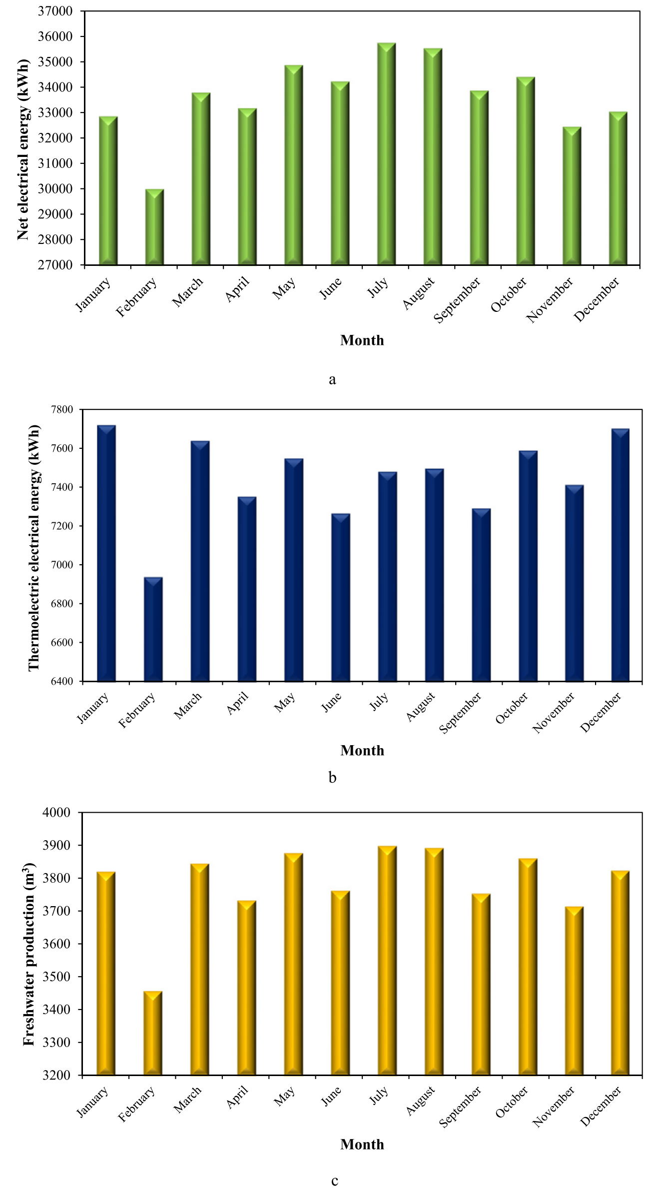

Fig. 17. (a) net electrical energy, (b) the thermoelectric electrical energy, and (c) freshwater production changes concerning ambient temperature in Isfahan.

various types of ANN architectures. One multilayer neural network (MLP) has been used in this study, and its general structure is shown in Fig. 18.

Fig. 19 and Fig. 20 show the regression for exergy efficiency and cost as objective functions.

Table 7 presents the related parameters for the input and output layers and the range of changes.

Based on the simulated system (Figs. 19 and 20), the neural network has a high level of accuracy. Fig. 21 shows the ANN model error histogram for different data, where most data are near zero, indicating the high reliability of the network.

3.4.2. NSGA-II Optimizer

Multi-objective optimization of the NSGA_II is applied to the suggested combined energy system. Fig. 22 shows the Pareto frontier. On the Pareto frontier, all solution points are optimal. Selection of the final optimal solution (which provides the best trade-off between objectives) among the optimal points requires a decision-making process; herein, a simple geometric method has been employed.

Fig. 18 verified that a considerable cost decrease could be achieved if the exergy efficiency is slightly compromised. A list of specifications for points 1, 2, and 3 is given in Table 8.

The population distribution is given in Fig. 23 to illustrate the optimal point characteristics.

Comparison of results is hindered due to the specific system configuration herein employed. However, there are similar studies, such as Rafiei et al. [48], who coupled a solar desalination system with an organic Rankine cycle for power and freshwater production. Smooth and corrugated receivers were employed, and the

Table 5
System outputs pertinent to DNI in Isfahan in one year.

Net electrical energy	Thermoelectric electrical energy	Freshwater production
928,017 kWh	34,238 kWh	24,487 m^3

Table 6
System outputs pertinent to ambient temperature in Isfahan in one year.

Net electrical energy	Thermoelectric electrical energy	Freshwater production
404371 kWh	89474 kWh	45463 m^3

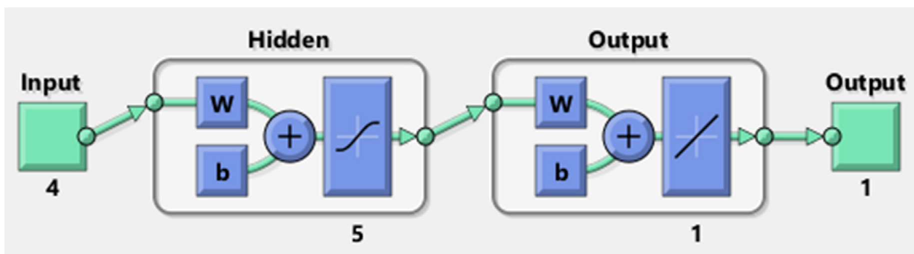

Fig. 18. The architecture of neural networks.

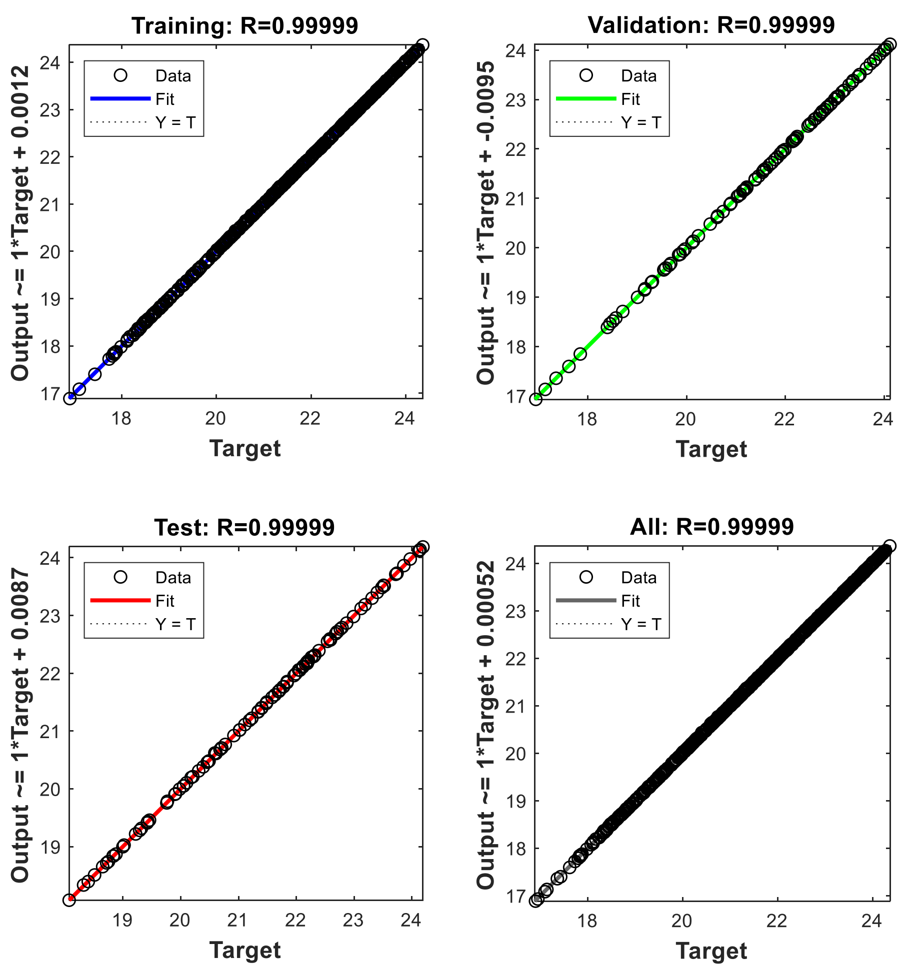

Fig. 19. Validation of the ANN algorithm for objective function (exergy efficiency). 1

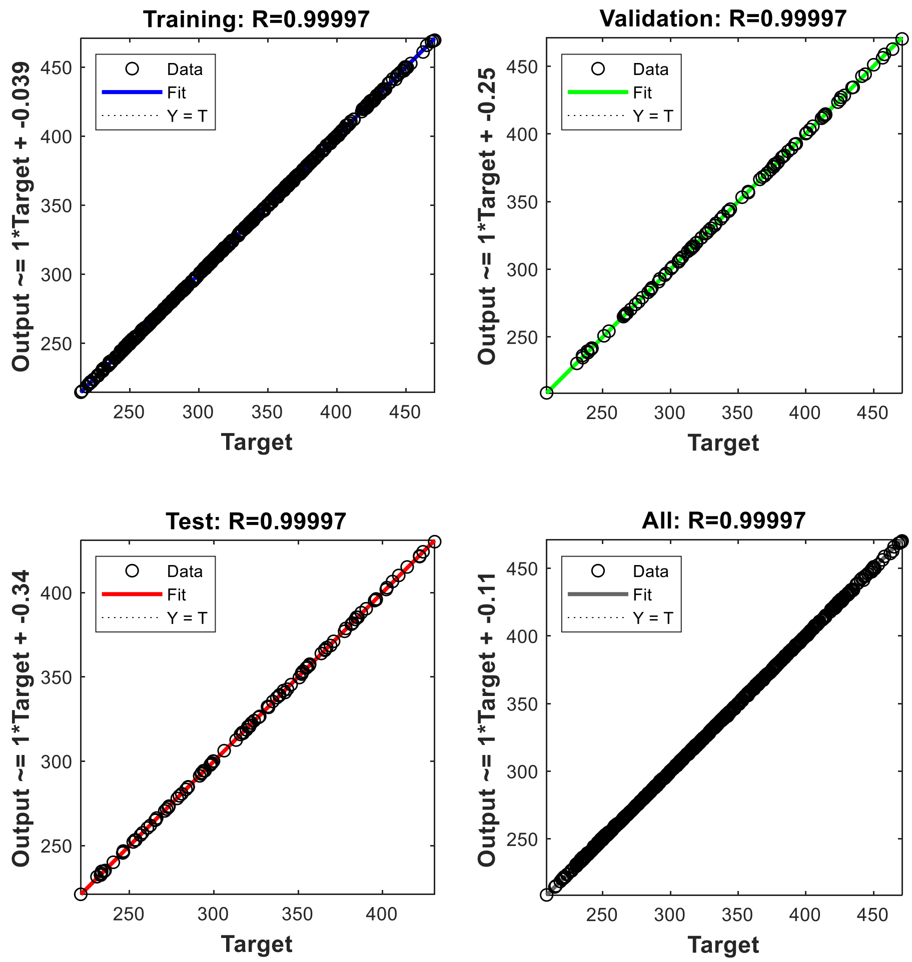

Fig. 20. Validation of the ANN algorithm for objective function (cost).

Table 7
Input and output layer data range.

Parameter	Lower band	Upper band	Reason
Pressure ratio (–)	5	15	Standard pressure ratio range for concentrated solar power.
Number of mirrors (–)	350	650	The usual range for the number of mirrors
Inlet steam turbine pressure (kPa)	2000	4000	Steam turbine material temperature limit
Evaporator pinch point (C)	3	10	Normal range for evaporator pinch point
Exergy efficiency (%)	–	–	Needs to be maximized
Cost ($/h)	–	–	Needs to be minimized

freshwater production increased with solar irradiance, reaching 12.71 kg/h and 13.09 kg/h, respectively. Ding et al. [49] presented a power and freshwater generation system, with a gas turbine cycle as the primary system and a Kalina cycle and humidification-dehumidification desalination unit as the waste heat recovery subsystems. The exergy efficiency of the system was 43.11%, with

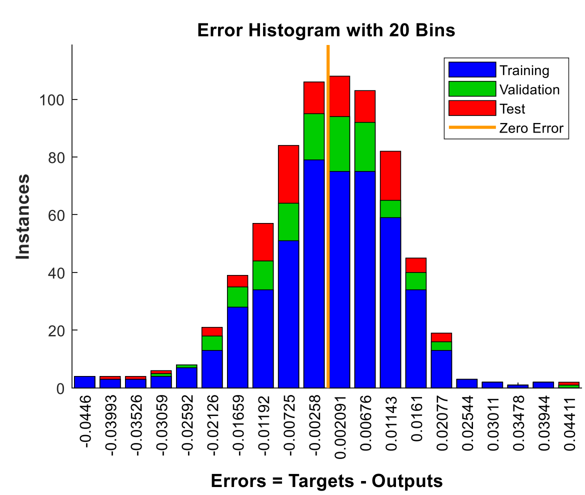

Fig. 21. ANN model error histogram.

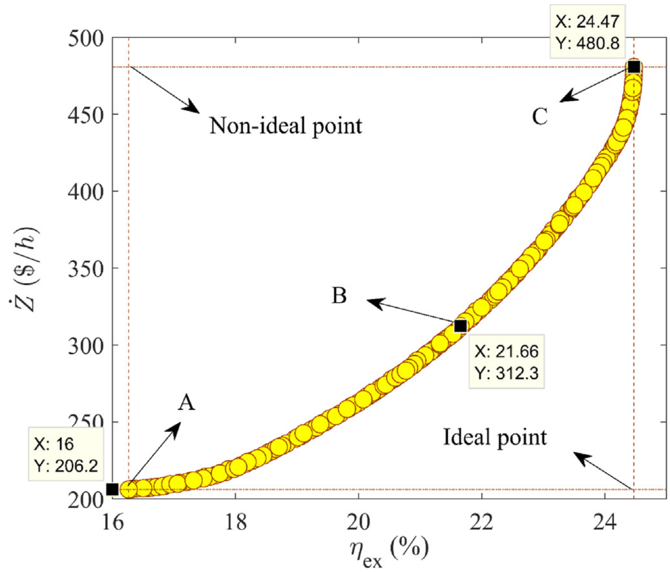

Fig. 22. Pareto front of the proposed system's optimal points.

Table 8
Optimization procedure.

	A	B	C
Objective function			
Exergy efficiency (%)	16	21.66	24.47
Cost ($/h)	206.2	312.3	480.8
Optimization parameters			
Pressure ratio (−)	5	8.5	14.6
Number of mirrors (−)	350	490	645
Inlet steam turbine pressure (kPa)	2000	3798	3709
Evaporator pinch point (C)	4.8	3.4	3

freshwater production at 10.39 kg/s. After optimization, exergy efficiency increased to 43.84%. The authors emphasize the necessity of considering highly integrated and multigeneration energy systems and highlight the case-specific complexity in establishing suitable combinations of technologies considering local energy regulations and the availability of resources. Biomass gasification, regenerative gas turbine with intercooling, and a syngas combustor were employed by Hamrang et al. [50] to produce freshwater and electricity. After multi-objective particle swarm optimization, optimal exergy efficiency, freshwater production rate, sum unit cost of products, and net output power were 45.10%, 14.27 kg/s, 12.95 USD/GJ, and 8141 kW, respectively.

Considering that only a very small portion of total desalinated water is currently obtained from renewable-assisted systems [3], there is a clear need for further research. Trends in desalination include the utilization of renewable energy resources, such as solar and biomass.

4. Conclusion

This study focused on a solar-assisted combined energy system located in Isfahan (central Iran), consisting of a concentrated solar power plant, steam Rankine cycle, Brayton cycle, organic Rankine cycle, reverse osmosis subsystem and thermoelectric generator. The energy system produced freshwater and clean electricity. The most influential parameters on system performance were direct normal irradiance, number of heliostats, turbine efficiency, turbine inlet pressure, compressor pressure ratio, and SRC pump inlet temperature. The proposed system was then optimized with a multi-objective genetic algorithm, considering exergy efficiency and the system cost rate. Multi-objective optimization yielded optimal exergy efficiency and cost rate of 21.66% and 312.3 $/h, respectively. A Pareto frontier was then charted, producing a set of optimal points. Ultimately, it can be asserted that the system introduced in this study, according to the results, is suitable for the required applications.

In the case considered, there was a strong relationship between system performance and ambient temperature. Recognizing that climate trends could affect the production of energy systems, consideration of the effects of climate change could provide a better prediction of energy outputs in future studies.

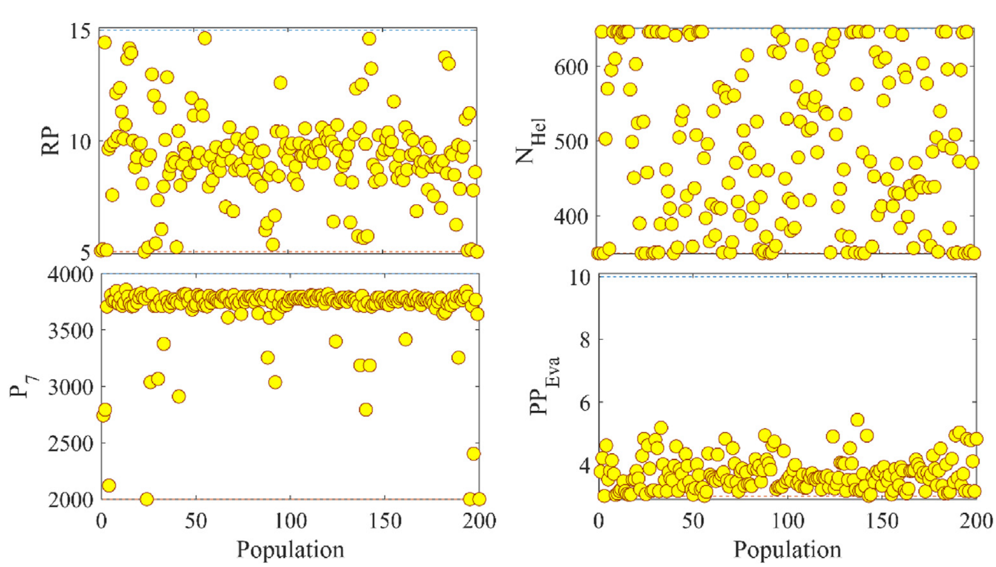

Fig. 23. Scatter distribution of decision variables.

References

[1] Carvalho M, Millar DL. Concept development of optimal mine site energy supply. Energies 2012;5:4726–45. https://doi.org/10.3390/en5114726.

[2] Sarafraz MM, Tlili I, Tian Z, Bakouri M, Safaei MR, Goodarzi M. Thermal evaluation of graphene nanoplatelets nanofluid in a fast-responding HP with the potential use in solar systems in smart cities. Appl Sci 2019;9:2101. https://doi.org/10.3390/APP9102101. 2019; 9:2101.

[3] Lourenço AB, Carvalho M. Exergoeconomic and exergoenvironmental analyses of an off-grid reverse osmosis system with internal combustion engine and waste heat recovery. Chem Eng J Adv 2020;4:100056. https://doi.org/10.1016/J.CEJA.2020.100056.

[4] Olia H, Torabi M, Bahiraei M, Ahmadi MH, Goodarzi M, Safaei MR. Application of nanofluids in thermal performance enhancement of parabolic trough solar collector: state-of-the-art. Appl Sci 2019;9:463. https://doi.org/10.3390/APP9030463. 2019; 9:463.

[5] Gunawan A, Simmons RA, Haynes MW, Moreno D, Menon AK, Hatzell MC, et al. Techno-economics of cogeneration approaches for combined power and desalination from concentrated solar power. J Sol Energy Eng 2019;141. https://doi.org/10.1115/1.4042061.

[6] Yilmaz F. Thermodynamic performance evaluation of a novel solar energy based multigeneration system. Appl Therm Eng 2018;143:429–37. https://doi.org/10.1016/j.applthermaleng.2018.07.125.

[7] Ghorbani B, Shirmohammadi R, Mehrpooya M. Development of an innovative cogeneration system for fresh water and power production by renewable energy using thermal energy storage system. Sustain Energy Technol Assessments 2020;37:100572. https://doi.org/10.1016/j.seta.2019.100572.

[8] Alirahmi SM, Assareh E. Energy, exergy, and exergoeconomics (3E) analysis and multi-objective optimization of a multigeneration energy system for day and night time power generation - case study: Dezful city. Int J Hydrogen Energy 2020;45:31555–73. https://doi.org/10.1016/j.ijhydene.2020.08.160.

[9] Salehi A, Mousavi SM, Fasihfar A, Ravanbakhsh M. Energy, exergy, and environmental (3E) assessments of an integrated molten carbonate fuel cell (MCFC), Stirling engine and organic Rankine cycle (ORC) cogeneration system fed by a biomass-fueled gasifier. Int J Hydrogen Energy 2019;44:31488–505. https://doi.org/10.1016/j.ijhydene.2019.10.038.

[10] Assareh E, Assareh M, Alirahmi SM, Jalilinasrabady S, Dejdar A, Izadi M. An extensive thermo-economic evaluation and optimization of an integrated system empowered by solar-wind-ocean energy converter for electricity generation - case study: Bandar Abas, Iran. Therm Sci Eng Prog 2021;25:100965. https://doi.org/10.1016/j.tsep.2021.100965.

[11] Ghorbani B, Mahyari KB, Mehrpooya M, Hamedi MH. Introducing a hybrid renewable energy system for production of power and fresh water using parabolic trough solar collectors and LNG cold energy recovery. Renew Energy 2020;148:1227–43. https://doi.org/10.1016/j.renene.2019.10.063.

[12] Anvari S, Khalilarya S, Zare V. Power generation enhancement in a biomass-based combined cycle using solar energy: thermodynamic and environmental analysis. Appl Therm Eng 2019;153:128–41. https://doi.org/10.1016/j.applthermaleng.2019.02.112.

[13] Ozturk M, Dincer I, Javani N. Thermodynamic modeling of a solar energy based combined cycle with rock bed heat storage system. Sol Energy 2020;200:51–60. https://doi.org/10.1016/j.solener.2019.03.053.

[14] Pourrahmani H, Moghimi M. Exergoeconomic analysis and multi-objective optimization of a novel continuous solar-driven hydrogen production system assisted by phase change material thermal storage system. Energy 2019;189:116170. https://doi.org/10.1016/j.energy.2019.116170.

[15] Behzadi A, Habibollahzade A, Ahmadi P, Gholamian E, Houshfar E, Ghorbani B, et al. Multi-objective design optimization of a solar based system for electricity, cooling, and hydrogen production. Handb Sustain Eng 2020;169:1065–107. https://doi.org/10.1007/978-1-4020-8939-8_117.

[16] Mohammadi K, Khaledi MSE, Saghafifar M, Powell K. Hybrid systems based on gas turbine combined cycle for trigeneration of power, cooling, and freshwater: a comparative techno-economic assessment. Sustain Energy Technol Assessments 2020;37:100632. https://doi.org/10.1016/J.SETA.2020.100632.

[17] Assareh E, Alirahmi SM, Ahmadi P. A Sustainable model for the integration of solar and geothermal energy boosted with thermoelectric generators (TEGs) for electricity, cooling and desalination purpose. Geothermics 2021;92:102042. https://doi.org/10.1016/j.geothermics.2021.102042.

[18] Lourenço AB, Carvalho M. Exergy, exergoeconomic and exergy-based emission cost analyses of a coconut husk-fired power and desalination plant. Int J Exergy 2020;32:267–91. https://doi.org/10.1504/IJEX.2020.108594.

[19] Lund H, Østergaard PA, Connolly D, Mathiesen BV. Smart energy and smart energy systems. Energy 2017;137:556–65. https://doi.org/10.1016/j.energy.2017.05.123.

[20] Lund H, Thellufsen JZ, Østergaard PA, Sorknæs P, Skov IR, Mathiesen BV. EnergyPLAN–Advanced analysis of smart energy systems. Smart Energy 2021;1:100007.

[21] Mathiesen BV, Lund H. Global smart energy systems redesign to meet the Paris agreement. Smart Energy; 2021, 100024.

[22] O'Dwyer E, Pan I, Acha S, Shah N. Smart energy systems for sustainable smart cities: current developments, trends and future directions. Appl Energy 2019;237:581–97. https://doi.org/10.1016/j.apenergy.2019.01.024.

[23] Sidnell T, Clarke F, Dorneanu B, Mechleri E, Arellano-Garcia H. Optimal design and operation of distributed energy resources systems for residential neighbourhoods. Smart Energy 2021;4:100049.

[24] Bačeković I, Østergaard PA. Local smart energy systems and cross-system integration. Energy 2018;151:812–25. https://doi.org/10.1016/j.energy.2018.03.098.

[25] Roustaei M, Niknam T, Salari S, Chabok H, Sheikh M, Kavousi-Fard A, et al. A scenario-based approach for the design of smart energy and water Hub. Energy 2020;195:116931. https://doi.org/10.1016/j.energy.2020.116931.

[26] Affi S, Cherif H, Belhadj J. Smart system management and techno-environmental optimal sizing of a desalination plant powered by renewables with energy storage. Int J Energy Res 2021;45:7501–20. https://doi.org/10.1002/er.6331.

[27] Dominković DF, Dobravec V, Jiang Y, Nielsen PS, Krajačić G. Modelling smart energy systems in tropical regions. Energy 2018;155:592–609. https://doi.org/10.1016/j.energy.2018.05.007.

[28] Bashiri Mousavi S, Adib M, Soltani M, Razmi AR, Nathwani J. Transient thermodynamic modeling and economic analysis of an adiabatic compressed air energy storage (A-CAES) based on cascade packed bed thermal energy storage with encapsulated phase change materials. Energy Convers Manag 2021;243:114379. https://doi.org/10.1016/J.ENCONMAN.2021.114379.

[29] Goshayeshi HR, Safaei MR. Effect of absorber plate surface shape and glass cover inclination angle on the performance of a passive solar still. Int J Numer Methods Heat Fluid Flow 2020;30:3183–98. https://doi.org/10.1108/HFF-01-2019-0018/FULL/XML.

[30] Jathar LD, Ganesan S, Shahapurkar K, Soudagar MEM, Mujtaba MA, Anqi AE, et al. Effect of various factors and diverse approaches to enhance the performance of solar stills: a comprehensive review. J Therm Anal Calorim 2021 2021:1–32. https://doi.org/10.1007/S10973-021-10826-Y.

[31] Khodabandeh E, Safaei MR, Akbari S, Akbari OA, Alrashed AAAA. Application of nanofluid to improve the thermal performance of horizontal spiral coil utilized in solar ponds: geometric study. Renew Energy 2018;122:1–16. https://doi.org/10.1016/J.RENENE.2018.01.023.

[32] Khosravi R, Rabiei S, Khaki M, Safaei MR, Goodarzi M. Entropy generation of graphene–platinum hybrid nanofluid flow through a wavy cylindrical microchannel solar receiver by using neural networks. J Therm Anal Calorim 2021;145:1949–67. https://doi.org/10.1007/S10973-021-10828-W. 1454 2021.

[33] Cao Y, Mohamed AM, Dahari M, Delpisheh M, Haghghi MA. Performance enhancement and multi-objective optimization of a solar-driven setup with storage process using an innovative modification. J Energy Storage 2020;32. https://doi.org/10.1016/j.est.2020.101956.

[34] Alirahmi SM, Razmi AR, Arabkoohsar A. Comprehensive assessment and multi-objective optimization of a green concept based on a combination of hydrogen and compressed air energy storage (CAES) systems. Renew Sustain Energy Rev 2021;142:110850. https://doi.org/10.1016/J.RSER.2021.110850.

[35] Mehrpooya M, Bahramian P, Pourfayaz F, Katooli H, Delpisheh M. A novel hybrid liquefied natural gas process with absorption refrigeration integrated with molten carbonate fuel cell. Int J Low Carbon Technol 2021. https://doi.org/10.1093/ijlct/ctab021.

[36] Alirahmi SM, Bashiri Mousavi S, Razmi AR, Ahmadi P. A comprehensive techno-economic analysis and multi-criteria optimization of a compressed air energy storage (CAES) hybridized with solar and desalination units. Energy Convers Manag 2021;236:114053. https://doi.org/10.1016/J.ENCONMAN.2021.114053.

[37] Cao Y, Dhahad HA, Sun Y-L, Abdollahi Haghghi M, Delpisheh M, Athari H, et al. The role of input gas species to the cathode in the oxygen-ion conducting and proton conducting solid oxide fuel cells and their applications: comparative 4E analysis. Int J Hydrogen Energy 2021. https://doi.org/10.1016/j.ijhydene.2021.03.111.

[38] Alirahmi SM, Mousavi SF, Ahmadi P, Arabkoohsar A. Soft computing analysis of a compressed air energy storage and SOFC system via different artificial neural network architecture and tri-objective grey wolf optimization. Energy 2021;236:121412. https://doi.org/10.1016/j.energy.2021.121412.

[39] Delpisheh M, Abdollahi Haghghi M, Mehrpooya M, Chitsaz A, Athari H. Design and financial parametric assessment and optimization of a novel solar-driven freshwater and hydrogen cogeneration system with thermal energy storage. Sustain Energy Technol Assessments 2021;45:101096. https://doi.org/10.1016/j.seta.2021.101096.

[40] Nafey AS, Sharaf MA. Combined solar organic Rankine cycle with reverse osmosis desalination process: energy, exergy, and cost evaluations. Renew Energy 2010;35:2571−80. https://doi.org/10.1016/j.renene.2010.03.034.

[41] Habibollahzade A, Gholamian E, Ahmadi P, Behzadi A. Multi-criteria optimization of an integrated energy system with thermoelectric generator, parabolic trough solar collector and electrolysis for hydrogen production. Int J Hydrogen Energy 2018;43:14140−57. https://doi.org/10.1016/j.ijhydene.2018.05.143.

[42] Zoghi M, Houshang Ehsani A, Sadat M, javad Amiri M, Karimi S. Optimization solar site selection by fuzzy logic model and weighted linear combination method in arid and semi-arid region: a case study Isfahan-Iran. Renew Sustain Energy Rev 2017;68:986−96. https://doi.org/10.1016/j.rser.2015.07.014.

[43] Meteonorm software worldwide irradiation data, global meteorological database for engineers, planners and education. Meteotest AG, fabrikstrasse 14 3012 Bern, Switz. https://meteonorm.com/en/. [Accessed 13 May 2021].

[44] Abdulrahim AH, Chung JN. Performance improvement of cogeneration plants in hot arid regions via sustainable turbine inlet air cooling technologies: an energy-water nexus comparative case study. Int J Energy Res 2021;45:10765−93. https://doi.org/10.1002/ER.6561.

[45] Parikhani T, Delpisheh M, Haghghi MA, Holagh SG, Athari H. Performance enhancement and multi-objective optimization of a double-flash binary geothermal power plant. Energy Nexus 2021:100012. https://doi.org/10.1016/J.NEXUS.2021.100012.

[46] Musharavati F, Khoshnevisan A, Alirahmi SM, Ahmadi P, Khanmohammadi S. Multi-objective optimization of a biomass gasification to generate electricity and desalinated water using Grey Wolf Optimizer and artificial neural network. Chemosphere 2022;287:131980. https://doi.org/10.1016/j.chemosphere.2021.131980.

[47] Alirahmi SM, Assareh E, Pourghassab NN, Delpisheh M, Barelli L, Baldinelli A. Green hydrogen & electricity production via geothermal-driven multi-generation system: thermodynamic modeling and optimization. Fuel 2022;308:122049. https://doi.org/10.1016/J.FUEL.2021.122049.

[48] Rafiei A, Loni R, Najafi G, Mahadzir SB, Bellos E, Sharifpur M, et al. Assessment of a solar-driven cogeneration system for electricity and desalination. J Therm Anal Calorim 2021 1453 2021;145:1711−31. https://doi.org/10.1007/S10973-020-10525-0.

[49] Ding P, Liu X, Qi H, Shen H, Liu X, Farkoush SG. Multi-objective optimization of a new cogeneration system driven by gas turbine cycle for power and freshwater production. J Clean Prod 2021;288:125639. https://doi.org/10.1016/j.jclepro.2020.125639.

[50] Hamrang F, Mahmoudi SMS, Rosen MA. A novel electricity and freshwater production system: performance analysis from reliability and exergoeconomic viewpoints with multi-objective optimization. Sustainability 2021;13. https://doi.org/10.3390/su13116448.

Conversion of Sewage Sludge to combined heat and power: Modeling and optimization

Tapas Ranjan Baitharu, *Department of Computer Sciencel Engineering, Aryan Institute of Engineering & Technology, Bhubaneswar, tkbaitharu11@gmail.com*

Romeo Jena, *Department of Electrical and Electronics Engineering, Capital Engineering College, Bhubaneswar, romeo_jena2@hotmail.com*

Sudesh Kumar Patel, *Department of Computer Scinece Engineering , Raajdhani Engineering College, Bhubaneswar, sk.patel331@yahoo.co.in*

Swaha Pattnaik, *Department of Electronics and Communication Engineering , NM Institute of Engineering & Technology, Bhubaneswar, swaha.pattanayak@gmail.com*

A R T I C L E I N F O

Keywords:
Aspen plus
Sewage sludge
Gasification
Syngas
Combined heat and power (CHP)

A B S T R A C T

Combined Heat and Power (CHP) generation from Sewage Sludge (SS) offers two simultaneous advantages: greenhouse gas emission reduction and increase of renewable energy generation as promoted by the European Union Green Deal 2021. In this work, a numerical model has been developed via Aspen Plus for the evaluation of CHP generation potentiality from SS through gasification integrated with an internal combustion engine system. The model is applied to the case of Italy and eight other European countries for the first time. The gasification model has been developed based on the experimental data on syngas generation from SS in a bench-scale rotary kiln reactor under laboratory conditions available in the literature. Sensitivity analysis revealed optimal operating temperature and equivalence ratios for gasification were 900 °C and 0.2 respectively. The CHP generation potentiality of SS resulted to be 2.73 kWh per kg SS as dry solid.

According to the statistical analysis used in the present study, SS generation will reach 680 kt per year as dry solid by 2030 based on the current sludge generation rate as well as improvement in the wastewater collection and treatment expected for the future in Italy. Within this time, the projected electrical and thermal energy generation rate per year can reach 714 GWh and 1142 GWh respectively. Electrical and thermal energy generation rates from sewage sludge have been estimated for eight EU countries in 2015 and compared with the Italian scenario, founding the highest one in Spain and the lowest in Luxembourg.

1. Introduction

World primary energy consumption has continuously risen from 5,519 Mtoe/year in 1971 to 14,282 Mtoe/year in 2018 due to the increase in population and industrial productivity. Fossil fuel (Oil, Coal, and Natural gas) is the major contributor to the global energy demand and accounted for 81% in 2018 [1]. Fossil fuel reserves are continuously declining due to the excessive dependency to meet up the energy demand [2,3]. Consequently, the world will face a severe energy crisis within the next few decades [4,5]. In addition to this, the level of GreenHouse Gas (GHG) is continuously increasing due to the emission of CO_2, CO, NOx, SOx, etc. from fossil fuel burning and the disposal of waste materials to open fields, landfilling, and incineration. According to the European Union (EU) Green Deal 2021, policies should be updated to reduce the GHG emission at least 55% by 2030 compared to the 1990 level and the contribution of renewable energy to the primary energy demand should increase to at least 40% within the same time [6]. Now EU policies are strengthened to the conversion of waste to energy to achieve these goals within the projected duration. Conversion of Sewage Sludge (SS) generated in WasteWater Treatment Plants (WWTPs) to energy can help to reduce GHG emissions compared to the current management practice of agricultural reuse, landfilling, and incineration and increase the renewable energy share to the primary energy demand.

Wastewater generated from daily activities needs to pass through primary treatment (for the removal of pollutants by screening that is either floating or settling out by gravity), secondary treatment (to remove dissolved and suspended biological matter), and tertiary treatment (for the removal of remaining inorganic substances e.g. nitrogen, phosphorous, sulfur) to reduce the pollutant load to ensure environmental security. SS generation has dramatically increased over the last few years due to the stringent directives on wastewater treatment all over the world.

Nomenclature

Abbreviations Symbols

CGE	Cold gas efficiency
CHP	Combined heat and power
DS	Dry solid
ER	Equivalence ratio
EU	European Union
FBR	Fluidized bed reactor
GHG	Greenhouse gas
HHV	Higher heating value
ICE	Internal combustion engine
IPCC	Intergovernmental panel on climate change
LHV	Lower heating value
S/B	Steam to biomass
SS	Sewage sludge
/WWTPs	Wastewater treatment plants

Symbols

LHV_{SS}	Lower Heating Value of sewage sludge
LHV_{Syng}	Lower Heating Value of syngas
M'_{SS}	Mass flow rate of sewage sludge
M'_{Syng}	Mass flow rate of syngas
n	Number of components considered in syngas
N_{TURB}	Electrical power
Q_{EX}	Thermal power
Q_{EXCH}	Heat energy
Q'_{INPUT}	Energy supply rate
ΔT_{Appr}	Limit of gasifier temperature
T_{Eqlm}	Equilibrium temperature
T_{Gasf}	Gasification temperature

Greek symbols

η_{CHP}	Cogeneration efficiency
η_{el}	Electrical efficiency
η_{th}	Thermal efficiency

Subscripts

Appr	Approach
Eqlm	Equilibrium
Gasf	Gasification
Syng	Syngas

According to Eurostat 2021 [7], the SS generation rate has varied from 5.82 to 8.0 Mt of Dry Solid (DS) per year in 27 EU countries (EU-27) from 2007 to 2016 and it is estimated to reach around 10 Mt of DS/year by 2030.

SS contains different kinds of solid suspension in impure water [8]. Solid particles are a mixture of organic carbonaceous matter of nontoxic nature (proteins, carbohydrates, oil, and fats), phosphorous, nitrogen, and sulfur-containing compounds, inorganic matter, a lighter fraction of heavy metals, and a wide variety of microorganisms. Based on the composition, the Lower Heating Value (LHV) of SS is in the range of 11–20 MJ/kg of DS [9–17]. SS can be used as fertilizer in agricultural land either directly or converted to compost due to the presence of organic compounds and nutrients (N, P, and S) [18]. Globally, SS is disposed of through agricultural reuse, landfilling, incineration, or it is sent to external plants for further treatment (mainly for physical treatments in combination with chemical processes) to eliminate impurities before final disposal [19].

CO, CO_2, CH_4, and N_2O are continuously formed and emitted to the environment where SS is disposed, in case of both agricultural reuse and landfilling, due to microbial activity on the carbonaceous matter and nutrients present in SS [20]. According to the fifth assessment report of the Intergovernmental Panel on Climate Change (IPCC) [21], CH_4 and N_2O have 28 and 265 times respectively more potential as a GHG as compared to CO_2. Moreover, the odor is continuously released from the disposed site and stakeholders have strong objections against agricultural reuse and landfilling of SS. Also, SS incineration releases pollutants (mainly NOx, SO_2, HCl) that are responsible for global pollution [22].

Energy recovery from SS either biologically or thermally can reduce the problem associated with current management practices. Biological treatment of SS (either anaerobic or aerobic digestion) to recover energy reduces the environmental impact, but it needs longer processing times up to 105 days due to the digestion process being highly sensitive to the activities of microorganisms and has lower efficiency (both electrical and thermal efficiency in the range of 30 to 40%) [23–25]. An effective and promising technique for energy recovery from SS is a thermal treatment, which can quickly handle a large quantity with high volume reduction, eliminate pathogens, heavy metals as well as other organic and inorganic pollutants with a higher conversion efficiency [26,27]. One of the most advantageous thermal treatments is gasification for energy recovery is particularly promising with higher conversion efficiency as well as less migration of heavy metals to the gaseous phase compared to pyrolysis, incineration, combustion, and hydrothermal carbonization [28,29–31].

The gaseous product formed during the gasification of SS or biomass is known as syngas, a mixture of CO, CO_2, H_2, CH_4, and other lighter hydrocarbons, and moisture with tar which can be used as a fuel in powerplant, district heat, or industry [28]. Based on the desired syngas specification, different gasifying agents are frequently used in the gasification of biomass, such as air, steam, O_2 [28,32–34], CO_2 [35,36], or a mixture of air, O_2, and steam [37,38]. Air is commonly used as a gasifying agent because of its easier availability and low cost.

Temperature and Equivalence Ratio (ER) is the main operating parameter for gasification of SS when using air as a gasifying agent. ER is defined as the ratio between the quantity of air fed to the reactor to the stoichiometric amount of air required for complete combustion [13]. Several experimental tests are required to optimize the operating parameters to generate syngas from SS in a sustainable way. Gasification modeling based on experimental data may be useful to identify the optimum operating parameters, saving time and reducing the economic costs compared to experimental campaigns. While SS gasification modeling through Aspen Plus to identify the best operating conditions and to estimate the process performances has been extensively studied [16,17,39], works on the use of the produced syngas for energy production are limited [40–42].

Abdelrahim et al. [16] completed an experimental campaign in an atmospheric Fluidized Bed Reactor (FBR) to generate syngas from SS at two different sets of operating conditions. Authors calibrated their developed model based on one set of experimental data and validated it for another and found a good agreement. Optimum operating parameters of temperature (780 °C) and ER (0.30) for the gasification are identified through the developed model. de Andres et al. [17] calibrated and validated a model on Aspen Plus to simulate the syngas generation from SS in an atmospheric FBR based on two different sets of experimental data available in the literature and a satisfactory agreement of the model with experimental data is observed. The researchers have predicted optimum operating parameters for gasification of temperature equal to 850 °C and an ER of 0.3 for the syngas generation in a sustainable way. Migliaccio et al. [39] conducted an experimental analysis to produce syngas from two different SS generated in the same WWTP at two different times of the year at a temperature of 850 °C for both SS and ER of 0.2 for the first one and 0.1 for the second sample in an FBR. The authors have simulated the gasifi-cation model through calibration based on the experimental out-comes and used it to predict optimum operating conditions (temperature of 850 °C and ER of 0.25 for the gasification of both SS).

Abdelrahim et al. [16], de Andres et al. [17], and Migliaccio et al. [39] identified optimum operating conditions for the gasification of SS based on the composition of the syngas, without considering the net power available from the treatment process. In the current work, the authors consider not only the conversion of SS to syngas but also its further application for Combined Heat and Power (CHP) generation. During model calibration researchers [16,17,39] are predicted temperatures to restrict the equilibrium of individual gasification reactions but the fraction of carbon moved to the gasifier and elute out as char is not presented.

Research on smart energy systems design is now a promising area to achieve 100% renewable energy systems by integrating the electricity, heating, and transportation sector [43–45]. Kofler and Clausen [43] proposed three different polygeneration plants to produce electricity, biofuels, and heat through air-gasification of wheat straw in a low temperature circulating FBR integrated with a gas engine as a smart energy system. The authors designed the first plant for the generation of electricity and heat with a CCE of 23%, the second plant to produce synthetic natural gas and heat with a CCE of 91% and the last plant to produce dimethyl ether, heat and electricity with a CCE equal to 50%. Furubayashi [44] designed a plant to convert wind energy to electricity, heat, and transportation fuel for Akita prefecture in Japan as a smart energy system. The author estimated the potentiality of wind energy to generate electricity equal to 35.2 TWh/year of which 32.10% is sufficient to fulfill the electric energy demand, whereas the remaining can be stored in batteries to generate heat and transportation fuel. Cirillo et al. [46] analyzed experimentally and numerically a smart energy system to produce CHP from wood chips based on gasification integrated with a spark-ignition Internal Combustion Engine (ICE). The researchers found a satisfactory agreement between the developed model and the experimental results and evaluated electrical and thermal efficiencies of 19.9% and 17.8% respectively.

To the best of the author's knowledge, there is no study related to model development on CHP generation from SS as a smart energy system but there are limited studies relevant to CHP generation modeling from waste biomass [40–42]. Francois et al. [40] developed a model on Aspen Plus to evaluate the CHP generation potentiality from wood through gasification integrated with the ICE system based on the experimental data available in the literature. Authors are assessed electrical (27%), thermal (39%), and cogeneration (66%) efficiencies. Villarini et al. [41] developed a model on biomass gasification incorporated with an ICE system to assess the potentiality of CHP generation from Hazelnut and Olive pruning and predicted electrical and cogeneration efficiencies of 30% and 60% respectively for the first one and 26% and 41% for another. Ruya et al. [42] developed a conceptual model on Aspen Plus to identify the specification of SS for the generation of syngas by supercritical water gasification and ultimately power based on exergy analysis. Researchers recommended that SS must be characterized by a minimum LHV of 12.63 MJ/kg with the DS content of at least 25% and highlighted the need for supplementary fuel (crude glycerol, waste cooking oil, or heavy oil) to ensure auto-thermal operation.

The first aim of the current study is to evaluate the energy recovery potentiality as CHP from Italian SS through gasification integrated with an ICE system as a smart energy system for the first time. The produced thermal energy is used to reduce the moisture content of mechanically dewatered SS to less than 10% as required for gasification treatment, whereas the produced electrical energy is employed to run the WWTPs. The gasification process was simulated through a restricted chemical equilibrium approach on Aspen Plus although there is limited study on model development for syngas generation from SS by applying restricted chemical equilibrium [16,17,39,46]. The gasification model was calibrated and validated based on two distinct sets of experimental data available in the literature on syngas generation from SS collected from a WWTP in Italy in a bench-scale rotary kiln reactor [47]. Optimum operating parameters (temperature and ER) were identified through a sensitivity analysis. A model to simulate the use of the generated syngas in an ICE system to produce CHP was also developed. The energy production rate was estimated from all the generated SS in Italy if the wastewater treatment system would be improved to fulfill the EU green deal 2021, on collection and treatment. Finally, CHP generation rates from the overall produced SS in 2015 were estimated also in eight different EU countries (Luxembourg, Slovakia, Bulgaria, Ireland, Greece, Romania, Poland, and Spain) by applying data obtained in the developed model and compared with the Italian scenario.

2. Modeling of energy recovery from sewage sludge

2.1. *Energy recovery from sewage sludge*

In this work, three consecutive processes are proposed for energy recovery from SS, as shown in Fig. 1.

SS is fed to a gasifier with air as a gasifying agent to complete the gasification at a specified temperature and ER. Gasification temperature is reached by pre-heating the incoming air. Syngas exiting from the gasifier presents a high temperature and it contains H_2, CO, CO_2, CH_4 along with other lighter hydrocarbons, N_2, steam, char, and ash. To use it in an ICE, syngas temperature must be reduced, and impurities have to be removed [41]. This is achieved through the cleaning and cooling process. Clean syngas is then combusted in an ICE to generate electrical energy and thermal energy from the exhaust of the engine. A detailed description of energy generation from SS is available in the literature [41,47]. A comprehensive description of the flowsheet developed in Aspen Plus is presented in the following section.

2.2. *Aspen Plus model*

The developed Aspen Plus flowsheet for the proposed plant to generate CHP from SS is shown in Fig. 2.

The feed stream SS enters to DECOMP block (RYield reactor) to convert the non-conventional component (SS) into conventional components of C, H_2, N_2, O_2 and H_2O and a non-conventional component of ash, according to the yield distribution that is specified by implementing the ultimate analysis of the substrate through a calculator from design specification tools. The temperature of the DECOMP block is 400 °C which is appropriate for the pyrolysis of biomass [48].

Off products from DECOMP move to the S-SEP block where they are divided into two sub-streams: GASFEED, which contains fractions of carbon participating in the gasification reactions with H_2, N_2, O_2 and H_2O, and C-CHAR that contains ash and unconverted carbon (char).

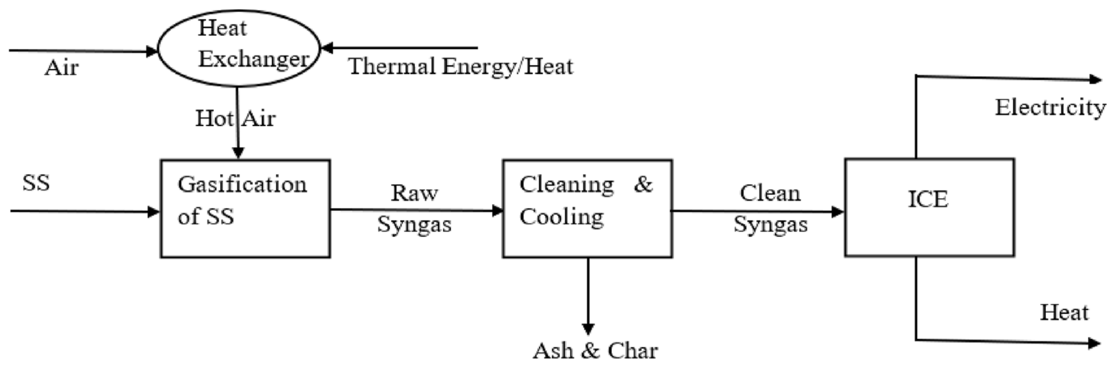

Fig. 1. Combined heat and power generation route from sewage sludge.

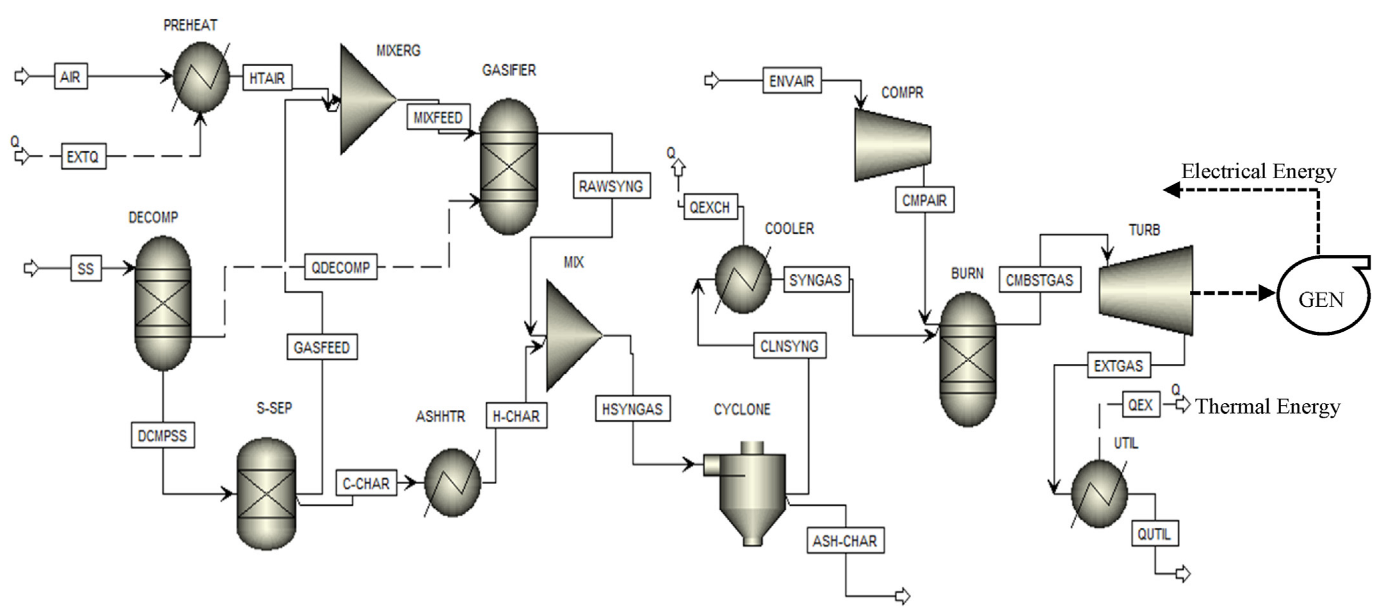

Fig. 2. Flowsheet of the proposed plant to generate CHP from SS.

GASFEED stream is mixed with preheated air in a Mixer of block MIXERG and moved to the gasification process. The RGibbs reactor is chosen to simulate gasification reactions and it is denoted by the GASIFIER block in the flowsheet. Individual reactions involved in gasification are restricted by specifying their temperature. Indeed, this empirical approach allows calibrating the model results with experimental data obtaining a syngas composition closer to the experimental one compared to the chemical equilibrium method [49]. Gasification temperature is maintained by heating the incoming air in a Heater of block PREHEAT.

C-CHAR flow exit from S-SEP block is passed through a heat exchanger of block ASHHTR to equalize the temperature to the generated product stream from GASIFIER of RAWSYNG and combined in the Mixer of block MIX. The flow of HSYNGAS exiting the block MIX is driven to the CYCLONE which simulates the cleaning process where ash and char are separated from syngas and form CLNSYNG stream which is passed through the Heater of block COOLER to cool down the syngas to meet the conditions required for ICE [41]. As suggested in the available literature [40,41,50], the ICE is simulated through three consecutive blocks:

- the compressor of block COMPR to increase the potential energy of incoming air through pressure raising;
- the BURN block, where the fuel combustion is simulated to transform the potential energy of air-syngas mixture to thermal energy;
- the turbine of block TURB to complete the conversion of thermal energy present in CMBSTGAS stream exiting from the combustion chamber to mechanical energy to drive a generator (block GEN) to produce electricity.

The EXITGAS stream passes through the UTIL block of a Heater to extract thermal energy that can be used for thermal drying of mechanically dewatered SS, office heating, or district heating based on the productivity of the thermal energy from the plant.

Unit operation blocks used in Aspen plus with specific functions are presented in Table 1.

2.3. Gasification modeling

The following assumptions are considered for gasification modeling in Aspen Plus to simplify the process:

- The gasification is isothermal and steady-state [37,51,52].
- Volatile products are mainly of H_2, CO, CO_2, CH_4, and H_2O formed by instantaneous pyrolysis of SS [53,54].

.

Table 1
Functional description of unit operation block used in Aspen Plus flowsheet.

Block ID	Name	Function
DECOMP	RYield	It converts the non-conventional feed of SS to conventional and non-conventional components.
S-SEP	Separator	It completes the separation of conventional and non-conventional streams.
PREHEAT	Heater	It completes the preheating of incoming air to reach the gasification temperature.
MIXERG	Mixer	It simulates the mixing of gasification reactants.
GASIFIER	RGibbs	It completes the gasification reaction by minimizing Gibbs free energy and restricts the chemical equilibrium of individual reactions for a specific temperature.
ASHHTR	Heater	It equalizes the temperature of C-CHAR and gasifier products.
MIX	Mixer	Blending the gasifier off products, ash, and char.
CYCLONE	Split	Completed the simulation to perform the separation of the gas-solid mixture to syngas and ash and char.
COOLER	Heater	It cools down the syngas to a specific temperature before entering the ICE.
COMPR	Compressor	Pressurizes the stoichiometric air required to perform complete combustion of syngas in ICE.
BURN	RGibbs	Perform the simulation on combustion of syngas by minimizing the Gibbs free energy.
TURB	Turbine	Completed the conversion of thermal energy into mechanical energy of the exhaust from the combustion chamber.
UTIL	Heater	Complete the recovery of thermal energy from the exhaust stream of the ICE.

- The developed model is kinetic-free and zero-dimensional.
- Produced char is full of carbon [55].
- All gases behave ideally.
- Gasification completed at atmospheric pressure.
- Tar formation is neglected.

Indeed, according to the available literature, tar is the complex mixtures of various hydrocarbons (e.g. phenols, olefins, benzene, naphthalene, acenaphthylene, anthracene, phenanthrene, pyrene, etc.). The formation of tar components is not reaching equilibrium within the shortest residence time creating destabilization of the gasification model used in the present study [40,56]. Development of the SS gasification model by considering tar components will be explored in our future work.

In the present analysis, seven reactions are considered during the simulation of the SS gasification model. The reactions are listed in Table 2.

The Boudouard reaction ($CO_2 + C \rightarrow 2CO$) does not achieve kinetic equilibrium within the shortest residence time and creates destabilization of the overall gasification process [34]. For this reason, the Boudouard reaction is not considered in the current equilibrium modeling.

2.3.1. Restricted chemical equilibrium

As mentioned above, the syngas composition obtained through the chemical equilibrium method may significantly deviate from experimental data due to the complexity of the whole process and the short residence time [57]. The deviation of the gasification model results can be reduced to a tolerable limit of less than 20% by using a restricted chemical equilibrium method [58]. For this reason, each reaction involved in the gasification process is restricted to equilibrium by assigning a specific temperature according to equation (1).

Table 2
List of chemical reactions considered during model simulation.

Reaction No.	Reaction	Name
R1	$C + H_2O \rightarrow H_2 + CO$	Water gas
R2	$C + O_2 \rightarrow CO_2$	Carbon combustion
R3	$C + 2H_2 \rightarrow CH_4$	Methanation
R4	$CO + H_2O \rightarrow H_2 + CO_2$	Water Gas Shift
R5	$C_2H_6 + 3.5O_2 \rightarrow 3H_2O + 2CO_2$	Ethane combustion
R6	$C_3H_8 + 5O_2 \rightarrow 4H_2O + 3CO_2$	Propane combustion
R7	$H_2 + 0.5O_2 \rightarrow H_2O$	Hydrogen combustion

$$T_{Eqlm} = T_{Gasf} + \Delta T_{Appr} \tag{1}$$

where, T_{Eqlm} is the equilibrium temperature, T_{Gasf} is the gasification temperature and ΔT_{Appr} is the limit of gasifier temperature where the reaction is restricted.

For the sake of completeness, the deviation is defined as the difference between the model results and experimental data and is calculated according to equation (2).

$$Deviation\ (\%) = \frac{Simulation\ result - Experimental\ result}{Experimental\ result} \cdot 100 \tag{2}$$

The average deviation is calculated from the deviation of individual syngas components according to equation (3)

$$Average\ Deviation\ (\%) = \frac{1}{n}\sum_{i=1}^{n}|Deviation| \tag{3}$$

where, n is the number of the considered component present in syngas.

2.4. ICE modeling: cogeneration process performances

Syngas from the gasification of SS is converted to electrical and thermal energy through an ICE system. Electrical (η_{el}), thermal (η_{th}) and system (η_{sys}) efficiencies are calculated according to equations (4)–(6) respectively. Electrical, thermal, and system efficiencies are used to evaluate the cogeneration process performance.

$$\eta_{el}(\%) = \frac{N_{TURB}}{LHV_{Syng}.M'_{Syng}} \cdot 100 \tag{4}$$

$$\eta_{th}(\%) = \frac{Q_{EX}}{LHV_{Syng}.M'_{Syng}} \cdot 100 \tag{5}$$

$$\eta_{sys}(\%) = \frac{N_{TURB} + Q_{EXCH} + Q_{EX}}{LHV_{SS}.M'_{SS} + Q'_{INPUT}} \cdot 100 \tag{6}$$

where, N_{TURB} represents the effective electrical power available in the turbine, Q_{EXCH} is the heat subtracted during the cooldown of syngas before entering the ICE, Q_{EX} is the thermal power obtained from the cooling of ICE exhausts to useable temperature, LHV_{Syng} and LHV_{SS} are the LHV of syngas and SS respectively, M'_{Syng} and M'_{SS} are the mass flow rate of syngas and SS respectively and Q'_{INPUT} is the power supply associated with the RGibbs reactor.

2.5. Input parameters

2.5.1. Characteristics of sewage sludge

Characteristics of SS used in the present analysis were available from the literature [47]. The proximate and ultimate analysis with the Higher Heating Value (HHV) of SS used in the present study is shown in Table 3.

2.5.2. Gasification conditions and syngas composition

Syngas composition obtained by gasification of SS for two distinct operating conditions available from the literature [47] is reported in Table 4.

Syngas composition from test condition I is used to calibrate the model. To identify an appropriate ΔT_{Appr} for every reaction mentioned in Table 2, a 2% standard deviation from the experimental results is set. The value of flow/fraction for unconverted carbon identification was set in the range of 0–1.0. The obtained ΔT_{Appr} and char fractions during model calibration are used to validate the model by comparing the results obtained from the developed model with test condition II.

2.5.3. Operating conditions for internal combustion engine

The operating parameters considered for the simulation of the ICE system are collected from literature [50,59,60] and reported in Table 5.

3. Energy generation potentiality from SS

Energy generation potentiality as CHP from all the generated SS in Italy and eight other EU countries are evaluated in this section.

3.1. CHP generation potentiality from SS in Italy

CHP generation potentiality from all the generated SS is assessed for Italy. According to the EU Environment Agency report 2020 [61], in 2015 only 60% of the total population in Italy are connected to sewage systems and WWTPs. A statistical model is developed to predict the SS generation rate by connecting all the population in Italy with the public sewage system.

3.1.1. Prediction of SS generation

In 2015 Mininni et al. [62] surveyed 84 Italian wastewater treatment utilities responsible for the collection and treatment of municipal wastewater for around 35 million peoples and the estimated production of SS was 395 kt of DS per year, which corresponds to a generation rate per capita of 11.29 kg/(person.year). The per capita SS generation rate in Italy is almost half compared to the average EU–27 which is 22.50 kg/(person.year) in 2015 due to the lower number (60%) of the population are connected to the sewage system [63]. In this work, three scenarios (first, second, and third) are assumed based on the improvement of wastewater collection and treatment rate. The first scenario is assumed by considering that the Italian existing wastewater treatment capacity will be enlarged to treat all generated wastewater by 2030 to fulfill the target mentioned in the EU green deal 2021. For the second and third scenarios, it is supposed that this aim will be reached by 2040 and 2050, respectively. The estimation takes into account also the projection for Italian population variation over the years proposed by Eurostat 2021 [64].

Table 4
Overview of operating conditions and syngas composition [47].

Parameters, Unit	Condition I	Condition II
Temperature (°C)	850	850
ER (–)	0.16	0.24
SS feed rate (g/h)	237	244
Air feed rate (g/h)	225	347
Syngas composition, vol% (Dry and N_2 free basis)		
CO	35.30	37.10
CO_2	20.60	24.20
H_2	33.80	32.30
CH_4	10.30	6.45

Table 5
Operating parameters applied for ICE simulation [50,59,60].

Operating conditions	Value
Temperature (incoming syngas to the ICE combustion chamber, °C)	30.0
Temperature (incoming air to the compressor, °C)	20.0
Stoichiometric air ratio (–)	3.0
Pressure of compressor and combustion chamber (bar)	20.0
Isentropic expansion coefficient (%)	90.0
Isentropic compression coefficient (%)	90.0
Pressure (fume exit from turbine, bar)	1.0
Utilization temperature of exhaust fume (°C)	80.0

3.2. Energy generation potential from SS in other EU countries

A fraction of generated SS is subjected to anaerobic digestion in 13 EU countries (e.g. Germany, France, Norway, Switzerland, Denmark, Sweden, Finland, Austria, Hungary, Czech Republic, Netherland, UK, and Turkey) with the purpose of energy recovery [65]. Eight EU countries where SS is disposed in agricultural reuse, landfilling, incineration, and further physical or chemical treatment are selected taking into account different geographical locations (e.g. Luxembourg, Slovakia, Bulgaria, Ireland, Greece, Romania, Poland, and Spain). CHP generation rates are estimated in the selected countries in 2015 by assuming that the electrical and thermal energy generation potential of SS is similar to the one obtained in the present study for Italy. SS generation rates in these EU countries have been collected from Eurostat 2021 [7]. Per capita, electrical, and thermal energy generation rate from SS in 2015 have been also estimated and compared with the Italian scenario.

Table 3
Proximate and Ultimate analysis of SS with heating values [47].

Proximate analysis (wt%)		Ultimate analysis (wt%)		Heating Value (MJ/kg, db)	
Moisture	3.53	C	41.2	HHV	14.1
Volatile matter (d.b.)	64.2	H_2	5.22		
Fixed carbon (d.b.)	2.58	N_2	3.21		
Ash (d.b.)	29.7	O_2	20.7		

*d.b: dry basis of material.

4. Results and discussion

4.1. Model calibration and validation

The temperatures to restrict the chemical equilibrium of gasification reactions presented in Table 2 are obtained during model calibration by using regression analysis tools in Aspen Plus and shown in Table 6 with the fraction of carbon participating in gasification reaction.

Considering the results presented in Table 6, 85.40% of carbon present in SS participate in gasification reactions, whereas the remaining fraction is inert and exit the gasifier as char.

The composition of syngas obtained from the simulation is compared with the experimental results accessible in literature [47]. The comparison, as well as the corresponding deviation during model calibration and validation, are shown in Table 7.

As presented in Table 7, the average deviation is found to be only 2.96% with the deviation of each component of syngas less than 5% for the model calibration. The average deviation rises to 13.7% for the validation case, whereas the deviation for individual components is lower than 20%. Therefore, it is assumed that the developed model has a good agreement with the experimental results [17,58]. Indeed, the average deviation (13.7%) obtained in the current simulation for model validation was substantially lowered compared to that of analogous simulations carried out by other researchers, e.g. Abdelrahim et al. [16] for SS (average deviation was 16%) and Gonzalez et al. [66] for oil sludge gasification (average deviation was 28.37%). In the current work, the highest deviation was found for the species with the lowest concentration (CH_4).

4.2. Sensitivity analysis

A sensitivity analysis is conducted by using the feed flow rate of 244 g/h mentioned for test condition II to investigate the optimum ER and gasification temperature. The energy available from syngas and that is required to preheat the incoming air to reach gasification temperature are considered to identify the optimum condition of operation.

4.2.1. Effect of ER

The gasification temperature of 850°C is considered in simulation model development to detect the ideal ER.

Reaction condition change with the change of ER due to the alteration of oxygen supply to the gasifier that has a clear impact on the syngas composition. The effect of ER on syngas compositions is presented in Fig. 3.

As clearly depicted in Fig. 3, the concentration of CO_2 in syngas increases continuously with ER, while that of H_2 rises slowly. The remaining constituents of syngas e.g. CO, CH_4, C_2H_6, and C_3H_8 decrease continuously with an increase of ER. This occurs due to the increase of O_2 entering the gasifier with ER that drives the combustion reactions of carbon, methane, ethane, and propane to the forward direction, and increases the concentration of CO_2 and H_2O in syngas. Increases in H_2O concentration in gasifier moves both water gas and water gas shift reaction to forward direction and the former one increases both CO and H_2 concentration but later one dropped the CO concentration in syngas. Water-gas shift reaction proceeds with a faster rate compared to water gas reaction because of the availability of reactants. Ultimately CO concentration in syngas decreases with the increase of ER.

The effect of ER on LHV of syngas, primary power available from syngas as well as thermal power required to preheat the incoming air to complete the gasification reactions cycle are shown in Fig. 4.

As clearly depicted in Fig. 4, the LHV and primary power available from syngas as well as thermal power required to preheat the incoming air to reach gasification temperature decrease continuously with ER. LHV depends on the concentration of H_2, CO, CH_4, and other hydrocarbons present in syngas [67]. LHV of syngas decreases continuously with the increase of ER due to the decreasing concentration of all the fuel compounds except for H_2. With the increase of ER, the rate of oxidation reactions moves forward, which are exothermic and rises the quantity of generated heat [68–70]. Consequently, the energy required to preheat the air decreases continuously with ER.

Based on the current simulation results, 0.2 is identified as the optimum ER for the gasification of the SS. Although LHV of syngas would be higher at ER equal to 0.15, gasification at ER < 0.2 may lead to incomplete gasification, and pyrolysis of SS occurred which increases char production as well as tar content [13,71–73], requiring higher cost for the cleaning of syngas to remove impurities for further use (for chemical synthesis or power generation).

4.2.2. Effect of temperature

The identified optimum value of ER in section 4.2.1 (0.2) is used to reveal the ideal gasification temperature.

The effect of gasification temperature on syngas composition is presented in Fig. 5.

As clearly depicted in Fig. 5, the concentration of H_2 and CO increases continuously with the increase of gasification temperature, whereas the concentration of CH_4 rises slowly with temperature up to 800 °C and afterward it decreases linearly. The concentration of remaining gas components in syngas e.g. CO_2, C_2H_6, and C_3H_8 decreases in the whole range of temperature, with a rapid decrease of CO_2 and a moderate drop of C_2H_6 and C_3H_8. With the temperature rise, endothermic reactions move to a forward direction whereas exothermic reactions experience the reverse. Combustion reactions that occur in the gasifier are exothermic and move to the backward direction with temperature, which drives the decrease of CO_2, C_2H_6, C_3H_8, and CH_4 concentration in syngas. In contrast, water gas and water gas shift reactions are endothermic and move in the forward direction with temperature rise, causing an increase in the concentration of CO and H_2 in syngas [68–70].

The effect of gasification temperature on LHV of syngas and power flow in the gasifier is depicted in Fig. 6.

Table 6
Temperatures to restrict the reactions and fraction of carbon participate in gasification.

Reaction No.	Temperature limit (ΔT_{Appr}), °C
R1	−133.0
R2	−84.5
R3	−337.0
R4	−376.0
R5	26.6
R6	51.6
R7	0
Fraction of C participate in gasification reaction	0.854

Table 7
Comparison of simulation results with experimental data and their corresponding deviation.

	Model Calibration			Model Validation		
Composition (%v/v)	Experimental results [47]	Simulation results	Deviation (%)	Experimental results [47]	Simulation results	Deviation (%)
CO	35.3	34.3	−2.76	37.1	31.3	−15.7
CO_2	20.6	20.2	−1.71	24.2	23.4	−3.22
H_2	33.8	34.6	2.40	32.3	37.8	17.2
CH_4	10.3	10.8	4.99	6.45	7.65	18.5
AD (%)			2.96			13.7

*AD = Average Deviation.

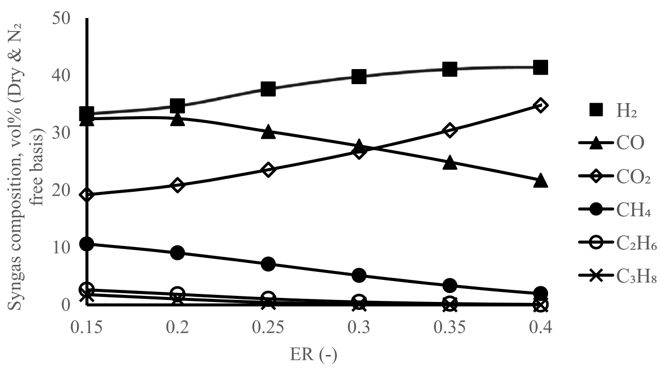

Fig. 3. Effect of ER on syngas composition [Gasification temperature = 850ºC].

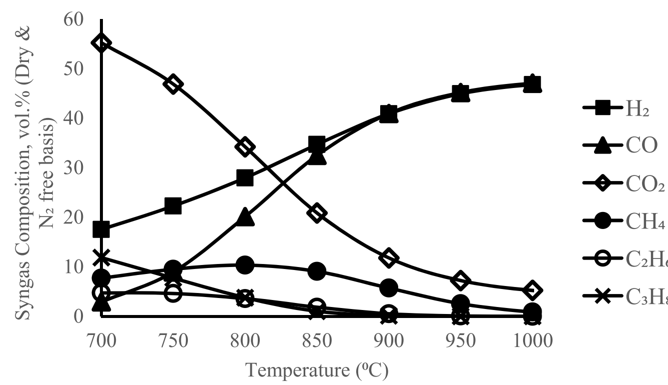

Fig. 5. Effect of gasification temperature on syngas composition [ER = 0.2].

As clearly observed in Fig. 6, the LHV of syngas, primary power accessible in syngas, and thermal power needed for preheating the incoming air increase with the rise of gasification temperature. With the increase of gasification temperature, the concentration of CO and H_2 in the syngas increases, and consequently the LHV rises [67]. However, the thermal power required to preheat the incoming air increases with the gasification temperature since at higher temperatures, exothermic reactions move to the backward direction whereas endothermic reactions experience the opposite, needing more energy to complete the cycle.

Based on the current simulation results, 900 °C is the identified optimum temperature for the gasification of SS. Indeed, the LHV and the available primary power in syngas increase as the gasification temperature rises from 900 to 950 °C. However, at the same time the thermal power required for pre-heating the gasifying agent increases as well, and such an increase (42.96 W) is higher than that related to the primary power available from syngas (31.26 W). Therefore, increasing the gasification temperature above 900 °C does not appear to be convenient.

The effect of ER and gasification temperature on syngas composition and LHV found in the current study is similar to that observed by other researchers in their developed model for the gasification of SS or waste biomass [13,16,17,47,68,74–77].

4.3. Evaluation of IC engine performance

Syngas obtained through simulation in this analysis at optimum operating conditions of gasification temperature 900 °C and ER of 0.2 is used to simulate CHP generation through an ICE system. The reason behind the identification of optimum ER and temperature for gasification of SS in the current analysis is mentioned clearly in sections 4.2.1 and 4.2.2 respectively. The predicted optimum operating conditions of gasification temperature, ER, LHV, gas yield, electrical, thermal, and cogeneration efficiencies found in the current simulation and comparison with similar results obtained by other researchers are mentioned in Table 8.

From the results presented in Table 8, the electrical efficiency

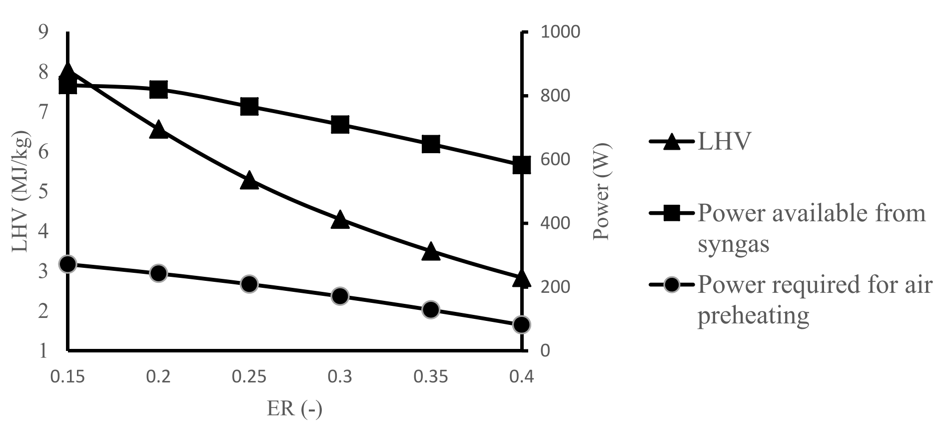

Fig. 4. Effect of ER on LHV of syngas, primary power available from syngas and required to reach gasification temperature [Gasification temperature = 850 ºC].

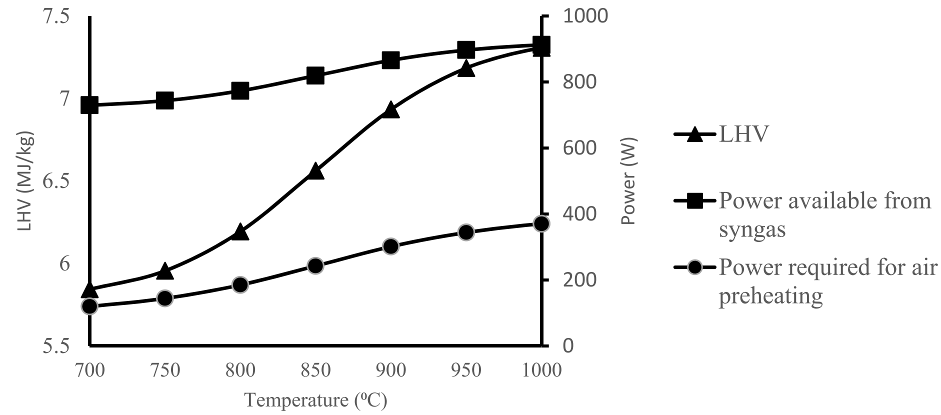

Fig. 6. Effect of temperature on LHV of syngas and primary power obtained from syngas and required to preheat the incoming air to the gasifier [ER = 0.2].

obtained from the proposed model is slightly higher compared to those of other biomass cogeneration systems analyzed in the available literature where the air is used as gasifying agent. This appears to be due to the different optimum operating parameters for gasification as well as the composition and LHV of feed materials. Thermal efficiency found in the current work is also higher than the one found by other authors, probably due to the simplifying hypothesis that all the generated heat can be exploited. Conversely, electrical and cogeneration efficiencies found in the current work are lower compared to the case of steam gasification (from Hazelnut shells) due to the difference of gasifying agent which has an impact on syngas LHV.

5. Estimated CHP generation rate from SS

The model developed in the present study is applied to evaluate the potentiality of electrical and thermal energy generation rate from all the SS produced in Italy as well as some EU countries mentioned in sections 3.1 and 3.2.

5.1. Potentiality of energy recovery from SS in Italy

5.1.1. Prediction of SS generation

The predicted SS generation rate in Italy based on the assumptions illustrated in subsection 3.1.1 are presented in Fig. 7.

Due to the improvement of wastewater collection and treatment facilities, the projected SS generation rate in Italy continuously increases for the considered scenarios. The expected SS generation rate is around 680 kt DS/year in 2030 for the first scenario, and in 2040 and 2050 for the second and third scenarios, respectively.

5.1.2. Projection of energy generation potential from SS

According to the results obtained from the developed model, electrical and thermal energy recovery potentiality of 1 kg of SS as DS is 1.05 kWh_{el} and 1.68 kWh_{th}, respectively. The potentiality of electrical and thermal energy generation from SS produced in Italy for the three scenarios are presented in Fig. 8(a) and (b), respectively, by assuming 7000 h of operation time every year for the ICE system.

As illustrated in Fig. 8 (a) and (b), the predicted electrical and thermal energy generation rate from SS can reach 714 GWh_{el}/year and 1142 GWh_{th}/year respectively.

5.2. Estimation of energy generation potential from SS in selected EU countries

The estimated electrical and thermal energy with per capita generation rate from SS in Italy and selected eight EU countries, considering the data related to 2015, are presented in Table 9.

Table 9 shows that the highest quantity of electrical and thermal energies from SS was found in Spain and the lowest in Luxembourg. CHP generation from SS in a country depends on the per capita SS generation rate which depends on the quantity of population connected to the sewage system and the total population. Spain has 46.5 million people after Italy with 60.8 million and 94.6% people are connected to the sewage system after Luxembourg of 98.5% in 2015. The per capita SS generation rate is the highest in Spain (24.81 kg of DS/(person.year)) among the EU countries presented in Table 9. In terms of per capita electrical and thermal energy generation potential from SS, Spain is in the top position and Italy is at the bottom. Italy has the second-lowest of both par capita SS generation (11.29 kg of DS/(person.year)) and population connection (60%) to the sewage system after Romania (10.59 kg of DS/(person.year) and 45.6% respectively) in 2015 [7,62,63].

In EU countries, the electrical energy consumed by the wastewater treatment sector is estimated to be around 1% of the national demand [80]. Considering this, it can be predicted that in the best scenario of complete collection and treatment of generated

Table 8
Gas yield, electrical, thermal, and cogeneration efficiencies found in the current study and comparison with studies available in the literature.

Feed material	Gasifying Agent	ER/SB	Gasification Temperature (ºC)	Gas Yield (Nm^3/kg)	LHV (MJ/Nm^3)	η_{el} (%)	η_{th} (%)	η_{sys} (%)	Ref.
SS	Air	0.20	900	1.83	4.12	29.20	45.92	53.10	Current study
Olive pruning		0.27	785	1.70	4.20	26.00	*n.r.	41.00	[41]
Wood		0.20	960	n.r.	n.r.	27.00	39.00	66.00	[40]
		0.3	800	n.r.	5.94	25.00	38.00	n.r.	[78]
*MSW		0.25	680	n.r.	5.80	19.08	20.00	40.05	[79]
Hazelnut shells	Steam	0.4	785	1.56	7.25	30.00	n.r.	64.00	[41]

*MSW = Municipal Solid Waste; n.r. = not reported.

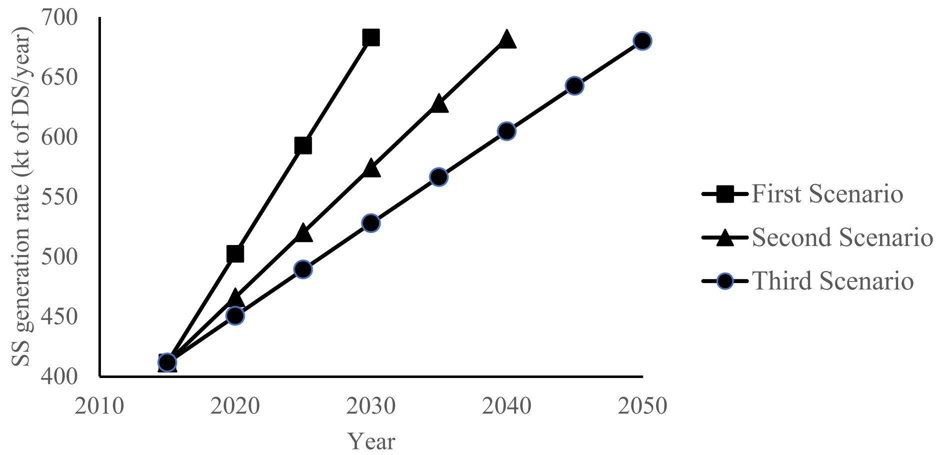

Fig. 7. Projection of the annual SS generation rate for three different scenarios in Italy.

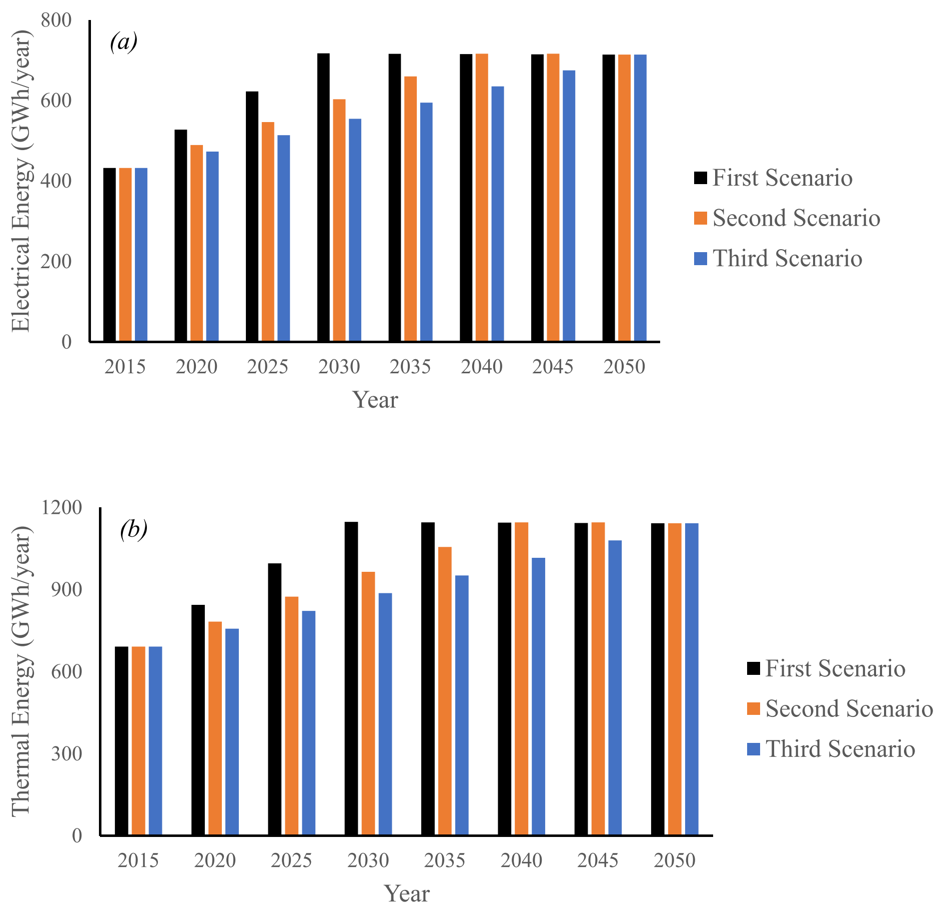

Fig. 8. Prediction of energy generation rate from SS in Italy through gasification in combination with an ICE system (a) Electrical (b) Thermal.

wastewater, around 23–29% of electrical energy needed by the wastewater treatment sector in Italy as well as in other EU countries could be self-produced. Mechanically dewatered SS needs to be dried before gasification to reduce the moisture content to less than 10 wt% [16,17] requiring high thermal energy consumption. Sludge drying could be carried out by using thermal energy available in the CHP generation system. More in detail, it could cover around 50–57% of the thermal energy demand of sludge drying, assuming an average moisture content equal to 70% for the wet SS and specific thermal energy consumption of drying equal to 0.85 kWh_{th} [81].

6. Conclusion

A simulation model in Aspen Plus is proposed as a smart energy system to assess the energy recovery from sewage sludge through gasification combined with an internal combustion engine system to produce electrical and thermal energy in Italy and applied to eight EU countries. To estimate syngas generation, the Aspen Plus model is calibrated and validated by using two distinct sets of

Table 9
Estimated total electrical and thermal energy generation from SS in some EU countries with per capita production potential in 2015.

Country	Electrical Energy (GWh/year)	Thermal Energy (GWh/year)	Per capita electrical energy (kWh/(person.year)	Per capita thermal energy (kWh/(person.year)
Luxembourg	9.61	15.4	17.1	27.3
Slovakia	59.1	94.5	10.9	17.4
Bulgaria	60.3	96.4	8.37	13.4
Ireland	61.3	98.1	13.1	21.0
Greece	126	201	11.6	18.6
Romania	221	354	11.1	17.8
Italy	432	692	7.11	11.4
Poland	596	954	15.7	25.1
Spain	1210	1936	26.1	41.7

experimental data available in the literature. The operating parameters involved during air gasification of sewage sludge are optimized through a sensitivity analysis aimed at investigating the effect of the equivalence ratio and gasification temperature on the system performance. Operating parameters related to the model development on combined heat and power generation from syngas in an internal combustion engine system are considered from the available literature. Under these operating conditions, the proposed system produces 1.05 kWh_{el} and 1.68 kWh_{th} per kg of sewage sludge as dry solid.

Considering the existing data and improvement of wastewater collection and treatment in the future, the sewage sludge generation rate in Italy is estimated to be equal to 680 kt per year as dry solid by 2030. Assuming that all sewage sludge is used for energy recovery through the system analyzed in the current work, around 714 GWh/year of electrical and 1142 GWh/year of thermal energy can be produced.

Electrical and thermal energy generation rates from sewage sludge in eight other EU countries in 2015 are estimated and compared with the Italian scenario. According to the estimated results, the highest quantity of electrical and thermal energy generated from sewage sludge was found for Spain whereas the lowest for Luxembourg. CHP generation from sludge through the proposed system would allow covering around 23–29% of the electrical energy demand of the wastewater treatment sector and 50–57% of the thermal energy demand for sewage sludge drying. Energy recovery from sewage sludge through the proposed system can beneficiary to fulfill the target of greenhouse gas emission reduction and increase of renewable energy contribution to the primary energy demand by 2030 mentioned in the EU green deal 2021.

Declaration of competing interest

The authors declare that they have no known competing financial interests or personal relationships that could have appeared to influence the work reported in this paper.

References

[1] IEA. World energy balances: Overview. Paris: IEA; 2020. https://www.iea.org/reports/world-energy-balances-overview.
[2] Bludowsky T, Agar DW. Thermally integrated bio-syngas-production for biorefineries. Chem Eng Res Des 2009;87(9):1328–39. https://doi.org/10.1016/j.cherd.2009.03.012.
[3] Shafiee S, Topal E. When will fossil fuel reserves be diminished? Energy pol. 2009;37(1):181–9. https://doi.org/10.1016/j.enpol.2008.08.016.
[4] Singh BR, Singh O. Global trends of fossil fuel reserves and climate change in the 21st century, 8; 2012. p. 167–92.
[5] Baliban RC, Elia JA, Floudas CA. Biomass to liquid transportation fuels (BTL) systems: process synthesis and global optimization framework. Energy Environ Sci 2013;6(1):267–87. https://doi.org/10.1039/C2EE23369J.
[6] European green deal. https://ec.europa.eu/commission/presscorner/detail/en/ip_21_3541; 2021.
[7] Eurostat. Sewage sludge production and disposal. https://ec.europa.eu/eurostat/databrowser/view/env_ww_spd/default/table?lang=en; 2021 (Access date March 2021).
[8] Vesilind PA. The role of water in sludge dewatering. Water Environ Res 1994;66(1):4–11.
[9] Magdziarz A, Dalai AK, Koziński JA. Chemical composition, character and reactivity of renewable fuel ashes. Fuel 2016;176:135–45. https://doi.org/10.1016/j.fuel.2016.02.069.
[10] Werle S. Impact of feedstock properties and operating conditions on sewage sludge gasification in a fixed bed gasifier. Waste Manag Res 2014;32(10):954–60. https://doi.org/10.1177/0734242X14535654.
[11] Chen G-B, Wu F-H, Fang T-L, Lin H-T, Chao Y-C. A study of Co-gasification of sewage sludge and palm kernel shells. Energy 2021;218:119532. https://doi.org/10.1016/j.energy.2020.119532.
[12] Fang S, Deng Z, Lin Y, Huang Z, Ding L, Deng L, et al. Investigation of the nitrogen migration characteristics in sewage sludge during chemical looping gasification. Energy 2021;216:119247. https://doi.org/10.1016/j.energy.2020.119247.
[13] de Andrés JM, Narros A, Rodríguez ME. Air-steam gasification of sewage sludge in a bubbling bed reactor: effect of alumina as a primary catalyst. Fuel Process Technol 2011;92:433–40. https://doi.org/10.1016/j.fuproc.2010.10.006.
[14] Jeong Y-S, Choi Y-K, Park K-B, Kim J-S. Air co-gasification of coal and dried sewage sludge in a two-stage gasifier: effect of blending ratio on the producer gas composition and tar removal. Energy 2019;185:708–16. https://doi.org/10.1016/j.energy.2019.07.093.
[15] Gai C, Chen M, Liu T, Peng N, Liu Z. Gasification characteristics of hydrochar and pyrochar derived from sewage sludge. Energy 2016;113:957–65. https://doi.org/10.1016/j.energy.2016.07.129.
[16] Abdelrahim A, Brachi P, Ruoppolo G, Di Fraia S, Vanoli L. Experimental and numerical investigation of biosolid gasification: equilibrium-based modeling with emphasis on the effects of different pretreatment methods. Ind Eng Chem Res 2020;59(1):299–307. https://doi.org/10.1021/acs.iecr.9b03902.
[17] de Andrés JM, Vedrenne M, Brambilla M, Rodríguez E. Modeling and model performance evaluation of sewage sludge gasification in fluidized-bed gasifiers using Aspen Plus. J. Air Waste Manage. 2019;69(1):23–33. https://doi.org/10.1080/10962247.2018.1500404.
[18] Raschid-Sally L. City waste for agriculture: emerging priorities which influence agenda setting. Aquat. Procedia. 2013;1:88–99. https://doi.org/10.1016/j.aqpro.2013.07.008.
[19] Wei L, Zhu F, Li Q, Xue C, Xia X, Yu H, et al. Development, current state and future trends of sludge management in China: based on exploratory data and CO_2-equivalent emissions analysis. Environ Int 2020;144:106093. https://doi.org/10.1016/j.envint.2020.106093.
[20] Islam KMN. Greenhouse gas footprint and the carbon flow associated with different solid waste management strategy for urban metabolism in Bangladesh. Sci Total Environ 2017;580:755–69. https://doi.org/10.1016/j.scitotenv.2016.12.022. PMID: 28024747.
[21] AR5 values: https://www.ipcc.ch/pdf/assessmentreport/ar5/wg1/WG1AR5_

Chapter08_FINAL.pdf (p. 73-79).

[22] Bunsow W, Dobberstein J. Refuse-derived fuel: composition and emissions from combustion. Resour Conserv 1987;14:249–56. https://doi.org/10.1016/0166-3097(87)90026-5.

[23] Huang YW, Chen MQ, Li Y, Guo J. Modeling of chemical exergy of agricultural biomass using improved general regression neural network. Energy 2016;114:1164–75. https://doi.org/10.1016/j.energy.2016.08.090.

[24] Martínez EJ, Stores A, Arenas CB, Blanco D, Martínez O, Gómez X. Improving anaerobic digestion of sewage sludge by hydrogen addition: analysis of microbial populations and process performance. Energies 2019;12:1228. https://doi.org/10.3390/en12071228.

[25] Marta G, Andrea L, Alicia S, Pierluigi L, Massimo S. Enhancing the energy efficiency of wastewater treatment plants through Co-digestion and fuel cell systems. Front Environ Sci 2017;5:70. https://doi.org/10.3389/fenvs.2017.00070.

[26] Chen S, Sun Z, Zhang Q, Hu J, Xiang W. Steam gasification of sewage sludge with CaO as CO_2 sorbent for hydrogen-rich syngas production. Biomass Bioenergy 2017;107:52–62. https://doi.org/10.1016/j.biombioe.2017.09.009.

[27] Ramachandran S, Yao Z, You S, Massier T, Stimming U, Wang C-H. Life cycle assessment of a sewage sludge and woody biomass co-gasification system. Energy 2017;137:369–76. https://doi.org/10.1016/j.energy.2017.04.139.

[28] Korberg AD, Mathiesen BV, Clausen LR, Skov IR. The role of biomass gasification in low-carbon energy and transport systems. Smart Energ. 2021;1:100006. https://doi.org/10.1016/j.segy.2021.100006.

[29] Thomsen TP, Sárossy Z, Gøbel B, Stoholm P, Ahrenfeldt J, Frandsen FJ, et al. Low temperature circulating fluidized bed gasification and co-gasification of municipal sewage sludge. Part 1: process performance and gas product characterization. Waste Manag. 2017;66:123–33. https://doi.org/10.1016/j.wasman.2017.04.028.

[30] Mehrpooya M, Khalili M, Sharifzadeh MMM. Model development and energy and exergy analysis of the biomass gasification process (Based on the various biomass sources). Renew Sustain Energy Rev 2018;91:869–87. https://doi.org/10.1016/j.rser.2018.04.076.

[31] Zhang Y, Xu P, Liang S, Liu B, Shuai B, Li B. Exergy analysis of hydrogen production from steam gasification of biomass: a review. Int. J. Hydrogen. Energy 2019;44(28):14290–302. https://doi.org/10.1016/j.ijhydene.2019.02.064.

[32] Roche E, Almeida JMA, Narros A, Rodriguez E. Air and air-steam gasification of sewage sludge. The influence of dolomite and throughput in tar production and composition. Fuel 2014;115:54–61. https://doi.org/10.1016/j.fuel.2013.07.003.

[33] Couto ND, Silva VB, Rouboa A. Assessment on steam gasification of municipal solid waste against biomass substrates. Energy Convers. Manag. 2016;124:92–103. https://doi.org/10.1016/j.enconman.2016.06.077.

[34] Franco C, Pinto F, Gulyurtlu I, Cabrita I. The study of reactions influencing the biomass steam gasification process. Fuel 2003;82(7):835–42. https://doi.org/10.1016/S0016-2361(02)00313-7.

[35] Prabowo B, Susanto H, Umeki K, Yan M, Yoshikawa K. Pilot scale autothermal gasification of coconut shell with CO_2-O_2 mixture. Front Energy 2015;9(3):362–70. https://doi.org/10.1007/s11708-015-0375-5.

[36] Irfan MF, Usman MR, Kusakabe K. Coal gasification in CO_2 atmosphere and its kinetics since 1948: a brief review. Energy 2011;36(1):12–40. https://doi.org/10.1016/j.energy.2010.10.034.

[37] Lv PM, Xiong ZH, Chang J, Wu CZ, Chen Y, Zhu JX. An experimental study on biomass airesteam gasification in a fluidized bed. Bioresour Technol 2004;95(1):95–101. https://doi.org/10.1016/j.biortech.2004.02.003.

[38] González JF, Román S, Bragado D, Calderón M. Investigation on the reactions influencing biomass air and air/steam gasification for hydrogen production. Fuel Process Technol 2008;89(8):764–72. https://doi.org/10.1016/j.fuproc.2008.01.011.

[39] Migliaccio R, Brachi P, Montagnaro F, Papa S, Tavano A, Montesarchio P, et al. Sewage sludge gasification in a fluidized bed: experimental investigation and modeling. Ind Eng Chem Res 2021;60:5034–47. https://doi.org/10.1021/acs.iecr.1c00084.

[40] Francois J, Abdelouahed L, Mauviel G, Patisson F, Mirgaux O, Rogaume C, et al. Detailed process modeling of a wood gasification combined heat and power plant. Biomass Bioenergy 2013;51:68–82. https://doi.org/10.1016/j.biombioe.2013.01.004.

[41] Villarini M, Marcantonio V, Colantoni A, Bocci E. Sensitivity analysis of different parameters on the performance of a CHP internal combustion engine system fed by a biomass waste gasifier. Energies 2019;12:688. https://doi.org/10.3390/en12040688.

[42] Ruya PM, Purwadi R, Lim SS. Supercritical water gasification of sewage sludge for power generation–thermodynamic study on auto-thermal operation using Aspen Plus. Energy Convers. Manag. 2020;206:112458. https://doi.org/10.1016/j.enconman.2019.112458.

[43] Kofler R, Clausen LR. Wheat straw based polygeneration systems integrating the electricity, heating and transport sector. Smart Energ. 2021;2:100015. https://doi.org/10.1016/j.segy.2021.100015.

[44] Furubayashi T. Design and analysis of a 100% renewable energy system for Akita prefecture, Japan. Smart Energ. 2021;2:100012. https://doi.org/10.1016/j.segy.2021.100012.

[45] Lund H, Østergaard PA, Connolly D, Mathiesen BV. Smart energy and smart energy systems. Energy 2017;137:556–65. https://doi.org/10.1016/j.energy.2017.05.123.

[46] Cirillo D, Di Palma M, La Villetta M, Macaluso A, Mauro A, Vanoli L. A novel biomass gasification micro-cogeneration plant: experimental and numerical analysis. Energy Convers. Manag. 2021;243:114349. https://doi.org/10.1016/j.enconman.2021.114349.

[47] Freda C, Cornacchia G, Romanelli A, Valerio V, Grieco M. Sewage sludge gasification in a bench scale rotary kiln. Fuel 2018;212:88–94. https://doi.org/10.1016/j.fuel.2017.10.013.

[48] Gao N, Kamran K, Quan C, Williams PT. Thermochemical conversion of sewage sludge: a critical review. Prog Energy Combust Sci 2020;79:100843. https://doi.org/10.1016/j.pecs.2020.100843.

[49] Acar MC, Böke YE. Simulation of biomass gasification in a BFBG using chemical equilibrium model and restricted chemical equilibrium method. Biomass Bioenergy 2019;125:131–8. https://doi.org/10.1016/j.biombioe.2019.04.012.

[50] Damartzis Th, Michailos S, Zabaniotou A. Energetic assessment of a combined heat and power integrated biomass gasification–internal combustion engine system by using Aspen Plus. Fuel Process Technol 2012;95:37–44. https://doi.org/10.1016/j.fuproc.2011.11.010.

[51] Ye G, Xie D, Qiao W, Grace JR, Lim CJ. Modeling of fluidized bed membrane reactors for hydrogen production from steam methane reforming with aspen plus. Int. J. Hydrogen. Energy 2009;34:4755–62. https://doi.org/10.1016/j.ijhydene.2009.03.047.

[52] Sadaka SS, Ghaly AE, Sabbah MA. Two phase biomass air-steam gasification model for fluidized bed reactors: Part I—model development. Biomass Bioenergy 2002;22(6):439–62. https://doi.org/10.1016/S0961-9534(02)00023-5.

[53] Lapuerta M, Hernández JJ, Pazo A, López J. Gasification and Co-gasification of biomass wastes: effect of the biomass origin and the gasifier operating conditions. Fuel Process Technol 2008;89(9):828–37. https://doi.org/10.1016/j.fuproc.2008.02.001.

[54] Thapa S, Bhoi PR, Kumar A, Huhnke RL. Effects of syngas cooling and biomass filter medium on tar removal. Energies 2017;10:349. https://doi.org/10.3390/en10030349.

[55] Demirbas A. Carbonization ranking of selected biomass for charcoal, liquid and gaseous products. Energy Convers. Manag. 2001;42(10):1229–38. https://doi.org/10.1016/S0196-8904(00)00110-2.

[56] Ahmed AMA, Salmiaton A, Choong TSY, Azlina WAKGW. Review of kinetic and equilibrium concepts for biomass tar modeling by using Aspen Plus. Renew Sustain Energy Rev 2015;52:1623–44. https://doi.org/10.1016/j.rser.2015.07.125.

[57] Loha C, Chatterjee PK, Chattopadhyay H. Performance of fluidized bed steam gasification of biomass – modeling and experiment. Energy Convers. Manag. 2011;52(3):1583–8. https://doi.org/10.1016/j.enconman.2010.11.003.

[58] Pala LPR, Wang Q, Kolb G, Hessel V. Steam gasification of biomass with subsequent syngas adjustment using shift reaction for syngas production: an aspen plus model. Renew Energy 2017;101:484–92. https://doi.org/10.1016/j.renene.2016.08.069.

[59] Baratieri M, Baggio P, Bosio B, Grigiante M, Longo GA. The use of biomass syngas in IC engines and CCGT plants: a comparative analysis. Appl Therm Eng 2009;29(16):3309–18. https://doi.org/10.1016/j.applthermaleng.2009.05.003.

[60] Martinez JD, Mahkamov K, Andrade RV, Lora EES. Syngas production in downdraft biomass gasifiers and its application using internal combustion engines. Renew Energy 2012;38(1):1–9. https://doi.org/10.1016/j.renene.2011.07.035.

[61] European Environment Agency. Urban wastewater treatment in Europe. https://www.eea.europa.eu/data-and-maps/indicators/urban-waste-water-treatment/urban-waste-water-treatment-assessment-4; 2020 (Access date: February 2021).

[62] Mininni G, Mauro E, Piccioli B, Colarullo G, Brandolini F, Giacomelli P. Production and characteristics of sewage sludge in Italy. Water Sci Technol 2019;79(4):619–26. https://doi.org/10.2166/wst.2019.064. PMID: 30975928.

[63] European Environment Agency. Water Statistics (Eurostat 2021); http://www.eea.europa.eu/data-and-maps/data/external/population-connected-to-wastewater-collection. (Accessed March 2021).

[64] Eurostat 2021. Population projections; https://ec.europa.eu/eurostat/databrowser/view/tps00002/default/table?lang=en. (Assess date: February 2021).

[65] Junior IV, de Almeida R, Cammarota MC. A review of sludge pretreatment methods and co-digestion to boost biogas production and energy self-sufficiency in wastewater treatment plants. J. Water Proc. Eng. 2021;40:101857. https://doi.org/10.1016/j.jwpe.2020.101857.

[66] Gonzalez AM, Lora EES, Palacio JCE. Syngas production from oil sludge gasification and its potential use in power generation systems: an energy and exergy analysis. Energy 2019;169:1175–90. https://doi.org/10.1016/j.energy.2018.11.087.

[67] Zheng X, Chen W, Ying Z, Huang J, Ji S, Wang B. Thermodynamic investigation on gasification performance of sewage sludge-derived hydrochar: effect of hydrothermal carbonization. Int. J. Hydrogen. Energy 2019;44(21):10374–83. https://doi.org/10.1016/j.ijhydene.2019.02.200.

[68] Nikoo MB, Mahinpey N. Simulation of biomass gasification in fluidized bed reactor using ASPEN PLUS. Biomass Bioenergy 2008;32(12):1245–54. https://doi.org/10.1016/j.biombioe.2008.02.020.

[69] Doherty W, Reynolds A, Kennedy D. Aspen plus simulation of biomass gasification in a steam blown dual fluidised bed. In: Méndez-Vilas A, editor. Materials and Processes for Energy: Communicating Current Research and Technological Developments. Spain: Formatex Research Centre: Badajoz; 2013.

[70] Begum S, Rasul MG, Akbar D, Ramzan N. Performance analysis of an integrated fixed bed gasifier model for different biomass feedstocks. Energies 2013;6(12):6508–24. https://doi.org/10.3390/en6126508.

[71] Caputo C, Cirillo D, Costa M, Villetta ML, Tuccillo R, Villani R. Numerical analysis of a combined heat and power generation technology from residual biomasses. J Energy Power Eng 2018;12:300–21. https://doi.org/10.17265/1934-8975/2018.06.003.

[72] Arjharn W, Hinsui T, Liplap P, Raghavan GSV. Evaluation of an energy production system from sewage sludge using a pilot-scale downdraft gasifier. Energy Fuels 2013;27(1):229–36. https://doi.org/10.1021/ef3012728.

[73] Mun TY, Kang BS, Kim JS. Production of a producer gas with high heating values and less tar from dried sewage sludge through air gasification using a two-stage gasifier and activated carbon. Energy Fuels 2009;23(6):3268–76. https://doi.org/10.1021/ef900028n.

[74] Tavares R, Monteiro E, Tabet F, Rouboa A. Numerical investigation of optimum operating conditions for syngas and hydrogen production from biomass gasification using Aspen Plus. Renew Energy 2020;146:1309–14. https://doi.org/10.1016/j.renene.2019.07.051.

[75] Kaushal P, Tyagi R. Advanced simulation of biomass gasification in a fluidized bed reactor using ASPEN PLUS. Renew Energy 2017;101:629–36. https://doi.org/10.1016/j.renene.2016.09.011.

[76] Garcia G, Monzon A, Bimbela F, Sanchez JL, Abrego J. Desulfurization and catalytic gas cleaning in fluidized-bed co-gasification of sewage sludge–coal blends. Energy Fuels 2013;27(5):2846–56. https://doi.org/10.1021/ef400259g.

[77] Lee KW, Lee WC, Lee HJ, Dong JI. Gasification characteristics of sewage sludge combined with wood biomass. J Mater Cycles Waste Manag 2014;16:642–9. https://doi.org/10.1007/s10163-014-0270-x.

[78] Gabbrielli R, Seggiani M, Frigo S, Puccini M, Vitolo S, Raggio G, et al. Validation of a small scale woody biomass downdraft gasification plant coupled with gas engine. Chem. Eng. Trans. 2016;50:241–6. https://doi.org/10.3303/CET1650041.

[79] Násner AML, Lora EES, Palacio JCE, Rocha MH, Restrepo JC, Venturini OJ. Refuse Derived Fuel (RDF) production and gasification in a pilot plant integrated with an Otto cycle ICE through Aspen plusTM modelling: thermodynamic and economic viability. Waste Manag. 2017;69:187–201. https://doi.org/10.1016/j.wasman.2017.08.006.

[80] Longo S, d'Antoni BM, Bongards M, Chaparro A, Cronrath A, Fatone F, et al. Monitoring and diagnosis of energy consumption in wastewater treatment plants. A state of the art and proposals for improvement. Appl Energy 2016;179:1251–68. https://doi.org/10.1016/j.apenergy.2016.07.043.

[81] Bennamoun L, Arlabosse P, Léonard A. Review on fundamental aspect of application of drying process to wastewater sludge. Renew Sustain Energy Rev 2013;28:29–43. https://doi.org/10.1016/j.rser.2013.07.043.

Fexible power-to-heat operation in district heating by redesigning electricity grid tariffs

Ajanta Priyadarshinee, *Department of Electrical Engineering, Aryan Institute of Engineering & Technology, Bhubaneswar, ajantapriyadarshinee10@gmail.com*

Balagoni Sampath Kumar, *Department of Electrical Engineering , NM Institute of Engineering & Technology, Bhubaneswar, bs.kumar456@gmail.com*

Prativa Barik, *Department of Electrical and Electronics Engineering, Raajdhani Engineering College, Bhubaneswar, p.barik213@gmail.com*

Satyajit Nayak, *Department of Electrical Engineering , Capital Engineering College, Bhubaneswar, satyajit_nayak@gmail.com*

Keywords:
District heating
Electricity grid tariffs
Flexibility
Wind power
EnergyPRO

A B S T R A C T

The Danish district heating sector constitutes a large potential for power-to-heat technology utilisation and thereby for increasing energy system flexibility and integration of the heat- and electricity sectors. Though the potential is there, it is uncertain whether the current flat-rate electricity grid tariff structure best incentivises a flexible integration. This study investigates how a redesign of the current flat-rate electricity grid tariffs influences the business-economic incentive for flexible power-to-heat operation in a district heating area, and how tariff schemes can incentivise increased integration of local wind power. The simulation tool energyPRO is used to investigate the influence of three redesigned tariff schemes; a flat-rate tariff reduction, a fixed time-of-use tariff scheme and a dynamic tariff scheme. It is concluded that the redesigned tariff schemes show potential for improving business-economic viability of flexible power-to-heat operation and increased integration of variable renewable electricity. However, measures and careful planning must be undertaken in the design of future tariff schemes to ensure that the necessary income for grid operators remains in place. The study thus suggests a redesign of the current tariff scheme and provides policymakers with tangible results of how a district heating company is affected by changes to the structure of electricity grid tariffs.

1. Introduction

Ensuring energy system and power system flexibility is a tremendous challenge to the integration of increased variable renewable electricity (VRE) in the transition to renewable energy systems [1]; a challenge that requires both technological advancements, regulatory changes, and new market mechanisms [2].

The concept of flexibility and its importance is discussed avidly in both academic research, governmental regulation, and political strategies, but regardless, no universal definition has emerged [3]. Traditionally, the term flexibility has been used solely to describe the flexibility of the electricity sector, e.g. the ability of power plants to maintain and balance voltage and frequency [4], but with increasing shares of VRE more flexibility options and mechanisms are needed [5]. This is evident in previous studies finding that when integrating more VRE into the energy systems a more holistic energy system approach tends to result in lower overall system costs [6]. Previous studies have also found that when the different energy sectors become more interrelated, market re-design to facilitate VRE integration have to be understood across the different energy sectors, as the different energy markets will to a larger extend affect each other [7].

Previous research has shown that the district heating (DH) sector can have an important role to play in the future integration and balancing of RE, due to a combination of existing storage capacity and technological diversity [8]. Furthermore, despite decreasing costs, battery storage remains an expensive solution for long-term electricity storage compared to heat storage alternatives found in the DH sector [9]. The storage potential in DH is especially relevant because of power to heat (P2H) technologies enabling the conversion of electricity to heat, typically based on conventional heating resistors, electrode boilers, or HPs. A transition towards P2H technologies, such as electric boilers (EBs) and electric heat pumps (HPs) in DH, coupled with heat storage could very well provide some of the critically needed flexibility and be an integral part of the future integration of VRE [10].

While both EBs and HPs enable the coupling of the heat and electricity sector and are useful technologies in integrating and utilizing VRE production, EBs and HPs provide vastly different benefits to the energy system [11]. HPs typically function as base-load units with many production hours due to high investment costs, low operation costs, and high efficiencies [12]. Therefore, HPs could prove to be an unreliable source of flexibility in the future, given the current operation mechanisms, where HPs only to a limited extent react to price signals from the day-ahead spot market and fluctuations in VRE production [12]. EBs are almost the exact opposite technology of HPs, providing a lower investment cost, but also lower efficiency. Enabling greater system flexibility through flexible operation of both EBs and HPs could prove to be a pivotal challenge for future RE systems.

The use of P2H technologies as a future flexibility mechanism is an area of growing interest among both academics and grid operators. However, as argued by Skytte [13], significant barriers to the realization of the P2H potential are present, including the market development and the regulatory setup. Key issues in the Danish context have been the preference for biomass heat only boilers; a result of the tax exemption for biomass, and the existing grid tariff structure hindering P2H utilisation.

A redesign of electricity grid tariffs could prove to be a useful mechanism for encouraging flexible operation. In an investigation of policy incentives for flexible DH in the Baltic countries, Sneum et al. [14] argue how flexibility is mainly provided by market incentives and very little by energy policy, raising the question of whether the existing market incentives are sufficient mechanisms for ensuring that the increased demand for flexibility is met. This is a challenge that is further exacerbated due to the conflict of ecological and financial efficiency of P2H control strategies, and the current lack of financial incentives for flexible P2H operation [15].

Through Balmorel simulations of the Nordic countries, Sandberg et al. [16] have investigated the impact of altering the grid tariff structure and found that the use of electricity in DH was significantly influenced. Likewise, a study of the North European power market based on Balmorel simulations concluded that the value of VRE increases, as the installed P2H capacity increased. In a study of a representative Danish DH system, Bergaentzlé et al. [17] analysed the impact of alternative tariff schemes on the operation of P2H technologies; this is however limited to only include EBs due to the site-specific nature of HPs. Similarly, Kirkerud et al. [18] investigated how changes to the grid tariffs influenced the operation of an EB in a typical Norwegian DH plant.

Tariffs are regulated locally by the distribution system operators (DSOs) and nationally by the transmission system operator (TSO). Danish DH companies are subject to a distribution tariff to the local DSO, in addition to transmission- and system tariffs paid to the TSO. All three are in the form of fixed tariff rates, where the total tariff payment is a result of the volumetric electricity consumption. The tariffs are supposed to be balanced to a level equal to the cost of operating and maintaining the grid, with a stated purpose from the Danish Electricity Supply Act of being cost-reflective, fair, and non-discriminating [19]. Thus, in theory, tariff rates should be cost-reflective. There is however notably no mentioning of encour-aging flexibility.

While traditionally electricity grid tariffs have been designed using a volumetric rate (EUR/kWh), independent of time and place of consumption, such fixed price structure may not be suitable for the on-going transition towards VRE and the ensuing changes to the electricity market. Reneses et al. [20] outline how the cost of supplying electricity is not static but instead varies according to both time of the day and location of consumption. In hours with excess renewable electricity, the marginal cost for supplying additional electricity on the distribution- and transmission grid is low. On the other hand, supplying electricity during peak load hours is expensive, both due to increased losses as a result of intensity and the expensive necessary investments in peak grid capacity [20]. Concerns like these cause Bergaentzlé et al. [17] to argue that traditional volumetric tariff distorts the price signals from tariffs as they do not properly reflect the marginal supply cost.

Perhaps a response to the challenges related to the traditional volumetric tariff schemes, three Danish DSOs Radius (part of Andel as of September 2020) [21], Cerius [22] and Konstant [23] have implemented an alternative tariff scheme within parts of their grid area for testing and demonstration purposes. While the specific tariff rates are slightly different for each DSO, the general structure applied is the same. In all three areas the tariffs have been changed to consist of three different price periods; low, high, and peak pricing. This, at least in theory, adds an element of time to electricity consumption, rewarding consumption outside of the typical peak demand hours. For all three DSOs a tariff reduction of 39%–42% is provided for consumption during low periods, no changes to the tariff rate during high periods, and a tariff increase of 42%–48% is added for consumption during peak periods.

As shown, while P2H flexibility and interactions with electricity grid tariffs already have seen some attention within research, significant gaps in this can be identified. One notable observation is the absence of studies on flexible operation of HPs in DH, whereas typically studies on P2H flexibility only investigate the potential for EBs. This may be a result of the site-specific nature of HPs, causing a need for case and site-specific investigations due to the need for a low-temperature energy source in connection to the HP, as opposed to either large-scale aggregated analysis or investigation of average cases. Furthermore, integration of VRE is only correlated to the changes in P2H operation as a result of tariff changes on a large-scale (e.g. for the North European power market [24]), but not on a local scale. The integration of VRE locally should however not be underestimated, where increased system flexibility may assist in reducing grid congestion and thus reduce grid expansion needs, in addition to supporting local renewable energy strategies due to a lower curtailment of VRE and improved integration.

1.1. Scope and case

This study investigates the challenge of system flexibility specifically in the context of Denmark, where approximately 64% of all households are supplied by DH [25] and 64% of the electricity demand is supplied from RE [26], thus making Denmark a prime candidate for investigations of P2H flexibility in DH. Furthermore, Denmark is committed to the transition to a 100% renewable energy (RE) system by 2050 [27]; a goal that requires a continued expansion of especially wind power production and thus an increased need for flexibility and VRE integration.

We hypothesise that a redesign of the existing rigid tariff scheme can incentivise flexible operation of P2H technologies, and thus result in increased integration of VRE as a result of increased P2H flexibility. Such a change should be understood not only in the context of the electricity market side but also consider the local heat market, as shown by the Smart Energy Markets concept [7], where we for this study thus consider the tariff structure as an important part of the energy market structure. While a redesign of the similarly rigid electricity tax structure could possibly also contribute to increased demand-side flexibility as investigated in Albertsen et al. [28], or flexible operation in DH as investigated in Østergaard and Andersen [29], the scope of this study is limited specifically to the electricity grid tariff schemes. Thus, this study sheds light on how a redesign of the existing electricity grid tariff schemes can increase the incentive for flexible operation of P2H technologies in the DH sector.

The study applies techno-economic modelling of a case DH plant with different P2H technologies installed, located in a region with large amounts of VRE production. The chosen case is Ringkøbing DH system, located in Ringkøbing-Skjern Municipality in Denmark. Ringkøbing DH is found relevant for investigating the effect of redesigned grid tariffs on flexibility in the local integration of VRE as Ringkøbing Municipality is in the process of developing a new energy strategy emphasising flexibility of the energy system and integration of the large amounts of locally produced VRE, thus following an increasing tendency among municipalities to actively engage in energy planning [30]. Ringkøbing DH has already installed EB capacity alongside a highly flexible and fast regulating hybrid natural gas and electricity HP, making the investigation of flexible P2H operation possible for both EB and HP. Also, Ringkøbing Municipality is home to the largest installed capacity of onshore wind turbines in Denmark, with electricity production in 2018 amounting to 178% of the electricity demand within the municipality, making the challenge of integrating VRE to the local energy system highly relevant. Ringkøbing DH is modelled in detail to investigate the effect of new tariff designs on the operation and business economic viability of P2H technologies. The operation of P2H technologies is correlated to the local wind power production, to assess how changes to the tariff structure influence local integration of VRE.

While it is not possible to decide on complex policy design such as electricity grid tariffs based solely on individual case studies, the aim of this study is to feed into the discussion of policy implications and evaluating the effect of new grid tariff schemes both on the operation of a DH company, and in terms of VRE integration.

2. Methods

The study applies the tool EnergyPRO for modelling Ringkøbing DH system, the selected case site, and testing redesigned tariff schemes. Tariff schemes are evaluated based on a combination of technical and economic parameters. This section outlines the process of choosing a suitable tool for modelling Ringkøbing DH system, followed by a description of the established model and key assumptions and data. Finally, the analytical framework consisting of the parameters of which the results are analysed according to, is presented.

2.1. Simulation tool

The purpose of this study's energy system analysis was to investigate the potential for increased flexible operation of P2H technologies and the influence of energy policy in the form of electricity tariffs. This was done by modelling and simulating the operation of Ringkøbing DH plant and testing how altering tariff schemes influence production and operation. For this analysis, a number of characteristics were necessary for the applied tool, including:

- Able to model DH at a local level including typical P2H technologies.
- Hourly calculation time steps.
- Possibility of including spot market and adhering both production and consumption accordingly.
- Able to simulate and optimize for a minimum of a one-year period.
- Possibility of including existing and potential future energy policy such as taxes and tariffs.

To simulate different system configurations and varying taxes and tariffs the software energyPRO [31] was used. energyPRO is mainly used for modelling and simulating local or site-specific energy systems such as a DH system. energyPRO is capable of optimising such systems operation according to existing conditions such as weather, fuel prices, taxes, and subsidies, and a variety of fossil fuel based-, renewable-, and storage technologies can be modelled. Furthermore, the possibility of simulating operation according to both existing and potential future market conditions makes energyPRO a relevant modelling tool for this specific study. energyPRO also has strong sector integration properties, highly relevant when investigating the potential for increased coupling of electricity and heating sectors. Finally, energyPRO is a proven and widely applied tool, utilized in many peer-reviewed studies, and is often the preferred choice for analyses focused on the DH sector. Examples of this include; modelling of scenarios for heat supply in a Danish municipality [32], an analysis on the use of booster HPs in combination with central HPs in DH [33] and simulations of DH systems in Finland with an increasing share of HPs [34].

The default optimisation principle of energyPRO, and the principle applied in this study, is to minimise operational expenditures, a result of a least-cost prioritisation strategy based on a priority list method. This is done by calculating a net heat production cost (NHPC), equal to the short-term marginal production costs for every production unit for every hour. The production unit with the lowest NHPC is activated first, followed by the second lowest if the demand (in this case heat demand) is still not fulfilled. As an alternative to this economic optimisation, it is possible to apply custom operation strategies. The energyPRO model in this study operates on a basis of perfect foresight, meaning that energyPRO is able to foresee electricity prices and demands for the entire optimisation period from the input time series. While this is a limitation of the tool and not entirely in accordance with real-life scenarios, it is not very different from practical operation where spot market prices are available 24 h before activating and heat demand and wind power production can be fairly accurately predicted due to forecasts.

This study applies hourly calculation steps for a one-year period (8,760 h) due to the coherence with the spot market data and other input data such as the electricity production from wind turbines and electricity consumption in Ringkøbing-Skjern Municipality. Since the purpose is to investigate the potential for flexible operation and the resulting integration of local wind power production, hourly calculation steps for a one year period is deemed sufficient.

2.2. Analytical framework

Analyses of technical and economic nature are conducted with the purpose of clarifying how the operation of P2H technologies is altered based on the changing of tariff schemes. For this study, technical analyses primarily revolve around how the changes in operation patterns interact with the local wind power production, while economic analyses relate to the tariff income of the DSO and TSO, as well as the business economic impact for the DH company.

2.2.1. Temporal operation of P2H technologies

The change in operation and integration of wind power is analysed through hourly comparisons of the wind power production relative to electricity consumption. Naturally, it is preferable to have the P2H technologies operate during hours of excess electricity production from renewable sources, such as wind power. To test this, the production hours are divided into two categories; hours with excess electricity produced by wind power and production hours with a deficit of electricity produced by wind power. For every hour it is determined whether there is an excess or deficit of electricity produced from wind power relative to the electricity consumption of Ringkøbing-Skjern Municipality. It is possible to determine incurred changes in operation due to changes to the tariff schemes, and whether it is possible to incentivise increased production during hours with excess electricity production.

2.2.2. Peak electricity production and export

The high wind power production of Ringkøbing-Skjern Municipality results in some hours with high peak power productions that must be exported, straining the grid. Grid expansions are expensive, so redesigned tariff schemes should preferably mitigate these peaks and reduce the export of electricity. To assess tariff schemes' influence on-peak hours, an assessment of how the most problematic peak hour is affected is included, in addition to an assessment of the 5% peak hours, and a total annual import-export balance.

2.2.3. Business economy

To investigate how the business economy of the DH company is affected a heat production cost is calculated. The evaluated heat price is a marginal heat production cost, meaning that only the short-term operational expenses are included, i.e., O&M costs, fuel and electricity costs, taxes, and tariffs. Long-term expenses such as investment costs are not included since no new investments are included for this study and such long-term expenses do not generally influence the operation strategy of the system. The simple approach for the heat price calculation is seen in Equation (1).

$$Heat\ price = \frac{Annual\ operation\ expenses}{Annual\ heat\ demand\ excl.\ heat\ loss} \tag{1}$$

Where.

Heat price	[EUR/MWh]
Annual operation expenses	[EUR]
Annual heat demand excl. heat loss	[MWh]

2.2.4. Recovering grid costs

An overview of tariff expenses, paid by the DH plant based on the electricity consumption of the P2H technologies to the DSO and TSO is also included. The total tariff expense is relevant to consider since the DSO and TSO will need to recover the cost of maintaining the electricity grid, and any potential deficits must be recovered elsewhere through other payment mechanisms. As the tariff rates are supposed to be cost-reflective as mentioned in Section 1, the current total tariff payment can be considered as a form of break-even point.

2.3. System details

Ringkøbing DH plant is split into three locations; Ringkøbing plant, Rindum plant, and two solar heating fields located close to each other and to the Rindum plant. This has no influence on the energyPRO model, since in reality the heat distribution grid allows heat to be transported between the different sites. From Fig. 1 it can be seen that Ringkøbing DH plant includes various different technologies; natural gas boilers, a natural gas CHP engine, an EB, an air to water HP able to run on either natural gas or electricity, hot water storage tanks and solar heating. Furthermore, it can also be seen that natural gas, electricity and solar energy are the only energy sources used in the DH plant.

In the energyPRO model, all the different heating technologies can utilise all three hot water storage tanks, allowing the system to benefit from periods of low heat demand and low electricity prices due to high VRE production to store heat for later use. The model does not include any requirements on minimum or maximum yearly operation hours. This means that the system is free to supply the heat demand based on what combination of technologies is found to be cheapest, according to the hourly prioritisation principle in energyPRO and the technologies NHPC. Furthermore it is seen how the only electricity market included in the energyPRO model is the spot market which is connected to the P2H technologies and the CHP unit; further details on the assumed hourly electricity prices are included in Section 2.5. Finally, it can be seen that there is also an annual heat demand which must be met and an annual heat loss, due to heat loss in the DH pipes connecting the DH plant to the heat consumers.

2.4. Technical- and economic parameters

In Table 1 the installed technologies along with corresponding technical and economic parameters can be seen.

In Table 1 the O&M costs are classified as fixed and variable, where fixed O&M costs are annual costs independent of production, and variable O&M depend on the total production (i.e. utilisation of the technology). In addition to the O&M costs included in Table 1, further economic assumptions include the taxes, tariffs, and CO_2 quota costs; these can be seen in Appendix 1. Furthermore, the natural gas CHP plant produces electricity which is assumed to be sold at the spot market price (see Fig. 3). The revenue generated from the sale of electricity is subtracted from the annual operational expenditures.

The EB installed in Ringkøbing DH is of 12 MW capacity and is capable of regulating within a few seconds. The efficiency of EBs range from 98% to 100% [36] due to the losses being resistive, and therefore heat-producing as well. For the purpose of the modelling in this study, the efficiency is assumed to be 100%. One thing to note is that an EB converts a high-quality energy resource (electricity) to a low-quality energy resource (heat). This is important to keep in mind when considering the efficiency since compared to for example a HP, the efficiency is quite low. The EB is mainly used as a peak load unit during hours with very low electricity prices, the current flat-rate grid tariffs are therefore typically a significant part of the operational expenditures.

The HP installed in Ringkøbing DH plant is an air to water HP capable of being powered by either natural gas or electricity, depending on which energy source is cheaper. For this study, it is assumed that the HP can freely operate on either natural gas or electricity, depending on the current NHPC. Table 2 provides an overview of how the efficiency and heat production varies according to the ambient temperature for both the natural gas and electric operation mode for the HP assuming a forward temperature of 70 °C. The data in Table 2 is used to model the heat pump in energyPRO and ensure that the efficiency and production correlate to the ambient air temperature as specified by the manufacturer.

To model the HP in the energyPRO model, two production units are modelled, one powered by natural gas and the other powered by electricity. The operation of the two units is restricted to one unit at a time. Microsoft Excel is used to produce time series for the heat output and fuel consumption since these vary throughout the year depending on the ambient temperature due to the nature of it being an air to water HP. The data from Table 2 is used to construct these time series for every hour of the year using linear interpolation and the hourly ambient temperature data described in Section 2.5. The output, in the form of heat production, is a system output, meaning that energy consumption for defrosting and air-coolers is included, explaining why the heat production is higher at higher temperatures.

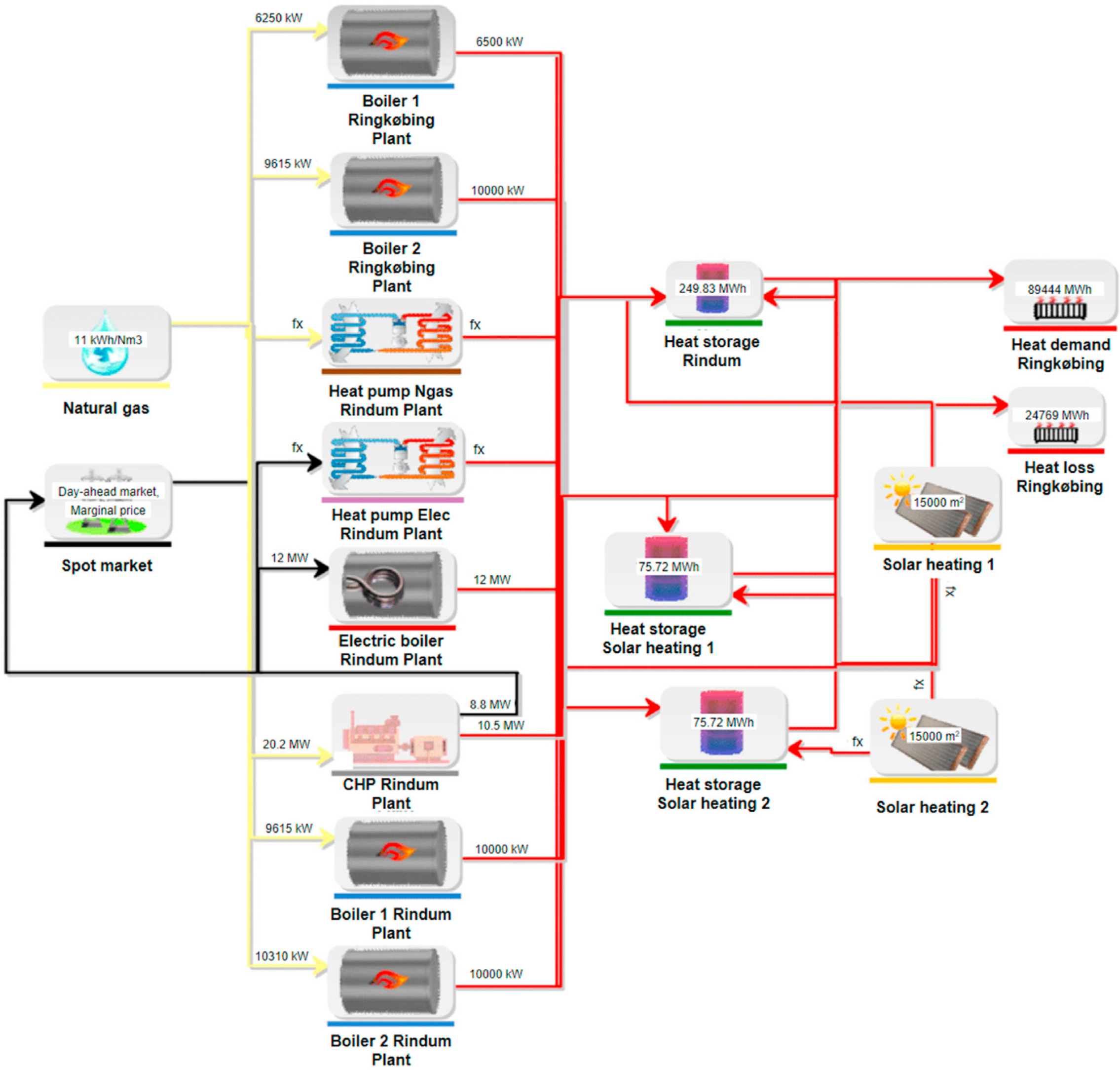

Fig. 1. Graphical overview of Ringkøbing DH plant as modelled in EnergyPRO.

Table 1
Key technical and economic parameters. Sizes and efficiencies are based on information from the DH plant. O&M costs are based on estimates from the Danish Energy Agency [36].

Technology	Size	Efficiency	Fixed O&M	Variable O&M
Natural gas boilers	36.5 MW	102.25%	2,000 EUR/MW/y	1.10 EUR/MWh
Natural gas CHP	10.5 MW_{th}	$52\%_{th}$ and $43.6\%_{e}$	10,000 EUR/MW/y	5.38 EUR/MWh
HP: Natural gas operation	4.29 MW	219%	10,000 EUR/MW_e/y[a]	7.99 EUR/MWh
HP: Electricity operation	3.28 MW	374%	2,000 EUR/MW_{th}/y	3.29 EUR/MWh
EB	12 MW	100%	1,100 EUR/MW/y	0.80 EUR/MWh
Solar heating	30,000 m^2	[b]	–	–
Heat storage	401.27 MWh	[c]	–	–

[a] Based on axle power delivered to HP.
[b] Based on solar radiation, ambient temperature, and solar collector efficiency parameters [35].
[c] Based on top/bottom temperatures, height, insulation thickness, thermal conductivity, and ambient temperature [35].

2.5. Input time series

Critical input data to the model include the wind power production of the municipality, the electricity spot market prices, and the heat demand. All of these are included as 8,760 hourly values, thus enabling the temporal comparisons essential to the study of flexibility. How these are included will be elaborated in the following. The included time series are all from 2018 as this is the most recent year with complete data sets available for all the needed inputs, at the time of this study. Time series on external conditions (ambient temperature and solar radiation) are also included in the model, used to determine the hourly heat demand and heat production from the solar heating fields respectively. Both originate from the Design Reference Year data made by the Danish Meteorological Institute [38]; these will however not be described in further details within this study.

Table 2
Coefficient of performance (COP) and heat production for the HP when operating based on electricity and natural gas respectively [37].

Hybrid natural gas and electricity HP (electricity operation)															
COP	3.02	3.09	3.16	3.24	3.32	3.41	3.49	3.59	3.74	3.89	4.00	4.12	4.24	4.36	4.49
Production [MW]	1.85	1.99	2.14	2.29	2.47	2.63	2.80	2.99	3.28	3.58	3.79	4.01	4.24	4.47	4.47
Temperature [°C]	−10	−8	−6	−4	−2	0	2	4	7	10	12	14	16	18	20
Hybrid natural gas and electricity HP (natural gas operation)															
COP	1.90	1.93	1.95	1.98	2.01	2.05	2.08	2.13	2.19	2.27	2.32	2.38	2.44	2.5	2.57
Production [MW]	2.60	2.77	2.96	3.15	3.34	3.54	3.75	3.96	4.29	4.63	4.87	5.11	5.36	5.61	5.6
Temperature [°C]	−10	−8	−6	−4	−2	0	2	4	7	10	12	14	16	18	20

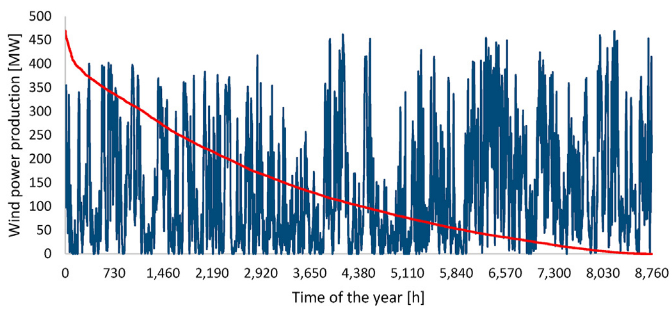

Fig. 2. Hourly wind power production in Ringkøbing-Skjern Municipality 2018. The red line is the corresponding duration curve. Data supplied by the Danish TSO Energinet. (For interpretation of the references to colour in this figure legend, the reader is referred to the Web version of this article.)

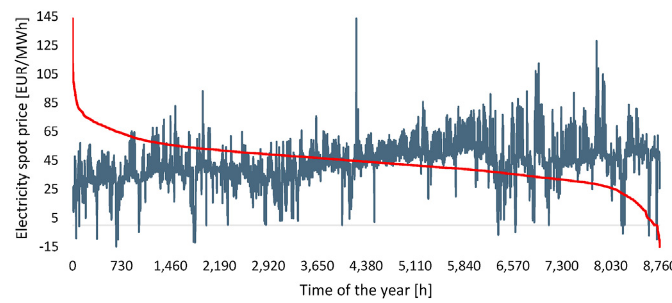

Fig. 3. Electricity spot market prices for Western Denmark (DK1) 2018; hourly values in blue and duration curve in red. Data available online [39]. (For interpretation of the references to colour in this figure legend, the reader is referred to the Web version of this article.)

2.5.1. *Wind power production*

From Fig. 2 it can be seen that the wind power production fluctuates throughout the year. The energyPRO model does not as such take into account the wind power production when simulating the system, which is based solely on a NHPC principle as described previously. Thus, to assess whether the changes to the grid tariffs result in increased utilisation of local wind energy, the hourly simulation output from energyPRO is compared to this wind power data in an Excel spreadsheet model.

2.5.2. *Electricity spot market prices*

The electricity spot market price seen in Fig. 3 is a critical input to the model because of the direct correlation to the NHPC and thus technology prioritisation. The average spot market price in 2018 was 43.9 EUR/MWh; higher than the average spot market price for 2000–2018 of 34.5 EUR/MWh, before adjusting for inflation.

2.5.3. *Heat demand*

The annual heat demand for Ringkøbing DH in 2018 was 89,444 MWh, excl. heat losses. This annual demand is distributed hourly using the degree-day method [35] based on the hourly ambient temperature, a temperature-dependent share of 70% for space heating, and a 30% temperature-independent share for hot water. It is assumed there is no demand for space heating during the summer months (June, July, August). The resulting time series can be seen in Fig. 4. In addition to the heat demand in Fig. 4, a heat loss of 27.7% is included in the model.

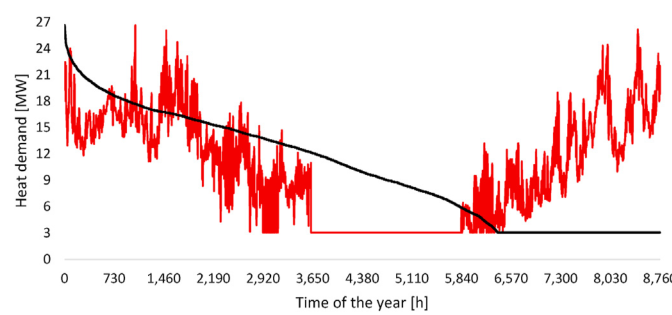

Fig. 4. Heat demand; hourly values and duration curve.

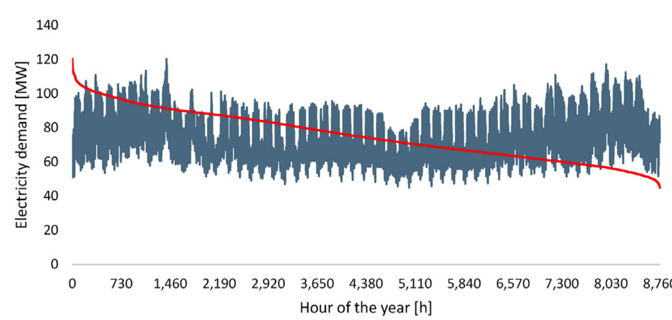

Fig. 5. Electricity demand for Ringkøbing-Skjern Municipality; hourly values and duration curve.

2.5.4. *Electricity demand*

The electricity demand shown in Fig. 5 is the demand of the entire municipality and is as such not needed for the energyPRO simulations of Ringkøbing DH plant. It is instead used to correlate the electricity consumption to the VRE production, and thus assess whether the changes to the grid tariffs enable increased local integration of VRE.

3. Investigated tariff schemes

This section presents the three tariff structures investigated (Table 3) and outlines how these could be a source of flexibility.

Re-designing tariff schemes will, almost inevitably, result in discussions on whether electricity grid tariffs are suitable as a flexibility enhancing mechanism, or whether e.g. market-based incentives should have this role. While this is an important and relevant discussion, this study assumes that the role and purpose of electricity grid tariffs can be extended to include grid flexibility and that they can thus be designed accordingly.

3.1. *Flat rate tariff*

For the flat-rate tariff structure (FRT), the tariff structure does not as such change from the existing tariff structure; payment is still dependent on the total electricity consumption without considering the time of consumption. A decrease in tariff payment would, however, lower the threshold for when the operation of EBs/HPs is feasible and could thus increase P2H utilisation. It can be argued that since neither electric HPs nor EBs are critical heat production units in the Danish energy system, an agreement ensuring flexibility in which the DSO/TSO is allowed to disconnect at will could be made, with a lower tariff rate to compensate for this option. The Danish TSO is working towards implementing such a principle as evident from the public hearing announced by Energinet in December 2019 [40]. Operation of P2H units would become more feasible at low electricity prices, where the fixed tariffs currently make up a significant portion of the operational costs, thus potentially increasing VRE integration and energy system flexibility.

A flat tariff reduction of 40% is tested for transmission-, system- and distribution tariffs in the model (Table 4). A 40% reduction is chosen because this closely resembles the decrease in tariff rate for the low price period in DSO areas where time-varying tariff rates have been implemented already, as described in Section 1. A flat-rate reduction of 40% is, therefore, a way to test the extent to which flexibility could be obtained from a very straightforward change where the low tariff rate is simply applied to all hours.

3.2. *Time-of-use tariff*

Fixed time-of-use (TOU) tariffs are becoming popular to implement by the various DSOs, and as previously mentioned in Section 1, fixed TOU tariffs have already to some extent been implemented in Denmark by the DSOs Radius, Konstant, and Cerius. For this study, the applied TOU tariff scheme is developed based on the average spot price fluctuations in West Denmark in 2018. This results in an average daily profile with higher prices during the peak morning and afternoon periods, and lower prices during the night, which is reflected in the tariff structure through low-, high-and peak load tariff rates. A schematic of the tested TOU scheme can be seen in Fig. 6.

The distribution tariff rates are based on the tariff rates implemented by the DSO Radius where TOU tariff rates were implemented in 2018. There are no existing experiences with also changing the tariffs to the TSO, therefore for this study, it is assumed that the TSO tariffs will vary in a similar pattern. This is done by increasing and decreasing the tariff rates by 50% for the low load and peak load hours respectively since this closely resembles the level of fluctuations implemented in the distribution tariff.

Table 4
Tested flat tariff rates. 0% constitute the tariff rates for Ringkøbing DH company in 2019.

Reduction	Transmission [EUR/MWh]	System [EUR/MWh]	Distribution [EUR/MWh]	Sum [EUR/MWh]
0%	5.9	4.8	5.2	15.9
40%	3.5	2.9	3.1	9.5

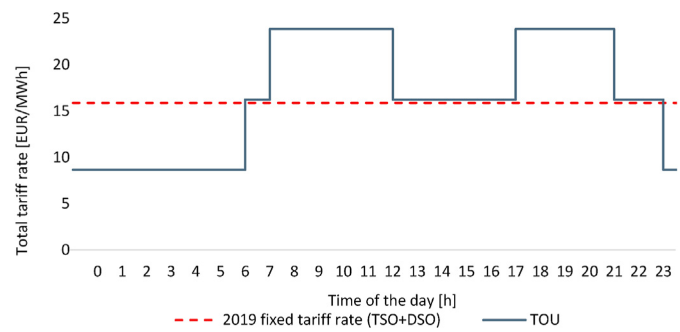

Fig. 6. TOU tariff scheme illustrated.

3.3. *Dynamic tariff*

Dynamic tariffs are, as opposed to fixed TOU tariffs, not based on a fixed time scheme. Such a structure could prove to be well-suited for future RE systems with uncertain VRE production and electricity prices. However, a dynamic tariff scheme is also significantly more complicated than a fixed TOU tariff scheme and relies on more sophisticated control mechanisms and automation on both consumption and production side. DH companies are generally familiar with adjusting their production according to price signals such as spot prices, which would make the introduction of dynamic tariffs easier here than in residential areas where knowledge, awareness, and ability to adjust electricity demand accordingly is likely lower.

In this study, dynamic tariff rates are generated as a function of the hourly spot price by calculating a percentage of the spot price, meaning that tariff rates will increase as the spot price increases and vice versa. This should, in theory, provide a greater incentive to utilise VRE since tariff rates are expected to be low during hours of high VRE production while aligning the price signals from spot prices and tariffs. This enables DH plants to place cost-reflective bids on the spot market. Such an approach would arguably also to a higher extent reflect the low marginal costs of supplying electricity when excess electricity is available and should reflect the high cost of supplying during peak load hours. In Fig. 7 the dynamic tariff scheme is illustrated through a duration curve, showing how the tariff rate varies depending on the hourly electricity price in 2018.

A spot price dependant tariff rate of 30% is chosen for this study. This is a combined total for all tariffs and is then separated into transmission-, system- and distribution tariffs based on the respective current share of each individual tariff. The tariff is designed so that the tariff rate cannot decrease below 0 EUR/MWh,

Table 3
Tariff schemes tested in simulations.

Tariff scheme	*Abbreviation*	*Description*
Flat-rate-tariff	FRT	A flat volumetric tariff rate. Payment is based on the total electricity consumption.
Time-of-use tariffs	TOU	A fixed temporal time structure is applied, making electricity consumption more expensive during typical peak load hours.
Dynamic tariffs	Dyn	Tariff rates fluctuate dynamically on an hour-to-hour basis as a function of the spot market price.

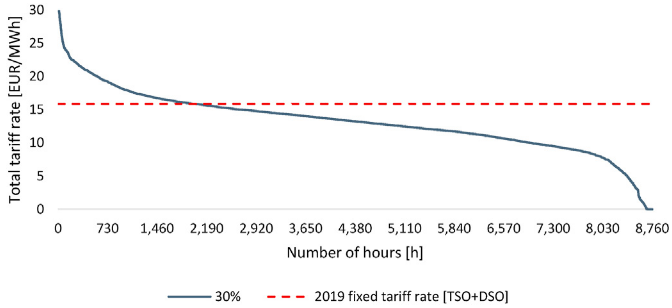

Fig. 7. Dynamic tariff scheme illustrated.

even if the spot price becomes negative. At a tariff rate of 30%, the tariff payment during hours of average electricity prices will resemble the reference tariff rates. The fluctuations will, however, be largely due to the nature of the electricity price dependency.

4. Results

The following section presents the results of the energyPRO model and the ensuing Excel data analysis, quantifying the effect of the investigated tariff schemes on the operation of the district heating plant.

4.1. Operation and integration of VRE

In Fig. 8 it can be seen that the utilisation of the P2H technologies varies depending on the applied tariff scheme. The highest utilisation is found for the Dyn tariff scheme, followed by the FRT tariff scheme. Especially the EB is utilized more in the Dyn tariff scheme compared to the Reference, FRT and TOU scenarios. This is a result of the low tariff rates during hours with low spot prices where EB operation is most relevant. However, depending on the individual perspective on flexibility and electricity consumption, this could be considered both a strength and a weakness of the Dyn tariff scheme.

As previously described, the wind power production in Ringkøbing-Skjern Municipality is at times very high, necessitating large grid capacity, at the expense of the DSO. Table 5 presents a comparison of how the different tariff schemes influence the peak excess wind production. This is a result of the difference between the wind power production and the electricity consumption of the municipality, combined with the consumption of the EB and the electric HP at Ringkøbing DH plant.

The TOU tariff scheme fails to decrease the maximum exported capacity compared to the Reference scenario (Table 5). The FRT tariff scheme and the Dyn tariff scheme is able to obtain a minor

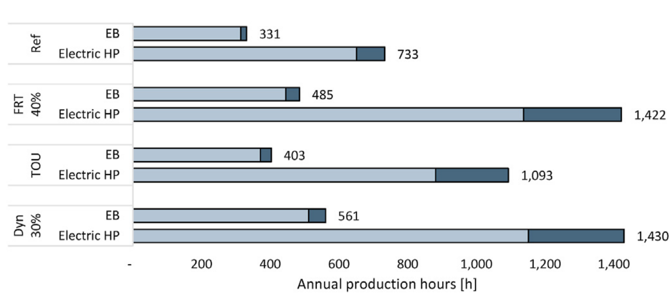

Fig. 8. Assessment of production hours and temporal distribution relative to local wind power production.

Table 5
Export of wind power relative to tariff scheme scenario.

	Ref	FRT 40%	TOU	Dyn 30%
Max export [MW]	−386.0	−385.2	−386.0	−384.5
Export [MWh]	513,810	−2,418	−1,140	−3,349
Top 5% export [MWh]	136,761	−330	62	−374

reduction due to operation of the electric HP. The reason for this is that while the wind power production for the specific peak hour was very high, the spot price was not low enough to incentivise operation of the EB.

All three tariff schemes reduce the annual exported electricity, with the largest reduction coming from the Dyn tariff scheme, followed by the FRT tariff scheme, and finally the TOU tariff scheme with the smallest change. Looking at the hours where the top 5% of the electricity is being exported, the TOU tariff scheme actually increases the need for electricity export during the most critical hours, which is an undesired effect. This indicates that the fixed nature of the TOU structure does not always correspond to the fluctuations from the wind and electricity consumption.

4.2. Tariff expense

The total annual tariff expense varies for the different tariff schemes, however, most significantly for the EB. An interesting observation is that despite the FRT tariff scheme having the lowest average tariff cost throughout the year, the annual tariff payment for the EB is the highest, excluding the Reference scenario (Table 6). The explanation is that during the hours where the EB is actually in operation, the tariff is lower, which is especially true for the Dyn tariff scheme. The most radical change in the annual tariff expenses is for the Dyn tariff scheme, where the decrease in the annual tariff payment for the EB and for the electric HP is much lower than for the other tariff schemes and for the Reference scenario.

A reduced income for the TSO and DSO is potentially problematic for sustaining the electricity grid, therefore a redesigned tariff scheme may need to be supplemented with other financial mechanisms to recover the costs; e.g. a larger fixed payment component. A fixed component would not influence the short term marginal costs and the resulting operation of P2H technologies; the design of such a mechanism is however beyond the scope of this study.

4.3. Temporal distribution of production

From Fig. 9 and Fig. 10 it can be seen how the operation of both the electric HP and the EB varies throughout the day, prioritising times when the hourly spot prices are low; often during the night. In fact, all three redesigned tariff schemes increase the average production during the night for both the HP and EB. The TOU tariff scheme most substantially reduces the production during the morning and evening peak periods, indicating that the tariff scheme is working as intended with regards to incentivising operation outside of these periods.

Table 6
Heat production cost and annual tariff expenses for EB and HP.

	Ref	FRT 40%	TOU	Dyn 30%
Heat production cost [EUR/MWh]	55	54.8	54.9	54.5
Tariff expense (HP) [EUR/year]	10,171	11,729	10,159	8,027
Tariff expense (EB) [EUR/year]	62,933	55,210	51,269	24,759

Note: Heat production costs shown are short-term marginal heat production costs.

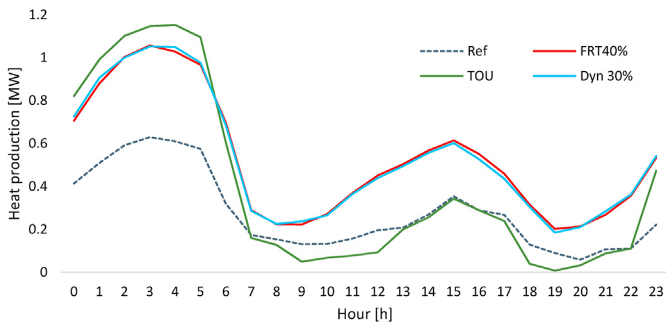

Fig. 9. Daily average production profile (heat pump).

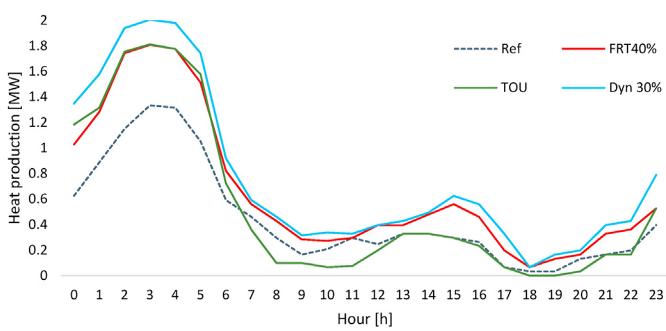

Fig. 10. Daily average production profile (electric boiler).

4.4. Excluding the hybrid natural gas HP

To evaluate how the system operates with a traditional electrical HP, the natural gas component is removed from the model, since this more closely resembles traditional DH plants with electrical HPs.

Removing the natural gas component of the HP takes away a significant portion of the annual production, in addition to removing a low-cost alternative to operation during hours of high electricity prices. This removes most of the flexibility of the electrical HP, since now the electrical HP will have the lowest NHPC almost regardless of electricity price and tariff rate, and the price incentives obtained from the tariff schemes are no longer sufficient mechanisms to incentivise flexible operation, resulting in a large number of operating hours for the electrical HP (Table 7).

There are no significant changes to the operation of the EB apart from minor changes to the total annual production hours, ranging from a 1-h decrease to an 18-h increase depending on the tariff scheme. This is mostly because the EB rarely directly competes with the HP regardless of whether it is running on natural gas or electricity. Instead, the EB primarily competes with the natural gas boilers as a peak load unit, and thus removing the natural gas HP does not influence operation significantly. As a result of the combined changes to the operation of the EB and electrical HP, the P2H share increases by 18–23%.

The electrical HP operates very differently in a system without a natural gas HP. In all the tested tariff schemes for this sensitivity analysis, the electric HPs annual production hours increase by 6,954 - 7,651 h, depending on the scheme. This results in the electric HP having more than 8,380 annual production hours for each scheme in the sensitivity analysis. A further observation is that due to the increase in production hours across the different tariff schemes, the resulting annual production hours for the electric HP is almost exactly equal for all the tested tariff schemes. This indicates that the tariff scheme does not influence the decision of whether or not to operate the electrical HP, and the tariff schemes do not appear to incentivise flexible operation of the HP in a system where the electrical HP operates as a base-load production unit.

5. Discussion and conclusion

The results of this study indicate that increasing P2H flexibility is feasible within a DH setting through the use of redesigned tariff schemes, resulting in increased P2H utilisation and local integration of VRE. In a techno-economic analysis three different tariff schemes are tested; a flat-rate tariff scheme, a fixed time-of-use tariff scheme, and a dynamic tariff scheme with hourly variations. Based on energy system modelling, the influence of these three tariff schemes on the operation of P2H technologies is tested for Ringkøbing DH plant in Denmark. Below key findings from the techno-economic analysis for the three tested tariff schemes can be seen.

5.1. Flat-rate tariff scheme

- Increases annual production hours by 47% for the EB, while decreasing the annual tariff expense by 12%.
- Increases annual production hours by 94% for the electric HP, while increasing the annual tariff expense by 15%.

5.2. Time of use tariff scheme

- Increases annual production hours by 22% for the EB, while decreasing the annual tariff expense by 19%.
- Increases annual production hours by 49% for the electric HP, while decreasing the annual tariff expense by 0.1%.

Table 7
Comparison of model results where the natural gas HP part is excluded.

	Original model					Without natural gas HP			
	Ref	*FRT 100%*	*FRT 40%*	*TOU*	*Dyn 30%*	*Ref*	*FRT 40%*	*TOU*	*Dyn 30%*
EB: Annual production hours [h]	331	1,376	485	403	562	7	13	17	17
- Excess electricity [h]	314	1,109	445	371	512	7	11	18	13
- Deficit electricity [h]	17	267	40	32	49	–	2	−1	4
HP: Annual production hours [h]	733	3,746	1,422	1,093	1,430	7,651	6,966	7,294	6,954
- Excess electricity [h]	651	2,596	1,137	881	1,151	4,413	3,929	4,170	3,912
- Deficit electricity [h]	82	1,150	285	212	279	3,238	3,037	3,123	3,041
P2H share [%]	6	25	9	7	13	23	21	22	18
EB: Tariff expense [EUR/year]	62,933	0	55,210	51,269	24,759	1,242	1,520	2,142	1,111
HP: Tariff expense [EUR/year]	10,171	0	11,729	10,159	8,027	107,127	58,716	113,279	88,580
Heat price [EUR/MWh]	55.0	54.2	54.8	54.9	54.4	24	19	24	22

Note: Results for the analysis without natural gas HP are shown as the changes relative to the results of the original model.

5.3. Dynamic tariff scheme

- Increases annual production hours by 69% for the EB, while decreasing the annual tariff expense by 61%.
- Increases annual production hours by 95% for the electric HP, while decreasing the annual tariff expense by 21%.

The dynamic tariff scheme resulted in the most significant increase in production hours, alongside significant decreases in tariff income for the DSO/TSO. This effect will have to be negated elsewhere to recover sufficient income to maintain the electricity grid. As an immediate alternative to very complex tariff schemes, a reduced flat-rate tariff of 40% resulted in a very similar level of operation hours and flexibility provided by the EB. The effect of fixed TOU tariffs proved to be more limited on both P2H operation and tariff income to the DSO/TSO. It could, however, function as a suitable first step in the transition towards flexible tariff schemes due to ease of implementation and low-risk change to grid operators. The potential for flexible operation of the electrical HP relies on the presence of the hybrid natural gas HP as a low-cost alternative, since without it the price signal provided by electricity grid tariffs proved to be insufficient to influence the operation of the electric HP. There are therefore no clear flexibility benefits to reducing the tariff rate for HPs in such a situation since flexible behaviour cannot be expected, and it would likely be more relevant to move towards technology-specific tariff schemes.

This study has only investigated tariff changes in the context of a DH plant, but other consumers, both large- and small-scale e.g. industries or private households, likely have very different consumption patterns. Therefore, the results of this study are likely unable to be transferred directly to other electricity consumers, where additional adaptations could be necessary to achieve the desired changes. All three tariff schemes investigated in this study (flat-rate, TOU, dynamic), could be further differentiated in the future if needed. Such differentiations could include differences in tariff rates for different technologies, consumer types, locations, or local grid congestion levels. As an example, areas primarily with vacation houses (or otherwise seasonal demands) may require one scheme, while areas with solely permanent housing would require a different scheme. TOU tariff schemes could become increasingly complex following some of the previously mentioned differentiation possibilities, which could perhaps to some extent increase the correlation between VRE production and electricity consumption. However, the nature of TOU schemes and the fixed structure will inevitably limit the potential for flexibility as electricity demand, VRE production, and thus grid strains, become increasingly difficult to predict. Peaks are expected to occur as the wind blows, and accounting for this with a system based on either a fixed tariff or a predetermined scheme will be difficult.

The dynamic tariff scheme considered for this study is based on the electricity spot price, a simple approach, which DH companies would likely find relatively simple to implement. A challenge with such a scheme is how adjustments in the average price from one year to another would be determine, e.g., if the average spot price increases or decreases significantly from one year to another, should the dynamic tariff rate also increase or decrease? And how would this work in a real-life scenario, since for this study, the spot prices for the entire year are known in advance and an appropriate tariff rate can be designed accordingly. However, choosing a correct tariff rate will be more challenging without the luxury of perfect foresight of the spot prices for a whole year.

Future research should be pursued with regards to how technologies, industries and sectors beyond the DH sector are expected to respond to changes to the electricity grid tariff scheme. System-wide analysis and modelling, optimally encompassing a multitude of energy sectors, should also be conducted in addition to case-oriented methodologies such as the approach applied in this study. Future discussions on tariff schemes should aim to clarify the role of electricity grid tariffs in energy systems, and the extent to which flexibility should be incorporated as a desirable mechanism.

Table 8
Overview of assumed operating expenditures.

Operating expenditures		
Fuel costs		
Natural gas	0.27	EUR/Nm^3
Taxes and tariffs		
Natural gas boilers		
Energy tax	22.31	EUR/MWh
CO_2 tax	6.65	EUR/MWh
NOx tax	0.00	EUR/Nm^3
Natural gas CHP		
Energy tax (Heat production only)	0.29	EUR/Nm^3
CO_2 tax (Heat production only)	0.05	EUR/Nm^3
NOx tax	0.00	EUR/Nm^3
Methane tax	0.01	EUR/Nm^3
Feed-in tariff	0.40	EUR/MWh
Electric boiler		
Electricity tax	28.92	EUR/MWh
Transmission tariff	5.89	EUR/MWh
System tariff	4.82	EUR/MWh
Distribution tariff	5.17	EUR/MWh
Heat pump (electricity)		
Electricity tax	34.67	EUR/MWh
Transmission tariff	5.89	EUR/MWh
System tariff	4.82	EUR/MWh
Distribution tariff	5.17	EUR/MWh
Heat pump (natural gas)		
Energy tax	0.29	EUR/Nm^3
CO_2 tax	0.05	EUR/Nm^3
NOx tax	0.00	EUR/Nm^3
Natural gas costs (all units)		
Transmission costs	0.04	EUR/Nm^3
CO_2 quotas	26.77	EUR/ton CO_2

References

[1] Auer H, Haas R. On integrating large shares of variable renewables into the electricity system. Energy 2016;115:1592–601. https://doi.org/10.1016/j.energy.2016.05.067.
[2] Lund PD, Lindgren J, Mikkola J, Salpakari J. Review of energy system flexibility measures to enable high levels of variable renewable electricity. Renew Sustain Energy Rev 2015;45:785–807. https://doi.org/10.1016/j.rser.2015.01.057.
[3] Hillberg E, Zegers A, Herndler B, Wong S, Pompee J, Bourmaud J-Y, et al. Flexibility needs in the future power system. 2019.
[4] Papaefthymiou G, Haesen E, Sach T. Power System Flexibility Tracker: indicators to track flexibility progress towards high-RES systems. Renew Energy 2018;127:1026–35. https://doi.org/10.1016/j.renene.2018.04.094.

[5] Hsieh E, Anderson R. Grid flexibility: the quiet revolution cumulative installed wind, solar, and storage capacity. Electr J 2017;30:1–8. https://doi.org/10.1016/j.tej.2017.01.009.
[6] Lund H, Østergaard PA, Connolly D, Mathiesen BV. Smart energy and smart energy systems. Energy 2017;137:556–65. https://doi.org/10.1016/j.energy.2017.05.123.
[7] Sorknæs P, Lund H, Skov IR, Djørup S, Skytte K, Morthorst PE, et al. Smart Energy Markets - future electricity, gas and heating markets. Renew Sustain Energy Rev 2020;119. https://doi.org/10.1016/j.rser.2019.109655.
[8] Lund H, Østergaard PA, Connolly D, Mathiesen BV. Smart energy and smart energy systems. Energy 2017. https://doi.org/10.1016/j.energy.2017.05.123.
[9] Lund H, Østergaard PA, Connolly D, Ridjan I, Mathiesen BV, Hvelplund F, et al. Energy storage and smart energy systems. Int. J. Sustain. Energy Plan. Manag. 2016;11:3–14. https://doi.org/10.5278/ijsepm.2016.11.2.
[10] Mathiesen BV, Lund H, Connolly D, Wenzel H, Østergaard PA, Möller B, et al. Smart Energy Systems for coherent 100% renewable energy and transport solutions. Appl Energy 2015;145:139–54. https://doi.org/10.1016/j.apenergy.2015.01.075.
[11] Lund R, Ilic DD, Trygg L. Socioeconomic potential for introducing large-scale heat pumps in district heating in Denmark. J Clean Prod 2016;139:219–29. https://doi.org/10.1016/j.jclepro.2016.07.135.
[12] David A, Mathiesen BV, Averfalk H, Werner S, Lund H. Heat Roadmap Europe: large-scale electric heat pumps in district heating systems. Energies 2017;10: 1–18. https://doi.org/10.3390/en10040578.
[13] Skytte K. Barriers for flexibility in the district heating-electricity interface. 2016.
[14] Sneum DM, Sandberg E, Koduvere H, Olsen OJ, Blumberga D. Policy incentives for flexible district heating in the Baltic countries. Util Pol 2018;51:61–72. https://doi.org/10.1016/j.jup.2018.02.001.
[15] Nolting L, Praktiknjo A. Techno-economic analysis of flexible heat pump controls. Appl Energy 2019;238:1417–33. https://doi.org/10.1016/j.apenergy.2019.01.177.
[16] Sandberg E, Kirkerud JG, Trømborg E, Bolkesjø TF. Energy system impacts of grid tariff structures for flexible power-to- district heat. Energy 2019;168: 772–81. https://doi.org/10.1016/j.energy.2018.11.035.
[17] Bergaentzlé C, Græsted I, Skytte K, Jess O. Electricity grid tariffs as a tool for flexible energy systems: A Danish case study126; 2019. p. 12–21. https://doi.org/10.1016/j.enpol.2018.11.021.
[18] Kirkerud JG, Trømborg E, Bolkesjø TF. Impacts of electricity grid tariffs on flexible use of electricity to heat generation. Energy 2016;115:1679–87. https://doi.org/10.1016/j.energy.2016.06.147.
[19] Danish Ministry of Climate E and U. Elforsyningsloven - Bekendtgørelse af lov om elforsyning - retsinformation.dk. 2019.
[20] Reneses J, Rodríguez MP, Pérez-Arriaga IJ. Electricity tariffs. In: Pérez-Arriaga IJ, editor. Regul. Power Sect. London: Springer London; 2013. p. 397–441. https://doi.org/10.1007/978-1-4471-5034-3_8.
[21] Radius. Tariffer og netabonnement. 2020.
[22] Cerius. Tarifmodel 2.0. 2020.
[23] Konstant. Tarifmodel - Nettariffer og abonnementer. 2020.
[24] Kirkerud JG, Bolkesjø TF, Trømborg E. Power-to-heat as a flexibility measure for integration of renewable energy. Energy 2017;128:776–84. https://doi.org/10.1016/j.energy.2017.03.153.
[25] Danish Energy Agency. Danish experiences on district heating. 2019.
[26] Danish Energy Agency. Key figures - Denmark 2017. 2017.
[27] Danish Energy Agency. Dansk Energipolitik. 2018.
[28] Albertsen LH, Andersen M, Boscán LR, Santos AQ. Implementing dynamic electricity taxation in Denmark. Energy Pol 2020;143:111543. https://doi.org/10.1016/j.enpol.2020.111543.
[29] Østergaard PA, Andersen AN. Variable taxes promoting district heating heat pump flexibility. Energy 2021. https://doi.org/10.1016/j.energy.2021.119839.
[30] Johannsen RM, Østergaard PA, Maya-Drysdale D, Krog L, Mouritsen E. Designing tools for energy system scenario making in municipal energy planning. Energies 2021;14:1442. https://doi.org/10.3390/en14051442.
[31] EMD International. EnergyPRO. 2019.
[32] Ben Amer-Allam S, Münster M, Petrović S. Scenarios for sustainable heat supply and heat savings in municipalities - the case of Helsingør, Denmark. Energy 2017;137:1252–63. https://doi.org/10.1016/j.energy.2017.06.091.
[33] Østergaard PA, Andersen AN. Booster heat pumps and central heat pumps in district heating. Appl Energy 2016;184:1374–88.
[34] Kontu K, Rinne S, Junnila S. Introducing modern heat pumps to existing district heating systems – global lessons from viable decarbonizing of district heating in Finland. Energy 2019;166:862–70. https://doi.org/10.1016/j.energy.2018.10.077.
[35] EMD International. User's guide energyPRO. 2019.
[36] Danish energy agency. Technology data for energy plants for electricity and district heating generation. 2016.
[37] Solid energy A/S. Solid energy AW502 heat pump. 2018.
[38] Wang PG, Scharling M, Nielsen KP, Wittchen KB, Kern-Hansen C. 2001 - 2010 Danish design reference year. 2013.
[39] Energinet. Elspot prices - Energi data service. 2020.
[40] Energinet. Energinet udsender de nye netprodukter (tarifkategorier) "Begrænset netadgang" og "Midlertidigt begrænset net" i høring fra 18. december 2019 til 4. februar 2020 | Energinet. 2019.

A Bi-objective AHP-MINLP-GA approach for Flexible Alternative Supplier Selection amid the COVID-19 Pandemic

Amiya Kumar sahoo, *Department of Computer Sciencel Engineering, Aryan Institute of Engineering & Technology, Bhubaneswar, aksahoo336@gmail.com*

Major Das, *Department of Computer Scinece Engineering , Raajdhani Engineering College, Bhubaneswar, major.das556@gmail.com*

Satyajit Nayak, *Department of Electrical Engineering , Capital Engineering College, Bhubaneswar, satyajit_nayak@gmail.com*

Subhendu Sahoo, *Department of Electrical and Electronics Engineering, NM Institute of Engineering & Technology, Bhubaneswar, s.sahoo95@outlook.com*

A R T I C L E I N F O

Keywords:
Analytic hierarchy process
Multiple criteria decision making, Consistency
Subjudgment matrix
Bi-objective

A B S T R A C T

A decision maker may hold multiple viewpoints regarding the relative priorities of criteria simultaneously, but this has rarely been considered in past studies. Therefore, this study proposes a bi-objective analytic hierarchy process (AHP)–mixed integer nonlinear programming (MINLP)–genetic algorithm (GA) approach. First, AHP is applied to decompose the decision maker's judgment matrix into several sub-judgment matrices. Each sub-judgment matrix represents a single viewpoint and generates a priority set. To generate diversified priority sets, a bi-objective MINLP problem is solved using a GA, and multiple alternatives can be selected based on these priority sets. The proposed approach has been applied to the real case of choosing diversified alternative suppliers amid the COVID-19 pandemic to assess its effectiveness. Several existing methods were also applied to this case for comparison. Experimental results showed that only the proposed approach was able to diversify the recommended alternative suppliers that were simultaneously optimal, thereby enhancing decision-making flexibility. In addition, the application of GA increased the solution efficiency by up to 75%.

1. Introduction

The analytic hierarchy process (AHP) is widely used in multicriteria decision making (MCDM) to derive the weights (or priorities) of criteria [1,2,3,4,5]. AHP can be extended to analytic network process to directly compare the overall performances of alternatives by considering the dependencies between criteria, criteria and alternatives, and/or alternatives [6,7].

Recent AHP research and applications have leveraged the advances in information, automation, and communication technologies, thereby developing several innovative applications. AHP and fuzzy AHP (FAHP) have been applied extensively to identify critical factors governing the success or sustainability of technology applications [8], including groundwater exploitation [9], wind farm siting [10], and aircraft fabrication using three-dimensional printing [11]. Group decision-making AHP is the most prevalent approach to prevent personal bias from a single decision maker (DM) skewing the analysis (e.g. [12,13]). Ho and Ma [14] showed that combining AHP and fuzzy logic has become the most popular AHP research direction [15]. However, Saaty [16] questioned whether fuzzy logic was helpful to improve AHP. Nevertheless, increasingly complex fuzzy sets have been applied to construct fuzzy judgment matrices [17], including intuitionistic fuzzy sets [18], hesitant fuzzy sets [19], neutrosophic sets [20], and Pythagorean fuzzy numbers [21]. The reasons for applying these types of fuzzy numbers are similar among scholars, but several studies have argued the possible overexploitation of AHP and FAHP.

AHP assumes that a DM can make pairwise comparisons of criteria that satisfy the multiplication requirement. However, this assumption is impractical because the DM may hold various viewpoints simultaneously [22,23]. Since pairwise comparison results are not identical from different perspectives, this leads to inconsistent results, reducing the credibility of an AHP analysis. Therefore, several studies proposed modified methods to measure consistency [24,25,26]. Others derived priorities using alternative methods [27,28]. However, these treatments change AHP rules, which is somewhat controversial. In contrast, the present study addresses this problem without changing AHP rules by observing the pairwise comparison process.

This study proposes a bi-objective AHP–mixed integer nonlinear programming (MINLP)–genetic algorithm (GA) approach to address the inconsistency of pairwise comparison results. Existing AHP methods usually employ a single objective function: minimizing the difference between the derived priorities and pairwise comparison results. In contrast, the proposed approach decomposes a judgment matrix into several sub-judgment matrices, each representing a single DM viewpoint. In this way, multiple priority sets can be derived to select multiple alternatives, thereby increasing the flexibility of decision making. All alternatives are optimal but correspond to different viewpoints, which provides flexibility and is distinct from the prevalent top-*k* policy [29]. The proposed approach also differs from existing group decision-making AHP methods that aggregate multiple judgment matrices into a single matrix. Sub-judgment matrices remain diverse since they represent different viewpoints, but they have higher consistency than the original judgment matrix because only one viewpoint is considered at a time. These considerations lead to the formulation of a bi-objective MINLP problem that is solved using a GA to decompose the judgment matrix. The novelty of the proposed methodology resides in the following:

(1) The proposed methodology attempts to discover the diverse viewpoints of a decision maker, which has rarely been investigated in the past. In contrast, recent studies on diversified decision-making have focused on problems in which decision makers adopted different sets of criteria to evaluate the performances of alternatives [30–32]. Obviously, the nature of these two types of methods are different.
(2) Diversification is the basic requirement of clustering methods [33,34,35]. However, the problem discussed in this study is an evaluation or ranking problem, not a clustering problem. In addition, in a clustering problem, each diversified cluster contains many objects. In contrast, in this study, each diversified choice is unique.

The remainder of this paper is organized as follows. Section 2 reviews conventional AHP methods and introduces the proposed bi-objective AHP-MINLP-GA approach. Section 3 applies the proposed approach to a real case of choosing diversified alternative suppliers amid the COVID-19 pandemic to assess its effectiveness. Several existing methods are also compared. Section 4 applies the proposed methodology to another case to elaborate its effectiveness. Section 5 summarizes and concludes this paper, and suggests possible topics for future studies.

2. The Proposed Methodology

2.1. AHP

AHP compares the relative priorities of factors using linguistic terms, such as "as equal as," "weakly more important than," "strongly more important than," "very strongly more important than," and "absolutely more important than." These linguistic terms are usually mapped to integers within [1, 9],

L1: "As equal as" = 1
L2: "Weakly more important than" = 3
L3: "Strongly more important than" = 5
L4: "Very strongly more important than" = 7
L5: "Absolutely more important than" = 9

2, 4, 6, and 8 can also be selected if the relative priority lies between two successive linguistic terms.

A judgment matrix is constructed from pairwise comparison results as

$$\mathbf{A}_{n\times n} = [a_{ij}] \tag{1}$$

where $i, j = 1 - n$;

$$a_{ij} = \begin{cases} 1 & if \quad i = j \\ \dfrac{1}{a_{ji}} & otherwise \end{cases} \tag{2}$$

is the relative priority of factor i over factor j; a_{ij} is a positive comparison if $a_{ij} \geq 1$. Eigenvalues and eigenvectors of $\mathbf{A}$ (λ and $\mathbf{x}$, respectively) satisfy

$$det(\mathbf{A} - \lambda\mathbf{I}) = 0 \tag{3}$$

and

$$(\mathbf{A} - \lambda\mathbf{I})\mathbf{x} = 0 \tag{4}$$

The maximum eigenvalue and the priority of each factor are

$$\lambda_{\max} = \max_i \lambda_i \tag{5}$$

and

$$w_i = \frac{x_i}{\sum_{j=1}^{n} x_j}, \tag{6}$$

respectively. The consistency of pairwise comparison results can be evaluated using indices

$$\text{Consistency inder : CI} = \frac{\lambda_{\max} - n}{n-1} \tag{7}$$

$$\text{Consistency ratio : } CR = \frac{CI}{RI} \tag{8}$$

where RI is the random consistency index (Satty, 1980), as shown in Table 1. CR needs to be smaller than 0.1 for a small AHP problem and 0.3 for a larger problem [36,37].

Theorem 1.

$$RI \cong 0.0053n^3 - 0.1273n^2 + 1.051n - 1.6125\,\forall\, \mathbf{2} \leq n \leq \mathbf{10} \tag{9}$$

The geometric mean can be employed to estimate the values of priorities as [38]

$$w_i = \frac{\sqrt[n]{\prod_{j=1}^{n} a_{ij}^{\infty}}}{\sum_{m=1}^{n} \sqrt[n]{\prod_{j=1}^{n} a_{mj}^{\infty}}} \tag{10}$$

and hence the maximal eigenvalue is derived as

$$\lambda_{\max} \cong \frac{1}{n}\sum_{i=1}^{n}\left(\frac{\sum_{j=1}^{n}(a_{ij}w_j)}{w_i}\right) \tag{11}$$

Substituting Equations (9) and (11) into (8),

$$CR(\mathbf{A}) \cong \frac{\frac{1}{n}\sum_{i=1}^{n}\left(\frac{\sum_{j=1}^{n}(a_{ij}w_j)}{w_i}\right) - n}{(n-1)(0.0053n^3 - 0.1273n^2 + 1.051n - 1.6125)} \tag{12}$$

Table 1
Random consistency index.

N	*RI*
1	0.00
2	0.00
3	0.58
4	0.90
5	1.12
6	1.24
7	1.32
8	1.41
9	1.45
10	1.49

2.2. Proposed bi-objective AHP-MINLP-GA approach

This study proposes a bi-objective AHP-MINLP-GA approach to decompose a judgment matrix into several sub-judgment matrices, each representing a unique viewpoint regarding the relative priorities of criteria, as shown in Fig. 1. Different priority sets can be generated from these viewpoints and used to select different alternatives that are simultaneously optimal. These viewpoints should be as diverse as possible and each sub-judgment matrix is expected to be more consistent than the original judgment matrix, resulting in a bi-objective problem.

Fig. 2 shows the proposed bi-objective AHP-MINLP-GA approach, which is composed of the following steps.

Step 1. Construct the judgment matrix.
Step 2. Evaluate the consistency of the judgment matrix in terms of CR.
Step 3. If the consistency is sufficiently high (i.e., CR < 0.1), proceed to Step 10; otherwise, proceed to Step 4.
Step 4. Construct the bi-objective MINLP model to decompose the judgment matrix into several sub-judgment matrices.
Step 5. If a compromise can be made between the two objective functions, proceed to Step 6; otherwise, proceed to Step 8.
Step 6. Convert the bi-objective MINLP model into a single-objective MINLP model.
Step 7. Apply a GA algorithm to solve the single-objective MINLP problem.
Step 8. Derive the priorities of criteria from each sub-judgment (or judgment) matrix.

2.3. The bi-objective MINLP model

The proposed bi-objective AHP-MINLP-GA approach decomposes a judgment matrix $\mathbf{A}$ into several sub-judgment matrices $\{\mathbf{A}(k)|\, k = 1 \sim K\}$ using the arithmetic average operator,

$$\mathbf{A} := \frac{\sum_{k=1}^{K}\mathbf{A}(k)}{K} \tag{13}$$

hence

$$a_{ij} = \frac{\sum_{k=1}^{K} a_{ij}(k)}{K}\ \forall\, a_{ij} > 1 \tag{14}$$

for each positive pairwise comparison, i.e., $\forall\ a_{ij} > 1$.

The relationship between negative pairwise comparisons will be a harmonic mean, as demonstrated by the following theorem.

Theorem 2.

$$a_{ji} = \frac{K}{\sum_{k=1}^{K}\frac{1}{a_{ji}(k)}} \tag{15}$$

where $\forall\ a_{ij} > 1$.

Proof.

$$\begin{aligned} a_{ji} &= \frac{1}{a_{ij}} \\ &= \frac{1}{\frac{\sum_{k=1}^{K} a_{ij}(k)}{K}} \\ &= \frac{1}{\frac{\sum_{k=1}^{K}\frac{1}{a_{ji}(k)}}{K}} \\ &= \frac{K}{\sum_{k=1}^{K}\frac{1}{a_{ji}(k)}} \end{aligned} \tag{16}$$

Theorem 2. is proved.

All sub-judgment matrices satisfy the basic requirements of a judgment matrix

$$det(\mathbf{A}(k) - \lambda(k)\mathbf{I}) = 0 \tag{17}$$

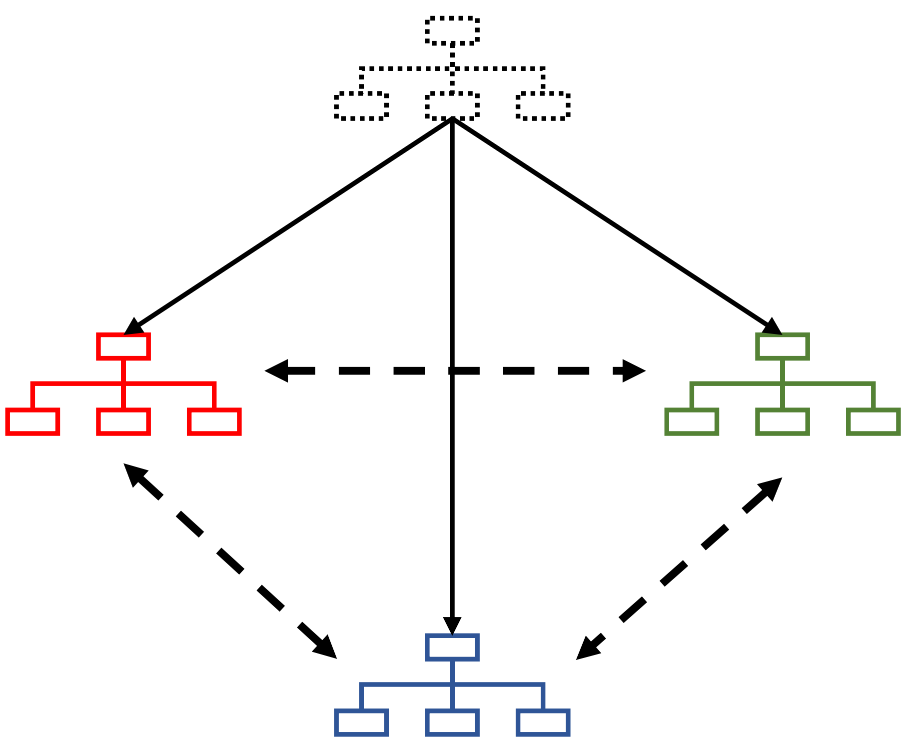

Fig. 1. Decomposition of a judgment matrix.

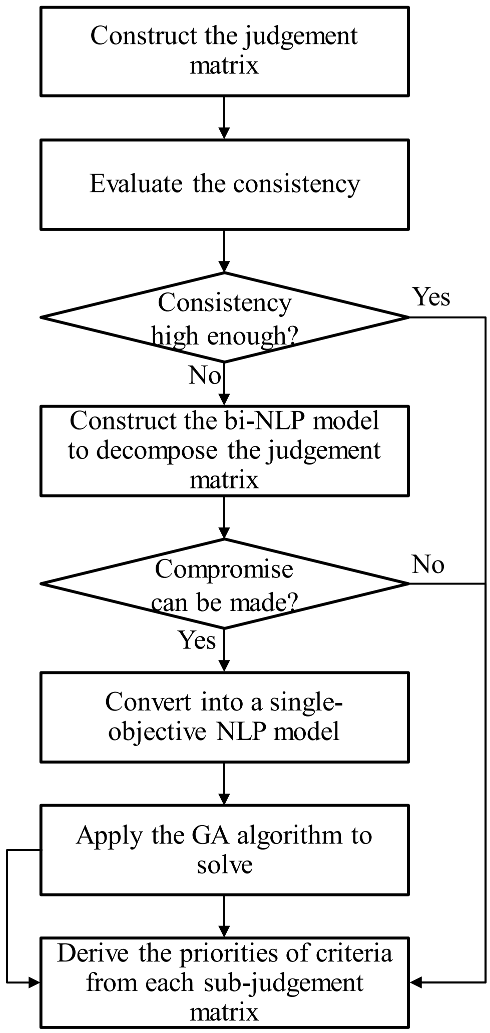

Fig. 2. Procedure of the bi-objective AHP-MINLP-GA approach.

and

$$(\mathbf{A}(k) - \lambda(k)\mathbf{I})\mathbf{x}(k) = 0 \tag{18}$$

A DM usually holds multiple viewpoints regarding the relative priorities of factors, which may conflict with each other, causing inconsistent pairwise comparison results. However, each sub-judgment matrix represents a single viewpoint held by the DM, and hence each sub-judgment matrix is expected to be more consistent than the original judgment matrix, i.e.,

$$CR(\mathbf{A}(k)) \le CR(\mathbf{A});\ k = 1 \sim K \tag{19}$$

Therefore, the proposed approach first optimizes the average improvement in CR,

$$\text{Max } Z_1 = \frac{1}{K}\sum_{k=1}^{K}(CR(\mathbf{A}) - CR(\mathbf{A}(k))) \tag{20}$$

The number of possible combinations of sub-judgment matrixes is large, and each sub-judgment matrix should be sufficiently far from each other to maximize viewpoint diversity. Therefore, the proposed approach then maximizes the distance between sub-judgment matrices,

$$\text{Max } Z_2 = \sum_{k=1}^{K-1}\sum_{l=k+1}^{K} d(\mathbf{A}(k),\ \mathbf{A}(l)) \tag{21}$$

where $d()$ is the Frobenius distance [39] between two matrices,

$$d(\mathbf{A}(k),\ \mathbf{A}(l)) = \sqrt{\sum_{i=1}^{n}\sum_{j=1}^{n}\left(a_{ij}(k) - a_{ij}(l)\right)^2} \tag{22}$$

Thus, the bi-objective MINLP model is formulated and optimized to decompose the judgment matrix into sub-judgment matrices that are not only diverse but also more consistent than the original judgment matrix.

(Bi-objective MINLP Model I)

$$\text{Max } Z_1 = \frac{1}{K}\sum_{k=1}^{K}(CR(\mathbf{A}) - CR(\mathbf{A}(k))) \tag{23}$$

$$\text{Max } Z_2 = \sum_{k=1}^{K-1}\sum_{l=k+1}^{K}\sqrt{\sum_{i=1}^{n}\sum_{j=1}^{n}\left(a_{ij}(k) - a_{ij}(l)\right)^2} \tag{24}$$

subject to

$$a_{ij} = \frac{\sum_{k=1}^{K} a_{ij}(k)}{K}\ \forall a_{ij} > 1 \tag{25}$$

$$a_{ij}(k)a_{ji}(k) = 1 \tag{26}$$

$$a_{ii}(k) = 1 \tag{27}$$

$$det(\mathbf{A}(k) - \lambda(k)\mathbf{I}) = 0 \tag{28}$$

$$CR(\mathbf{A}(k)) \le CR(\mathbf{A}) \tag{29}$$

$$a_{ij}(k) \in \{1,\ \ldots,\ 9\}\ \forall a_{ij} > 1 \tag{30}$$

where $i, j = 1 - n$; $k = 1 - K$.

Constraints (26) and (27) are the basic requirements for judgment (or sub-judgment) matrices, and the other constraints have been explained above. The bi-objective MINLP model must be converted into a more tractable form so that it can be more easily solved.

2.4. Converting the bi-objective MINLP model into a more tractable form

In the first objective function, $CR(\mathbf{A}(k))$ can be calculated using Equation (7) if $\lambda(k)$ is known,

$$CR(\mathbf{A}(k)) = \frac{\lambda(k) - n}{(n-1)(0.0053n^3 - 0.1273n^2 + 1.051n - 1.6125)} \tag{31}$$

The second objective function can be replaced with

$$\text{Max } Z_2 = \sum_{k=1}^{K-1}\sum_{l=k+1}^{K} d_{kl} \tag{32}$$

where

$$d_{kl}^2 = \sum_{i=1}^{n}\sum_{j=1}^{n}\left(a_{ij}(k) - a_{ij}(l)\right)^2 \tag{33}$$

Applying Constraints (10) and (11) to approximate Constraint (28),

$$w_i(k) = \frac{\sqrt[n]{\prod_{j=1}^{n} a_{ij}^{\infty}(k)}}{\sum_{m=1}^{n}\sqrt[n]{\prod_{j=1}^{n} a_{mj}^{\infty}(k)}} \tag{34}$$

$$\lambda(k) = \frac{1}{n}\sum_{i=1}^{n}\left(\frac{\sum_{j=1}^{n}(a_{ij}(k)w_j(k))}{w_i(k)}\right) \tag{35}$$

Let

$$b_i(k) = n\sqrt{\prod_{j=1}^{n} a_{ij}^{\infty}(k)} \tag{36}$$

and

$$\omega_i(k) = \frac{\sum_{j=1}^{n}\left(a_{ij}(k)w_j(k)\right)}{w_i(k)} \tag{37}$$

Then Constraints (34) and (35) can be simplified to

$$w_i(k)\sum_{m=1}^{n} b_m(k) = b_i(k) \tag{38}$$

and

$$n\lambda(k) = \sum_{i=1}^{n} \omega_i(k) \tag{39}$$

respectively, and the bi-objective MINLP problem can be expressed as follows.

(Bi-objective MINLP Model II)

$$\text{Max } Z_1 = \frac{1}{K}\sum_{k=1}^{K}(CR(\mathbf{A}) - CR(\mathbf{A}(k))) \tag{40}$$

$$\text{Max } Z_2 = \sum_{k=1}^{K-1}\sum_{l=k+1}^{K} d_{kl} \tag{41}$$

subject to

$$d_{kl}^2 = \sum_{i=1}^{n}\sum_{j=1}^{n}\left(a_{ij}(k) - a_{ij}(l)\right)^2; k = 1 \sim K-1; / = k \tag{42}$$

$$a_{ij} = \frac{\sum_{k=1}^{K} a_{ij}(k)}{K} \forall a_{ij} > 1, ij = 1 \sim n \tag{43}$$

$$a_{ij}(k)a_{ji}(k) = 1 \forall i, j = 1 \sim n; k = 1 \sim K \tag{44}$$

$$a_{ii}(k) = 1 \forall i = 1 \sim n; k = 1 \sim K \tag{45}$$

$$b_i^n(k) = \prod_{j=1}^{n} a_{ij}^{\infty}(k); i = 1 \sim n; k = 1 \sim K \tag{46}$$

$$w_i(k)\sum_{m=1}^{n} b_m(k) = b_i(k); i = 1 \sim n; k = 1 \sim K \tag{47}$$

$$\omega_i(k)w_i(k) = \sum_{j=1}^{n}\left(a_{ij}(k)w_j(k)\right); i = 1 \sim n; k = 1 \sim K \tag{48}$$

$$n\lambda(k) = \sum_{i=1}^{n} \omega_i(k); k = 1 \sim K \tag{49}$$

$$CR(\mathbf{A}(k)) \le CR(\mathbf{A}); k = 1 \sim K \tag{50}$$

$$CR(\mathbf{A}(k)) = \frac{\lambda(k) - n}{(n-1)(0.0053n^3 - 0.1273n^2 + 1.051n - 1.6125)}; k = 1 \sim K \tag{51}$$

$$a_{ij}(k) \in \{1, \ldots, 9\} \forall a_{ij} > 1; ij = 1 \sim n; k = 1 \sim K \tag{52}$$

2.5. *Converting into a single-objective problem*

Various approaches can be employed to convert a bi-objective problem into a single-objective problem, including simultaneous (or Pareto), utility (or compromise), goal programming (or satisfying), hierarchical, and interactive approaches [40]. This study applies a goal programming (or satisfying) approach by changing the first objective function into a constraint,

$$\frac{1}{K}\sum_{k=1}^{K}(CR(\mathbf{A}) - CR(\mathbf{A}(k)) \ge \xi \tag{53}$$

and solving the subsequent single-objective MINLP problem as follows.

(Single-objective MINLP Model)

$$\text{Max } Z_2 = \sum_{k=1}^{K-1}\sum_{l=k+1}^{K} d_{kl} \tag{54}$$

subject to

$$d_{kl}^2 = \sum_{i=1}^{n}\sum_{j=1}^{n}\left(a_{ij}(k) - a_{ij}(l)\right)^2 k = 1 \sim K-1; / = k+1 \sim K \tag{55}$$

$$\frac{1}{K}\sum_{k=1}^{K}(CR(\mathbf{A}) - CR(\mathbf{A}(k)) \ge \xi; k = 1 \sim K \tag{56}$$

$$a_{ij} = \frac{\sum_{k=1}^{K} a_{ij}(k)}{K} \forall a_{ij} > 1; i,j = 1 \sim n \tag{57}$$

$$a_{ij}(k)a_{ji}(k) = 1 \forall i, j = 1 \sim n; k = 1 \sim K \tag{58}$$

$$a_{ii}(k) = 1 \forall i = 1 \sim n; k = 1 \sim K \tag{59}$$

$$b_i^n(k) = \prod_{j=1}^{n} a_{ij}^{\infty}(k);\ i = 1 \sim n; k = 1 \sim K \tag{60}$$

$$w_i(k)\sum_{m=1}^{n} b_m(k) = b_i(k);\ i = 1 \sim n; k = 1 \sim K \tag{61}$$

$$\omega_i(k)w_i(k) = \sum_{j=1}^{n}\left(a_{ij}(k)w_j(k)\right);\ i = 1 \sim n; k = 1 \sim K \tag{62}$$

$$n\lambda(k) = \sum_{i=1}^{n} \omega_i(k); k = 1 \sim K \tag{63}$$

$$CR(\mathbf{A}(k)) \le CR(\mathbf{A}); k = 1 \sim K \tag{64}$$

$$CR(\mathbf{A}(k)) = \frac{\lambda(k) - n}{(n-1)(0.0053n^3 - 0.1273n^2 + 1.051n - 1.6125)}; k = 1 \sim K \tag{65}$$

$$a_{ij}(k) \in \{1, \ldots, 9\} \forall a_{ij} > 1; i,j = 1 \sim n; k = 1 \sim K \tag{66}$$

The MINLP models are not easy to solve [41].

2.6. *GA*

GA have been extensively applied to help solve MINLP problems [42,43,44]. For this reason, we designed a GA algorithm to solve the single-objective MINLP problem. Fig. 3 shows a typical example. The original judgment matrix **A** has $a_{12} = 3$, $a_{13} = 4$, and $a_{23} = 1$, and can be decomposed into two sub-judgment matrices **A**(1) and **A**(2), with $a_{12}(1) = 2$, $a_{13}(1) = 6$, and $a_{23}(1) = 1$. **A**(2) can derived from **A**(1) as

$$a_{12}(2) = 2a_{12} - a_{12}(1) = 4$$

$$a_{13}(2) = 2a_{13} - a_{13}(1) = 2$$

$$a_{23}(2) = 2a_{23} - a_{23}(1) = 1$$

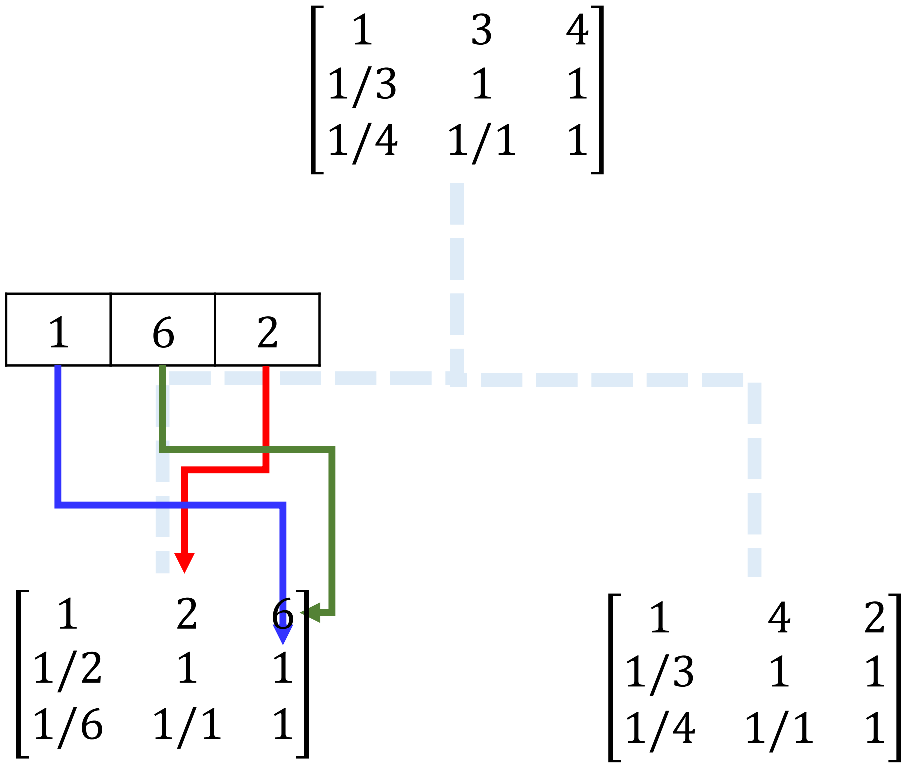

Fig. 3. Encoding of a chromosome.

A single chromosome with three genes within [1, 9] suffices to represent this decomposition, where A(1) is represented as [1 6 2].

Constraint (57) is incorporated into the objective function as a penalty term to form the fitness function

$$\text{Max}\, fitness = \sum_{k=1}^{K-1} \sum_{l=k+1}^{K} d_{kl} + M\left(\frac{1}{K}\sum_{k=1}^{K}(CR(\mathbf{A}) - CR(\mathbf{A}(k)) - \xi\right) \tag{67}$$

where M is a large positive value. If sub-judgment matrixes are well separated, d_{kl} is large and *fitness* increases. We expect that CR improves considerably after decomposition, i.e., $CR(\mathbf{A}) - CR(\mathbf{A}(k)) \geq \xi$, and hence *fitness* also increases.

Each population includes 10 chromosomes. Monte Carlo method is applied to choose parent chromosomes to be paired based on their fitness values. Specifically speaking, the probability of choosing chromosome z is set to

$$p(z) = \frac{fitness(z)}{\sum_{w=1}^{10} fitness(w)} \tag{68}$$

A single crossover point is chosen at random with crossover probability $= 0.4$. Offspring chromosomes are generated by exchanging their parent's genes between themselves until the crossover point is reached, as illustrated in Fig. 4.

Gene mutation is achieved by slightly incrementing or decrementing the gene's value, i.e., $5 \rightarrow 4$ or 6, and mutation rate $= 0.1$, as illustrated in Fig. 5.

Stopping criteria include

(1) 100 populations have been generated.
(2) The improvement in the average fitness of a population < 0.5.
(3) The improvement in the fitness of the best individual in a given generation < 0.1.

The GA algorithm is implemented in MATLAB using the eig() function to derive the eigenvalues and eigenvectors of judgment (or sub-judgment) matrixes.

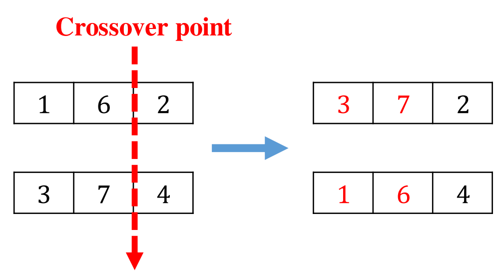

Fig. 4. The crossover mechanism.

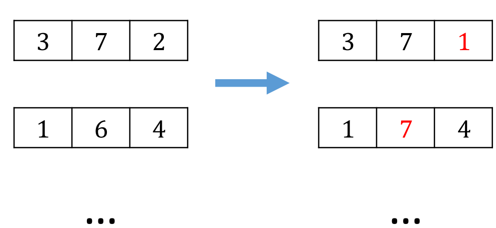

Fig. 5. The mutation mechanism.

3. Case Study: Supplier Selection

3.1. Case description

Although a manufacturer usually has multiple suppliers, most suppliers are similar and may be affected by the same risks [45]. Consequently, when the industry is hit, these suppliers will lose effectiveness at the same time, breaking the supply chain. The COVID-19 pandemic is an obvious example. Thus, manufacturers need to find diversified suppliers to eliminate such risks [46,47,48].

In this case, a wafer foundry would like to choose diversified alternative suppliers amid the COVID-19 pandemic, because the shipments from regular suppliers were backlogged owing to the limited capacity of cross-border transportation. To this end, the proposed bi-objective AHP-MINLP-GA approach was applied. In the literature, de Boer et al. [49] classified existing supplier selection methods into five categories: linear weighting, total cost-of-ownership, mathematical programming, statistical, and artificial intelligence methods. AHP and variants are linear weighting methods and are among the most widely used supplier selection methods [50,51,52,53,54,55,56]. Tirkolaee et al. [57] applied a fuzzy analytic network process (FANP) method to derive the priorities of criteria for evaluating a sustainable and reliable supplier. Then, they applied the fuzzy technique for order of preference by similarity to ideal solution (fuzzy TOPSIS) method to evaluate and compare the overall performances of suppliers. Tirkolaee et al. [58] proposed a similar method, in which a multi-objective mixed-integer linear programming (MOMILP) problem was solved to distribute the required quantity of raw materials among the chosen suppliers.

The alternative supplier selection problem considered in the present study assessed the performance of an alternative supplier according to the following criteria [46]

- pandemic severity [59],
- pandemic containment performance [59],
- company reputation [56,60,61,62],
- delivery speed [56,60,61,62], and
- level of buyer–supplier cooperation ([63]; . [64]).

A DM constructed the following judgment matrix for this problem,

$$\mathbf{A} = \begin{bmatrix} 1 & 5 & 3 & 3 & 7 \\ 1/5 & 1 & 1/3 & 1/9 & 1/7 \\ 1/3 & 3 & 1 & 1/3 & 1 \\ 1/3 & 9 & 3 & 1 & 7 \\ 1/7 & 7 & 1/1 & 1/7 & 1 \end{bmatrix}$$

$$\widetilde{O}(x, \mu_{\widetilde{O}}(x)) = \left\{ \left(\#5, \ \frac{1/0.150}{\max(1/0.150, 1/0.129)} \right), \ \left(\#1, \ \frac{1/0.150}{\max(1/0.150, 1/0.129)} \right) \right\}$$
$$= \{(\#5, \ 0.86), \ (\#1, \ 1)\}$$

Thus, $CR = 0.154$, i.e., the matrix is inconsistent. Therefore, the proposed approach was applied to enhance the consistency of the AHP analysis.

3.2. Application of the proposed methodology

First, the judgment matrix was decomposed into two sub-judgment matrices, and the required single-objective MINLP problem was solved using the GA algorithm on a PC equipped with i7-7700 CPU 3.6 GHz (Intel Corp., CA, USA) and 8 GB RAM. We set $\xi = 0.015$, and the optimal solution was

$$\mathbf{A}^*(1) = \begin{bmatrix} 1 & 4 & 2 & 1 & 5 \\ 1/4 & 1 & 1/3 & 1/9 & 1/9 \\ 1/2 & 3 & 1 & 1/4 & 1 \\ 1 & 9 & 4 & 1 & 9 \\ 1/5 & 9 & 1/1 & 1/9 & 1 \end{bmatrix}; \mathbf{A}^*(2) = \begin{bmatrix} 1 & 6 & 4 & 5 & 9 \\ 1/6 & 1 & 1/3 & 1/9 & 1/5 \\ 1/4 & 3 & 1 & 1/2 & 1 \\ 1/5 & 9 & 2 & 1 & 5 \\ 1/9 & 5 & 1 & 1/5 & 1 \end{bmatrix}$$

$Z_2^* = 8.763$; $CR(\mathbf{A}^*(1)) = 0.150$; and $CR(\mathbf{A}^*(2)) = 0.129$. The global optimality of the optimal solution was confirmed using an enumeration procedure in MATLAB R2017a (The MathWorks, Inc., MA, USA) on the same PC. The execution time was 11.94 s. The MATLAB code of the enumeration procedure is shown in Appendix A. The enumeration procedure generated all possible decomposition results, evaluated the improvement in the consistency ratio by each sub-judgment matrix, and measured the distance between two sub-judgment matrixes. Decomposition results with less improvement in the consistency ratio and shorter distance between sub-judgment matrixes were eliminated. The rest formed the Pareto optimal set.

Although we express

$$\mathbf{A} := \frac{\mathbf{A}^*(1) + \mathbf{A}^*(2)}{2}$$

A was not the arithmetic mean of $\mathbf{A}^*(1)$ and $\mathbf{A}^*(2)$, but rather **A** could be decomposed into $\mathbf{A}^*(1)$ and $\mathbf{A}^*(2)$. The consistency improved since both sub-judgment matrices were more consistent than the original judgment matrix.

The priorities of criteria derived from the two sub-judgment matrices were {0.279, 0.056, 0.101, 0.459, 0.105} and {0.555, 0.028, 0.098, 0.222, 0.097}, respectively. Two priority sets were generated, enabling the selection of multiple alternative suppliers that were simultaneously optimal from different viewpoints. The first viewpoint emphasized delivery speed, whereas the second viewpoint emphasized pandemic severity.

Table 2 summarizes the performances of six possible alternative suppliers on various criteria. All performances were scored as integers within [1, 10]. Two alternative suppliers (#5 and #1) were identified as simultaneously optimal solutions. Such results can be represented with a fuzzy set $\widetilde{O}$ to which the membership of belonging is set to

$$\mu_{\widetilde{O}}(x^*(k)) = \frac{1/CR(k)}{\max_l(1/CR(l))} \tag{69}$$

Therefore,

3.3. Comparison with existing methods

Table 4 summarizes the results obtained using a conventional AHP approach. In contrast to the proposed approach, the conventional AHP approach selected Alternative Suppliers #6 and #5, with only alternative supplier 6 achieving an optimal performance. In contrast, both Alternative Suppliers #5 and #1 selected using the proposed approach were top performers from different viewpoints.

We also applied the conventional ordered weighted average (OWA) method [65] to this problem for comparison. OWA sorts the performances of an alternative supplier in optimizing various criteria before aggregation. Weights assigned to these sorted performances depend on the decision strategy, as shown in Table 5. Table 6 summarizes the OWA results. None of the decision strategies yielded the same result as obtained using the proposed approach. Nevertheless, the “moderately optimistic” decision strategy led to OWA results close to those obtained using the proposed approach. However, only a single optimal alternative supplier (Alternative Supplier #6) was identified using the OWA

Table 2
Performances of six alternative suppliers in optimizing various criteria.

Alternative Supplier #	Pandemic Severity	Pandemic Containment Performance	Company Reputation	Delivery Speed	Level of Buyer–supplier Cooperation
1	7	7	8	6	3
2	5	9	9	6	7
3	5	7	3	8	7
4	4	6	8	6	9
5	5	6	4	9	9
6	5	7	8	8	8

Table 3
Selections based on the two viewpoints.

Point of View	Choice
$\mathbf{A}^*(1)$	Alternative supplier #5
$\mathbf{A}^*(2)$	Alternative supplier #1

method.

We also compared with the results obtained using the measure attractiveness based on categorical evaluation (MACBETH) method (Bana e Costa et al., 2005). MACBETH is similar to AHP in that both methods are ranking approaches based on pairwise comparison results performed by a DM. However, MACBETH uses an interval scale, whereas AHP adopts a ratio scale. The calculation process of MACBETH differs considerably from that of AHP. MACBETH adopts a comparison scale within [0, 8], rather than within [1, 9].

A quadratic programming (QP) problem was solved for the alternative supplier selection problem to derive the priorities of criteria, with results $\{w_i^*\} = \{0.353, 0.000, 0.184, 0.310, 0.153\}$. Alternative Supplier #6 was the top performer, then Alternative Supplier #5, similar to the result using OWA with a neutral decision strategy but different from the result using traditional AHP or the proposed approach.

Table 7 shows differences between the proposed methodology and existing methods for the case.

3.4. Parametric analysis

Table 8 shows the results of a parametric analysis to examine the effect of ξ on the existence of an optimal solution. Obviously, a careful selection of ξ is required to ensure the existence of valid solutions for improving *CR*.

3.5. Pareto solutions

We employed an enumeration procedure to generate all Pareto solutions to the bi-objective MINLP problem. We found 203 feasible solutions to the bi-objective MINLP problem, but only five were Pareto solutions, as shown in Table 9. Fig. 6 shows the corresponding approximate Pareto front. All Pareto solutions were simultaneously optimal. Therefore, in principle $5 \times 2 = 10$ simultaneously optimal alternative suppliers could be selected using the bi-objective AHP-MINLP-GA approach, which greatly enhanced the flexibility of alternative supplier selection.

Table 5
Weights assigned to the sorted performances.

Decision Strategy	Weights
Optimistic	{1.00, 0.00, 0.00, 0.00, 0.00}
Moderately Optimistic	{0.62, 0.14, 0.10, 0.08, 0.06}
Neutral	{0.20, 0.20, 0.20, 0.20, 0.20}
Moderately Pessimistic	{0.01, 0.06, 0.15, 0.30, 0.49}
Pessimistic	{0.00, 0.00, 0.01, 0.10, 0.89}

4. Discussion

The following conclusions and points were evident from the experimental results.

(1) Determining the best method was difficult by comparing the results obtained using various methods, since these methods resulted in different outcomes. Selecting multiple optimal alternative suppliers was only possible using the proposed methodology. However, the possibility cannot be attributed to the formation of numerous ties in comparing the performances of alternative suppliers but to the various viewpoints considered by the DM.
(2) Two distinct optimal alternative suppliers could be selected for each Pareto solution, which enhanced the flexibility of alternative supplier selection. Although the advantages of the proposed bi-criteria model over single-objective models were clear, it was difficult to exclude the possibility that two optimal alternative suppliers based on one Pareto solution might be similar to those based on another Pareto solution.
(3) Although alternative supplier selection based on priority sets with higher consistency (i.e., lower *CR*) is preferred, alternative supplier chosen based on a priority set with higher consistency is not necessarily superior to that based on a priority set with lower consistency.
(4) Although judgment matrix decomposition may be possible, decomposing a completely consistent matrix may worsen consistency. In addition, a judgment matrix with extreme values (i.e., 1 or 9) cannot be decomposed.
(5) The proposed methodology has two superior aspects compared with existing methods. First, selecting diversified alternative suppliers was only possible using the proposed methodology. In Table 7, Alternative Supplier #1 differed from other top performers and was selected only when the proposed methodology was applied. Second, the GA significantly enhanced the efficiency judgment of matrix decomposition. Enumeration takes tens of

Table 4
Results obtained using the conventional AHP approach.

Alternative Supplier #	Overall Performance	Sequence
1	6.389	3
2	6.056	4
3	6.016	5
4	5.593	6
5	6.590	2
6	6.610	1

Table 6
Results obtained using the OWA method.

Decision Strategy	Top 1 Alternative Supplier	Top 2 Alternative Supplier
Optimistic	#2, #4, #5	
Moderately Optimistic	#5	#4
Neutral	#6	#4, #5
Moderately Pessimistic	#6	#2
Pessimistic	#6	#2

Table 7
Differences between the proposed approach and existing methods.

Method	Number of Judgment Matrices	Number of Priority Sets	Number of Objectives	Top 1 Alternative Supplier	Top 2 Alternative Supplier
Conventional AHP	1	1	1	#6	#5
OWA (moderately optimistic)	-	1	-	#5	#4
MACBETH	1	1	1	#6	#5
The proposed methodology	1	2	2	#5, #1	#6

Table 8
Effect of ξ on the existence of optimal solutions.

Value of ξ	Existence of optimal solutions
0.10	Yes
0.15	Yes
0.20	No
0.25	No
0.30	No

minutes to hours to decompose a judgment matrix with dimensionality > 7, whereas GA usually requires only a few minutes.

(6) The effectiveness of a method was measured in terms of the distance between the two top performers. The proposed approach achieved a distance of 5.745, whereas OWA (moderately optimistic), conventional AHP, and MACBETH approaches achieved 5.099, 4.359, and 4.359, respectively. Thus, the proposed methodology maximized diversity. Table 10 summarizes the efficiency of a method measured in terms of the execution time. Since alternative supplier selection was not a time-critical task, the efficiency of the proposed methodology was considered acceptable.

The practical implications of the experimental results are discussed as follow:

(1) If the wafer foundry needed only one alternative supplier, then either of the two recommended alternative suppliers could be chosen, since they are simultaneously optimal. Another feasible way was to divide the required quantity of raw materials between the two alternative suppliers.

Table 9
Pareto solutions to the bi-objective MINLP problem.

Pareto Solution #	Z_1	Z_2
1	5.915E-03	10.630
2	6.332E-03	9.454
3	6.489E-03	9.425
4	6.884E-03	9.236
5	1.404E-02	8.993

(2) During the COVID-19 pandemic, the selected alternative suppliers may not be able to support the wafer foundry. Different types of alternative suppliers face different risks. Therefore, choosing diversified alternative suppliers may be a good way to reduce the risk that both alternative suppliers cannot support the wafer foundry.

4.1. *Another Case Study: Metro Tunnel Risk Assessment*

We also elaborated the effectiveness of the proposed methodology with a higher-dimensional case: metro tunnel risk assessment [66]. Fig. 5 shows that factors affecting metro tunnel construction risk assessment were categorized into a four-layer hierarchy. The second layer contained four risk factor categories A1–A4: investment, security, environmental, and construction risks, respectively. These categories were affected by five risk factors in the third layer B1–B5: collapse, water inrush, structural failure, surface deformation, and uneven settlement, respectively. Each of these risk factors was then affected by seven subfactors in the fourth layer C1–C7: spring group, groundwater, geological features, rock and oil properties, peripheral roads, neighboring buildings, and underground pipelines, respectively.

Table 11 summarizes the original judgment matrixes, which restricted values within very narrow ranges to increase the consistency. However, this also reduced the flexibility of decision making. Therefore, we applied the proposed methodology to decompose each judgment (or sub-judgment) matrix into two distinct sub-judgment matrixes with better consistency and wider ranges, as shown in Table 12. As a result, each risk factor category had at most 2 priorities; each risk factor had at most 4 priorities; and each subfactor could have up to 8 priorities. Thus, the DM has considerable planning flexibility to minimize metro tunnel risks.

5. Conclusions

Decision makers commonly hold multiple viewpoints when comparing factors pairwise. Conventional AHP assumes that the DM can effectively resolve conflicts among these viewpoints and produce a single result. However, this assumption is somewhat impractical, and DMs tend to generate inconsistent pairwise comparison results.

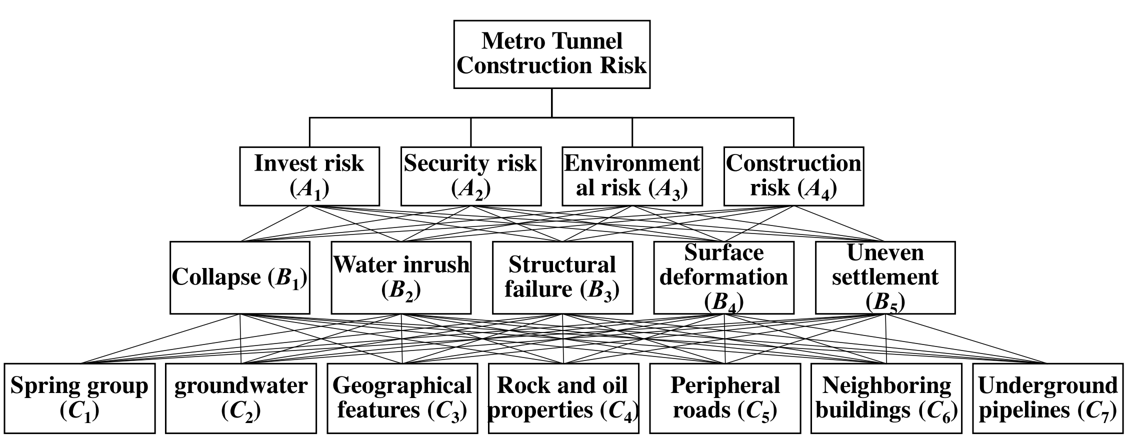

Fig. 6. Pareto solutions to the bi-objective MINLP problem.

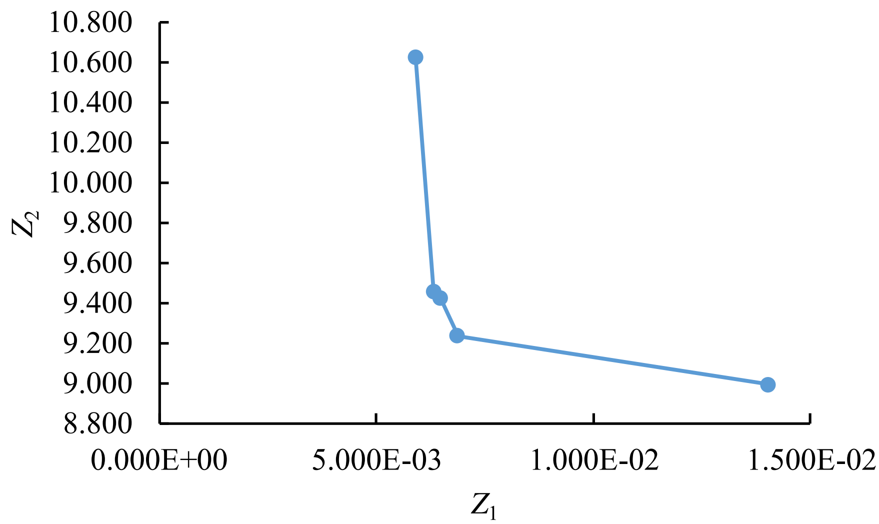

Fig. 7. The case of metro tunnel risk assessment.

Table 10
The execution time.

Method	Execution Time (s)
Conventional AHP	< 1
OWA	< 1
MACBETH	5
The proposed methodology (decomposition using the enumeration procedure)	11.94
The proposed methodology (decomposition using GA)	3

Therefore, this study proposed a bi-objective AHP-MINLP-GA approach that preserves the original AHP rules by decomposing an inconsistent judgment matrix into several more consistent sub-judgment matrices, where each sub-judgment matrix represents a unique DM viewpoint and is used to generate a priority set. Multiple alternatives are simultaneously selected as the optimal alternative for each viewpoint. The two objective functions optimized in the proposed bi-objective AHP-MINLP-GA approach are maximizing the average improvement in *CR* and maximizing the distance between sub-judgment matrices. In addition,

Table 11
Original judgment matrixes.

Subhierarchy	Judgment Matrix	*CR*
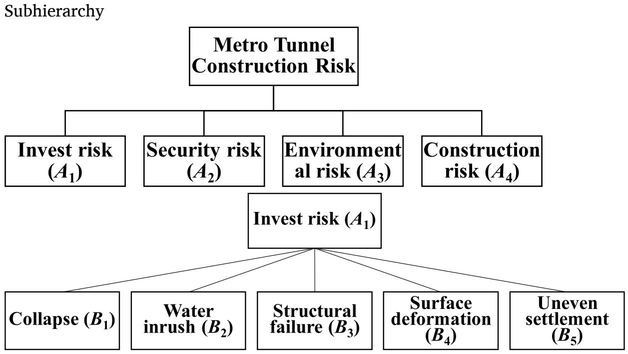	$\begin{bmatrix} 1 & 0.333 & 0.5 & 1 \\ 3 & 1 & 2 & 3 \\ 2 & 0.5 & 1 & 2 \\ 1 & 0.333 & 0.5 & 1 \end{bmatrix}$	0.004
	$\begin{bmatrix} 1 & 1 & 2 & 3 & 3 \\ 1 & 1 & 1 & 2 & 2 \\ 0.5 & 1 & 1 & 3 & 5 \\ 0.333 & 0.5 & 0.333 & 1 & 1 \\ 0.333 & 0.5 & 0.2 & 1 & 1 \end{bmatrix}$	0.037
…		

Table 12
Decomposition results.

Subhierarchy	Subjudgment Matrixes	*CR*
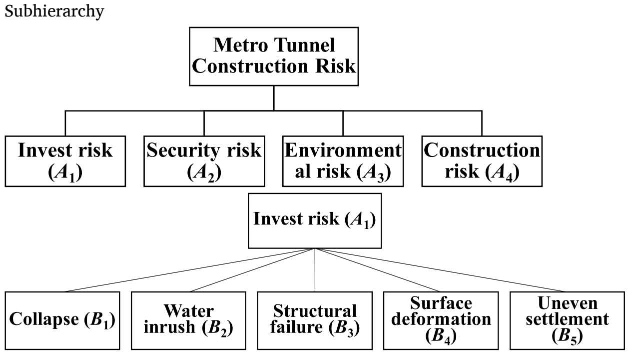	$\begin{bmatrix} 1 & 0.333 & 0.5 & 1 \\ 3 & 1 & 2 & 3 \\ 2 & 0.5 & 1 & 2 \\ 1 & 0.333 & 0.5 & 1 \end{bmatrix}, \begin{bmatrix} 1 & 0.333 & 0.5 & 1 \\ 3 & 1 & 2 & 3 \\ 2 & 0.5 & 1 & 2 \\ 1 & 0.333 & 0.5 & 1 \end{bmatrix}$	0.004, 0.004
	$\begin{bmatrix} 1 & 1 & 1 & 5 & 5 \\ 1 & 1 & 1 & 3 & 3 \\ 1 & 1 & 1 & 5 & 9 \\ 0.2 & 0.333 & 0.2 & 1 & 1 \\ 0.2 & 0.333 & 0.111 & 1 & 1 \end{bmatrix}, \begin{bmatrix} 1 & 1 & 3 & 1 & 1 \\ 1 & 1 & 1 & 1 & 1 \\ 0.333 & 1 & 1 & 1 & 1 \\ 1 & 1 & 1 & 1 & 1 \\ 1 & 1 & 1 & 1 & 1 \end{bmatrix}$	0.024, 0.034
…		

an enumeration procedure was established to identify all feasible solutions and Pareto optimal solutions to the bi-objective MINLP model, and a GA was applied to solve the resulting single-objective MINLP problem.

The proposed approach was applied to an alternative supplier selection problem amid the COVID-19 pandemic to examine its effectiveness. Experimental results verified the following outcomes.

(1) Multiple sub-judgment matrices could be generated from the judgment matrix, with all sub-judgment matrices being more consistent than the original judgment matrix.
(2) The distance between sub-judgment matrices was maximized, thereby diversifying the matrices.
(3) The bi-objective MINLP problem had a discrete feasible region with limited solutions, hence enumerating all feasible solutions was possible.
(4) The proposed approach selected distinct alternative suppliers for two different viewpoints, whereas existing methods could only select a single optimal alterative supplier. Suppliers selected using the proposed approach differed from those selected using existing methods.

The limitations of the proposed methodology include:

(1) It is not always possible to decompose a judgement matrix into subjudgment matrixes that are more consistent.
(2) As the size of the judgment matrix increases, it becomes more and more difficult to find the optimal decomposition result.

The pros and cons of the proposed methodology are:

(1) Using the proposed methodology, multiple alternatives that are quite different from each other can be selected. In contrast, the multiple alternatives selected using an existing method are usually similar – these alternatives all have good performances in optimizing high-priority criteria. The decision maker will feel compelled to accept some poorer alternatives.
(2) Involving the use of GA to solve a MINLP problem, the proposed methodology may be a bit complicated and difficult to be applied in practice.

Future research should resolve the inefficiency problem of the enumeration procedure for large problem sizes, and investigate the potential of different methods for decomposing a judgment matrix, such as geometric, harmonic, or weighted means.

Appendix A. Enumeration Procedure

```
t1=now;
A=[1 8 4 5 9;0.125 1 0.25 0.111 0.111;0.25 4 1 0.5 1; 0.2 9 2 1 5; 0.111 9 1 0.2 1];
[E V]=eig(A);
CI=(V(1,1)-5)/(5-1);
A1best=zeros(5,5);
A2best=zeros(5,5);
CI1best=0;
CI2best=0;
E1best=zeros(5,5);
E2best=zeros(5,5);
distbest=0;
for i1=7:9
for i2=1:7
for i3=1:9
for i4=9:9
for i5=1:7
for i6=1:1
for i7=9:9
for i8=1:3
for i9=1:9
for i10=9:9
A1=A;
A2=A;
A1(1,2)=i1; A1(2,1)=1/A1(1,2);
A1(1,3)=i2; A1(3,1)=1/A1(1,3);
…
A2(1,2)=2*A(1,2)-A1(1,2); A2(2,1)=1/A2(1,2);
A2(1,3)=2*A(1,3)-A1(1,3); A2(3,1)=1/A2(1,3);
…
[E2,V2]=eig(A2);
CI1=(V1(1,1)-5)/(5-1);
CI2=(V2(1,1)-5)/(5-1);
if CI1<=CI & CI2<=CI
A1
A2
dist=sqrt(sum(sum((A1-A2).^2)))
CI1
CI2
if dist>distbest
distbest=dist
A1best=A1
A2best=A2
```

(*continued on next page*)

(*continued*)

```
CI1best=CI1
CI2best=CI2
E1best=E1
E2best=E2
end
end
end
end
end
end
end
end
end
end
end
end
t2=now;
(t2-t1)*24*60*60;
```

References

[1] A. Banasik, J.M. Bloemhof-Ruwaard, A. Kanellopoulos, G.D.H. Claassen, J.G. van der Vorst, Multi-criteria decision making approaches for green supply chains: A review, Flexible Services and Manufacturing Journal 30 (3) (2018) 366–396.
[2] C.F. Chien, J.Z. Wu, Y.D. Weng, Modeling order assignment for semiconductor assembly hierarchical outsourcing and developing the decision support system, Flexible Services and Manufacturing Journal 22 (1-2) (2010) 109–139.
[3] T.L. Saaty, Decision making with the analytic hierarchy process, International journal of Services Sciences 1 (1) (2008) 83–98.
[4] J. Chen, C. Zhao, L. Chen, Collaborative filtering recommendation algorithm based on user correlation and evolutionary clustering, Complex & Intelligent Systems (2019) 1–10.
[5] M. Hasan, İ.E. Büyüktahtakın, E. Elamin, A multi-criteria ranking algorithm (MCRA) for determining breast cancer therapy, Omega 82 (2019) 83–101.
[6] T.L. Saaty, Analytic Network Process, Springer, US, 2013.
[7] Y.C. Wang, T. Chen, Y.L. Yeh, Advanced 3D printing technologies for the aircraft industry: a fuzzy systematic approach for assessing the critical factors, The International Journal of Advanced Manufacturing Technology 105 (10) (2019) 4059–4069.
[8] J. Wątróbski, J. Jankowski, P. Ziemba, A. Karczmarczyk, M. Zioło, Generalised framework for multi-criteria method selection, Omega 86 (2019) 107–124.
[9] O. Rahmati, A.N. Samani, M. Mahdavi, H.R. Pourghasemi, H. Zeinivand, Groundwater potential mapping at Kurdistan region of Iran using analytic hierarchy process and GIS, Arabian Journal of Geosciences 8 (9) (2015) 7059–7071.
[10] T. Höfer, Y. Sunak, H. Siddique, R. Madlener, Wind farm siting using a spatial Analytic Hierarchy Process approach: A case study of the Städteregion Aachen, Applied energy 163 (2016) 222–243.
[11] C.W. Lin, T. Chen, 3D printing technologies for enhancing the sustainability of an aircraft manufacturing or MRO company—a multi-expert partial consensus-FAHP analysis, The International Journal of Advanced Manufacturing Technology (2019) 1–10.
[12] P. Grošelj, L.Z. Stirn, N. Ayrilmis, M.K. Kuzman, Comparison of some aggregation techniques using group analytic hierarchy process, Expert Systems with Applications 42 (4) (2015) 2198–2204.
[13] W. Ossadnik, S. Schinke, R.H. Kaspar, Group aggregation techniques for analytic hierarchy process and analytic network process: a comparative analysis, Group Decision and Negotiation 25 (2) (2016) 421–457.
[14] W. Ho, X. Ma, The state-of-the-art integrations and applications of the analytic hierarchy process, European Journal of Operational Research 267 (2) (2018) 399–414.
[15] T.C.T. Chen, Evaluating the sustainability of a smart technology application to mobile health care: the FGM–ACO–FWA approach, Complex & Intelligent Systems (2019) 1–13.
[16] T.L. Saaty, There is no mathematical validity for using fuzzy number crunching in the analytic hierarchy process, Journal of Systems Science and Systems Engineering 15 (4) (2006) 457–464.
[17] B.S. Ahn, The analytic hierarchy process with interval preference statements, Omega 67 (2017) 177–185.
[18] L. Abdullah, L. Najib, Sustainable energy planning decision using the intuitionistic fuzzy analytic hierarchy process: Choosing energy technology in Malaysia, International Journal of Sustainable Energy 35 (4) (2016) 360–377.
[19] B. Zhu, Z. Xu, R. Zhang, M. Hong, Hesitant analytic hierarchy process, European Journal of Operational Research 250 (2) (2016) 602–614.
[20] M. Abdel-Basset, M. Mohamed, Y. Zhou, I. Hezam, Multi-criteria group decision making based on neutrosophic analytic hierarchy process, Journal of Intelligent & Fuzzy Systems 33 (6) (2017) 4055–4066.
[21] E. Ilbahar, A. Karaşan, S. Cebi, C. Kahraman, A novel approach to risk assessment for occupational health and safety using Pythagorean fuzzy AHP & fuzzy inference system, Safety Science 103 (2018) 124–136.
[22] T.C.T. Chen, Y.C. Lin, Diverse three-dimensional printing capacity planning for manufacturers, 67, Robotics and Computer-Integrated Manufacturing, 2021, 102052.
[23] Y.C. Lin, T. Chen, A multibelief analytic hierarchy process and nonlinear programming approach for diversifying product designs: Smart backpack design as an example, Proceedings of the Institution of Mechanical Engineers, Part B: Journal of Engineering Manufacture, 234 (6-7) (2020) 1044–1056.
[24] Business Performance Management Singapore, (2013). https://bpmsg.com/ahp-high-consistency-ratio/.
[25] J. Franek, A. Kresta, Judgment scales and consistency measure in AHP, Procedia Economics and Finance 12 (2014) 164–173.
[26] W.C. Wedley, Consistency prediction for incomplete AHP matrices, Mathematical and Computer Modelling 17 (4-5) (1993) 151–161.
[27] G. Crawford, C. Williams, A note on the analysis of subjective judgement matrices, Journal of Mathematical Psychology 29 (1985) 387–405.
[28] T.C. Wang, Y.H. Chen, Applying fuzzy linguistic preference relations to the improvement of consistency of fuzzy AHP, Information Sciences 178 (19) (2008) 3755–3765.
[29] A. Jeang, C.P. Chung, C.K. Hsieh, Simultaneous process mean and process tolerance determination with asymmetrical loss function, The International Journal of Advanced Manufacturing Technology 31 (7-8) (2007) 694–704.
[30] B. Sun, X. Zhou, N. Lin, Diversified binary relation-based fuzzy multigranulation rough set over two universes and application to multiple attribute group decision making, Information Fusion 55 (2020) 91–104.
[31] B. Sun, C. Qi, W. Ma, T. Wang, L. Zhang, C. Jiang, Variable precision diversified attribute multigranulation fuzzy rough set-based multi-attribute group decision making problems, Computers & Industrial Engineering 142 (2020), 106331.
[32] B. Sun, M. Zhang, T. Wang, X. Zhang, Diversified multiple attribute group decision-making based on multigranulation soft fuzzy rough set and TODIM method, Computational and Applied Mathematics 39 (3) (2020) 1–30.
[33] K. Honda, N. Yamamoto, S. Ubukata, A. Notsu, Noise rejection in MMMs-induced fuzzy co-clustering, Journal of Advanced Computational Intelligence and Intelligent Informatics 21 (7) (2017) 1144–1151.
[34] R. Logesh, V. Subramaniyaswamy, V. Vijayakumar, X.Z. Gao, G.G. Wang, Hybrid bio-inspired user clustering for the generation of diversified recommendations, Neural Computing and Applications 32 (7) (2020) 2487–2506.
[35] Y. Yan, G. Liu, S. Wang, J. Zhang, K. Zheng, Graph-based clustering and ranking for diversified image search, Multimedia Systems 23 (1) (2017) 41–52.
[36] Y.C. Lin, Y.C. Wang, T.C.T. Chen, H.F. Lin, Evaluating the suitability of a smart technology application for fall detection using a fuzzy collaborative intelligence approach, Mathematics 7 (11) (2019) 1097.
[37] H.C. Wu, T. Chen, C.H. Huang, A piecewise linear FGM approach for efficient and accurate FAHP analysis: Smart backpack design as an example, Mathematics 8 (8) (2020) 1319.
[38] Y. Dong, G. Zhang, W.C. Hong, Y. Xu, Consensus models for AHP group decision making under row geometric mean prioritization method, Decision Support Systems 49 (3) (2010) 281–289.
[39] G.H. Golub, C.F. Van Loan, Matrix Computations, Johns Hopkins, Baltimore, MD, 1996.
[40] E. Triantaphyllou, Multi-criteria decision making methods, Multi-criteria Decision Making Methods: A Comparative Study (2000) 5–21.
[41] Y.C. Wang, M.C. Chiu, T. Chen, A fuzzy nonlinear programming approach for planning energy-efficient wafer fabrication factories, Applied Soft Computing 95 (2020), 106506.
[42] K. Jankauskas, L.G. Papageorgiou, S.S. Farid, Fast genetic algorithm approaches to solving discrete-time mixed integer linear programming problems of capacity

planning and scheduling of biopharmaceutical manufacture, Computers & Chemical Engineering 121 (2019) 212–223.

[43] A.K. Maiti, A.K. Bhunia, M. Maiti, An application of real-coded genetic algorithm (RCGA) for mixed integer non-linear programming in two-storage multi-item inventory model with discount policy, Applied Mathematics and Computation 183 (2) (2006) 903–915.

[44] M. Nemati, M. Braun, S. Tenbohlen, Optimization of unit commitment and economic dispatch in microgrids based on genetic algorithm and mixed integer linear programming, Applied Energy 210 (2018) 944–963.

[45] D. Huang, T. Chen, M.J.J. Wang, A fuzzy set approach for event tree analysis, Fuzzy Sets and Systems 118 (1) (2001) 153–165.

[46] T. Chen, Y.C. Wang, H.C. Wu, Analyzing the impact of vaccine availability on alternative supplier selection amid the COVID-19 pandemic: A cFGM-FTOPSIS-FWI approach, Healthcare 9 (1) (2021) 71.

[47] G.Y. Gao, E. Xie, K.Z. Zhou, How does technological diversity in supplier network drive buyer innovation? Relational process and contingencies, Journal of Operations Management 36 (2015) 165–177.

[48] S.M. Ordoobadi, S. Wang, A multiple perspectives approach to supplier selection, Industrial Management & Data Systems 111 (4) (2011) 629–648.

[49] L. de Boer, E. Labro, P. Morlacchi, A review of methods supporting supplier selection, European Journal of Purchasing & Supply Management 7 (2) (2001) 75–89.

[50] F.T. Chan, N. Kumar, M.K. Tiwari, H.C. Lau, K.L. Choy, Global supplier selection: a fuzzy-AHP approach, International Journal of Production Research 46 (14) (2008) 3825–3857.

[51] X. Deng, Y. Hu, Y. Deng, S. Mahadevan, Supplier selection using AHP methodology extended by D numbers, Expert Systems with Applications 41 (1) (2014) 156–167.

[52] F. Dweiri, S. Kumar, S.A. Khan, V. Jain, Designing an integrated AHP based decision support system for supplier selection in automotive industry, Expert Systems with Applications 62 (2016) 273–283.

[53] C. Kahraman, U. Cebeci, Z. Ulukan, Multi-criteria supplier selection using fuzzy AHP, Logistics Information Management 16 (6) (2003) 382–394.

[54] O. Kilincci, S.A. Onal, Fuzzy AHP approach for supplier selection in a washing machine company, Expert Systems with Applications 38 (8) (2011) 9656–9664.

[55] P. Sirisawat, T. Kiatcharoenpol, Fuzzy AHP-TOPSIS approaches to prioritizing solutions for reverse logistics barriers, Computers & Industrial Engineering 117 (2018) 303–318.

[56] Y.C. Wang, T.C.T. Chen, A partial-consensus posterior-aggregation FAHP method—Supplier selection problem as an example, Mathematics 7 (2) (2019) 179.

[57] E.B. Tirkolaee, A. Mardani, Z. Dashtian, M. Soltani, G.W. Weber, A novel hybrid method using fuzzy decision making and multi-objective programming for sustainable-reliable supplier selection in two-echelon supply chain design, Journal of Cleaner Production 250 (2020), 119517.

[58] E.B. Tirkolaee, Z. Dashtian, G.W. Weber, H. Tomaskova, M. Soltani, N.S. Mousavi, An integrated decision-making approach for green supplier selection in an agri-food supply chain: threshold of robustness worthiness, Mathematics 9 (11) (2021) 1304.

[59] T. Chen, Y.C. Wang, M.C. Chiu, Assessing the robustness of a factory amid the COVID-19 pandemic: A fuzzy collaborative intelligence approach, Healthcare 8 (4) (2020) 481.

[60] R. Alikhani, S.A. Torabi, N. Altay, Strategic supplier selection under sustainability and risk criteria, International Journal of Production Economics 208 (2019) 69–82.

[61] S. Hosseini, N. Morshedlou, D. Ivanov, M.D. Sarder, K. Barker, A. Al Khaled, Resilient supplier selection and optimal order allocation under disruption risks, International Journal of Production Economics 213 (2019) 124–137.

[62] M. Yazdani, P. Chatterjee, E.K. Zavadskas, S.H. Zolfani, Integrated QFD-MCDM framework for green supplier selection, Journal of Cleaner Production 142 (2017) 3728–3740.

[63] M. Bensaou, Interorganizational cooperation: The role of information technology an empirical comparison of US and Japanese supplier relations, Inf. Syst. Res. 8 (1997) 107–124.

[64] K.K. Kim, S.H. Park, S.Y. Ryoo, S.K. Park, Inter-organizational cooperation in buyer–supplier relationships: Both perspectives, Journal of Business Research 63 (8) (2010) 863–869.

[65] R.R. Yager, J. Kacprzyk, The Ordered Weighted Averaging Operators: Theory and Applications, Springer Science & Business Media, 2012.

[66] H.M. Lyu, W.J. Sun, S.L. Shen, A.N. Zhou, Risk assessment using a new consulting process in fuzzy, AHP. Journal of Construction Engineering and Management 146 (3) (2020), 04019112.

A fuzzy optimization model for methane gas production from municipal solid waste

Srinivas, *Department of Electrical and Electronics Engineering, Aryan Institute of Engineering & Technology, Bhubaneswar, srinivas225@gmail.com*

Smruti Ranjan Panda, *Department of Electrical and Electronics Engineering, Raajdhani Engineering College, Bhubaneswar, sr_panda@outlook.com*

Arabinda Dash, *Department of Computer Scinece Engineering , Capital Engineering College, Bhubaneswar, arabindadash56@hotmail.com*

Prasanna Kumar Chhotaray, *Department of Computer Scinece Engineering , NM Institute of Engineering & Technology, Bhubaneswar, pkchhotaray85@gmail.com*

A R T I C L E I N F O

Keywords:
Municipal solid waste (MSW)
Optimization
Multi-period
Greenhouse gas (GHG) emission
Transportation
Waste
Waste management

A B S T R A C T

The availability of non-renewable fossil fuels in Jordan continues to decrease, which increases reliance on energy sources, such as, methane gas produced from municipal solid waste (MSW). Furthermore, during the COVID-19 pandemic, solid wastes were significantly increased, especially in lockdown periods and this increase requires an immediate response to this global emergency by improving MSW management system. Unfortunately, little previous research efforts have been directed to propose optimization models that optimize concurrently economic and environmental aspects with the utilization of the available resources from transportation trucks of different types and capacities. This research, therefore, develops an optimization model for efficient MSW management system to increase the percentage of waste transported from multiple depots to anaerobic digestion plants (ADP) or recycling centers. The objective function of the optimization model is two-fold; maximizing quantities of transported waste and minimizing both transportation costs and greenhouse gas (GHG) emissions generated from different types of transport trucks over a six-day period. A case study was presented, where the optimization results showed that on average 1236.36 mega Watt-hour (MWh) of energy potential at a minimal average processing cost of 165.22 $/ton could be generated from transported 3540 tons of waste over six days. Such energy can be utilized to promote sustainability and develop an eco-city powered by renewable energy. In conclusion, the proposed model is found efficient in enhancing the performance of the existing MSW and results in significant reductions in environmental impacts and transportation costs and maximizing trucks and facilities utilizations.

1. Introduction

For low-income countries, Municipal Solid Waste (MSW) management is a critical issue, which impacts the environment, socio-economic, health, aesthetics, and infrastructure, due to the generated volume of wastes, treatment, and disposal methods. Typically, the MSW system deals with wastes from its source of generation to final disposal, including all the operations and transformation of this waste [1]. Typically, the MSW has several sources, i.e., residential, commercial, and municipal services [2], which makes the management of MSW a persistent challenge for many developing countries [3].

Practically, MSW landfills cause very harmful effects on the environment and hence many treatment methods, including recycling, incineration, and mechanical biological treatment, can be implemented to reduce negative environmental impacts [4]. The decomposition of organic wastes via anaerobic processes produced methane gas. Although, the upgrading process of emitted gases to methane gas is complex and expensive, the generated methane gas can be used as energy to promote sustainability.

Over the years, the net amount of MSW generated and its impact on the environment in Jordan have increased significantly [5]. Studies showed [6] that around 70–90% of waste was collected, but only about 5–10% of solid waste has been recycled. A major problem is that this system does not include separation of the recyclable and non-recyclable solid waste. Ideally, waste separation requires strong individual's commitment, long-term information, and educational campaigns [6], however weak initiatives have been directed towards these aspects in Jordan. Further, the current MSW management lacks critical dedicated facilities, such as, recycling centers, and aerobic digestion plants, which are necessary to increase the ability of controlling and utilizing dumped quantities of generated solid waste. As a result, large amounts of waste are accumulated in landfills, which alerts decision makers for the necessity of establishing of recycling centers, and aerobic digestion plant and developing cost-effective and environmentally friendly transportation system. Moreover, the existing waste transportation system between facilities suffers poor planning of transportation trucks, which may lead to negative impacts on environment due to excessive number of trips between facilities and incurs high transportation costs. In order to improve the current MSW management system and enhance its efficiency, this research analyzes the effectiveness of the current MSW and then develops an optimization model to maximize methane gas collection in MSW management system through maximizing transported waste and minimizing both transportation costs and greenhouse gas emissions while considering truck types and capacities. The remaining of this paper including the introduction is outlined as follows. Section 2 presents literature review. Section 3 develops the optimization model. Section 4 illustrates the optimization model and discusses research results. Section 5 summarizes research conclusions. The results of this research can provide great assistance to decision makers in Jordanian municipalities on how to establish and develop a sustainable MSW management system.

2. Literature review

Recently, the MSW management has received significant research attention. For example, Badran and El-Haggar [1] proposed a mixed integer programming model for a municipal solid waste management system in Port Said, Egypt. It included the use of the concept of collection stations, which have not yet been used in Egypt. The results showed that the best model would include 27 collection stations of 15-ton daily capacity and 2 collection stations of 10-ton daily capacity. Any transfer of waste between the collection station and the landfill should not occur. Mora et al. [7] presented a mixed integer linear model to reduce the economic and environmental impacts by minimizing different costs at 'kerbside' waste collection system in a municipality in Italy. A heuristic procedure was applied to obtain some admissible solutions of the real problem. Five alternative configurations of kerbside system, diverging in number of sub-areas, synchrony of vehicles and directionality of the arcs, were compared in an economic point of view. Finally, Life-Cycle Assessment was used as a tool to compare the overall potential environmental impacts of the alternative of kerbside collection systems and to compare the kerbside system with the traditional bring one. Põldnurk [8] assessed the environmental and economic feasibility of source sorting paper and bio-waste in rural municipalities, improvement of administrative efficiency, and economic cost-effectiveness resulting in reorganization of waste management administration, and optimization options of the municipal waste collection logistics through inter-municipal waste collection districts. The results showed that in rural areas central collection of sources sorted bio-waste is not economically and environmentally feasible, however the central collection of source-sorted paper waste may be considered environmentally beneficial if applied through inter-municipal cooperation. Zhao and Zhu [9] developed a multi-depot vehicle-routing model with the minimization of total cost and total risk through two-commodity flow formulation, and simultaneous of planning tours and vehicle acquisitions for the explosive waste collection and designing the return-trips between collection centers and recycling centers. A case study in Nanchuan of South-west China and related test instances were presented to elucidate their developed approach. Habibi et al. [3] proposed a multi-objective robust optimization model for a MSW management system and addressed the economic, environmental, and social perspectives simultaneously by minimizing the total cost, the greenhouse gas emission, and the resulting visual pollution. Their model was validated using real data for long-term planning of Tehran's MSW management system by examining five candidate sites for the construction of new facilities. Trochu et al. [10] addressed the reverse logistics network design problem under environmental policies targeting recycled wood materials from the construction, renovation, and demolition (CRD) industry. The main objective was to determine the location and the capacities of the sorting facilities to ensure compliance with the new regulation and prevent the wood from being massively landfilled using a mixed-integer linear programming model (MILP) to minimize the total cost of the wood recycling process collected from CRD sites. The proposed MILP model was applied for a case study in the CRD industry within the province of Quebec, Canada. Tsai et al. [11] applied exploratory factor analysis to test the validity and reliability of MSW attributes of cities in Vietnam under uncertainty. Fuzzy set theory was used to translate the linguistic references into the qualitative attributes of MSW management. The decision-making trial and evaluation laboratory was used to address the interrelationships among the attributes. The causal interrelationships among 14 attributes were identified. The results showed that technical integration and social acceptability were the aspects that drive MSW management, while treatment innovations, safety and health, economic benefits, and technology functionality and appropriateness were determined to be the linkage criteria. Finally, the distinctions between cities were presented. Tsai et al. [12] presented a systematic data-driven bibliometric analysis on MSW management as a foundation in a circular economy and applied the entropy weight method to convert the frequencies to weights and performed regional comparisons based on a database. A bibliographic coupling analysis was conducted and revealed that Africa and North America have less studies than other regions. Xiao et al. [13] proposed system dynamic model, which simulates the entire process of MSW production, sorting, collection, and final treatment and then analyzed policy impacts on MSW management from a dynamic and complex perspective in Shanghai. Seven scenarios were set to simulate the impacts of these policies. Results showed that economic policy has the largest impact on future MSW management, where MSW generation in 2035 will decline by 3.25 million tons if Gross Domestic Production growth rate decrease by 1%. Istrate et al. [14] fulfilled the review on published life-cycle assessment studies on MSW management systems with the aim of identifying waste-to-energy solutions and their impact on the system's environmental performance. Discrepancies were observed with respect to the environmental consequences of both the diversion of organic waste from incineration to anaerobic digestion and the diversion of waste from incineration to mechanical-biological treatment plants. Deus et al. [15] developed an aggregate indicator for environmental impact assessment of MSW management in the small municipalities of the state of Sao Paulo (Brazil). Additionally, the study aimed at creating a classification of the municipalities considered to identify the best management practices. The results showed that the average waste generation was 223.89 kg, the average carbon dioxide equivalent (CO2e) emissions was 0.166 tons (inhabitant−1 year−1) and the average amount of energy savings was 51.37 kWh. Tong et al. [16] employed a system thinking approach to analyze the crucial roles of the informal sector in SWM system in Vietnam. The analysis was built on the field survey including elements and key driving forces of the systems with 36 scrap dealers, 127 scrap buyers, and 760 households and in-depth interviews with experts in the Mekong Delta region, Vietnam. Results stated that informal systems should be integrated into the SWM process. Batur et al. [17] formulated a mixed integer linear programming model for long-term planning of municipal solid waste management system taking into consideration different process, capacity, and location possibilities that may occur in complex waste management processes at the same time. The results that the developed model provides significant convenience for the multi-objective optimization of financial-environmental-social costs and the solution of some uncertainty problems of decision-making tools, such as, life cycle assessment. Iyamu et al. [18] reviewed the common themes limiting MSW management sustainability in the BRIC (Brazil, Russia, India and China) countries, as well as the historical transition of MSW management to a sustainable level in some high-income countries such as United States, Japan, Denmark, and Australia. They focused on the interaction of MSW management with technology systems, socioeconomic factors, related environmental issues, influence on policy and decision making. The key MSWM findings was used to develop a thematic framework, underpinned by the different interacting factors of policy; environmental; socio-economic; and technology. Pinha and Sagawa [19] presented a system dynamics model for MSW management which involved resources, destinations of waste and cost structure of service/system. As a case study, the context of a Brazilian city of 230, 000 inhabitants was modelled and scenarios for 10 years were proposed. The scenario that presented better results with feasible investments prescribes an increase from 8.5% to 15% in the public collection of dry waste together with a productivity improvement of the sorting process. The simulations showed that the revenues from the recyclables do not cover the expenditures of the service provider and allowed pointing out scenarios that make the provider less dependent of governmental subsidy. Paul and Bussemaker [20] developed a web-based decision support system that can be used in planning and management of MSW for assessing the suitability of waste valorization in a particular location, such as, waste types, waste quantities and related waste contractors in England. Waste market opportunities and circular economy partners were also identified through the web application and these results were presented in context of waste-derived supply chain decisions. Hajar et al. [21] examined the development of the MSW management sector in Jordan from sustainability standpoint and developed potential scenarios to attain Jordan Vision 2025 target and gradually place this sector on a green growth path. The Sustainability Window analysis tool was used to assess the sustainability of the studied sector over the 2010–2015 period. Three scenarios were proposed and compared using the Sustainability Window tool: Mechanical biological treatment-anaerobic digestion, mechanical biological treatment-composting, and incineration. It was concluded from the Sustainability Window analysis that the 2010–2015 Jordanian municipal solid waste sector growth did not fulfill all sustainability criteria. Pinupolu and raja Kommineni [22] suggested a method of MSW management through public-private partnership (PPP) for Vijayawada city, which faced the problem of disposal and handling of municipal solid waste. Installation cost, land required for the proposed solid waste treatment and population were assessed by the geometrical progression method for the anticipated year 2051. Results indicated that the total quantity of evaluated solid waste created in the year 2051 is 2788 tons/day. Sarbassov et al. [23] performed compositional analysis of the municipal solid waste produced at the Astana International Airport and evaluated different waste management scenarios in terms of greenhouse gas emissions. Recyclable and combustible fractions were found to be the major fractions (over 50%) of the total municipal solid waste generated in the Astana International Airport. Four base greenhouse gas emissions scenarios were proposed and discussed. Viau et al. [24] aimed to critically evaluate the modelling of substitution in life cycle cost of recovered material from MSW management systems. They performed a systematic analysis of 51 life cycle assessment studies on MSW management systems published in the peer-reviewed literature and found that 22% of the substitution ratios are only implicitly expressed. Finally, guidance for the documentation of substitution ratios, with the aim of reaching more credible and robust analyses were developed. Kulkarni and Anantharama [25] presented a global backdrop of MSW management during COVID-19 outbreak and examined various aspects of MSW management. The data and information were collected from several scientific research papers from different disciplines, publications from governments and multilateral agencies and media reports. They presented challenges and opportunities in the aftermath of the ongoing pandemic and recommended alternatives approaches for MSW treatment and disposal and outlines the future scope of work to achieve sustainable waste management during and aftermath of the pandemics. Lately during the COVID-19 crisis, the transition from fossil fuel energy sources to green energy sources is urgent and crucial issue for globe to address the emergency pandemics and secure sustainable economies. Thus, new studies for generating energy were considered from different green sources such as Mostafaeipour et al. [26] who studied the feasibility of a new power generation system from wind for urban applications. Also, Rezaei et al. [27] evaluated the production of hydrogen by establishing hybrid wind and solar power plants. With the same manner, Wang et al. [28] considered the solar energy by identifying optimal sites for constructing the solar photovoltaic panels. Wang et al. [29] offered an assessment approach for cleaner energy sources using data envelopment analysis and fuzzy model.

Recently in the MSW management system, little research efforts were directed to develop optimization models with multiple objective functions that integrate the concurrent economic and environmental aspects with the utilization of the available resources from transportation trucks. In addition, most of the proposed MSW management system ignored truck types with different capacity and GHG emission for each type. Therefore, this paper proposes optimization model with multiple objective functions, including, minimizing total transportation, minimizing GHG emissions and unfilled trucks' capacities, maximizing total transported quantities, and maximizing satisfaction levels on utilization of collection stations and recycling centers, while considering various truck types and capacities for transporting collected and processed waste quantities.

3. Optimization model development

The key elements of solid waste chain are shown in Fig. 1, which includes I depots; i= [1, …, I], J collection stations; j= [1, …, J], R recycling plants; r= [1, …, R], L landfills, l= [1, …, L], and M anaerobic digestion plants; m= [1, …, M]. In any selected area, the waste bins will be divided into clusters which are assigned to depots. The trucks will collect wastes from each cluster's bins and accumulate wastes in the assigned depot of this cluster [30]. Then, waste will be transported from depot i to collection station j for processing. Because waste separation at source is not applicable in many areas, the waste separation is performed in collection stations to sort the recyclable and non-recyclable wastes. After processing, recyclable waste is transported from collection station j to recycling center r, whereas non-recyclable waste is transported to the L landfill. Finally, the organic recyclable waste is converted to a special compost amendment, which is transported from recycling center r to anaerobic digestion plant m. For tth period, the amount of waste presented in each stage from previous period, is defined as beginning inventories, $E^{b}_{(t-1)}$, while the amount of waste that will be remained in each stage for the present period, is defined as ending inventories, E^{f}_{t}, and both inventories are considered. Let NT^{u}_{ijt}, NT^{u}_{jlt}, and NT^{u}_{rmt} denote the number of trips taken by truck u at day t for transporting waste from the $i\underline{th}$ depot to the $j\underline{th}$ collection station; the $j\underline{th}$ collection station to the $r\underline{th}$ recycling center; the $j\underline{th}$ collection station to the $l\underline{th}$ landfill; and the $r\underline{th}$ recycling center to the $m\underline{th}$ anaerobic digestion plant, respectively. Let GH^{I}, GH^{J}, GH^{R} and GH^{L} denote the amount of GHG emitted from processing one ton of waste (g/ton) at the depots, collection stations, recycling centers and landfills, respectively. Let GH^{u} denotes the amount of GHG emitted (g/km) by truck type u. Each stage has its own associated GHG emissions resulting from processing of waste, transportation of waste in trucks, or both as shown in Fig. 2.

It is assumed that: *(i)* waste is separated and sorted at collection stations, *(ii)* fixed cost daily rates for depots, collection stations, recycling centers, landfills, and anaerobic digestion plants are calculated as total fixed cost divided by expected economic lifespan in days, *(iii)* variable rates ($/ton) of depots, collection stations, recycling centers, landfills, and anaerobic digestion plants are calculated as operational costs per ton divided by the daily capacity of the collection stations, *(iv)* fuel and maintenance costs are proportional to traveled distance, *(v)* distances are measured from the centroids of the destinations, and *(vi)* the beginning inventory at the first period is zero for all stages.

3.1. Model description

There are several decision variables and parameters are shown in Appendix A (Nomenclature). Let FC_i, FC_j, FC_r, FC_l and FC_m denote the fixed costs per day t for depots, collection stations, landfills, recycling centers and anaerobic digestion plants, respectively. Then, the total

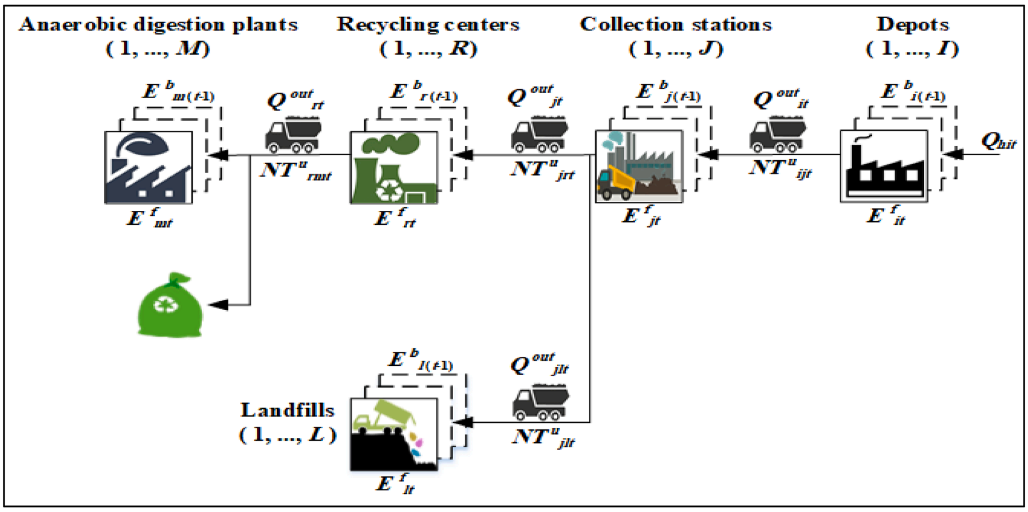

Fig. 1. Illustration of stages for the optimization model.

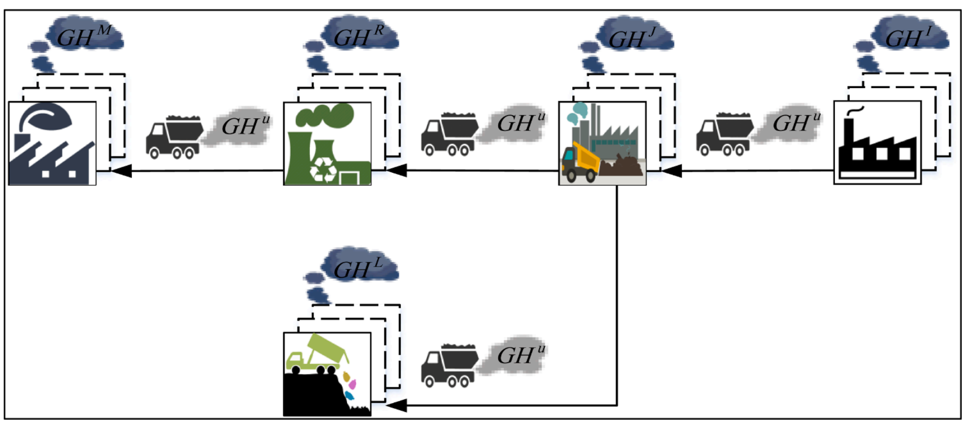

Fig. 2. Illustration of stages for the optimization model.

daily fixed cost, TFC, incurred in the system is calculated as given in Eq. (1).

$$TFC = \sum_{i=1}^{I} FC_i + \sum_{j=1}^{J} FC_j + \sum_{r=1}^{R} FC_r + \sum_{l=1}^{L} FL_l + \sum_{m=1}^{M} FC_m \quad (1)$$

Variable costs are incurred due to processing waste in each stage on day t. Let v_j, v_r, v_l, and v_m denote the variable costs per ton of the processing for the collection stations, recycling centers, landfills, and anaerobic digestion plants, respectively. Also, let Q_{jt}, Q_{rt}, Q_{lt} and Q_{mt} denote the total waste quantities at collection station j, recycling center r, landfills l, and anaerobic digestion plant m on day t, respectively. Then, the total daily variable cost, TVC, is calculated as stated in Eq. (2):

$$TVC = \sum_{t=1}^{T}\sum_{j=1}^{J} v_j \times Q_{jt} + \sum_{t=1}^{T}\sum_{r=1}^{R} v_r \times Q_{rt} + \sum_{t=1}^{T}\sum_{l=1}^{L} v_l \times Q_{lt} + \sum_{t=1}^{T} \times \sum_{m=1}^{M} v_m \times Q_{mt} \quad (2)$$

The total transportation cost of waste quantities is calculated by multiplying the transportation cost rate (*$/ton.km*) by the distance travelled and quantity carried by truck type u. Let α-denotes the cost rate of transportation (*$/ton.km*). Also, let d_{ij}, d_{jr}, d_{jl} and d_{rm} denote the distance travelled from depot i to collection station j, from collection station j to recycling center r and to landfill l, and from recycling center r to anaerobic digestion plant m, respectively. Finally, let Q_{ijt}, Q_{jrt}, Q_{jlt} and Q_{rmt} denote the quantity of waste transported on day t from depot I to collection station j, from collection station j to recycling center r, and to landfill l, and from recycling center r to anaerobic digestion plant m, respectively. The total cost of transporting waste quantities, TQC, is estimated using Eq. (3).

$$TQC = \alpha \times \left(\sum_{t=1}^{T}\sum_{i=1}^{I}\sum_{j=1}^{J} d_{ij} \times Q_{ijt} + \sum_{t=1}^{T}\sum_{j=1}^{J}\sum_{r=1}^{R} d_{jr} \times Q_{jrt} + \sum_{t=1}^{T}\sum_{j=1}^{J} \times \sum_{l=1}^{L} d_{jl} \times Q_{jlt} + \sum_{t=1}^{T}\sum_{r=1}^{R}\sum_{m=1}^{M} d_{rm} \times Q_{rmt} \right) \quad (3)$$

The total cost of fuel consumption is calculated by multiplying the unit cost of fuel, τ ($/L), by fuel consumed (*Liter/km*) by U truck types, travelled distance between any two stations, and number of trips over T days. Let TC_u denotes the fuel consumption of truck type u. Then, the total cost, TTC, of fuel consumption by all U trucks between all stages over T days is obtained as given in Eq. (4).

$$TTC = \tau \times \left(\sum_{u=1}^{U} \sum_{t=1}^{T} \sum_{i=1}^{I} \sum_{j=1}^{J} TC_u \times d_{ij} \times NT_{uij} + \sum_{u=1}^{U} \sum_{t=1}^{T} \sum_{j=1}^{J} \sum_{l=1}^{L} TC_u \times d_{jl} \times NT_{ujl} + \sum_{u=1}^{U} \sum_{t=1}^{T} \sum_{j=1}^{J} \sum_{r=1}^{R} TC_u \times d_{jr} \times NT_{ujr} + \sum_{u=1}^{U} \sum_{t=1}^{T} \sum_{r=1}^{R} \sum_{m=1}^{M} TC_u \times d_{rm} \times NT_{urm} \right) \tag{4}$$

Note that the transportation cost depends on a cost rate of the transported quantities. Consequently, if the quantities transported increased then the transportation cost will increase proportionally. While the fuel consumption cost depends on the travelled distance by each operated truck. Realistically, the cost rate for transported quantities is different from the fuel consumption cost.

Let GH^I, GH^J, GH^R, GH^L and GH^M denote the amount of GHG emitted from processing one ton of waste (g/ton) at I depots, J collection stations, R recycling centers, L landfills and M anaerobic digestion plants, respectively. Then, the total amount of GHG emissions, GHE, in the system is calculated as stated in Eq. (5).

$$GHE = GH^I \times \sum_{t=1}^{T} \sum_{i=1}^{I} Q_{it} + GH^J \times \sum_{t=1}^{T} \sum_{j=1}^{J} Q_{jt} + GH^R \times \sum_{t=1}^{T} \sum_{r=1}^{R} Q_{rt} + GH^L \times \sum_{t=1}^{T} \sum_{l=1}^{L} Q_{lt} + GH^M \times \sum_{t=1}^{T} \sum_{m=1}^{M} Q_{mt} \tag{5}$$

Let NT^u_{ijt}, NT^u_{jlt}, and NT^u_{rmt} denote the number of trips taken by truck type u to transport waste on day t from depot i to collection station j, the collection station j to recycling center r; from collection station j to landfill l, and from recycling center r to anaerobic digestion plant m, respectively. The GHG emitted from U truck types over T days is calculated by multiplying the amount of GHG emissions by both the total distance travelled between any pair of stages and number of trips. Then, the total amount, GHT, of GHG emitted due to transporting waste from depot i to anaerobic digestion plant m, is estimated as in Eq. (6):

$$GHT = GH^u \times \left(\sum_{u=1}^{U} \sum_{t=1}^{T} \sum_{i=1}^{I} \sum_{j=1}^{J} d_{ij} \times NT_{uijt} + \sum_{u=1}^{U} \sum_{t=1}^{T} \sum_{j=1}^{J} \times \sum_{r=1}^{R} d_{jr} \times NT_{ujrt} + \sum_{u=1}^{U} \sum_{t=1}^{T} \sum_{j=1}^{J} \sum_{l=1}^{L} d_{jl} \times NT_{ujlt} + \sum_{u=1}^{U} \sum_{t=1}^{T} \sum_{r=1}^{R} \times \sum_{m=1}^{M} d_{rm} \times NT_{urmt} \right) \tag{6}$$

The unfilled capacity in transportation truck type u is calculated by subtracting the total transported quantity between two stages by truck type u on day t from its capacity. Let R_u denotes the capacity of truck type u. Then, the total unfilled capacities, Q^{TOT}, for U truck types over T days between all pairs of stages is calculated using Eq. (7).

$$Q^{TOT} = \sum_{u=1}^{U} \sum_{t=1}^{T} \sum_{i=1}^{I} \sum_{j=1}^{J} \left(\left(NT^u_{ijt} \times R_u \right) - Q_{ijt} \right) + \sum_{u=1}^{U} \sum_{t=1}^{T} \sum_{j=1}^{J} \sum_{l=1}^{L} \left(\left(NT^u_{jlt} \times R_u \right) - Q_{jlt} \right) + \sum_{u=1}^{U} \sum_{t=1}^{T} \sum_{j=1}^{J} \sum_{r=1}^{R} \left(\left(NT^u_{jrt} \times R_u \right) - Q_{jrt} \right) + \sum_{u=1}^{U} \sum_{t=1}^{T} \sum_{r=1}^{R} \sum_{m=1}^{M} \left(\left(NT^u_{rmt} \times R_u \right) - Q_{rmt} \right) \tag{7}$$

Utilizing formulas 1 to 7, two objective functions will be developed; the first objective function, Z_1, aims at minimizing the total costs and environmental impacts of the waste management system as shown in Formula (8). The second objective function, Z_2, seeks maximizing the total of transported quantities between all pairs of stages and thereby optimizing methane production as stated in Formula (9).

$$Z_1 = \left(TFC + TVC + TQC + TTC + GHE + GHT + Q^{TOT} \right) \quad Min \ Z_1 \tag{8}$$

$$Z_2 = \sum_{t=1}^{T} \sum_{i=1}^{I} \sum_{j=1}^{J} Q_{ijt} + \sum_{t=1}^{T} \sum_{j=1}^{J} \sum_{r=1}^{R} Q_{jrt} + \sum_{t=1}^{T} \sum_{r=1}^{R} \sum_{m=1}^{M} Q_{rmt} \quad MaxZ_2 \tag{9}$$

The main constraints are as follows:

1 The waste quantity, Q_{it}, of at depot i on day t is equal to the total quantity, Q_{hit}, of waste transported to depot i from different areas on day t and the beginning inventory at depot i, $E^b_{i(t-1)}$, from previous day (t-1). That is in Eq. (10).

$$\sum_{h=1}^{H} Q_{hit} + E^b_{i(t-1)} = Q_{it} \tag{10}$$

2 The total quantity, Q_{it}, of waste at depot i on day t shall not exceed its capacity, C_i, as stated in Inequality (11).

$$Q_{it} \le C_i, \forall i, t \tag{11}$$

3 Let NTA_{uijt} denotes the number of trucks that travel from depot i to collection station j on day t. The total quantity transported from depot i to collection station j on day t shall not exceed capacity of truck type u as stated in Inequality (12).

$$\sum_{j=1}^{J} Q_{ijt} \le \sum_{u=1}^{U} NTA_{uijt} \times R_u, \forall i, t \tag{12}$$

4 The total quantity of waste, Q_{ijt}, transported from depot i to collection station j on day t is equal to the waste quantity, Q^{out}_{it}, leaving from depot i on day t as stated in Eq. (13).

$$\sum_{j=1}^{J} Q_{ijt} = \sum_{j=1}^{J} Q_{it}^{out}, \forall i, t \tag{13}$$

5 The number of trips to J collection stations on day t shall not exceed the number of available trips on the same day as given by Inequality (14).

$$\sum_{j=1}^{J} NT_{uijt} \leq NTA_{uijt}, \forall i, t, u \tag{14}$$

6 The ending inventory, E^f_{it}, at depot i on day t is equal to the total quantity of waste in depot i minus the quantity of waste leaving this depot on the same day, or Eq. (15)

$$Q_{it} - Q_{it}^{out} = E_{it}^{f}, \forall i, t \tag{15}$$

7 The ending inventory, E^f_{it}, at depot i should not exceed the percentage, λ, of the total waste which enters this depot as given in Inequality (16).

$$E_{it}^{f} \leq \lambda \times \sum_{h=1}^{H} Q_{hit}, \forall i, t \tag{16}$$

8 The total quantity, Q_{jt}, of waste at collection station j on day t cannot exceed its capacity, C_j, as shown by Inequality (17).

$$Q_{jt} \leq C_j, \forall j, t \tag{17}$$

9 The quantity of waste, Q_{ijt}, at collection station j on day t is equal to the waste transported quantity to collection station j from depot i on day t plus the beginning inventory, $E^b_{j(t\text{-}1)}$, at collection station j from previous day (t-1) as shown in Eq. (18).

$$\sum_{i=1}^{I} Q_{ijt} + E_{j(t-1)}^{b} = Q_{jt}, \forall j, t \tag{18}$$

10 A certain proportion, R_L, of the waste transported from depot i to collection station j goes to landfills as given in Eq. (19).

$$R_L \times \sum_{i=1}^{I} Q_{ijt} = \sum_{l=1}^{L} Q_{jlt}, \forall j, t \tag{19}$$

11 Let NTA_{ujlt} denotes the number of available trips by truck type u on day t from collection station j to landfill l. The quantity transported from collection station j to landfill l on day t must not exceed the capacity of the available trips as stated in Formula (20).

$$\sum_{l=1}^{L} Q_{jlt} \leq \sum_{u=1}^{U} NTA_{ujlt} \times R_u, \forall j, t \tag{20}$$

12 The waste quantity enters landfill l from collection station j on day t is equal to the waste quantity, Q^{out}_{jlt}, that leaves collection station j towards landfill l as stated in Eq. (21).

$$\sum_{l=1}^{L} Q_{jlt} = \sum_{l=1}^{L} Q_{jlt}^{out}, \forall j, t \tag{21}$$

13 Let NTA_{ujrt} denotes the number of available trips on day t from collection station to recycling center r by truck u. The quantity transported from collection station j to recycling center r on day t cannot exceed the capacity of the available trips as given in Eq. (22).

$$\sum_{r=1}^{R} Q_{jrt} \leq \sum_{u=1}^{U} NTA_{ujrt} \times R_u, \forall j, t \tag{22}$$

14 The quantity of waste that enters recycling center r from collection station j on day t, is equal to the quantity of waste, Q^{out}_{jrt}, that leaves collection station j towards R recycling centers on day t as stated in Eq. (23).

$$\sum_{r=1}^{R} Q_{jrt} = \sum_{r=1}^{R} Q_{jrt}^{out}, \forall j, t \tag{23}$$

15 The ending inventory, E^f_{jt}, at collection station j on day t is equal to the total quantity of waste in J collection stations minus the quantity of waste leaving the collection stations to R recycling centers and L landfills on the same day t as given in Eq. (24).

$$Q_{jt} - \sum_{r=1}^{R} Q_{jrt}^{out} - \sum_{l=1}^{L} Q_{jlt}^{out} = E_{jt}^{f}, \forall j, t \tag{24}$$

16 The number of trips to L landfills and R recycling centers on day t does not exceed the number of available trips on the same day as given in inequalities (25a) and (25b), respectively.

$$\sum_{l=1}^{L} NT_{ujlt} \leq NTA_{ujlt}, \forall u, j, l, t \tag{25a}$$

$$\sum_{r=1}^{R} NT_{ujrt} \leq NTA_{ujrt}, \forall u, j, r, t \tag{25b}$$

17 The ending inventory, E^f_{jt}, at collection station j cannot exceed the ratio λ of the total waste which enters that collection station j from all I depots as stated in Eq. (26).

$$E_{jt}^{f} \leq \lambda \times \sum_{i=1}^{I} Q_{ijt}, \forall j, t \tag{26}$$

18 The quantity of waste, Q_{lt}, at landfill l on a given day t is equal to the sum of total quantity of waste, Q_{jlt}, transported from all J collection stations to landfill l plus the beginning inventory, $E^b_{l(t\text{-}1)}$ at landfill l from previous day as given in Eq. (27).

$$\sum_{j=1}^{J} Q_{jlt} + E_{l(t-1)}^{b} = Q_{lt}, \forall l, t \tag{27}$$

19 The total waste quantity, Q_{lt}, at landfill l at any given day t, cannot exceed the landfill's capacity, C_l, as stated in Formula (28).

$$Q_{lt} \leq C_l, \forall l, t \tag{28}$$

20 The quantity of waste, Q_{jrt}, at recycling center *r* on day *t* is equal to the sum of total waste quantity transported to recycling center *r* from all *J* collection stations and the beginning inventory, $E^{b}_{r(t\text{-}1)}$, at recycling center *r* from previous day *t*-1 as given in Eq. (29).

$$\sum_{j=1}^{J} Q_{jrt} + E^{b}_{r(t-1)} = Q_{rt}, \forall r, t \tag{29}$$

21 The total waste quantity, Q_{rt}, at recycling center *r* on day t cannot exceed its capacity, C_r, as stated in Inequality (30).

$$Q_{rt} \leq C_r, \forall r, t \tag{30}$$

22 Let NTA_{urmt} denotes the number of available trips by truck *u* on day *t* from recycling center *r* to anaerobic digestion plant *m*. The quantity transported from recycling center *r* to *M* anaerobic digestion plants on day *t* by *U* truck types cannot exceed the capacity of the available trips as stated in Inequality (31).

$$\sum_{m=1}^{M} Q_{rmt} \leq \sum_{u=1}^{U} NTA_{urmt} \times R_u, \forall r, m, t \tag{31}$$

23 To ensure efficiency, the total waste quantity transported from recycling center *r* to anaerobic digestion plant *m* on day *t*, is equal to the waste quantity, Q^{out}_{rmt}, leaving from recycling center *r* on the same day as stated in Eq. (32).

$$\sum_{m=1}^{M} Q_{rmt} = \sum_{m=1}^{M} Q^{out}_{rmt}, \forall r, t \tag{32}$$

24 A certain proportion R_R of the quantity of the waste transported from *J* collection stations to recycling center *r* on day *t* generates revenue, REV_t, as given in Eq. (33).

$$R_R \times \sum_{j=1}^{J} Q_{jrt} = REV_t, \forall r, t \tag{33}$$

25 The ending inventory, E^{f}_{rt}, at recycling center *r* on day *t* is equal to the total quantity of waste at recycling center, *r*, minus both the quantity of waste leaving that recycling center to anaerobic digestion plant *m* and the quantity used to generate revenues on the same day. Mathematically as stated in Eq. (34).

$$Q_{rt} - \sum_{m=1}^{M} Q^{out}_{rmt} - REV_t = E^{f}_{rt}, \forall r, t \tag{34}$$

26 The number of trips to anaerobic digestion plant on any given day *t*, does not exceed the number of available trips on the same day as stated in Eq. (35).

$$\sum_{m=1}^{M} NT_{urmt} \leq NTA_{urmt}, \forall r, m, t \tag{35}$$

27 The ending inventory, E^{f}_{rt}, at recycling center *r* on day *t* cannot exceed the ratio λ of the total waste which enters the recycling center as mentioned in Formula (36).

$$E^{f}_{rt} \leq \lambda \times \sum_{j=1}^{J} Q_{jrt}, \forall r, t \tag{36}$$

28 The quantity of waste at anaerobic digestion plant *m* on day *t* is equal to the sum of total quantity of waste transported to anaerobic digestion plant *m* from *R* recycling centers and the beginning inventory at anaerobic digestion plant *m*, $E^{b}_{m(t\text{-}1)}$, from previous day *t*-1 as expressed in Eq. (37).

$$\sum_{r=1}^{R} Q_{rmt} + E^{b}_{m(t-1)} = Q_{mt}, \forall m, t \tag{37}$$

29 The quantity of waste at anaerobic digestion plant *m* cannot exceed the capacity of the m^{th} anaerobic digestion plant, C_m, as explained in Inequality (38).

$$Q_{mt} \leq C_m, \forall m, t \tag{38}$$

30 On any given day *t*, transported waste from depot *i* to collection station *j* must not exceed the capacity of the available trips by *U* truck types from all *I* depots to collection station *j* on the same day, as shown in Inequality (39).

$$\sum_{u=1}^{U} \sum_{i=1}^{I} NT_{uijt} \times R_u \geq \sum_{i=1}^{I} Q_{ijt}, \forall j, t \tag{39}$$

31 On day *t*, the transported waste from *J* collection stations to the landfill *l* must not exceed the capacity of the available trips from all collection station to landfill *l* by *U* truck types on the same day, as shown in Formula (40).

$$\sum_{u=1}^{U} \sum_{j=1}^{J} NT_{ujlt} \times R_u \geq \sum_{j=1}^{J} Q_{jlt}, \forall l, t \tag{40}$$

32 On day *t*, the capacity of the number of trucks which shall transport the waste from *J* collection stations to recycling center *r* on day *t* by *U* trucks must be greater than or equal to the quantity of waste transported from *J* collection stations to recycling center *r* by *U* truck types on the same day, as given in Inequality (41).

$$\sum_{u=1}^{U} \sum_{j=1}^{J} NT_{ujrt} \times R_u \geq \sum_{j=1}^{J} Q_{jrt}, \forall r, t \tag{41}$$

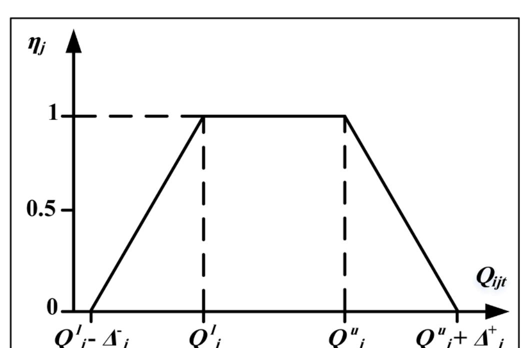

Fig. 3. Trapezoidal membership function for utilization of collection stations.

33 The capacity of the number of trucks, NT_{urmt}, used to transport waste from R recycling centers to anaerobic digestion plant m on day t must be greater than or equal to the quantity of waste transported from R recycling centers to digestion plant m by u truck types, as shown in the Inequality (42).

$$\sum_{u=1}^{U}\sum_{r=1}^{R} NT_{urmt} \times R_u \geq \sum_{r=1}^{R} Q_{rmt}, \forall m, t \tag{42}$$

34 Some variables should be integers and always positive as stated Inequality (43).

$$NT_{uijt},\ NT_{ujrt}, NT_{ujlt}, NT_{urmt} \ \geq 0 \ \& \ Integer, \forall u, i, j, l, r, m, t \tag{43}$$

3.2. Satisfaction on utilization of collection stations

The aim of this satisfaction model is to maximize the daily utilization of collection stations while processing waste quantities. Let the upper and lower limits of the preferable target of quantities be denoted by Q^u_j and Q^l_j, respectively. Let Δ^-_j and Δ^+_j denote the maximum negative and positive allowable deviation from the preferable quantity target at collection station j, respectively. Also, let δ^-_j and δ^+_j denote any negative or positive deviation from the preferable quantity target at collection station j, respectively. Considering the capacity and costs issues at collection stations, the utilization of any collection station should range between averages of daily quantity of 150 to 200 ton and hence results in 100% satisfaction on utilization. However, quantities fall beyond Q^u_j or below Q^l_j will incur overtime or under time costs, respectively. The trapezoidal membership function for collection station j, η_j, shown in Figure 3 is, therefore, found appropriate for measuring the satisfaction level on utilization of collection stations. If the transported quantity, Q_{ijt}, to collection station j on day t falls within the preferable limits, then the satisfaction on utilization of collection station j will be 100%.

The objective function is then to maximize the sum of the membership functions of utilization at J collection stations as formulated in Formula (44).

$$Max \sum_{j=1}^{J} \eta_j \tag{44}$$

The objective function in Formula (44) is subjected to the following constraints:

a The amount of any negative deviation, δ^-_j and is how far is the transported quantity from the lower limit as shown in Inequality (45).

$$\sum_{i=1}^{I} Q_{ijt} + \delta^-_j \geq \Delta^-_j, \forall j, t \tag{45}$$

b The amount of any positive deviation, δ^+_j, is how far is the transported quantity from the upper limit as given in Formula (46).

$$\sum_{i=1}^{I} Q_{ijt} - \delta^+_j \geq \Delta^+_j, \forall j, t \tag{46}$$

c The value of the utilization membership function is calculated using Eq. (47).

$$\eta_j + \frac{\delta^-_j}{\Delta^-_j} + \frac{\delta^+_j}{\Delta^+_j} = 1, \forall j \tag{47}$$

d The value of the membership function should not be lower than the minimum required utilization, θ_j, of collection station j as stated in Inequality (48).

$$\eta_j \geq \theta_j, \forall j \tag{48}$$

e The ranges of the negative and positive deviations are decided as given in inequalities (49) and (50), respectively.

$$0 \leq \delta^-_j \leq \Delta^-_j, \forall j \tag{49}$$

$$0 \leq \delta^+_j \leq \Delta^+_j, \forall j \tag{50}$$

3.3. Satisfaction on utilization of recycling centers

The goal of this model is to maximize the membership function of the utilization of the recycling centers while processing waste quantities on day t. If the quantities transported, Q_{jrt}, to recycling center r on day t are within the preferable target, then the utilization membership function, η_r, of the recycling centers will be 100%. Let the upper and lower limits of the preferable target of quantities be denoted by Q^u_r and Q^l_r, respectively. Let Δ^-_r and Δ^+_r denote the maximum negative and positive allowable deviation from the preferable quantity target at recycling center r, respectively. Also, let δ^-_r and δ^+_r denote any negative or positive deviation from the preferable quantity target at recycling center r. The objective function is to maximize the satisfaction on the utilization of the R recycling centers for processing waste as stated in Formula (51).

$$Max \sum_{r=1}^{R} \eta_r \tag{51}$$

The objective function is subjected to the following constraints:

i The amount of any negative deviation, δ^-_r, at recycling center r is how far is the transported quantity from J collection stations from the lower limit as in Inequality (52).

$$\sum_{j=1}^{J} Q_{jrt} + \delta^-_r \geq \Delta^-_r, \forall r, t \tag{52}$$

ii The amount of any positive deviation, δ^+_r, at recycling center r for is how far is the transported quantity J collection stations from the upper limit. That is stated in Eq. (53).

$$\sum_{j=1}^{J} Q_{jrt} - \delta^+_r \geq \Delta^+_r, \forall r, t \tag{53}$$

iii The value of the utilization membership function at recycling center r is calculated using Eq. (54).

$$\eta_r + \frac{\delta^-_r}{\Delta^-_r} + \frac{\delta^+_r}{\Delta^+_r} = 1, \forall r \tag{54}$$

iv The membership function value should not be lower than the minimum required utilization, θ_r, of recycling center r as stated in Eq. (55).

$$\eta_r \geq \theta_r, \forall r \tag{55}$$

v The range of the negative and positive deviations are shown in inequalities (56) and (57), respectively.

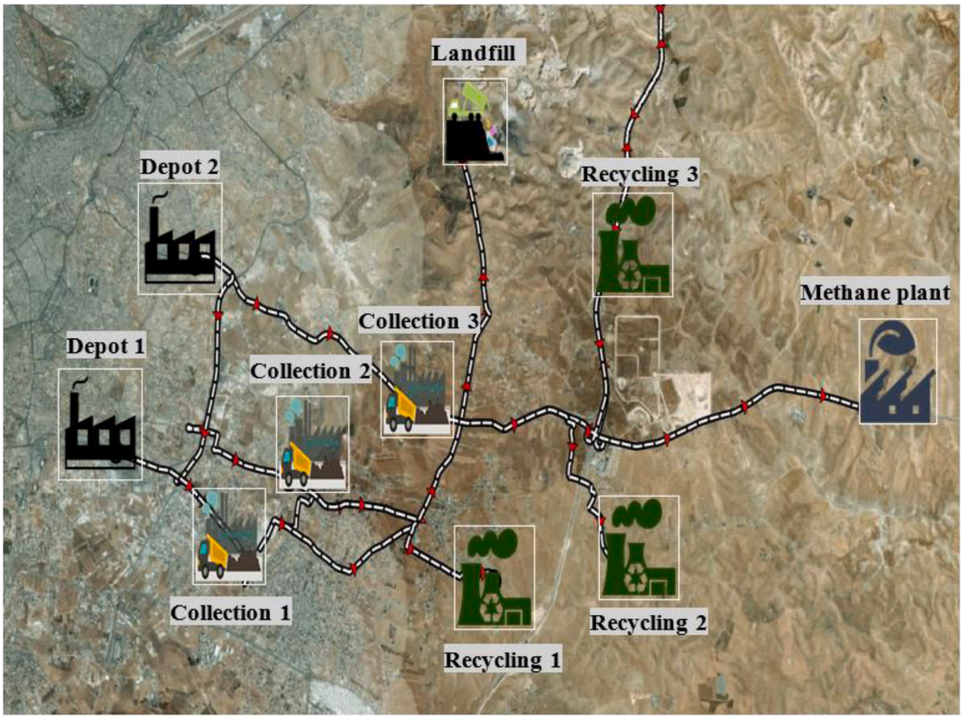

Fig. 4. Representation of case study on QGIS map.

Table 1
Values of model parameters.

Depot Parameter	Value	Anaerobic digestion plant (ADP) Parameter	Value
Fixed cost, FC_i	75 ($)	Fixed cost, FC_m	250 ($)
Variable cost	-	Variable cost, v_m	8 ($/ton)
Capacity, C_i	32000 (tons)	Capacity, C_m	10000 (tons)
GH^I	0.9 (g/km)	GH^M	6.9 (g/km)
Landfill (L)		**Recycling center (RC)**	
Fixed cost, FC_l	100 ($)	Fixed cost, FC_r	200 ($)
Variable cost, v_l	4.5 ($/ton)	Variable cost, v_r	7 ($/ton)
Capacity, C_l	1000000 (tons)	Capacity, C_r	20000 (tons)
GH^L	0.6 (g/km)	GH^R	6.8 (g/km)
Collection station (CS)		**Distances**	
Fixed cost, FC_j	150 ($)	d_{ij}	30 (km)
Variable cost, v_j	5 ($/ton)	d_{jl}	29 (km)
Capacity, C_j	32000 (tons)	d_{jr}	25 (km)
GH^J	5.2 (g/km)	d_{rm}	35 (km)
R_1	10 (tons)	GH_1	1.30 (g/km)
R_2	8 (tons)	GH_2	1.26 (g/km)
R_3	4 (tons)	GH_3	1.18 (g/km)
τ	0.61 ($/L)	$\propto$	0.3 ($/km × g)
$\Delta^-{}_j$	250 (tons)	$\Delta^+{}_j$	100 (tons)
$\Delta^-{}_r$	20 (tons)	$\Delta^+{}_r$	150 (tons)
θ_j	0.8	θ_r	0.9
$Q^u{}_j$	200 (tons)	$Q^l{}_j$	150 (tons)
$Q^u{}_r$	70 (tons)	$Q^l{}_r$	100 (tons)
R_R	0.25	R_L	0.2

$$0 \leq \delta_r^- \leq \Delta_r^-, \forall r \tag{56}$$

$$0 \leq \delta_r^+ \leq \Delta_r^+, \forall r \tag{57}$$

The complete optimization model is formulated by combining the presented three models: minimizing both total cost and GHG emission and maximizing satisfaction membership functions for the utilization of collection stations and recycling centers.

4. Analysis and results

A selected area in Amman, the capital of Jordan, was mainly considered to test the validity of the modelling contribution developed in this study. The population of the selected area is 250 thousand and the waste production per capita is 1.4 kg/day. On average, the collected waste per year is 120 thousand tons. This case study considers two depots (I =2), three collection stations (J=3), three recycling centers (R =3), one landfill (L =1), and a single anaerobic digestion plant (M =1) as represented on the QGIS map in Fig. 4.

Three types of trucks (U = 3) will be used to transport the waste quantities. Table 1 displays the general model parameters [1, 3], including fixed and variable costs for all stages with their capacities, the environmental parameters, and distances measured using QGIS software. Due to insufficient database about GHG emissions and costs for MSW management system in Jordan, the parameters values, such as, the operational costs (fixed and variable costs) and GHG emissions from trucks and facilities were adopted from some related studies [3].

The waste is tracked over a period of 6 days (T =6). The beginning inventories are zeros for all stages. The quantities that entered the depots on days (t= 1) to (t= 6) are 650, 440, 440, 710, 750, and 550 tons, respectively. Solving the proposed model using Lingo 18.0 software (Processor: Intel (R) Core (TM) i7-7700U; CPU @ 3.60 GHz, 3.60 GHz), the obtained optimal results for transported quantities and ending inventories for all stages were calculated by the model as displayed in Table B-1 shown in Appendix B. Given a certain number of available trips, *NTA*, the model calculates the optimal number of trips needed by each truck types (R_1, R_2, R_3) to transport all the waste. The obtained optimal trip numbers between stages are displayed in Table B-2 in Appendix B.

4.1. Results of optimization model

The optimal total cost of the system over six-day period was calculated for each stage and then displayed in Table 2. It is found that the average processing cost was 165.22 $/ton. From Table 2, collection center 1 on average over 6 days incurred variable costs, *TVC,* 2528.84

Table 2
Costs of the system.

	Day	Depot		Collection station			Landfill	Recyclingcenter			Aerobic Digestion Plant
		1	2	1	2	3		1	2	3	ADP
***TVC* ($)**	1	-	-	2150.00	1200.00	1200.00	409.50	1919.00	1197.00	1206.50	1535.63
	2	-	-	2690.00	1560.00	1560.00	809.55	2665.70	2449.10	2220.15	4397.40
	3	-	-	2807.00	1681.50	1668.00	206.82	2889.71	2789.01	1863.05	7511.02
	4	-	-	2806.02	1670.51	1558.00	306.52	2889.71	2789.01	1863.05	7511.02
	5	-	-	2150.00	1355.80	1106.60	417.50	1939.00	1197.00	1206.50	1535.63
	6	-	-	2570.00	1560.00	1560.00	709.55	2665.70	2449.10	2220.15	4397.40
On average ($/day)		-	-	2528.84	1504.63	1442.10	476.57	2494.80	2145.04	1763.23	4481.35
***TQC* ($)**	1	1753.50	1449.00	1280.55	792.00	986.40	-	472.50	342.90	285.12	-
	2	1744.05	1392.30	1656.03	1018.80	1255.44	-	742.46	752.76	567.72	-
	3	1681.05	1429.16	348.00	254.84	302.40	-	1105.65	689.58	857.76	-
	4	1744.05	1392.30	1656.03	1018.80	1255.44	-	742.46	752.76	567.72	-
	5	1681.05	1429.16	348.00	254.84	302.40	-	1105.65	689.58	857.76	-
	6	1753.50	1449.00	1280.55	792.00	986.40	-	472.50	342.90	285.12	-
On average ($/day)		1726.20	1423.49	1094.86	688.55	848.08	-	773.54	595.08	570.12	-
***TTC* ($)**	1	389.39	320.43	279.29	172.63	216.00	-	108.89	80.52	66.43	-
	2	385.31	309.91	372.92	236.68	279.08	-	166.53	164.70	132.86	-
	3	374.75	315.25	335.50	226.55	261.26	-	187.88	148.84	159.03	-
	4	374.75	315.25	335.50	226.55	261.26	-	166.53	164.70	132.86	-
	5	385.31	309.91	279.29	172.63	216.00	-	187.88	148.84	159.03	-
	6	385.31	309.91	372.92	236.68	279.08	-	108.89	80.52	66.43	-
On average ($/day)		382.47	313.44	329.24	211.95	252.11	-	154.43	131.35	119.44	-

Table 3
Total emissions resulting from system.

Stage	Component	Sources	Total (g)
Depots	Depot 1	Emissions (g)	1851.30
		Emissions from NT_{ijt} (g)	5223.04
	Depot 2	Emissions (g)	1596.60
		Emissions from NT_{ijt} (g)	3978.20
	Total = 12649.20		
Collection Station (CS)	CS1	Emissions (g)	7952.88
		Emissions from NT_{jlt} and NT_{jrt} (g)	4452.70
	CS2	Emissions (g)	4619.16
		Emissions from NT_{jlt} and NT_{jrt} (g)	2876.58
	CS3	Emissions (g)	4605.12
		Emissions from NT_{jlt} and NT_{jrt} (g)	3251.80
	Total= 27758.20		
Landfill	L1	Emissions	323.44
Recycling Center (RC)	RC1	Emissions (g)	5350.10
		Emissions from NT_{rmt} (g)	1974.00
	RC2	Emissions (g)	4606.18
		Emissions from NT_{rmt} (g)	1915.60
	RC3	Emissions (g)	3786.30
		Emissions from NT_{rmt} (g)	1525.92
	Total = 60211.60		
Anaerobic digestion plant	ADP	Emissions (g)	3024.70
The average amount of emissions from the system over 6 days			16820 g/day

Table 4
Utilization results for collection stations and recycling centers.

Utilization in Collection Stations							
Day (*t*)	**1**	**2**	**3**	**4**	**5**	**6**	**On average**
CS1	93%	98%	100%	84%	88%	89%	92%
CS2	80%	80%	81%	89%	83%	87%	83%
CS3	80%	80%	80%	90%	90%	81%	84%
Utilization in Recycling Centers							
Day (*t*)	**1**	**2**	**3**	**4**	**5**	**6**	**On average**
RC1	99%	90%	90%	95%	96%	96%	94%
RC2	90%	94%	92%	91%	95%	93%	93%
RC3	91%	98%	90%	94%	92%	92%	93%

($/day); thus, collection center 1 required higher variable costs with respect to collection station 2 and 3. Conversely, collection center 3 on average required lower variable costs, 1442.10 ($/day). However, the highest variable cost, *TVC*, in the system was incurred in aerobic digestion plant on average with 4481.35 ($/day); because of high-tech operations are needed to process waste at such plants. Moreover, on average landfills required the lowest variable costs in the system 476.57 ($/day).

On the other hand, the total transportation costs, *TQC*, were slightly different on average over six-day period for all stages. The close *TQC* results was incurred due to insignificant differences between distances of the trips. However, depot 1 incurred the highest *TQC* over the six days with average of 1726.20 ($/day). While recycling centers incurred on average the lower *TQC*, especially recycling center 3 which required 570.12 ($/day). In addition, it is noticed that the fuel consumption costs for trucks, *TTC*, will not seriously change over time except for unconditional incidents. On average, the *TTC* costs were changed from 119.44 ($/day) in recycling center 3 to 382.47 ($/day) in depot 1.

Finally, the emissions resulting from processing and transporting waste in the waste management system were estimated and displayed in Table 3, where it is noted that the average emission from depots, collection stations, and recycling centers is 16.82 kg/day. The higher emissions were emitted from recycling centers 60211.60 g; because of the advanced processes applied in recycling centers. In contrast, at the depots the waste does not require advance processes, so the emissions were 12649.20 g. These values can provide valuable information to transportation planning engineering on the effect of system emission on environment sustainability.

The utilization results for all collection stations and recycling centers over six-day period are displayed in Table 4. It is noted that the smallest satisfaction values for collection stations and recycling centers are 80% and 90%, respectively, which indicates acceptable utilization. The transported quantities for collection station 1 and recycling center 1 were the highest because the lower transportation costs. Thus, the highest average utilization for collection stations was found in collection station 1. As well, recycling center 1 achieved the highest utilization. The differences in utilization percentages were occurred because of the transported quantities.

The generated energy from processing wastes is different due to the operational capacities and waste types. Currently, the ADP are not operated in Jordan and there is lack of data about wastes. In similar studies, it was reported that the energy potential of 584 tons/day MSW is

.

Table 5
The expected generated energy in ADP.

Day (t)	Entering Q, Q_{rmt}	Energy potential (MWh)	Electrical power (MW)	Power to grid (MW)
1	102.38	568.70	7.19	4.73
2	190.79	1059.80	13.39	8.82
3	207.57	1153.01	14.57	9.60
4	250.62	1392.14	17.59	11.59
5	294.9	1638.11	20.70	13.63
6	289.19	1606.39	20.30	13.37
On average	222.58	1236.36	15.63	10.29

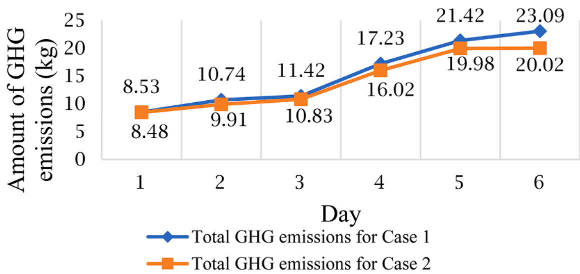

Fig. 5. Comparison between total emissions for Case 1 and Case 2.

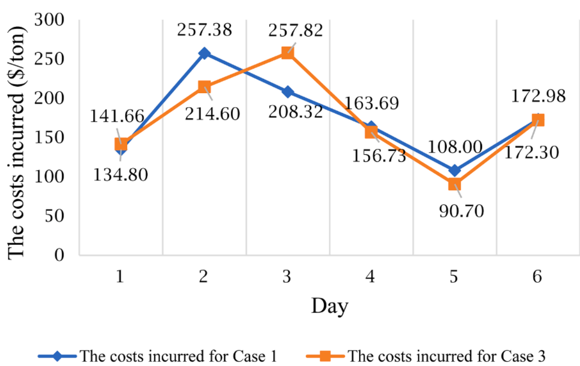

Fig. 6. Comparison between costs for Case 1 and Case 3.

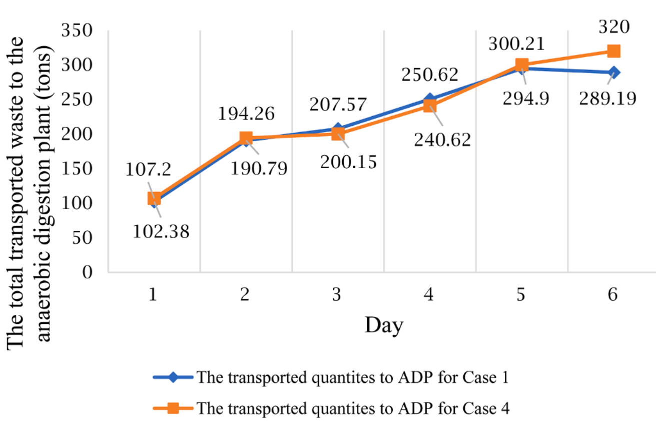

Fig. 7. Comparison between the quantities for Case 1 and Case 4.

about 3244 MWh, and the electrical power of the same quantity is about 41 MW whereas the power to grid is about 27 MW [31]. Table 5 summarized the expected generated energy from the transported quantities to ADP.

Table 6
Comparison between all applied case studies.

Case study	Total costs ($/ton)	Total GHG emissions (kg/day)	The transported quantities (ton/day)
Case 1 (All objective functions were considered)	165.22	16.82	222.58
Case 2 (Minimizing GHG emissions only)	138.78	14.21	282.52
Case 3 (Minimizing incurred costs only)	155.91	19.4	298.76
Case 4 (Maximizing the transported quantities only)	236.73	20.64	451.22

4.2. *Sensitivity analysis*

Further analysis was conducted on each objective function over six-day period. The beginning inventories are zero for all stages on the first day. The quantities that entered the depot are 650, 440, 440, 710, 750, and 550 tons on days 1 to 6, respectively. When the objective function only considered minimizing the GHG emissions (case 2) from waste transportation, the average GHG emissions per day are 14.21 kg/day. However, the average processing cost incurred is 138.78 $/ton and the average quantity transferred to the anaerobic digestion plant is 282.52 ton/day. A comparison between the total emissions is displayed in Fig. 5. In this case 2, the optimization model only aims to minimize the GHG emissions. In all days, the total emissions were slightly reduced. The results showed a reduction of GHG emissions by 0.05, 0.83, 0.59, 1.21, 1.44, and 3.07 kg over six-day period, respectively.

However, when only minimizing total costs (case 3) was considered as the objective function, the average processing cost over six-day period is 155.91 $/ton. While the average GHG emissions per day are 19.40 kg/day and the average quantity transferred to the anaerobic digestion plant is 298.76 ton/day. A comparison between the optimal costs is displayed in Fig. 6, where it is noticed that the incurred costs fluctuated between 257.82 ($/ton) on day 3 and 90.70 ($/ton) on day 5. The largest cost reduction was achieved in day 3 by 49.5 ($/ton). On the other hand, the smallest reduction was found to be 0.68 ($/ton) in day 6. The rates of cost reduction over the 6 days change in response to the transported quantities, and transportation.

Finally, when solving the model to maximize the total quantities only (case 4), and the average quantity transferred to the anaerobic digestion plant over the six-day period is 451.22 ton/day, while the average processing cost is 236.73 $/ton and the average GHG emissions are 20.64 kg/day. A comparison between the total quantities transported is displayed in Fig. 7. The objective function in case 4 was aimed to maximize the total transported quantities to ADP. Mostly, over the six-day period the transported quantities to ADP were increased. For example, an increasing by 4.82, 5.31, and 30.81 ton were achieved in days 1, 5, and 6, respectively.

Table 6 shows a comparison between all case studies with respect to the objective functions (Total costs, GHG emissions, and Transported quantities). In conclusion, the introduced optimization model is not

Table B-1
Optimal waste quantities to be transported (tons).

Day (t)	**Day 1**			**Day 2**			**Day 3**		
Depot	**Depot 1**	**Depot 2**		**Depot 1**	**Depot 2**		**Depot 1**	**Depot 2**	
Beginning Inv., $E^b_{i(t-1)}$	0.00	0.00		105.00	90.00		103.50	87.00	
Entering Q, Q_{hit}	350.00	300.00		240.00	200.00		230.00	210.00	
Q in depot, Q_{it}	350.00	300.00		345.00	290.00		333.50	297.00	
Exiting Q, Q_{it}^{out}	245.00	210.00		241.50	203.00		233.45	207.90	
Ending Inv., E^f_{it}	105.00	90.00		103.50	87.00		100.05	89.10	
Day (t)	**Day 4**			**Day 5**			**Day 6**		
Beginning Inv., $E^b_{i(t-1)}$	100.05	89.10		123.02	146.73		141.90	164.02	
Entering Q, Q_{hit}	310.00	400.00		350.00	400.00		250.00	300.00	
Q in depot, Q_{it}	410.05	489.10		473.02	546.73		391.90	464.02	
Exiting Q, Q_{it}^{out}	287.04	342.37		331.11	382.71		274.33	324.81	
Ending Inv., E^f_{it}	123.02	146.73		141.90	164.02		117.57	139.21	
Day (t)	**Day 1**			**Day 2**			**Day 3**		
Collection Center	**CS1**	**CS2**	**CS3**	**CS1**	**CS2**	**CS3**	**CS1**	**CS2**	**CS3**
Beginning Inv., $E^b_{j(t-1)}$	0.00	0.00	0.00	64.50	36.00	36.00	80.70	46.80	46.80
Entering Q, Q_{ijt}	215.00	120.00	120.00	204.50	120.00	120.00	199.45	121.90	120.00
Q in collection, Q_{jt}	215.00	120.00	120.00	269.00	156.00	156.00	280.15	168.70	166.80
Q to landfill, Q_{jlt}	43.00	24.00	24.00	40.90	24.00	24.00	39.89	24.38	24.00
Q to recycling, Q_{jrt}	107.50	60.00	60.00	147.40	85.20	85.20	128.20	76.84	76.08
Ending Inv., E^f_{jt}	64.50	36.00	36.00	80.70	46.80	46.80	112.06	67.48	66.72
Day (t)	**Day 4**			**Day 5**			**Day 6**		
Beginning Inv., $E^b_{j(t-1)}$	112.06	67.48	66.72	93.62	80.37	88.72	89.23	102.11	101.61
Entering Q, Q_{ijt}	200.00	200.41	229.00	203.82	260.00	250.00	200.15	200.00	199.00
Q in collection, Q_{jt}	312.06	267.89	295.72	297.44	340.37	338.72	289.38	302.11	300.61
Q to landfill, Q_{jlt}	62.41	53.58	59.14	59.49	68.07	67.74	57.88	60.42	60.12
Q to recycling, Q_{jrt}	156.03	133.94	147.86	148.72	170.18	169.36	144.69	151.05	150.31
Ending Inv., E^f_{jt}	93.62	80.37	88.72	89.23	102.11	101.61	86.81	90.63	90.18
Day (t)	**Day 1**			**Day 2**			**Day 3**		
Landfill	**L1**			**L1**			**L1**		
Beginning Inv., $E^b_{l(t-1)}$	0.00			91.00			179.90		
Entering Q, Q_{jlt}	91.00			88.90			88.27		
Q in landfill, Q_{lt}	91.00			179.90			268.17		
Ending Inv., E^f_{lt}	91.00			179.90			268.17		
Day (t)	**Day 4**			**Day 5**			**Day 6**		
Beginning Inv., $E^b_{l(t-1)}$	268.17			443.30			638.61		
Entering Q, Q_{jlt}	175.13			195.30			178.42		
Q in landfill, Q_{lt}	443.30			638.61			817.03		
Ending Inv., E^f_{lt}	443.30			638.61			817.03		
Day (t)	**Day 1**			**Day 2**			**Day 3**		
Recycling Center	**RC1**	**RC2**	**RC3**	**RC1**	**RC2**	**RC3**	**RC1**	**RC2**	**RC3**
Beginning Inv., $E^b_{r(t-1)}$	0.00	0.00	0.00	30.00	19.05	19.20	42.00	37.46	36.36
Entering Q, Q_{jrt}	100.00	63.50	64.00	110.00	110.00	97.80	109.92	63.00	108.20
Q in recycling, Q_{rt}	100.00	63.50	64.00	140.00	124.85	121.20	151.92	100.46	144.56
REV_t	25.00	15.88	16.00	27.50	26.45	25.50	27.48	15.75	27.05
Q to plant, Q_{rmt}	45.00	28.58	28.80	70.50	60.95	59.34	78.86	54.57	74.14
Ending Inv., E^f_{rt}	30.00	19.05	19.20	42.00	37.46	36.36	45.58	30.14	43.37
Day (t)	**Day 4**			**Day 5**			**Day 6**		
Beginning Inv., $E^b_{r(t-1)}$	45.58	30.14	43.37	43.67	50.39	73.01	73.10	45.12	78.38
Entering Q, Q_{jrt}	100.00	137.83	200.00	200.00	100.00	188.26	106.00	200.05	140.00
Q in recycling, Q_{rt}	145.58	167.97	243.37	243.67	150.39	261.27	179.10	245.17	218.38
REV_t	36.40	41.99	60.84	60.92	37.60	65.32	44.78	61.29	54.60
Q to plant, Q_{rmt}	65.51	75.59	109.52	109.65	67.68	117.57	80.60	110.33	98.27
Ending Inv., E^f_{rt}	43.67	50.39	73.01	73.10	45.12	78.38	53.73	73.55	65.51
Day (t)	**Day 1**			**Day 2**			**Day 3**		
Anaerobic digestion plants	**M1**			**M1**			**M1**		
Beginning Inv., $E^b_{m(t-1)}$	0.00			102.38			293.16		
Entering Q, Q_{rmt}	102.38			190.79			207.57		
Q in plant, Q_{mt}	102.38			293.16			500.73		
Ending Inv., E^f_{mt}	102.38			293.16			500.73		
Day (t)	**Day 4**			**Day 5**			**Day 6**		
Beginning Inv., $E^b_{m(t-1)}$	500.73			751.35			1046.25		
Entering Q, Q_{rmt}	250.62			294.90			289.19		
Q in plant, Q_{mt}	751.35			1046.25			1335.44		
Ending Inv., E^f_{mt}	751.35			1046.25			1335.44		

Table B-2
Optimal number of trips between stages.

Depot to collection station						
Day (*t*)	**Day 1**		**Day 2**		**Day 3**	
Depot *i*	**Available Trips** (R_1, R_2, R_3)	**Actual Trips** (R_1, R_2, R_3)	**Available Trips** (R_1, R_2, R_3)	**Actual Trips** (R_1, R_2, R_3)	**Available Trips** (R_1, R_2, R_3)	**Actual Trips** (R_1, R_2, R_3)
Depot 1	(12,15,4)	(12,15,2)	(12,12,10)	(12,12,7)	(14,12,6)	(14,12,0)
Depot 2	(16,15,4)	(13,10,0)	(16,9,4)	(14,8,0)	(14,12,4)	(12,11,0)
Day (*t*)	**Day 4**		**Day 5**		**Day 6**	
Depot 1	(14,12,6)	(14,12,0)	(16,15,4)	(13,10,0)	(16,9,4)	(14,8,0)
Depot 2	(12,15,4)	(12,15,2)	(14,12,4)	(12,11,0)	(12,12,10)	(12,12,7)
Collection station (CS) to Landfill						
Day (*t*)	**Day 1**		**Day 2**		**Day 3**	
CS *j*	**Available Trips** (R_1, R_2, R_3)	**Actual Trips** (R_1, R_2, R_3)	**Available Trips** (R_1, R_2, R_3)	**Actual Trips** (R_1, R_2, R_3)	**Available Trips** (R_1, R_2, R_3)	**Actual Trips** (R_1, R_2, R_3)
CS1	(4,3,0)	(2,3,0)	(2,3,0)	(2,3,0)	(4,3,4)	(4,0,0)
CS2	(4,2,4)	(2,0,1)	(2,0,4)	(2,0,1)	(6,0,0)	(3,0,0)
CS3	(4,3,0)	(0,3,0)	(4,6,0)	(0,3,0)	(2,6,4)	(0,3,0)
Day (*t*)	**Day 4**		**Day 5**		**Day 6**	
CS1	(6,0,0)	(3,0,0)	(2,6,4)	(0,3,0)	(4,6,0)	(0,3,0)
CS2	(4,3,0)	(0,3,0)	(4,2,4)	(2,0,1)	(2,3,0)	(2,3,0)
CS3	(2,0,4)	(2,0,1)	(4,3,4)	(4,0,0)	(4,3,0)	(2,3,0)
Collection station (CS) to Recycling Centers (RCs)						
Day (*t*)	**Day 1**		**Day 2**		**Day 3**	
CS *j*	**Available Trips** (R_1, R_2, R_3)	**Actual Trips** (R_1, R_2, R_3)	**Available Trips** (R_1, R_2, R_3)	**Actual Trips** (R_1, R_2, R_3)	**Available Trips** (R_1, R_2, R_3)	**Actual Trips** (R_1, R_2, R_3)
CS1	(4,3,12)	(4,3,11)	(10,6,4)	(10,6,0)	(14,3,0)	(13,0,0)
CS2	(4,0,12)	(4,0,5)	(10,0,0)	(9,0,0)	(6,6,9)	(5,3,1)
CS3	(4,3,8)	(4,2,1)	(8,3,0)	(7,2,0)	(8,0,4)	(8,0,0)
Day (*t*)	**Day 4**		**Day 5**		**Day 6**	
CS1	(10,0,0)	(9,0,0)	(4,3,12)	(4,3,11)	(8,3,0)	(7,2,0)
CS2	(6,6,9)	(5,3,1)	(4,3,8)	(4,2,1)	(4,0,12)	(4,0,5)
CS3	(14,3,0)	(13,0,0)	(8,0,4)	(8,0,0)	(10,6,4)	(10,6,0)
Recycling centers to Anaerobic digestion plants						
Day (*t*)	**Day 1**		**Day 2**		**Day 3**	
RC *r*	**Available Trips** (R_1, R_2, R_3)	**Actual Trips** (R_1, R_2, R_3)	**Available Trips** (R_1, R_2, R_3)	**Actual Trips** (R_1, R_2, R_3)	**Available Trips** (R_1, R_2, R_3)	**Actual Trips** (R_1, R_2, R_3)
RC1	(0,6,9)	(0,6,0)	(4,4,3)	(4,4,0)	(8,6,0)	(8,0,0)
RC2	(0,2,4)	(0,2,4)	(8,2,2)	(5,1,1)	(8,2,2)	(4,2,0)
RC3	(4,4,6)	(3,0,0)	(6,0,0)	(6,0,0)	(3,10,4)	(2,7,0)
Day (*t*)	**Day 4**		**Day 5**		**Day 6**	
RC1	(8,2,2)	(4,2,0)	(0,6,9)	(0,6,0)	(3,10,4)	(2,7,0)
RC2	(8,6,0)	(8,0,0)	(6,0,0)	(6,0,0)	(0,2,4)	(0,2,4)
RC3	(4,4,3)	(4,4,0)	(4,4,6)	(3,0,0)	(8,2,2)	(5,1,1)

biased for specific objective function. Moreover, the formulated constraints should control the absence of any eliminated objective function. Case 1 (all objective functions were considered) showed more moderate results. Although case 2 (minimizing GHG emissions only) presented more optimal results in costs, GHG emissions, and transported quantities; but because the higher transported quantities that exceeded the preferable limits the utilization of collection stations and recycling centers were decreased. In case 3 (minimizing incurred costs only), with enforcing the optimization model to minimize the incurred costs only; it showed a good response but with higher GHG emissions. For case 4 (maximizing the transported quantities only), in response to the objective function high quantities were transported without restrictions on costs and GHG emissions.

5. Conclusions

MSW management system is a crucial public health service, which requires instant and powerful attention from decision makers during and aftermath of the COVID-19 crisis. However, the COVID-19 crisis has affected the industries on many levels. The volume of recyclable wastes was significantly increased during COVID-19 outbreak especially in the lockdown periods. Then, the decision makers should respond to this public health emergency by improving the MSW management system. Consequently, the objective of this article was to establish a more efficient MSW management system which maximizes the percentage of waste transported from depots to anaerobic digestion plants for recovery and recycling using mathematical optimization model. The model was built to maximize waste transported while minimizing both transportation costs and greenhouse gas emissions using different types of available trucks and ensuring sufficient utilization of the system. Results showed that, a quantity of 3540 tons of waste was assumed to enter the depot over a period of six-days. Accordingly, the model determined that an optimal quantity of waste could be transported from all depots to anaerobic digestion plants using 686 trips out of 1026 available trips with minimal environmental impacts. Revenues could be generated using 670.35 tons of non-organic recyclable waste.

In addition, the average optimal quantity which entered the anaerobic digestion plant was 222.58 ton/day of waste and this could potentially generate approximately 1236.36 MWh of energy potential, 15.63 MW of electrical power, and 10.29 MW power to grid. The minimal average system cost of this would be 165.22 $/ton. With the aid of the recommended waste management system and its optimization model, the public municipalities could utilize research results in developing effects plans that lead to reduce SWM transportations costs and enhance facilities utilization. In addition, the proposed optimization models supports building a sustainable MSW system that is valuable under normal and unexpected conditions; such as, COVID-19 outbreak. More importantly, 1 MW of electricity can be generated for each 50 tons of waste thus contributing to the major goal of the “green city” concept, which are found consistent with the obtained results by relevant studies on the same field. Future research considers analyzing the MSW system over longer periods with separation process at the source and stochastic collected quantities.

Funding

Not applicable.

Data availability statement

Not applicable.

CRediT authorship contribution statement

Abbas Al-Refaie: Conceptualization, Methodology, Data curation, Formal analysis. **Ahmad Al-Hawadi:** Conceptualization, Methodology, Data curation, Formal analysis. **Natalija Lepkova:** Writing – review & editing, Formal analysis, Methodology.

Declaration of Competing Interest

The authors declare no conflict of interest.

Appendix A. Nomenclature

(a) Decision variables

Variable	Description
Qit	Waste quantity at depot *i* on day *t*.
Qjt	Waste quantity at collection station *j* on day *t*.
Qrt	Waste quantity at recycling center *r* on day *t*.
Qlt	Waste quantity at the landfill *l* on day *t*.
Qmt	Waste quantity at anaerobic digestion plant *m* on day *t*.
Qijt	Waste quantity transported from depot *i* to collection station *j* on day *t*.
Qjrt	Waste quantity which is transported from collection station *j* to recycling center *r* on day *t*.
Qjlt	Waste quantity which is transported from collection station *j* to landfill *l* on day *t*.
Qrmt	Waste quantity that is transported from recycling center *r* to anaerobic digestion plant *m* on day *t*.
NTuijt	Number of trips by truck type *u* from depot *i* to collection station *j* on day *t*.
NTujrt	Number of trips by truck type *u* from collection station *j* to recycling center *r* on day *t*.
NTujlt	Number of trips by truck type *u* from collection station *j* to landfill *l* on day *t*.
NTurmt	Number of trips by truck type *u* from recycling center *r* to anaerobic digestion plant *m* on day *t*.
REVt	Generated revenues on day *t*.
E^f_{it}	Ending inventory at depot *i* on day *t*.
E^f_{jt}	Ending inventory at collection station *j* on day *t*.
E^f_{lt}	Ending inventory at landfill *l* at on day *t*.
E^f_{rt}	Ending inventory at recycling center *r* on day *t*.
E^f_{mt}	Ending inventory at anaerobic digestion plant *m* on day *t*.
δ^-_j	Negative deviation from the preferable target for collection station *j*.
δ^+_j	Positive deviation from the preferable target for collection station *j*.
δ^-_r	Negative deviation from the preferable target for recycling center *r*.
δ^+_r	Positive deviation from the preferable target for recycling center *r*.
η_j	Utilization membership function of collection station *j*.
η_r	Utilization membership function of recycling center *r*.

(a) Model parameters

Parameter	Description
Q_{hit}	Quantity of waste transported to depot *i* from cluster *h* on day *t*.
$E^b_{i(t-1)}$	Beginning inventory at depot *i* on day (*t*-1).
$E^b_{j(t-1)}$	Beginning inventory at collection station *j* from previous day (*t*-1).
$E^b_{l(t-1)}$	Beginning inventory at landfill *l* from previous day (*t*-1).
$E^b_{r(t-1)}$	Beginning inventory at recycling center *r* from previous day (*t*-1).
$E^b_{m(t-1)}$	Beginning inventory at anaerobic digestion plant *m* from previous day (*t*-1).
Λ	Ratio of ending inventory.
R_L	A proportion of waste that is moved to *L* landfill.
R_R	A proportion of waste that generates *R* revenues.
C_i	Capacity of depot *i*.
C_j	Capacity of collection station *j*.
C_l	Capacity of landfill *l*.
C_r	Capacity of recycling center *r*.
C_m	Capacity of anaerobic digestion plant *m*.
NTA_{uijt}	Available trips of trucks type *u* on day *t* to ship waste from depot *i* to collection station *j*.
NTA_{ujrt}	Available trips of trucks type *u* on day *t* to ship waste from collection station *j* to recycling center *r*.
NTA_{ujlt}	Available trips of trucks type *u* on day *t* to ship waste from collection station *j* to landfill *l*.
NTA_{urmt}	Available trips of trucks type *u* on day *t* to ship waste from recycling center *r* to digestion plant *m*.
GH^I	Amount of of GHG emitted from processing one ton of waste (g/ton) at *I* depots.

(*continued on next page*)

(*continued*)

Parameter	Description
GH^J	Amount of of GHG emitted from processing one ton of waste (g/ton) at *J* collection stations.
GH^R	Amount of GHG emitted from processing one ton of waste (g/ton) at *R* recycling centers.
GH^L	Amount of of GHG emitted from processing one ton of waste (g/ton) at *L* landfills.
GH^M	Amount of of GHG emitted from processing one ton of waste (g/ton) at M digestion plants.
GH^u	Amount of of GHG emitted (g/km) from truck type *u*.
FC_i	Fixed cost per day for depot *i*.
FC_j	Fixed cost per day for collection station *j*.
FC_r	Fixed cost per day for recycling center *r*.
FC_l	Fixed cost per day for landfill *l*.
FC_m	Fixed cost per day for anaerobic digestion plant *m*.
VC_j	Variable cost per day at collection station *j*.
VC_r	Variable cost per day at recycling center *r*.
VC_l	Variable cost per day at landfill *l*.
VC_m	Variable cost per day at digestion plant *m*.
α	Transportation cost ($/ton × km).
d_{ij}	Distance travelled from depot *i* to collection station *j*.
d_{jr}	Distance travelled from collection station *j* to recycling center, *r*.
d_{jl}	Distance travelled from collection station *j* to landfill *l*.
d_{rm}	Distance travelled from recycling center *r* to anaerobic digestion plant *m*.
T	Fuel cost per Litre ($/L).
TC^u	Fuel consumption of truck type *u*.
R_u	Capacity of transportation truck type *u*.
Q_j^u	Upper limit of the preferable quantity target at collection station *j*.
Q_j^l	Lower limit of the preferable quantity target at collection station.
Q_r^u	Upper limit of the preferable quantity target of recycling center *r*.
Q_r^l	Lower limit of the preferable quantity target of recycling center *r*.
Δ_j^-	Maximum negative allowable deviation from the lower preferable target $Q^l{}_j$ at collection station *j*.
Δ_j^+	The maximum positive allowable deviation from the upper preferable target $Q^u{}_j$ at collection station *j*.
Δ_r^-	The maximum negative allowable deviation from the lower preferable target $Q^l{}_r$ at recycling center *r*.
Δ_r^+	The maximum positive allowable deviation from the upper preferable target $Q^u{}_r$ at recycling center *r*.
θ_j	The minimum required utilization of collection station *j*.
θ_r	Minimum acceptable utilization of recycling center *r*.

Appendix B. Table

Table

References

[1] M.F. Badran, S.M. El-Haggar, Optimization of municipal solid waste management in port said – Egypt, Waste Manag. 26 (5) (2006) 534–545, https://doi.org/10.1016/j.wasman.2005.05.005.
[2] G. Tchobanoglous, H. Theisen, S. Vigil, Integrated Solid Waste Management, McGraw-Hill, New York, 1993.
[3] F. Habibi, E. Asadi, S.J. Sadjadi, F. Barzinpour, A multi-objective robust optimization model for site-selection and capacity allocation of municipal solid waste facilities: a case study in Tehran, J. Clean. Prod. 166 (2017) 816–834, https://doi.org/10.1016/j.jclepro.2017.08.063.
[4] S.C. Paolo, G. Manuela, L. Claudio, European trends in greenhouse gases emissions from integrated solid waste management, Environ. Technol. 2125 (2015), 1022230, https://doi.org/10.1080/09593330.2015.1022230.
[5] Jordan Green Building Council, Your Guide to Waste Management in Jordan Waste Sorting Informative Booklet, Jordan Green Building Council, 2016.
[6] P.S. Calabro, A. Satira, Recent advancements towards resilient and sustainable municipal solid waste collection systems, Curr. Opin. Green Sustain. Chem. (2020), 100375, https://doi.org/10.1016/j.cogsc.2020.100375.
[7] C. Mora, R. Manzini, M. Gamberi, A. Cascini, Environmental and economic assessment for the optimal configuration of a sustainable solid waste collection system: a 'kerbside' case study, Prod. Plan. Control 25 (9) (2013) 737–761, https://doi.org/10.1080/09537287.2012.750386.
[8] J. Põldnurk, Optimisation of the economic, environmental, and administrative efficiency of the municipal waste management model in rural areas, Resour. Conserv. Recycl. 97 (2015) 55–65, https://doi.org/10.1016/j.resconrec.2015.02.003.
[9] J. Zhao, F. Zhu, A multi-depot vehicle-routing model for the explosive waste recycling, Int. J. Prod. Res. 54 (2) (2016) 550–563, https://doi.org/10.1080/00207543.2015.1111533.
[10] J. Trochu, A. Chaabane, M. Ouhimmou, Reverse logistics network redesign under uncertainty for wood waste in the CRD industry, Resour. Conserv. Recycl. 128 (2018) 32–47, https://doi.org/10.1016/j.resconrec.2017.09.011.
[11] F.M. Tsai, T.D. Bui, M.L. Tseng, K.J. Wu, A causal municipal solid waste management model for sustainable cities in Vietnam under uncertainty: a comparison, Resour. Conserv. Recycl. 154 (2020), 104599, https://doi.org/10.1016/j.resconrec.2019.104599.
[12] F.M. Tsai, T.D. Bui, M.L. Tseng, M.K. Lim, J. Hu, Municipal solid waste management in a circular economy: a data-driven bibliometric analysis, J. Clean. Prod. 275 (2020), 124132, https://doi.org/10.1016/j.jclepro.2020.124132.
[13] S. Xiao, H. Dong, Y. Geng, X. Tian, C. Liu, H. Li, Policy impacts on municipal solid waste management in Shanghai: a system dynamics model analysis, J. Clean. Prod. 262 (2020), 121366, https://doi.org/10.1016/j.jclepro.2020.121366.
[14] I.R. Istrate, D. Iribarren, J.L. Gálvez-Martos, J. Dufour, Review of life-cycle environmental consequences of waste-to-energy solutions on the municipal solid waste management system, Resour. Conserv. Recycl. 157 (2020), 104778, https://doi.org/10.1016/j.resconrec.2020.104778.
[15] R.M. Deus, F.D. Mele, B.S. Bezerra, R.A.G. Battistelle, A municipal solid waste indicator for environmental impact: assessment and identification of best management practices, J. Clean. Prod. 242 (2020), 118433, https://doi.org/10.1016/j.jclepro.2019.118433.
[16] Y.D. Tong, T.D.X. Huynh, T.D. Khong, Understanding the role of informal sector for sustainable development of municipal solid waste management system: a case study in Vietnam, Waste Manag. 124 (2021) 118–127, https://doi.org/10.1016/j.wasman.2021.01.033.
[17] M.E. Batur, A. Cihan, M.K. Korucu, N. Bektaş, B. Keskinler, A mixed integer linear programming model for long-term planning of municipal solid waste management systems: against restricted mass balances, Waste Manag. 105 (2020) 211–222, https://doi.org/10.1016/j.wasman.2020.02.003.
[18] H.O. Iyamu, M. Anda, G. Ho, A review of municipal solid waste management in the BRIC and high-income countries: a thematic framework for low-income countries, Habitat Int. 95 (2020), 102097, https://doi.org/10.1016/j.habitatint.2019.102097.
[19] A.C.H. Pinha, J.K. Sagawa, A system dynamic modelling approach for municipal solid waste management and financial analysis, J. Clean. Prod. 269 (2020), 122350, https://doi.org/10.1016/j.jclepro.2020.122350.
[20] M. Paul, M.J. Bussemaker, A web-based geographic interface system to support decision making for municipal solid waste management in England, J. Clean. Prod. 263 (2020), 121461, https://doi.org/10.1016/j.jclepro.2020.121461.
[21] ... H.A.A. Hajar, A. Tweissi, Y.A.A. Hajar, R. Al-Weshah, K.M. Shatanawi, R. Imam, M.A.A. Hajer, Assessment of the municipal solid waste management sector development in Jordan towards green growth by sustainability window analysis

J. Clean. Prod. 258 (2020), 120539 https://doi.org/10.1016/j.jclepro.2020.120539.

A. P. Pinupolu, H. raja Kommineni, Best method of municipal solid waste management through public-private partnership for Vijayawada city, in: Proceedings of the Materials Today 33, 2020, pp. 217–222, https://doi.org/ 10.1016/j.matpr.2020.03.816.

B. ... & Y. Sarbassov, C. Venetis, B. Aiymbetov, B. Abylkhani, A. Yagofarova, D. Tokmurzin, V.J. Inglezakis, Municipal solid waste management and greenhouse gas emissions at international airports: a case study of Astana international airport,

J. Air Transp. Manag. 85 (2020), 101789 https://doi.org/10.1016/j.jairtraman.2020.101789.

[24] S. Viau, G. Majeau-Bettez, L. Spreutels, R. Legros, M. Margni, R. Samson, Substitution modelling in life cycle assessment of municipal solid waste management, Waste Manag. 102 (2020) 795–803, https://doi.org/10.1016/j.wasman.2019.11.042.

[25] B.N. Kulkarni, V. Anantharama, Repercussions of COVID-19 pandemic on municipal solid waste management: challenges and opportunities, Sci. Total Environ. 743 (2020), 140693, https://doi.org/10.1016/j.scitotenv.2020.140693.

[26] A. Mostafaeipour, M. Rezaei, M. Jahangiri, M. Qolipour, Feasibility analysis of a new tree-shaped wind turbine for urban application: a case study, Energy Environ. 31 (7) (2020) 1230–1256, https://doi.org/10.1177/2F0958305X19888878.

[27] M. Rezaei, K.R. Khalilpour, M. Jahangiri, Multi-criteria location identification for wind/solar based hydrogen generation: the case of capital cities of a developing country, Int. J. Hydrog. Energy 45 (58) (2020) 33151–33168, https://doi.org/10.1016/j.ijhydene.2020.09.138.

[28] C. Wang, N.T. Nguyen, T. Dang, J.A Bayer, Two-stage multiple criteria decision making for site selection of solar photovoltaic (PV) power plant: a case study in Taiwan, IEEE Access 9 (2021) 75509–75525, https://doi.org/10.1109/ACCESS.2021.3081995.

[29] C. Wang, T. Dang, H. Tibo, D. Duong, Assessing renewable energy production capabilities using DEA window and fuzzy TOPSIS model, Symmetry 13 (2) (2021) 334, https://doi.org/10.3390/sym13020334.

[30] A. Al-Refaie, A. Al-Hawadi, S. Fraij, Optimization models for clustering of solid waste collection process, Eng. Optim. (2020) 1–14, https://doi.org/10.1080/0305215X.2020.1843165.

[31] R.A. Ibikunle, I.F. Titiladunayo, B.O. Akinnuli, S.O. Dahunsi, T.M.A. Olayanju, Estimation of power generation from municipal solid wastes: a case study of ilorin metropolis, Nigeria, Energy Rep. 5 (2020) 126–135, https://doi.org/10.1016/j.egyr.2019.01.005.

POSTER PRESENTATION

A fuzzy proximity relation approach for outlier detection in the mixed dataset by using rough entropy-based weighted density method

Rakhi Jha, Department of Computer Scinece Engineering , NM Institute of Engineering & Technology, Bhubaneswar, rakhijha91@yahoo.co.in

Sunil Kumar Mahapatro, Department of Electrical Engineering, Aryan Institute of Engineering & Technology, Bhubaneswar, skmahapatro78@outlook.com

Sandip Kar Mazumdar, Department of Electrical Engineering , Raajdhani Engineering College, Bhubaneswar, sk_mazumdar1@gmail.com

Manoj Mohanta, Department of Electrical and Electronics Engineering, Capital Engineering College, Bhubaneswar, manoj.mohanta62@outlook.com

A R T I C L E I N F O

Keywords:
Data Mining
Entropy
Fuzzy Proximity
Mixed Data
Rough sets
Weighted Density

A B S T R A C T

Data mining is an emerging technology where researchers explore innovative ideas in different domains, particularly detecting anomalies. Instances in the dataset which considerably deviate from others by their common patterns are known as anomalies. The state of being ambiguous and not affording certainty of data exists in this world of nature. Rough Set Theory is a proven methodology which deals with ambiguity and uncertainty of data. Research works that have been done until this point were focused on numeric or categorical type, which fails when the attributes are mixed type. By using fuzzy proximity and ordering relations, the numerical data has been converted to categorical data. This article presented an idea for detecting outliers in mixed data where the weighted density values of attributes and objects are calculated. The proposed approach has been compared with existing outlier detection methods by taking the hiring dataset as an example and benchmarked with Harvard dataverse datasets to prove its efficiency and performance.

1. Introduction

Data can be defined as any matter, numerals, or content easily handled by a system. Nowadays, companies have a huge volume of data in various styles and aspects. It comprises operational information such as stock and finance, non-operational information like weather forecasting and monetary information, and meta information (the information about the information itself), like the design of different databases or definitions for a word given in a dictionary [3]. Modeling of data or providing the link between these objects will provide some information. The point of sale system provides information regarding when the products are sold. The information can be translated into knowledge based on previous facts and by future predictions. The point of sale system can be improved by knowing the buying behavior of the customers. In recent years, massive data acquisition are amassed at the supermarkets, images produced by the satellites, and data present in the networking system [29]

A dataset may contain instances that have not adhered to normal behavior or deviate from the rest of the objects are termed as outliers [11]. A dataset may be comprised of numerical, categorical, or mixed types of data. It also alludes to discovering designs in the information system that does not adjust to expected behavior. Exceptions have likewise been alluded to as abnormalities, dissonant perceptions, exemptions, issues, abandons, distortions, commotion, or contaminants in various application domains. In earlier days, outliers were discarded as noise or exceptions.

An anomaly may demonstrate wrong information. For instance, the information may have been coded mistakenly, or the analysis might not have been run accurately[16]. If the outlying point is erroneous, then it can be corrected or removed from the dataset. It may not be conceivable to decide whether an outlying point has invalid information. If the information contains critical anomalies, we may need to think about the utilization of powerful,measurable systems[6]. But nowadays, much importance will be given to identify outliers. Because sometimes it may hold some valuable information. It is vital to identify outliers in major domains such as criminal activities like misuse of mobile phones and credit card activities, pattern recognition of malignant tumors, secured communication in the presence of third parties, malfunction of an airplane engine, and artificial intelligence [2]

The intra region anomalies are determined by density-based and inter-region anomalies are determined by distance-based methods[10]. Also, outliers can be identified in exceptional cases and the generation of novel patterns. Mostly clustering techniques provide efficient outlier detection rather than classification method. The statistical approach, probability model, will also be used to determine outliers[17].

Outliers are reported in two categories: the labeled objects are

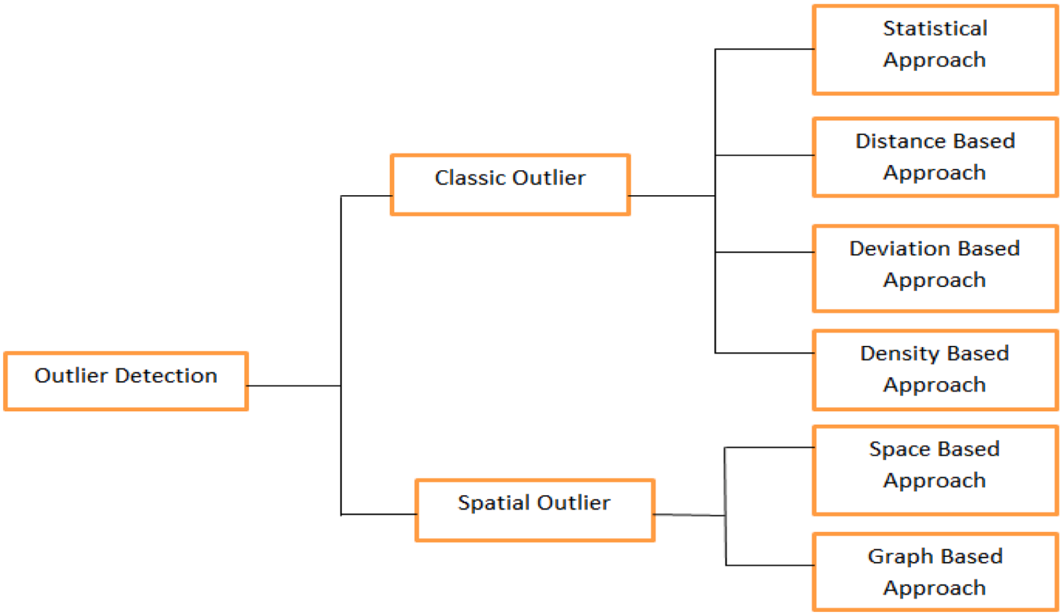

Fig. 1. Different Methodologies of outlier detection.

treated as normal objects, and the remaining objects that are not labeled are identified as outliers. Each pattern will be assigned an outlier score by fixing the threshold value to determine the degree of outliers [18]. The similitude of data cannot be correspondingly measured if there exists much noise. But the similarity measure and density measure do not suit high dimensional data [8]. Nowadays, researchers are focussing on detecting outliers in high-dimensional data. Because so many works were carried out to detect outliers for qualitative and quantitative data [23]. The proposed approach probably suits mixed data with a high level of significance. Different methodologies for outlier detection techniques are shown in Fig. 1.

2. Outlier detection method

2.1. Supervised method

This technique displays data uniformity and anomaly. The specialists label similar objects and objects that do not coordinate the model of ordinary objects as exceptions or outliers [1]. The normal data objects appear much than the outlier objects. This method has two classes (normal and outliers) which are imbalanced. The small amount of sample data taken for training will not suitably be considered for outlier distribution. But labeling the true object as an outlier should not be allowed. It is more important than outlier detection.

2.2. Unsupervised methods

In a few applications, labeling objects as "usual" or "exception" are not made. Consequently, an unsupervised learning technique must be utilized. Clustering can be done between normal objects and outlier objects[9]. Objects which deviate from normal behavior form one cluster, and the remaining objects fall into a normal category. The issues in unsupervised strategies are sometimes data that does not belong to any group might be considered noise but not an outlier[35]. Also, it is regularly expensive to design clusters first and to find anomalies. It is typically expected that outlier objects are distant than objects which are considered to be normal.

2.3. Semi-supervised methods

It can be viewed as the utilization of semi-supervised learning strategies. In particular, while accessing labeling objects, it can be utilized, or with the closer unlabelled objects that are close by preparing a layout for normal objects. The layout of the ordinary object at that point can be utilized to identify outliers - the items which do not fit into the layout of normal objects are anomalies [4]. To enhance the nature of exception location, one can get assistance from models of unsupervised strategies.

3. Rough set theory and fuzzy approximation space

During the 1980s, Zdzislaw Pawlak[27], a Polish mathematician, developed a mathematical tool called rough sets with lower and upper approximation concepts, which have crisp sets. However, it does not need any prior or extra information about concerned data. There exists a strict association between vague and uncertain data. The rough set approach demonstrates a clear association between these two ideas. Vagueness is associated with sets, while uncertainty is associated with components of sets. The data analysis with rough sets uses decision tables with structured rows and columns[12]. The columns of a table are attributes classified into two groups: condition and decision attributes. Each row specifies an object which induces some decision or result. If some conditions are satisfied, then the decision rule is certain; otherwise, it is uncertain.

It also implicates the thought of similarity. Let us consider the information table $IT=(W, X, Y, Z)$ where W is the universe which should be nonempty, X is the set of attributes, Y and Z are the conditional and decisional attributes[13]. The components of W are objects, entities, items, or investigations. Attributes are also represented as features, aspects, or characteristics.

Assume $S=(V, RT)$ then the subset $Y\subseteq V$ and an equivalence relation $RT\in IND(S)$. The subsets of X, such as lower and upper approximation, are defined as follows:

$$\underline{RT}Y = \cup^{\{X\in V/RT:\ X\subseteq Y\}}$$
$$\overline{RT}Y = \cup^{\{X\in V/RT:\ X\cap^{Y}=\emptyset\}}$$
$$or$$
$$x \in \underline{RT}X \ \ if\ and\ only\ if\ \ [x]_{RT}\subseteq X$$
$$x \in \overline{RT}X if and only if [x]_{RT}\cap^{X} \neq 0$$

From this, $Boundary(X) = \overline{RT}X - \underline{RT}X$ will be called the RT boundary of X. The boundary sets are included in the upper approximation but not in the lower approximation. Rough sets are defined through the lower

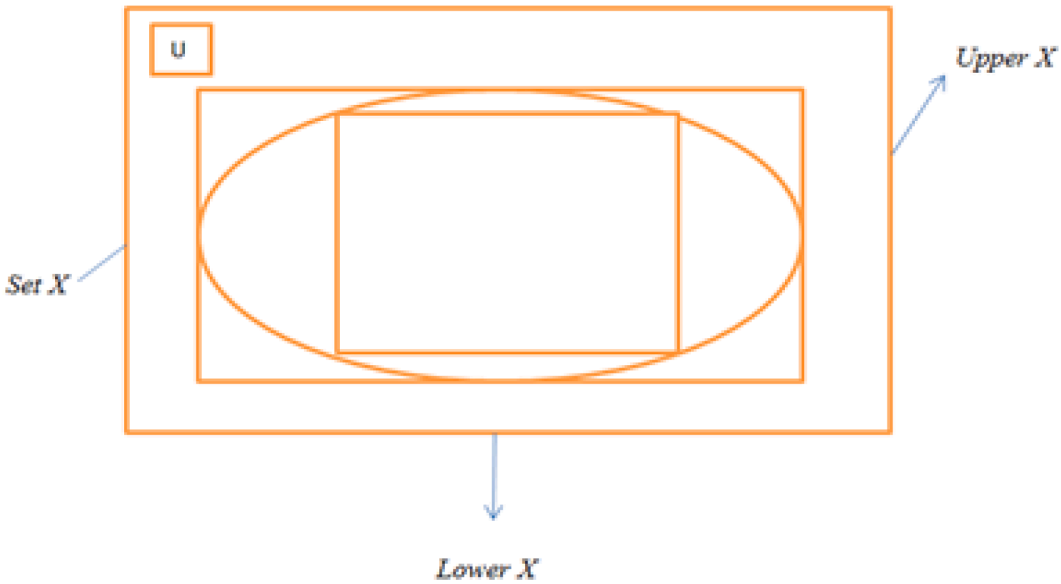

Fig. 2. Set Approximation

and upper approximation. Also, a boundary region is a devoid set ($\overline{RT}\, X \neq \underline{RT}\, X$).

3.1. *Membership relation and approximation*

Membership relation is derived from approximation spaces. Both membership and set approximation are related to knowledge only[28]. The representation is shown below:

$$l \underline{\in}_T L then l \in \underline{T} L$$
$$l_T \overline{\in} L then l \in \overline{T} L$$

In which, $\underline{\in}_T$ reads "l surely belongs to L for T" and $\overline{\in} T$, "l possibly belongs to L concerning T", is the lower and upper membership relation, respectively. Fig. 2 depicts the set approximation.

3.2. *Fuzzy approximation space with Rough Sets*

In general, fuzzy sets are used to handle the issues in understandability of the patterns, incomplete and noisy data, multimedia information, and intercommunication between persons resolves quickly within the determined time [14]. The minimal and maximal approximation for a fuzzy set B in Z as the fuzzy sets $T \downarrow B$, $T \uparrow B$ in Z *as*

$$(T{\downarrow}B)(r) = inf_{s \in S}\ (R(s,\ r),\ A(s))$$
$$(T{\uparrow}B)(r) = sup_{s \in S} T(R(s,\ r),\ A(s))$$

$T{\downarrow}B$ and $T{\uparrow}B$ can also be determined as how much inclusion T_r in B and overlap of T_r and B respectively [10], which is related to $r \in T \downarrow A$ *only* $[r]_T \subseteq B$ and $r \in T \uparrow B$ *only* $[r]_T \cap B \neq 0$.

4. Related work

Datasets make different clusters based on different labeling techniques. A data item to be compared with these formed clusters that don't belong to any cluster will be identified as an outlier[7]. For a single class classification, a support vector data description (SVDD) method was used. It determines a hypersphere that includes all normal data within its space. The objects which out lies from the hypersphere are termed outliers. In k-means clustering, objects that are found to be similar under a feature vector are formed into clusters, and any object that does not group under any cluster is outliers. In the local outlier factor method (LOF), the relative distance of an object with its neighborhood points is to be calculated. If the value has a high deviation, then it is an outlier [34].

Multivariate Outlier Detection (MOD) is a traditional strategy for the detection of outliers. It regularly demonstrates those perceptions that are found generally a long way from the focal point of the information distributed. A few distance measures are executed for such detection [19]. The Mahalanobis distance is an outstanding rule which relies upon evaluated parameters of the multivariate distribution.

The rough membership function also is used to detect outliers from the real-world dataset. One of the most popular distance-based approaches is the Manhattan distance. When the threshold value increases, this technique outdoes the performance of statistical approaches and distance-based methods. The efficiency can be improved by fixing the proper threshold value. The clustering technique provides more accuracy than the distance-based approach[37,38]. Small clusters can be constructed by using Partitioning Around Medoids (PAM) to detect outliers from the dataset.

In neural networks, the data will be trained and tested. It is used to clear the ambiguity in patterns and is also an effective tool to retrieve knowledge from large databases. The rough set method with the neural network is defined well to handle data mining problems. A backpropagation algorithm has been employed using rough sets to avoid inconsistencies between data. The neural system learning model uses backpropagation. Neurobiologists and therapists initially ignited this field to create and test neuron's computational analog. The neural system is arranged so that input/yield units are associated with weights related to it [25].

Backpropagation learns by preparing an informational index of tuples iteratively, which contrasts the system's expectation of an individual tuple with the known target. The objective target might be the class name known for the preparation tuple (characterization issues) or consistent instance (forecast). Each preparation tuple has weights altered to limit the error of mean squared value between the system's expectation and the real target instance [20]

Rough Entropy has been used to measure the uncertainty of data. Each object and attribute is calculated with a weighted density value to detect outliers. But clustering of data had not been done[21]. The clustering approach can be improved by using RKM (rough K-means) with a preliminary centroid selection method [22]. Cluster validity index will be achieved by improved entropy-based rough K-means (ERKM) method. In multi granulation rough sets, the decision was made by "OR" instead of "AND" logic. When the two attributes have

Table 1
Study on different outlier detection methods

S. No	Outlier Detection Method	Advantages	Disadvantages
1	Support Vector Data description (SVDD)	It detects outliers well in smaller sample sizes and produces effective results for more intricate and scanty datasets.	If the sample sizes become larger, outlier detection is difficult.
2	k means clustering	Even if the dataset is huge,outlier detection is possible	Generally, outliers are to be discarded, but in this method, outliers form a separate group.
3	Local Outlier Factor(LOF)	The point at the smallest distance is considered an outlier to the cluster, which is at a denser level. But in general outlier detection approaches, the point at the smallest distance will not be considered an outlier.	The threshold value will be fixed to detect outliers. The fixation of the threshold value will be based on the problem and the user.
4	Multivariate Outlier Detection (MOD)	It detects outliers (of n features)in n-dimensional space.	Finding distributions of n-dimensional space is difficult, so training of the dataset would be required.
5	Partitioning Around Medoids (PAM)	When compared to other available partitioning algorithms, outliers are less noticeable in the PAM method	Choosing k medoids is random; it gives a different result for the same dataset.
6	Backpropagation Method	A deeper understanding of the data is not required.	Particularly sensitive to noisy data.
7	Rough k Means(RKM)	The weighted density method uses the Gaussian function to detect outliers in a vague dataset.	When separating objects which are overlapped between clusters, the approach is susceptible.
8	Entropy Rough k Means (ERKM)	Effectively outliers are removed, which results in the formation of quality clusters.	Centroid selection is random based on the Rough k means Method(RKM)

contradictions and inconsistencies, multi granulation with a rough set framework has been used [40]. So that, it needs effective computation.

The traditional approach of outlier detection was the statistical method where it applies to single-dimensional datasets alone. The model suitably fits for perceptible real-world datasets where the categorical data has been converted into numerical data for the processing of statistical methods [5]. So it increases the processing time for tangled datasets. The simple outlier detection method with no prior information needed for the processing of data is the proximity-based technique. But, the calculation of distances between all objects results in high exponential growth. The number of objects n and its dimensionality m is directly proportional to its time complexity. So it will not be suitable for high dimensional data.

The parametric method is suitable for larger datasets because it has a built-in distribution model. If any model fits the prescribed dataset, then the outcome will be accurate. The data model grows with paradigmatic complexity, not with the size of data. The only condition is the predefined model should be fit for the available dataset. The nonparametric methods need prior information to process.

In some cases, the prior knowledge will not be available, or the computation cost will be high[32]. Many datasets use not only a determined data model but also follow a random distribution model. It may be applicable for regression and principal component analysis methods. In the pre-processing stage, parameter settings are to be made, and later they should be processed.

An outer perception, or anomaly, seems to diverge extraordinarily from other individuals where it occurs. A perception (or a subset of perceptions) gives off an impression of conflicting with the rest of the data [24]. Exceptions are defined as the focuses lie outwards from the cluster but at the same time are isolated from the noise[30]. Patterns with the well-defined notion of normal behavior, which are not confirmed, are outliers, and the regions of network structure differs from expected under the normal behavior [26].

Social network anomaly detection focuses on outlier detection techniques developed in machine learning and statistical domains [31]. Intrusion detection with anomaly detection was proposed through system calls[33]. First, evaluate decision-makers preferences for each choice and introduce the concept of pre-decisions, resulting in an incomplete fuzzy decision system[43]. Then, using the defined similarity relation, the weighted conditional probabilities are determined. The concept of relative utility functions is next introduced, followed by a method for determining relative utility function values. Then, in incomplete fuzzy decision systems, we build a three-way decision model and apply it to the modeling of incomplete multi-attribute decision--making issues[44].

On IFVIS(intuitionistic fuzzy-valued information systems), three alternative sorting decision-making procedures include subtracting intuitionistic fuzzy numbers, sorting functions, and intimacy coefficients [45].We create the outranked set for each alternative and present a hybrid information table that includes a Multi-Attribute Decision-Making matrix and a loss function table.Multi-attribute decision-making (MADM) is a crucial component of modern decision sciences[46]. It refers to a decision problem of selecting the best alternative or ranking alternatives based on numerous attributes.A three-way decision has been included in a multi-scale decision information system, which offers a novel approach to addressing multi-attribute decision-making concerns in a multi-scale decision information system[47]. In addition, a review has been made for outlier detection using data mining methods. The pros and cons of different outlier detection methods are shown in Table 1.

5. Proposed model

Detecting outliers is a major data mining technique that has significant consideration inside different research groups and application domains. Numerous methods have been created to identify outliers but only on numerical data. Those methods cannot be applied directly to categorical data. So the fuzzy proximity relation is introduced to convert numerical data to categorical[36]. Then the Density and uncertainty of every object and attribute are calculated. For a stable dataset, the fixation of the threshold value is high, and for the unstable dataset, the lower threshold value is fixed. In this way, outliers are removed incredibly to improve the execution of data mining algorithms. In Fig. 3, at the pre-processing stage, the mixed data is converted to categorical by using fuzzy proximity relation in post-processing. Finally, a rough set entropy-based weighted density outlier detection approach is applied to determine outliers.

5.1. Roughset entropy-based weighted density outlier detection algorithm

A dataset may include missing data and some negative and null values, which are outliers. So the dataset is defined to be vague and incomplete. To handle this scenario, a rough set with a weighted density-based outlier detection method is proposed. In the pre-processing stage, numerical data is converted to categorical data by using fuzzy proximity relation, and then it is ordered. In the post-processing stage, similar objects are identified concerning attributes using indiscernibility relation, and complement entropy measure is used to calculate uncertainty values; the weighted density values are calculated by identifying indiscernible objects divided by the total number of objects to each attribute. Finally, the user fixes the threshold value. If the calculated value is lesser than the threshold, then they are treated as outlier objects. The following definitions will be used to detect outliers when the table has been converted from mixed to categorical type,

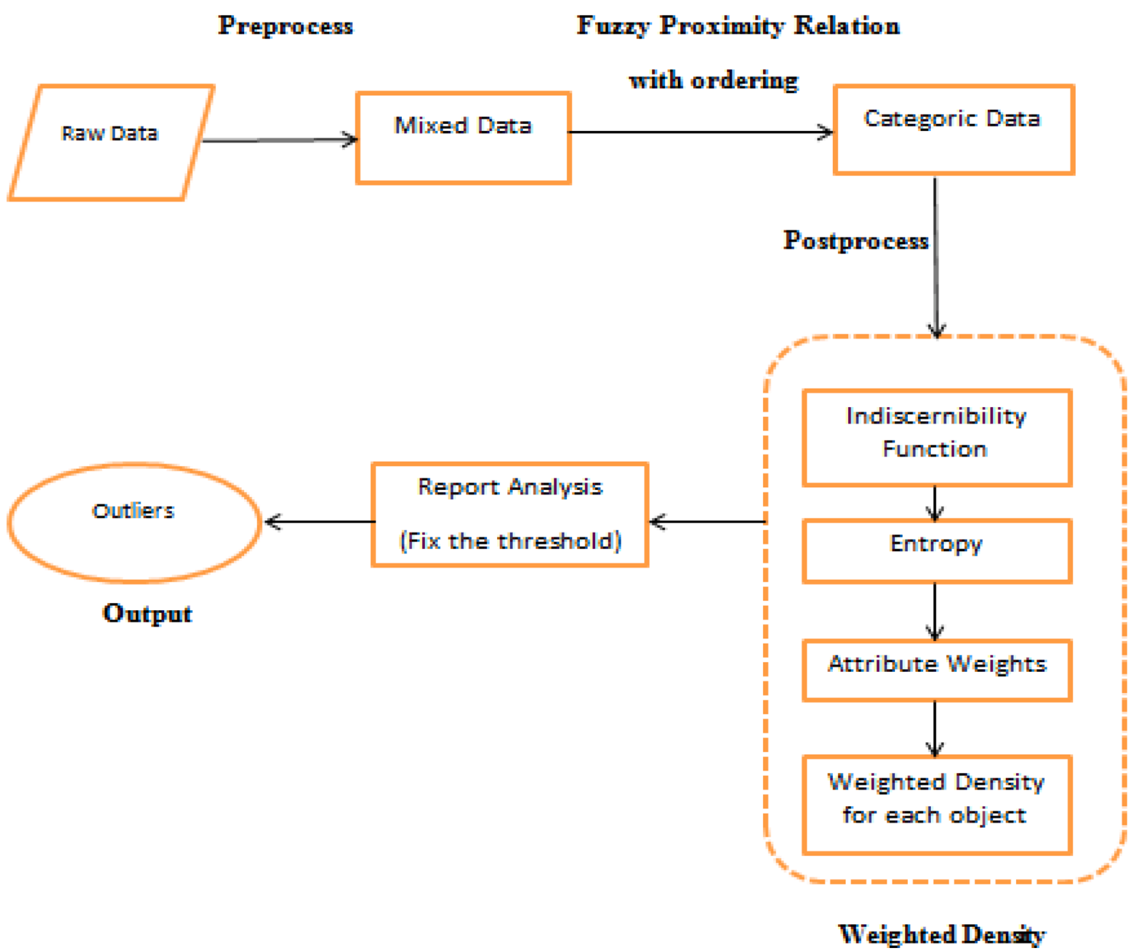

Fig. 3. Proposed Model for Outlier Detection using Rough Sets.

which is discussed below:

Definition 1:A. dataset DS is defined by the triplet $DS=(Z, R, C)$ where Z represents the universe, R represents the objects, and C represents the attributes in a dataset.

Definition 2. Let $DS= (Z, R, C)$ and $RT \subseteqq C$. The indiscernibility relation RT for r in R or s in C is represented as

$$\{Z|IND(RT)\} = \{[r]_{RT}|\ r\epsilon Z\ \}$$

Definition 3:Let. $DS=(Z, R, C)$, and $RT \subseteqq C$ and $\frac{Z}{IND(RT)} = \{C_1, C_2, \ldots C_m\}$.The complement entropy *(CPE)* with respect to RT is defined as

$$CPE(RT) = \sum_{j=1}^{n} \frac{|C|}{|R|}\frac{|C|_j^c}{|R|}$$

where C_j^c denotes complement set of C_j, which is $C_j^c = R - C$;

Definition 4. Let $DS= (Z, R, C)$, the weight of every attribute for C is defined as

$$Weight(C) = \frac{1 - CPE(RT)}{\sum_{j=1}^{n}(C_j)}$$

Definition 5:The. average Density of each attribute will be determined as

$$AverageDensity(R_j) = \frac{|[R_j]_C|}{|Z|}$$

From that, the weighted Density of each object will be determined as follows:

$$WeightedDensity(C) = \sum_{r_j \epsilon R}(Average\ Density(R_j), Z(C))$$

Definition 6. Let us consider the dataset $DS=(Z, R, C)$, and θ is a fixed threshold value from the weighted density objects. If the value of *Weighted Density(R)* $< \theta$ then r is termed an outlier.

6. An empirical study on hiring dataset

A fabricated mixed dataset "Hiring" is designed with four conditional attributes Degree, Experience, French, and Reference for the effective proposed approach. The attribute experience has numerical values, and the remaining attributes such as degree, french, and reference have categorical values. So many algorithms are available for numerical data to detect outliers. But, our proposed method uses fuzzy proximity relation to convert numerical data to categorical data. The $FPR(o_i, o_j)$,which derives binary relation for the numerical attribute experience by using the formula,finds the almost similarity among the objects o_i &o_j.

$$FPR(o_i, o_j) = 1 - \frac{|o_i - o_j|}{(o_i + o_j)}$$

Based on calculated values, the attribute experience is ordered. The proposed algorithm has been applied to this dataset to detect outliers and graphs have also been plotted using the nominal values. The author has been conducted evaluations by comparing existing methods with the proposed method for hiring dataset. The hiring dataset with 10 objects and mixedattributes are shown in Table 2 and Table 3 shows fuzzy proximity relation for the attribute experience.

Table 2
Hiring Dataset - Mixed Type

Objects	*Degree*	*Experience*	*French*	*Reference*
E_1	*MBA*	*5.2*	*Yes*	*Excellent*
E_2	*MSc*	*4.3*	*Yes*	*Good*
E_3	*MSc*	*3.4*	*No*	*Neutral*
E_4	*MBA*	*2.5*	*No*	*Good*
E_5	*MCA*	*6.2*	*Yes*	*Good*
E_6	*MCA*	*3.1*	*Yes*	*Neutral*
E_7	*MBA*	*2.2*	*Yes*	*Excellent*
E_8	*MSc*	*3.2*	*No*	*Excellent*
E_9	*MCA*	*2.7*	*No*	*Good*
E_{10}	*MBA*	*2.4*	*Yes*	*Neutral*

Let the almost indiscernibility be $\omega \geq 90\%$, From Table 2, thus, the objects E_1, E_2, E_5 are ω- identical. Similarly, $E_3, E_4, E_6, E_7, E_8, E_9, E_{10}$ are ω – identical.

$$U/R_1^{\omega} = \{\{E_1, E_2, E_5\}, \{E_3, E_4, E_6, E_7, E_8, E_9, E_{10}\}\}$$

Based on the similarity value of ω, the attribute experience is ordered into two groups. The numerical values of the attribute experience for objects $\{E_1, E_2, E_5\}$ are having greater values. So it is classified as High and the remaining objects $\{E_3, E_4, E_6, E_7, E_8, E_9, E_{10}\}$ are classified as Low. Now the numeric type of experience attribute is converted to categorical, which is shown in Table 4.

Obtain indiscernible relation for each attribute. Objects that possess indiscernible values for attributes are:

$$U/IND\ (Degree) = \ \{E_1, E_4, E_7, E_{10}\}, \{E_2, E_3, E_8\}, \{E_5, E_6, E_9\}$$

$$U/IND(Experience) \ = \ \{E_1, E_2, E_5\}, \{E_3, E_4, E_6, E_7, E_8, E_9, E_{10}\}$$

$$U/\ IND(French) = \{E_1, E_2, E_5, E_6, E_7, E_{10}\}, \{E_3, E_4, E_8, E_9\}$$

$$U/IND(Reference) = \{E_1, E_7, E_8\}, \{E_2, E_4, E_5, E_9\}, \{E_3, E_6, E_{10}\}$$

The complement entropy function is to be calculated for each attribute with the obtained indiscernible relation.

$$CE(Degree) = \frac{4}{10}\left(1 - \frac{4}{10}\right) + \frac{3}{10}\left(1 - \frac{3}{10}\right) + \frac{3}{10}\left(1 - \frac{3}{10}\right) = \frac{33}{50}$$

$$CE(Experience) = \frac{3}{10}\left(1 - \frac{3}{10}\right) + \frac{7}{10}\left(1 - \frac{7}{10}\right) = \frac{21}{50}$$

$$CE(French) = \frac{24}{50}\ ; CE(Reference) = \frac{33}{50}$$

Calculate each attribute weight by adding the total number of attributes with the complement entropy function.

$$Weight\ of\ Attribute(Degree) = \frac{17}{54};\ Weight\ \ of\ Attribute(Experience) = \frac{29}{54}$$

$$Weight\ \ of\ Attribute(French) = \frac{26}{54};\ Weight\ of\ Attribute(Reference) = \frac{17}{54}$$

The weight of each object should be calculated by the summation of the product of the weight of attributes with indiscernible objects.

$$W\ (E_1) = \frac{4}{10} \times \frac{17}{54} + \ \frac{3}{10} \times \frac{29}{54} + \frac{6}{10} \times \frac{26}{54} + \frac{3}{10} \times \frac{17}{54} = 0.67;$$

$$W(E_2) = \ 0.67; W(E_3) = \ 0.75; W(E_4) = 0.82; W(E_5) = 0.67\ ;$$

$$W(E_6) = 0.85; W(E_7) = 0.88; W(E_8) = 0.75;\ W(E_9) = 0.78;$$

$$W(E_{10}) = 0.88.$$

If $\theta < 0.7$, then the objects E_1, $E_2$and E_5 are outliers. The normal and outlier objects are shown in Fig. 4.

7. Experimental results

The working model of outlier detection algorithm in mixed datasets will be understood by, conducted experiments on a hiring dataset that has 120 objects with four conditional attributes of numerical and categorical values. It has been implemented with Processor-Intel Pentium,1GigaByte RAM, and the Windows10 operating system. Existing methods like Distance-based, Density-based, Local Outlier Factor and Class outlier factor were analyzed using Rapid Miner 7.0. The concept of Rough sets was implemented using C. It is a flexible language that is used to implement mathematical models. The proposed algorithm has been run on a hiring dataset that is of mixed type. The fuzzy proximity relation method was used to convert numerical value to categorical value, and then it was ordered.

A rough set entropy-based weighted density outlier detection

Table 4
Converted Table – Mixed to Categoric Type

Objects	*Degree*	*Experience*	*French*	*Reference*
E_1	*MBA*	*High*	*Yes*	*Excellent*
E_2	*MSc*	*High*	*Yes*	*Good*
E_3	*MSc*	*Low*	*No*	*Neutral*
E_4	*MBA*	*Low*	*No*	*Good*
E_5	*MCA*	*High*	*Yes*	*Good*
E_6	*MCA*	*Low*	*Yes*	*Neutral*
E_7	*MBA*	*Low*	*Yes*	*Excellent*
E_8	*MSc*	*Low*	*No*	*Excellent*
E_9	*MCA*	*Low*	*No*	*Good*
E_{10}	*MBA*	*Low*	*Yes*	*Neutral*

Table 3
Fuzzy Proximity Relation -Experience Attribute

R_1	E_1	E_2	E_3	E_4	E_5	E_6	E_7	E_8	E_9	E_{10}
E_1	1.0000	0.9053	0.7907	0.6494	0.9123	0.747	0.5946	0.7620	0.6836	0.6316
E_2	0.9053	1.0000	0.8832	0.7353	0.8191	0.8379	0.677	0.8534	0.7715	0.7165
E_3	0.7907	0.8832	1.0000	0.8475	0.7084	0.9539	0.7858	0.9697	0.8853	0.8276
E_4	0.6494	0.7353	0.8475	1.0000	0.5748	0.8929	0.9362	0.8772	0.9616	0.9796
E_5	0.9123	0.8191	0.7084	0.5748	1.0000	0.6667	0.5239	0.6809	0.6068	0.5582
E_6	0.747	0.8379	0.9539	0.8929	0.6667	1.0000	0.8302	0.9842	0.9311	0.8728
E_7	0.5946	0.677	0.7858	0.9362	0.5239	0.8302	1.0000	0.8149	0.898	0.9566
E_8	0.762	0.8534	0.9697	0.8772	0.6809	0.9842	0.8149	1.0000	0.9153	08572
E_9	0.6836	0.7715	0.8853	0.9616	0.6068	0.9311	0.8980	0.9153	1.0000	0.9412
E_{10}	0.6316	0.7165	0.8276	0.9796	0.5582	0.8728	0.9566	0.8572	0.9412	1.0000

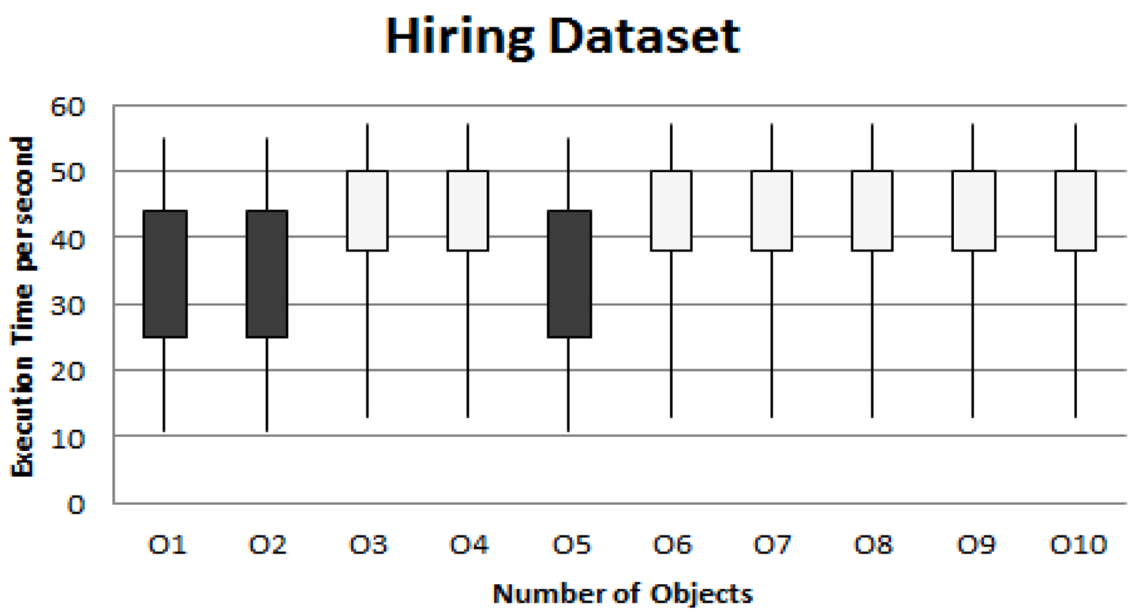

Fig. 4. Showing Normal and Outlier objects.

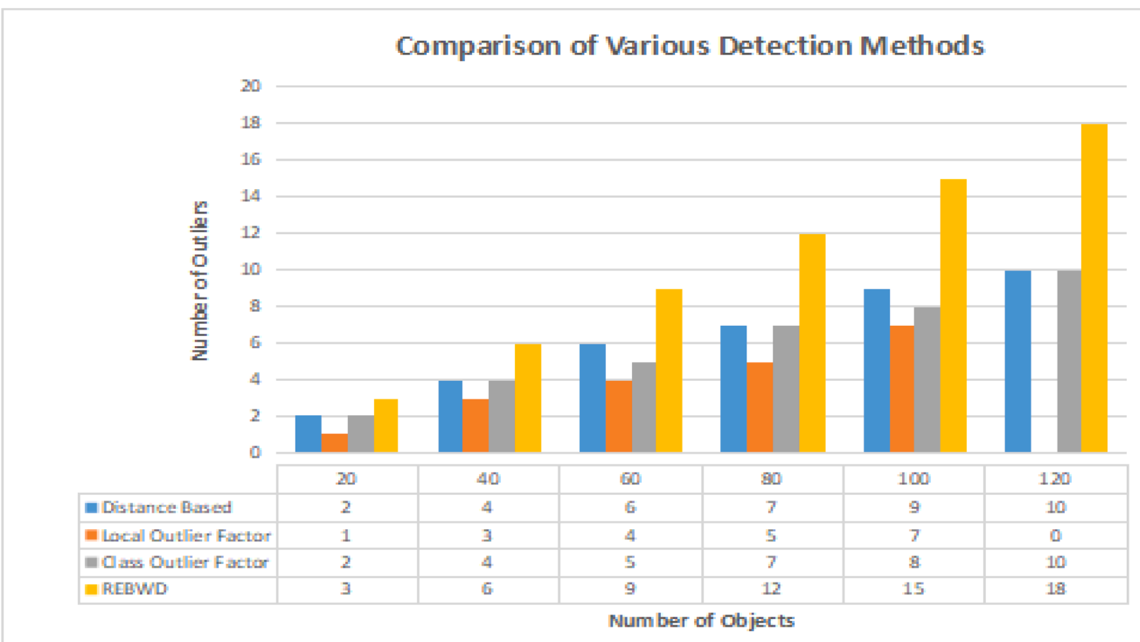

Fig. 5. Comparison Chart for Existing Methods with Proposed Method

method has been applied for effective outlier detection. Fig. 5 shows that the comparison chart for an existing and proposed method for outlier detection. In the distance-based outlier detection method, each data point has been ranked based on the distance to its *k-th* nearest neighbor [39] so that the top *n* data points are declared as outliers. It detects ten outlier objects. In density-based outlier detection method *DensityBased (p, P)*, an object that deviates at least P distance from the p, the proportion of all data objects is considered outliers. This method does not detect any outlier objects. In the local outlier factor method, each object should be calculated with a local outlier factor based upon the local density measure. Then it is compared with their *l* nearest neighbors [41].

The objects which are having lower density values when compared with their neighbors are termed to be outliers. It detects seven outlier objects. In the class outlier factor method, each data point in the sample will be ranked based on ClassOutlierFactor=(S, N) where S represents top-class outlier and N represents the number of nearest neighbors. This algorithm detects ten outlier objects. Further, our proposed method rough set entropy-based weighted density outlier detection method detects outliers by computing the weighted density value of all objects and attributes. It detects 18 outlier objects[42]. Our proposed algorithm's performance and efficiency are high compared to existing methods because it calculates weighted density values for every object and attribute so that a true object will never be detected as an outlier. The comparison chart showing various outlier detection methods is shown in Fig. 5.

Also, benchmark datasets such as the annthyroid dataset, breast cancer dataset, and letter dataset have been taken from Harvard dataverse to show the proposed algorithm efficiency, which has been compared with other existing outlier detection methodologies such as local outlier factor (LOF), feature-based(FB), isolation forest(IF), K-

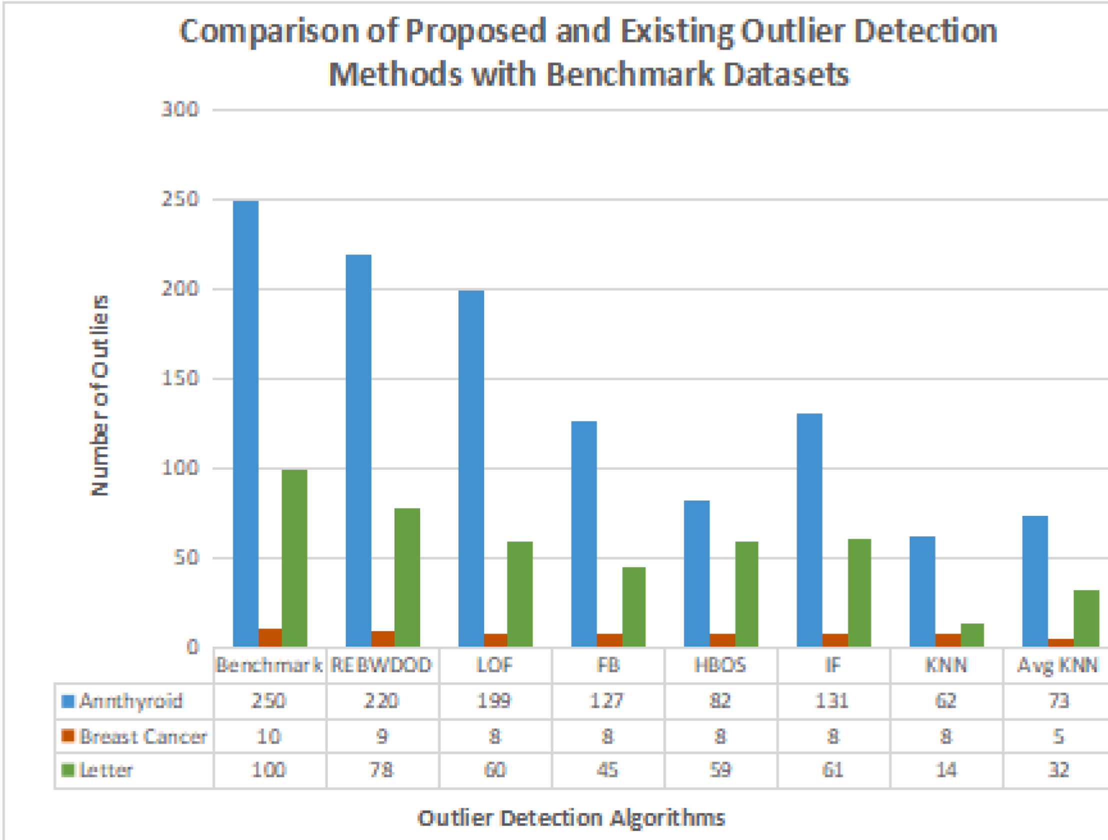

	Benchmark	REBWDOD	LOF	FB	HBOS	IF	KNN	Avg KNN
Annthyroid	250	220	199	127	82	131	62	73
Breast Cancer	10	9	8	8	8	8	8	5
Letter	100	78	60	45	59	61	14	32

Fig. 6. Comparison of Proposed and Existing Outlier Detection Methods with Benchmark Datasets.

nearest neighbor (KNN), average KNN and histogram-based outlier score (HBOS). The local outlier factor determines the Density of an object with the distance of its neighbors. Feature bagging selects features of the subsamples randomly and finally combines the values of all base detectors, using the local outlier factor. Isolation forest observes data by constructing a tree[15]. The isolated value score is determined as outliers that are well suitable for high dimensional data. By constructing histograms, outliers are detected in the histogram-based outlier score approach. It is an unsupervised learning method that generates scores by considering the independent features.KNN identifies the nearest neighbor to an object. Based on the distance, it calculates scores, and outliers are identified. In the Average KNN method, super samples are constructed for individual classes. The test data is given as an input, and Average KNN searches samples available in super samples or closer. Others are identified as outliers. The comparison chart of the proposed method with existing outlier detection algorithms for the benchmark datasets is shown in Fig. 6.

Other approaches like fuzzy bipolar soft set and Pythagorean fuzzy bipolar soft set are compared with the proposed method to prove its efficiency. The fuzzy-based bipolar soft set is used to analyze the patients with the help of membership degrees and decide whether the patient is hypomania, depression, or bipolar. Mostly it is used in decision-making systems.On the other hand, the pythagorean fuzzy bipolar soft setis mostly used in group decision-making situations. Personalization of the findings acquired is avoided because a common idea is derived from the opinions of all doctors. But the proposed method identifies indiscernible values, computesEntropy, and then calculates each object's weighted density value and attribute to detect outliers.

7.1. Measures for performance evaluation

The performance evaluation of benchmark datasets is measured by calculating their accuracy, specificity, sensitivity, precision, and F1 score. The accuracy of a classifier is calculated as the total number of objects which are correctly classified to the total number of objects available. The formula to calculate accuracy is as follows:

$$Accuracy = \frac{TP + TN}{TP + FN + TN + FP}$$

where TP is True Positive, FP is False Positive, TN is True Negative, and FN is False Negative. Thus, sensitivity or recall measures the true positive values proportion, which is correctly identified, whereas specificity measures the true negative values proportion, which is correctly detected. The values are obtained from the formulas shown below:

$$Specificity = \frac{TN}{TN + FP}$$

$$Sensitivity = \frac{TP}{TP + FN}$$

$$Recall = \frac{TP}{TP + FN}$$

Precision or positive predictive value is the one that measures relevant objects from the retrieved objects. The formula to calculate precision is as follows:

$$Precision = \frac{TP}{TP + FP}$$

F1 score measure provides the balance between precision and recalls when the distribution of classes is not even. It becomes worse when its value is 0 and best when it is 1. The formula to calculate the F1 score is as follows:

$$F1\ Score = \frac{2 * Precision * Recall}{Precision + Recall}$$

Table 5
Performance Evaluation - Annthyroid Dataset

Sl.No	Measures	LOF	REBWDOD
1	Accuracy	98.16%	99.57%
2	Specificity	1.0	1.0
3	Sensitivity	0.9813	0.9955
4	Precision	1.0	1.0
5	F1 Score	0.9906	0.9978

Table 6
Performance Evaluation - Breast Cancer Dataset

Sl.No	Measures	LOF	REBWDOD
1	Accuracy	99.18%	99.46%
2	Specificity	1.0	1.0
3	Sensitivity	0.99	0.99
4	Precision	1.0	1.0
5	F1 Score	0.9958	0.9972

Table 7
Performance Evaluation - Letter Dataset

Sl.No	Measures	LOF	REBWDOD
1	Accuracy	97.56%	98.69%
2	Specificity	1.0	1.0
3	Sensitivity	0.97	0.98
4	Precision	1.0	1.0
5	F1 Score	0.9872	0.9930

The performance evaluation of benchmark datasets such as annthyroid, breast cancer, and letter dataset are shown in Table 5, Table 6, and Table 7.

7.2. *Analysis of efficacy*

The following three sorts of tests have been conducted to see how each algorithm's performance changes as factors change, such as the size of the data set, the dimensionality of the data set, and the number of outliers[48].In comparison to the local outlier factor method, the WDOD approach takes less time in terms of data size, data dimensionality, and mark the number of outliers.

The WDOD technique appears to be particularly suitable for big data sets with high dimensionality and data sets with a high number of outliers, based on the results of these experiments. The WDOD algorithm's growing rate of execution time is substantially slower than the local outlier factor algorithm. As a result, when the data size is huge, attributes are more the suggested WDOD algorithm can ensure efficient execution in detecting outliers which are shown in Fig. 7, Fig. 8, and Fig. 9.

8. Conclusion

In this paper, outlier detection for a mixed dataset has been proposed. In the pre-processing stage, fuzzy proximity relations with order information rules convert numeric to categorical attributes. The rough set-based Entropy weighted density outlier detection method has been carried out to detect outliers in the post-processing stage. Research works carried out so far detect outliers only for numeric or categorical data, where mixed data was not considered. The proposed model detects outliers in the hiring dataset, which has mixed data, by calculating their weighted density value so that the normal object will not be detected as an outlier. However, the proposed algorithm is benchmarked with Harvard dataverse datasets such as the annthyroid dataset,breast cancer dataset, and letter dataset compared with the existing local outlier factor outlier method to prove its efficiency and performance level. As the number of increasing objects and attributes, the proposed method ensures efficient execution in detecting outliers.Future work will be focused on detecting outliers where input is dynamic and in multi-granulation sets. The proposed work has some limitations, such that the fixation of threshold value sometimes results in regular objects become outlier and outliers become regular objects.This research did not receive any specific grant from funding agencies in the public, commercial, or not-for-profit sectors.

9. Acknowledgements

Funding

No funding received for this research.

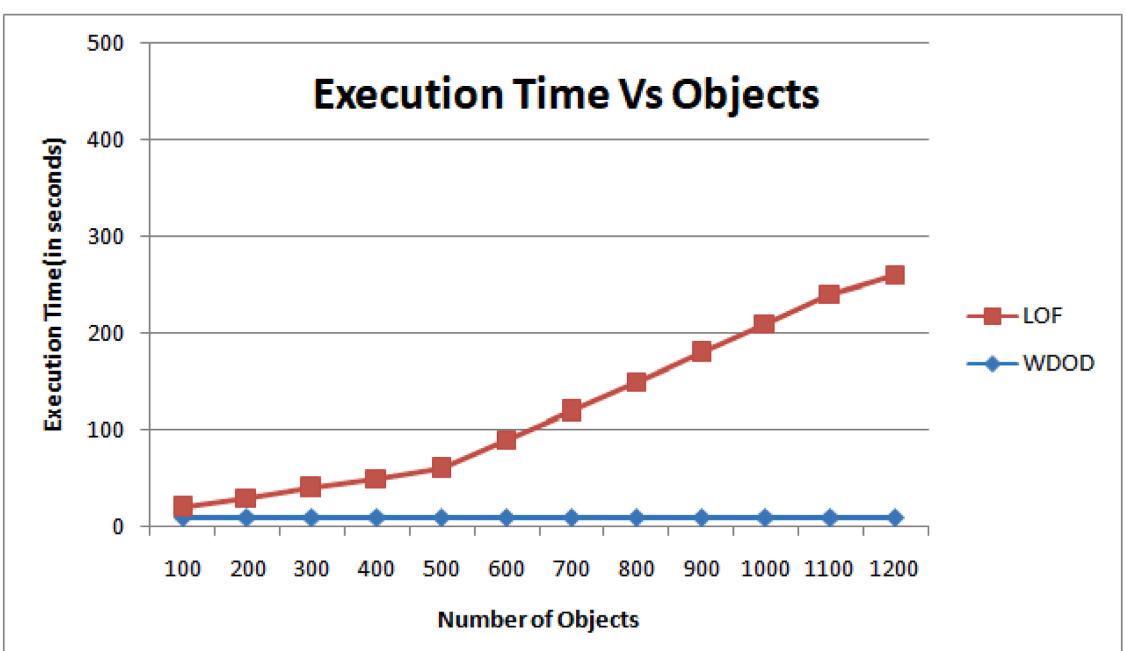

Fig. 7. Comparing execution time as the number of objects grows

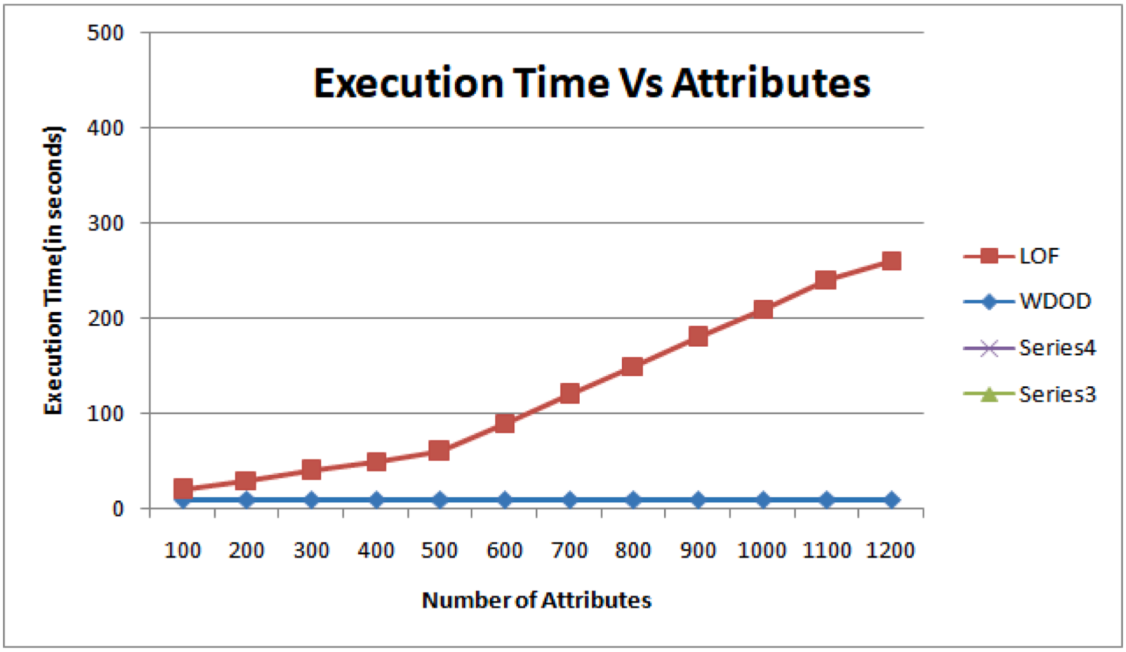

Fig. 8. Comparing execution time as the number of attributes grows

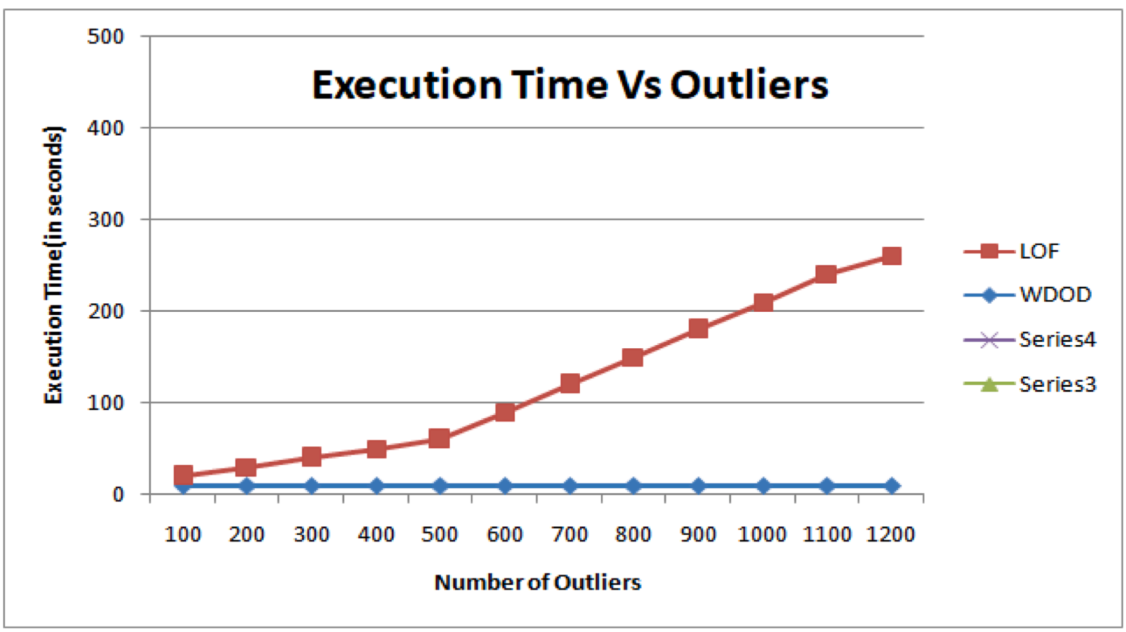

Fig. 9. Comparing execution time with an increased number of outliers

Competing interests

The process of writing and the content of the article does not give grounds for raising the issue of a conflict of interest.

Availability of data and material

Not applicable

Code availability

Not applicable

Author contributions

The corresponding author claims the major contribution of the paper including formulation, analysis and editing. The Second author provides guidance to verify the analysis result and manuscript editing.

Compliance with ethical standards

This article is a completely original work of its authors; it has not been published before and will not be sent to other publications until the journal's editorial board decides not to accept it for publication (Definations 1 & 6) (Algorithm 1)

Algorithm 1
The algorithm for the proposed model has been shown below:

Input: Dataset $DS(W,\alpha,\beta)$ and θ be threshold values.
Output: Set S holds outlier objects.

Step 1:Start
Step 2: Input the dataset of mixed type.
Step 3: Use fuzzy proximity relation and ordering to convert numeric into categorical data.
Step 4: Let $S = \emptyset$
Step 5: For each attribute $\beta_i \in \beta$
Step 6: Calculate the indiscernibility function $U/IND(\alpha_i)$ according to definition2;
Step 7: Calculate the complement entropy according to definition3;
Step 8:For each attribute $\beta_i \in \beta$, compute weighted Density according to definition4;
Step 9:For each object $\alpha_i \in W$, calculate the weighted Density according to definition5;
Step 10: If (*Weighted Density*(α_i) $<\theta$)
Step 11: $S = S \cup \{\alpha_i\}$.
Step 12: Return S.
Step 13: Stop.

References

[1] H.P. Achtert, L. Kriegel, E Reichert, R. Schubert, Zimek Wojdanowski, A Visual Evaluation of Outlier Detection Models, in: *Proc.* International Conference on Database Systems for Advanced Applications (DASFAA), Tsukuba, Japan, 2010. https://link.springer.com/chapter/10.1007/978-3-642-12098-5_34.
[2] C.C. Aggarwal, P.S. Yu, Outlier detection for high dimensional data, in: Proc.ACM-SIGMOD, Int. Conf. Management of Data (SIGMOD'01), 2001, pp. 37–46. Santa Barbara,CA, https://dl.acm.org/doi/abs/10.1145/375663.375668.
[3] A. Arning, R. Agrawal, &P. Raghavan, A linear method for deviation detection in large databases, in: Proc. Int. Conf. on Knowledge Discovery and Data Mining (KDD), Portland, 1996. OR, https://www.aaai.org/Papers/KDD/1996/KDD96-027.pdf.
[4] P. Ashok, &G.M.K. Nawaz, Outlier Detection Method on UCI Repository Dataset by Entropy-Based Rough K-means, J. Defence Science 11 (2016) 113–121.
[5] V. Barnett, &T. Lewis, Outliers in statistical data, John Wiley and sons, 1994.
[6] S.D. Bay, &M. Schwabacher, Mining distance-based outliers in near-linear time with randomization and a simple pruning rule, in: Proc. Int. Conf. on Knowledge Discovery and Data Mining (KDD), Washington, DC., 2003. https://dl.acm.org/doi/abs/10.1145/956750.956758.
[7] R.J. Beckman, R.D. Cook, Outliers Technometrics 25 (2) (1983) 119–149, https://doi.org/10.1080/00401706.1983.10487840.
[8] M.M. Breunig, H.P. Kriegel, J. Sander, Identifying density-based local outliers, in: Proc Acm Sigmod Conference, 2021, pp. 93–104. https://dl.acm.org/doi/abs/10.1145/342009.335388.
[9] V. Chandola, A. Banerjee, V. Kumar, Anomaly Detection A Survey, ACM ComputingSurveys 41 (1) (2011) 58–66, 2011, https://dl.acm.org/doi/abs/10.1145/1541880.1541882.
[10] A.G. Christy, M. Gandhi, S.V. Subramaniyan, Cluster based outlier detection for cluster data 5 (5) (2012) 363–387.
[11] D. Dasgupta, F.A. Nino, Comparison of negative and positive selection algorithms in novel pattern detection, in: Proceedings of the IEEE International Conferenceon Systems, Man, and Cybernetics. Nashville, TN 1, 2000, pp. 125–130. https://ieeexplore.ieee.org/abstract/document/884976.
[12] M. Ester, H.P. Kriegel, J. Sander, X. Xu, A density-based algorithm for discovering clusters in large spatial databases with noise, in: Proc. Int. Conf. on Knowledge Discovery and Data Mining (KDD), Portland, OR, 1996. https://www.aaai.org/Papers/KDD/1996/KDD96-037.pdf?source=post_page.
[13] F. Jiang, Y. Sui, C. Cao, Outlier Detection Based on RoughMembership Function, Rough Sets and Current Trends in Computing 4259 (2006) 388–397. https://link.springer.com/chapter/10.1007/11908029_41.
[14] S. Forrest, C. Warrender, B. Pearlmutter, Detecting intrusions using system calls: Alternate data models, in: Proceedings of the IEEE Symposium on Security and Privacy, IEEE Computer Society, Washington, DC, USA, 1999, pp. 133–145. https://ieeexplore.ieee.org/abstract/document/766910.
[15] A. Ghoting, S. Parthasarathy, M. Otey, Fast mining of distance-based outliers in high dimensional spaces, in: Proc SIAM Int Conf on Data Mining(SDM) dimensional spaces, Bethesda, ML, 2006. https://link.springer.com/article/10.1007/s10618-008-0093-2.
[16] F.E. Grubbs, Procedures for detecting outlying observations in samples, Technometrics 11 (1) (1969) 19–21. https://www.tandfonline.com/doi/abs/10.1080/00401706.1969.10490657.
[17] D. Hawkins, Identification of outliers, Monographs on Applied Probability and Statistics (1980).
[18] V. Hodge, J.A. Austin, Survey of outlier detection methodologies, Artificial Intelligence Review 22 (2) (2004) 85–126. https://link.springer.com/article/10.1023/B:AIRE.0000045502.10941.a9.
[19] J. Han, M. Kamber & J. Pei, Data Mining concepts and techniques, 2012.
[20] E.M. Knorr, R.T. Ng, A unified approach for mining outliers, in: Proc. Conf. of the Centre for Advanced Studies on Collaborative Research (CASCON), Toronto, Canada, 1997. https://www.aaai.org/Papers/KDD/1997/KDD97-044.pdf.
[21] E.M. Knorr, N.G. RT, Algorithms for mining distance-based outliers in large datasets, in: Proc. Int. Conf. on Very Large Data Bases (VLDB), New York, NY, 1998. https://citeseerx.ist.psu.edu/viewdoc/download?doi=10.1.1.55.8026&rep=rep1&type=pdf.
[22] E.M. Knorr, R.T. Ng, Finding intensional knowledge of distance-based outliers, in: Proc. Int. Conf. onVeryLargeDataBases(VLDB)Edinburgh Scotland on Very Large Data Bases (VLDB), Edinburgh, Scotland, 1999. http://citeseerx.ist.psu.edu/viewdoc/download?doi=10.1.1.45.9005&rep=rep1&type=pdf.
[23] A. Lazarevic, L. Ertoz, V. Kumar, A. Ozgur, J.A. Srivastava, Comparative study of anomaly detection schemes in network intrusion detection, in: Proceedings of theThirdInternational Conference on Data Mining. *SIAM*, 2021. https://epubs.siam.org/doi/abs/10.1137/1.9781611972733.3.
[24] A. McCallum, K. Nigam, L.H. Ungar, Efficient clustering of high-dimensional data sets with application to reference matching, in: Proc. ACM SIGKDD Int. Conf. on Knowledge Discovery and Data Mining (SIGKDD), Boston, MA, 2000. https://dl.acm.org/doi/abs/10.1145/347090.347123.
[25] M. Markou, S. Singh, Novelty detection: A Review - Part1:Statistical Approaches, Signal Processing 83 (12) (2003) 2481–2497. https://www.sciencedirect.com/science/article/abs/pii/S0165168403002020.
[26] M. Markou, S. Singh, Novelty detection: A Review-Part 2: Neural Network based approaches, Signal Processing 83 (12) (2003) 2499–2521. https://www.sciencedirect.com/science/article/abs/pii/S0165168403002032.
[27] Z. Pawlak, Rough Sets, J. Computer and Information Sciences 11 (1982) 341–356. https://link.springer.com/article/10.1007/BF01001956.
[28] M.I. Petrovskiy, Outlier detection algorithms in data mining systems, Programming and Computer Software 29 (4) (1988) 228–237. https://link.springer.com/article/10.1023/A:1024974810270.
[29] F. Preparata & M. Shamos, Computational Geometry: an Introduction. Springer Verlag.
[30] R. Banshal, N. Gaur, S.N. Singh, Outlier detection-Applications and Techniques in Data Mining, IEEE Conference 44 (12) (2016) 2862–2870. https://ieeexplore.ieee.org/abstract/document/7508146.
[31] R. Kannan, H. Woo, C.C. Aggarwal, Outlier Detection for text data-An extended version 23 (2000) 61–69. https://arxiv.org/abs/1701.01325.
[32] R. Kaur, S. Singh, A review of social network-centric anomaly detection techniques 23 (1) (2016) 61–69. https://www.inderscienceonline.com/doi/abs/10.1504/IJCNDS.2016.080582.
[33] P. J. Rousseeuw, & A.M. Leroy Robust regression and outlier detection. John Wiley & Sons, Inc., New York, NY, USA.
[34] P.I.J. Ruts, Rousseeuw, Computing depth contours of bivariate point clouds, Computational Statistics and Data Analysis 23 (2021) 153–168. https://www.sciencedirect.com/science/article/abs/pii/S0167947396000278.
[35] D. Synder, MS thesis, Department of Computer Science, Florida State University, 2001.
[36] S. Mitra, Sankar, P. Mitra, Data Mining in soft computing framework: A Survey, J. IEEE transactions on neural networks, 13 (2002) 132. https://ieeexplore.ieee.org/abstract/document/977258.
[37] E. Savage, G. Becker, R. Zamudio, A survey of link mining and anomaly detection 34 (3) (2015) 645–654.
[38] J. Tang, Z. Chen, A.W. Fu, D.W. Cheung, Capabilities of outlier detection schemes in large datasets, framework, and methodologies, Knowledge and Information Systems 11 (1) (2006) 45–84. https://link.springer.com/article/10.1007/s10115-005-0233-6.
[39] V. Kumar, S Kumar, A.K. Singh, Outlier detection – A clustering based approach, IJISME I (7) (2021) 383–387. ISSN:2319-6386.
[40] X. Zhao, J. Liang, F. Cao, A simple and effective outlier detection algorithm for categorical data, J.Machine Learning and Cybernetics 5 (2014) 469–477. https://link.springer.com/article/10.1007%2Fs13042-013-0202-4.
[41] Z.A. Bakar, R. Mohamed, A. Ahmad, M.M. Deris, A comparative study for outlier detection techniques in data mining 10 (4) (2006) 371–395. https://ieeexplore.ieee.org/abstract/document/4017846.
[42] T. Zhang, R. Ramakrishnan, M. Livny, BIRCH: an efficient data clustering method for very large databases, in: Proc. ACM SIGMOD Int. Conf. on Management of Data (SIGMOD), Montreal, Canada, 2021. https://dl.acm.org/doi/abs/10.1145/235968.233324.
[43] J. Zhan, J. Ye, W. Ding, P. Liu, A novel three-way decision model based on utility theory in incomplete fuzzy decision systems, IEEE Transactions on Fuzzy Systems (2021).

[44] K. Zhang, J. Zhan, W.Z. Wu, On multi-criteria decision-making method based on a fuzzy rough set model with fuzzy α-neighborhoods, IEEE Transactions on Fuzzy Systems (2020).

[45] J. Zhan, H. Jiang, Y. Yao, Three-way multi-attribute decision-making based on outranking relations, IEEE Transactions on Fuzzy Systems (2020).

[46] J. Ye, J. Zhan, W. Ding, H. Fujita, A novel fuzzy rough set model with fuzzy neighborhood operators, Information Sciences 544 (2021) 266–297.

[47] W. Wang, J. Zhan, C. Zhang, Three -way decisions based multi-attribute decision making with probabilistic dominance relations, Information Sciences 559 (2021) 75–96.

[48] J. Deng, J. Zhan, W.Z. Wu, A three-way decision methodology to multi-attribute decision-making in multi-scale decision information systems, Information Sciences 568 (2021) 175–198.

A hybrid heuristic approach for traffic light synchronization based on the MAXBAND

Sachikanta Pati, *Department of Computer Scinece Engineering , NM Institute of Engineering & Technology, Bhubaneswar, sachikantapati98@outlook.com*

Debasish Mishra, *Department of Electrical Engineering, Aryan Institute of Engineering & Technology, Bhubaneswar, debasishmishra1@gmail.com*

Malaya Tripathy, *Department of Electronics and Communication Engineering , Capital Engineering College, Bhubaneswar, malaya.tripathy43@gmail.com*

Smruti Ranjan Panda, *Department of Electrical and Electronics Engineering, Raajdhani Engineering College, Bhubaneswar, sr_panda@outlook.com*

A R T I C L E I N F O

Keywords:
Traffic light synchronization
Hybrid heuristics
Tabu search
Variable neighborhood search
MAXBAND

A B S T R A C T

This study addresses a high resolution model for the synchronization of traffic lights on transport networks. A hybrid heuristic algorithm optimizes the mixed integer linear model, referred as MAXBAND, seeking to achieve maximal bandwidth by setting arterial signals. The assessed algorithm corresponds to a hybrid metaheuristic which combines Tabu Search and Variable Neighborhood Search. The algorithm uses a memory structure within an iterative local search, allowing a broader diversity of solutions. In addition, some adjustments were incorporated to the MAXBAND such as the revision of the constraints of the mixed integer linear model, including those that describe all the cyclic routes in the graph, and some bounds were generalized for integer variables. Extensive computational experiments were carried out evidencing a competitive performance for large instances.

1. Introduction

Over recent years, traffic congestion has become an issue of remarkable importance due to an increase of vehicles on the roads in urban areas. For controlling the flow of vehicles, traffic lights have been used as regulators since the late 19th century. Nevertheless, its use also leads to other problems which include time delays for vehicles moving from one place to another, and an increase in pollution due to the constant changes in the speed of vehicles [1]. In this sense, traffic light synchronization, which embraces the regulation in the timing of traffic lights, is a topic of noteworthy importance. This problem is commonly tackled following two approaches, by minimizing the delays or some other measures which assess the performance of traffic, or by maximizing the time in which vehicles move without stopping at the red lights, referred also as the bandwidth maximization [2].

In terms of traffic flow measures, usually a minimization problem is formulated to reduce the overall delay, or to reduce the number of stops vehicles complete. In a classic study, a convex nonlinear formulation with a piece-wise linearization and an increased number of constraints was proposed by Gartner et al. (1975) [3]. Similarly, an analogous linear model permitted to decide among different signal timing plans while relaxing the assumption of a common red-green period width [4]. However, the latter is not a hard constraint because in that case the least common multiple of all red-green periods could be used as a uniform period, as mentioned in [5].

Concerning the bandwidth maximization, initial formulations with preassigned vehicles velocity deemed a geometric method for a two-way street given a fixed and common red-green time period on each signal [6]. Subsequently, a mixed integer linear program (MILP) was proposed to solve a more complete version of the problem [7]. The selection of the red-green time period occurred between given bounds. Speed variations and bounds on the velocity limits between adjacent signals were included. Additionally, an extension was provided to solve the same problem on general networks, but only very small instances could be solved. This is a more difficult problem because it is necessary to introduce the so-called loop constraints, which permit to model the circular movements that vehicles can do. The introduction of a generalization containing left turns at the junctions led to the MAXBAND model [8]. On its first version, the MAXBAND handled problems on networks with only 3 arteries and up to 17 traffic signals. The MAXBAND was extended to work with a variable bandwidth for each street segment originating the MULTIBAND model [9]. This modification incorporated a traffic factor on the objective function. Recent variations have derived a new version referred as the AM-BAND, which attempts to use better the available green times on both road directions by relaxing the symmetric assumption with respect to the progression line [10]. Finally, the inclusion of variable bandwidths permitted to consider the impact of the speed variation to the model [11,12].

Metaheuristic approaches are flexible and robust strategies that have demonstrated to be computationally efficient in terms of CPU time. They

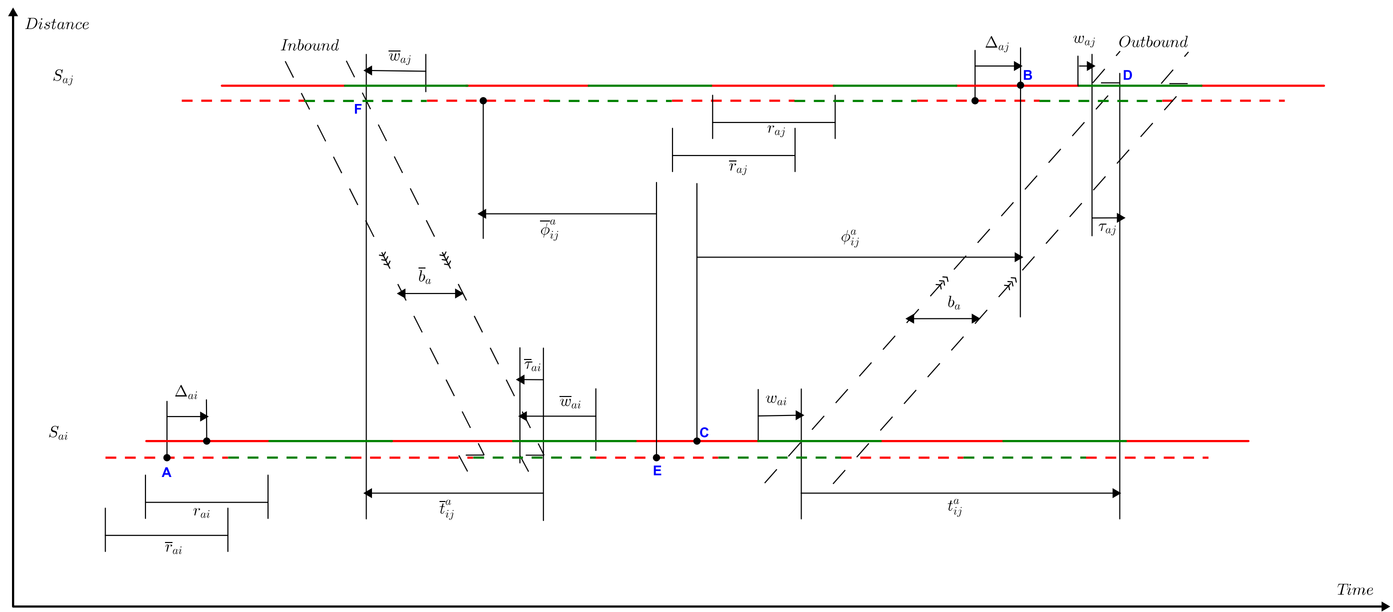

Fig. 1. Geometry for MAXBAND model on artery a.

have the competency of solving large-scale problems such as the traffic light synchronization [13]. For instance, the commercial software for synchronization of traffic signals and traffic management TRANSYT provides a heuristic solution for a complete and robust objective function [14,15]. TRANSYT uses microscopic simulations of traffic behavior ensemble with genetic algorithms. In the case of the MAXBAND model, a heuristic method was implemented for the network problem by initially solving a tree sub-problem which considered measures of interest. The integer variables were fixed to the values obtained and used in a second stage to obtain a solution for the whole problem [16]. In addition, numerous heuristics have been employed in traffic light scheduling including, evolutionary methods [17,18], particle swarm optimization [19], and a hybrid heuristic which combined harmony search with local search [20]. The hybridization of a metaheuristic with local search strategies enhances significantly the success rate in much less CPU time [21,22].

Tabu Search is a global optimization algorithm originally proposed by Glover (1986) [23]. It has proven applicability in operations research applications including scheduling [24,25], vehicle routing problems [26], and health care [27]. In this work, a hybrid heuristic algorithm based on Tabu Search is developed for bandwidth maximization. The algorithm is enhanced by intensifying its search using a sequence of neighborhood solution processes, which follows the idea of the Variable Neighborhood Search (VNS) [28]. The MAXBAND problem is typically solved for very small instances by optimization solvers. In this sense, this contribution aims to adapt a hybrid heuristic algorithm for bandwidth maximization to expand its capabilities and to solve the problem for complete networks. To the best of our knowledge, there are no references in the literature about solving the MAXBAND on a complete network nor using other metaheuristic approaches.

The rest of the paper is structured as follows. Section 2 introduces and reviews the MAXBAND model, including a detailed explanation of its elements and the notation to be used in the manuscript. Section 2.4 explains the approach for modelling the loop constraints with a small number of binary variables. Section 3 includes a generalization of the bounds for arterial integer variables. Section 4 introduces the MILP-based hybrid heuristic algorithm based on Tabu Search and VNS. Later, computational evaluations are carried out to verify the efficiency and effectiveness of the proposed method for large instances. Finally, in Section 5 conclusions and future research are discussed.

2. MAXBAND modelling for a network

Let us consider a group of two-way *arteries* (streets) that meet each other at *junctions* to form a transport *network*. This network has some traffic signals to regulate its traffic. They work with a common *period* that splits into red and green time. Even though it is sometimes referred as *cycle length*, to avoid confusion with the *loops* (also known as cycles), the term to be used through the paper is *period length*. The distances (time units) that allow to measure the relative location between two signals on the same artery and on different arteries are called *internode offset* and *intranode offset*, respectively. A list of offsets for the signals is said to be a *synchronization*.

The MAXBAND model relies on the geometry illustrated in Fig. 1. Information for two signals S_{ai} and S_{aj} is provided on an artery a. The notation is similar to the one proposed in [8].

The parameters in Fig. 1 are defined as follows,

- T: Period length, in seconds.
- n_a: Number of traffic lights (signals) on artery a.
- r_{ai} $(\overline{r}_{ai})$: Outbound (inbound) red time of signal i on artery a, in periods.
- τ_{ai} $(\overline{\tau}_{ai})$: An advancement of the outbound (inbound) bandwidth upon leaving S_i, in periods.

The variables in Fig. 1 are defined as follows,

- z: Signal frequency, in periods per second.
- b_a $(\overline{b}_a)$: Outbound (inbound) bandwidth on artery a, in periods.
- t^a_{ij} $(\overline{t}^a_{ij})$: Travel time from S_{ai} to S_{aj} in outbound (from S_{aj} to S_{ai} in inbound) direction, in periods.
- ϕ^a_{ij} $(\overline{\phi}^a_{ij})$: Time from the center of red at S_{ai} to the center of red at S_{aj}, in periods. The two reds are chosen so that each is immediately to the left (right) of the same outbound (inbound) green band. ϕ^a_{ij} $(\overline{\phi}^a_{ij})$ is positive if S_{aj}'s center of red lies to the right (left) of S_{ai}'s.
- w_{ai} $(\overline{w}_{ai})$: Time from the right (left) side of S_{ai}'s red to the left (right) side of green band in outbound (inbound) direction, in periods.
- Δ_{ai}: Time from center of $\overline{r}_{ai}$ to the nearest center of r_{ai}, in periods. It is positive from left to right.

For the complete formulation of the MAXBAND please refer to LM 2.1, which holds additional parameters and variables not included

LM 2.1 MAXBAND, Maximal Bandwidth Formulation.

$$\text{Maximize} \quad \sum_{a \in A} \left(k_a b_a + \overline{k}_a \overline{b}_a \right) \tag{1}$$

subject to :

$$\frac{1}{T_2} \leq z \leq \frac{1}{T_1}, \tag{2}$$

$$w_{ai} + b_a \leq 1 - r_{ai}, \forall a \in A, \forall i = 1, \ldots, n_a, \tag{3}$$

$$\overline{w}_{ai} + \overline{b}_a \leq 1 - \overline{r}_{ai}, \forall a \in A, \forall i = 1, \ldots, n_a, \tag{4}$$

$$\begin{aligned} &(w_{ai} + \overline{w}_{ai}) - (w_{a,i+1} + \overline{w}_{a,i+1}) + (t_i^a + \overline{t}_i^a) \\ &+(\delta_{ai}\ell_{ai} - \overline{\delta}_{ai}\overline{\ell}_{ai}) - (\delta_{a,i+1}\ell_{a,i+1} - \overline{\delta}_{a,i+1}\overline{\ell}_{a,i+1}) + (r_{ai} - r_{a,i+1}) \\ &-(\tau_{a,i+1} + \overline{\tau}_{ai}) = m_i^a, \forall a \in A, \forall i = 1, \ldots, n_a - 1, \end{aligned} \tag{5}$$

$$\left(\frac{d_i^a}{f_i^a} \right) z \leq t_i^a \leq \left(\frac{d_i^a}{e_i^a} \right) z, \forall a \in A, \forall i = 1, \ldots, n_a - 1, \tag{6}$$

$$\left(\frac{\overline{d}_i^a}{\overline{f}_i^a} \right) z \leq \overline{t}_i^a \leq \left(\frac{\overline{d}_i^a}{\overline{e}_i^a} \right) z, \forall a \in A, \forall i = 1, \ldots, n_a - 1, \tag{7}$$

$$\left(\frac{d_i^a}{h_i^a} \right) z \leq \left(\frac{d_i^a}{d_{i+1}^a} \right) t_{i+1}^a - t_i^a \leq \left(\frac{d_i^a}{g_i^a} \right) z, \forall a \in A, \forall i = 1, \ldots, n_a - 2, \tag{8}$$

$$\left(\frac{\overline{d}_i^a}{\overline{h}_i^a} \right) z \leq \left(\frac{\overline{d}_i^a}{\overline{d}_{i+1}^a} \right) \overline{t}_{i+1}^a - \overline{t}_i^a \leq \left(\frac{\overline{d}_i^a}{\overline{g}_i^a} \right) z, \forall a \in A, \forall i = 1, \ldots, n_a - 2, \tag{9}$$

$$\sum_{(i,j):a \in A_\zeta^F} \phi_{ij}^a - \sum_{(i,j):a \in A_\zeta^B} \phi_{ij}^a + \sum_{(b,j,i,c,k) \in J_\zeta} \Psi^i_{S_{bj},S_{ck}} = C_\zeta, \forall \zeta \in \mathcal{B}_\zeta, \tag{10}$$

$$C_\zeta \in \mathbb{Z}, \forall \zeta \in \mathcal{B}_\zeta, \tag{11}$$

$$m_i^a \in \mathbb{Z}, \forall a \in A, \forall i = 1, \ldots, n_a - 1, \tag{12}$$

$$\delta_{ai}, \overline{\delta}_{ai} \in \{0, 1\}, \forall a \in A, \forall i = 1, \ldots, n_a - 1, \tag{13}$$

$$b_a, \overline{b}_a, t_i^a, \overline{t}_i^a, w_{ai}, \overline{w}_{ai}, z \geq 0, \forall a \in A, \forall i = 1, \ldots, n_a - 1. \tag{14}$$

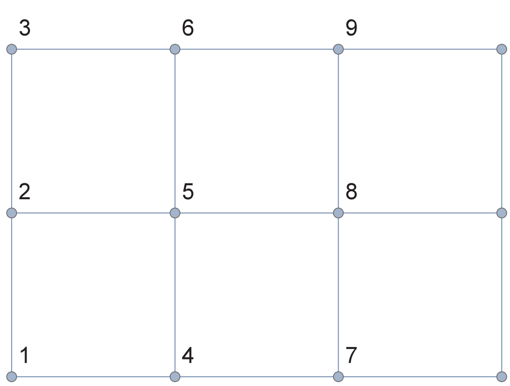

Fig. 2. A grid graph $G_{3\times 4}(V, E)$.

in Fig. 1. In addition, α_i^a for any parameter or variable α, and their corresponding names with bars for the opposite direction on an artery are considered.

The model takes into account only networks that can be represented by two dimensional grid graphs $G_{r\times c}(V, E)$, where r and c are the number of rows and columns, respectively. V is the set of nodes, E is the set of edges, $|V| = n = rc$ and $|E| = m = 2rc - r - c$. Grid graphs are a good representation of many real-world networks. Fig. 2 shows an example with $n = 12$ and $m = 17$.

2.1. Objective function

In our practice, the goal is to maximize the weighted sum of the bandwidths. Let A be the set of arteries on the network; thus, the objective function to be maximized is:

$$\sum_{a \in A} \left(k_a b_a + \overline{k}_a \overline{b}_a \right).$$

Here, k_a and $\overline{k}_a$ are the weights for the outbound and inbound bandwidth, respectively.

2.2. Arterial constraints

As mentioned beforalgorithme, all signals are assumed to work into a common signal period which length is introduced in the model as a decision variable. They must lie on an interval $[T_1, T_2]$, see (2). The decision variable z is the reciprocal of the period length, that is, $z = 1/T$. The inequalities (3)-(4) guarantee that the bandwidth remains within the green time. The velocities v_i^a between each signal on each artery are decision variables that are bounded in between e_i^a and f_i^a, representing the lower and upper limits, and d_i^a is the distance between two consecutive arteries, see (6)-(7). In order to avoid sudden changes in the velocities between consecutive signals, they are limited by imposing lower and upper bounds $1/h_i^a$ and $1/g_i^a$ on changes in reciprocal velocities. The reason for using reciprocal bounds for velocities and changes in velocities is that linear constraints can be formulated in this manner. It is not possible to consider directly the inequalities $e_i^a \leq v_i^a \leq f_i^a$ because the period length is also a variable. Thus, if v_i^a is converted from meters/second to meters/period, the inequality becomes $e_i^a T \leq v_i^a T \leq f_i^a T$, which resembles nonlinear constraints. Therefore, we use the reciprocals of e_i^a and f_i^a,

$$e_i^a \leq v_i^a \leq f_i^a \quad \rightarrow \quad \frac{d_i^a}{f_i^a} \leq \frac{d_i^a}{v_i^a} \leq \frac{d_i^a}{e_i^a} \quad \rightarrow \quad \frac{d_i^a}{f_i^a} z \leq t_i^a \leq \frac{d_i^a}{e_i^a} z.$$

The same applies to the changes in the velocities.

Additionally, Fig. 1 denotes that $Time_{\text{A-B}} = \Delta_{ai}$+integer number of periods+ϕ_{ij}^a and that $Time_{\text{A-B}}$ =integer number of periods$-\overline{\phi}_{ij}^a$+integer number of periods+Δ_{aj}. Consequently,

$$\phi_{ij}^a + \overline{\phi}_{ij}^a + \Delta_{ai} - \Delta_{aj} = m_{ij}^a, \tag{15}$$

where m_{ij}^a is an integer decision variable (number of periods). In addition, $Time_{\text{C-D}} = \phi_{ij}^a + \frac{1}{2}r_{aj} + w_{aj} + \tau_{aj} = \frac{1}{2}r_{ai} + w_{ai} + t_{ij}^a$ and $Time_{\text{E-F}} = \overline{\phi}_{ij}^a + \frac{1}{2}\overline{r}_{aj} + \overline{w}_{aj} = \frac{1}{2}\overline{r}_{ai} + \overline{w}_{ai} - \overline{\tau}_{ai} + \overline{t}_{ij}^a$. So, if (15) is substituted,

$$\begin{aligned} &t_{ij}^a + \overline{t}_{ij}^a + \frac{1}{2}(r_{ai} + \overline{r}_{ai}) + (w_{ai} + \overline{w}_{ai}) - \frac{1}{2}(r_{aj} + \overline{r}_{aj}) - (w_{aj} + \overline{w}_{aj}) - (\tau_{aj} \\ &+ \overline{\tau}_{ai}) + (\Delta_{ai} - \Delta_{aj}) = m_{ij}^a. \end{aligned} \tag{16}$$

Eq. (16) is named *arterial loop constraint* for artery a between signals S_{ai} and S_{aj}.

In addition, there are constraints that model left turn decisions if they are allowed by the green lights. The MAXBAND permits to decide among four possible patterns of left turns which are resembled in Fig. 3 (for more details please refer to Little et al. [8]).

Parameters ℓ_{ai} and $\overline{\ell}_{ai}$ in Fig. 3 represent, for a signal i on an artery a, the time (periods) of outbound and inbound left turn phases respectively. R is the common red time. For instance, Fig. 4 shows the three possible movements for vehicles on a main street in three different moments. As can be seen at area 2, the traffic lights are green for outbound and inbound directions, so no car in the horizontal street can cross to the other side. On the common red time R a possible different left turn pattern can be given for cross street.

Furthermore, Δ_{ai} can be expressed as a function of ℓ_{ai} and $\overline{\ell}_{ai}$. For example, if we consider Pattern 1 and calculate the difference between the center of total red time of outbound and the total red of inbound (in that order), the following is obtained

$$\Delta_{ai} = \frac{\overline{\ell}_{ai} + R}{2} - \left(\frac{R + \ell_{ai}}{2} + \overline{\ell}_{ai} \right) = -\frac{\ell_{ai} + \overline{\ell}_{ai}}{2}.$$

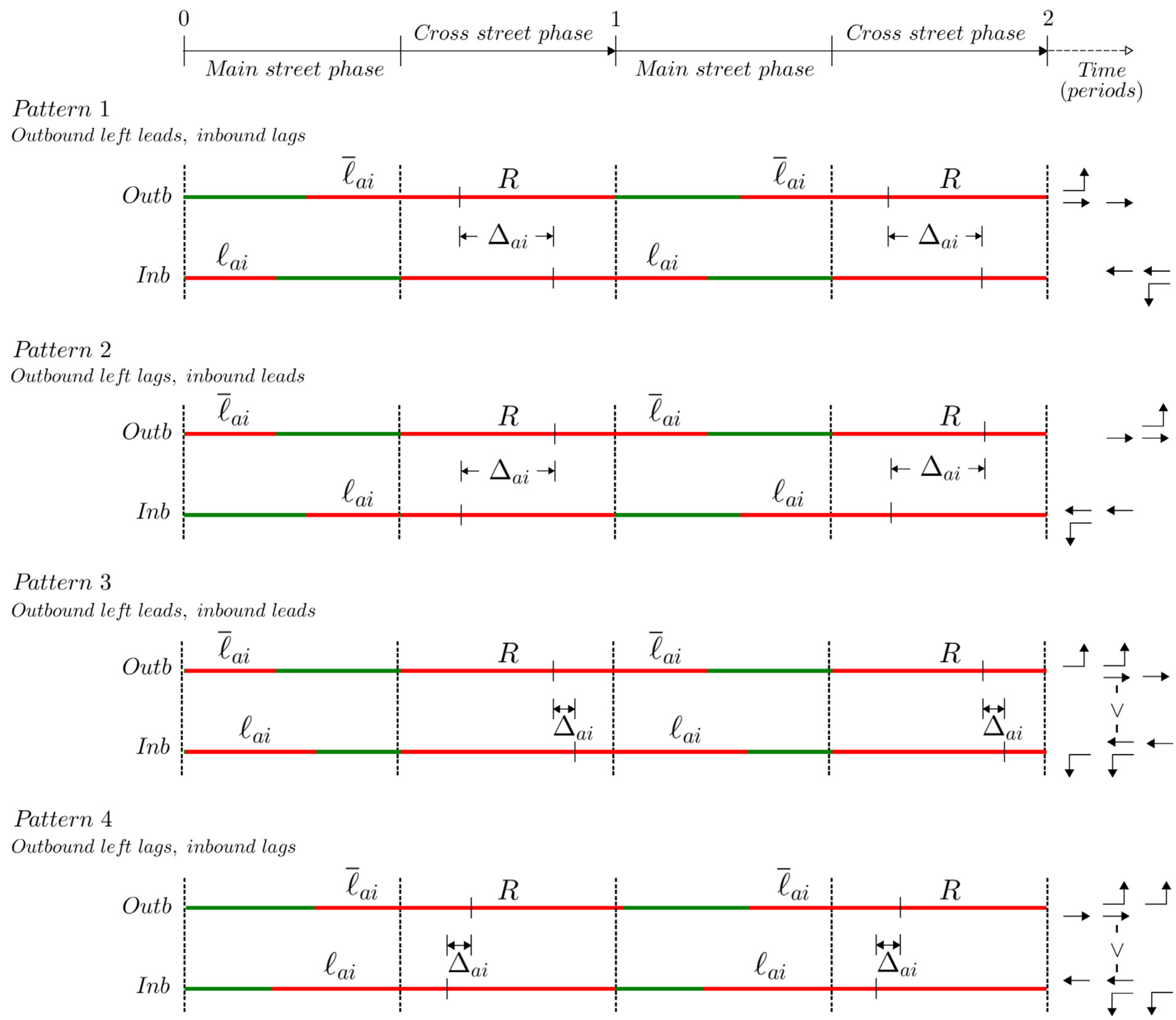

Fig. 3. Patterns of left turn phases.

Table 1
Expressions for Δ_{ai}'s.

Pattern	Δ_{ai}	δ_{ai}	$\bar{\delta}_{ai}$
1	$-\frac{\ell_{ai}+\bar{\ell}_{ai}}{2}$	0	1
2	$\frac{\ell_{ai}+\bar{\ell}_{ai}}{2}$	1	0
3	$-\frac{\ell_{ai}-\bar{\ell}_{ai}}{2}$	0	0
4	$\frac{\ell_{ai}-\bar{\ell}_{ai}}{2}$	1	1

The results for the other left turn phases are listed in Table 1. These expressions can be obtained with the following formula

$$\Delta_{ai} = \frac{1}{2}[(2\delta_{ai} - 1)\ell_{ai} - (2\bar{\delta}_{ai} - 1)\bar{\ell}_{ai}], \tag{17}$$

where, δ_{ai}, $\bar{\delta}_{ai} \in \{0, 1\}$ are additional binary variables. The decisions on left turns are included in the model by substituting Eq. (16) in (17), as can be seen in the constraint (5).

2.3. Loop constraints

The network case is a natural generalization of the arterial case, and the corresponding model includes all the aforementioned constraints for each artery. The arterial loop constraint (16) can be seen as a cycle for two nodes because it represents the movement of going to and returning from a signal. If this idea is extended to larger cycles, it is clear that the sum of all the offsets in the cycle must be an integer number as well.

For observing how to write the equation of the cycle constraints, let us start with an example. A cycle consisting of 4 arteries $A = \{a, b, c, d\}$ and 4 junctions $J = \{J_1, J_2, J_3, J_4\}$ is exhibited in Fig. 5. Each artery $a \in A$ has signals S_{aj}, where j is the index for signals on a increasing in the outbound direction given by the arrows. Heading in the clockwise direction and starting from junction J_1, the cycle constraint for this example would be

$$\phi^b_{jk} + \Psi^{J_2}_{S_{bk},S_{co}} + \phi^c_{op} + \Psi^{J_3}_{S_{cp},S_{dq}} + \phi^d_{qr} + \Psi^{J_4}_{S_{dr},S_{ah}} + \phi^a_{hi} + \Psi^{J_1}_{S_{ai},S_{bj}} = C_\zeta,$$

where C_ζ is an integer decision variable and $\Psi^i_{S_{aj},S_{bk}}$ is a decision variable expressed as *intranode offset* which represents the time between consecutive centers of reds for signals S_{aj} and S_{bk} that meet at junction i, i.e, it is a link time between arteries a and b.

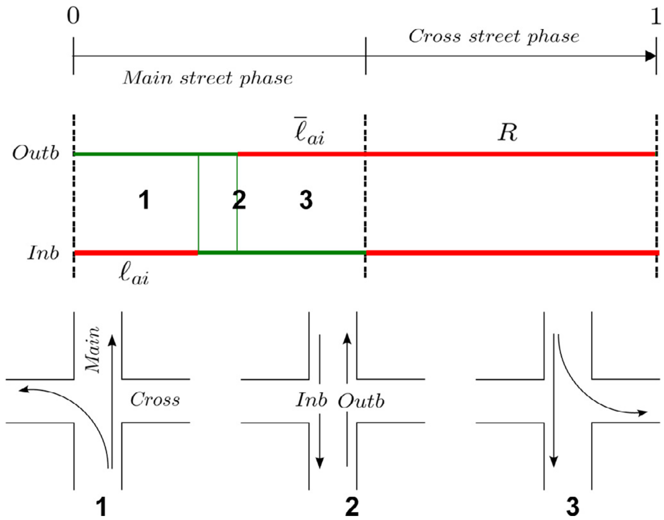

Fig. 4. Left turn phase example with Pattern 1.

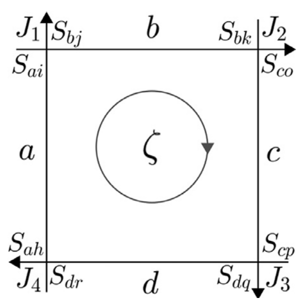

Fig. 5. Clockwise loop with 4 junctions.

To generalize this expression for any cycle, the following sets are defined:

- A^F_ζ (A^B_ζ): Set of all segments of forward (backward) arteries with edges (i, j) in the clockwise direction of cycle ζ,
- J_ζ: All sets of the form (b, j, i, c, k) in ζ, where i is the junction between arteries b and c in the signals S_{bj} and S_{ck},

Afterwards, the *network loop constraint* (cycle constraint) becomes:

$$\sum_{(i,j):a\in A^F_\zeta} \phi^a_{ij} - \sum_{(i,j):a\in A^B_\zeta} \phi^a_{ij} + \sum_{(b,j,i,c,k)\in J_\zeta} \Psi^i_{S_{bj},S_{ck}} = C_\zeta.$$

The number of cycle constraints in the model depend on the quantity of edges and nodes of the network. In fact, this number can be very high, which makes the problem very difficult to solve. The following result permits to alleviate the mentioned problem. It is well known that the set of all cycles ζ on any single graph can be spanned by a basis $\mathcal{B}_\zeta$ with cardinality $m - n + 1$, where m represents the number of edges and n the number of nodes on the underlying undirected graph related to the directed graph, which represents the original network. So, a cycle basis must be found before writing the model. The interested reader is encouraged to consult [29] for more details.

2.4. Computing intranode offset

In general, a grid graph $G_{k\times k}$ requires $(k-1)^2$ network loop constraints and, consequently, several intranodes must be computed for each of these equations. The values of intranode offsets $\Psi^i_{S_{aj},S_{bk}}$'s depend on red time positions of the signals S_{aj} and S_{bk} on a main and cross street, respectively. For instance, if left turns are not permitted, then the red and green times for main and cross streets will have the same length and in this case the intradone offset will be clearly 0.5 periods. Because

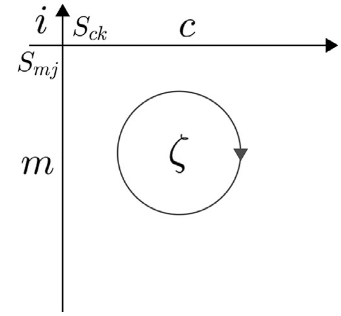

Fig. 6. A junction i of arteries main (m) and cross (c).

Table 2
Expressions for $\psi^{p_m p_c}_{mc}$'s.

	Patterns	Cross Street 1	2	3	4
Main Street	1	$\frac{1-\bar{\ell}_{ck}+\bar{\ell}_{mj}}{2}$	$\frac{1+\bar{\ell}_{ck}+\bar{\ell}_{mj}}{2}$	$\frac{1+\bar{\ell}_{ck}+\bar{\ell}_{mj}}{2}$	$\frac{1-\bar{\ell}_{ck}+\bar{\ell}_{mj}}{2}$
	2	$\frac{1-\bar{\ell}_{ck}-\bar{\ell}_{mj}}{2}$	$\frac{1+\bar{\ell}_{ck}-\bar{\ell}_{mj}}{2}$	$\frac{1+\bar{\ell}_{ck}-\bar{\ell}_{mj}}{2}$	$\frac{1-\bar{\ell}_{ck}-\bar{\ell}_{mj}}{2}$
	3	$\frac{1-\bar{\ell}_{ck}-\bar{\ell}_{mj}}{2}$	$\frac{1+\bar{\ell}_{ck}-\bar{\ell}_{mj}}{2}$	$\frac{1+\bar{\ell}_{ck}-\bar{\ell}_{mj}}{2}$	$\frac{1-\bar{\ell}_{ck}-\bar{\ell}_{mj}}{2}$
	4	$\frac{1-\bar{\ell}_{ck}+\bar{\ell}_{mj}}{2}$	$\frac{1+\bar{\ell}_{ck}+\bar{\ell}_{mj}}{2}$	$\frac{1+\bar{\ell}_{ck}+\bar{\ell}_{mj}}{2}$	$\frac{1-\bar{\ell}_{ck}+\bar{\ell}_{mj}}{2}$

the MAXBAND model must decide among four different left turn patterns on each junction i, the computation of each intranode should take into account all the possible values of binary variables involved in such choice. The following result provides a simple expression to compute intranode offsets without requiring extra variables beyond those included in the model LM 2.1.

Theorem 1. *Consider the patterns of left turn phases exhibited in Fig. 3. Let $\psi^{p_m p_c}_{mc}$ be the value of $\Psi^i_{S_{mj},S_{ck}}$ when the arteries m and c meet at the junction i for signals S_{mj} and S_{ck} with left turn phases patterns p_m and p_c, respectively (See Fig. 6). Then, for all possible values of p_m and p_c, it is defined:*

$$\Psi^i_{S_m,S_{ck}} = \frac{1}{2} - \frac{1}{2}\left[(2\bar{\delta}_{ck} - 1)\bar{\ell}_{ck} - (2\bar{\delta}_{mj} - 1)\bar{\ell}_{mj}\right].$$

Proof. Let us consider Fig. 7, which shows the different forms that $\psi^{p_m p_c}_{mc}$ may acquire for all possible permutations of left turn phases in Fig. 3. The cross street phase takes place during the red time R_m in the main street and vice versa.

All values of $\psi^{p_m p_c}_{mc}$ are summarized in Table 2. Since only the ϕ's in equation (10) of the MAXBAND model are being used, only the outbound directions phases are taken into account.

Moreover, Table 2 reveals that:
$\psi^{1,1}_{mc} = \psi^{1,4}_{mc} = \psi^{4,1}_{mc} = \psi^{4,4}_{mc} = \frac{1-\bar{\ell}_{ck}+\bar{\ell}_{mj}}{2}$, $\psi^{2,1}_{mc} = \psi^{2,4}_{mc} = \psi^{3,1}_{mc} = \psi^{3,4}_{mc} = \frac{1-\bar{\ell}_{ck}-\bar{\ell}_{mj}}{2}$, $\psi^{1,2}_{mc} = \psi^{1,3}_{mc} = \psi^{4,2}_{mc} = \psi^{4,3}_{mc} = \frac{1+\bar{\ell}_{ck}+\bar{\ell}_{mj}}{2}$, and $\psi^{2,2}_{mc} = \psi^{2,3}_{mc} = \psi^{3,2}_{mc} = \psi^{3,3}_{mc} = \frac{1+\bar{\ell}_{ck}-\bar{\ell}_{mj}}{2}$.

Table 3 shows all the different values of the binaries variables δ's and $\bar{\delta}$'s for each left turn phase that the model needs to compute Δ's with Eq. (17). The $\psi^{p_m p_c}_{mc}$'s are arranged in four groups determined just for the values of $\bar{\delta}$'s on the signals S_{mj} and S_{ck}.

Now, it is easy to verify that a single expression to compute any $\Psi^i_{S_m,S_{ck}}$ is given by:

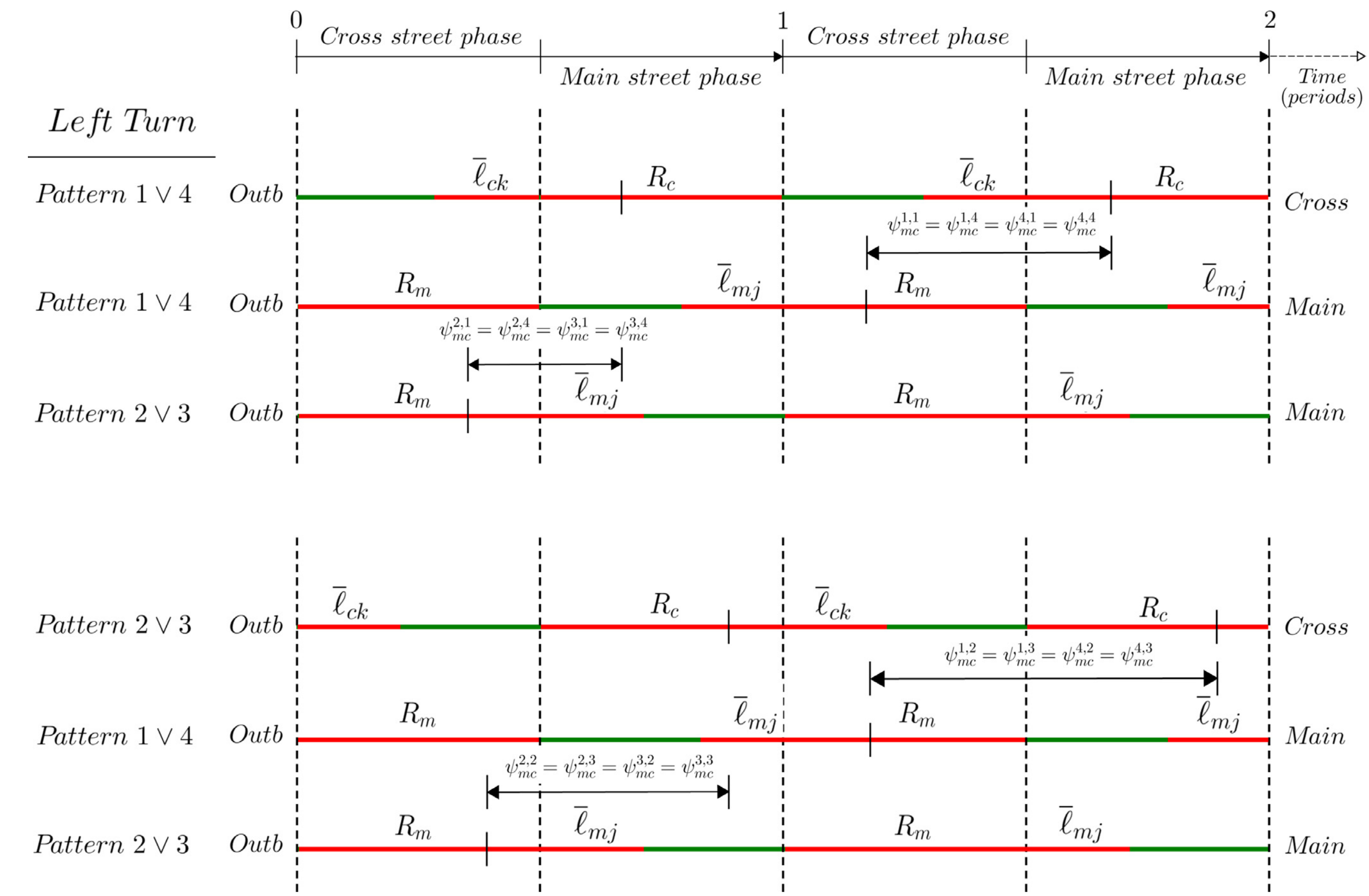

Fig. 7. Geometry for $\psi_{mc}^{p_m p_c}$.

Table 3
Four different groups of $\psi_{mc}^{p_m p_c}$'s on junction i.

Patterns						
p_m	p_c	δ_{mj}	$\bar{\delta}_{mj}$	δ_{ck}	$\bar{\delta}_{ck}$	$\psi_{mc}^{p_m p_c}$
4	4	1	1	1	1	$\psi_{mc}^{4,4}$
4	1	1	1	0	1	$\psi_{mc}^{4,1}$
1	4	0	1	1	1	$\psi_{mc}^{1,4}$
1	1	0	1	0	1	$\psi_{mc}^{1,1}$
3	4	0	0	1	1	$\psi_{mc}^{3,4}$
2	1	1	0	0	1	$\psi_{mc}^{2,1}$
3	1	0	0	0	1	$\psi_{mc}^{3,1}$
2	4	1	0	1	1	$\psi_{mc}^{2,4}$
1	2	0	1	1	0	$\psi_{mc}^{1,2}$
4	2	1	1	1	0	$\psi_{mc}^{4,2}$
4	3	1	1	0	0	$\psi_{mc}^{4,3}$
1	3	0	1	0	0	$\psi_{mc}^{1,3}$
2	2	1	0	1	0	$\psi_{mc}^{2,2}$
2	3	1	0	0	0	$\psi_{mc}^{2,3}$
3	2	0	0	1	0	$\psi_{mc}^{3,2}$
3	3	0	0	0	0	$\psi_{mc}^{3,3}$

$$\Psi^i_{S_m,S_{ck}} = \frac{1}{2} - \frac{1}{2}\Big[(2\bar{\delta}_{ck}-1)\bar{\ell}_{ck} - (2\bar{\delta}_{mj}-1)\bar{\ell}_{mj}\Big]. \tag{18}$$

□

A comparable proposition can be found in [30]. However, no attempt to expand it was made.

3. Bounds for integer variables

In this section, the bounds for the integer variables in the arterial loop constraints when left turns phases, given in [7], are extended for the network loop constraints.

From Fig. 1, clearly $0 \le w_{ai} \le 1 - r_{ai}$, and $0 \le \overline{w}_{ai} \le 1 - \bar{r}_{ai}$ for any signal i on artery a. By using the constraints (2), (6) and (7), it is obtained $\frac{d^a_{ij}}{f^a_{ij}T_2} \le t^a_{ij} \le \frac{d^a_{ij}}{e^a_{ij}T_1}$, and $\frac{d^a_{ij}}{\bar{f}^a_{ij}T_2} \le \bar{t}^a_{ij} \le \frac{d^a_{ij}}{\bar{e}^a_{ij}T_1}$. Eq. (17) provides $\Delta_{ai} = \delta_{ai}\ell_{ai} - \frac{\ell_{ai}}{2} - \bar{\delta}_{ai}\bar{\ell}_{ai} - \frac{\bar{\ell}_{ai}}{2}$. Thus, $-(\frac{\ell_{ai}}{2} + \frac{\bar{\ell}_{ai}}{2}) \le \Delta_{ai} \le (\frac{\ell_{ai}}{2} + \frac{\bar{\ell}_{ai}}{2})$, as δ's take values in $\{0, 1\}$.

By using the bounds in constraints (5), the following limits for m's in terms of the MAXBAND parameters, $\underline{m^a_{ij}} \le m^a_{ij} \le \overline{m^a_{ij}}$, can be expressed.

$$\overline{m^a_{ij}} = \Big\lfloor 2 - \frac{1}{2}(r_{ai}+\bar{r}_{ai}) - \frac{1}{2}(r_{aj}+\bar{r}_{aj}) + \frac{1}{2}(l_{ai}+\bar{l}_{ai}) + \frac{1}{2}(l_{aj}+\bar{l}_{aj}) - (\tau_{aj}+\bar{\tau}_{ai}) + \frac{d^a_{ij}}{e^a_{ij}T_1} + \frac{d^a_{ij}}{\bar{e}^a_{ij}T_1}\Big\rfloor, \tag{19}$$

$$\underline{m^a_{ij}} = \Big\lceil -2 + \frac{1}{2}(r_{ai}+\bar{r}_{ai}) + \frac{1}{2}(r_{aj}+\bar{r}_{aj}) - \frac{1}{2}(\ell_{ai}+\bar{\ell}_{ai}) - \frac{1}{2}(\ell_{aj}+\bar{\ell}_{aj}) - (\tau_{aj}+\bar{\tau}_{ai}) + \frac{d^a_{ij}}{f^a_{ij}T_2} + \frac{d^a_{ij}}{\bar{f}^a_{ij}T_2}\Big\rceil. \tag{20}$$

Therefore, using the notation in LM 2.1, i.e., $m^a_{i,i+1} = m^a_i$:

$$\underline{m^a_i} \le m^a_i \le \overline{m^a_i}, \quad \forall a \in A, \forall i = 1, \ldots, n_a - 1. \tag{21}$$

Furthermore, let $a \in A^F_\zeta$ be an artery with signals S_{ai}, where $i \in I^a_\zeta = \{1^a_\zeta, \ldots, n^a_\zeta\}$ and increasing in the outbound direction. The time between

Table 4
Sizes of some MAXBAND problems.

	Grid Graph $G_{r\times c}$								
	3x3	5x5	6x6	7x7	8x8	9x9	10x10	15x15	20x20
Equalities	16	56	85	120	161	208	261	616	1121
m's	12	40	60	84	112	144	180	420	760
C's	4	16	25	36	49	64	81	196	361
δ's	36	100	144	196	256	324	400	900	1600
Integer variables	52	156	229	316	417	532	661	1516	2721

the first signal and the last one in the artery segment is:

$$t^a_{1^a_\zeta,n^a_\zeta} = \sum_{i\in I^a_\zeta\setminus\{n^a_\zeta\}} t^a_i - \sum_{i\in I^a_\zeta\setminus/1^a_\zeta/} \tau_{ai}. \tag{22}$$

Hence, $\underline{t^a_{1^a_\zeta,n^a_\zeta}} \le t^a_{1^a_\zeta,n^a_\zeta} \le \overline{t^a_{1^a_\zeta,n^a_\zeta}}$, in which

$$\overline{t^a_{1^a_\zeta,n^a_\zeta}} = \sum_{i\in I^a_\zeta\setminus\{n^a_\zeta\}} \frac{d^a_i}{e^a_i T_1} - \sum_{i\in I^a_\zeta\setminus\{1^a_\zeta\}} \tau_{ai}, \tag{23}$$

$$\underline{t^a_{1^a_\zeta,n^a_\zeta}} = \sum_{i\in I^a_\zeta\setminus\{n^a_\zeta\}} \frac{d^a_i}{f^a_i T_2} - \sum_{i\in I^a_\zeta\setminus\{1^a_\zeta\}} \tau_{ai}. \tag{24}$$

By using the same means mentioned before and considering $\phi^a_{ij} + \frac{1}{2}r_{aj} + w_{aj} + \tau_{aj} = \frac{1}{2}r_{ai} + w_{ai} + t^a_{ij}$, it is obtained $\underline{\phi^a_{i^a_\zeta,n^a_\zeta}} \le \phi^a_{i^a_\zeta,n^a_\zeta} \le \overline{\phi^a_{i^a_\zeta,n^a_\zeta}}$, for,

$$\overline{\phi^a_{i^a_\zeta,n^a_\zeta}} = -\frac{1}{2}(r_{a,1^a_\zeta} + r_{a,n^a_\zeta}) + \overline{t^a_{1^a_\zeta,n^a_\zeta}} + 1, \tag{25}$$

$$\underline{\phi^a_{i^a_\zeta,n^a_\zeta}} = \frac{1}{2}(r_{a,1^a_\zeta} + r_{a,n^a_\zeta}) + \underline{t^a_{1^a_\zeta,n^a_\zeta}} - 1. \tag{26}$$

Following Eq. (18), we also have $\underline{\Psi^i_{bc}} \le \Psi^i_{bc} \le \overline{\Psi^i_{bc}}$, where

$$\overline{\Psi^i_{bc}} = \frac{1}{2}(1 + \overline{\ell}_{ck} + \overline{\ell}_{bj}), \tag{27}$$

$$\underline{\Psi^i_{bc}} = \frac{1}{2}(1 - \overline{\ell}_{ck} - \overline{\ell}_{bj}). \tag{28}$$

Finally, the bounds for C_ζ, in the set of constrains (10), become

$$\overline{C_\zeta} = \left\lfloor \sum_{a\in A^F_\zeta} \overline{\phi^a_{i^a_\zeta,n^a_\zeta}} - \sum_{a\in A^B_\zeta} \underline{\phi^a_{i^a_\zeta,n^a_\zeta}} + \sum_{(b,i,c)\in J_\zeta} \overline{\Psi^i_{bc}} \right\rfloor, \tag{29}$$

$$\underline{C_\zeta} = \left\lceil \sum_{a\in A^F_\zeta} \underline{\phi^a_{i^a_\zeta,n^a_\zeta}} - \sum_{a\in A^B_\zeta} \overline{\phi^a_{i^a_\zeta,n^a_\zeta}} + \sum_{(b,i,c)\in J_\zeta} \underline{\Psi^i_{bc}} \right\rceil. \tag{30}$$

The next set of constraints can be added to the linear model:

$$\underline{C_\zeta} \le C_\zeta \le \overline{C_\zeta}, \quad \forall \zeta \in \mathcal{B}_\zeta. \tag{31}$$

For reducing the space of search of the integer variables, the above-mentioned limits are utilized in the coming computational experiments.

4. Hybrid heuristic for MAXBAND

4.1. A MILP-based heuristic with tabu search for MAXBAND

On a network, the MAXBAND model requires a large number of initial data points as well as several variables defined on each segment of an artery, signals and cycles in the cycle basis. Even though the instances presented in Table 4 may not seem to be very large, the formulation has many equalities which contain integer and binary variables, making the problem difficult to solve.

Because the proposed algorithm includes Tabu Search [23], it requires an initial solution for later exploring its neighbourhood. Despite many attempts to find a systematic procedure to generate this solution, due to the high number of equalities involved, the optimization solver XPRESS provided the first feasible solution [31].

Moreover, the set of the variables m's ($2rc - r - c$), δ's ($4rc$) and C's ($r(c-1) - c + 1$) require to take integer values in the optimal solution. A number of *rm, rd* and *rC* variables are chosen randomly from them respectively to be modified later with one of the following procedures. The rest of the integer variables are fixed to the values they have in the initial solution.

- TSILP-LSF: The values of *rm, rd* and *rC* variables are fixed to values within the inequality Eqs. (21), {0, 1} and (31), respectively.
- TSILP-LSU: The *rm, rd* and *rC* variables with values given by a solution become variables again (i.e., unfixed).
- TSILP-LSVNS: TSILP-LSF and TSILP-LSU are applied one after the other.

The current problem is solved using XPRESS to attain a new feasible neighbour solution. This is repeated to generate a set of solutions (*candidate list*) of size *SizeList*. The list of candidates may contain many unfeasible solutions when using TSILP-LSF. Thus, if some variables are unfixed, the number of unfeasible solutions reduces considerably. In this sense, TSILP-LSU generates the candidate list. In our experience, if a memory structure is applied, releasing (unfixing) variables to solve the problem, it generates a diverse set of solutions. TSILP-LSU is applied on the selected variables *rm, rd* and *rC* only if it is not forbidden by a *tabu list*. The list is an array which contains *tt* values for each variable representing the number of iterations that cannot be modified. This is sorted by decreasing in order the objective value (i.e., the best first), and the first solution becomes the *current solution*. After saving the *tabu list* and updating each integer variable, the *tt* values decrease if different from zero, otherwise they are fixed to a value *maxtt*. Subsequently, a greedy local search is applied to the *current solution*. This is simply an iterative application of TSILP-LSVNS (Algorithm 1), TSILP-LSF (Algorithm 2) or TSILP-LSU (Algorithm 3). The termination criteria is met when a maximum number of iterations occur (see Algorithm 4).

4.2. Computational results

The algorithms performance is tested using artificial data. All random data hold the same values for outbound and inbound directions. Notice that even small grid graphs are very dense.

Let $U(a, b)$ be a continuous uniform distribution on interval (a, b),

- The lengths of the arcs of the grid follow a distribution $U(140, 600)$ (meters).
- Red times r follow a distribution $U(0.4, 0.6)$ (periods).
- Times to turn left ℓ follow a distribution $U(0.25r, 0.38r)$ (seconds).
- Min/max common period $T_{\min}/T_{\max}$, follows a distribution $U(40, 60)/U(90, 110)$ (seconds).
- Limits of velocities lower/upper e/f follow a distribution $U(12, 14)/U(15, 16)$ (meters/second).
- Limits on changes in reciprocal speed lower/upper $1/h/1/g = 0.012/{-0.012}$ (meters/second)$^{-1}$.

Table 5
Computational Results for TSILP procedure (small instances).

		Exact		Global			Global/LS				TSILP-LSF				TSILP-LSU				TSILP-LSVNS			
size	#	OF*	t	iter	sl	tt	iLS	rm	rd	rC	avg	worst	best	avgt	avg	worst	best	avgt	avg	worst	best	avgt
3x3	1	3.22	0	10	5	3	5	2	2	2	2.73	2.71	2.91	6	3.01	3.01	3.02	7	3.00	2.83	3.02	9
				10	5	3	10	2	2	2	2.72	2.71	2.81	8	3.01	3.01	3.02	10	3.02	3.01	3.02	15
				30	10	3	10	4	4	4	2.71	2.71	2.76	33	3.02	3.02	3.02	45	3.02	3.02	3.02	59
				50	10	3	20	4	4	4	2.71	2.71	2.71	73	3.02	3.02	3.02	123	3.02	3.02	3.02	174
	2	3.80	0	10	5	3	5	2	2	2	2.61	1.24	3.76	5	3.48	1.38	3.80	6	3.79	3.67	3.80	8
				10	5	3	10	2	2	2	3.24	1.24	3.77	10	3.78	3.72	3.80	9	3.80	3.76	3.80	13
				30	10	3	10	4	4	4	3.69	3.69	3.69	31	3.69	3.69	3.69	39	3.69	3.69	3.69	52
				50	10	3	20	4	4	4	3.69	3.69	3.69	72	3.69	3.69	3.69	102	3.69	3.69	3.69	145
5x5	3	4.77	7	10	5	3	5	2	2	2	3.57	2.63	4.16	11	4.05	3.43	4.31	14	4.11	3.73	4.29	17
				10	5	3	10	2	2	2	3.86	3.29	4.06	14	4.08	3.52	4.30	17	4.17	3.83	4.35	19
				30	10	3	10	4	4	4	4.16	4.01	4.41	55	4.31	4.18	4.73	96	4.36	4.18	4.73	117
				50	10	3	20	4	4	4	4.14	3.94	4.18	145	4.33	3.95	4.71	257	4.42	4.23	4.72	332
	4	5.20	6	10	5	3	5	2	2	2	3.88	3.75	3.98	7	4.09	3.84	4.43	11	4.24	3.98	4.49	11
				10	5	3	10	2	2	2	3.91	3.74	4.11	14	4.25	3.78	4.77	22	4.21	4.11	4.26	29
				30	10	3	10	4	4	4	4.47	3.97	4.61	58	4.77	4.66	4.86	84	4.74	4.46	4.86	120
				50	10	3	20	4	4	4	4.45	3.97	4.61	145	4.78	4.66	4.86	260	4.83	4.77	4.86	326
6x6	5	5.18	116	10	5	3	5	2	2	2	3.11	2.01	3.52	15	3.51	3.28	3.94	17	3.54	3.18	3.97	20
				10	5	3	10	2	2	2	3.12	2.49	3.48	21	3.49	3.07	3.79	33	3.48	3.07	3.86	39
				30	10	3	10	4	4	4	3.58	3.38	3.73	85	4.07	3.57	4.24	128	4.16	3.91	4.24	152
				50	10	3	20	4	4	4	3.73	3.49	4.18	190	4.23	3.93	4.46	345	4.31	4.12	4.46	420
	6	4.74	1270	10	5	3	5	2	2	2	3.35	1.63	4.16	12	4.18	3.92	4.31	17	4.16	3.92	4.31	19
				10	5	3	10	2	2	2	3.57	1.63	4.15	17	4.19	3.74	4.35	25	4.26	4.10	4.35	36
				30	10	3	10	4	4	4	4.24	4.17	4.33	92	4.32	4.14	4.37	128	4.36	4.35	4.37	152
				50	10	3	20	4	4	4	4.28	4.22	4.33	193	4.36	4.35	4.37	274	4.36	4.35	4.37	295

Algorithm 1 VNS Local Search Procedure (LSVNS).

Let:
S : A problem with best objective function value on a *candidate list*.

Step 1. Choose rm, rd and rC from m's, δ's and C's on S.
Step 2. If $tt = 0$, fix their values with random numbers within their bounds.
Step 3. Solve the instance using an LP solver (XPRESS) and set this solution as a *current solution*.
Step 4. Choose other integer variables rm, rd and rC from m's, δ's and C's on the *current solution*.
Step 5. If $tt = 0$, these variables are unfixed.
Step 6. Solve the instance using branch and bound (XPRESS).
Step 7. Update the *current solution* only if it is better than the previous one.
Step 8. Repeat the process until the maximum number of iterations is reached.

Algorithm 2 Fix local search procedure (LSF).

Let:
S : A problem with best objective function value on a *candidate list*.

Steps 1 …3 and 7 …8 are as in LSVNS.

- All τ_{ai}'s and $\overline{\tau}_{ai}$'s were set to 0.
- All weights on the objective function were set to 1.

Computational experiments are carried out using a PC Intel(R) Xeon(R) 3.40GHz 16.0 (RAM). The fundamental cycle basis [29,32] for each graph $G_{r\times c}$ were obtained using *Mathematica* version 10.1. The algorithms were coded with *Xpress Mosel* version 3.4.2, and the solver used was Xpress Optimizer version 24.01.04.

Algorithm 3 Unfix local search procedure (LSU).

Let:
S : A problem with best objective function value on a *candidate list*.

Steps 4 …6 and 7 …8 are as in LSVNS.

Algorithm 4 Tabu Search for MAXBAND (TSILP-LS/F/U/VNS).

Let:
P: A complete MAXBAND problem on a grid graph.

Step 1. For all m, δ and C, $tt = 0$ in a *tabu list*.
Step 2. Find the first integer solution for P by XPRESS and set it as *current solution*.
Step 3. Create a *candidate list* of size *SizeList*:
1. Choose randomly rm, rd and rC from m's, δ's and C's in *current solution*.
2. If $tt = 0$, unfix these variables.
3. Solve the problem using branch and bound (XPRESS).
4. Repeat *SizeList* times.

Step 4. Sort the $candidate\ list$ in decreasing order of the objective function value.
Step 5. Apply procedure LSF, LSU or LSVNS with the best first in the candidate list as input.
Step 6. Set the *current solution* as the best solution in the *candidate list*.
Step 7. Update the *tabu list* for each m, δ and C on the *current solution*:
1. If current $tt = 0$ then $tt = maxtt$, else
2. $tt = tt - 1$.

Step 8. Repeat Steps $3-7$ until a maximum number of iterations is reached.

Table 5 presents results for different small grid graph instances generated randomly, considering all parameters and variables in the model 1 including the bounds (21) and (31).

Table 6
Computational Results for TSILP procedure (large instances).

		Global			Global/LS				TSILP-LSF				TSILP-LSU				TSILP-LSVNS			
size	#	iter	sl	tt	iLS	rm	rd	rC	avg	worst	best	avgt	avg	worst	best	avgt	avg	worst	best	avgt
7x7	7	30	10	5	20	5	5	5	4.33	4.24	4.34	292	4.51	4.35	4.66	484	4.63	4.56	4.68	546
		30	10	5	30	5	5	5	4.34	4.27	4.46	213	4.51	4.35	4.72	440	4.58	4.36	4.72	520
		50	10	5	30	5	5	5	4.34	4.34	4.35	300	4.56	4.35	4.70	625	4.66	4.53	4.72	815
		50	20	5	30	10	10	10	4.37	4.24	4.55	623	4.67	4.56	4.72	1469	4.70	4.66	4.72	1700
	8	30	10	5	20	5	5	5	3.11	2.88	3.19	175	3.28	3.19	3.46	347	3.40	3.19	3.55	417
		30	10	5	30	5	5	5	3.15	2.88	3.19	162	3.31	3.12	3.48	329	3.41	3.19	3.83	425
		50	10	5	30	5	5	5	3.21	3.19	3.38	399	3.35	3.19	3.55	613	3.63	3.23	3.99	817
		50	20	5	30	10	10	10	3.29	3.19	3.82	581	3.52	3.22	4.30	1113	3.81	3.36	4.39	1323
8x8	9	30	10	5	20	5	5	5	4.08	3.85	4.28	219	4.22	4.20	4.28	398	4.23	4.20	4.28	483
		30	10	5	30	5	5	5	3.99	3.85	4.19	281	4.21	4.20	4.24	715	4.24	4.20	4.28	910
		50	10	5	30	5	5	5	4.04	3.85	4.19	472	4.23	4.20	4.33	806	4.25	4.20	4.33	900
		50	20	5	30	10	10	10	4.22	4.19	4.28	778	4.28	4.20	4.33	1710	4.30	4.24	4.33	1760
	10	30	10	5	20	5	5	5	2.25	2.08	2.84	167	3.07	2.54	3.37	397	3.10	2.75	3.53	524
		30	10	5	30	5	5	5	2.25	2.01	2.84	218	3.03	2.38	3.49	601	3.12	2.77	3.49	727
		50	10	5	30	5	5	5	2.33	2.08	2.96	382	3.35	2.84	3.72	710	3.42	2.84	3.61	1186
		50	20	5	30	10	10	10	3.01	2.68	3.22	567	3.54	3.27	3.92	1345	3.72	3.29	4.10	1688
9x9	11	30	10	5	20	5	5	5	3.33	3.00	3.70	282	4.15	3.61	4.35	524	4.15	3.61	4.31	620
		30	10	5	30	5	5	5	3.40	3.00	4.02	324	4.04	3.61	4.31	620	4.20	3.61	4.49	755
		50	10	5	30	5	5	5	3.43	3.00	3.65	522	4.25	3.61	4.88	893	4.93	4.75	5.01	928
		50	20	5	30	10	10	10	4.14	3.79	4.42	479	4.36	4.26	4.49	1131	4.80	4.38	5.20	1206
	12	30	10	5	20	5	5	5	4.17	4.07	4.31	270	4.31	4.24	4.71	541	4.36	4.24	4.71	646
		30	10	5	30	5	5	5	4.18	4.07	4.31	316	4.25	4.22	4.31	699	4.28	4.24	4.42	848
		50	10	5	30	5	5	5	4.18	4.07	4.42	539	4.26	4.24	4.31	901	4.39	4.24	4.74	1223
		50	20	5	30	10	10	10	4.27	4.12	4.42	658	4.43	4.24	4.56	1324	4.45	4.31	4.61	1698
10x10	13	30	10	5	20	5	5	5	1.63	1.55	1.91	9937	1.85	1.76	1.91	10,123	1.86	1.76	1.91	10,259
		30	10	5	30	5	5	5	1.75	1.55	1.91	10,007	1.84	1.57	1.91	10,278	1.89	1.72	1.91	10,488
		50	10	5	30	5	5	5	1.71	1.55	1.91	10,218	1.86	1.66	1.91	10,714	1.91	1.90	1.91	11,058
		50	20	5	30	10	10	10	1.89	1.72	1.91	10,553	1.91	1.91	1.91	11,341	1.94	1.73	2.01	11,729
	14	30	10	5	20	5	5	5	2.36	2.30	2.46	474	2.86	2.56	2.97	778	2.91	2.75	2.97	918
		30	10	5	30	5	5	5	2.45	2.30	2.90	554	2.85	2.52	3.03	769	2.94	2.79	3.05	958
		50	10	5	30	5	5	5	2.40	2.30	2.55	648	2.93	2.84	3.05	1407	2.95	2.79	3.05	2016
		50	20	5	30	10	10	10	2.98	2.77	3.05	876	3.13	3.04	3.21	2082	3.20	3.05	3.24	3238

Table 7
10 × 10 instances vs XPRESS.

		Exact			TSILP_LSF		TSILP_LSU		TSILP_LSVNS	
size	#	f_OF	t_fs	t > 3h	worst	best	worst	best	worst	best
10x10	13	0.14	9657	1.55	1.55	1.91	1.57	1.91	1.72	2.01
	14	0.54	152	2.19	2.30	3.05	2.52	3.21	2.75	3.24

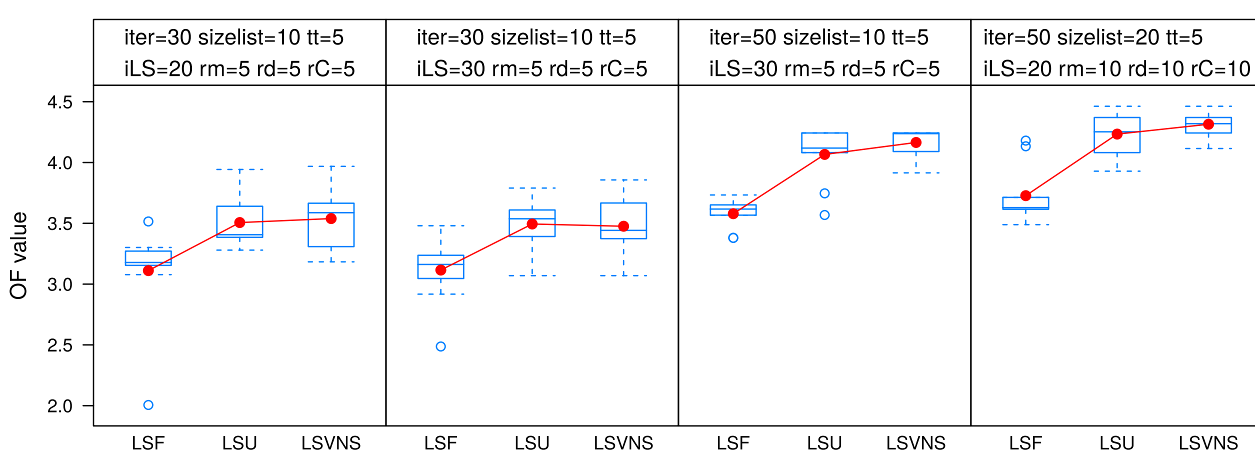

Fig. 8. Box-Plot of 10 runs for experiments TSILP-LS on $G_{6\times 6}$ (instance 5).

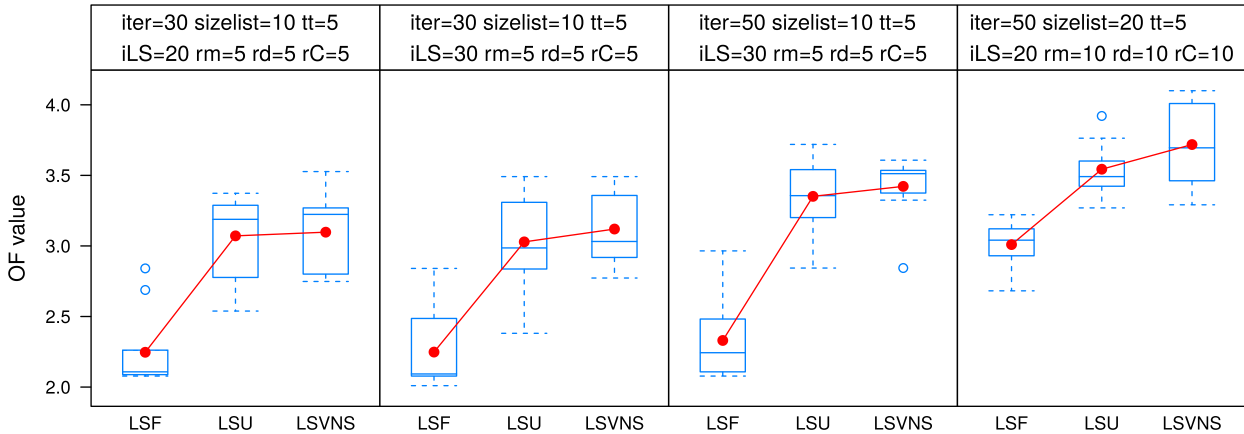

Fig. 9. Box-Plot of 10 runs for experiments TSILP-LS on $G_{8\times8}$ (instance 10).

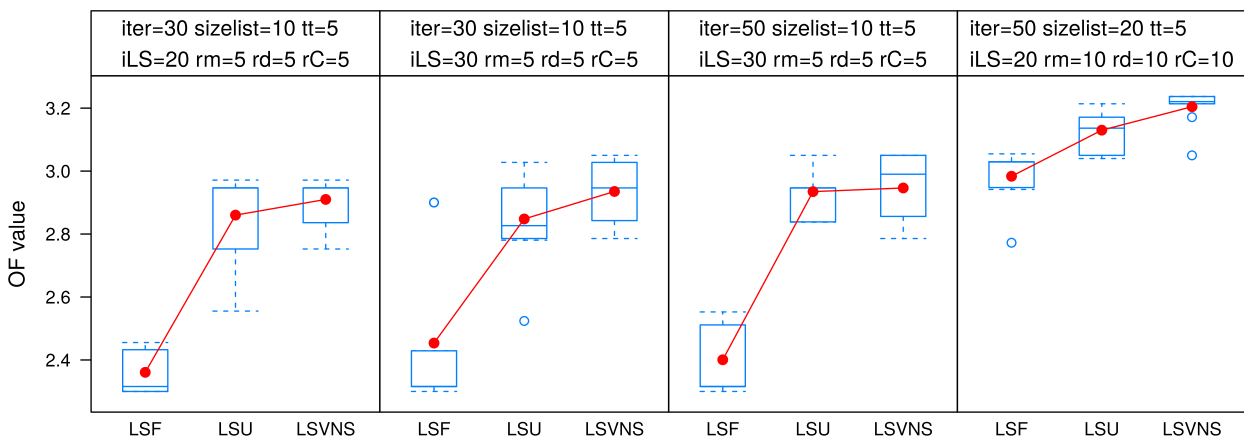

Fig. 10. Box-Plot of 10 runs for experiments TSILP-LS on $G_{10\times10}$ (instance 14).

The headers are as follows:

- size: size of the problem.
- #: instance number.
- Exact (XPRESS branch and bound).
  - OF*: optimal value of the objective function.
  - t: running time (seconds).
- Global (stands for whole procedure).
  - iter: number of tabu search iterations.
  - sl: size list.
  - tt: tenure time in the memory list (iterations).
- Global/LS (stands for whole and local search procedures).
  - iLS: number of iterations of local search.
  - rm, rd, rC: number of variables m's, δ's and C's chosen for the candidate list and the local search.
- TSILP-(LSF, LSU, LSVNS).
  - avg, worst, best: Average, worst and best case objective function value.
  - avgt: average time (seconds).

Each problem is solved ten times using four different parameter settings. An equal number of integer variables *rm, rd* and *rC* were used in both cases to create the candidate list and to run the local search procedure. The best objective function values obtained among the different heuristic algorithms are underlined. For each instances, XPRESS permmited to obtain optimal solutions in short time.

TSILP-LSU and TSILP-LSVNS met the optimal for problem #2 and both algorithms performed almost the same in most of the evaluated cases. Fig. 8 resembles, as an example, the mean OF values represented in red dots.

For problems of 5 × 5 and 6 × 6 size, the increase in the number of iterations, size list and selected random variables generated better results. Clearly, as the problem size increases, the heuristics times are more competitive.

Table 6 presents results for larger instances. In this case, XPRESS was not able to find the optimal solution for any of them within a time limit of 3 h. On the other hand, TSILP-LSVNS showed better results as it is portrayed in Figs. 9 and 10.

The running times, which include the time required to achieve the first initial feasible solution using standard branch and bound in XPRESS, were as explained next. For instance #13, the CPU time was more or less 9657 s, 152 for instance #14, and the remainder took less than 11 s.

In most of the cases, the average solution of TSILP-LSVNS improved the average solutions obtained with the first two methods. TSILP-LSF took less time, but almost never found the best objective function value, which was obtained by the other algorithms.

Due to the vast amount of initial data, and the need of having the integer model ready and before applying any algorithm, requires some time which was not included in the running times. Nevertheless, the largest instance tested had an average of 20.73 s, which is time needed by XPRESS to generate the model to be solved.

The best results was found for the largest instances. In this case, the three algorithms, even in the worst cases, reached much better solution than those obtained using XPRESS. Table 7 lists the first integer solution (f_OF), the time to meet that solution (t_fs) and the best integer solution after 3 h of running time (t > 3h) of the XPRESS branch and bound.

5. Conclusions

In this contribution, a complete review of the MAXBAND model and a generalization of the integer variable bounds proposed in [7] were performed to establish the network case study. Cycle integer variable bounds were provided as well.

Additionally, a hybrid heuristic algorithm based on Tabu Search and VNS took advantage of the mixed integer linear MAXBAND model to obtain feasible solutions. During the search of optimal solutions, the problems were solved in a reduced feasible space due to the initial solution. The proposed algorithm begins with a feasible solution for later obtaining integer values to be used in the subsequent iterations. Results were better when a serial application of LSF and LSU was included by local search using VNS. As attested in the computational experiments, the best results were obtained for large instances.

Future work in this subject embraces to include further attention in prioritizing certain arteries with high traffic, and other real-life traffic aspects that were not included. The incorporation of such real aspect would modify the weights composing the objective function.

References

[1] M. Péres, G. Ruiz, S. Nesmachnow, A.C. Olivera, Multiobjective evolutionary optimization of traffic flow and pollution in montevideo, uruguay, Appl. Soft Comput. 70 (2018) 472–485.
[2] M. Papageorgiou, C. Diakaki, V. Dinopoulou, A. Kotsialos, Y. Wang, Review of road traffic control strategies, Proceed. IEEE 91 (12) (2003) 2043–2067.
[3] N. Gartner, D. Little, H. Gabbay, Optimization of traffic signal settings by mixed-integer linear programming; part I: the network coordination problem; part II: The network synchronization problem, Transport. Sci. 9 (1975) 321–363.
[4] G. Wünsch, Coordination of traffic signals in networks, Ph.D. thesis, Technische Universität Berlin, 2008.
[5] E. Köhler, M. Strehler, Traffic signal optimization using cyclically expanded networks, Wiley Period. Netw. 65 (2015) 244–261.
[6] J. Morgan, D. Little, Synchronizing traffic signals for maximal bandwidth, Opera. Res. Spec. Transport. Sci. Issue 12 (6) (1964) 896–912.
[7] D. Little, The synchronization of traffic signals by mixed-integer linear programming, Oper. Res. 14 (4) (1966) 568–594.
[8] D. Little, M. Kelson, N. Gartner, MAXBAND: a versatile program for setting signal on arteries and triangular networks, Transport. Res. Rec. 795 (1980) 40–46.
[9] t Gartner, S. Assmann, F. Lasaga, D. Hou, A multi-band approach to arterial traffic signal, Transport. Res. 25B (1) (1991) 55–74.
[10] C. Zhang, Y. Xie, N. Gartner, C. Stamatiadis, T. Arsava, AM-BAND: an asymmetrical multi-band model for arterial traffic signal coordination, Transport. Res. Part C: Emerg. Technol. 58 (2015) 515–531.
[11] X. Wu, Z. Tian, P. Hu, Z. Yuan, Bandwidth optimization of coordinated arterials based on group partition method, Procedia-Soc. Behav. Sci. 43 (2012) 232–244.
[12] W. Xianyu, H. Peifeng, Y. Zhenzhou, Link-based signalized arterial progression optimization with practical travel speed, J. Appl. Math. (2013).
[13] K. Gao, Y. Zhang, R. Su, F. Yang, P.N. Suganthan, M. Zhou, Solving traffic signal scheduling problems in heterogeneous traffic network by using meta-heuristics, IEEE Trans. Intell. Transport. Syst. (2018).
[14] D. Robertson, TRANSYT, a Traffic Network Study Tool. Technical Report, Crowthorne, Berkshire, 1969.
[15] S. Cohen, Concurrent use of MAXBAND and TRANSYT signal timing programs for arterial signal optimization, Transport. Res. Rec. 906 (1983) 81–84.
[16] t Gartner, C. Stamatiadis, Arterial-based control of traffic flow in urban grid networks, Math. Comput. Model. 35 (2002) 657–671.
[17] R. Braun, F. Weichenmeier, Automatic offline-optimization of coordinated traffic signal control in urban networks using genetic algorithms, in: Proceedings of the 12th World Congress on Intelligent Transport Systems, 2005.
[18] L. Singh, S. Tripathi, H. Arora, Time optimization for traffic signal control using genetic algorithm, Expert Syst. Applica. 2 (2) (2009).
[19] J. García-Nieto, E. Alba, A.C. Olivera, Swarm intelligence for traffic light scheduling: application to real urban areas, Eng. Applica. Artif. Intell. 25 (2) (2012) 274–283.
[20] K. Gao, Y. Zhang, A. Sadollah, R. Su, Optimizing urban traffic light scheduling problem using harmony search with ensemble of local search, Appl. Soft Comput. 48 (2016) 359–372.
[21] H. Yi, Q. Duan, T.W. Liao, Three improved hybrid metaheuristic algorithms for engineering design optimization, Appl. Soft Comput. 13 (5) (2013) 2433–2444.
[22] Q. Duan, T.W. Liao, H. Yi, A comparative study of different local search application strategies in hybrid metaheuristics, Appl. Soft Comput. 13 (3) (2013) 1464–1477.
[23] F. Glover, Future paths for integer programming and links to artificial intelligence, Comput. Opera. Res. 13 (1986) 533–549.
[24] J. Brandao, A. Mercer, A tabu search algorithm for the multi-trip vehicle routing and scheduling problem, Eur. J. Opera. Res. 100 (1) (1997) 180–191.
[25] O. Shahvari, R. Logendran, An enhanced tabu search algorithm to minimize a bi-criteria objective in batching and scheduling problems on unrelated-parallel machines with desired lower bounds on batch sizes, Comput. Opera. Res. 77 (2017) 154–176.
[26] L. Berbotto, S. García, F.J. Nogales, A randomized granular tabu search heuristic for the split delivery vehicle routing problem, Ann. Oper. Res. 222 (1) (2014) 153–173.
[27] P. Demeester, W. Souffriau, P. De Causmaecker, G.V. Berghe, A hybrid tabu search algorithm for automatically assigning patients to beds, Artifi. Intell. Med. 48 (1) (2010) 61–70.
[28] N. Mladenović, P. Hansen, Variable neighbourhood search, Comput. Oper. Res. 24 (1997) 1097–1100.
[29] C. Liebchen, R. Rizzi, Classes of cycle bases, Disc. Appl. Math. 155 (3) (2007) 337–355.
[30] N. Chaudhary, A mixed integer linear programming approach for obtaining an optimal signal timing plan in general traffic networks, Texas A&M University, 1987 Ph.D. thesis.
[31] FICO, Xpress optimization suite, January 19, 2017, Retrieved from https://www.fico.com/en/products/fico-xpress-optimization.
[32] T. Kavitha, C. Liebchen, K. Mehlhorn, D. Michail, R. Rizzi, T. Ueckerdt, K. Zweig, Cycle bases in graphs: characterization, algorithms, complexity and applications, Comput. Sci. 3 (4) (2009) 199–243.

A modified fuzzy approach to project team selection

Binayini Pradhan, Department of Computer Scinece Engineering , Raajdhani Engineering College, Bhubaneswar, binayini.pradhan@gmail.com

Ajit Kumar Panda, *Department of Electrical Engineering, Aryan Institute of Engineering & Technology, Bhubaneswar, akpanda555@hotmail.com*

Subhendu Sahoo, *Department of Electrical and Electronics Engineering, NM Institute of Engineering & Technology, Bhubaneswar, s.sahoo95@outlook.com*

Pratik Mohanty, *Department of Electrical Engineering , Capital Engineering College, Bhubaneswar, pratikmohanty92@hotmail.com*

A R T I C L E I N F O

Keywords:
Fuzzy set
Soft set
Intuitionistic fuzzy soft Set
Project team selection

A B S T R A C T

Selecting a team for executing a project is not an easy task. As any project involves monetary implications, management of a company employs a careful approach in choosing a project team. Several variations of Multi Criteria Decision Making (MCDM) Models are available in the literature and practice. We propose a modified intutionistic fuzzy approach to project team selection. We have combined the MCDM with dynamic weightage for each parameter. The main design parameters in this model are the conversion of input data into the fuzzified form, design of non - membership grade and the calculation of indeterministic values from membership and non-membership grades. Finally, the fuzzified output is converted into a crisp set, known as defuzzification. This method helps in determining the most skilled candidates in the order of their ability from a group of applicants.

1. Introduction

A project is a temporary endeavour designed to produce a unique product, service or result with a defined beginning and end satisfying the predetermined goals and objectives, typically to bring about beneficial change or added value [7]. The phases of project management include initiating, planning, executing, monitoring and controlling, and closing the work of a team. All those activities are aimed to achieve defined goals at the defined time.

Projects are usually time constrained, and often constrained by funding and staffing. These constraints impact the quality of the deliverables. The success of project management can always be filtered through the Triple Constraints, viz., the budget, time and scope. Though the origins of Triple Constraints are unclear, they have been used since at least the 1950s.

This paper is presented in 8 sections. Review of relevant literature is available in Sections 2 and 6. The motivation of the work and the relevance of the work are available in Section 3. The role of fuzzy set theory in the project management is presented in Section 4. The model construction is given in Section 5. In Sections 6 and 7, an experiment, its result, discussion and the sensitivity analysis are included. The paper concludes with Section 8.

1.1. History of project management

Most scholars consider that modern project management has started with the innovative scheduling diagram Gantt chart by Henry Gantt in 1917. This scheduling tool created a new way of thinking for project management and gave birth to dozens of process and tools for project managers to manage the complexities of budget, quality and time. Some notable techniques included the Critical Path Method (CPM), the Program Evaluation Review Technique (PERT) and the Work Breakdown Structure (WBS). The CPM identifies the earliest completion time without discarding all the crucial activities to complete the project. The PERT helps to analyse the task involved in completing a project. The WBS helps to decompose projects into smaller deliverables. These tools help monitoring and controlling the projects to minimize the impacts of the Triple Constraints and improve quality.

In the last couple of decades, markets have become more competitive. Many isolated economies shifted to global approaches. Quality has become the de facto standard for winning a customer. The definition of quality becomes more refined to conformance to requirement. Project management processes received wider attention to predict and improve quality of the product. Total Quality Management (TQM), International Organization for Standardization (ISO), Capability Maturity Model Integration (CMMI) and many more standards were born, refined and streamlined during this time to manage the Triple Constraint and thereby the quality. All these standards provide fundamental management techniques, optimizing processes and efficient tools towards continuous improvements for an organization by conforming customer needs and expectations, encouraging innovation and employee participation, respecting societal values and belief and obeying governmental regulations and statues.

Though the term Triple Constraint was introduced as part of modern project management in 1950s, there are historical evidences that in the early civilization these concepts were heavily used. In 2570 BC, the Pharaohs completed The Great Pyramid of Giza, the tallest human-made structure existing for more than 3800 years, conforming to the quality requirements of Pharaoh. The project had clear time span of 20 years, budget of 100,000 workers and clear dimensions of Pyramid as the scope. Without the service of modern management concepts, tools such as cranes, bulldozers, the Egyptians managed the triple constraints and completed mammoth structures of admirable precision within time. Archaeologists suggests that Egyptians conquered the concept of Work Breakdown Structure (WBS) to employee 100,000 skilled craftsmen for the project. These employees were arranged in a highly organized tiered management structure with each side of the pyramids having a dedicated supervisor. They understood the concepts of modern Human Resources Management (HRM) very well. The importance was given for their skills, knowledge management and experience. The workers' safety and health were considered important. They lived near the construction sites with well-equipped and furnished labour camps. Employees were paid in food and accommodation, well looked after and were allowed one day in ten to rest. Another such large project were huge manpower was used is Construction of the Great Wall of China in 208 BC. According to historical data, the labour force was organized into soldiers, common people and prisoners.

1.2. Project management in modern times

The modern project management techniques focus more on the aspects of monitoring and controlling of project which happens after a team has been selected. With the examples of these two ancient projects, one can observe the importance of highly skilled people in right position for the success of the project. Rightly skilled people placed at right position brings in competitive advantage to any company.

Teamwork is one of the pivot factors that influence the engineering and management structure. Software fields now greatly work by forming small teams which carry out assignments relating to system management, product development, analysis, etc. This reduces the error tendencies as prominent skilled people are made part of the team. Each team comprises of people who can directly contribute to the requirements of the project.

2. Review of literature

Katzenbach and Smith [17] defined the concept of an optimal cross functional team required for a project. They presented that an optimal cross functional team is a group of people, few from each required functional area, who are chosen carefully for complementary skills and who are mutually amenable and can work for a common goal for the project success. They will have a shared mission and approach and a fixed timeline. The members will return to their functional units or move to a different project once the project task is accomplished. Hence the project team formation is recognized to be an intricate multi-criteria problem in decision making.

Topcu [13] indicated that the constraints on the cost of development and establishment also lead to quality issues during the completion of the project. He also says that, evaluating the team members with respect to their skills, past performances, work quality, competency and mutual agreeability may help in resolving this issue. All of the project activities undoubtedly rely on the team structure. Thus team selection which is one of the incipient tasks of the project becomes the most relevant. Hence a strategic decision making study on the team selection procedure has now become a necessity. Though a lot of work regarding the behavioural traits of the team members that can affect the smooth functioning of the project were categorically studied, a talent-based (quantitative) research in this domain is yet very limited. A fuzzified approach to this aspect was noticeably brought by Yakoob and Kawata [14], by making use of triangular fuzzy numbers in the selection of the candidates for work team formation.

3. Project management

3.1. Team and role structure

Success or failure of project is directly linked to the quality of the human resources selected to execute the project and the hierarchical structure adopted. In the last 50 years, Human Resources Management (HRM) has pioneered many concepts from hiring, training and development, performance review, compensation, safety and health, welfare industrial relations to termination of employees. The strategic HRM movement reinforces these concepts that any individual in a company who has responsibility for people is the HR manager, no matter which functional division the employee reports to. The following 3 step process ensures that the employees are motivated and productive.

3.1.1. Step 1: Job Analysis and Job Description

The first step of project management is to conduct a job analysis for the project and define all the job descriptions (JD). The Job Analysis is more exhaustive than just technical skills. It shall include analysing the entire work process, internal and external communications, work structure, etc. The JD shall include the details of jobs, remuneration, years of experience, knowledge, skill set, expected results, behavioural and technical competencies, soft skills, etc. The JD ensures to broadly cover both psychological and sociological dimensions of work and workforce.

3.1.2. Step 2: Hierarchical Structure

The second step is to create the hierarchical structure needed for the workforce and define the responsibility matrix. The RASCI matrix is a common framework used for allocation and assignment of responsibilities to the team members in projects. The letters of RASCI in the matrix describe the level of responsibility. The levels are Responsibility, Accountability, Supported, Consulted and Informed in that order.

3.1.3. Step 3: Job Design

The last step is to ensure a proper Job Design approach for the project by considering characteristics of the task, work flow, ergonomics, work practices, autonomy, employee abilities and availability and social and cultural expectations. Job Design ensures job satisfaction with enriched jobs. With proper job description, reporting structure and job design in place, team members from the available pool can be selected.

3.2. Selecting members to the project team

The team is comparable to human body. Like various organs collaborate to make things happen in a body, the varied different individuals collaborate day by day to bring success to the project. The key quality to be part of the project team is teamwork, which is a behavioural competency. Members bring something unique to the project team and are always gunning to make things happen [18].

Team selection is not different from match-making. One side of the spectrum is the requirement - clear roles and job descriptions. The other side is the available talents with their various capability parameters. The objective is to gain the best talents in the market that can make a difference to the project. There should be a fit between job description and the capabilities of available talent to discharge the tasks. Any mismatch is likely to result in job dissatisfaction that carries dysfunctional consequences like low productivity, increased absenteeism and attrition. The Assignment Problem and the Classical Marriage Problem are similar scenarios.

There are many criteria available for comparing a talent against the job description. Each project may choose the right blend of criteria that are important for that environment. These criteria help the workforce to execute project with agility and quality. In people selection process for a project, we must identify the criteria needed for each position in that project, align available human resources to business positions.

Table 1
Example of SS.

H	Υ_1	Υ_2	Υ_3	Υ_4
Ω_1	1	0	1	0
Ω_2	1	0	1	1
Ω_3	0	1	1	1
Ω_4	1	0	0	0
Ω_5	0	1	0	1

Table 2
Example of FSS.

H	Υ_1	Υ_2	Υ_3	Υ_4
ϖ_1	0.85	0.23	0.92	0.34
ϖ_2	0.65	0.31	0.87	0.95
ϖ_3	0.22	0.79	0.89	0.93
ϖ_4	0.89	0.12	0.41	0.87
ϖ_5	0.25	0.87	0.27	0.91

Today, the normal ways of doing business has changed. Globalization and digitization have brought in level playing fields across international markets. Every business is facing VUCA (volatility, uncertainty, complexity and ambiguity) threats from markets that were unknown few years back. At the same time, organizations are attempting constantly to improve productivity, performance and return on investment. The strength of the organization is strength of its team. Each organization is always on the lookout for making a dream team. The MCDM (Multi-Criteria Decision Making) Method ensures that the organization can build a dream team.

4. Fuzzy set theory and its application in project management

Nowadays, fuzzy technology is increasingly used in Project team selection studies. Project team selection is a complex process. The model presented should only be used for those cases in which there are minor divergence among the DMs. This enables them to define an interval of variation for the weight of each criterion. i. e., a lower and an upper limit for the weight of each criterion. In this work, the MCDM with dynamic weightage for each parameter is considered.

In 1965, Zadeh [16] introduced the concept of fuzzy set theory. This theory acts as a bridge between certainty and uncertainty. So many researchers have applied this theory in real time applications. This theory is efficiently effective when the relationships are not fully defined. The fuzzy set is defined from a universal set H to [0,1]. Normally the range of a crisp function is taken as a very large interval from $-\infty$ to $+\infty$. This very large range of crisp function can be mapped in to a closed interval [0,1]. That is a very large range can be transformed into a small interval between 0 and 1 both values are inclusive. From $(-\infty, +\infty)$ can be shrunk to the interval [0,1]. Then there arises a question: Is this possible? This question brings out a solution. The solution is the fuzzy set which is the most powerful and universal set in reality. The function associated with the fuzzy set is called the membership function (MF) and the set defined by it is called fuzzy set.

The MF μ_C is defined as

$$\mu_C : H \to [0,1]. \tag{1}$$

4.1. Fuzzy soft sets

Molodtsov [6] introduced soft set (SS) which is capable of handling uncertainties. This theory has several applications in computer science, electrical engineering and boolean algebra because it contains only two elements 0 and 1. The ordered pair $(\mathcal{F}, C)$ is called a soft set over H, where $\mathcal{F} : C \to R(H)$, where $R(H)$ is the set of all subsets of a universal set H and C is a collection of attributes.

4.2. An SLCM Model

Let $H = \{\Omega_1, \Omega_2, \Omega_3, \Omega_4, \Omega_5\}$ be the five Software Life Cycle Models (SLCM) in software engineering. Let $C = \{\Upsilon_1, \Upsilon_2, \Upsilon_3, \Upsilon_4\}$ be the parameters (attributes) related to this models. Suppose that $\mathcal{F}(\Upsilon_1) = \{\Omega_1, \Omega_2, \Omega_4\}$, $\mathcal{F}(\Upsilon_2) = \{\Omega_3, \Omega_5\}$, $\mathcal{F}(\Upsilon_3) = \{\Omega_1, \Omega_2, \Omega_3\}$, and $\mathcal{F}(\Upsilon_4) = \{\Omega_2, \Omega_3, \Omega_5\}$. This is represented as a $0-1$ matrix in Table 1.

The Soft Set (SS) has rich potential applications in computer science and boolean algebra. The major drawback of the soft set theory is that it deals with two extremes only. To avoid these problems Maji et al.[4] introduced the concept called fuzzy soft set theory which also deals with uncertainties. There are infinite number of possibilities in fuzzy soft set theory because there are infinite number of real numbers that lie between 0 and 1. The ordered pair $(\mathcal{F}, E)$ is called a fuzzy soft set over H, where $\mathcal{F} : E \to A(H)$, where $A(H)$ is the set of all fuzzy sets of a universal set H.

In the previous example, suppose that

$$\mathcal{F}(\Upsilon_1) = \{\varpi_1/.85, \varpi_2/.65, \varpi_3/.22, \varpi_4/.89, \varpi_5/.25\},$$
$$\mathcal{F}(\Upsilon_1) = \{\varpi_1/.85, \varpi_2/.65, \varpi_3/.22, \varpi_4/.89, \varpi_5/.25\},$$
$$\mathcal{F}(\Upsilon_2) = \{\varpi_1/.23, \varpi_2/.31, \varpi_3/.79, \varpi_4/.12, \varpi_5/.87\},$$
$$\mathcal{F}(\Upsilon_3) = \{\varpi_1/.92, \varpi_2/.87, \varpi_3/.89, \varpi_4/.41, \varpi_5/.27\},$$
$$\text{and } \mathcal{F}(\Upsilon_4) = \{\varpi_1/.34, \varpi_2/.95, \varpi_3/.93, \varpi_4/.87, \varpi_5/.91\}.$$

Then the corresponding Fuzzy Soft Set is given in Table 2.

Determining the appropriate input variables is probably one of the most critical decision variables in developing a successful project team selection model since it contains important information about correlation structures in the data series. After determining the appropriate input variables that have a significant influence on the selection, appropriate model architecture and parameters must be chosen for the project team selection model.

5. Model construction

We consider another similarity measure known as Intutionistic Fuzzy Soft Set (IFSS) IFSS [5]. The IFSS is also called vague set because it contains vague information. The IFSS theory is applied in logic programming, medical diagnosis, artificial intelligence, database systems etc. Dengfeng et al. [3] introduced concentrated, dilated, normalized IFS and derived some properties. Different types of uncertainty can be modelled through fuzzy logic programming [2,15]. Some researchers derived the properties of IFSS such as containment, convertibility, interaction, monotonicity, union and intersection.

The main design parameters are concerned with the conversion of input data into the fuzzified form, design of non - membership grade and the calculation of indeterministic values from membership and non-membership grades. Finally, the fuzzified output is converted into a crisp set, known as defuzzification. Next, we give a real time example of IFSS.

5.1. Basic concepts of the IFSS

An IFSS [1] is defined as

$$C = \{\langle z, \mu_c(z), \nu_c(z)\rangle | z \in G\} \tag{2}$$

where, the function $\mu_C : G \to [0,1]$ and $\nu_C : G \to [0,1]$. The functions $\mu_c(z)$ and $\nu_c(z)$ are called membership value (MV) and non-membership value (NV), respectively. It is to be noted that

$$0 \le \mu_c(z) + \nu_c(z) \le 1 \tag{3}$$

$$\pi_c(z) = 1 - \mu_c(z) - \nu_c(z) \tag{4}$$

$$0 \le \pi_c(z) \le 1 \tag{5}$$

The value $\pi_c(z)$ is called the indeterministic part for z.

Table 3
Example of IFSS.

U	Υ_1	Υ_2	Υ_3	Υ_4
x^1	(0.65,0.3)	(0.66,0.23)	(0.58,0.31)	(0.89,0.10)
x^2	(0.65,0.33)	(0.48,0.31)	(0.77,0.13)	(0.73,0.21)
x^3	(0.76,0.12)	(0.90,0.0)	(1.0,0.0)	(0.85,0.05)
x^4	(0.8,0.0)	(0.56,0.3)	(0.72,0.23)	(0.78,0.11)
x^5	(0.55,0.33)	(0.9,0.0)	(0.68,0.21)	(0.9,0.0)

5.2. An IFSS model

Let x^1, x^2, x^3, x^4 and x^5 be five houses. Let the parameters be $P = \{\Upsilon_1, \Upsilon_2, \Upsilon_3$ and $\Upsilon_4\}$, where Υ_1 = green environment, Υ_2= good looking, Υ_3 = good painting, Υ_4 = good architecture. The IFSS of this model provided in the Table 3.

The non- membership value is calculated by using the following formula.

$$\nu_c(z) = \begin{cases} \dfrac{0.5 * \beta[1-\mu_c(z)]}{\max[\mu_c(z), 1-\mu_c(z)]} & \text{if } \mu_c(z) \geq 0.5 \\ \dfrac{0.5 * \beta[(1-\mu_c(z)]^2}{\min[\mu_c(z), 1-\mu_c(z)]} & \text{if } 0 < \mu_c(z) < 0.5 \\ 1 & \text{if } \mu_c(z) = 0 \end{cases} \tag{6}$$

where β is a dominating fuzzy index and $0 \leq \beta \leq 1$.

Many authors developed the similarity measures between fuzzy sets. See [8–12] for more details.

5.3. Modified intuitionistic fuzzy soft set model

In the context of a project many qualities are desirable. Some of them are technical skill, communication skill, problem solving skill, behavioural competency, inter-personal relationship, leadership skill, total experience, team spirit, organizing capacity, planning skill, decision-making skill, persuasion skill, conflict resolution, influencing skill etc.

In this modified IFSS model, we discuss the similarity measures between IFSSs. The idea of similarity measures between IFSSs has so many applications in computer science including software engineering.

Let $\Gamma_{r_1}(Q,R)$, $\Gamma_{r_2}(Q,R)$ and $\Gamma_{r_3}(Q,R)$ be the various forms of similarity measures between two IFSSs Q and R. They are determined using the formulas given in the Eqs. (7)–(9). The formulas are coined for this model such that values of $\Gamma_{r_1}(Q,R)$, $\Gamma_{r_2}(Q,R)$ and $\Gamma_{r_3}(Q,R)$ lie between 0 and 1.

$$\Gamma_{r_1}(Q,R) = 1 - \sqrt{\frac{\sum_{i=1}^{m}[|\psi_1(i)| + |\psi_2(i)| + |\psi_3(i)|]}{\sum_{i=1}^{m}[|\psi_4(i)| + |\psi_5(i)| + |\psi_6(i)|]}} \tag{7}$$

$$\Gamma_{r_2}(Q,R) = 1 - \frac{1}{2}\sqrt{\sum_{i=1}^{m}\frac{4}{3m}[|\psi_1(i)| + |\psi_2(i)| + |\psi_3(i)|]} \tag{8}$$

$$\Gamma_{r_3}(Q,R) = 1 - \sqrt{\frac{1}{3m}\sum_{i=1}^{m}[|\psi_1(i)| + |\psi_2(i)| + |\psi_7(i)|]} \tag{9}$$

where

$\psi_1(i) = \mu_Q(z_i) - \mu_R(z_i)$,

$\psi_2(i) = \nu_Q(z_i) - \nu_R(z_i)$,

$\psi_3(i) = \pi_Q(z_i) - \pi_R(z_i)$,

$\psi_4(i) = \mu_Q(z_i) + \mu_R(z_i)$,

$\psi_5(i) = \nu_Q(z_i) + \nu_R(z_i)$,

$\psi_6(i) = \pi_Q(z_i) + \pi_R(z_i)$.

$\psi_7(i) = \phi_Q(z_i) - \phi_R(z_i)$

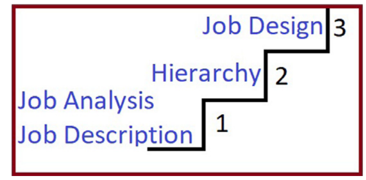

Fig. 1. The 3-step process.

$$\phi_Q(z_i) = \frac{\mu_Q(z_i) + \nu_Q(z_i)}{2}, z_i \in G$$

$$\phi_R(z_i) = \frac{\mu_R(z_i) + \nu_R(z_i)}{2}, z_i \in G$$

and m is the number of attributes.

6. Experiment and results

There are umpteen number of skills that are desirable for the team members. Considering primarily the literature [7,13,14], then the opinions collected from the experts, we have identified four skills as the most important skills needed for the members in a team. These skills are communication skill (CS), technical skill (TS), problem solving skill (PS) and decision-making skill (DM).

They are denoted by $\Upsilon_1, \Upsilon_2, \Upsilon_3$ and Υ_4, respectively. In the experimental case, we consider 10 individuals, $\{\zeta_i\}_{i=1}^{10}$. The intuitionistic fuzzy soft sets are

$(F,E) = \{\{\Upsilon_1\}, \{\Upsilon_2\}, \{\Upsilon_3\}, \{\Upsilon_4\}\}$,

where

$$\Upsilon_1 = \begin{cases} \{\{\zeta_1/(.925,.05), \zeta_2/(.725,.2), \zeta_3/(.95,.03), \zeta_4/(.4725,.45), \zeta_5/(.48,.35), \\ \zeta_6/(.9925,.0075), \zeta_7/(.98,.02), \zeta_8/(.7025,.25), \zeta_9/(.9625,.02), \zeta_{10}/(.7375,.25)\}, \end{cases}$$

$$\Upsilon_2 = \begin{cases} \{\{\zeta_1/(.4375,.45), \zeta_2/(.95,.05), \zeta_3/(.67,.2), \zeta_4/(.975,.025), \zeta_5/(.49,.35), \\ \zeta_6/(.7375,.25), \zeta_7/(.9875,.0125), \zeta_8/(.5,.4), \zeta_9/(.93,.05), \zeta_{10}/(.4925,.41)\}, \end{cases}$$

$$\Upsilon_3 = \begin{cases} \{\{\zeta_1/(.7,.207), \zeta_2/(.9375,.05), \zeta_3/(.4575,.4), \zeta_4/(.735,.25), \zeta_5/(.96,.04), \\ \zeta_6/(.7275,.2), \zeta_7/(.4675,.4), \zeta_8/(.715,.2), \zeta_9/(.445,.4), \zeta_{10}/(.75,.23)\} \end{cases}$$

and

$$\Upsilon_4 = \begin{cases} \{\{\zeta_1/(.4625,.50), \zeta_2/(.95,.04), \zeta_3/(0.715,0.2), \zeta_4/(.99,.01), \zeta_5/(.725,.25), \\ \zeta_6/(.99,.01), \zeta_7/(.735,.2), \zeta_8/(.9375,.05), \zeta_9/(.4725,.42), \zeta_{10}/(.7475,.2)\}. \end{cases}$$

7. Discussion

The model presented is helpful in determining the appropriate selection. These intuitionistic values are computed with the support of other computations. We have followed the fuzzification and de-fuzzification methods scientifically. We had also calculated the indeterministic values from membership and non- membership grades.

The IFSS evaluates the skill of each of the potential candidates. The selection procedure is based on the following criteria: Communication skill (CS), Technical skill (TS), Problem solving capacity (PC), Decision making skill (DM). The minimum requirements (weights) for CS is (GD), TS is (VG), PS is (GD), DM is (GD). If any of the candidates do not satisfy the minimum requirements, the selectors will not assign the candidate in labour pool.

The management has decided to fix the fuzzy membership value for each category as PR $\in [0, 0.25]$, FR $\in [0.25, 0.5]$, GD $\in [0.5, 0.75]$ and VG $\in [0.75, 1.0]$. i. e., $0 \leq PR \leq 0.25$, $0.25 \leq FR \leq 0.5$, $0.5 \leq GD \leq 0.75$ and $0.75 \leq VG \leq 1$ (Fig. 2). The width of each class interval is 0.25. The upper bound of each category lies in the prefix or postfix category. The selectors also give the weightage of each category as: CS - 0.2, TS - 0.5, PS - 0.2, DM - 0.1 such that the sum of all the weightages is 1. A selection is considered as 1 and non-selection is 0. Hence, CS, TS, PS and DM are the components of selection that constitutes 1.

Table 4
The values of $\psi_1(i)$, $\psi_2(i)$, $\psi_3(i)$, $\psi_4(i)$ and $\psi_5(i)$ of project team selection.

ζ_n	ζ_1	ζ_2	ζ_3	ζ_4	ζ_5	ζ_6	ζ_7	ζ_8	ζ_9	ζ_{10}
Υ_1	.075	.275	.05	.5275	.52	.007	.02	.2975	.0375	.2625
Υ_2	.5625	.05	.33	.025	.51	.2625	.0125	.5	.07	.5075
Υ_3	.3	.0625	.5425	.265	.04	.5325	.2725	.285	.555	.25
Υ_4	.5375	.05	.285	.01	.275	.01	.265	.0625	.5275	.2525
						$\mid \psi_1(i) \mid$				
Υ_1	.05	.2	.03	.45	.35	.0075	.02	.25	.02	.25
Υ_2	.45	.05	.2	.025	.35	.01	.0125	.4	.05	.41
Υ_3	.207	.05	.4	.25	.04	.2	.4	.2	.4	.23
Υ_4	.50	.04	.2	. 01	.25	.01	.2	. 05	.42	.2
						$\mid \psi_2(i) \mid$				
Υ_1	.025	.075	.02	.0775	.17	0	0	.0475	.0175	.0125
Υ_2	.1125	.05	.31	0	.16	.0125	0	.1	.02	.0975
Υ_3	.093	. 0125	.1425	.015	0	.0725	.1325	.085	.155	.02
Υ_4	.0375	.01	.085	0	.075	0	.065	.0125	.1075	.0525
						$\mid \psi_3(i) \mid$				
Υ_1	1.925	1.725	1.95	1.4725	1.48	1.9925	1.98	1.7025	1.9625	1.7375
Υ_2	1.4375	1.95	1.67	1.975	1.49	1.7375	1.9875	1.5	1.93	1.4925
Υ_3	1.7	1.9375	1.4575	1.735	1.96	1.7275	1.4675	1.715	1.445	1.75
Υ_4	1.4625	1.95	1.715	1.99	1.725	1.99	1.735	1.9375	1.4725	1.7475
						$\mid \psi_4(i) \mid$				
Υ_1	.05	.2	.03	.45	.35	.0075	.02	.25	.02	.25
Υ_2	.45	.05	.2	.025	.35	.25	.0125	.4	.05	.41
Υ_3	.207	. 05	.4	.25	.04	.2	.4	.2	.4	.23
Υ_4	.50	.04	.2	.01	.25	.01	.2	.05	.42	.2
						$\mid \psi_5(i) \mid$				

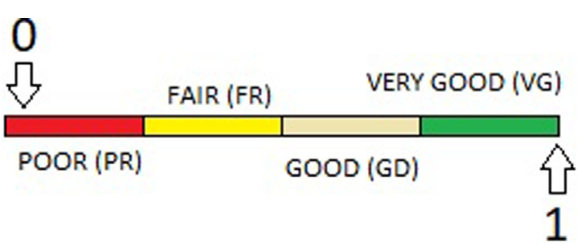

Fig. 2. Scale of evaluation.

Table 5
$\phi_Q(z_i)$ values of IFSS.

Employees ζ_n	Υ_1	Υ_2	Υ_3	Υ_4
ζ_1	0.4875	0.44375	0.4535	0.48125)
ζ_2	0.4625	0.5	0.49375	0.495
ζ_3	0.49	0.435	0.42875	0.4575
ζ_4	0.46125	0.5	0.4925	0.5
ζ_5	0.415	0.42	0.5	0.4875
ζ_6	0.5	0.49375	0.46375	0.5
ζ_7	0.5	0.5	0.43375	0.4675
ζ_8	0.47625	0.45	0.4575	0.49375
ζ_9	0.49125	0.49	0.4225	0.44625
ζ_{10}	0.49375	0.45125	0.49	0.47375

Table 6
$\mid \psi_7(i) \mid$ values of IFSS.

Employees ζ_n	Υ_1	Υ_2	Υ_3	Υ_4
ζ_1	0.0125	0.05625	0.0465	0.01875)
ζ_2	0.0375	0	0..00625	0.005
ζ_3	0.01	0.065	0.07125	0.0425
ζ_4	0.03875	0	0.0075	0
ζ_5	0.085	0.08	0	0.0125
ζ_6	0	0.00625	0.03625	0
ζ_7	0	0	0.06625	0.0325
ζ_8	0.02375	0.05	0.0425	0.00625
ζ_9	0.00875	0.01	0.0775	0.05375
ζ_{10}	0.00625	0.04875	0.01	0.02625

Table 7
Optimum selection for project team.

H	$\Gamma_{r_1}(Super, \zeta_i)$	$\Gamma_{r_2}(Super, \zeta_i)$	$\Gamma_{r_3}(Super, \zeta_i)$	Flag
ζ_1	0.3927	0.5042	0.5156	0
ζ_2	0.6692	0.7300	0.7376	1
ζ_3	0.4505	0.5514	0.5692	0
ζ_4	0.5455	0.6286	0.6338	1
ζ_5	0.4201	0.5265	0.5424	0
ζ_6	0.7250	0.7755	0.7816	1
ζ_7	0.6000	0.6734	0.6836	1
ζ_8	0.4649	0.5631	0.5750	0
ζ_9	0.4545	0.5546	0.5689	0
ζ_{10}	0.4359	0.5395	0.5487	0

It is to be noted that $\psi_1(i)$ is the difference of the membership values and $\psi_4(i)$ is the sum of the membership values. Further, $\psi_2(i)$ and $\psi_5(i)$ are respectively the difference and sum of the non-membership values. The difference and sum of the indeterministic values are $\psi_3(i)$ and $\psi_6(i)$, respectively. The values of $\psi_1(i)$, $\psi_2(i)$, $\psi_3(i)$, $\psi_4(i)$ and $\psi_5(i)$ are provided in the Table 4.

They are computed using the formula given in Section 5.3. Since the values of indeterminate terms are close to zero, their difference and sum are also close to zero. We have used both the values for computing the rank.

Table 5 consists of the values of $\phi_Q(z_i)$ which is the average of the membership and non-membership values. A intuitionistic fuzzy set is said be be superintuitionistic fuzzy set if the membership value is 1 and non-membership value is 0. It is the perfect state. Crisp sets are super intutionistic fuzzy sets. Since R is taken as the superintutionistic set $(1, 0)$ which is the most ideal situation, $\phi_R(z_i)$ would be consisting of the average of the crisp values 1 and 0. i. e., 0.5.

For the final team selection, we set a minimum value for the parameters Γ_{r_1}, Γ_{r_2} and Γ_{r_3} as 0.5. The minimum requirement is set as a cut-off so that the selection presupposes a minimum quality. This minimum requirement could be changed from situation to situation. These three parameters and the condition we had set, have substantial impact on the project team selection. From the ten candidates only four candidates qualify. They are ζ_2, ζ_4, ζ_6 and ζ_7. They are flagged 1 and others are flagged 0. See Table 7 for details. They are selected in the order ζ_6, ζ_2, ζ_7 and ζ_4 considering their average scores. When we take average scores, ζ_3, ζ_8, ζ_9 and ζ_{10} also have scores above 0.5. However, since we had taken the minimum value for each parameter as 0.5, they are not qualified. This helps us to select the best teams excelling in each of the desirable qualities.

7.1. Sensitivity analysis

A very important point to note is that all the four parameters are inconsistent. This inconsistency brings more fuzziness. In the test explained, the cut-off decided is 0.5. However, instead of keeping the cut-off for each of the parameters, if we keep it for the average score, except ζ_1 and ζ_5, everyone will find a place in the team. Nevertheless, if we consider the real quality of the people, lowest value of all the selected candidates is 0.602. The other three got the scores 0.7607, 0.7123 and 0.6523, respectively. The maximum difference between the consecutive levels of these top-rank holders is 0.0599. But the difference of the scores of the fourth and the fifth rank holders is 0.683. This is comparatively large. Hence, the decision to take individual minimum is justified.

It is also interesting to note that none of the rank holders from 5 to 10 excels the top rank holders in any of the categories. If a team is requiring a member with a desirable quality in particular needs, based on this evaluation, further training can be given. If it is done, several members could be enhanced in their skills and more teams can be formed. In case, if there are emergency vacancies in teams, those trained personnels could be made use of.

The membership and non-membership values have been very close in many cases. Hence, the indeterminate value became negligible. This is not an ideal situation as in the superintutionistic fuzzy set, the ideal difference of membership and non-membership is always 1 and the indeterminate part is 0. In the problem considered, both the tables of $\psi_3(i)$ and $\psi_6(i)$ are the same.

If the membership value is 0 and the non-membership value is 1, then the intuitionistic fuzzy set is null-intutionistic fuzzy set. In such a case, we can take the similarity measure between the original set and the null-intutionistic fuzzy set (0, 1). This makes the optimization table (Table 7) with fuzzy complement values. In such a case, instead of the maximum of the averages, we can take the minimum of the averages and we get the same result.

8. Conclusion

Fuzzy set theory had contributed extensively to the optimization problems ever since it came into existence. There is no realm in the human endeavour, where fuzzy theories cannot be applied. We presented here a model of team selection based on the intutionistic fuzzy set theory. We compared the similarity measures and hence we named it as modified method. This method provides relative consistency in decision-making regarding the team selection for the project management. Although the experiment is done for only 10 candidates, it could be extended to quite large values. Moreover, we had considered only four skills in the process of selecting team members. With the support of efficient computers, more variables can be included. Further, depending on the type of team, skills could be changed. The more the skills are qualitative, the more is the difficulty in getting a convincing decision. The selection process could be extended to other types of team selection with sub-teams, vendor-selection, service provider selection for institutions etc.

References

[1] Krassimir T. Atanassov, Intuitionistic fuzzy sets, Fuzzy Sets and Systems 20 (1) (1986) 87–96, doi:10.1016/S0165-0114(86)80034-3.
[2] Shyi-Ming Chen, A new approach to handling fuzzy decision-making problems, IEEE Transactions on Systems, Man, and Cybernetics 18 (6) (1988) 1012–1016, doi:10.1109/21.23100.
[3] Li Dengfeng, Cheng Chuntian, New similarity measures of intuitionistic fuzzy sets and application to pattern recognitions, Pattern Recognition Letters 23 (1–3) (2002) 221–225, doi:10.1016/S0167-8655(01)00110-6.
[4] Pabitra Kumar Maji, Ranjit Biswas, A Ranjan Roy, Fuzzy soft sets, Journal of Fuzzy Mathematics 9 (3) (2001) 589–602.
[5] Pabitra Kumar Maji, Ranjit Biswas, A Ranjan Roy, Intuitionistic fuzzy soft sets, Journal of Fuzzy Mathematics 9 (3) (2001) 677–692.
[6] D. Molodtsov, Soft set theory—First results, Computers & Mathematics with Applications 37 (1999) 19–31, doi:10.1016/S0898-1221(99)00056-5.
[7] Sebastian Nokes, The Definitive Guide to Project Management: The fast track to getting the job done on time and on budget, 2nd, Prentice Hall, London, 2007.
[8] Sunny Joseph Kalayathankal, G. Suresh Singh, P. B. Vinodkumar, Ordered intuitionistic fuzzy soft sets, Journal of Fuzzy Mathematics 18 (4) (2010) 991–998.
[9] Sunny Joseph Kalayathankal, G. Suresh Singh, P. B. Vinodkumar, S. Joseph, J. Thomas, Ordered intuitionistic fuzzy soft model of flood alarm, Iranian Journal of Fuzzy Systems 8 (1) (2011) 29–39.
[10] Sunny Joseph Kalayathankal, John T. Abraham, A fuzzy decision making approach to SLCM selection, International Journal of Civil Engineering and Technology 8 (6) (2017) 178–185.
[11] Sunny Joseph Kalayathankal, John T. Abraham, A fuzzy soft software lifecycle model, International Journal of Civil Engineering and Technology 8 (8) (2017) 755–761.
[12] Sunny Joseph Kalayathankal, John T. Abraham, Joseph Varghese Kureethara, A modified fuzzy similarity measure decision making approach to SLCM selection, International Journal of Computer Science and Engineering 5 (9) (2017) 32–39.
[13] Y. Ilker Topcu, A decision model proposal for construction contractor selection in Turkey, Building and Environment 39 (4) (2004) 469–481, doi:10.1016/j.buildenv.2003.09.009.
[14] Shamshul Bahar Yaakob, Shigeo Kawata, Workers' placement in an industrial environment, Fuzzy Sets and Systems 106 (3) (1999) 289–297, doi:10.1016/S0165-0114(97)00274-1.
[15] Zeshui Xu, Some similarity measures of intuitionistic fuzzy sets and their applications to multiple attribute decision making, Fuzzy Optimization and Decision Making 6 (June) (2007) 109–121, doi:10.1007/s10700-007-9004-z.
[16] L. A. Zadeh, Fuzzy sets, Information and Control 8 (3) (1965) 338–353, doi:10.1016/S0019-9958(65)90241-X.
[17] Jon R. Katzenbach, Douglas K. Smith, The Discipline of Teams, Harvard Business Review (March–April) (1993) 111–120.
[18] Adil Baykasoglu, Turkay Dereli, Sena Das, Project team selection using fuzzy optimization approach, Cybernetics and Systems 38 (2) (2007) 155–185, doi:10.1080/01969720601139041.

A new auditory algorithm in stock market prediction on oil and gas sector in Nigerian stock exchange

Biraja Nayak, *Department of Computer Scinece Engineering , Capital Engineering College, Bhubaneswar, birajanayak21@gmail.com*

Prakash Dehury, *Department of Computer Sciencel Engineering, Aryan Institute of Engineering & Technology, Bhubaneswar, prakashdehury1@hotmail.com*

Prasanna Kumar Chhotaray, *Department of Computer Scinece Engineering , NM Institute of Engineering & Technology, Bhubaneswar, pkchhotaray85@gmail.com*

Soumya Mishra, *Department of Electronics and Communication Engineering , Raajdhani Engineering College, Bhubaneswar, soumyamishra96@gmail.com*

A R T I C L E I N F O

Keywords:
Auditory algorithm
Geometric Brownian motion
Stochastic process
Machine learning
Support vector machine

A B S T R A C T

Stock market prediction is the process of forecasting future prices of stocks. Stock market prediction is a challenging process as a result of uncertainties that influence the market change of price. This paper proposes a nature-inspired algorithm, called Auditory Algorithm (AA), which follows the pathway of the auditory system like that of the human ear. The performance of AA is compared with that of high performance machine learning algorithms and continuous-time stochastic process. The machine learning algorithms used in this paper are Logistic Regression (LR), Support Vector Machine (SVM), Feed forward neural network (FFN) and Recurrent Neural Network (RNN) while continuous-time models such as Stochastic Differential Equation (SDE) and Geometric Brownian Motion (GBM) are also used. The results show that the overall performance of AA is superior to that of other algorithms compared in this paper, as it drastically reduced the forecast error to the barest minimum.

1. Introduction

Stock market prediction is a very difficult task due to different uncertainties that influence the market price which includes political events, economic, investor sentiment [1–6]. This was due to stock market price fluctuations which resulted in random fluctuation. The stock market in nature is dynamic and noisy [7]. To predict the stock exchange, advanced knowledge of the stocks is mandatory. Investors prefer to buy stock whose price increase in future, and refrain from stock whose value decline over time in future. However, it is important to develop a robust stock market algorithm that can predict the stock behavior accurately to maximize gain and minimize the loss of the investor.

Moreover, the stock market is vulnerable to different factors which influence its fluctuation in the exchange market. Incomplete information about stock market data is also a challenge to forecast the stock future price. Investors in stock rely on different technical indicators to predict the stock price movement. Although these indicators are used to assess the stock, it is difficult to predict market trends. Factors such as economic and non-economic influence the behavior of the stock trends [15]. The stock market prediction is therefore seen as a significant challenge to the growth of production. To address this issue, we propose an Auditory Algorithm to predict accurately the stock market behavior.

This paper focuses on Auditory Algorithm (AA) for stock market prediction. The researchers considered six popular algorithms that have been used for stock market prediction which are machine learning and continuous-time stochastic processes and then compared their performance with that of AA. We considered six algorithms and these are Logistic Regression, Support Vector Machine, Feed Forward Neural Network, Recurrent Neural Network, Geometric Brownian Motion and Stochastic Differential Equation. The summary of contributions of this work include:

- A novel AA algorithm that has the capacity to accurately predict the stock market prices to yield high significant financial profit for the investors was presented.
- The ability to detect exponential decay of the stock market which is one of the advantages of adopting AA for stock market prediction was eloquently demonstrated through experimental results in this paper. Stock market prediction is of great interest to investors, AA will enable investors to determine the stock that will yield high value.
- Study of how exponential decay will help the investor to know when the stock is stable, upward and downward trend.

- An analysis of how the exponential growth obtained from the AA will enable the investor to determine the growth of the stock market prices as presented.
- Analysis of the statistical differences of all the seven algorithms using the Friedman test and post hoc analysis using a Wilcoxon test was performed.

The rest of this paper is organized as follows: Section 2 discusses the related work in the field of stock market prediction. The proposed methodology used in this work is explained in Section 4. The results and the discussion of the results are presented in Section 5 and Section 6 is the conclusion of the paper.

2. Related work

This section briefly discussed the recent researches done in the field of stock market prediction. The stochastic process was developed by Bachelier [17] who developed the first model of stock prediction by utilizing it to predict future price and options. In a paper by Antwi [19], the author studied the price behavior of the Ghana Stock Exchange by utilizing geometric Brownian motion. After comparing the actual price with forecast prices, their model predicted stock behavior in more than 80% of the cases as shown in their findings.

Recently, machine learning models were developed to overcome drawback of continuous-time models. The authors in [21, 24] utilized time series and technical indicators to predict stock market. They observed that combining technical indicator with their probabilistic model makes the uncertainty in stock price to reduce. Giacomelet al. [13] proposed an ensemble neural network that predicts if one stock is going to rise or fall. Oyewolaet al. [14] in their paper utilized logistic regression, random forest, support vector machine, and neural network for stock market prediction. They also used an ensemble of three different machine learning algorithms to predict stock market prices and showed that when the random forest is at the top layer the algorithms perform better than other algorithms. However, [8] in their paper used recurrent neural network and back propagation network to predict stock prices. They observed that their model achieved better prediction results compared to existing techniques. A computational efficient functional link artificial neural network (CEFLANN) proposed by [16] produces a continuous trading signal within the range of 0 and 1 by integrating technical indicators with CEFLANN. They compared the performance of their results with Support vector machine, naïve Bayesian model, K nearest neighbor model and Decision Tree. The result shows that the proposed model provides superior profit compared to other selected machine learning algorithms.

Chen and Fang [16] in their work utilized Artificial Neural Network, Generalized Auto-Regressive Conditional Heteroskescatic and Random walk models in predicting Asian Currency Unit. They observed that Artificial Neural Network outperform others which are GARCH and random walk models. The deep learning network for stock market analysis was presented by [9]. The authors developed a method to extract features from data and also study the effects of unsupervised feature extraction such as Boltzmann machine, auto-encoder and principal component analysis on the Korean stock market. It was found that a deep neural network with three-layer performed better than the autoregressive model.

Recently, a hybrid model has been developed for stock market prediction. Shipra, Khan and Mohammad Anwer [18] utilized rough set model, neural network and hybrid neural network for buy and sell off stock in Dhaka stock exchange. Their results indicated that their proposed model performs effectively than other model used in the paper. Oussama and Mohamed [10] presented a hierarchical deep neural network with 75 stocks of Tunisian stock exchange for 5 min returns. Their study shows an accuracy of 71%.

3. Auditory system

Hearing involves a step by step process that converts sound waves that pass through the medium (air) into an electrical signal [20]. The auditory nerves are responsible to transfer the signals receives from the cochlea to the brain. There are three major parts of an ear which consists of:

1 The outer ear
2 The middle ear
3 The inner ear
4 ***The outer ear***

The outer ear has two parts which consist of the ear canal and the pinna. Sound waves pass through the pinna then to the ear canal. The outside ear is called the pinna which is at the side of the head which was made of cartilage. The sound waves pass through a passage called the ear canal. The pinna is responsible to collect sound to the ear canal [11].

1 ***The middle ear***

Sound waves pass through the eardrum which causes it to vibrate and transfer the vibration to malleus, incus and stapes. The three bones which consist of the malleus, incus and stapes increase the sound vibration from the eardrum and transfer it to the cochlea [22]. The cochlea is in the form of a spiral structure filled with fluid.

1 ***The inner ear***

The cochlea is in the form of a spiral structure filled with fluid. The cochlea is split into an elastic partition that runs from the upper and lower part called the basilar membrane. The hair cells beside the cochlea detect a high-pitched sound [12]. Movement of the hair cells will cause the stereocilia to open up and the chemicals rush into the cells which create an electrical signal. The auditory nerves are responsible to carry the electrical signal to the brain, which changes it into the sound we recognize.

3.1. Proposed auditory algorithm (AA)

The auditory algorithm takes inspiration from the auditory process. In this algorithm, the sound waves that pass through the pinna are represented as Pinna. The sound waves are represented as follows:

$$\text{Pinna} = [x_1,\ x_2,\ x_3, \ldots, x_n] \tag{1}$$

The sound waves $(x_1,\ x_2, \ldots, x_n)$ passes through the pinna to the narrow part called the ear canal. From the ear canal, it transfers the sound waves to the eardrum and then vibrates. The vibrating eardrum equations are given as the wave equation with zero boundary condition

$$\frac{\partial^2 u}{\partial x^2} = \frac{1}{c^2} \times \frac{\partial^2 u}{\partial t^2} \tag{2}$$

Eq. (2) has a solution $u = f(x,t)$ which can be written as $u(x,t)$
Assuming $u(x,t) = X(x)T(t)$
Where $X(x)$ is a function of x and $T(t)$ is a function of t
Let $u = XT$

$$\frac{\partial u}{\partial x} = X'T \text{ and } \frac{\partial^2 u}{\partial x^2} = X''T \tag{3}$$

Then

$$\frac{\partial u}{\partial t} = XT' \text{ and } \frac{\partial^2 u}{\partial t^2} = XT'' \tag{4}$$

Substitute Eqs. (3) and (4) to Eq. (1)

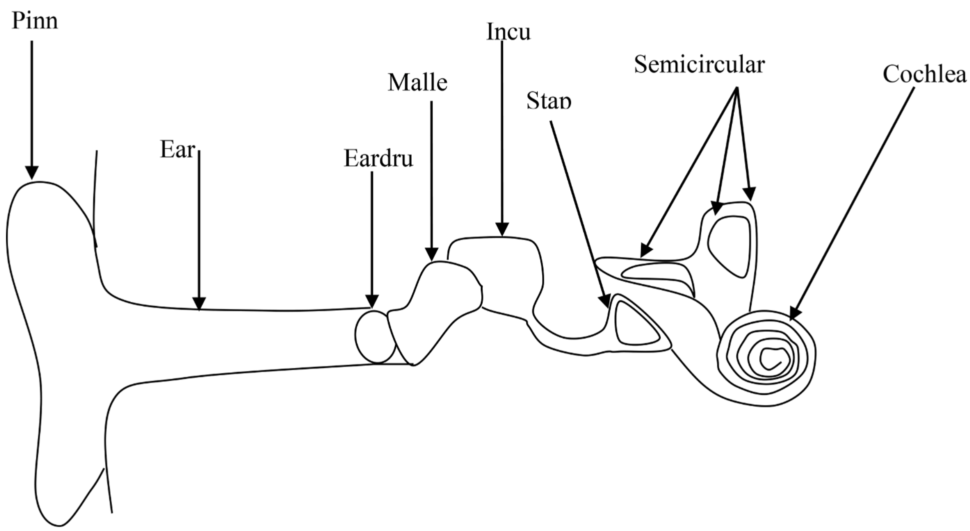

Fig. 1. Auditory System

$$X''T = \frac{1}{c^2}XT'' \tag{5}$$

Divide Eq. (5) by XT we have

$$\frac{X''}{X} = \frac{1}{c^2}\frac{T''}{T} \tag{6}$$

We assume Eq. (6) $=\varphi$ that is $\varphi > 0$. Then Eq. (6) becomes

$$\frac{X''}{X} = \frac{1}{c^2}\frac{T''}{T} = \varphi \tag{7}$$

Eq. (7) can be separated in this form

$$\frac{X''}{X} = \varphi \text{ and } \frac{1}{c^2}\frac{T''}{T} = \varphi$$

$$\therefore X'' - X\varphi = 0 \text{ and } T'' - c^2\varphi T = 0$$

Let $\varphi = r^2$
The auxiliary equation of $X'' - X\varphi = 0$ is given as

$$m^2 - r^2 = 0$$

$$\therefore m = \pm r$$

$$X = Ae^{rx} + Be^{-rx} \tag{8}$$

For the second equation

$$T'' - c^2\varphi T = 0$$

Let $\varphi = r^2$
The auxiliary equation of $T'' - c^2\varphi T = 0$ is given as

$$m^2 - c^2r^2 = 0$$

$$\therefore m = \pm cr$$

$$T = Ae^{crt} + Be^{-crt} \tag{9}$$

Recall that we let $u = XT$
Substitute Eqs. (7) and (8) to $u = XT$

$$\therefore u(x,t) = (Ae^{rx} + Be^{-rx})(Ae^{crt} + Be^{-crt})$$

Assuming $A = B = 1$ and $t = 0$, we have

$$u(x,0) = e^{rx} + e^{-rx}$$

The general equation of the vibration of the eardrum is given as

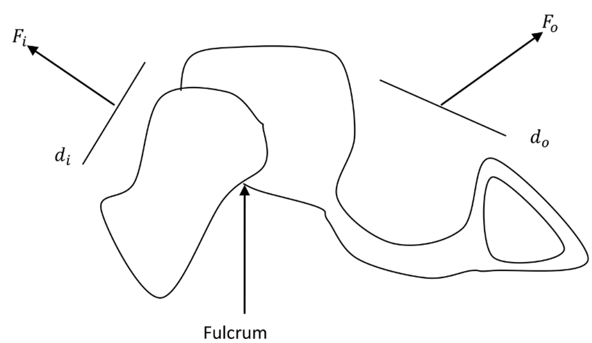

Fig. 2. Malleus, Incus and Stapes

$$u(x_i,0) = e^{rx_i} + e^{-rx_i} \text{ where } i = 1,2,3,\ldots \tag{10}$$

$x = soundwaves$ and $r = exponentialgrowthordecay$
The result obtained from the vibration of eardrum given as $u(x_i,0)$ will then be transferred to the middle ear which consists of the three bones malleus, incus and stapes. The diagrammatical representation of the three bones is in Fig. 2

Fig. 2 consists of the three bones in the middle ear. The diagram represents a first class lever with the fulcrum at the center. Where F_i is the input force exerted by the vibration of the sound waves, d_i is input distance of the sound waves at input i given as the sound waves vibration $u(x_i,0)$. F_o is the output force exerted by the sound waves and the d_o is the output distance of the sound waves.

Fig. 1, Fig. 12, Fig. 8, Fig. 8.

The first class lever equation of malleus, incus and stapes is given as

$$F_id_i = F_od_o \tag{11}$$

$$d_i = u(x_i,0),\ d_o = u(x_o,0)$$

$$\therefore u(x_o,0) = \frac{u(x_i,0)F_i}{F_o} \tag{12}$$

The Eq. (12) is the output distance of the vibration of the sound waves which transfer it to the cochlea. The cochlea is in the form of the Archimedean spiral. The Archimedean equation is given as:

$$u(r_o,0) = u(x_o,0)a \text{ where } a \text{ is constant.} \tag{13}$$

substitute Eq. (12) to (13) we have

$$u(r_o,0) = \frac{u(x_i,0)aF_i}{F_o} \quad (14)$$

The auditory nerves then carry $u(r_o,0)$ to the brain which changes it to sound we recognize.

4. Methodology

We test the performance of the proposed Auditory Algorithm (AA) on five stock market obtained from the Nigerian Stock Exchange (NSE). On the performance of the proposed algorithm with other machine learning, we consider four machine learning and two continuous-time models:

- Logistic Regression (LR): Logistic regression is a technique used to analyze data with one dependent variable and one or more independent variable. LR measures the relationship between the categorical dependent variable and one or more independent variables by estimating probabilities using a logistic function [23, 25]. It models the probability of an event.

  The LR equation is given as:

  $$P(C_t = 1) = \frac{1}{1 + e^{-(w \times C_t + b)}} \quad (15)$$

  Where $P(C_t = 1)$ is interpreted as the probability of the dependent variable equating a success, e denotes the exponential function,C_t is the closing price at time t, w is the weight and b is the bias

- Support Vector Machine (SVM): Support vector machine is a regression predictive tool which uses a hyperplane to separate classes [26–28]. The kernel function used in SVM is to indicate a weight function for a weighted sum.

  The SVM equation is given as:

  $$W \times C_t + b = 0 \quad (16)$$

  Where W is the weight vector and b is the bias

- Feed Forward Neural Network (FNN): Feed Forward neural network consists of input, hidden and output layer. The input layer is responsible to receive data while acts as an intermediate layer which separates the input layer from the output layer [29, 30]. The output layer gives the result of the data sent to the input layer. FFN is called feed forward neural network due to its capability to move from one layer to the other layers. It moves forward from input to hidden and to the output layer.

  The FNN equation is given as:

  $$y_j = f\left(u_j^1\right) = f\left(\sum_{i=1}^{N} w_{ij}\vartheta_i\right) \quad (17)$$

  Where $\vartheta_i = f(u_i) = f(\sum_{t=0}^{K} w_{ti}C_t)$, ϑ_i is the hidden layer at i hidden neuron,$f(u_i)$ is the activation function and y_j is the output value.

- Recurrent Neural Network (RNN): RNN is different from feed forward neural network in the sense that it has the capability to travels both forward and backward in the network. RNN consists of all loops which allow information to pass from one network to the next network. It has multiple copies of the same network and passes the information to the inheritor [31].

Table I
Oil and Gas Sector in Nigerian Stock Exchange (NSE).

S/ No.	Company	Symbol	Date Listed	Date of Incorporation
1.	ANINO INTERNATIONAL PLC.	ANINO	January 2nd 1990	June 3rd 1981
2.	CAPITAL OIL PLC.	CAPOIL	Invalid date	August 29th 1985
3.	CONOIL PLC.	CONOIL	Invalid date	June 30th 1970
4.	CAVERTON OFFSHORE SUPPORT GROUP	CAVERTON	February 6th 2014	June 2nd 2008
5.	ETERNA PLC.	ETERNA	Invalid date	January 13th 1989
6.	JAPAUL OIL & MARITIME SERVICE PLC	JAPAULOIL	August 10th 2005	June 29th 1994
7.	MRS OIL NIGERIA PLC.	MRS	Invalid date	August 12th 1969
8.	OANDO PLC.	OANDO	February 24th 1992	August 12th 1969
9.	RAK UNITY PET. COMP. PLC.	RAKUNITY	Invalid date	December 20th 1982
10.	SEPLAT PETROLEUM DEVELOPMENT COMP. PLC.	SEPLAT	Invalid date	June 17th 2009
11.	TOTAL NIGERIA PLC.	TOTAL	Invalid date	January 6th 1956
12.	11 PLC.	MOBIL	July 25th 1991	December 31st 1951
13.	FORTE OIL	FO	Invalid date	1964

  The RNN equation is given as:

  $$Y_t = f_n\left(W_{dy}d_t + b_y\right) \quad (18)$$

  Where $d_t = f_n(W_{cd}C_t + W_{dd}d_{t-1} + b_d)$, d_t is the hidden layer at t instant,f_n is the activation function,W_{cd} is the input to the hidden layer, b_d is the bias of the input layer,W_{dy} is the weight of the output layer and b_y is the bias of the output layer.

- Stochastic Differential Equations (SDE):- SDE is an equation in which coefficients are random functions or stochastic process of the independent variables [32]. The equation can be used in various phenomena like stock price or physical systems.

  The equation is given as:

  $$dC_t = F(t, C_t)dt + G(t, C_t)dW_t \quad (19)$$

  Where C_t closing price to stimulate at time t, F is the drift rate function, G is the diffusion rate function, W_tBrownian motion or wiener process.

- Geometric Brownian Motion (GBM):- GBM is a stochastic process in which the varying quantity follows a Brownian motion. It has a constant called drift, volatility and wiener process or Brownian motion [33].

  $$dC_t = \mu C_t dt + \sigma C_t dW_t \quad (20)$$

Where μ is the mean of closing price at time t or drift rate, σ is the volatility and dW_t is the Brownian motion.

Stock data used in this paper was extracted from the Nigerian Stock Exchange (NSE). The oil and gas sector was extracted from it which consists of Stocks which has been in existence before Nigeria's independence and after the independence. The table I is the oil and gas sector company selected in this paper which started operation in Nigeria. The date listed on Nigeria stock market and the date of incorporation is

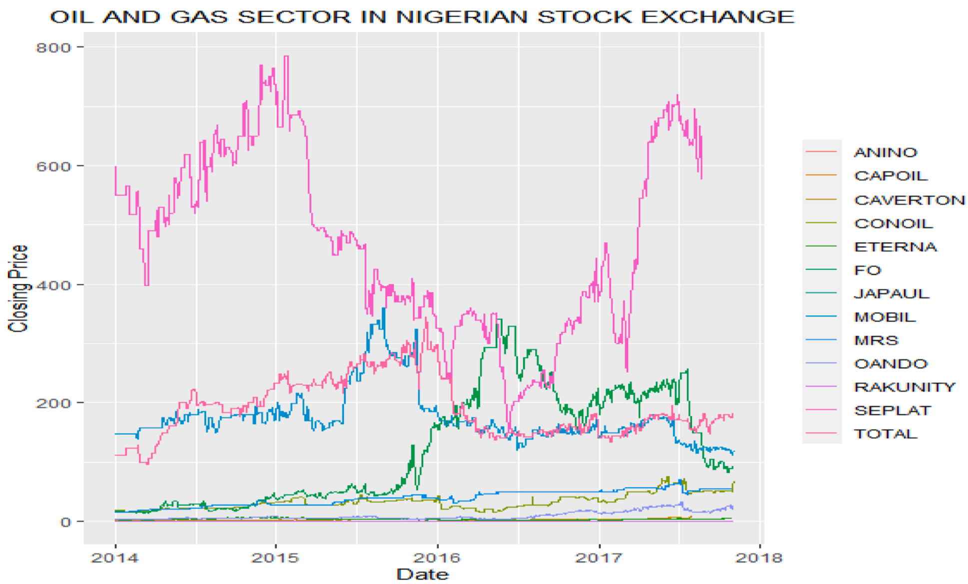

Fig. 3. The closing price of Oil and Gas Sector in Nigerian Stock Exchange.

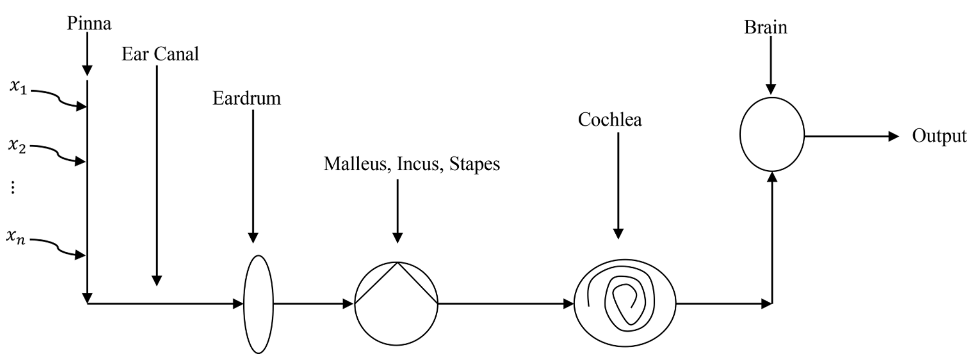

Fig. 4. Schematic diagram of Auditory Algorithm.

included.

Table I displayed the 13 major stocks in oil and gas sector, ANINO, CAPOIL, CONOIL, CAVERTON, ETERNA, JAPAULOIL, MRS, OANDO, RAKUNITY, SEPLAT, TOTAL, MOBIL and FO are selected to predict the stock price using six selected model and the proposed model. We considered the daily closing price, from 1 January 2014 to 31 December 2019 and three technical indicators. Time series plot for the thirteen selected stocks is shown in Fig. 3. Fig. 3 indicated that SEPLAT and MOBIL oil was rated high than TOTAL, FO and CONOIL.

Fig. 4 is the proposed Schematic diagram of Auditory Algorithm which consists of sound waves $(x_1, x_2, \ldots, x_n)$. In this paper, the sound waves are the oil and gas sectors of the Nigerian Stock Exchange while n is the trading days of the closing price of the selected five stock market. The sound waves $(x_1, x_2, \ldots, x_n)$ enters through the ear canal to the eardrum using Eq. (10) then to the malleus, incus and stapes as in Eq. (12) for balance. The cochlea is in form of a spiral as shown in Fig. 4 which utilized Eq. (13) and the output of the electrical signal of the sound waves is obtained from the brain.

Substitute Eq. (10) to Eq. (13)

$$u(r_o, 0) = \frac{(e^{rx} + e^{-rx})aF_i}{F_o} \tag{21}$$

We assume $rx = \log\left(C_t - \frac{\beta\gamma}{SMA}\right)$, since exponential growth of the stock depends on the stock price and output, input exerted force, a, r is the unit values. Where C_t is the closing price of the stock at time t, $\beta = \max(C_t) + \min(C_t)$, $\gamma = 0.01$ and SMA is the simple moving average.

$$u(r_o, 0) = \frac{\left(e^{\log\left(C_t - \frac{\beta\gamma}{SMA}\right)} + e^{-\log\left(C_t - \frac{\beta\gamma}{SMA}\right)}\right)aF_i}{F_o} \tag{22}$$

The input force F_i and the output force F_o of the eardrum is used to balance the sound waves while the parameter a is to control the exponential growth of the stock given as $e^{\log\left(C_t - \frac{\beta\gamma}{SMA}\right)}$ and exponential decay of the stock given as $e^{-\log\left(C_t - \frac{\beta\gamma}{SMA}\right)}$.

$$y_s = \frac{\left(a_1 e^{\log\left(C_t - \frac{\beta\gamma}{SMA}\right)} + a_2 e^{-\log\left(C_t - \frac{\beta\gamma}{SMA}\right)}\right)F_i}{F_o} \tag{23}$$

replacing $u(r_o, 0)$ with y_s

Where y_s is the output of the sound waves, F_i is the inputforce of the stock, F_o is the output force of the stock,a_1 parameter control the exponential growth of the stock and a_2 parameter controls the exponential decay of the stock.

Technical Indicator

The different researcher has utilized various ways of determining when to buy and sell in the stock market. In this paper, we will utilize four technical indicators:

Table II
Descriptive statistics of Oil and Gas Sector.

Descriptive Statistics	Minimum	1st Quartile	Median	Mean	3rd Quartile	Maximum	Standard Deviation
ANINO	0.2100	0.2400	0.2500	0.2427	0.2500	0.2500	0.0142
CAPOIL	0.2000	0.3300	0.5000	0.4299	0.5000	0.5000	0.1170
CAVERTON	0.6400	1.4030	2.2500	2.4010	3.0000	9.5000	1.3194
CONOIL	15.15	23.0000	31.8000	32.97	39.30	75.73	12.2336
ETERNA	1.4500	2.7500	3.4450	3.6310	4.2150	7.2600	1.3284
FO	14.00	38.6700	90.1600	123.00	209.00	342.00	95.31
JAPAUL	0.2000	0.3900	0.5000	0.4404	0.5000	0.9700	0.1264
MOBIL	111.7	150.0	165.0	175.3	180.0	360.0	45.24
MRS	15.30	28.35	39.03	39.40	50.54	70.00	12.70
OANDO	2.970	4.950	5.990	9.627	14.15	33.47	6.8378
RAKUNITY	0.3000	0.3100	0.3100	0.3849	0.5000	0.5000	0.0870
SEPLAT	151.7	345.0	465.0	469.9	619.0	785.0	154.3
TOTAL	96.50	152.0	180.0	190.6	230.0	345.0	49.30

- Relative Strength Index (RSI): RSI is a momentum used in the financial market to determine if a price change of the stock is over-bought or oversold in the stock market [34].

RSI can be expressed as:

$$RSI = 100 - \frac{100}{1 + \frac{\sum_{i=1}^{n} U_p}{\sum_{i=1}^{n} D_w}} \tag{24}$$

Where U_p is the upward closing price and D_w is the downward closing price

- Moving Average Convergence Divergence (MACD): MACD was developed to reveal direction and momentum in a stock price. It helps to indicate whether the stock market is upward or downward [35].

MACD can be expressed as:

$$MACD = EMA_{12}(C_t) - EMA_{26}(C_t) \tag{25}$$

Where EMA is the exponential moving average

- Momentum (MOM): MOM is a technical indicator to compares the changes in price over a given period time [37].

MOM can be expressed as:

$$MOM = C_t - C_{t-n} \tag{26}$$

Where C_t is the present closing price at time t and C_{t-n} is the closing price at n period ago

- Simple Moving Average (SMA): SMA is a technical indicator of an average of closing price over a given period time [36].

SMA can be expressed as:

$$SMA = \frac{1}{t}\sum_{i=1}^{t} C_t \tag{27}$$

Performance evaluation

The accuracy test of the five selected stock is evaluated using:

A. Mean Absolute Error (MAE)

Consider a set of the actual closing price C_p and the predicted values $\widehat{C_p}$. MAE is given as follows:

$$\frac{1}{n}\sum_{n=1}^{n}\left|C_p - \widehat{C_p}\right|$$

B. Root Mean Square Error (RMSE)

RMSE is given as:

$$\sqrt{\frac{1}{n}\sum_{n=1}^{n}\left(C_p - \widehat{C_p}\right)^2}$$

C. Mean Square Error (MSE)

MSE is given as

$$\frac{1}{n}\sum_{n=1}^{n}\left(C_p - \widehat{C_p}\right)^2$$

Table III
Summary Statistics of Selected Technical Indicator.

Stock	Technical Indicator											
	RSI				MACD				MOM			
	Minimum	Median	Mean	Maximum	Minimum	Median	Mean	Maximum	Minimum	Median	Mean	Maximum
ANINO	0.00	66.67	50.35	100.00	−4.06	0.00	−0.09	1.13	−0.00	0.00	0.00	0.00
CAPOIL	0.00	50.00	75.20	100.00	−1.11	0.00	0.44	12.65	−0.17	0.00	0.00	0.00
CAVERTON	0.00	66.67	53.32	100.00	−17.46	0.15	0.30	18.53	−1.64	−0.02	0.00	0.04
CONOIL	0.00	100	57.49	100.00	−15.49	0.61	0.41	8.64	−13.44	0.00	0.07	13.46
ETERNA	0.00	66.67	53.92	100.00	−16.27	0.28	0.15	7.67	−1.16	0.00	0.00	0.08
FO	0.00	76.94	55.36	100.00	−15.04	0.88	0.62	16.05	−43.13	0.00	0.11	48.77
JAPAUL	0.00	66.67	55.80	100.00	−15.21	0.00	0.45	17.22	−0.16	0.00	0.00	0.00
MOBIL	0.00	66.67	52.06	100.00	−11.11	0.07	−0.16	9.25	−57.46	0.00	−0.04	35.99
MRS	0.00	100.00	64.04	100.00	−8.81	0.19	0.61	7.05	−8.61	0.00	0.06	8.30
OANDO	0.00	66.67	56.35	100.00	−12.48	1.11	0.75	11.78	−5.91	−0.15	0.03	5.96
RAKUNITY	0.00	66.67	52.22	100.00	−12.34	0.00	−0.02	8.81	−0.19	0.00	0.00	0.19
SEPLAT	0.00	52.98	49.78	100.00	−17.35	0.13	−0.03	10.30	−108.10	−3.00	−0.03	92.30
TOTAL	0.00	65.70	52.09	100.00	−8.95	0.15	0.19	7.07	−53.64	0.00	0.09	32.58

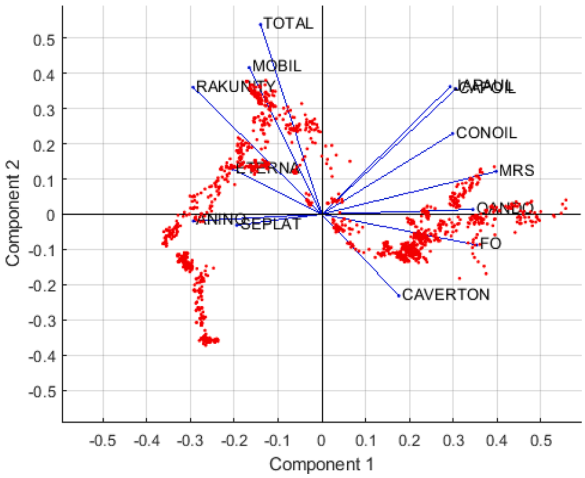

Fig. 5. 2-D Biplot of Oil and Gas Sector.

D. Mean Absolute Scaled Error (MASE)
MASE is given as

$$\frac{1}{n}\sum_{n=1}^{n}\frac{\left|C_p-\widehat{C_p}\right|}{\frac{1}{n-m}\sum_{n=m+1}^{n}\left|C_p-\widehat{C_p}\right|}$$

Where m is the seasonal period of the closing price and n is the trading days.

5. Experimental result

Table II shows the summary statistics of each of the selected Oil and gas sector of the Nigerian Stock Exchange from January 2014 to December 2019. The daily mean, median, 1st quartile, 3rd quartile, median, maximum and standard deviation. The daily mean of ANINO is small compared to other selected stocks. ANINO also has small volatility of 0.0142 compared with other stocks which indicate that the stock price fluctuates slowly and tends to be more stable. SEPLAT has a maximum price of 785 due to supply and demand. The summary statistics of selected technical indicators of RSI, MACD and MOM is also presented in Table III. MACD, MOM has a negative minimum in all the stocks while RSI has a maximum price in all the stocks. Fig. 5 is the 2-D bi-plot of the oil and gas sector of all the thirteen stock used in this paper. Bi-plot shows the direction and length of the vector of the principal component one and principal component two. The largest positive coefficients in the first principal component are MRS and OANDO the least negative coefficients in the first principal component are: CAVERTON and FO. On this, positive variables obtained from the second principal component: TOTAL, MOBIL and RAKUNITY which are more preferable to the least negative variables: ANINO and SEPLAT. In essence, TOTAL, MOBIL and RAKUNITY are among the stock with the high stock prices.

The performance metrics of each machine learning, deep learning and the stochastic process were shown in Table IV. Logistic Regression (LR) and Support vector machine (SVM) are selected among different machine learning algorithms considered in this paper while two deep learning are utilized. The deep learning models used are feed forward network (FFN) and recurrent neural network (RNN). The Continuous-Time stochastic process considered in this paper include Stochastic differential equation (SDE) and geometric Brownian motion (GBM). Four performance measures were considered: Root Mean Square Error (RMSE), Mean Square Error (MSE), Mean Absolute Error (MAE) and Mean Absolute Scaled Error (MASE). Table IV is a summary of the result obtained from the performance measure. The results show that the proposed model AA can predict accurately the stock price movement of all the selected stock price. The second best performance is the deep

Table IV
Performance Metrics of Oil and Gas Sector.

Stock	Model	Performance Metrics			
		RMSE	MSE	MAE	MASE
ANINO	LR	0.0128	0.0002	0.0091	8.0176
	SVM	0.0135	0.0002	0.0063	5.5713
	FFN	0.0121	0.0001	0.0078	6.8939
	RNN	0.0120	0.0001	0.0080	7.1494
	GBM	0.0933	0.0087	0.0822	72.7625
	SDE	0.0402	0.0016	0.0320	28.3089
	AA	0.0042	0.0000	0.0041	3.6686
CAPOIL	LR	0.1157	0.0134	0.0982	64.789
	SVM	0.1228	0.0151	0.0705	46.5082
	FFN	0.1084	0.0118	0.0854	56.3775
	RNN	0.1095	0.0120	0.0873	57.6327
	GBM	0.3104	0.0964	0.2734	180.4110
	SDE	0.1685	0.0284	0.1416	93.4546
	AA	0.0028	0.0000	0.0026	1.7308
CAVERTON	LR	1.2177	1.4828	0.9131	6.7647
	SVM	1.0755	1.1565	0.7980	5.9119
	FFN	1.0227	1.0460	0.8035	5.9528
	RNN	1.0674	1.1393	0.8452	6.2615
	GBM	1.9921	3.9686	1.4114	10.4554
	SDE	6.4934	42.1642	5.0196	37.1857
	AA	0.0006	0.0000	0.0005	0.0041
CONOIL	LR	11.6770	136.3536	9.1943	8.4803
	SVM	11.5031	132.3230	8.9471	8.2523
	FFN	11.3904	129.7425	9.0962	8.3899
	RNN	19.6673	386.8063	15.9852	14.7439
	GBM	22.9947	528.7569	17.6405	16.2706
	SDE	27.7448	769.7751	20.9903	19.3604
	AA	0.0003	0.0000	0.0000	0.0000
ETERNA	LR	1.2858	1.6533	0.9942	5.8808
	SVM	1.1769	1.3852	0.8716	5.1558
	FFN	1.1584	1.3420	0.8689	5.1394
	RNN	1.1589	1.3430	0.8862	5.2419
	GBM	2.1262	4.5208	1.8061	10.6827
	SDE	3.1107	9.6768	2.6206	15.5001
	AA	0.0004	0.0000	0.0003	0.0019
FO	LR	95.1844	9060.0832	87.3436	13.6993
	SVM	94.8192	8990.6860	68.4187	10.7310
	FFN	82.1877	6754.8252	68.7521	10.7833
	RNN	79.2008	6272.7772	65.3822	10.2548
	GBM	146.0618	21,334.0817	108.3942	17.0009
	SDE	98.2136	9645.9290	69.1310	10.8427
	AA	0.0002	0.0000	0.0000	0.0000
JAPAUL	LR	0.1174	0.0138	0.0915	8.3746
	SVM	0.1153	0.0133	0.0655	5.9999
	FFN	0.0973	0.0094	0.0609	5.5760
	RNN	0.0943	0.0088	0.0610	5.5873
	GBM	0.3296	0.1086	0.2900	26.5391
	SDE	0.2227	0.0496	0.1820	16.6617
	AA	0.0028	0.0000	0.0025	0.2368
MOBIL	LR	42.3607	1794.4318	28.3588	4.7783
	SVM	38.6753	1495.7849	23.1840	3.9064
	FFN	35.2272	1240.9616	22.9190	3.8617
	RNN	36.0828	1301.9743	22.7448	3.8324
	GBM	110.0848	12,118.6773	97.7899	16.477
	SDE	72.9839	5326.6505	51.4967	8.6770
	AA	0.0003	0.0000	0.0000	0.0000
MRS	LR	12.6598	160.2725	11.0793	24.0398
	SVM	12.6012	158.7921	11.0215	23.9144
	FFN	12.0883	146.1272	10.3022	22.3537
	RNN	12.0486	145.1708	10.2880	22.3230
	GBM	24.7196	611.0611	21.5698	46.8020
	SDE	10.2553	105.1728	8.3612	18.1422
	AA	0.0003	0.0000	0.0000	0.0000
OANDO	LR	6.6260	43.9049	5.4341	9.0401
	SVM	6.0903	37.0924	3.7815	6.2908
	FFN	5.5617	30.9332	4.2363	7.0474
	RNN	5.6185	31.5683	4.1731	6.9422
	GBM	9.8245	96.52106	6.3589	10.5786
	SDE	13.1531	173.0047	8.9597	14.9050
	AA	0.0003	0.0000	0.0001	0.0002
RAKUNITY	LR	0.0814	0.0066	0.0744	10.1157
	SVM	0.0928	0.0086	0.0723	9.8230
	FFN	0.0772	0.0059	0.0662	9.0024

(continued on next page)

Table IV (*continued*)

Stock	Model	Performance Metrics			
		RMSE	MSE	MAE	MASE
	RNN	0.0768	0.0059	0.0667	9.0697
	GBM	0.3277	0.1073	0.3118	42.3586
	SDE	0.4618	0.2133	0.3506	47.6272
	AA	0.0028	0.0000	0.0027	0.3714
SEPLAT	LR	148.2094	21,966.0413	128.0943	7.73466
	SVM	144.5021	20,880.8686	120.8583	7.2977
	FFN	144.6246	20,916.2923	123.1089	7.4336
	RNN	143.9400	20,718.7353	122.2034	7.3789
	GBM	219.0488	47,982.3857	152.3325	9.1982
	SDE	348.7254	121,609.4097	282.4359	17.0541
	AA	0.0003	0.0000	0.0000	0.0000
TOTAL	LR	48.2120	2324.4010	40.4635	7.2990
	SVM	47.5486	2260.8783	37.1902	6.7085
	FFN	45.6891	2087.4962	38.1208	6.8764
	RNN	45.7364	2091.8216	38.2157	6.8935
	GBM	123.7989	15,326.1738	114.0260	20.5685
	SDE	92.3292	8524.6858	78.7073	14.1976
	AA	0.0003	0.0000	0.0000	0.0000

learning followed by machine learning. The Continuous-Time stochastic processes fail to achieve any result when compared with others. This indicated that further research and studies needs to be considered in predicting the stock market using the continuous-time stochastic process as explained in (Osei Antwi, 2017). Fig. 6-11 is the price paths of all the algorithms utilized in this paper which shows that SDE and GBM fail to perform accurately with the actual price.

Fig. 7, Fig. 9. Fig. 10.

Another important advantage of AA over other algorithm considered is the ability to detect exponential decay of a stock price. Fig. 6 is the exponential decay of all the oil and gas sector obtained from AA. This shows that the higher the price of the stock the lower the exponential decay of the stock while the lower the price of the stock the higher the exponential decay of the stock price. However, the exponential decay also indicates the stability of the price, uptrend and downward trend of the price as shown in Fig. 6 and Table V. This may provide an opportunity for the investor to determine when the stock will fall or rise.

In this paper, we compared the performance of all the seven algorithms such as LR, SVM, FFN, RNN, GBM, SDE and AA using Friedman test which is a non-parametric statistical test [23]. The Friedman test is used to detect a significant difference among all the seven algorithms. If the p-value is less than 0.05, it means that there are significant differences among all the algorithms. Table VI shows the chi-squared and the p-value obtained from the Friedman test. In all the thirteen stock price of the oil and gas sector in comparison with all the seven algorithms, the p-value is less than 0.005. This shows that there is a significant difference among all the seven algorithms. To find out which pair is different from all the thirteen oil and gas sector utilized in this paper. We carry out post hoc analysis using Wilcoxon tests. We adjusted the results by multiplying the number of pairs with the p-value obtained from the Friedman test. Since we have 8 samples, it means we have 28possible pairs. The p-value of the test of ANINO, CAPOIL and JAPAUL oil are all

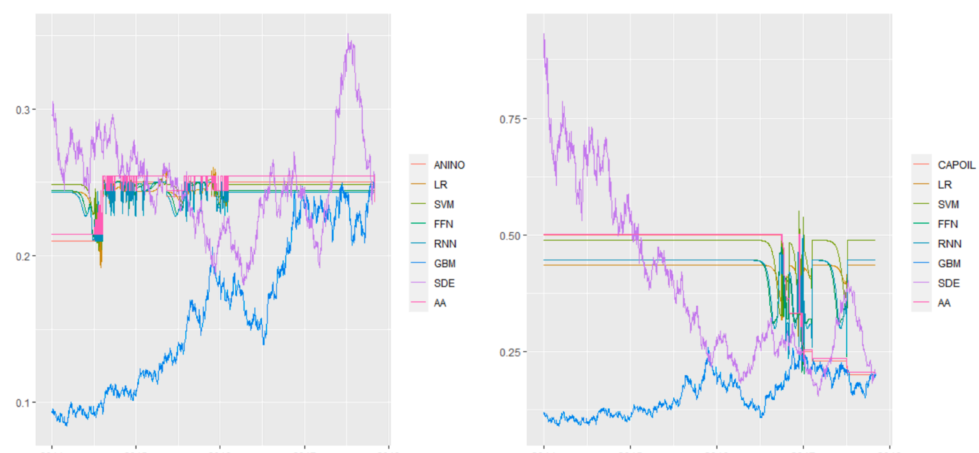

Fig. 6. Stock price prediction of ANINO oil, CAPOIL oil, LR, SVM, FFN, RNN, SDE, GBM and AA.

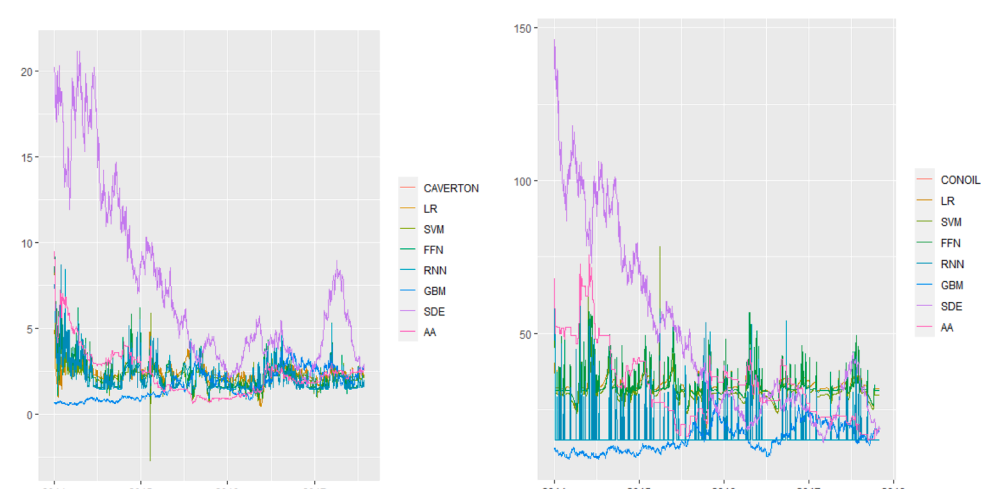

Fig. 7. CAVERTON oil, CONOIL oil stock price prediction of LR, SVM, FFN, RNN, SDE, GBM and AA.

Fig. 8. ETERNA oil, FO oil stock price prediction of LR, SVM, FFN, RNN, SDE, GBM and AA.

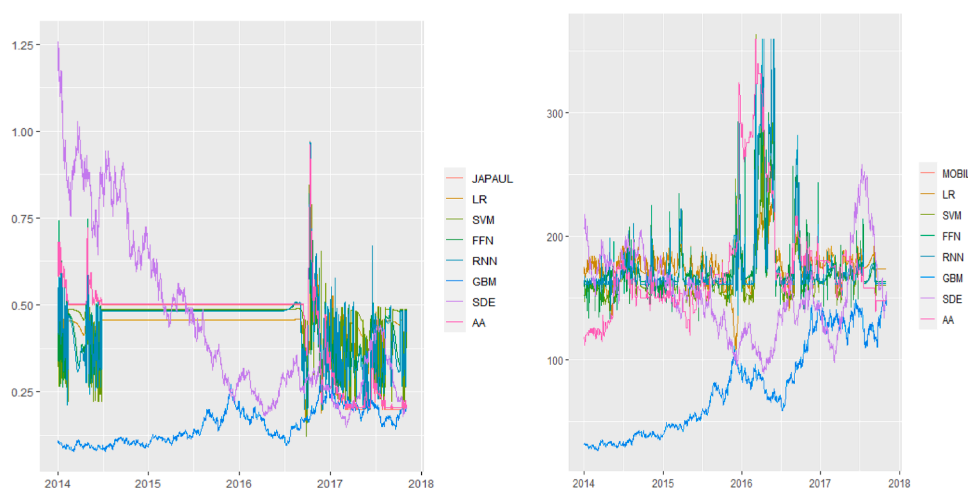

Fig. 8. JAPAUL oil, MOBIL oil stock price prediction of LR, SVM, FFN, RNN, SDE, GBM and AA.

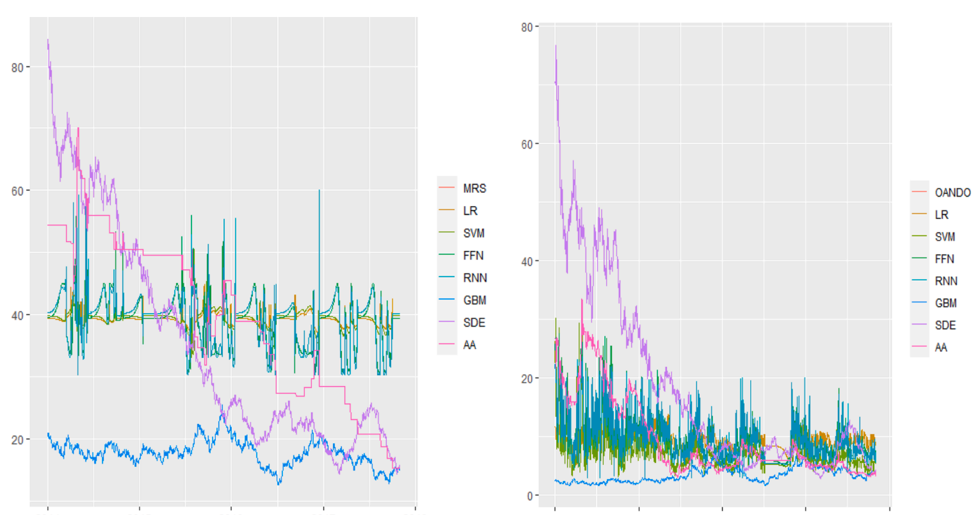

Fig. 9. MRS oil, OANDO oil stock price prediction of LR, SVM, FFN, RNN, SDE, GBM and AA.

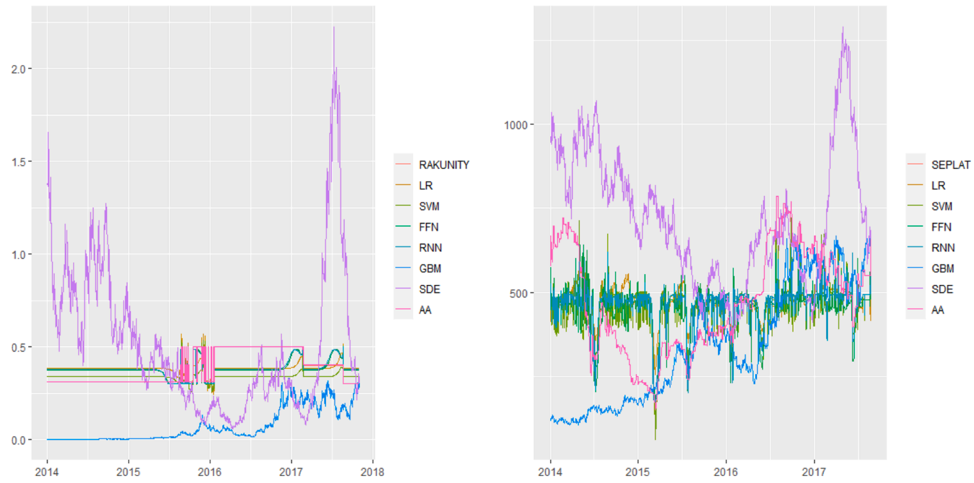

Fig. 10. RAKUNITY oil, SEPLAT oil stock price prediction of LR, SVM, FFN, RNN, SDE, GBM and AA.

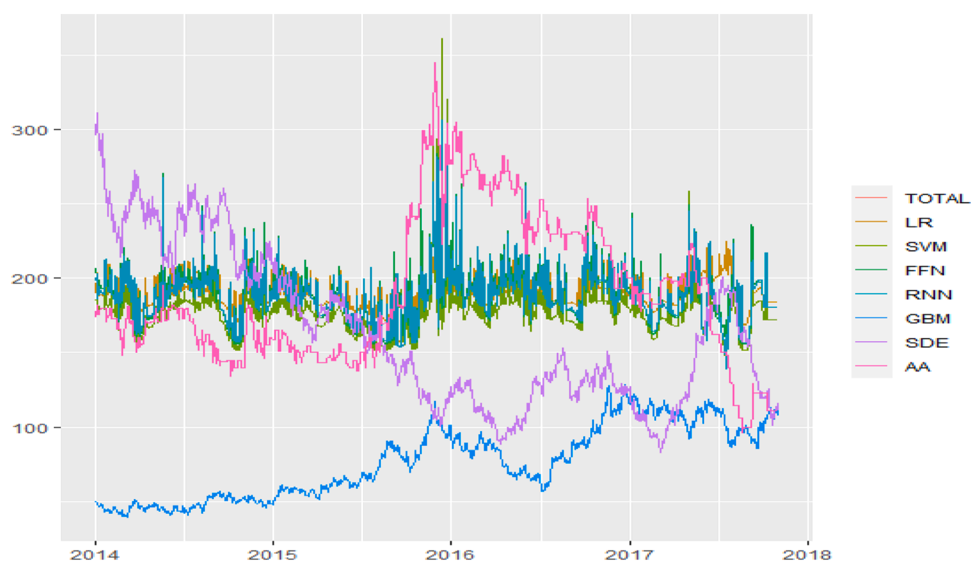

Fig. 11. TOTAL oil stock price prediction of LR, SVM, FFN, RNN, SDE, GBM and AA.

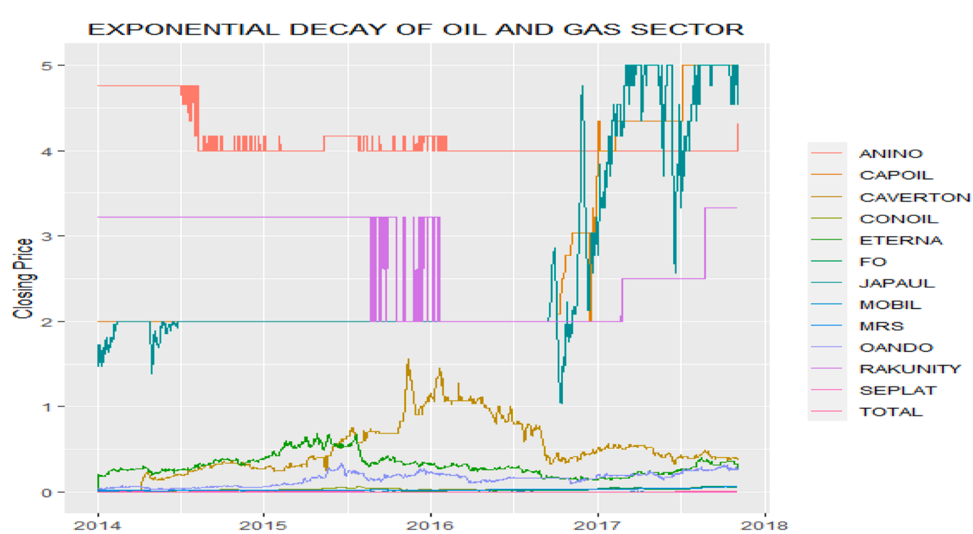

Fig. 12. Exponential decay of Oil and Gas Sector in Nigeria.

Table V
Exponential decay of Oil and Gas Sector.

Stock	Minimum	Mean	Variance
ANINO	4.0000	4.1400	0.0800
CAPOIL	2.0000	2.6200	1.1400
CAVERTON	0.0000	0.5100	0.0900
CONOIL	0.0132	0.0345	0.0001
ETERNA	0.0000	0.3140	0.0142
FO	0.0000	0.0189	0.0000
JAPAUL	1.0417	2.5820	1.2413
MOBIL	0.0028	0.0060	0.0000
MRS	0.0000	0.0289	0.0001
OANDO	0.0299	0.1507	0.0055
RAKUNITY	2.0000	2.7263	0.3236
SEPLAT	0.0000	0.0023	0.0000
TOTAL	0.0000	0.0056	0.0000

Table VI
Result of Friedman Test to detect differences in LR, SVM, FFN, RNN, GBM, SDE and AA.

Stock	Chi-squared (χ^2)	p-value
ANINO	5144.20	2.2×10^{-16}
CAPOIL	4901.90	2.2×10^{-16}
CAVERTON	3203.10	2.2×10^{-16}
CONOIL	5395.90	2.2×10^{-16}
ETERNA	3720.50	2.2×10^{-16}
FO	4409.40	2.2×10^{-16}
JAPAUL	4029.60	2.2×10^{-16}
MOBIL	4222.10	2.2×10^{-16}
MRS	3639.30	2.2×10^{-16}
OANDO	4431.00	2.2×10^{-16}
RAKUNITY	4086.30	2.2×10^{-16}
SEPLAT	2621.90	2.2×10^{-16}
TOTAL	4141.90	2.2×10^{-16}

less than the significant level alpha = 0.05. We can conclude that ANINO, CAPOIL and JAPAUL oil median stock oil price is significantly different from median of all the seven algorithms. However, CAVERTON, CONOIL, ETERNA, FO, MOBIL, MRS, OANDO, RAKUNITY, SEPLAT and TOTAL in some of the algorithms show no significant difference as shown in Table VII. Since they are greater than the significant level of 0.05. From the results in Table VII, it was identified that AA algorithm is superior to all the other thirteen algorithms due to the fact that it shows no significant difference in nine out of 13 oil and gas sector.

Conclusion

In this paper, a robust auditory algorithm inspired by an auditory system of the human ear was developed. The development of a new nature-inspired auditory algorithm method called AA was inspired by the human auditory system. The method considers the pathway of sound waves from the pinna to the ear canal, eardrum, malleus, incus, stapes, cochlea and to the brain in predicting stock market behavior.

The performance of AA was compared with that of six other algorithms. The results showed that the overall performance of AA ranks first followed second is the deep learning and third is machine learning. The study indicated that stochastic process SDE and GBM failed to achieve any results. The study was limited by the difficulty in accessing data and lack of funds on the part of the researcher. It is believed that this work will help investors in the stock market to make accurate decisions when predicting stock. Further research work will focus on the prediction of cryptocurrency, gold, other stock market and other commodities like silver, copper, oil and gas using the proposed Auditory Algorithm (AA).

Table VII
Result of Post Hoc Analysis using Wilcox Test.

Stock	Model	p-value
ANINO	LR	1.61×10^{-88}
	SVM	1.73×10^{-56}
	FFN	1.22×10^{-117}
	RNN	3.78×10^{-86}
	GBM	0.00
	SDE	1.17×10^{-6}
	AA	4.29×10^{-160}
CAPOIL	LR	1.57×10^{-101}
	SVM	1.07×10^{-95}
	FFN	1.09×10^{-104}
	RNN	8.17×10^{-105}
	GBM	0.00
	SDE	1.18×10^{-13}
	AA	4.60×10^{-146}
CAVERTON	LR	8.51×10^{-7}
	SVM	8.97
	FFN	18.65
	RNN	9.03
	GBM	5.30×10^{-43}
	SDE	7.30×10^{-270}
	AA	13.91
CONOIL	LR	1.28×10^{-5}
	SVM	9.42
	FFN	0.0008
	RNN	0.00
	GBM	0.00
	SDE	1.07×10^{-31}
	AA	10.18
ETERNA	LR	8.90×10^{-11}
	SVM	9.54
	FFN	0.61
	RNN	1.25×10^{-5}
	GBM	1.03×10^{-226}
	SDE	1.55×10^{-115}
	AA	15.37
FO	LR	2.60×10^{-5}
	SVM	4.77
	FFN	2.21×10^{-6}
	RNN	4.89×10^{-6}
	GBM	0.00
	SDE	1.42×10^{-48}
	AA	17.87
JAPAUL	LR	7.16×10^{-98}
	SVM	9.17×10^{-97}
	FFN	1.62×10^{-82}
	RNN	7.02×10^{-77}
	GBM	0.00
	SDE	0.0029
	AA	6.70×10^{-86}
MOBIL	LR	5.23×10^{-37}
	SVM	3.76
	FFN	1.64×10^{-8}
	RNN	7.97×10^{-7}
	GBM	0.00
	SDE	9.99×10^{-38}
	AA	10.68
MRS	LR	15.24
	SVM	15.58
	FFN	11.40
	RNN	19.93
	GBM	0.00
	SDE	2.70×10^{-22}
	AA	0.59
OANDO	LR	1.99×10^{-52}

(*continued on next page*)

Table VII (*continued*)

Stock	Model	p-value
	SVM	10.86
	FFN	3.98×10^{-40}
	RNN	1.01×10^{-31}
	GBM	0.00
	SDE	4.01×10^{-67}
	AA	12.95
RAKUNITY	LR	0.03
	SVM	1.76
	FFN	7.01
	RNN	7.13
	GBM	0.00
	SDE	1.15
	AA	4.74×10^{-64}
SEPLAT	LR	3.67
	SVM	18.90
	FFN	1.04
	RNN	14.66
	GBM	5.04×10^{-81}
	SDE	8.23×10^{-204}
	AA	15.87
TOTAL	LR	3.14×10^{-14}
	SVM	6.78
	FFN	5.01×10^{-8}
	RNN	4.80×10^{-7}
	GBM	0.00
	SDE	5.69×10^{-44}
	AA	14.15

Declaration of Competing Interest

None.

References

[1] J.L. Ticknor, A Bayesian regularized artificial neural network for stockmarket forecasting, Expert Syst. Appl. 40 (14) (2013) 5501–5506 (2013).

[2] R.G. Ahangar, M. Yahyazadehfar, H. Pournaghshband, The comparison of methods artificial neural network with linear regression using specific variables for prediction stock price in tehran stock exchange, Int. J. Comput. Sci. Inf. Sec. 7 (2) (2010) 38–46.

[3] Andrés Arévalo, Jaime Niño, German Hernández, Javier Sandoval, High-frequency Trading Strategy Based on Deep Neural Networks.Ininternational Conference on Intelligent Computing, Springer, Cham, 2016, pp. 424–436, 2016.

[4] Dattatray P. Gandhmal, K. Kumar, Systematic analysis and review of stock market prediction techniques, Comput. Sci. Rev. 34 (2019) 1–13 (2019).

[5] C.Y. Yeh, C.W. Huang, S.J. Lee, A multiple-kernel support vector regression approach for stock market price forecasting, Expert Syst. Appl. 38 (3) (2011) 2177–2186 (2011).

[6] N. Cristianini., J. Shawe-Taylor, An Introduction to Support Vector Machines, University Press, Cambridge, 2000, 2000.

[7] K. Chourmouziadis, P.D. Chatzoglou, An intelligent short term stock trading fuzzy system for assisting investors in portfolio management, Expert Syst. Appl. 43 (2016) 298–311.

[8] David Enke, Suraphan Thawornwong, The use of data mining and neural networks for forecasting stock market returns, Expert Syst. Appl. 29 (4) (2005) 927–940, no. (2005).

[9] L. Bachelier, The orie de la speculation, Ann. Sci. l'E'coleNormaleSupe'rieure Se'r. 3 (17) (1900) 21–86.

[10] Antwi Osei, Stochastic Modeling of Stock price behavior on Ghana stock exchange, Int. J. Syst. Sci. Appl. Math. 2 (6) (2017) 116–125.

[11] D. Bao, Z. Yang, Intelligent stock trading system by turning point confirming and Probabilistic reasoning, Expert Syst. Appl. 34 (1) (2008) 620–627, 2008.

[12] A. Timmermann, W.C. Granger, Efficient market hypothesis and forecasting, Int. J. Forecast. 20 (1) (2004) 15–27, 2004.

[13] Galante Giacomel, Pareira, An algorithmic trading agent based on a neural network ensemble: a case of study in North American and Brazilian stock markets, in: IEEE/WIC/ACM International Conference on Web Intelligence and Intelligent Agent Technology, 2015.

[14] David Oyewola, Emmanuel Gbenga Dada, Ezekiel Olaoluwa Omole, K.A. Al-Mustapha, Predicting Nigerian stock returns using technical analysis and machine learning, Eur. J. Electric. Comput. Eng. 3 (2) (2019) 1–8.

[15] E. Avci, Forecasting daily and seasonal returns of the ISE-100 Index with neuralnetwork models, Dogus Univ. J. 8 (2) (2007) 128–142.

[16] Rajashree Dash, PradiptaKishoreln Dash, A hybrid stock trading framework integrating technical analysis with machine learning techniques, J. Finance Data Sci. (2016) 42–57 (2016).

[17] J. Chen, Y. Fang, Forecasting the performance of the Asian currency unit and the causes of contagion of the Asian financial crisis, Asia Pac. Manag. Rev. 13 (4) (2008) 665–684.

[18] A.A. Adebiyi, A.O. Adewumi, C.K. Ayo, Comparison of arima and artificialneural networks models for stock price prediction, J. Appl. Math. (2014), 2014.

[19] ShipraBanik, A.F.M.Khodadad Khan, Mohammad Anwer, Hybrid machine learning technique for forecasting dhaka stock market timing decisions, Comput. Intell. Neurosci. (2014) 1–8 (2014).

[20] OussamaLachiheb, Mohamed Salah Gouider, A hierarchical deep neural network design for stock returns prediction, Procedia Comput. Sci. 126 (2018) 264–272 (2018).

[21] R. Litovsky, Development of the auditory system, Handb. Clin. Neurol. (2015) 55–72.

[22] N. Anthwal, H. Thompson, The development of the mammalian outer and middle ear, J. Anat. 228 (2) (2015) 217–232.

[23] R. Glueckert, L. Johnson Chacko, H. Rask-Andersen, W. Liu, S. Handschuh, A. Schrott-Fischer, Anatomical basis of drug delivery to the inner ear, Hear. Res. (2018).

[24] D.O. Oyewola, K.A. Al-Mustapha, E.G. Dada, O.A. Kennedy, Stock market movement direction with ensemble deep learning network, J. Niger. Assoc. Math. Phys. 53 (2019) 103–116 (2019).

[25] Eunsuk Chong, Chulwoo Han, Frank C. Park, Deep learning networks for stock market analysis and prediction:methodology, data representations, and case studies, Expert Syst. Appl. 83 (2017) 187–205 (2017).

[26] D. MacKay, Probable networks and plausible predictions—a review of practical Bayesian methods for supervised neuralnetworks, Netw.: Comput. Neural Syst. 6 (1995) 469–505 (1995).

[27] Serrano Cinca, Self-organizing neural networks for financial diagnosis, Decis. Support Syst. 17 (1996) 227–238 (1996).

[28] B. Wong, T. Bodnovich, Y. Selvi, Neural network applications in business: a review and analysis of the literature (1988–1995), Decis. Support. Syst. 19 (4) (1997) 301–320 (1997).

[29] David O. Oyewola, Aye Patrick Olabanji, A.U. Terrang., Jayeola Dare, Deep continuous-time models in Nigerian stock exchange sector, J. Sci. Technol. Research 2 (1) (2020) 99–113, 2020.

[30] Da Silva, N. F., E.R. Hruschka, E.R &Hruschka, Tweet sentiment analysis with classifier ensembles, Decis. Support Syst. 66 (2014) 170–179.

[31] David Oyewola, Danladi Hakimi, Kayode Adeboye, Musa DanjumaShehu, Using five machine learning for breast cancer biopsy predictions based on mammographic diagnosis, Int. J. Eng. Technol.-Ijet 2 (4) (2016) 142–145.

[32] J.A.K. Suykens, T. Van Gestel, J. De Brabanter, B. De Moor, J. Vandewalle, Least Squares Support Vector Machines, World Scientific, New Jersey, 2002, 2002.

[33] T. Eftimov, P. Korošec, A novel statistical approach for comparing metaheuristic stochastic optimization algorithms according to the distribution of solutions in the search space, Inf. Sci. (Ny) 489 (2019) 255–273, 2019.

[34] Bing Anderson, Shuyun Li, An investigation of the relative strength index, Banks Bank Syst. 10 (1) (2015) 92–96.

[35] Mohammad Alalaya, Hani.A. Alrawshdeh, Akram Alawad, Moving average convergence /devergerance and relative strength index applied to predict price of ASE, Int. J. Bus. Soc. Sci. 9 (6) (2018) 35–42.

[36] V. Zakamulin, J. Giner, Trend following with momentum versus moving averages: a tale of differences, Quant. Finance (2020) 1–23.

[37] Lijun Wang, Haizhong An, Xiaohua Xia, Xiaojia Liu, Xiaoqi Sun, Xuan Huang, Generating moving average trading rules on the oil futures market with genetic algorithms, Math. Prob. Eng. 2014 (2014) 1–10.

An analysis of Harmony Search for solving Sudoku puzzles

Namrata Khamari, *Department of Computer Scinece Engineering , NM Institute of Engineering & Technology, Bhubaneswar, namrayakhamari@outlook.com*

Tapas Ranjan Baitharu, *Department of Computer Sciencel Engineering, Aryan Institute of Engineering & Technology, Bhubaneswar, tkbaitharu11@gmail.com*

Arabinda Dash, *Department of Computer Scinece Engineering , Capital Engineering College, Bhubaneswar, arabindadash56@hotmail.com*

Smruti Ranjan Panda, *Department of Electrical and Electronics Engineering, Raajdhani Engineering College, Bhubaneswar, sr_panda@outlook.com*

ARTICLE INFO

Keywords:
Sudoku puzzle
Harmony search
Metaheuristics
Local search

ABSTRACT

The Harmony Search metaheuristic has been used to solve many different optimization problems. Several papers examined its effectiveness for solving Sudoku puzzles. Another paper claims that it is ineffective for solving Sudoku puzzles and further that the method itself lacks novelty compared to other evolutionary algorithms. Our paper analyzes the search process in harmony search when applied to a specific Sudoku puzzle examined in earlier research. The basic harmony search procedure is re-implemented and tested to evaluate its performance and verify its applicability to the specific example. We found that the while the criticisms of the method for this problem are valid, that the performance can be improved with a rather simple modification. First, we propose a new objective function for the search procedure. This proposed objective function facilitates the search method to find a proper solution. Second, the modified version of the harmony search, where harmony search is combined with local search is introduced and analyzed for its contribution of 'improvisation' in harmony search procedure by comparing the performance of local search and the modified search. For a specific problem, the modified version of harmony search generates a unique solution with new objective function in favorable time. Then extended experiments were performed for various Sudoku problems. We find that while the modified search procedure produces solutions more quickly, that it suffers the same issue that the original method has in that it sometimes fails to find a feasible solution.

1. Introduction

In recent years, a tremendous amount of research has been conducted related to the application of metaheuristics to combinatorial optimization problems. While some of these efforts have gained recognition and respect, others face criticism due to unpredictable performance and lack of theoretical foundations. The Harmony Search (HS) algorithm based on jazz music was proposed by Geem [9]. Since its introduction, HS has been applied to problems in areas such as scheduling optimization [6], reliability problem [27] and facility layout design [11] because of its simple structure and easiness to be applied. HS is even capable of derivative for discrete variables [7] and the result can be independent from parameter setting [10]. However, Weyland [25] raised the issue of its novelty, and also its limitations, and Weyland [26] presented criticism of its application to Sudoku, which was proposed in Geem [8]. The result provided in Geem [8] could not be verified by Weyland [26] and the question about the applicability of the HS algorithm came to the front. Our study is focused on the analysis of HS for its usability as a Sudoku solver, the introduction of a modified search method, and a comparison between the original search method and our modified one. Note that we are not addressing the arguments surrounding the novelty of Harmony search that were mentioned in Weyland [25] and then rebutted several times, for example in Kim [12] and Saka et al. [20]. We are simply demonstrating that some simple improvements can improve the performance of the method on Sudoku problems.

A Sudoku puzzle assigns a single-digit number between 1 through 9 to each location in a 9×9 matrix. A number must not be repeated in each row, column, and within each of the nine 3×3 blocks. As shown in Fig. 1, each puzzle has some cells that have already been filled with numbers. This puzzle, which is well known for its addictive nature [13], has been further popularized by the many versions which have been developed and released as mobile applications. The level of difficulty of a Sudoku puzzle depends not only on the number of pre-filled cells but also on the techniques required to find the proper values for each cell [19]. An empty Sudoku grid has 6.67×10^{21} possible combinations [5, 19], but the pre-filled cells serve as constraints and reduce the number of possible combinations.

	5		3		6			7
				8	5		2	4
	9	8	4	2		6		3
9		1			3	2		6
	3						1	
5		7	2	6		9		8
4		5		9		3	8	
	1		5	7				2
8			1		4		7	

Fig. 1. Example of Sudoku Puzzle [8].

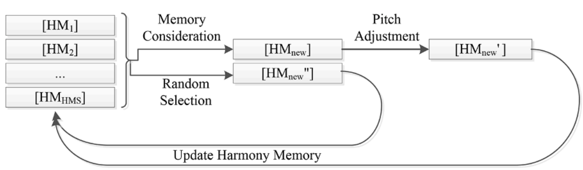

Fig. 2. Procedure of Harmony Search.

In recent years, many research efforts involving Suduku have applied evolutionary search algorithms such as genetic algorithms [14], particle swarm optimization [17], artificial bee colony algorithms [18]. A detailed discussion of meta-heuristic approaches can be found in Lewis [13] and Mishra et al. [15]. In Mishra et al. [15], more than 10 meta-heuristics were introduced and analyzed on their performance on Sudoku, but the HS was not included in this discussion. As previously mentioned, our paper analyzes the performance of HS and its applicability to Sudoku and it is not intended to support or contradict the previous research presented in Weyland [26] or Geem [8]. Heuristics that are designed specifically for Sudoku puzzles and have excellent solution times were introduced in Coelho and Laporte [3]. Thus, comparing the performance of HS to other heuristics that are specifically designed-to-solve Sudoku puzzles would not be a new contribution. Our study is mainly interested in exploring the performance of HS and in proposing a modification which will improve it for these puzzles. We propose the HS algorithm with some modification, embedding local search to solve Sudoku puzzle. Furthermore, we analyze the effect of harmony search procedure by comparing its result to the variant containing the local search.

In the following section, we explored the mathematical form of Sudoku prior to discussing the harmony search. Section 3 describes a basic harmony search used in Geem [8], and we propose a possible objective function to solve Sudoku more accurately. An extended form of HS algorithm is introduced and detailed in this section. Section 4 presents a comparison of results of previous research to this study. Additional analysis for the proposed algorithm and further applications of the proposed algorithm are presented. Finally, we draw our conclusion in Section 5.

2. Sudoku problem formulation

The Sudoku puzzle found in Fig. 1 can be modeled as a linear program [2]. Specifically, it can be modeled as a binary integer program (BIP) for general $n \times n$ puzzles. The decision variables are defined as follows:

$$x_{ij}^{k} = \begin{cases} 1, & \textit{if element } (i,j) \textit{ of the } n \times n \textit{ matrix contains the integer } k \\ 0, & \textit{otherwise} \end{cases}$$

This problem is a special case of a linear program because it only considers the constraints and can be modeled as a constraint program [1, 2]. Thus, the objective function is just set to zero as in Eq. (1) and the constraints are set to work for its satisfiability.

$$\text{Min}0 \tag{1}$$

$$\text{s.t.} \sum_{i=1}^{9} x_{ij}^{k} = 1,\ j = 1..9,\ k = 1, \ldots.., 9 \tag{2}$$

$$\sum_{j=1}^{9} x_{ij}^{k} = 1,\ i = 1..9,\ k = 1, \ldots.., 9 \tag{3}$$

$$\sum_{j=3q-2}^{3q} \sum_{i=3p-2}^{3p} x_{ij}^{k} = 1,\ p = 1..3, q = 1..3,\ k = 1, \ldots.., 9 \tag{4}$$

(a)	2	3	7	5	1	3	9	8	6
(b)	2	4	7	5	1	3	9	8	6
(c)	2	3	7	5	1	4	9	8	6

Fig. 4. re-adjustment procedure.

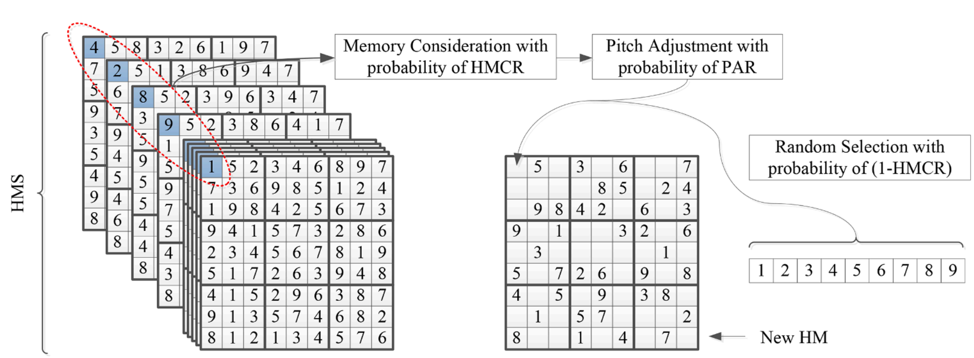

Fig. 3. HM construction process.

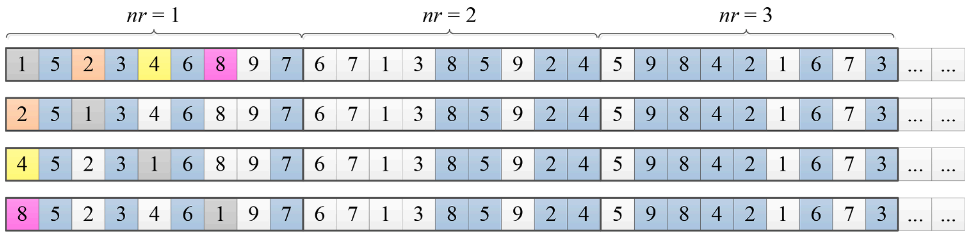

Fig. 5. Example of two-way exchange in a *2-opt* algorithm.

Table 1
the result of the experiments.

HMS	HMCR	PAR	Runs finding the unique solution in 10^4 iterations in Weyland [26] and this study	10^6 iterations in Weyland [26] and this study	Iterations to obtain the optimal solution in Geem [8]	by HS with Re-adjustment		by HS with embedded local search (HS2E)
1	0.5	0.01	0	0	66	395167	(0.05)	2
		0.1	0	0	337	655541	(0.1)	15
		0.5	0	0	422	n/a	(0)	14
	0.7	0.01	0	0	287	3978	(0.35)	1
		0.1	0	0	3413	297840	(0.15)	7
		0.5	0	0	56	n/a	(0)	3
	0.9	0.01	0	0	260	828969	(0.05)	136
		0.1	0	0	n/a	90892	(0.1)	61
		0.5	0	0	1003	88848	(0.25)	19
2	0.5	0.01	0	0	31	180210	(0.05)	12
		0.1	0	0	94	502616	(0.1)	12
		0.5	0	0	175	n/a	(0)	14
	0.7	0.01	0	0	102	15930	(0.3)	2
		0.1	0	0	77	364327	(0.1)	16
		0.5	0	0	99	n/a	(0)	11
	0.9	0.01	0	0	n/a	203425	(0.15)	11
		0.1	0	0	n/a	54147	(0.2)	19
		0.5	0	0	1325	126627	(0.15)	3
10	0.5	0.01	0	0	49	450860	(0.35)	25
		0.1	0	0	280	825597	(0.05)	7
		0.5	0	0	188	n/a	(0)	18
	0.7	0.01	0	0	56	546484	(0.05)	2
		0.1	0	0	146	33106	(0.15)	11
		0.5	0	0	259	n/a	(0)	33
	0.9	0.01	0	0	180	8199	(0.15)	4
		0.1	0	0	217	1798	(0.25)	7
		0.5	0	0	350	198292	(0.15)	10
50	0.5	0.01	0	0	147	n/a	(0)	2
		0.1	0	0	372	n/a	(0)	2
		0.5	0	0	649	n/a	(0)	7
	0.7	0.01	0	0	165	55735	(0.05)	5
		0.1	0	0	285	133542	(0.1)	23
		0.5	0	0	453	n/a	(0)	19
	0.9	0.01	0	0	87	n/a	(0)	2
		0.1	0	0	329	10781	(0.05)	26
		0.5	0	0	352	638784	(0.15)	30

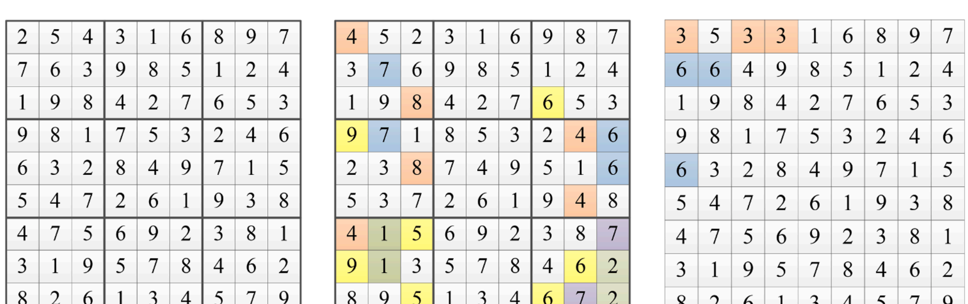

(a) The unique solution

(b) An optimal solution with Eq. (12) in this study

(c) An optimal solution with Eq. (12) in Weyland (2015)

Fig. 6. The example of solutions that generate the optimal objective value of 0 in Eq. (12).

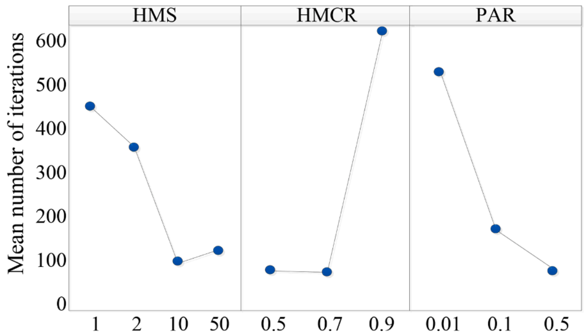

Fig. 7. Main effects plot for the number of iterations.

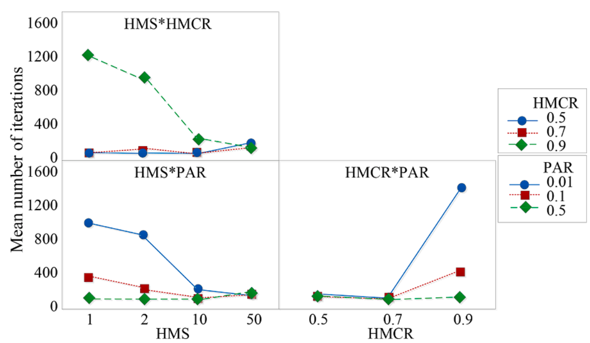

Fig. 8. Interaction effects plots for the number of iterations.

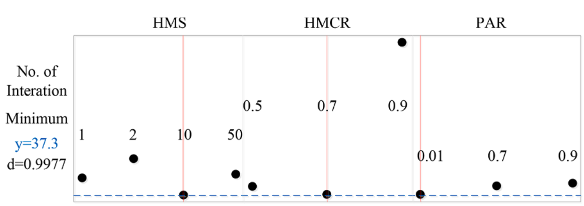

Fig. 9. Response optimization.

$$\sum_{k=1}^{9} x_{ij}^{k} = 1,\ \ i = 1..9,\ \ j = 1,\ldots\ldots,9 \tag{5}$$

$$x_{ij}^{k} = 1,\ \ \forall (i,j,k) \in G \tag{6}$$

$$x_{ij}^{k} \in \{0,1\},\ \ \forall i,\ j \tag{7}$$

Eq. (2) through Eq. (4) indicates that the single number should be assigned to each row, column, and block, where m indicates the dimension of submatrix. Eq. (5) ensures that every cell must have a number. The given number is set to 1 at Eq. (6) where G indicates the set of cell location and the number specifically given at that cell. Eq. (7) restricts the variable uses to only binary.

This constraint program can be formulated another way as follows:

$$\text{Min}\ \left|\sum_{i=1}^{9} x_{ij}^{k} - 1\right| + \left|\sum_{j=1}^{9} x_{ij}^{k} - 1\right| + \left|\sum_{j=3q-2}^{3q}\ \sum_{i=3p-2}^{3p} x_{ij}^{k} - 1\right| \tag{8}$$

$$\text{s.t. } i = 1,\ldots,9,\ j = 1,\ldots,9,\ k = 1,\ldots,9,\ p = 1,\ldots,3,\ q = 1,\ldots,3 \qquad \sum\nolimits_{k=1}^{9} x_{ij}^{k} = 1,\ i = 1,\ldots,9,\ j = 1,\ldots,9 \tag{9}$$

$$x_{ij}^{k} = 1,\ \forall (i,j,k) \in G \tag{10}$$

$$x_{ij}^{k} \in \{0,1\},\ \forall i,\ j \tag{11}$$

Due to differences in objective function, the method of construction in harmony search could not be compared with that of a search procedure. However, we were able to compare the unique solution and the solving time of a specific Sudoku problem in the two algorithms. The formulation was coded and executed using CPLEX 12.6 on an Intel Core i5 CPU, 8G memory computer, which generated the optimal solution within 0.01 second for the example problem given in Geem [8]. Additional tests using extended examples (Section 4.3) were examined through the CPLEX application. The additional tests generated the optimal solutions within 0.02 s for even the hardest problem. Thus, rating the performance of each algorithm in terms of solving time was ineffective. Instead, the search procedure itself is tested for its effectiveness.

3. Harmony Search

Harmony Search's approach is inspired by the improvisation process used by jazz musicians. There are three phases of this approach: initialization, improvisation, and memory updates. The harmony memory size (HMS) is defined as the number of solution vectors called harmony memory (HM). The HMS, harmony memory consideration rate (HMCR) and pitch adjustment rate (PAR) should be determined at the initialization phase. Two parameters, HMCR and PAR, are used for constructing a solution for the next generation in improvisation phase with the use of random selection for a new HM. After generating new HM, the new group of HM is updated based on its solution quality; if a newly generated HM is better than the HM in the previous group, then the new HM is included to a new generation of HM where the worst value is removed. Fig. 2 illustrates the procedure of HM.

3.1. Basic HS Model for Sudoku

As it was mentioned, Sudoku is solved by filling in the cells with numbers 1 through 9 while abiding to the 'single number' rule [2] in the matrix. Thus, the objective function of BIP is not the focus of the problem—the constraints are. However, one of the characteristics of

Table 3
Number of iterations needed to solve the Sudoku puzzle using HS2E.

	Easy (36)	Medium (29)	Hard (23)	SD1 (24)	SD2 (23)	SD3(22)
Min	24	196	9765	16626	26450	20708
(run time)	(0.6s)	(6.8s)	(354s)	(891s)	(1523s)	(1098s)
Median	882	22645	256780	46365	191397	216998.5
Probability of Success	100%	77%	63%	87%	67%	80%

Table 2
The comparison of HS2E and *2-opt* algorithm.

	Number of iterations				Time to Solve (in s)			
	Min	Median	Mean	Max	Min	Median	Mean	Max
HS2E	1	39.5	54.2	384	0.07	0.75	0.91	4.95
2-opt	20	379.5	584.1	3442	0.48	9.33	14.22	83.53

improvement type heuristics such as HS is that they have a guided approach to a given problem. In other words, the algorithm decides whether to adapt the new solution or to keep the previous solution in each iteration depending on the resulting value. Thus, setting the objective function would be very important to develop a proper solution procedure. Mishra et al. [15] introduced various objective functions used to solve Sudoku using evolutionary metaheuristics. In Geem [8], the objective function is based on the sum of each row, column, and block as follows:

$$\text{Minimize } Z = \sum_{i=1}^{9}\left|\sum_{j=1}^{9} x_{ij} - 45\right| + \sum_{j=1}^{9}\left|\sum_{i=1}^{9} x_{ij} - 45\right| + \sum_{r=1}^{9}\left|\sum_{(s,t)\in B_r}^{9} x_{st} - 45\right| \tag{12}$$

where x_{ij} = cell at row i and column j, and B_r = set of coordinates for block r. The characteristic of the Sudoku matrix requires that sum of each row, column, and block should be 45. Therefore, the given objective function should be zero when the allocation of single number satisfies its constraints. It has been mentioned that the given objective function does not guarantee that the numbers 1 through 9 are shown exactly once in a row, column, and block [8]. However, there is no specific method introduced to avoid this violation in Geem [8], and it is expected that the iteration itself would drive the process to generate the intended solutions. The violation of constraints with zero objective function value (OFV) has been reported in Weyland [26]. Therefore, we propose a modified objective function as follows.

$$\begin{aligned}\text{Minimize } Z = &\sum_{i=1}^{9}\left(\sum_{j=1}^{9} x_{ij} - 45\right)^2 + \sum_{j=1}^{9}\left(\sum_{i=1}^{9} x_{ij} - 45\right)^2 \\ &+ \sum_{r=1}^{9}\left(\sum_{(s,t)\in B_r}^{9} x_{st} - 45\right)^2 + \sum_{i=1}^{9}\left(\sum_{j=1}^{9} S_{ij} - 60\right)^2 + \sum_{j=1}^{9}\left(\sum_{i=1}^{9} S_{ij} - 60\right)^2 \\ &+ \sum_{r=1}^{9}\left(\sum_{(s,t)\in B_r}^{9} S_{st} - 60\right)^2\end{aligned} \tag{13}$$

where $S_{ij} = (x_{ij} - \overline{x})^2$ and $\overline{x} = 5$, which are the deviation and mean value of 1 through 9, respectively. The summation of the deviation for each row is expected to be 60 if the number 1 through 9 are evenly distributed. The use of a square instead of an absolute sign places increased emphasis on the non-negativity condition. Furthermore, the term including S_{ij}, a deviation, ensures that numbers 1 through 9 appears only once in a row, column, and block.

For HS to solve Sudoku in this study, the process follows exactly as indicated in Weyland [26] and Geem [8]. The whole process is summarized in Fig. 2. The solution was generated randomly in accordance with the HMS. New solutions are continuously generated until the maximum number of iterations is met. Each new solution is modified using one of the three methods: memory consideration, pitch adjustment, and random selection. In each step, memory consideration is used to choose a value from one of the existing HM with the probability of HMCR and the random selection was used to choose a value from 1 through 9 in uniformly random with the probability of 1-HMCR. This means that every number in each cell in Sudoku matrix is assigned by either memory consideration or random selection. An additional method with the probability of PAR, called pitch adjustment, is applied to the one already assigned by memory consideration. According to Geem [8], the pitch adjustment adds or subtracts 1 from the originally assigned number with a chance of 1/2 except when the number 1 and 9 has a lower and upper limit. The HM constriction process is presented in Fig. 3.

3.2. *Modification: re-adjustment*

The HS in Geem [8] does not explicitly consider avoiding duplication of each number in each row, column, and block. However, many heuristic approaches adopt certain methods to avoid such duplication. In Pacurib et al. [18], a penalty function is used to avoid duplication, and many other researchers have used a blocking mechanism in methods [14, 16, 22, 23]. The objective function we present in Eq. (9) is much tighter and therefore *encourages* solutions without any duplication in each row, column, and bock, but it does not *require* these solutions. Therefore, at the final stage of each iteration, a number that appeared more than once in each row is replaced with another number that is not present in the current row.

Fig. 4 shows the process of re-adjustment in the final stage of each iteration. Since number 3 appears twice in (a), the first 3 is replaced with a 4 as shown in (b). 4 is an acceptable substitute because it was not present in the row before substitution. If the second cell in (a) is a given number that cannot be replaced, then the second 3 is replaced with a 4. In the case in which there are more than three identical numbers in a row, the substitution process is the same as explained in Fig. 4 except there are additional numbers for substitution. The process finds the position for replacement from left to right. Once the process finds the specific position for the number to replace, a randomly generated number which has not been shown in a row are chosen for the substation. Once done, the next position requiring a substitute is found. It proceeds until all the numbers, 1 to 9, are shown a row. This process increases the chances of finding a solution.

3.3. *Modification: embedding local search*

The performance of local search is in general not as effective as well developed metaheuristics, but it can be embedded into a heuristic to improve the search process of the original method. The *2-opt* algorithm is an improvement technique used for a variety of combinatorial problems, and it can be easily adapted due to its simplicity and easy implementation. The algorithm was first introduced by Croes [4] to solve a traveling salesmen problem, and it has been adapted to many other combinatorial problems since then. To apply the procedure to Sudoku, a single two-way exchange is performed in each row. This is because the final HM of each iteration has a feasible arrangement of numbers in each row after the re-adjustment procedure, and the feasibility of each column is not considered at this stage. However, the number exchange in each row forces the algorithm to search for the best objective function possible by placing each cell's 'single number' in each column as well as each block. Shown below is a *2-opt* algorithm adapted for this study. Fig. 5 presents an example of number exchange in the beginning of an algorithm.

Step 1. Let C be the initial solution provided by the HM with re-adjustment and z its OFV. Set $C^* = c$, $Z^* = z$, $i = 1, j = i + 1$, $nr = 1$, and $i, j \notin G$, where G is set of fixed cell as in Eq. (6)
Step 2. Exchange the numbers in cell i and j in the solution C. If the result of this exchange, C', improve the OFV, $z' < z^*$, then set $z^* = z'$ and $C^* = C'$. If $j < g_{nr}$, where g_{nr} is max number in G^c in each row, then $j = j + 1$; otherwise $i = i + 1$ and $j = i + 1$. If $i < g_{nr}$ then repeat step 2; otherwise set $nr = nr + 1$. If $nr \leq 9$, then repeat step 2; otherwise go to step 3.
Step 3. If $C \neq C^*$, set $C = C^*$, $z = z^*$, $i = 1, j = i + 1$, $nr = 1$ and go to step 2. Otherwise, stop the process and return C^* as the best solution.

4. Experimental results

As mentioned in Weyland [26], the issue of the objective function and the result in Geem [8] demonstrates the need to repeat the experiments before pursuing further analysis for the extendibility of HS. Table 1 shows the result of the problem instance used throughout this study. To compare the specific value, we use the result of HS run in Weyland [26] and Geem [8]. This study verifies that the classic (or original) HS could not find a unique solution for Sudoku puzzle within

10^6 iterations, the number cited in Weyland [26]. Hence, it is logical that the original HS could not find a unique solution within 10^4 times of iterations, the maximum number of iterations cited in Geem [8]. Each set of parameters were tested 20 times for a total of 720 runs. The HS with an objective function in Eq. (12) generates an optimal solution, which is not a feasible solution as shown in Fig. 6. The number placements that violate the single number rule are highlighted.

The proposed objective function, Eq. (13), was used for the rest of the experiments and the classic HS did not generate a unique solution in the given number of iterations. However, as mentioned before, it was reported that HS has been successfully applied to other type of optimization problems and that there are many hybridized HS methods that are capable of generating favorable solutions for a certain problem. Therefore, we modified the procedure as explained in 3.2; the re-adjustment process was added to make each row feasible at the final stage of HM in each iteration. The result of the modification is shown on the second and third column in the right side of Table 1. The value in parenthesis indicates the probability of finding the solution. As shown in the table, the modification seems to be unsuccessful. Many iterations are necessary to increase the probability of finding the optimal solution. However, the re-adjustment modification would be embedded in the beginning of the local search *2-opt* because this two-way exchange algorithm requires a feasible configuration to improve its performance. After adapting the *2-opt* to HS, the result is dramatic as shown in the last column of Table 1. The number indicates the minimum number of iterations to find the optimal solution among the 20 trials in each parameter set.

Through this experiment, it was verified that the HS with embedded *2-opt* — which we refer to as HS2E — generated favorable results for the specific Sudoku problem. However, it was uncertain whether the *2-opt* algorithm was capable of replicating HS2E's performance by itself. This uncertainty questioned the contribution of HS in HS2E. To verify the contribution of 'HS' in HS2E, a randomly generated initial solution was given to a *2-opt* procedure instead of HM in HS2E, and the random solution was compared to the improvised solution in HS. For this evaluation, the parameters were set for HS2E and the test for parameter selection was done.

4.1. Parameter Selection

To select the parameter set, a general full factorial analysis with three factors, multiple levels, and 20 replications generated to provide for Table 1 was conducted. Since there is no dependable OFV for each factor, the number of iterations to find zero OFV serves as the response for this analysis. It was concluded that each of the factors and their interaction—HMS, HMCR, and PAR—are influential to determine the number of iterations necessary.

The main effects graphed in Fig. 7 indicates that the parameter set would be the most effective with (HMS, HMCR, PAR) = (10, 0.7, 0.5). However, the interaction effect does not provide a clear distinction of each parameter as shown in Fig. 8, with the exception of a few sets that must not be combined as a parameter: HMS = 1, HMCR = 0.9, and PAR=0.01. Finally, the tool named 'Response Optimizer', provided in Minitab® and used as a parameter tuning tool, was used to select the best combination of parameters to minimize the number of iterations needed to find the optimal solution; the tool provided the parameter set (HMS, HMCR, PAR) =(10, 0.7, 0.01) as shown in Fig. 9.

The number of iterations is expected to be 37.3 with use of 'the parameter set'. $d = 0.9977$ indicates that the setting is well fit to overall response ($d = 1$ represents ideal case).

4.2. HS2E vs. 2-opt algorithm

With a given parameter set, additional 50 runs were tested. The procedure for HS2E and *2-opt* algorithm were implemented in C++, and executed on an Intel Core i5 class computer with 8GB of memory. Table 2 summarizes the result of these two algorithms.

As shown in Table 2, the proposed HS2E is superior to *2-opt* algorithm because HS2E requires fewer iterations and less solution time than the *2-opt* algorithm. We noticed that the median value of the number of iterations for HS2E is very close to the one generated by a response optimizer ($y = 37.3$). Overall performance indicates that the application of HS as a Sudoku solver is effective for this specific problem when combined with the local search, *2-opt*. We expect that statistical analysis would provide the same result.

4.3. Additional experiments

As mentioned in Section 1, the level of difficulty of a Sudoku puzzle depends on the numbers that are given to the grid in the theoretical count. The example problem in Weyland [26] and Geem [8] has 40 given numbers. The Sudoku puzzles with more than 30 given numbers fall into the 'easy' categories based on the example used in Mantere and Koljonen [14], Pacurib et al. [18], Sato and Inoue [22], and Wang et al. [24]. Thus, we performed additional experiments to test the method's applicability in Sudoku puzzles of varying difficulty. Three instances used in Pacurib et al. [18] were tested for HS2E: easy, medium, and hard. Additional instances in Sato et al. [21] were used for extremely difficult cases: SD1, SD2, and SD3. Table 3 shows the result of the experiment for these six instances. The numbers in parenthesis indicate the number of givens in Sudoku grid. The experiment was repeated 30 times for each problem within 10^6 iterations.

The average iterations are not significant in this experiment because some trials did not find an optimal solution within 10^6 iterations and because we do not have information regarding how far the iterations might proceed. However, the median can be calculated since the majority of trials reached the solution. Through these experiments, it can be inferred that when fewer numbers are given to a Sudoku grid, HS needs more iterations to find a unique solution. This is expected since the given number in Sudoku grid is related to the number of combinations the Sudoku puzzle can have. However, the probability of success is not directly related to the number of givens in Sudoku. The method generated a solution for SD2, named 'Al Escargot' known as the one of the hardest Sudoku puzzles, with 67% of probability of success, which is less than that of SD3. A medium difficulty problem with 29 givens had lower probability of success than that of SD1 with only 24 givens. The data structure inside of a Sudoku grid could affect the chance of finding a solution. We observed that it takes around 8 h to have 10^6 iterations for the medium and hard problems and around 12 h for the very difficult SD1 through SD3.

5. Conclusion and discussion

In this paper, we analyzed the effectiveness of basic harmony search for solving Sudoku puzzles. The effectiveness of harmony search in Sudoku has been a subject of debate. In this research, the contribution of the harmony search was evaluated and the effect of harmony memory construction to local search algorithm was shown by comparing the results of harmony search with that of the local search with a randomly generated initial solution. The improvised procedure in harmony search facilitated the local search to find the optimal solution with a proposed objective function, which was much more specific to the optimality condition.

Even though HS2E was proposed to explore the HS effect as a search procedure to a specific given problem, the HS2E was applied to solve general Sudoku instances other than the one given in the previous research. The experimental result showed that HS2E generated the optimal solution satisfactorily and it is capable of solving extremely difficult problems. However, its probability of success for medium to extremely hard problem is not 100%. Thus, identifying other search methods to embed which will increase the probability of success on difficult problems is an area of focus in the future.

Declaration of Competing Interest

None.

References

[1] K Apt, Principles of Constraint Programming, Cambridge University Press, Cambridge, 2003.

[2] AC Bartlett, TP Chartier, AN Langville, TD Rankin, Integer programming model for the Sudoku problem, J Online Math. Appl 8 (1) (2008).

[3] LC Coelho, G Laporte, A comparison of several enumerative algorithms for Sudoku, J. Oper. Res. Soc. 65 (2014) 1602–1610, https://doi.org/10.1057/jors.2013.114.

[4] GA Croes, A method for solving traveling-salesman problems, Oper. Res. 6 (1958) 791–812, https://doi.org/10.1287/opre.6.6.791.

[5] B Felgenhouer, F Jarvis, Mathematics of Sudoku I, Math Spectr 39 (2006) 15–22.

[6] a ZW Geem, Optimal scheduling of multiple dam system using Harmony Search Algorithm, in: F Sandoval, A Prieto, J Cabestany, M Graña (Eds.), Computational and Ambient Intelligence, Springer, Berlin, Heidelberg, 2007, pp. 316–323.

[7] ZW Geem, Novel derivative of harmony search algorithm for discrete design variables, Appl. Math. Comput. 199 (2008) 223–230, https://doi.org/10.1016/j.amc.2007.09.049.

[8] b ZW Geem, Harmony search algorithm for solving Sudoku, in: B Apolloni, RJ Howlett, L Jain (Eds.), Knowledge-Based Intelligent Information and Engineering Systems, Springer, Berlin, Heidelberg, 2007, pp. 371–378.

[9] ZW Geem, JH Kim, G V Loganathan, A new heuristic optimization algorithm: Harmony Search, Simulation 76 (2001) 60–68, https://doi.org/10.1177/003754970107600201.

[10] ZW Geem, KB Sim, Parameter-setting-free harmony search algorithm, Appl. Math. Comput. 217 (2010) 3881–3889, https://doi.org/10.1016/j.amc.2010.09.049.

[11] S Kang, J Chae, Harmony search for the layout design of an unequal area facility, Expert Syst. Appl. 79 (2017) 269–281, https://doi.org/10.1016/j.eswa.2017.02.047.

[12] JH Kim, Harmony Search algorithm: a unique music-inspired algorithm, Procedia Eng 154 (2016) 1401–1405, https://doi.org/10.1016/j.proeng.2016.07.510.

[13] R Lewis, Metaheuristics can solve sudoku puzzles, J. Heuristics. 13 (2007) 387–401, https://doi.org/10.1007/s10732-007-9012-8.

[14] T Mantere, J Koljonen, Solving, rating and generating sudoku puzzles with GA, in: Proceedings of the 2007 IEEE Congress on Evolutionary Computation, CEC 2007, 2007, pp. 1382–1389, https://doi.org/10.1109/CEC.2007.4424632.

[15] DB Mishra, R Mishra, KN Das, AA Acharya, et al., Solving Sudoku puzzles using evolutionary techniques—a systematic survey, in: M Pant, K Ray, TK Sharma, et al. (Eds.), Soft Computing: Theories and Applications, Springer, Singapore, 2018, pp. 791–802.

[16] TK Moon, JH Gunther, JJ Kupin, Sinkhorn solves Sudoku, IEEE Trans. Inf. Theory 55 (2009) 1741–1746, https://doi.org/10.1109/TIT.2009.2013004.

[17] A Moraglio, J Togelius, Geometric particle swarm optimization for the sudoku puzzle, in: Proceedings of the Ninth annual conference on Genetic and evolutionary computation - GECCO '07, ACM Press, New York, 2007, p. 118.

[18] JA Pacurib, GMM Seno, JPT Yusiong, Solving Sudoku puzzles using improved Artificial Bee Colony Algorithm, in: Proceedings of the 2009 Fourth International Conference on Innovative Computing, Information and Control (ICICIC), IEEE, 2009, pp. 885–888.

[19] R Pelánek, Difficulty rating of Sudoku puzzles by a computational model, in: Proceedings of the FLAIRS Conference, 2011.

[20] MP Saka, O Hasançebi, ZW Geem, Metaheuristics in structural optimization and discussions on harmony search algorithm, Swarm Evol. Comput. 28 (2016) 88–97, https://doi.org/10.1016/j.swevo.2016.01.005.

[21] Y Sato, N Hasegawa, M Sato, GPU acceleration for Sudoku solution with genetic operations, in: Proceedings of the 2011 IEEE Congress of Evolutionary Computation, CEC 2011, 2011, pp. 296–303.

[22] Y Sato, H Inoue, Solving Sudoku with genetic operations that preserve building blocks, in: Proceedings of the 2010 IEEE Conference on Computational Intelligence and Games, CIG2010, 2010, pp. 23–29.

[23] H Simonis, Sudoku as a constraint problem, in: B Hnich, P Prosser, B Smith (Eds.), Proceedings of the Fourth International Workshop on Modelling and Reformulating Constraint Satisfaction Problems, 2005, pp. 13–27.

[24] Z Wang, T Yasuda, K Ohkura, An evolutionary approach to sudoku puzzles with filtered mutations, in: Proceedings of the 2015 IEEE Congress on Evolutionary Computation (CEC), 2015, pp. 1732–1737.

[25] D Weyland, A Rigorous Analysis of the Harmony Search Algorithm: How the research community can be misled by a "Novel" methodology. Modeling, Analysis, and Applications in Metaheuristic Computing, IGI Global, 2010, pp. 72–83.

[26] D Weyland, A critical analysis of the harmony search algorithm-How not to solve sudoku, Oper. Res. Perspect. 2 (2015) 97–105, https://doi.org/10.1016/j.orp.2015.04.001.

[27] D Zou, L Gao, J Wu, et al., A novel global harmony search algorithm for reliability problems, Comput. Ind. Eng. 58 (2010) 307–316, https://doi.org/10.1016/j.cie.2009.11.003.

An ensemble machine learning model for the prediction of danger zones: Towards a global counter-terrorism

Major Das, *Department of Computer Scinece Engineering , Raajdhani Engineering College, Bhubaneswar, major.das556@gmail.com*

Srimanta Mohapatra, *Department of Computer Scinece Engineering , NM Institute of Engineering & Technology, Bhubaneswar, srimantamohaparta66@gmail.com*

Sanjay Kumar Padhi, *Department of Computer Sciencel Engineering, Aryan Institute of Engineering & Technology, Bhubaneswar, sk.padhi2@gmail.com*

Subrat Dash, *Department of Computer Scinece Engineering , Capital Engineering College, Bhubaneswar, subratdash43@gmail.com*

A R T I C L E I N F O

Keywords:
Terrorism
Ensemble machine learning
Danger zones
Support vector machine

A B S T R A C T

Terrorism can be described as the use of violence against persons or properties to intimidate or coerce a government or its citizens to some certain political or social objectives. It is a global problem which has led to loss of lives and properties and known to have negative impacts on tourism and global economy. Terrorism has also been associated with high level of insecurity and most nations of the world are interested in any research efforts that can reduce its menace. Most of the research efforts on terrorism have focused on measures to fight terrorism or how to reduce the activities of terrorists but there are limited efforts on terrorism prediction. The aim of this work is to develop an ensemble machine learning model which combines Support Vector Machine and K-Nearest Neighbor for prediction of continents susceptible to terrorism. Data was obtained from Global Terrorism Database and data preprocessing included data cleaning and dimensionality reduction. Two feature selection techniques, Chi-squared, Information Gain and a hybrid of both were applied to the dataset before modeling. Ensemble machine learning models were then constructed and applied on the selected features. Chi-squared, Information Gain and the hybrid-based features produced an accuracy of 94.17%, 97.34% and 97.81% respectively at predicting danger zones with respective sensitivity scores of 82.3%, 88.7% and 92.2% and specificity scores of 98%, 90.5% and 99.67% respectively. These imply that the hybrid-based selected features produced the best results among the feature selection techniques at predicting terrorism locations. Our results show that ensemble machine learning model can accurately predict terrorism locations.

1. Introduction

Terrorism is a global menace which has stayed with humanity since the ancient times. It is a global concern because it has led to loss of lives, properties and insecurity, both nationally and globally. Previous studies have shown that the level of insecurity and uncertainty caused by terrorism has influenced decision-making to the extent that many people now make more conservative and less risky decisions often as a way of compensating for the feelings of insecurity caused by the disasters associated with terrorism [1]. One of the most popular terrorist activities is the 9/11 which has not only been recorded as one of the deadliest single attacks in history but also has attracted world's attention to the dire need of investigating, predicting and cubing this social and economic enemy called terrorism. Although terrorism has often been defined in a way that is specific to the subject-matter of the particular convention, it is described by Title 22 of the U. S. code as politically motivated violence perpetrated in a clandestine manner against non-combatants [2]. It is often committed so as to create a fearful state of mind in an audience very often different from the victims. Although some have argued that terrorism has some positive implications, the fact is that it cannot be reasonable even if it was later discovered to be benign [3]. This was premised on the fact that any action exhibited against a representative public order is an illicit act and can be characterized as oppressive and illegitimate. This is because terrorism itself is associated with violence, extremism, intimidation and acts against public and social order [4]. Terrorism has also been found to be associated with anti-colonial movement, cruelty and rivalry among political opponents [5, 6].

The inclinations and impacts of terrorist activities are often quantified and assessed by the number of incidents and casualties [4]. The causes of terrorism can be categorized into three layers; the situational factor, the strategic factors and the individual factors [6]. The situational factors include conditions that allow the possibility of radicalization and motivate feelings against the enemy as well as specific triggers for actions. The factors may, in the short run, mean an act to advertise a course; but its long term (strategic) factors may point to a political change, nationalists, and revolution or separatist movements. It may also seek to disrupt and discredit the process of government, influence public attitude and prevent good governance, instill fear and sympathy as well as provoke a counter-reaction to legitimize their grievances. The individual factors deal with the worldview, psychology and character traits of terrorists. It assumes that terroristic personality or predisposition exists in humans.

The danger of terrorism to lives and properties in a global sense and the need to cub it is a good justification for this work. The impact of the application of machine learning and artificial intelligence to curbing the spread of terrorism cannot be overemphasized, the techniques of which can help prevent and combat terrorism, help the government and other policy-makers make informed decisions, concertize citizens and pilgrims on the kind of terrorism activities a particular region is exposed to and, indeed provide a cost-effective means of protecting lives and properties of citizens [5-9]. Machine learning can be used to make predictions about terrorism with such information as financial transactions, travel patterns, activities, as well as publicly available information such as social media. The expected outcome of this study will highlight the importance of global terrorism data and the ability to obtain useful information from them vis-à-vis counter-terrorism [10, 11].

Datasets for machine learning prediction may contain hundreds of attributes, many of which may be irrelevant to the mining task, hence, the need for feature selection. Feature selection is an important exercise for providing further insights and pre-insights into any given dataset. It can also form a crucial part of data preprocessing especially in the case of machine learning models [12, 13]. It helps in assigning a score to the predictive variables based on how the explain the target variable [14]. Feature importance can be manual, statistical or machine learning based. Chi-Square feature selection compares each feature against the target variable to measure their relative dependence which has been widely used in literature [15-17]. Information gain is another effective feature selection technique. It works by calculating the reduction in entropy by splitting the dataset according to a given value of a random variable. Information gain is defined in Eqs. (1), (2) and (3).

$$\mathrm{Gain}(\mathrm{S_j}) = E(\mathrm{P_i}) - E(\mathrm{S_j}) \tag{1}$$

whereas

$$\mathrm{E}(\mathrm{P_i}) = \sum_{i=1}^{n} \mathrm{P_i}\log_2 \mathrm{P_i} \tag{2}$$

and

$$\mathrm{E}(\mathrm{S_j}) = \sum_{i=1}^{s_j} \mathrm{I_j} * \mathrm{E}(\mathrm{Y_j}) \tag{3}$$

where $\mathrm{P_i}$ is the ratio of conditional attribute P in the given dataset, $\mathrm{S_j}$ is the index for each attribute. The information gain implementation yields scores for each attribute which ranks based on importance. The higher the information gain score, the more contributive the feature is to the target variable.

Some research works have been done in the application of statistical, machine learning and deep learning techniques to the Global Terrorism Database (GTD) towards countering global terrorisms. Some authors have applied machine learning techniques such as Naïve Bayes (NB), K-Nearest Neighbors (KNN), Decision Trees and Support Vector Machine (SVM) to predict the terrorist groups responsible for a given incident [18, 19]. Some authors have also developed a recommender system using deep learning to predict the rate at which terrorists spread online propaganda [20]. A hazard grading model has been developed for the quantification of terrorist attacks using K-Means clustering [21]. The success of terrorist activities has also been predicted using Decision Tree Algorithms [22]. Some researchers also predicted if a particular terrorist attack is targeted at a government official, civilians, military, business or others [23]. Similar work on the computational approaches to terrorism prediction have also been reported in previous studies [24, 25] and [26]. Whether a given terrorist attack will be claimed by a known group or not has also been established by recent researchers using different machine learning techniques [27]. In another dimension, it is noted that none of these works has predicted locations, that is, continents where a given kind of terrorism can occur. This is a novelty of this work. Such information can aid the War on Terrorism, improve security consciousness and serves as good advice for tourists. In this work, we proposed an ensemble computational model for the prediction of danger zones as it relates to terrorism attacks.

2. Materials and methods

2.1. Study workflow

We developed a workflow for the study to guide the project execution. This workflow includes preprocessing, feature selection, training, testing and prediction (Fig. 1). It shows the systematic approach taken by the researchers in actualizing the study. The Global Terrorism Database (GTD) was used for this study. The dataset was preprocessed and split into training and testing. The ensemble machine learning model consists of Support Vector Machine (SVM) and K-Nearest Neighbors (KNN). The system learned from the training set and its efficiency was evaluated with the testing set. This bottom up approach helped us to anticipate all that could be needed for the study and we made efforts towards getting them. These components are described in the following sub-sections.

2.2. Data description

In this study, we obtained terrorism dataset from the University of Maryland's online repository known as the Global Terrorism Database (GTD). The data is maintained by the National Consortium for the Study of Terrorism and Responses to Terrorism (START). The data description shows that an incident is categorized and recorded as terrorism if it meets any two of these three criteria: (1) if it is intentional, (2) if it entails some level of violence or immediate threat of violence and (3) if the perpetrators of the violence are sub-national actors. This dataset contains incidents of terrorism and attacks that were collected from news sources all over the world [28]. The GTD contains 181,691 instances of recorded incidents of terrorism attacks recorded from July 1970 to December 2017 from all countries of the world (Fig. 2, Table 1). The dataset has 139 attributes, many of which are sparse due to missing data. Detailed description of this dataset is available elsewhere [28-30]. In order to give our model a very good statistical power and to reduce fitting error, we removed all the attacks that do not have complete information required for the modeling.

2.3. Data pre-processing

The GTD was preprocessed via data cleaning, discretization, duplicate removal and normalization. To clean the data, columns which describe the same features were combined and only one of such was retained and some extracted features replaced some feature subset. For instance, we removed the column for event ID and retained day, month and year of occurrence. Columns with 20% or less of missing data were also removed to reduce the effect of missing data on our model. This reduced the number of features from 139 to 46. Data discretization was

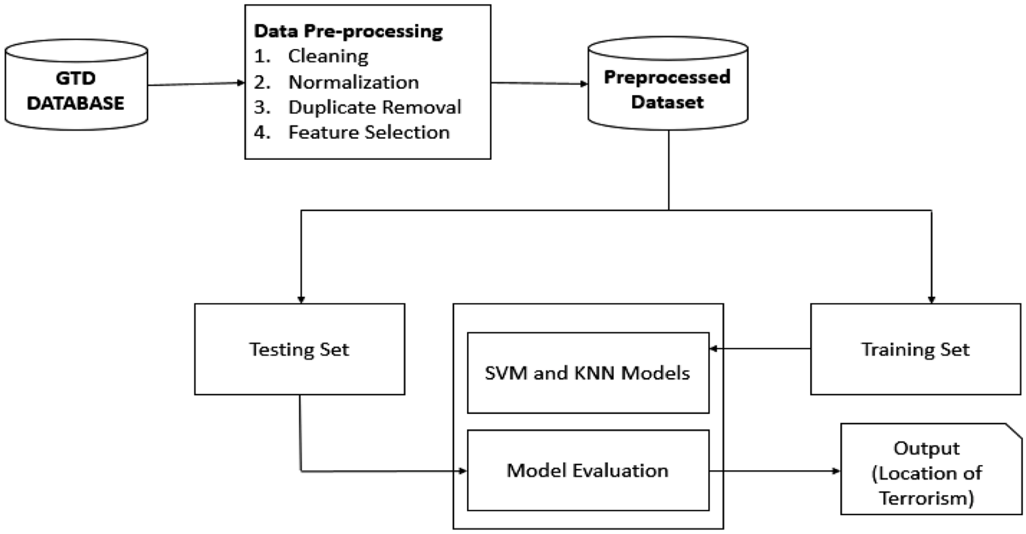

Fig. 1.. Workflow of the proposed model.

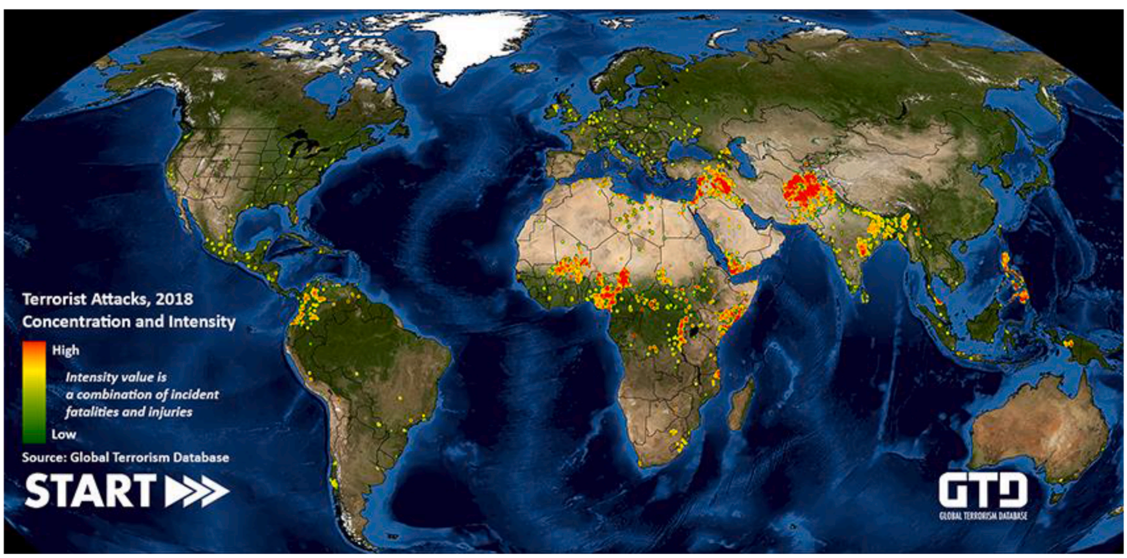

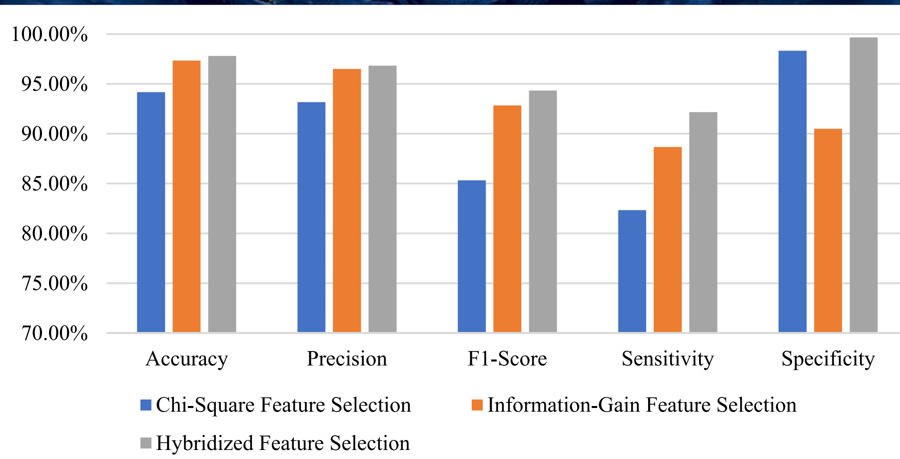

Fig. 2.. Map of the world showing the incidence of Terrorism
Source: Global Terrorism Data (https://start.umd.edu/news/global-terrorism-decreases-2018-recent-uptick-us-terrorist-attacks-was-sustained); Fig. 2: Performance metrics visualization.

Table 1.
Confusion matrix of the model predicting continents of terrorist attacks.

CLASS LABELS		Predicted						
		NA	AS	EU	SA	AF	OC	Total
	NA	4403	29	0	61	1	0	4494
Actual	AS	14	33,401	139	78	159	2	33,793
	EU	1	179	6747	0	73	0	7000
	SA	61	48	3	6109	0	0	6221
	AF	5	354	67	0	7920	3	8349
	OC	0	9	0	0	25	68	102
	Total	4484	34,020	6956	6248	8178	73	59,959

Note: NA → North America, AS → Asia, EU → Europe, SA → South America, AF → Africa, OC → Oceania.

done by converting the nominal fields in the GTD dataset into corresponding numerical values and data normalization was done using Eq. (4).

$$z = (x - \min(x))/(\max(x) - \min(x)) \tag{4}$$

where min and max are the respective minimum and maximum values for feature x and z is the normalized feature. Normalization is important because it reduces the variance of dataset thereby improving the fitness of our model and reducing bias. The countries were grouped into continents and each instance was assigned a continent code generated using longitude and latitude.

2.4. Feature selection

Two filter-based feature selection methods (Chi-Square and Mutual Information Gain) were used in this study to determine the "best fit" features in the pre-processed GTD datasets. This allowed us to:

I identify and focus on the most important features and
II reduce computation time because less features are relatively computationally less expensive.

Chi Squared and Mutual Information Gain helped in the individual ranking of the GTD features from which we selected features with higher scores. Hybrid selection was done by selecting the intersection of both selection techniques.

2.5. Modelling and implementation

Following data pre-processing and feature selection, we proceeded to the development of a predictive model using the selected features. Our target was to predict the continents of terrorist attack. Our prediction model is a mapping function which consists of the training dataset S of the original features. If n datasets are selected randomly for training the models using the known relevant attributes, the mapping $\xi : X_{j.k} \rightarrow Y_k$ defined as $\xi(X_{j.k}) = Y_k \ \forall$ terrorism incidents, k; where $X_{j.k}$ are the set of attributes, j is the incident counter Y is the output – predicted – class. Ensemble models are preferred to single models in order to reduce bias and increase the predictive power of the developed system. The motivation for using ensemble models is to reduce the generalization error of the prediction [31]. The base models used for the ensemble model were SVM and KNN. The dataset was divided to training and testing using ratio 70:30.

SVM and KNN are well known machine learning techniques used for classification and they are well described elsewhere [32-34]. SVM is a supervised machine learning technique used for labelled prediction. It uses the training set to learn the differences between groups to be classified. It is also called a maximum-margin classifier because it works by finding the optimal margin that best separates the groups to be classified SVM has a wide area of application because it can work with both linear and non-linear data. It also works well with high dimensional data and has high flexibility in modeling data from different sources [35]. In the SVM model, radial basis function (RBF) was used to handle the non-linearity in the data because it gave a very good result during experimentation. Details of KNN models can be found elsewhere [36-38]. KNN is also a supervised machine learning algorithm used for classification. Similar to SVM, KNN has application in many fields such as pattern recognition, data mining and intrusion detection. It is non-parametric which means that it does not make any assumption about the distribution of the data. It also uses the training set to learn the differences between groups to be classified. We evaluated the predictive power of the model using measures of sensitivity, specificity, accuracy and Area Under Curve (AUC).

3. Results

The data preprocessing reduced the number of features in the dataset to 21, these are Month of occurrence, Day of occurrence, Region of occurrence, Location, if it is intentional, if it entails some level of violence or immediate threat of violence and if the perpetrators of the violence must be sub-national actors, Is event clearly a terrorism, Connected to other Attacks, Is Suicide, Type of Attack, Target Type, Nationality of Target, Group Name Known, Not Affiliated to Group, Type of Weapon, Number of Fatalities, Property Damaged, Victims in Hostage, Ransom Given, Terrorism successful. The features selected from the hybridized feature selection process were collated and passed to the implemented ensemble classifier. The result of the prediction is presented in the confusion matrix in Table 1 while Table 2 shows the sensitivity, specificity and Area Under Curve (AUC).

The result shows that North America, Asia and South America have a high sensitivity of 0.98 while North America and Europe have a high sensitivity of 0.98. North America and South America produced the highest Area Under Curve of 0.99.

Table 2 shows that the AUC for the classes ranged from 0.83 to 0.99 with North America having the highest area and Oceania having the least. Also, the sensitivity ranged from 0.63 to 0.98 with the North America having the highest value and Oceania with the least value. The specificity ranged from 0.92 to 0.98 with North America having the highest value and South America having the least value.

Table 3 shows the summary result for the performance of the three models, i.e. the ensemble model using Chi Square feature selection, Information Gain feature selection and the hybridized method which combines the two. The result shows that the model built using the hybridized feature selection method gave the best performance in all the

Table 2.
Performance of the model per continent showing the sensitivity, specificity and AUC.

	Sensitivity	Specificity	AUC
NA	0.98	0.98	0.99
AS	0.98	0.96	0.98
EU	0.96	0.98	0.98
SA	0.98	0.92	0.99
AF	0.95	0.97	0.97
OC	0.67	0.93	0.83

Note: NA → North America, AS → Asia, EU → Europe, SA → South America, AF → Africa, OC → Oceania, AUC – Area Under the Curve.

Table 3.
Summary results of all the ensemble model using three feature selection techniques.

Performance Metrics	Chi-Square Feature Selection	Information-Gain Feature Selection	Hybridized Feature Selection
Accuracy	94.17%	97.34%	97.81%
Precision	93.17%	96.50%	96.83%
F1-Score	85.33%	92.83%	94.33%
Sensitivity	82.33%	88.67%	92.17%
Specificity	98.33%	90.50%	99.67%
Execution time	83.50s	81.47s	60.13s

performance metrics i.e. sensitivity, specificity, accuracy, precision and execution time. This is further visualized in Fig. 2.

4. Discussion

We developed 3 models for predicting the continent of terrorist attack using ensemble algorithm. The first one was based on Chi-Square future selection, the second was based on Information Gain feature selection while the third was based on the combination of Chi-Square and Information Gain called the hybridized method. Our results show that the hybridized model performed better than the other two. The hybridized model gave accuracy, sensitivity and specificity of 97.81%, 92.17% and 99.67% respectively which suggests that our model gave an excellent performance. These results depicts that the variables selected using the combination of Chi-Square and Information Gain predicts with a high accuracy the continent in which such a terrorism incident can occur

The main strength of this work is the use of machine learning in the prediction of location in which a given terrorism incident can occur. Previous works on the GTD have investigated features such as the extent of damage of attacks, likelihood of success of a terrorism attempt, likely targets of a terrorism incident and groups likely to be perpetrate an attack. To the best of our knowledge, none of the existing study worked on predicting the location of a terrorist attack. Another strength is the use of ensemble model that allowed us to combine two machine learning techniques namely SVM and KNN. This could explain the reason why the proposed model gave an excellent result. The choice of KNN and SVM was another strength. They are known to be fast and perform to be good with large dataset [39, 40]. GTD is a large dataset and the proposed model ran within 60.13 s which shows that it was time efficient.

One weakness identified in this study is that continent was predicted even though we believed that predicting countries will be better. However, this was avoided because this will amount to too many categories and machine learning models may not give a good result when the categories are many.

5. Conclusion

This study proposed an ensemble machine learning model which combines Support Vector Machine and K-Nearest Neighbor for prediction of continents susceptible to terrorism. Feature selection was used three feature selection techniques, Chi-squared, Information Gain and a hybrid of both methods. Our results show that ensemble machine learning model can accurately predict terrorism locations. Our results further showed that a combination of feature selection techniques offer an advantage over a single technique. This work established that terrorist location can be predicted using computational technique. This has a huge implication in the fight against terrorism and in protection of life and properties.

References

[1] K. Sacco, V. Galletto, E. Blanzieri, How has the 9/11 terrorist attack influenced decision making? Appl. Cogn. Psychol. 17 (2003) 1113–1127.
[2] T. Kapitan, Terrorism in the Arab-Israeli conflict, Terrorism (2004) 175–191.
[3] J.M. Sorel, Some questions about the definition of terrorism and the fight against its financing, Eur. J. Int. Law 14 (2003) 365–378.
[4] B.S. Frey, S. Luechinger, A. Stutzer, Calculating tragedy: assessing the costs of terrorism, J. Econ. Surv. 21 (2007) 1–24.
[5] M. Abdalsalam, C. Li, A. Dahou, S. Noor, A Study of the Effects of Textual Features on Prediction of Terrorism Attacks in GTD Dataset, Eng. Lett. 29 (2021).
[6] D.D. Atsa'am, R. Wario, F.E. Okpo, TerrorClassify: an algorithm for terror groups placement into hierarchical categories of casualties and consequences, J. Appl. Secur. Res. 15 (2020) 568–579.
[7] L. Hellmueller, V. Hase, P. Lindner, Terrorist Organizations in the News: A Computational Approach to Measure Media Attention towards Terrorism, Mass Communication and Society, 2021.
[8] S. Tickle, I. Eckley, P. Fearnhead, A Computationally efficient, High-Dimensional Multiple Changepoint Procedure with Application to Global Terrorism Incidence, arXiv preprint, 2020 arXiv:2011.03599.
[9] G.M. Campedelli, M. Bartulovic, K.M. Carley, Learning future terrorist targets through temporal meta-graphs, Sci Rep 11 (2021) 1–15.
[10] M.I. Uddin, N. Zada, F. Aziz, Y. Saeed, A. Zeb, S.A. Ali Shah, et al., Prediction of future terrorist activities using deep neural networks, Complexity 2020 (2020).
[11] A.S. Tawadros, Mapping terrorist groups using network analysis: egypt case study, J. Humanit. Appl. Soc. Sci. (2020).
[12] S. Hooker, D. Erhan, P.-J. Kindermans, and B. Kim, "Evaluating feature importance estimates," 2018.
[13] G. König, C. Molnar, B. Bischl, M. Grosse-Wentrup, Relative feature importance, in: 2020 25th International Conference on Pattern Recognition (ICPR), 2021, pp. 9318–9325.
[14] C. Liu, S. Gong, C.C. Loy, On-the-fly feature importance mining for person re-identification, Pattern Recognit 47 (2014) 1602–1615.
[15] X. Jin, A. Xu, R. Bie, P. Guo, Machine learning techniques and chi-square feature selection for cancer classification using SAGE gene expression profiles, in: International Workshop on Data Mining for Biomedical Applications, 2006, pp. 106–115.
[16] Y. Zhai, W. Song, X. Liu, L. Liu, X. Zhao, A chi-square statistics based feature selection method in text classification, in: 2018 IEEE 9th International Conference on Software Engineering and Service Science (ICSESS), 2018, pp. 160–163.
[17] I.S. Thaseen, C.A. Kumar, A. Ahmad, Integrated intrusion detection model using chi-square feature selection and ensemble of classifiers, Arab. J. Sci. Eng. 44 (2019) 3357–3368.
[18] G.M. Tolan, O.S. Soliman, An experimental study of classification algorithms for terrorism prediction, Int. J. Knowl. Eng.-IACSIT 1 (2015) 107–112.
[19] M. Khorshid, T. Abou-El-Enien, G. Soliman, A comparison among support vector machine and other machine learning classification algorithms, IPASJ Int. J. Comp. Sci. 3 (2015) 26–35.
[20] R.S. Alhamdani, M.N. Abdullah, I.A. Sattar, Recommender System for Global Terrorist Database Based on Deep Learning, Int. J. Mach. Learn. Comput. 8 (2018).
[21] Y. Jun, X. Tong, H. Zhiyi, and L. Yutong, "Hazard Grading Model of Terrorist Attack Based on Machine Learning," 2019.
[22] T. Jani, "Predicting success of global terrorist," 2019.
[23] S.B. Salem, S. Naouali, Pattern recognition approach in multidimensional databases: application to the global terrorism database, Int. J. Adv. Comp. Sci. Appl. (IJACSA) 7 (2016).
[24] M.M. Khorshid, T.H. Abou-El-Enien, G.M. Soliman, Hybrid Classification Algorithms For Terrorism Prediction in Middle East and North Africa, Int. J. Emerg. Trend. Tech. Comp. Sci. 4 (2015) 23–29.
[25] S. Nieves, A. Cruz, Finding Patterns of Terrorist Groups in Iraq: a Knowledge Discovery Analysis, in: Ninth LACCEI Latin American and Caribbean Conference (LACCEI'2011), Engineering for a Smart Planet, Innovation, Information Technology and Computational Tools for Sustainable Development., Medellín, 2011.
[26] M. Adnan, M. Rafi, Extracting patterns from Global Terrorist Dataset (GTD) Using Co-Clustering approach, J. Independ. Stud. Res. 13 (2015) 7.
[27] V. Kumar, M. Mazzara, A. Messina, J. Lee, A Conjoint Application of Data Mining Techniques for Analysis of Global Terrorist Attacks, in: International Conference in Software Engineering for Defence Applications, 2018, pp. 146–158.
[28] G. LaFree, L. Dugan, Introducing the global terrorism database, Terror. Pol. Viol. 19 (2007) 181–204.
[29] L. Dugan, The Making of the Global Terrorism Database and Its Applicability to Studying the Life Cycles of Terrorist, The SAGE handbook of criminological research methods, 2011, p. 175.
[30] G. LaFree, The global terrorism database (GTD) accomplishments and challenges, Perspect. Terror. 4 (2010) 24–46.
[31] A. Diop, N. Emad, T. Winter, M. Hilia, Design of an Ensemble Learning Behavior Anomaly Detection Framework, Int. J. Comp. Inform. Eng. 13 (2019) 551–559.
[32] W.H. Land, J.D. Schaffer, The Support Vector Machine. The Art and Science of Machine Intelligence, ed, Springer, 2020, pp. 45–76.
[33] N. Shafiabady, L.H. Lee, R. Rajkumar, V. Kallimani, N.A. Akram, D. Isa, Using unsupervised clustering approach to train the Support Vector Machine for text classification, Neurocomputing 211 (2016) 4–10.
[34] Y. Zhang, G. Cao, B. Wang, X. Li, A novel ensemble method for k-nearest neighbor, Pattern Recognit 85 (2019) 13–25.
[35] B. Schölkopf, K. Tsuda, J. Vert, Kernel Methods in Computational Biology, ed, MIT Press, 2004, 2004.
[36] T. Thomas, A.P. Vijayaraghavan, S. Emmanuel, Nearest Neighbor and Fingerprint Classification. Machine Learning Approaches in Cyber Security Analytics, ed, Springer, 2020, pp. 107–128.

[37] R. Bandyopadhyay, Varying k-Nearest Neighbours: an Attempt to Improve a Widely Used Classification Model. Smart Intelligent Computing and Applications, ed, Springer, 2020, pp. 1–8.
[38] A.V. Joshi, Support vector machines. Machine Learning and Artificial Intelligence, ed, Springer, 2020, pp. 65–71.
[39] L. Demidova, I. Klyueva, A. Pylkin, Hybrid Approach to Improving the Results of the SVM Classification Using the Random Forest Algorithm, Procedia Comput. Sci. 150 (2019) 455–461.
[40] J. Weston, S. Mukherjee, O. Chapelle, M. Pontil, T. Poggio, V. Vapnik, Feature selection for SVMs, in: Advances in neural information processing systems, 2001, pp. 668–674.

Analysis of French phonetic idiosyncrasies for accent recognition

Ajaya Kumar swain, *Department of Electrical and Electronics Engineering, Aryan Institute of Engineering & Technology, Bhubaneswar, ajayaswain9@gmail.com*

Swarna Manjari Samal, *Department of Electrical Engineering, Aryan Institute of Engineering & Technology, Bhubaneswar, swarnamanjari88@gmail.com*

Sidhanta Kumar Balabantaray, *Department of Computer Scinece Engineering , Raajdhani Engineering College, Bhubaneswar, sk.balabantaray111@gmail.com*

Susmita Mohapatra, *Department of Computer Scinece Engineering , Raajdhani Engineering College, Bhubaneswar, susmitamohapatra963@gmail.com*

A R T I C L E I N F O

Keywords:
Accent recognition
French accent classification

A B S T R A C T

Speech recognition systems have made tremendous progress since the last few decades. They have developed significantly in identifying the speech of the speaker. However, there is a scope of improvement in speech recognition systems in identifying the nuances and accents of a speaker. It is known that any specific natural language may possess at least one accent. Despite the identical word phonemic composition, if it is pronounced in different accents, we will have sound waves, which are different from each other. Differences in pronunciation, in accent and intonation of speech in general, create one of the most common problems of speech recognition. If there are a lot of accents in language we should create the acoustic model for each separately. We carry out a systematic analysis of the problem in the accurate classification of accents. We use traditional machine learning techniques and convolutional neural networks, and show that the classical techniques are not sufficiently efficient to solve this problem. Using spectrograms of speech signals, we propose a multi-class classification framework for accent recognition. In this paper, we focus our attention on the French accent. We also identify its limitation by understanding the impact of French idiosyncrasies on its spectrograms.

1. Introduction

Accent recognition is one of the most important topics in automatic speaker and speaker-independent speech recognition (SI-ASR) systems in recent years. The growth of voice-controlled technologies has becoming part of our daily life, nevertheless variability in speech makes these spoken language technologies relatively difficult. One of the profound variability in a speech signal is the accent. Different models could be developed to handle SI-ASR by accurately classifying the various accent types [1]. Such a successful accent recognition module can be integrated into a natural language processor, leading to its wide ranging impact in finance [2], medical science [3], and sustainable environment [4].

Dialect/accent refers to the different ways of pronouncing/speaking a language within a community. Some illustrative examples could be American English versus British English speakers or the Spanish speakers in Spain versus Caribbean. During the past few years, there have been significant attempt to automatically recognize the dialect or accent of a speaker given his or her speech utterance. Recognition of dialects or accents of speakers prior to automatic speech recognition (ASR) helps in improving performance of the ASR systems by adapting the ASR acoustic and/or language models appropriately. Moreover, in applications such as smart assistants as the ones used in smartphones, by recognizing the accent of the caller and then connecting the caller to agent with similar dialect or accent will produce more user-friendly environment for the users of the application.

Most of the existing techniques do not possess good accuracy in identifying the various accents. One of the reasons we are having trouble to have a good accuracy in the accent recognition problem is the lack of knowledge we have of English syllabic structure. In order to approximate English phonology, we have to understand the native language similarities of articulation, intonation, and rhythm. In the past, the research has focused on phone inventories and sequences, acoustic realizations, and intonation patterns. Therefore, it is important to study the English syllable structure. The main problem behind word recognition is the understanding of the syllable. It usually consists of an obligatory vowel with optional initial and final consonants. One familiar way of subdividing a syllable is into *onset* and *rhyme*. All syllables in all languages phonetically at least consist of onset and rhyme. However, these categories alone do not indicate where the syllable is placed within the word. In order to capture foreign accents in English, we want to highlight those constituents of the syllable that are most likely to prove difficult for speakers of languages in which they are not contained [5].

In this paper, we focus on the specifications of the French language. We are interested in identifying the idiosyncrasies [6] of French people that lead a model into predicting the wrong accent.

1.1. Related work

Berkling et al. [5] discussed the tonal and non-tonal languages and their treatment in speech recognition systems. In Kardava et al. [7], they have developed an approach to solve the above mentioned problems and create more effective, improved speech recognition system of Georgian language and of languages, that are similar to Georgian language. Katarina et al. proposed [8], an automatic method of detection of the degree of foreign accent and the results are compared with accent labeling carried out by an expert phonetician. In [9], they give a new approach for modeling allophones in a speech recognition system based on hidden Markov models.

In [10], they studied mutual influences between native and non-native vowel production during learning, *i.e.*, before and after short-term visual articulatory feedback training with non-native sounds. To obtain a speaker's pronunciation characteristics, [11] gave a method based on an idea from bionics, which uses spectrogram statistics to achieve a characteristic spectrogram to give a stable representation of the speaker's pronunciation from a linear superposition of short-time spectrograms. Hossari et al. in [12] used a two-stage cascading model using Facebook's fastTex implementation [13] to learn the word embeddings. Davies et al. presented advanced computer vision methods, emphasizing machine and deep learning techniques that have emerged during the past 5–10 years [14]. The book provides clear explanations of principles and algorithms supported with applications. In [15], Farris present the Gini index and several measures of integrity.

1.2. Contributions of the paper

The main contributions of this paper[1] can be summarized as follows:

- Highlighting the problem of the limit in the context of the study of accent recognition. In this paper, we will show there exists a "natural" limit of the accuracy when it comes to accent classification. The main aim of this work will be to address that limit and give a solution to that problem.
- Highlighting French idiosyncrasies restricting the accuracy values of deep learning models. In this paper, we focused our work on the French speakers. We decided to study the language habits of French speakers that could explain the decrease in precision. Indeed, the English language is an Indo-European Germanic language while the French is a Latin language, which means that their structure is very different. Thus, we will find strongly similar words between the two languages, but the way of pronouncing them will often vary a lot. Thus, the study of these Latin habits is particularly interesting in the context of our work: understanding which aspects of the French language reduce the effectiveness of our models will allow us to better recognize a French accent later on.
- Highlighting the incidence of these idiosyncrasies in the spectrograms, and therefore the models in question. Once we have isolated more clearly the responsible French idiosyncrasies, we determine their real impact on the models used (CNN in our case) by the precise study of spectrograms of vocal samples used. In this case, we will compare different spectrograms for the same sentence and determine the differences between a "French" and "English" spectrogram, for a specific idiosyncrasy.

[1] With the spirit of reproducible research, the code to reproduce the results in this paper is shared at https://github.com/pberjon/Article-Accent-Recognition.

Table 1
Highlighting of French main mispronunciations of the English language.

Usual English pronunciations and French pronunciation
short A, as in fat `French Accent` : pronounced "ah" as in father
long A followed by a consonant, as in gate `French Accent` : pronounced like the short e in get
ER at the end of a word, as in water `French Accent` : pronounced air
short I, as in sip `French Accent` : pronounced "ee" as in seep
long I, as in kite `French Accent` : elongated and almost turned into two syllables: [ka it]
short O, as in cot `French Accent` : pronounced either "uh" as in cut, or "oh" as in coat
U in words like full `French Accent` : pronounced "oo" as in fool

The rest of the paper is structured as follows. Section 2 discusses the data and the methods we used in our preliminary study (dataset and neural networks) and Section 3 discusses results we obtained with these methods. In Sections 4 and 5, we analyzed the French speakers idiosyncrasies and their consequences on spectrograms. Finally, Section 6 concludes the work and discusses our future works.

2. A primer on French speakers idiosyncrasies

In this section, we provide a primer to the readers on the various types of speech idiosyncrasies exhibited by French speakers.

2.1. French-infused vowels

Nearly every English vowel is affected by the French accent [10]. French has no diphthongs, so vowels are always shorter than their English counterparts. The long A, O, and U sounds in English, as in say, so, and Sue, are pronounced by French speakers like their similar but un-diphthonged French equivalents, as in the French words sais, seau, and sou. For example, English speakers pronounce say as [seI], with a diphthong made up of a long "a" sound followed by a sort of "y" sound. But French speakers will say [se] - no diphthong, no "y" sound. English vowel sounds which do not have close French equivalents are systematically replaced by other sounds, as it is showed in Table 1.

2.2. Dropped vowels, syllabification, and word stress

French people pronounce all schwas (unstressed vowels). Native English speakers tend toward "r'mind'r", but French speakers say "ree-ma-een-dair". They will pronounce amazes "ah-may-zez", with the final e fully stressed, unlike native speakers who will gloss over it: "amaz's". And the French often emphasize the -ed at the end of a verb, even if that means adding a syllable: amazed becomes "ah-may-zed".

Short words that native English speakers tend to skim over or swallow will always be carefully pronounced by French speakers. The latter will say "peanoot boo-tair and jelly", whereas native English speakers opt for pean't butt'r 'n' jelly.

Because French has no word stress (all syllables are pronounced with the same emphasis), French speakers have a hard time with stressed syllables in English, and will usually pronounce everything at the same stress, like actually, which becomes "ahk chew ah lee". Or they might stress the last syllable — particularly in words with more than two: computer is often said "com-pu-TAIR".

2.3. French-accented consonants

H is always silent in French, so the French will pronounce happy as “appy”. Once in a while, they might make a particular effort, usually resulting in an overly forceful H sound — even with words like hour and honest, in which the H is silent in English. J is likely to be pronounced “zh” like the G in massage. R will be pronounced either as in French or as a tricky sound somewhere between W and L. Interestingly, if a word starting with a vowel has an R in the middle, some French speakers will mistakenly add an (overly forceful) English H in front of it. For example, arm might be pronounced “hahrm”.

TH’s pronunciation will vary, depending on how it is supposed to be pronounced in English:

- voiced TH [ð] is pronounced Z or DZ: “this” becomes “zees” or “dzees”
- unvoiced TH is pronounced S or T: “thin” turns into “seen” or “teen”

Letters that should be silent at the beginning and end of words (psychology, lamb) are often pronounced.

3. Accent recognition system

3.1. Features for detecting accents

Spectrograms are pictorial representation of sound we can use for speech recognition [11]. The x-axis represents time in seconds while the y-axis represents frequency in Hertz. Different colors represent the different magnitude of frequency at a particular time. We can think of the spectrogram as an image. Fig. 1 represents a sample speech single and its corresponding spectogram. Once the audio file is converted to an image, the problem reduces to an image classification task. Based on the number of images, algorithms like Support Vector Machines (SVM), *etc.* are used to classify sound, validate the speaker.

3.2. Our proposed framework for detecting accents

We used different Machine Learning and Deep Learning models, and the first one is a two convolutional layers neural network with 5 different accents as shown in Fig. 2. This neural network is a 2-layer Convolutional Neural Network: one with 32 filters and a ReLu activation function, and another one with 64 filters and a ReLu activation function.

We will focus on this 2-layer CNN for the rest of our work.

4. Results and discussion

4.1. Dataset

Everyone who speaks a language, speaks it with an accent. A particular accent essentially reflects a person’s linguistic background. When people listen to someone speak with a different accent from their own, they notice the difference, and they may even make certain biased social judgments about the speaker. In this paper, we used the Speech Accent Archive [16]. It has been established to uniformly exhibit a large set of speech accents from a variety of language backgrounds. The distribution of speech signals across the five languages is represented in Fig. 3. Native and non-native speakers of English all read the same English paragraph and are carefully recorded.

This dataset allows us to compare the demographic and linguistic backgrounds of the speakers in order to determine which variables are key predictors of each accent. The speech accent archive demonstrates that accents are systematic rather than merely mistaken speech. It contains 2140 speech samples, each from a different talker reading the same reading passage. Talkers come from 177 countries and have 214 different native languages. Each talker is speaking in English. The samples were collected by many individuals under the supervision of Steven H. Weinberger, the most up-to-date version of the archive is hosted by George Mason University and can be found here: https://www.kaggle.com/rtatman/speech-accent-archive. [16]

Table 2
Average accent classification accuracy across the different languages using various benchmarking models.

Comparison of SVM and CNNs				
Model	Overall ACC	F1 Macro	F1 Micro	Hamming Loss
SVM	0.3518	0.33458	0.33458	0.38043
2-layer CNN	0.70652	0.405	0.70652	0.29348
4-layer CNN	0.6529	0.52	0.73913	0.26087

4.2. Accent recognition metric

In order to provide an objective evaluation of the accent recognition task, we compute the overall accuracy, F1-macro, F1-micro and hamming loss [17]. These metrics are defined as:

$$ACC = \frac{tp + tn}{(tp + fp) + (tn + fn)}$$

$$F1_{macro} = \frac{1}{N}\sum_{i=1}^{N} F1_i$$

$$F1_{micro} = 2\frac{Micro-precision * Micro-recall}{\text{Micro-precision} + \text{Micro-recall}}$$

$$HL = \frac{1}{NL}\sum_{i=1}^{N}\sum_{l=1}^{L} Y_{i,l} \oplus X_{i,l}$$

In the overall accuracy formula, tp, tn, fp, fn stand respectively for true positive, true negative, false positive and false negative. In the Hamming loss formula, $\oplus$ denotes exlusive-or, $X_{i,l}$ ($Y_{i,l}$) stands for boolean that the ith datum (ith prediction) contains the lth label

Table 2 demonstrates the evaluation metric obtained via SVM technique and two variants of CNN model.

With regular machine learning methods as SVM, we obtained low accuracy of 0.35. As expected, the impact of Deep Learning methods [14] is quite clear here. We observe from Table 2, that the Convolutional Neural Networks achieves an accuracy of 0.65. However, we observe that we do not obtain an optimal score if we use too many layers in our model. Depending upon how large our dataset is, the CNN architecture is implemented. Adding layers unnecessarily to any CNN will increase our number of parameters only for the smaller dataset. It is true for some reasons that on adding more hidden layers, it will give a better accuracy. That is true for larger datasets, as more layers with less stride factor will extract more features for the input data. In CNN, how we play with the architecture is completely dependent on what our requirement is and how our data is. Increasing unnecessary parameters will only overfit your network, and that is the reason why our CNN with 2 layers has better results than with 4.

A macro-average will compute the metric independently for each class and then take the average (hence treating all classes equally), whereas a micro-average will aggregate the contributions of all classes to compute the average metric. In a multi-class classification setup, micro-average is preferable if we suspect there might be class imbalance issue (*i.e.* we may have many more examples of one class, as compared to other classes). Table 2 explains this scenario clearly. We observe that neural networks show better F1-score values in the context of multi-class classification. In such situation, Hamming Loss is a good measure of model performance. The lower the Hamming loss, the better is the model performance. In our case, Hamming loss ranges from 0.26 till 0.39, which is considered as good results, especially in the context of 5-class multi-class classification problem.

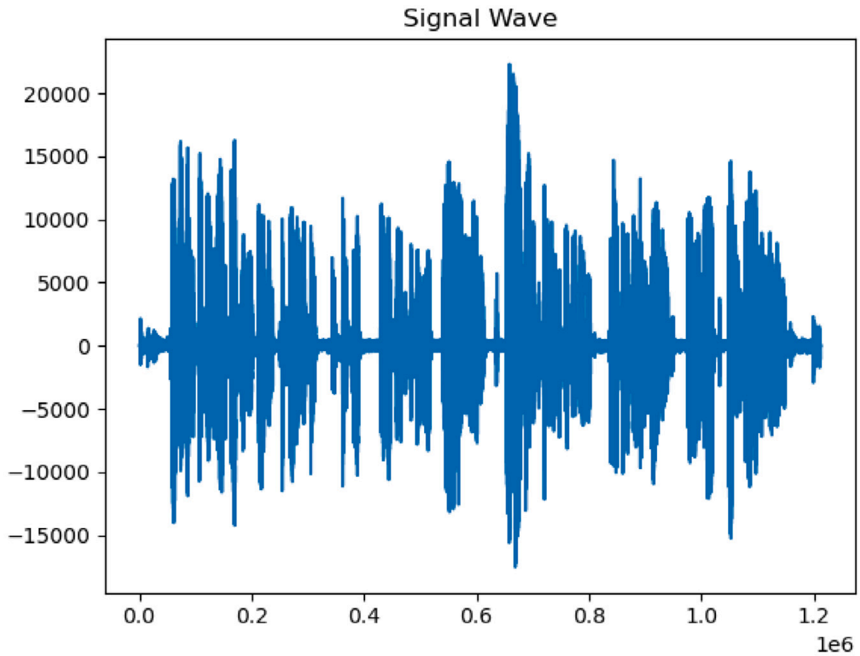

(a) Signal

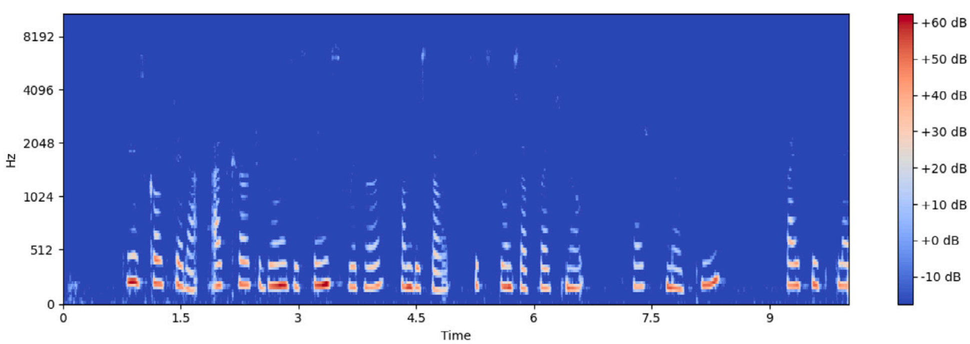

(b) Spectrogram

Fig. 1. Signal and spectrogram of a french accent sample.

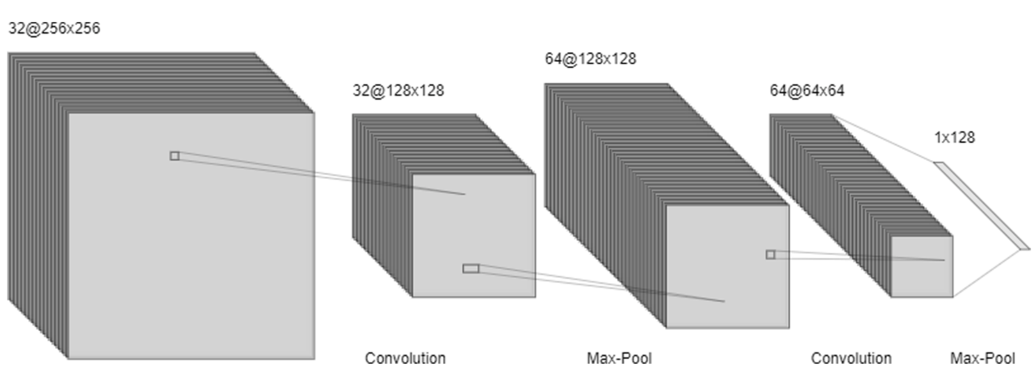

Fig. 2. CNN with 2 layers with ReLu activation function.

Table 3
Multi-class classification metric values using the SVM model.

SVM				
Classes	ACC	AGF	AUC	GI
English	0.42391	0.21774	0.36781	−0.26437
Arabic	0.71739	0.0	0.5	0.0
French	0.34783	0.51315	0.49171	−0.01658
German	0.92391	0.0	0.5	0.0
Hindi	0.95652	0.0	0.5	−0.01124

Table 4
Multi-class classification metric values using our proposed 2-layer CNN model.

2-layer CNN				
Classes	ACC	AGF	AUC	GI
English	1.0	1.0	1.0	1.0
Arabic	0.95	0.71	0.74	0.48
French	0.85	0.84	0.84	0.69
German	0.84	0.80	0.80	0.61
Hindi	0.87	0.32	0.53	0.06

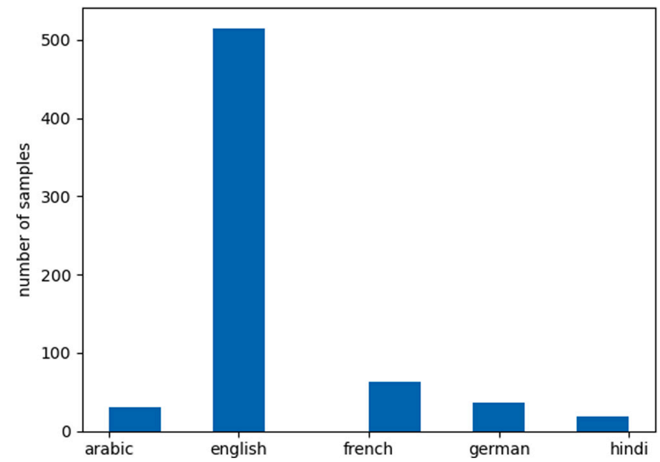

Fig. 3. The distribution of the samples across the five languages in the dataset.

4.3. Multi-class accent recognition metric

In this case of multi-class classification, we are considering ACC, AGF, AUC and GI.

$$ACC = \frac{tp + tn}{tp + tn + tp + tn}$$

$$AGF = (1 + \beta^2)\frac{precision * recall}{(\beta^2 * precision) + recall}$$

$$AUC = \frac{recall + sensibility}{2}$$

$$GI = 1 - \sum_{j=1}^{n} p_j^2 = 1$$

We obtained these results in the confusion matrices with the 2-layer CNN and the SVM method:

Table 3 indicates that the results for Arabic, Hindi and German accents are better. This can easily be explained by the size of the data sets corresponding to each accent. This is a result that shows fairly well the limit of *classical* machine learning algorithms. This limit in the evaluation scores for classical machine learning models are also observed in the broad areas of network security [18] and computer vision [19]. In this specific application of accent recognition, we observe that an increase in the number of vocal samples do not lead to an increased accuracy values. This difference is due to the lack of capacity of the SVM which has difficulty processing information as complex as images.

Table 4 indicates that the results are much more harmonized between the different accents. We still do not have a perfect match between the size of the dataset and the performance of the model, but the disparities between accents disappear.

We can observe from Tables 3 and 4 that the *classical* machine learning methods are quite ineffective and that the deep learning methods stand out clearly in accent recognition; that is why we will use the 2-layer CNNs as a reference for the rest of the paper. In most case, the SVM method is not powerful enough for us to have a good accuracy. That can be explained with the results we obtained on the Gini Index [15]. The values obtained by the index are quite low (negative values are considered quite low positive values), which means that in the case of SVM, the spectrograms are similar in nature. Such SVM methods are not selective enough to clearly determine the accent (which is also shown by the AGF values). However, the SVM method is not totally to be excluded: in the context of the Hindi accent or the German accent, the SVM turns out to be more effective than all the deep learning methods used.

The total computing time is 1 min and 23 s when our proposed model is executed on Google Colab using GPU.

5. Impact of idiosyncrasies on speech spectrograms

We will now study the idiosyncrasies of the French language and how it impacts the corresponding spectograms of the speech signals.

The spectrogram is a representation allowing to observe the whole of the decomposition spectral voice and speech on the same graphic representation. This tool is precise, informative and reliable to analyze the characteristics of sound production. In a first-cut analysis, we associate the spectrogram with the temporal pace, the power profile and segmentation. More extensively, there are a significant number of indicators, metrics and tools. This includes the fundamental frequency and its derivatives, the alteration of voice and speech, and more generally the assessment of intelligibility. It is its ability to measure vocal alteration that will interest us here. We will focus on primarily two pieces of information given by the spectrogram: amplitude and frequency in our study.

5.0.1. The un-diphthonged "y"

Firstly, we will analyze differences on the spectrograms for the word "Wednesday", where the French speaker is not supposed to use the "y" sound, like it was explained in French-infused Vowels. Here are the spectrograms of an English speaker and a French speaker of the sentence "and we will go meet her Wednesday at the train station" in Fig. 4 and Fig. 5.

We can see, as expected, that at the end of the word (1.3-1.4 for English and 1.05-1.1 for French), the "y" is almost not even pronounced by the French speaker, while the English speaker pronounced it clearly. Indeed, the frequencies used are relatively similar on the whole of the audio sample, but certain syllables are *pressed* with a much higher frequency by a French speaker. Consequently, the corresponding amplitude will be low in magnitude. This explains a clear difference between the perception of a word between a French speaker and an English speaker: the non-native will tend to pronounce English less loudly, but will support certain syllables much more than an English speaker.

5.0.2. Voiced TH [ð] is pronounced Z or DZ

French people tend to say "zees" instead of "these". That is what we can see in the sentence "Please call Stella, ask her to bring these things from the store.".

It is quite complicated to delimit the word "these" in this sentence because it is quite quick, so we will delimit "bring these", as the word "bring" does not represent a major problem for French speakers.

Here, we see that French speakers tend to diminish the importance of the word "bring" but accentuate the word "these", whereas English speakers seem to pronounce the sequence "bring these" at the same

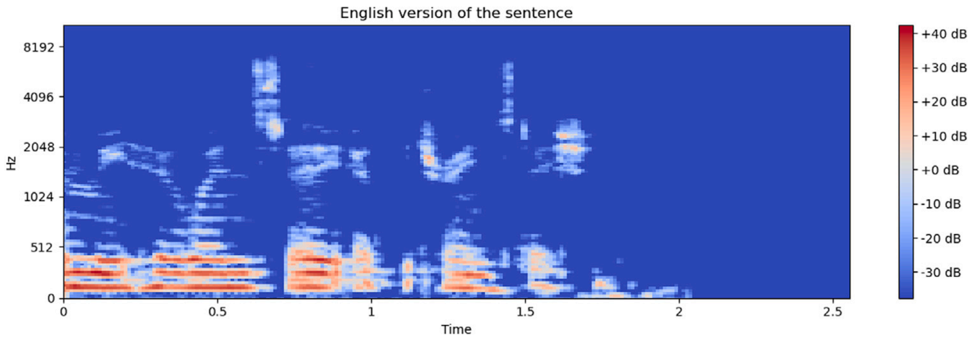

Fig. 4. "Wednesday" in English version: 0.8s-1.4s.

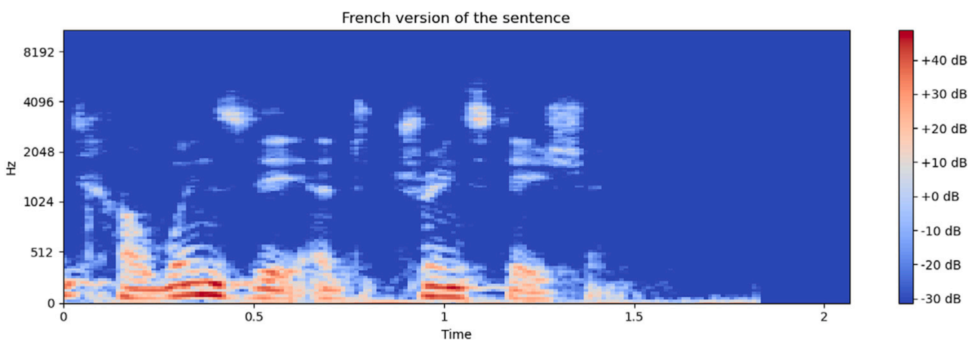

Fig. 5. "Wednesday" in French version: 0.7s-1.10s.

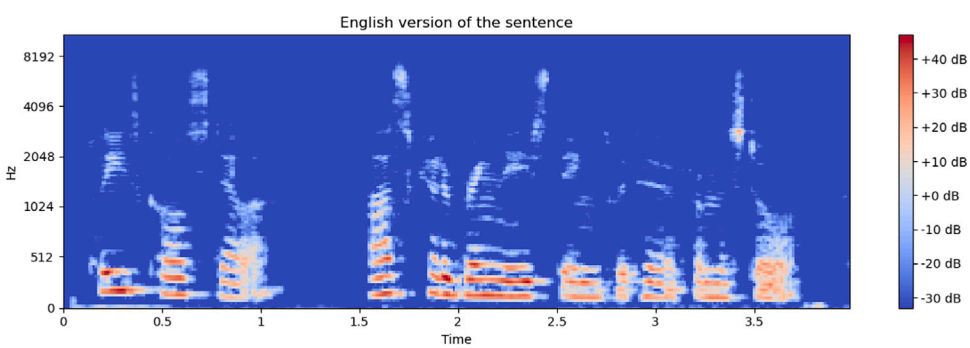

Fig. 6. "Bring these" in English version: 2.5s-3s.

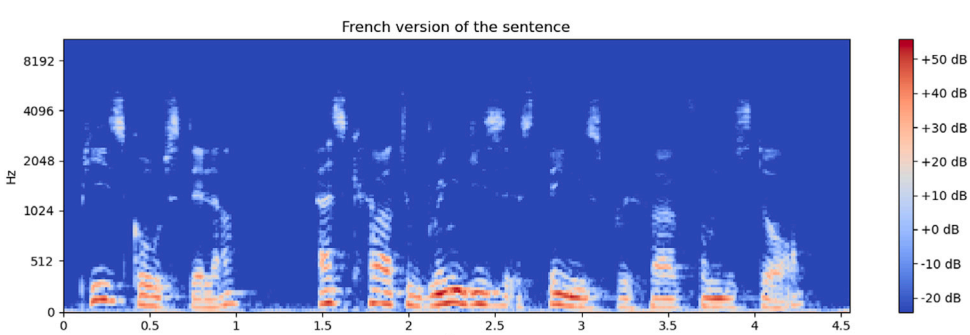

Fig. 7. "Bring these" in French version: 2.6s-3.2s.

frequency (see Fig. 6 and Fig. 7). We remark that is why, for French speakers, the "th" sounds like "z". Indeed, the closest sound to "th" is "z" in the French language, so it is only natural for us to use it. Nevertheless, we believe the reason why they accentuate it (because we could just use the sound "z" more discreetly) is because of the role of words like "these", "the", "this"... They are articles, and in the French language, they tend to accentuate the most important parts of the sentence, which made this French speaker diminish "bring", and accentuate "these".

Thus, French speakers idiosyncrasies have a direct impact on audio samples spectrograms. Then, we can easily understand why these idiosyncrasies have a direct impact on the results of deep learning models:

the first reason why we use spectrograms in order to develop Speech Recognition Systems is to turn an audio classification problem into an image classification problem. Then, if the idiosyncrasies of a specific language have that much effect on spectrograms, that means that the different languages have different spectrograms and this should help the deep learning models to get a better classification between English and French.

6. Conclusions and future work

In this paper, we have concluded that the classical deep learning models are not powerful enough to accurately predict the accent of an user. Therefore, we decided to study the differences between tonal and non-tonal languages, in order to clearly identify the obstacles that prevent us from achieving better results in accent recognition. To fulfill this purpose, we decided to devote our analysis on the French accent, which is a non-tonal language. In this paper, we studied the idiosyncrasies of French speakers: the characteristics of the spoken French language that have a direct impact on the pronunciation of English words by French speakers. In addition, we determined the consequences these idiosyncrasies have on spectrograms, and consequently on the accuracy of deep learning models. In the future, we would like to work further on the subject of French idiosyncrasies, by building a model which determines if an idiosyncrasy is present in an audio sample or not. This would allow us to more easily determine the presence of a French accent in an audio sample. Such accurate recognition of accents in a speech signal will lead to better automatic speech recognition systems.

References

[1] O. Omidvar, J. Dayhoff, Neural Networks and Pattern Recognition, Oxford University Press, 1996, pp. 23–26.
[2] M.S. Islam, E. Hossain, Foreign exchange currency rate prediction using a GRU-LSTM hybrid network, Soft Comput. Lett. (2020) 100009.
[3] H.Y. Raji-Lawal, A.T. Akinwale, O. Folorunsho, A.O. Mustapha, Decision support system for dementia patients using intuitionistic fuzzy similarity measure, Soft Comput. Lett. 2 (2020) 100005.
[4] J. Wu, F. Orlandi, T. Alskaif, D. O'Sullivan, S. Dev, Ontology modeling for decentralized household energy systems, in: 2021 International Conference on Smart Energy Systems and Technologies, SEST, IEEE, 2021.
[5] K. Berkling, J. Vonwiller, C. Cleirigh, Scope, syllable core and periphery evaluation: Automatic syllabification and application to foreign accent identification, Speech Commun. 35 (2001) 125–138.
[6] S. Awang, M. Maros, N. Ibrahim, Language idiosyncrasies in second language learners' use of communication strategies, Asian Soc. Sci. 11 (2015) 55–70.
[7] I. Kardava, J. Antidze, N. Gulua, Solving the problem of the accents for speech recognition systems, Int. J. Signal Process. Syst. 4 (2016) 235–238.
[8] B. Katarina, D. Jouvet, Automatic detection of foreign accent for automatic speech recognition, in: Proc. 16th Int. Con. Phon. Sc., 2007, pp. 2185–2188.
[9] D. Jouvet, K. Bartkova, J. Monné, On the modelization of allophones in an HMM based speech recognition system, in: Second European Conference on Speech Communication and Technology, 1991.
[10] N. Kartushina, A. Hervais-Adelman, U.H. Frauenfelder, N. Golestani, Mutual influences between native and non-native vowels in production: Evidence from short-term visual articulatory feedback training, J. Phonetics 57 (2016) 21–39.
[11] J. Yanjie, X. Chen, J. Yu, L. Wang, Y. Xu, S. Liu, Y. Wang, Speaker recognition based on characteristic spectrograms and an improved self-organizing feature map neural network, Complex Intell. Syst. (2020).
[12] M. Hossari, S. Dev, J.D. Kelleher, TEST: A terminology extraction system for technology related terms, in: Proceedings of the 2019 11th International Conference on Computer and Automation Engineering, 2019, pp. 78–81.
[13] A. Joulin, E. Grave, P. Bojanowski, T. Mikolov, Bag of tricks for efficient text classification, 2016, arXiv preprint arXiv:1607.01759.
[14] E.R. Davies, O. Camps, M. Turk, Advanced Methods and Deep Learning in Computer Vision, Academic Press, 2021, pp. 441–452.
[15] F.A. Farris, The gini index and measures of inequality, Amer. Math. Monthly 117 (2010) 851–864.
[16] S. Weinberger, Speech accent archive. George Mason University. This dataset is distributed under a ccby-nc-sa 2.0 license, 2013.
[17] S. Dev, H. Javidnia, M. Hossari, M. Nicholson, K. McCabe, A. Nautiyal, C. Conran, J. Tang, W. Xu, F. Pitié, Identifying candidate spaces for advert implantation, 2019 IEEE 7th International Conference on Computer Science and Network Technology, ICCSNT, IEEE, 2019, pp. 503–507.
[18] M.S. Elsayed, N.-A. Le-Khac, S. Dev, A.D. Jurcut, Machine-learning techniques for detecting attacks in SDN, in: 2019 IEEE 7th International Conference on Computer Science and Network Technology, ICCSNT, IEEE, 2019.
[19] M. Jain, C. Meegan, S. Dev, Using GANs to augment data for cloud image segmentation task, in: 2021 IEEE International Geoscience and Remote Sensing Symposium, IGARSS, IEEE, 2021.

Application of Swarm Robotic System in a Dynamic Environment using Cohort Intelligence

Ashis Acharya, *Department of Computer Scinece Engineering , Capital Engineering College, Bhubaneswar, ashisacharya12@gmail.com*

Subhasish Mohanty, *Department of Electrical Engineering, Aryan Institute of Engineering & Technology, Bhubaneswar, subhasish.mohanty@hotmail.com*

Pratik Mohanty, *Department of Electrical Engineering , Capital Engineering College, Bhubaneswar, pratikmohanty92@hotmail.com*

Subhendu Sahoo, *Department of Electrical and Electronics Engineering, NM Institute of Engineering & Technology, Bhubaneswar, s.sahoo95@outlook.com*

A R T I C L E I N F O

Keywords:
Cohort Intelligence
Search and Rescue
Swarm Robotics
Metaheuristics
Artificial Intelligence

A B S T R A C T

The nature inspired Swarm Intelligence has laid the foundation for many eclectic applications. This work considers a solution to one such application of Search and Rescue operation, based on Cohort Intelligence (CI) methodology which aims at modelling the behaviour of candidates based on the interaction amongst each other to achieve a common goal. Every candidate improves its own behaviour by observing all other candidates in the cohort. This method results in the refinement of the performance of the entire system. The research done so far in this application using CI is associated with robots deployed in a static alien establishment. However, this assumption is not suitable in real-life scenarios. In this paper, the obstacle avoidance and path planning of a swarm of robots was implemented while considering a dynamic alien establishment. The problem of robots occasionally getting stuck in the non-convex obstacles has also been solved using a perturbation technique. The following test cases were implemented - No Obstacle Case (NOC), Stationary Obstacles Case (SOC), Single Dynamic Obstacle Case (SDOC), Multiple Dynamic Obstacles Case with Same Velocity (MDOC-SV) and Multiple Dynamic Obstacles Case with Different Velocities (MDOC-DV).

1. Introduction

Artificial Intelligence (AI) has been instrumental in almost every sector of human life. Some of the AI driven and benefited fields are Agriculture [8], Transportation [1], Healthcare [10], Manufacturing [14], Military Guidance and Surveillance [17], and many more. Importantly, Robotics is the most significantly affected field so far. For example, Assistive Intelligent Robotic Wheelchairs [9], Collaborative Smart Drones [3], Marine Environment Monitoring [7], Autonomous Robotic Surgery [2], Assistive Swarm Robots for Fire-fighters [13] and Robot-assisted Urban Search and Rescue [4] are few of the examples of intelligent robotic systems.

This paper considers an application of a robotic system in search and rescue operations. Path planning and obstacle avoidance is a major concern in this domain. Some of the remarkable research done in this field includes a velocity-based motion planning technique where sensors were used to avoid collisions with the obstacles [16], a new algorithm based on the Simultaneous Replanning concept was introduced by Biswas et al. [5], a Fuzzy Ant Colony Optimization methodology was proposed [18] that uses ultrasonic transducers for obstacle detection and a swarm robotic method for dynamic obstacle avoidance called Self-organizing migrating algorithm was developed by Diep et al. [6].

Recently, an application inspired by the role of AI-based robots in the rescue operations was implemented in Self-organizing Multi-Agent Cooperative Robotic System [15] using the Cohort Intelligence (CI) methodology developed by Kulkarni et al. [11]. This implementation considered robots deployed in an alien establishment with obstacle(s). The robots in the arena try to reach the target by interacting and following the behavior of other robots in order to improve their own behavior and eventually of the entire cohort. This alien establishment was considered to be of static nature. Whenever the robot encountered any obstacle it moved along the boundary of the obstacle. All the obstacles were of convex nature. However, these assumptions are not close to real-life scenarios. This paper proposes a more realistic approach to this application using the same CI methodology. The path planning and obstacle avoidance of a swarm of robots were implemented while considering a dynamic environment. The obstacles in the environment can move in a random direction with a certain velocity. The robots do not collide with the obstacle(s), rather they maintain a safe distance with the obstacle(s) while moving in the arena. The problem of robots getting stuck in the nonconvex obstacles has also been resolved using a perturbation technique. Furthermore, this application was implemented with two variations in the context of candidate following one another, the roulette wheel approach where candidate to be followed is selected based on roulette wheel selection methodology and the follow median approach

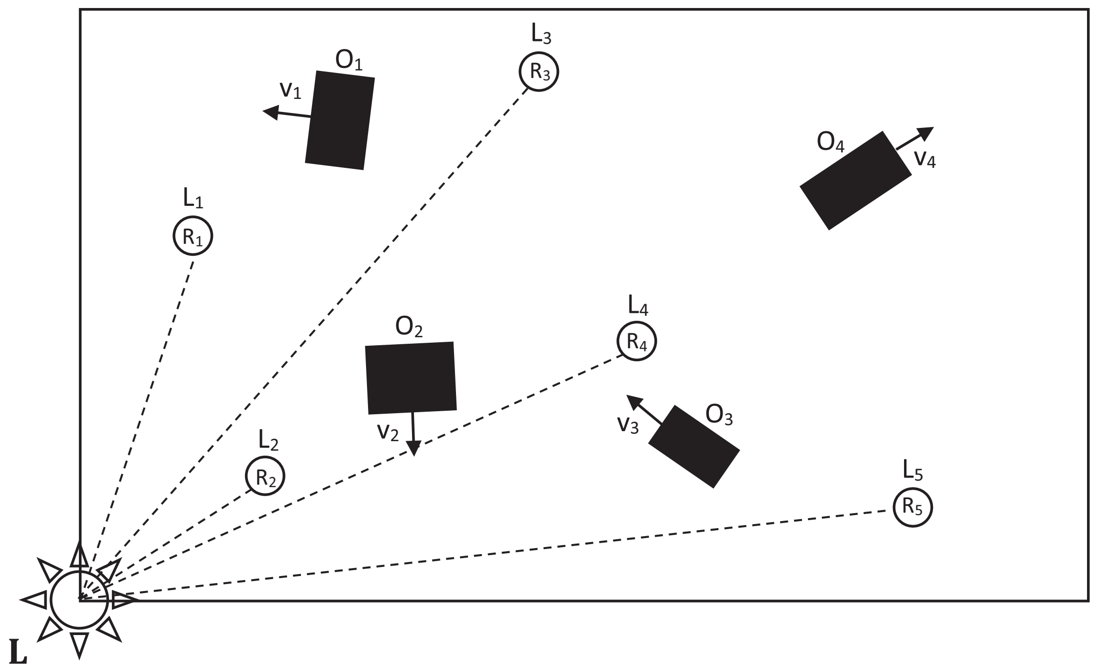

Fig. 1. A representation of the arena with robots and obstacles

where candidate to be followed is selected based on the median probability to reach the target. [12].

The remainder of this paper is structured as follows: Section 2 describes the mathematical formulation and experimental setup of the application. The validation of this implementation is presented in Section 3 by solving five test cases: No Obstacle Case (NOC), Stationary Obstacles Case (SOC), Single Dynamic Obstacle Case (SDOC), Multiple Dynamic Obstacles Case with Same Velocity (MDOC-SV) and Multiple Dynamic Obstacles Case with Different Velocities (MDOC-DV). The conclusion and a note on future directions are presented in Section 4 of this paper.

2. CI Framework for Swarm of Robots in Dynamic Environment

This endeavor is based on CI methodology which aims at modeling the behavior of the swarm of robots in a dynamic alien establishment. The nature of this approach is collaborative where all robots are self-adaptive and inter-dependent amongst one another. They cooperate with one another to achieve a common goal. A perturbation technique is devised to help the robots come out of the non-convex obstacle space. This resilience results in the refinement of the overall performance of the system.

Consider an arena of dimension $l \times b$ having robots and dynamic obstacles moving randomly (Fig. 1). The activity of robots, as well as the obstacles, is restricted within the limits of the arena. Assume the target of the system is a single light source $\boldsymbol{L}$. The goal of every robot R_i is to reach the light source $\boldsymbol{L}$ from their initial position without colliding with one another as well as with the obstacle(s). Every robot is assumed to have light and proximity sensors. Step length distance s is the distance with which every robot maneuvers in the arena in each iteration. The entire system is assumed to be on the same plane.

n	number of robots	
m	number of obstacles	
R_i	i^{th} robot	$i = 1, \dots, n$
L_i	light Intensity of i^{th} robot	$i = 1, \dots, n$
d_i	Euclidean distance of i^{th} robot from the light source	$i = 1, \dots, n$
p_i	probability of i^{th} robot	$i = 1, \dots, n$
O_j	j^{th} obstacle	$j = 1, \dots, m$
v_j	velocity of j^{th} obstacle	$j = 1, \dots, m$
s	step length distance	

The objective of this proposition is to maximize the light intensity sensed by each robot as follows,

$$Maximize \sum_{i=1}^{n} L_i \tag{1}$$

According to the inverse square law, L_i is inversely proportional to the square of the distance from the source,

$$L_i \propto 1/\left(d_i\right)^2 \tag{2}$$

The probability of selecting a robot to follow is calculated as follows,

$$p_i = L_i / \sum_{i=1}^{n} L_i \tag{3}$$

Initially, the configuration (position of robots as well as the obstacles, the velocity of obstacles v_i and the step length distance s) is random and the maximum number of iterations is k_{max}.

Step 1: The probability of each robot to reach the light source is calculated using eq. (3). In roulette wheel approach, every robot generates a random number $\in [0, 1)$ that decides which robot to follow. Whereas, in follow median approach every candidate follows the candidate which has the median probability.

Step 2: New positions of the robots are generated step length distance away, in the direction of the robot to be followed. If any robot follows itself, the direction of movement is chosen at random. If any obstacle is encountered, the robot moves by keeping a safe distance from the obstacle.

Step 3: If any robot gets stuck in the non-convex space of obstacles for a significant number of iterations, then the robot is perturbed with some distance. An illustration of the same is shown in Fig. 2. Here, R_4 is perturbed to a new position R_4' as it was stuck in the non-convex space created by obstacles O_2 and O_3.

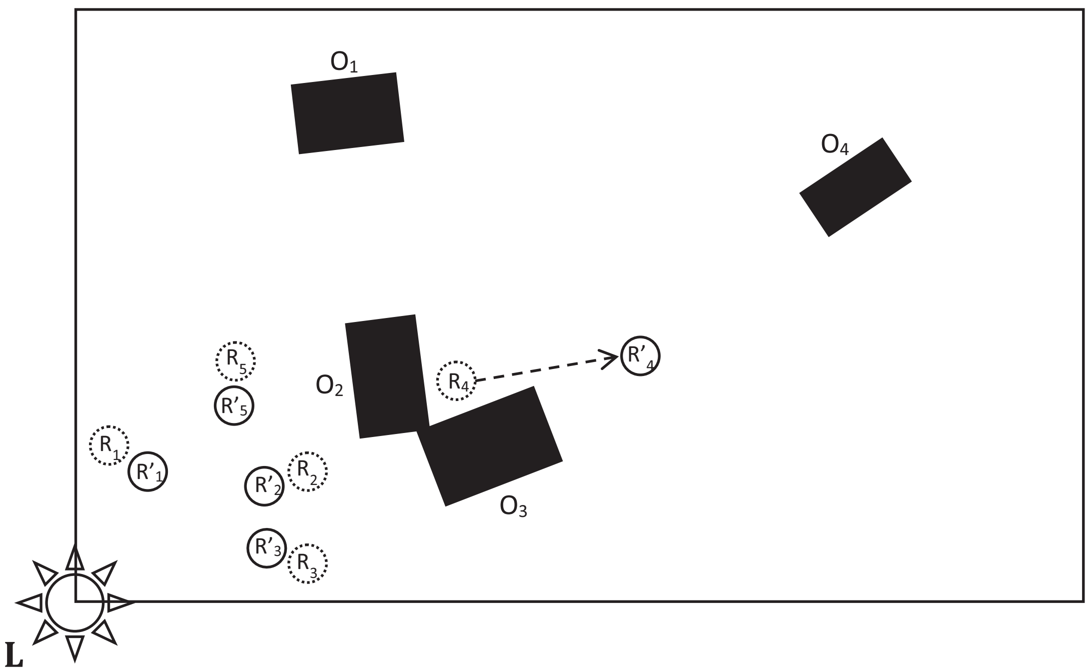

Fig. 2. An illustration of perturbation of robot

Step 4: The steps 1 to 3 are repeated until either the target is reached, or the maximum number of iterations is reached. The detailed flowchart of the procedure is presented in Fig. 3.

3. Numerical experiments and discussions

The algorithm was coded in Python 3.7 on Anaconda 4.8 platform and the simulations were run on Windows 10 operating system with Intel Core i5 2.5 GHz processor speed with 8 GB RAM. The following test cases were considered: No Obstacle Case (NOC), Stationary Obstacles Case (SOC), Single Dynamic Obstacle Case (SDOC), Multiple Dynamic Obstacles Case with Same Velocity (MDOC-SV) and Multiple Dynamic Obstacles Case with Different Velocities (MDOC-DV). For the roulette wheel approach as well as the follow median approach, every case was solved 30 times with 5 different initial configurations for each case. In every case, 5 robots were located randomly in a 5×5 arena. In addition, every robot maneuvers in the arena with step length (1 step = 0.14 units).

The NOC and SOC are illustrated in Fig. 4(a) and Fig. 4(b) respectively. The mean total time was observed to be significantly less than that of the same cases solved by Roychowdhury et al. [15]. Whenever a robot senses an obstacle in its path it diverts itself maintaining a safe distance from the obstacle without colliding with it. While simulating this case, a certain anomaly was encountered which restricted the movement of a robot due to nonconvex orientation of obstacles. To overcome this, a perturbation technique was devised which reconfigures its position. One such illustration is shown in Fig. 4(c). Similarly, the SDOC, MDOC-SV and MDOC-DV are illustrated in the Fig. 4(d), Fig. 4(e) and Fig. 4(f) respectively.

The results of execution of all five cases are presented in Table 1. The relative difference shown in Table 1 is used to gauge the performance of the robots in each case. It is the absolute difference of the mean of total traveled distance with respect to the mean of initial distance of the robots from the light source. As evident in Table 1, the execution time of both the approaches was comparable, however, the mean of total traveled distance is significantly less in the follow median approach than in the roulette wheel approach. This is due to the fact that the follow median approach avoids getting stuck in the local minima and simultaneously improves the solution, while in the roulette wheel selection approach there is some possibility that the robots may

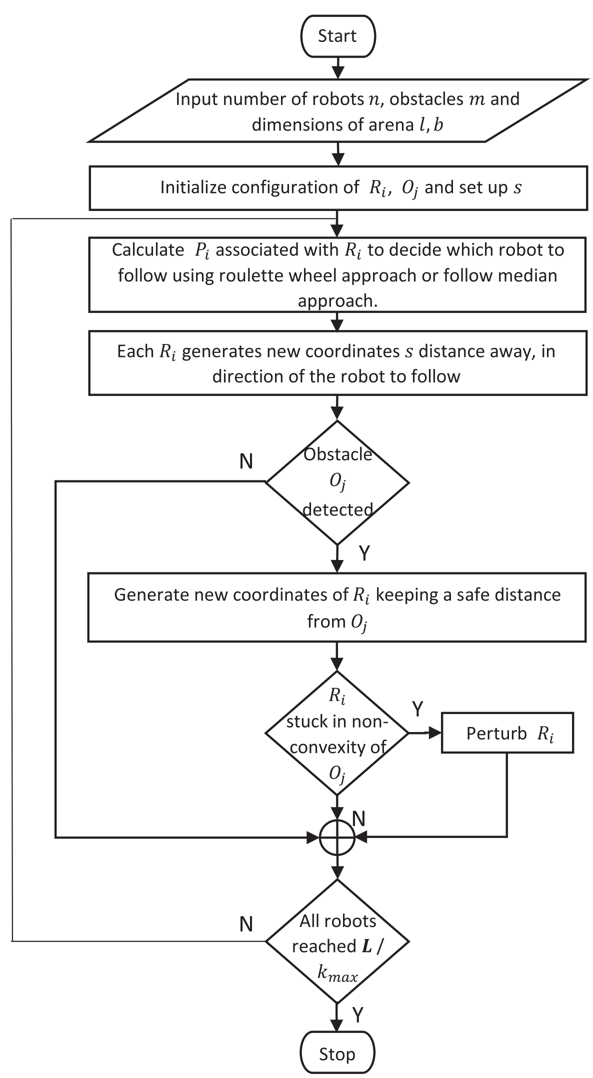

Fig. 3. Flowchart of the algorithm

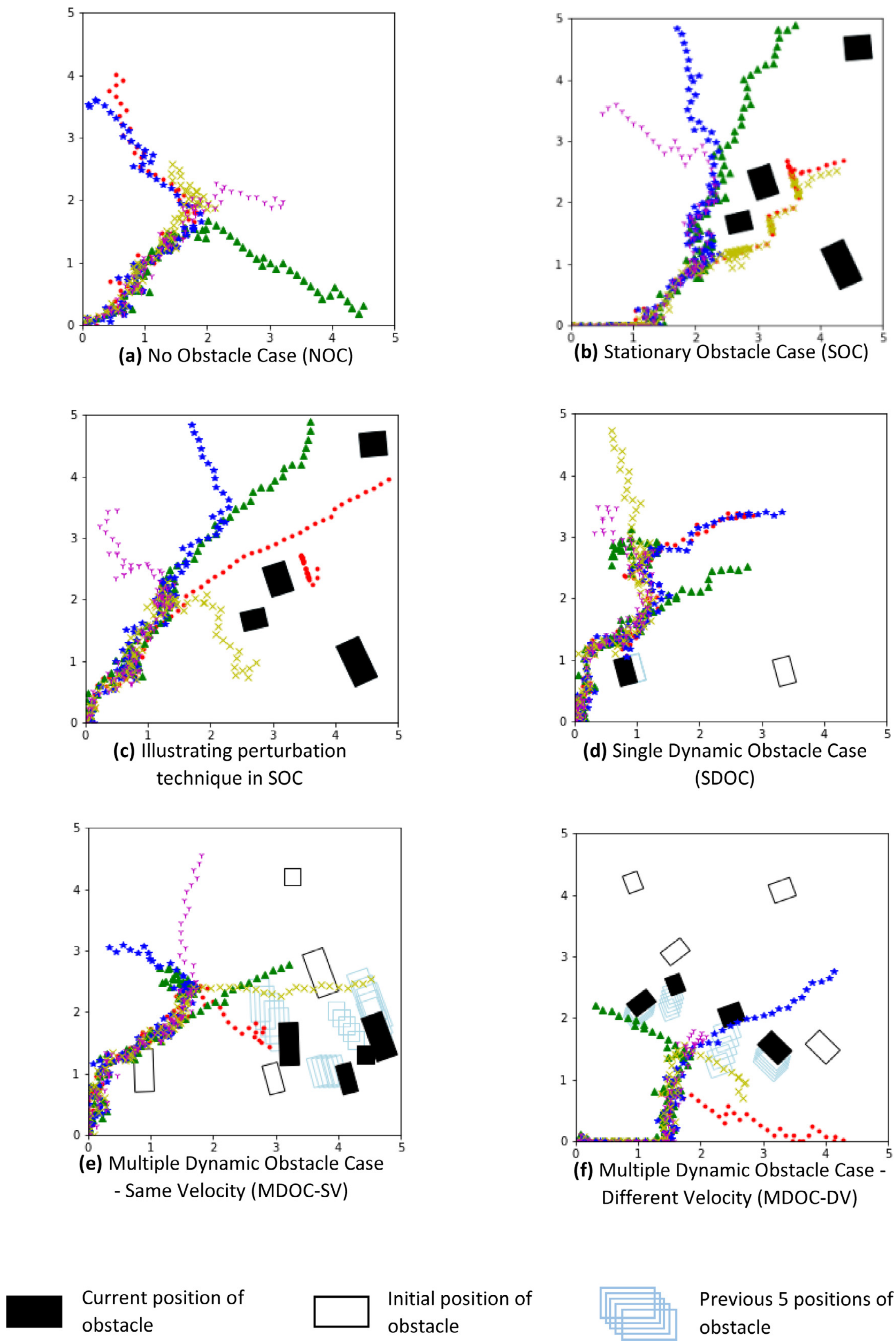

Fig. 4. Graphical representation of various cases by roulette wheel approach

Table 1
Performance of CI for different cases.

Cases	Config.	Mean of Initial Distance	Roulette wheel approach: Mean of Total Time (seconds)	Roulette wheel approach: Standard Deviation of Time (seconds)	Roulette wheel approach: Mean of Total Traveled Distance	Roulette wheel approach: Standard Deviation of Traveled Distance	Roulette wheel approach: Relative Difference of Traveled Distance	Follow median approach: Mean of Total Time (seconds)	Follow median approach: Standard Deviation of Time (seconds)	Follow median approach: Mean of Total Traveled Distance	Follow median approach: Standard Deviation of Traveled Distance	Follow median approach: Relative Difference of Traveled Distance
NOC	1	3.42	0.02	0.01	11.58	2.30	2.39	0.02	0.00	5.94	0.00	0.74
	2	3.76	0.02	0.01	12.90	2.56	2.43	0.04	0.00	10.32	0.00	1.74
	3	3.10	0.01	0.00	6.10	1.28	0.97	0.05	0.00	12.02	0.00	2.88
	4	3.47	0.02	0.01	13.10	3.18	2.78	0.04	0.00	9.90	0.00	1.85
	5	3.74	0.02	0.01	7.64	0.93	1.04	0.06	0.00	13.29	0.00	2.55
SOC	1	3.43	0.03	0.01	10.13	2.08	1.95	0.02	0.00	5.09	0.00	0.48
	2	4.45	0.10	0.03	30.17	8.44	5.78	0.06	0.00	7.49	0.00	0.68
	3	4.41	0.05	0.02	16.49	4.19	2.74	0.03	0.00	6.51	0.00	0.48
	4	3.25	0.05	0.02	12.47	4.89	2.84	0.03	0.00	5.80	0.00	0.78
	5	5.69	0.08	0.03	25.71	6.38	3.52	0.08	0.00	13.29	0.00	1.34
SDOC	1	3.84	0.05	0.03	10.25	3.79	1.67	0.05	0.02	5.94	0.56	0.80
	2	2.32	0.03	0.01	6.10	0.69	1.63	0.03	0.01	5.23	0.00	0.34
	3	4.04	0.06	0.02	19.08	6.72	3.72	0.04	0.03	5.43	0.33	0.44
	4	2.66	0.03	0.01	9.56	2.75	2.59	0.03	0.01	4.50	0.27	0.70
	5	4.07	0.02	0.01	15.09	3.67	2.71	0.04	0.01	5.91	0.15	0.43
MDOC-SV	1	3.62	0.04	0.02	9.58	3.81	1.65	0.05	0.02	5.92	0.11	0.53
	2	3.87	0.06	0.02	15.96	4.53	3.12	0.06	0.01	6.41	0.48	0.59
	3	4.03	0.05	0.02	12.92	3.54	2.21	0.06	0.02	6.74	0.38	0.67
	4	2.75	0.06	0.02	8.37	1.84	2.04	0.03	0.00	4.50	0.30	0.64
	5	4.29	0.14	0.10	15.55	8.68	2.62	0.05	0.00	6.26	0.07	0.46
MDOC-DV	1	2.88	0.04	0.01	6.42	1.32	1.23	0.15	0.04	70.71	0.00	23.55
	2	3.95	0.04	0.04	10.43	5.85	1.64	0.05	0.01	6.15	0.55	0.56
	3	3.39	0.06	0.02	9.99	1.67	1.95	0.06	0.01	5.30	0.08	0.56
	4	2.81	0.06	0.02	7.52	1.32	1.68	0.27	0.03	70.71	0.00	24.16
	5	3.28	0.05	0.03	8.93	3.95	1.72	0.04	0.02	5.16	0.62	0.57

follow the worse performing robots. In the roulette wheel approach, all robots successfully reached the light source in all configurations, whereas in two configurations of MDOC-DV using follow median approach the robots failed to do so. It was observed that, in all the cases, the standard deviation of time is not significant, hence this system proves to be adaptive to any initial configuration. There is no deviation of traveled distance for the NOC and SDOC using the follow median approach as the environment in these cases is of static nature and hence the robots follow the same median robot for all trials without any exception.

4. Conclusion and Future Directions

The application of Swarm robotics in Search and Rescue operation was implemented using CI methodology with two different approaches: the roulette wheel selection approach and the follow median approach. The same application was implemented by Roychowdhury et al. [15], considering an ideal scenario of static nature of environment, which is rarely observed. Hence, to make it closer to real-life scenario, the entire system was considered to be dynamic in nature. This implementation was successfully validated for following independent static test cases like No Obstacle Case (NOC), Stationary Obstacles Case (SOC), as well as dynamic test cases like Single Dynamic Obstacle Case (SDOC), Multiple Dynamic Obstacles Case with Same Velocity (MDOC-SV) and Multiple Dynamic Obstacles Case with Different Velocities (MDOC-DV). The tests were conducted by arbitrarily positioning the robots and obstacles which can move randomly in the arena. This implementation was tested on non-convex orientation of obstacles and a new perturbation technique was devised for the same.

Swarm robotics considered in dynamic nature can have a wide range of applications. This paper shows the implementation of an application considering a single plane while more complex real-life problems can also be solved using this methodology considering the robots and obstacles in different planes. Furthermore, this work uses a perturbation technique to overcome the problem of robots getting stuck in the non-convex region formed due to dynamic configuration of obstacles. A better approach can be designed for this by making use of multiple proximity sensors on the robots or by making use of computer vision technology. However, these approaches may increase the heftiness which needs to be worked upon. This work can have strong potential in implementing applications like assistive swarm-robotics in healthcare, aerial swarm-robotics and aquatic swarm-robotics. Authors intend to apply this dynamic CI approach in such fields.

References

[1] R. Abduljabbar, H. Dia, S. Liyanage, S.A. Bagloee, Applications of artificial intelligence in transport: an overview, Sustainability 11 (1) (2019) 189.

[2] I. Andras, E. Mazzone, F.W.B. van Leeuwen, G. De Naeyer, M.N. van Oosterom, S. Beato, T. Buckle, S. O'Sullivan, P.J. van Leeuwen, A. Beulens, N. Crisan, F. D'Hondt, P. Schatteman, H. van Der Poel, P. Dell'Oglio, A. Mottrie, Artificial intelligence and robotics: a combination that is changing the operating room, World J. Urol. (2019).

[3] S.H. Alsamhi, O. Ma, M.S. Ansari, F.A. Almalki, Survey on collaborative smart drones and internet of things for improving smartness of smart cities, IEEE Access 7 (2019) 128125–128152.

[4] J.G. Blitch, Artificial intelligence technologies for robot assisted urban search and rescue, Expert Syst. Appl. 11 (2) (1996) 109–124.

[5] S. Biswas, S.G. Anavatti, M.A. Garatt, Obstacle avoidance for multi-agent path planning based on vectorized particle swarm optimization", in: G. Leu, H. Singh, S. Elsayed (Eds.), Intelligent and Evolutionary System, Proceedings in Adaptation, Learning and Optimization, 8, Springer, Cham, 2017, pp. 61–74.

[6] Q.B. Diep, I. Zelinka, R. Senkerik, "An algorithm for swarm robot to avoid multiple dynamic obstacles and to catch the moving target, in: International Conference on Artificial Intelligence and Soft Computing, 2019, 2019, pp. 666–675.

[7] M. Duarte, J. Gomes, V. Costa, T. Rodrigues, F. Silva, V. Lobo, M.M. Marques, S.M. Oliveria, A.L. Christensen, Application of swarm robotics systems to marine environmental monitoring", in: Proceedings of the OCEANS 2016 - Shanghai, Shanghai, 2016, pp. 1–8. 10-13 April 2016.

[8] N.C. Eli-Chukwu, Applications of artificial intelligence in agriculture: a review, Eng., Technol. Appl. Sci. Res. 9 (4) (2019) 4377–4383.

[9] I.P. Ktistakis, N.G. Bourbakis, Assistive Intelligent Robotic Wheelchairs, IEEE Potentials 36 (1) (2017) 10–13.

[10] A.J. Kulkarni, M.F. Baki, B.A. Chaouch, Application of the Cohort-intelligence optimization method to three selected combinatorial optimization problems, Eur. J. Oper. Res. 250 (2) (2016) 427–447.

[11] A.J. Kulkarni, I.P. Durugkar, M. Kumar, Cohort intelligence: a self supervised learning behavior, in: Proceedings of the 2013 IEEE International Conference on Systems, Man, and Cybernetics, Manchester, 2013, pp. 1396–1400. 13-16 October 2013.

[12] N.S. Patankar, A.J. Kulkarni, in: Variations of cohort intelligence, 22, Soft Computing, Springer, 2017, pp. 1731–1747.

[13] J. Penders, L. Alboul, U. Witkowski, A. Naghsh, J. Saez-Pons, S. Herbrechtsmeier, M. El-Habbal, A Robot Swarm Assisting a Human Fire-Fighter, Adv. Robot. 25 (1-2) (2011) 93–117.

[14] C. Renzi, F. Leali, M. Cavazzuti, A.O. Andrisano, A review on artificial intelligence applications to the optimal design of dedicated and reconfigurable manufacturing systems, Int. J. Adv. Manuf. Technol. 72 (1-4) (2014) 403–418.

[15] P. Roychowdhury, S. Mehra, R. Devarakonda, P. Shrivastava, S. Basu, A.J. Kulkarni, "A Self-organizing multi-agent cooperative robotic system: an application of cohort intelligence algorithm, in: A.J. Kulkarni, P.K. Singh, S.C. Satapathy, K.A. Husseinzadeh, K. Tai (Eds.), Socio-cultural Inspired Metaheuristics, Studies in Computational Intelligence, 828, Springer, 2019, pp. 121–135.

[16] C. Stachniss, W. Burgard, "An integrated approach to goal-directed obstacle avoidance under dynamic constraints for dynamic environments, in: IEEE/RSJ International Conference on Intelligent Robots and Systems, Lausanne, Switzerland, 2002, pp. 508–513. 30 September-4 October 2002.

[17] P. Svenmarck, L. Luotsinen, M. Nilsson, J. Schubert, "Possibilities and challenges for artificial intelligence in military applications", in: Proceedings of the NATO Big Data and Artificial Intelligence for Military Decision Making Specialists' Meeting, Neuilly-sur-Seine, France, 2018, pp. 1–16. 30 May-1 June 2018.

[18] C.T. Yen, M.F. Cheng, A study of fuzzy control with ant colony algorithm used in mobile robot for shortest path planning and obstacle avoidance, Microsyst. Technol. 24 (1) (2016) 125–135.

Bus journey simulation to develop public transport predictive algorithms

Sidhanta Kumar Balabantaray, *Department of Computer Scinece Engineering , Raajdhani Engineering College, Bhubaneswar, sk.balabantaray111@gmail.com*

Chinmaya Ranjan Pradhan, *Department of Electrical and Electronics Engineering, NM Institute of Engineering & Technology, Bhubaneswar, cr.pradhan23@gmail.com*

Alekha Sahoo, *Department of Electrical Engineering , Raajdhani Engineering College, Bhubaneswar, alekha.sahoo241@gmail.com*

V. Raja, *Department of Electronics and Communication Engineering , NM Institute of Engineering & Technology, Bhubaneswar, v_raja241@outlook.com*

ARTICLE INFO

Keywords:
Public transport
Arrival time prediction
Data simulation
Data quality
Machine learning
Deep learning

ABSTRACT

Encouraging the use of public transport is essential to combat congestion and pollution in an urban environment. To achieve this, the reliability of arrival time prediction should be improved as this is one area of improvement frequently requested by passengers. The development of accurate predictive algorithms requires good quality data, which is often not available. Here we demonstrate a method to synthesise data using a reference curve approach derived from very limited real world data without reliable ground truth. This approach allows the controlled introduction of artefacts and noise to simulate their impact on prediction accuracy. To illustrate these impacts, a recurrent neural network next-step prediction is used to compare different scenarios in two different UK cities. The results show that a realistic data synthesis is possible, allowing for controlled testing of predictive algorithms. It also highlights the importance of reliable data transmission to gain such data from real world sources. Our main contribution is the demonstration of a synthetic data generator for public transport data, which can be used to compensate for low data quality. We further show that this data generator can be used to develop and enhance predictive algorithms in the context of urban bus networks if high-quality data is limited, by mixing synthetic and real data.

1. Introduction

Cities around the world are trying to shift personal traffic to public transport to reduce congestion and environmental impact. A crucial part of such a strategy is to make public transport as convenient as possible. Bus passengers often rely on Real-Time Passenger Information (RTPI) systems at bus stops, online and in mobile apps. These RTPI systems can be unreliable [1] which is inconvenient for passengers. In general, passengers assign different priorities to certain aspects of public transport. Reliability and safety are considered the two most important [2].

The importance of making especially buses as attractive as possible in comparison to private vehicles is highlighted in the historical statistical records. In the UK, 4.8 billion bus trips were made in 2018/19, accounting for 58% of all public transport journeys [3]. These journeys amounted to 27.4 billion km travelled and saved approximately 96 million tonnes of CO_2 [4]. However, since 1985, bus travel has been steadily decreasing by a total of 0.7 billion journeys. As other public transport modes such as trains in most areas cannot be a replacement for local bus services, this suggests that a larger share of passengers opt for private vehicles. This is mirrored in the continuous upward trend of car traffic on British roads [3]. To encourage potential passengers to use public transport, it is crucial to make it as attractive as possible to reverse the above trends, ultimately having a positive impact on the environment as well as congestion levels in urban settings. However, the mentioned data are pre-pandemic, thus the long-term impact of the pandemic on public transport cannot currently be anticipated.

Other studies also highlighted the importance of accurate Estimated Time of Arrival (ETA) predictions to improve customer experience [5]. Many public transport providers have developed mobile apps, which give 'live' positions of vehicles. Passengers can use such technology to decide when to leave the house to catch a bus without having long wait times at a bus stop. However, we previously noted the latency of this information caused by delays of wireless network infrastructure and the fact that the data in our operational area passes through a number of 3rd party systems [6]. Therefore, the RTPI system might suggest a vehicle is further away than it is in reality. This could cause a passenger to miss a bus and thus unnecessarily inconvenience them. In Bournemouth, one of the two cities used as an example in this study, the latency of the internet-based 'live position' is approximately 30–40 s. To alleviate this issue, we have proposed a short-horizon prediction which will be useful in the further development of ETA and long-term predictions, and in bringing the 'live' locations closer to reality. The commonly deployed Automatic Vehicle Location (AVL) systems [7], could supply data for such approaches.

To compare any potential model, the assessment of their performance is of crucial importance, this has to be reported in a way that allows to replicate and compare the results. However, this is not possible in all cases as some authors report relative errors [8–10] and no consistency in the reported parameters can be distinguished. The precondition for all machine learning algorithms should be verifiable, and the RoyalSociety's report highlights this as a central feature [11]. This has also been recognised in the healthcare sector where guidelines for the development and reporting of predictive models exist [12]. The difference in standards might be explained because ETA predictions do not affect the health or safety of a passenger and a spurious algorithm might at most cause inconvenience rather than physical harm. However, for an operating company, this might cause a loss of revenue through a decline in patronage, and the society as a whole might be subjected to more congestion that could simply be reduced by providing accurate ETA predictions. Furthermore, the doctrine of science is replicability. The reproducibility crisis is most prominently known from psychological research [13] however due to its notoriety, it has been actively addressed [14]. It has also been identified as a problem in 'harder' sciences such as biomedicine [15] and also artificial intelligence [16]. Although results gained from machine learning techniques might be considered hard evidence, because the final model is based on mathematical concepts, they often suffer from similar problems as seen in psychology where the research is often subjective to the researcher. The similarities between the two fields are that the findings cannot usually be explained due to the 'black box' effect. The field of psychology has now started to apply lessons from problems seen in machine learning research [14]. A suggested way of addressing such problems is meta-science that could shed light on the true accuracy of findings [17]. However, this relies on comparable measurements of accuracy, which is not found in a large proportion of the public transport literature. Therefore, comprehensive standards of reporting are urgently needed in the field of predictive bus transportation research. This as a consequence poses the issue that high-quality data is required to develop good predictive models. We and other researchers have highlighted that data quality issues need to be considered in the context of public transport research [6,18–20]. Therefore, in this study we demonstrate a method to synthesis bus journeys based on limited and low quality data. This allows on the one hand to generate a hybrid dataset to develop models from. On the other hand it has the potential to be used to generate synthetic datasets that can be used for benchmarking in an attempt to combat the highlighted replicability issues faced by public transport research.

In our data, a notable lack of quality hampers the development of predictive algorithms. The quality issues include the lack of clear journey identification, linkable to a timetable, artefacts such as gaps in recordings, falsely reported line numbers, and direction of travel (inbound vs. outbound). These quality issues make it impossible to develop accurate predictive algorithms. Unfortunately, the simplest solution of recording high-quality historical data is not feasible due to closed source data collection by 3rd party companies. To address this issue, this study describes a reference curve-based synthetic data generator, which bases its assumptions on limited real-world data. This allows to test algorithms in a controlled environment and enables the injection of user-defined artefacts into the dataset to test their effect on prediction quality. We also show that mixing real and synthetic data improves the prediction accuracy.

2. Background

Methods for ETA prediction can include simple historical averages or be based on statistical models. However, due to the complexity of the ETA prediction, machine learning methods have become increasingly popular [21]. In recent years, artificial Neural Networks (NN) have revolutionised a number of other domains. Therefore, NNs should be expected to have similar potential when applied to bus ETA prediction problems. A comprehensive review specifically investigating NN applications in public transport [22] found that only 16% (12) addressed ETA of buses, whereas the rest of the studies applied the technique to other modes of transport. This suggests that the area of bus ETA prediction using NNs might be underrepresented in the context of public transport research. This relative absence of NNs to predict bus ETA is striking as NNs have revolutionised other areas of data science such as image and speech recognition [23,24].

The challenge of all machine learning approaches is to fine tune the model parameters, one solution is to use genetic algorithms [25] to optimise machine learning algorithms inspired by nature. Several innovative variations have been demonstrated in the recent literature, such as an algorithm inspired by the mating of red deer populations [26], or the simplification of parameter search with a simplified metaheuristic [27]. The same authors also demonstrate methods applicable to supply chain management using the Taguchi method to outperform conventional genetic algorithms [28] as well as the potential use of blockchain algorithms in the management of supply chains [29], additionally they show applications to predict photovoltaic electricity generation [30] as well as bioremediation [31].

Nowadays, the majority of buses have onboard AVL systems, which are equipped with GPS sensors and transmit the location of the bus at frequent intervals, typically ranging between 20 and 60 s. The availability of vehicle locations are the basis for any ETA prediction and are accessible through the AVL system and do not necessarily need any additional investment in static sensors.

The biggest hurdle in developing machine learning solutions generally is the difficulty to acquire enough good-quality data to develop a useful algorithm. In some fields, this has led to the use of simulated data ranging from medicine [32] to geophysics [33]. Regarding public transport journey simulation, the literature is scarce. Some examples related to bus data simulation include bus platooning [34] as well as traffic simulation [35]. However, to the best of our knowledge, no study has investigated the use of simulated data to train a next step prediction model for urban bus networks. In many areas of machine learning research, benchmark datasets are common [36]. These allow researchers to objectively compare algorithms against each other. This is missing in the field of urban bus networks. Therefore, the presented data generator could allow the generation of a standardised benchmark dataset that could lay the foundation for further research in public transport.

3. Real-world data processing

3.1. Data collection

Data is accessible via the infrastructure of our collaborators, and two British cities have been selected with the largest number of vehicles and access to recorded travel data. AVL data was collected from two different bus operators from Reading (UK) line 17 and Bournemouth (UK) line 1 (Fig. 1). Each vehicle transmits its position approximately every 40 s, which is recorded by the company providing the Electronic Ticketing Machines (ETMs) with the integrated AVL-system. Due to data handling by several independent entities, only a limited amount of information is transmitted. The available data are:

- Timestamp
- Position (latitude and longitude)
- Line number
- Direction (outbound or inbound)

For the Bournemouth operator, it became apparent that the transmitted directions are often incorrect and so are the line numbers when a vehicle changes its line during an operational run. The data collected in Reading had a better integrity with reliably transmitted direction, thus simplifying the data processing steps. Based on this limited information, it is not possible to match a vehicle to a timetable corresponding to the journey it is currently serving. A journey is a specific trip found in the

Fig. 1. Location of both example cities and the journey shape used for all experiments. The line 1 in Bournemouth is shown yellow and the line 17 in Reading in blue. (For interpretation of the references to colour in this figure legend, the reader is referred to the web version of this article.)

timetable of a bus line, e.g., the outbound 9 AM service 1. In contrast, a route pattern (also referred to as 'shape') is the route as travelled on the road, which can vary slightly for each journey for the same bus service. In the example of line 1 in Bournemouth, there are several patterns which can include different starting points along the route, resulting in shorter overall journeys or slightly different routes. In both cities, reliably matching a vehicle directly to a specific route pattern is not possible as the unique route pattern identifiers were not accessible to us. Therefore, one route pattern for each city was arbitrarily selected and used to generate synthetic data, which is an acceptable approach as in the selected cities the differences between patterns are negligible.

3.2. Identifying route sections for filtering

The bus route used in Bournemouth is line 1, starting in the town centre towards Christchurch (Fig. 1). The complete route shape includes longer journeys and therefore needs to be truncated. In the second example of Reading line 17 was used, which can have up to 90 different route patterns per direction with different runtimes and minor variations in route shapes (Fig. 1). Additionally, a complicating factor is that the route follows a one-way system in the city centre, meaning that the routes are different depending on the served direction. Therefore, a two-pronged approach was used. To initially filter journeys that were too far away from the shape, all available shapes for both directions were combined to a template shape. Any journey outside a radius of 3 x the mean distance to the template shape was excluded. The final filtering with the ability to enforce the direction was done using an arbitrarily selected route pattern from the many different patterns available for each line covering the entire length of the route. In the case of Reading these route patterns are mostly identical, however, in Bournemouth the patterns can be very different. We have described these issues previously [6].

3.3. Identification of individual journeys

Due to the lack of explicit journey identification, a heuristic approach was used to separate individual journeys that will then be used as a basis to generate synthetic data.

Bournemouth operator does not reliably transmit the direction a vehicle currently serves. However, an observation made was that at the end of a journey vehicles stopped transmitting data for a short period of time. Thus, once it reappears in the data stream, a gap in the timestamps can be detected. A new journey was defined as a time gap of more than 15 min. If such a gap is detected, it is assumed a new journey has started.

Reading operator reliably reports the direction of travel, making the identification of an individual journey easier. Furthermore, vehicles tend to serve the same line and do not change lines between runs, by selecting a single direction, large gaps in transmission timestamps can be observed, making the separation of journeys accurate.

3.4. Trajectory generation

It is assumed that the vehicles follow the identified outbound journey shape. This allows us to represent a journey as a trajectory which is the distance travelled along the route shape. Using such a trajectory, a journey can be represented in two dimensions based on the distance travelled and the run time from the start of the journey.

3.5. Additional processing steps

To ensure a clean dataset, repetitions at the start where the vehicle did not move further than 10 m were removed and a journey is assumed to start once the vehicle has moved further than this threshold. The journey was presumed to have ended as soon as it had reached its maximum trajectory.

4. Synthetic data generation

The data generation process uses a heuristic data-based approach to generate synthetic journeys. This process is broken down into several sub steps:

- The interpolation of the route shape as the reported points are not evenly distributed along the route.
- The identification of the normal run time for a journey is based on historical data, which also allows the identification of delays.
- The probability-based simulation of the delays.

The above steps are described in detail in the following subsections.

4.1. Interpolating the journey based on the route shape

A synthetic journey is generated based on future timetables. To avoid all vehicles starting at the same point, a time offset is added to the start time of the timetable, which is a random number between 0 and 40 s (the transmission interval). This is added to the scheduled start time. The distance that should be offset is then calculated by multiplying the offset by the average speed observed in the real world data 8 m/s (30 km/h). The timestamps are then interpolated to a user-defined interval — 40 s in the presented example. Calculating the time difference between two subsequent stops on the route segment gives the overall runtime. This can be divided by the transmission frequency of 40 s to give the number of transmissions expected on this route section. By assuming the vehicle travels at a constant speed, the progress along the shape can be estimated and the coordinates of the shape at the transmission points can be extracted. However, the coordinates of the reference journey pattern are not equidistant; the distances between consecutive reported locations vary between 6 m and 100 m. Therefore, interpolation solely based on the shape would give very different speeds depending on the road shape. This is avoided by generating an interpolation based on the distance along the route. The closest calculated distance of the shape coordinates is used to calculate the difference between the interpolation coordinate and the shape coordinate. If this distance is greater than 5 m, the two neighbouring points on the shape are used to interpolate the positions between these two coordinates to make the data more realistic. This does not account for variations in the speed or the curvature of the earth, but as the distance is at most 100 m, it is a reasonable omittance. Additionally, it appears that wider gaps are found on straight road sections and the frequency increases in meandering sections, making the proposed approach a good compromise.

4.2. The problem of determining delays

As arrival times at bus stops are not recorded, it cannot be determined whether a vehicle was running on time or was delayed. An additional difficulty is that the journey times vary and depend on the time of the day and weekdays. This variation in timetabled runtime compensates for the expected traffic status. TomTom, a location technology company, records congestion characteristics for different cities based on consumer GPS data. The data for Bournemouth indicates the percentage of delay that needs to be added to a journey at a certain time of day. The maximum in Bournemouth is on a Wednesday afternoon with an expected 71% increase in travel time (pre-pandemic) [37].

Most times of the day, the timetable overestimates the travel time compared to the expected time based on TomTom's data. However, it needs to be kept in mind that the vehicles travel between Bournemouth and Christchurch and the data only accounts for Bournemouth. Furthermore, stops to let passengers board or debark are not considered in the TomTom dataset. This means the timetable accounts for expected variations in traffic conditions and thus cannot be used to simulate vehicle delays.

Another avenue explored was the use of Google services to predict delays based on consumer data, which was not possible as buses travel in bus lanes, making the route very different from a prediction based on Google Maps.

4.2.1. Probability based simulation of delays

By assessing all journeys within the real-world dataset by weekday and hours of day, a reference trajectory can be derived. This reference trajectory is simply the mean trajectory of all observed journeys (Fig. 2(a)). As a result, the outliers are removed and the reference curve represents the baseline of a 'normal' journey (Figs. 2(b) and 2(c)). This allows to calculate the probability that a journey will be delayed or early for every time of each week day. Reference curves were generated using a centred moving 3 h window except for the first and last hour where a truncated window was used. This gives the advantage that the time dependency of delays is simulated, meaning that a vehicle following a delayed bus will most likely also be delayed, thus approximating the delay propagation along a single line.

4.2.2. Journey generation

To generate a journey, the timetables of one week are queried and used as a template. The reason for this approach is that although the timetables for Bournemouth are available until the end of the current calendar year, this is not the case in Reading where only one week is available. As the timetable normally does not drastically change within the same year, this is a justifiable approach. Subsequently, the reference curve queried and the following relevant data points are extracted:

- The mean reference trajectory.
- The standard deviation as well as 95% confidence intervals.
- The probabilities of delayed or early arrival with respect to the reference curve (Fig. 2).

4.2.3. Delays

Based on the reference curve, the probability of a journey being delayed or early can be calculated. Whether a journey is delayed is decided by sampling from a normal distribution for each entry of the reference table, a random number r is generated and stored in a probability list $\{r_o \dots r_n\}$. These parameters double as a modification parameter to generate the delay or time gain. To remove variations of the list of probabilities, a Savitzky–Golay filter is applied with a window of 7 and a polynomial order of 3. A decision whether a vehicle will be on time, early or delayed is made based on the smoothed probability list. A vehicle will arrive early if $r < p_{early}$. If $p_{early} < r < p_{early} + p_{delayed}$ vehicle is delayed. If neither of the conditions is true, the vehicle is assumed to be on time. To simulate the variations in time gained, the initially expected runtime t of the reference curve is calculated as well as the difference of the last position of the reference curve γ. The ratio of expected variation is calculated based on the confidence interval of the reference curve ν. Thus, the progress along the trajectory under the influence of a time gain can be calculated as follows:

$$\nu = (\sigma_i/\gamma_i) * (R = \{^1_0)$$
$$P = P_{i-1} + t - (t \times ((0.9 \times \nu) \times 1.25))$$

Where: ν=volatility, γ=reference, P=position, t =expected time at position

If the next position will be delayed, a random modification factor m is generated by sampling from a beta continuous random distribution (α=1, β=2). This tailed distribution was chosen as it makes large reductions in delay less likely and a vehicle will in most circumstances make up no or very little time. The delay *volatility* is defined as the ratio of the reference curve standard deviation to the reference curve itself multiplied by m. Additionally, the delay of the previous step d_{i-1} is calculated and subtracted from the current delay to prevent an exponential increase in delay. To account for random major changes outside the 'norm' of delay or time gains observed in the real data, GPS *noise* is generated using a uniformly sampled random number R which also acts as a weight of the additional delay. Thus, a position with simulated noise can be described as:

$$\eta = \nu \times (R = \{^1_0 + 1)$$
$$P = P_{i-1} + (t + [(\nu \times m) - d_{i-1} \pm \eta])$$

Where: η= noise to be added, ν=volatility, P=position, t =expected time at next position

If the bus is most likely on time, the probability p of it being on time is used to generate an adjustment towards the reference curve as follows:

$$P = [P_{i-1} + t] - [p \times t]$$

Where: P=position, p = probability a vehicle is on time t =expected time at next position

The generated trajectory is then interpolated to give positions in time intervals of 40 s consistent with the transmission rates of the recorded data.

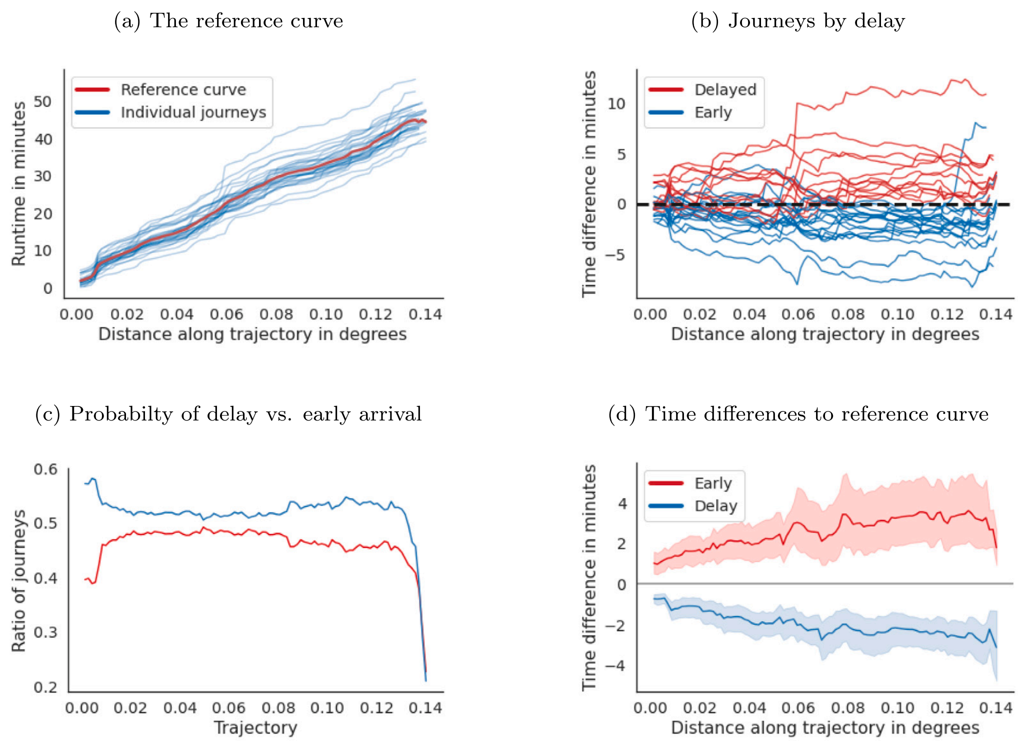

Fig. 2. (a) The historical trajectories of a one day block in Bournemouth (Tuesday 9–12 am). (b) The relative difference from the reference curve along the trajectory. Journeys delayed at more than 60% of the positions are highlighted in red. (c) Probability of travelling early or late on the trajectory. The discrepancy in the sum of the two conditions represents the fraction of vehicles that arrive on time. (c) The average time difference to the reference curve with the uncertainty highlighted. (For interpretation of the references to colour in this figure legend, the reader is referred to the web version of this article.)

4.3. *Injection of artefacts*

The original data is affected by artefacts caused by the behaviour of vehicles as well as data collection issues. Three noteworthy artefacts have been incorporated into the simulation of the synthetic data and are described below.

4.3.1. *Injection of GPS noise*

GPS recordings are affected by noise which can depend on the surrounding environment, such as high-rise buildings. In the cities used in this study, buildings tend to be low and thus effects due to reflection of the GPS signal are unlikely and have not been observed. To simulate the inaccuracies of the GPS recording, random noise sampled from a normal distribution (mean=0, σ=7) is added to latitude and longitude.

4.3.2. *Injection of repeated locations*

Due to operational reasons, journeys have scheduled buffers to allow vehicles to catch up with the timetable. This means that the vehicle often repeatedly transmits the same location at the start or end of a journey. At the journey start, 83% of the journeys have repeated locations, whereas end-repetitions are seen in 67% of journeys. The number of repeats varies depending on how long a vehicle is stationary. A skew-normal distribution [38] was fitted to both the start and end repetitions and this reference distribution is used to sample the number of repeats at either end of the journey. This artefact is optional and datasets with as well as without have been generated as in theory it is possible to gather journey data only for the journey itself without buffer times at either end.

4.3.3. *Geofencing artefacts*

The original data collected contained characteristic circular patterns. We empirically demonstrated previously [6] that the origin of such characteristic artefacts are the geofencing methods used by some AVL-systems to determine if a vehicle has arrived at a bus stop [6]. Unless the bus has been very close to the stop, the AVL-system ‘snaps’ the real position of the vehicle to a circular geofencing boundary with a radius of 10 m. As this is an unusual artefact, it is generated optionally.

4.4. *Data generation*

For both cities, datasets were generated for 145 days and for three different conditions:

- a journey only with GPS noise,
- a journey with GPS noise and circular artefacts,
- a journey with GPS noise, and start and end repeats.

Additionally, a hybrid dataset was generated for the city of Reading containing 5000 journeys, of which 50% were synthetically generated and the remaining half were taken from the original dataset.

5. Prediction methods

5.1. *Benchmarks*

Two naïve benchmark algorithms were used to compare all models against.

Average speed: This method uses the average speed of a vehicle since the start of its current journey. Thus, it does not reflect any short-term speed variation. The calculated speed is used to interpolate the position of the vehicle from the trajectory of its journey pattern for the next 40 s.

Current speed: This method uses the last three transmitted positions of a vehicle to calculate its current average speed, hence accounting for temporary speed variations. The prediction is made by interpolating the position for the next 40 s from the journey trajectory.

5.2. Target representation

The target was represented as a trajectory, by projecting the coordinates onto the route pattern of a journey. This ensures that inaccuracies locating a vehicle off-route are removed. In practice, this method predicts a number representing the progress along the trajectory with a max of 1, which is the final destination. To illustrate the performance of the model, the trajectory can be decoded into coordinates to allow the calculation of a Haversine distance between the predicted and actual location, which is more intuitive than a loss based on the trajectory. Two variations of this target representation were used: **a.** the unconstrained progress along the trajectory, which could lead to a vehicle appearing to move backwards, **b.** the distance travelled in the next time interval added to the last known position, which enforces a forward prediction.

5.3. Input features

The features included were: coordinates normalised to a bounding box representing the operational area of the bus company, the time delta between consecutive recordings, the elapsed time from the start of the journey, and time embeddings as described below. The input features were min–max normalised.

5.4. Handling of time

The time information was split into its components to make it possible for the algorithms to learn periodic patterns. To achieve this, the timestamp was translated into the minute of the day, the hour of the day, and day of the week. These were embedded in a multidimensional space as detailed in the architecture description 5.6.

5.5. Input windows

A moving window was applied to each journey. The window size was a minimum of 10 data points growing by one time step at a time until the end of the journey. This ensures a realistic simulation of the progress of a journey as would be observed in a real world application.

5.6. Architecture

Two neural networks were used with identical architecture except for the Recurrent Neural Network (RNN) module [39], which was either a Gated Recurrent Unit (GRU) [40] or a Long Short Term Memory (LSTM) network [41]. The time embeddings were learned by the network in a multidimensional space. The dimensions were chosen as half of the possible number of values for each embedded variable. As an example, the hour of the day was embedded in 12 dimensions as the maximum number of hours is 24. These embeddings with a total of 52 dimensions were fed into a linear layer to reduce their dimensions back to the original number of time-based features. The output of the linear layer was concatenated with the remaining input features and fed into either a GRU or LSTM layer followed sequentially by a 1D batchnorm, a linear layer, a leaky ReLU, a second batchnorm and a final linear layer. To ensure the outputs were bounded, a sigmoid function was applied.

5.7. Hyper-parameters

To allow for direct comparison between the models, all training hyper-parameters were kept constant between the two cities. It is appreciated that this might not always yield the best performance but will illustrate the influence of the modifications made on the performance. The variables used were chosen through empirical exploration following the recommendations described by [42]. Each model was trained for 50 epochs using the one-cycle policy [42] with a maximum learning rate of 10^{-1} (Bournemouth) and 10^{-2} (Reading). As a loss function, the mean average error (MAE) was used.

6. Results and discussion

It is crucial to compare predictive algorithms using several different metrics to ensure a balanced interpretation of the results. Furthermore, it has to be kept in mind that in the presented example the two cities are considerably different. The most striking difference is the practice regarding journey shapes. The idea behind a journey shape is that it gives the exact route along the road of a certain journey. This, however, is handled differently by the bus operators. In the example of Reading each journey has an individual shape amounting to 90 shapes a day. These are mostly very similar or identical. In the example of Bournemouth fewer shapes are used, however, the shapes are significantly different in length as well as route, highlighting the need for standardisation of public transport data. As a result, only a subset of the journeys in Bournemouth are similar enough to be simulated in one approach, thus this dataset contains fewer journeys than the dataset generated for Reading (17,115 vs 7839 journeys). These differences have to be kept in mind and are crucial for the interpretation of the results. The median accuracies for mean speed benchmarks in Reading are lower in all datasets compared to the current speed benchmark and are shown in Fig. 3. The current speed benchmark for Bournemouth is comparable to the average speed benchmark. In the example of Reading this is not the case and the current speed benchmark suffers from higher prediction errors compared to the average speed benchmark (Fig. 3). An explanation could be that vehicles in Reading are more likely to stop for brief periods, which is reflected in a 13% increase of standard deviation of the travelling speed compared to Bournemouth. Interestingly, the histogram for the Reading benchmarks shows a peak around 80 m for the dataset with repeated start and ends (Fig. 4). This is explained by the benchmarking method, which uses the last three positions to estimate the average speed. Thus, a vehicle's speed can change from stationary to moving within 120 s or vice versa. Considering this time frame, 80 m/120 s corresponds to an average speed of 24 km/h, which is a realistic prediction for an urban bus network and in accordance with the estimated speed from the mean speed benchmark (Figs. 3 & 4)).

6.1. Perfect journeys

The first set of experiments shows the 'perfect' synthetic journey. These are generated without any of the discussed artefacts and therefore, should represent the simplest prediction problem. Poor performance of both architectures can be observed in the Bournemouth dataset. Both architectures perform virtually identical with a mean error of 63.8 m (σ=55 m) (Fig. 5(a)). This is an accuracy comparable to the benchmarks (current speed: 64.2 m, mean speed: 62.1 m). This underwhelming performance could be explained by the smaller dataset compared to the Reading data, however, a more likely explanation is the variability of the journey shape and routes in Bournemouth, which naturally results in less realistic synthetic data. As a consequence, it is difficult to identify individual journeys from the original data. Furthermore, the data generation suffers from the fact that the vehicles do not follow a consistent route, which would be expected to cause unrealistic synthetic journeys. In contrast, the prediction for Reading performs well with a mean error of 41.5 m (σ=46.5) and 47.5 m (σ=47.2) for the GRU and LSTM respectively (Fig. 5(a)). Both models significantly improve on the error compared to the benchmark (current speed: 68 m, mean speed 50.7 m). As mentioned previously, this dataset contains more journeys per day, however, the most likely explanation of this performance improvement can be attributed to the uniform journey shape, which will reduce errors in the data generation.

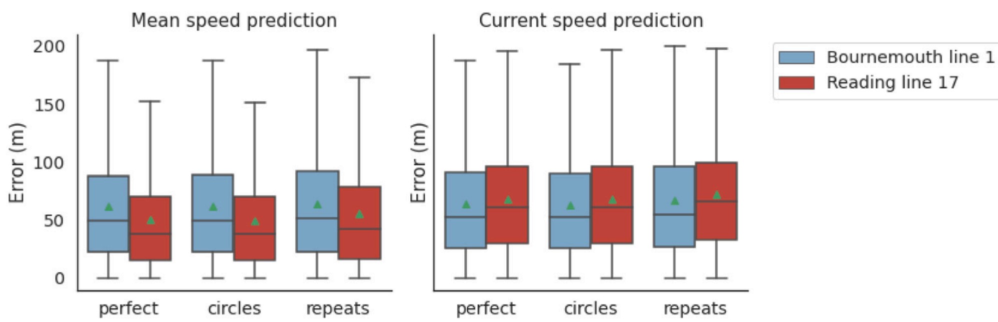

Fig. 3. Boxplot illustrating the prediction errors of the two nïve benchmark algorithms for both cities.

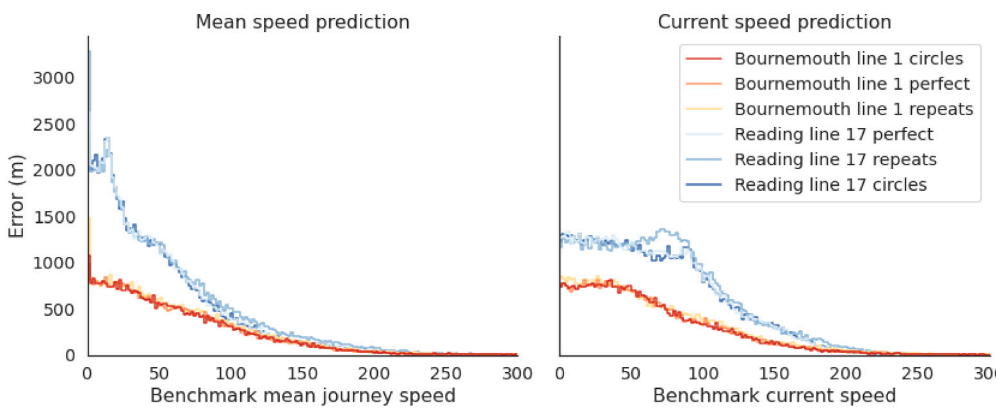

Fig. 4. Boxplot illustrating the prediction errors of the two nïve benchmark algorithms for both cities.

6.2. Ticketing machine artefacts

The introduction of the characteristic circular artefacts into the dataset would be expected to make any prediction more difficult. This is indeed observed in the predictions for Bournemouth. The average GRU performance was reduced by 2.5 m compared to the artefact free journeys. Notably, the performance of the LSTM did not significantly decrease and remained at 63.9 m (Fig. 5(a)). Similar findings were observed in Reading where the mean error of the GRU increased by 5 m. Interestingly, the mean error of the LSTM decreased by 2 m.

6.3. Repeats at start and end

The introduction of repeats at the start and end of the journey did have a strong impact on the prediction performance. The mean prediction error in Bournemouth increased by 5 m and 2 m for the GRU and LSTM, respectively. In Reading, the GRU prediction worsened drastically by 24 m, whereas the LSTM was not affected and remained at 47.8 m (Fig. 5). This is an intuitive response of the LSTM which, due to its ability to forget irrelevant information, is able to focus on the data relevant for the next step prediction.

6.4. Using hybrid data to improve predictions

The described hybrid dataset was used to demonstrate a possible application. As an intuition, it was assumed that the addition of synthetic data, which are cleaner and not affected by uncontrollable artefacts, should improve the overall prediction. When using an unconstrained prediction along the trajectory, this however is not observed and a model trained on purely synthetic or hybrid data performs worse on inference on real data (Fig. 5). This, however, is not the case if the prediction is forced forward as described in Section 4.4. If the prediction space is limited, an improvement in the inference accuracy of networks trained on both the real world dataset can be observed both in the purely synthetic and the hybrid dataset. The largest improvement can be observed if hybrid data were used for training (Fig. 5(b)).

6.5. Discussion of results

The results of this study show that the addition of synthetic data can improve predictive algorithms, which suffer from data quality issues. The use of synthetic data is used in many settings [43], such as healthcare settings to preserve privacy [44] but is also used in the assessment of algorithms such as feature selection methods where the control of features is important [45]. Some authors have also used synthetic data to estimate the upper theoretical limits of predictive algorithms [46]. The generation of hybrid datasets consisting of both real and synthetic data is less common, but examples such as from computer vision exist [47] or for classification problems with heavily unbalanced data [48]. Furthermore, some studies used synthetic data to augment small datasets, for example to improve pandemic datasets and the associated machine learning models [49]. Examples from the field of public transport are rare and mostly focus on optimisation of transport networks and specifically bus routes to minimise delays [50–52]. However, in general, a knowledge gap appears to prevent the combination of simulated data with machine learning algorithms [53], which could be beneficial to improve many areas especially in public transport research. This study demonstrates the use of such hybrid datasets to improve prediction quality. Furthermore, it highlights the lack of framework previously noted by us [54]. A prediction accuracy comparison with the wider literature for this study is not possible as similar research aims to solve different problems. The reason for this is that the research focus regarding short horizon predictions are focused on time frames of >5 min [55,56] or are defined as a distance rather than a time horizon [57]. Shorter prediction horizons are found in the literature but are aimed at predicting different metrics such as speed [58] or the elimination of bus-bunching [59]. As there are, to the author's knowledge, no examples in the literature predicting the position of urban buses in an ultrashort prediction horizon, a comparison with other studies cannot be drawn. Additionally, this study does not claim predictive superiority but demonstrates that the use of hybrid

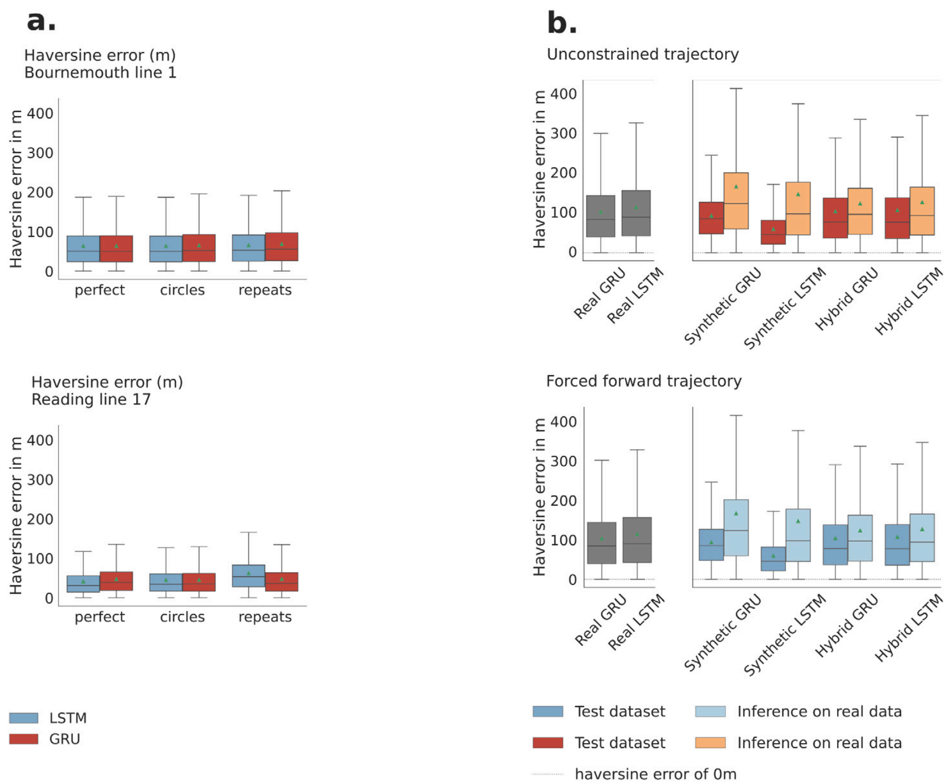

Fig. 5. (a) Boxplots for both cities and for each of the dataset and network architecture combinations. It is apparent that the performance in Reading is considerably better and the expected deterioration with the introduction of artefact can be observed. **(b) top:** Boxplots showing the error ranges in meters for the unconstrained networks the grey boxes show a network trained on real data as reference. The red boxes show the error of the holdout portion of the synthetic or hybrid dataset the orange boxes show the inference errors on the real dataset. **(b) bottom:** Boxplots showing the error ranges in meters for the forced forward networks the grey boxes show a network trained on real data as reference. The dark blue boxes show the error of the holdout portion of the synthetic or hybrid dataset the light blue boxes show the inference errors on the real dataset. (For interpretation of the references to colour in this figure legend, the reader is referred to the web version of this article.)

data can improve prediction accuracy. This knowledge will be of value to public transport researchers and can be applied to any prediction problem as well as to any model architecture to push the limits of the available data.

7. Conclusion

The importance of making public transport as convenient as possible is self-evident and could help increase passenger numbers and reduce urban congestion and pollution. Reliable predictions of current vehicle position and arrival times play a crucial part in this endeavour. However, this is being inhibited by the lack of reliable data, making any such algorithm development difficult.

Therefore, the described method of generating realistic journeys builds a bridge between the low quality recordable data and the real world. As a result, it is a platform to develop algorithms in a simulated and controlled environment, which can later be deployed in a real world scenario. Additionally, this platform allows simulation of user-specified artefacts as demonstrated by the repetition of positions or geofencing based disturbances. This study has highlighted several areas of improvement for urban bus network data to allow the development of reliable predictive solutions. The most striking observation was that any RNN based predictions in Bournemouth barely outperformed the naïve benchmark. This is due to the varied route shapes and lengths of the same bus line, making generalisation unfeasible. Thus, it can be recommended from a managerial as well as software development point of view that either route shapes should be standardised between the lines or that the lines are subdivided based on their route shapes. This will greatly improve the potential of the data collected and the development of data-based software solutions.

The second observation was that the prediction performance can be improved if the data is as clean as possible. This means that technology providers need to collaborate to ensure the best possible outcome for public transport as a whole. Although geofencing methods to determine the arrival at a stop are useful, the produced artefacts of some systems do have a negative impact on the tested predictive algorithms. Furthermore, an indication whether a vehicle has started or ended a journey will help in the overall prediction accuracy. The differences between the two example cities highlight the need for a national standard if accurate predictions are desired, universally preventing the need to develop a predictive system from the ground up for each city and operational line. This would be a big step forward to an implementation of mobility as a service and would benefit all public transport operators.

The limitations of this study are that the ground truth can only be approximated due to the lack of high-quality data. This, however, is also the driving force behind the demonstrated approach to further advance this research and any other research relying on public transport data, the following key points should be considered for future research:

- Develop a standardised framework to transmit and record public transport data.
- Standardise the use of route patterns to ensure they can be used for data driven applications.
- Develop a benchmarking framework specifically for predictive algorithms in urban bus networks.

In the meantime, until such standardisations become reality, our data generation method described here is a good approximation of reality and a useful tool in simulating effects on urban bus networks.

References

[1] M.M. Salvador, M. Budka, T. Quay, Automatic transport network matching using deep learning, Transp. Res. Proc. 31 (2016) (2018) 67–73, http://dx.doi.org/10.1016/j.trpro.2018.09.053, URL https://linkinghub.elsevier.com/retrieve/pii/S2352146518301273.

[2] G.-J. Peek, M. van Hagen, Creating synergy in and around stations: Three strategies for adding value, Transp. Res. Rec. J. Transp. Res. Board 1793 (1) (2002) 1–6, http://dx.doi.org/10.3141/1793-01, URL http://trrjournalonline.trb.org/doi/10.3141/1793-01.

[3] Department for Transport, Transport Statistics Great Britain 2019 Moving Britain Ahead, Tech. rep., 2019, p. 10.

[4] Department for Business Energy & Industrial Strategy, Greenhouse gas reporting: conversion factors 2019, Research and Analysis (2019) URL https://www.gov.uk/government/publications/greenhouse-gas-reporting-conversion-factors-2019.

[5] R.G. Mishalani, M.M. Mccord, J. Wirtz, Passenger wait time perceptions at bus stops : Empirical results and impact on evaluating real- time bus arrival information, J. Publ. Transp. 9 (2) (2006) 89–106, http://dx.doi.org/10.5038/2375-0901.9.2.5.

[6] T. Reich, M. Budka, D. Hulbert, Impact of data quality and target representation on predictions for urban bus networks, in: 2020 IEEE Symposium Series on Computational Intelligence, SSCI 2020, IEEE, 2020, pp. 2843–2852, http://dx.doi.org/10.1109/SSCI47803.2020.9308166, URL https://ieeexplore.ieee.org/document/9308166/.

[7] M. Hickman, Bus automatic vehicle location (AVL) systems, in: Assessing the Benefits and Costs of ITS, Kluwer Academic Publishers, Boston, 2006, pp. 59–88, http://dx.doi.org/10.1007/1-4020-7874-9{_}5, URL http://link.springer.com/10.1007/1-4020-7874-9_5.

[8] Z. Junyou, W. Fanyu, W. Shufeng, Application of support vector machine in bus travel time prediction, Int. J. Syst. Eng. 2 (1) (2018) 21–25, http://dx.doi.org/10.11648/j.ijse.20180201.15, URL https://www.tandfonline.com/doi/full/10.1080/21680566.2017.1353449.

[9] J. Li, J. Gao, Y. Yang, H. Wei, Bus arrival time prediction based on mixed model, China Commun. 14 (5) (2017) 38–47, http://dx.doi.org/10.1109/CC.2017.7942193, URL http://ieeexplore.ieee.org/document/7942193/.

[10] L. Meng, P. Li, J. Wang, Z. Zhou, Research on the prediction algorithm of the arrival time of campus bus, in: Advances in Intelligent Systems Research, AISR, Vol. 142, 2017, pp. 31–33.

[11] The Royal Society, Machine learning: the power and promise of computers that learn by example, in: Report By the Royal Society, Vol. 66, The Royal Society, 2017, p. 125, http://dx.doi.org/10.1126/scitranslmed.3002564, URL https://royalsociety.org/~/media/policy/projects/machine-learning/publications/machine-learning-report.pdf.

[12] W. Luo, D. Phung, T. Tran, S. Gupta, S. Rana, C. Karmakar, A. Shilton, J. Yearwood, N. Dimitrova, T.B. Ho, S. Venkatesh, M. Berk, Guidelines for developing and reporting machine learning predictive models in biomedical research: A multidisciplinary view., J. Med. Int. Res. 18 (12) (2016) e323, http://dx.doi.org/10.2196/jmir.5870, http://www.ncbi.nlm.nih.gov/pubmed/27986644.

[13] M. Baker, Over half of psychology studies fail reproducibility test, Nature (2015) http://dx.doi.org/10.1038/nature.2015.18248, http://www.nature.com/doifinder/10.1038/nature.2015.18248 http://www.nature.com/articles/nature.2015.18248.

[14] T. Yarkoni, J. Westfall, Choosing prediction over explanation in psychology: Lessons from machine learning, Perspect. Psychol. Sci. 12 (6) (2017) 1100–1122, http://dx.doi.org/10.1177/1745691617693393.

[15] M. Baker, 1,500 Scientists lift the lid on reproducibility, Nature 533 (7604) (2016) 452–454, http://dx.doi.org/10.1038/533452a, URL http://www.nature.com/doifinder/10.1038/533452a.

[16] M. Hutson, Artificial intelligence faces reproducibility crisis unpublished code and sensitivity to training conditions make many claims hard to verify, Science 359 (6377) (2018) 725–726, http://dx.doi.org/10.1126/science.359.6377.725, URL http://www.ncbi.nlm.nih.gov/pubmed/29449469.

[17] J.W. Schooler, Metascience could rescue the 'replication crisis', Nature 515 (7525) (2014) 9, http://dx.doi.org/10.1038/515009a, URL http://www.nature.com/doifinder/10.1038/515009a.

[18] W. Rasdorf, H. Cai, C. Tilley, S. Brun, H. Karimi, F. Robson, Transportation distance measurement data quality, J. Comput. Civ. Eng. 17 (2) (2003) http://dx.doi.org/10.1061/(ASCE)0887-3801(2003)17:2(75).

[19] S. Robinson, B. Narayanan, N. Toh, F. Pereira, Methods for pre-processing smartcard data to improve data quality, Transp. Res. C 49 (2014) http://dx.doi.org/10.1016/j.trc.2014.10.006.

[20] R. Arbex, C.B. Cunha, Estimating the influence of crowding and travel time variability on accessibility to jobs in a large public transport network using smart card big data, J. Transp. Geogr. 85 (2020) http://dx.doi.org/10.1016/j.jtrangeo.2020.102671.

[21] R. Choudhary, A. Khamparia, A.K. Gahier, Real time prediction of bus arrival time: A review, in: 2016 2nd International Conference on Next Generation Computing Technologies, NGCT, IEEE, 2016, pp. 25–29, http://dx.doi.org/10.1109/NGCT.2016.7877384, URL http://ieeexplore.ieee.org/document/7877384/.

[22] E. Pekel, S.S. Kara, A comprehensive review for artificial neural network application to public transportation, Sigma J. Eng. Nat. Sci. 35 (1) (2017) 157–179.

[23] I. Sutskever, O. Vinyals, Q.V. Le, Sequence to sequence learning with neural networks, 2014, pp. 1–9, http://dx.doi.org/10.1007/s10107-014-0839-0, URL http://arxiv.org/abs/1409.3215.

[24] R. Yamashita, M. Nishio, R.K.G. Do, K. Togashi, Convolutional neural networks: an overview and application in radiology, Insights Imaging 9 (4) (2018) 611–629, http://dx.doi.org/10.1007/s13244-018-0639-9.

[25] O. Theophilus, M.A. Dulebenets, J. Pasha, Y.y. Lau, A.M. Fathollahi-Fard, A. Mazaheri, Truck scheduling optimization at a cold-chain cross-docking terminal with product perishability considerations, Comput. Ind. Eng. 156 (March) (2021) http://dx.doi.org/10.1016/j.cie.2021.107240.

[26] A.M. Fathollahi-Fard, M. Hajiaghaei-Keshteli, R. Tavakkoli-Moghaddam, Red deer algorithm (RDA): a new nature-inspired meta-heuristic, Soft Comput. 24 (19) (2020) 14637–14665, http://dx.doi.org/10.1007/s00500-020-04812-z.

[27] A.M. Fathollahi-Fard, M. Hajiaghaei-Keshteli, R. Tavakkoli-Moghaddam, The social engineering optimizer (SEO), Eng. Appl. Artif. Intell. 72 (April) (2018) 267–293, http://dx.doi.org/10.1016/j.engappai.2018.04.009.

[28] M.R. Islam, S.M. Ali, A.M. Fathollahi-Fard, G. Kabir, A novel particle swarm optimization-based grey model for the prediction of warehouse performance, J. Comput. Design Eng. 8 (2) (2021) 705–727, http://dx.doi.org/10.1093/jcde/qwab009.

[29] J. Moosavi, L.M. Naeni, A.M. Fathollahi-Fard, U. Fiore, Blockchain in supply chain management: a review, bibliometric, and network analysis, Environ. Sci. Pollut. Res. (July) (2021) http://dx.doi.org/10.1007/s11356-021-13094-3.

[30] N. Ghadami, M. Gheibi, Z. Kian, M.G. Faramarz, R. Naghedi, M. Eftekhari, A.M. Fathollahi-Fard, M.A. Dulebenets, G. Tian, Implementation of solar energy in smart cities using an integration of artificial neural network, photovoltaic system and classical delphi methods, Sustainable Cities Soc. 74 (2021) 103149, http://dx.doi.org/10.1016/j.scs.2021.103149, https://www.sciencedirect.com/science/article/abs/pii/S2210670721004315 https://linkinghub.elsevier.com/retrieve/pii/S2210670721004315.

[31] M. Mohammadi, M. Gheibi, A.M. Fathollahi-Fard, M. Eftekhari, Z. Kian, G. Tian, A hybrid computational intelligence approach for bioremediation of amoxicillin based on fungus activities from soil resources and aflatoxin B1 controls, J. Environ. Manag. 299 (2021) 113594, http://dx.doi.org/10.1016/j.jenvman.2021.113594, URL https://linkinghub.elsevier.com/retrieve/pii/S030147972101656X.

[32] J.M. Huttunen, L. Kärkkäinen, H. Lindholm, Pulse transit time estimation of aortic pulse wave velocity and blood pressure using machine learning and simulated training data, PLoS Comput. Biol. 15 (8) (2019) e1007259, http://dx.doi.org/10.1371/journal.pcbi.1007259.

[33] K.B. Withers, M.P. Moschetti, E.M. Thompson, A machine learning approach to developing ground motion models from simulated ground motions, Geophys. Res. Lett. 47 (6) (2020) http://dx.doi.org/10.1029/2019GL086690, https://agupubs.onlinelibrary.wiley.com/doi/epdf/10.1029/2019GL086690 https://onlinelibrary.wiley.com/doi/abs/10.1029/2019GL086690.

[34] G. Sethuraman, X. Liu, F.R. Bachmann, M. Xie, A. Ongel, F. Busch, Effects of bus platooning in an urban environment, in: 2019 IEEE Intelligent Transportation Systems Conference, ITSC 2019, Institute of Electrical and Electronics Engineers Inc., 2019, pp. 974–980, http://dx.doi.org/10.1109/ITSC.2019.8917041.

[35] Y. Ding, S.I.-J. Chien, N.A. Zayas, Simulating bus operations with enhanced corridor simulator: Case study of new jersey transit bus route 39, Transp. Res. Rec. (1731) (2000) 104–111, http://dx.doi.org/10.3141/1731-13.

[36] P. Ristoski, G.K.D. De Vries, H. Paulheim, A collection of benchmark datasets for systematic evaluations of machine learning on the semantic web, in: Lecture Notes in Computer Science (Including Subseries Lecture Notes in Artificial Intelligence and Lecture Notes in Bioinformatics), 9982 LNCS, Springer Verlag, 2016, pp. 186–194, http://dx.doi.org/10.1007/978-3-319-46547-0{_}20, URL https://link.springer.com/chapter/10.1007/978-3-319-46547-0_20.

[37] TomTom, Bournemouth traffic report | TomTom traffic index, 2020, Bournemouth Traffic URL https://www.tomtom.com/en_gb/traffic-index/bournemouth-traffic/.

[38] A. Azzalini, A. Capitanio, Statistical applications of the multivariate skew normal distribution, J. R. Stat. Soc. Ser. B Stat. Methodol. 61 (3) (1999) 579–602, http://dx.doi.org/10.1111/1467-9868.00194.

[39] D.E. Rumelhart, G.E. Hinton, R.J. Williams, Learning internal representations by error propagation, Read. Cogn. Sci. A Perspect. Psychol. Artif. Intell. (V) (2013) 399–421, http://dx.doi.org/10.1016/B978-1-4832-1446-7.50035-2.

[40] K. Cho, B. van Merrienboer, C. Gulcehre, D. Bahdanau, F. Bougares, H. Schwenk, Y. Bengio, Learning phrase representations using RNN encoder–decoder for statistical machine translation, in: Proceedings of the 2014 Conference on Empirical Methods in Natural Language Processing, EMNLP, Vol. 4, (January) Association for Computational Linguistics, Stroudsburg, PA, USA, 2014, pp. 1724–1734, http://dx.doi.org/10.3115/v1/D14-1179, URL http://arxiv.org/abs/1409.3215 http://aclweb.org/anthology/D14-1179.

[41] S. Hochreiter, J. Schmidhuber, Long short-term memory, Neural Comput. 9 (8) (1997) 1735–1780, http://dx.doi.org/10.1162/neco.1997.9.8.1735.

[42] L.N. Smith, A disciplined approach to neural network hyper-parameters: Part 1 – learning rate, batch size, momentum, and weight decay, 2018, pp. 1–21, arXiv CoRR abs/1803.09820 URL http://arxiv.org/abs/1803.09820.

[43] M. Hittmeir, A. Ekelhart, R. Mayer, On the utility of synthetic data: An empirical evaluation on machine learning tasks, PervasiveHealth Pervasive Comput. Technol. Healthc. (2019) http://dx.doi.org/10.1145/3339252.3339281.

[44] D. Rankin, M. Black, R. Bond, J. Wallace, M. Mulvenna, G. Epelde, Reliability of supervised machine learning using synthetic data in health care: Model to preserve privacy for data sharing, JMIR Med. Inform. 8 (7) (2020) http://dx.doi.org/10.2196/18910.

[45] V. Bolón-Canedo, N. Sánchez-Maroño, A. Alonso-Betanzos, A review of feature selection methods on synthetic data, Knowl. Inf. Syst. 34 (3) (2013) 483–519, http://dx.doi.org/10.1007/s10115-012-0487-8.

[46] Y.I. Kuchin, R.I. Mukhamediev, K.O. Yakunin, One method of generating synthetic data to assess the upper limit of machine learning algorithms performance, Cogent Eng. 7 (1) (2020) http://dx.doi.org/10.1080/23311916.2020.1718821.

[47] D. Dai, C. Sakaridis, S. Hecker, L. Van Gool, Curriculum model adaptation with synthetic and real data for semantic foggy scene understanding, Int. J. Comput. Vis. 128 (5) (2020) 1182–1204, http://dx.doi.org/10.1007/s11263-019-01182-4.

[48] H. Kaur, H.S. Pannu, A.K. Malhi, A systematic review on imbalanced data challenges in machine learning: Applications and solutions, ACM Comput. Surv. 52 (4) (2019) http://dx.doi.org/10.1145/3343440.

[49] H.P. Das, R. Tran, J. Singh, X. Yue, G. Tison, A. Sangiovanni-Vincentelli, C.J. Spanos, Conditional synthetic data generation for robust machine learning applications with limited pandemic data, 19, 2021, URL http://arxiv.org/abs/2109.06486.

[50] R.K. Kalle, P. Kumar, S. Mohan, M. Sakata, Simulation-driven optimization of urban bus transport, WIT Trans. Built Environ. 186 (2019) 97–108, http://dx.doi.org/10.2495/UT190091.

[51] S.M.H. Moosavi, A. Ismail, C.W. Yuen, Using simulation model as a tool for analyzing bus service reliability and implementing improvement strategies, PLoS One 15 (5) (2020) 1–26, http://dx.doi.org/10.1371/journal.pone.0232799.

[52] S.R. Pells, An approach to the simulation of bus passenger journey times for the journey to work, Transp. Plan. Technol. 14 (1) (1989) 19–35, http://dx.doi.org/10.1080/03081068908717411, https://www.witpress.com/Secure/elibrary/papers/UT19/UT19009FU1.pdf http://www.tandfonline.com/doi/abs/10.1080/03081068908717411.

[53] L. von Rueden, S. Mayer, R. Sifa, C. Bauckhage, J. Garcke, Combining Machine Learning and Simulation to a Hybrid Modelling Approach: Current and Future Directions, in: Lecture Notes in Computer Science (Including Subseries Lecture Notes in Artificial Intelligence and Lecture Notes in Bioinformatics), vol. 12080 LNCS, Springer International Publishing, 2020, pp. 548–560, http://dx.doi.org/10.1007/978-3-030-44584-3{_}43.

[54] T. Reich, M. Budka, D. Robbins, D. Hulbert, Survey of ETA prediction methods in public transport networks, 2019, arXiv.

[55] T. Zhou, W. Wu, L. Peng, M. Zhang, Z. Li, Y. Xiong, Y. Bai, Evaluation of urban bus service reliability on variable time horizons using a hybrid deep learning method, Reliab. Eng. Syst. Saf. 217 (May 2021) (2021) 108090, http://dx.doi.org/10.1016/j.ress.2021.108090.

[56] E. Hans, N. Chiabaut, L. Leclercq, R.L. Bertini, Real-time bus route state forecasting using particle filter and mesoscopic modeling, Transp. Res. C 61 (2015) 121–140, http://dx.doi.org/10.1016/j.trc.2015.10.017.

[57] C. Coffey, A. Pozdnoukhov, F. Calabrese, Time of arrival predictability horizons for public bus routes, in: 4th ACM SIGSPATIAL International Workshop on Computational Transportation Science 2011, CTS'11, in Conjunction with ACM SIGSPATIAL GIS 2011, 2011, pp. 1–5, http://dx.doi.org/10.1145/2068984.2068985.

[58] Q. Ye, W.Y. Szeto, S.C. Wong, Short-term traffic speed forecasting based on data recorded at irregular intervals, IEEE Trans. Intell. Transp. Syst. 13 (4) (2012) 1727–1737, http://dx.doi.org/10.1109/TITS.2012.2203122.

[59] B. Varga, T. Tettamanti, B. Kulcsár, Energy-aware predictive control for electrified bus networks, Appl. Energy 252 (August) (2019) 113477, http://dx.doi.org/10.1016/j.apenergy.2019.113477.

Decision support system for dementia patients using intuitionistic fuzzy similarity measure

Debendra Kumar Sahoo, *Department of Electrical Engineering, Aryan Institute of Engineering & Technology, Bhubaneswar, dksahoo312@gmail.com*

Malaya Tripathy, *Department of Electronics and Communication Engineering , Capital Engineering College, Bhubaneswar, malaya.tripathy43@gmail.com*

Sudesh Kumar Patel, *Department of Computer Scinece Engineering , Raajdhani Engineering College, Bhubaneswar, sk.patel331@yahoo.co.in*

Subhendu Sahoo, *Department of Electrical Engineering , NM Institute of Engineering & Technology, Bhubaneswar, srikant.p@yahoo.co.in*

A R T I C L E I N F O

Key words:
Similarity measure
Word cognition assessment
Crisp measure
Fuzzy similarity measure
Intuitionistic fuzzy similarity measure
Efficiency

A B S T R A C T

Similarity measure confirms the proximity of two objects to each other. This concept can be applied as fuzzy or intuitionistic fuzzy. There are lots of fuzzy similarity measures which had been extended to intuitionistic fuzzy similarity measure, with application in different domain. There is need to investigate these methods based on their application for further modification. Thus, the aim of this research is to modify existing fuzzy and intuitionistic fuzzy similarity measures, and apply it to cognitive domain for better performance.

Existing intuitionistic fuzzy similarity methods were extended and modified. These research showed that the existing methods had been applied to various domains, and researchers had improved and extended most fuzzy similarity measure to intuitionistic fuzzy similarity measure for optimal performance. Experiment showed that the proposed methods gives higher similarity value and lower processing time.

1. Introduction

Similarity is such that if all substrings from one argument of comparison are found in the other, the final similarity degree is evaluated as '1' which is interpreted as the identity of the two strings [19]. It plays a great role in problem solving including real life problems. Similarity measure is a scientific measure for determining the degree of similarity between two objects. In the same way distance measure is an important tool which describes the difference between two sets, and it is considered as a dual concept of similarity measure. Several approaches had been scientifically opined for evaluating similarity measure These measures are as many as the broad significance and applicability of similarity measure, whose suitability depends on the application areas like pattern recognition, hierarchical cluster analysis, approximate analogical reasoning, rule matching in fuzzy control, neural networks, query processing with different fuzzy semantics. Similarity measures are based on set operations like union, intersection, maximum difference, symmetric difference etc. Similarity measure may not be effective in some cases, especially where classification is paramount.

Sets represents elements or group of elements that has common properties [22]. A set is a tool that can be used to model real life problems. Set can be represented in various forms like crisp set, fuzzy set, and intuitionistic fuzzy set among others. A crisp set evaluates to either 0 or 1. It does not depict the degree of membership. Fuzzy set is preferred to crisp set because it represents how human mind perceives and manipulates information. Human mind process hedges like weak, moderate, strong, good, very good, tall, very tall, brilliant, more brilliant to mention but few. These hedges are modelled as linguistic property, for instance type-1 linguistic fuzzy set gives overlapping partition which leads from one set to another such as small, medium and big. Fuzzy considers only membership function, to improve this it is extended to intuitionistic fuzzy set which considers membership and vagueness of a set with respect to the universal set. Intuitionistic fuzzy sets make descriptions of the objective world become more realistic, practical, accurate and promising. It has diverse application to fields like data processing, identification of functional dependency relationship between concepts in data mining systems, approximate reasoning, pattern recognition, decision making, medical diagnosis, logic programming, sale analysis and new product marketing. Other diverse application include financial services, negotiation process, psychological investigations, machine learning, image processing, fuzzy risk analysis, fault tree analysis etc.

Measures of similarity between sets is an important tool for decision making, pattern recognition, machine learning etc. [33]. Intuitionistic fuzzy set similarity measure entails comparing the information carried by intuitionistic fuzzy set. Many similarity measures had been proposed in this context but a few of them comes from the well-known distance measures. Intuitionistic fuzzy similarity measure bridges the gap of similarity measures by classifying data based on linguistic variable quintuple.

An area of psychology popularly known as cognition is an area that needs more attention, due to its relevance to keeping track of working memory capacity. Anagram and word cognition are not exempted in this context. It has to do with evaluating user's response to anagram or word scrabble task. Application of intuitionistic fuzzy set to this area is not common. Application of intuitionistic fuzzy similarity measure on anagram or word permutation would permit to test patient's sick situation. It would detect weather patient's response is okay or otherwise. The use of ply card for scrambling and unscrambling cards moved to storing set of words of a user's register in the database such that words are presented to users in scrambled form on the computer screen, users supplies the correct anagram. Researches had applied methods like brute-force, sorting, neighbourhood frequency i.e. the use of histogram or counting for verifying if supplied anagram or word are correct or not.

Thus, previous researches that modelled anagram cognition using crisp set, stated the membership or non-membership of word supplied by user without specifying the degree of membership. Previous model analysed anagram with respect to character entailment, whereby syllabic complexity is left out. This research seeks this further to model this problem using intuitionistic fuzzy set, which can depict the membership degree of words supplied, and also putting into consideration the vagueness of the anagram or word. The degree of membership would thus be based on type-1 linguistic fuzzy terms. Other characteristics such as character length, character entailment and syllabic complexity were used as characteristic variable to model anagram or word cognition. The degree of membership is measured by intuitionistic fuzzy similarity measure. The aim of this research is to test the estimated values of common existing similarity and distance measures in psychology domain, specifically cognition assessment, and come up with accurate similarity or distance measures of high values for the context.

2. Literature review

2.1. Similarity measures and applications

Similarity and distance functions are inter-related and recent researches have combined them to improve the performances of string processing for different applications [20]. Distance measures represent similarity measure as the proximity of observations to one another across the variable in cross variant. Distance measure is a measure of dissimilarity for continuous variables, where a larger value denotes less similarity, and is converted into a similarity measure by using an inverse relationship. The distance measure best represent the concept of proximity. It focuses on the magnitude of the values and portray similar cases of the objects that are closer together as the characteristics measured by metric variables are used, distance measure is the best method to assess similarity in clusters [5].

Shun Li and Jin Wen used pattern matching method to locate periods of operation from a historical data set. This was achieved by calculating the degree of similarity between historical data window and current snapshot data in order to locate periods of historical operation that are similar to current operating conditions. This enhanced the fault detection strategy [40].

An empirical study was done to reveal the behaviour of similarity measures when dealing with high dimensional data sets. A technical frame work was proposed to analyse, compare and bench mark the influence of different similarity measures on the result of distance based clustering algorithm. The relevance of this is to be able to identify suitable distance measures for data sets, and also facilitate a comparison and evaluation of newly proposed similarity or distance measures with traditional ones.

Aahul B. Diwate et al. did a systemic review on pattern matching. They stated that pattern matching concept was used in applications like: parser, spam filters, digital libraries, computational molecular biology, natural language processing, word processors [1].

Adio Akinwale and Adam Newiadomski explored the grammatical properties of generalized n-gram matching technique of similarity measures to find exact text in electronic computer applications. The authors proposed new similarity measures of improved generalized n-gram matching, which were tested and found to be universal. It was useful in words that could be derived from the word list as a group, and retrieve relevant medical terms from data base. One of the methods achieved best correlation of values for the evaluation of subjective examination. The authors proposed best similarity measures for closeness measurement of a particular domain [3].

Grigori, Alexander, Helena and David worked on soft similarity and soft cosine measure, they generalize the well-known cosine similarity measure in vector space model by introducing soft cosine measure. Authors proposed various formulas for exact or approximate calculation of soft cosine measure. Experiments shows that soft cosine measure gives better performance in case study entrance exam question answering task. One of the proposed measures is distance weighed cosine measure, it is calculated by averaging cosine similarity measure with hamming distance. Hamming distance counts how many features two vectors do not share, it decrease the similarity value of two vectors that share less features. This is because authors claim that cosine similarity is overly biased by features with higher values and does not care about how many features two vectors share [21].

2.2. Dissimilarity measures and applications

Dissimilarity coefficients, $d(S_1, S_2)$assess the degree to which patterns differ, S_1 and S_2 are string of character. Smaller values indicates closer or higher resemblance. Distances, differences, reciprocal of similarities, all constitute examples of dissimilarity measures.

Globally, similarity and dissimilarity are referred to as proximity measures $prox(S_1, S_2)$. Proximity values are positive numbers, its range being either bounded, such as the interval [0,1] or right unbounded: $prox(S_1, S_2) \in [0; +\infty]$. Similarity and dissimilarity measures have an inverse relationship [42].

Divergence measure has to do with discrimination and inferences. A new exponential divergence measure for intuitionistic fuzzy sets was proposed by Rajesh and Satish, [23], and applied to medical investigation and pattern recognition [26].

Rajesh and Satish, [24] proposed a divergence measure called intuitionistic fuzzy Jensen-Tsalli divergence measure, the essence of this is to measure the vagueness and underlying intuitionistic fuzzy sets. It was applied to pattern recognition problem and in diagnosis of some diseases.

Authors Rajesh and others proposed a new dissimilarity measure based on Jensen inequality and α-nominal divergence measure. This method was proposed to solve multi-attribute decision making (MADM), its performance is better than other well known MADM method [25].

Rajesh and Satish proposed a new suitable divergence measure for discrimination of two probability distributions. The proposed dissimilarity measure was applied to pattern recognition [27].

A suitable divergence measure was introduced to find the distance between two probability distributions, which is very relevant in problems based on discrimination and inferences. The divergence measure is based on Shanon entropy. Proposed measure was applied to pattern recognition, and performed better than existing divergence measures. Proposed measure was extended to intuitionistic fuzzy dissimilarity measure [28].

2.3. Intuitionistic fuzzy set

Fuzziness is a concept of human thinking and speaking [11], which deals with subjectivity and vague concept. This is in contrast to crisp set which gives a true or false concept Fuzzy sets expresses the imprecision of human thinking and behaviour by appropriate mathematical tools. A fuzzy set is built from a reference set called universe of discourse.

Let X be the universe of discourse

$X = \{x1, x2, ..., xn\}$

Fuzzy set A is in $X(A \subset X)$

$\{(xi, \mu(xi))\}$

Where $xi \in x \, and \, \mu A: x \to [0, 1]$ is the membership function of A.

$VA: x \to [0, 1]$ is a non-membership function of A.

Intuitionistic fuzzy set [IFS] is a tool for modelling real life problems like sale analysis, new product marketing, financial services, negotiation process, psychological investigation etc. [7].

One of the most important fact of human thinking is its ability to summarize information into fuzzy set that bear an approximation relation to the primary data. In fuzzy sets, a membership function assigns to each element of the universe of discourse a number from the unit interval to indicate the degree of belongingness to the set under consideration. In most cases, when the degree of membership is expressed, the degree of non-membership is not expressed. Atanassov introduced the concept of IFS to resolve this. Intuitionistic fuzzy set expresses the degree of membership and non-membership with a degree of hesitancy [11].

IFS within the same universe of discourse can be evaluated for similarity. Lots of researches had been conducted on review of intuitionistic similarity and distance measures, and also extension and generation of new measures for enhancement. Intuitionistic fuzzy set similarity measure had been applied extensively to decision making [34,38], pattern recognition [12,35] and linguistic summaries [6,38,39].

2.4. Related works on existing intuitionistic fuzzy similarity measures and application

A new similarity measure was generated from the distance. It was proven from the research that the new similarity measure is simpler and more easily interpreted than the existing methods, and is well suited to be used with linguistic variables. Proposed similarity measures were used to characterize the similarity between linguistic variables. The proposed similarity measures are reliable in applications with compound linguistic variables. Existing measures are not that friendly with fuzzy queries, and defining the degree of similarity between fuzzy sets. [10]

Xu Zeshui and J Chen reviewed distance and similarity measures of intuitionistic fuzzy set comprehensively. This shows that distance and similarity measures of IFSs are based on geometric distance model, and set theoretic approach. Their review indicates that the most widely used tools are Hamming distance, Euclidean distance and Hausdourff distance. The authors defined distance measures between interval valued intuitionistic fuzzy set based on extension of hamming distance, Normalized Hamming distance, weighted Hamming distance, Euclidean distance Normalized Euclidean Distance, Weighted Euclidean distance to interval value intuitionistic fuzzy set. Two other measures were defined by combining Hausdorff metric with weight Hamming distance and weight Euclidean distance. There were non-extended methods and new proposed methods that satisfied the conditions of the metric. These methods have some good geometric properties, that are not as fit as proposed ones [11].

Jun Ye considered the information carried by membership and non-membership degree in IFSs as a vector representation with two elements. The author proposed a cosine similarity measure and a weighted cosine similarity measure between intuitionistic fuzzy similarity based on the concept of cosine similarity measure for fuzzy sets. The proposed measures were compared with the existing measures to test for efficiency. Research revealed that cosine similarity measure is the most reasonable. This was demonstrated with application to pattern recognition and medical diagnosis. Existing similarity measures cannot carry out pattern recognition in some cases [36].

Jun Ye developed a decision making method with optimism, neutralism and pessimism by use of the Dice similarity measure based on the reduct IFSs of interval valued intuitionistic fuzzy set [IVIFS]. The author addressed the issue of decision making method using the dice similarity measure between the reduct IFSs of IVIFS to treat the influences of optimism neutralism and persimism on the multicriteria decision making problem. The author also proposed Jacccard, Dice and cosine similarity measures between intutionistic trapezoidal fuzzy numbers that are treated as continuous and applied to multicriteria group decision making problems. In fuzzy environment, information available is imprecise/uncertain, which is a torment for decision maker in the decision making process. Dice is preferred to Jaccard and cosine because it gives better result when second vector is undefined. Result of Dice similarity measure based on expected interval of trapezoidal fuzzy numbers was compared with Zeng's single expected value method with known criteria weight. This proposed method is simple and effective in the decision making problem with completely unknown criteria weights [37].

Chandresegar and Seithikurmer applied intuitionistic fuzzy network for Customer to Business decision making. The method attained intuitionistic fuzzy optimization for customer to business, and resolved multi decision making problem. The method reduced the complexity of the customers to take best decision with less effort. The method minimized the decision making criteria by means of assigning the range of sets with the contribution of similarity degree measures. The method optimized customer to business decision making, and optimize decision making problem. Its application to customer to business has not received much attention over the internet [34].

Dimitris and Elpikini proposed a novel approach to the construction of cognitive map based on intuitionistic fuzzy logic. The new model called intuitionistic fuzzy cognitive map extends fuzzy cognitive map by considering expert hesitancy in determination of causal relation between the concept of a domain. It's advantage over fuzzy cognitive map model is that it can incorporate additional information regarding the hesitancy of the experts in the definition of the cause-effect relations between the concepts involved in a domain. Intuitionistic fuzzy cognitive map is capable of modelling real world medical decision making tasks closer to the way human perceive them. Existing methods lack ability to perform approximate reasoning and handle incomplete information [13].

Boran and other authors proposed intuitionistic fuzzy TOPSIS method for evaluation of supplier's multi-criteria group decision. Intuitionistic fuzzy weighted averaging operator was utilized to aggregate individual opinions of decision making for rating the important criteria and alternative. The weight of each criteria was given as linguistic terms characterized by intuitionistic fuzzy numbers. Intuitionistic fuzzy operator was utilized to aggregate opinions of decision makers. Ideal solutions were calculated based on Euclidean distance. This approach created a huge success for multi-criteria decision making problems because of vague perception of decision maker's opinions. Proposed method is more suitable in this context because criteria provided by decision makers are difficult to precisely express by crisp data in the selection of supplier problem [4].

Chao-Ming et al. proposed a new similarity measure formula for intuitionistic fuzzy set induced by Sugeno integral. This was compared with other existing similarity measures for intuitionistic fuzzy set and Sugeno performs better than existing ones, because it provides an operation similar to expected value. The proposed similarity measure uses a robust clustering method to recognize the pattern of intuitionistic fuzzy set. There was no existing method that considered Sugeno integral technique [12]

Ejagwa et al. authors showed a novel application of intuitionistic fuzzy set to model the uncertainty and vagueness in career determining using normalized Euclidean distance method to measure the distance between each student and each career respectively. Career was prescribed based on smallest distance between each student and each career. Existing career determination tool lacked the vagueness and hesitancy factor. Career determination using intuitionistic fuzzy set gave accurate and proper career choice based on academic performance [7].

Table 1
Intuitionistic Fuzzy similarity values for pattern/text with unequal length.

S/No.	Pattern/Text	IFV [jaccard, modified canbera, modified bigram]	IFV [jaccard, modified canbera, dice]
1	NAILS/NAIL	[0.8, 0.2] [0.8, 0.2] [0.25, 0.75]	[0.8, 0.2] [0.8, 0.2] [0.14, 0.86]
2	Gallery/Real	[0.57, 0.43] [0.667, 0.333] [0.833, 0.167]	[0.57, 0.43] [0.667, 0.333] [0.78, 0.22]
3	ANTLER/LATER	[0.83, 0.167] [0.83, 0.167] [0.8, 0.2]	[0.83, 0.167] [0.83, 0.167] [0.78, 0.22]
4	ANTLER/RENT	[0.667, 0.333] [0.667, 0.333] [0.8, 0.2]	[0.667, 0.333] [0.667, 0.333] [0.75, 0.25]
5	RENTAL/TEN	[0.5, 0.5] [0.5, 0.5] [0.8, 0.2]	[0.5, 0.5] [0.5, 0.5] [0.714, 0.286]
6	RENTAL/NET	[0.5, 0.5] [0.5, 0.5] [1.0, 0.0]	[0.5, 0.5] [0.5, 0.5] [1.0, 0.0]
7	RENTAL/RENT	[0.67, 0.33] [0.67, 0.33] [0.4, 0.6]	[0.67, 0.33] [0.67, 0.33] [0.25, 0.75]
8	GALLERY/GALL	[0.57, 0.43] [0.5, 0.5] [0.5, 0.5]	[0.57, 0.43] [0.5, 0.5] [0.33, 0.67]
9	GALLERY/ALL	[0.43, 0.57] [0.33, 0.67] [0.67, 0.33]	[0.43, 0.57] [0.33, 0.67] [0.50, 0.50]
10	BROAD/ROAD	[0.80, 0.20] [0.80, 0.20] [0.25 , 0.75]	[0.80, 0.20] [0.80, 0.20] [0.75, 0.25]
11	LARGELY/LAY	[0.43, 0.57] [0.50, 0.50] [0.83 , 0.17]	[0.43, 0.57] [0.50, 0.50] [0.75, 0.25]
12	LARGELY/GEAR	[0.57, 0.43] [0.67, 0.33] [0.67 , 0.33]	[0.57, 0.43] [0.67, 0.33] [0.56, 0.44]
13	ACRE/ACE	[0.75, 0.25] [0.75, 0.25] [0.67 , 0.33]	[0.75, 0.25] [0.75, 0.25] [0.60, 0.40]
14	ACRE/ARE	[0.75, 0.25] [0.75, 0.25] [0.67 , 0.33]	[0.75, 0.25] [0.75, 0.25] [0.60, 0.40]
15	Alter/Tar	[0.6, 0.4] [0.6, 0.4] [1.0, 0.0]	[0.6, 0.4] [0.6, 0.4] [1.0, 0.0]
16	Alter/Tear	[0.8, 0.2] [0.8, 0.2] [0.75, 0.25]	[0.8, 0.2] [0.8, 0.2] [0.71, 0.29]
17	Wean/An	[0.5, 0.5] [0.5, 0.5] [0.667, 0.333]	[0.5, 0.5] [0.5, 0.5] [0.5, 0.5]
18	SLAIN/SIN	[0.60, 0.40] [0.60, 0.40] [0.75, 0.25]	[0.60, 0.40] [0.60, 0.40] [0.67, 0.33]
19	SLAIN/AN	[0.40, 0.60] [0.40, 0.60] [1.0 , 0.0]	[0.40, 0.60] [0.40, 0.60] [1.0 , 0.0]
20	SLAIN/IN	[0.40, 0.60] [0.40, 0.60] [0.75 , 0.25]	[0.40, 0.60] [0.40, 0.60] [0.60 , 0.40]
21	ACRITICAL/CRITIC	[0.67, 0.33] [0.67, 0.33] [0.38 , 0.63]	[0.67, 0.33] [0.67, 0.33] [0.30 , 0.70]

2.5. Effect of cognition task on dementia patients

One of the tools used in psychology to investigate cognitive processes is anagram task. Adam et al. made a useful contribution to measurement models of human cognitive problem solving [2]. Robert, [29] worked on anagram software for cognitive research, the software provides different modes of operation: interactive and automatic. All possible anagrams are identified using sorting technique, and the lemma frequency information for all orthographically identical word forms is summed and printed. The research did not consider bi-gram frequency in anagrams.

Ktori presents series of orthographic measures for psycholinguistic research. Orthographic measure factors are word length, word-form frequency, lemma frequency, neighbourhood density, neighbourhood frequency, transposition neighbours [15]. Anagram tasks are frequently used in behavioural research to investigate a wide array of cognitive phenomena. Most prominently, they are used to study the cognitive stages involved in problem solving, specifically insight [29]. Researches on anagram had explored different methods for detecting orthographic similarity between anagrams. Methods like Brute force [18], Sorting [29], Bubble sort [9], Neighbourhood frequency of counting and histogram [14,16,17], have been used to detect anagram.

In previous researches on the use of anagram task for cognition there are drawbacks such as restriction of anagram letters to five [30,32]. There is no standard software for anagram detection, and statistical analysis tool was only used. [14,16]. Oral conduction of anagram test, no standard software was developed [31].

The existing cognitive software does not incorporate bigram orthographic structure. It only uses sorting detection technique, and there was no syllabic structure relationship detection [29]. It makes use of bigram frequency with bubble sort anagram detection without consideration of position of characters [9]. The processing time of Anagram detection is very high [9,18]

3. Method

3.1. Metrics and dissimilarity property

A distance or metric, d, is a real valued function of two points that obeys the following properties:

1. $Positivity$:
$d(S_1, S_2) \geq 0\, and\ d(S_1, S_2) = 0 \Leftrightarrow S_1 = S_2$ (1)

2. $Symmetryproperty$:
$d(S_1, S_2) = d(S_2, S_1)$ (2)

3. $Triangleinequity$:
$d(S_1, S_3) \leq d(S_1, S_2) + d(S_2, S_3)$ (3)

$Thepositivitysubsumesthefollowingtwodistanceaxioms$:
1. $Consistenceofself - similarity$:
$d(S_1, S_1) = d(S_2, S_2)$ (4)

2. $Minimalityofself - similarity$:
$d(S_1, S_2) \leq d(S_2, S_1)$ (5)

3.2. Similarity as a relation

$AsimilarityrelationonasetUisafuzzybinaryrelation$
$R : U \times R \rightarrow [0, 1]\ Holdingthefollowingproperties$:
$Reflexive$:
$R(x, x) = 1\ for\ any\ x \in U$ (6)

$Symmetric$:
$R(x, y) = R(y, x)\ for\ any\ x, y \in U$ (7)

$Transitive$:
$R(x, z) \geq R(x, y) \Delta R(y, z) for\ any\ x, y, z \in U$ (8)
$Where\ the\ operator\ is\ an\ arbitrary\ t - norm : [0, 1] \times [0, 1] \rightarrow [0, 1]$

It is a binary operator which is commutative, associative, monotone in both arguments and$1 \Delta x = x$. Hence it subsumes the classical two valued conjuction operator. A relation of similarity x_1 *and* x_2 is written as $x_1 \sim x_2$ [3].

3.3. Concept of intuitionistic fuzzy similarity measure

Let X be a nonempty set. An intuitionistic fuzzy set A in X is an object having the form:

$A = \left\{ \left(x, \mu_A(x), V_A(x) \right) : x \in X \right\}$

Where $\mu_A(x)$, $V_A(x)$: $x \rightarrow [0, 1]$ define respectively the degree of membership and nonmembership of the element $x \in X$to the set A, which is the subset of X.

Also, for every element $x \in X$, $0 \leq \mu_A(x)$, $V_A(x) \leq 1$.

Thus, $\pi_A(x) = 1 - \mu_A(x) - V_A(x)$ is called the intuitionistic fuzzy set index or is called hesitation margin of $x$in A. $\pi_A(x)$ is the degree of indeterminacy of $x \in X$ to the IFS A and $\pi_A(x) \in [0, 1]$ i.e. $\pi_A(x)$: $x \rightarrow$ [0, 1] and $0 \leq \pi_A(x) \leq 1$ for every $x \in X$ [41].

Table 2
Intuitionistic Fuzzy similarity measure [IFSM] of pattern/text with unequal lengths.

Pattern/Text	Linguistic Variable (anagram)	Euc. New Bigram	Euc. Dice	Can. New Bigram	Can. Dice	Ham. New Bigram	Ham. Dice
NAILS/NAIL	Simple	0.710	0.680	0.728	0.703	0.387	0.347
	Moderate	0.816	0.749	0.896	0.751	0.720	0.424
	Hard	0.739	0.649	0.833	0.803	0.577	0.518
Gallery/Real	Weak	0.73	0.77	0.748	0.762	0.419	0.442
	Moderate	0.91	0.94	0.896	0.913	0.720	0.760
	Hard	0.93	0.93	0.876	0.880	0.674	0.681
ANTLER/LATER	Simple	0.586	0.596	0.656	0.660	0.282	0.288
	Moderate	0.862	0.869	0.801	0.807	0.514	0.525
	Hard	0.998	0.997	0.978	0.971	0.936	0.916
ANTLER/RENT	Weak	0.733	0.76	0.731	0.74	0.393	0.413
	Moderate	0.95	0.97	0.904	0.913	0.716	0.753
	Hard	0.95	0.95	0.895	0.89	0.766	0.729
RENTAL/TEN	Weak	0.835	0.888	0.819	0.843	0.549	0.598
	Moderate	0.942	0.835	0.875	0.819	0.670	0.549
	Hard	0.835	0.803	0.819	0.766	0.549	0.449
RENTAL/NET	Weak	0.684	0.684	0.766	0.766	0.449	0.449
	Moderate	0.835	0.835	0.819	0.819	0.549	0.549
	Hard	0.803	0.803	0.766	0.766	0.449	0.449
RENTAL/RENT	Weak	0.867	0.848	0.837	0.796	0.586	0.505
	Moderate	0.952	0.877	0.895	0.851	0.716	0.616
	Hard	0.823	0.713	0.801	0.762	0.514	0.442
GALLERY/GALL	Weak	0.952	0.957	0.883	0.893	0.690	0.713
	Moderate	0.979	0.921	0.927	0.876	0.795	0.673
	Hard	0.793	0.697	0.759	0.717	0.436	0.369
GALLERY/ALL	Weak	0.926	0.985	0.886	0.937	0.696	0.822
	Moderate	0.900	0.895	0.845	0.836	0.604	0.584
	Hard	0.689	0.640	0.723	0.685	0.379	0.320
BROAD/ROAD	Weak	0.710	0.680	0.728	0.703	0.387	0.347
	Moderate	0.816	0.749	0.779	0.751	0.472	0.424
	Hard	0.739	0.649	0.833	0.803	0.577	0.518
LARGELY/LAY	Weak	0.820	0.875	0.829	0.852	0.570	0.619
	Moderate	0.910	0.940	0.845	0.869	0.604	0.656
	Hard	0.795	0.795	0.791	0.787	0.495	0.486
LARGELY/GEAR	Weak	0.842	0.882	0.791	0.820	0.495	0.486
	Moderate	0.990	0.993	0.947	0.954	0.494	0.552
	Hard	0.916	0.878	0.848	0.817	0.850	0.869
ACRE/ACE	Weak	0.729	0.752	0.725	0.741	0.380	0.407
	Moderate	0.952	0.956	0.885	0.905	0.693	0.741
	Hard	0.977	0.956	0.925	0.905	0.972	0.741
ACRE/ARE	Weak	0.729	0.752	0.725	0.741	0.380	0.407
	Moderate	0.952	0.956	0.885	0.905	0.693	0.741
	Hard	0.977	0.956	0.925	0.905	0.972	0.741
SLAIN/SIN	Weak	0.816	0.860	0.779	0.801	0.472	0.513
	Moderate	0.978	0.996	0.951	0.978	0.861	0.935
	Hard	0.921	0.907	0.861	0.837	0.638	0.587
SLAIN/AN	Weak	0.698	0.698	0.819	0.819	0.549	0.549
	Moderate	0.787	0.787	0.766	0.766	0.449	0.449
	Hard	0.698	0.698	0.717	0.717	0.368	0.368
SLAIN/IN	Weak	0.884	0.961	0.890	0.935	0.705	0.819
	Moderate	0.902	0.923	0.833	0.875	0.577	0.670
	Hard	0.724	0.698	0.754	0.717	0.427	0.368
ACRITICAL/CRITIC	Weak	0.867	0.843	0.830	0.791	0.572	0.495
	Moderate	0.942	0.865	0.887	0.845	0.698	0.605
	Hard	0.806	0.698	0.795	0.757	0.501	0.434
	Sum	45.606	44.94	44.71	44.22	31.59	30.41
	Average	0.84456	0.8323	0.8278	0.8189	0.5849	0.5631

3.3.1. Conditions for intuitionistic fuzzy similarity measure

A mapping S: $IFS \times IFS \rightarrow [0, 1], S(A, B)$ is said to be the degree of similarity between $A \in IFSs(x)\, and\, B \in IFSs(x)$, if $S(A, B)$ satisfies the following condition:

Let S be real function S such that:

$IFS \times IFS \rightarrow R^{+}.S$ is called a similarity measure if it satisfies the following conditions [11]:

$IS1 - 0 \leq S(A, B) \leq 1$
$IS2 - S(A, B) = 1\ if\ and\ only\ if\ A = B$
$IS3 - S(A, B) = S(B, A)$
$IS4 - S(A, C) \leq S(A, B)\, and\, S(A, C)$
$if\ A \subseteq B \subseteq C, C \in IFSs(X)$

3.3.2. Properties of intuitionistic fuzzy relation

Reflexive:

An intuitionistic fuzzy relation $R(x_1 \times x_2)$ is said to be reflexive if

$R(x_1 \times x_2)$
$\forall x_1, x_2 \in X, \mu R(x_1, x_1) = 1$

Symmetric: if $x_1, x_2 \in X$

$\mu R(x_1, x_2) = \mu R(x_2, x_1)\, and$
$V R(x_1, x_2) = V R(x_2, x_1)$

Transitive:

If R^2 is a subset of R where

$R^2 = R\, o\, R$

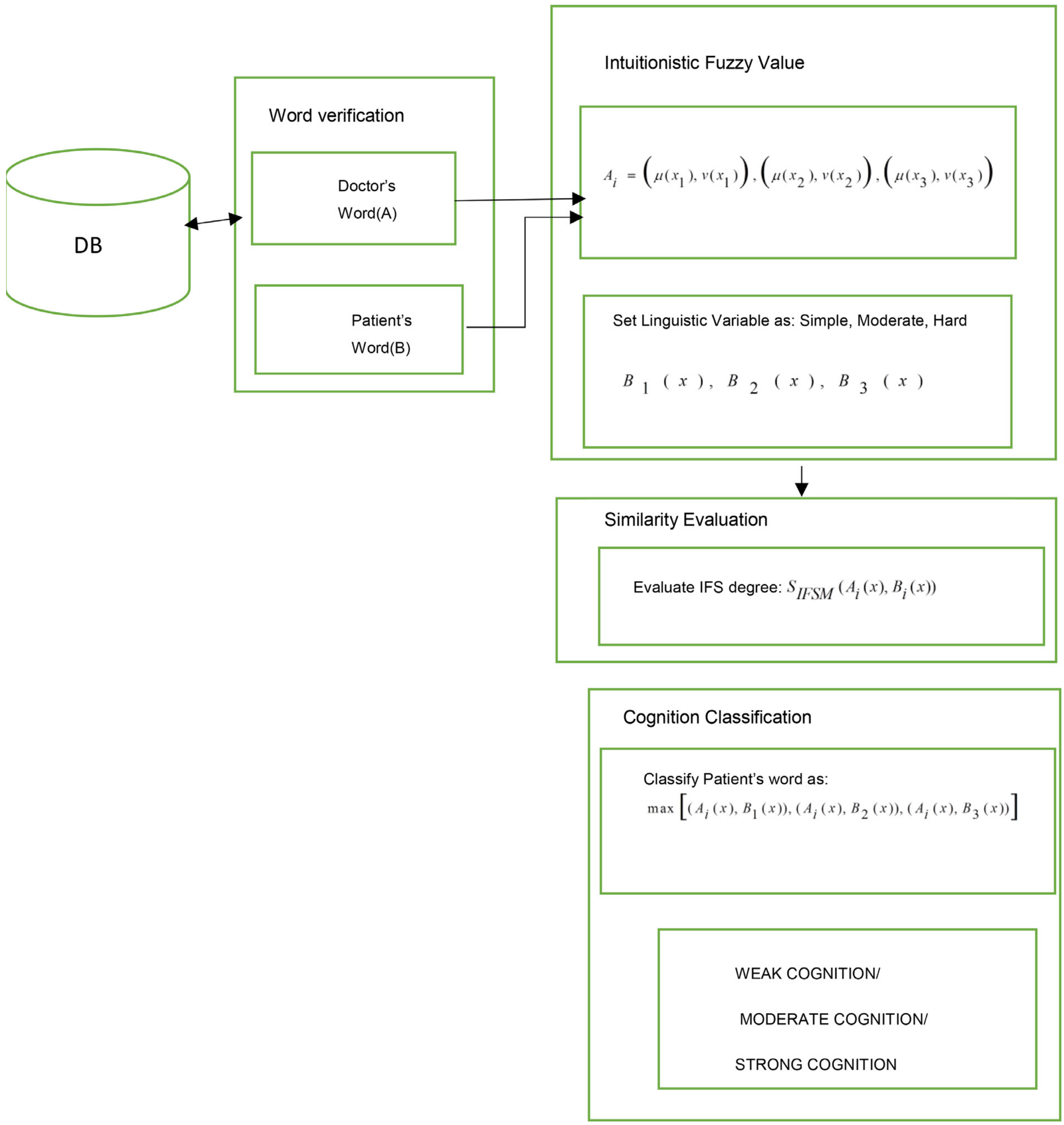

Fig. 1. Representation of the working principle of Cognition Assessment Decision Making.

3.4. Algorithm for intuitionistic fuzzy cognition assessment decision making

1 Calculate the system word and patient's word for characteristic featurex_1: character length using modified Canberra similarity and distance measures for determination of membership and non-membership μ, v respectively.

$$\mu(x_1) = 1 - \frac{|A| - |B|}{|A|} \tag{9}$$

$$\upsilon(x_1) = \frac{|A| - |B|}{|A|} \tag{10}$$

2 Calculate the system word and patient's word for characteristic featurex_2: character entailment using Jaccard similarity and distance measures for determination of membership and non-membership μ, v respectively.

$$\mu(x_2) = \frac{|A \cap B|}{|A \cup B|} \tag{11}$$

$$\upsilon(x_2) = 1 - \frac{|A \cap B|}{|A \cup B|} \tag{12}$$

3 Calculate the system word and patient's word for characteristic featurex_3: character entailment using modified Bigram (proposed method) distance and similarity measures for determination of membership and non-membership μ, v respectively.

$$\mu(x_3) = 1 - \frac{bigram(|A \cap B|)}{\max(|bigramA|, |bigramB|)} \tag{13}$$

$$\upsilon(x_3) = \frac{bigram(|A \cap B|)}{\max(|bigramA|, |bigramB|)} \tag{14}$$

Table 3
Processing Time of IFSM with modified bigram and IFSM dice for selected text and pattern.

S/No.	Euclidean Dice(ms)	Euclidean Bigram (ms)	Canberra Dice (ms)	Canberra Bigram (ms)	Hamming Dice (ms)	Hamming Bigram (ms)
1	1.00	0.992	1.00	1.00	0.999	1.00
2	1.00	0.999	1.00	1.00	0.999	0.999
3	1.00	0.995	0.999	1.00	1.00	1.00
4	1.00	0.999	1.015	0.999	1.00	1.00
5	0.999	0.997	1.00	0.999	1.00	0.999
6	0.999	0.998	1.000	1.00	1.00	1.00
7	1.00	0.999	1.000	0.999	1.00	1.00
8	1.00	1.015	0.999	1.00	1.015	1.00
9	1.015	1.015	1.000	1.00	1.00	1.015
10	0.999	0.999	1.000	1.00	1.00	0.999
11	1.00	0.999	1.000	1.001	1.00	1.015
12	1.00	0.999	1.000	0.999	1.015	1.00
13	1.00	1.013	1.015	1.015	1.00	0.999
14	1.00	0.997	1.00	1.015	1.015	1.00
15	1.00	0.997	1.015	1.00	1.00	1.015
Sum	15.012	15.003	15.043	15.027	15.043	15.031
Avg	1.8765	1.8754	1.8804	1.8784	1.8804	1.8789
Cost	0.450072	0.443805	0.44026	0.435067	0.311071	0.299727

4 Intuitionistic fuzzy value is generated as:

$$A_i(x) = (\mu(x_1), \upsilon(x_1)), (\mu(x_2), \upsilon(x_2)), (\mu(x_3), \upsilon(x_3))$$

5 Set the linguistic variables as:

$$\begin{aligned} &Simple\ : [0.4,\ 0.6]\,[0.4,\ 0.6]\,[0.4, 0.6] = B_1(x)\\ &Moderate\ : [0.6,\ 0.4]\,[0.6,\ 0.4]\,[0.6, 0.4] = B_2(x)\\ &Hard\ : [0.8,\ 0.2]\,[0.8,\ 0.2]\,[0.8, 0.2] = B_3(x)\end{aligned}$$

6 Intuitionistic fuzzy degree is evaluated between the set IFV and generated IFV for linguistic variables:

$$S_{IFSM}(A_i(x), B_i(x))$$

7 The patient's input is classified as IFV and linguistic variable with highest intuitionistic fuzzy similarity value:

$$\max\left[(A_i(x), B_1(x)), (A_i(x), B_2(x)), (A_i(x), B_3(x))\right]$$

Equations 9 – 14 are for converting Doctor's and Patient's Words to IFV. Eqs. (10) and (14) are modified Canberra and Dice respectively. The modified methods gives higher IFV values, emphasis is more on the modified method in Eq. (14) i.e. modified bigram because it is used to measure the characteristic word permutation. This characteristic is added to character entailment and length measure, to improve word cognition measure. Step 5 shows the threshold for classifying IFSMs, this is based on Evan's calibration. Steps 6 and 7 indicates how IFV are converted to IFSM and classified to simple, moderate and hard.

3.5. Modified and extended intuitionistic fuzzy distance measures for classification of intuitionistic fuzzy values of text and pattern

The formulas for conversion of strings into intuitionistic fuzzy values above in Eqs. (9)-14 will be adapted into IFSM.Anagram detection will be broadened by improving detection from [True/False] to Type-1 Anagram Detection i.e. using the linguistic terms A1- Not Anagram, A2- weak Anagram, A3- Average Anagram and A4- Hard Anagram. The IFV obtained from Eq. (9)-14 will be classified to type-1 anagram using modified and extended methods in Eqs. (18)–(20).

The similarity measure between IFS A and B as follows:

$$\begin{aligned} &S(A, B) = \frac{f(d_H(A,B)) - f(1)}{f(0) - f(1)}\\ &S(A, B)\ satisfies\ the\ properties\ of\ similarity\ measure\\ &The\ simplest\ f\ that\ can\ be\ chosen\ is\ :\\ &f(x) = 1 - x\end{aligned} \tag{15}$$

Similarity measure between A and B is denoted as follows:

$$\begin{aligned} &S(A, B) = 1 - d_H(A, B)\\ &d_H(A, B) = \left[\sum_{i=1}^{n} |a_i - b_i|^H\right]^{1/H}\\ &This\ denotes\ distance\ function,\ it\ represents\ the\ Hth\\ &order\ between\ points\ a\ and\ b.\\ &When\ H = 1\ and\ H = \infty\\ &d_1(A, B) = \left[\sum_{i=1}^{n} |a_i - b_i|^H\right]\\ &d_\infty(A, B) = \max_i |a_i - b_i|\end{aligned} \tag{16}$$

Also an exponential operation is highly useful in dealing with a similarity relation. Thus

$$f(x) = e^{-x} \tag{17}$$

3.5.1. Modified Euclidean intuitionistic fuzzy similarity measure based on exponential function

$$\begin{aligned} &E_{IFS}(A, B) = \sum_{i=1}^{n} \frac{|\mu_A(x_i) - \mu_B(x_i)|^2 + |V_A(x_i) - V_B(x_i)|^2}{2(|\mu_A(x_i) + \mu_B(x_i)| + |V_A(x_i) + V_B(x_i)|)}\\ &S_{new1}(A, B) = e^{-E_{IFS}(A,B)}\end{aligned} \tag{18}$$

3.5.2. Modified Canberra intuitionistic fuzzy similarity measure based on exponential function

$$\begin{aligned} &CA_{IFS}(A, B) = \sum_{i=1}^{n} \frac{|\mu_A(x_i) - \mu_B(x_i)| + |V_A(x_i) - V_B(x_i)|}{|\mu_A(x_i) + \mu_B(x_i)| + |V_A(x_i) + V_B(x_i)|}\\ &CA_{IFS}(A, B)\ -\ represent\ Canberra\ Intuitionistic\ Fuzzy\ distance\ measure\\ &S_{new2} = e^{-CA_{IFS}(A,B)}\end{aligned} \tag{19}$$

3.5.3. 3.11.3 modified hamming intuitionistic fuzzy similarity measure based on exponential function

$$\begin{aligned} &H_{IFS}(A, B) = \frac{\sum_{i=1}^{n} |\mu_A(x_i) - \mu_B(x_i)| + |V_A(x_i) - V_B(x_i)|}{2}\\ &S_{new3} = e^{-H_{IFS}(A,B)}\\ &H_{IFS}(A, B) - Hamming\ intuitionistic\ fuzzy\ similarity\ measure\end{aligned} \tag{20}$$

4. Result

Previous researches explored the use of anagram detection techniques like brute force, sorting, counting and histogram with

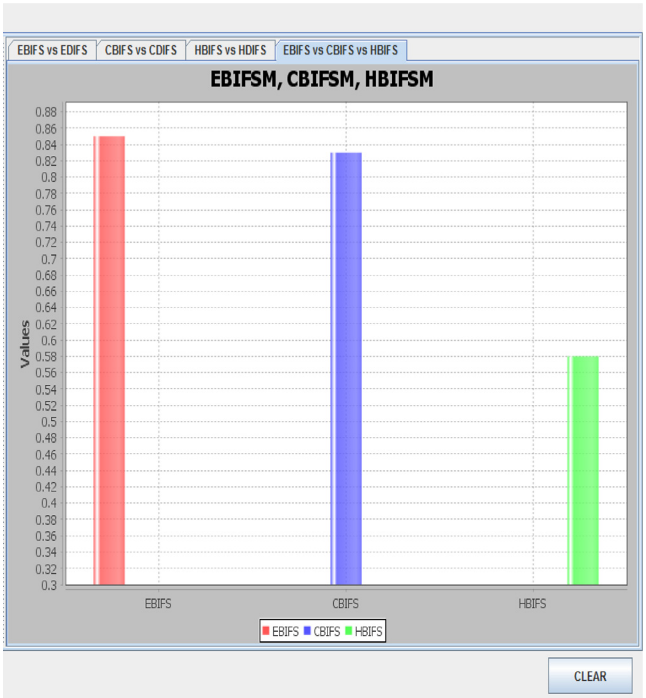

Fig. 2. EBIFSM, CBIFSM, HBIFSM.

complexities$O(n!)$,$O(n^2)$,$O(n)$, $O(n)$respectively. They all returns crisp values i.e. gives information on the pattern and text been anagram or not anagram. The only difference is their processing time. Old methods compares pattern and text, to return crisp value i.e. 0 or 1, it returns true or false without giving any idea about the level of membership/ non-membership. The existing algorithms for anagram detection method such as sorting, counting, neighbourhood frequency considers character length and character entailment. These characteristics cannot reveal the degree of anagram membership i.e. strong/moderate/simple. The best existing anagram detection technique is counting, it gives the same crisp value like other techniques but runs at a faster processing time.

Similarity values for existing and proposed methods:

Experiment was performed using 250 words, some of these were represented on Tables 1 and 2. The IFV generated for character length, entailment and permutation of character using modified Canberra, Jaccard, Dice (old method for permutation of characters) and Modified bigram (modified dice proposed method for permutation of characters) as stated in algorithm 3.4 steps 1–3, Table 1 depicts generated IFV for some data set. IFVs were passed for classification to proposed IFSMs Exponential base Euclidean, Canberra and Hamming in steps 4–7, Table 2 depicts this. All these steps are depicted in Fig. 1. Similarity values of existing methods are lower than that of proposed methods, the same goes with the cost which is determined by similarity value with respect to processing time, Table 3 depicts processing time. The proposed method IFSMs Exponential base Euclidean with modified bigram gives the highest similarity value and cost, hence the most effective value, followed by Canberra and Hamming with modified bigram. Fig. 2 depicts these, Table 6 shows the processing time of the existing and proposed methods respectively .

$$cost = \frac{value}{time} \tag{21}$$

5. Conclusion

The measure of patient's word cognition is dependent on the text supplied by the patient. The character length, entailment and syllabic complexity relationship between the text/ pattern of patient/doctor's randomly generated word is measured by selected and modified similarity measures of the text. These measures gives the intuitionistic fuzzy value of text supplied by patient. The generated IFV is classified using type-1 intuitionistic fuzzy threshold by author in [8] This classifies into simple, moderate and hard.

The tool intuitionistic fuzzy similarity measures gives a better word cognition measure compared to existing crisp measure. This is to enhance classification to type-1 technique in contrast to Boolean method. Also the Boolean/ crisp method is restricted to character length and entailment in feature. Thus it is not easy to determine the relationship between pattern/ text.

Previous approaches to orthographic similarity of anagrams were based on Brute force, Sorting, Orthographic neighbourhood frequency. User defined vocabularies and orthographic parameters were used for orthographic verification. Experiment revealed that the measures has the capacity to test for orthographic similarity of anagram through character entailment verification only. The drawback thus, lies in lack of character position verification and syllabic relationship test which are very vital while testing user's working memory capacity i.e. the wellness of the state of mind. These draw backs can be adapted into an enhanced anagram/scrabble measure through intuitionistic fuzzy set similarity measures, existing and modified IFSM measures were tested with numerical examples. These shows that a more accurate detection and classification can be derived through IFSM of anagrams/scrabble words.

References

[1] Aahul B. Diwate, Satish J. Alaspurkar, Systemic review on pattern matching, in: Proceedings of the International Journal of Advanced Research in Computer Science and Software Engineering, 2013.
[2] J.W. Adams, M. Stone, R.D. Vincent, S.J. Muncer, "The role of syllables in anagram solution: a Rasch analysis, J. Gen. Psychol. 138 (2) (2011) 94–109.
[3] Adio Akinwale, Nieweiadomski Adam, Efficient similarity measure for text matching, J. Appl. Comput. Sci. 23 (1) (2015) 21.
[4] F.E. Boran, S. Genç, M. Kurt, D. Akay, A multi-criteria intuitionistic fuzzy group decision making for supplier selection with TOPSIS method, Expert Syst. Appl. 36 (8) (2009) 11363–11368.
[5] S. Dahal, Effect of different measures in result of cluster analysis, Aalto University School of Engineering, 2015.
[6] M. Dziedzic, S. Zadrożny, J. Kacprzyk, Towards bipolar linguistic summaries: a novel fuzzy bipolar querying based approach, in: Proceedings of the IEEE International Conference on Fuzzy Systems (FUZZ-IEEE), 2012.
[7] P.A. Ejagwa, A.J. Kubo, O.M. Joshua, Intuitionistic fuzzy set and it' s application in career determination via normalized euclidean distance method, Eur. Sci. J. 10 (15) (2014).
[8] J.D. Evan, Straight Forward Statistics For Behavioral Sciences, Brooks 1 Cole Publishing, Pacific Groove, CA, 1996.
[9] J. Henin, E. Accorsi, P. Cho, W. Tabor, Extraordinary natural ability: anagram solution as an extension of normal reading ability, in: Proceedings of the 31st Annual Meeting of the Cognitive Science Society, 2009.
[10] Wen-Liang Hung, Miin-Shen Yang, Similarity measures of intuitionistic fuzzy sets based on Hausdorff distance, Pattern Recognit. Lett. 25 (14) (2004) 1603–1611.
[11] W.L. Hung, M.S. Yang, On similarity measures between intuitionistic fuzzy sets, Int. J. Intell. Syst. 23 (3) (2008) 364–383.
[12] Chao-Ming Hwang, Miin-Shen Yang, Wen-Liang Hung, Ming-Gay Lee, A similarity measure of intuitionistic fuzzy sets based on the Sugeno integral with its application to pattern recognition, Inf. Sci. (Ny) 189 (2012) 93–109.
[13] D.K. Lakovidis, E. Papageorgiou, Intuitionistic fuzzy cognitive maps for medical decision making, IEEE Trans. Inf. Technol. Biomed. 15 (1) (2011) 100–107.
[14] Lequex, C.P.a. (2004). anagram effect in visual word recognition, https://archives-onverts.fr/hat0042984.
[15] Ktori Maria, J.B. Walter, Nicola Van Heuven, J. Ptchford, Greek Lex: a lexical database of modern greek, Behav. Res. Methods 40 (3) (2008) 773–783.
[16] A.F. Mary, J.F. Hugh, W. Alice, R. Leslie, Anagram solving: does effort have an effect, Memory Cognit. 17 (6) (1989) 755–758.
[17] E.S. Menelaos, T.P. Chris, Linguistic effect on anagram solution: the case of transparent language, World Class J. Educ. 3 (4) (2013) 41–51.
[18] Timothy R. Jordan, Axel Monteiro, Generating anagrams from multiple core strings employing user defined vocabularies and orthographic parameters, Behav. Res. Methods, Instrum. Comput. 35 (1) (2003) 129–135.
[19] A. Niewiadomski, J. Ochelska, P. Szczepaniak, "Interval-valued linguistic summaries of databases, Control Cybern 35 (2006) 415–443.
[20] Akinwale Adio, Niewiadomski Adam, Effective similarity measure in electronic testing at programming languages, J. Appl. Comput. Sci. (2012).
[21] Sidrov Grigori, Gelbukh Alexander, Gomez-Adorno Helena, Pinto David, Soft similarity and soft cosine measure: similarity of features in vector space model, Comput. Syst. 18 (3) (2014) 14.

[22] Laijun Luo, Haiping Ren, "A new similarity measure for intuitionistic fuzzy set and application in MADM problem, AMSE J. -Ser. Adv. A 59 (1) (2016) 20.

[23] Rajesh Joshi, Satish Kumar, Exponential Jensen intuitionistic fuzzy divergence measure with applications in medical investigation and pattern recognition, Soft Computing 23 (18) (2018) 8995–9008, doi:10.1007/s00500-018-3505-2.

[24] Rajesh Joshi, Satish Kumar, "Jensen-Tsalli's intuitionistic fuzzy divergence measure and its applications in medical analysis and pattern recognition, International J. Uncertaint. Fuzziness Knowl. Based Syst. 27 (1) (2019) 145–169, doi:10.1142/S0218488519500077.

[25] Rajesh Joshi, Satish Kumar, Deepak Gupta, Hans Kaur, A Jensen-α-norm dissimilarity measure for intuitionistic fuzzy sets and its applications in multiple attribute decision making, Int. J. Fuzzy Syst. 20 (4) (2017) 1188–1202, doi:10.1007/s40815-017-0389-8.

[26] Rajesh Joshi, Satish Kumar, An exponential Jesen fuzzy divergence measure with applications in multiple attribute decision making, Hindawi, Math. Probl. Eng. (2018), doi:10.1155/2018/4342098.

[27] Rajesh Joshi, Satish Kumar, A dissimilarity jensen-shannon divergence measure for intuitionistic fuzzy sets, Int. J. Intell. Syst. 33 (11) (2018) 2216–2235, doi:10.1002/int.22026.

[28] Rajesh Joshi, Satish Kumar, A dissimilarity measure based on jensen-shannon divergence measure, Int. J. Gen. Syst. 48 (3) (2018) 280–301, doi:10.1080/03081079.2018.1552685.

[29] D.V. Robert, K.G. Yael, A.T. Debra, "Anagram software for cognitive research that enables specification of Pscholinguistic variables, Behav. Res. Methods, Instrum. Comput. (2006), doi:10.3758/BF0319558738(2).

[30] L.R. Norvick, S...J. Sharman, Type based bigram frequencies for five letter words, Behav. Res. Methods, Instrum. Comput. (2004), doi:10.3758/BF0319558736(3):397-401.

[31] W. Sandra, M. M.-Marse, W. Christina, R. Alfred, J.R. Emily, K.T. Cynthia, "The Northerwestern Test: measuring sentence production in primary progressive Aphasia, Am. J. Alzhheinder's Dis. Other Dementias (2009).

[32] P. Sergio, O. A., E.T. Juan, P. Pedro, Randomized Anagram revisited." Cosec Laboratory, Elsevier, 2014.

[33] Y. Song, X. Wang, L. Lei, A. Xue, A novel similarity measure on intuitionistic fuzzy sets with its applications, Appl. Intell. 42 (2) (2015) 252–261.

[34] C. Thirumalai, M. Senthilkumar, An assessment framework of intuitionistic fuzzy network for C2B decision making, in: Proceedings of the 4th International Conference on Electronics and Communication Systems (ICECS), 2017.

[35] A.P. Wibawa, A. Nafalski, A.E. Kadarisman, W.F. Mahmudy, Indonesian-to-Javanese machine translation, Int. J. Innov. Manag. Technol. 4 (4) (2013) 451.

[36] J. Ye, Cosine similarity measures for intuitionistic fuzzy sets and their applications, Math. Comput. Model. 53 (1) (2011) 91–97.

[37] J. Ye, Multicriteria group decision-making method using vector similarity measures for trapezoidal intuitionistic fuzzy numbers, Group Decis. Negotiat. (2012).

[38] S. Zadrożny, J. Kacprzyk, Z. Raś, Supporting consensus reaching processes under fuzzy preferences and a fuzzy majority via linguistic summaries and action rules, Consensual Processes 289-314 (2011).

[39] S. Zadrozny, J. Kacprzyk, G. Sobota, Avoiding duplicate records in a /database using a linguistic quantifier based aggregation-a practical approach. Fuzzy Systems, 2008, in: Proceedings of the IEEE International Conference on FUZZ-IEEE (IEEE World Congress on Computational Intelligence), 2008.

[40] S. Li, J. Wen, Application of pattern matching method for detecting faults in air handling unit system, Automation in Construction, Elsevier 43 (2014) 49–59.

[41] K.T. Atanassov, Intuitionistic fuzzy sets: theory and application, Springer (1999).

[42] D Chen, X Chang, Similarity measure and clustering of pattern, Pattern Recognition and String Matching (2002).

PLOTTING

Citicon Engineers has now come up with this new township to give ownership of the land to aspiring and potential buyers.However, most of the buyers are sceptical about the authenticity of land they purchase;

INDEPENDENT HOUSES

A way of living that is kinder to the planet. Citicon Engineers belief has inspire to create a lush,tropical villa community where nature and innovation walk hand in hand. Where the gift of solar energy...

APARTMENT

Citicon Engineers focuses on building aesthetically and structurally remarkable projects. A full service landholding development company that offers the best commercial properties and residential properties .